V.C. LAKHAN

(editor)

ADVANCES IN COASTAL MODELING

ADVANCES IN COASTAL MODELING

Elsevier Oceanography Series
Series Editor: David Halpern (1993-)

ADVANCES IN COASTAL MODELING

Editor
V.C. Lakhan
School of Physical Sciences,
Windsor, Canada

Preface

Overview of Advances in Coastal Modeling

It is now established that models are becoming indispensable not only for understanding and predicting the dynamics at work in the coastal system, but also for effective decision making and efficient solutions to complex problems in the coastal environment. Progressively more sophisticated models are now illuminating the complex dynamics operating in the large-scale coastal system and its interacting subsystems, thereby leading to major advances in our comprehension of the various coastal characteristics (for example, morphology, water quality, and ecology), and the governing physical processes such as waves, tides, currents, and sediment movement.

With the understanding that the proliferation of coastal models in the diverse literature increases the difficulty of obtaining from one source an integrated account of recent advances and present state-of-the-art knowledge in the various aspects of coastal modeling, it is becomes academically justified to unify and enhance the accessibility of contemporary coastal modeling research. This book, therefore, has the primary purpose of consolidating a comprehensive range of current coastal models and enlightening, timely review chapters to emphasize advances in significant areas of coastal modeling. The expected readership of senior students, academics, researchers, practicing professionals and all those interested in the modeling of coastal and oceanic processes and characteristics will obtain invaluable insights in scholarly research on coastal modeling.

To address the wide diversity of coastal models efforts have been made to present a book which is neither a narrowly specialized nor an all encompassing presentation on advances in coastal modeling. In choosing and organizing a representative selection of models from the broad spectrum of coastal models, critical decisions were required on what to include and what to exclude. Apart from considering the overall scope of the book, chapter selection was also aided by several criteria, including contents of an extensive coastal modeling database established in the late 1980's when I was first contracted to edit a book on coastal modeling, knowledge of articles for a forthcoming issue on coastal morphodynamic modeling which I am now editing, and an understanding of modeling skills required to encourage active participation in the coastal modeling process.

While the preferential selection of chapters provides a broad perspective on coastal modeling it should, nevertheless, be emphasized that the book is not intended to be an exhaustive account of advances in coastal modeling. The omission of certain topics does not imply that they are unimportant, but space limitations prevented including as many as are needed to do justice to the multifaceted aspects of coastal modeling. One of the unique strengths of the book is that the selected chapters bring together, from fourteen different countries, the special knowledge and expertise of coastal modelers who are with universities, the military, consulting and research institutions. The twenty-one chapters are representative of the scholarly advancement of contemporary research in coastal modeling. In addition to chapters modeling the dynamic natural processes of waves, currents, circulatory flows and sediment transport there are also chapters that focus on the modeling of beaches, shorelines, tidal basins, and shore platforms. The substantial scope of the book is further strengthened with chapters concentrating on the effects of coastal structures on nearshore flows, coastal water quality, coastal pollution, coastal ecological modeling, statistical data modeling, and coupling of coastal models with geographical information systems.

In editing each chapter, efforts have been made to maintain clarity and coherency, without sacrificing the personal writing styles of each of the contributors. Each chapter is self-contained and can be read on an individual basis, but greater insights of the coastal system can be obtained when the chapters are read in selected groupings. In the contextual framework of the book, the subject matter is organized according to broad thematic groupings or specific topic areas. As shown in the overview

presented below, there are chapters on waves and nearshore currents (**Chapters 1** to **4**), spectral and probabilistic modeling of waves (**Chapters 5** and **6**), effects of coastal structures on waves and nearshore flows (**Chapter 7**), sediment transport mechanics (**Chapters 8** to **10**), coastal morphological characteristics (**Chapters 11** to **14**), water circulation (**Chapter 15** and **16**), water quality and pollution of coastal waters (**Chapter 17** and **18**), coastal ecological modeling (**Chapter 19**), statistical modeling of beach and shoreline data (**Chapter 20**), and geographical information systems and coastal modeling (**Chapter 21**).

The first group of chapters includes state-of-the-art models on the dynamics of waves and nearshore current processes. Given the robust basis and widespread acceptance of the extended Boussinesq equations for computing surface wave motion in coastal areas, the book begins with a comprehensive discussion of Boussinesq models and applications to nearshore wave propagation, surf zone processes and wave-induced currents. **Chapter 1** reviews a number of recent developments, and then evaluates the strengths and limitations of the present state of the modeling technique. In a very informative presentation, the author makes it very clear that recent extensions to the theoretical and empirical basis for modeling systems based on these equations now cover wave propagation from deep to shallow water, and allow for the prediction of most surf zone phenomena, including wave breaking, longshore currents, and swash behavior. In a continuation of advanced research on wave modeling **Chapter 2** presents a state-of-the-art account of nonlinear frequency domain models for the nearshore and surf zones. The frequency domain transformations of extended Boussinesq models are detailed with special emphasis given to the models' linear properties (frequency, dispersion and shoaling). Nonlinear mild-slope equation models are outlined, and it is highlighted that frequency domain development is performed in the context of parabolic models. The author also elaborates on stochastic models based on the phase-resolving frequency domain models, and provides suggestions for future research. To further our understanding of coastal hydrodynamics **Chapter 3** presents advanced numerical techniques to solve the two-dimensional shallow water equations. These equations are solved numerically using a modern, conservative, high resolution, Godunov-type scheme on a Cartesian Cut Cell grid. The accurate and robust results from the numerical modeling provide the author with justification to emphasize that the state-of-the-art solver is capable of not only resolving complex flow phenomena such as bore waves and hydraulic jumps, but can also be utilized to investigate numerous practical problems in coastal engineering.

To overcome existing limitations in the modeling of nearshore currents **Chapter 4** describes an advanced numerical model of nearshore currents in a quasi three-dimensional field. The equations associated with the wave and current modules are solved with efficient numerical methods. After performing rigorous tests the author is able to demonstrate clearly that the model has immense practical applications because it can produce results which are in close agreement with measured data. Among the operational uses of the model are the prediction of cross-shore current velocities, the computation of longshore current velocity distributions, and the prediction of nearshore current velocities around coastal structures.

The next two chapters focus on the spectral and probabilistic modeling of waves and their attributes. **Chapter 5** emphasizes the development, utilization and application of spectral wave models for global and regional wave forecasts. The author presents an elaborate review of the present state-of-the-art in spectral wave modeling in coastal environments. Differences between the SWAN and the WAVEWATCH models are discussed, and the WAM-PRO model is highlighted. After presenting two examples demonstrating the use of a spectral wave model, the chapter concludes with a thorough analytical discussion on prospects for expected developments in spectral wave modeling. With the understanding that stochastic models provide a useful description of the spatial and temporal variabilities of wave fields in the ocean and coastal waters, **Chapter 6** focuses on advances in probabilistic models of waves in the coastal zone. The author selects and presents extensive state-of-the-art reviews on wave heights, wave periods, wave groups, time series models of sea states,

long-term models and joint long-term models. In a critical assessment the author emphasizes that the various models are used for either the analysis or the design and construction of coastal and offshore structures.

Apart from understanding the dynamics and characteristics of waves and currents, it is also vital to understand how waves and nearshore flows are affected by coastal structures. **Chapter 7**, therefore, elaborates on advanced research in modeling the effects of permeable and reflective structures on waves and nearshore flows. Recently developed models and their applications are reviewed, emphasizing the consequences of including the effects of porous flow in the general hydrodynamic model. Models based on Boussinesq-type equations and the Navier-Stokes equation are advanced. In an analytical conclusion the author discusses the state-of-the-art, and expected trends in the modeling of wave and porous structure interaction.

The waves and currents discussed in the preceding chapters have a strong influence on sediment movement so the next group of chapters (8, 9 and 10) is on sediment transport modeling. In **Chapter 8** the author communicates, in an informative, comprehensible style, his special knowledge on evolution in sediment modeling. Analytical perspectives are presented on advanced capabilities in numerical modeling of sediment dynamics, with emphasis placed on modeling of the boundary layer within millimeters of the sea bed. Various empirical case studies are used to discuss modeling strengths and weaknesses. The author concludes by providing meaningful potential solutions to sediment modeling problems in the coastal environment. The next chapter presents an innovative, advanced modeling technique for large-scale simulations of flow and sediment transport processes in coastal waters. In **Chapter 9** the author employs parallel computation techniques to increase the computational efficiency of a three-dimensional finite element sediment transport model. The parallelized model is run on a multiple instruction, multiple data Beowulf parallel computer system. The simulated model results show good correlation with field measurements, thereby allowing the authors to justify the computationally efficient model as being capable of simulating hydrodynamic and sediment transport patterns in coastal waters. **Chapter 10** emphasizes the importance of the material presented in Chapter 1 because it combines a wave model based on the higher-order Boussinesq-type equations with two sediment transport modules (based on a detailed and on an energetics approach) to investigate the process of sediment transport and morphological evolution in the nearshore zone. By incorporating in the model recent advances in wave and sediment dynamics the author executes the robust model to produce results in the cross-shore direction, indicating not only erosion and formation of a bar but also the recession of the shoreline. Moreover, the model results on longshore transport rates are in excellent agreement with established findings.

The models presented in Chapters 11, 12, 13 and 14 concentrate on characteristics of coastal morphology which, to a great extent, are influenced by the waves, currents, sediments and other processes discussed in the preceding chapters. In **Chapter 11** the author considers the dynamics of a coastal zone using analogy to a generalized dynamic system. By initializing an original coastal morphodynamic model with bathymetry, wave parameters, sediment characteristics, storm duration, and mean water level, and then linking several coastal process modules the author presents the modeling of short-term storm-induced deformations of nearshore morphology and long-term coastal evolution. Model applications in two and three spatial dimensions permit the prediction of beach profiles with time scales in the order of the duration of a storm event or an ensemble of storms and morphological evolution during longer periods of several years to decades. After reviewing numerical beach change modeling the authors of **Chapter 12** provide a robust, state-of-the-art numerical model to simulate the topographic evolution in the nearshore due to breaking waves and surf zone related processes. The model calculates waves, mean water elevation, longshore currents, and cross-shore, longshore, and swash zone sediment transport, and then computes beach changes from the sediment volume conservation equation. Testing of the model with data from field measurements demonstrates that it is computationally efficient, and very useful in engineering projects where time scales from individ-

ual storms to seasonal variations are to be considered. **Chapter 13** presents an advanced operational model for understanding the morphodynamics and complexities of tidal basins and coastal inlets, which on a world-wide basis, have immense social, economic and ecological importance. With the recognition that there is inadequate knowledge to predict the evolution of tidal basins and their interaction with the coast on time scales much longer than the process scale, the authors concentrate on expanding an aggregated-scale model. The significant findings from the operational model substantiate the process-aggregated approach, which allows for the hindcasting and possibly forecasting of the morphodynamic behavior of tidal basins to natural and anthropogenic impacts on engineering time scales. To improve on previous shore platform models concerned mainly with submarine erosion in tideless seas, the author of **Chapter 14** presents an advanced model to study the evolution of shore platforms and associated cliff recession on rocky coasts in wave dominated environments. The model considers such factors as the tidal expenditure of wave energy, deep water wave conditions, the rate of wave and surf attenuation in shallow water, offshore and submarine gradients, the height of the breakers, the width of the surf zone, and the minimum or threshold wave force capable of causing rock erosion. Extensive testing shows that the model can be used to simulate the erosion of rock coasts in the inter-tidal zone.

The next two chapters are necessary because modeling of water circulation is important for understanding the physical, chemical, and biological processes operating in the near and offshore coastal environment. **Chapter 15** focuses on the dynamics of large-scale water circulation around a complex bathymetry. The domain of the Great Barrier Reef is used to emphasize that a better understanding of large-scale water circulation can be obtained by merging models with different spatial scales. With the use of different two-dimensional and three-dimensional models the authors provide valuable insights on how processes operating at very different spatial and temporal scales interact. In an analytical discussion it is recognized that feedback exists between scales, thereby making it necessary to identify small-scale processes that are relevant at larger scales, and then parameterizing these processes in larger scale models. **Chapter 16** highlights the operational use of the Princeton Ocean Model (POM) to simulate not only water circulation, but also the thermohaline structure. With the POM, a time-dependent, primitive equation circulation model that includes a realistic bottom topography, the authors judiciously analyze from a series of numerical experiments the qualitative and quantitative effects of nonlinearity, wind forcing, and lateral boundary transport on the Japan/East Sea. The results on temperature, salinity and velocity fields are consistent with observational studies thereby demonstrating that the numerical simulation can provide considerable insights into the external factors affecting regional and coastal oceanography.

With the understanding that water quality and pollution of coastal waters and estuaries are issues of great public concern, it becomes vital to utilize models on coastal pollution and water quality. In **Chapter 17** two analytical models are described for estimating the concentration of a dissolved conservative constituent within a semi-enclosed tidal basin. Both models are based upon a "tidal prism" or "zero-dimensional" approach, and use an analytical method to predict the temporal variations in pollutant concentration. From the substantial modeling results the author is able to highlight the finding that the analytical approach offers a viable and computationally inexpensive alternative to conventional multi-dimensional pollutant transport simulations, and also increases our understanding of the flushing characteristics of tidal basins. In **Chapter 18** the author uses several case studies from the United States to accentuate advances made in the past twenty years in coastal water quality modeling. By deciding not to focus on the advances in the fundamental techniques of water quality modeling, the author places special emphasis on a detailed analysis of the progress in coastal water quality modeling from the aspects of computing power, linkages among models, model frameworks, and process descriptions. While significant advancements have been documented the author, nevertheless, suggests the need for several improvements including developing dynamic linkages from

coastal water quality models to various types of living resource models, such as bioenergetics and population models.

The tremendous ecological significance of the coastal zone necessitates discussing the advances in coastal ecological modeling. **Chapter 19** concentrates on neural network applications in coastal ecological modeling. Recognizing that neural network applications to ecological modeling are quite recent, the author introduces neural networks as computational tools, and then provides relevant information on their main features and technical particulars. Appropriate examples of neural network models applied to coastal ecosystems are provided and analyzed. The chapter concludes with an enlightening discussion of the state-of-the-art in neural network modeling, and provides perspectives on their future development.

The use of statistical models in beach and shoreline monitoring programs is emphasized in **Chapter 20**. The author demonstrates that insights on the long-term temporal and spatial dynamics of the nearshore system can be obtained by fitting statistical models to collected data. Box-Jenkins Transfer Function modeling procedures are utilized to identify models which best describe a time series (1978–2001) of beach and shoreline data. Modeling results highlight the influence of temporal stochastic processes on the long range behavior of beach and shoreline variations. In monitoring programs the transfer modeling approach is found to be useful to detect shifts in phase states of beaches and shorelines that occur through time and space.

It is now widely recognized that geographical information systems (GIS) bring an important new dimension to coastal modeling. **Chapter 21** explores some of the recent developments, progress made, and some of the problems encountered in integrating GIS with coastal models. While space limitations prevented the discussion of methodological developments in GIS the authors, nevertheless, elucidate that advances in computer hardware, software, display and visualization capabilities, and user interfaces are enabling more widespread use of coastal modeling tools, facilitating opportunities for collaborative distributed networking and integrated spatial decision support system tools to aid the coastal manager and practitioner in planning and decision making tasks. It is emphasized that developments are continuing, and success is being achieved in integrating GIS with coastal models.

<div align="right">

Dr. V. CHRIS LAKHAN
Professor, Earth Sciences
School of Physical Sciences
University of Windsor
November, 2002

</div>

This Page Intentionally Left Blank

Acknowledgments

List of Contributors

Robert W. Barber   Research Scientist
Centre for Microfluidics
Computational Engineering Group
CLRC Daresbury Laboratory, Daresbury
Warrington, Cheshire WA4 4AD, United Kingdom
E-mail: r.w.barber@dl.ac.uk

Kerry Black   Scientist/Research Consultant
ASR Limited
Marine and Freshwater Consultants
P.O. Box 13048
Hamilton, New Zealand
E-mail: kblack@asrltd.co.nz

Richard Brinkman   Australian Institute of Marine Science, PMB No. 3
Townsville MC, Queensland 4810, Australia

Peter C. Chu   Professor and Head
Naval Ocean Analysis and Prediction Laboratory
Department of Oceanography
Naval Postgraduate School
Monterey, CA 93943, USA
E-mail: pcchu@nps.navy.mil

Eric Deleersnijder   Institut d'Astronomie et de Geophysique G. Lemaitre
Universite Catholique de Louvain
2 Chemin du Cyclotron
B-1348 Louvain-La-Neuve, Belgium

Mark S. Dortch   Chief
Water Quality and Contaminant Modeling Branch
US Army Engineer Research and Development Center
Waterways Experiment Station, 3909 Halls Ferry Road
Vicksburg, MS 39180-6199, USA
E-mail: dortchm@wes.army.mil

Chenwu Fan   Department of Oceanography
Naval Postgraduate School
Monterey, CA 93943, USA

David R. Green   Professor
Centre for Marine and Coastal Zone Management
Centre for Remote Sensing & Mapping Science
Department of Geography & Environment
University of Aberdeen, Elphinstone Road
AB24 3UF, Aberdeen, Scotland, United Kingdom
E-mail: d.r.green@abdn.ac.uk

Carlos Guedes Soares Professor
 Unit of Marine Technology and Engineering
 Technical University of Lisbon
 Instituto Superior Técnico
 Av. Rovisco Pais
 1049-001 Lisboa, Portugal
 E-mail: guedess@mar.ist.utl.pt

Hans Hanson Professor
 Department of Water Resources Engineering
 Lund University
 Box 118
 S-221 00 Lund, Sweden

Yu-Wu Jiang Department of Civil & Structural Engineering
 The Hong Kong Polytechnic University
 Hung Hom, Kowloon, Hong Kong

James M. Kaihatu Senior Scientist
 Ocean Dynamics and Prediction Branch
 Oceanography Division (Code 7322)
 Naval Research Laboratory
 Stennis Space Center, MS 39529-5004, USA
 E-mail: kaihatu@nrlssc.navy.mil

Theophanis V. Karambas Professor
 Department of Civil Engineering
 Technological Education Institute of Serres
 Terma Magnesias, 621 24 Serres
 Greece
 E-mail: karambas@civil.auth.gr

Chang S. Kim Korea Ocean R&D Institute
 Ansan 425–170, South Korea

Stephen D. King Department of Geography and Environment
 University of Aberdeen
 AB24 3UF Aberdeen, Scotland, United Kingdom

James T. Kirby Professor
 Center for Applied Coastal Research
 University of Delaware
 Newark, DE 19716, USA
 E-mail: kirby@udel.edu

Nicholas C. Kraus Research Physical Scientist
 Coastal and Hydraulics Laboratory
 U.S. Army Engineer Research and Development Center
 3909 Halls Ferry Road
 Vicksburg, MS 39180–6199, USA

Magnus Larson Professor
 Department of Water Resources Engineering
 Lund University
 Box 118
 S-221 00 Lund, Sweden
 E-mail: magnus.larson@tvrl.lth.se

Placido D. LaValle   Professor
Department of Earth Sciences
University of Windsor
Windsor, Ontario, Canada N9B 3P4
E-mail: plavall@uwindsor.ca

Igor O. Leont'yev   Principal Researcher
Russian Academy of Sciences
P.P. Shirshov Institute of Oceanology
Nakhimov Prospect, 36
Moscow 117851, Russian Federation
E-mail: leontev@geo.sio.rssi.ru

Inigo J. Losada   Professor
Ocean & Coastal Research Group
University de Cantabria
E.T.S.I. de Caminos, Canales y Puertos
Avda. de los Castros s/n
39005 Santander, Spain
E-mail: losadai@unican.es

Qi-Miao Lu   Baird and Associates
627 Lyons Lane, Suite 200
Oakville, Ontario, Canada L6J 5Z7

Shihua Lu   Department of Oceanography
Naval Postgraduate School
Monterey, CA 93943, USA

Felicity McAllister   Australian Institute of Marine Science, PMB No. 3
Townsville MC, Queensland 4810, Australia

Clive G. Mingham   Professor
Department of Computing and Mathematics
Centre for Mathematical Modelling and Flow Analysis
Manchester Metropolitan University, Chester Street
Manchester M1 5GD, United Kingdom
E:mail: c.mingham@mmu.ac.uk

Jaak Monbaliu   Professor
Hydraulics Laboratory
Katholieke Universiteit Leuven
Kasteelpark Arenberg 40
B-3001 Heverlee, Belgium
E-mail: jaak.monbaliu@bwk.kuleuven.ac.be

Hideaki Noda   Professor and Vice-President
Department of Environmental Design
Tottori University of Environmental Studies
1-1-1 Wakabadai-Kita, Tottori City
Tottori Prefecture, 689-1111 Japan
E-mail: noda <hidenoda@kankyo-u.ac.jp>

Michele Scardi   Professor
                          Department of Biology
                          University of Roma "Tor Vergata"
                          Via della Ricerca Scientifica
                          00133 Roma, Italy
                          E-mail: mscardi@mclink.it

William Skirving   Australian Institute of Marine Science, PMB No. 3
                          Townsville MC, Queensland 4810, Australia

Simon Spagnol   Australian Institute of Marine Science, PMB No. 3
                          Townsville MC, Queensland 4810, Australia

Craig Steinberg   Australian Institute of Marine Science, PMB No. 3
                          Townsville MC, Queensland 4810, Australia

Marcel J.F. Stive   Professor of Coastal Engineering
                          Delft University of Technology
                          Faculty of Civil Engineering and Geosciences
                          Stevinweg 1, PO Box 5048
                          2600 GA Delft, The Netherlands
                          E-mail: m.j.f.stive@ct.tudelft.nl

Alan S. Trenhaile   Professor
                          Department of Earth Sciences
                          University of Windsor
                          Windsor, Ontario, Canada N9B 3P4
                          E-mail: tren@uwindsor.ca

Onyx Wing-Hong Wai   Professor
                          Department of Civil & Structural Engineering
                          The Hong Kong Polytechnic University
                          Hung Hom, Kowloon, Hong Kong
                          E-mail: ceonyx@polyu.edu.hk

Z.B. Wang   Professor
                          Delft Hydraulics
                          Delft, The Netherlands

Eric Wolanski   Leading Chief Scientist
                          Australian Institute of Marine Science, PMB No. 3
                          Townsville MC, Queensland 4810, Australia
                          E-mail: e.wolanski@aims.gov.au

Contents

Chapter 1

Boussinesq Models and Applications to Nearshore Wave Propagation, Surf Zone Processes and Wave-Induced Currents

James T. Kirby

Center for Applied Coastal Research, University of Delaware, Newark, DE 19716, USA

1. INTRODUCTION

Classical Boussinesq theory provides a set of evolution equations for surface water waves in the combined limit of weak nonlinearity (characterized by $\delta \ll 1$) and weak dispersion ($\mu \ll 1$) with the ratio $\delta/\mu^2 = O(1)$. The parameters represent a wave height to water depth ratio, and a water depth to wavelength ratio, respectively. In an early review of the state of modeling efforts directed at predicting wave-induced nearshore circulation, Basco (1983, p. 352–353) concluded that

> "The Boussinesq theory offers the possibility to eventually raise the fundamental knowledge of coastal hydrodynamics to a higher level. No time-averaging is involved. Nonlinear wave propagation and resulting wave height variations are automatically produced as part of the calculation procedure. The unsteady asymmetrical currents and instantaneous water surface variations as solutions to the governing equations are only obtainable with the aid of large, high-speed computers. Solution techniques and applications are in their infancy. Wave breaking and surf zone simulations have yet to be implemented."

At the time of this prediction, Boussinesq models were scarce, difficult and time consuming to run, and relatively undeveloped for practical physical applications. Very few explicit calculations of coastal wave propagation, and none of surf zone processes, had been made using models based on the Boussinesq theory, and the long-term averaging of model results needed to obtain predictions of mean currents had not been performed. The conclusion that the Boussinesq model approach could provide an advantage over the more well-established procedure of using a radiation stress field to drive a slowly varying mean current field (for a recent example see Özkan-Haller and Kirby, 1999) was met by occasional skepticism, as evidenced for example by the discussion of Basco's paper by Kirby and Dalrymple (1984).

In the years from 1983 to the present, events have firmly indicated that Basco was correct in his original assessment. Modeling schemes based on Boussinesq equations coupled with innovative extensions to the theoretical framework have been shown to be accurate and revealing predictors of a wide range of nearshore hydrodynamic behavior, including wave propagation and shoaling, wave current interaction, wave breaking and the generation of nearshore circulation, wave-structure interaction and a range of additional topics. The availability of faster computers is bringing the modeling technique into the realm of practical calculations, and model codes have been documented and are, in some cases (for example, Kirby et al., 1998) freely available to the public.

This chapter provides an overview of several aspects of the recent development of the Boussinesq modeling technique, aimed especially at providing a description or predictive capability in the nearshore ocean. The review highlights the work of this author and collaborating colleagues at the University of Delaware over the past decade, and is thus in some sense somewhat narrow in its orientation. Attempts have been made to provide balanced indications of the work of other groups in the field, but for omissions apologies are offered.

The chapter proceeds by providing an overview of the development of modern fully nonlinear Boussinesq theory in Section 2, and provides several examples illustrating wave shoaling and propagation properties as well as a test of the generation and advection of a vertical-core vortex structure. Section 3 turns to practical extensions to the $O(\mu^2)$ theory, which provides the foundation of most operational Boussinesq models at this time. Extensions to curvilinear coordinates and the inclusion of wave breaking, bottom friction and subgrid-scale mixing are described and illustrated. Section 4 discusses the problem of nearshore circulation, and describes example calculations addressing the generation of longshore currents, longshore current instability and formation of shear waves, and the generation and destabilization of rip currents. Section 5 discusses recent results including vertical shear effects (or the presence of horizontal vorticity). Miscellaneous topics are discussed in Section 6, including the use of Boussinesq models to assist in the depth inversion problem, and an application to tsunami propagation and inundation.

2. BOUSSINESQ EQUATIONS FOR WAVE PROPAGATION

The onset of recent developments in the field of Boussinesq models was triggered by two events. The first was the increasing availability of the computer resources needed to run the models. The second was the development of variants of the theory which could be optimized to obtain better dispersion properties at larger kh values, thus allowing the model to treat a larger range of water depths. Critical steps in this process were provided by Madsen et al. (1991), who established a procedure for optimizing model performance through rearrangement of dispersive terms, and Nwogu (1993), who demonstrated the flexibility obtained by using the horizontal velocity at a given elevation in the water column as a dependent variable. Both procedures have been extensively utilized in the development of subsequent theory. The review articles of Kirby (1997) and Madsen and Schäffer (1999) and the book by Dingemans (1997) provide extensive reviews of these developments up to 1999, and therefore the material here is concentrated on more recent developments. In addition, the subjects of wave interaction with permeable structures, surf and swash zone sediment transport, and frequency domain modeling are covered elsewhere in this book and are thus largely neglected here.

2.1. Hydrodynamic Fundamentals

Almost all Boussinesq-type models are derived from the framework of incompressible, inviscid flow. (The exception will be the case of waves with horizontal vorticity or vertical shear, considered in Section 5) To proceed, a scaling which is appropriate to the regime where wavelength exceeds water depth is chosen.

$$(x, y) = (k_0 x', k_0 y'); \ z = z'/h_0; \ t = \sqrt{gh_0 k_0^2} \, t'; \ \eta = \eta'/a_0; \ \phi = \left(\frac{a_0 \sqrt{gh_0}}{k_0 h_0} \right)^{-1} \phi' \tag{1}$$

where primes denote dimensional variables, and where h_0 is a depth scale, a_0 is a wave amplitude scale, and k_0 is an inverse horizontal length scale. The dependent variables are surface displacement η and velocity potential ϕ. Velocity components are then given by

$$\mathbf{u} = (u, v) = \nabla \phi \tag{2}$$

for horizontal velocities, where $\nabla = (\partial/\partial x, \partial/\partial y)$, and

$$w = \phi_z \tag{3}$$

for vertical velocity, where subscripts x, y, z or t will denote partial derivatives. The resulting scaled problem is characterized by the dimensionless ratios

$$\mu = k_0 h_0; \qquad \delta = a_0 / h_0 \tag{4}$$

The parameter μ characterizes frequency dispersion, and the limit $\mu \to 0$ represents the non-dispersive limit. The designation *weakly dispersive* refers to the regime $\mu \ll 1$. The parameter δ characterizes nonlinearity, and the limit $\delta \to 0$ represents the linear limit. The designation *weakly nonlinear* refers to the regime $\delta \ll 1$. In the present context, we will use the terminology *fully nonlinear* to indicate that no truncation based on powers of δ is employed in obtaining the corresponding model equations. The resulting set of scaled equations is given by

$$\nabla^2 \phi + \frac{1}{\mu^2} \phi_{zz} = 0, \qquad -h \leqslant z \leqslant \delta\eta \tag{5}$$

$$\nabla h \cdot \nabla \phi + \frac{1}{\mu^2} \phi_z = 0, \qquad z = -h \tag{6}$$

$$\eta + \phi_t + \frac{\delta}{2} \left(|\nabla\phi|^2 + \frac{1}{\mu^2}(\phi_z)^2 \right) = 0, \qquad z = \delta\eta \tag{7}$$

$$\eta_t + \delta\nabla\eta \cdot \nabla\phi - \frac{1}{\mu^2}\phi_z = 0, \qquad z = \delta\eta \tag{8}$$

Equation (8) is often replaced by a depth-integrated form of equation (5) which uses equations (6) and (8) to resolve boundary terms, giving

$$\eta_t + \nabla \cdot \mathbf{M} = 0; \qquad \mathbf{M} = \int_{-h}^{\delta\eta} \nabla\phi \, dz \tag{9}$$

The central feature of Boussinesq wave theories is that the solution to equations (5)–(6) is usually given as a power series in z, after which the surface boundary conditions are employed to obtain evolution equations. The choice of a reference elevation for the series expansion in z is initially fairly arbitrary. Following Madsen and Schäffer (1998), an expansion about the still water level of the form

$$\phi(x, y, z, t) = \sum_{n=0}^{\infty} z^n \phi^{(n)}(x, y, t) \tag{10}$$

gives, after substitution in equation (5),

$$\phi(x, y, z, t) = \sum_{n=0}^{\infty} (-1)^n \mu^{2n} \left(\frac{z^{2n}}{(2n)!} \nabla^{2n} \phi^{(0)} + \frac{z^{2n+1}}{(2n+1)!} \nabla^{2n} \phi^{(1)} \right) \tag{11}$$

where $\phi^{(0)}$ and $\phi^{(1)}$ represent ϕ and ϕ_z evaluated at $z = 0$ and are unknown prior to applying boundary conditions. Agnon et al. (1999) demonstrate that equation (11) recovers the full linear solution for a slowly varying plane wave over a mild bottom slope.

The standard procedure for developing Boussinesq models follows from using the bottom boundary condition (equation (6)) to eliminate the $\phi^{(1)}$ unknown in favor of $\phi^{(0)}$ (or a suitably defined replacement), after which the development proceeds using a truncated expansion for ϕ. We concentrate on this procedure below. More recently, Agnon et al. (1999) and Madsen et al. (2003) have pursued a path where the identity of horizontal and vertical velocities is maintained through much

of the derivation, adding a dependent variable but increasing flexibility in optimizing results. This procedure will be discussed in Section 2.4.

2.2. The Weakly Dispersive Problem

The full linear problem taken from equations (5)–(8) describes propagating water waves with a dispersion relation given by

$$\omega^2 = gk \tanh kh \tag{12}$$

or, equivalently,

$$c^2 = gh \frac{\tanh kh}{kh} \tag{13}$$

where ω denotes angular frequency, k denotes magnitude of a wave number vector $\mathbf{k}$, and c denotes phase speed for a monochromatic wave component. In the limit $\mu \ll 1$, the ratio in equation (13) should approach 1, and hence $c^2 \sim gh$. The resulting waves are nearly non-dispersive, with a leading order correction of the form

$$c^2 = gh(1 + O(kh)^2) \tag{14}$$

Obviously, an approximation of this form can impose severe restrictions when the problem of propagating water waves in a general domain with a range of water depths is considered. In modern terms, the principal goal of most derivations of Boussinesq models is to obtain an approximation to the ratio in equation (13) which is fairly robust over a range of values of kh; i.e., extending outside of the limit $\mu \to 0$.

Following Nwogu (1993), we define a reference elevation z_α located within the water column, and re-express the series expansion for ϕ in terms of the value at z_α. Using the bottom boundary condition (equation (6)) and truncating the resulting series after $O(\mu^2)$ gives

$$\phi(x, y, z, t) = \phi_\alpha(x, y, t) + \mu^2(z_\alpha - z)\nabla \cdot (h\nabla\phi_\alpha) - \frac{1}{2}\mu^2(z_\alpha^2 - z^2)\nabla^2\phi_\alpha + O(\mu^4) \tag{15}$$

Substituting equation (15) in linearized versions of equations (7) and (9) (with $\delta = 0$) and using $\phi_\alpha \sim \exp i(kx - \omega t)$ gives the dispersion relation

$$\omega^2 = gk^2 h \frac{1 - (\alpha + 1/3)(kh)^2}{1 - \alpha(kh)^2} \tag{16}$$

where

$$\alpha = \frac{1}{2}\left(\frac{z_\alpha}{h}\right)^2 + \frac{z_\alpha}{h} \tag{17}$$

The choice of α fixes the resulting dispersion relation and the corresponding value of z_α. $\alpha = -1/3$ reproduces the classical Boussinesq theory based on depth-averaged velocity, while the choice $\alpha = -2/5$ reproduces the (2, 2) Padé approximant to equation (13). Nwogu further adjusted the second result by choosing α to minimize a measure of phase speed error over a range of kh values, and obtained $\alpha = -0.39$. A comparison of the true linear dispersion relation (equation (13)) and the approximate form (equation (16)) is shown in Fig. 1, and shows that reasonably accurate dispersion can be obtained for a range of μ values up to about 3. The next order of approximation is discussed in Section 2.4.
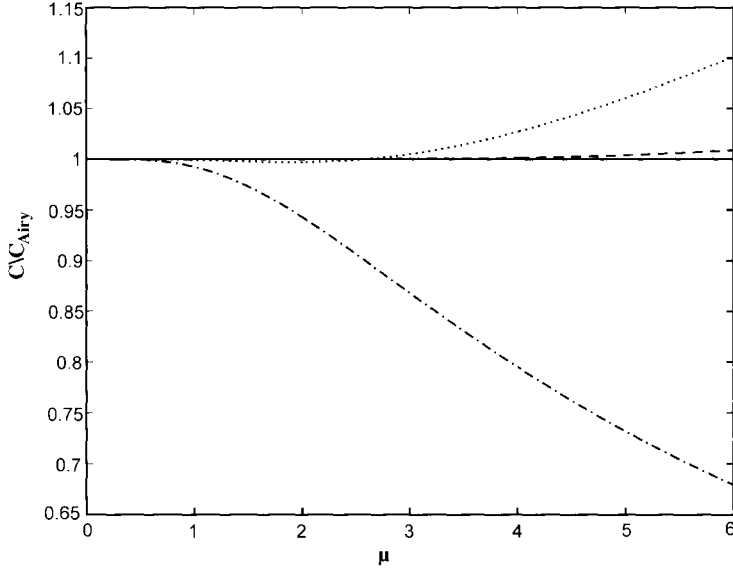
Figure 1. Ratio of model linear phase speed c to exact linear phase speed c_{Airy} given by equation (13). Standard Boussinesq dispersion with $\alpha = -1/3$ in equation (16) (dash-dot); optimized $O(\mu^2)$ dispersion based on the (2,2) Padé approximant with minimization of phase speed errors to obtain $\alpha = -0.39$ in (16), following Nwogu (1993) (dotted); $O(\mu^4)$ dispersion based on (4,4) Padé approximant in (31) (dash). (From Gobbi et al., 2000).

2.3. Weak vs. Full Nonlinearity in the $O(\mu^2)$ Boussinesq Formulation

Subsequent to the initial work on improved linear dispersion, the next topic to receive attention was the problem of relaxing the restriction of weak nonlinearity in the problem formulation. The need for this extension is clear when one realizes that the wave height to water depth ratio essentially is of $O(1)$ in the surf zone and just seaward of it. The most obvious line of approach staying within the Boussinesq type of formulation is to drop the notion of pursuing an expansion in powers of δ, and instead use the weakly dispersive expression for ϕ or horizontal velocity **u** in the form of a power series in μ^2 to evaluate the complete surface boundary condition. We will subsequently refer to models resulting from this procedure as *fully nonlinear models*, in the sense that all of the available information on velocities is used to evaluate the full boundary conditions. Numerous early examples of this approach appear in the literature and have been reviewed by Dingemans (1997), Kirby (1997) and Madsen and Schäffer (1999). We restrict our attention here to two examples; those of Wei et al. (1995) and Liu (1994). Following the procedure of Nwogu (1993), each study derived a set of model equations for potential flow written initially in terms of ϕ_α and η given by the volume conservation equation (9) and the Bernoulli equation (7). Using expression (15) in equations (9) and (7) gives

$$
\mathbf{M} = H\left[\nabla\phi_\alpha + \mu^2 \left\{ \nabla\left[z_\alpha \nabla \cdot (h\nabla\phi_\alpha) + \frac{z_\alpha^2}{2}\nabla^2\phi_\alpha \right] \right.\right.
$$
$$
\left.\left. + \frac{(h - \delta\eta)}{2}\nabla(\nabla \cdot (h\nabla\phi_\alpha)) - \frac{(h^2 - h\delta\eta + (\delta\eta)^2)}{6}\nabla^2\nabla\phi_\alpha \right\} \right] \tag{18}
$$

for volume flux (where $H = h + \delta\eta$ is the total water depth), and

$$\eta + \phi_{\alpha t} + \frac{\delta}{2}\nabla\phi_\alpha \cdot \nabla\phi_\alpha + \mu^2\left[(z_\alpha - \delta\eta)\nabla\cdot(h\nabla\phi_{\alpha t}) + \frac{1}{2}(z_\alpha^2 - (\delta\eta)^2)\nabla^2\phi_{\alpha t}\right]$$

$$+ \delta\mu^2\left\{\nabla\phi_\alpha \cdot \left[\nabla z_\alpha \nabla\cdot(h\nabla\phi_\alpha) + (z_\alpha - \delta\eta)\nabla(\nabla\cdot(h\nabla\phi_\alpha))\right]\right\}$$

$$+ \delta\mu^2\left\{\nabla\phi_\alpha \cdot \left[z_\alpha\nabla z_\alpha \nabla^2\phi_\alpha + \frac{1}{2}(z_\alpha^2 - (\delta\eta)^2)\nabla(\nabla^2\phi_\alpha)\right]\right\}$$

$$+ \delta\mu^2\left\{\frac{1}{2}[\nabla\cdot(h\nabla\phi_\alpha)]^2 + \delta\eta\nabla\cdot(h\nabla\phi_\alpha)\nabla^2\phi_\alpha + \frac{1}{2}(\delta\eta)^2(\nabla^2\phi_\alpha)^2\right\} = 0 \tag{19}$$

for the Bernoulli equation. These results were found independently by Liu (1994) and Wei et al. (1995).

An alternate model in terms of η and horizontal velocity $\mathbf{u}_\alpha$ at the reference level z_α is preferred for practical use, as it is extendable to include breaking, frictional and mixing effects. Substituting for $\nabla\phi_\alpha$ in equation (18) using

$$\nabla\phi_\alpha = \mathbf{u}_\alpha - \mu^2[\nabla z_\alpha \nabla\cdot(h\mathbf{u}_\alpha) + z_\alpha\nabla z_\alpha\nabla\cdot\mathbf{u}_\alpha] + O(\mu^4) \tag{20}$$

gives

$$\mathbf{M} = H\left[\mathbf{u}_\alpha + \mu^2\left\{\left[\frac{1}{2}z_\alpha^2 - \frac{1}{6}(h^2 - h\delta\eta + (\delta\eta)^2)\right]\nabla(\nabla\cdot\mathbf{u}_\alpha)\right.\right.$$

$$\left.\left. + \left[z_\alpha + \frac{1}{2}(h - \delta\eta)\right]\nabla(\nabla\cdot(h\mathbf{u}_\alpha))\right\}\right] + O(\mu^4) \tag{21}$$

for volume flux. Taking the horizontal gradient of equation (19) leads to a horizontal momentum equation which may be written schematically in the form

$$\mathbf{u}_{\alpha t} + \delta(\mathbf{u}_\alpha \cdot \nabla)\mathbf{u}_\alpha + \nabla\eta + \mu^2\mathbf{V_1} + \delta\mu^2\mathbf{V_2} = O(\mu^4) \tag{22}$$

In deriving their version of the model equation, Wei et al. (1995) erroneously made the substitution

$$\frac{\delta}{2}\nabla(\mathbf{u}_\alpha \cdot \mathbf{u}_\alpha) \rightarrow \delta(\mathbf{u}_\alpha \cdot \nabla)\mathbf{u}_\alpha \tag{23}$$

after using equation (20) in the Bernoulli equation. The substitution (equation (23)) implies the incorporation of a vorticity term $\omega \times \mathbf{u}_\alpha$, but, as will be shown below, the $O(\mu^2)$ contribution to ω is missed in this substitution, as pointed out by Chen et al. (2000b) and Hsaio et al. (2002). Wei et al. (1995) obtained the dispersive terms

$$\mathbf{V_1} = \frac{1}{2}z_\alpha^2\nabla(\nabla\cdot\mathbf{u}_{\alpha t}) + z_\alpha\nabla(\nabla\cdot(h\mathbf{u}_{\alpha t})) - \nabla\left[\frac{1}{2}(\delta\eta)^2\nabla\cdot\mathbf{u}_{\alpha t} + \delta\eta\nabla\cdot(h\mathbf{u}_{\alpha t})\right] \tag{24}$$

$$\mathbf{V_2} = \mathbf{V_{2W}} = \nabla\left[(z_\alpha - \delta\eta)(\mathbf{u}_\alpha \cdot \nabla)(\nabla\cdot(h\mathbf{u}_\alpha)) + \frac{1}{2}(z_\alpha^2 - (\delta\eta)^2)(\mathbf{u}_\alpha \cdot \nabla)(\nabla\cdot\mathbf{u}_\alpha)\right]$$

$$+ \frac{1}{2}\nabla\left[(\nabla\cdot(h\mathbf{u}_\alpha) + \delta\eta\nabla\cdot\mathbf{u}_\alpha)^2\right] \tag{25}$$

where the $\mathbf{W}$ subscript in $\mathbf{V_{2W}}$ denotes the Wei et al. version. In contrast, Liu (1994) (see corrected versions in Lynett et al., 2002) invoked the substitution

$$\frac{\delta}{2}\nabla(\nabla\phi_\alpha \cdot \nabla\phi_\alpha) = \delta(\nabla\phi_\alpha \cdot \nabla)\nabla\phi_\alpha \tag{26}$$

within the original gradient of the Bernoulli equation, and obtained the expression V_1 as in equation (24). After some rearrangement to get a form close to the Wei et al. form V_{2W}, which is a pure gradient, Liu's V_2 may be written as

$$V_{2L} = V_{2W} + V_{2r} \tag{27}$$

where

$$
\begin{aligned}
V_{2r} &= (\mathbf{u}_\alpha \cdot \nabla z_\alpha)\left[z_\alpha \nabla(\nabla \cdot \mathbf{u}_\alpha) + \nabla(\nabla \cdot (h\mathbf{u}_\alpha))\right] \\
&\quad - \nabla z_\alpha(\mathbf{u}_\alpha \cdot \nabla)(\nabla \cdot (h\mathbf{u}_\alpha)) - z_\alpha \nabla z_\alpha(\mathbf{u}_\alpha \cdot \nabla)(\nabla \cdot \mathbf{u}_\alpha)
\end{aligned}
\tag{28}
$$

The physical interpretation of this extra term was discovered by Chen et al. (2000b). After some manipulation, V_{2r} may be written in the compact form

$$V_{2r} = \omega_1 \times \mathbf{u}_\alpha \tag{29}$$

where ω_1 denotes the $O(\mu^2)$ contribution to vertical vorticity, given by

$$
\begin{aligned}
\omega_1 &= \mathbf{i}_z\left[z_{\alpha,x}\left[(\nabla \cdot (h\mathbf{u}_\alpha))_{,y} + z_\alpha(\nabla \cdot \mathbf{u}_\alpha)_{,y}\right] - z_{\alpha,y}\left[(\nabla \cdot (h\mathbf{u}_\alpha))_{,x} + z_\alpha(\nabla \cdot \mathbf{u}_\alpha)_{,x}\right]\right] \\
&= \nabla z_\alpha \times \nabla[\nabla \cdot (h\mathbf{u}_\alpha) + z_\alpha \nabla \cdot \mathbf{u}_\alpha]
\end{aligned}
\tag{30}
$$

Adding V_{2r} to equation (25) corrects the original model of Wei et al. (1995). We will refer to the combined set of terms simply as V_2 subsequently. Note that the correction term does not appear in weakly-nonlinear formulations, where terms of $O(\delta\mu^2)$, and hence all of V_2, are neglected. The term also vanishes in water of constant depth, where z_α is constant.

Wei and Kirby (1995) have described a numerical scheme for equations of this type which has come into fairly wide usage. Time stepping is treated using a fourth-order Adams-Bashforth-Moulton scheme, while spatial differencing is handled using a mixed-order scheme, employing fourth-order accurate centered differences for first derivatives and second-order accurate derivatives for third derivatives. The latter choice is made in order to move leading truncation errors to one order higher than the $O(\mu^2)$ dispersive terms, while maintaining the tridiagonal structure of spatial derivatives within time-derivative terms. Wei and Kirby (1995) used a non-staggered grid scheme with $\mathbf{u}_\alpha$ and η defined at the same locations. More recently, Shi et al. (2001a) have used a staggered grid approach which has less apparent sensitivity to treatment of boundary conditions. The staggered grid scheme has become our preferred approach. Methods for generating waves at internal sources have been described by Wei et al. (1999) and Chawla and Kirby (2000). Kirby et al. (1998) document a version of the non-staggered code, known as *FUNWAVE*, which is available at http://chinacat.coastal.udel.edu/~kirby/programs/funwave.

Properties of this model for wave propagation problems have been reviewed by Kirby (1997) and Madsen and Schäffer (1999). The ability of the model to provide an accurate representation of the evolution and transport of the vertical vorticity component was tested by Hommel et al. (2000), who compared model results to laboratory data for the case of a vertical vortex core shed during the passage of a solitary wave past a vertical plane wall blocking half the width of a wave flume. These tests were partially motivated by a previous study by Roddier and Ertekin (1999), who had considered the diffraction of a solitary wave at the tip of a breakwater using a potential flow model analogous to the Bernoulli equation formulation (equation (19)). Roddier and Ertekin indicated the formation of a deep depression at the breakwater tip, which they explained to be a "bathtub vortex". However, a consideration of their geometry shows that a vortex core could not be forming at a position attached to the tip of the wall, since the presence of the wall would interrupt the circulation of fluid around the
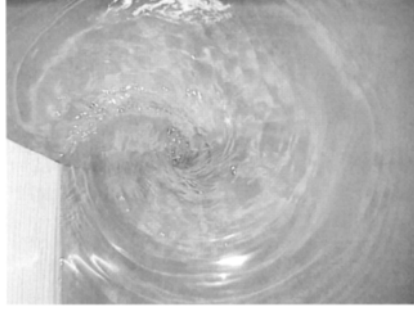
Figure 2. Shed vortex formed during passage of solitary wave past a vertical wall. (From Hommel et al., 2000. Reproduced with permission of ASCE).
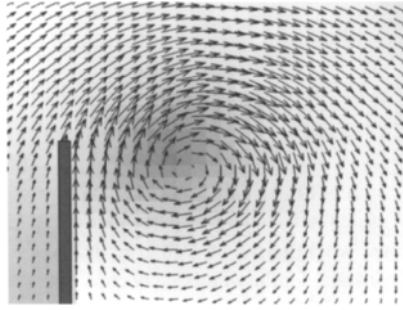
Figure 3. Calculated velocity field corresponding to vortex in Fig. 2. (From Hommel et al., 2000. Reproduced with permission of ASCE).

depression. The depression is simply the manifestation of a singularity in the solution at the break-water tip, caused by the approach to infinite acceleration as fluid turns the 180° corner. This result shows conclusively that the truly irrotational models in the form of a Bernoulli equation will not spontaneously generate a vortex due to flow separation or advect the vortex away from the generation region. Hommel et al. (2000) considered the somewhat different case of a breakwater oriented parallel to the crest of the approaching solitary wave. Fig. 2 shows a photograph of a vortex core shed during passage of a solitary wave from the left, with the core rotation in the clockwise direction. Fig. 3 shows the corresponding numerical result, with velocity vectors overlying a colormap of the vorticity field. In general, agreement between modeled and measured velocity time series were good for these cases. Results are omitted here, and the reader is referred to Hommel et al. (2000).

2.4. Extensions to Higher Order

The $O(\mu^2)$ model described above has provided a robust framework for predicting wave propagation in shallow to intermediate water depths, but still exhibits limitations in predicting water particle kinematics. In particular, predictions of wave-induced horizontal velocity near the sea bed breaks down for values of μ far smaller than implied by the limitations on model dispersion accuracy. For example, the horizontal velocity predicted by the model of Wei et al. (1995) falls to zero at $\mu = \sqrt{10}$ and becomes negative in sign (relative to the surface velocity) in deeper water, as illustrated in Fig. 4. This type of result renders the $O(\mu^2)$ models useless for prediction of near bed kinematics (as would
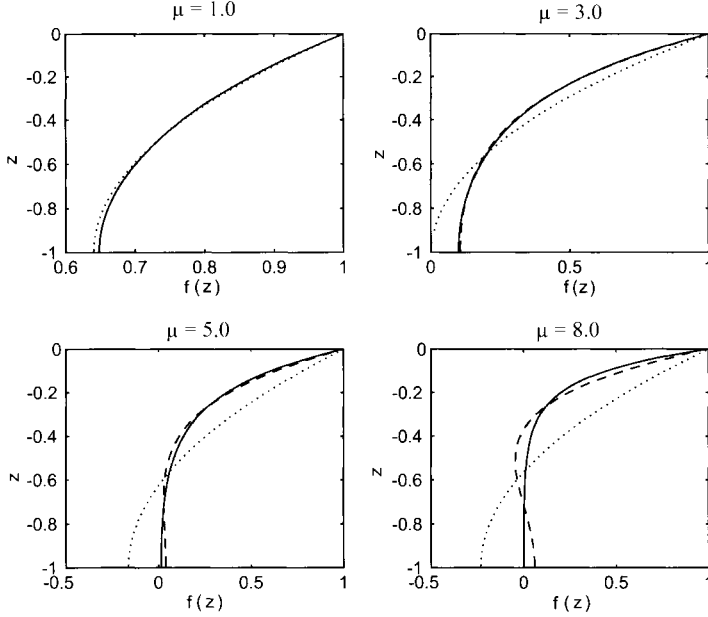
Figure 4. Normalized vertical profile of linear horizontal velocity at four values of μ. Exact linear solutions (solid), $O(\mu^2)$ approximate solution (dot), $O(\mu^4)$ approximate solution (dash) (From Gobbi et al., 2000).

be needed in sediment transport calculations) at water depths far smaller than implied by the accuracy of the dispersion relation, unless an artificial means is employed to estimate near bed velocities from surface values. As a result, the development of higher-order approximations in the Boussinesq model has proceeded with the intent both of increasing the range of allowed water depths and with improving the accuracy of kinematic predictions within the allowed range of depths. Two avenues of approach are reviewed here.

2.4.1. Model of Gobbi et al. (2000)

One avenue of approach is to retain higher-order terms in the expansion for ϕ, and then proceed in constructing either the two-equation model in η, ϕ^* or the three-equation model in $\eta, \mathbf{u}^*$, where superscript $*$ indicates a particular choice of reference level or combination of reference levels used to specify the value of the potential or horizontal velocity. This procedure poses difficulties right away, as the method proposed by Nwogu (1993) does not provide access to higher-order versions of the Padé form of the dispersion relation (Dingemans, 1997). For example, at $O(\mu^4)$ in the expansion for ϕ, the desired expansion of the usual dispersion relation is given by

$$\frac{\tanh\mu}{\mu} = \frac{1 + (1/9)\mu^2 + (1/945)\mu^4}{1 + (4/9)\mu^2 + (1/63)\mu^4} + O(\mu^{10}) \tag{31}$$

The resulting phase speed estimate is shown in Fig. 1. Gobbi et al. (2000) approached this problem by constructing a potential formulated as the weighted average of the potential at two Nwogu-type reference levels

$$\tilde{\phi} = \beta\phi_a + (1 - \beta)\phi_b \tag{32}$$

where ϕ_a and ϕ_b are defined as in the previous section and are evaluated at levels z_a and z_b. Relationships between these parameters giving the appropriate dispersion relationship are given by (Gobbi et al., 2000)

$$z_a = \left[\frac{1}{9} - \left\{ \frac{8\beta}{567(1-\beta)} \right\}^{1/2} + \left\{ \frac{8}{567\beta(1-\beta)} \right\}^{1/2} \right]^{1/2} - 1 \tag{33}$$

$$z_b = \left[\frac{1}{9} - \left\{ \frac{8\beta}{567(1-\beta)} \right\}^{1/2} \right]^{1/2} - 1 \tag{34}$$

Values $0.018 < \beta < 0.467$ give z_a and z_b levels lying within the water column and recover the form (equation (31)). The resulting truncated potential is given by

$$\phi = \tilde{\phi} + \mu^2 \left[(Ah - \zeta) F_1(\tilde{\phi}) + \left(Bh^2 - \zeta^2 \right) F_2(\tilde{\phi}) \right] + \mu^4 \left[(Ah - \zeta) F_3(\tilde{\phi}) \right.$$
$$\left. + \left(Bh^2 - \zeta^2 \right) F_4(\tilde{\phi}) + \left(Ch^3 - \zeta^3 \right) F_5(\tilde{\phi}) + \left(Dh^4 - \zeta^4 \right) F_6(\tilde{\phi}) \right] \tag{35}$$

where $\zeta = h + z$, and where

$$A \equiv \frac{1}{h} \left[\beta(h + z_a) + (1 - \beta)(h + z_b) \right] \tag{36}$$

$$B \equiv \frac{1}{h^2} \left[\beta(h + z_a)^2 + (1 - \beta)(h + z_b)^2 \right] \tag{37}$$

$$C \equiv \frac{1}{h^3} \left[\beta(h + z_a)^3 + (1 - \beta)(h + z_b)^3 \right] \tag{38}$$

$$D \equiv \frac{1}{h^4} \left[\beta(h + z_a)^4 + (1 - \beta)(h + z_b)^4 \right] \tag{39}$$

and

$$F_1(\tilde{\phi}) \equiv G\nabla h \cdot \nabla\tilde{\phi} \tag{40}$$

$$F_2(\tilde{\phi}) \equiv \frac{1}{2} G\nabla^2\tilde{\phi} \tag{41}$$

$$F_3(\tilde{\phi}) \equiv \nabla h \cdot \nabla \left(Ah\nabla h \cdot \nabla\tilde{\phi} \right) + \frac{1}{2}\nabla h \cdot \nabla \left(Bh^2\nabla^2\tilde{\phi} \right) \tag{42}$$

$$F_4(\tilde{\phi}) \equiv \frac{1}{2}\nabla^2 \left(Ah\nabla h \cdot \nabla\tilde{\phi} \right) + \frac{1}{4}\nabla^2 \left(Bh^2\nabla^2\tilde{\phi} \right)$$
$$- \frac{1}{2}\nabla^2 h\nabla h \cdot \nabla\tilde{\phi} - \nabla h \cdot \nabla \left(\nabla h \cdot \nabla\tilde{\phi} \right) \tag{43}$$

$$F_5(\tilde{\phi}) \equiv -\frac{1}{6}\nabla^2 h\nabla^2\tilde{\phi} - \frac{1}{3}\nabla h \cdot \nabla \left(\nabla^2\tilde{\phi} \right) - \frac{1}{6}\nabla^2 \left(\nabla h \cdot \nabla\tilde{\phi} \right) \tag{44}$$

$$F_6(\tilde{\phi}) \equiv -\frac{1}{24}\nabla^2 \left(\nabla^2\tilde{\phi} \right) \tag{45}$$

where $G = (1 + \mu^2|\nabla h|^2)^{-1}$. Seeking a model system in terms of a horizontal velocity, Gobbi and Kirby (1999) introduced the definition

$$\tilde{\mathbf{u}}(x, y, t) = \beta \left[\nabla\phi \right]_{z=z_a} + (1 - \beta) \left[\nabla\phi \right]_{z=z_b} \tag{46}$$

where the relationship between $\tilde{\mathbf{u}}$ and $\tilde{\phi}$ is given by

$$\nabla\tilde{\phi} = \tilde{\mathbf{u}} - \mu^2\nabla h\left[(A-1)F_{21} + 2(B-A)hF_{22}\right]$$
$$- \mu^4\nabla h\left[(A-1)(F_{41}+F_{43}) + 2(B-A)h(F_{42}+F_{44})\right.$$
$$\left. + 3(C-B)h^2F_{45} + 4(D-C)h^3F_{46}\right] \tag{47}$$

where

$$F_{21}(\tilde{\mathbf{u}}) \equiv G\nabla h \cdot \tilde{\mathbf{u}} \tag{48}$$

$$F_{22}(\tilde{\mathbf{u}}) \equiv \frac{1}{2}G\nabla \cdot \tilde{\mathbf{u}} \tag{49}$$

$$F_{41}(\tilde{\mathbf{u}}) \equiv -|\nabla h|^2\left[(A-1)\nabla h \cdot \tilde{\mathbf{u}} + (B-A)h\nabla \cdot \tilde{\mathbf{u}}\right] \tag{50}$$

$$F_{42}(\tilde{\mathbf{u}}) \equiv -\frac{1}{2}\nabla \cdot \left\{\nabla h\left[(A-1)\nabla h \cdot \tilde{\mathbf{u}} + (B-A)h\nabla \cdot \tilde{\mathbf{u}}\right]\right\} \tag{51}$$

$$F_{43}(\tilde{\mathbf{u}}) \equiv \nabla h \cdot \nabla\left(Ah\nabla h \cdot \tilde{\mathbf{u}}\right) + \frac{1}{2}\nabla h \cdot \nabla\left(Bh^2\nabla \cdot \tilde{\mathbf{u}}\right) \tag{52}$$

$$F_{44}(\tilde{\mathbf{u}}) \equiv \frac{1}{2}\nabla^2\left(Ah\nabla h \cdot \tilde{\mathbf{u}}\right) + \frac{1}{4}\nabla^2\left(Bh^2\nabla \cdot \tilde{\mathbf{u}}\right)$$
$$- \frac{1}{2}\nabla^2 h\nabla h \cdot \tilde{\mathbf{u}} - \nabla h \cdot \nabla\left(\nabla h \cdot \tilde{\mathbf{u}}\right) \tag{53}$$

$$F_{45}(\tilde{\mathbf{u}}) \equiv -\frac{1}{6}\nabla^2 h\nabla \cdot \tilde{\mathbf{u}} - \frac{1}{3}\nabla h \cdot \nabla\left(\nabla \cdot \tilde{\mathbf{u}}\right) - \frac{1}{6}\nabla^2\left(\nabla h \cdot \tilde{\mathbf{u}}\right) \tag{54}$$

$$F_{46}(\tilde{\mathbf{u}}) \equiv -\frac{1}{24}\nabla^2\left(\nabla \cdot \tilde{\mathbf{u}}\right) \tag{55}$$

The volume flux $\mathbf{M}$ in equation (9) is then given by

$$\mathbf{M} = H\left\{\tilde{\mathbf{u}} + \mu^2\left[\left(Ah - \frac{H}{2}\right)(2\nabla h F_{22} + \nabla F_{21}) + \left(Bh^2 - \frac{H^2}{3}\right)\nabla F_{22}\right]\right.$$
$$+ \mu^4\left[\left(Ah - \frac{H}{2}\right)(2\nabla h F_{42} + \nabla F_{41} + 2\nabla h F_{44} + \nabla F_{43})\right.$$
$$+ \left(Bh^2 - \frac{H^2}{3}\right)(\nabla F_{42} + 3\nabla h F_{45} + \nabla F_{44})$$
$$\left.\left.+ \left(Ch^3 - \frac{H^3}{4}\right)(4\nabla h F_{46} + \nabla F_{45}) + \left(Dh^4 - \frac{H^4}{5}\right)\nabla F_{46}\right]\right\} \tag{56}$$

where $H = h + \delta\eta$ denotes total water depth. The momentum equation may be written as

$$\mathbf{U}_t = -\nabla\eta - \frac{\delta}{2}\nabla\left(|\tilde{\mathbf{u}}|^2\right) + \Gamma_1\left(\eta, \tilde{\mathbf{u}}_t\right) + \Gamma_2\left(\eta, \tilde{\mathbf{u}}\right) \tag{57}$$

where

$$\mathbf{U} \equiv \tilde{\mathbf{u}} + \mu^2\left[(A-1)h\left(2\nabla h F_{22} + \nabla F_{21}\right) + (B-1)h^2\nabla F_{22}\right]$$

$$+ \mu^4 \left[(A-1)h \left(2\nabla h F_{42} + \nabla F_{41} + 2\nabla h F_{44} + \nabla F_{43} \right) \right.$$

$$+ (B-1)h^2 \left(\nabla F_{42} + 3\nabla h F_{45} + \nabla F_{44} \right)$$

$$+ \left. (C-1)h^3 \left(4\nabla h F_{46} + \nabla F_{45} \right) + (D-1)h^4 \nabla F_{46} \right] \tag{58}$$

$$\Gamma_1 \equiv \mu^2 \nabla \left[\delta\eta F_{21_t} + \left(2h\delta\eta + \delta^2\eta^2 \right) F_{22_t} \right]$$

$$+ \mu^4 \nabla \left[\delta\eta \left(F_{41_t} + F_{43_t} \right) + \left(2h\delta\eta + \delta^2\eta^2 \right) \left(F_{42_t} + F_{44_t} \right) \right.$$

$$+ \left(3h^2\delta\eta + 3h\delta^2\eta^2 + \delta^3\eta^3 \right) F_{45_t}$$

$$+ \left. \left(4h^3\delta\eta + 6h^2\delta^2\eta^2 + 4h\delta^3\eta^3 + \delta^4\eta^4 \right) F_{46_t} \right] \tag{59}$$

$$\Gamma_2 \equiv - \mu^2 \delta\nabla \left\{ \tilde{\mathbf{u}} \cdot \left[(Ah-H)(\nabla F_{21} + 2\nabla h F_{22}) + \left(Bh^2 - H^2 \right) \nabla F_{22} \right] \right.$$

$$+ \left. \frac{1}{2} (F_{21} + 2H F_{22})^2 \right\}$$

$$- \mu^4 \delta\nabla \left\{ \tilde{\mathbf{u}} \cdot \left[(Ah-H)(\nabla F_{41} + 2\nabla h F_{42} + \nabla F_{43} + 2\nabla h F_{44}) \right. \right.$$

$$+ \left(Bh^2 - H^2 \right) (\nabla F_{42} + \nabla F_{44} + 3\nabla h F_{45})$$

$$+ \left. \left(Ch^3 - H^3 \right) (\nabla F_{45} + 4\nabla h F_{46}) + \left(Dh^4 - H^4 \right) \nabla F_{46} \right]$$

$$+ \frac{1}{2} \left| (Ah-H))(\nabla F_{21} + 2\nabla h F_{22}) + \left(Bh^2 - H^2 \right) \nabla F_{42} \right|^2$$

$$+ \frac{1}{2} \left[(F_{21} + 2H F_{22})(F_{41} + 2H F_{42} \right.$$

$$+ \left. \left. F_{43} + 2H F_{44} + 3H^2 F_{45} + 4H^3 F_{46} \right) \right] \right\} \tag{60}$$

Note that equation (57) retains the form of the Bernoulli term and thus is only applicable to irrotational motion. Uses of the model by Gobbi and Kirby (1999) were limited to one horizontal dimension, and thus no vertical vorticity is generated in any existing results.

The extension to $O(\mu^4)$ of the vertical structure of ϕ in the Gobbi et al. model provides a dramatic enhancement of the prediction of velocity components. For example, Fig. 4 shows a comparison of vertical profiles of horizontal velocity for the linear, periodic wave case. The prediction is fairly robust up to $\mu = 5$, with a spurious flow reversal first occurring at $\mu = 5.54$ at a dimensionless elevation $z = -0.628$. Similar results are obtained for vertical velocities. Improvements are also documented in prediction of second-harmonic amplitudes over the lower order theory. Systematic improvements in leading order amplitude dispersion were, however, not noted.

Systematic improvements were also noted in solitary wave properties, including wave height, water particle velocity at crest, and total energy as functions of normalized phase speed. Fig. 5 shows plots of a crest speed parameter ω_s given by

$$\omega_s = 1 - (u_c - F_r)^2 \tag{61}$$

where u_c and F_r are horizontal particle velocity at the crest and wave phase speed both normalized by $\sqrt{gh}$. As the particle velocity varies from zero in linear waves to F_r at limiting wave height, ω_s varies
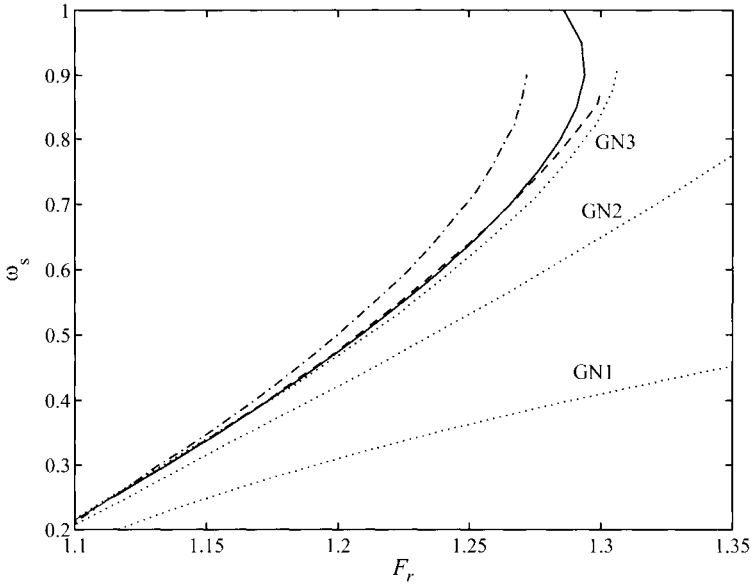
Figure 5. ω_s vs. phase speed for solitary waves. Exact (solid line), Gobbi et al. (dash), Wei et al. (dash-dot), Shields and Webster (dot). (From Gobbi et al., 2000).
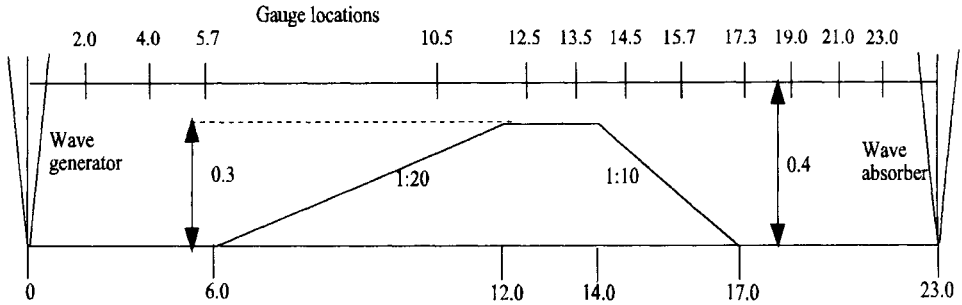
Figure 6. Sketch of wave flume in Delft experiments. All dimensions in (m). (From Gobbi and Kirby, 1999).

from zero to one. Fig. 5 shows exact results due to Tanaka (1986), three levels of a Green-Naghdi theory due to Shields and Webster (1988), and results of the $O(\mu^2)$ theory of Wei et al. (1995) and the $O(\mu^4)$ theory of Gobbi et al. (2000). Results generally indicate that the present theory has accuracy comparable to level 3 Green-Naghdi theory, which has not been applied in realistic computational settings to date.

The most striking improvement in a practical sense is seen in a study of waves propagating from relatively deep water, over the shallow crest of a bar, and back into deep water, as presented originally in Beji and Battjes (1993). The test geometry and location of wave gauges is shown in Fig. 6. Gobbi and Kirby considered two test cases for periodic wave propagation over the bar crest, using the theory of Gobbi and Kirby and the $O(\mu^2)$ theory of Wei et al. (1995). Figs. 7 and 8 show results for Case (c), where waves with an initial $\mu = 1.69$ propagate from deeper water, over the shoal, and back into

14
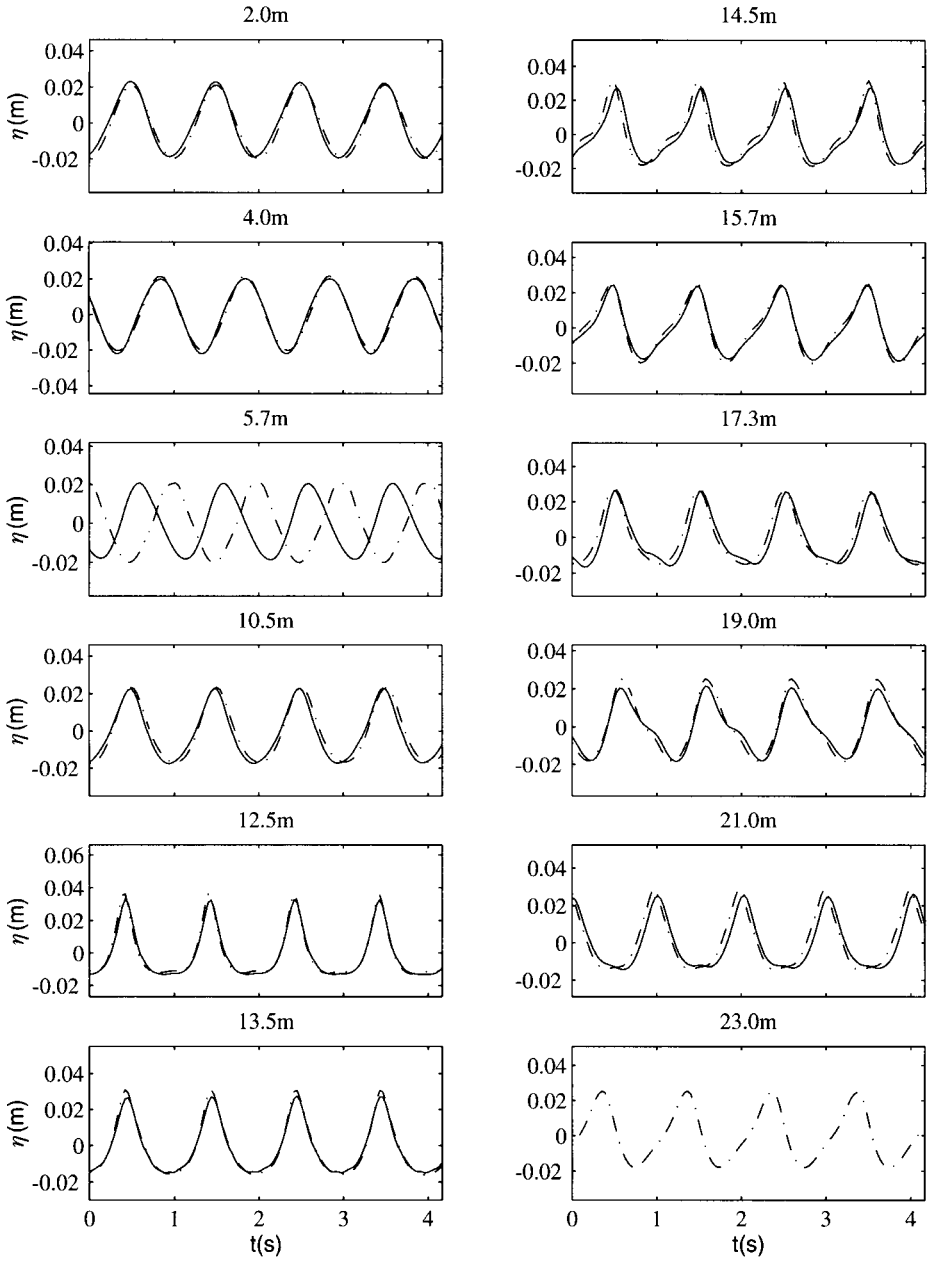
Figure 7. Comparisons of free surface displacement for case (c) of Delft experimental data at various gauge locations. Model of Gobbi and Kirby (dash-dot), data (solid). (From Gobbi and Kirby, 1999).
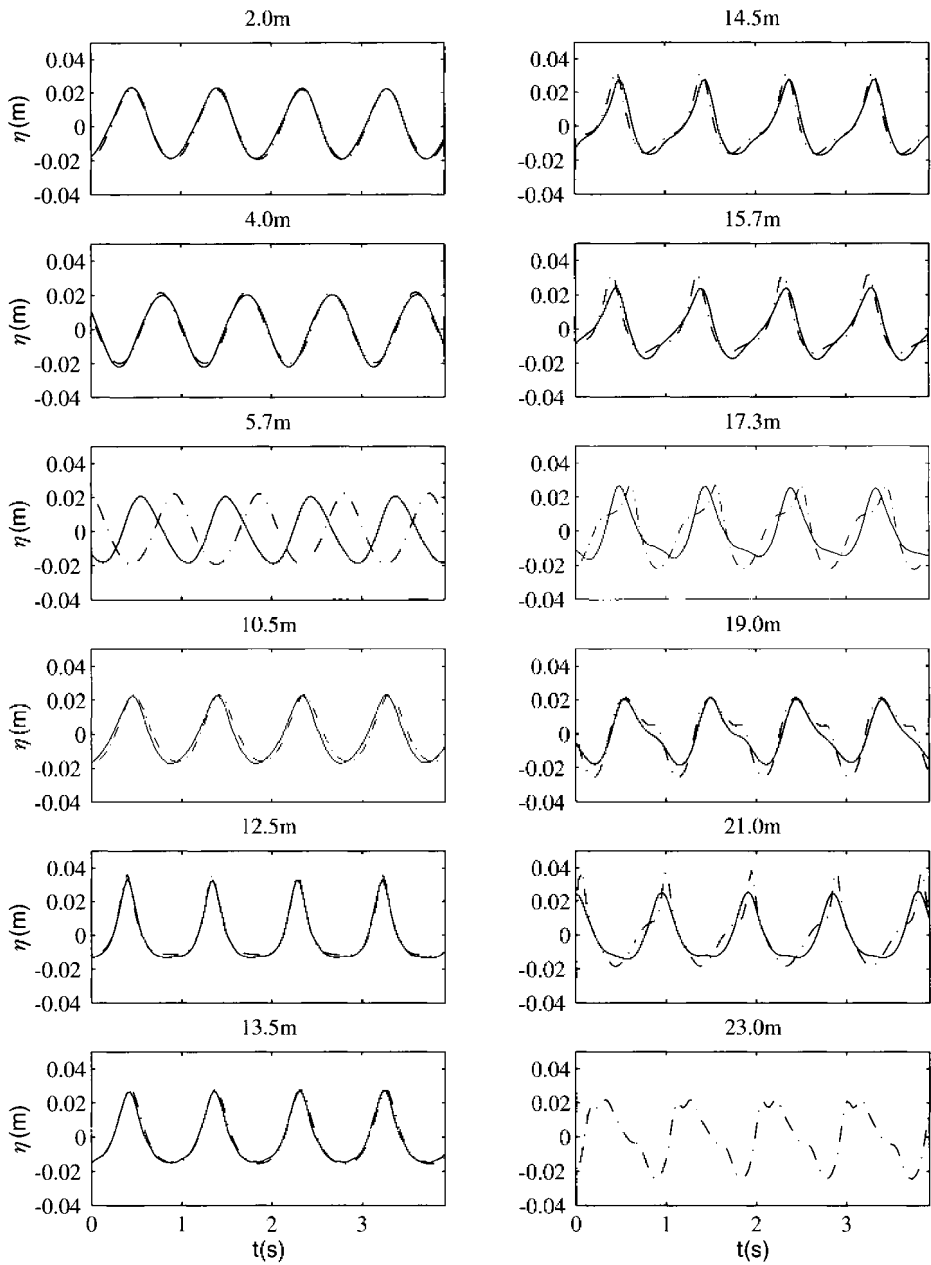
Figure 8. Comparisons of free surface displacement for case (c) of Delft experimental data at various gauge locations. Model of Wei et al. (dash-dot), data (solid). (From Gobbi and Kirby, 1999).

deeper water. Fig. 7 shows results for the Gobbi and Kirby model, and indicates that the model is capable of preserving the overall shape of transmitted waves downstream of the bar, which is the most difficult region to obtain good results in. In contrast, Fig. 8 shows results obtained using the Wei et al. model. In this case, there is clear damage to phase information in the transmitted wave, despite the fact that shoaling from deeper water to the bar crest was modeled relatively accurately. The accumulation of phase errors beyond the bar crest in the lower order model could be interpreted as being due to dispersion errors in the relatively less accurate model. However, this is not an entirely satisfactory explanation. In order to test this explanation, Gobbi and Kirby constructed a weakly nonlinear ($\delta = O(\mu^2)$) model system by truncating the Gobbi-Kirby model to $O(\mu^4, \delta\mu^2)$. Results from this case show a similar tendency to accumulate phase errors downwave of the shallow bar crest. Clearly, both full nonlinearity and enhanced dispersion effects play a crucial role in the accuracy of solutions in this case.

2.4.2. Model of Agnon et al. (1999) and Successors

An alternate approach to extending model derivation to higher order and increased accuracy was originally proposed by Agnon et al. (1999), with continuing development, for example, in Madsen et al. (2003). In this approach, the reduction of the problem to a description in terms of a velocity potential is dropped, and the identity of horizontal velocity $\mathbf{u}$ and vertical velocity w is retained instead. Following Madsen and Schäffer (1998), the irrotational solutions for the velocities may be written as

$$\mathbf{u}(\mathbf{x}, z, t) = \sum_{n=0}^{\infty} (-1)^n \left(\frac{z^{2n}}{(2n)!} \mu^{2n} \nabla(\nabla^{2n-2}(\nabla \cdot \mathbf{u_0})) + \frac{z^{2n+1}}{(2n+1)!} \mu^{2n+2} \nabla(\nabla^{2n} w_0) \right) \tag{62}$$

$$w(\mathbf{x}, z, t) = \sum_{n=0}^{\infty} (-1)^n \left(-\frac{z^{2n+1}}{(2n+1)!} \mu^{2n+2} \nabla^{2n}(\nabla \cdot \mathbf{u_0}) + \frac{z^{2n}}{(2n)!} \mu^{2n+2} \nabla^{2n} w_0 \right) \tag{63}$$

where, following equation (11),

$$\mathbf{u_0} = \nabla\phi^{(0)}; \qquad w_0 = \phi^{(1)} \tag{64}$$

are the velocities at $z = 0$. The two velocities are related through the bottom boundary condition (equation (6)), giving a relation of the form

$$L_c\{w_0\} + L_s \cdot \{\mathbf{u_0}\} + \nabla h \cdot (L_c\{\mathbf{u_0}\} + L_s\{w_0\}) = 0 \tag{65}$$

where

$$L_c = \sum_{n=0}^{\infty} (-1)^n \frac{h^{2n}}{(2n)!} \nabla^{2n}, \qquad L_s = \sum_{n=0}^{\infty} (-1)^n \frac{h^{2n+1}}{(2n+1)!} \nabla^{2n+1} \tag{66}$$

A great deal of flexibility is left in choosing a procedure for improving the truncated series appearing in equation (65) during the development of a finite order theory. In Agnon et al. (1999), the series form of equation (65) is multiplied by a differential operator of the form

$$A = 1 + a_2 h^2 \nabla^2 + a_4 h^4 \nabla^4 + \cdots \tag{67}$$

and coefficients are then chosen to force terms to disappear in the resulting equation up to the required order. For example, for constant depth and a truncation level $N = 4$, the resulting equation is

$$(1 - \frac{4}{9}h^2\nabla^2 + \frac{1}{63}h^4\nabla^4)w_0 + (h\nabla - \frac{1}{9}h^3\nabla^3 + \frac{1}{945}h^5\nabla^5) \cdot \mathbf{u_0} \tag{68}$$

which is correct to $O(\mu^8)$ and reproduces (4,4) Padé dispersion as in Gobbi et al. Agnon et al. extend this procedure to include mild-slope terms limited to $O(\nabla h)$, possibly limiting the accuracy of the resulting model when applied to abrupt nearshore bathymetry. Once the form of the relation between $\mathbf{u}_0$ and w_0 is obtained, Agnon et al. develop expressions for velocities at the free surface in terms of the velocities at $z = 0$, and then employ the evolution equations in terms of $\mathbf{V} = \nabla \Phi$, where $\Phi = \phi(\mathbf{x}, z = \eta, t)$ as in Dommermuth and Yue (1987) and others. Madsen et al. (2003) further generalize this procedure by choosing to develop series for the velocities at the arbitrary reference level z_α rather than the still water level $z = 0$. The additional freedom in the system of equations is then utilized to improve the vertical profile of horizontal velocity rather than the dispersion relation, which is already quite accurate.

The line of investigation initiated in these studies holds a great deal of promise. In particular, it is much more likely that any access to an actual model system for cases of higher accuracy than that in Gobbi et al. would come from this procedure rather than from direct expansion in terms of the velocity potential. Additional publications detailing both theoretical aspects and numerical treatments of the method will be forthcoming.

3. PRACTICAL EXTENSIONS TO THE $O(\mu^2)$ BOUSSINESQ MODEL

The $O(\mu^2)$ model written in terms of a velocity variable provides an easily extensible framework for the development of a nearshore processes model. In order to achieve this goal, various additional physical processes are incorporated, often on an ad hoc basis. In this section, we consider the extension of the model equation (22) to the form

$$\mathbf{u}_{\alpha t} + \delta(\mathbf{u}_\alpha \cdot \nabla)\mathbf{u}_\alpha + \nabla \eta + \mu^2 \mathbf{V_1} + \delta \mu^2 \mathbf{V_2} - \mathbf{R_b} - \mathbf{R_s} + \mathbf{R_f} = O(\mu^4) \tag{69}$$

where $\mathbf{R_b}$ denotes wave breaking effects, $\mathbf{R_f}$ denotes bottom friction, and $\mathbf{R_s}$ denotes subgrid-scale lateral mixing effects.

3.1. Improving Model Dispersion, Shoaling and Nonlinear Properties

As has been shown in a number of studies starting with Madsen et al. (1991), improvements in Boussinesq model performance can be introduced by employing rearrangements that alter the definitions of $\mathbf{M}$, $\mathbf{V_1}$ and $\mathbf{V_2}$ terms in the model equations, or by redefining the reference configuration of the dependent variables, leading to the same sort of rearrangement. The effectiveness of any modification can be established by examining linear properties such as shoaling and dispersion, along with nonlinear properties such as the amplitudes of harmonics or the magnitude of amplitude dispersion in Stokes wave solutions. We consider two cases in particular.

In order to provide a degree of freedom for use in optimizing nonlinear model properties, Kennedy et al. (2001) modified the formulation of Wei et al. (1995) by allowing the reference elevation z_α to depend on time and thus follow the rise and fall of the local water surface in some manner. The most general case considered defined z_α as

$$z_\alpha = \zeta h + \beta \delta \eta \tag{70}$$

where the original theory of Wei et al. is recovered by taking $\beta = 0$ and $\zeta = -1 + \sqrt{1/5}$, corresponding to the (2,2) Padé case. A special case of this relationship occurs when $\beta = \zeta + 1 = \sqrt{1/5}$, which gives

$$z_\alpha = -h + \beta H \tag{71}$$

This case corresponds to choosing a reference level which remains at a fixed proportion of the instantaneous total water depth, and would be equivalent to choosing a fixed σ_α reference level in a σ−coordinate model. The revision to the model equations is contained entirely within the $\mathbf{V}_1$ term (equation (24)), which is revised to read

$$\mathbf{V}_1 = \left[\frac{1}{2}z_\alpha^2 \nabla(\nabla \cdot \mathbf{u}_\alpha) + z_\alpha \nabla(\nabla \cdot (h\mathbf{u}_\alpha))\right]_t - \nabla\left[\frac{1}{2}(\delta\eta)^2 \nabla \cdot \mathbf{u}_{\alpha t} + \delta\eta \nabla \cdot (h\mathbf{u}_{\alpha t})\right] \tag{72}$$

Kennedy et al. (2001) examined the optimal choice of β by examining a Stokes wave solution of the form

$$\eta = a_1[\cos(kx - \omega t) + a_+ \cos 2(kx - \omega t) + a_-] \tag{73}$$

where a_+ is a normalized second harmonic amplitude and a_- represents the steady set-down. Forcing the Taylor series expansions of the resulting second harmonic amplitude to match the Taylor series for the second harmonic amplitude of a regular Stokes wave for the full dispersive theory gives the choice $\beta = 17\sqrt{5}/200$. Fig. 9 shows plots of the resulting second harmonic amplitudes and set-down, normalized by the correct solutions, for a range of $\mu = kh$ values. The second harmonic amplitude from the optimized model behaves quite well in comparison to the result from the original Wei et al. theory, and thus this revision to the original model is highly recommended.

Several studies have examined the enhancement of the $O(\mu^2)$ evolution equations in order to obtain higher-order dispersion. Schäffer and Madsen (1995) applied operators to rearrange dispersive terms in the weakly nonlinear model equations of Nwogu (1993) and obtained four sets of operator coefficients that would recover the more accurate (4,4) Padé dispersion relation in the model system, without adding higher-order terms as in the model of Gobbi et al. Madsen and Schäffer (1998) extended this procedure to the fully nonlinear equations of Wei et al. (1995). Madsen and Schäffer also
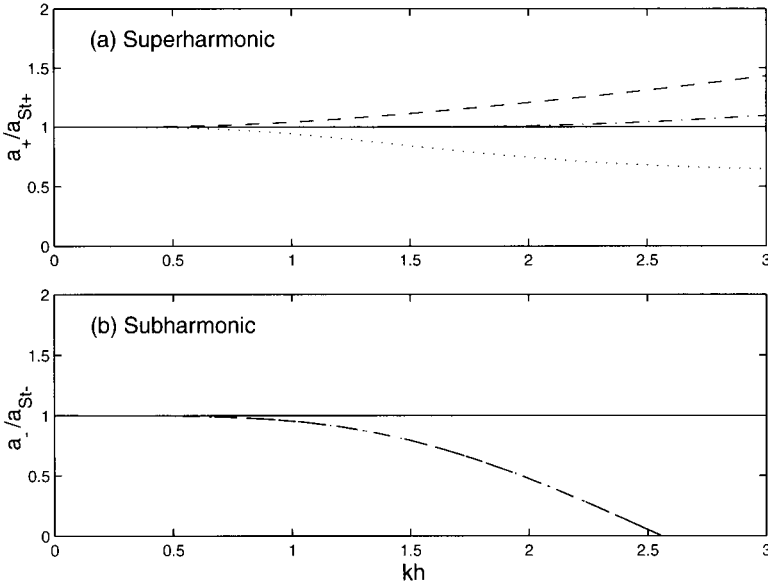
Figure 9. Self interaction superharmonics (a) and subharmonics (or set-down) (b) relative to the Stokes solution for the fully-dispersive problem. Original Wei et al. theory (dash), constant σ level theory (dot), optimized moving z_α theory (dash-dot). (From Kennedy et al., 2001).
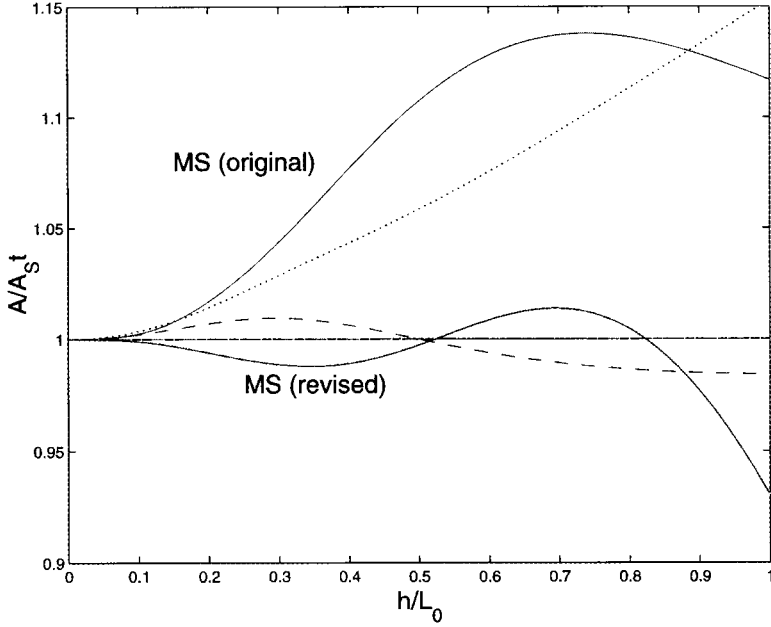
Figure 10. Integrated shoaling amplitudes for shore normal waves. (dash) Model optimized by coefficient choice alone, (dash-dot) model optimized by operator rearrangement and coefficient choice (obscured behind level line), (dot) linearized model of Nwogu (1993) or Wei et al. (1995), plus results from Madsen and Schäffer (1998). (From Kennedy et al., 2002).

demonstrated a procedure for recovering a model expressed entirely in terms of $O(\mu^2)$ terms at the highest, but starting with an $O(\mu^4)$ model and then choosing a form which was expressed only in $O(\mu^2)$ terms by means of operator rearrangements and choice of coefficients. Kennedy et al. (2002) have extended this procedure, starting with the $O(\mu^4)$ model of Gobbi and Kirby (1999) in order to retain the very accurate vertical velocity profile given there. Kennedy et al. employed two procedures, one based solely on choice of coefficients, and the second based on a combination of operator rearrangement and choice of coefficients, to obtain model equations expressed in terms of $O(\mu^2)$ terms at the highest. The resulting model retains the (4,4) Padé dispersion of the Gobbi and Kirby model. Following Madsen and Schäffer, Kennedy et al. choose the remaining free parameters in order to optimize an integrated shoaling coefficient, which represents a measure of error in local shoaling effects integrated across the entire shoaling zone. Results for this measure are shown in Fig. 10 in comparison to results derived from Nwogu's model and from the study of Madsen and Schäffer. The results for the more involved optimization are almost graphically indistinguishable from the exact linear shoaling theory for the vertical resolution chosen in the plot.

3.2. Extensions to Non-Cartesian Coordinate Systems

It is often necessary to apply Boussinesq models in complex geometries. This problem has classically been approached by employing stair-step boundaries in existing Cartesian grid finite difference codes. Resulting models can be robust, but there is evidence (as discussed below) that such an approach can lead to spurious wave scattering behavior along oblique wall sections. Several more modern approaches have been employed to solve this problem.

The first approach involves switching to a numerical solution method which is not tied to a regular gridding scheme. Finite element techniques are often the principal choice in this approach, and the technique has been extensively developed for application to Boussinesq models. Recent examples include the work of Li et al. (1999), Walkley and Berzins (1999), Sørensen and Sørensen (2000) and Woo and Liu (2001).

A second approach is based on employing either analytic or numerically determined coordinate transformations in order to obtain a boundary fitted coordinate system, in which major boundary segments lie along constant values of the fitted coordinates. Methods for obtaining coordinate transformations numerically are well-developed in the computational fluid dynamics literature; for example, Shi et al. (2001a) employ the scheme of Brackbill and Saltzman (1982) and have developed a publically available Matlab code which may be obtained at http://chinacat.coastal.udel.edu/~kirby/programs/. Several levels of transformation can be employed in such an approach. At the simplest level, the transformation can be applied to the coordinate system only, while the identity of the surface elevation η, x velocity component u and y velocity component v are retained but determined at grid points in the new coordinate system. Results obtained with this approach are perhaps somewhat easier to interpret, but the resulting transformed governing equations are quite cumbersome; see, for example, the discussion of model equations in Li and Zhan (2001).

A more involved approach involves defining a tensor transformation applied to the velocity components as well as the coordinate system. Shi et al. (2001a; 2001b) employed such an approach, and chose to formulate the resulting model in terms of contravariant velocity components, which are defined to be the velocity components perpendicular to coordinate lines at each point in the modeled domain. Warsi (1993) provides an extensive discussion of the geometric considerations. While the overhead of learning the details of the metric tensor geometry can be considerable, the approach leads to a much more compact representation of the governing equations than is obtained in a method based on the primitive variables.

Shi et al. (2001a; 2001b) provide a number of examples illustrating computations in generalized curvilinear coordinates. Figs. 11 and 12 illustrate the propagation of an initially plane wave into a circular channel. The computation in a polar coordinate system corresponds closely to the analytic solution in the linear limit, as shown by Shi et al. (2001a). In contrast, a similar calculation in a reasonably finely-resolved Cartesian grid with stair-step boundaries produces a clear excess of scattered wave components in comparison to the polar case.
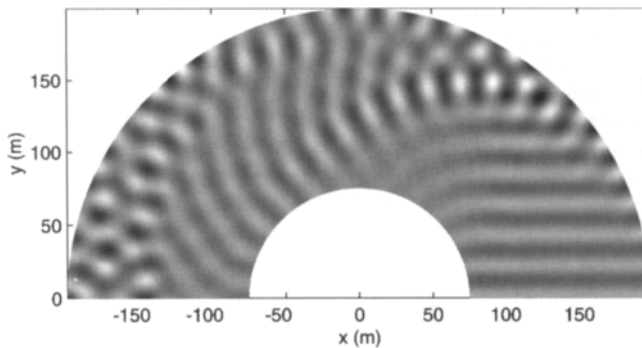
Figure 11. An example of initially plane wave propagation into a circular channel of constant depth. Boundary fitted coordinate system. (From Shi et al., 2001a).
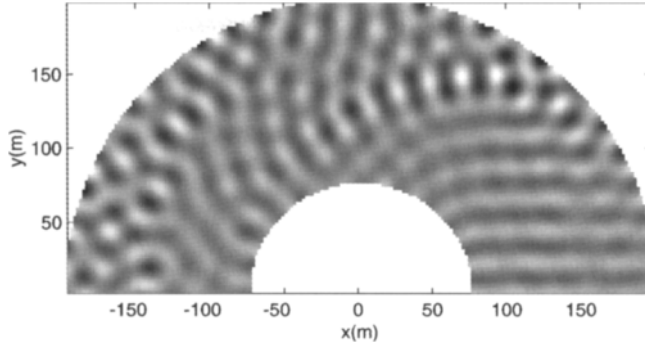
Figure 12. Example of 11 repeated on a Cartesian grid with stair-step boundaries. Note the appearance of spurious reflected components close to the incident wave entrance on the right. (From Shi et al., 2001a).

Shi et al. (2001b) have also applied the model to the case of a coastal inlet and have compared model results to measurements of surface elevation, skewness and asymmetry obtained from a laboratory scale model. Detailed model-data comparisons for this case will appear in other publications.

3.3. Shoreline Conditions

The waterline on a beach subjected to wave action is highly variable, and thus the physical domain in a nearshore Boussinesq model application changes in time. Although it is possible to utilize a time-dependent, shoreline-following grid system in order to resolve the fluid domain only up to the waterline (for example, Özkan-Haller and Kirby, 1997), it is difficult to do so if the shoreline does not remain single valued or becomes multiply connected. For this reason, it is more standard to employ techniques whereby the entire region which is potentially wetted is treated as an active part of the computational grid. One of the earliest methods along this line is the "slot" method of Tao (1984), in which deep, narrow, flooded slots are added to each grid row, extending down at least to the lowest elevation that will be experienced during shoreface rundown. Kennedy et al. (2000a) employed the slot technique of Tao but modified it to better enforce mass conservation. Details can be found in the aforementioned study. To date, utilization of slot methods remains something of an art form. Slots which are too wide relative to the model grid spacing admit too much fluid before filling during runup, and cause both a reduction in amplitude and a phase lag in modeled runup events. At the other extreme, slots which are too narrow tend to induce a great deal of numerical noise, leading to the need for intermittent or even fairly frequent filtering of swash zone solutions.

Alternatively, several moving boundary techniques where the occurrence of a shoreline is traced on a fixed grid have been proposed. In one such method, Lynett et al. (2002) determine the position of the shoreline on a beach face by linearly extrapolating the surface and velocities from the two wetted grid points closest to shore. Derivatives at wetted grid points are then computed using the regular finite difference stencil including extrapolated values, eliminating the need for conditional application of off-centered difference stencils near the shore. The time stepping solution is then only performed for the wetted grid points. Although this method does not impose any apparent constraints on mass conservation at the shoreline, results for runup of regular and solitary waves are seen to be quite accurate, indicating that the method holds promise for general application.

3.4. Wave Breaking

Simulation of wave breaking in Boussinesq models has been approached with a number of techniques, ranging from fairly ad-hoc additions of eddy viscosity formulations up to reasonably detailed

calculations of the generation and transport of vorticity or turbulent kinetic energy under the breaking wave crest. Regardless of the formulation, each of the approaches can be thought of as a means for adding the breaking wave force term $\mathbf{R_b}$ to the momentum equation. At minimum, these terms must be scaled similarly in order to reproduce the correct amount of energy dissipation. They must also be localized in the region of the front face of the breaking wave, in order to provide the correct distribution of dissipation in the frequency domain and preserve the proper relative phasing of harmonic components in the wave. Beyond these requirements, the range of physical approaches taken has a great deal of variety.

3.4.1. Eddy Viscosity Models

Zelt (1991) provided an early model for Boussinesq wave breaking, in the form of an eddy viscosity model applied in a one-dimensional (1-D) horizontal model. Extended to two-dimensions, the breaking wave force term $\mathbf{R_b}$ can be written as

$$R_b^x = \frac{1}{H} \left(\{v_b[Hu_\alpha]_x\}_x + \frac{1}{2}\{v_b[Hu_\alpha]_y + v_b[Hv_\alpha]_x\}_y \right) \tag{74}$$

$$R_b^y = \frac{1}{H} \left(\{v_b[Hv_\alpha]_y\}_y + \frac{1}{2}\{v_b[Hv_\alpha]_x + v_b[Hu_\alpha]_y\}_x \right) \tag{75}$$

Following Zelt, Kennedy et al. (2000a) give the breaking wave eddy viscosity as

$$v_b = B\delta_b^2 H\eta_t \tag{76}$$

where δ_b is a mixing length coefficient which is calibrated to a value of 1.2. The coefficient B is used to turn the breaking term off or on depending on a criterion based on the vertical velocity of the surface. Again, following Zelt but using time derivatives in place of space derivatives, Kennedy et al. used

$$B = \begin{cases} 1, & \eta_t \geq 2\eta_t^* \\[2mm] \dfrac{\eta_t}{\eta_t^*} - 1, & \eta_t^* < \eta_t \leq 2\eta_t^* \\[2mm] 0, & \eta_t \leq \eta_t^* \end{cases} \tag{77}$$

The parameter η_t^* determines the onset and cessation of breaking. Zelt chose this criterion to have a constant value, but Kennedy et al. use a model for the parameter which involves a time history in order to allow the slope of the breaking wave crest to relax after the onset of breaking, as in the roller model described below. The relationship is

$$\eta_t^* = \begin{cases} \eta_t^{(F)}, & t \geq T^* \\[2mm] \eta_t^{(I)} + \dfrac{t - t_0}{T^*}(\eta_t^{(F)} - \eta_t^{(I)}), & 0 \leq t - t_0 < T^* \end{cases} \tag{78}$$

Here, T^* is the elapsed time since the onset of the local breaking event, and the initiation and relaxed critical surface velocities are given by $\eta_t^{(I)} = 0.65\sqrt{gh}$ and $\eta_t^{(F)} = 0.15\sqrt{gh}$. In 2-D applications, the relationship must be augmented with a tracking algorithm to follow events along rays (see Chen et al., 2000a).
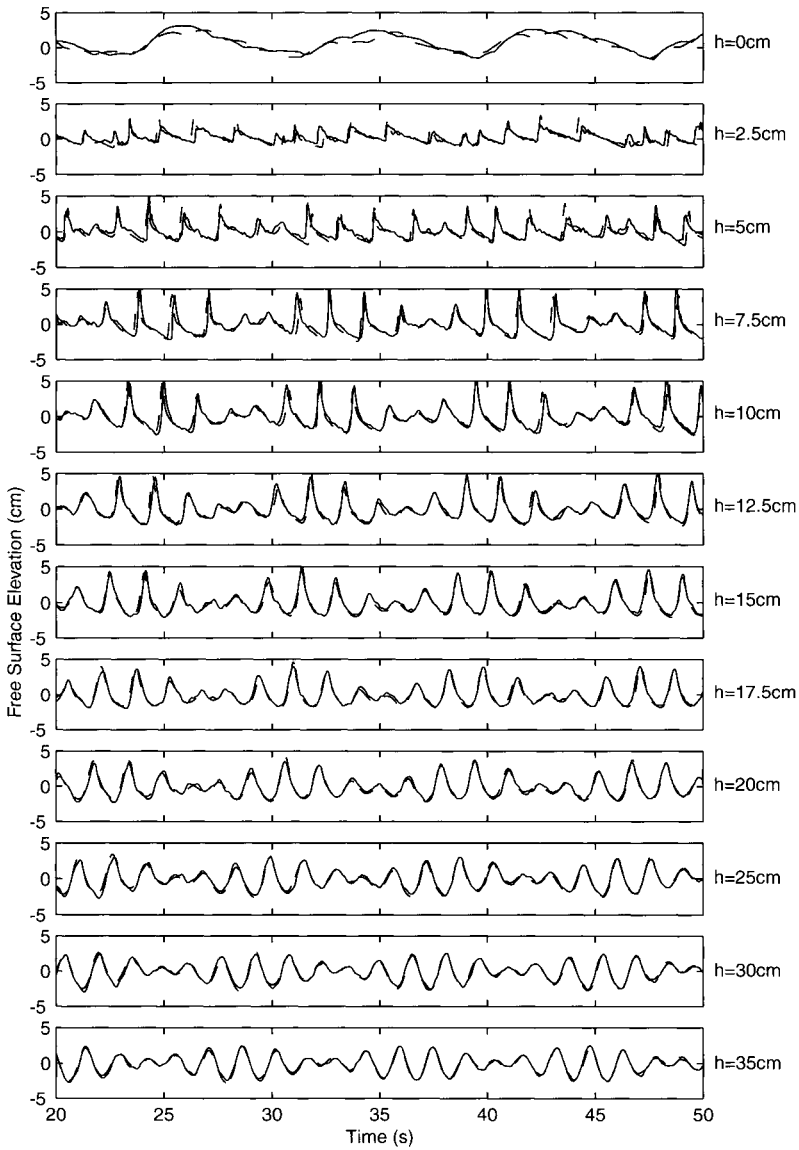
Figure 13. Computed (dash line) and measured (solid line) free surface elevations and shoreline runup for a bichromatic wave train shoaling on a plane beach. Data from Mase (1995). (From Kennedy et al., 2000a. Reproduced with permission of ASCE).

Fig. 13 shows an example of bichromatic waves shoaling over a plane beach, including breaking and runup effects. Data is from the laboratory study of Mase (1995). The test verifies the basic features of both the breaking process and the runup using the slot method. Additional two-dimensional calculations for wave breaking and runup on a circular island may be found in Chen et al. (2000a).

Nwogu and Demirbilek (2001) present a more sophisticated eddy viscosity model in which the eddy viscosity is expressed in terms of turbulent kinetic energy k and a length scale l_t,

$$v_b = \sqrt{k}l_t \tag{79}$$

The turbulent kinetic energy is computed using a one-equation model which expresses the generation, horizontal advection, and dissipation of total depth-integrated k. Breaking is triggered when horizontal fluid velocity at the surface exceeds the linear estimate of the wave phase speed. Turbulence production falls immediately to zero when this criterion is not exceeded, so there is no relaxation effect as described above or as in the roller model described below.

3.4.2. Roller Models

A simplified formulation with a more direct physical interpretation, was developed by Schäffer et al. (1993), using the surface roller concept of Svendsen (1984). The model is developed using a two-layer velocity profile, where it is assumed that the velocity u below the elevation of the roller bottom corresponds to the depth-averaged value from irrotational theory, while the roller volume itself is moving at the phase speed c of the wave. The effect of the roller is expressed as a modification to the momentum balance for the organized wave motion. The resulting momentum equation for depth-integrated volume flux Q may be written as (in one horizontal dimension)

$$Q_t + \delta \left(\frac{Q^2}{H} \right)_x + gH\eta_x - \mu^2 \frac{h^2}{2} Q_{xxt} + \mu^2 \frac{h^3}{6} \left(\frac{Q}{h} \right)_{xxt} + R_x \tag{80}$$

where R is the excess momentum flux in the roller, given by

$$R = d \left(c - \frac{Q}{H} \right)^2 \left(1 - \frac{d}{H} \right)^{-1} \tag{81}$$

where d is the local roller thickness. Calibration of the model and testing against data are described in Madsen et al. (1997), and results are of comparable accuracy to the eddy viscosity models described above.

3.4.3. Vorticity Transport Models

The most elaborate model of Boussinesq model wave breaking is the vorticity transport model of Veeramony and Svendsen (2000). In this model, there is no a priori separation between roller region and a zone of irrotational flow beneath. Instead, the entire vertical fluid column is treated as a rotational flow, and the vorticity transport equation is solved with simplifying assumptions in order to determine the entire velocity profile over depth. The resulting model is similar to the model of Schäffer et al. (1993) in overall form, but the resulting wave breaking terms require more evaluation.

Since the flow is rotational over depth in this treatment, the basic formulation of the problem in terms of a velocity potential is not valid. Veeramony and Svendsen restricted their attention to propagation in one horizontal dimension and formulate the problem in terms of a scalar stream function in the vertical plane,

$$\mu^2 \psi_{xx} + \psi_{zz} = \xi \tag{82}$$

where ψ is the stream function and ξ is the magnitude of the out-of-plane vorticity vector. Boundary conditions are given by

$$\psi(z = -h) = \psi_z(z = -h) = 0 \tag{83}$$

Within the weakly dispersive approximation, equation (82) may be solved to give

$$\psi = u_0(z+h) - \frac{1}{2}\mu^2(z+h)^2(h_{xx}u_0 + 2h_x u_{0,x}) - \frac{1}{6}\mu^2(z+h)^3 u_{0,xx}$$

$$+ \int_{-h}^{z}\int_{-h}^{z}\xi dz dz - \mu^2\int_{-h}^{z}\int_{-h}^{z}\int_{-h}^{z}\int_{-h}^{z}\xi_{xx}dzdzdzdz \tag{84}$$

where u_0 is the value of the irrotational velocity at the bottom and where terms in u_0 correspond to the usual irrotational theory. In terms of scalar volume flux Q, the resulting Boussinesq momentum equation (without dispersion enhancement) takes on the form

$$Q_t + H\eta_x + \delta\left(\frac{Q^2}{H}\right)_x - \mu^2\frac{h^2}{2}Q_{xxt} + \mu^2\frac{h^3}{6}\left(\frac{Q}{h}\right)_{xxt} + \delta(\Delta M)_x + \mu^2(\Delta P)_{xxt} = 0 \tag{85}$$

Breaking effects are expressed through the quantities ΔM and ΔP, given by

$$\Delta P = \int_{-h}^{\delta\eta}\int_{z}^{\delta\eta}\int_{-h}^{z}(u_r - \overline{u_r})dzdzdz \tag{86}$$

$$\Delta M = \int_{-h}^{\delta\eta}(u_r^2 - \overline{u_r}^2)dz \tag{87}$$

where $\overline{(*)}$ denotes a depth average. u_r is the rotational component of the horizontal velocity, given by

$$u_r = \int_{-h}^{z}\xi dz - \mu^2\int_{-h}^{z}\int_{-h}^{z}\int_{-h}^{z}\xi_{xx}dzdzdz + O(\mu^4) \tag{88}$$

The vorticity ξ is formally unknown at this point, and Veeramony and Svendsen (2000) use the leading order terms of the vorticity transport equation, neglecting advective effects to get

$$\xi_t = \kappa\xi_{\sigma\sigma}; \qquad \kappa = \frac{\nu_t}{h^2}; \qquad \sigma = \frac{h+z}{H} \tag{89}$$

Boundary conditions for the vorticity are derived from hydraulic jump experiments described in Svendsen et al. (2000). Veeramony and Svendsen solve equation (89) analytically for the case of eddy viscosity held constant over depth. Fig. 14 illustrates the evolution of a vorticity field under a breaking wave crest. Results for undertow profiles were also obtained and show general agreement with laboratory measurements.

Further development of the theory of Veeramony and Svendsen would involve the use of a numerical solution of equation (89) so that more realistic values of eddy viscosity could be used. However, the extension of the model to two horizontal dimensions is hampered by the use of the stream function formulation, and thus an alternative formulation allowing a three-dimensional flow field is required. The key to this future development may lie in the formulation of Shen (2001), mentioned in Section 5 below.

3.5. Bottom Friction and Subgrid-Scale Mixing

Since the velocity field in a Boussinesq calculation resolves the instantaneous wave orbital motion, the choice of a bottom friction formulation is relatively straightforward, and is given in the applications below by

$$\mathbf{R_f} = \frac{f}{H}|\mathbf{u}_\alpha|\mathbf{u}_\alpha \tag{90}$$
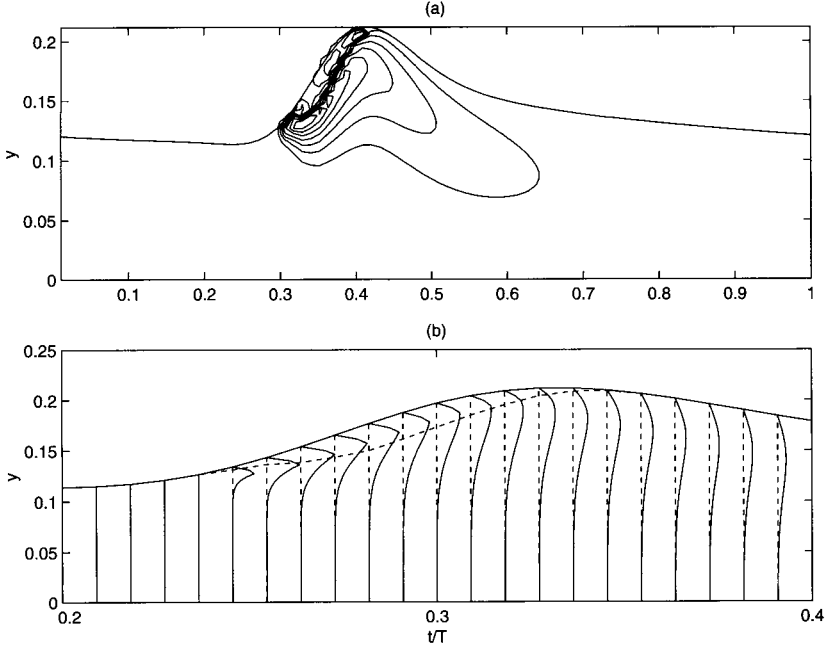
Figure 14. (a) Contours of vorticity at $h = 14.29$ cm. (b) Vertical profiles of vorticity under the roller and behind the crest at $h = 14.29$ cm. The ordinate $y = h + z$ is zero at the bottom. (From Veeramony and Svendsen, 2000).

where the friction factor is on the order of 10^{-3} in most simulations (Chen et al., 1999; 2000a). Note that the term is written in terms of the reference velocity rather than the bottom velocity, which would tend to somewhat reduce the size of f.

Nearshore current systems are affected by several lateral mixing effects, including both turbulent mixing and lateral shear dispersion resulting from the three-dimensional structure of real currents and their interaction with the wave orbital velocity. Of these, the shear dispersion can be an order of magnitude larger (Svendsen and Putrevu, 1994), and an attempt has been made to incorporate its effect in most of our nearshore simulations. Chen et al. (1999) formulate the effect as a Smagorinsky subgrid model with the form

$$R_s^x = \frac{1}{H} \left(\{\nu_s [Hu_\alpha]_x\}_x + \frac{1}{2} \{\nu_s [Hu_\alpha]_y + \nu_s [Hv_\alpha]_x\}_y \right) \tag{91}$$

$$R_s^y = \frac{1}{H} \left(\{\nu_s [Hv_\alpha]_y\}_y + \frac{1}{2} \{\nu_s [Hv_\alpha]_x + \nu_s [Hu_\alpha]_y\}_x \right) \tag{92}$$

where ν_s is an eddy viscosity arising from the mean flow field,

$$\nu_s = c_m \Delta x \Delta y \left[(U_x)^2 + (V_y)^2 + \frac{1}{2} (U_y + V_x)^2 \right]^{1/2} \tag{93}$$

and where U and V are suitable time averages of the velocity field. Chen et al. (1999) and subsequent studies have used time averages over two wave periods for regular waves or over ten peak wave periods for irregular waves, and typically use $c_m = 0.25$. This aspect of the model application has

not been extensively evaluated. Ongoing work is examining the evolution of shear instabilities in model results as an indicator of the correct level of lateral mixing.

4. BOUSSINESQ MODELING OF NEARSHORE CIRCULATION

Once the effectiveness of breaking and runup models for Boussinesq codes was established, attention turned to the question of whether the models could provide an accurate rendition of mean currents in the surf zone. A classical analysis of wave-averaged surf zone dynamics shows that both cross- and longshore mean currents arise due to the presence of gradients of radiation stresses, which represent fluxes of wave-averaged momentum. An analysis of wave-averaged forms of the Boussinesq equations readily shows that the relevant forcing mechanisms are present in the time-dependent form of the evolution equations (Yoon and Liu, 1989), and hence mean currents should be generated in models which account for wave energy dissipation through breaking, which in general would be expressed as $-\rho H \mathbf{u}_\alpha \cdot \mathbf{R_b} + O(\mu^2)$ following from equation (69). Such a demonstration was provided by Madsen et al. (1997). More recently, Peregrine (1998) examined the instantaneous vorticity dynamics, with particular attention to the idea that vertical vorticity generation in the surf zone is mainly provided by the mechanism

$$\frac{d\omega}{dt} = \nabla \times \mathbf{R_b} \tag{94}$$

where ω is discussed in Section 2.3. Peregrine examines the generation of circulation in finite patches of the surf zone and relates its generation to variations in breaking intensity along wave crests. An example of this mechanism in action is provided in Section 4.3 for the case of a rip current stabilized in place by the presence of a channel in a longshore-uniform bar.

4.1. Longshore Currents

Chen et al. (2000b) have considered the case of longshore current generation in field conditions, using data from the DELILAH field experiment at Duck, North Carolina in October 1990. Fig. 15 shows the bathymetry at the experimental site for October 10, 1990. The bar field in this case is nearly longshore uniform aside from a slight kink in bottom contours near the location of an array of cross-shore current measurements, indicated by the dashed line. Cross-shore decay of breaking wave heights and resulting longshore currents are indicated by circles in Figs. 16c and d, respectively. The longshore current has a strong maximum in the trough between the shoreface and the longshore bar crest, at a location where local forcing due to radiation stress gradients should be weak. Chen et al. simulated this experiment using a version of *FUNWAVE* and the wave generation algorithm of Wei et al. (1999) which was extended to cover periodic longshore conditions. A TMA directional wave spectrum was used to provide input conditions (improved simulations using actual measured directional spectra are presently under review for publication). Fig. 16 illustrates a snapshot of the surface wave field over the simulated area in panel (a). Refraction of the wave pattern, which is propagating from the lower right, is evident, as is crest splitting in several locations as waves pass over the bar crest. Panel (b) illustrates the time-averaged mean currents in the area. Chen et al. show that there is a time-steady net longshore pressure gradient over the stretch of beach in the vicinity of the current measurements, and thus the strong longshore current in the trough is at least partially hydraulically driven. Note that time averaged currents in the Boussinesq model do not reproduce a sufficiently strong undertow, even though the velocity being averaged is located near mid depth. This deficiency is also noted in results of Madsen et al. (1997), and occurs because there is no explicit treatment of breaking wave roller volume in the volume conservation equation (9). This deficiency is removed in the 1-D cross-shore model of Veeramony and Svendsen (2000), which recovers undertow
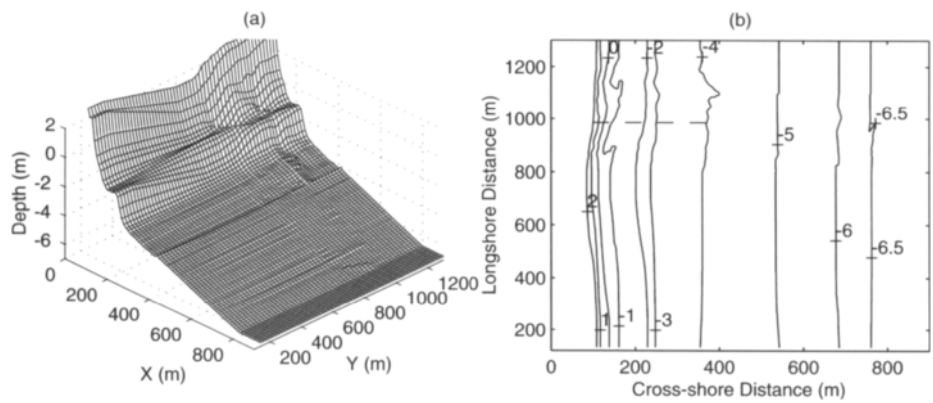
Figure 15. The bathymetry at the Field Research Facility, Duck, NC, Oct. 10, 1992: (a) topography, (b) depth contours. (From Chen et al., 2000b. Reproduced with permission of ASCE).
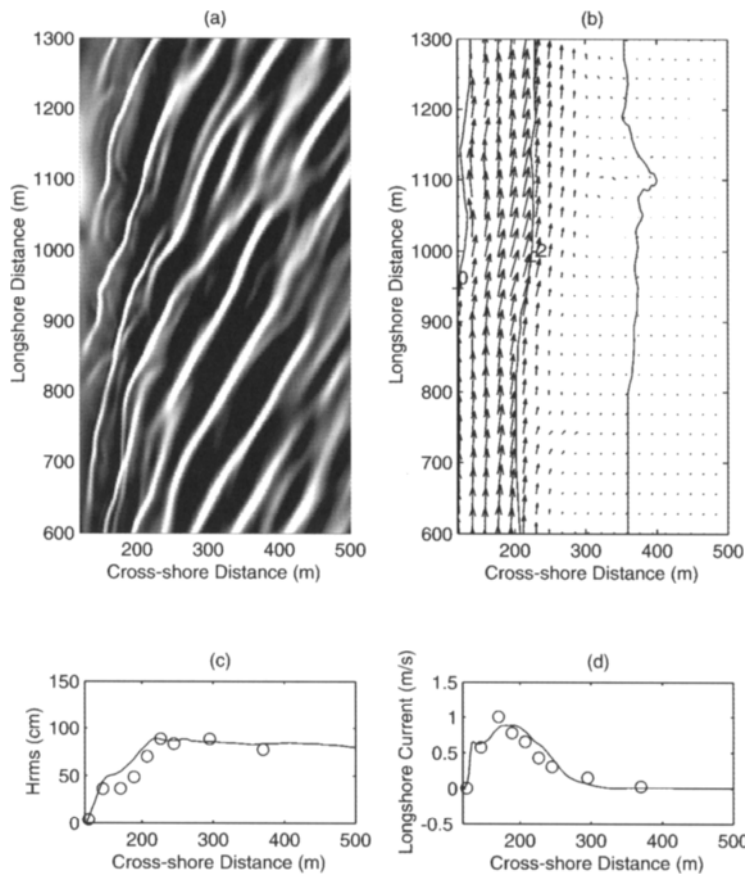
Figure 16. Model results: (a) snapshot of computed free surface elevation, light areas indicate wave crests; (b) computed time-averaged longshore current. (From Chen et al., 2000b. Reproduced with permission of ASCE).

values reasonably well, but the correction still remains to be made in most two-dimensional (2-D) models. Overall, results for longshore currents agree well with data in both laboratory and field settings, providing encouragement that the models are ready to use in realistic settings.

4.2. Shear Waves

Based on observations by Oltman-Shay et al. (1989), Bowen and Holman (1989) examined the linear stability problem for longshore currents and showed that currents are likely to be unstable for a range of realistic conditions. Özkan-Haller and Kirby (1999) carried out numerical simulations of the same experiment using a radiation stress formulation, and have illustrated the growth to finite amplitude of the instabilities, or *shear waves*. They have shown that the presence of shear waves contributes to the cross-shore mixing that leads to the determination of the longshore current profile, and they have shown that the increase or decrease of imposed dispersive mixing (i.e., the mechanism of Svendsen and Putrevu, 1994) leads to a corresponding decrease or increase in the energetics of the shear wave climate, in such a way that the overall longshore current profile is insensitive to the relative importance of the two mechanisms. This result has not been explained to date, or examined fully in other modeling schemes.

Since shear waves are essentially unsteady motions, it is not immediately clear how to separate them from the incident wave field in a time domain simulation. Chen et al. (1999) approached this problem, in the context of rip currents, by applying a time average over several wave periods in order to suppress the incident wave signature in the modeled velocity field. The resulting filtered velocity field was then differentiated to provide a vertical vorticity field. During this study, Chen et al. discovered that a vorticity field constructed directly from the instantaneous horizontal velocities was similar to the wave-averaged field. In particular, the signature of incident waves in the instantaneous vorticity field is very slight, even after interaction with the underlying vortical current field, and is mainly limited to strong local bottom friction events associated with the passage of wave crests. At the same time, the instantaneous vorticity plots showed more detail in the structure of vortical features such as eddies, since these were not being subjected to an arbitrary low-pass filter.

Fig. 17 shows an overlay of a wave-averaged current field and resulting derived vorticity field for the October 10, 1990 DELILAH case described above. For the field cases, the choice of an averaging period is not obvious since the wave field is unsteady in time. Averages here are over a period corresponding to 10 peak wave periods. Vorticity computed from the instantaneous flow field is illustrated in the bottom panel, and shows an energetic flow field associated with growth of instabilities and shedding of eddies to the region offshore of the surf zone (to the right in each panel). Ongoing studies are examining whether these depictions of the flow field are consistent with more detailed array measurements of currents in the field, primarily using data from the Sandyduck experiment in 1997.

4.3. Rip Currents

Haller and Dalrymple (2001) performed a laboratory study of a rip current generated on a beach with a fixed channel in an otherwise longshore-uniform bar. The rip was observed to be unstable, leading to lateral motion of the rip both in the rip channel and offshore. An instability analysis provided information on the time scales of fluctuations and the downstream evolution of mean current profiles which agreed qualitatively with laboratory observations.

Chen et al. (1999) examined the experiment of Haller and Dalrymple using the *FUNWAVE* code. The Boussinesq model was shown to reproduce most features of the laboratory experiment, although it was impossible to perform model runs long enough to examine whether the longest time scales observed in the fluctuating laboratory flow field (on the order of 100 seconds) were reproduced in model simulations. Fig. 18 illustrates the state of the wave-averaged flow field soon after the initiation of breaking over the bar crest in the simulation. The position of the longshore bar and the
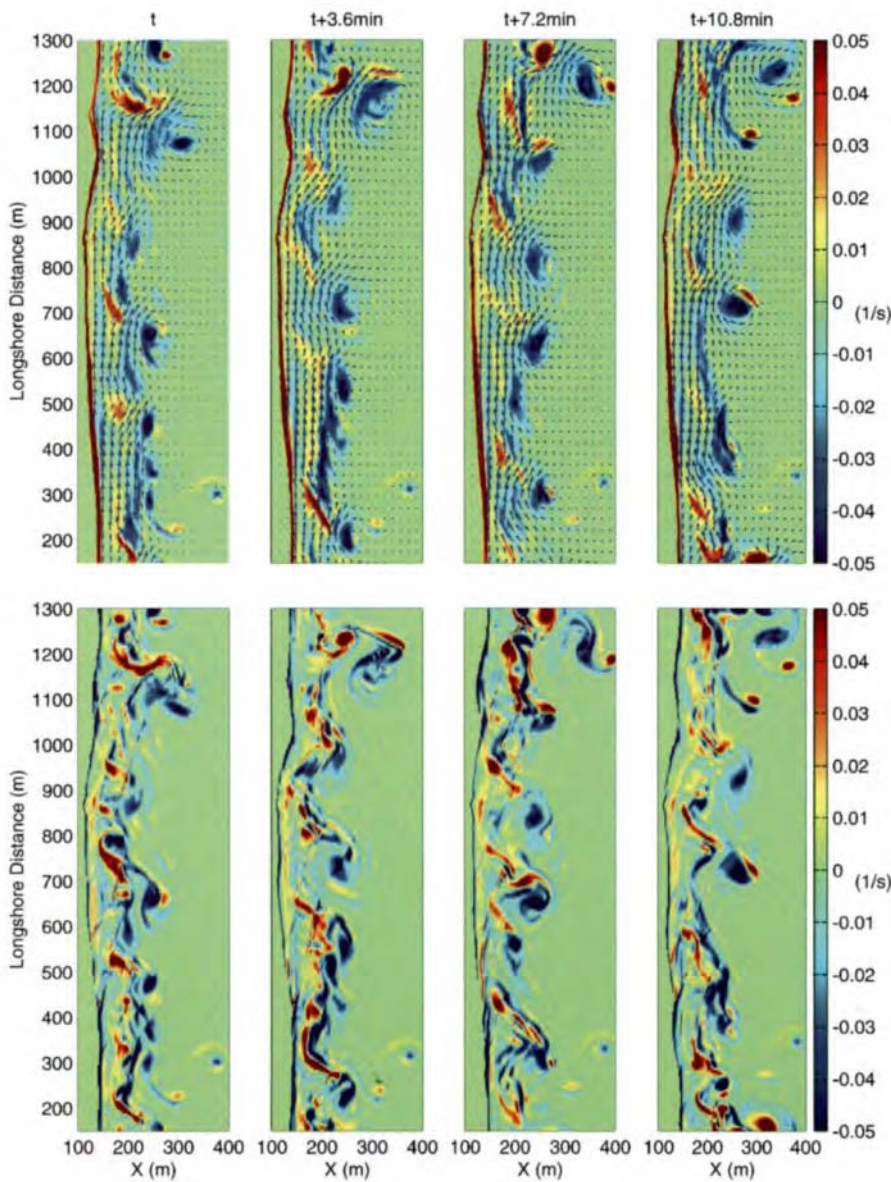
Figure 17. Time sequence of vorticity field, indicating presence of shear waves. Top panels display velocities and vorticity averaged over ten peak wave periods. Bottom panels display instantaneous vorticity. (From Chen et al., 2000b. Reproduced with permission of ASCE).

rip channel are outlined by dashed lines in each of the three panels. The middle and lower panel show the presence of strong, localized vorticies fixed at the transition between bar crest and deep rip channel. These are presumably driven at these locations by the mechanism described by Peregrine (1998), and are responsible for the initiation of the rip current jet, which is driven primarily by the
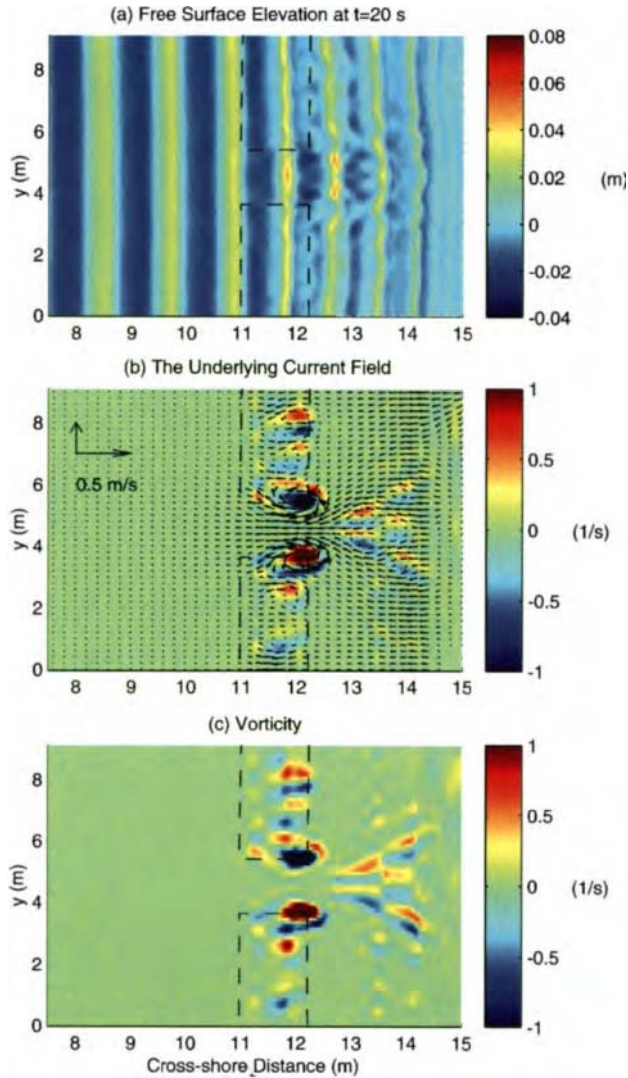
Figure 18. A snapshot of (a) the computed free surface elevation, (b) the underlying current field and associated mean vorticity, and (c) the instantaneous vorticity field at $t = 20s$, shortly after initiation of wave breaking over the longshore bar. Dashed lines indicate outline of longshore bar geometry in the laboratory. (From Chen et al., 1999, copyright [1999] by the American Geophysical Union).

dipole forcing provided by the pair of counter-rotating eddies. As the current field evolves further, these vortex pairs are ejected as coherent eddy pairs and advected offshore by the instantaneous jet, after which subsequent eddy pairs form and are also ejected. A portion of such a sequence is illustrated in Fig. 19. Fig. 20 shows a comparison of long-time averages of cross-shore velocities along 4 longshore transects. The extreme unsteadiness of the rip current leads to a rapid decay of the time-mean cross-shore velocity offshore of the rip channel. This result is deceptive as a measure of
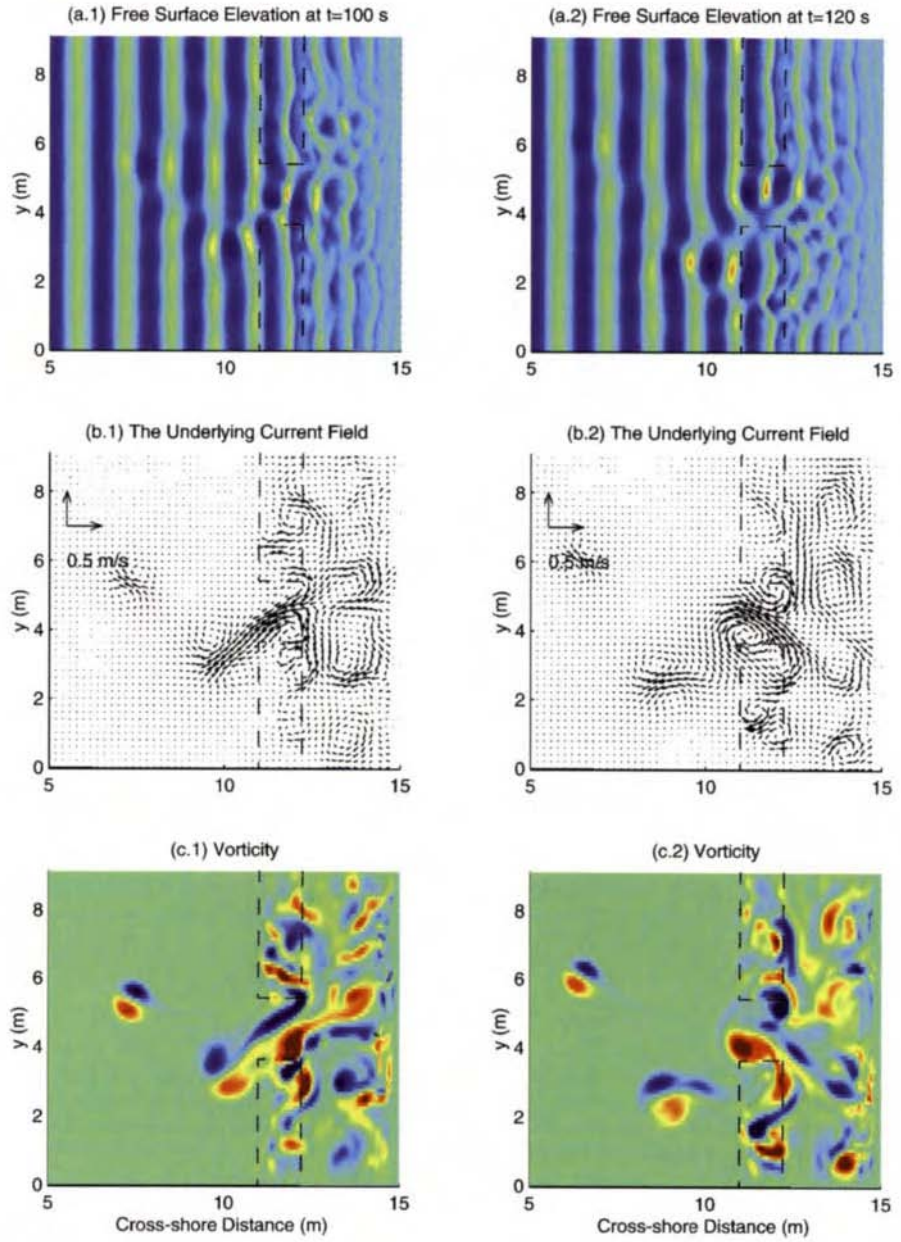
Figure 19. Snapshots of (a) the computed free surface elevation, (b) the underlying current field, and (c) vorticity at (left) $t = 100s$ and (right) $t = 120s$, illustrating unsteady behavior of rip current jet. (From Chen et al., 1999, copyright [1999] by the American Geophysical Union).
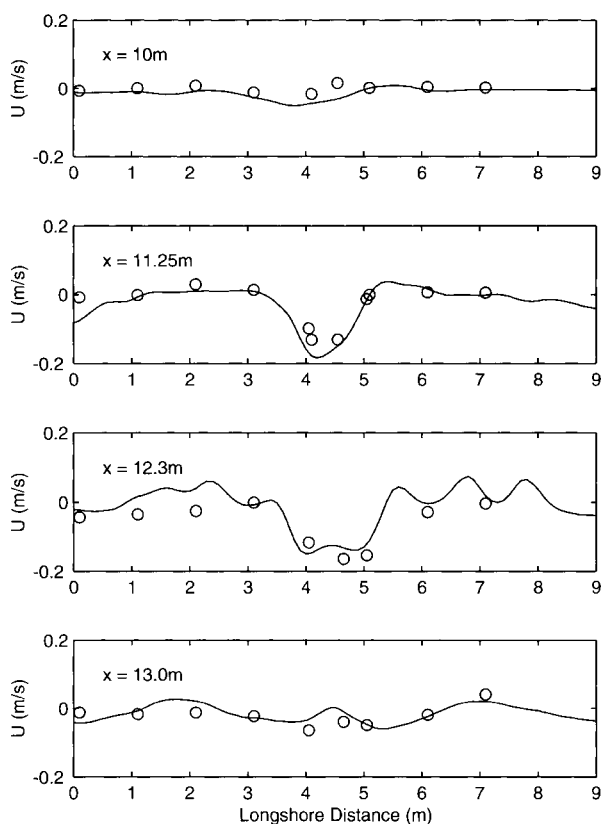
Figure 20. Comparison of computed (solid lines) and measured (circles) cross-shore mean velocity, resulting from time averages of velocities in the unsteady rip current illustrated in Figs. 18 and 19. (From Chen et al., 1999, copyright [1999] by the American Geophysical Union).

rip strength and must be tempered with the indication of the strength of the instantaneous flow, as indicated in Fig. 19.

Overall, Boussinesq models have performed quite well in comparison to both laboratory and field measurements, in situations where flow fields are strongly affected by instability mechanisms and become extremely complex. Further work to examine the energetics of shear wave climates and the mixing of tracers in the cross-shore direction needs to be carried out. In addition, the application of Boussinesq models to the problem of sediment transport and evolution of coastal morphology is underway, and will be a fertile area of work for the next several years.

5. WAVES ON VERTICALLY SHEARED CURRENTS

Water in coastal regions can be stratified due to the presence of net freshwater runoff, and it is therefore not uncommon to see tidal currents which are sheared over the vertical. The presence of vertical shear greatly complicates the development of appropriate propagation models, since the use of a velocity potential is no longer valid except for the special case of horizontal vorticity components which are uniform over depth (linear current shear).

For the case of propagation in one horizontal dimension, a formulation in terms of a scalar stream function can be employed as in the wave breaking model of Veeramony and Svendsen, described above. This approach has been explored by Rego et al. (2001). Starting with the Poisson equation (82), Rego et al. developed a fully nonlinear Boussinesq type equation to $O(\mu^2)$ using a dependent variable $\bar{u}_\alpha$ defined as the horizontal velocity at reference elevation z_α. For the case of linearized, periodic waves and an imposed current shear, the rather complex model equations yield a dispersion relation given by (in dimensional form)

$$\hat{\omega}^2[1 - \alpha(kh)^2] = (gk - \hat{\omega}\gamma_0)kh[1 - (\alpha + \frac{1}{3})(kh)^2] + \hat{\omega}k(\gamma_1 + k^2\gamma_2)$$

$$-\hat{\omega}kh\gamma_0[1 - \alpha(kh)^2] \tag{95}$$

where the intrinsic frequency is given by

$$\hat{\omega} = \omega - ku_s^c \tag{96}$$

and where ω is absolute frequency, u_s^c is the current velocity at $z = 0$,

$$\gamma_0 = \frac{1}{h} \int_{-h}^{0} \xi \, dz \qquad \gamma_1 = \frac{2}{h} \int_{-h}^{0} \int_{-h}^{z} \xi \, dz^2 \tag{97}$$

and

$$\gamma_2 = \frac{1}{h} \left\{ \int_{-h}^{0} \left[\left((z+h)^2 - (z_\alpha + h)^2 \right) \int_{-h}^{z} \xi \, dz \right] dz + \int_{-h}^{0} \int_{z}^{0} \left((z+h) \int_{-h}^{z} \xi \, dz \right) dz^2 \right\} \tag{98}$$

The accuracy of the resulting dispersion relation was checked for several cases by comparing to numerical solutions of the Rayleigh equation following the method of Fenton (1973). Fig. 21 shows
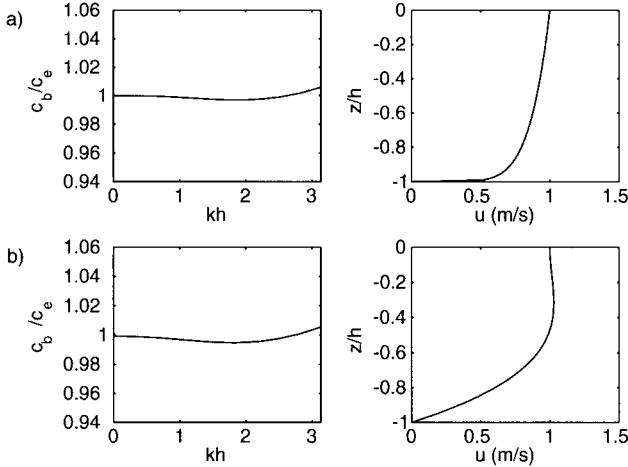
Figure 21. Normalized phase velocity (model phase velocity c_b divided by exact phase velocity c_e calculated from the Rayleigh equation) and associated current profiles: a) 1/7 power law, b) cubic polynomial. (From Rego et al., 2001. Reproduced with permission of ASCE).

results for the case of a 1/7 power law profile and a profile given by a cubic polynomial. The results indicate that the model dispersion relation retains accuracy over a range of wave numbers comparable to the (2,2) Padé dispersion relation for the no-current (or uniform over depth current) case.

As with the wave breaking model of Veeramony and Svendsen (2000), the use of the scalar stream function in the present case makes a general extension to two horizontal dimensions difficult. A way around this can be seen by noting that the derivative of equation (82) with respect to x gives

$$\mu^2 w_{xx} + w_{zz} = \xi_x \tag{99}$$

giving a problem formulated in terms of vertical velocity w. Starting from the general three-dimensional Euler equations, it is straightforward to show that this relation is generalized by

$$\mu^2 \nabla^2 w + w_{zz} = \nabla \cdot \boldsymbol{\xi} \tag{100}$$

where $\boldsymbol{\xi}$ is now a vector formed by the two horizontal components of the general three-dimensional vorticity vector. Shen (2001) has explored the use of equation (100) as a starting point for deriving Boussinesq model equations.

6. MISCELLANEOUS APPLICATIONS

6.1. Depth Inversion

The question of whether the spatial pattern of water depths in the surf zone can be deduced from images of the water surface has been with us since the early days of military amphibious operations. Recently, several successful video-based techniques have been described for waves in slowly varying depth in open water (Dugan et al., 2001) or in the surf zone (Stockdon and Holman, 2000). Each of these methods depends on having dense spatial information and long time series so that both frequency and wave number content of the signal can be determined. The direct need for a model-based simulation is then avoided by using the linear wave dispersion relation to relate frequency to wave number in order to determine the unknown water depth. Methods of this type are not readily applicable to data streams obtained during a rapid overflight of the target area, as in typical airborne INSAR or LIDAR measurements, and thus the question of using a model to determine the relation between spatial and temporal information arises. Kennedy et al. (2000b) considered the question of whether the Boussinesq model could be used as a bridge between two images of dynamic variables with small separation in time. Considering an artificial example where both $\mathbf{u}_\alpha$ and η are given at two times over a dense spatial image, they developed a realizable method in which the model is initialized with the first image and an assumed bathymetry, and then integrated forward in time to the time of the second image. The mismatch between computed and measured dynamic variables at the time of the second image is used as a basis for iterative correction of the bathymetry. Kennedy et al. showed that the iteration converged rapidly and that separations on the order of 1/4 to 1/3 of a dominant wave period were adequate. Subsequently, Misra et al. (2003) have considered a more realistic case where one or more dynamic variables are missing.

6.2. Tsunami Propagation and Runup

An important and rapidly growing area of Boussinesq model application is in the modeling of the generation, propagation and runup of tsunamis. This process has traditionally been approached using models based on nonlinear shallow water equations (see, for example, Synolakis et al., 2002), but there are obvious advantages to using Boussinesq models, particularly in the better representation of vertical flow structure near source regions, a better prediction of wave crest geometry and crest
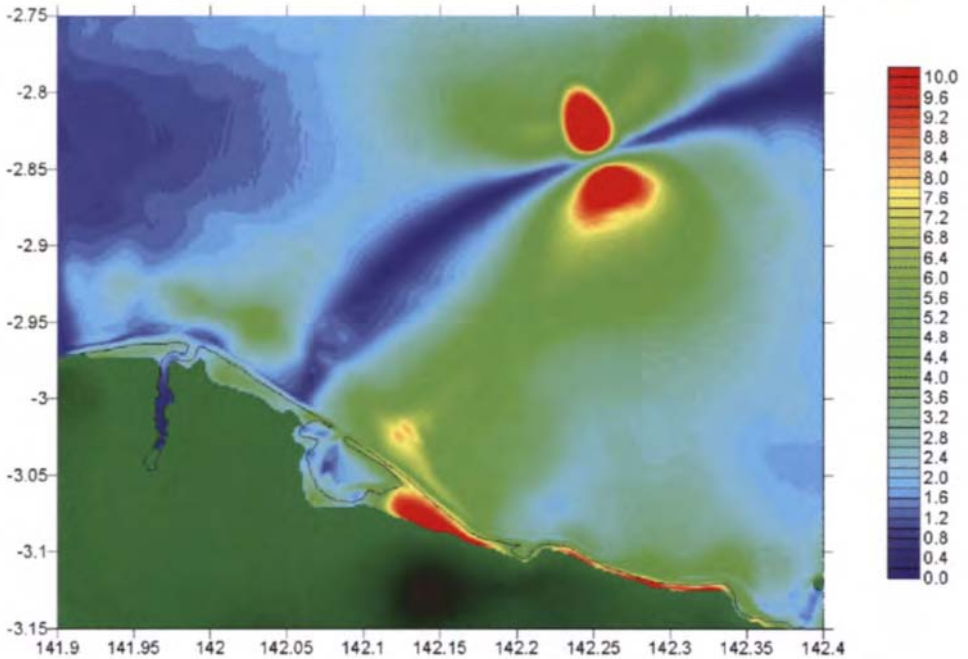
Figure 22. Model estimates of maximum local water surface elevations during July 17, 1998 Papua New Guinea tsunami event. Slump region is in vicinity of strong surface displacements offshore (upper right in picture). Shoreline is indicated by black line. Results indicate inundation beyond the mean shoreline, with runup amplitudes in excess of 10 m in the region East of Sissano Lagoon, the main embayment in the figure (after Watts et al., 2002).

disintegration during propagation over complex topography, and in the modeling of accumulated frequency dispersion effects in ocean-basin scale propagation problems. Applications of this sort are in their infancy, but will play a prominent role in the future. Lynett and Liu (2002) have presented an initial study of the generation of tsunamis due to bottom slumping, concentrating on one-dimensional and symmetric two-dimensional bottom motions. Watts et al. (2002) have described a modeling system called *GEOWAVE*, which consists of a modified version of the *FUNWAVE* model coupled to a three-dimensional nearfield tsunami source model. Fig. 22 shows an example calculation based on a slump-type source for the Papua New Guinea tsunami of July 17, 1998. The figure indicates maximum surface elevation occurring at each location in the modeled domain, and indicates runup and inundation of the shoreline facing the source region. Results of this study are preliminary, and detailed quantitative comparisons to estimated runup elevations in the field will be described elsewhere.

7. CONCLUSIONS

The development of Boussinesq models for application to coastal hydrodynamics problems has reached a level of maturity that would probably not have been expected a decade ago. The model formulation has been extended to allow for wave propagation in almost all finite water depths, rendering the notion of the models being only applicable in shallow water obsolete. A wide range of associated physical phenomena have been incorporated in model formulations, making it possible to apply Boussinesq model technology to the surf zone. The technology is also beginning to supplant

the nonlinear shallow water equations (NLS) in a number of areas where the NLS has long been the dominant player; in calculation of wave runup and overtopping on coastal structures and in calculation of tsunami propagation and inundation. In addition, the application of Boussinesq models to problems of coastal sediment transport is just beginning (see Chapter 10). The long computational times involved in present calculations still hinder this line of research, but increasing computer capacity and speed will make it possible, in time, to approach the problem of morphological planform evolution with direct application of Boussinesq model codes.

It is apparent from several of the sections above that the existing versions of higher-accuracy Boussinesq models are dauntingly complex in form, and it becomes relevant to address the question of whether further development along these lines is warranted relative to direct utilization of the Navier-Stokes equations. This concern is well placed. However, there is a great deal of room in numerical efficiency between the practical $O(\mu^2)$ models described above and any competing formulation of the Navier-Stokes or Euler equations in three-dimensions, and thus the models described here are likely to be the basis for practical computations for a number of years. Indeed, the examples of Navier-Stokes based wave propagation calculations which are presently available (for example, Casulli, 1999 or Lin and Li, 2002) show results for the shoaling example of Beji and Battjes (1993) which are less accurate than corresponding Boussinesq calculations, even using $O(\mu^2)$ models for comparison. It is likely that the typical second-order accurate numerical schemes used in Navier-Stokes solvers to date are a limiting factor in obtaining accurate results, indicating a need for further development in this area.

ACKNOWLEDGMENTS

LIST OF SYMBOLS

a_0	—	wave amplitude scale
c	—	wave phase speed
c_m	—	coefficient in expression for vorticity in Smagorinsky scheme
f	—	bottom friction factor
g	—	gravitational constant
$k, \mathbf{k}$	—	scalar wave number, vector wave number
k_0	—	wave number (or inverse wavelength) scale
$h(\mathbf{x})$	—	still water depth
h_0	—	water depth scale
$H(\mathbf{x}, t) = h + \delta\eta$	—	total instantaneous water depth
$\mathbf{M}(\mathbf{x}, t)$	—	horizontal depth-integrated volume flux vector
Q	—	horizontal volume flux in 1-D theory
$\mathbf{R_b}, \mathbf{R_s}, \mathbf{R_f}$	—	wave breaking, subgrid mixing and bottom friction terms in horizontal momentum equations
t	—	time coordinate
$\mathbf{u} = (u, v)$	—	horizontal velocity vector

$\mathbf{u}_\alpha = (u_\alpha, v_\alpha)$	—	horizontal velocity at reference elevation
$\tilde{\mathbf{u}} = (\tilde{u}, \tilde{v})$	—	weighted horizontal velocity in Gobbi's theory
$\mathbf{V}_1, \mathbf{V}_2$	—	$O(\mu^2)$, dispersive terms in Boussinesq equations
w	—	vertical velocity
$\mathbf{x} = (x, y)$	—	horizontal coordinate
$\Delta x, \Delta y$	—	finite difference grid spacings
z	—	vertical coordinate
z_a, z_b, z_α	—	reference elevations
α	—	dispersion enhancement parameter, see equation (17)
β	—	weighting factor in theory of Gobbi
$\delta = a_0/h_0$	—	nonlinearity parameter
$\eta(\mathbf{x}, t)$	—	water surface elevation
$\mu = k_0 h_0$	—	dispersion parameter
ν	—	viscosity coefficient
ν_b	—	eddy viscosity coefficient in Zelt-type breaker model
ν_s	—	eddy viscosity coefficient in Smagorinsky subgrid scheme
ω	—	wave angular frequency
ω, ω_1	—	total and $O(\mu^2)$ contribution to vertical vorticity vector
$\phi(\mathbf{x}, z, t)$	—	velocity potential
$\phi_a, \phi_b, \phi_\alpha(\mathbf{x}, t)$	—	velocity potential at reference elevations
$\tilde{\phi}(\mathbf{x}, t)$	—	weighted velocity potential in Gobbi's theory
$\phi^{(n)}$	—	components of series solution for ϕ
$\psi(x, z, t)$	—	scalar stream function
ξ	—	scalar magnitude of horizontal vorticity
$\boldsymbol{\xi} = (\xi_x, \xi_y)$	—	projection of total vorticity vector in horizontal plane
ζ	—	parameter in Kennedy's moving reference elevation model
$\nabla = \left(\dfrac{\partial}{\partial x}, \dfrac{\partial}{\partial y} \right)$	—	horizontal gradient operator

REFERENCES

Agnon, Y., Madsen, P.A., and Schäffer, H.A., 1999. A new approach to high-order Boussinesq models. Journal of Fluid Mechanics, 399: 319–333.

Basco, D.R., 1983. Surfzone currents. Coastal Engineering, 7: 331–355.

Beji, S., and Battjes, J.A., 1993. Experimental investigations of wave propagation over a bar. Coastal Engineering, 19: 151–162.

Bowen, A.J., and Holman, R.A., 1989. Shear instabilities of the mean longshore current. 1. Theory. Journal of Geophysical Research, 94: 18,023–18,030.

Brackbill, J.U., and Saltzman, J.S., 1982. Adaptive zoning for singular problems in two dimensions. Journal of Computational Physics, 46: 342–368.

Casulli, V., 1999. A semi-implicit finite difference method for non-hydrostatic, free surface flows. International Journal for Numerical Methods in Fluids, 30: 425–440.

Chawla, A., and Kirby, J.T., 2000. A source function method for generation of waves on currents in Boussinesq models. Applied Ocean Research, 22: 75–83.

Chen, Q., Dalrymple, R.A., Kirby, J.T., Kennedy, A.B. and Haller, M.C., 1999. Boussinesq modeling of a rip current system. Journal of Geophysical Research, 104: 20,617–20,637.

Chen, Q., Kirby, J.T., Dalrymple, R.A., Kennedy, A.B., and Chawla, A., 2000a. Boussinesq modeling of wave transformation, breaking and runup. II: 2-D. Journal of Waterway, Port, Coastal and Ocean Engineering, 126: 48–56.

Chen, Q., Kirby, J.T., Dalrymple, R.A., Kennedy, A.B., Thornton, E.B., and Shi, F., 2000b. Boussinesq modeling of waves and longshore currents under field conditions. Proceedings of the 27th International Conference on Coastal Engineering, ASCE, pp. 651–663.

Dingemans, M.W., 1997. Water Wave Propagation over Uneven Bottoms. Part 2—Non-linear Wave Propagation. Singapore: World Scientific Publishing Co.

Dommermuth, D.G., and Yue, D.K.P., 1987. A high-order spectral method for the study of nonlinear gravity waves. Journal of Fluid Mechanics, 184: 267–288.

Dugan, J.P., Piotrowski, C.C., and Williams, J.Z., 2001. Water depth and surface current retrievals from airborne optical measurements of surface gravity wave dispersion. Journal of Geophysical Research, 106: 16,903–16,915.

Fenton, J.D., 1973. Some results for surface gravity waves in shear flows. Journal of the Institute of Mathematics and its Applications, 12: 1–20.

Gobbi, M.F., and Kirby, J.T., 1999. Wave evolution over submerged sills: Tests of a high-order Boussinesq model. Coastal Engineering, 37: 57–96.

Gobbi, M.F., Kirby, J.T., and Wei, G., 2000. A fully nonlinear Boussinesq model for surface waves. II. Extension to $O(kh^4)$. Journal of Fluid Mechanics, 405: 181–210.

Haller, M.C., and Dalrymple, R.A., 2001. Rip current instabilities. Journal of Fluid Mechanics, 433: 161–192.

Hommel, D., Shi, F., Kirby, J.T., Dalrymple, R.A., and Chen, Q., 2000. Modelling of a wave-induced vortex near a breakwater. Proceedings of the 27th International Conference on Coastal Engineering, ASCE, pp. 2318–2330.

Hsiao, S.-C., Liu, P.L.-F., and Chen, Y., 2002. Nonlinear water waves propagating over a permeable bed. Proceedings: Mathematical, Physical & Engineering Sciences (The Royal Society), 458 (2022): 1291–1322.

Kennedy, A.B, Chen, Q., Kirby, J.T., and Dalrymple, R.A., 2000a. Boussinesq modeling of wave transformation, breaking and runup. I: 1-D. Journal of Waterway, Port, Coastal and Ocean Engineering, 126: 39–47.

Kennedy, A.B., Dalrymple, R.A., Kirby, J.T., and Chen, Q., 2000b. Determination of inverse depths using direct Boussinesq modelling. Journal of Waterway, Port, Coastal and Ocean Engineering, 126: 206–214.

Kennedy, A.B., Kirby, J.T., Chen, Q., and Dalrymple, R.A., 2001. Boussinesq-type equations with improved nonlinear performance. Wave Motion, 33: 225–243.

Kennedy, A.B., Kirby, J.T., and Gobbi, M.F., 2002. Simplified higher order Boussinesq equations. 1: Linear simplifications. Coastal Engineering, 44: 205–229.

Kirby, J.T., 1997. Nonlinear, dispersive long waves in water of variable depth. In: Hunt, J.N. (Editor), Gravity Waves in Water of Finite Depth. Advances in Fluid Mechanics, Vol. 10, pp. 55–125. Southampton, UK: Computational Mechanics Publications.

Kirby, J.T., and Dalrymple, R.A., 1984. Surfzone Currents, by D.R. Basco—Discussion. Coastal Engineering, 8: 387–392.

Kirby, J.T., Wei, G., Chen, Q., Kennedy, A.B., and Dalrymple, R.A., 1998. FUNWAVE 1.0. Fully nonlinear Boussinesq wave model. Documentation and user's manual. Report CACR-98-06. Newark, DE: Center for Applied Coastal Research, Department of Civil and Environmental Engineering, University of Delaware.

Li, Y.S., Liu, S.X., Yu, Y.X., and Lai, G.Z., 1999. Numerical modeling of Boussinesq equations by finite element method. Coastal Engineering, 37: 97–122.

Li, Y.S., and Zhan, J.M., 2001. Boussinesq-type model with boundary-fitted coordinate system. Journal of Waterway, Port, Coastal and Ocean Engineering, 127: 152–160.

Lin, P., and Li, C.W., 2002. A σ-coordinate three-dimensional numerical model for surface wave propagation. International Journal for Numerical Methods in Fluids, 38: 1045–1068.

Liu, P.L.-F., 1994. Model equations for wave propagations from deep to shallow water. In: Liu, P.L-F. (Editor), Advances in Coastal and Ocean Engineering, Vol. 1, pp. 125–157. Singapore: World Scientific Publishing Co.

Lynett, P.J., and Liu, P.L.-F., 2002. A numerical study of submarine landslide generated waves and runup. Proceedings of the Royal Society of London A, 458: 2885–2910.

Lynett, P.J., Wu, T.-R., and Liu, P.L.-F., 2002. Modeling wave runup with depth-integrated equations. Coastal Engineering, 46: 89–107.

Madsen, P.A., Bingham, H.B., and Schäffer, H.A., 2003. Boussinesq-type formulations for fully non-linear and extremely dispersive water waves: Derivation and analysis. Proceedings: Mathematical, Physical & Engineering Sciences (The Royal Society), 459 (2033): 1075–1104.

Madsen, P.A., Murray, R., and Sørensen, O.R., 1991. A new form of Boussinesq equations with improved linear dispersion characteristics. Part 1. Coastal Engineering, 15: 371–388.

Madsen, P.A., and Schäffer, H.A., 1998. Higher-order Boussinesq-type equations for surface gravity waves: Derivation and analysis. Philosophical Transactions of the Royal Society of London A, 356: 3123–3184.

Madsen, P.A., and Schäffer, H.A., 1999. Review of Boussinesq-type equations for surface gravity waves. In: Liu, P.L-F. (Editor), Advances in Coastal and Ocean Engineering, Vol. 5, pp. 1–94. Singapore: World Scientific Publishing Co.

Madsen, P.A., Sørensen, O.R., and Schäffer, H.A., 1997. Surfzone dynamics simulated by a Boussinesq type model. Part 1: Model description and cross-shore motion of regular waves. Coastal Engineering, 32: 255–288.

Mase, H., 1995. Frequency downshift of swash oscillation compared to incident waves. Journal of Hydraulic Research, 33: 397–411.

Misra, S., Kennedy, A.B., and Kirby, J.T., 2003. An approach to determining nearshore bathymetry using remotely sensed ocean surface dynamics. Coastal Engineering, 47: 265–293.

Nwogu, O., 1993. Alternative form of Boussinesq equations for nearshore wave propagation. Journal of Waterway, Port, Coastal and Ocean Engineering, 119: 618–638.

Nwogu, O., and Demirbilek, Z., 2001. BOUSS-2D: A Boussinesq wave model for coastal regions and harbors. ERDC/CHL TR-01-25. Vicksburg, MS: Coastal and Hydraulics Laboratory, USACOE Engineer Research and Development Center.

Oltman-Shay, J., Howd, P.A., and Birkemeier, W.A., 1989. Shear instabilities of the mean longshore current. 2. Field observations. Journal of Geophysical Research, 94: pp. 18,031–18,042.

Özkan-Haller, H.T., and Kirby, J.T., 1997. A Fourier-Chebyshev collocation method for the shallow water equations including shoreline runup. Applied Ocean Research, 19: 21–34.

Özkan-Haller, H.T., and Kirby, J.T., 1999. Nonlinear evolution of shear instabilities of the longshore current: A comparison of observations and computations. Journal of Geophysical Research, 104: 25,953–25,984.

Peregrine, D.H., 1998. Surf zone currents. Theoretical and Computational Fluid Dynamics, 10: 295–309.

Rego, V.S., Kirby, J.T., and Thompson, D., 2001. Boussinesq waves on flows with arbitrary vorticity. Proceedings of the 4th International Symposium on Ocean Wave Measurement and Analysis, Waves'01, ASCE, pp. 904–913.

Roddier, D., and Ertekin, R.C., 1999. Diffraction and remodelization of solitons around a false wall. Chaos, Solitons and Fractals, 10: 1221–1240.

Schäffer, H.A., and Madsen, P.A., 1995. Further enhancements of Boussinesq-type equations. Coastal Engineering, 26: 1–14.

Schäffer, H.A., Madsen, P.A., and Deigaard, R., 1993. A Boussinesq model for waves breaking in shallow water. Coastal Engineering, 20: 185–202.

Shen, C.Y., 2001. Constituent Boussinesq equations for waves and currents. Journal of Physical Oceanography, 31: 850–859.

Shi, F., Dalrymple, R.A., Kirby, J.T., Chen, Q., and Kennedy, A., 2001a. A fully nonlinear Boussinesq model in generalized curvilinear coordinates. Coastal Engineering, 42: 337–358.

Shi, F., Kirby, J.T., Dalrymple, R.A., and Chen, Q., 2001b. A curvilinear Boussinesq model and its application. Proceedings of the 4th International Symposium on Ocean Wave Measurement and Analysis, Waves'01, ASCE, pp. 844–853.

Shields, J.J., and Webster, W.C., 1988. On direct methods in water-wave theory. Journal of Fluid Mechanics, 197: 171–199.

Sørensen, O.R., and Sørensen, L.S., 2000. Boussinesq type modelling using unstructured finite element technique. Proceedings of the 27th International Conference on Coastal Engineering, ASCE, pp. 190–202.

Stockdon, H.F., and Holman, R.A., 2000. Estimation of wave phase speed and nearshore bathymetry from video imagery. Journal of Geophysical Research, 105: 22,105–22,033.

Svendsen, I.A., 1984. Wave heights and setup in a surfzone. Coastal Engineering, 8: 303–329.

Svendsen, I.A., and Putrevu, U., 1994. Nearshore mixing and dispersion. Proceedings of the Royal Society of London A, 445: 1–16.

Svendsen, I.A., Veeramony, J., Bakunin, J., and Kirby, J.T., 2000. The flow in weak turbulent hydraulic jumps. Journal of Fluid Mechanics, 418: 25–57.

Synolakis, C.E., Bardet, J.-P., Borrero, J.C., Davies, H.L., Okal, E.A., Silver, E.A., Sweet, S., and Tappin, D.R., 2002. The slump origin of the 1998 Papua New Guinea tsunami. Proceedings of the Royal Society of London A, 458: 763–789.

Tanaka, M., 1986. The stability of solitary waves. Physics of Fluids, 29: 650–655.

Tao, J., 1984. Numerical modelling of wave runup and breaking on the beach. Acta Oceanologica Sinica, 6: 692–700 (in Chinese).

Veeramony, J., and Svendsen, I.A., 2000. The flow in surf-zone waves. Coastal Engineering, 39: 93–122.

Walkley, M., and Berzins, M., 1999. A finite element method for the one-dimensional extended Boussinesq equations. International Journal for Numerical Methods in Fluids, 29: 143–157.

Warsi, Z.U.A., 1993. Fluid Dynamics: Theoretical and Computational Approaches. Boca Raton, FL: CRC Press.

Watts, P., Grilli, S.T., and Kirby, J.T., 2002. Simulation of landslide tsunamis. Case studies using a Boussinesq model coupled to a fully nonlinear tsunami source model. Proceedings of the 27th European Geophysical Society General Assembly, in press.

Wei, G., and Kirby, J.T., 1995. A time-dependent numerical code for extended Boussinesq equations. Journal of Waterway, Port, Coastal and Ocean Engineering, 120: 251–261.

Wei, G., Kirby, J.T., Grilli, S.T., and Subramanya, R., 1995. A fully nonlinear Boussinesq model for surface waves. I. Highly nonlinear, unsteady waves. Journal of Fluid Mechanics, 294: 71–92.

Wei, G., Kirby, J.T., and Sinha, A., 1999. Generation of waves in Boussinesq models using a source function method. Coastal Engineering, 36: 271–299.

Woo, S.-B., and Liu, P.L.-F., 2001. A Petrov-Galerkin finite element model for one-dimensional fully non-linear and weakly dispersive wave propagation. International Journal for Numerical Methods in Fluids, 37: 541–575.

Yoon, S.B., and Liu, P.L.-F., 1989. Interactions of currents and weakly nonlinear water waves in shallow water. Journal of Fluid Mechanics, 205: 397–419.

Zelt, J.A., 1991. The runup of nonbreaking and breaking solitary waves. Coastal Engineering, 15: 205–246.

This Page Intentionally Left Blank

Chapter 2

Frequency Domain Wave Models in the Nearshore and Surf Zones

James M. Kaihatu

Ocean Dynamics and Prediction Branch, Oceanography Division (Code 7322)
Naval Research Laboratory, Stennis Space Center, MS 39529-5004

1. INTRODUCTION

In deep water ($kh >> 1$, where k is the wave number and h the water depth), second-order wave nonlinearity can be described as a small correction to the underlying linear wave. Perturbation expansions in wave steepness $\epsilon = ka$, where a is the wave amplitude, are used (Phillips, 1960), and at second-order only non-resonant (bound) waves are possible among triads of wave frequencies. Thus the interacting waves with the frequency-vector wave number combination $(\omega_1, \mathbf{k}_1)$ and $(\omega_2, \mathbf{k}_2)$ excite secondary waves at $(\omega_1 + \omega_2, \mathbf{k}_1 + \mathbf{k}_2)$, but these secondary wave amplitudes always remain small relative to the primary amplitudes. At the next order, resonant interaction occurs between quartets of waves, with the resultant slow energy exchange between the interacting waves.

In shallow water ($kh << 1$) waves become less dispersive and more collinear, and triads of waves at second-order begin to more closely satisfy the resonant conditions for wave interaction. The perturbation solutions of finite depth do not apply in the nearshore, since significant energy transfer occurs over much shorter distances ($O(10)$ wavelengths) than in deep water. The Ursell number $U_r = a/k^2 h^3$ (Ursell, 1953) is the typical measure for the validity of these perturbation solutions, which are only applicable if $U_r << 1$. Though the resonant conditions between triads are only exactly satisfied in the collinear, non-dispersive limit, the nonlinearity inherent in shoaling waves in the nearshore is strong enough for significant energy transfer to occur at near-resonance (Bryant, 1973). Recourse is often made to the Boussinesq equations (Peregrine, 1967) for simulation of nonlinear energy transfer in shallow water, as they are valid for $U_r = O(1)$, where weak nonlinearity and weak dispersion are balanced.

1.1. The Frequency Domain

One model framework which has been used in simulating ocean wave propagation in the nearshore has involved the application of Fourier transforms to the dynamical equations governing the propagation. This transformation involves imposing the following constraint on the dependent variable of these equations (usually the free surface η)

$$\eta(x, y, t) = \sum_{n=1}^{N} \hat{\eta}_n(x, y) e^{-i\omega_n t} + c.c. \tag{1}$$

where ω_n is the nth frequency in the spectrum, N is the total number of frequency components in the spectrum, $\hat{\eta}_n$ is a complex Fourier amplitude and $c.c.$ denotes complex conjugate. Assumption of temporal periodicity is a natural application to ocean waves.

The frequency domain format allows explicit detail of nonlinear wave-wave interaction and wave transformation properties. Nonlinearities in the equations appear as products of amplitudes at discrete frequencies in the spectrum, which can then be investigated in detail. Since the resulting equations are

in terms of evolving amplitudes rather than the free surface, spatial resolution requirements are usually less restrictive than in time domain models. Overall computational time, however, is a function of the number of frequency components kept in the simulation, whereas (outside of ensuring sufficient resolution for the shortest waves) this is not germane for time domain models. Additionally, there is often a disconnect between properties of a time domain model and those of the corresponding frequency domain models. A good example is seen in Rygg (1988), who used a time domain model of the classical (shallow water) Boussinesq equations of Peregrine (1967) to simulate intermediate depth cases of laboratory wave propagation experiments successfully. Similar experiments with corresponding frequency domain models (Liu et al., 1985, as used by Kaihatu and Kirby, 1995) have proven less favorable.

2. CLASSICAL BOUSSINESQ MODELS IN THE FREQUENCY DOMAIN

The Boussinesq equations can be derived from either the Euler equations (Peregrine, 1967) or the boundary value problem for water waves (Mei, 1983). In shallow water, it is reasonable to assume that vertical velocities in the water column are much smaller than horizontal velocities. This imposes the following scales on the independent variables

$$(x', y') = \frac{(x, y)}{L}; \quad z' = \frac{z}{h_o}; \quad t' = \frac{\sqrt{gh_o}}{L}t \tag{2}$$

where L is a characteristic wavelength, h_o a characteristic water depth, and the primes denote dimensionless variables. These scales are then applied to the physical quantities

$$(u', v') = \frac{h_o}{a\sqrt{gh_o}}(u, v); \quad w' = \frac{h_o^2}{aL\sqrt{gh_o}}w \tag{3}$$

$$\eta' = \frac{\eta}{a}; \quad h' = \frac{h}{h_o}; \quad p' = \frac{p}{\rho ga} \tag{4}$$

where a is a characteristic amplitude, (u, v, w) are the water particle velocity components, p is the pressure and ρ is the fluid density. When substituted into the Euler equations, the following dimensionless parameters become evident

$$\mu^2 = (kh_o)^2; \quad \delta = \frac{a}{h_o} \tag{5}$$

which are measures of frequency dispersion and nonlinearity, respectively. The Boussinesq equations can be derived by assuming

$$O(\mu^2) \approx O(\delta) \ll O(1) \tag{6}$$

Using the scaled Euler equations, Peregrine (1967) derived the Boussinesq equations for a varying bathymetry

$$\eta_t + \nabla \cdot (h + \eta)\bar{\mathbf{u}} = O(\mu^4, \delta\mu^2, \delta^2) \tag{7}$$

$$\bar{\mathbf{u}}_t + \bar{\mathbf{u}} \cdot \nabla\bar{\mathbf{u}} + g\nabla\eta = \frac{h}{2}\nabla\left[\nabla \cdot (h\bar{\mathbf{u}}_t)\right] - \frac{h^2}{6}\nabla\left[\nabla \cdot \bar{\mathbf{u}}\right] + O(\mu^4, \delta\mu^2, \delta^2) \tag{8}$$

where $\bar{\mathbf{u}}$ is the depth-averaged velocity vector. The quadratic nonlinear terms in the equation above represent the lowest-order nonlinearity of $O(\delta)$. Application of Fourier series to these terms requires

special treatment (see Mei, 1983), and thus gives rise to the triadic cross-spectral energy transfer which is the manifestation of nonlinearity in the frequency domain. Freilich and Guza (1984) derived frequency domain models from the one-dimensional form of these equations. The first (the "consistent" model) can be written

$$A_{nx} + \frac{h_x}{4h} A_n - \frac{in^3 k^3 h^2}{6} A_n + \frac{3ink}{8h} \left(\sum_{l=1}^{n-1} A_l A_{n-l} + 2 \sum_{l=1}^{N-n} A_l^* A_{n+l} \right) \tag{9}$$

where A_n are complex amplitudes of the free surface and asterisks denote complex conjugate. Freilich and Guza (1984) solved the equation in terms of coupled amplitude and phase equations rather than the complex amplitudes seen in equation (9). The second model (the "dispersive" model) was also derived from the standard Boussinesq equations, but does not contain the phase-shifting dispersive term (third term in equation (9)). Instead, the weak dispersion is incorporated through the use of the dispersion relation for the Boussinesq equations

$$\omega^2 = \frac{ghk^2}{1 + \frac{1}{3}(kh)^2} \tag{10}$$

One consequence of the use of this dispersion relation is that the wave number k_n is no longer a linear function of ω. Thus, the interacting amplitudes $(A_n, A_{n \pm l}, A_{\mp l})$, while resonant in frequency, are in *near* resonance in wave number. Freilich and Guza (1984) then compared both models to field data, using offshore wave spectra to initialize the model and ably demonstrating the utility of frequency domain models to nearshore wave propagation problems. Their comparisons of wave spectra showed that the dispersive shoaling model performed slightly better than the consistent model; however, both models clearly deviated from the data in the higher frequency range, where kh was no longer small.

Two-dimensional frequency domain models of both the Boussinesq equations (7) and (8) and the Kadomtsev-Petviashvili (KP) equations (Kadomtsev and Petviashvili, 1970) were developed by Liu et al. (1985) in the form of parabolic models, which are formulated based on the assumption that the angle between the wave direction and the x-axis of the grid is small. Kirby (1990) developed angular spectrum models based on the Boussinesq equations of Peregrine (1967). Periodicity in both time and longshore direction was assumed, thus imposing resonant interaction among longshore wave number modes as well as frequency modes.

3. EXTENDED BOUSSINESQ MODELS IN THE FREQUENCY DOMAIN

One fundamental problem with frequency domain models of the classical Boussinesq equations is their lack of applicability in deeper water than that for which the shallow water theory is valid. Recent efforts, beginning with Witting (1984), have focused on improving the deep water behavior of Boussinesq models such that their linear properties (dispersion, shoaling, etc.) better mimic those of fully-dispersive linear theory for a wide range of water depths. McCowan and Blackman (1989), Madsen et al. (1991) and Nwogu (1993) represent some of the first attempts to improve time domain Boussinesq models in this regard; the resulting models were generally dubbed "extended" Boussinesq models because their linear properties were extendable to intermediate and deep water. Madsen et al. (1991) added terms to the classical Boussinesq momentum equation, multiplied by a free parameter, which would be zero in shallow water but have significant effect in deeper water. This free parameter was tuned via Padé approximations so that the dispersion relation of the equations would compare favorably to that of linear theory for a wide range of depths. Madsen and Sørensen (1992) extended the Madsen et al. (1991) model to include varying bathymetry. Madsen and Sørensen (1993)

investigated frequency domain formulations of the model of Madsen et al. (1991) for wave evolution over a flat bottom, and sloping-bottom extensions of this equation became the basis for further development in the frequency domain (Eldeberky and Battjes, 1996; Kofoed-Hansen and Rasmussen, 1998; Becq-Girard et al., 1999). The equations of Madsen et al. (1991), and their various nonlinear and dispersive enhancements, have been analyzed extensively by Schäffer and Madsen (1995), Madsen and Schäffer (1998) and Madsen and Schäffer (1999).

In contrast, but to the same end, Nwogu (1993) used the velocity variable at an arbitrary location in the water column (rather than the depth-averaged velocity as in the classical Boussinesq equations) as a basis for deriving extended Boussinesq equations from the inviscid Euler equations. The resulting equations contained higher-order terms in both the continuity and momentum equations, and are

$$
\eta_t + \nabla \cdot [(h + \eta)\mathbf{u}_\alpha] + \nabla \cdot \left\{ \left(\frac{z_\alpha^2}{2} - \frac{h^2}{6} \right) h\nabla(\nabla \cdot \mathbf{u}_\alpha + \left(z_\alpha + \frac{h}{2} \right) h\nabla[\nabla \cdot (h\mathbf{u}_\alpha)] \right\}
$$
$$
= O(\mu^4, \delta\mu^2, \delta^2) \tag{11}
$$

$$
\mathbf{u}_{\alpha t} + g\nabla\eta + (\mathbf{u}_\alpha \cdot \nabla)\mathbf{u}_\alpha + z_\alpha \left\{ \frac{z_\alpha}{2} \nabla(\nabla \cdot \mathbf{u}_{\alpha t}) + \nabla[\nabla \cdot (h\mathbf{u}_{\alpha t})] \right\} = O(\mu^4, \delta\mu^2, \delta^2) \tag{12}
$$

where $\mathbf{u}_\alpha$ is the horizontal velocity at a location z_α in the water column. The dispersion relation of this set of equations is found by isolating the linear terms and substituting in a periodic, progressive wave, leading to

$$
C^2 = \frac{\omega^2}{k^2} = gh \left[\frac{1 - \left(\alpha + \frac{1}{3} \right)(kh)^2}{1 - \alpha(kh)^2} \right] \tag{13}
$$

where α is a free parameter related to z_α by

$$
\alpha = \left(\frac{z_\alpha^2}{2h^2} + \frac{z_\alpha}{h} \right) \tag{14}
$$

This free parameter α is then best-fit to that of fully-dispersive linear theory for a wide range of water depths. Nwogu (1993) determined that $\alpha = -0.390$ was the best-fit parameter value for the range $0 \leq h/L_o \leq 0.5$, where L_o is the deep water wavelength. This value of α corresponds to $z_\alpha = -0.522h$.

3.1. Frequency Domain Transformation of the Equations of Nwogu (1993): Linear Properties

Usually the first step undertaken in a frequency domain transformation is to combine the continuity and momentum equations into one via the use of first-order substitutions. Noting the extra dispersive terms in both the continuity equation (11) and momentum equation (12), Chen and Liu (1995) commented on the difficulty in determining a frequency domain form of the equations such that the linear dispersion relation (see equation (13)) would remain applicable to the resulting equation. Later, Kaihatu and Kirby (1998) determined a series of first-order substitutions which would lead to a set of equations retaining the original dispersion relation.

To illustrate the difficulty, we reduce equations (11) and (12) to their linear, one-dimensional form for a flat bottom

$$
\eta_t + hu_{\alpha x} + \left(\alpha + \frac{1}{3} \right) h^3 u_{\alpha xxx} = 0 \tag{15}
$$

$$
u_{\alpha t} + g\eta_x + \alpha h^2 u_{xxt} = 0 \tag{16}
$$

We follow the procedure of Liu et al. (1985) to formulate the frequency domain model. The first step involves combining the continuity (15) and momentum (16) equations. We make use of the following first-order relations

$$\eta_t = -hu_{\alpha x} \tag{17}$$

$$u_{\alpha t} = -g\eta_x \tag{18}$$

We then take the time derivative of equation (15), the x-derivative of equation (16), and combine the resulting equations. We then use equation (18) to eliminate u_α in favor of η. This results in

$$\eta_{tt} - gh\eta_{xx} + gh^3\eta_{xxxx} - g\left(\alpha + \frac{1}{3}\right)h^3\eta_{xxxx} = 0 \tag{19}$$

To obtain the linear dispersion relation, we substitute

$$\eta = Ae^{i(kx-\omega t)} \tag{20}$$

into equation (19) and obtain

$$\omega^2 = ghk^2\left[1 - \frac{1}{3}(kh)^2\right] \tag{21}$$

which is essentially the linear dispersion relation to weakly-dispersive Boussinesq theory to within a binomial expansion. The substitution sequence used to collapse the two equations did not retain the dispersion relation of the original equation. Schäffer and Madsen (1995) addressed this issue by applying differential operators of $O(\mu^2)$ (multiplied by free parameters) to the equations of Nwogu (1993) and then used a Padé [4, 4] expansion to determine the set of parameters which best fit the linear dispersion and shoaling characteristics from linear theory, with the results of Nwogu (1993) representing a subset of the parameters. In contrast, Kaihatu and Kirby (1998) used a different series of substitutions to retain the dispersion properties of the original equation; this is examined here. If we had taken the time derivative of equation (15), and then used equation (18) to replace u_α with η, we would have obtained

$$\eta_{tt} + hu_{\alpha xt} - g\left(\alpha + \frac{1}{3}\right)h^3\eta_{xxxx} = 0 \tag{22}$$

We then multiply equation (16) by h and substitute the time derivative of equation (17) to eliminate u_α. Substituting the result into equation (22) results in

$$\eta_{tt} - gh\eta_{xx} - \alpha h^2\eta_{xxtt} - gh^3\left(\alpha + \frac{1}{3}\right)\eta_{xxxx} = 0 \tag{23}$$

It can be shown that the linear dispersion relation of equation (23) is equation (13), the original dispersion relation of Nwogu (1993).

The complicated substitution sequence required to retain the linear dispersion relation also affects the shoaling behavior of the frequency domain model. To examine this, we return to the derivation of equation (23), but retain bottom slope terms. Performing the same series of substitutions and neglecting h_{xx} and $(h_x)^2$ terms leads to

$$\eta_{tt} - g(h\eta_x)_x + 2\alpha hh_x\eta_{xtt} + \alpha h^2\eta_{xxtt} - gh^2(5\alpha + 2)h_x\eta_{xxx} - gh^3\left(\alpha + \frac{1}{3}\right)\eta_{xxxx} = 0 \tag{24}$$

Substituting equation (20) into equation (24) leads to

$$A_x + WA = 0 \tag{25}$$

where

$$W = \frac{Ek_x + Fh_x}{G} \tag{26}$$

$$E = gh + \omega^2 h^2 \alpha - 6gh^3 \left(\alpha + \frac{1}{3} \right) k^2 \tag{27}$$

$$F = gk + 2\alpha \omega^2 kh - gh^2(5\alpha + 2)k^3 \tag{28}$$

$$G = 2 \left[gkh + \omega^2 h^2 \alpha k - 2gk^3 h^3 \left(\alpha + \frac{1}{3} \right) \right] \tag{29}$$

Though the derivation appears to be fairly straightforward, it will be shown that the linear shoaling term (equation (26)) compares very poorly to that of linear theory. Further analysis reveals that the balance between the η_{ttx} and $g(h\eta_{xx})_x$ terms governs the effectiveness of the wave shoaling relation. Kaihatu and Kirby (1998) addressed this by adding the following term to the equation

$$\beta(\eta_{tt} - gh\eta_{xx})_x = 0 \tag{30}$$

which is true at lowest order. In this equation β is a free parameter to be optimized. This changes equation (24) to

$$\eta_{tt} - g(h\eta_x)_x + (2\alpha + \beta)hh_x\eta_{xtt} + \alpha h^2 \eta_{xxtt} - gh^2(5\alpha + 2 + \beta)h_x\eta_{xxx}$$
$$- gh^3 \left(\alpha + \frac{1}{3} \right) \eta_{xxxx} = 0 \tag{31}$$

Carrying the calculation forward to the point of obtaining a shoaling relation results in a slight modification to the expression F in equation (28)

$$F = gk + (2\alpha + \beta)\omega^2 kh - gh^2(5\alpha + 2 + \beta)k^3 \tag{32}$$

Kaihatu and Kirby (1998) determined the free parameters α (for dispersion) and β (for shoaling) using a least squares optimization integrated as a function of h/L_o. Two sets of parameters were found. The first set optimized the shoaling while using the optimum α determined by Chen and Liu (1995). This set ($\alpha = -0.3855$, $\beta = -0.3540$) was known as the "dispersion optimized" (DO) set. The second parameter set was determined by finding the values of α and β which minimized the global error in (α, β) parameter space. This set ($\alpha = -0.4111$, $\beta = -0.3188$) was denoted the "dispersion and shoaling optimized" (DSO) parameter set. It is noted that the DSO parameter value of $\alpha = -0.4111$ is very close to Witting's (1984) optimum dispersion parameter value (found via Padé approximants) of $\alpha = -2/5$.

3.2. Frequency Domain Transformation of the Equations of Nwogu (1993): Nonlinear Parabolic Model

If nonlinearity and two-dimensionality had been retained when deriving equation (31), the result would have been (Kaihatu and Kirby, 1998)

$$
\eta_{tt} - g\nabla \cdot (h\nabla\eta) - h\nabla \cdot [(\mathbf{u}_\alpha \cdot \nabla)\mathbf{u}_\alpha] + (2\alpha + \beta)h\nabla h \cdot \nabla\eta_{tt} + \alpha h^2 \nabla^2 \eta_{tt} + \nabla \cdot (\eta\mathbf{u}_\alpha)_t
$$

$$
- gh^2(5\alpha + 2 + \beta)\nabla h \cdot \nabla(\nabla^2\eta) - gh^3 \left(\alpha + \frac{1}{3}\right)\nabla^2\nabla^2\eta = 0 \tag{33}
$$

Complete elimination of the velocity $\mathbf{u}_\alpha$ requires assumption of time periodicity for both η and $\mathbf{u}_\alpha$. To eliminate $\mathbf{u}_\alpha$ from the nonlinear terms, we can use the time-periodic form of equation (18)

$$
\hat{\mathbf{u}}_{\alpha n} = \frac{ig}{n\omega}\nabla\hat{\eta}_n \tag{34}
$$

leading to the time-periodic equation for $\hat{\eta}_n$. To facilitate convenient numerical treatment, we make use of the parabolic approximation, first developed by Radder (1979) and Lozano and Liu (1980) for the linear mild-slope equation. We first make an explicit assumption that the waves are propagating forward

$$
\hat{\eta}_n = A_n(x, y)e^{i\int k_n(x,y)dx} \tag{35}
$$

The complex amplitudes $A_n(x, y)$ represent phase-like behavior in both x and y. The phase function is integrated only in x; this places all phase-like behavior in y in the complex amplitude A_n, while allowing explicit slow and fast variations in x. The consequence is that the angle between the incident wave and the x direction of the grid remains small in order to maintain slowly-varying wave-like behavior of A_n in the y direction.

Because of the third and fourth derivatives of η present in equation (33), terms proportional to $k_{nx}A_{nx}$, A_{nxx}, and other higher-order derivatives will be generated. We thus keep a higher degree of modulation in the y direction than in the x direction (following the ordering of Liu et al., 1985), leading to a parabolic evolution equation for A_n. However, because the phase function in equation (35) is integrated only in x, but k is a function of both x and y, a redefinition is required

$$
A_n = a_n e^{i\int \bar{k}_n(x) - k_n(x,y)dx} \tag{36}
$$

where $\bar{k}_n$ is a reference wave number that is the result of averaging along the y direction. With this redefinition, the model equation reads

$$
2i\left[ghk_n + n^2\omega^2\alpha k_n h^2 - 2gh^3 k_n^3 \left(\alpha + \frac{1}{3}\right)\right]a_{nx}
$$

$$
- 2\left[ghk_n + n^2\omega^2\alpha k_n h^2 - 2gh^3 k_n^3 \left(\alpha + \frac{1}{3}\right)\right](\bar{k}_n - k_n)a_n
$$

$$
+ i[gk_n + n^2\omega^2(2\alpha + \beta)k_n h - gh^3 k_n^3(5\alpha + 2 + \beta)]h_x a_n
$$

$$
+ i\left[gh + n^2\omega^2\alpha h^2 - 6gh^3 k_n^2 \left(\alpha + \frac{1}{3}\right)\right]k_{nx}a_n
$$

$$
+ \left[g + n^2\omega^2(2\alpha + \beta)h - gh^2 k_n^2(5\alpha + 2 + \beta)\right]h_y a_{ny}
$$

$$
+ \left[gh + n^2\omega^2\alpha h^2 - 2gh^3 k_n^2 \left(\alpha + \frac{1}{3}\right)\right]a_{nyy}
$$

$$-\frac{g}{4}\left(\sum_{l=1}^{n-1} Ra_l a_{n-l} e^{i\int(\bar{k}_l+\bar{k}_{n-l}-\bar{k}_n)dx} + 2\sum_{l=1}^{N-n} Sa_l^* a_{n+l} e^{i\int(\bar{k}_{n+l}-\bar{k}_l-\bar{k}_n)dx}\right) = 0 \tag{37}$$

where

$$R = \frac{gh}{l(n-l)\omega^2}[k_l k_{n-l}(k_l + k_{n-l})^2] + \frac{n^2 k_l k_{n-l}}{l(n-l)} + \frac{n^2\omega^2}{gh} \tag{38}$$

$$S = \frac{gh}{l(n+l)\omega^2}[k_l k_{n+l}(k_l - k_{n+l})^2] + \frac{n^2 k_l k_{n+l}}{l(n+l)} + \frac{n^2\omega^2}{gh} \tag{39}$$

This is the primary result from Kaihatu and Kirby (1998).

Kaihatu (1994) noted that the ambiguity which affected the substitution process in the linear terms also appears in the formulation of the nonlinear terms, to the effect that several different nonlinear coefficient sets are possible. Unlike the linear terms, however, there are no corresponding analytical metrics for determining which set of coefficients have the most desirable properties, outside of comparisons to nonlinear permanent form solutions. The general complexity of the Boussinesq equations of Nwogu (1993), particularly in retaining shoaling and dispersive properties during transformation into the frequency domain, has motivated investigations into developing simpler forms of the equations. This is explored in the next section.

3.3. Frequency Domain Transformation of the Equations of Chen and Liu (1995)

Chen and Liu (1995) and Kaihatu and Kirby (1994) investigated using the extended Boussinesq equations of Nwogu (1993) in the form of velocity potential (rather than velocity) and free surface elevation. The resulting equations would be an analogue to the Boussinesq equations of Wu (1981), which were a (ϕ, η) form of the classical Boussinesq equations of Peregrine (1967). The use of velocity potential as a dependent variable simplifies the treatment of the extended Boussinesq equations considerably, since ϕ is a scalar quantity.

Chen and Liu (1995) began with the boundary value problem for water waves, with surface boundary conditions scaled for shallow water waves and expanded to $O(\delta, \mu^2)$. The derivation is similar to that seen in Mei (1983), except that the velocity potential is taken at an unknown level in the water column rather than averaged over depth. Kaihatu and Kirby (1994) expanded the equations to $O(\delta, \mu^2, \delta\mu^2)$, thereby including dispersive effects in the nonlinear terms. The resulting equations are

$$\eta_t + \nabla \cdot \left[(h + \eta)\nabla\phi_\alpha\right] + \nabla \cdot \left[h\nabla\left\{z_\alpha\nabla \cdot (h\nabla\phi_\alpha) + \frac{z_\alpha^2}{2}\nabla^2\phi_\alpha\right\}\right.$$

$$\left. + \frac{h^2}{2}\nabla[\nabla \cdot (h\nabla\phi_\alpha)] - \frac{h^3}{6}\nabla\nabla^2\phi_\alpha\right] + \Upsilon = 0 \tag{40}$$

$$\phi_{\alpha t} + g\eta + \frac{1}{2}(\nabla\phi_\alpha)^2 + \left[z_\alpha\nabla \cdot (h\nabla\phi_{\alpha t}) + \frac{z_\alpha^2}{2}\nabla^2\phi_{\alpha t}\right] + \Lambda = 0 \tag{41}$$

where ϕ_α is the velocity potential at z_α. The terms Υ and Λ represent terms of $O(\delta\mu^2)$, which are zero in Chen and Liu (1995). In Kaihatu and Kirby (1994) they are

$$\Upsilon = \nabla \cdot (\eta\nabla\phi_\alpha) + \nabla \cdot (\eta\nabla[z_\alpha\nabla \cdot (h\nabla\phi_\alpha)])$$

$$+ \eta \nabla \left(\frac{z_\alpha^2}{2} \nabla^2 \phi_\alpha \right) \tag{42}$$

$$\Lambda = -\eta \nabla \cdot (h \nabla \phi_{\alpha t}) + \nabla \phi_\alpha \cdot [\nabla z_\alpha \nabla \cdot (h \nabla \phi_\alpha)] + z_\alpha (\nabla \phi_\alpha \cdot \nabla)(\nabla \cdot (h \nabla \phi_\alpha))$$

$$+ \nabla \phi_\alpha \cdot \left(z_\alpha \nabla z_\alpha \nabla^2 \phi_\alpha \right) + \frac{1}{2} \nabla \phi_\alpha z_\alpha^2 \cdot \nabla (\nabla^2 \phi_\alpha) + \frac{1}{2} \nabla \cdot (h \nabla \phi_\alpha) \tag{43}$$

Temporal periodicity was assumed for the velocity potential ϕ_α and the following equation developed for the amplitudes of the velocity potential b_n (Chen and Liu, 1995, although expressed somewhat differently)

$$\left[h + \frac{\omega_n^2 h^2 \alpha}{g} - 2 \left(\alpha + \frac{1}{3} \right) h^3 k_n^2 \right] b_{nyy} + 2i \left[k_n \left(h + \frac{\omega_n^2 h^2 \alpha}{g} \right) - 2 k_n^3 h^3 \left(\alpha + \frac{1}{3} \right) \right] b_{nx}$$

$$+ \left[1 + \frac{\omega_n^2 z_\alpha}{g} - (1 + 5\alpha + \sqrt{1 + 2\alpha}) k_n^2 h^2 \right] h_y b_{ny}$$

$$+ i \left\{ k_n \left(1 + \frac{\omega^2 z_\alpha}{g} \right) - [k_n^3 h^2 (1 + 5\alpha + \sqrt{1 + 2\alpha})] \right\} h_x b_n$$

$$- 2 \left[k_n \left(h + \frac{\omega_n^2 h^2 \alpha}{g} \right) - 2 k_n^3 h^3 \left(\alpha + \frac{1}{3} \right) \right] (\bar{k}_n - k_n) b_n$$

$$+ i \left[h + \frac{\omega_n^2 h^2 \alpha}{g} - 6 \left(\alpha + \frac{1}{3} \right) h^3 k_n^2 \right] k_{nx} b_n$$

$$- \frac{i\omega}{4g} \left(\sum_{l=1}^{n-1} \tilde{R} b_l b_{n-l} e^{i \int (\bar{k}_l + \bar{k}_{n-l} - \bar{k}_n) dx} + 2 \sum_{l=1}^{N-n} \tilde{S} b_l^* b_{n+l} e^{i \int (\bar{k}_{n+l} - \bar{k}_l - \bar{k}_n) dx} \right) \tag{44}$$

where

$$\tilde{R} = l k_{n-l}^2 + 2n k_l k_{n-l} + (n-l) k_l^2 - \alpha h^2 \left(l k_l^3 k_{n-l} + n k_l^2 + (n-l) k_l k_{n-l}^3 \right) \tag{45}$$

$$\tilde{S} = (n+l) k_l^2 - 2n k_l k_{n+l} - l k_{n+l}^2 + \alpha h^2 \left((n+l) k_l k_{n+l}^3 - n k_l^2 k_{n+l}^2 - l k_{n+l} k_l^3 \right) \tag{46}$$

From the second-order dynamic free surface boundary condition, the nonlinear relation between the amplitudes of ϕ_α and those of the free surface η can be derived

$$a_n = \frac{i\omega_n}{g} \alpha h^2 b_{nyy} + \frac{i\omega_n z_\alpha}{g} h_y b_{ny} - \frac{2\omega_n \alpha h^2 k_n}{g} b_{nx} - \frac{\omega_n z_\alpha k_n}{g} h_x b_n$$

$$- \frac{\omega_n \alpha h^2}{g} k_{nx} b_n + \frac{i\omega_n}{g} [1 - \alpha k_n^2 h^2 - 2\alpha h^2 k_n (\bar{k}_n - k_n)] b_n$$

$$+ \frac{1}{4g} \left(\sum_{l=1}^{n-1} \tilde{R}' b_l b_{n-l} e^{i \int (\bar{k}_l + \bar{k}_{n-l} - \bar{k}_n) dx} - 2 \sum_{l=1}^{N-n} \tilde{S}' b_l^* b_{n+l} e^{i \int (\bar{k}_{n+l} - \bar{k}_l - \bar{k}_n) dx} \right) \tag{47}$$

where

$$\tilde{R}' = k_l k_{n-l} \tag{48}$$

$$\tilde{S}' = k_l k_{n+l} \tag{49}$$

The extension to $O(\delta\mu^2)$ results in the nonlinear coefficients (Kaihatu and Kirby, 1994)

$$\tilde{\tilde{R}} = \tilde{R} - \alpha h^2 \left((n-l)k_l^4 + (2n-l)k_l^3 k_{n-l} + (n+l)k_l k_{n-l}^3 + l k_{n-l}^4 \right)$$

$$- n h^2 \left(\frac{(n-l)^2 + l(n-l) + l^2}{l(n-l)} \right) k_l^2 k_{n-l}^2 \tag{50}$$

$$\tilde{\tilde{S}} = \tilde{S} + \alpha h^2 \left(l k_{n+l}^4 + (2n+l)k_l^3 k_{n+l} + (n-l)k_l k_{n+l}^3 - (n+l)k_l^4 \right)$$

$$+ n h^2 \left(\frac{(n+l)^2 - l(n+l) + l^2}{l(n+l)} \right) k_l^2 k_{n+l}^2 \tag{51}$$

$$\tilde{\tilde{R}}' = \tilde{R}' - \alpha h^2 \left[k_l k_{n-l}^3 + k_l^3 k_{n-l} \right] - h^2 \left[\frac{(n-l)^2 + l(n-l) + l^2}{l(n-l)} \right] k_l^2 k_{n-l}^2 \tag{52}$$

$$\tilde{\tilde{S}}' = \tilde{S}' - \alpha h^2 \left[k_l k_{n+l}^3 + k_l^3 k_{n+l} \right] - h^2 \left[\frac{(n+l)^2 - l(n+l) + l^2}{l(n+l)} \right] k_l^2 k_{n+l}^2 \tag{53}$$

The $O(\delta\mu^2)$ terms generally tend to induce a slower growth in the generated higher harmonics in shoaling wave applications. Truncation of the extended Boussinesq model to $O(\mu^2)$ (with all nonlinearity retained) was performed by Wei et al. (1995). We note that the ambiguities which arose in the previous frequency domain treatment of the equations of Nwogu (1993) are not present here.

3.4. Model Evaluation

We noted earlier that a primary motivation for development of the extended Boussinesq models was to impart linear properties which mimicked those of fully-dispersive linear theory for a wide range of water depths, thus removing a substantial obstacle to general model application. In this section we examine how well the resulting frequency domain models capture wave shoaling, having insured (via the substitution process) that linear dispersion is well represented. Additionally, because the resulting models are parabolic, we will also examine the wide-angle behavior of the equations.

3.4.1. Wave Shoaling

As mentioned previously, one of the consequences of frequency domain transformation of the equations of Nwogu (1993) has been the lack of any guarantee that the characteristics of the original equations survive the transformation process. Great care had to be exercised in the combination of the equations such that the advantageous linear dispersion properties could be maintained. Additional steps were required for handling shoaling. In contrast, the equations of Chen and Liu (1995) were relatively simple to transform into the frequency domain, particularly with respect to retaining the dispersion relation of the equations of Nwogu (1993).

Madsen and Sørensen (1992) noted that the most reliable measure of the effectiveness of the shoaling mechanism was the shoaling gradient

$$\frac{|A|_x}{|A|} = -\frac{h_x}{h}\gamma \tag{54}$$

where γ is the shoaling gradient. While deviation of the shoaling gradient from linear theory may exaggerate that seen in the shoaling model itself, particularly in intermediate water depth (Chen and Liu, 1995), it is a convenient measure since integration is not required. The resulting expressions for γ for the shoaling models compared herein can be found in the original publications. Kaihatu and Kirby (1998), as mentioned previously, used two sets of parameters: the DO parameters ($\alpha = -0.3855, \beta = -0.3540$) and the DSO parameters ($\alpha = -0.4111, \beta = -0.3188$). To demonstrate the effect of the β term, we also include the ($\alpha = -0.3855, \beta = 0$) case; this is what would result if the ambiguity in the substitution process detailed earlier had not been realized. The shoaling mechanisms of Madsen and Sørensen (1992) and Chen and Liu (1995) will be used with the optimized free parameters determined by the authors in the original publications. We note that the model of Kaihatu and Kirby (1994) shares the same shoaling characteristics as that of Chen and Liu (1995).

As a benchmark, the shoaling gradient from fully-dispersive linear theory is used (Madsen and Sørensen, 1992)

$$\gamma = \frac{G'\left(1 + \frac{1}{2}G'(1 - \cosh 2kh)\right)}{(1 + G')^2} \tag{55}$$

where

$$G' = \frac{2kh}{\sinh 2kh} \tag{56}$$

Fig. 1 shows a comparison between the different shoaling mechanisms and that of linear theory. Of the five shoaling mechanisms, those of Madsen and Sørensen (1992) and Kaihatu and Kirby (1998) with DSO parameters compare the best, with a slight improvement yielded by the free parameterization of the latter model. In contrast, the shoaling mechanisms of Chen and Liu (1995) and Kaihatu and Kirby (1998) with $\beta = 0$ compare poorly, particularly the latter model. The model of Kaihatu and Kirby (1998) may represent the limit of optimum shoaling performance possible with two free parameters. Schäffer and Madsen (1995), using a Padé [4, 4] approximation and more free parameters, developed an expression for γ which exhibited virtually no deviation from linear theory for the complete range of water depths.

3.4.2. Wide-Angle Behavior of the Parabolic Equations

One consequence of the parabolic approximation is the assumption that the angle between the x-coordinate of the grid and the incident wave direction remains small. Methods for ameliorating this problem have generally taken the form of retention of higher-order derivative terms with coefficients which can be determined by Padé approximations (Booij, 1981; Kirby, 1986a) or by rational approximations (Kirby, 1986b), and have been shown to work well for parabolic approximations of the mild-slope equation (Berkhoff, 1972; Smith and Sprinks, 1975). The suitability for parabolic approximations of the Boussinesq equations, however, have not been established except by comparisons with data (for example, Kirby, 1990). In this section we analyze the effectiveness of the parabolic approximation used in the development of the frequency domain extended Boussinesq models. We note that the models of Chen and Liu (1995) and Kaihatu and Kirby (1994; 1998) reduce to the same basic parabolic form in the linear limit.
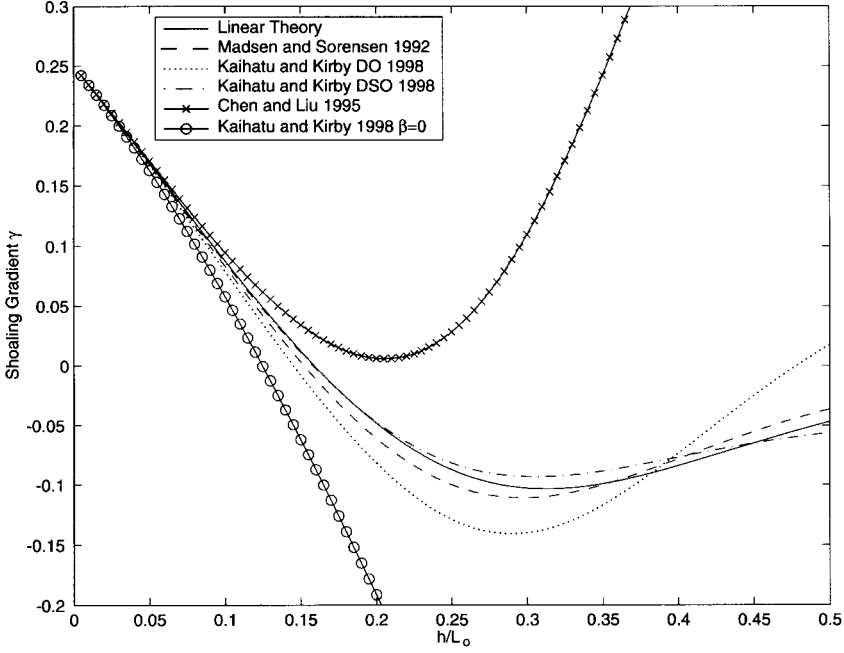
Figure 1. Comparison of shoaling mechanisms from various extended Boussinesq models to that of linear theory.

Numerical treatment of parabolic wave models generally involves the Crank-Nicholson discretization scheme, which is second-order accurate in both horizontal directions. A tridiagonal matrix is formed at each x location and is usually solved using a Thomas algorithm. The highest order derivative of A which would allow this treatment is A_{xyy} (Kirby, 1986a), which was not retained in our previous development. Expanding the time-periodic form of equation (33) into its horizontal components, neglecting nonlinear and bottom slope terms, substituting in equation (35) and retaining the A_{xyy} term that results yields

$$2i \left[ghk + \omega^2 kh^2 - 2g(kh)^3 \left(\alpha + \frac{1}{3} \right) \right] A_x + \left[gh + \omega^2 h^2 \alpha - 2gh^3 k^2 \left(\alpha + \frac{1}{3} \right) \right] A_{yy}$$

$$+ 4igh^3 k \left(\alpha + \frac{1}{3} \right) A_{xyy} = 0 \tag{57}$$

We note that many terms were truncated in the substitution process used to derive equation (57), specifically third and fourth derivatives with respect to y. Additionally, similar derivatives with respect to x are represented only in the differentiation of the phase function, generating terms proportional to k^4. To ascertain the effect this truncation has on the accuracy of wave propagation, we need to transform the equation back into $\hat{\eta}$ by

$$A = \hat{\eta} e^{-ikx} \tag{58}$$

leading to

$$2i \left[ghk + \omega^2 kh^2 \alpha - 2gk^3 h^3 \left(\alpha + \frac{1}{3} \right) \right] \hat{\eta}_x + 2k \left[ghk + \omega^2 kh^2 \alpha - 2gk^3 h^3 \left(\alpha + \frac{1}{3} \right) \right] \hat{\eta}$$

$$+ \left[gh + \omega^2 h^2 \alpha - 2gh^3 k^2 \left(\alpha + \frac{1}{3} \right) \right] \hat{\eta}_{yy} + 4igh^3 k \left(\alpha + \frac{1}{3} \right) \hat{\eta}_{xyy}$$

$$+ 4k^2 gh^3 \left(\alpha + \frac{1}{3} \right) \hat{\eta}_{yy} = 0 \tag{59}$$

Making a final substitution

$$\hat{\eta} = ae^{i(k_x x + k_y y)} \tag{60}$$

where k_x and k_y denote wave number vector components in the x and y directions, respectively, we can obtain an expression for k_y in terms of k and k_x

$$k_y = \sqrt{\frac{2(k - k_x) \left[ghk + \omega^2 k h^2 \alpha - 2gk^3 h^3 \left(\alpha + \frac{1}{3} \right) \right]}{gh \left[4h^2 (k^2 - kk_x) \left(\alpha + \frac{1}{3} \right) + \left[1 + \frac{\omega^2 h \alpha}{g} - 2k^2 h^2 \left(\alpha + \frac{1}{3} \right) \right] \right]}} \tag{61}$$

The neglect of the A_{xyy} term would have the effect of zeroing out the kk_x term in the denominator of equation (61). The baseline for comparison is the circle

$$k_y = \sqrt{k^2 - k_x^2} \tag{62}$$

which was derived by substitution of equation (60) into the Helmholtz equation. Additionally, we also compare to the small-angle parabolic approximations used in the mild-slope equation (Kirby, 1986b)

$$k_y = \sqrt{2(k^2 - kk_x)} \tag{63}$$

and the wide angle expression from the Padé approximation of Kirby (1986a)

$$k_y = \sqrt{\frac{4k^2 \left(1 - \frac{k_x}{k} \right)}{\left(3 - \frac{k_x}{k} \right)}} \tag{64}$$

Fig. 2 shows a comparison of the above expressions relating k_x to k_y. It appears that the parabolic models of the extended Boussinesq equation have slightly worse characteristics at oblique angles than the small-angle approximation of the mild-slope equation, with the A_{xyy} term imparting no appreciable improvement. This could be due to the considerable amount of information contained in the $\nabla^2 \nabla^2 \eta$ terms (among others) discarded when the form (equation (35)) is substituted and the parabolic approximation made. Optimizations similar to Kirby's (1986a; 1986b) developments with the mild-slope equation could be implemented here.

4. NONLINEAR MILD-SLOPE EQUATION MODELS

An alternative approach to developing nonlinear frequency domain models involves incorporating nonlinear effects into models already equipped with fully-dispersive transformation characteristics. The mild-slope equation (Berkhoff, 1972; Smith and Sprinks, 1975) simulates wave refraction, shoaling and diffraction over mildly-varying bathymetry; its applicability has been greatly increased with the advent of the parabolic approximation (Radder, 1979; Lozano and Liu, 1980) encountered in earlier sections.
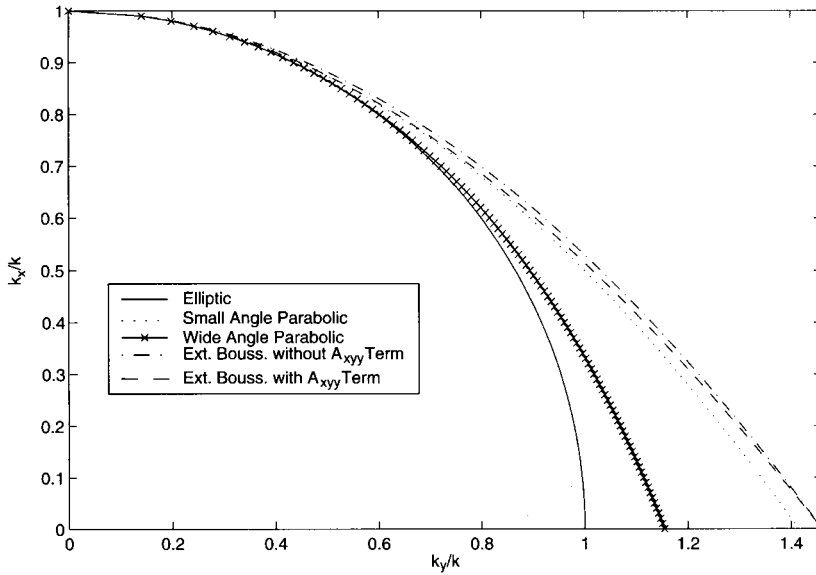
Figure 2. Analysis of the parabolic approximations used for various models. Relation from elliptic model is benchmark.

Bryant (1973, 1974) first studied the efficacy of developing fully-dispersive models with second-order nonlinear characteristics. He developed a spatially-periodic solution to the truncated Laplace boundary value problem (thereby retaining full frequency dispersion) and compared numerical evaluations of this solution to those from various forms of the Korteweg-deVries (KdV) equation. Furthermore, Bryant (1974) also demonstrated that three harmonic amplitudes of his spatially-periodic solution matched those of third-order Stokes waves, as did the nonlinear dispersion characteristics.

Keller (1988) derived coupled nonlinear equations derived from the shallow water equations, the Boussinesq equations and the Euler equations, all truncated to two harmonics. He showed that, in the shallow water limit, the equations reduced to identical forms.

Agnon et al. (1993) developed a unidirectional shoaling model based on a nonlinear extension of fully-dispersive linear shoaling. The linear part of the resulting model contained fully-dispersive shoaling, and triad interactions between wave components described the nonlinear evolution. This was later extended to two-dimensional propagation by Kaihatu and Kirby (1995), Tang and Ouelette (1997) (both parabolic models) and Agnon and Sheremet (1997) (hyperbolic model). The paper by Kaihatu and Kirby (1995) also detailed the inclusion of a surf zone dissipation mechanism. Tang and Ouelette (1997) extended the model of Kaihatu and Kirby (1995) by including diffraction and bottom slope effects in the nonlinear terms of their model.

To explain some of the subtle points outlined later in this section, we briefly outline the development of the nonlinear mild-slope equation described by Kaihatu and Kirby (1995). We start from the boundary value problem for water waves, with free surface conditions expanded to second-order in wave amplitude. We first assume that the solution can be expressed as a superposition

$$\phi(x, y, z, t) = \sum_{n=1}^{N} \tilde{f}_n(z)\hat{\phi}_n(x, y)e^{-i\omega_n t} + c.c. \tag{65}$$

where $\hat{\phi}_n$ is complex, and

$$\tilde{f}_n = \frac{\cosh k_n(h+z)}{\cosh k_n h} \tag{66}$$

where the dispersion relation is that of linear theory

$$\omega_n^2 = g k_n \tanh k_n h \tag{67}$$

We then make use of Green's Second Identity on the variables $\tilde{f}_n$ and $\hat{\phi}_n$, and then use resonant triad interaction theory to create a time-periodic evolution equation for $\hat{\phi}_n$. We then assume a propagating wave

$$\hat{\phi}_n = -\frac{ig}{\omega_n} A_n e^{i \int k_n dx} \tag{68}$$

We substitute equation (68) and its conjugate into the time-periodic equation for $\hat{\phi}_n$, and employ the parabolic approximation to justify neglecting $\partial^2 A_n / \partial x^2$ terms in the resulting equation. We then make use of a phase function redefinition similar to that done for the extended Boussinesq models in earlier sections. This results in

$$2i(kCC_g)_n a_{nx} - 2(kCC_g)_n(\bar{k}_n - k_n)a_n + i(kCC_g)_{nx}a_n + [(CC_g)_n(a_n)_y]_y$$

$$= \frac{1}{4}\left(\sum_{l=1}^{n-1} Y a_l a_{n-l} e^{i\int(\bar{k}_l + \bar{k}_{n-l} - \bar{k}_n)dx} + 2\sum_{l=1}^{N-n} Z a_l^* a_{n+l} e^{i\int(\bar{k}_{n+l} - \bar{k}_l - \bar{k}_n)dx}\right) \tag{69}$$

where

$$Y = \frac{g}{\omega_l \omega_{n-l}}[\omega_n^2 k_l k_{n-l} + (k_l + k_{n-l})(\omega_{n-l}k_l + \omega_l k_{n-l})\omega_n]$$

$$- \frac{\omega_n^2}{g}(\omega_l^2 + \omega_l \omega_{n-l} + \omega_{n-l}^2) \tag{70}$$

$$Z = \frac{g}{\omega_l \omega_{n+l}}[\omega_n^2 k_l k_{n+l} + (k_{n+l} - k_l)(\omega_{n+l}k_l + \omega_l k_{n+l})\omega_n]$$

$$- \frac{\omega_n^2}{g}(\omega_l^2 - \omega_l \omega_{n+l} + \omega_{n+l}^2) \tag{71}$$

Equation (69) comprises the model of Kaihatu and Kirby (1995).

Equation (68) is derived from the first-order dynamic free surface boundary condition

$$\phi_t + g\eta = 0; \qquad z = 0 \tag{72}$$

and is a transformation from amplitudes of velocity potential to those of the free-surface elevation. This transformation is first-order, and does not include the nonlinear terms inherent in the dynamic free surface boundary condition. Eldeberky and Madsen (1999) determined that the neglect of these second-order terms had the effect of underpredicting the nonlinear energy transfer, particularly with respect to the superharmonic energy transfer. They used successive approximations to invert the second-order dynamic free surface boundary condition and eliminate the velocity potential, resulting

in an evolution equation that could be conveniently solved for the free surface amplitudes alone. The linear terms are the same as those of earlier models, but the nonlinear coefficients are

$$Y' = Y - \frac{g}{\omega_l \omega_{n-l}} \Gamma^+ \omega_n k_l k_{n-l} + \frac{\Gamma^+ \omega_n^2}{g} (\omega_l^2 + \omega_l \omega_{n-l} + \omega_{n-l}^2) \tag{73}$$

$$Z' = Z - \frac{g}{\omega_l \omega_{n+l}} \Gamma^- \omega_n k_l k_{n+l} - \frac{\Gamma^- \omega_n^2}{g} (\omega_l^2 - \omega_l \omega_{n+l} + \omega_{n+l}^2) \tag{74}$$

where

$$\Gamma^+ = \frac{2(k_l + k_{n-l} - k_n) C_{gn}}{\omega_n} \tag{75}$$

$$\Gamma^- = \frac{2(k_{n+l} - k_l - k_n) C_{gn}}{\omega_n} \tag{76}$$

Eldeberky and Madsen (1999) demonstrated that the above terms contributed substantially to the superharmonic energy transfer. We note here that Tang and Ouelette (1997) also took the second-order terms in this transformation into account, though in a manner different than Eldeberky and Madsen (1999).

Kaihatu (2001) took a different approach and derived the required correction to make the resulting equations consistent. This correction was derived from the second-order dynamic free surface boundary condition, and is applied whenever the free surface is required

$$\tilde{a}_n = a_n + \frac{1}{4g} \left(\sum_{l=1}^{n-1} Y'' a_l a_{n-l} e^{i \int (\bar{k}_l + \bar{k}_{n-l} - \bar{k}_n) dx} + 2 \sum_{l=1}^{N-n} Z'' a_l^* a_{n+l} e^{i \int (\bar{k}_{n+l} - \bar{k}_l - \bar{k}_n) dx} \right) \tag{77}$$

where $\tilde{a}_n$ is the total amplitude of the free surface to second-order, a_n is the solution to equation (69), and

$$Y'' = \omega_l^2 + \omega_l \omega_{n-l} + \omega_{n-l}^2 - g^2 \frac{k_l k_{n-l}}{\omega_l \omega_{n-l}} \tag{78}$$

$$Z'' = \omega_l^2 - \omega_l \omega_{n+l} + \omega_{n+l}^2 - g^2 \frac{k_l k_{n+l}}{\omega_l \omega_{n+l}} \tag{79}$$

Kaihatu (2001) also investigated the effect of this correction by comparing permanent form solutions of the one-dimensional version of equation (69), with and without the correction (equation (77)), to third-order Stokes theory. While the correction did not noticeably enhance phase speed comparisons to the theory, it did improve comparisons of the respective free surfaces. Additionally, Kaihatu (2001) also extended the parabolic model to include wide-angle propagation terms, which notably improved model performance when compared to laboratory measurements of waves propagating over a shoal (Chawla et al., 1998). These wide-angle propagation terms are essentially those of Kirby (1986a) and therefore share the same accuracy in oblique-angle propagation as equation (64).

5. BREAKING WAVE MODELS

For general utility in solving nearshore wave propagation problems, consideration of wave breaking and surf zone decay is required. Due to the nature of the evolution equations, such breaking and decay descriptions must necessarily be statistical. Two formulations are generally used for this application; those of Battjes and Janssen (1978) and Thornton and Guza (1983), though several others are extant (for example, Dally, 1990; Battjes and Groenendijk, 2000).

Battjes and Janssen (1978) assumed that the probability distribution of breaking waves could be described as a Rayleigh distribution, where the percentage of breaking waves at a particular location is related to the area under the truncated probability distribution. This percentage Q_b was determined by solution of the following implicit relation

$$\frac{1 - Q_b}{\ln Q_b} = -\left(\frac{H_{rms}}{H_{max}}\right)^2 \tag{80}$$

where H_{rms} is the root-mean-square wave height and H_{max} the maximum wave height in the distribution. Framing the energy dissipation from breaking waves as an energy balance

$$\left(\overline{E}\sqrt{gh}\right)_x = -\epsilon_b \tag{81}$$

where $\overline{E}$ is wave energy, Battjes and Janssen (1978) determined an expression for the energy dissipation ϵ_b

$$\epsilon_b = \frac{1}{4} Q_b \overline{f} \rho g H_{max}^2 \tag{82}$$

where $\overline{f}$ is the average frequency of the spectrum. The maximum wave height H_{max} is determined by

$$H_{max} = \frac{0.88}{\overline{k}} \tanh\left(\frac{\tilde{\gamma}\overline{k}h}{0.88}\right) \tag{83}$$

where $\overline{k}$ is the average wave number. An expression for $\tilde{\gamma}$ based on the deep water wave steepness was found by Battjes and Stive (1985).

Thornton and Guza (1983) extended the Battjes and Janssen (1978) model by accounting for the transformation of the wave height probability distribution through the surf zone. They hypothesized a distribution of breaking waves as being a weighted Rayleigh distribution with tunable parameters. The energy dissipation for a single bore was then integrated through this probability distribution to obtain

$$\epsilon_b = \frac{3\sqrt{\pi}}{4\sqrt{gh}} \frac{B^3 \overline{f} H_{rms}^5}{\overline{\gamma}^4 h^5} \tag{84}$$

where B and $\overline{\gamma}$ are free parameters. Reasonable fit to field data was found with $\overline{\gamma} = 0.42$ and $B = 1.3 - 1.7$ (Thornton and Guza, 1983). Mase and Kirby (1992) incorporated this dissipation mechanism into their "hybrid KdV" shoaling model, which used full linear shoaling with shallow water nonlinearity. This particular study also detailed a laboratory experiment in which a spectrum of waves was allowed to shoal and break over a long sloping bottom. The unique feature of this experiment is that the energy at the peak of the spectrum is in intermediate water depth at the wave maker; this would serve as a severe test of shoaling models, and would invalidate those limited to

weak dispersion (for example, models based on the classical Boussinesq equations). This dissipation mechanism was also included in the linear spectral parabolic model of Chawla et al. (1998), as well as the nonlinear shoaling model of Kaihatu and Kirby (1995).

Both Battjes and Janssen (1978) and Thornton and Guza (1983) developed their dissipation mechanisms purely as lumped parameter models, dependent only on integrated properties of the spectrum with no other details. For use in phase-resolving frequency domain models such as those detailed in this study, some assumptions concerning the distribution of the dissipation over the frequency range must be made. The majority of nonlinear models of this type assume an equal weighting of dissipation across the entire frequency range (Eldeberky and Battjes, 1996; Eldeberky and Madsen, 1999); this assumption is also used in linear spectral models (Chawla et al. 1998). Alternatively, Mase and Kirby (1992), Kaihatu and Kirby (1995) and Kirby and Kaihatu (1996) used a distribution which assumes a frequency-squared weighting of the dissipation term, thus accounting for nonlinear transfer of energy from low to high frequencies due to triad interactions. Chen et al. (1997) demonstrated (using the model of Chen and Liu 1995) that, while the frequency-squared weighting did not affect the spectral shape significantly, it did offer greater accuracy in estimating skewness and asymmetry. Both quantities are indications of wave shape; for example, negative asymmetry corresponds to a forward-pitched shape of the wave field, redolent of surf zone waves.

The dissipation mechanisms are usually formulated in terms of energy $\overline{E}$. Some manipulation is required to implement these into complex-amplitude evolution equations. Mase and Kirby (1992) implemented the Thornton and Guza (1983) dissipation by starting with the conservation of energy flux equation with a damping term added

$$A_{nx} + \frac{C_{gnx}}{2C_{gn}} A_n + \tilde{\alpha} A_n = 0 \tag{85}$$

where $\tilde{\alpha}$ is the dissipation coefficient. Multiplying this equation by the conjugate amplitude, adding it to its conjugate equation, then summing over all components, we obtain

$$\sum_{n=1}^{N} \left(C_{gn} |A_n|^2 \right)_x = -2 \sum_{n=1}^{N} \tilde{\alpha}_n C_{gn} |A_n|^2 \tag{86}$$

Then, assuming shallow water and switching to an energy definition, we obtain

$$\left(\overline{E} \sqrt{gh} \right)_x = \rho g \sqrt{gh} \left(\sum_{n=1}^{N} \tilde{\alpha}_n |A_n|^2 \right) \tag{87}$$

where ρ is mass density of water. Equating this to the dissipation function in equation (84) yields

$$\sum_{n=1}^{N} \tilde{\alpha}_n |A_n|^2 = \frac{3\sqrt{\pi}}{4\sqrt{gh}} \frac{B^3 f_{peak} H_{rms}^5}{\gamma^2 h^3} = \tilde{\beta}(x) \sum_{n=1}^{N} |A_n|^2 \tag{88}$$

We now require a frequency distribution for $\tilde{\alpha}_n$. Mase and Kirby (1992) investigated the trends evidenced in a back-calculation of $\tilde{\alpha}_n$ from the data, and determined that a strong f_n^2 dependence for the dissipation existed, analogous to a frequency domain transformation of the Burgher's equation with viscous damping. A reasonable representation of this frequency dependence can be achieved by assuming the following form for $\tilde{\alpha}_n$

$$\tilde{\alpha}_n = \tilde{\alpha}_{n0} + \left(\frac{f_n}{f_{peak}} \right)^2 \tilde{\alpha}_{n1} \tag{89}$$

where

$$\tilde{\alpha}_{n0} = \tilde{F}\tilde{\beta}(x) \tag{90}$$

$$\tilde{\alpha}_{n1} = \left(\tilde{\beta}(x) - \tilde{\alpha}_{n0}\right) \frac{f_{peak}^2 \sum_{n=1}^{N} |A_n|^2}{\sum_{n=1}^{N} f_n^2 |A_n|^2} \tag{91}$$

This essentially splits the frequency dependence into a balance between one that is flat across the frequency range ($\tilde{\alpha}_{n0}$) and one that is weighted to the square of the frequency ($\tilde{\alpha}_{n1}$). This split is controlled by the parameter $\tilde{F}$. Mase and Kirby (1992) found that $\tilde{F} = 0.5$ seemed to work best for their experimental data, though Chen et al. (1997) noted that $\tilde{F} = 0$ worked best if the comparison at the shallowest gauge of the experiment ($h = .025$ m) was neglected.

Eldeberky and Battjes (1996) and Eldeberky and Madsen (1999) both used the dissipation of Battjes and Janssen (1978), and assumed that the dissipation was weighted equally across all frequencies. By realizing that amplitude changes are half those of changes in energy, they found that

$$\tilde{\alpha}_n = \frac{1}{2} \frac{\epsilon_b}{\sum_{n=1}^{N} C_{gn}|A_n|^2} \tag{92}$$

where the denominator represents the total energy flux in the spectrum. Eldeberky and Madsen (1999) show comparisons of their model (with the inclusion of the second-order relation between ϕ and η discussed earlier) with the data of Mase and Kirby (1992). While they showed improved comparisons of skewness relative to the original model of Kaihatu and Kirby (1995), they were unable to replicate the increase in negative asymmetry seen in the data. Kaihatu (2001), using the f_n^2 dissipation weighting detailed in Mase and Kirby (1992) as well as the second-order transformation between ϕ and η, demonstrated improved asymmetry predictions relative to those seen in Eldeberky and Madsen (1999) by using $\tilde{F} = 0$ in equation (90).

6. COMPARISONS TO DATA

6.1. Whalin (1971)

In this section we compare several of the described models to the experimental data of Whalin (1971), who conducted a laboratory study to investigate the limits of linear refractive wave propagation theory. He generated sinusoidal waves with periods of 1, 2 and 3 seconds and ran them over bathymetry resembling a tilted cylinder. The plan view of the experimental layout is shown in Fig. 3. Wave gauges located down the centerline of the tank measured the free surface elevation; these measurements were then processed to yield wave harmonic amplitudes. The experimental conditions ranged from deep ($\mu^2 \approx 2$) to shallow ($\mu^2 \approx 0.2$) water at the wave maker. We will concentrate on the 1 second period case. Comparisons to other cases in the experiment are detailed in the original papers.

For this $T = 1$ s case ($a_o = 0.0195$ m) $N = 2$ harmonics were used. This is in concert with the work detailed in the original studies; the inclusion of additional harmonics did not make a significant difference. For each case, all wave energy was placed in the first harmonic, with the higher harmonics initialized with zero energy. We compare the following models: the extended Boussinesq model of Kaihatu and Kirby (1998) with DSO parameters ($\alpha = -0.4111, \beta = -0.3188$); the extended Boussinesq model (expressed in terms of ϕ and η) of Kaihatu and Kirby (1994); and the nonlinear mild-slope equation model of Kaihatu and Kirby (1995) with the second-order correction of Kaihatu (2001). The exclusion of the second-order correction of Kaihatu (2001) did
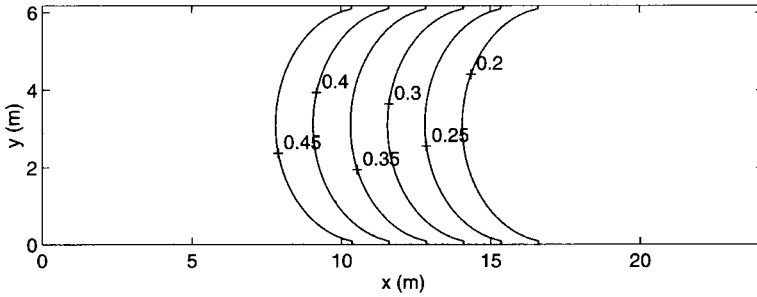
Figure 3. Plan view of experiment of Whalin (1971). Bathymetric contours labeled in meters.

not yield significant difference relative to inclusion. Additionally, comparisons between the DO ($\alpha = -0.3855, \beta = -0.3540$) and DSO parameters for this experiment are shown in the original paper of Kaihatu and Kirby (1998) and are not included here. Lastly, the model of Chen and Liu (1995) was not used in these comparisons; they used a second-order bound wave solution to force their model for the $T = 1$ s case, citing a large phase mismatch between the free and bound second harmonic otherwise. However, we are more interested in testing the model in general wave propagation scenarios, where *a priori* consideration of the free or bound wave nature of the forcing would not be desirable. Linear wave forcing of the model of Chen and Liu (1995) for this case reveals significant oscillation of the second harmonic over the domain.

Comparisons of the model to the $T = 1$ s, $a_o = 0.0195$ m case are shown in Fig. 4. In this case the model of Kaihatu and Kirby (1995) with the second-order correction (Kaihatu, 2001) seems to work best for capturing evolution characteristics of both harmonics. The extended Boussinesq models of Kaihatu and Kirby (1994; 1998) appear to underpredict the energy transfer to the second harmonic in the focal region. The oscillations in the second harmonic as predicted by Kaihatu and Kirby (1994) are of the same order as those shown in Chen and Liu (1995), and are less severe than would be seen if the Chen and Liu (1995) model had been forced with a linear wave. This indicates that the presence of $O(\delta\mu^2)$ terms appear to have a stabilizing effect on the model, as commented by Tang and Ouelette (1997). We also note here that the model of Chen and Liu (1995) with bound wave forcing agrees with the second harmonic data for this case better than the model of Kaihatu and Kirby (1994) with linear wave forcing. Lastly, Tang and Ouelette (1997) show a better match to the $T = 1$ s case than seen here, possibly due to the inclusion of nonlinear diffraction terms.

6.2. Mase and Kirby (1992)

Mase and Kirby (1992) conducted a series of laboratory experiments in which irregular waves (Pierson-Moskowitz spectrum) were generated and allowed to shoal and break over a slope. The experimental set-up is shown in Fig. 5. The case studied here had a peak period $T_p = 1$ s, leading to $kh \approx 2$ at the wave maker. Significant wave breaking occurred in this experiment beginning near the gauge at $h = 0.175$ m. Time series of free surface elevations were collected at 20 Hz and divided into 7 realizations of 2048 points each. Each realization was then put into a Fast Fourier Transform (FFT); the resulting energy density spectra were both Bartlett-averaged across all seven realizations and band-averaged across eight neighboring frequency bands. A gauge located 0.20 m offshore of the toe of the slope provided the initial condition. Tests with $N = 300$ and $N = 500$ frequency components were run through the models for each realization, leading to a maximum frequency of 3 Hz and 5 Hz respectively.

We compare two models to the experimental data: the nonlinear mild-slope equation model of Kaihatu and Kirby (1995), with corrections by Kaihatu (2001); and the extended Boussinesq frequency
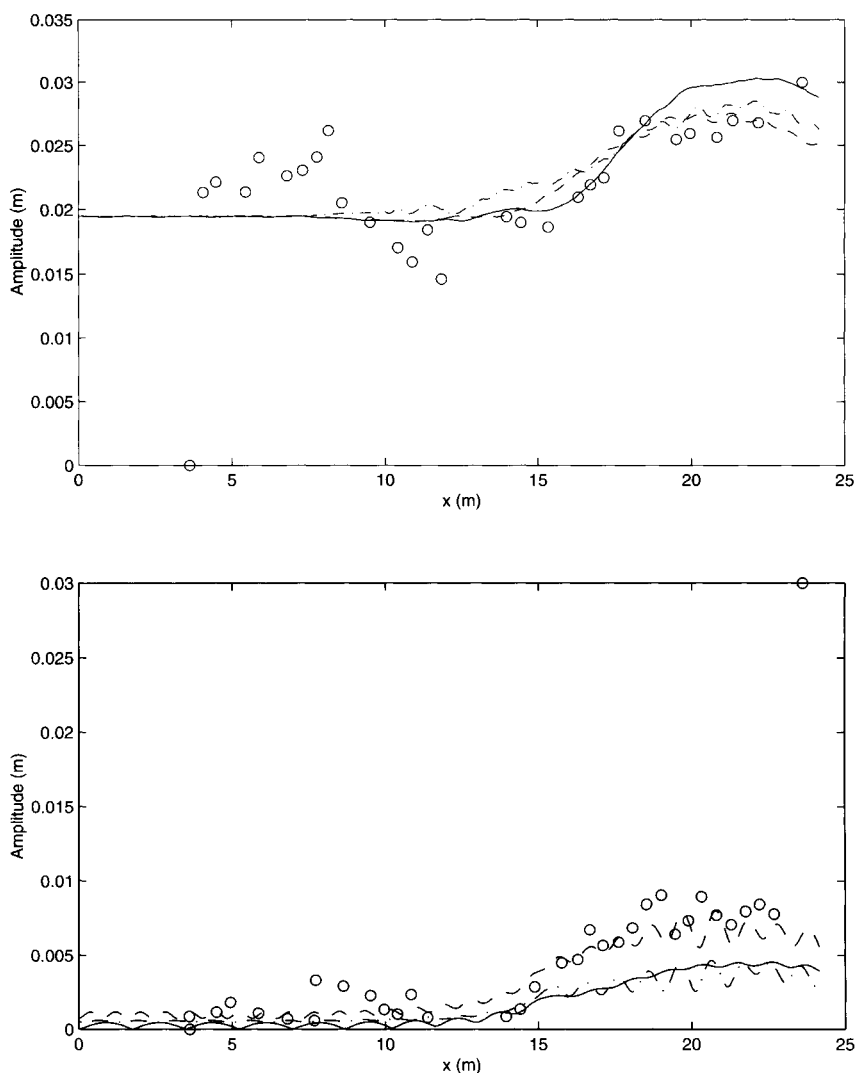
Figure 4. Comparison of nonlinear frequency domain models data of Whalin (1971). Solid line: model of Kaihatu and Kirby (1998) with DSO parameters. Dashed line: model of Kaihatu and Kirby (1995) with corrections from Kaihatu (2001). Dash-dot line: model of Kaihatu and Kirby (1994). Top: first harmonic amplitudes. Bottom: second harmonic amplitudes.

domain model of Kaihatu and Kirby (1998) with the DSO parameters. Both models were equipped with the dissipation mechanism of Thornton and Guza (1983) and the frequency-distribution methodology detailed by Mase and Kirby (1992). Both $\tilde{F} = 0.5$ and $\tilde{F} = 0$ were used, the latter corresponding to a full frequency-squared weighting of dissipation.

Comparisons of spectra at various locations are shown in Fig. 6, with $N = 300$ and $\tilde{F} = 0$. It is apparent that, while both models tend to compare well to the data at the frequency peak and lower,
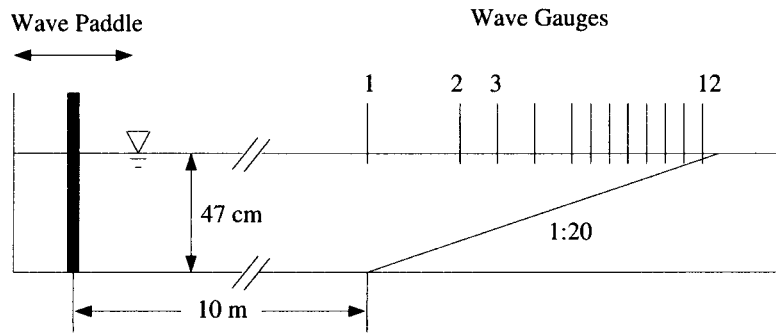
Figure 5. Layout of experiment of Mase and Kirby (1992).
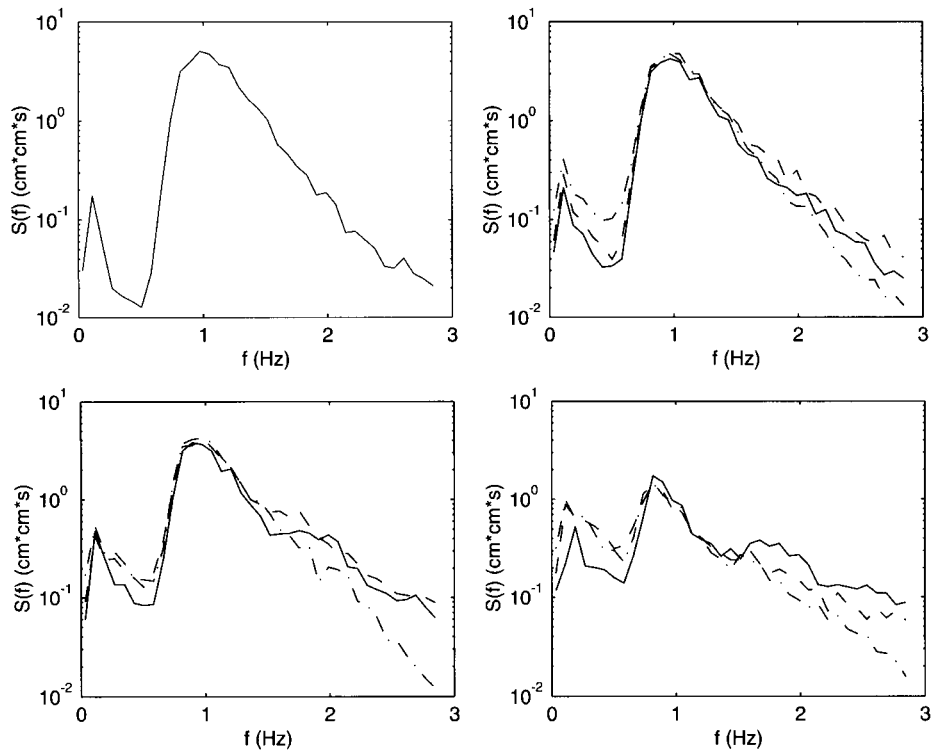
Figure 6. Comparisons of spectra from models to data from Mase and Kirby (1992): $N = 300$ frequencies, $F = 0$. Solid line: data. Dashed line: model of Kaihatu and Kirby (1995) with correction of Kaihatu (2001). Dash-dot line: model of Kaihatu and Kirby (1998) with DSO parameters. Top left: $h = 0.47$ m. Top right: $h = 0.2$ m. Bottom left: $h = 0.125$ m. Bottom right: $h = 0.05$ m.

the extended Boussinesq model of Kaihatu and Kirby (1998) significantly underpredicts the high frequency evolution ($f > 1.75$ Hz). The case of $N = 500$ components reveal similar trends. No significant differences occur between the $\tilde{F} = 0$ and $\tilde{F} = 0.5$ cases.
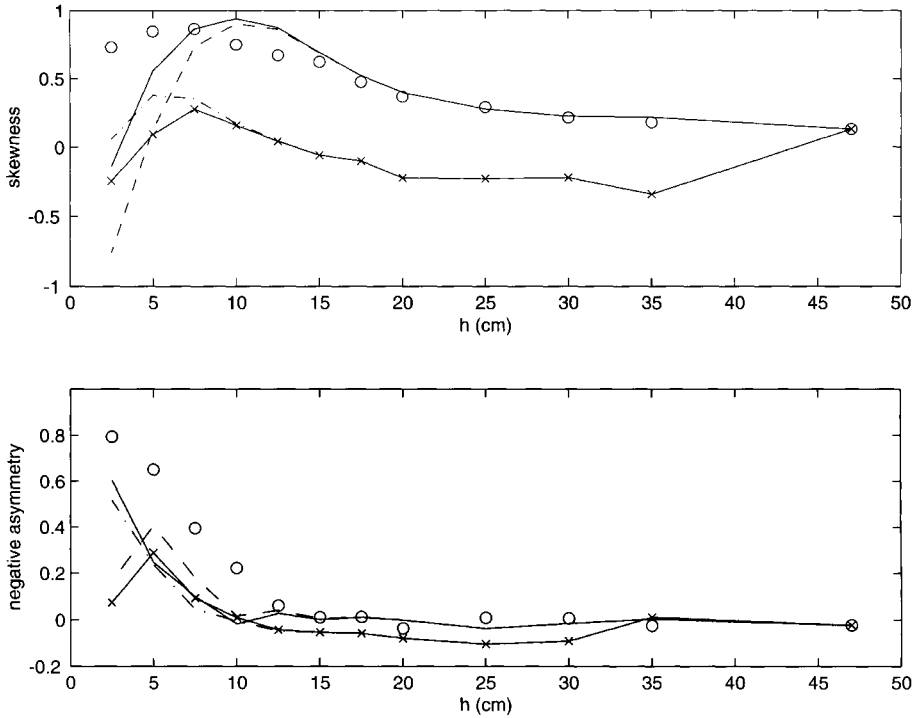
Figure 7. Comparisons of skewness and asymmetry from models to data from Mase and Kirby (1992): $N = 500$ frequencies. Open circles: data. Solid and dashed lines: model of Kaihatu and Kirby (1995) with correction of Kaihatu (2001) with $F = 0.5$ and $F = 0$, respectively. Dash-dot and dash-x lines: model of Kaihatu and Kirby (1998) with DSO parameters and $F = 0.5$ and $F = 0$, respectively. Top: skewness. Bottom: Negative asymmetry.

Differences between the $\tilde{F} = 0$ and $\tilde{F} = 0.5$ cases begin to appear when comparing skewness and asymmetry. Fig. 7 shows a comparison of both models, each using $\tilde{F} = 0.5$ and $\tilde{F} = 0$, to the skewness and asymmetry values from the data for the case of $N = 500$. (It was shown by Kaihatu, 2001 that good comparisons to higher-order moments required $N = 500$ frequency components.) Both skewness and asymmetry are better predicted by the model of Kaihatu and Kirby (1995), with corrections by Kaihatu (2001), than with the extended Boussinesq model of Kaihatu and Kirby (1998). Additionally, $\tilde{F} = 0.5$ results in a slightly better skewness prediction and a slightly worse asymmetry prediction than $\tilde{F} = 0$, except for the gauge nearest to shore. At that location the modeled asymmetry falls off dramatically if $\tilde{F} = 0$ in either shoaling model. The reason for this sudden dropoff is not clear. We note here that this behavior at the last gauge is not an indictment of the $\tilde{F} = 0$ value; Kennedy et al. (2000) showed excellent agreement between the time domain Boussinesq model of Wei et al. (1995) and the Mase and Kirby (1992) data. An eddy viscosity mechanism was used for dissipation in the time domain model, the formulation of which is equivalent to $\tilde{F} = 0$ in the frequency domain. Rather, the problem in the frequency domain may lie in the use of the bulk energy dissipation mechanism used here; it is quite likely that a frequency domain formulation of the local eddy viscosity mechanism in the Kennedy et al. (2000) model would address the problems seen at the shallowest gauge.

6.3. Discussion

Based on the data-model comparisons shown, it appears that frequency domain formulations of the extended Boussinesq model of Nwogu (1993) may be inferior to those based on the nonlinear mild-slope equation (Kaihatu and Kirby, 1995; Kaihatu, 2001). One possible reason for the relatively poor performance of the frequency domain model of Kaihatu and Kirby (1998) may lie in the order of truncation of the original equations of Nwogu (1993). These equations were truncated to retain only $O(\delta, \mu^2)$ terms. As seen in the (ϕ, η) model of Kaihatu and Kirby (1994), it is possible to retain $O(\delta\mu^2)$ terms and still treat the equations using the frequency domain transformation; perhaps the inclusion of these terms in the frequency domain model of Kaihatu and Kirby (1998) would improve the results (though, in the author's experience, the derivation process is exceedingly complicated and ambiguous).

Interestingly, however, Wei and Kirby (1995) show very good agreement between their numerical treatment of the model of Nwogu (1993) and the Mase and Kirby (1992) data. As mentioned early in the chapter, there is often some discrepancy between the performance of the original time domain model and its corresponding frequency domain formulation. Additionally, Kofoed-Hansen and Rasmussen (1998) showed that the model of Madsen and Sørensen (1993) (a frequency domain shoaling model based on the extended Boussinesq model of Madsen et al., 1991) demonstrates favorable agreement with the Mase and Kirby (1992) data set, despite the order of truncation being the same as that in Kaihatu and Kirby (1998). This is likely due to differences in the underlying time domain equations and in the derivation procedure of the corresponding frequency domain models.

7. STOCHASTIC MODELS

While frequency domain models offer great utility in simulating shallow water processes, this is done at some computational expense, particularly when they are initialized with smoothed spectra (as would be the case for field studies, for example). Initial phases are required for these models, so multiple temporal realizations are run with random initial phases and the results averaged until acceptably smooth, which can require considerable computation time. This has motivated research into stochastic models of triad interactions. In this section, we briefly describe a few approaches, referring interested readers to the papers cited herein and the overview of Agnon and Sheremet (2000) for further details.

Abreau et al. (1992) developed a statistical model for triad wave evolution, suitable as a source function in a spectral balance model such as WAM (Komen et al., 1994) or SWAN (Booij et al., 1999). The model was developed using the non-dispersive asymptote, with the concomitant assumption that resonant interactions are only possible among collinear shallow water waves. This inherently disallows vector-sum interactions among spectral components in the wave field, negating a significant portion of the potential nonlinear behavior.

Eldeberky and Battjes (1995) developed a parameterized triad energy exchange mechanism which depends on the evolution of the biphase, a higher-order statistical quantity of the wave train which is zero at low nonlinearity (low Ursell number) and asymptotically approaches $-\pi/2$ as the Ursell number increases. The evolution of this quantity was determined from experimental measurements as a function of Ursell number. Additionally, nonlinear interaction was further limited to self-self interactions at the spectral peak. This allowed energy to move from the peak to its second harmonic, but did not allow for any feedback transfer. This parameterized model is a selectable option in the SWAN model (see Chapter 5).

Recently, much has been done on developing stochastic models from the phase-resolving dynamical equations (for example, Boussinesq equations). The evolution equation and its conjugate are each multiplied by their corresponding conjugates, then added together, resulting in an energy equation

with triple products of amplitudes in the nonlinear summations. These triple products are related to the bispectrum (a higher-order spectrum), for which an additional evolution equation is needed for system closure. The bispectral evolution equation is derived by applying the triple product definition of the bispectrum to the original evolution equation, resulting in an equation for bispectra with quadruple products of amplitudes in the nonlinear terms (the trispectrum). At this point a Gaussian closure assumption is made, which has the effect of reducing the trispectrum to products of the spectrum, thus creating a finite system of equations. Herbers and Burton (1997) developed a directional stochastic model from the Boussinesq equations of Peregrine (1967) using the same periodicity assumptions as Kirby (1990) and the procedure described above. Agnon and Sheremet (1997) worked from the nonlinear dispersive model of Agnon et al. (1993) to develop a stochastic model using the same closure hypothesis as Herbers and Burton (1997), but in the form of a single equation model for the spectral energy. Kofoed-Hansen and Rasmussen (1998) operated on the extended Boussinesq equations of Madsen and Sørensen (1993) and developed a corresponding stochastic model. They showed that good model comparisons were possible so long as the Ursell number $U_r < 1.5$, was in accord with the observations of Agnon and Sheremet (1997). Eldeberky and Madsen (1999) revisited Agnon and Sheremet (1997) and rederived a stochastic model, taking an additional second-order effect (noted earlier) into account.

One potential limitation has been the specification of the closure required to truncate the system to a finite number of solvable equations; the subset of trispectra used in the bispectral evolution equation represent the lowest order contributions. However, Holloway (1980), in the context of triad interactions among internal waves, hypothesized a different closure for the system. Rather than discarding a significant portion of the trispectra, Holloway (1980) suggested that the trispectrum is also proportional to the bispectrum; this, in addition to the products of energy terms, make up the contributions from the trispectrum. Becq-Girard et al. (1999), working from the extended Boussinesq model of Madsen and Sørensen (1993), developed a stochastic model with Holloway's (1980) closure hypothesis included. This inclusion essentially adds a linear term (multiplied by an empirical proportionality coefficient) to the bispectral evolution equation, with the effect of broadening the resonance condition, and adding higher-order contributions that may improve overall performance at moderate Ursell numbers.

8. CONCLUSIONS

Nonlinear frequency domain models have undergone rapid development, apace with corresponding advances in the time domain realm (particularly with respect to Boussinesq models). They have also increased in utility with the incorporation of enhanced frequency dispersion effects, improved shoaling and energy dissipation from wave breaking. We investigated several formulations for nonlinear frequency domain models; ensuing data-model comparisons demonstrate that nonlinear models based on the mild-slope equations appear to be more accurate than frequency domain transformations of the extended Boussinesq equations explored herein.

Initial phases of the irregular wave train were available to drive the models for data-model comparisons to the laboratory data. In most general field situations, however, smoothed spectra from pressure gauges, wave buoys or forecast model output would be the only source of data. Using smoothed spectra as an initial condition requires multiple runs of the model with random phases, a time consuming task. With the advent of the SWAN model, the consideration of triad interactions (even in the parameterized form used by the model) has become more widespread, and the need for a useful operational form of these interactions more apparent. This is particularly evident as more model systems linking wave, hydrodynamic and sediment modules are developed. The stochastic models described previously exhibit great potential for operational use; more development in this area is warranted.

ACKNOWLEDGMENTS

LIST OF SYMBOLS

α	—	dispersion optimization parameter from Nwogu (1993)
$\tilde{\alpha}$	—	dissipation coefficient from Mase and Kirby (1992)
β	—	shoaling optimization parameter from Kaihatu and Kirby (1998)
$\tilde{\beta}$	—	dissipation coefficient from Mase and Kirby (1992)
Γ^+, Γ^-	—	nonlinear coefficients from Eldeberky and Madsen (1999)
γ	—	shoaling gradient
$\tilde{\gamma}$	—	free parameter in calculation of H_{max} from Battjes and Janssen (1978)
$\overline{\gamma}$	—	dissipation free parameter from Thornton and Guza (1983)
δ	—	nonlinearity scaling parameter
ϵ_b	—	dissipation
η	—	free surface elevation
$\hat{\eta}$	—	time-periodic free surface elevation
Λ	—	$O(\delta\mu^2)$ term in extended Boussinesq model of Kaihatu and Kirby (1994)
μ	—	dispersion scaling parameter
π	—	3.1415927....
ρ	—	mass density
ϕ	—	velocity potential
$\hat{\phi}$	—	time-periodic velocity potential
ϕ_α	—	velocity potential at depth z_α
$\hat{\phi}_\alpha$	—	time-periodic velocity potential at depth z_α
Υ	—	$O(\delta\mu^2)$ term in extended Boussinesq model of Kaihatu and Kirby (1994)
ω	—	radian frequency
A	—	complex amplitude of free surface
a	—	complex amplitude of free surface in parabolic model
a_o	—	reference amplitude
$\tilde{a}$	—	complex amplitude of free surface with second-order correction of Kaihatu (2001)
b	—	complex amplitude of velocity potential
C	—	phase speed
C_g	—	group velocity
$c.c.$	—	complex conjugate
E	—	term in shoaling relation of Kaihatu and Kirby (1998)

$\overline{E}$	—	energy
F	—	term in shoaling relation of Kaihatu and Kirby (1998)
$\tilde{F}$	—	breaking parameter controlling frequency dependence of dissipation from Mase and Kirby (1992)
f	—	cyclic frequency
f_{peak}	—	peak frequency
$\tilde{f}$	—	depth dependence from linear theory
$\overline{f}$	—	average frequency
G	—	term in shoaling relation of Kaihatu and Kirby (1998)
G'	—	depth dependence term
g	—	gravitational acceleration
H_{max}	—	maximum wave height
H_{rms}	—	root-mean-square wave height
h	—	water depth
h_o	—	reference water depth
i	—	$\sqrt{-1}$
k	—	wave number
$\mathbf{k}$	—	wave number vector
$\overline{k}$	—	longshore-averaged wave number
k_x	—	cross-shore component of wave number vector
k_y	—	longshore component of wave number vector
N	—	total number of frequencies
n	—	frequency index
p	—	pressure
Q_b	—	percentage of breaking waves
R	—	nonlinear coefficient term from Kaihatu and Kirby (1998)
$\tilde{R}, \tilde{R}'$	—	nonlinear coefficient from Chen and Liu (1994)
$\tilde{\tilde{R}}, \tilde{\tilde{R}}'$	—	nonlinear coefficient from Kaihatu and Kirby (1994)
S	—	nonlinear coefficient term from Kaihatu and Kirby (1998)
$\tilde{S}, \tilde{S}'$	—	nonlinear coefficient from Chen and Liu (1994)
$\tilde{\tilde{S}}, \tilde{\tilde{S}}'$	—	nonlinear coefficient from Kaihatu and Kirby (1994)
T	—	wave period
T_p	—	peak period
t	—	time
u	—	cross-shore velocity
u_α	—	cross-shore velocity at z_α
$\mathbf{u}_\alpha$	—	horizontal velocity vector at z_α
$\hat{\mathbf{u}}_\alpha$	—	time-periodic horizontal velocity vector at z_α
$\overline{\mathbf{u}}$	—	depth-averaged horizontal velocity vector
U_r	—	Ursell number (δ/μ^2)
v	—	longshore velocity
W	—	shoaling coefficient term
x	—	cross-shore coordinate
Y	—	nonlinear coefficient of Kaihatu and Kirby (1995)
Y'	—	nonlinear coefficient from Eldeberky and Madsen (1999)
Y''	—	nonlinear coefficient from Kaihatu (2001)
y	—	longshore coordinate
Z	—	nonlinear coefficient from Kaihatu and Kirby (1995)

Z'	—	nonlinear coefficient from Eldeberky and Madsen (1999)
Z''	—	nonlinear coefficient from Kaihatu (2001)
z	—	vertical coordinate
∇	—	horizontal gradient operator

REFERENCES

Abreau, M., Larraza, A., and Thornton, E.B., 1992. Nonlinear transformation of directional wave spectra in shallow water, Journal of Geophysical Research, 97: 15,579–15,589.

Agnon, Y., Sheremet, A., Gonsalves, J., and Stiassnie, M., 1993. Nonlinear evolution of a unidirectional shoaling wave field. Coastal Engineering, 20: 29–58.

Agnon, Y., and Sheremet, A., 1997. Stochastic nonlinear shoaling of directional spectra. Journal of Fluid Mechanics, 345: 79–99.

Agnon, Y., and Sheremet, A., 2000. Stochastic evolution models for nonlinear gravity waves over uneven topography. In: Liu, P.L.-F. (Editor), Advances in Coastal and Ocean Engineering, Vol. 6. Singapore: World Scientific Publishing Co.

Battjes, J.A., and Groenendijk, H.W., 2000. Wave height distributions on shallow foreshores. Coastal Engineering, 40: 161–182.

Battjes, J.A., and Janssen, J.P.F.M., 1978. Energy loss and set-up due to breaking of random waves. Proceedings of the 16th International Conference on Coastal Engineering, ASCE, pp. 569–587.

Battjes, J.A., and Stive, M., 1985. Calibration and verification of a dissipation model for random breaking waves. Journal of Geophysical Research, 90: 9159–9167.

Becq-Girard, F., Forget, P., and Benoit, M., 1999. Non-linear propagation of unidirectional wave fields over varying topography. Coastal Engineering, 38: 91–113.

Berkhoff, J.C.W., 1972. Computation of combined refraction-diffraction. Proceedings of the 13th International Conference on Coastal Engineering, ASCE, pp. 471–490.

Booij, N., 1981. Gravity waves on water with non-uniform depth and current. Report 81-1. Delft, The Netherlands: Department of Civil Engineering, Delft University of Technology.

Booij, N., Ris, R.C., and Holthuijsen, L.H., 1999. A third-generation wave model for coastal regions. 1. Model description and validation. Journal of Geophysical Research, 104: 7649–7666.

Bryant, P.J., 1973. Periodic waves in shallow water. Journal of Fluid Mechanics, 59: 625–644.

Bryant, P.J., 1974. Stability of periodic waves in shallow water. Journal of Fluid Mechanics, 66: 81–96.

Chawla, A., Özkan-Haller, H.T., and Kirby, J.T., 1998. Spectral model for wave evolution over irregular bathymetry. Journal of Waterway, Port, Coastal and Ocean Engineering, 124: 189–198.

Chen, Y., and Liu, P.L.-F., 1995. Modified Boussinesq equations and associated parabolic models for water wave propagation. Journal of Fluid Mechanics, 288: 351–381.

Chen, Y., Guza, R.T., and Elgar, S., 1997. Modeling spectra of breaking surface waves in shallow water. Journal of Geophysical Research, 102: 25,035–25,046.

Dally, W.R., 1990. Random breaking waves: A closed-form solution for planar beaches. Coastal Engineering, 14: 233–263.

Eldeberky, Y., and Battjes, J.A., 1995. Parameterization of triad interaction in wave energy models. Proceedings of Coastal Dynamics '95, pp. 140–148.

Eldeberky, Y., and Battjes, J.A., 1996. Spectral modeling of wave breaking: Application to Boussinesq equations. Journal of Geophysical Research, 101: 1253–1264.

Eldeberky, Y., and Madsen, P.A., 1999. Deterministic and stochastic evolution equations for fully dispersive and weakly nonlinear waves. Coastal Engineering, 38: 1–24.

Freilich, M.H., and Guza, R.T., 1984. Nonlinear effects on shoaling surface gravity waves. Philosophical Transactions of the Royal Society of London, Series A, 311: 1–41.

Herbers, T.H.C., and Burton, M.C., 1997. Nonlinear shoaling of directionally spread waves on a beach. Journal of Geophysical Research, 102: 21,101–21,114.

Holloway, G., 1980. Oceanic internal waves are not weak waves. Journal of Physical Oceanography, 10: 906–914.

Kadomtsev, B.B., and Petviashvili, V.I., 1970. On the stability of solitary waves in weakly dispersing media. Soviet Physics - Doklady, 15: 539–541.

Kaihatu, J.M., 1994. Frequency domain models for nonlinear finite depth water wave propagation. Ph.D. thesis. Newark, DE: University of Delaware, 169p.

Kaihatu, J.M., 2001. Improvement of nonlinear parabolic dispersive wave model. Journal of Waterway, Port, Coastal and Ocean Engineering, 127: 113–121.

Kaihatu, J.M., and Kirby, J.T., 1994. Parabolic and angular spectrum modeling of a fully nonlinear extended Boussinesq equation. Proceedings of the International Symposium: Waves—Physical and Numerical Modeling, pp. 514–523.

Kaihatu, J.M., and Kirby, J.T., 1995. Nonlinear transformation of waves in finite water depth. Physics of Fluids, 7: 1903–1914.

Kaihatu, J.M., and Kirby, J.T., 1998. Two-dimensional parabolic modeling of extended Boussinesq equations. Journal of Waterway, Port, Coastal and Ocean Engineering, 124: 57–67.

Keller, J.B., 1988. Resonantly interacting water waves. Journal of Fluid Mechanics, 191: 529–534.

Kennedy, A.B., Chen, Q., Kirby, J.T., and Dalrymple, R.A., 2000. Boussinesq modeling of wave transformation, breaking, and runup. I: 1-D. Journal of Waterway, Port, Coastal and Ocean Engineering, 126: 39–47.

Kirby, J.T., 1986a. Higher-order approximations in the parabolic equation method for water waves. Journal of Geophysical Research, 91: 933–952.

Kirby, J.T., 1986b. Rational approximations in the parabolic equation method for water waves. Coastal Engineering, 10: 355–378.

Kirby, J.T., 1990. Modeling shoaling directional wave spectra in shallow water. Proceedings of the 22nd International Conference on Coastal Engineering, ASCE, pp. 109–122.

Kirby, J.T., and Kaihatu, J.M., 1996. Structure of frequency domain models for random wave breaking. Proceedings of the 25th International Conference on Coastal Engineering, ASCE, pp. 1144–1155.

Kofoed-Hansen, H., and Rasmussen, J.H., 1998. Modelling of nonlinear shoaling based on stochastic evolution equations. Coastal Engineering, 33: 203–232.

Komen, G.J., Cavaleri, L., Donelan, M.A., Hasselmann, K., Hasselmann, S., and Janssen, P.A.E.M., 1994. Dynamics and Modeling of Ocean Waves. Cambridge: Cambridge University Press. 531p.

Liu, P.L.-F., Yoon, S.B., and Kirby, J.T., 1985. Nonlinear refraction-diffraction of waves in shallow water. Journal of Fluid Mechanics, 153: 185–201.

Lozano, C.J., and Liu, P.L.-F., 1980. Refraction-diffraction model for linear surface water waves. Journal of Fluid Mechanics, 101: 705–720.

Madsen, P.A., Murray, R., and Sørensen, O.R., 1991. A new form of the Boussinesq equations with improved linear dispersion characteristics. Coastal Engineering, 15: 371–388.

Madsen, P.A., and Schäffer, H.A., 1998. Higher-order Boussinesq-type equations for surface gravity waves: Derivation and analysis. Philosophical Transactions of the Royal Society of London, Series A, 356: 3123–3184.

Madsen, P.A., and Schäffer, H.A., 1999. A review of Boussinesq-type equations for surface gravity waves. In: Liu, P.L.-F. (Editor), Advances in Coastal and Ocean Engineering, Vol. 5. Singapore: World Scientific Publishing Co.

Madsen, P.A., and Sørensen, O.R., 1992. A new form of the Boussinesq equations with improved linear dispersion characteristics. Part 2. A slowly-varying bathymetry. Coastal Engineering, 18: 183–204.

Madsen, P.A., and Sørensen, O.R., 1993. Bound waves and triad interactions in shallow water. Ocean Engineering, 20: 359–388.

Mase, H., and Kirby, J.T., 1992. Hybrid KdV frequency domain equation for random wave transformation. Proceedings of the 23rd International Conference on Coastal Engineering, ASCE, pp. 474–482.

McCowan, A.D., and Blackman, D.R., 1989. Proceedings of the 9th Australasian Conference on Coastal and Ocean Engineering, pp. 412–416.

Mei, C.C., 1983. The Dynamics of Ocean Surface Waves. Singapore: World Scientific Publishing Co. 740p.

Nwogu, O., 1993. Alternative form of Boussinesq equations for nearshore wave propagation. Journal of Waterway, Port, Coastal and Ocean Engineering, 119: 618–638.

Peregrine, D.H., 1967. Long waves on a beach. Journal of Fluid Mechanics, 27: 815–827.

Phillips, O.M., 1960. On the dynamics of unsteady gravity waves of finite amplitude. Part 1. The elementary interactions. Journal of Fluid Mechanics, 9: 193–217.

Radder, A.C., 1979. On the parabolic equation method for water-wave propagation. Journal of Fluid Mechanics, 95: 159–176.

Rygg, O.B., 1988. Nonlinear refraction-diffraction of surface waves in intermediate and shallow water. Coastal Engineering, 12: 191–211.

Schäffer, H.A., and Madsen, P.A., 1995. Further enhancements of Boussinesq-type equations. Coastal Engineering, 26: 1–14.

Smith, R., and Sprinks, T., 1975. Scattering of surface waves by a conical island. Journal of Fluid Mechanics, 72: 373–384.

Tang, Y., and Ouelette, Y., 1997. A new kind of nonlinear mild-slope equation for combined refraction-diffraction of multifrequency waves. Coastal Engineering, 31: 3–36.

Thornton, E.B., and Guza, R.G., 1983. Transformation of wave height distribution. Journal of Geophysical Research, 88: 5925–5938.

Ursell, F., 1953. The long wave paradox in the theory of gravity waves. Proceedings of the Cambridge Philosophical Society, 49: 685–694.

Wei, G., and Kirby, J.T., 1995. A time-domain numerical code for extended Boussinesq equations. Journal of Waterway, Port, Coastal and Ocean Engineering, 120: 251–261.

Wei, G., Kirby, J.T., Grilli, S.T., and Subramanya, R., 1995. A fully nonlinear Boussinesq model for surface waves. 1: Highly nonlinear, unsteady waves. Journal of Fluid Mechanics, 294: 71–92.

Whalin, R.W., 1971. The limit of application of linear wave refraction theory in a convergence zone. Report. H-71-3. Vicksburg, MS: U.S. Army Corps of Engineers Waterways Experiment Station.

Witting, J.M., 1984. A unified model for the evolution of nonlinear water waves. Journal of Computational Physics, 56: 203–236.

Wu, T.Y., 1981. Long waves in ocean and coastal waters. Journal of Engineering Mechanics, 107: 501–522.

Chapter 3

Advanced Numerical Methods for Coastal Hydrodynamics

Clive G. Mingham

Centre for Mathematical Modelling and Flow Analysis, Manchester Metropolitan University, Chester Street, Manchester, M1 5GD, United Kingdom

1. INTRODUCTION

As a result of increasing public interest in environmental issues more attention is now being paid to the coastal environment and humankind's impact upon it. Some of the many recent problems relating to the coastal environment include beach erosion, silting of shipping channels, pollutant dispersal, wakes from high-speed ferries, oil spill trajectories, the design of breakwaters, tsunamis, tidal flushing of harbors and estuaries and the effects of sea level rise due to global warming. All these problems have economic and social consequences in addition to the obvious environmental ones. The root of understanding these problems is an accurate description of the underlying hydrodynamics, and this may be investigated in two very different ways.

Historically, engineers have constructed physical scale models of a particular scenario within a wave tank or flume. This approach is very expensive, time consuming and requires extensive expertise in order to capture the relevant features of the problem and to measure the resulting data accurately. Furthermore, physical scale models contain intrinsic scaling errors and are difficult to adapt to even slightly different situations. Examples of this approach can be found in Owen (1980, 1982), Goda (1985), Allsop et al. (1995; 1996), Besley et al. (1998), and Bruce et al. (2001).

An alternative approach is to use mathematical models. The equations describing water flow have been known for a long time and now, with the development of modern high-speed digital computers, it has become feasible to obtain approximate solutions to these equations and thus simulate realistic flow scenarios. In many cases this computational approach is quicker and cheaper than the scale model approach and, given a suitably well written computer package, may not require the same degree of engineering expertise to obtain the required results. Furthermore, numerical simulation is unaffected by scaling errors and is very flexible—the geometry, wave height and bathymetry can be changed easily by simply modifying input files. Examples of this approach can be found in Abbot et al. (1973), Falconer (1980), Fennema and Chaudhry (1990), Watson et al. (1996), Dodd (1998), and Mingham and Causon (1998). This chapter presents some modern numerical techniques and results for a range of coastal problems.

There are two main problems with numerical simulation. Firstly, the underlying physics must be described in enough detail to capture the essential features of the flow. A complete description of the flow, even it this were possible, would yield a system of equations which would be so complex that they could not be solved in a reasonable time. In reality, a complete description is not possible because terms such as turbulent shear stresses and bed stresses are not sufficiently well understood and have to be approximated or modeled empirically. In practice, the engineer often only requires fairly coarse detail, and is satisfied with the prediction of a small number of key parameters. This allows the full equation set to be simplified enough to become computationally tractable and the lesser requirement for engineering accuracy permits the approximation of terms within the model without invalidating its results.

The second problem with numerical simulation concerns the algorithms used to approximate the solution of the flow model. The resulting set of equations must be solved using numerical schemes capable of resolving the essential flow features accurately. Solvers that are constructed only on the basis of the mathematics do not always respect the underlying physics. These solvers may fail to conserve mass or momentum which can lead to large errors in the solution. Schemes containing high levels of numerical diffusion also tend to be inaccurate as they obscure potentially interesting features of the flow. Simplifying assumptions, like inviscid flow, may lead to the formation of bore waves which traditional solvers have been unable to handle, and many solvers fail on problems involving transcritical flow or abrupt changes in bathymetry (Leendertse, 1967; Falconer, 1992). The solvers presented in this chapter respect the underlying physics and address all of these problems.

There is one further issue concerning the numerical simulation method that relates to the gridding of the computational domain. Problems in coastal hydrodynamics often occur over complicated geometries with highly irregular coastlines, the presence of islands and complex harbor and breakwater configurations. Classical finite difference approaches based on Cartesian grids use crude saw-tooth approximations to the boundaries of the domain which lead to unnecessary solution errors (Abbot et al., 1973; Falconer, 1980). One approach to overcome this problem and produce a boundary fitted grid is to employ curvilinear coordinates to transform the computational domain to a rectangular domain (Borthwick and Barber, 1992; Pearson, 1996). This technique complicates the original equation set and may lead to additional approximation errors. A better approach uses the finite volume method (Mingham and Causon, 1998). In this method the flow equations are written in integral form and discretized using fluxes projected normal to grid interfaces. The finite volume method permits the use of grid cells of arbitrary shape and size which allows the computational domain to be boundary fitted accurately. Additionally, grid points can easily be concentrated in regions of particular interest without enriching the whole grid and suffering subsequent loss of computational speed. No coordinate transformations are required; all the analysis is performed with respect to the usual Cartesian coordinates, and the flow equations remain unchanged. Although the finite volume method is, in principle, superior to the previous two methods it contains a potential weakness from a practical standpoint. The drawback is that many coastal problems contain complicated domains which include interior solid regions such as islands, and this makes the generation of a boundary conforming grid a difficult task requiring significant expertise (Hu et al., 1997). In order to overcome this problem a Cartesian Cut Cell approach may be used (Causon et al., 2000). The method works by overlaying a background Cartesian grid on to the computational domain and simply cutting out from it any solid regions such as coastlines and islands. This gives rise to a computational grid containing a majority of rectangular cells away from the solid boundaries and a small number of cut cells next to the solid boundaries. Grid generation is **automatic and boundary fitting**. Moreover, the cut cell technique permits automatic grid refinement in regions of particular interest (Pearson et al., 1997). It also allows moving boundaries to be represented without the need for complicated and time consuming regridding of the whole domain (Causon et al., 2001a) as it is only necessary to recompute the intersections between the boundary and the background Cartesian grid as the body moves through it.

The following sections present some advanced numerical techniques for simulating coastal hydrodynamics which are contained within the AMAZON-CC computer code developed by the Centre for Mathematical Modelling and Flow Analysis (CMMFA) at Manchester Metropolitan University. AMAZON-CC is a state-of-the-art numerical package that uses the Cartesian Cut Cell gridding technique and incorporates a new method for source term discretization. A copy of the code may be available by contacting the CMMFA (http://cmmfa.mmu.ac.uk/). AMAZON-CC is a robust, high resolution computer code for solving the two-dimensional Shallow Water Equations. The solver is an explicit time-marching algorithm of the Godunov type (Mingham and Causon, 1998; Mingham and Causon, 1999). At the heart of the code is an explicit two-stage advective solver. In the first stage, cell center data is extrapolated to cell interfaces using Monotone Upstream Schemes for Con-

servation Laws (MUSCL) reconstruction to eliminate non-physical oscillations (van Leer, 1974). The solution is then updated to an intermediate time level. In the second stage, extrapolation is repeated on the new data to provide a pair of flux values at each cell interface. The resulting Riemann problem at each interface is solved by the HLL (Harten-Lax-van Leer) approach which is robust, accurate and computationally efficient (Harten et al., 1983). The resulting fluxes are then used to update the solution to the next time level. AMAZON-CC is capable of simulating transcritical flow over arbitrary geometries and can capture complex flow phenomena such as bore waves and hydraulic jumps. The code has been extensively validated against a large number of test problems which include dam breaks, surge waves in a channel with varying bed slope, oblique hydraulic jumps, jet forced circulation in a basin, tidal circulation in a harbor, tidal bore wave propagation, wave runup and reflection at a sloping beach and wave overtopping at sloping and vertical seawalls (Causon et al., 2000; Causon et al., 2001b; Zhou et al., 2001). In these tests the results were found to be accurate and contain very little numerical diffusion or dispersion.

2. NUMERICAL METHODS

A complete mathematical model of water flow is provided by the continuity equation which expresses the physical law of conservation of mass together with the Navier-Stokes equations which are an expression of the physical law of conservation of momentum. These equations include time and the three space dimensions. Enormous computing power is needed to solve this system of partial differential equations which means that such a model is impractical for all but the simplest of flow problems. A simplification of these equations is obtained by time-averaging to give the Reynolds equations. For many coastal problems the flow in the vertical direction is insignificant and so may be averaged out to reduce the number of spatial dimensions to two (Whitam, 1973). This depth-averaging of the Reynolds equations gives the Shallow Water Equations (SWE) which can provide the coastal engineer with a useful flow model. Furthermore, for practical problems, the SWE can be solved numerically in an acceptable time. It should be noted that the SWE are normally only applicable when the vertical acceleration of the flow is small compared to gravity. A further SWE limitation is that the ratio of wavelength to depth should be less than around 0.04 (Chadwick and Morfett, 1993). That said, recent work on landslide generated bores (Richardson et al., 2001a) and wave overtopping (Richardson et al., 2001b) has shown that the SWE do give reasonably accurate results even outside their formal range of applicability. A comprehensive treatment of the SWE is given in (Weiyan, 1992).

2.1. Shallow Water Equations

In differential form the 2-D Shallow Water Equations are

$$\frac{\partial U}{\partial t} + \frac{\partial F}{\partial x} + \frac{\partial G}{\partial y} = Q + \frac{\partial F_v}{\partial x} + \frac{\partial G_v}{\partial y} \tag{1}$$

where

$$U = \begin{pmatrix} \phi \\ \phi\,u \\ \phi\,v \end{pmatrix}, \quad H = F\,i + G\,j = \begin{pmatrix} \phi\,q \\ \phi\,uq + \phi^2\,i/2 \\ \phi\,vq + \phi^2\,j/2 \end{pmatrix},$$

$$H_v = F_v\,i + G_v\,j = \begin{pmatrix} 0 \\ (\phi/\rho)\,\sigma_{xx}\,i + (\phi/\rho)\,\tau_{xy}\,j \\ (\phi/\rho)\,\tau_{yx}\,i + (\phi/\rho)\,\sigma_{yy}\,j \end{pmatrix}, \quad Q = B + C + D + E,$$

$$B = \begin{pmatrix} 0 \\ fv\phi \\ -fu\phi \end{pmatrix}, \ C = \begin{pmatrix} 0 \\ (g/\rho)\,\tau_{xw} \\ (g/\rho)\,\tau_{yw} \end{pmatrix}, \ D = \begin{pmatrix} 0 \\ -(g/\rho)\,\tau_{xf} \\ -(g/\rho)\,\tau_{yf} \end{pmatrix}, \ E = \begin{pmatrix} 0 \\ \phi g b_x \\ \phi g b_y \end{pmatrix},$$

$\phi = g$ h is the geopotential, g is acceleration due to gravity, h is water depth, $\mathbf{q} = u\,\mathbf{i} + v\,\mathbf{j}$ is water velocity, f is coriolis force, ρ is water density, τ_{xw}, τ_{yw} are wind shear stresses, τ_{xf}, τ_{yf} are bed shear stresses, σ_{xx}, σ_{yy}, τ_{xy}, τ_{yx} are normal and shear stresses respectively, and b_x, b_y are bed slopes in the x and y directions (measured downwards). U is the matrix of conserved quantities, Q is the matrix of source terms, and $\mathbf{H}$ and $\mathbf{H_v}$ are the inviscid and viscous flux tensors respectively.

The following numerical scheme is based on the finite volume method that requires that equation (1) be re-cast in integral form. Integrating equation (1) over a planar region of area A with boundary S and outward pointing unit normal vector $\hat{\mathbf{n}}$ and applying Gauss' divergence theorem to the flux integrals gives the integral form of the SWE

$$\frac{\partial}{\partial t} \iint_A U \, dA + \oint_S \mathbf{H} \cdot \hat{\mathbf{n}} \, dS = \iint_A Q \, dA = \oint_S \mathbf{H_v} \cdot \hat{\mathbf{n}} \, dS \tag{2}$$

In the following, for clarity of exposition, viscous flux terms are neglected and only the bed slopes are included in the source term matrix (i.e., Q = E). It should also be noted that the advective terms present the most difficulty from a numerical standpoint and the following scheme is designed with this in mind.

2.2. Discretization

The physical region over which equation (2) is to be solved is partitioned by a computational grid of cells. This grid may be structured or unstructured. For notational convenience it will be assumed that the grid is structured which allows each grid cell to be located by an ordered pair of integers. In this case each grid cell has four sides. Let the area of cell ij be A_{ij}. Let U_{ij} be the integral average of U over cell ij located at the cell center (Fig. 1). Q_{ij} is defined similarly.

Since equation (2) holds for an arbitrary region it can be approximated over each cell by the semi-discrete equation

$$\frac{\partial U_{ij}}{\partial t} = -\frac{1}{A_{ij}} \sum_{k=1}^{m} \mathbf{H_k} \cdot \mathbf{n_k} + Q_{ij} \tag{3}$$

where m = 4 is the number of sides of cell ij, and $\mathbf{n_k}$ is the outward pointing normal vector to side k whose magnitude is the length of side k as shown in Fig. 2. $\mathbf{n_k}$ are known as side vectors, and $\mathbf{H_k} \cdot \mathbf{n_k}$
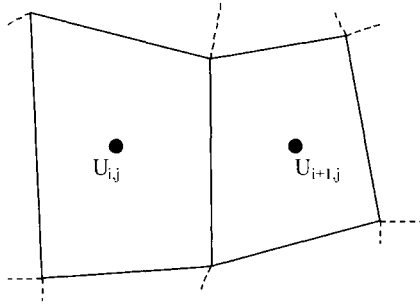
Figure 1. Computational cells showing conserved variable matrix U at cell centers.
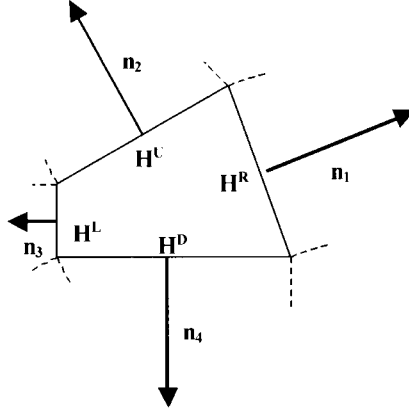
Figure 2. Cell ij showing side vectors, **n**, and interface fluxes, **H**.

is essentially the component of the flux in cell ij flowing outwards normal to side k. It should be noted that for a code based on Cartesian Cut Cells the calculation of side vectors and dot products is trivial away from solid boundaries since these cells are rectangular with sides parallel to the coordinate axes. Special treatments for cut cells will be given in Section 3.

2.3. Solver

To solve equation (2), equation (3) is fully discretized by a two step Godunov type scheme which is due to Hancock (van Leer, 1984). The scheme is explicit and second-order accurate in time. In smooth regions the scheme is second-order accurate in space and first-order accurate around discontinuities. Second-order time accuracy is provided by a two step process in which the solution is advanced to a fictitious half-time level which provides data to advance through a whole time step. Second-order accuracy in space is provided by piecewise linear extrapolation of data based on gradients calculated from neighboring cells together with a slope limiter to prevent non-physical under- or overshoots of the data at cell interfaces. The extrapolation process produces two flux values at each cell interface which form a so-called Riemann problem. The scheme respects the underlying physics by employing Riemann solutions at cell interfaces which permits the resolution of high spatial gradients and the solution of transcritical flow problems.

In the following scheme, U_{ij}^n is the value of U_{ij} at time $n\Delta t$. Q_{ij}^n is defined similarly. The time step is Δt (to be determined). $\mathbf{H}_{ij}^R$, $\mathbf{H}_{ij}^L$, $\mathbf{H}_{ij}^U$, $\mathbf{H}_{ij}^D$ are the fluxes at the right, left, up and down cell interfaces in cell ij respectively (see Fig. 2). The subscript $1/2$ refers to a cell interface so that, for example, $i, j +1/2$ refers to the interface between cell ij and cell i, j+1. $\mathbf{H}_{i+1/2, j}^*$ is the solution to the Riemann problem at the indicated cell interface. The scheme is

Predictor

$$U_{ij}^{n+1/2} = U_{ij}^n - \frac{\Delta t/2}{A_{ij}} (\mathbf{H}_{ij}^R \cdot \mathbf{n}_{i+1/2, j} + \mathbf{H}_{ij}^L \cdot \mathbf{n}_{i-1/2, j} + \mathbf{H}_{ij}^U \cdot \mathbf{n}_{i, j+1/2} +$$

$$\mathbf{H}_{ij}^D \cdot \mathbf{n}_{i, j-1/2} - Q_{ij}^n) \tag{4}$$

Corrector

$$U_{ij}^{n+1} = U_{ij}^n - \frac{\Delta t}{A_{ij}} (H_{i+1/2,j}^* \cdot n_{i+1/2,j} + H_{i-1/2,j}^* \cdot n_{i-1/2,j} + H_{i,j+1/2}^* \cdot n_{i,j+1/2} +$$

$$H_{i,j-1/2}^* \cdot n_{i,j-1/2} - Q_{ij}^{n+1/2}) \tag{5}$$

Since $H = H(U)$, the interface fluxes in the predictor step are obtained by extrapolating U_{ij} to the corresponding cell interfaces by calculating the (limited) gradient vector of U_{ij}. This process, known as MUSCL reconstruction, is described in Section 2.4.

The extrapolation process is repeated in the corrector step using the half-time level data, $U_{ij}^{n+1/2}$, and the gradients obtained in the predictor step. At each cell interface the extrapolation process produces two values of H. The solution of the resulting Riemann problem is denoted by H^*. There is no closed form for H^* and its evaluation by an iterative technique (Toro, 1992) becomes computationally expensive since this needs to be done at every cell interface and at every time step. A computationally efficient method for approximating H^* is provided by the HLL algorithm which is described in Section 2.5.

A straightforward discretization of the source terms, Q, leads to errors because of the conservative nature of the overall scheme. Accurate discretization of the source terms is addressed by the Surface Gradient Method which is described in Section 2.6.

Since the scheme is explicit the time step, Δt, is limited by stability considerations. At each iteration of the scheme Δt is given by

$$\Delta t = \nu \min_{i,j} \frac{A_{ij}}{|q_{ij}| + \sqrt{\phi_{ij}}} \tag{6}$$

where, for stability, the Courant number, ν is less than 1.0, A_{ij} is the cell area, q_{ij} is the water velocity, and ϕ_{ij} is the geopotential as stated previously.

2.4. MUSCL Reconstruction

In order to obtain the interface fluxes in equation (4) it is necessary to extrapolate U, the matrix of conserved variables, to each cell interface based on its gradients within each cell. U is assumed to be piecewise linear in each cell and gradients are estimated from neighboring cell center values. To avoid non-physical extrapolated values (for example, negative water heights) these gradients must be limited so that estimated interface values do not undershoot or overshoot their adjacent cell center values. This is done using a MUSCL (Monotonic Upstream Schemes for Conservation Laws) reconstruction scheme (van Leer, 1974). For clarity, attention is restricted to one dimension and the homogeneous Shallow Water Equation is used (i.e., Q = 0). Cell i has center x_i and length Δx_i. The required left and right interface values of U_i are denoted by U_i^L and U_i^R respectively, and are given by

$$U_i^R = U_i + 0.5 \Delta x_i \Delta U_i \tag{7}$$

$$U_i^L = U_i - 0.5 \Delta x_i \Delta U_i \tag{8}$$

where ΔU_i is the *limited* gradient of U_i in cell i given by

$$\Delta U_i = f \left(\frac{U_{i+1} - U_i}{x_{i+1} - x_i}, \frac{U_i - U_{i-1}}{x_i - x_{i-1}} \right), \tag{9}$$

f(x, y) is a slope limiter function defined by

$$f(x, y) = \begin{cases} \max[0, \min(kx, y), \min(x, ky)], & x > 0 \\ \min[0, \max(kx, y), \max(x, ky)], & \text{otherwise}, \end{cases} \tag{10}$$

and, $k = 1$ and $k = 2$ give the well-known Minmod and Superbee limiters respectively. A more general treatment for non-uniform grids in 2-D can be found in Mingham and Causon (1998).

2.5. HLL Approximate Riemann Solver

To obtain the $\mathbf{H}^*$ values in equation (5) an approximate Riemann solver is used for computational efficiency. There are many such solvers; a review can be found in Toro (1997). The HLL solver, based on the work of Harten et al. (1983), is used here and it has been shown to be accurate, robust and adaptable to dry beds which are a feature of wetting and drying problems.

In the HLL solver the Riemann solution at each cell interface is simplified by assuming it to consist of three constant states separated by two left and right waves travelling at speeds q_L and q_R respectively. The required solution lies in the star region between the two waves. The simplified Riemann fan is shown in Fig. 3 where the horizontal axis denotes distance normal to the cell interface. It can be shown (Mingham and Causon, 1998) that the approximate HLL Riemann solution at cell interface $i + 1/2, j$ is given by

$$\mathbf{H}^*_{i+1/2,j} \cdot \hat{\mathbf{n}}_{i+1/2,j} = \begin{cases} \mathbf{H}^R_{ij} \cdot \hat{\mathbf{n}}_{i+1/2,j}, & q_L > 0, \\[2mm] \mathbf{H}^L_{i+1,j} \cdot \hat{\mathbf{n}}_{i+1/2,j}, & q_R < 0, \\[2mm] \dfrac{q_R \mathbf{H}^R_{ij} \cdot \hat{\mathbf{n}}_{i+1/2,j} - q_L \mathbf{H}^L_{i+1,j} \cdot \hat{\mathbf{n}}_{i+1/2,j} + q_R q_L (U_R - U_L)}{q_R - q_L}, & \text{else}. \end{cases} \tag{11}$$

The solutions at other interfaces are given similarly. Waves speeds are provided by the 'two rarefaction' estimates (Davis, 1988), and are given by

$$q_L = \min\left(\mathbf{q}^R_{ij} \cdot \hat{\mathbf{n}}_{i+1/2,j} - \sqrt{\phi^R_{ij}},\ u^* - \sqrt{\phi^*}\right) \tag{12}$$

Figure 3. Wave diagram for the HLL approximate Riemann solver showing Riemann solution U*, and left and right wave speeds, q_L and q_R.

$$q_R = \max \left(\mathbf{q}^L_{i+1,j} \cdot \hat{\mathbf{n}}_{i+1/2,j} + \sqrt{\phi^L_{i+1,j}}, \ u^* + \sqrt{\phi^*} \right) \tag{13}$$

where

$$u^* = 0.5 \left(\mathbf{q}^R_{ij} + \mathbf{q}^L_{i+1,j} \right) \cdot \hat{\mathbf{n}}_{i+1/2,j} + \sqrt{\phi^R_{ij}} - \sqrt{\phi^L_{i+1,j}} \tag{14}$$

and

$$\sqrt{\phi^*} = 0.5 \left(\sqrt{\phi^R_{ij}} + \sqrt{\phi^L_{i+1,j}} \right) - 0.25 \left(\mathbf{q}^R_{ij} - \mathbf{q}^L_{i+1,j} \right) \cdot \hat{\mathbf{n}}_{i+1/2,j} \tag{15}$$

These wave speed estimates may be modified for the dry bed solution (Fraccorollo and Toro, 1995) to give

$$q_L = \mathbf{q}^R_{ij} \cdot \hat{\mathbf{n}}_{i+1/2,j} - \sqrt{\phi^R_{ij}}, \quad q_R = \mathbf{q}^R_{ij} \cdot \hat{\mathbf{n}}_{i+1/2,j} + 2\sqrt{\phi^R_{ij}}, \quad \text{(right dry bed)} \tag{16}$$

$$q_L = \mathbf{q}^L_{i+1,j} \cdot \hat{\mathbf{n}}_{i+1/2,j} - 2\sqrt{\phi^L_{i+1,j}}, \quad q_R = \mathbf{q}^L_{i+1,j} \cdot \hat{\mathbf{n}}_{i+1/2,j} + \sqrt{\phi^L_{i+1,j}}, \quad \text{(left dry bed)} \tag{17}$$

2.6. Surface Gradient Method

Accurate discretization of source terms in the Shallow Water Equations is a non-trivial problem for conservative Godunov-type schemes because of the inherent difficulty in balancing them with the flux gradients. There has been some recent progress in this field but these methods are complicated and may be inaccurate for transcritical flows (Bermudez and Vazquez, 1994; LeVeque, 1998; Vazquez-Cendon, 1999). The Surface Gradient Method, developed at Manchester Metropolitan University, is both accurate, simple and is a general scheme for source term discretization. In the following, the Surface Gradient Method is applied to the bed slope source terms and uses, η, the water surface level above a datum, instead of, h, the true water depth, as a basis for data reconstruction at cell interfaces. For clarity, the Surface Gradient Method is described for one dimension. The water surface level is given by

$$\eta = h + z \tag{18}$$

where z is the bed height above the horizontal datum used to measure η (Fig. 4). Denoting the left and right water levels at cell interface i+1/2 by η^L and η^R respectively, and using MUSCL reconstruction, these values are given by

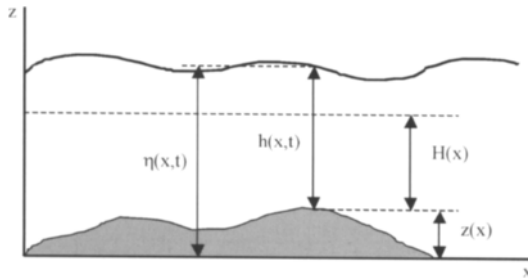$$\eta^R = \eta_{i+1} - 0.5 \Delta x_i \Delta \eta_{i+1} \tag{19}$$

Figure 4. Free surface and bathymetry showing η, height above datum, h, depth, H, depth below datum and z, bed height above datum.

$$\eta^L = \eta_i + 0.5 \, \Delta x_i \, \Delta \eta_i \qquad (20)$$

where $\Delta \eta_i$ is the (limited) gradient of η_i in cell i.

The corresponding left and right values of the geopotential are then calculated from equation (18), and are

$$\phi^R = g(\eta^R - z_{i+1/2}) \qquad (21)$$

$$\phi^L = g(\eta^L - z_{i+1/2}) \qquad (22)$$

This gives accurate interface values for the conservative variable ϕ and accounts for the variation in bed topography. It is assumed that bathymetric information is known at cell interfaces. To complete the discretization of the bed slope, b_x is approximated at cell centers by a simple central difference of data at neighboring cell interfaces. In cell i

$$b_x = -(z_{i+1/2} - z_{i-1/2})/\Delta x_i \qquad (23)$$

The Surface Gradient Method has been extensively tested on a range of demanding problems with highly variable bathymetry, and full details are reported in Zhou et al. (2001).

3. CARTESIAN CUT CELL MODIFICATIONS

Classical Cartesian grids give rise to saw-tooth representations of solid objects within the computational domain (Fig. 5a). The AMAZON-CC solver uses Cartesian Cut Cell technology to give a boundary fitted grid (Fig. 5b). This creates three types of grid cell: solid, flow and cut. Solid cells are completely 'filled' by solid objects. Flow cells are completely 'filled' with water and are rectangular (for example, cell c, Fig. 5b). Computations on flow cells completely surrounded by other flow cells are described previously. Cut cells are cells in the flow domain which are not rectangular as a result of being cut by a solid boundary (for example, cell a, Fig. 5b). The following special treatment is required for cut cells in order to obtain conserved variable gradients and to solve the Riemann problems at their solid interfaces.

The computation for a cut cell requires a fictitious 'ghost' cell in the solid region. Let U_g denote the conserved variable matrix in the ghost cell. U_g is obtained from the usual reflective boundary conditions applied to U_{ij}. Let $\mathbf{q}_s$ denote the velocity of the solid interface (which obviously is zero for a static boundary), and let $\hat{\mathbf{n}}$ be the outward pointing unit normal vector to cut cell ij. This is summarized in Fig. 5c.

U_g is determined once the ghost values of velocity and geopotential are known. These are given by

$$\mathbf{q}_g = \mathbf{q}_{ij} - 2\left(\mathbf{q}_{ij} \cdot \hat{\mathbf{n}}\right)\mathbf{n} + 2\left(\mathbf{q}_s \cdot \hat{\mathbf{n}}\right)\hat{\mathbf{n}} \qquad (24)$$

$$\phi_g = \phi_{ij} \qquad (25)$$

Since cut cell ij borders both solid and fluid cells, gradients in U may be of two types: fluid and solid. Furthermore, unlike fluid cells, the line joining neighboring cell centers is no longer parallel to the coordinate directions, and so a gradient *vector* must be calculated which can then be projected in the correct direction when extrapolating U to a cell interface. Denoting fluid and solid gradients of U in the x direction by ∇U_x^f, ∇U_x^s respectively gives

$$\nabla U_x^f = f\left(\frac{U_{i+1,j} - U_{i,j}}{\Delta x_{i+1/2,j}}, \frac{U_{i,j} - U_{i-1,j}}{\Delta x_{i-1/2,j}}\right) \qquad (26)$$
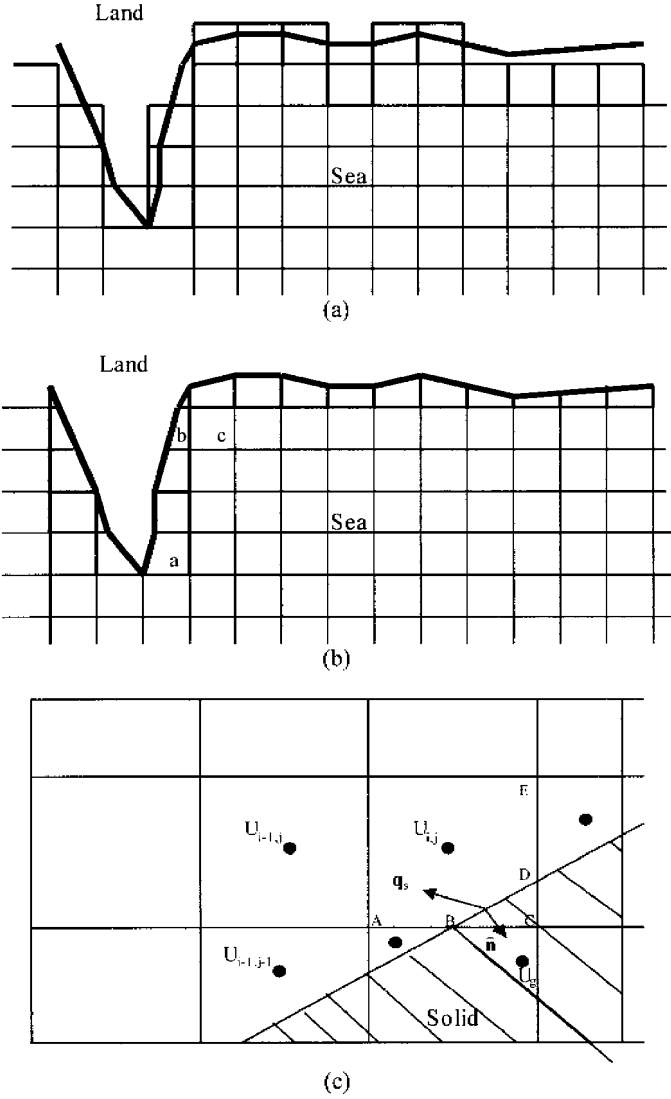
Figure 5. (a) Saw-tooth representation of a coastline, (b) Cartesian Cut Cell representation of a coastline, (c) Treatment at a cut cell solid boundary.

$$\nabla U_x^s = f \left(\frac{U_g - U_{i,j}}{\Delta x_{i,g}}, \frac{U_{i,j} - U_{i-1,j}}{\Delta x_{i-1/2,j}} \right) \tag{27}$$

where $\Delta x_{i+1/2,j}$ is the horizontal distance between the centers of cells i+1,j and ij, $\Delta x_{i,g}$ is the horizontal distance between cell ij and the ghost cell, and f is the slope limiter function defined by equation (10). Values for the fluid and solid gradients in the y direction are denoted and calculated similarly. A unique gradient vector for cell ij is obtained by a weighted average of the fluid and solid

gradients giving

$$\nabla U_{ij} = \left(\frac{\Delta y_s U_x^s + \Delta y_f U_x^f}{\Delta y} \right) \mathbf{i} + \left(\frac{\Delta x_s U_y^s + \Delta x_f U_y^f}{\Delta x} \right) \mathbf{j} \tag{28}$$

where Δx, Δy are the uncut cell side lengths, and $\Delta x_f = |AB|$, $\Delta x_s = |BC|$, $\Delta y_f = |CD|$, $\Delta y_f = |DE|$ (see Fig. 5c).

U_{ij} can now be extrapolated to side k of cut cell ij. This value, U_{ij}^k, is given by

$$U_{ij}^k = U_{ij} + \nabla U_{ij} \cdot \mathbf{r}_{ij}^k \tag{29}$$

where $\mathbf{r}_{ij}^k$ is the vector from the center of cell ij normal to side k. Hence, the predictor step in the solver (equation (4)) can be computed for cut cells.

It now remains to solve the Riemann problem at a solid interface of a cut cell in order to compute the corrector step (equation (5)) for cut cells. Let $\mathbf{q}_f$ be the interface velocity extrapolated from the velocity at the center of cell ij. Since the solver only requires velocity components normal to cell interfaces, let q_{fn}, q_{sn} denote the 'fluid' and solid normal velocity components. These are given by

$$q_{fn} = \mathbf{q}_f \cdot \hat{\mathbf{n}} \tag{30}$$

$$q_{sn} = \mathbf{q}_s \cdot (-\hat{\mathbf{n}}) \tag{31}$$

The exact Riemann solution for a moving piston is used (Stoker, 1992). Denoting the Riemann solutions for geopotential and normal velocity by ϕ^* and q_n^* respectively, the latter is simply

$$q_n^* = q_{sn} \tag{32}$$

If $q_{fn} < q_{sn}$ both left and right waves are rarefactions, and

$$\phi^* = 0.25 \left(q_{fn} - q_n^* + 2\sqrt{\phi_f} \right)^2 \tag{33}$$

otherwise both waves are bores, and ϕ^* is obtained from the Rankine-Hugoniot condition

$$\left(\phi^* - \phi_f \right) \sqrt{\frac{\phi^* + \phi_f}{2\phi^* \phi_f}} + q_n^* - q_{fn} = 0 \tag{34}$$

which can be solved approximately and efficiently by the Newton-Raphson method. Since there is no flow through a solid boundary (i.e., $\mathbf{q} \cdot \mathbf{n} = 0$), the normal flux reduces to a function of the geopotential at the interface, and it is easy to show that in equation (5)

$$\mathbf{H}^* \cdot \mathbf{n} = \begin{pmatrix} 0 \\ 0.5\,\phi^{*^2}\, n_y \\ 0.5\,\phi^{*^2}\, n_x \end{pmatrix} \tag{35}$$

where n_x and n_y are the $\mathbf{i}$ and $\mathbf{j}$ components of the side vector corresponding to the moving solid cell interface. This completes the main cut cell modifications for the solver.

There is one further practical consideration concerning cut cell size. Since the solver is explicit, the time step is restricted for stability. Equation (6) shows that a small cell area reduces the time step. The cut cell methodology may give rise to extremely small cells that could give impractically small time steps for realistic computations. To overcome this problem a 'small' cell is merged with

the neighboring cell which has the longest common interface. Typically, 'small' means a cell area of less than $0.5\Delta x\Delta y$. In Fig. 5b, cell b merges with cell c; a new cell center is calculated and new cell center values of U are obtained using conservation of mass and momentum. Full details of cut cell modifications are given in Causon at al. (2001a).

4. NUMERICAL SIMULATIONS

The purpose of this section is to demonstrate the capability of the modern high resolution solver and novel gridding scheme to simulate a range of model coastal problems. Full details of set-up conditions for each problem can be found in the accompanying references.

4.1. Waves Generated by a Moving Vessel

This simulation shows the moving boundary capability of the Cartesian Cut Cell method, and also the ability of the solver to deal with supercritical flow and steep wave fronts. The computational domain is an open rectangular region in which there is a solid object in the shape of a ship which is symmetrical about its longitudinal axis (note that since the scheme solves the Shallow Water Equations, the ship extends to the sea bed and has vertical walls which cannot be overtopped). The grid is automatically body fitted to the ship that is then impulsively started and allowed to travel across the domain in the x direction at a supercritical velocity (at a Froude number of 3). At each time step in the computation the grid is re-cut and remains body fitted.

In order to assess the results, the computation was repeated using the physically identical situation of a static ship and moving water. Fig. 6 shows a composite plot of the wave fields for static and moving cases. The port side wave pattern was generated by the moving ship, and the starboard pattern

(a)

(b)
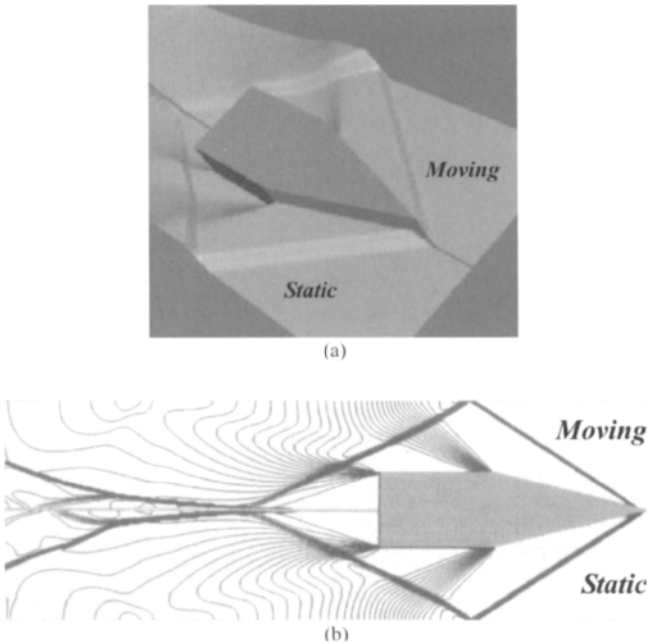
Figure 6. Moving vessel. (a) plot of water surface, (b) contour plot of water depth.

was generated by water moving past a fixed ship. Fig. 6a shows a surface plot of the water height around the ship, and Fig. 6b shows the corresponding contour plot. Results are virtually identical and the steep bow wave is well resolved. This problem has an analytic solution which is closely approximated by the numerical results. Further details can be found in Causon et al. (2001a).

4.2. Wave-Structure Interaction

This problem demonstrates the ability of the new Surface Gradient Method together with the high resolution solver to model wave overtopping at a seawall. The problem also demonstrates the limitations of the Shallow Water Equations in this context.

Fig. 7a shows a pair of surface plots of water height as a result of a bore wave hitting a seawall at an oblique angle. In the upper plot the seawall is modeled by a solid boundary in the computational

(a)

(b)

(c)
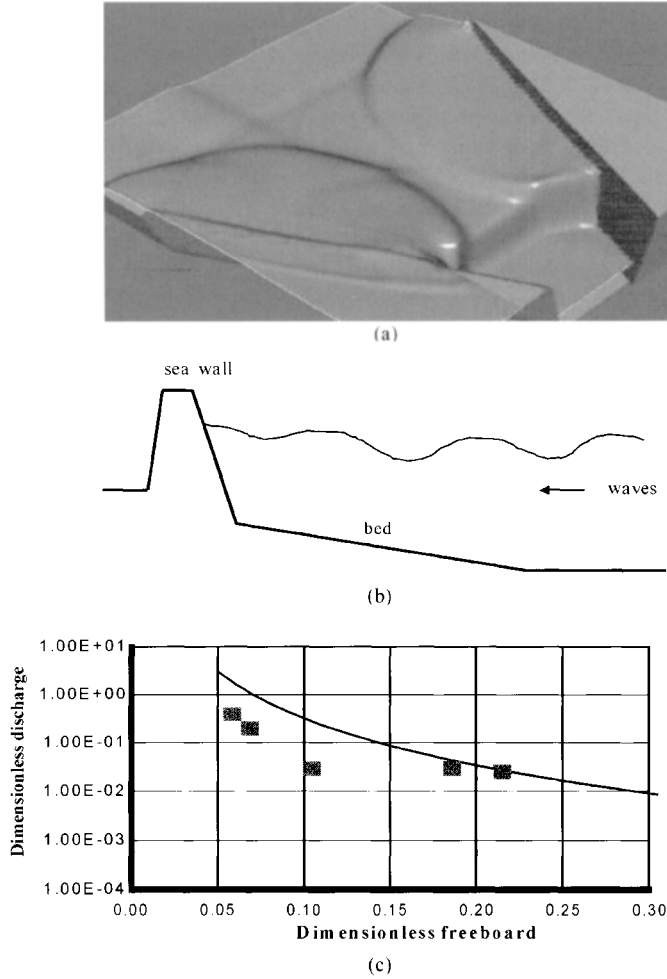
Figure 7. Wave-structure interaction. (a) Oblique wave reflection (upper plot), overtopping (lower plot), (b) Schematic of seawall, (c) Experimental (line) and numerical (squares) overtopping results for a seawall.

domain and cannot be overtopped. The incident wave is reflected back from the wall, and the curved reflected wave can clearly be seen. The lower half of Fig. 7a presents a similar picture except that the seawall is modeled by a steep bed which allows for it to be overtopped. The overtopping water can be clearly seen on the seawall. There is also a reflected wave and, although not clear from the picture, it is weaker than the reflected wave in the upper part of the figure. Full details of this simulation can be found in Zhou et al. (2001).

An application of the above is a study of violent wave impacts on seawalls. A one-dimensional version of AMAZON-CC is used to simulate a long, narrow wave tank which is used in a corresponding experimental study (see www.vows.ac.uk). Fig. 7b shows a schematic of the computational domain. As previously, the seawall is modeled by regarding it as a steep bed. The Surface Gradient Method is used for accuracy. Random waves are generated and allowed to impinge on the seawall. Some of the waves are reflected but in some cases the water overtops the wall. The discharge over the seawall is calculated and results for different wave conditions are plotted against various wall freeboard. In Fig. 7c, numerical results (squares) are compared to an experimentally derived curve (Besley, 1999). The two numerical results around a freeboard of 0.2 are in quite good agreement with the experimental curve. These results correspond to less impacting waves. The other numerical results show significant differences from the experimental curve and these correspond to highly impacting waves. These waves break on the seawall and, as this cannot be modeled properly using the Shallow Water Equations, discrepancies are to be expected. Further details of these numerical experiments can be found in Richardson et al. (2001b).

4.3. Landslide Generated Waves in a Fjord

This simulation demonstrates the body fitted and moving boundary gridding capabilities of AMAZON-CC and its ability to resolve complex wave fields. Additionally, the simulation uses the Surface Gradient Method to model an island which permits runup and overtopping.

Fig. 8 shows a hypothetical branched fjord containing an island. The open sea is on the bottom of the picture. A landslide into the left branch is simulated by a moving solid boundary (not shown) which generates a strong bore wave. Part of this wave hits the side of the left branch and is reflected back, and some of it is diffracted round the headland into the right branch. Fig. 8 shows a contour plot of water height just before the bore wave hits the island (which is modeled by a bed slope term). Further details of this type of problem can be found in Richardson et al. (2001a).
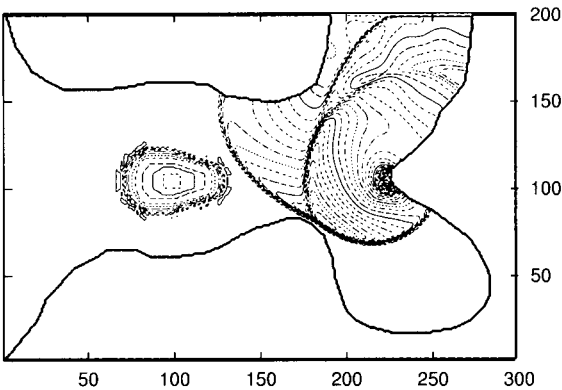

Figure 8. Landslide into a fjord: contour plot of water height.

5. CONCLUSIONS AND FURTHER WORK

Numerical simulations of a range of coastal problems have been presented. The two-dimensional Shallow Water Equations were chosen to model the hydrodynamics. These equations were solved numerically using a modern, conservative, high resolution, Godunov-type scheme on a Cartesian Cut Cell grid. The solver was able to resolve complex wave fields including bore waves. The gridding method produced a body fitted grid automatically and was able to handle moving bodies. The Surface Gradient Method was used to discretize source terms accurately.

The simulations presented demonstrate the potential of the numerical methods to investigate a wide range of practical problems in coastal engineering. The moving boundary capability can be used to construct a numerical wave maker in a wave basin which could then be used for a numerical study of wave-breakwater interactions. This capability could also ultimately be used to generate waves from moving ships and assess the effects of ship wash on the shore. The body fitted gridding capability can be used to represent accurately complex configurations such as harbors or shorelines. In this way, tidal-induced problems such as circulation patterns in marinas or the flushing characteristics of estuaries can be investigated. The numerical solver respects the underlying physics and can simulate complex wave patterns including steep wave fronts which are a feature of nearly breaking waves and tsunamis. Such an accurate solver will also be useful in numerical studies of pollutant and sediment transport. The techniques presented here are not confined to the Shallow Water Equations, but are generic and may be used on more sophisticated equation sets which will be dictated by the problem and the level of understanding required. Such equations may include physical effects such as dispersion if this is deemed to be an important component of the model. Equations may also be extended from two to three dimensions if a detailed understanding of the water column is required.

An example of the need for more sophisticated models was alluded to in the study of wave overtopping at seawalls. Storm waves may break at a wall and this cannot be modeled by the Shallow Water Equations since breaking waves become multi-valued in height. A multi-component model based on the Euler Equations in conjunction with a water/air interface tracking algorithm has been used in a preliminary study of wave overtopping. Fig. 9 shows a wave produced by a collapsing cylinder of water hitting an obstruction. The water overtops the obstruction and its height becomes multi-valued. This simulation forms a basis for wave-structure interaction studies in the future.
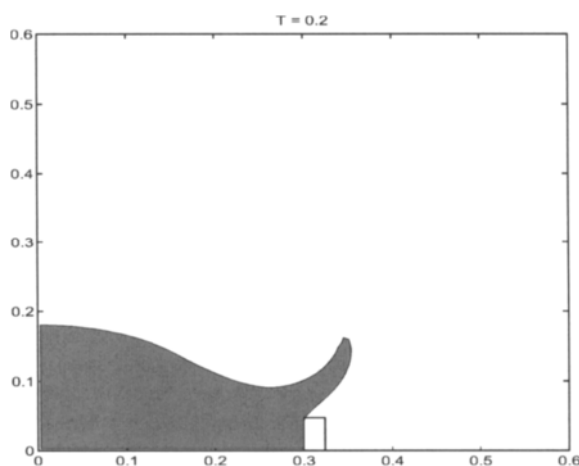
Figure 9. Multi-fluid simulation of wave-structure interaction.
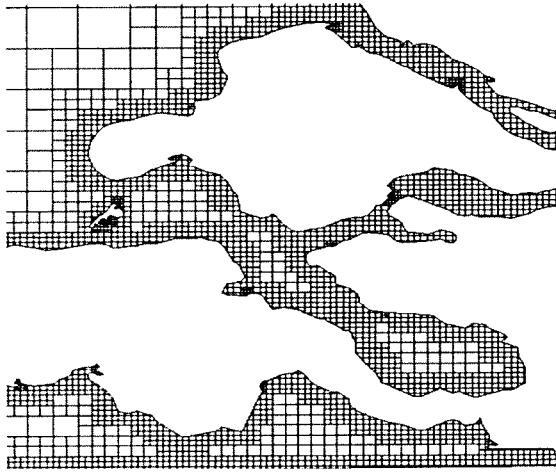
Figure 10. Adaptive Cartesian Cut Cell grid for part of the Dutch coastline.

Further developments concern the grid topology. At present, the grid density is constant through-out the domain, which may be inefficient. In many coastal problems the nearshore area is of greater interest than the far field. In the Cartesian Cut Cell grid generation method described previously, enriching the grid around the nearshore to obtain greater solution detail automatically enriches the whole grid. This is computationally inefficient. One solution is to locally refine the grid by using a quad-tree approach (Pearson et al., 1997). Fig. 10 shows a grid of part of the Dutch coastline. Grid cells are concentrated around the nearshore and around islands. The grid is still body fitted and is still generated automatically as in the Cartesian Cut Cell method.

Numerical methods are becoming ever more sophisticated and, in conjunction with the rapid rise in computing power, a greater range of problems than ever before can now be addressed. Numerical modeling, because of its flexibility and relative low cost, plays an important role in coastal engineering and its importance will continue to increase.

ACKNOWLEDGMENTS

LIST OF SYMBOLS

A_{ij}	—	is area of cell ij
b_x, b_y	—	are bed slopes (measured downwards)
Δt	—	is the time step
Δx_i	—	is the cell side length
$\Delta x_{i+1/2,j}$	—	is the horizontal distance between the centers of cells i+1,j and ij
f	—	is coriolis force

$f(x,y)$	—	is a slope limiter function
ϕ	—	is geopotential
g	—	is acceleration due to gravity
ΔU	—	is the gradient of U
h	—	is water depth
$\mathbf{H}$	—	is inviscid flux
$\mathbf{H}_v$	—	is the viscous flux
$\mathbf{H}_{ij}^R$	—	is the flux at right interface of cell ij
$\mathbf{H}^*$	—	is the Riemann solution
$\mathbf{i}, \mathbf{j}$	—	are Cartesian basis vectors
$\mathbf{n}_k$	—	is the outward pointing normal vector to side k
$\hat{\mathbf{n}}$	—	is a unit normal vector
n_x, n_y	—	are side vector components
ν	—	is the Courant number
η	—	is water level above datum
$\mathbf{q} = u\mathbf{i} + v\mathbf{j}$	—	is the water velocity
Q	—	is the matrix of source terms
$\mathbf{r}_{ij}^k$	—	is the vector from the center of cell ij normal to side k
ρ	—	is water density
t	—	is time
τ_{xw}, τ_{yw}	—	are wind shear stresses
τ_{xf}, τ_{yf}	—	are bed shear stresses
σ_{xx}, σ_{yy}	—	are normal stresses
τ_{xy}, τ_{yx}	—	are shear stresses
u	—	is water speed in the x direction
U	—	is the matrix of conserved quantities
U_{ij}	—	is the integral average of U over cell ij
U_{ij}^n	—	is U_{ij} at time $n\Delta t$
U_g	—	is the ghost value of U_{ij}^n
U_i^L	—	is the left interface value of U_i
v	—	is water speed in the y direction
x_i	—	is center of cell i
z	—	is bed height above datum

REFERENCES

Abbot, M., Damsgaard, A., and Rodenhuis, G., 1973. SYSTEM 21, "Jupiter", (a design system for two dimensional nearly horizontal flows). Journal of Hydraulic Research, 11: 1–28.

Allsop, N.W.H., Besley, P., and Madurini, L., 1995. Overtopping performance of vertical walls and composite breakwaters, seawalls and low reflection alternatives. MCS Final Report, Paper 4.7. Hannover, Germany: University of Hannover.

Allsop, N.W.H., McKenna, J.E., Vicinanza, D., and Whittaker, T.T.J., 1996. New design methods for wave impact loadings on vertical breakwaters and seawalls. Proceedings of the 25th International Conference on Coastal Engineering, ASCE, pp. 2508–2521.

Bermudez, A., and Vazquez, M.E., 1994. Upwind methods for hyperbolic conservation laws with source terms. Computers and Fluids, 23: 1049–1071.

Besley, P., 1999. Overtopping of seawalls—Design and assessment manual. R & D Technical Report W 178. Bristol: Environment Agency (ISBN 1 85705 069 X).

Besley, P.B., Stewart, T., and Allsop, N.W.H., 1998. Overtopping of vertical structures: New methods to account for shallow water conditions. In: Allsop, N.W.H. (Editor), Coastlines, Structures and Breakwaters. Proceedings of the International Conference '98. Institution of Civil Engineers. London: Thomas Telford, pp. 46–57.

Borthwick, A., and Barber, R., 1992. River and reservoir flow modelling using the transformed shallow water equations. International Journal of Numerical Methods in Fluids, 14: 1193–1217.

Bruce, T., Allsop, N.W.H., and Pearson, J., 2001. Violent overtopping of seawalls—Extended prediction methods. Proceedings, Coastlines, Seawalls and Breakwaters '01. Institution of Civil Engineers. London: Thomas Telford.

Causon, D.M., Ingram, D.M, Mingham, C.G., Yang, G, and Pearson, R.V., 2000. Calculation of shallow water flows using a Cartesian Cut Cell approach. Advances in Water Resources, 23: 545–562.

Causon, D.M., Ingram, D.M., and Mingham, C.G., 2001a. A Cartesian Cut Cell Method for shallow water flows with moving boundaries. Advances in Water Resources, 24: 899–911.

Causon, D.M., Ingram, D.M., Mingham, C.G., Zang, J., Hu, K., and Zhou, J.G., 2001b. Numerically simulating seawall overtopping. Proceedings of the 27th International Conference on Coastal Engineering, ASCE, pp. 2086–2099.

Chadwick, A., and Morfett, J., 1993. Hydraulics in Civil Engineering. New York: Chapman and Hall.

Davis, S.F., 1988. Simplified second-order Godunov-type methods. SIAM Journal of Statistical and Scientific Computing, 9: 445–473.

Dodd, N., 1998. A numerical model of wave run-up, overtopping and regeneration. Journal of Waterway, Port, Coastal and Ocean Engineering, 124 (2): 73–81.

Falconer, R.A., 1980. Numerical modelling of tidal circulation in harbours. Journal of Waterway, Port, Coastal and Ocean Division, 106 (10): 31–48.

Falconer, R.A., 1992. Flow and water quality modelling in coastal and inland water. Journal of Hydraulic Research, 30 (4): 437–452.

Fennema, R.J., and Chaudhry, M.H., 1990. Explicit methods for 2-d transient free-surface flows. Journal of Hydraulic Engineering, 116: 1013–1034.

Fraccarollo, L., and Toro, E.F., 1995. Experimental and numerical assessment of the shallow water model for two-dimensional dam-break type problems. Journal of Hydraulic Research, 33: 843.

Goda, Y., 1985. Random Seas and Maritime Structures. Tokyo: University of Tokyo Press.

Harten, A., Lax, P.D., van Leer, B., 1983. On upstream differencing and Godunov-type schemes for hyperbolic conservation laws. SIAM Review, 25: 35–61.

Hu, K., Mingham, C.G., and Causon, D.M., 1997. Numerical simulation of wave induced circulation in harbours. In: Acinas, J.R., and Brebbia, C.A. (Editors), Computer Modelling of Seas and Coastal Regions. Proceedings of the 3rd International Conference, pp. 325–334. Southhampton, UK: Computational Mechanics Publications.

LeVeque, R. J., 1998. Balancing source terms and flux gradients in high-resolution Godunov methods: The quasi-steady wave-propagation algorithm. Journal of Computational Physics, 146: 346.

Leendertse, J.J., 1967. Aspects of a Computational Model for Long Period Water Wave Propagation. The Rand Corporation, RM-5294-PR.

Mingham, C.G., and Causon, D.M., 1998. A high resolution finite volume method for shallow water flows. Journal of Hydraulic Engineering, 124 (6): 605–614.

Mingham, C.G., and Causon, D.M., 1999. Calculation of unsteady bore diffraction using a high resolution finite volume method. Journal of Hydraulic Research, 38 (1): 49–56.

Owen, M.W., 1980. Design of Sea Walls Allowing for Wave Overtopping. Report EX 924. Wallingford, UK: Hydraulics Research.

Owen M.W., 1982. The hydraulic design of sea-wall profiles. Proceedings, Institution of Civil Engineers Conference on Shoreline Protection, pp. 185–192. London: Thomas Telford.

Pearson, R.V., 1996. Simulation of Shallow Water Hydrodynamics and Species Transport Using Elliptically Generated Boundary-Fitted Coordinate Systems. Ph.D. Thesis. Salford, UK: University of Salford.

Pearson, R.V., Mingham, C.G., and Causon, D.M., 1997. Simulation of shallow water hydrodynamics using a high resolution finite volume technique on hierarchically structured Cartesian grids. In: Rajar, R., and Brebbia, C.A. (Editors), Water Pollution IV. Proceedings of the 4th International Conference, pp. 617–626. Southampton, UK: Computational Mechanics Publications.

Richardson, S.R., Ingram, D.M., and Causon, D.M., 2001a. Landslide generated shallow water flows using a Cartesian Cut Cell approach. In: Weatherill, N., and Morgan, K. (Editors), ECCOMAS CFD 2001. Proceedings, European Congress on Computational Methods in Applied Sciences and Engineering. Swansea: Institution of Mathematics and its Applications, CDROM.

Richardson, S.R., Ingram, D.M., Mingham, C.G., and Causon, D.M., 2001b. On the validity of the Shallow Water Equations for violent wave overtopping. Ocean Wave Measurement and Analysis. Proceedings of the 4th International Symposium, pp. 1112–1125. Reston, VA: ASCE.

Stoker, J., 1992. Water Waves: The Mathematical Theory with Applications. New York: Wiley Classics Library Edition.

Toro, E.F., 1992. Riemann problems and the WAF method for solving the two-dimensional shallow water equations. Philosophical Transactions of the Royal Society of London, Series A, 338: 43–68.

Toro, E.F., 1997. Riemann Solvers and Numerical Methods for Fluid Dynamics. Berlin/ Heidelberg: Springer-Verlag.

van Leer, B., 1974. Towards the ultimate conservative difference scheme II: Monotonicity and conservation combined in a single scheme. Journal of Computational Physics, 14: 361–370.

van Leer, B., 1984. On the relation between the upwind differencing schemes of Godunov, Enquist-Osher and Roe. SIAM Journal of Science and Statistical Computing, 5 (1): 1–20.

Vazquez-Cendon, M.E., 1999. Improved treatment of source terms in upwind schemes for shallow water equations in channels with irregular geometry. Journal of Computational Physics, 148: 497.

Watson, G., Barnes, T.C.C., and Peregrine, D.H., 1996. Numerical modelling of solitary wave propagation and breaking on a beach and runup on a vertical wall. In: Yeh, H., Liu, P., and Synolakis, C. (Editors), Long-wave Runup Models, pp. 291–297. Singapore: World Scientific Publishing Co.

Weiyan, T., 1992. Shallow Water Hydrodynamics. Amsterdam, The Netherlands: Elsevier Science Publishers.

Whitam, G. B., 1973. Linear and Nonlinear Waves. New York: Wiley Publishers.

Zhou, J.G., Causon, D.M., Mingham, C.G., and Ingram, D.M., 2001. The surface gradient method for the treatment of source terms in the Shallow Water Equations. Journal of Computational Physics, 168: 1–25.

This Page Intentionally Left Blank

93

Chapter 4

Numerical Models for Nearshore Currents

Hideaki Noda

Department of Environmental Design, Tottori University of Environmental Studies, Tottori, 689-1111, Japan

1. INTRODUCTION

Nearshore currents have previously been estimated by using two-dimensional (2-D) models in the horizontal plane. Yoo et al. (1988) presented a mathematical 2-D model estimating waves and currents for the port design. Madsen and Schäffer (1999) reviewed Boussinesq equations describing almost every aspect of wave transformation over varying depth and in depth-uniform currents. The depth-averaged current model is not suitable to predict the medium- or short-term sea bed level changes affected by the construction of coastal structures, because this method cannot accurately evaluate the effect of undertow and suspended sediment in the surf zone. Furthermore, the two-dimensional current model is unable to describe the direction and magnitude of current velocity near the sea bottom, which affects sediment transport and spiral profiles of nearshore currents observed in the field by many researchers. In order to predict the changes of sea bottom topography accurately, the estimation of sediment transport rate, taking into account the vertical profiles of both nearshore current and suspended sediment concentration, is necessary.

Kuroiwa et al. (1998) have previously proposed a quasi three-dimensional (3-D) model for the nearshore current field on straight beaches. The objective of this chapter is to describe the numerical model of nearshore currents in a quasi three-dimensional field, developed by Kuroiwa et al.

Recently, models for estimating three-dimensional currents have been proposed. Svendsen and Lorenz (1989) presented an analytical model composed of cross-shore and alongshore current velocities. Sanchez et al. (1992) proposed a quasi three-dimensional numerical model by combining a 2-D model in the horizontal plane and a one-dimensional (1-D) model in the vertical direction. Okayasu et al. (1994) proposed a quasi three-dimensional numerical model taking into account the effect of the momentum flux caused by large vortices formed on the front face of breaking waves. However, these models have been only applied to straight coastlines without coastal structures. On the other hand, Pechon and Teisson (1994) developed a quasi three-dimensional numerical model and attempted to calculate the nearshore currents around coastal structures.

2. WAVE FIELD MODULE

The wave field can be obtained from the time-dependent mild-slope equations proposed by Watanabe et al. (1984). Taking the x-(cross-shore), y-(alongshore) axes and z-axis vertically upwards as shown in Fig. 1, the governing equations are expressed as follows

$$\frac{\partial Q_x}{\partial t} + \frac{1}{n} C^2 \frac{\partial n \eta}{\partial x} + f_D Q_x = 0 \tag{1}$$

$$\frac{\partial Q_y}{\partial t} + \frac{1}{n} C^2 \frac{\partial n \eta}{\partial y} + f_D Q_y = 0 \tag{2}$$
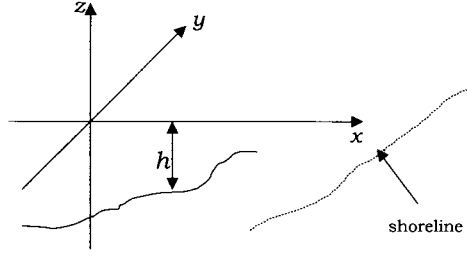
Figure 1. Schematic representation of axes.

$$\frac{\partial \eta}{\partial t} + \frac{\partial Q_x}{\partial x} + \frac{\partial Q_y}{\partial y} = 0 \tag{3}$$

in which C is the wave celerity, η is surface elevation, n is the ratio of group velocity to wave celerity and t is time. The wave-induced depth-integrated flow rates per unit width in the x and y directions are defined by

$$Q_x = \int_{-h}^{\eta} u_w \, dz \tag{4}$$

$$Q_y = \int_{-h}^{\eta} v_w \, dz \tag{5}$$

where u_w and v_w are the horizontal components of water particle velocities in the x and y directions, corresponding to the wave motion, and h is the water depth at x and y. Finally, f_D is the attenuation factor due to wave breaking and is estimated by

$$f_D = \alpha_D \, \tan\beta \sqrt{\frac{g}{h} \left(\frac{\widehat{Q}}{Q_r} - 1 \right)} \tag{6}$$

in which the amplitude of flow rate $\widehat{Q}$ is expressed by

$$\widehat{Q} = \sqrt{Q_x^2 + Q_y^2} \tag{7}$$

the amplitude of the flow rate of recovered waves Q_r is

$$Q_r = 0.25 \, h\sqrt{gh} \tag{8}$$

and α_D is a non-dimensional coefficient, $\tan\beta$ is the bottom slope and g is the gravitational acceleration. The governing equations for the wave field are numerically solved by using an explicit finite difference method on a staggered rectangular grid.

3. NEARSHORE CURRENT MODULE

The quasi three-dimensional equations are derived from Navier-Stokes equations referring to the equation of motion proposed by Svendsen and Lorenz (1989), that is

$$\frac{\partial u}{\partial t} + u\frac{\partial u}{\partial x} + v\frac{\partial u}{\partial y} + w\frac{\partial u}{\partial z} = -\frac{1}{\rho}\frac{\partial p}{\partial x} + \nu\left(\frac{\partial^2 u}{\partial x^2} + \frac{\partial^2 u}{\partial y^2} + \frac{\partial^2 u}{\partial z^2}\right) \tag{9}$$

$$\frac{\partial v}{\partial t} + u\frac{\partial v}{\partial x} + v\frac{\partial v}{\partial y} + w\frac{\partial v}{\partial z} = -\frac{1}{\rho}\frac{\partial p}{\partial y} + \nu\left(\frac{\partial^2 v}{\partial x^2} + \frac{\partial^2 v}{\partial y^2} + \frac{\partial^2 v}{\partial z^2}\right) \tag{10}$$

$$\frac{\partial w}{\partial t} + u\frac{\partial w}{\partial x} + v\frac{\partial w}{\partial y} + w\frac{\partial w}{\partial z} = -g - \frac{1}{\rho}\frac{\partial p}{\partial z} + \nu\left(\frac{\partial^2 w}{\partial x^2} + \frac{\partial^2 w}{\partial y^2} + \frac{\partial^2 w}{\partial z^2}\right) \tag{11}$$

where ρ is the density of fluid, ν is the kinematic viscosity and p is the pressure.

In these equations, the total instantaneous water particle velocities are termed u, v, w, and the velocity components are given in the x, y, z coordinate system shown in Fig. 2. The velocity components u, v, w are divided into three parts: the component of steady current velocities U, V, W; a purely periodic component u_w, v_w, w_w corresponding to the wave motion, and a turbulent velocity fluctuation u', v', w'.

Thus, the velocity components are defined by

$$\left.\begin{array}{l} u = U + u_w + u' \\ v = V + v_w + v' \\ w = W + w_w + w' \end{array}\right\} \tag{12}$$

In addition, the pressure p is divided into three parts: $\overline{p}$ is the mean component, p_w is the periodic component corresponding to wave motion and p' is the turbulent fluctuation. Hence, the pressure p is given by
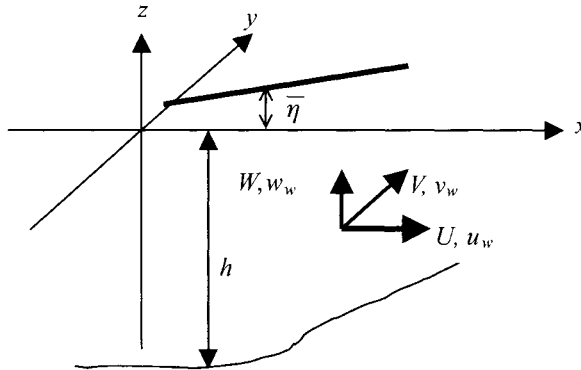
$$p = \overline{p} + p_w + p' \tag{13}$$

Figure 2. Illustration of velocity components.

The ensemble average of the velocity components $\tilde{u}$, $\tilde{v}$, $\tilde{w}$ and pressure $\tilde{p}$ are denoted by

$$
\begin{aligned}
\tilde{u} &= \tilde{U} + \tilde{u}_w + \tilde{u}' = U + u_w = u_p \\
\tilde{v} &= \tilde{V} + \tilde{v}_w + \tilde{v}' = V + v_w = v_p \\
\tilde{w} &= \tilde{W} + \tilde{w}_w + \tilde{w}' = W + w_w = w_p \\
\tilde{p} &= \tilde{\tilde{p}} + \tilde{p}_w + \tilde{p}' = \overline{p} + p_w = p_p
\end{aligned}
\tag{14}
$$

in which superscript$\sim$denotes ensemble averaging, and $\tilde{u}' = \tilde{v}' = \tilde{w}' = \tilde{p}' = 0$ due to the statistical behavior of turbulent fluctuations. Furthermore, introducing the superscript $-$ to indicate averaging over a wave period and taking into account $\overline{u}_w = \overline{v}_w = \overline{w}_w = \overline{p}_w = 0$, the quantities in equation (14) are given by

$$
\left.
\begin{aligned}
\overline{\tilde{u}} &= \overline{u}_p = \overline{u}_w + \overline{U} = U \\
\overline{\tilde{v}} &= \overline{v}_p = \overline{v}_w + \overline{V} = V \\
\overline{\tilde{w}} &= \overline{w}_p = \overline{w}_w + \overline{W} = W \\
\overline{\tilde{p}} &= \overline{p}_p = \overline{p} + \overline{p}_w = \overline{p}
\end{aligned}
\right\}
\tag{15}
$$

Substituting equations (12) and (13) into the Navier-Stokes equations (9), (10) and (11), and taking the ensemble average, the equations of motion are given by

$$
\frac{\partial u_p}{\partial t} + \frac{\partial u_p^2}{\partial x} + \frac{\partial u_p v_p}{\partial y} + \frac{\partial u_p w_p}{\partial z} = -\frac{1}{\rho}\frac{\partial p_p}{\partial x}
$$
$$
+ \frac{\partial}{\partial x}\left(-\widetilde{u'^2}\right) + \frac{\partial}{\partial y}\left(-\widetilde{u'v'}\right) + \frac{\partial}{\partial z}\left(-\widetilde{u'w'}\right) + \nu\left(\frac{\partial^2 u_p}{\partial x^2} + \frac{\partial^2 u_p}{\partial y^2} + \frac{\partial^2 u_p}{\partial z^2}\right)
\tag{16}
$$

$$
\frac{\partial v_p}{\partial t} + \frac{\partial u_p v_p}{\partial x} + \frac{\partial v_p^2}{\partial y} + \frac{\partial v_p w_p}{\partial z} = -\frac{1}{\rho}\frac{\partial p_p}{\partial y}
$$
$$
+ \frac{\partial}{\partial x}\left(-\widetilde{u'v'}\right) + \frac{\partial}{\partial y}\left(-\widetilde{v_p'^2}\right) + \frac{\partial}{\partial z}\left(-\widetilde{v'w'}\right) + \nu\left(\frac{\partial^2 v_p}{\partial x^2} + \frac{\partial^2 v_p}{\partial y^2} + \frac{\partial^2 v_p}{\partial z^2}\right)
\tag{17}
$$

$$
\frac{\partial w_p}{\partial t} + \frac{\partial u_p w_p}{\partial x} + \frac{\partial v_p w_p}{\partial y} + \frac{\partial w_p^2}{\partial z} = -\frac{1}{\rho}\frac{\partial p}{\partial z} - g
$$
$$
+ \frac{\partial}{\partial x}\left(-\widetilde{u'w'}\right) + \frac{\partial}{\partial y}\left(-\widetilde{v'w'}\right) + \frac{\partial}{\partial z}\left(-\widetilde{w_p'^2}\right) + \nu\left(\frac{\partial^2 w_p}{\partial x^2} + \frac{\partial^2 w_p}{\partial y^2} + \frac{\partial^2 w_p}{\partial z^2}\right)
\tag{18}
$$

and then, after averaging over a wave period, equations (16) and (17) become

$$
\frac{\partial U}{\partial t} + U\frac{\partial U}{\partial x} + V\frac{\partial U}{\partial y} + W\frac{\partial U}{\partial z} = -\frac{1}{\rho}\frac{\partial \overline{p}}{\partial x} - \frac{\partial}{\partial x}\left(\overline{u_w^2}\right) - \frac{\partial}{\partial y}\left(\overline{u_w v_w}\right) - \frac{\partial}{\partial z}\left(\overline{u_w w_w}\right)
$$
$$
+ \frac{\partial}{\partial x}\left(-\overline{u'^2}\right) + \frac{\partial}{\partial y}\left(-\overline{u'v'}\right) + \frac{\partial}{\partial z}\left(-\overline{u'w'}\right) + \nu\left(\frac{\partial^2 U}{\partial x^2} + \frac{\partial^2 U}{\partial y^2} + \frac{\partial^2 U}{\partial z^2}\right)
\tag{19}
$$

$$
\frac{\partial V}{\partial t} + U\frac{\partial V}{\partial x} + V\frac{\partial V}{\partial y} + W\frac{\partial V}{\partial z} = -\frac{1}{\rho}\frac{\partial \overline{p}}{\partial y} - \frac{\partial}{\partial x}\left(\overline{u_w v_w}\right) - \frac{\partial}{\partial y}\left(\overline{v_w^2}\right) - \frac{\partial}{\partial z}\left(\overline{v_w w_w}\right)
$$

$$+\frac{\partial}{\partial x}\left(-\overline{u'v'}\right)+\frac{\partial}{\partial y}\left(-\overline{v'^2}\right)+\frac{\partial}{\partial z}\left(-\overline{u'w'}\right)+v\left(\frac{\partial^2 V}{\partial x^2}+\frac{\partial^2 V}{\partial y^2}+\frac{\partial^2 V}{\partial z^2}\right) \tag{20}$$

In order to solve the current velocities by using a quasi 3-D numerical model, the vertical component in equation (18) is integrated from a depth z to the water surface η before time-averaging, to give

$$p_p = \rho g\,(\eta-z)+\rho\left[\frac{\partial}{\partial t}\int_z^\eta w_p\,dz+\frac{\partial}{\partial x}\int_z^\eta u_p w_p\,dz+\frac{\partial}{\partial y}\int_z^\eta v_p w_p\,dz\right]-\rho\,w_p^2$$

$$-\rho\left[w_p\left(\frac{\partial\eta}{\partial t}+u_p\frac{\partial\eta}{\partial x}+v_p\frac{\partial\eta}{\partial y}-w_p\right)\right]_{z=\eta} \tag{21}$$

The viscous and turbulent shear stress terms in equation (18) are neglected in the estimation of the above equation, due to the assumption that those terms are smaller than the other terms in equation (18). In addition, the last term on the right-hand side in equation (18) is equal to zero, taking into account the free surface boundary condition.

Integrating equation (21) following Mei (1983) over a wave period, equation (21) can be expressed as follows

$$\overline{p}=\rho g\,(\overline{\eta}-z)-\rho\left(W^2+\overline{w_w^2}\right)+\rho\left(\frac{\partial}{\partial t}\int_z^{\overline{\eta}}\overline{w_w}\,dz+\frac{\partial}{\partial x}\int_z^{\overline{\eta}}\overline{u_w w_w}\,dz\right.$$

$$\left.+\frac{\partial}{\partial y}\int_z^{\overline{\eta}}\overline{v_w w_w}\,dz\right)+\rho\left(\frac{\partial}{\partial t}\int_z^{\overline{\eta}}W\,dz+\frac{\partial}{\partial x}\int_z^{\overline{\eta}}UW\,dz+\frac{\partial}{\partial y}\int_z^{\overline{\eta}}VW\,dz\right) \tag{22}$$

in which $\overline{\eta}$ is the mean water level. Finally, omitting small quantities and the terms being equal to zero by applying linear theory the right-hand side of equation (22), the time-averaged pressure $\overline{p}$ can be expressed as

$$\overline{p}=\rho g\,(\overline{\eta-z})-\rho\,\overline{w_w^2} \tag{23}$$

Substituting equation (23) into equations (19) and (20), the equations of motion in the quasi three-dimensional current system become respectively

$$\frac{\partial U}{\partial t}+U\frac{\partial U}{\partial x}+V\frac{\partial U}{\partial y}+W\frac{\partial U}{\partial z}=-g\frac{\partial\overline{\eta}}{\partial x}-\frac{\partial}{\partial x}\left(\overline{u_w^2}-\overline{w_w^2}\right)-\frac{\partial}{\partial y}\left(\overline{u_w\,v_w}\right)$$

$$+\frac{\partial}{\partial x}\left(v_h\frac{\partial U}{\partial x}\right)+\frac{\partial}{\partial y}\left(v_h\frac{\partial U}{\partial y}\right)+\frac{\partial}{\partial z}\left(v_v\frac{\partial U}{\partial z}\right) \tag{24}$$

$$\frac{\partial V}{\partial t}+U\frac{\partial V}{\partial x}+V\frac{\partial V}{\partial y}+W\frac{\partial V}{\partial z}=-g\frac{\partial\overline{\eta}}{\partial y}-\frac{\partial}{\partial x}\left(\overline{u_w\,v_w}\right)-\frac{\partial}{\partial y}\left(\overline{v_w^2}-\overline{w_w^2}\right)$$

$$+\frac{\partial}{\partial x}\left(v_h\frac{\partial V}{\partial x}\right)+\frac{\partial}{\partial y}\left(v_h\frac{\partial V}{\partial y}\right)+\frac{\partial}{\partial z}\left(v_v\frac{\partial V}{\partial z}\right) \tag{25}$$

in which v_h and v_v are the coefficients of eddy viscosity in the horizontal and vertical direction respectively. In these equations, the eddy viscosity, which is analogous to the kinematic viscosity,

is introduced for the Reynolds' stresses and viscous terms in equations (19) and (20) are neglected because they are much smaller than the turbulent shear terms.

The quantities $\overline{u_w^2} - \overline{w_w^2}$, $\overline{v_w^2} - \overline{w_w^2}$ and $\overline{u_w\,v_w}$ represent excess momentum fluxes (wave radiation stresses) due to wave action and provide the driving force that creates the nearshore currents.

The continuity equation is given by

$$\frac{\partial U}{\partial x} + \frac{\partial V}{\partial y} + \frac{\partial W}{\partial z} = 0 \tag{26}$$

In order to obtain the mean water level $\bar{\eta}$, the other continuity equation for which equation (26) is integrated from bottom to water surface in the vertical direction is given by

$$\frac{\partial \bar{\eta}}{\partial t} + \frac{\partial \widetilde{U}\,(h + \bar{\eta})}{\partial x} + \frac{\partial \widetilde{V}\,(h + \bar{\eta})}{\partial y} = 0 \tag{27}$$

where $\widetilde{U}$ and $\widetilde{V}$ are the velocities of the depth-averaged currents.

4. EVALUATION OF RADIATION STRESSES

In order to obtain the velocity of the currents, the radiation stresses must be determined using the water surface elevation η and the flow rates Q_x, Q_y. The radiation stresses S_{xx}, S_{yy}, and $S_{xy}(= S_{yx})$ are estimated using the method proposed by Watanabe and Siozaki (1982), which includes the effect of superimposed waves, such as the combination of progressive and reflected waves.

$$S_{xx} = \int_{-h}^{0} \rho \left(\overline{u_w^2} - \overline{w_w^2}\right) dz + S_0 \tag{28}$$

$$S_{yy} = \int_{-h}^{0} \rho \left(\overline{v_w^2} - \overline{w_w^2}\right) dz + S_0 \tag{29}$$

$$S_{xy} = \int_{-h}^{0} \rho \,\overline{u_w\,v_w}\, dz \tag{30}$$

and

$$S_0 = \frac{1}{2}\rho\,g\,\overline{\eta^2} + \rho\,g\,h\,\overline{\eta'} + \int_{-h}^{0} \rho \left[\frac{\partial}{\partial x}\int_{-h}^{0}\overline{u_w\,w_w}\,dz + \frac{\partial}{\partial y}\int_{-h}^{0}\overline{v_w\,w_w}\,dz\right] dz \tag{31}$$

in which h is not the mean water depth over a wave period, but the spatially mean water depth determined so as to eliminate the small fluctuations, η', in water surface elevation caused by wave superimposition due to interaction processes such as reflection and diffraction.

The time variation of water elevation η, and the flow rates Q_x and Q_y computed by the wave field module are expressed by

$$\left.\begin{array}{l} \eta = \hat{\eta}\,\sin\left(\sigma t + \varepsilon_\eta\right) \\ Q_x = \widehat{Q}_x\,\sin\left(\sigma t + \varepsilon_x\right) \\ Q_y = \widehat{Q}_y\,\sin\left(\sigma t + \varepsilon_y\right) \end{array}\right\} \tag{32}$$

where $\hat{\eta}$, $\widehat{Q}_x$ and $\widehat{Q}_y$ are the amplitude of water surface elevation and the flow rates in the x- and y-directions, respectively, ε_x and ε_y are the phase angles of Q_x and Q_y for η, ε_η is the phase angle of water surface elevation, $\sigma = 2\pi/T$ is the angular frequency and T is the wave period. Therefore, the water particle velocities induced by waves are given by

$$u_w = k\widehat{Q}_x \left[\cosh k(h+z)/\sinh kh\right] \sin(\sigma t + \varepsilon_x) \tag{33}$$

$$v_w = k\widehat{Q}_y \left[\cosh k(h+z)/\sinh kh\right] \sin(\sigma t + \varepsilon_y) \tag{34}$$

$$w_w = \sigma\hat{\eta} \left[\sinh k(h+z)/\sinh kh\right] \cos(\sigma t + \varepsilon_\eta) \tag{35}$$

where $k = 2\pi/L$ is the wave number, and L is the wavelength. Substituting equations (33) through (35) into equations (28) through (31), the radiation stresses are expressed by

$$\frac{S_{xx}}{\rho g} = \frac{Q_{xs}^2 + Q_{xc}^2}{4C^2}\left(1 + \frac{2kh}{\sinh 2kh}\right) + \Gamma \tag{36}$$

$$\frac{S_{yy}}{\rho g} = \frac{Q_{ys}^2 + Q_{yc}^2}{4C^2}\left(1 + \frac{2kh}{\sinh 2kh}\right) + \Gamma \tag{37}$$

$$\frac{S_{xy}}{\rho g} = \frac{Q_{xc}\,Q_{xs} + Q_{yc}\,Q_{ys}}{4C^2}\left(1 + \frac{2kh}{\sinh 2kh}\right) \tag{38}$$

in which

$$\Gamma = \frac{\eta_c^2 + \eta_s^2}{4}\frac{2kh}{\sinh 2kh} - \frac{1}{8\sigma}\left[\frac{\partial}{\partial x}\left(\eta_c Q_{xs} - \eta_s Q_{xc}\right) + \frac{\partial}{\partial y}\left(\eta_c Q_{ys} - \eta_s Q_{yc}\right)\right] \tag{39}$$

and

$$\begin{aligned}
&\eta_s = \hat{\eta}\sin\varepsilon_\eta\,, &&\eta_c = \hat{\eta}\cos\varepsilon_\eta\,, \\
&Q_{xs} = \widehat{Q}_x\sin\varepsilon_x\,, &&Q_{xc} = \widehat{Q}_x\cos\varepsilon_x\,, \\
&Q_{ys} = \widehat{Q}_y\sin\varepsilon_y\,, &&Q_{yc} = \widehat{Q}_y\cos\varepsilon_y\,.
\end{aligned} \tag{40}$$

A methodology for calculating η_s, η_c, Q_{xs}, Q_{xc}, Q_{ys} and Q_{yc} is as follows: for example, multiplying both sides of equation (32) by $\cos\sigma t$ and integrating time t over a wave period, the following equation is obtained

$$\int_0^T Q_x \cos\sigma t\, dt = \widehat{Q}_x \int_0^T \sin(\sigma t + \varepsilon_\eta)\cos\sigma t\, dt = \widehat{Q}_x \sin\varepsilon_x \int_0^T \cos^2\sigma t\, dt = \frac{T}{2}\widehat{Q}_x \sin\varepsilon_x = \frac{T}{2}Q_{xs}$$

and then

$$Q_{xs} = \frac{2}{T}\int_0^T Q\cos\sigma t\, dt$$

and the right-hand side of the above equation can be calculated by a numerical integration. On the other hand, multiplying both sides of equation (32) by $\sin\sigma t$ and integrating with time over a wave period, Q_{xc} can be calculated in a similar manner as mentioned above. Furthermore, the methodology for calculating η_s, η_c, Q_{ys} and Q_{yc} is similar to that mentioned above.

5. EVALUATION OF EDDY VISCOSITY

(1) Eddy viscosity ν_h in the horizontal direction

Longuet-Higgins (1970) proposed that the eddy viscosity ν_h is proportional to the product of the long wave celerity $C = \sqrt{g(h + \overline{\eta})}$ and distance from the shoreline, that is

$$\nu_h = Nx'\sqrt{g\,(h + \overline{\eta})} \tag{41}$$

in which N is a non-dimensional constant, x' is the horizontal distance from the shoreline and $h + \overline{\eta}$ is the real water depth. In this equation, using $\tan\beta$ for the slope of the sea bottom

$$x' = (h + \overline{\eta})/\tan\beta$$

Hence

$$\nu_h = N\,(h + \overline{\eta})\,\sqrt{g\,(h + \overline{\eta})}/\tan\beta \tag{42}$$

(2) Eddy viscosity ν_v in the vertical direction

The eddy viscosity ν_v plays a very important role in the determination of the vertical distribution for the velocity of nearshore currents. Tsuchiya et al. (1986) introduced the coefficient of eddy viscosity by putting

$$\nu_v = A_v C H \tag{43}$$

where C is the wave celerity, H is the wave height and A_v is a non-dimensional parameter. This equation shows that the eddy viscosity is constant in the vertical direction. However, another hypothesis for the eddy viscosity is to assume that the coefficient ν_v is a function of z. These hypotheses will be examined experimentally in Section 8.

6. BOUNDARY CONDITIONS

The boundary conditions at the mean water surface and bottom are important for determining the vertical distribution of the steady currents. During computation, it is possible to treat the bottom boundary as non-slip by increasing the number of divisions in the bottom boundary layer. However, it is useful to utilize the bottom shear stress as the bottom boundary condition instead of the non-slip one, and so reduce the computer memory requirement.

The boundary conditions on the sea bottom are given as

$$\nu_v \frac{\partial U}{\partial z} = \frac{\tau_{bx}}{\rho} \quad \text{and} \quad \nu_v \frac{\partial V}{\partial z} = \frac{\tau_{by}}{\rho} \quad \text{at } z = -h \tag{44}$$

where τ_{bx} and τ_{by} are the shear stresses due to bottom friction in the x and y directions, and which include the effect of interaction between the steady current and oscillatory motion in water waves. Horikawa (1985) indicated that the mean bottom shear stress components over a wave period including the effect of the interaction between current and wave motion are expressed by

$$\tau_{bx} = C_f\,\rho\,(U + u_b)\,\sqrt{(U + u_b)^2 + (V + v_b)^2} \tag{45}$$

$$\tau_{by} = C_f\,\rho\,(V + v_b)\,\sqrt{(U + u_b)^2 + (V + v_b)^2} \tag{46}$$

in which u_b and v_b are the wave-induced water particle velocity components at the bed, in the x and y directions respectively, and C_f is the coefficient of bottom friction. The water particle velocities u_b and v_b are expressed by

$$u_b = \hat{u}_b \cos(\sigma t - \psi_x) \tag{47}$$

$$v_b = \hat{v}_b \cos(\sigma t - \psi_y) \tag{48}$$

In addition, the amplitudes of water particle velocity components are given by

$$\hat{u}_b = \frac{k\,\widehat{Q}_x}{\sinh k\,(h + \overline{\eta})} \quad \text{and} \quad \hat{v}_b = \frac{k\,\widehat{Q}_y}{\sinh k(h + \overline{\eta})} \tag{49}$$

in which ψ_x and ψ_y are phase angles in the x and y directions, in the case of superimposed waves due to reflection and diffraction, and ψ_x (or ψ_y) is determined by the time difference in the same phase of Q_x (or Q_y) between a reference point and the desired point. Finally, the bottom shear stresses are given by

$$\tau_{bx} = \frac{\rho\,C_f}{4}\left[(\widetilde{U} + \hat{u}_b \cos\delta)\sqrt{(\widetilde{U} + \hat{u}_b \cos\delta)^2 + (\widetilde{V} + \hat{v}_b \cos\delta)^2} + \right.$$
$$\sqrt{(\widetilde{U} + \hat{u}_b \sin\delta)^2 + (\widetilde{V} - \hat{v}_b \sin\delta)^2} + \sqrt{(\widetilde{U} - \hat{u}_b \cos\delta)^2 + (\widetilde{V} - \hat{v}_b \cos\delta)^2} + \tag{50}$$
$$\left. \sqrt{(\widetilde{U} - \hat{u}_b \sin\delta)^2 + (\widetilde{V} + \hat{v}_b \sin\delta)^2} \right]$$

$$\tau_{by} = \frac{\rho\,C_f}{4}\left[(\widetilde{V} + \hat{v}_b \cos\delta)\sqrt{(\widetilde{V} + \hat{v}_b \cos\delta)^2 + (\widetilde{U} + \hat{u}_b \cos\delta)^2} + \right.$$
$$\sqrt{(\widetilde{V} + \hat{v}_b \sin\delta)^2 + (\widetilde{U} - \hat{u}_b \sin\delta)^2} + \sqrt{(\widetilde{V} - \hat{v}_b \cos\delta)^2 + (\widetilde{U} - \hat{u}_b \cos\delta)^2} + \tag{51}$$
$$\left. \sqrt{(\widetilde{V} - \hat{v}_b \sin\delta)^2 + (\widetilde{U} + \hat{u}_b \sin\delta)^2} \right]$$

in which $\delta = (\psi_x - \psi_y)/2$ and $\widetilde{U}$, $\widetilde{V}$ are the average at $\sigma t = (\psi_x + \psi_y + n\pi)/2$ ($n = 0,1,2,3$) of a wave period. Although the boundary condition at the free surface is generally that of no-flux, the shear stress due to water surface rollers must be considered in the surf zone where the mass transport caused by wave breaking is dominant. Taking account of the surface roller effects based on Svendsen and Lorenz's model (1989), the stress is given by

$$\tau_s = A_s \rho\,g\,h \tan\beta \left(\frac{H}{h}\right)^2 \left(2.7\,\frac{h}{L}\right) \tag{52}$$

in which H is the wave height, L is the wavelength, h is the water depth, $\tan\beta$ is the bottom slope and A_s is a constant value which is determined empirically by comparing computed nearshore currents with experimental data.

The shoreline can be regarded as a fixed boundary of the computational domain, if wave runup is neglected and the depth in the vicinity of the shoreline is very shallow. Coastal structures can also be considered to be fixed. The seaward boundary may also be regarded as fixed by locating it in deep water where there is no current and the mean water level set-up is zero. Therefore, current velocity components normal to these boundaries can be taken as zero. On the other hand, both the alongshore current velocity and the water level are uniform alongshore at lateral boundaries.

7. METHOD OF NUMERICAL COMPUTATION

The present model consists of two modules as shown in Fig. 3: (1) the wave field, and (2) the nearshore current field.

The set of equations (1) to (3) governing the wave climate can be solved numerically by using an explicit finite difference discretization on a staggered grid. Calculations are carried out in the time domain and must be continued until a steady periodic solution is obtained. In this model, it is important to determine the location of wave breaking accurately. Many researchers (see Dean, 1968; Goda, 1970; Goda, 1973; Ostendorf and Madsen, 1979; Sunamura, 1983) have proposed breaking conditions for progressive waves. The empirical formula of breaker indices proposed by Goda (1970) is applied in this model, that is,

$$\frac{H_b}{L_0} = 0.17\left[1 - \exp\left(-1.5\,\frac{h_b}{L_0}\,(1 + 1.5\,(\tan\beta)^{4/3})\right)\right] \tag{53}$$

in which H_b is the breaker height, h_b is the breaking water depth, L_0 is the wavelength in deep water, and $\tan\beta$ is the bottom slope. Furthermore, in order to calculate Goda's formula numerically, Watanabe et al. (1983) proposed the following relationship between the horizontal compo-
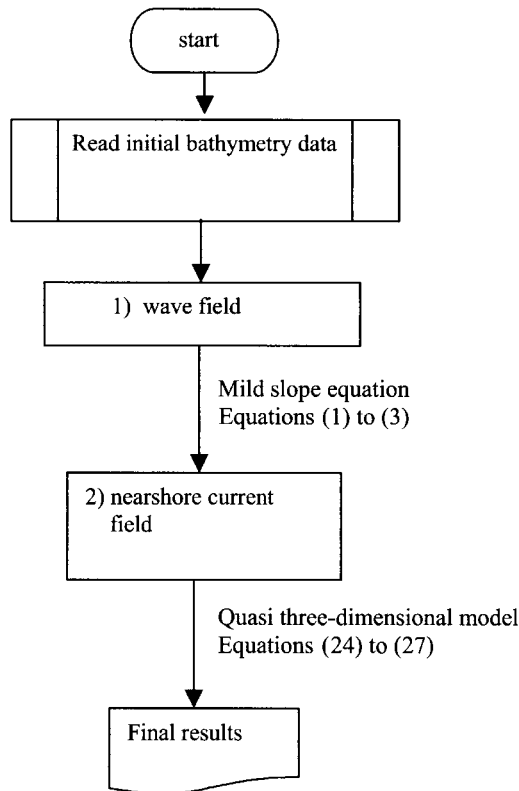
Figure 3. Flowchart of model to simulate nearshore currents.

nent of wave particle velocity at the still water level u_{wb} and the wave celerity C_b at the breaking point

$$\frac{u_{wb}}{C_b} = \pi \frac{H_b}{L_0} \coth^2 \left(2\pi \frac{h_b}{L_b} \right) \tag{54}$$

in which L_b is the wavelength at the breaking point. u_{wb}/C_b is the function of h_b/L_0 and the bottom slope, and is also the function of wave steepness in deep water H_0/L_0. Therefore, if the relationships between u_{wb}/C_b and H_0/L_0, or between u_{wb}/C_b and h_b/L_0 are calculated beforehand, the value of h_b/L_0 is determined.

In order to determine the velocities of nearshore currents in the quasi 3-D model, equations (24) and (25) must be solved so as to satisfy the continuity equations (26), (27) and boundary conditions. The method is the hybrid method proposed by Koutitas and O'Connor (1980), who combined the fractional step finite difference method in the horizontal plane with a Galerkin finite element one in the vertical direction.

FRACTIONAL STEP FINITE DIFFERENCE METHOD: This method proposed by Chorin (1968) is applied to integrate equations (24) and (25) over time. Equations (24) and (25) become the following by using an operator L

$$\frac{\partial U}{\partial t} = L(U) + \alpha_1 \tag{55}$$

$$\frac{\partial V}{\partial t} = L(V) + \alpha_2 \tag{56}$$

in which

$$L = -U\frac{\partial}{\partial x} - V\frac{\partial}{\partial y} - W\frac{\partial}{\partial z} + \frac{\partial}{\partial x}\left(v_h\frac{\partial}{\partial x}\right) + \frac{\partial}{\partial y}\left(v_h\frac{\partial}{\partial y}\right) + \frac{\partial}{\partial z}\left(v_v\frac{\partial}{\partial z}\right) \tag{57}$$

$$\alpha_1 = -g\frac{\partial \overline{\eta}}{\partial x} - \frac{\partial R_{xx}}{\partial x} - \frac{\partial R_{xy}}{\partial y}, \quad \alpha_2 = -g\frac{\partial \overline{\eta}}{\partial y} - \frac{\partial R_{yx}}{\partial x} - \frac{\partial R_{yy}}{\partial y} \tag{58}$$

and, in addition

$$R_{xx} = \overline{u_w^2} - \overline{w_w^2} \tag{59}$$

$$R_{yy} = \overline{v_w^2} - \overline{w_w^2} \tag{60}$$

$$R_{xy} = R_{yx} = \overline{u_w\,v_w} \tag{61}$$

If the operator L is independent of U, V and W over an infinitesimal time interval, the operator can be divided into two parts, L_1 and L_2. Therefore, the operators L_1 and L_2 are rewritten as

$$L_1 = -U^{(m)}\frac{\partial}{\partial x} - V^{(m)}\frac{\partial}{\partial y} - W^{(m)}\frac{\partial}{\partial z} + \frac{\partial}{\partial x}\left(v_h\frac{\partial}{\partial x}\right) + \frac{\partial}{\partial y}\left(v_h\frac{\partial}{\partial y}\right) \tag{62}$$

and

$$L_2 = \frac{\partial}{\partial z}\left(v_v\frac{\partial}{\partial z}\right) \tag{63}$$

Finally, the difference analogue of the governing equation in the x-direction (equation (55)) becomes

$$\text{Step1}: \quad \frac{\partial U^{(m)}}{\partial t} = \frac{U^{(d)} - U^{(m)}}{\Delta t} = L_1\left(U^{(m)}\right) + \alpha_1 \tag{64}$$

$$\text{Step2}: \quad \frac{\partial U^{(m+1)}}{\partial t} = \frac{U^{(m+1)} - U^{(d)}}{\Delta t} = L_2\left(U^{(m+1)}\right) + \alpha_2 \tag{65}$$

in which $U^{(d)}$ is a hypothetical velocity component and the superscripts (m), etc. refer to the time increment. In calculation, the hypothetical velocity component, $U^{(d)}$, is obtained from equation (64) by using a known value, $U^{(m)}$, and then substituting $U^{(d)}$ computed into equation (65), giving $U^{(m+1)}$. The calculation must be continued until a steady periodic solution is obtained.

GALERKIN FINITE ELEMENT METHOD: The above-mentioned equations are discretized by using the finite element method. Firstly, the variables are located on each element according to the staggered method shown in Fig. 4, and each individual element is divided so as to satisfy the following equation, that is,

$$\frac{\ell_{i,j,k}}{d_{i,j}} = \frac{\ell_{i+1,j,k}}{d_{i+1,j}} \tag{66}$$

in which subscripts i and j are the discrete points of mesh in the x- and y-direction, respectively, and subscript k shows the discrete point in the vertical direction. In addition, d is real water depth $(= h + \overline{\eta})$ and $\ell_k = z_{k+1} - z_k$.

It is assumed that velocity components U, V, W and the eddy viscosity ν_v between k and $k+1$ are expressed as follows

$$\left.\begin{aligned} U &= N_k\, U_k + N_{k+1}\, U_{k+1} \\ V &= N_k\, V_k + N_{k+1}\, V_{k+1} \\ W &= N_k\, W_k + N_{k+1}\, W_{k+1} \end{aligned}\right\} \tag{67}$$

$$\nu_v = N_k\, \nu_{vk} + N_{k+1}\, \nu_{vk+1}$$

in which N_k and N_{k+1} are the linear form functions which are described by
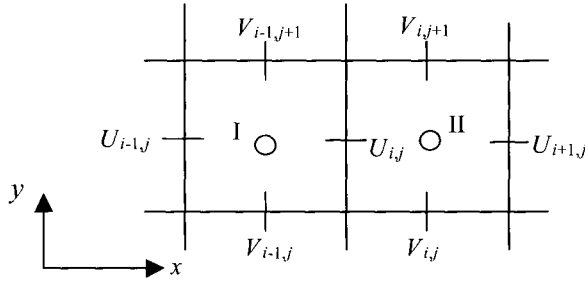
$$N_k = \frac{z_{k+1} - z}{z_{k+1} - z_k} \tag{68}$$

$$N_{k+1} = \frac{z - z_k}{z_{k+1} - z_k} \tag{69}$$

By applying the Galerkin finite element method, the matrices in element ℓ_k are given by

$$\begin{pmatrix} A_{k,k} & A_{k,k+1} \\ A_{k+1,k} & A_{k+1,k+1} \end{pmatrix} \{U_k, U_{k+1}\}^{(d)} = \{a_k, a_{k+1}\}^{(m)} \tag{70}$$

$$\begin{pmatrix} A_{k,k} & A_{k,k+1} \\ A_{k+1,k} & A_{k+1,k+1} \end{pmatrix} \{V_k, V_{k+1}\}^{(d)} = \{b_k, b_{k+1}\}^{(m)} \tag{71}$$

$$\begin{pmatrix} B_{k,k} & B_{k,k+1} \\ B_{k+1,k} & B_{k+1,k+1} \end{pmatrix} \{U_k, U_{k+1}\}^{(m+1)} = \{c_k, c_{k+1}\}^{(d)} \tag{72}$$
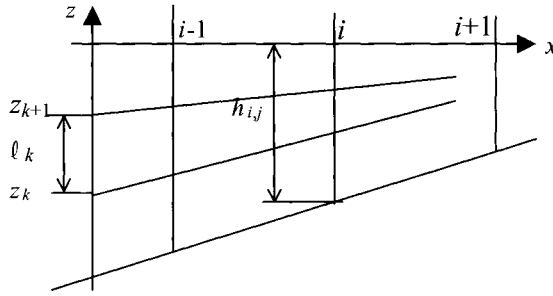
Figure 4. Grid used in computation of currents.

$$\begin{pmatrix} B_{k,k} & B_{k,k+1} \\ B_{k+1,k} & B_{k+1,k+1} \end{pmatrix} \{V_k, V_{k+1}\}^{(m+1)} = \{d_k, d_{k+1}\}^{(d)} \tag{73}$$

The whole matrix can be solved by the summation of these element matrices including the bottom and water surface boundary conditions. Details of matrices (A), (B) and vectors $\{a\}$, $\{b\}$, $\{c\}$, $\{d\}$ are given in the Appendix.

As shown in Fig. 4, the computational domain in the x-y plane is divided into a rectangular grid ($\Delta x = \Delta y$). The vertical component of current velocity W and mean water level η are computed at the center of each grid cell, whereas the horizontal velocity components U and V, are corrected midway along the cell faces. The mean water surface level η for the next time step ($m + 1/2$) is evaluated using that at the previous time step ($m - 1/2$), based upon the difference equation of continuity equation (27), that is,

$$\overline{\eta}^{(m+1/2)} = \overline{\eta}^{(m-1/2)} - \frac{\Delta t}{\Delta x} \left(U_{i+1,j} \cdot h_{U_{i+1,j}}^{(m-1/2)} - U_{i,j} \cdot h_{U_{i,j}}^{(m-1/2)} \right)$$
$$+ \frac{\Delta t}{\Delta y} \left(V_{i,j+1} \cdot h_{V_{i,j+1}}^{(m-1/2)} - V_{i,j} \cdot h_{V_{i,j}}^{(m-1/2)} \right) \tag{74}$$

In a similar manner, the difference equation of the vertical velocity component expressed by equation (26) can be obtained as follows

$$W_{i,j,k}^{(m+1)} = W_{i,j,k-1} - \frac{\overline{U}_{i+1,j}^{(m+1)} \cdot \ell_{kU_{i+1,j}}^{(m+1/2)} - \overline{U}_{i,j}^{(m+1)} \cdot \ell_{kU_{i,j}}^{(m+1/2)}}{\Delta x}$$

$$+ \frac{\overline{V}_{i,j+1}^{(m+1)} \cdot \ell_{kV_{i,j+1}}^{(m+1/2)} - \overline{V}_{i,j}^{(m+1)} \cdot \ell_{kV_{i,j}}^{(m+1/2)}}{\Delta y} \tag{75}$$

in which subscripts $_U$ and $_V$ refer to values at the computational points of U and V, respectively. Furthermore, U and V are the average of the velocity components at grid points k and $k + 1$. Finally, the time step for stability according to the current condition may be written as

$$\Delta t < \frac{\Delta x}{|U| + \sqrt{g(h + \overline{\eta})}} \tag{76}$$

in which this condition relates to the Galerkin sub-model alone.

8. UNDERTOW

In order to predict nearshore currents, it is necessary to evaluate the eddy viscosity coefficient as accurately as possible. In this section, the characteristic eddy viscosity profile is described by a simple method for estimating the vertical distributions of the undertow velocity.

The fundamental equation can be introduced on the basis of Svendsen (1984), that is,

$$\frac{\partial}{\partial z} \left(\nu_v \frac{\partial U}{\partial z} \right) = \frac{\partial}{\partial x} \left(\overline{u_w^2} + g\overline{\eta} \right) \tag{77}$$

Applying long wave theory to the right-hand side of the above equation, equation (77) is rewritten as

$$\frac{\partial}{\partial x} \left(\overline{u_w^2} + g\overline{\eta} \right) = C^2 \left(\frac{H}{h} \right)^2 B_0 \left[2 \left(\frac{C_x}{C} + \frac{(H/h)_x}{H/h} \right) + \frac{B_{0x}}{B_0} \right] + g\overline{\eta}_x \tag{78}$$

in which the subscript x is differentiation with respect to x, C is the wave celerity, and B_0 is defined as follows

$$B_0 = \frac{1}{T} \int_0^T \left(\frac{\eta}{H} \right)^2 dt \tag{79}$$

An experimental equation for equation (79) proposed by Hansen (1990) is given by

$$B_0 = 0.125 \tanh \left(\frac{11.40}{\sqrt{U_{rb}}} \right) \cdot \left[1 - \frac{0.025}{h_x} \left(1.3 - 10 \frac{h_x}{\sqrt{H_0/L_0}} \right. \right.$$
$$\left. \left. \left(1 - 2.654 \sqrt{\frac{H_0}{L_0}} - \frac{h}{h_b} \right) \left(1 - \frac{h}{h_b} \right) \right) \right] \tag{80}$$

in which U_{rb} is the Ursell number ($U_r = HL^2/h^3$) and h_b is the water depth at the breaking point. If the eddy viscosity coefficient, ν_v has a constant value, the right-hand side of equation (77) is independent with respect to z, and then equation (77) is rewritten as follows

$$\frac{\partial^2 U}{\partial z^2} = \omega \tag{81}$$

in which

$$\omega = \frac{1}{\nu_v} \left[C^2 \left(\frac{H}{h} \right)^2 B_0 \left[2 \left(\frac{C_x}{C} + \frac{(H/h)_x}{H/h} \right) + \frac{B_{0x}}{B_0} \right] + g\overline{\eta}_x \right] \tag{82}$$

The bottom boundary condition satisfying equation (77) is given by the undertow velocity U_b at the bottom, proposed by Kuroiwa et al. (1994), that is,

$$U_b = A_b \frac{H^2}{Td} \tanh\left(\frac{d}{d_b} - 1\right) \tag{83}$$

in which A_b is a constant determined experimentally and $d_b = (h + \bar{\eta})_b$ the mean water depth at the breaking point. The continuity condition at the trough level of waves is defined by

$$U_m d_{tr} = \int\limits_{-h}^{-h+d_{tr}} U(z)\,dz \tag{84}$$

in which d_{tr} is the depth from the still water surface to trough level of waves and U_m the mean velocity from the bottom to the trough level. The solution of equation (81) satisfying both boundary conditions is analytically given by

$$U = \frac{1}{2}\omega(z+h)^2 + \left(2\frac{U_m - U_b}{d_{tr}} - \frac{1}{3}\omega d_{tr}\right)(z+h) \tag{85}$$

As mentioned above, the depth d_{tr} and the mean velocity U_m must be determined empirically. The depth of the trough level proposed by Hansen (1990) is given by

$$d_{tr} = h - 0.5\,H\,\frac{\tanh 4.85}{\sqrt{U_r}} \tag{86}$$

and also the mean velocity indicated by Svendsen (1984) is given by

$$U_m = -C\left(\frac{H}{h}\right)^2\left(B_0 + A_r\frac{h}{H^2 L}\right) \tag{87}$$

in which A_r is the cross-sectional area of the surface roller caused by breaking waves, that is, $A_r = 0.9H^2$.

Fig. 5a compares experimental measurements of the distribution of wave heights, mean water level and trough level with numerical predictions based upon equations (1), (3) and (86). In addition, Fig. 5b presents a comparison of the measured undertow velocity distribution cross-shore, at the stations 2 mm above the bottom with the corresponding distribution obtained using equation (83) where $A_b = 2.6$. It is found that the calculated results of wave height and trough level closely match the experimental measurements and the predictions of bottom velocity agree approximately with experimental data.

In cases when the eddy viscosity varies in the vertical direction, it is necessary to solve equation (77) numerically by using the difference method. Okayasu et al. (1986) assumed the eddy viscosity to be as follows

$$\nu_v = 0.013\,C\,(h+z) \tag{88}$$

Equation (83) was used as the bottom boundary condition, and equation (89)

$$\nu_v\frac{\partial U}{\partial z'} = \frac{\tau}{\rho} = 0.0016\,C^2 \quad \text{at } z' = d_{tr} \tag{89}$$

as the surface boundary condition at the trough level of waves, in which $z' = h + z$ and τ is the shear stress at trough level. On the other hand, Deigaard et al. (1986) attempted to evaluate the eddy
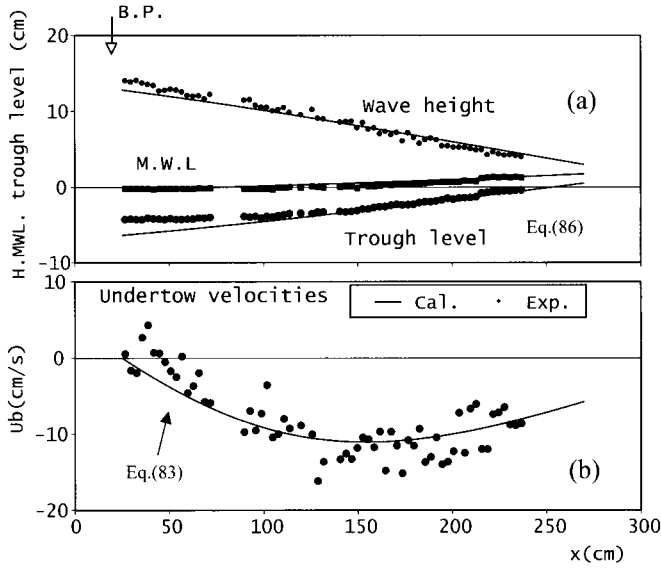
Figure 5. Comparison of the calculated bottom velocity and the depth at trough level with those measured. Wave height $H = 13.1$ cm at water depth $h = 40$ cm, Wave period $T = 1.01$ sec, Wave height $H_b = 13.7$ cm at water depth of breaking point $h_b = 17.6$ cm, Breaker type: spilling.

viscosity by using the turbulent energy due to wave breaking, and calculated the undertow velocities numerically.

Fig. 6 presents a comparison of the calculated results for vertical distributions of undertow velocity using the eddy viscosity coefficient proposed by Tuchiya et al. (1986) (equation (43)), Okayasu et al. (1986) (equation (88)) and Deigaard et al. (1986) with experimental measurements. It is clear that there are none of the assumed eddy viscosity coefficients applicable over a wide range of h/h_b values. Therefore, the relatively simple description of eddy viscosity in the vertical direction, proposed by Tuchiya et al. will be used in later sections of nearshore current computation.

The quasi two-dimensional equations for nearshore currents are rewritten from equations (24) to (27) as follows

$$\frac{\partial U}{\partial t} + U\frac{\partial U}{\partial x} + W\frac{\partial U}{\partial z} = -g\frac{\partial \overline{\eta}}{\partial x} - \frac{\partial}{\partial x}\left(\overline{u_w^2} - \overline{w_w^2}\right) - \frac{\partial}{\partial z}\left(\overline{u_w\,w_w}\right) +$$

$$\frac{\partial}{\partial x}\left(\nu_h\frac{\partial U}{\partial x}\right) + \frac{\partial}{\partial z}\left(\nu_v\frac{\partial U}{\partial z}\right) \tag{90}$$

$$\frac{\partial U}{\partial x} + \frac{\partial W}{\partial z} = 0 \tag{91}$$

and

$$\frac{\partial \overline{\eta}}{\partial t} + \frac{\partial \widetilde{U}(h + \overline{\eta})}{\partial x} = 0 \tag{92}$$

In order to solve these equations numerically, it is necessary to determine the momentum flux corresponding to radiation stresses and eddy viscosity coefficient beforehand. It is clear from previous
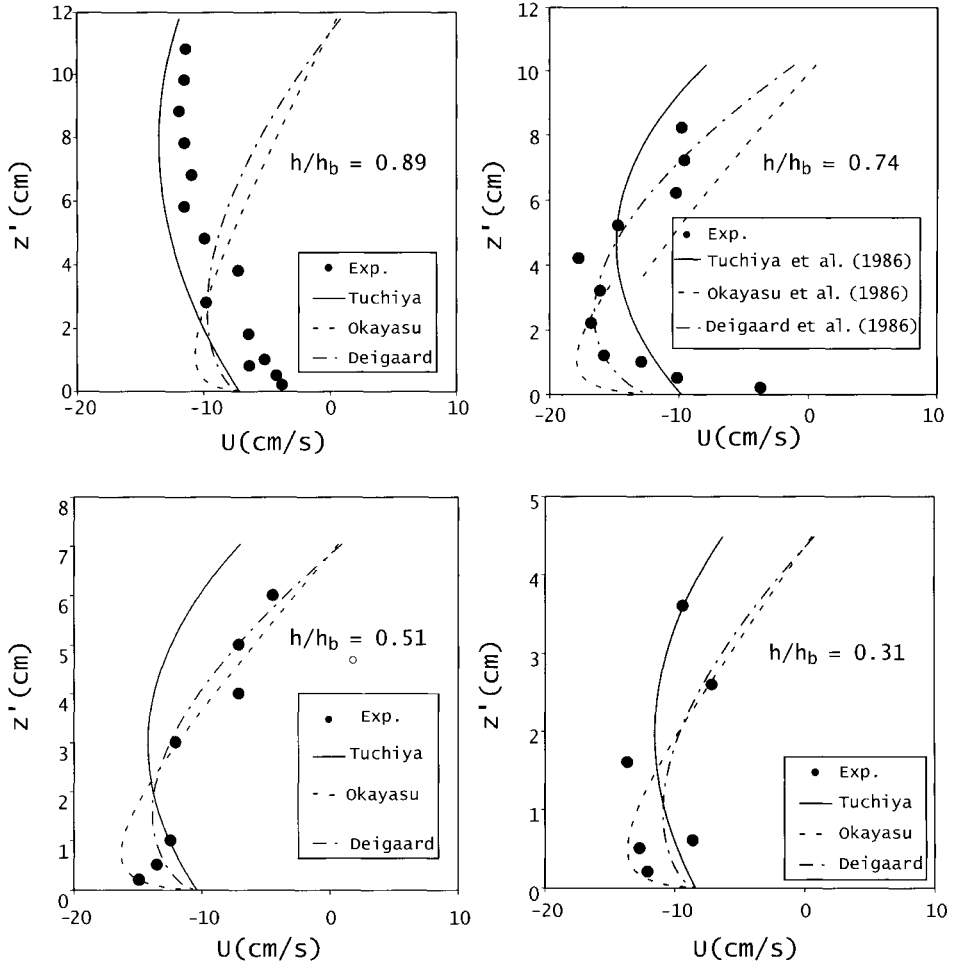
Figure 6. Comparison of calculated results for vertical distributions of undertow velocity based upon experiments done by several researchers. Characteristics of waves used in experiments are the same as those in Fig. 5.

experiments (see Kuroiwa, 1999) that the momentum flux in the surf zone is constant in the vertical direction. Although wave characteristics in the surf zone have strong dispersion and nonlinearity, the radiation stresses and momentum flux are evaluated on the basis of linear theory for simplicity. Francisco and Arcilla (1992) presented the momentum flux based upon linear wave theory as follows

$$\overline{u_w^2} - \overline{w_w^2} = G\left(\frac{E}{\rho h}\right) \tag{93}$$

in which E is wave energy, and

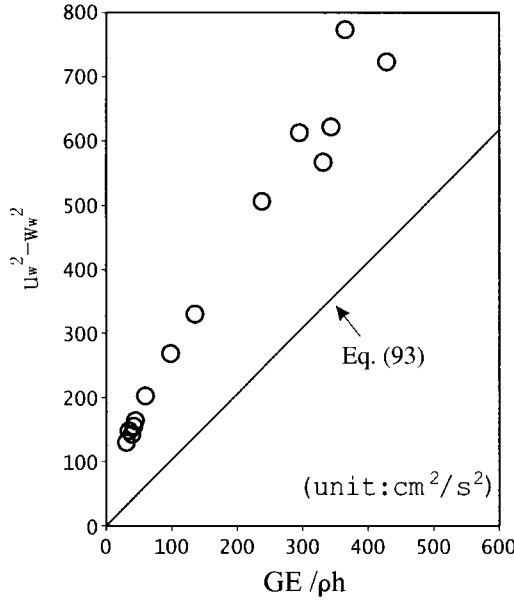$$G = \frac{2kh}{\sinh 2kh} \tag{94}$$

Figure 7. Relationship between momentum flux and $GE/\rho h$.

where k is the wave number. Surface waves induce a momentum M in the direction of wave propagation. The value of M is given by $M = E/C$, and current velocity U is proportional to $M/\rho h = E/\rho h C$. Dividing equation (93) by C^2, it is clear that the right-hand side of equation (93) is proportional to U/C (see Horikawa, 1978).

Fig. 7 shows the calculated result (solid line) of equation (93) and the experimental relationship (circles) between the momentum flux and $GE/\rho h$. It is shown that the relationship between the momentum flux and $GE/\rho h$ obtained from experiments is given by

$$\overline{u_w^2} - \overline{w_w^2} = 2G\left(\frac{E}{\rho h}\right) \tag{95}$$

On the other hand, the radiation stress S_{xx} obtained from depth-averaged flow rate is given by

$$\frac{S_{xx}}{\rho g} = \frac{Q_{xs}^2 + Q_{xc}^2}{4C^2}\left(1 + \frac{2kh}{\sinh 2kh}\right) + \frac{\eta_s^2 + \eta_c^2}{4}\frac{2kh}{\sinh 2kh} \tag{96}$$

Substituting calculated results obtained by the mild-slope equations into the momentum flux and integrating from the bottom to the water surface, the momentum flux is rewritten as

$$\frac{h(\overline{u_w^2} - \overline{w_w^2})}{g} = \frac{1}{g}\int_{-h}^{0}(\overline{u_w^2} - \overline{w_w^2})\,dz = \frac{Q_{xs}^2 + Q_{xc}^2}{4C^2}\left(1 + \frac{2kh}{\sinh 2kh}\right) +$$

$$\frac{\eta_s^2 + \eta_c^2}{4}\left(\frac{2kh}{\sinh 2kh} - 1\right) \tag{97}$$
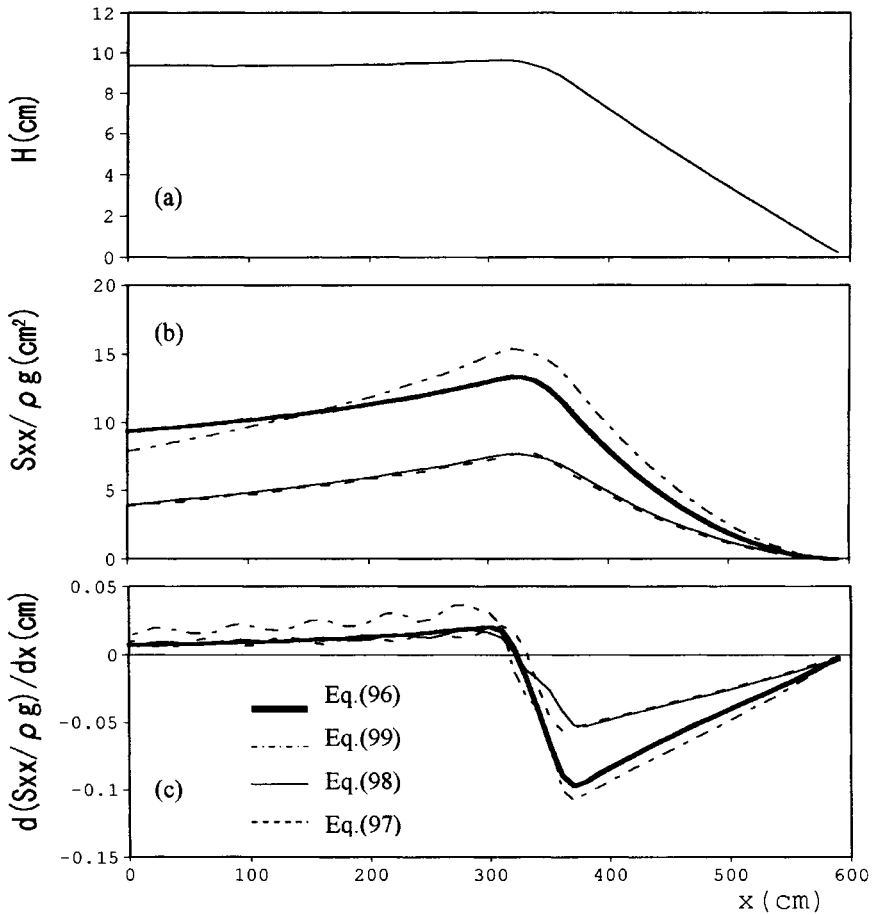
Figure 8. Computed spatial variations of wave height, momentum flux and the differentiation. Wave characteristics: Deep water wave height $H_0 = 10.26$ cm, Wave period $T = 1.0$ sec. Beach slope $\tan \beta = 1/20$, depth at breaking point $h_b = 11.5$ cm, Breaker type: spilling-plunging.

Equations (93) and (94) are rewritten so as to have the same dimensions as equation (96), that is,

$$\frac{h(\overline{u_w^2} - \overline{w_w^2})}{g} = G\left(\frac{E}{\rho g}\right) \tag{98}$$

and

$$\frac{h(\overline{u_w^2} - \overline{w_w^2})}{g} = 2G\left(\frac{E}{\rho g}\right) \tag{99}$$

Figs. 8a, b and c show the calculated results for spatial variation of wave height H, the momentum flux (or radiation stress) and the spatial differentiation of momentum flux, respectively, of waves as they progress cross-shore. As shown in Fig. 8b, the cross-shore distributions of the momentum flux calculated by equation (97) coincide with those calculated by equation (98). However, the results
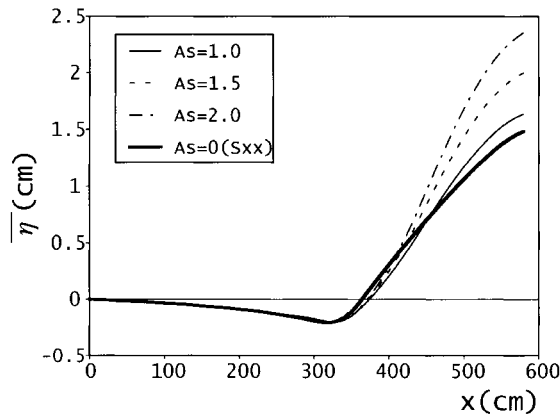
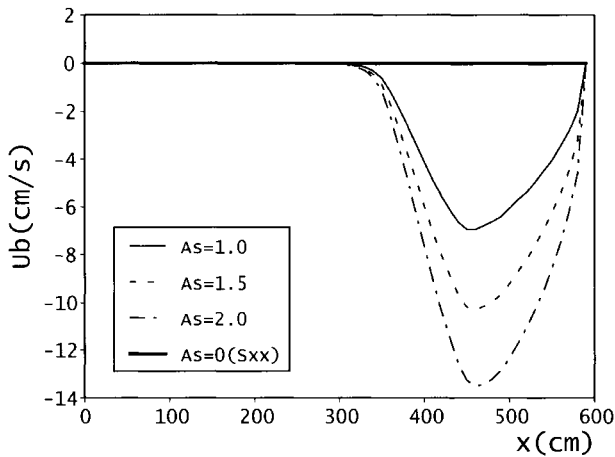**Figure 9.** Effect of shear stress at free surface on mean water level.

Figure 10. Effect of shear stress at free surface on current velocities at bottom.

calculated by equations (96) and (99), of which values are greater than equation (98), are different from those of equations (97) and (98). The quantity which influences the spatial variation of mean water surface level and current is not the momentum flux, but the variations of spatial differentiation for momentum flux. As shown in Fig. 8c, the results calculated by equations (96), (97) and (98) have almost the same values (unlike equation (99)) seaward of the breaker zone. However, the results calculated by equations (97) and (98) are smaller than those from equations (96) and (99) within and immediately shoreward of the breaker zone.

As a result, it is suggested that smaller values, which show the spatial differentiation of momentum flux calculated from equations (97) and (98), influence the variation of mean water level. To supplement the effect in practical calculation, the shear stress given by equation (52), which is the added momentum flux due to the surface roller caused by breaking waves, is applied as the surface boundary condition. Fig. 9 shows that the computed mean water level in the cross-shore direction increases with increasing values of the coefficient of A_s in equation (52) for the free surface shear
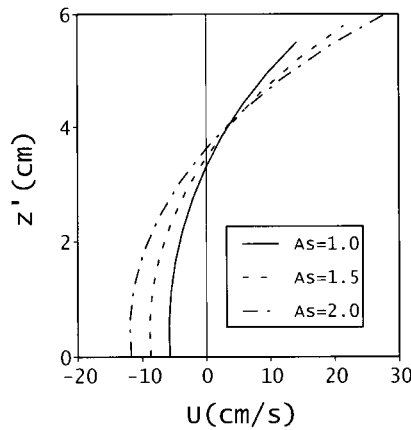
Figure 11. An example of computed results for vertical distributions of current velocity.
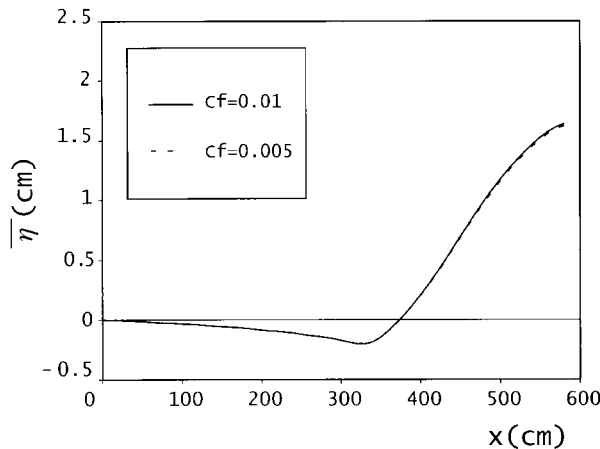

Figure 12. Computed results for spatial variation of mean water level influenced by eddy viscosity C_f.

stress. In this calculation, the bottom friction factor $C_f = 0.01$ and the coefficient including the eddy viscosity in equation (43) is taken to be $A_v = 0.01$. Fig. 10 shows the variation of bottom current velocities associated with increasing A_s. In this figure, it is remarkable that the bottom current velocity is not induced in the case of $A_s = 0$ which means the shear stress is almost equal to zero. Fig. 11 shows the calculated results for the vertical distributions of steady current for $A_s = 1.0$, 1.5 and 2.0. It is observable that the greater the value of A_s becomes, the larger the near bed undertow velocity becomes, and the steady current velocity at the bottom increases shoreward whereas the steady current at the free surface increases seaward as the value of A_s increases.

Figs. 12 and 13 show the computed results for the spatial variation of mean water level and current velocity at bottom with A_v (included in coefficient of eddy viscosity equation (43)). The following values have been used for the parameters: $A_s = 1.0$ and $C_f = 0.01$. The mean water level calculated using $A_v = 0.005$ is not different from that of $A_v = 0.01$, but the bottom current velocity prediction
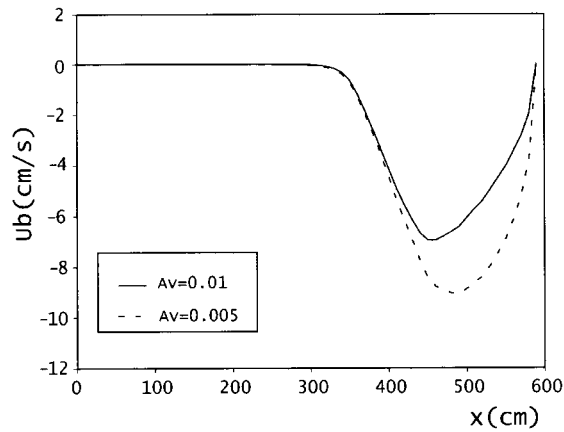
Figure 13. Computed results for spatial variation of bottom current velocity influenced by eddy viscosity C_f.
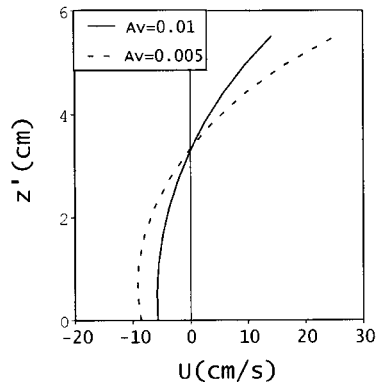

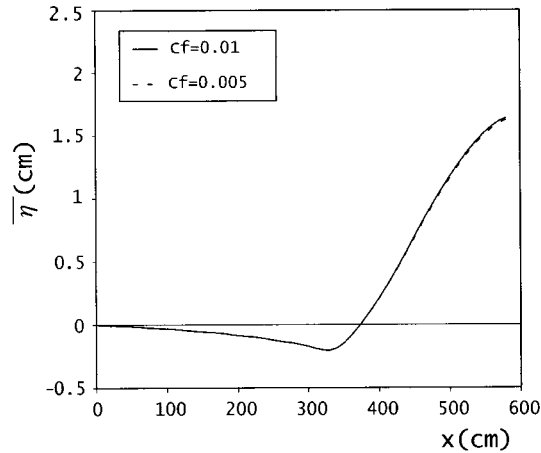**Figure 14.** The effect of vertical eddy viscosity on current velocities.

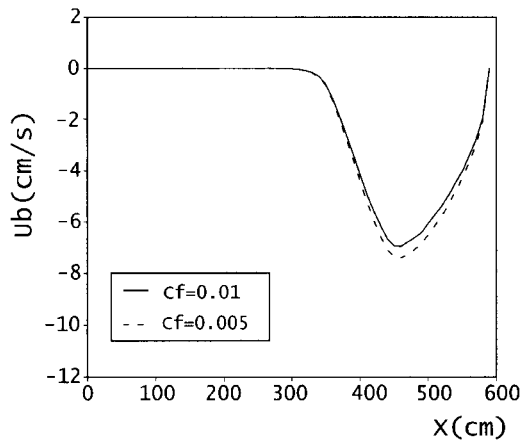**Figure 15.** The effect of friction factor on mean water level.

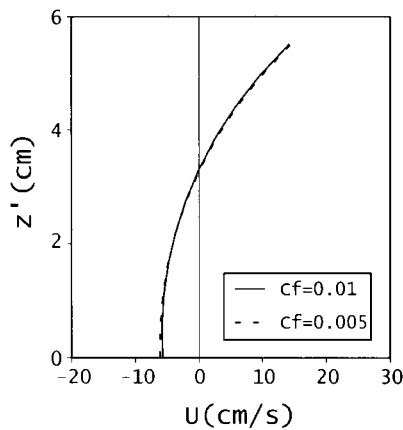**Figure 16.** The effect of friction factor on bottom current velocity.

Figure 17. The effect of friction factor on vertical distribution of current velocity.

are different in the surf zone as shown in Fig. 13. Fig. 14 shows the vertical distributions of current velocity computed for the same conditions as Figs. 12 and 13. In this figure, the current velocities at the bottom and at the free surface increase seaward and shoreward respectively, as the values of A_v decrease. An outstanding feature shown in this figure is that the vertical eddy viscosity influences not only the vertical distributions of current velocity but also those in the cross-shore direction.

Figs. 15 and 16 show the variations of mean water level and bottom current velocity with z' computed for the case of $A_v = 0.01$, $A_s = 1.0$ and various values of friction factor C_f, respectively. Fig. 17 shows the variations of current velocity with the vertical axis computed for the same case as Fig. 15. It is evident that the effects of friction factor on both mean water level and bottom current velocity are negligible.

Figs. 18a, b and c show the observed variations of wave height, mean water level and bottom current velocity in the cross-shore direction, respectively. The experimental conditions are summarized in Table 1. The predicted and measured cross-shore variations of wave height are in close agree-
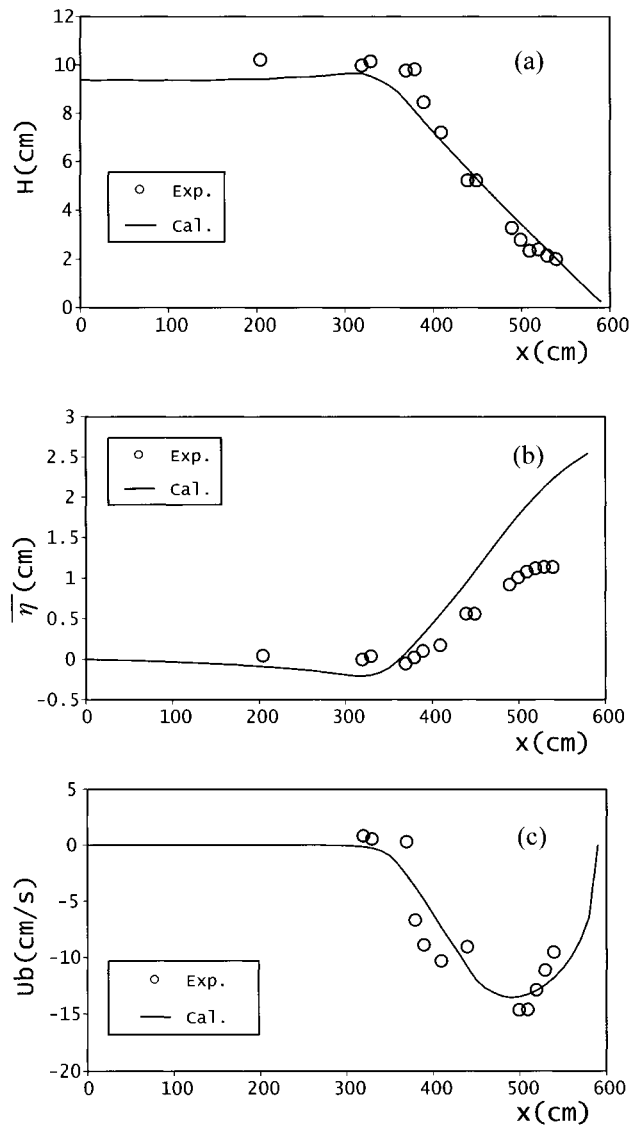
Figure 18. Comparisons of experimental results with those computed. (a) Wave height, (b) mean water level, and (c) bottom current velocity.

Table 1
The conditions of experiments.

$\tan \beta$	H_0 (cm)	T (sec)	H_b (cm)	h_b (cm)	H_0/L_0	Breaker type
1/20	10.26	1.00	9.74	11.5	0.066	spilling-plunging
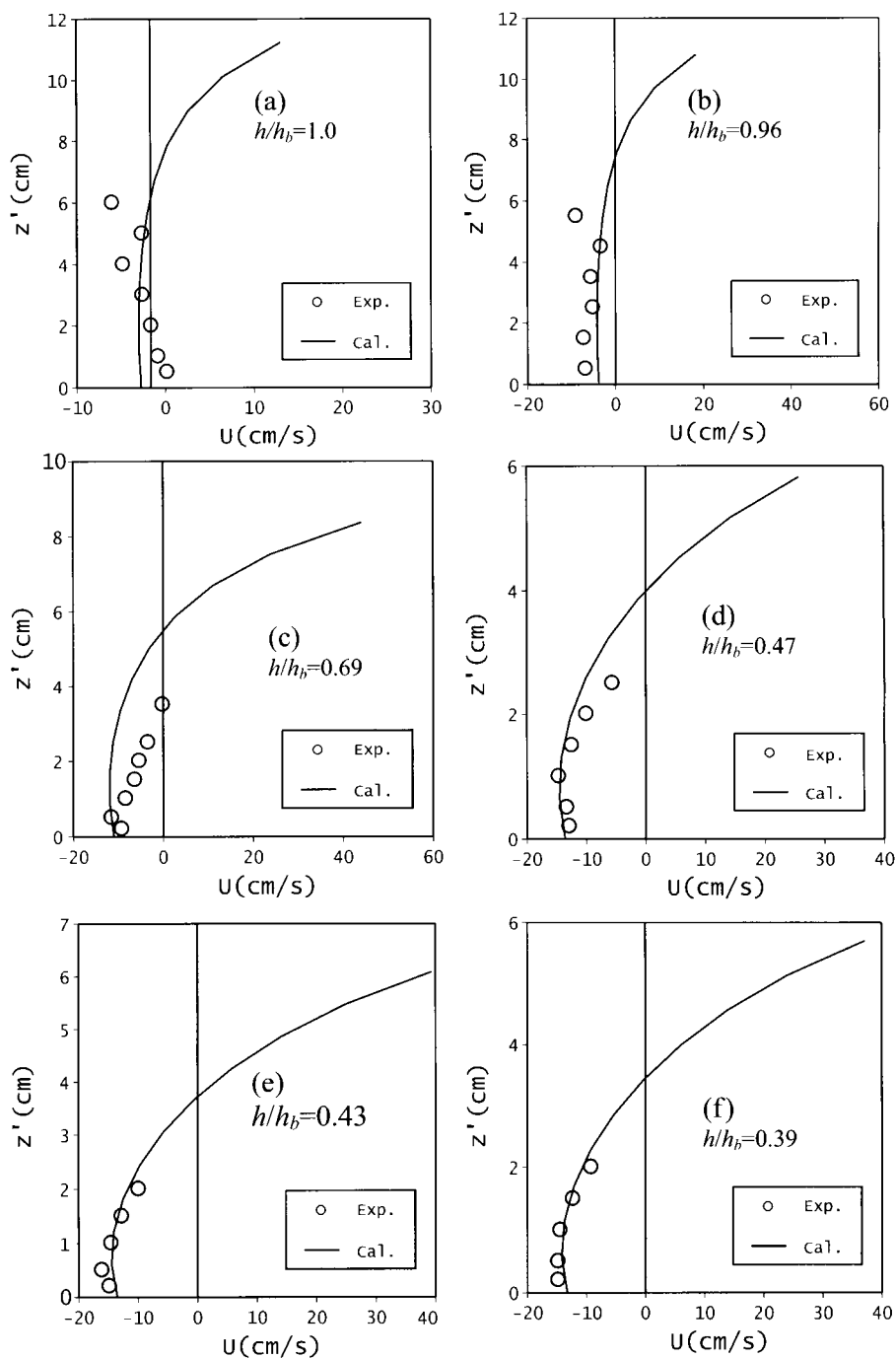
Figure 19. Comparison of vertical distributions for cross-shore current velocities of experiments with those computed.

ment. However, Fig. 18b shows that the computed mean water level is overestimated in comparison with the experimental data. Although a scatter of points can be seen, Fig. 18c shows that the results of experiments are in approximate agreement with the computed result. In these computations, the following parameters have been used: $A_s = 1.5$, $C_f = 0.01$ and $A_v = 0.005$. Fig. 19 compares the experimental results for the vertical distributions of cross-shore current velocities with those computed for the cases in the range of $0.39 \leqslant h/h_b \leqslant 1.0$. In these figures, the predicted current velocity near the bottom is in the opposite direction for the experimental measurement at the breaking point $(h/h_b = 1.0)$. The other cases of the computed results are in reasonable agreement with those of the experiments.

9. LONGSHORE CURRENTS

The present model is applied to determine the vertical profile of longshore currents. The computed results are compared with those of experiments carried out by Visser (1991). Figs. 20a, b and c

Figure 20. Comparison of mean water levels and longshore currents between the computed and experimental results.
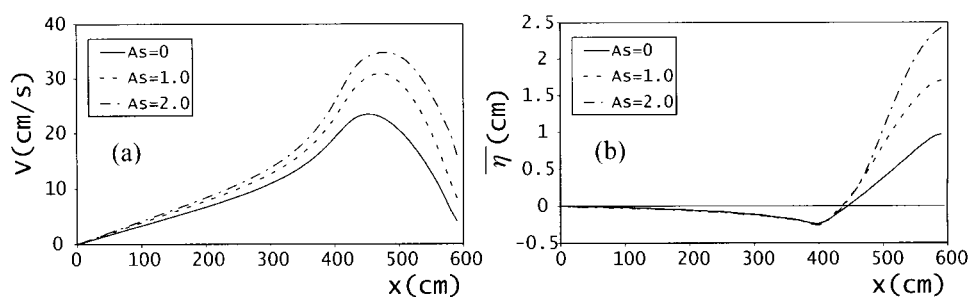
Figure 21. Effects of parameter A_s on mean water level and longshore current velocity.

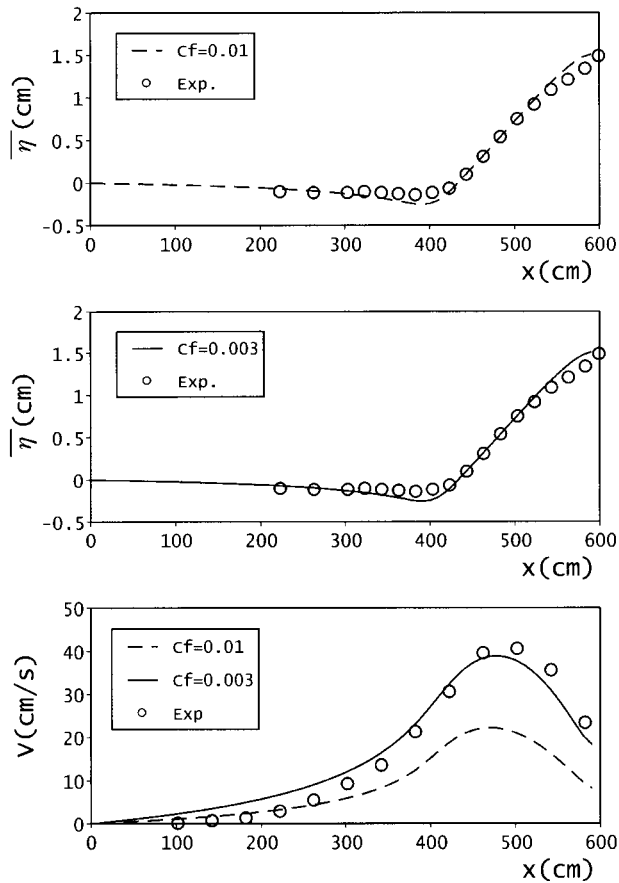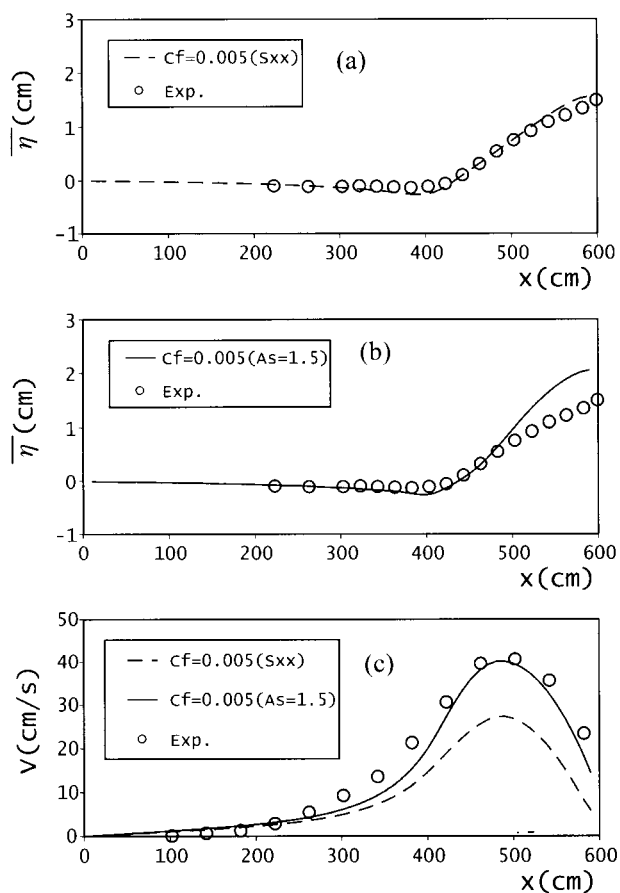**Figure 22.** Comparison of experimental results with those of computation related to mean water level and longshore current velocity calculated by quasi three-dimensional model.
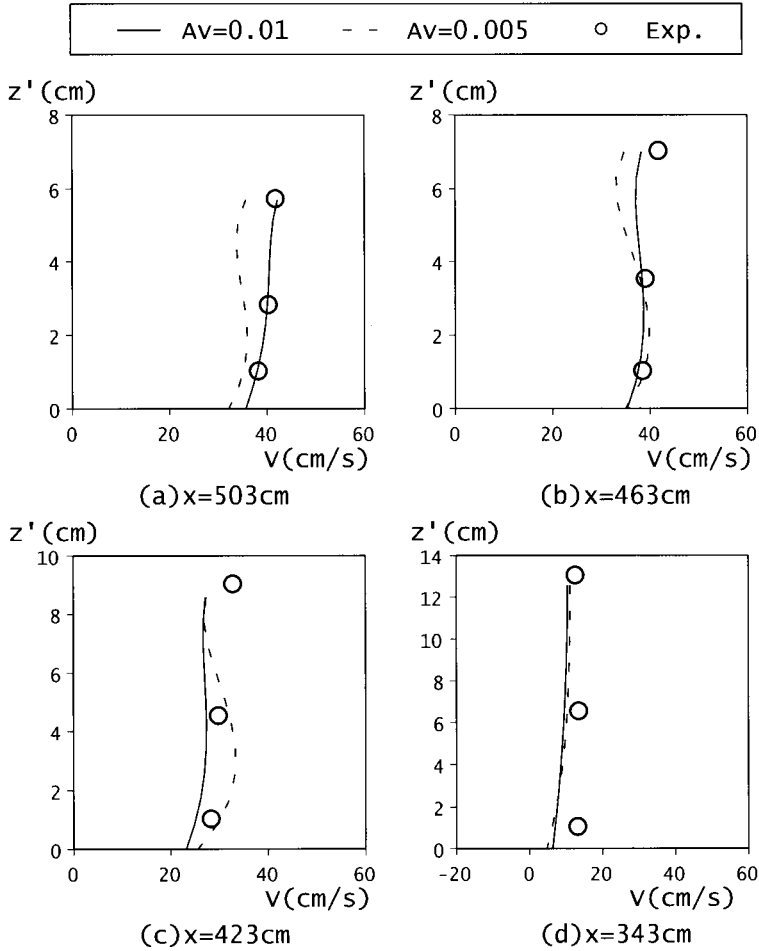
Figure 23. Comparison of experimental results with those of computation with respect to vertical distributions of longshore current velocities.

show the experimental results for the cross-shore distributions of the mean water levels and the depth-integrated longshore current velocity. In addition, solid and dotted lines in these figures show the results computed by the 2-D horizontal numerical model for $C_f = 0.003$ and 0.01. The other parameters: $A_s = 1.0$ and $A_v = 0.01$. It is found that C_f does not affect the mean water level, but the longshore current velocities are greatly influenced by the values of C_f. Figs. 21a and b show the computed cross-shore distributions of the mean water level and the longshore current velocity obtained by putting $A_v = 0.01$, $C_f = 0.01$ and varying with $A_s = 0$, 1.0 and 2.0. The results indicate that the mean water levels and longshore current velocities increase with the increasing A_s. On the other hand, the effect of the eddy viscosity parameter A_v, on the mean water level and longshore current velocity is only somewhat significant. It is found from the above computation that the shear stresses caused by breaking waves at the free surface influence the elevation of mean water level,

Figure 24. Numerical results for velocity vectors of longshore current at mean water level and near bottom (C_f = 0.005 and $\tau_s \neq 0$).

and that the friction factor at bottom C_f influences the cross-shore distributions of longshore current velocity but not mean water level.

Figs. 22a and b compare mean water levels calculated by the quasi 3-D model with those experimentally determined by Visser (1991). The following parameters have been used: $C_f = 0.005$, $A_v = 0.01$ and $A_s = 0$ in Fig. 22a, and $A_s = 1.5$ in Fig. 22b. Fig. 22c presents computed and measured depth-integrated velocities of longshore current. In this figure, the solid and dotted lines correspond to Figs. 22b and a, respectively. From these figures, it is found that the computed value of mean water surface level agrees with the experimental result in the case of $A_s = 0$, but the computed result of longshore current velocities is underestimated. On the other hand, the computed result of mean water level is overestimated in the case of $A_s = 1.5$, but the computed result of longshore current velocities agrees with the experimental one.

Fig. 23 shows that the vertical distributions of longshore current velocities under the conditions of $A_s = 1.5$ and $A_v = 0.01$ are compared with experimental results and in this figure, the computed results in the case of $A_v = 0.005$ are also shown by dotted lines. It is indicated that the results in the case of $A_v = 0.01$ agree well with those of experiments.

Figs. 24a and b show the computed velocity vectors of longshore current at the mean water surface level and near the bottom, respectively. In these figures, it is clear that the directions of currents at the mean water surface level are shoreward and seaward near the bottom, and so the longshore currents have a spiral profile in the vertical direction.

122

50cm/s

50cm/s

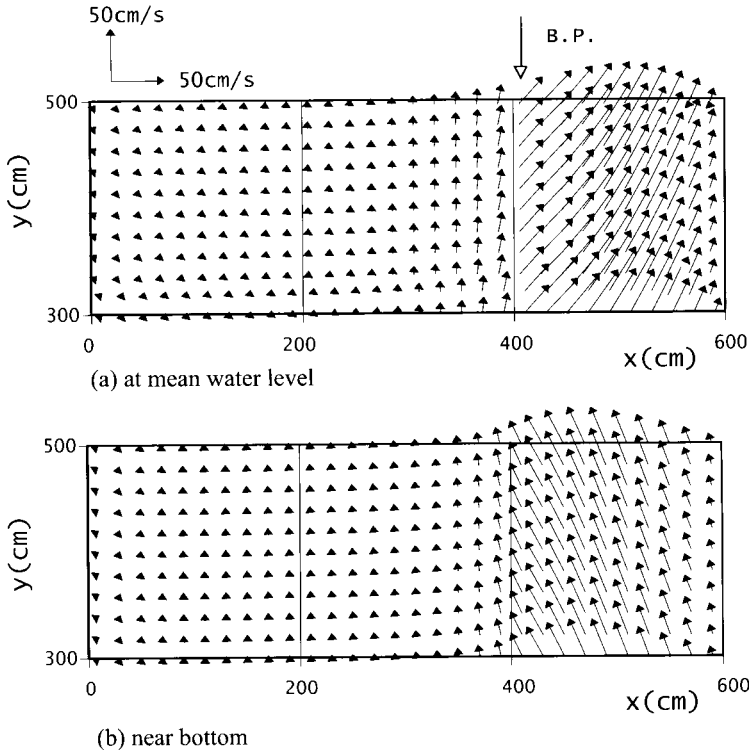B.P.

(a) at mean water level
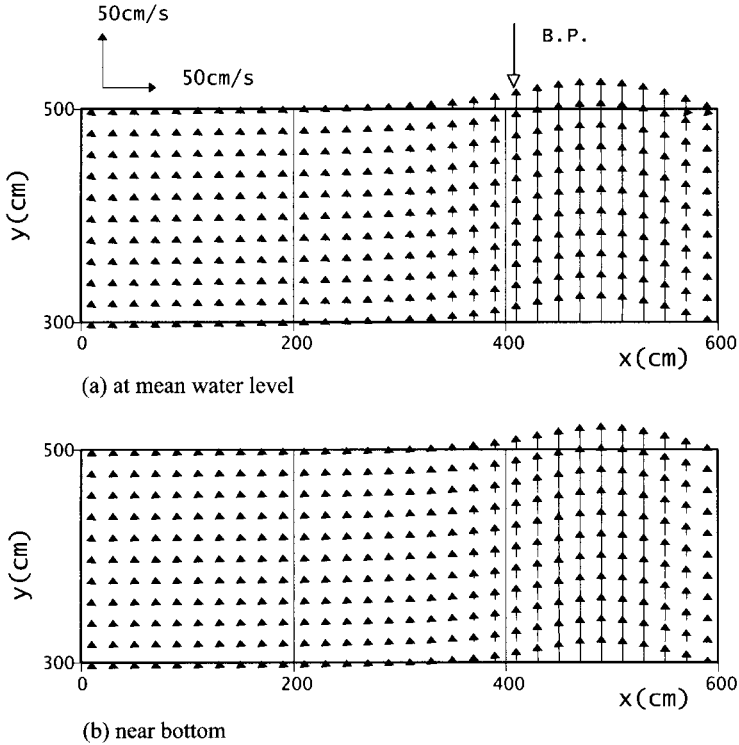
(b) near bottom

Figure 25. Numerical results for velocity vectors of longshore currents at mean water level (a) and near bottom (b) ($C_f = 0.05$ and $\tau_s = 0$).

Figs. 25a and b show the same results for velocity vectors of longshore currents computed for $\tau_s = 0$. These figures indicate that both directions of longshore currents are almost the same and longshore currents have no spiral profile in the vertical direction.

From the results mentioned above, it is concluded that: (1) two-dimensional circulation flows in the vertical plane may be formed by giving the shear stresses at the mean water level, caused by the surface roller, (2) it is found that the vertical distribution of current velocity and the cross-shore distribution of the mean water surface level are not affected by varying the parameter C_f ($= 0.005$ to 0.01), and (3) from experimental results, the vertical distributions of current velocity are the best fit in the case of $C_f = 0.01$, $A_v = 0.005$ and $A_s = 1.5$, but the elevations of mean water surface level are overestimated.

10. NEARSHORE CURRENTS AROUND DETACHED BREAKWATER

In order to examine the applicability of the quasi 3-D model to nearshore currents around coastal structures, the numerical computation and experiment have been carried out for the following case of a semi-detached breakwater situated in a wave basin. The wave basin is 12 m long, 5.0 m wide and 0.6 m deep, the beach slope is 1 in 10, the water depth at the toe of beach slope is 0.3 m and the semi-detached breakwater width of 1.0 m is installed normal to the incident waves as shown

Figure 26. Illustration of wave basin.

in Fig. 26. Wave characteristics used in the computation and the experiment are as follows: wave height at water depth 30 cm, $H = 6.9$ cm, wave period $T = 1.0$ sec and plunging breaker type. For the numerical model, the rectangular grid has spatial increments of size $\Delta x = 2.5$ cm in the wave module and $\Delta x = 5.0$ cm in the current module in the x-y plane. The depth is divided into 10 eleme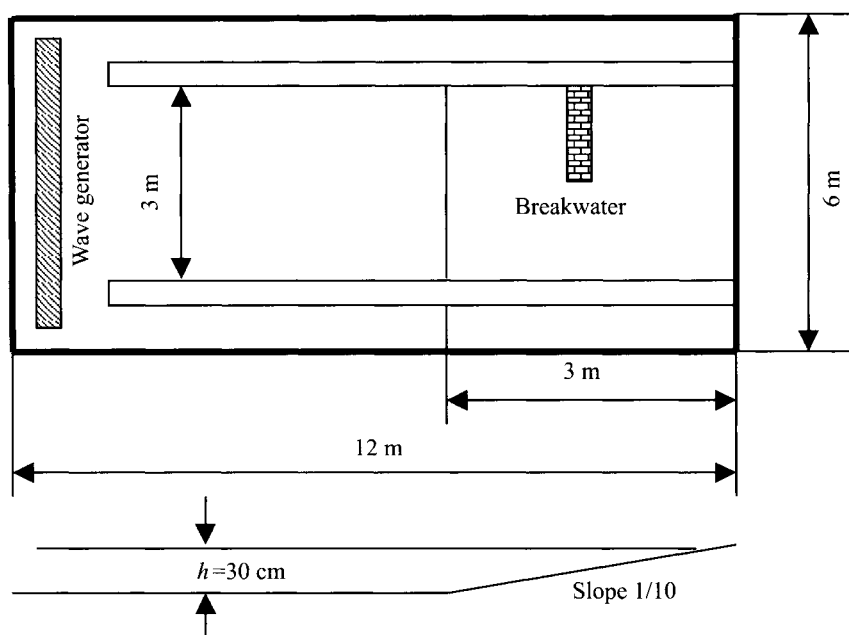nts in the z-axis when applying the finite element method. Fig. 27a shows the calculation domain and the predicted wave height distribution around the detached breakwater, calculated by the mild-slope equation. Fig. 27b shows the experimental result for the distribution of wave height. In Figs. 27a and b, the thick line and the piecewise solid line represent the breaking points which is determined as the ratio of water particle velocity to wave celerity, $u_w/C > 0.45$ and observed by experiment, respectively. In addition, the values indicated in these figures refer to wave height. Fig. 28 shows the comparison predicted wave height with experimental data at $y = 60, 100, 240$ and 280 cm shown in Fig. 27. The predicted cross-shore profile of wave height is in close agreement with the experimental data and those measured, as may be seen in Fig. 28.

Figs. 29a and b show the computed current vectors at the mean water surface level and those at the bottom, respectively. In both figures, it is found that the magnitudes and directions of current vectors at the mean water surface level are different from those at the bottom. Undertow velocities in the surf zone can be reproduced in the opening of the detached breakwater and the spiral profiles can also be reproduced in the surf zone. Figs. 30a and b show the current vectors behind the detached breakwater measured at 2 cm above the bottom and 5 cm under the mean water surface, respectively. In these figures, the solid line shows breaking points. It is found that the circulation flows are generated behind the breakwater but the directions of such flows near the water surface are different from those near the bottom, especially at the corner of the breakwater.

Fig. 31 shows a comparison of the vertical profiles of computed results with those of experiments. In this figure, Notation (a-1), (a-2) and (a-3) correspond to results at the stations $x = 152$ cm, $x =$
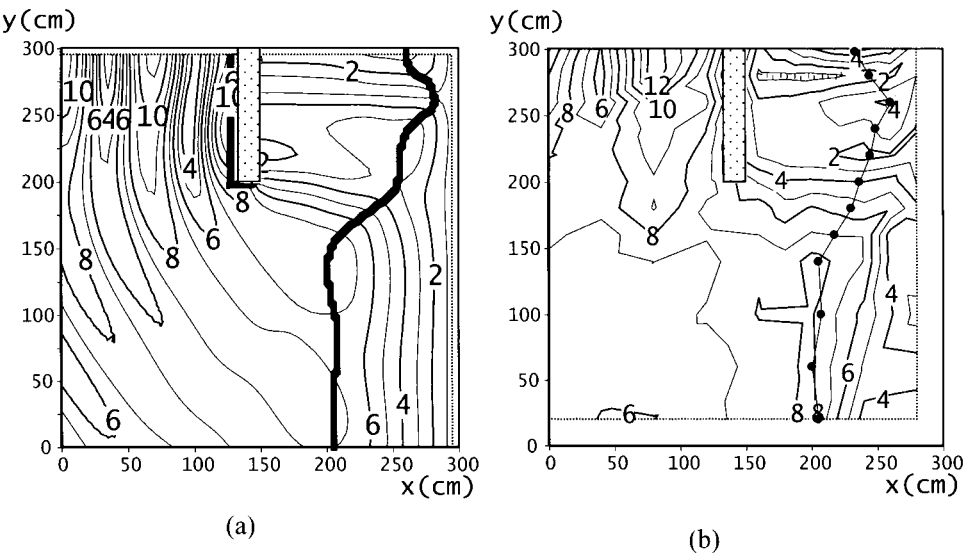
Figure 27. Distribution of wave height around breakwater: (a) computation and (b) experiment. (Unit: cm).
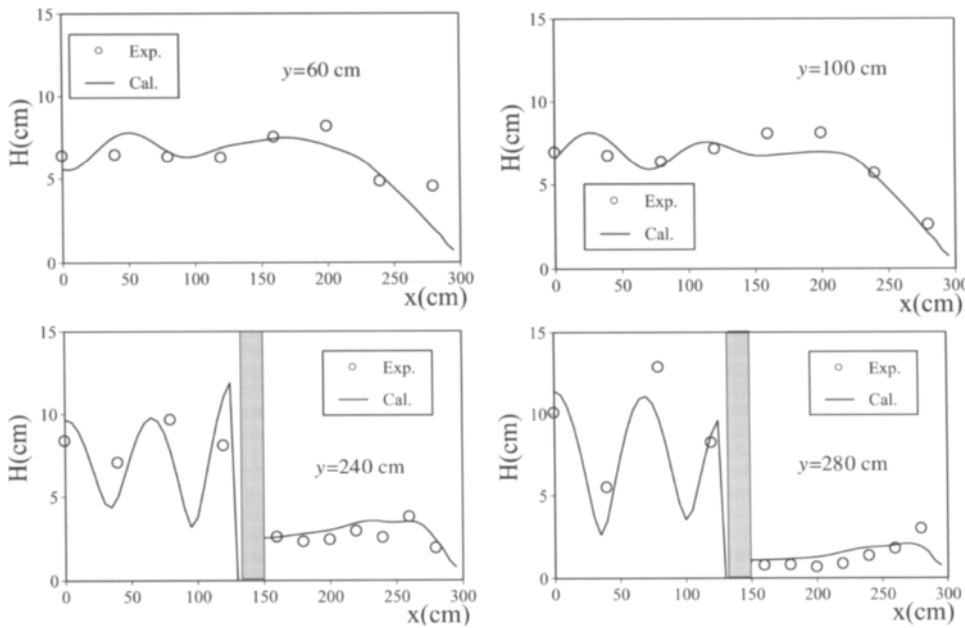
Figure 28. Comparison of wave height distribution between computation and experiment.
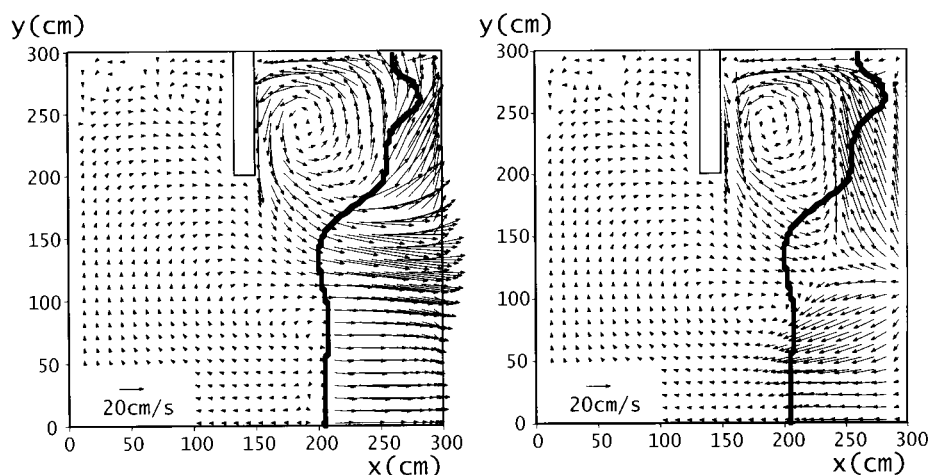
Figure 29. Distributions of current vectors computed: (a) at mean water surface level, and (b) at bottom.
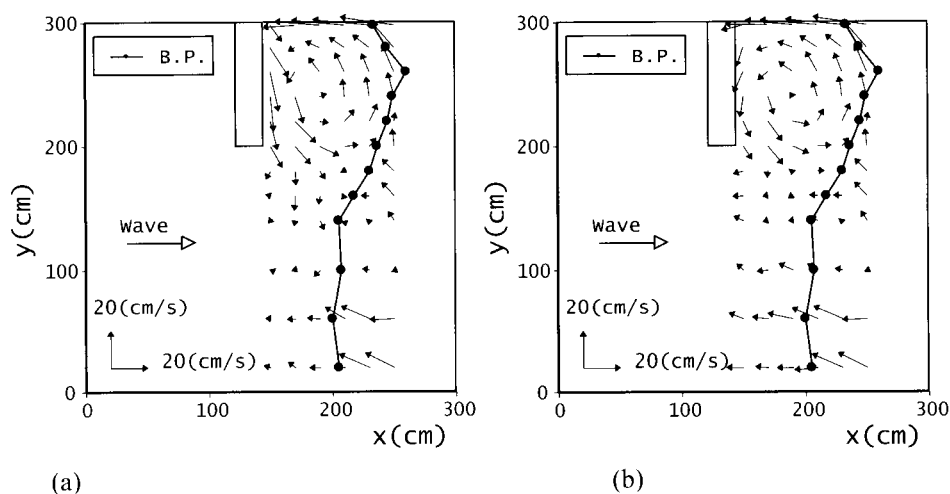
Figure 30. Distributions of current vectors obtained from experiments: (a) at 2 cm above bottom, and (b) at 5 cm under mean water surface.

170 cm and $x = 190$ cm along measured line $y = 200$ cm as shown in Fig. 29a, respectively. In addition, Notation (b-1), (b-2) and (b-3) correspond to the stations $x = 152$ cm, $x = 170$ cm and $x = 190$ cm along the measured line $y = 280$ cm, respectively. The cross-shore current velocity U and the longshore current velocity V are constant over depth at the stations shown in (a-1), (a-2) and (a-3) and the computed results coincide with the measured data. However, the computed cross-shore current velocities U are quite different from those of the experiment at the stations shown in (b-2) and (b-3). Although the numerical method in the vicinity of the breakwater should be improved, it is

126
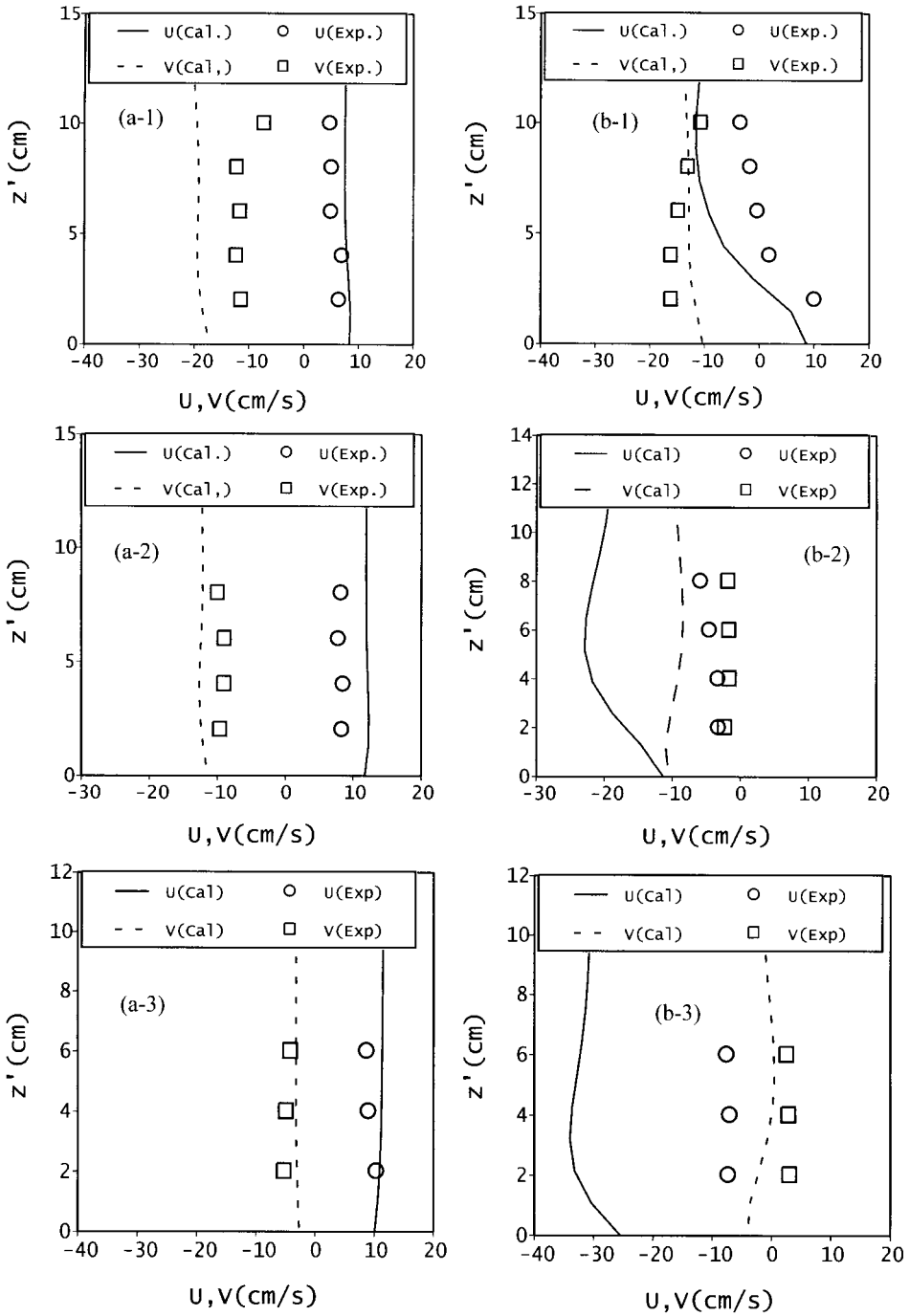
Figure 31. Comparisons of computed results for vertical distributions of nearshore currents behind detached breakwater with those of experiments.

confirmed that the quasi 3-D model could apply to the prediction of nearshore currents around such coastal structures.

11. CONCLUSIONS

A quasi 3-D model for predicting the nearshore current has been developed. The main conclusions are summarized as follows:

1. Owing to the recent studies (see Watanabe and Siozaki, 1982; Watanabe et al., 1983) made in the mathematical formulation of fundamental equations, the wave transformation in any complex coastal environment can be estimated accurately by using their mathematical model.
2. It was found that the predicted undertow profiles were in reasonable agreement with the measured cross-shore current velocities.
3. From the comparison with the measured longshore current, it was found that the shear stresses caused by breaking waves at the free surface influence the elevation of mean water level, and that the friction factor at the bottom influences the cross-shore distributions of longshore current velocity but not the mean water level. The computed longshore current velocity distribution was qualitatively consistent with the measured data.
4. The predicted nearshore current velocities around the detached breakwater show quantitative agreement with measured data. It was found that the circulation pattern behind the detached breakwater obtained by using the proposed model was reproduced with comparative accuracy (see Figs. 29 and 30).

LIST OF SYMBOLS

b	—	subscript that indicates breaking wave
C	—	local wave celerity
C_f	—	friction factor
d_{tr}	—	depth from still water level to trough level of wave
E	—	wave energy
f_D	—	attenuation factor
g	—	acceleration due to gravity
h	—	water depth
H	—	local wave height
H_0	—	deep water wave height
k	—	wave number $2\pi/L$
L	—	local wavelength
L_0	—	deep water wavelength
n	—	ratio of group velocity to wave celerity
p	—	pressure
Q	—	mass flux due to wave
S	—	radiation stress
T	—	wave period
$\tan\beta$	—	bottom slope
u_w	—	horizontal component of water particle velocity in x-axis
v_w	—	horizontal component of water particle velocity in y-axis
w_w	—	vertical component of water particle velocity
U	—	current velocity in x direction

V	—	current velocity in y direction
W	—	current velocity in z direction
U_r	—	Ursell number
ε	—	phase angle
η	—	water surface elevation
ν_h	—	eddy viscosity in horizontal direction
ν_v	—	eddy viscosity in vertical direction
ρ	—	density of fluid
σ	—	wave angular frequency $2\pi/T$
τ_b	—	shear stress at bottom
τ_s	—	shear stress at mean water surface

APPENDIX

$$A_{k,k} = A_{k+1,k+1} = \frac{\ell_k}{3\Delta t} \tag{A--1}$$

$$A_{k,k+1} = A_{k+1,k} = \frac{\ell_k}{6\Delta t} \tag{A--2}$$

$$B_{k,k} = B_{k+1,k+1} = \frac{\ell_k}{6\Delta t} + \frac{\nu_{vk} + \nu_{vk+1}}{2\ell_k} \tag{A--3}$$

$$B_{k,k+1} = B_{k+1,k} = \frac{\ell_k}{6\Delta t} - \frac{\nu_{vk} + \nu_{vk+1}}{2\ell_k} \tag{A--4}$$

$$
\begin{aligned}
a_k =\ & \frac{\ell_k\left(2U_k + U_{k+1}\right)}{6\Delta t} - \frac{\ell_k}{12}\left(3U_k + U_{k+1}\right)\frac{\partial U_k}{\partial x} + \frac{1}{12}\frac{\partial \ell_k}{\partial x}\left(3U_k^2 + 2U_k U_{k+1} + U_{k+1}^2\right) \\
& - \frac{\ell_k}{12}\left(U_k + U_{k+1}\right)\frac{\partial U_{k+1}}{\partial x} - \frac{\ell_k}{12}\left(3V_k + V_{k+1}\right)\frac{\partial U_k}{\partial y} - \frac{\ell_k}{12}\left(V_k + V_{k+1}\right)\frac{\partial U_{k+1}}{\partial y} \\
& + \frac{1}{12}\frac{\partial \ell_k}{\partial y}\left(3U_k V_k + U_k V_{k+1} + U_{k+1}V_k + U_{k+1}V_{k+1}\right) - \frac{1}{6}\left(U_{k+1} - U_k\right)\left(2W_k + W_{k+1}\right)
\end{aligned}
$$

$$
+\nu_h
\begin{bmatrix}
\left(\dfrac{\partial^2 U_k}{\partial x^2} + \dfrac{\partial^2 U_k}{\partial y^2}\right)\dfrac{\ell_k}{3} + \left(\dfrac{\partial^2 U_{k+1}}{\partial x^2} + \dfrac{\partial^2 U_{k+1}}{\partial y^2}\right)\dfrac{\ell_k}{6} \\[2ex]
-\dfrac{1}{3}\left\{\left(2\dfrac{\partial U_k}{\partial x} + \dfrac{\partial U_{k+1}}{\partial x}\right)\dfrac{\partial \ell_k}{\partial x} + \left(2\dfrac{\partial U_k}{\partial y} + \dfrac{\partial U_{k+1}}{\partial y}\right)\dfrac{\partial \ell_k}{\partial y}\right\} \\[2ex]
+\dfrac{2U_k + U_{k+1}}{3\ell_k}\left\{\left(\dfrac{\partial \ell_k}{\partial x}\right)^2 + \left(\dfrac{\partial \ell_k}{\partial y}\right)^2\right\} - \dfrac{2U_k + U_{k+1}}{6}\left(\dfrac{\partial^2 \ell_k}{\partial x^2} + \dfrac{\partial^2 \ell_k}{\partial y^2}\right)
\end{bmatrix}
$$

$$
-\frac{\partial \nu_h}{\partial x}\left[\frac{1}{6}\left(2U_k + U_{k+1}\right)\frac{\partial \ell_k}{\partial x} - \frac{\ell_k}{6}\left(2\frac{\partial U_k}{\partial x} + \frac{\partial U_{k+1}}{\partial x}\right)\right] - \frac{1}{2}\ell_k\left(\frac{\partial R_{xx}}{\partial x} + \frac{\partial R_{xy}}{\partial y} + g\frac{\partial \bar{\eta}}{\partial x}\right)
$$

$$
-\frac{\partial \nu_h}{\partial y}\left[\frac{1}{6}\frac{\partial \ell_k}{\partial y}\left(2U_k + U_{k+1}\right) - \frac{\ell_k}{6}\left(2\frac{\partial U_k}{\partial y} + \frac{\partial U_{k+1}}{\partial y}\right)\right] \tag{A--5}
$$

$$a_{k+1} = \frac{\ell_k \left(U_k + 2U_{k+1}\right)}{6\Delta t} - \frac{\ell_k}{12} \left(U_k + 3U_{k-1}\right) \frac{\partial U_{k+1}}{\partial x} + \frac{1}{12} \frac{\partial \ell_k}{\partial x} \left(U_k^2 + 2U_k U_{k+1} + 3U_{k+1}^2\right)$$

$$- \frac{\ell_k}{12} \frac{\partial U_k}{\partial x} \left(U_k + U_{k+1}\right) - \frac{\ell_k}{12} \left[\left(V_k + V_{k+1}\right) \frac{\partial U_k}{\partial y} + \left(V_k + 3V_{k+1}\right) \frac{\partial U_{k+1}}{\partial y} \right]$$

$$+ \frac{1}{12} \frac{\partial \ell_k}{\partial y} \left(U_k V_k + U_k V_{k+1} + U_{k+1} V_k + 3U_{k+1} V_{k+1}\right)$$

$$- \frac{1}{6} \left(U_{k+1} - U_k\right) \left(W_k + 2W_{k+1}\right) + \nu_h \left[\frac{\ell_k}{6} \left(\frac{\partial^2 U_k}{\partial x^2} + \frac{\partial^2 U_k}{\partial y^2} \right) \right.$$

$$\left. + \frac{\ell_k}{3} \left(\frac{\partial^2 U_{k+1}}{\partial x^2} + \frac{\partial^2 U_{k-1}}{\partial y^2} \right) \right] - \frac{\nu_h}{3} \left[\left(\frac{\partial U_k}{\partial x} + 2\frac{\partial U_{k+1}}{\partial x} \right) \frac{\partial \ell_k}{\partial x} \right.$$

$$\left. + \left(\frac{\partial U_k}{\partial y} + 2\frac{\partial U_{k+1}}{\partial y} \right) \frac{\partial \ell_k}{\partial y} \right] + \frac{\nu_h}{3\ell_k} \left(U_k + 2U_{k+1}\right) \left[\left(\frac{\partial \ell_k}{\partial x} \right)^2 + \left(\frac{\partial \ell_k}{\partial y} \right)^2 \right]$$

$$- \frac{\nu_h}{6} \left(U_k + U_{k+1}\right) \left(\frac{\partial^2 \ell_k}{\partial x^2} + \frac{\partial^2 \ell_k}{\partial y^2} \right) - \frac{1}{6} \left(U_k + 2U_{k+1}\right) \left(\frac{\partial \nu_h}{\partial x} \frac{\partial \ell_k}{\partial x} + \frac{\partial \nu_k}{\partial y} \frac{\partial \ell_k}{\partial y} \right)$$

$$+ \frac{\ell_k}{6} \left[\frac{\partial \nu_h}{\partial x} \left(\frac{\partial U_k}{\partial x} + 2\frac{\partial U_{k+1}}{\partial x} \right) + \frac{\partial \nu_h}{\partial y} \left(\frac{\partial U_k}{\partial y} + 2\frac{\partial U_{k+1}}{\partial y} \right) \right]$$

$$- \frac{\ell_k}{2} \left(\frac{\partial R_{xx}}{\partial x} + \frac{\partial R_{xy}}{\partial y} + g\frac{\partial \overline{\eta}}{\partial x} \right) \tag{A–6}$$

$$b_k = \frac{\ell_k \left(2V_k + V_{k+1}\right)}{6\Delta t} - \frac{\ell_k}{12} \frac{\partial V_k}{\partial y} \left(3V_k + V_{k+1}\right) + \frac{\ell_k}{12} \frac{\partial \ell_k}{\partial y} \left(3V_k^2 + 2V_k V_{k+1} + V_{k+1}^2\right)$$

$$- \frac{\ell_k}{12} \left[\frac{\partial V_{k+1}}{\partial y} \left(V_k + V_{k+1}\right) + \frac{\partial V_k}{\partial x} \left(3U_k + U_{k-1}\right) + \frac{\partial V_{k+1}}{\partial x} \left(U_k + U_{k+1}\right) \right]$$

$$+ \frac{1}{12} \frac{\partial \ell_k}{\partial x} \left(3U_k V_k + U_k V_{k+1} + U_{k+1} V_k + U_{k+1} V_{k+1}\right) - \frac{1}{6} \left(V_{k+1} - V_k\right) \left(2W_k + W_{k+1}\right)$$

$$+ \frac{\nu_h \ell_k}{6} \left[2\left(\frac{\partial^2 V_k}{\partial x^2} + \frac{\partial^2 V_k}{\partial y^2} \right) + \left(\frac{\partial^2 V_{k+1}}{\partial x^2} + \frac{\partial^2 V_{k+1}}{\partial y^2} \right) \right]$$

$$- \frac{\nu_h}{3} \left[\left(2\frac{\partial V_k}{\partial x} + \frac{\partial V_{k+1}}{\partial x} \right) \frac{\partial \ell_k}{\partial x} + \left(2\frac{\partial V_k}{\partial y} + \frac{\partial V_{k+1}}{\partial y} \right) \frac{\partial \ell_k}{\partial y} \right] + \frac{\nu_h}{3\ell_k} \left(2V_k + V_{k+1}\right)$$

$$\left[\left(\frac{\partial \ell_k}{\partial x} \right)^2 + \left(\frac{\partial \ell_k}{\partial y} \right)^2 \right] - \frac{\nu_h}{6} \left(2V_k + V_{k+1}\right) \left(\frac{\partial^2 \ell_k}{\partial x^2} + \frac{\partial^2 \ell_k}{\partial y^2} \right) - \frac{2V_k + V_{k+1}}{6}$$

$$\left(\frac{\partial \ell_k}{\partial x} \frac{\partial \nu_h}{\partial x} + \frac{\partial \ell_k}{\partial y} \frac{\partial \nu_h}{\partial y} \right) + \frac{\ell_k}{6} \left[\left(2\frac{\partial \overline{V}_k}{\partial x} + \frac{\partial \overline{V}_{k+1}}{\partial x} \right) \frac{\partial V_h}{\partial x} + \left(2\frac{\partial \overline{V}_k}{\partial y} + \frac{\partial \overline{V}_{k+1}}{\partial y} \right) \frac{\partial V_h}{\partial y} \right]$$

$$- \frac{\ell_k}{2} \left(\frac{\partial R_{yy}}{\partial y} + \frac{\partial R_{yx}}{\partial x} + g\frac{\partial \overline{\eta}}{\partial y} \right) \tag{A–7}$$

$$b_{k+1} = \frac{\ell_k \left(V_k + 2V_{k+1}\right)}{6\Delta t} - \frac{\ell_k}{12} \left[\frac{\partial V_{k+1}}{\partial y} \left(V_k + 3V_{k+1}\right) + \frac{\partial V_k}{\partial y} \left(V_k + V_{k+1}\right) \right]$$

$$- \frac{\ell_k}{12} \left[\frac{\partial V_k}{\partial x} \left(U_k + U_{k+1}\right) + \frac{\partial V_{k+1}}{\partial x} \left(U_k + 3U_{k+1}\right) \right]$$

$$+ \frac{1}{12} \frac{\partial \ell_k}{\partial y} \left(V_k^2 + 2V_k V_{k+1} + 3V_{k+1}^2 \right)$$

$$+ \frac{1}{12} \frac{\partial \ell_k}{\partial x} \left(U_k V_k + U_k V_{k+1} + U_{k+1} V_k + 3U_{k+1} V_{k+1} \right) - \frac{\left(V_{k+1} - V_k\right)\left(W_k + 2W_{k+1}\right)}{6}$$

$$+ \frac{v_h \ell_k}{6} \left[\left(\frac{\partial^2 V_k}{\partial x^2} + \frac{\partial^2 V_k}{\partial y^2} \right) + 2 \left(\frac{\partial^2 V_{k+1}}{\partial x^2} + \frac{\partial^2 V_{k+1}}{\partial y^2} \right) \right] + \frac{v_h \left(V_k + 2V_{k+1}\right)}{3\ell_k}$$

$$\left[\left(\frac{\partial \ell_k}{\partial x} \right)^2 + \left(\frac{\partial \ell_k}{\partial y} \right)^2 \right] - \frac{v_h}{3} \left[\left(\frac{\partial V_k}{\partial x} + 2\frac{\partial V_{k+1}}{\partial x} \right) \frac{\partial \ell_k}{\partial x} + \left(\frac{\partial V_k}{\partial y} + 2\frac{\partial V_{k+1}}{\partial y} \right) \frac{\partial \ell_k}{\partial y} \right]$$

$$- \frac{v_h \left(V_k + 2V_{k+1}\right)}{6} \left(\frac{\partial^2 \ell_k}{\partial x^2} + \frac{\partial^2 \ell_k}{\partial y^2} \right) - \frac{\left(V_k + 2V_{k+1}\right)}{6} \left(\frac{\partial v_h}{\partial x} \frac{\partial \ell_k}{\partial x} + \frac{\partial v_h}{\partial y} \frac{\partial \ell_k}{\partial y} \right)$$

$$+ \frac{\ell_k}{6} \left[\left(\frac{\partial V_k}{\partial x} + 2\frac{\partial V_{k+1}}{\partial x} \right) \frac{\partial v_h}{\partial x} + \left(\frac{\partial V_k}{\partial y} + 2\frac{\partial V_{k+1}}{\partial y} \right) \frac{\partial v_h}{\partial y} \right]$$

$$- \frac{\ell_k}{2} \left(\frac{\partial R_{yy}}{\partial y} + \frac{\partial R_{yx}}{\partial x} + \frac{\partial \overline{\eta}}{\partial y} \right) \tag{A-8}$$

$$c_k = \frac{\ell_k \left(2U_k + U_{k+1}\right)}{6\Delta t} \tag{A-9}$$

$$c_{k+1} = \frac{\ell_k \left(U_k + 2U_{k+1}\right)}{6\Delta t} \tag{A-10}$$

$$d_k = \frac{\ell_k \left(2V_k + V_{k+1}\right)}{6\Delta t} \tag{A-11}$$

$$d_{k+1} = \frac{\ell_k \left(V_k + 2V_{k+1}\right)}{6\Delta t} \tag{A-12}$$

REFERENCES

Chorin, A.J., 1968. Numerical solution of the Navier Stokes equations. Mathematics of Computation, 22: 745–762.

Dean, R.G., 1968. Breaking wave criteria—A study employing a numerical wave theory. Proceedings of the 11th International Conference on Coastal Engineering, ASCE, pp. 108–123.

Deigaard, R., Fredsoe, J., and Hedgaard, I.B., 1986. Suspended sediment in the surf zone. Journal of Waterway, Port, Coastal and Ocean Engineering, 112 (1): 115–128.

Francisco, J.R., and Arcilla, A.S., 1992. On the vertical distribution of $<\overline{uw}>$. Coastal Engineering, 25: 137–151.

Goda, Y., 1970. A synthesis of breaker indices. Journal of the Japan Society of Civil Engineers, 180: 39–49.

Goda, Y., 1973. Breaker indices of irregular waves. Report of Research Institute of Port and Harbor, 14 (3): 59–106 (in Japanese).

Hansen, J.B., 1990. Periodic waves in the surf zone: Analysis of experimental data. Coastal Engineering, 14: 19–41.

Horikawa, K., 1978. Coastal Engineering. Tokyo: University of Tokyo Press, pp. 190–191.

Horikawa, K., 1985. Coastal Engineering in Environment. Tokyo: University of Tokyo Press, 582p. (in Japanese)

Kuroiwa, M., 1999. A numerical prediction using quasi-three dimensional nearshore current model and the applicability. Doctoral thesis. Tottori, Japan: Tottori University, 153p. (in Japanese).

Kuroiwa, M., Noda, H., and Hirokawa, H., 1994. Experimental study on undertow and sediment transport in the surf zone. Proceedings of the 41st Conference of Coastal Engineering, JSCE, pp. 146–150 (in Japanese).

Kuroiwa, M., Noda, H., and Matsubara, Y., 1998. Applicability of a quasi three-dimensional numerical model to nearshore currents. Coastal Engineering, 1: 815–827.

Koutitas, C., and O'Connor, B., 1980. Modeling three-dimensional wind-induced flows. Proceedings of the American Society of Civil Engineers (ASCE), Hydraulics Division, 11, pp. 1843–1865.

Longuet-Higgins, M.S., 1970. Longshore currents generated by obliquely incident sea waves, 1, 2. Journal of Geophysical Research, 75 (33): 6778–6801.

Madsen, P. A., and Schäffer, H.A., 1999. A review of Boussinesq equation for gravity waves. In: Lui, P.L-F. (Editor), Advances in Coastal and Ocean Engineering, Chapter 1, Vol. 5, pp. 1–94. Singapore: World Scientific Publishing Co.

Mei, C.C., 1983. The Applied Dynamics of Ocean Waves. New York: John Wiley & Sons, 740p.

Okayasu, A., Hara, K., and Shibayama, T., 1994. Laboratory experiments on three-dimensional nearshore currents and a model with momentum flux by breaking wave. Proceedings of the 24th International Conference on Coastal Engineering, ASCE, pp. 2461–2475.

Okayasu, A., Shibayama, T., and Horikawa, K., 1986. Prediction of two-dimensional currents in the surf zone. Proceedings of the 33rd Conference of Coastal Engineering, JSCE, Vol. 33, pp. 1–5. (in Japanese)

Ostendorf, D.W., and Madsen, O.S., 1979. An analysis of longshore currents and associated sediment transport in the surf zone. MIT Report, Sea Grant, pp. 79–83.

Pechon, P., and Teisson C., 1994. Numerical modeling of three-dimensional wave-driven currents in the surf zone. Proceedings of the 24th International Conference on Coastal Engineering, ASCE, pp. 2503–2512.

Sanchez, A.A., Collado, F., and Rodriguez, A., 1992. Vertical varying velocity field in quasi three-dimensional nearshore circulation. Proceedings of the 23rd International Conference on Coastal Engineering, ASCE, pp. 2811–2824.

Sunamura, T., 1983. Determination of breaker height and depth in the field, Annual Report, Institute of Geoscience, University of Tsukuba, No. 8, pp. 53–54.

Svendsen, I.A., 1984. Mass flux and undertow in a surf zone. Coastal Engineering, 8: 347–363.

Svendsen, I.A., and Lorenz, R.S., 1989. Velocities in combined undertow and longshore currents. Coastal Engineering, 13: 55–79.

Tsuchiya, Y., Yamashita, T., and Uemoto, M., 1986. A model of undertow in the surf zone. Proceedings of the 33rd Conference of Coastal Engineering, JSCE, pp. 31–35 (in Japanese).

Visser, P.J., 1991. Laboratory measurements of uniform longshore currents. Coastal Engineering, 15: 563–593.

Watanabe, A., Hara, A., and Horikawa, K., 1983. Breaking waves in the superimposed wave field. Proceedings of the 30th Conference of Coastal Engineering, JSCE, Vol. 30, pp. 5–9 (in Japanese).

Watanabe, A., Hara, A., and Horikawa, A., 1984. Breaking waves under combined refraction and diffraction. Proceedings of the 30th Conference of Coastal Engineering, JSCE, Vol. 30, pp. 5–9 (in Japanese).

Watanabe, A., and Siozaki, M., 1982. Waves and nearshore currents around the coastal structure. Proceedings of the 29th Conference of Coastal Engineering, JSCE, Vol. 29, pp. 110–114. (in Japanese).

Yoo, D., O'Connor, B.A., and McDowell, D.M., 1988. Mathematical modelling of wave climate for port design. Proceedings, Institution of Civil Engineers, Part 1, Vol. 86, pp. 513–530.

Chapter 5

Spectral Wave Models in Coastal Areas

Jaak Monbaliu

Hydraulics Laboratory, Katholieke Universiteit Leuven, Kasteelpark Arenberg 40, B-3001 Heverlee, Belgium

1. INTRODUCTION

The main use of spectral wave models has been and still is the operational use for global and regional wave forecasts. A world-wide overview of operational spectral wave modeling is outside the scope of this chapter. The scope of the chapter is outlined in Section 1.4. Essentially, the chapter presents a comprehensive review of the present state-of-the-art in spectral wave modeling in coastal environments.

1.1. Phase-Averaged Models

Battjes (1994) considers two families of shallow water wave models. They are phase-resolving (for rapidly varying waves, i.e., waves that have phase-averaged local properties which vary rapidly within distances of the order of one wavelength), and phase-averaged models (for slowly varying waves). A phase-averaged or spectral wave model describes the evolution of the wave energy spectrum (i.e., a superposition of sinusoidal waves of different frequencies with random phase and traveling in different directions). The statistical description assumes stationarity and homogeneity of the wave field at the model mesh size scale. These assumptions break down when the scales of the relevant processes become the same length and period of the characteristic waves. In most cases the assumption of phase randomness is a good approximation for the description of wind generated waves. It is known that the spectral wave energy distribution contains sufficient information to determine the most important parameters of the wave field. Phase-resolving models describe the sea surface as a function of time but are computationally very demanding because these models reconstruct the sea surface elevation in space and time. To this end they need space and time scales which are only a fraction of the wavelengths and periods considered. Although they implicitly account for shallow water effects and nonlinear interactions between different wave components, they should be used only when strictly needed. Only the mathematical description of strong diffraction and possibly of triad interaction requires phase-resolving models such as mild-slope equation or Boussinesq models. It is most economical to compute the energy spectrum (a phase-averaged quantity). With a phase-averaged model the exact location of the sea surface is not known in the strict sense, but it is in a statistical sense.

1.2. History

Khandekar (1989) gives an excellent overview of spectral wave models up to, and partially including the development of third generation wave models. The first generation discrete spectral wave models included energy propagation, wind input (S_{in}) and dissipation (S_{ds}). S_{in} and S_{ds} were tuned to observed fetch and duration limited characteristics.

The JONSWAP experiment (Hasselmann et al., 1973) clearly illustrated the rapid growth of wave energy on the forward (low frequency) face of the spectrum. This feature together with the observa-

tion of the so-called 'overshoot' effect could be explained by nonlinear wave-wave interactions. This led to the development of second and third generation spectral wave models.

Second generation models limit the computational effort. In the 'coupled hybrid' models, the wind-sea is described by a limited number of parameters. Swell is propagated independently along rays. In the 'coupled discrete' models both the swell and the wind-sea peak are represented at discrete frequencies. The tail beyond the peak is treated parametrically. The nonlinear interactions, which control strongly the wind-sea evolution, are parameterized in both types of models. A mechanism is built in to transfer energy between wind-sea and swell after every integration time step. These models are still very much in use today; for example, U.K. Met Office (UKMO) and Météo-France among others use them as their operational global model.

Third generation wave models solve the wave transport equation explicitly without any a priori assumption on the shape of the wave energy spectrum. The breakthrough was the fact that the nonlinear interactions could be calculated explicitly by approximating the total integral by a limited number of interaction configurations. Hasselmann and Hasselmann (1985) and Hasselmann et al. (1985) found that the exact nonlinear transfer could be represented reasonably well by considering just one mirror-image pair of interaction configurations. Although the calculation of the nonlinear transfer still was computationally expensive, it was no longer prohibitive. The method is known as the Discrete Interaction Approximation (DIA), and is still the most widely used method in third generation wave models.

The WAM-model can be seen as a standard for this type of model (WAMDI, 1988). A detailed description of the WAM-Cycle 4 model (hereafter referred to as WAM-C4) can be found in Günther et al. (1992) and Komen et al. (1994). The WAM-model is a state-of-the-art third generation spectral wave model specifically designed for global and shelf sea applications. It can be run in deep or shallow water and includes depth and current refraction (steady depth and current field only). It can be set up for any local or global grid with a prescribed data set, and grids may be nested for fine scale applications. The model is used in many operational centers in the world (for example, at the European Centre for Medium Range Weather Forecasts, (ECMWF)). Examples of other third generation models are Tolman's WAVEWATCH (Tolman, 1999), the SWAN model developed at Technical University Delft (Booij et al., 1999; Ris et al., 1999) and the TOMAWAC-model (Benoit et al., 1996). It should be noted that the SWAN model was developed specifically for coastal applications.

1.3. The Use of Spectral Wave Models

Discussions on operational spectral wave modeling can be found in several studies. Bidlot and Holt (1999) recently described the current practice of operational wave forecasting at ECMWF at Reading and at UKMO at Bracknell, supplemented with some information of the operations at Météo-France (J.-M. Lefèvre, personal communications, 2001). Other centers use similar model set-ups, of course, adjusted to the needs of the possible clients. The UKMO model is a second generation model (as is the model of Météo-France) with 13 frequency components between 0.04 and 0.324 Hz and 16 directional components. UKMO, Météo-France and ECMWF run wave models globally and regionally. UKMO runs a wave model globally on a regular lat-lon grid with a resolution of 1.25° in longitude and 0.833° in latitude and a wave model regionally. It covers the European continental shelf including the Mediterranean and Black Sea at a resolution of 0.4° in longitude and 0.25° in latitude. Météo-France runs a global wave model on a regular lat-lon grid with a resolution of 1° in longitude and 1° in latitude, and a regional one covering the European continental shelf and including the Mediterranean and Black Sea at a resolution of 0.25° in latitude and 0.25° in longitude. A high resolution model (0.1°) driven by the ALADIN model winds with similar resolution was to be implemented in 2001 over a domain covering the French continental shelf. ECMWF runs the WAM model globally on an irregular lat-lon grid with an effective resolution of 55 km and regionally for the entire North Atlantic, the North Sea, the Baltic Sea, the Mediterranean and Black Sea with an effective resolution

of 27 km. Since the 20th of November, 2000 they use 30 frequencies between 0.035 and 0.55 Hz and 24 directions (Bidlot, personal communication).

Bidlot and Holt (1999) indicate that the performance of operational wave models has improved over the last decade. Errors can be attributed to internal wave model errors (incomplete knowledge and/or representation of source terms, inaccurate numerics, etc.) and to external errors related to wind field inaccuracies. Especially in forecasting, errors in predicted wind fields soon dominate the other error sources (internal errors).

Engineers are also making more and more use of spectral wave models for coastal applications. Compared to global or regional applications, obviously a much better spatial resolution is needed in order to capture the details of the coastal bathymetry. Spectral wave models have been run in coastal areas with a spatial resolution of 100 m and have even been used to simulate laboratory experiments where a spatial resolution of 0.5 m was used (Ris, 1997). It should also be noted that spectral wave models in coastal areas are very often run in stationary mode, assuming no time variation in the domain considered. In particular for wave climate studies, spectral models are increasingly being used as a tool to transfer offshore wave information (local buoy measurements, remote sensing, regional model output or a combination of these) to a nearshore location (see for example the EC-project EUROWAVES, Barstow et al., 2000).

1.4. Scope

In what follows, the general equations of wave action conservation will be outlined. The different source terms that drive the model will be explained in more detail. It will become clear that our knowledge of these source terms remains incomplete.

The more practical side of the implementation of the equations will be illustrated using the WAM-model code as an example, but some differences between the SWAN and WAVEWATCH models will be pointed out. Note however that some modifications of the 'original' WAM-C4 code were necessary to make it run economically in coastal areas. These changes have been brought together in the EC-project PROMISE (PRe-Operational Modelling In the Seas of Europe, see Prandle, 2000). They have been described in detail in Monbaliu et al. (2000) with regard to the shallow water aspects, and in Ozer et al. (2000) with regard to the dynamic coupling with a surge model. This version of the WAM-model will hereafter be referred to as the WAM-PRO model.

The use of a spectral wave model will be illustrated by two examples in the southern North Sea area. Emphasis will be on the interaction of tide and surge with waves and on the importance of using directional information as input to a coastal wave model.

Finally, an outlook toward expected developments will be given.

2. A SPECTRAL WAVE MODEL

2.1. General Equation: The Action Balance Equation

In the general case incorporating the presence of currents, the equation to be solved is the action balance equation. Following Battjes (1994)

$$\frac{dN}{dt} = \frac{\partial N}{\partial t} + \dot{x}_\alpha \frac{\partial N}{\partial x_\alpha} + \dot{k}_\alpha \frac{\partial N}{\partial k_\alpha} = \sum_i \frac{S_i}{\sigma} \tag{1}$$

where

$$\sigma = \sqrt{gk \tanh kh} = \omega - \vec{k}_\alpha \cdot \vec{U}_\alpha \tag{2}$$

σ is the intrinsic frequency, ω is the absolute frequency, $\vec{k}_\alpha = (k_1, k_2)$ is the wave number vector, k is the modulus of the wave number, $\alpha = 1$ or 2 indicate the vector components

$$\dot{x}_\alpha = c_{g\alpha} + U_\alpha = \frac{\partial \sigma}{\partial k_\alpha} + U_\alpha \tag{3}$$

$$\dot{k}_\alpha = \frac{\partial k_\alpha}{\partial t} + \dot{x}_\beta \frac{\partial k_\alpha}{\partial x_\beta} = -\frac{\partial \sigma}{\partial h} \frac{\partial h}{\partial x_\alpha} - k_\beta \frac{\partial U_\beta}{\partial x_\alpha} \tag{4}$$

$$N(\vec{k}, \vec{x}, t) = E(\vec{k}, \vec{x}, t)/\sigma \tag{5}$$

where E is the energy density and N is called the action density, c_g is the wave group velocity; the geographical co-ordinates are given by $\vec{x}$ $(= (x_1, x_2))$, the dot terms indicate time derivatives (i.e., propagation velocities in geographical and spectral space), U $(= (u_1, u_2))$ is the horizontal current velocity; the right-hand side represents the source terms (see Section 2.2 and Section 2.3).

2.2. Implementation in a Spectral Wave Model

Most measurements of the wave spectrum are in terms of frequency or frequency-direction. Although model codes in k-space exist and have been applied successfully in coastal areas (Schneggenburger et al., 2000), formulations in terms of the energy balance or action density balance in terms of frequency and direction are most common.

Writing the action density equation (1) in terms of absolute frequency and direction, then the rate of change of action density for irregular waves is given by (here in Cartesian coordinates for simplicity)

$$\frac{dN}{dt} = \frac{\partial N}{\partial t} + \frac{\partial}{\partial x_1}(\dot{x}_1 N) + \frac{\partial}{\partial x_2}(\dot{x}_2 N) + \frac{\partial}{\partial \omega}(\dot{\omega}N) + \frac{\partial}{\partial \theta}(\dot{\theta}N) = \sum_i \frac{S_i}{\sigma} \tag{6}$$

where $N(t, x, y, \omega, \theta)$ is the action density spectrum, t is the time, ω is the absolute frequency, θ is the wave propagation direction measured clockwise from the true north, $\dot{x}_1$ and $\dot{x}_2$ are the propagation velocities in the geographical space, and $\dot{\omega}$ and $\dot{\theta}$ are the propagation velocities in the spectral space (frequency and directional space). In simple words equation (6) says that the total change of action density in the water column is due to the source terms applied. The total change in turn can be written as the sum of local change and advection in geographical and spectral space (frequency and angle, or wave number). In the case that currents do not play a role, the action density can be replaced by the energy density.

The absolute or angular frequency ω in a fixed reference frame is given by the dispersion relation in equation (2), which includes the water depth h and the current vector U_α. The propagation velocity in frequency space is given by (Tolman, 1990)

$$c_\omega = \dot{\omega} = \frac{\partial \omega}{\partial t} + \dot{x}_\alpha \frac{\partial \omega}{\partial x_\alpha} = \frac{\partial \sigma}{\partial h} \frac{\partial h}{\partial t} + k_\alpha \frac{\partial U_\alpha}{\partial t} \tag{7}$$

Formulation (6) has the advantage that the absolute frequency is conserved for stationary currents and water depths, i.e.,

$$\frac{d}{dt}(\omega) = 0 = \dot{\omega} \tag{8}$$

and consequently the term $\partial/\partial\omega\,(\dot{\omega}N)$ drops out in equation (6). However, one of the problems in solving equation (6) is the computation of the wave number modulus k from the dispersion relation

(equation (2)). In case of strong opposing currents for high frequency waves two solutions exist and the group velocity for certain frequencies becomes zero (wave trapping, see Mei, 1989).

To overcome the problem of strong opposing currents spectral wave models, such as WAM and SWAN, use internally the intrinsic frequency σ as coordinate. Equation (6) remains identical, except that the action density now becomes a function of the intrinsic frequency ($N = N(t, x_1, x_2, \sigma, \theta)$). The advantage of this expression is that the relation between the intrinsic frequency and the wave number modulus is unique and valid for all frequencies.

In SWAN the action density is kept in the transport equation (see Booij et al., 1999). In WAM equation (6) is then multiplied by σ and the partial derivatives with respect to t, x_1, x_2 and θ are exchanged with the multiplication. Together with the definition of the energy density spectrum (equation (5)), the action density equation (6) transforms to the following balance equation for the energy density spectrum (Günther, personal communications).

$$\frac{\partial F}{\partial t} + \frac{\partial}{\partial x}(\dot{x}_1 F) + \frac{\partial}{\partial y}(\dot{x}_2 F) + \sigma \frac{\partial}{\partial \sigma}\left(\dot{\sigma}\frac{F}{\sigma}\right) + \frac{\partial}{\partial \theta}(\dot{\theta} N) = \sum_i S_i \tag{9}$$

where $F = F(t, x_1, x_2, \sigma, \theta)$ is the energy density in function of frequency and direction (F is used instead of E to make a distinction between wave number space and frequency-direction space). The first term on the left-hand side of this equation therefore represents the rate of change of energy density in time. The second and third term represent rectilinear propagation of energy in geographical space (with propagation velocities $\dot{x}_1$, $\dot{x}_2$ respectively). The fourth term represents the effects of shifting of relative frequency due to variation in depths and currents (with propagation velocity $\dot{\sigma}$). The fifth term represents propagation in directional space due to current and/or depth-induced refraction (with propagation velocity $\dot{\theta}$). The terms $\dot{\sigma}$ and $\dot{\theta}$ are given by

$$\dot{\sigma} = \frac{\partial \sigma}{\partial t} + \dot{x}_\alpha \frac{\partial \sigma}{\partial x_\alpha} = \frac{\partial \sigma}{\partial h}\left[\frac{\partial h}{\partial t} + U_\alpha \cdot \nabla h\right] - c_g \alpha k_\alpha \cdot \frac{\partial U_\alpha}{\partial s} \tag{10}$$

$$\dot{\theta} = \frac{d\theta}{dt} = -\frac{1}{k}\left[\frac{\partial \sigma}{\partial h}\frac{\partial h}{\partial m} + k_\alpha \cdot \frac{\partial U_\alpha}{\partial m}\right] \tag{11}$$

where s is the space coordinate in the propagation direction θ, and m is a spatial coordinate perpendicular to s (Tolman, 1990). The right-hand side represents all effects of generation and dissipation of the waves including wind input S_{in}, whitecapping dissipation S_{ds}, nonlinear wave-wave interactions S_{nl}, bottom friction dissipation S_{bf} and in very shallow water depth-induced breaking S_{br}. Section 2.3 gives more details on the formulations of the individual source terms.

Equation (9) takes into account implicitly the interaction of waves with the mean flow through the term

$$\sigma \frac{\partial}{\partial \sigma}\left(\dot{\sigma}\frac{F}{\sigma}\right) = \frac{\partial}{\partial \sigma}(\dot{\sigma}F) - \frac{F}{\sigma}\dot{\sigma} = \frac{\partial}{\partial \sigma}(\dot{\sigma}F) - \frac{F}{\sigma}\left[\frac{\partial \sigma}{\partial t} + (U + c_g) \cdot \nabla \sigma\right] \tag{12}$$

The first term on the right-hand side is the flux of energy in σ space, and the second one, according to Phillips (1957), describes the interaction of the wave energy with the mean flow.

In contrast to the ω term in equation (6) which is already zero for stationary currents, the σ term in equation (9) only drops out if the current speed is zero (and water depth does not change). In this case both intrinsic and absolute frequency are the same. If a current is present, the spectrum has to be transformed from σ to ω frequencies using the Doppler term in equation (2). In the WAM model this transformation is carried out for all outputs.

2.3. Source Term Formulations

2.3.1. Wind Input

Two main mechanisms are considered responsible for the generation of waves by wind. The first mechanism is a resonance mechanism caused by pressure fluctuations moving over the sea surface due to the wind. If the pressure fluctuations and the waves travel together at the right speed, it was shown by Phillips (1957) that energy input to the wave field is possible. The second mechanism is attributed to Miles (1957). It takes into account the disturbance of the air flow due to the presence of the waves. This mechanism has been analyzed by coupling the air and water motion and looking at the stability of the interface.

Although the resonance mechanism of Phillips accounts for the start of wave motion on a still water surface, it is quickly taken over by the feedback mechanism of Miles. This is directly reflected in the description of the source term

$$S_{in}(\sigma, \theta) = A + BF(\sigma, \theta) \tag{13}$$

where A and B are some function of σ and θ as well.

Cavaleri and Rizzoli (1981) give an expression for the A-term representing the Phillips' mechanism. As soon as there is some wave energy in the system, the term is negligible compared to the second term and, for example, in the WAM-model it is not implemented. Different forms of the second term exist. In WAM-Cycle 3 (WAMDI, 1988), the expression of Komen et al. (1984) was used

$$S_{in}(\sigma, \theta) = \max\{0, 0.25 \frac{\rho_a}{\rho_w} (28\beta \frac{u_{*a}}{c} \cos(\theta - \psi) - 1)\}\sigma F(\sigma, \theta) \tag{14}$$

In WAM-Cycle 4, the expression of Janssen (1991) is used

$$S_{in}(\sigma, \theta) = \max\{0, 1.2 \frac{\rho_a}{\rho_w} \left[\frac{u_{*a}}{\kappa c} \cos(\theta - \psi) \right]^2 \mu \ln^4 \mu\}\sigma F(\sigma, \theta) \tag{15}$$

In equations (14) and (15), ρ_a and ρ_w are the density of air and water respectively, c is the wave propagation speed, u_{*a} is the air friction velocity, θ is the wave propagation angle, ψ the angle of the wind, κ is the von Karman constant, and μ is a parameter that depends on the effective roughness of the sea surface, which in turn depends on the sea state through the wave-induced stress. Note that total stress at the sea surface is the sum of the turbulent stress and the wave-induced stress. A good description of the implementation of Janssen's theory can be found in Mastenbroek et al. (1993). In the SWAN-model both options have been implemented (see also the section on whitecapping dissipation).

Young (1999) remarks that the theories (and measurements) for wind input are essentially restricted to deep water situations, and little is known of the effects shallow water has on wind input.

2.3.2. Quadruplets

The concept of the ocean as a superposition of free and independent components is only correct to the first-order. Nonlinear interactions between the different wave components can transfer energy to other wave components. In deep water interactions between four waves (quadruplets) are possible if the following resonance conditions for wave numbers $\vec{k}_i$ and frequencies σ_i are satisfied

$$\begin{aligned} \vec{k}_1 + \vec{k}_2 &= \vec{k}_3 + \vec{k}_4 \\ \sigma_1 + \sigma_2 &= \sigma_3 + \sigma_4 \end{aligned} \tag{16}$$

The end result is a rather complicated integral, the so-called Boltzmann integral, which describes the rate of change of the action density due to resonance. The full integral representing the four-wave interactions is very time consuming to solve, and has therefore only been used as a research

tool (Resio, 1993). Hasselmann and Hasselmann (1985) found that to a large extent, the effect of the quadruplets could be reproduced by taking only a limited number of possible interaction combinations. In fact Hasselmann et al. (1985), reduced the effort to only one set of the possible sets of interaction configurations, reducing the computational effort to such an extent that it could be used in operational models. The method of Hasselmann et al. (1985) is known as the Discrete Interaction Approximation (DIA) and is still the preferred method used in operational third generation spectral models today. For shallow water, they introduced a simple scaling factor.

For more details and an excellent overview of solution techniques the reader is referred to Young (1999). Due to the increased computational power, it is however worth noting that in the last few years quite a bit of research work has been done to reexamine and to improve the DIA-approximation to the quadruplet interaction term. Van Vledder (2001) and Hashimoto and Kawaguchi (2001) describe extensions to the DIA-approach. Van Vledder (2001) indicated that by adding optimally chosen configurations, it should in principle be possible to approach the exact solution as closely as desired. Also in the "Advanced Wave Prediction Program" (www.onr.navy.mil/sci_tech/ocean/info/cd99/advwvprd.htm) of the U.S. Office of Naval Research (ONR) considerable attention is being paid to the subject of nonlinear interactions.

2.3.3. Whitecapping

Hasselmann (1974) investigated the effects of whitecapping on the spectral balance. He showed that under very general conditions interaction processes that are weak in the mean, even if they are strongly nonlinear locally, are quasi-linear with respect to the wave spectrum. He suggested a proportionality coefficient that was a function of the square of the frequency multiplied by a parameter dependent on integral parameters of the spectrum such as the wave steepness. Other theories have been developed (see Young, 1999 for an extensive overview).

Komen et al. (1984) worked on the assumption of Hasselmann (1974) and proposed a dissipation function that allowed the existence of an equilibrium solution of the energy balance equation when waves were fully developed. Using their expression for the wind input term, Komen et al. (1984) obtained

$$S_{ds}(\sigma,\theta) = -C_{ds}\left(\frac{\sigma}{\overline{\sigma}}\right)^n \left(\frac{\overline{\alpha}}{\overline{\alpha}_{PM}}\right)^m \overline{\sigma}\, F(\sigma,\theta) \tag{17}$$

where C_{ds}, m and n are dissipation coefficients (a value of 2 was assigned), $\overline{\sigma}$ is the mean intrinsic frequency and $\overline{\alpha}$ is the integral wave steepness. The subscript PM refers to the value for a theoretical Pierson-Moskowitz-spectrum.

However, when the wind input source term in the WAM-model was changed from the expression of Komen et al. (1984) to the one from Janssen (1991), the whitecapping dissipation source term needed to be reconsidered. In order to obtain a proper energy balance at the high frequency end of the spectrum, the dissipation by whitecapping was extended by adding a k^2 term (Günther et al., 1992) and the expression became

$$S_{ds}(\sigma,\theta) = -C_{ds}\left(\hat{k}^2 E_{tot}\right)^2 \left((1-c_{dx})\frac{k}{\hat{k}} + c_{dx}\left(\frac{k}{\hat{k}}\right)^2\right)\hat{\sigma}\, F(\sigma,\theta) \tag{18}$$

The hat refers to taking the mean weighted by the inverse. C_{ds} and c_{dx} are dissipation coefficients. Note that in order to keep the dependence on wave steepness for the whitecapping source term, it needs to be implemented in terms of wave number for shallow water applications (Weber, 1991) as is done in equation (18).

In other words, the whitecapping dissipation source term is still relatively poorly understood and its form is chosen and tuned (in deep water) in order to obtain a balance of the spectrum. In this

respect it is interesting to note that Tolman (1999) uses the source term package of Tolman and Chalikov (1996) to account for wind input and dissipation through whitecapping. Also, Monbaliu (1992) showed that by tuning selected parameters in wind input and whitecapping dissipation, fetch limited evolution of total energy and peak frequency could be reproduced.

A fundamental problem, however, with the current formulations for whitecapping is that they do not really consider the different dissipation behavior of wind-sea waves and swell waves.

2.3.4. Triads

In shallow water, such as when waves pass over a bar, energy can be transferred from lower to higher frequencies. In contrast to deep water, where at least four waves are needed for interaction, in shallow water nonlinear interactions are also possible between three wave components (triads). The wave characteristics need to satisfy the following conditions (Young, 1999)

$$\vec{k}_1 \pm \vec{k}_2 = \vec{k}_3$$
$$\sigma_1 \pm \sigma_2 = \sigma_3 \tag{19}$$

Difference is made between resonant and non-resonant (also called bound) interactions. For resonant interactions, the third component of the interaction satisfies the dispersion relation (equation (2)). For non-resonant interaction the dispersion relation is not satisfied, but bound harmonics are created. Evidence of triad interactions have been observed and described. Young (1999) gives an overview.

At the moment SWAN is probably the only widely available (public domain) spectral wave model which includes a routine to take into account the effect of three wave-wave interactions. The parameterization of Eldeberky (1996), also known as the lumped triad approximation (LTA), has been implemented (see Booij et al., 1999).

Becq-Girard et al. (1999) described some experiments of wave evolution over a bar with a phase-resolving and two phase-averaged models for triad interaction, one being the LTA approach mentioned above. They concluded that the three approaches were able to reproduce the main features of nonlinear mechanisms affecting a wave field in the nearshore zone. The phase-resolving model gave the most accurate results. It correctly reproduced the nonlinear coupling effect in decreasing water depths due to wave-wave interactions, as well as the harmonic release after a bar. The phase-averaged models gave satisfactory results for the harmonic generation, but did not reproduce the release of harmonics as water depth increased after passing the bar. However, the computational requirements were considerably reduced using phase-averaged models.

2.3.5. Bottom Friction

The general form of the bottom friction dissipation can be written as (Weber, 1991)

$$S_{bf}(\sigma, \theta) = -C \frac{k}{\sinh(2kh)} F(\sigma, \theta) \tag{20}$$

where h is the water depth. The coefficient C will depend on the formulation used and of course on the flow conditions and bottom roughness.

In the WAM-C4 model only the JONSWAP formulation was implemented (Hasselmann et al., 1973). Four additional bottom friction formulations for pure wave conditions have been implemented in WAM-PRO (Monbaliu et al., 2000). They are the formulations of Hasselmann and Collins (1968), Collins (1972), Madsen et al. (1988) and Weber (1991). A detailed discussion on these formulations as well as on the empirical JONSWAP formulation, which is implemented in the standard WAM-C4, can be found in Luo and Monbaliu (1994). An illustration of their use in a practical situation can be found in Young and Gorman (1995) and Luo et al. (1996).

Luo and Monbaliu (1994) pointed out that growth curves and associated asymptotic values for fully developed seas in shallow water can be quite different depending on the friction formulation

and roughness coefficient used. They argued that the analytical expressions for non-dimensional growth curve limits in shallow water that are given in a function of a non-dimensional water depth, $\delta = gh/u_{*a}^2$ (see Young, 1999), should be questioned. The bottom friction plays a major role in the energy balance and therefore the bed roughness or another bed frictional parameter should be involved. This was also demonstrated by Padilla-Hernández and Monbaliu (2001) in an attempt to reproduce the fetch limited growth curves measured in Lake George, Australia (Young and Verhagen, 1996a; 1996b).

Bottom friction formulations accounting for a combined wave-current field have been introduced as well. Several theoretical models for the bottom friction in combined wave-current flows have been developed and advanced our knowledge of wave-current interactions (for example, Grant and Madsen, 1979; Christoffersen and Jonsson, 1985). However, these models were derived for a wave motion corresponding to a single period wave. Only recently Madsen (1994) derived a model for turbulent wave-current bottom boundary layer flows with wave motion described by its directional spectrum. The formulations of Christoffersen and Jonsson (1985) and Madsen (1994) have been implemented in WAM-PRO, but they have not yet been fully tested. An interesting discussion on wave-current interaction observations in the Holderness area is given by Wolf and Prandle (1999) and Wolf (1999).

2.3.6. Depth-Induced Breaking

To simulate depth-induced wave breaking, a source term based on the theory of Battjes-Janssen (1978) is widely used. In this theory it is assumed that depth-induced wave breaking does not affect the shape of the spectrum itself, which has been experimentally verified by Beji and Battjes (1993). This is translated in the following mathematical expression

$$S_{br}(\sigma, \theta) = -\frac{1}{4}\alpha_{br}\,\bar{k}\,Q_b\,H_{\max}^2\,F(\sigma, \theta) \tag{21}$$

where α_{br} is a constant of the order of one, Q_b is the local fraction of breaking waves, $\bar{k}$ is the mean wave number and H_{max} $(= \gamma h)$ is the maximum wave height, which is determined as a fraction γ of the water depth h.

For the practical implementation and interpretation, the reader is referred to Van Vledder et al. (1994) and Booij et al. (1999). The Battjes-Janssen theory is used in SWAN and WAM-PRO. Note that in principle the parameters α_{br} and especially γ are location dependent and should be calibrated.

An interesting study of other model formulations for depth-induced wave breaking has been executed by Becq and Benoit (1996). Next to the Battjes-Janssen model, which they supplemented with a wave breaking persistence parameter (Southgate and Wallace, 1994), they also studied the Thornton and Guza (1983) model, the Izumiya and Horikawa (1984) model, the Roelvink (1993) model, and the Larson (1993) model. Except for the Larson (1993) model, they all have been implemented in the TOMAWAC spectral wave model (Benoit et al., 1996).

2.4. Numerics
2.4.1. Advection

The action balance equation needs to be solved by numerical integration. The numerics for the WAM model are explained in more detail in the 'WAM'-book (Komen et al., 1994; see also WAMDI, 1988). The propagation of the energy density is solved by discretization of the left-hand side, setting the right-hand side equal to zero, into a first-order explicit upwind scheme. The time step for this part is limited by the Courant-Friedrich-Lewy (CFL) stability condition, and may be calculated on either a spherical or a Cartesian grid. Then the source term contribution is added using a semi-implicit forward in time scheme. This combination gives acceptable results for large-scale application (global or coarse grid shelf sea applications), but it is known that swell energy which can travel over a

long distance with a minimal loss of energy is underestimated, and can largely be attributed to the relatively large diffusion in the upwind numerical scheme. On the other hand, the garden sprinkler effect is well-known in spectral wave models that use higher-order schemes, in particular when the spectral resolution ($\Delta\theta$ and Δf) are coarse. Booij and Holthuijsen (1987) have proposed a solution for the problem.

In contrast to WAM, SWAN makes use of an implicit scheme to solve the action balance equation. Booij et al. (1999) provide more details of the scheme that has been implemented for the model. The scheme is unconditionally stable and therefore allows for much larger time steps than would be imposed by the CFL-criterion. Originally the model was designed for coastal applications and the large numerical diffusion introduced by the numerical scheme was not a major problem.

Rogers et al. (1999) have done extensive tests with different numerical schemes in order to come up with an alternative scheme to the one used in the SWAN-model. The scheme they selected requires more computational resources. They state that the advantages of their proposed scheme are best seen in large-scale propagation cases and in cases where the bathymetry is very rugged. Their final conclusion is that for oceanic cases there is an advantage to use the proposed scheme. However, for shelf and coastal scales (except for propagation behind islands) the higher cost of the scheme is not justified.

In summary, the numerics involved are always a compromise between accuracy, ease of implementation and demand of computational resources. Based on the application the need will be different.

2.4.2. Source Term Integration

Although in theory, a third generation model describes all the source terms explicitly, in practice it effectively integrates the spectrum up to a certain cut-off frequency. Beyond this cut-off frequency a parametric tail is attached. Note that the tail depends on the model implementation (Tolman, 1999).

In the standard WAM-C4 the source term equation (equation (1) without the advection terms) is solved by the following finite difference approximation

$$\frac{\Delta_{\text{int}} F_{i,j,k,l}}{\Delta t} = \frac{F_{i,j,k,l}^{n+1} - F_{i,j,k,l}^{n}}{\Delta t} = (1-\alpha)S_{i,j,k,l}^{n} + \alpha S_{i,j,k,l}^{n+1} \tag{22}$$

where i and j denote the position in geographical space, k and l represent the position in the wave direction and relative frequency space and α is in the range [0,1]. The superscript n refers to the time level.

Since the source functions depend nonlinearly on the spectrum F, Taylor expansions were introduced. By disregarding the negligible off-diagonal contribution of the function derivatives (Komen et al., 1994) in the Taylor expansions, the increments in spectral energy density due to the source terms for one time step may be expressed as

$$\Delta_{\text{int}} F_{i,j,k,l}^{n} = \Delta t S_{i,j,k,l}^{n} \left[1 - \Delta t\, \alpha\, \Lambda_{i,j,k,l}^{n} \right]^{-1} \tag{23}$$

where $\Lambda_{i,j,k,l}^{n}$ is the diagonal matrix of the partial derivatives of the source function. A forward time splitting technique is used ($\alpha = 1$) except for positive $\Lambda_{i,j,k,l}^{n}$ where, because of the obvious numerical instability, an explicit technique is used ($\alpha = 0$). However, the explicit implementation is not generally stable, so a limiter on the increments in wave energy is imposed. For further discussion on limiters, see Tolman (1992), and for the specific case of WAM, see Hersbach and Janssen (1999), Hargreaves and Annan (2001) and Monbaliu et al. (2000). Also the SWAN-model imposes a limit on wave growth (see Booij et al., 1999).

In WAM-C4, an additional restriction was built in to make the source term time step smaller than or equal to the advection time step. This restriction was successfully removed in the WAM-PRO

version. Although this modification made it possible to run the model efficiently in coastal areas where high spatial resolution is needed, the time step for source term integration should not be too large in order to be able to respond accurately to changing wave conditions (Monbaliu et al., 2000).

3. EXAMPLE APPLICATIONS

3.1. The Use of Directional Information

Directional information is particularly important in coastal studies. The wave climate close to the coast, the design of harbor protection, the layout of harbor entrance channels, coastal protection measures such as beach-fill or artificial dikes all depend critically on correct directional information. Wave models and/or directional wave measurements can provide, at selected points, full details of the wave energy spectrum.

The following example of an application at the Belgian coast illustrates this clearly. To do the calculations, the SWAN-model (Cycle 2, version 40.01) was implemented for this area and run in stationary mode. The bathymetry in this area is rather complex. The hydrodynamic characteristics of the Southern North Sea and the presence of sandy sediments resulted in the formation of large sandbanks more or less parallel to the coast. Typical length scales are 5 km for the width and 10 km for the length. They extend to within a few meters of the sea surface (Williams et al., 2000).

The 'offshore' boundary condition for the model area is located on a line parallel to the coast and going through the Westhinder (WHI) buoy, a location some 25 km away from the coast (water depth about 30 m). In Fig. 1 the measured directional spectrum (Wavec buoy) is shown at Westhinder. Also shown is the 'representative' spectrum as it would be constructed if only the significant wave height ($H_s = 5.2$ m), the peak period (7.14 s), the wind direction (338.5°) and wind speed (19.3 m/s) were given. On the same figure, the measured directional spectrum at Bol van Heist (BVH), a location some 5 km from the coast with a water depth of about 10 m, is compared to the numerically simulated spectrum. The low frequency peak in the spectrum is completely missed. However, if the full directional spectrum is imposed at the boundary, the agreement between model results and measurement is more reasonable (Fig. 2). Note that there is a small mismatch of the spectrum imposed at the boundary due to fact that SWAN eliminates all energy going out of the domain. Although it seems obvious by itself that the representation of a bimodal spectrum by a significant wave height, a period and a direction cannot describe the full details of the spectrum, it is very often the only information available for wave climate studies. As illustrated here this might lead to an inaccurate determination of the wave climate in the nearshore zone. All consequent studies using this information will be questionable as well.

3.2. Tidal Influence on Wave Characteristics

Next to having a rather complicated bathymetry, the Belgian coastal area is also subjected to considerable tide and surge effects. The tidal range is in the order of 5 m, surge can be up to about 2 m and the order of magnitude of the current speed is about 1 m/s. The area is located at the southern end of the North Sea. The North Sea is an enclosed area on a relatively wide shelf with an average depth of about 75 m.

To investigate the interaction between tide, surge and waves in the Belgian coastal area, Osuna (2002) implemented a fully coupled model system for tide-surge (TS) and waves on a series of nested grids, following the work carried out in the EU-project PROMISE (Ozer et al., 2000). The characteristics of the grids and the model time steps are given in Table 1 and Fig. 3. In Table 2 the locations of a number of buoys are given.
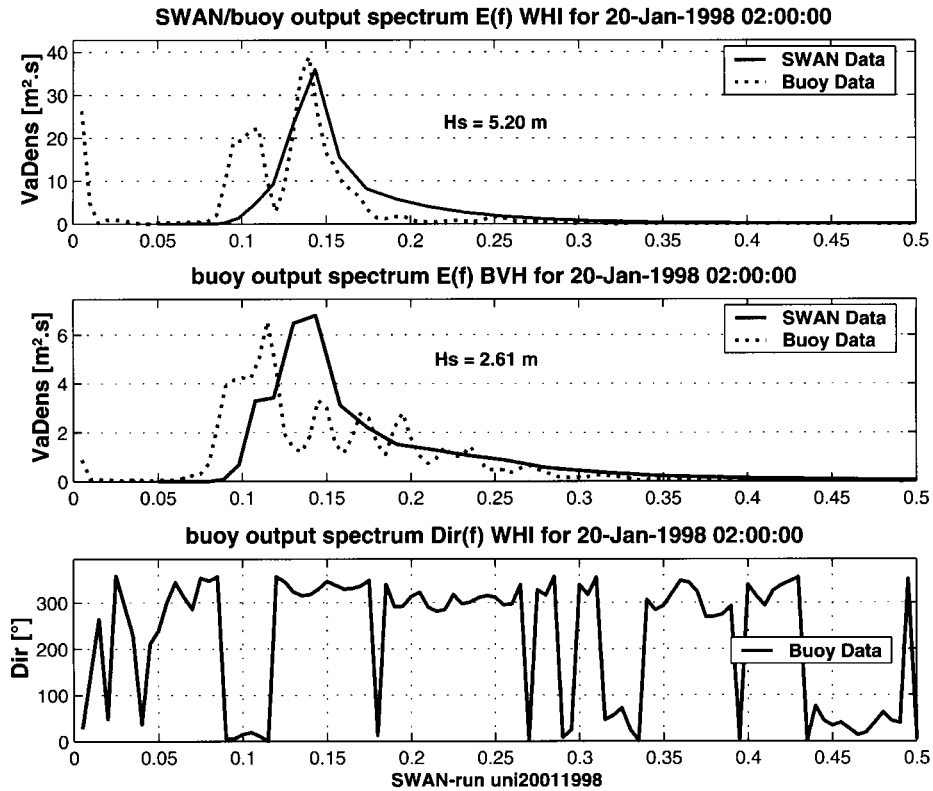
SWAN/buoy output spectrum E(f) WHI for 20-Jan-1998 02:00:00

buoy output spectrum E(f) BVH for 20-Jan-1998 02:00:00

buoy output spectrum Dir(f) WHI for 20-Jan-1998 02:00:00

Figure 1. Measured and simulated representative spectrum offshore (WHI-location) and nearshore (BVH-location).

The tide-surge model is a classical implementation of the depth-averaged shallow water equations. It calculates water elevations and current vectors at the grid points if the surface stress (or wind speed), the pressure (to account for the inverse barometric effect) and the necessary tidal elevations at the boundary of the domain are given (for more details, see Ozer et al., 2000). The tide-surge model was adapted to be forced by surface stresses calculated by the wave model. When running in uncoupled mode the surge model uses a piecewise linear drag-law according to Heaps (1965).

The largest grid extends far north in order to catch the swell waves propagating from the north to the south end of the North Sea. No wave information is provided for the Atlantic boundary. Although this has consequences for the modeled wave characteristics in the northern part of the North Sea, it does not affect the ability to model waves in the southern part of the North Sea. Successive nesting is used (and needed) to avoid large interpolation (and extrapolation) errors, and therefore to provide accurate boundary conditions for the fine grid model (Fig. 4).

Fully-coupled indicates that the model system allows for a dynamic information exchange between the wave model and the tide-surge model. For the wave model this means that it receives at predetermined intervals new values for tide-surge levels (update of the water depths and consequently of all model terms related to water depth) and for current speeds (update of current dependent terms). In fact, almost all terms in equation (9) are affected. For the $\dot{\sigma}$ and $\dot{\theta}$ terms this is directly seen from equations (10) and (11). But also $\dot{x}_1$ and $\dot{x}_2$ are affected through changes in the group
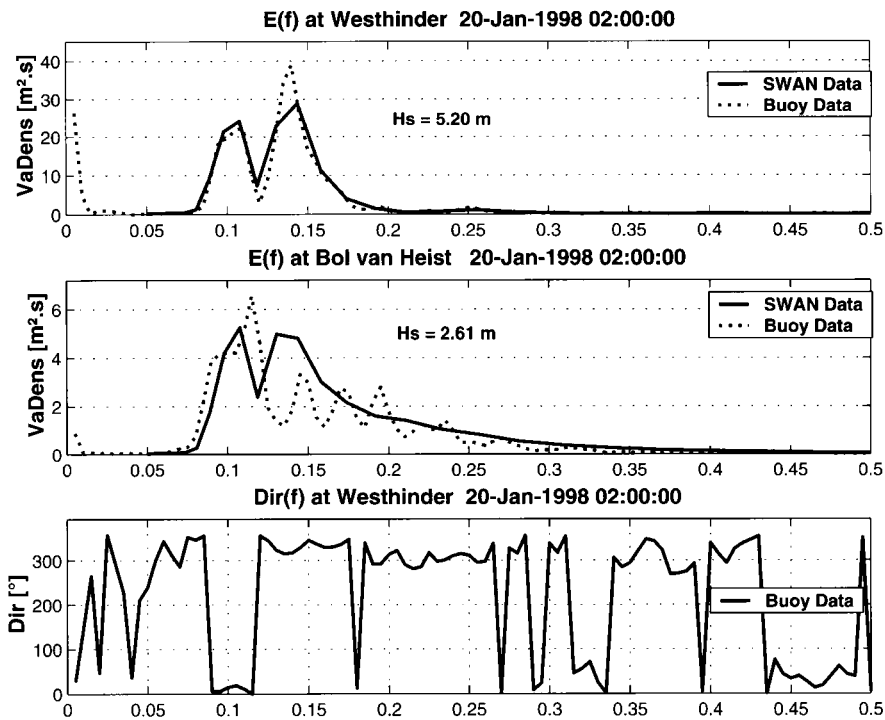
Figure 2. Measured and simulated spectrum offshore (WHI-location) and nearshore (BVH-location).

Table 1
Characteristics of nested grids.

GRID	AREA	RESOLUTION (LAT x LON)	TIME STEP Advection		Source
coarse	47° 50′ N - 70° 10′ N 12° 15′ W - 12° 15′ E	1/3° x 2/3°	WAM TS	10 min 1 min	10 min
nested 1	48° 30′ N - 55° 30′ N 02° 45′ W - 09° 15′ E	1/15° x 1/10°	WAM TS	2 min 1 min	10 min
nested 2	47° 14′ N - 52° 38′ N 00° 03′ W - 04° 45′ E	1/45° x 1/30°	WAM TS	1 min 1 min	10 min
fine	50° 59′ N - 51° 30′ N 02° 27′ W - 03° 53′ E	1/135° x 1/90°	WAM TS	30 sec 15 sec	5 min

Table 2
Buoy locations.

Station	Latitude	Longitude	Approximate depth (in m)
AUK	56° 23′ 59″ N	02° 03′ 56″ E	80
K13	56° 23′ 59″ N	03° 13′ 13″ E	31
WHI	51° 23′ 04″ N	02° 26′ 40″ E	30
BVH	51° 22′ 45″ N	03° 12′ 29″ E	10
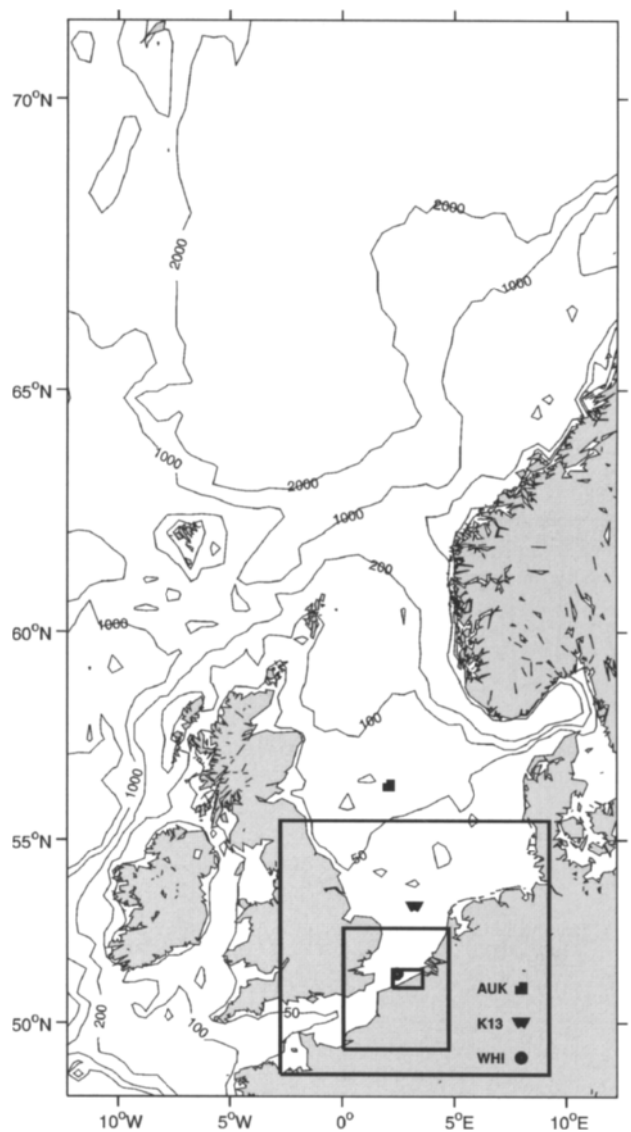
Figure 3. Model area with successive nested grids of the coupled tide-surge and spectral wave model. Buoy locations (AUK, K13 and WHI) are indicated.

velocity C_g and changes in the current speed (equations (3) and (2)). For the surge model this means that it receives at regular intervals updated values of the stress at the sea surface (sea state dependent according to Janssen's theory). Also, the radiation stress can be transferred from the wave model to the surge model. The gradient of the radiation stress (or excess momentum flux) is responsible for wave-induced set-up and wave-driven currents in the nearshore zone (see for example, Dean and Dalrymple, 1991).
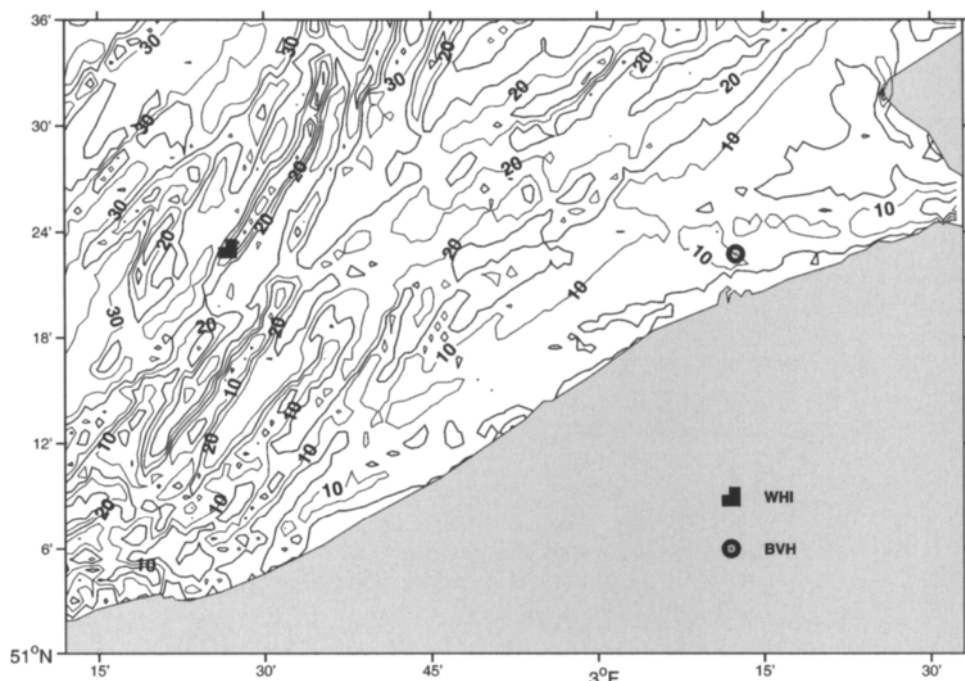
Figure 4. Bathymetry of the Belgian coastal area with indication of the two directional buoy locations (WHI and BVH).

As an illustration simulations were carried out for October 1997. To have some idea about the meteo-conditions, the wind speed and directions at three of the buoy locations are shown in Fig. 5. Note that the wind fields used are 6-hourly winds provided by UKMO (see Ozer et al., 2000, for additional details). Measurements at the WHI location indicate an underestimation of the modeled wind speed for the period considered. However, no attempt has been made to compensate for this. It should, therefore, be expected that modeled wave heights are underestimated.

In Figs. 6 and 7, the results of the coupled and uncoupled coarse grid model system are shown together with the buoy measurements. The calculated wave heights are barely affected by the coupling (Fig. 6). The absolute value of the difference is less than 10 cm at the three stations shown. The influence on the calculated period (here the second moment period Tm_{02} is chosen) is evident in Fig. 7. The modulation is not only visible in the calculations; it is also prominent in the measurements. Although the Doppler effect (equation (2)) is important for the modulation (see below), it is not the only mechanism involved (see also Ozer et al., 2000).

Through the successive nested models it is now also possible to look at the wave evolution in the coastal area. The fine grid results at the locations WHI and BVH are shown in Fig. 8. The tidal modulation mainly due to the Doppler shift in the wave period is clearly visible at WHI where waves and currents are quite often aligned. Nearshore at BVH, some tidal modulation is visible in the calculated wave heights due to the considerable changes in water depth. For given waves and current conditions the angle between wave propagation direction and current direction determines the strength of the tidal modulation in the wave period. For example, little or no modulation is present between October 13 and 15, when the wind was predominantly from the north.
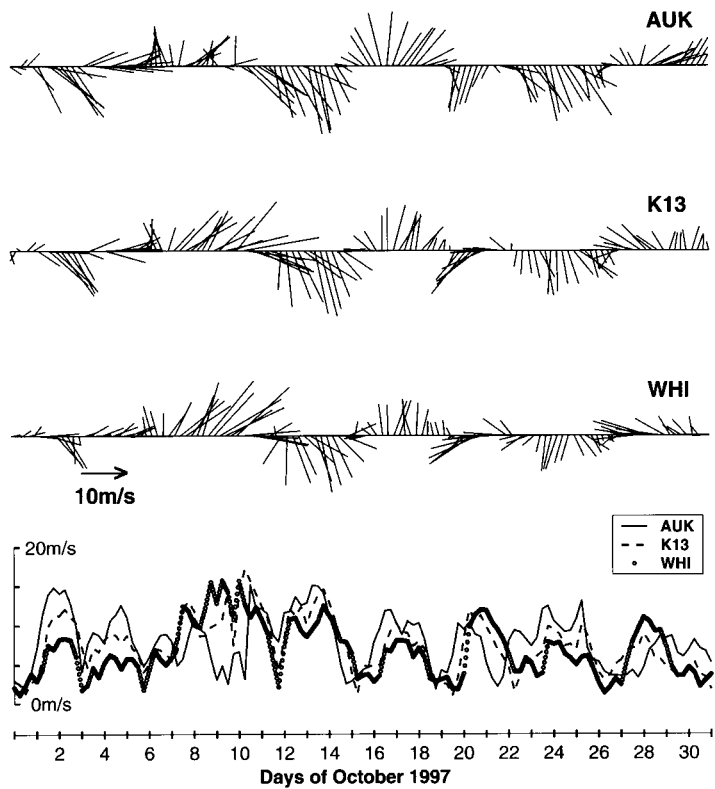
Figure 5. Model wind speed and direction at the three buoy locations shown in Fig. 3.

4. OUTLOOK

Developments will continue in spectral wave modeling. It has become clear that the DIA-approach for calculation of the resonant four-wave interactions is a relatively poor representation of the theoretical source. More accurate, yet efficient algorithms are being developed. Since the nonlinear transfer is crucial in the evolution of the wave energy spectrum, a better representation of this process will improve our understanding of the directional features of this evolution. The other source terms will need to be tuned in order to get a proper energy balance (see Section 2.3). But also the other source terms are under discussion and are being investigated. New insights will find their way to operational models.

Triad wave-wave interactions still need more attention. In particular the inability to release bound harmonics after passing over a bar in the current spectral implementation, limit their use in cases with complicated bathymetry.

Whitecapping dissipation needs to make a distinction between the behavior of wind waves and swell waves. Also the behavior of bottom friction dissipation in wave-current flows needs to be investigated in more detail.

In some cases diffraction is an important process, for example in coastal areas near breakwaters or in seas with many islands. It is expected that at least some parametric formulation of this effect will become available in spectral wave models.
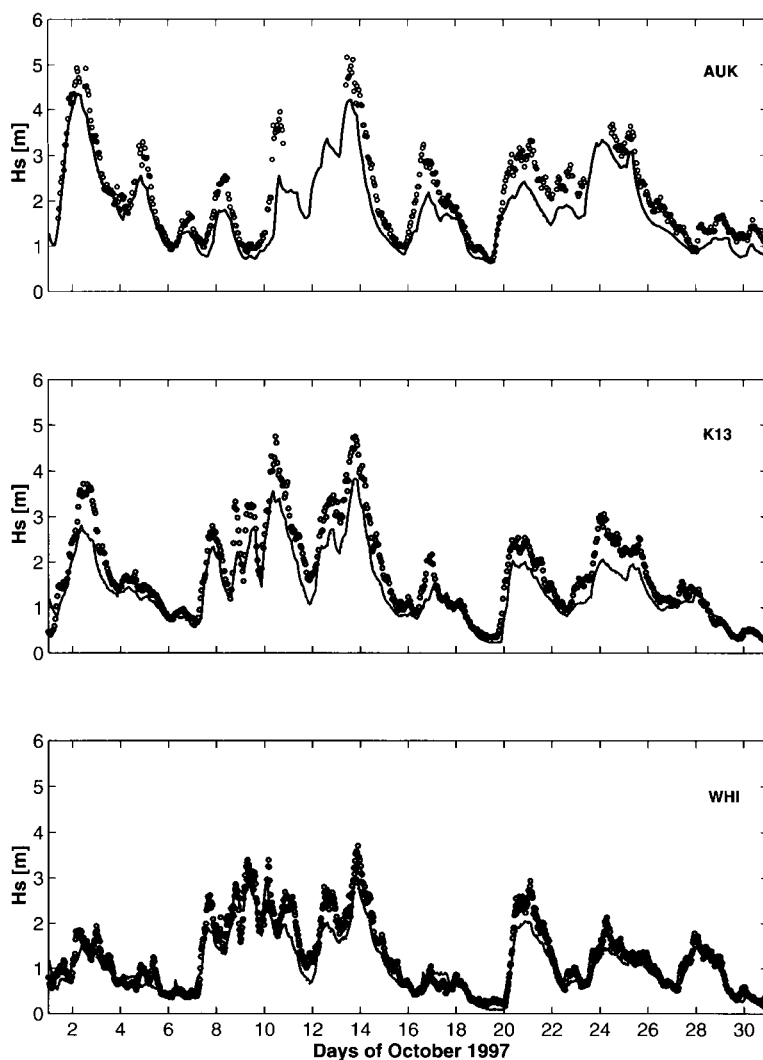
Figure 6. Coarse grid modeled and measured wave height at the three buoy locations shown in Fig. 3: measured (open circles), fully coupled (full line) and uncoupled (dotted line).

The use of parallel computers and, therefore, of a parallel version of a wave model code is common in large operational centers. ECMWF, for example, runs parallel since late 1996 (Bidlot et al., 2000). NCEP (National Center for Environmental Prediction, USA) has replaced their WAM-Cycle4 implementation in early 2000 by the parallel version of the WAVEWATCH-III model (Tolman, 1999). On the other hand personal computers have become so powerful, that coastal engineering consultant companies no longer hesitate to use third generation wave models.

It is obvious that validation of an operational model needs a systematic comparison with observed data for an extended period of time. Operational centers verify the performance of their operational system against measurements (see for example Janssen et al., 1997). For global applications, readily
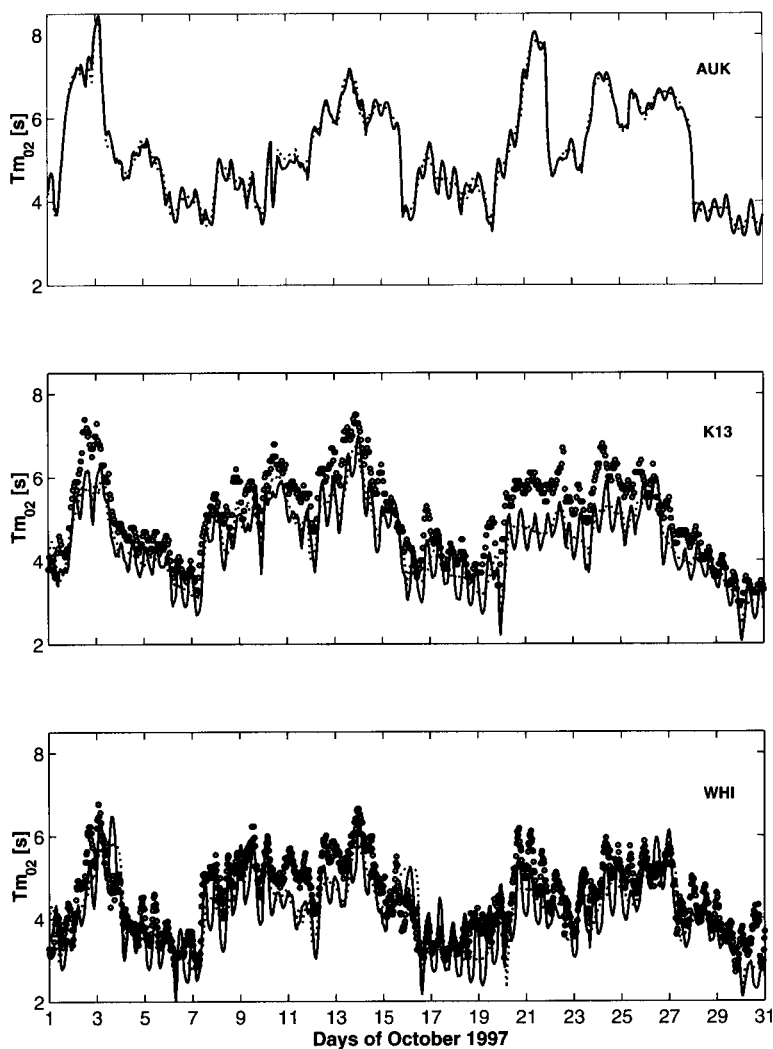
Figure 7. The same as Fig. 6 but for the second moment period.

available and reliable wave measurements from buoys are limited. Even fewer buoys provide directional information. They employ the usual parameters of bias, root mean square (rms) error and scatter index. For comparisons with altimeter data, significant wave height only is used. When buoy data are used in the comparison the peak or mean period is also used. Also scatter plots of observed versus modeled data are produced. These comparisons do not say much about how well the full spectrum is reproduced. For a large number of applications a correct match of all frequencies involved in the wave spectrum is essential. For some engineering applications such as dredging operations or surveying, only knowledge of low frequency swell energy is really important. Operational centers acknowledge this and, therefore, also give the wave parameters in terms of total sea, wind-sea and swell. For other applications such as trying to understand the mechanisms of gas transfer across the air-sea
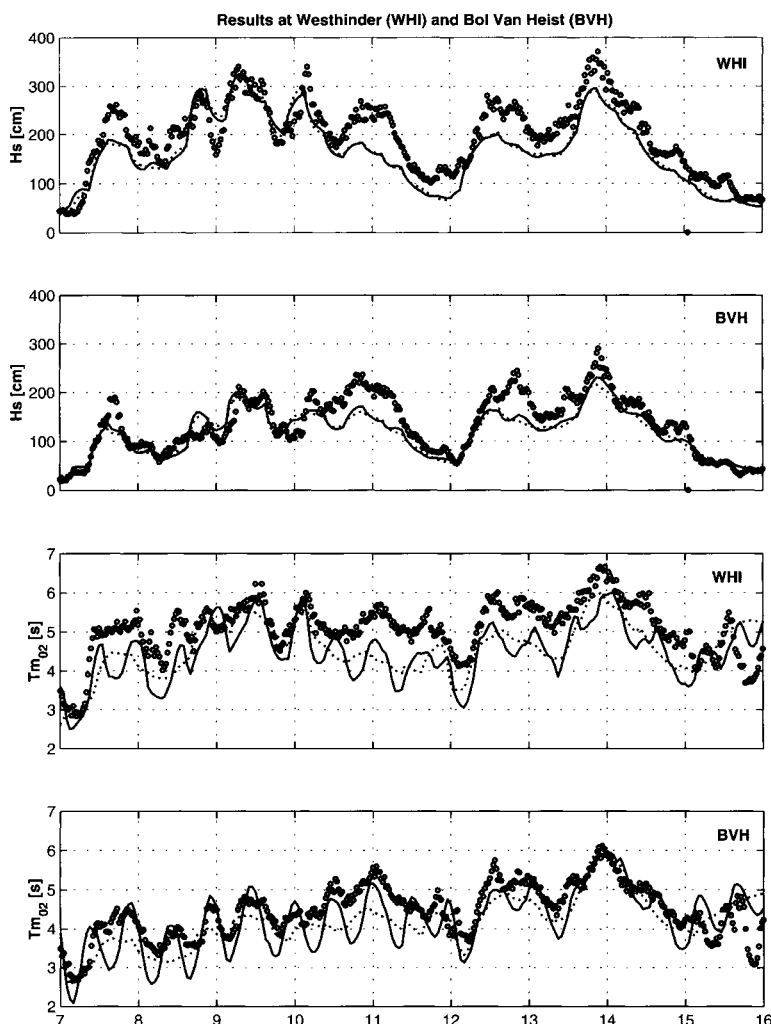
Figure 8. The same as Figs. 6 and 7, but now for the fine grid implementation.

interface, probably all frequency components in the spectrum play a role. Heimbach et al. (1998) for example found that swell energy in the WAM-model set-up they employed (the operational version of ECMWF since July 1994) was underpredicted by 20–30%, while the wind-sea was overpredicted by some 10%, when they compared ERS-1 synthetic aperture radar (SAR) with collocated WAM wave model data for the period between January 1993 and December 1995. Such additional information possibly points at shortcomings such as excessive damping in the WAM model propagation scheme at low frequencies. There is, therefore, a need for additional parameters that reflect the performance of a spectral wave model over the whole spectral domain.

Many operational models include data assimilation of some sort. For example, the current practice at ECMWF, UKMO, and Météo-France for the global model includes assimilation of the ERS-2 altimeter wave height and surface wind speed. At UKMO they use the analysis correction scheme

described by Thomas (1988). At ECMWF and Météo-France, an optimum interpolation scheme as developed by Lionello et al. (1992) is adopted. Assimilation of wave height and wind speed have been pointed at as important reasons for improved forecasting skills (see for example Janssen et al., 1997). Voorrips et al. (1997) illustrated clearly that assimilating directional wave information from pitch-and-roll (Wavec) buoys improved the KNMI (Royal Netherlands Meteorological Institute) operational forecast. The impact was greatest (up to 24 hours in the forecast) when swell coming from the Norwegian Sea was timely detected and assimilated. The assimilation method uses an optimal interpolation technique on wave partitions (i.e., before assimilation model and buoy data are partitioned into wind-sea and swell components). The methods above are referred to as single-time level methods, because they adjust the (forecasted) wave field at the time level of assimilation only. Assimilation techniques should preferably be based on multi-time level methods because they allow for integration of model data and observations in a dynamically consistent framework. Some methods have been proposed in the literature, see for example Hersbach (1998) and Voorrips (1998), but they are not used operationally, because they are still in the development stage or computationally too expensive. One should not forget that data assimilation of wave observations may be common practice now, but only fairly recently, for the practical reason that reliable wave measurements were not available for the largest part of the world. Only about one hundred moored buoys in the world, located in coastal areas, transmit wave data on a regular basis on the Global Transmitting System (GTS) and they are almost all located in the Northern Hemisphere. It is only since the advent of large amounts of reliable remotely sensed wave information (for example, ERS-1 wave data are available since 1991) that research and application interest to assimilate this information has grown considerably. It can, therefore, be expected that improvements in assimilation techniques for directional wave data will go hand in hand with the availability and amount of reliable directional wave information. Remote sensing will probably be the only technique capable of providing sufficient information in both time and space.

Directional information is important for global wave forecasting/hindcasting. Bauer and Heimbach (1999) demonstrated that the ERS-1 synthetic aperture radar measures wave heights quite well. There seems to be a small but systematic underestimation of the significant wave height compared to the wave height as measured by the TOPEX/POSEIDON and ERS-1 altimeters, but it can be attributed to the underestimation of the wind-sea part. Swell energy is captured quite accurately. The frequency and directional information present in the SAR signal, however, makes it very suitable for operational wave data assimilation. When compared to buoys, the quality of the SAR significant wave height seems however comparable to the ECMWF/WAM model one (Voorrips 1998, personal communication). This means that to improve wave analyses and forecasts, additional information from the SAR should be used (period and direction of wave trains).

One may wonder if improvements in physics are still needed. For ocean and shelf applications inaccurate wind predictions are often blamed for poor forecasts. The expected increase in observations and the consequent use of assimilation techniques could overcome shortcomings in our knowledge of the physics and in our ability to forecast wave conditions. Although the above might indeed be true for wave forecasts on ocean and shelf scale, this is not necessarily true to the same extent for coastal applications. There is no doubt that this will lead to improved knowledge of the wave boundary conditions for coastal applications and it is a *conditio sine qua non* for improved modeling skills. However, the effect of assimilating information at or close to the offshore boundary of a coastal region (typically some 20 to 40 km away from the coast) is short lived due to the short time needed for wave propagation toward the coast. Moreover, in shallow water, mainly the dissipation source terms are dominant. Only better knowledge of these processes will help coastal engineers to get more accurate wave parameters for the estimation of, for example, sediment transport or of the wave characteristics for the design of coastal structures.

There is also a tendency to couple wave models with other models. The coupling with current models is receiving more attention, both in regional and global applications (Buckley, 1999; Ozer et al., 2000). ECMWF has been running a coupled wave-atmospheric model since mid-1998 with apparent success (Bidlot et al., 2000). The idea behind the coupling of an atmospheric and a wave model is that waves integrate the effect of wind (see for example Kudryavtsev et al., 1999; Makin and Kudryavtsev, 1999). Together with the assimilation of altimeter data, it allows for a feedback from the waves to the surface winds. In this respect, assimilation of wave data will become more and more important in the future.

One of the limitations of spectral wave models is the lack of information about the phase of the wave components. Although knowledge of the significant wave height and a measure of the wave period give us a first estimate of what we can expect, information about groupiness is important to estimate maximum waves. This is of considerable importance in many engineering applications, such as the level of overtopping of coastal defense structures or design or operational levels for offshore platforms. Efforts are underway to overcome these shortcomings by trying to model the bi-phase evolution of the spectrum (for example, Norheim et al., 1998). Most probably this will still take many years before it is a standard feature in a spectral wave model.

An excellent informal forum to discuss difficulties and developments in shallow water wave modeling is available in the form of the yearly WISE (Waves In Shallow Environments) workshop (Cavaleri and Holthuijsen, 1998). Together with other platforms such as journal publications and conferences, it can be concluded that progress is guaranteed.

LIST OF SYMBOLS

CFL	—	Courant-Friedrich-Lewy
ECMWF	—	European Centre for Medium Range Weather Forecast
PROMISE	—	PRe-Operational Modeling In the Seas of Europe
SWAN	—	Simulating WAves Nearshore
TS	—	Tide-Surge
UKMO	—	United Kingdom Met Office
WAM	—	WAve Model
WAM-C3	—	WAM Cycle 3 version
WAM-C4	—	WAM Cycle 4 version
WAM-PRO	—	PROmise version of WAM-C4
c	—	wave celerity $(m.s^{-1})$
c_g	—	wave group velocity $(m.s^{-1})$
E	—	energy density in wave number space (m^4)
F	—	energy density in frequency-direction space $(m^2.s^1.rad^{-1})$
g	—	acceleration due to gravity $(m.s^{-2})$
H	—	wave height (m)
h	—	water depth (m)
k	—	wave number (m^{-1})
m	—	spatial co-ordinate perpendicular to wave propagation direction (m)
N	—	action density $(m^4.s)$ or $(m^2.s^2.rad^{-1})$
S	—	source term $(m^4.s^{-1})$ or $(m^2.rad^{-1})$
s	—	spatial co-ordinate in wave propagation direction (m)
t	—	time (s)
U	—	current velocity $(m.s^{-1})$
u_{*a}	—	air friction velocity $(m.s^{-1})$

x	—	geographical co-ordinate (m)
α	—	coefficient in numerical scheme
α	—	wave steepness
δ	—	non-dimensional water depth
κ	—	von Karman constant (-)
θ	—	wave propagation angle (°)
ρ_a	—	air density (kg.m^{-3})
ρ_w	—	water density (kg.m^{-3})
σ	—	intrinsic or relative frequency (s^{-1})
ω	—	absolute frequency (s^{-1})
ψ	—	angle of the wind (°)
bf	—	bottom friction
br	—	depth-induced breaking
ds	—	whitecapping dissipation
i	—	process counter
in	—	wind input
nl	—	nonlinear wave-wave interaction
max	—	maximum
PM	—	Pierson-Moskowitz
$\rightarrow$	—	vector indicator
.	—	time derivative
$-$	—	mean quantity
$\wedge$	—	mean weighted by inverse
n	—	time level

REFERENCES

Barstow, S., Athanassoulis, G.A., and Cavaleri, L., 2000. EUROWAVES—Integration of data from many sources in a user-friendly software package for calculation of wave statistics in European coastal waters. Oceanology International Conference, Brighton, UK, 7–10 March 2000, pp. 269–277.

Battjes, J.A., and Janssen, J.P.F.M., 1978. Energy loss and set-up due to breaking of random waves. Proceedings of the 16th International Conference on Coastal Engineering, ASCE, pp. 569–587.

Battjes, J. A., 1994. Shallow water wave modelling. Proceedings of the International Symposium on Waves—Physical and Numerical Modelling, Vol. I, pp. 1–23.

Bauer, E., and Heimbach, P., 1999. Annual validation of significant wave heights of ERS-1 synthetic aperture radar wave mode spectra using TOPEX/POSEIDON and ERS-1 altimeter data. Journal of Geophysical Research, 104 (C6): 13,345–13,357.

Becq, F., and Benoit, M., 1996. Implementation et comparaison de differents modèles de houle dans la zone de déferlement. EDF, HE-42/96/037/A, 56 pp. + app. (in French).

Becq-Girard, F., Forget, P., Benoit, M., 1999. Nonlinear propagation of unidirectional wave fields over varying topography. Coastal Engineering, 38: 91–113.

Beji, S., and Battjes, J.A., 1993. Experimental investigation of wave propagation over a bar. Coastal Engineering, 19: 151–162.

Benoit, M., Marcos, F., and Becq, F., 1996. Development of a third-generation wave shallow-water wave model with unstructured spatial meshing. Proceedings of the 25th International Conference on Coastal Engineering, ASCE, pp. 465–478.

Bidlot, J.-R., and Holt, M.W., 1999. Numerical wave modelling at operational weather centres. Coastal Engineering, 37: 409–429.

Bidlot, J.-R., Holmes, J.D., Wittmann, P.A., Lalbeharry, R., and Chen, H.S., 2000. Intercomparison of the performance of operational ocean wave forecasting systems with buoy data. ECMWF Technical Memorandum 315.

Booij, N., and Holthuijsen, L.H., 1987. Propagation of ocean waves in discrete spectral wave models. Journal of Computational Mechanics, 68: 307–326.

Booij, N., Ris, R.C., and Holthuijsen, L.H., 1999. A third-generation wave model for coastal regions. 1. Model description and validation. Journal of Geophysical Research, 104 (C4): 7649–7666.

Buckley, A.L., 1999. Wave current interaction for the Met Office Wave Model. Met Office (Ocean Applications) Internal Paper No. 22.

Cavaleri, L., and Holthuijsen, L.H., 1998. Wave modeling in the WISE group. Proceedings of the 26th International Conference on Coastal Engineering, ASCE, pp. 498–508.

Cavaleri, L., and Rizzoli, P.M., 1981. Wind wave prediction in shallow water: Theory and applications. Journal of Geophysical Research, 86: 10961–10973.

Christoffersen, J.B., and Jonsson, I.G., 1985. Bed friction and dissipation in a combined current and wave motion. Ocean Engineering, 12: 387–423.

Collins, J.I., 1972. Prediction of shallow water spectra. Journal of Geophysical Research, 93 (C1): 491–508.

Dean, R.G., and Dalrymple, R.A., 1991. Water wave mechanics for engineers and scientists. Advanced Series on Ocean Engineering. Vol. 2. Singapore: World Scientific Publishing Co., 353p.

Eldeberky, Y., 1996. Nonlinear transformation of triad interactions in wave energy models. Ph.D. thesis. Delft, The Netherlands: Department of Engineering, Delft University of Technology, 199p.

Grant, W.D., and Madsen, O.S., 1979. Combined wave and current interaction with a rough bottom. Journal of Geophysical Research, 84: 1797–1808.

Günther, H., Hasselmann, S., and Janssen, P.A.E.M., 1992. The WAM model Cycle 4, Report No. 4, Hamburg, Germany.

Hargreaves, J.C., and Annan, J.D., 2001. Comments on: Improvement of the short-fetch behavior in the wave ocean model (WAM). Journal of Atmospheric and Oceanic Technology, 18 (4): 711–715.

Hashimoto, N., and Kawaguchi, K., 2001. Extension of and modification of the discrete interaction approximation (DIA) for computing nonlinear energy transfer of gravity wave spectra. Proceedings, WAVES 2001 Conference, San Fransisco, USA.

Hasselmann, K., 1974. On the spectral dissipation of ocean waves due to whitecapping. Boundary Layer Meteorology 6: 107–127.

Hasselmann, K., and Collins, J.I., 1968. Spectral dissipation of finite-depth gravity waves due to turbulent bottom friction. Journal of Marine Research, 26: 1–12.

Hasselmann, K., Barnett, T.P., Bouws, E., Carlson, H., Cartwright, D.E., Enke, K., Ewing, J.I., Gienapp, H., Hasselmann, D.E., Kruseman, P., Meerbrug, A., Müller, P., Olbers, P.J., Richter, K., Sell, W., and Walden, H., 1973. Measurements of wind-wave growth and swell decay during the Joint North Sea Wave Project (JONSWAP). Deutsche Hydrographische Zeitschrift, A8(12), 95p.

Hasselmann, S., and Hasselmann, K., 1985. Computations and parameterizations of the nonlinear energy transfer in a gravity-wave spectrum. Part. I: A new method for efficient computations of the exact nonlinear transfer integral. Journal of Physical Oceanography, 15: 1369–1377.

Hasselmann, S., Hasselmann, K., Allender, J.H., and Barnett, T.P., 1985. Computations and parameterizations of the nonlinear energy transfer in a gravity-wave spectrum. Part. II: Parameterizations of the nonlinear energy transfer for application in wave models. Journal of Physical Oceanography, 15: 1378–1391.

Heaps, N.S., 1965. Storm surges on the continental shelf. Philosophical Transactions of the Royal Society of London, Series A, 257: 351–383.

Heimbach, P., Hasselmann, S., and Hasselmann, K., 1998. Statistical analysis and intercomparison of WAM model data with global ERS-1 SAR wave mode spectral retrievals over 3 years. Journal of Geophysical Research, 103 (C4): 7931–7977.

Hersbach, H., 1998. Application of the adjoint of the WAM model to inverse wave modelling, Journal of Geophysical Research, 103 (C5): 10,469–10,487.

Hersbach, H., and Janssen, P.A.E.M., 1999. Improvements of the short fetch behavior in the Wave Ocean Model (WAM). Journal of Atmospheric and Oceanic Technology, 16: 884–892.

Izumiya, T., and Horikawa, K., 1984. Wave energy equation applicable in and outside the surf zone. Coastal Engineering Japan, 27: 119–137.

Janssen, P.A.E.M., 1991. Quasi-linear theory of wind-wave generation applied to wave forecasting. Journal of Physical Oceanography, 21: 1631–1642.

Janssen, P.A.E.M., Hansen, B., and Bidlot, J.-R., 1997. Verification of the ECMWF Wave Forecasting System Against Buoy and Altimeter Data. Weather and Forecasting, 12: 763–784.

Khandekar, M.L., 1989. Operational Analysis and Prediction of Ocean Wind Waves. Berlin: Springer Verlag, 214p.

Komen, G.J., Cavaleri, L., Donelan, M., Hasselmann, K., Hasselmann, S., and Janssen, P.A.E.M., 1994. Dynamics and Modelling of Ocean Waves. Cambridge: Cambridge University Press, 532p.

Komen, G., Hasselmann, S., and Hasselmann, K., 1984. On the existence of a fully developed wind-sea spectrum. Journal of Physical Oceanography, 14: 1271–1285.

Kudryavtsev, V.N., Makin, V.K., and Chapron, B., 1999. Coupled sea surface atmosphere model: 2. Spectrum of short V.N. wind waves. Journal of Geophysical Research, 104 (C4): 7625–7639.

Larson, M., 1993. Decay of random waves in the surf zone. Proceedings of the International Conference, Waves '93, pp. 503–517.

Lionello, P., Günther, H., and Janssen, P.A.E.M., 1992. Assimilation of altimeter data in a global third generation wave model. Journal of Geophysical Research, 97 (C9): 14,453–14,474.

Luo, W., and Monbaliu, J., 1994. Effects of the bottom dissipation formulation on the energy balance for gravity waves in shallow water. Journal of Geophysical Research, 99 (C9): 18,501–18,511.

Luo, W.J., Monbaliu, J., and Berlamont, J., 1996. Bottom Friction Dissipation in the Belgian Coastal Waters. Proceedings of the 25th International Conference on Coastal Engineering, pp. 836–849.

Madsen O.S., 1994. Spectral wave-current bottom boundary layer flows. Proceedings of the 24th Conference on Coastal Engineering, ASCE, pp. 384–398.

Madsen O.S., Poon, Y.K., and Graber, H.C., 1988. Spectral wave attenuation by bottom friction: Theory. Proceedings of the 21st Conference on Coastal Engineering, ASCE, pp. 492–504.

Makin, V.K., and Kudryavtsev, V.N., 1999. Coupled sea surface-atmosphere model: 1. Wind over waves coupling. Journal of Geophysical Research, 104 (C4): 7613–7623.

Mastenbroek, C., Burgers, G., and Janssen, P.A.E.M., 1993. The dynamical coupling of a wave model and a storm surge model through the atmospheric boundary layer. Journal of Physical Oceanography, 23: 1856–1866.

Mei, 1989. The applied dynamics of ocean surface waves. Advanced Series on Ocean Engineering, Vol. 1. Singapore: World Scientific Publishing Co.

Miles, J.W., 1957. On the generation of surface waves by shear flows. Journal of Fluid Mechanics, 3: 185–204.

Monbaliu, J., 1992. Wind-drives seas: Optimal parameter choice for the wind input term. Journal Wind Engineering and Industrial Aerodynamics, 44: 2499–2510.

Monbaliu, J., Padilla-Hernández, R., Hargreaves, J.C., Albiach, J.C.C., Luo, W., Sclavo, M., Günther, H., 2000. The spectral wave model, WAM, adapted for applications with high spatial resolution. Coastal Engineering, 41: 41–62.

Norheim, C.A., Herbers, T.H.C., and Elgar, S., 1998. Nonlinear evolution of surface wave spectra on a beach. Journal of Physical Oceanography, 28 (7): 1534–1551.

Osuna, P., 2002. On the high resolution simulation of the dynamic interaction between current and waves in coastal waters: An application to the Southern North Sea. Ph.D. thesis. Heverlee, Belgium: Faculty of Sciences, Katholieke Universiteit Leuven.

Ozer, J., Padilla-Hernández, R., Monbaliu, J., Alvarez Fanjul, E., Carretero Albiach, J.C., Osuna, P., Yu, C.S., Wolf, J., 2000. A coupling module for tides, surges and waves. Coastal Engineering, 41: 95–124.

Padilla-Hernández, R., and Monbaliu, J., 2001. Energy balance of wind waves as a function of the bottom friction formulation. Coastal Engineering, 43: 131–148.

Phillips, O.M., 1957. On the generation of waves by turbulent wind. Journal of Fluid Mechanics, 2: 417–445.

Prandle, D., 2000. Operational oceanography in coastal waters. Coastal Engineering, 41: 3–12.

Resio, D.T., 1993. Full Boltzmann discrete spectral wave model, implementation and nondimensional tests. Vicksburg, MS: US Army Corps of Engineers, Waterways Experiment Station, Contract Report CERC-93-1.

Ris, R.C., 1997. Spectral modelling of wind waves in coastal areas. Ph.D. Thesis. Delft, The Netherlands: Delft University of Technology.

Ris, R.C., Holthuijsen, L.H., and Booij, N., 1999. A third-generation wave model for coastal regions. 2. Verification. Journal of Geophysical Research, 104 (C4): 7667–7681.

Roelvink, J.A., 1993. Dissipation in random wave groups incident on a beach. Coastal Engineering, 19: 127–150.

Rogers, W.E., Kaihatu, J.M., Booij, N., and Holtuijsen, L., 1999. Improving the Numerics of a Third-Generation Wave Action Model. Stennis Space Center, MS: Naval Research Laboratory. NRL/FR/7320–99-9695, 1–66.

Schneggenburger, C., Günther, H., and Rosenthal, W., 2000. Spectral wave modelling with nonlinear dissipation: Validation and applications in a coastal tidal environment. Coastal Engineering, 41: 201–235.

Southgate, H.N., and Wallace, H.M., 1994. Breaking wave persistence in parametric surf zone models. Proceedings, Coastal Dynamics '94, pp. 543–555.

Thomas, J.P., 1988. Retrieval of energy spectra from measured data for assimilation into a wave model. Quarterly Journal of the Royal Meteorological Society, 114: 781–800.

Thornton, E.B., and Guza, R.B., 1983. Transformation of wave height distribution. Journal of Geophysical Research, 88 (C10): 5925–5938.

Tolman, H.L., 1990. Wind wave propagation on tidal seas. Communications on hydraulic and geotechnical engineering. Delft, The Netherlands: Delft University of Technology, Report 90–1.

Tolman, H.L., 1992. Effect of numerics on the physics in a third generation wind-wave model. Journal of Physical Oceanography, 22 (10): 1095–1111.

Tolman, H.L., 1999. User manual and system documentation of WAVEWATCH-III version 1.18. NOAA / NWS / NCEP /OMB Technical Note 166, 110p.

Tolman, H.L., and Chalikov, D., 1996. Source terms in a third-generation wind-wave model. Journal of Physical Oceanography, 26: 2497–2518.

Van Vledder, G.Ph., 2001. Extension of the discrete interaction approximation for computing nonlinear quadruplet wave-wave interaction in operational wave prediction models. Proceedings, WAVES 2001 Conference, San Fransisco, USA.

Van Vledder, G.Ph., de Ronde, J.G., and Stive, M.J.F., 1994. Performance of a spectral wind-wave model in shallow water. Proceedings of the 24th International Conference on Coastal Engineering, ASCE, pp. 761–774.

Voorrips, A.C., 1998. Sequential data assimilation methods for ocean wave models. Ph.D. thesis. Delft, The Netherlands: Delft University of Technology, 168p.

Voorrips, A.C., Makin, V.K., and Hasselmann, S., 1997. Assimilation of wave spectra from pitch- and roll-buoys in a North Sea wave model. Journal of Geophysical Research, 102 (C3): 5829–5849.

WAMDI Group, 1988. The WAM model—A third generation ocean wave prediction model. Journal of Physical Oceanography, 18: 1775–1810.

Weber, S.L., 1991. Eddy-viscosity and drag-law models for random ocean wave dissipation. Journal Fluid Mechanics, 232: 73–98.

Williams, J.J., MacDonald, N.J., O'Connor, B.A., and Pan, S., 2000. Offshore sand bank dynamics. Journal of Marine Systems, 24 (1-2): 153–173.

Wolf, J., 1999. The estimation of shear stresses from near-bed turbulent velocities for combined wave-current flows. Coastal Engineering, 37: 529–543.

Wolf, J., and Prandle, D., 1999. Some observations of wave-current interaction. Coastal Engineering, 37: 471–485.

Young, I.R., 1999. Wind Generated Ocean Waves. Oxford, UK: Elsevier Science Ltd., 288p.

Young, I.R., and Gorman, R.M., 1995. Measurements of the evolution of ocean wave spectra due to bottom friction. Journal of Geophysical Research, 100 (C6): 10,987–11,004.

Young, I.R., and Verhagen, L.A., 1996a. The growth of fetch limited waves in water of finite depth. Part 1: Total energy and peak frequency. Coastal Engineering, 29: 47–78.

Young, I.R., and Verhagen, L.A.., 1996b. The growth of fetch limited waves in water of finite depth. Part 2: Spectral evolution. Coastal Engineering, 29: 79–99.

159

Chapter 6

Probabilistic Models of Waves in the Coastal Zone

Carlos Guedes Soares

Unit of Marine Technology and Engineering, Technical University of Lisbon, Instituto Superior Técnico, Av. Rovisco Pais, 1049–001 Lisboa, Portugal

1. INTRODUCTION

The variability of the processes associated with wave generation governs its basic nature even when propagation is being considered. Therefore, only stochastic models provide a satisfactory description of the spatial and temporal variations of wave fields in ocean and coastal waters.

The basic models that have been developed are based on the assumption that the free surface elevation of the sea surface at a point follows a Gaussian distribution. Furthermore, the ergodicity assumption is invoked to allow the same type of Gaussian models to provide a description of the variability of the process in space. The models developed describe different properties of the wave fields as required for different engineering purposes. Typically, in ocean areas, the waves are of interest to shipping as they govern ship motions and sometimes affect the choices of their routes. In the offshore areas both shipping and offshore platforms are of concern. Closer to the coast there is still coastal shipping, but also other coastal developments such as harbors and coastal defenses which need consideration. Furthermore, beaches and sediment transport are important issues close to the surf zone.

This wide variety of situations suggests that several properties of waves need to be described in order to meet the engineering needs for information which then can be applied to the different problems. Typically, one wants to describe the sea surface elevation, but in view of its periodic nature some models address the amplitude and the period or frequency of the motion. Still of interest is to study the properties of the envelopes of the process, which shows a lower frequency of oscillation than the basic process. This can be used to study several problems, ranging for example from the occurrence of maxima in the process to the occurrence of groups in the wave time series. Specific problems may require a description of the steepness of the waves, and how their shape changes when they interact with currents. Extreme steepness leads to breaking, which is a way in which the wave system dissipates energy. Breaking waves are also important to engineering because the accelerations that are involved in those situations are often large and potentially damaging if they impact a structure.

The foregoing gives an idea of the type of properties that are often of interest. However, in addition to describing the time and space variabilities of these properties, there is also interest in knowing the variability over longer time periods. This variability can be of interest for the basic wave parameters such as height and period, but also for derived quantities such as the significant wave height and any of the mean period parameters.

For design problems interest is often on the most likely maxima or on the extreme values that occur within very long periods of time, which is known as the long-term problem as opposed to the short-term models that describe the variability in time scales of minutes instead of years. Less studied are intermediate time scales on the order of days or of weeks, which are of interest in operability situations. Some examples of marine operations that have such time durations are towing of any large structure, installation or major work in offshore structures, and building and repair of coastal

structures. The typical problem is to determine windows of time during which the wave conditions are below a certain threshold that limits the operation due, for instance, to excessive motions or too high forces on the structures.

One additional complication is created by the bottom topography, which can affect the wave properties. For depths typically greater than half the wavelength the bottom topography does not affect the water waves, but in very shallow water all waves propagate at the same group velocity irrespective of the frequency. The transition zone in which the dispersion relation depends on the water depth is called the finite water depth. This means that the entire set of probabilistic models in all time scales can be different in each of the water depth ranges.

Since wave fields are described by stochastic models, it is possible to describe them both in the frequency and in the time domains. A Gaussian process can be completely described by its variance or energy spectrum or by its autocorrelation function. The time series of events can be used to describe the probability of occurrence of any property at a random point in time. While the first are normally called spectral models, the latter are denoted as probabilistic models, and both describe the variability of the same process.

This brief introduction has given an idea of the multitude of models that are available for different situations and it is obvious that it will be very difficult to cover them all in a review chapter. Therefore, this chapter will concentrate only on probabilistic models, mainly in deep water and finite water depth. In some coastal areas the continental shelf becomes very deep relatively close to the coast, making the area of intermediate depth models relatively narrow, while in other areas the region of intermediate water depth has a considerable extent.

Sections 2 and 3 describe the free surface elevation in short-term periods of stationarity, with Section 2 adopting a frequency domain discretization while Section 3 is based on the digitalization of time domain records. Section 4 deals with joint probabilities of wave heights and periods, while Section 5 describes wave groups, which are very important for the analysis of coastal structures. Section 6 deals with the medium-term models in which the modeled parameter is no longer the individual wave, but the parameters such as significant wave height that describe sea state intensity. The models account for the correlation among sea states and are useful for planning maritime operations, including construction of coastal structures. The last two sections (7 and 8) deal with long-term models that describe the variability of sea states in time scales on the order of 20 to 100 years, as is required for design decisions.

2. SPECTRAL MODELS

Spectral models of the sea surface elevation provide a frequency domain description of the stochastic process and the basic theory was well documented many years ago. Depending on the nature of the sea state they will be described by different shapes of spectra. After several models were proposed based on different considerations, the one that has been generally accepted to describe fully developed wind-driven wave systems was introduced by Pierson and Moskowitz (1964). These situations occur after stable conditions have been prevailing for some time and in a long enough fetch.

However, in younger seas and for shorter fetches as may occur in coastal waters, the wave system may not have time enough to fully develop and in this case the spectrum is more peaked and has, in general, higher peak frequencies. This was observed in the JONSWAP experiment (Hasselmann et al., 1973), which produced a model widely used since then to describe developing sea states. As the sea state develops, the nonlinear wave-wave interactions move the peak toward lower frequencies and make it flatter, converging to the Pierson-Moskowitz model. These are the two main models that describe wind-driven sea states. Huang et al. (1981) suggested a model that generalizes these.

Swell systems are more complicated to describe as no single self-similar form exists as in the case of wind-driven sea states. After the wind system ceases to provide input to the waves, they propagate freely as swell, traveling away from the storm area. In this process the long waves travel faster than the shorter ones and, as a consequence, the swell system looses its high frequency components as it moves away from the storm, becoming more peaked and less broad banded. Thus, for the same initial spectrum in the storm area, the shape of the swell spectrum depends on the distance traveled. There is very little data available for swell but Goda (1983) found that a JONSWAP spectrum with peak enhancement factor ranging from 7 to 10 can be adequate in those cases.

When a swell system coming from a distant storm arrives at an area with local wind generated sea a mixed wave system results. If the peak frequencies of the spectra are relatively close, the spectrum of the combined sea state may still look single peaked although the directional spectrum may indicate that the two wave systems come from the same or from different directions. When the peak frequencies are well separated the spectrum has a double peak and none of the spectral models indicated can describe them. These sea states can occur as much as 25% of the time, depending on the location. However, in all locations its probability of occurrence always decreases as the significant wave height increases (Guedes Soares, 1991).

One of the first models proposed to describe double-peaked spectra was by Strekalov et al. (1972) who suggested that it would be obtained by one high frequency spectrum describing the wind-driven component and a Gaussian shaped model describing the swell system. Ochi and Hubble (1976) proposed another form by combining a JONSWAP and a Pierson-Moskowitz spectrum describing the two individual wave systems, and they showed that by choosing different values of the spectral parameters one would be generating spectra with a different appearance.

When Guedes Soares (1984) studied the problem and tried to fit measured wave spectra by a combination of a JONSWAP and a Pierson-Moskowitz spectrum, he realized that the peak of the Pierson-Moskowitz spectrum was too broad to allow the two peak frequencies to still appear separately. Therefore, he proposed a model that represents both sea components by JONSWAP spectra of different peak frequencies. While the choice of the model for the wind-sea component is obvious, the choice to model the swell component was made because the JONSWAP model is able to fit very peaked spectra as would be appropriate for the narrow swell spectral component as shown by Goda (1983).

Torsethaugen (1993) also adopted two JONSWAP models to describe the two-peaked spectra but instead of using average JONSWAP parameters as done by Guedes Soares (1984), he used more adjustable parameters of the JONSWAP model. As a result, while the model of Guedes Soares is described by four parameters, the Torsethaugen model requires seven parameters. This is less practical but having a large database, it also allows a better fit. Indeed, Torsethaugen determined the values of these parameters for many classes of spectra of the Norwegian sea and his results are being used within the Norwegian offshore industry.

Guedes Soares (1984) proposed the ratio of spectral ordinates of the sea and swell components and the ratio of the peak frequencies of the two components as spectral parameters to describe the relation of the two wave systems. Rodriguez and Guedes Soares (1999) proposed two other related parameters, the Sea Swell Energy Ratio (SSER) and the Intermodal Distance (ID). The SSER is the ratio of energies associated with each wave system, defined as the ratio between the wind-sea zero order spectral moment, and the zero order moment of the frequency spectrum corresponding to the swell wave field as follows

$$SSER = \left(\frac{m_{0_{ws}}}{m_{0_{sw}}} \right) \tag{1}$$

where m_n is the n-th order moment of the spectrum $s(f)$

$$m_n = \int\limits_0^\infty f^n S(f)\, df \; ; \; n = 0, 1, 2, \ldots \tag{2}$$

where f is the frequency, and the subscripts sw and ws stand for swell and wind-sea parameters, respectively. The wave fields that have the SSER value smaller than one represent swell dominated sea states while the ones with the SSER value greater than one correspond to the wind-sea dominated category. If the SSER value is close to one it is included in the category of sea states with two spectral peaks with comparable energy content.

The other parameter is the frequency separation between the spectral frequency peaks, f_p, corresponding to the swell and wind-wave systems, called the *Intermodal Distance* (ID) and is calculated with the following expression

$$\text{ID} = \left(\frac{f_{p_{ws}} - f_{p_{sw}}}{f_{p_{ws}} + f_{p_{sw}}} \right) \tag{3}$$

All of these models have a tail that is proportional to the frequency to the power -5, as follows from the argument of the saturation condition (Phillips, 1958). However, several laboratory and full scale measurements have shown that the tail is closer to -4 than to -5 (for example, Toba, 1973; Forristall, 1981; Donelan et al., 1985; Ewans and Kibblewhite, 1990; Prevosto et al., 1996). As a consequence, Kitaigorodskii (1983) and Phillips (1985) proposed revised equilibrium spectral balances in which the wind input, nonlinear energy transfer and dissipation processes assume different levels of relative importance in determining the equilibrium spectral shape for the short gravity wave range of the spectrum. These energy balances are consistent with a -4 power law, as empirically derived by Toba (1973). In fact, a more detailed analysis indicated that for frequencies between the peak frequency and a frequency two or three times larger than the tail follows the -4 law while for larger frequencies the law of -5 predominates (Mitsuyasu et al., 1980; Forristall, 1981; Hansen et al., 1990; Rodriguez et al., 1999). The fact that the two slopes can be found in the high frequency part of the spectrum associated with the uncertainty in the estimation procedure (Rodriguez and Guedes Soares, 1998) can explain why different authors have obtained values between -4 and -5. Therefore, although there is some agreement now about the high frequency part of the spectrum, it is clear that these results have not yet been incorporated in the proposed spectral formulations of Pierson-Moskowitz and JONSWAP, which are recommended in some codes of practice.

In finite water depth the wave spectrum changes as a result of the interaction with the bottom. Bouws et al. (1985) proposed a spectral model of wind waves in finite water depth which became known as the TMA spectrum, and is the product of the JONSWAP spectrum by a depth function of Kitaigorodskii et al. (1975). Gentile et al. (1994) carried out a reexamination of the TMA spectrum by taking into account the dependence of the equilibrium parameter on depth, and claimed that the spectral energy density on finite depth could be higher than the one predicted by the TMA spectrum. Guedes Soares and Caires (1995) presented a method of accounting for shoaling and refraction so as to predict the evolution of the TMA spectrum as the wave system propagates in water of finite depth. Young and Verhagen, (1996) presented the results of an experimental study of wave propagation in a lake, which generally supported the work of Bouws et al. (1985).

A final aspect worth mentioning is the effect of current, which distorts the shape of wave spectra and modifies the models described above. This is particularly important in coastal waters, where currents are sometimes intense. Huang et al. (1972) proposed a formulation that is based on the conservation of energy and of wave kinematics. Hedges et al. (1985) modified it to account for the effect of wave breaking in the saturation limit of the spectra and compared the results with experiments in

a wave flume. Suh et al. (2000) presented additional experimental results on a flume concentrating in finite water depths. Finally, experimental work on three-dimensional wave tanks was presented by Nwogu (1993) and by Guedes Soares et al. (2000), showing that while the theory provides a good description of the spectral changes, some improvements in accuracy are still required.

3. DISTRIBUTIONS OF FREE SURFACE ELEVATION AND WAVE HEIGHTS

The surface elevation can be represented by a zero mean Gaussian density function

$$f(\eta) = \frac{1}{\sqrt{2\pi}\sigma_n} \exp -\frac{\eta^2}{2\sigma_\eta^2} \tag{4}$$

where σ_η^2 is the variance of $\eta(t)$.

Longuet-Higgins (1952) demonstrated that for narrow band processes the amplitude of the waves can be described by a Rayleigh distribution. This distribution has also been used to describe the probabilistic properties of the wave height H, which is approximated by twice the amplitude. The general expression for the Rayleigh probability density function is

$$f(x) = \frac{2x}{R} \exp\left(-\frac{x^2}{R}\right), \ 0 \leq x \leq \infty \tag{5}$$

The Rayleigh parameter R is

$$R = \begin{cases} 2\sigma_\eta^2 & \text{for } x \text{ representing wave amplitude} \\ 8\sigma_\eta^2 & \text{for } x \text{ representing wave height} \end{cases} \tag{6}$$

The Rayleigh distribution has a peak value of $\sqrt{2/R}$ at $x = \sqrt{R/2}$. The mean value and variance are given by

$$\mu_x = \frac{\sqrt{\pi R}}{2}$$

$$\sigma_x^2 = \left(1 - \frac{\pi}{4}\right)R \tag{7}$$

The fractiles of this distribution are often used as descriptive statistics. The average of the $1/n$-th highest observations $x_{1/n}$ is defined as

$$\bar{x}_{1/n} = n \int_{x_{1/n}}^{\infty} \frac{2x^2}{R} \exp\left(-\frac{x^2}{R}\right) dx \tag{8}$$

where $x_{1/n}$ is such that the probability of exceeding it is equal to $1/n$

$$P\left[x > x_{1/n}\right] = \int_{x_{1/n}}^{\infty} \frac{2x}{R} \exp\left(-\frac{x^2}{R}\right) dx = \frac{1}{n} \tag{9}$$

It can be shown that the expression for $\bar{x}_{1/n}$ results in

$$\bar{x}_{1/n} = n\sqrt{2\sigma_\eta^2}\left[\frac{1}{n}\sqrt{\ln n} + \sqrt{\pi}\left(0.5 - \text{erf}\sqrt{2\ln n}\right)\right] \tag{10}$$

where erf is the error function. This results in the significant wave height, which is defined as the average of the 1/3 highest waves, given by

$$H_s = \overline{H}_{1/3} = 4\sigma_\eta \tag{11}$$

The formulation just described is applicable for narrow band situations. One can define the spectral bandwidth ε by

$$\varepsilon^2 = 1 - \frac{m_2^2}{m_0\, m_4} \tag{12}$$

where m_i is the i-th moment of the spectrum given by equation (2).

When the bandwidth parameter is different from zero, the probability density function of the maxima is the Rice (1945) distribution as shown by Cartwright and Longuet-Higgins (1956)

$$f_X(x) = \frac{1}{\sqrt{2\pi}}\, \varepsilon \exp\left\{-\frac{1}{2}\left(\frac{x}{\varepsilon}\right)^2\right\} + \sqrt{(1-\varepsilon^2)}x \, \exp\left\{-\frac{1}{2}x^2\right\} \Phi\left[\frac{x\sqrt{(1-\varepsilon^2)}}{\varepsilon}\right] \tag{13}$$

where Φ is the standardized normal distribution. It should be noticed that this distribution reduces to the Rayleigh for $\varepsilon = 0$.

Assuming that all maxima are identically distributed and statistically independent, the cumulative distribution function for the maximum x_η out of n maxima is given by

$$F_{X_n}(x) = \left[F_X(x)\right]^n \tag{14}$$

When n becomes large, the expected value of the largest of n maxima is approximated by

$$E[x_n] = \sqrt{2}\left\{\left(\ln\sqrt{1-\varepsilon^2}n\right)^{1/2} + \frac{1}{2}\gamma\left(\ln\sqrt{1-\varepsilon^2}n\right)^{1/2}\right\} \tag{15}$$

where γ is the Euler constant ($= 0.57722\ldots$).

These results of the maxima of n waves are based on the assumption of independence between successive waves, which is known to be incorrect. Naess (1984) formulated the distribution of the maximum wave height accounting for the correlation between consecutive crests. However, he assumed that the wave height is twice the wave crest. Tayfun (1981) improved the definition of local wave height by considering it was the sum of the amplitude of a crest and the following trough.

Massel and Sobey (2000) reviewed these developments and concluded that none of them accounted simultaneously for all factors that exist in the real waves, and suggested that only a simulation procedure could do so. They developed probability distributions for the maximum wave height in samples of n waves in sea states of different characteristics. Although their distributions can be considered to be more accurate they are not analytical and this makes them very difficult to use in practice.

These theoretical models have been compared with measured data and found to give good agreement in general. Some discrepancies were found on some occasions when the narrow band assumption did not hold, but Longuet-Higgins (1980) showed that even in this case the Rayleigh distribution could be used if the parameter R was determined from the definition of significant wave height or if a correction factor was applied to the zero moment of the spectrum.

Forristall (1978) proposed the Weibull distribution

$$P(\eta > \eta_o) = \exp\left(-\frac{\eta^\alpha}{\beta m_0}\right) \tag{16}$$

where α and β are shape and location parameters to be determined from fitting empirical data. He used a data set from the Gulf of Mexico and obtained a shape factor of 2.126 while Nolte and Hsu (1979), using the same data, obtained 2.138. Myrhaug and Kjeldsen (1986) obtained 2.39 with another data set. Since the Rayleigh distribution is a special case of the Weibull distribution with a shape factor of two, one can see that the shape of these distributions is not too different from the Rayleigh distribution. These distributions predict a smaller probability for large wave heights than predicted by the Rayleigh distribution, the difference increasing with wave height. This deviation from the Rayleigh distribution results from the difference between the crest height and the following trough, which increases as the spectrum becomes broad banded.

A theory that includes the spectral bandwidth was proposed by Tayfun (1981) and compared with field data by Forristall (1984). It is based on the calculation of the amplitudes of the wave envelope at two points separated by half wave period.

Naess (1985) proposed another distribution

$$P\left(\eta > \eta_\circ\right) = \exp\left[-\frac{\eta^2}{4\left(1 - \rho\left(\tau/2\right)\right)m_0} \right] \tag{17}$$

where $\rho(\tau/2)$ represents the value of the normalized autocorrelation function of the sea surface elevation at half of the period away, the time when it attains its first minimum

$$\rho\left(\tau/2\right) = \frac{R\left(\tau/2\right)}{R(0)} \tag{18}$$

Tayfun (1990) developed asymptotic approximations to obtain close form expressions that are easy to use in practical applications but the usefulness of which are restricted to wave heights greater than the mean wave height.

While the approaches described in this section have been used to describe sea states with a single wave system, Rodriguez et al. (2002) examined combined sea states based on numerically simulated time series. They observed that, while the superposition of a swell with a low energy content to a dominant wind sea has unimportant effects on the wave height distribution, at least when using the zero up-crossing definition, the addition of a low energy wind sea to a dominant swell produces a significant effect on the observed probabilities. This gives rise to an increase of small and large wave heights and a decrease of intermediate wave heights. In the case of a wind dominated sea state co-existing with a low energy swell very close in frequency, there is an increase of large wave heights exceeding the predictions of all the models examined in this work. On the other hand, the super-position of two wave fields of different dominant frequencies, but similar energy content produces a decrease in the probability of wave heights larger than the mean wave height, and this effect is more pronounced as the intermodal distance increases. Guedes Soares and Carvalho (2001) exam-ined measured coastal data of this type of sea state and confirmed that, indeed, in some types of sea states the distributions used for single wave systems are not appropriate.

The Gaussian assumption, which is the underlying assumption for several of the distributions considered here, implies that the sea surface elevation is symmetric with respect to the waterline. However, this is not always observed in measured data, in particular in storms or as the water depth decreases. Large amplitude waves as well as waves in water of finite depth tend to be asymmetric, with higher crests and lower troughs. These nonlinear waves are appropriately described by higher-order Stokes models. In irregular sea states this asymmetry of the second-order Stokes waves is re-flected in the skewness of the surface elevation record as noted by Longuet-Higgins (1963) for deep water waves. Longuet-Higgins (1963) modeled the non-Gaussianity of the waves with the Edge-worth's form of the type A Gram-Charlier series. His work was extended to water of finite depth by Bitner (1980).

Irregular second-order waves include waves that have wave numbers equal to the sums and differences of those of first-order waves. The slowly varying difference wave numbers correspond to wave groups, which in intermediate water depths start feeling the bottom even when the individual wave components do not. Therefore, the second-order waves are more sensitive to bottom effects than the linear waves. Empirical probability distributions applicable for these nonlinear waves have been developed from observed data by Kuo and Kuo (1975), Goda (1975) and Hughes and Borgman (1987).

In the case of narrow band wave processes analytical expressions of the probability density function of the skewness in nonlinear free surface elevation have been obtained by Tayfun (1980), Arhan and Plaisted (1981) and Huang et al. (1983). Tayfun (1980) obtained the probability density function of deep water second-order Stokes waves. He assumed the amplitude as Rayleigh distributed and the phase uniformly distributed, being both slowly variant. Arhan and Plaisted (1981) analyzed field data from the Gulf of Mexico based on a third-order Stokes wave formulation. They found that the skewness of the field data was between 50% and 70% of their theoretical values. Winterstein et al. (1991) found that it was 80–85% in the case of deeper water North Sea data. Huang et al. (1983) adopted a perturbation scheme based on the assumption that the skewness is small, and obtained the probability distribution using a third-order Stokes expansion both for deep and shallow water. The probability density function for deep water is specified by the root mean square of the elevation and the significant slope. In water of finite depth one additional depth dependent factor is required.

Ochi and Wang (1984) derived the probability distribution of amplitudes of coastal waves applying the Gram-Charlier series distribution. However, the approach is not very practical as this distribution is not given in closed form and the density function becomes negative for large negative displacements.

Marthisen and Winterstein (1992) used the skewness of the sea state as the input to a Hermite polynomial transformation model proposed by Winterstein (1988), from which the extreme value of the non-Gaussian wave crests can be derived analytically.

Longuet-Higgins (1963) showed that at infinite water depth the skewness is always positive. Marthisen and Winterstein (1992) have shown that the slowly varying component of the second-order waves, which looks like a wave group, gives a negative contribution to the wave skewness in any water depth.

Longuet-Higgins and Stewart (1962) demonstrated that the slowly varying sea level associated with a group of waves is depressed, which was also shown by Langley (1987) for deep water waves. This effect becomes stronger as the water depth decreases, and thus reduces the increased skewness that is often assumed for shallower waters (Ochi, 1986).

Ochi (1998a) applied a closed form expression for the probability density function of peaks, troughs and peak-to-trough excursions of non-Gaussian processes (Ochi, 1998b) to the case of finite water depth waves. The approach is applicable only when the wave skewness is smaller than 1.2. In this case, a Rayleigh distribution is applicable, in which its parameter is a function of three parameters that represents the non-Gaussian waves.

Cieslikiewicz (1990) proposed an approach to derive a probability density function of wave height from the maximum entropy approach and Cieslikiewicz (1998) applied it to coastal waves. Ahn (1998) presented a formulation based on the maximum entropy method, which provides the probability density function of wave heights in finite water depth, including shallow water. The distribution can be expressed in terms of the breaking wave height as well as the mean and root-mean-square wave height. When third and higher moments are available a numerical solution can be obtained.

4. JOINT DISTRIBUTIONS OF WAVE HEIGHT AND PERIOD

Several theoretical models for the bivariate distribution of wave heights, H, and periods, T, have been proposed during the last two decades. Longuet-Higgins (1975), based on the assumption of a spectral narrow banded process, presented the first theoretical model for the bivariate distribution of wave heights and periods. He considered the statistics of the joint distribution of the wave envelope amplitude and the time derivative of the envelope phase. This distribution is expressed in terms of the spectral bandwidth parameter, given by

$$v = \left(\frac{m_0 m_2}{m_1^2} - 1 \right)^{1/2} \tag{19}$$

Furthermore, it shows symmetry about the mean period, $\overline{T} = (m_0/m_1)$. However, the joint distribution of H and T of wave records with finite spectral bandwidth displays a clear asymmetry about $\overline{T}$, mainly in the range of low heights (Goda, 1978). Thus, this model seldom matches the observed bivariate distribution of measured data, but can be appropriate for the upper portion of the distribution that corresponds to high waves.

Longuet-Higgins (1983) revised his earlier model to account for the effect of finite bandwidth and presented an alternative approach, which is also given in terms of the spectral bandwidth parameter. This model reproduces properly the asymmetrical shape of the joint distributions observed in practice, but it is also only valid for narrow-banded processes.

Cavanié et al. (1976) presented a bivariate model that reproduces the asymmetrical distributions often observed in measured wave records. To estimate wave heights and periods, they considered the joint distribution of positive maxima and their associated second derivatives. Furthermore, they assumed a sinusoidal profile for each wave, which is similar to a narrow band approximation. Hence, this model is not suitable to describe the bivariate distribution of T and H in broad-banded sea states. This distribution is expressed in terms of the following spectral bandwidth parameter ε given by equation (12).

Lindgren and Rychlik (1982) proposed an analytical model capable of describing the joint distribution of H and T in wave records with arbitrary spectral bandwidth. The key of this model lies in its dependence on the full covariance and its first four derivatives, which are estimated from the spectra of the wave records. In other words, it depends on the full spectral structure and not only on a few spectral moments, such as in all models previously mentioned. However, this model is computationally intensive, which has probably hampered its generalized adoption by the industry.

A problem of the Cavanié et al. (1976) and Lindgren and Rychlik (1982) models is the critical dependence on the fourth-order moment of the spectral function, and hence on the structure of the spectral high frequency range. As a consequence, measurement and computational factors, such as the sampling rate and filtering properties of the measurement equipment, and the high frequency cut-off used to estimate the spectral moments significantly affect them.

These studies have shown that the properties of the bivariate distribution of wave heights and periods from sea states with single peaked spectra are mainly controlled by the spectral bandwidth and the spectral shape of the wave field. Thus, it has been observed that, generally, $p(H, T)$ presents a high symmetry about the mean period for narrow band spectra and a progressive loss of symmetry with the increase of the spectral bandwidth, v, reflected by a more pronounced sharper decay of the probability levels at the high periods range as increases. Rodriguez and Guedes Soares (1999) showed that for moderate bandwidth the models of Longuet-Higgins (1983) and of Cavanié et al. (1976) are able to represent the asymmetry appropriately.

In view of the effects of spectral shape in the joint probability distributions, Sobey (1992) proposed to derive the joint distribution from numerical simulation of the sea states. Although this approach

can be claimed to lead to a distribution that matches the data well, it does not yield an analytical expression that can be adopted in subsequent studies. As in the case of the distribution of wave heights, the approaches described in this section have been used mainly to describe sea states with a single wave system (Earle et al., 1974; Chakrabarti and Cooley, 1977; Srokosz and Challenor, 1987).

Rodriguez and Guedes Soares (1999) examined combined sea states based on numerically simulated time series. They observed that, in general, the asymmetry of the bivariate distribution rises as the intermodal distance of the component spectra (ID) increases. However, this effect is very slight for the wind-sea dominated sea states. The joint distribution in sea states included in this category may be described with the Longuet-Higgins (1983) or the Cavanié et al. (1976) models, at least for small intermodal distances.

In sea states resulting from the combination of swell and wind-sea with comparable energy content a significant loss of symmetry can be observed as ID increases and the range of periods results amplified. This asymmetry can be characterized by the models of Longuet-Higgins (1983) or Cavanié et al. (1976), for small values of ID. However, for large values of ID, the only model capable of reproducing adequately the observed asymmetric shape of the joint distribution is that proposed by Lindgren and Rychlik (1982).

In swell dominated sea states, the asymmetry increases as ID takes larger values. Thus, the Longuet-Higgins (1983) and Cavanié et al. (1976) models may adequately fit the bivariate distributions associated with the wave fields in this category for low values of ID. The distributions obtained for large values of ID should be described with the Lindgren and Rychlik (1982) model.

The joint distributions can be used as the starting point to obtain the marginal distribution of wave periods, a topic much less studied than the distributions of wave height. This was adopted by Longuet-Higgins (1975), who derived the expression of the marginal distribution of wave periods

$$p(\tau) = \frac{v^2}{2\left[v^2 + (\tau - 1)^2\right]^{3/2}} \tag{20}$$

where v is the spectral bandwidth parameter and wave periods were normalized as

$$\tau = \frac{T m_1}{m_0} \tag{21}$$

Another theoretical expression for the wave period distribution was derived in a similar way by Cavanié et al. (1976)

$$p(\tau) = \frac{\alpha^3 \beta^2 \tau}{\left[\left(\tau^2 - \alpha^2\right)^2 + \alpha^4 \beta^2\right]^{3/2}} \tag{22}$$

where

$$\alpha = \frac{1}{2}\left(1 + \sqrt{1 - \varepsilon^2}\right) ; \beta = \frac{\varepsilon}{\sqrt{1 - \varepsilon^2}} \tag{23}$$

and ε is a spectral bandwidth parameter. It should be noted that their dimensionless period is given by

$$\hat{\tau} = \bar{\zeta}\tau = \bar{\zeta}\frac{T m_1}{m_0} \tag{24}$$

where $\bar{\zeta}$ is a function of ε that remains close to one for values of ε from 0 to 0.95.

Longuet-Higgins (1983) revised his model and presented an alternative expression

$$p(\tau) = \left(1 + \frac{\nu^2}{4}\right) \frac{1}{2\nu\tau^2} \left[1 + \left(1 - \frac{1}{\tau}\right)^2 \frac{1}{\nu^2}\right]^{-3/2} \tag{25}$$

Based on the behavior of experimental wave period distributions represented in Weibull scale presented by Myrhaug and Rue (1998), Myrhaug and Slaattelid (1999) proposed a combination of two two-parameter Weibull distribution functions given by

$$P_1(\tau) = 1 - \exp\left[-\left(\frac{\tau}{\alpha_1}\right)^{\beta_1}\right] ; \; 0 \le \tau \le \tau_c \tag{26}$$

and

$$P_2(\tau) = 1 - \exp\left[-\left(\frac{\tau}{\alpha_2}\right)^{\beta_2}\right] ; \; \tau > \tau_c \tag{27}$$

with α and β, being the Weibull parameters, and τ_c the intersection point between $P_1(\tau)$ and $P_2(\tau)$ given by

$$\tau_c = \left(\frac{\alpha_1^{\beta_1}}{\alpha_2^{\beta_2}}\right)^{1/(\beta_1 - \beta_2)} \tag{28}$$

Rodriguez and Guedes Soares (2000) examined the distribution of wave periods in combined sea states based on numerically simulated time series. The theoretical distributions of Longuet-Higgins (1983) and Cavanié et al. (1976) seemed to be useful to predict the obtained wave period distributions, at least approximately, only in the cases of mixed sea states with a dominant wind-sea field. However, even in these cases models gave rise to a systematic underprediction of the probability of intermediate wave periods, mainly for large intermodal distances. Another case in which the theoretical models seem to reproduce approximately the observed distributions is that in which a wind-sea and a swell with similar energy content and closed peak frequencies are superposed. The largest deviations between the observed and the expected probability distributions appear in swell dominated sea states, where none of the compared models is able to characterize the observed wave period probability distribution. The deviation between the theoretical models and the observed distribution increases with ID.

Guedes Soares and Carvalho (2001) examined the applicability of these models to fit measured data from a coastal station. They observed that for wind-sea dominated spectra the shape of the distribution is more regular and the models are able to characterize the wave period distribution for intermediate and large intermodal distance. When the energy is comparable the shape of the distribution is close to symmetric, except for the case of small intermodal distance, which tends to be bimodal. Thus, the models are able to predict the distribution of wave periods except for the last case. However, there is an overestimation of both models around the mean period. In the swell dominated case, especially for small and large intermodal distance, the distribution tends to bimodal and none of the models are able to characterize the empirical distribution of wave periods.

Doering and Donelan (1993) extended the model of Longuet-Higgins (1983) by parameterizing the ν parameter of the distribution with respect to Ursell's parameter, extending the applicability of the model to shoaling waters.

Memos (1994) and Memos and Tzanis (2000) presented an approach to extend the formulation of the joint distribution of wave height and period to finite water depth and to shoaling water. While

most models discussed here are applicable to narrow-banded waves, Memos (1994) developed the theory of the joint distribution for deep water waves of any bandwidth. The model accounts explicitly for the correlation between height and period of the waves and for the average wave steepness in a sea state.

From this deep water model, a shallow water model was developed by Memos (1994) and further improved by Memos and Tzanis (2000). This was achieved by employing the wave-by-wave approach used, for example, by Mase and Iwagaki (1982), and Dally (1992). This approach consists in selecting randomly from a deep water distribution of waves a sample of waves, which are then propagated and transformed into shallow water. There the sample is reassembled and the applicable probability distribution is reconstructed. Memos and Tzanis (2000) have extended the approach by accounting for two additional processes: wave breaking and wave reforming after breaking. Measured data from Isobe (1985), Mase (1989) and Kamphuis (1994) have been used to demonstrate the adequacy of the proposed model. The shallow water model was presented in a non-dimensional form depending only on the local depth and bed slope in addition to the parameters required for the deep water formulation.

5. WAVE GROUPS

Wave groups are important for the design of coastal structures. Attention to this problem was raised by Goda (1970) who used linear simulations to demonstrate that ocean waves in a random field are not completely randomly distributed but show a tendency to appear in groups. A wave group is a sequence of consecutive wave heights that exceed a certain threshold level, followed by a sequence of waves that fall below that referred level. Goda (1970) introduced the concept of the length of a total run of waves as the total number of wave heights that occur between the time of first exceedance above a specified threshold value and the time of the first re-exceedance above the same threshold. He assumed that the wave heights are uncorrelated and Rayleigh distributed and derived a probability distribution for the run lengths.

The analysis of wave groups in real sea wave data made by Rye (1982), Goda (1983), Elgar et al. (1984) and Battjes and van Veddler (1984) verified the results of the numerical simulations confirming that the linear theory could be used to properly describe wave groups. However, the probability density functions for the mean run lengths derived by Goda (1970) underestimated the values obtained from numerical simulations and from real sea waves. This was later understood to be the result of the existence of correlation among successive waves. In fact, several results have shown that successive individual waves are not independent. The correlation coefficient was reported to be around 0.20 for sea conditions (Rye, 1974; Arhan and Ezraty, 1978; Su et al., 1982) and about 0.65 for swell (Goda, 1983).

Kimura (1980) introduced a Markov chain hypothesis for the sequence of waves, considering that wave grouping is strongly dependent on the structure of the sea state, as measured by the correlation coefficient between successive wave heights. For a very broad banded spectrum the correlation between waves tends to zero and the results of Kimura (1980) reduce to the ones of Goda (1970). Recent results of Sobey (1996), who analyzed field data, supported the Markov assumption of the Kimura theory.

Wind-wave groups may also be described as a level crossing problem associated with the envelope of a random process (Nolte and Hsu, 1972; Tayfun, 1983). Longuet-Higgins (1984) combined this approach and that of Kimura and related them with the wind-wave spectrum, enhancing the application of both the basic descriptions for evaluating group wave characteristics.

Based on the envelope approach, it is possible to obtain analytical expressions for several variables such as the mean number of exceedances of a certain level, the mean length of wave groups, the

length of a total run of waves, or the average number of successive waves exceeding a specific level. The probability distribution of a number of waves in a group was also derived. Ochi and Sahinoglou (1989a; 1989b) have derived the probability density functions of the time duration associated with wave groups and of the occurrence of the wave groups.

Dawson et al. (1991) conducted a series of experiments on wave groups generated in a laboratory and found that only 25% of the wave crests crossing a threshold level formed a wave group while all others were single crossings.

Goda (1970) showed that the characteristics of wave groups in irregular wave trains are related with a dimensionless spectral peakedness parameter

$$Q_p = \frac{2 \int_0^\infty f \, S(f) \, df}{\left[2 \int_0^\infty S(f) \, df \right]^2} \tag{29}$$

Medina and Hudspeth (1987) proposed a related peakedness parameter

$$Q_e = \frac{2 m_1}{m_0^3} \int_0^\infty S^2(f) \, df \tag{30}$$

and Medina and Hudspeth (1990) showed a functional relationship between the coefficient of the joint Rayleigh distribution of Kimura (1980), the correlation coefficient between successive wave heights with lag m and the peakedness parameters Q_p and Q_e.

The various studies about the correlation of successive waves have concentrated on sea states that are described with spectra of one peak. The relative usefulness of the Kimura model to predict the statistical properties of wave groups in mixed sea states has been examined by Rodriguez et al. (2000), and it was observed that it always overestimates the observed mean run lengths.

In view of the importance that correlation between successive waves has on the description of wave groups, several researchers have addressed this problem. Arhan and Ezraty (1978) developed a theoretical formulation for the joint probability distribution of two successive wave heights. They used as a basis for the development of the joint distribution the work by Rice (1945) on the joint distribution of two lagged values of the envelope of a Gaussian process. Furthermore, they used the bivariate distribution of wave heights and periods presented by Cavanié et al. (1976). Kimura (1980), in relation with the groupiness of sea waves, considered a bivariate Rayleigh distribution to model the joint distribution of successive wave heights.

The joint distribution between successive wave periods has been studied by Myrhaug and Rue (1998). They presented a theoretical expression based on the assumption that the squared wave periods are reasonably well represented by a Rayleigh distribution.

In studying mixed sea states, Rodriguez and Guedes Soares (2001) concluded that the superposition of a swell wave and a wind-sea wave system enhances considerably the correlation between successive wave heights as compared with the single sea state. This fact is also true for consecutive wave periods in the case of a swell dominated sea state.

An extension of the approach of the envelope formulations also consists of using phase information. This can be achieved by representing the waves as the real part of a complex analytical formulation based on the envelope and phase function (Melville, 1983). The use of the Hilbert transformation allows the study of these processes and the identification of wave groups (Hudspeth and Medina, 1988). Cherneva and Velcheva (1993) used this approach to study coastal waves, and Cherneva and Guedes Soares (2001) analyzed storm deep water waves, showing that it is possible to use in both cases the local phase of waves to identify the wave groups.

6. TIME SERIES MODELS OF SEA STATES

The spectral density function describes a stationary random process, which in the case of a wave environment has duration from 20 minutes to few hours. The probability density functions discussed in the previous sections apply to these situations. However, for design and operation purposes, one is interested in having load models that are valid for longer periods. In those time spans the wave and response processes are no longer stationary.

The common practice is to separate the time scales. The periods of stationarity are the short-term ones governed by parameters such as significant wave height and mean period. The medium-term formulations discussed in this section and the long-term formulations described in the following sections describe the probability distribution of these parameters.

Models of long-term time series of sea state parameters are important for the planning of various offshore operations that have durations on the order of several days. In these cases the correlation that exists among the parameters of the successive sea states are very important for the outcome of the operation.

Autoregressive moving average process (ARMA) are a general class of processes that can be used to model wave data. Spanos (1983) used ARMA processes to simulate individual waves in short-term periods of stationarity. Scheffner and Borgman (1992) also simulated individual waves but they took into account the long-term variability. They adopted a piecewise month by month multivariate simulation approach in which the seasonal and the non-stationary changes are imposed by simulating each month separately and using an interpolation scheme to smooth the transition from month to month.

Guedes Soares et al. (1994) and Athanassoulis and Stefanakos (1995) demonstrated that linear autoregressive models can describe adequately time series of significant wave height at a site. These models have been applied to different sites and it was found that the same type of regression model could be applicable in the same geographical area. Models with orders up to 19 were required for a good modeling, although the most significant coefficients were only up to the order 10 (Guedes Soares et al., 1996).

Two main types of problems have to be solved in order to apply these type of models to the long-term series of wave parameters. One has to do with the non-stationarity of the series, in particular with its seasonality, and the other with the gaps in the time series, which sometimes can be relatively long. The seasonality of this type of data was studied by Guedes Soares and Ferreira (1995a) who showed that a Fourier model would describe it appropriately. Even after removing the seasonality the series is not stationary, and thus transformations of the data are required before ARMA models can be applied. Some different options have been considered in Cunha and Guedes Soares (1999).

One of the problems in the time series analysis of wave measurements is the missing values, which present difficulties in the application of linear and nonlinear models to the continuous series. The method used to fill gaps in a time series depends basically on their duration. Hidalgo et al. (1995) developed a method based on appropriate transfer functions in order to fill very long gaps. Smaller gaps are filled forecasting half gap with the model based on observations of the left side of the gap and the other half with the one from the right side. Stefanakos and Athanassoulis (2001) reviewed these types of approaches and applied them to some examples.

In many situations it is not enough to have a description of the significant wave height, but the associated mean period is also necessary. These two parameters of a sea state are positively correlated as demonstrated by several studies. The bivariate autoregressive models proposed by Guedes Soares and Cunha (2000) described the time evolution of the occurrence of such pairs of values taking into account the memory effects that exist in the process.

If interest is in modeling only the first two moments of the series, as occurs in many situations, the linear models are adequate, otherwise nonlinear models may be required. A study of nonlinear

autoregressive models has shown that the improved description provided by these models could only be noticed on the third and fourth statistical moments of the simulated series (Scotto and Guedes Soares, 2000).

7. LONG-TERM MODELS

The single most important parameter describing the severity of the sea states is the significant wave height. Thus, most marginal long-term parametric distributions describing the sea state are based on this variable. The interest of fitting parametric models to H_s data can be two-fold. On one hand, adopting a parametric model to fit the data is the means of smoothing the frequency histogram and providing appropriate functional descriptions of it. On the other hand, fitting a model may allow extrapolation outside the range of the data by calculating return values corresponding to high probability quantiles.

To fit H_s data the log-normal distribution was one of the first of the distributions to be proposed (Jasper, 1956). Later, Guedes Soares et al. (1988) found it adequate to model the long-term trends of significant wave height. However, this is true for the lower and moderate wave heights, which are the most important ones from the point of view of fatigue design of structures.

A better fit of the upper tail can be obtained by the Weibull distribution as shown by Battjes (1972). This distribution, although being better in the range of extreme waves is not so good for the lower wave heights, which led Haver (1985) to propose combining the log-normal and the Weibull distributions to provide a complete description of the whole range of significant wave heights.

For design purposes it is often necessary to estimate values of very low probability of occurrence. In some cases, the long-term distribution of H_s fit to the initial wave data has also been used to predict the occurrence of extreme values using the concept of return period, which can be related to the reference lifetime of interest, as discussed by Borgman (1963).

The log-normal and Weibull distribution functions have been used frequently to model H_s data. However, when estimating return values with a low probability level they are not very good models, as often the log-normal distribution overestimates, and the Weibull distribution underestimates the true return values.

Other possibilities are the Generalized Gamma distribution proposed by Ochi (1992) who showed that it gives a better graphical fit than both the log-normal and Weibull distributions. Ferreira and Guedes Soares (1999) have used Beta distributions, showing that they are more flexible than the other distributions.

The use of the statistical tests of fit to distinguish between the quality of fit of competing distributions is often not robust enough with this type of data, in which the concern is often with the tails of the distribution. This has been demonstrated with some examples in Guedes Soares and Ferreira (1995b). Therefore, from the point of view of return values estimation, it is necessary to have an extra reason for deciding whether a particular model is appropriate or not. Extreme Value Theory provides such an extra reason based on asymptotic distributional results about some of maxima over fixed periods and exceedances over high thresholds. Several authors have recommended or used Extreme Value Theory by applying the Annual Maxima Method to wave data (for example, Thom, 1971; Carter and Challenor, 1983; Muir Langley and El-Shaarawi, 1986).

The Peaks Over Threshold (POT) method (Davison and Smith, 1990) provides a more modern and soundly based solution to extrapolation problems (Elsinghorst et al., 1998; Ferreira and Guedes Soares, 1998). The method is particularly suited for dealing with realizations of a stochastic process, which is approximately stationary or can be split into stationary parts. It consists of fitting the Generalized Pareto distribution to the peaks of clustered excesses over a threshold—defined as the amounts by which observations exceed a given threshold—and calculating return values by taking into account

the average number of clusters. The rationale behind the procedure is that (i) if the threshold level is taken high enough, the distribution of the peak excesses is expected to be close to one among only three forms of the Generalized Pareto distribution; (ii) observations, in particular cluster peaks, belonging to different clusters are expected to be independent. While (i) avoids the choice of arbitrary models, (ii) ensures that the fundamental concept of return value is applicable.

Adopting different models for predicting the most likely maximum value during the structure's lifetime will yield significant differences in the predicted design values as pointed out by Earle and Baer (1982), Wang and Le Mehaute (1983), van Vledder et al. (1993) and Guedes Soares and Scotto (2001).

While the uncertainty involved in the choice of the different methods of extrapolation can be classified as a model uncertainty (Guedes Soares, 1989; Bitner-Gregersen and Hagen, 1990), the one that is involved in the statistical procedures to assess which probabilistic model describes a given population is called the statistical uncertainty. The statistical uncertainty can result from the choice of the population sample that is chosen to represent it or from the estimation of the parameters from the samples. The first aspect was studied for North Atlantic wave data, by comparing the predictions based on large samples of visual data and measurements (Guedes Soares and Viana, 1988) or by including hindcast data (Guedes Soares and Trovão, 1991). The samples had typical sizes of 10 to 20 years and significant differences in the return values were obtained. On the second aspect, Guedes Soares and Henriques (1996) compared three methods of fitting distributions to data, namely the methods of moments of least squares and of maximum likelihood. It was shown that often the method of moments was yielding different fits than the other two methods, and thus it should be avoided not withstanding its greater simplicity.

The uncertainty in the estimation of the values of return periods may also be associated with the size of the database used to fit the distribution as related to the period of concern. Using too short databases will lead to large variability, as shown by Guedes Soares (1986).

Another important issue in applying a probabilistic model to describe a population is the definition of the population under consideration and its samples. Guedes Soares and Nolasco (1992) argued that the current practice of pooling all type of wave data before fitting a distribution will combine data from populations with different characteristics. They have separated a data set from a coastal station into samples with single wave systems and with combined sea states, both swell dominated and wind-sea dominated showing that they are all described by different probabilistic models. This argument was further pursued by Guedes Soares and Henriques (1996), where it was noted that monthly data sets will be described by slightly different probabilistic models, which can be pooled in different seasonal data sets. The variability of the distributions fit to yearly data was shown to exist although it was smaller than the seasonal differences (Guedes Soares and Henriques, 1994).

The variability among years of the data of the same season was analyzed by Guedes Soares and Ferreira (1995b) based on the data from a location on the coast of Portugal. It was found that the data sets were statistically different, and thus, being from different populations they should not be pooled together. It appears, therefore, that pooling all wave data and fitting one probabilistic model may not be strictly correct from a statistical point of view. Furthermore, the choice of a parametric distribution to fit the data also introduces additional uncertainties. To cope with this situation Ferreira and Guedes Soares (2000) proposed a parametric model for the long-term data, which uses the Box-Cox transformation (Box and Cox, 1964) to transform the data set to a normal one, which is then fit by a normal distribution. It considers that the yearly populations have random properties and the transformation should be applied to each yearly data set. In this way the variability of the Box-Cox parameters would reflect the yearly variability of the data while the normal distribution of the transformed data would represent the variability of the wave parameters.

The long-term distributions of individual wave heights or of corresponding responses are obtained by considering that at a random point in time the variance of the sea state is itself a random variable

with a marginal density function $f_R(r)$ which depends only on the joint distribution of wave parameters just mentioned. Thus, the marginal distribution of sea state elevation is obtained by weighting the conditional distribution of amplitudes by the probability density function of the variances

$$Q_L(x) = \int_0^\infty Q_s(x|r) f_r(r) w(r) dr \qquad (31)$$

where $w(r)$ is a weighting factor that accounts for the relative number of peaks in each sea state and Q_s is a short-term distribution, conditional on the variance r. As discussed in Section 2, these distributions can be Rayleigh or any of the others discussed in that section.

Other methods have been used to obtain extreme values of significant wave height as described in various review papers (Nolte, 1973; Isaacson and Mackenzie, 1981; Muir Langley and El-Shaarawi, 1986). One method of extrapolation uses the most probable maximum wave height in each sea state and makes extrapolations based on these values instead of using the H_s. One problem of this approach as well as of the first one discussed is that in using all sea states the successive sea states are not independent. To avoid the problem of correlation between successive sea states one may use the annual maxima of wave height, which are then fitted by a Gumbel distribution. In fact one year is the period of climatological and environmental processes, which implies that yearly maxima should be statistically independent.

Still a different procedure that has been adopted is to extrapolate the sea state parameters based on the assumption that the largest wave will occur during the most severe sea state. Once the sea state parameters H_s and T_m are determined, the largest wave to occur in that sea state is determined from a short-term model.

A last model described in the literature reviews is the extrapolation based on storms. Storms in a given location are assumed to be independent events occurring with a constant arrival rate, which can be described by a Poisson process. A storm is modeled as a succession of sea states with increasing H_s up to a maximum value after which they decrease again. In this case, the extrapolation is made associating the Poisson model of storm occurrence with the maximum wave height in each storm.

The storm or event approach, which should not be confused with the POT method, is preferred in cases in which the weather is very calm most of the time, and there are few very intense events, such as for example in the Gulf of Mexico. In these cases it is often preferred to model the rate of occurrence of events such as hurricanes together with the probability of maximum waves in hurricanes such as proposed by Petruaskas and Aagaard (1970) or Jahns and Wheeler (1972).

When applying different methods to a specific problem very large scatter in the results are produced, as shown by Guedes Soares (1989). One possible way to deal with the problem is for the whole industry to adopt as a standard one of these methods and then calibrate the design process using its predictions. Another alternative is to use the information provided by all methods and combine them in a Bayesian way, using the opinions of experts to properly give weight to the different methods (Kerstens et al., 1988; Guedes Soares, 1989). This procedure, although not improving the accuracy of the estimation, will decrease the risk of choosing a wrong value and will decrease the model uncertainty of the estimate.

This section has discussed the long-term distributions as tools to extrapolate the wave conditions to some return value of interest to design. However, in several applications no extrapolation is needed and information is only required of the probability of occurrence of some defined conditions. For this purpose, it is not required to fit a parametric model to the data and one may resort to use it directly, although smoothed. Guedes Soares and Ferreira (1995b) and Ferreira and Guedes Soares (1999; 2000) discussed this problem and suggested that a good alternative would be to use the Kernel of the distribution, which can be smoothed by different schemes. This approach would not introduce unnecessarily any tendency on the data as might happen when fitting a parametric model to it.

The long-term models discussed here have contemplated data from one location. Very often one is interested in characterizing a wider region in which there is more than one measuring station. Using a much larger data set including samples from positions spatially distributed allows better confidence in the models estimated. It may also allow the identification of the space in which a given probabilistic model is applicable.

Regional analysis has been used for some time in hydrology and a good account is given by Hosking and Wallis (1997). van Gelder et al. (1999) used regional analysis to study the maximum sea level data from the North Sea, while van Gelder et al. (2000) and Goda et al. (2000) applied regional analysis to determine extremes of significant wave heights.

8. JOINT LONG-TERM MODELS

Although the long-term distributions of H_s provide a probabilistic description of the sea state severity, for many applications this description is too crude. Often it is necessary to describe also the associated mean period and direction. On other occasions joint distributions of waves and storm surges are required or joint distributions of waves, wind and current. Different approaches have been developed for specific applications, but possibly the most widely used is the conditional modeling approach in which the joint density function is defined in terms of a marginal distribution and a series of conditional density functions modeled by parametric functions that are fitted to the conditioned data by some form of estimation process.

The single most used joint distributions of wave parameters are the bivariate probability density functions of H_s and T_m which are available for different areas of the ocean and coastal areas. Most wave data banks provide information of the scatter diagram at a point, although some also provide directional information. In this case, it is normal that a scatter diagram is given for each of eight directional sectors. Thus, one has

$$f(H_s, T_m, \theta) = f(H_s, T_m | \theta) f(\theta) \tag{32}$$

where θ indicates the directional sector.

Normally the bivariate distribution of significant wave height and mean period is constructed from a conditional distribution of average or peak periods and a marginal distribution of significant wave height

$$f_{H_s T_m}(h, t) = f_{H_s}(h) f_{T_m | H_s}(t | h) \tag{33}$$

The distributions of wave period conditional on significant wave height have been shown to be well modeled by a log-normal distribution (Haver, 1985; Guedes Soares et al., 1988). Thus, a joint model can be approximated by the 3-parameter Weibull distribution for significant wave height

$$f_{H_{m0|\theta}}(h | \theta_1) = \frac{\beta}{\alpha} \left(\frac{h_{m0} - \gamma}{\alpha} \right)^{\beta - 1} \exp\left(-\left(\frac{h_{m0} - \gamma}{\alpha} \right)^{\beta} \right) \tag{34}$$

where α, β and γ are the scale, shape and location parameters, and θ is the main wave direction. The conditional log-normal distribution for the peak wave period given the significant wave height is

$$f_{T_p | H_{m0|\theta}}(t_p | h, \theta_i) = \frac{1}{\sqrt{2\pi} \sigma t_p} \exp\left[-\frac{(\ln t_p - \mu)^2}{2\sigma^2} \right] \tag{35}$$

where

$$\mu = E(\ln T_p) = a_t + a_2 h_{m0}^{a_3} \tag{36}$$

$$\sigma = Std\left(\ln T_p\right) = b_1 + b_2 e^{b_3 h_{m0}} \tag{37}$$

The parameters a_1, a_2, a_3, b_1, b_2 and b_3 are determined from the data. The estimation of these parameters is sometimes problematic, as few observations exist in some ranges of the variables, especially in the tails.

An alternative approach to conditional modeling has been to adopt different ways to transform the data to a multivariate normal, which is then fit by that model. Ochi (1978) used an exponential transformation to model a bivariate log-normal distribution to the H_s, T_z data. This transformation allows avoiding the use of conditional distributions and a single bivariate distribution is used for the whole sample. Prince-Wright (1995) used an extended version of a Box-Cox transformation to fit this joint distribution, where the additional parameter aimed at improving the fit in the tails. Bitner-Gregersen et al. (1998) compared the fits using this approach and the conditional modeling formulation and obtained fairly similar patterns for moderate wave heights.

Within the line of data transformation, Ferreira and Guedes Soares (2002) noticed that there was a non-negligible variability among the yearly data sets and this led to the proposal of considering random yearly populations. Thus, each yearly sample is transformed into a normal variable using appropriate Box-Cox transformation parameters for H_s and T_z. The variability of these parameters reflects the yearly variability of the data. The transformed data is then fit by a bivariate normal distribution.

Athanassoulis et al. (1994) proposed a different type of transformation. They adopted the Plackett bivariate model, which although not being completely general, allows the specification of any two marginal distributions and leaves the subsequent modeling of the dependence structure to be made with the estimation of a parameter related to the correlation between the variables.

The joint models of Ochi (1978), Athanassoulis et al. (1994), Prince-Wright (1995), and Ferreira and Guedes Soares (2002), and the Conditional Modeling Approach, for example, of Bitner-Gregersen and Haver (1989), utilized the complete probabilistic information obtained from simultaneous observations of the environmental variables. In some cases, only the marginal distributions for a set of stochastic variables are given, and information about the dependencies between the variables exist in terms of a correlation matrix R. For these cases Bitner-Gregersen and Hagen (1999) proposed to use a consistent and simple formulation based on the Nataf correlation model (Der Kiureghian and Liu, 1986). The Nataf model gives a good approximation for the distribution of the physical variables if the vector of the transformed standard normal variables is close to being multi-normal. It requires the first four statistical moments of each of the two variables in the joint distribution as well as the correlation between the variables.

An alternative to the joint distribution of H_s and T_z or T_p is to consider the joint distribution of H_s and a representative wave steepness parameter. Repko et al. (2000) compared some of the models described here with a joint distribution of H_s and a peak steepness defined as

$$s_p = \frac{2\pi H_s}{g T_p^2} \tag{38}$$

which was proposed by Vrijling and Bruinsma (1980), and concluded that the last approach provided better agreement with the data.

A related parameter, the average wave steepness was adopted by Bitner-Gregersen et al. (1998) and Bitner-Gregersen and Hagen (1999), showing that in different wave data sets the extreme values of the mean steepness decreased with increasing return period both for offshore and coastal data.

Although only bivariate models of H_s and one of the representative wave periods have been considered in this section, other joint models are possible and available. In general, the conditional modeling approach is very flexible for extension to any number of variables, but the drawback is that sometimes the number of observations in each of the conditioned distributions may be too small.

Reference is made to Bitner-Gregersen and Guedes Soares, (1997) for a review of some other applications.

9. CONCLUSION

From this review chapter it can be concluded that since wave fields are described by stochastic models, it is possible to describe them both in the frequency and in the time domains. While the focus of past research has been mainly on Gaussian waves in deep water it should, nevertheless, be emphasized that the characteristics of waves in finite water depths are substantially different than those in deep water in that the probability distribution is non-Gaussian as discussed mainly in Section 3. Refinements to the various models will continue in order to provide solutions to different problems, and to meet required design and engineering considerations.

ACKNOWLEDGMENTS

LIST OF SYMBOLS

SSER	—	Double Peaked Spectrum, Sea-Swell Energy Ratio, (equation (1))
m_n	—	n-th spectral moment, (equation (2))
$s(f)$	—	wave spectrum
f	—	wave frequency
sw	—	swell (subscript), (equation (2))
ws	—	wind-sea (subscript), (equation (2))
f_p	—	peak frequency
ID	—	Double Peaked Spectrum, Intermodal Distance, (equation (3))
σ_η^2	—	variance of sea surface elevation, (equation (4))
$\eta(t)$	—	sea surface elevation, (equation (4))
R	—	Rayleigh parameter, (equations (5), (6))
μ_x	—	mean value
σ_x^2	—	variance
$\bar{x}_{1/n}$	—	mean of the $1/n$-th highest observation
erf	—	error function
H_s	—	significant wave height
ε	—	spectral bandwidth, (equation (12))
Φ	—	standard normal distribution
x_n	—	maximum of n observations
γ	—	peak enhancement factor for JONSWAP spectrum
$\rho(t)$	—	normalized autocorrelation function for time lag t
$R(t)$	—	autocorrelation function for time lag t
H	—	wave height
T	—	wave period

υ	—	spectral bandwidth, (equation (9))
$\overline{T}$	—	mean wave period
τ	—	non-dimensional period
$\overline{\zeta}$	—	bandwidth function, (equation (24))
κ	—	Kimura correlation parameter
ρ	—	Kimura correlation coefficient
τ_c	—	cross-over point, (equation (28))
T_m	—	mean wave period
$Q_L(x)$	—	long-term probability of exceedance of x
$w(r)$	—	normalization factor
$Q_s(x)$	—	short-term probability of exceedance of x
r	—	sea state variance, (equation (31))
θ	—	wave direction
α	—	scale parameter
β	—	shape parameter
T_p	—	peak period
h	—	threshold level
s_p	—	peak steepness, (equation (38))
Q_e	—	Medina and Hudspeth spectral peakedness parameter, (equation (30))
Q_p	—	Goda spectral peakedness parameter, (equation (29))

REFERENCES

Ahn, K., 1998. Statistical distribution of wave heights in finite water depth. Proceedings of the 26th International Conference on Coastal Engineering, ASCE, pp. 533–544.

Arhan, M., and Ezraty, R., 1978. Statistical relations between successive wave heights. Oceanologica Acta, 1 (2): 151–158.

Arhan, M.F., and Plaisted, R.O., 1981. Nonlinear deformation of sea wave profiles in intermediate and shallow water. Oceanology Acta, 2: 107–115.

Athanassoulis, G.A., Skarsoulis, E.K., and Belibassakis, K.A., 1994. Bivariate distributions with given marginals with an application to wave climate description. Applied Ocean Research, 16: 1–17.

Athanassoulis, G.A., and Stefanakos, C.N., 1995. A nonstationary stochastic model for long-term time series of significant wave height. Journal of Geophysical Research, 100 (8): 16,149–16,162.

Battjes, J.A., 1972. Long-Term wave height distributions at seven stations around the British Isles. Deutsche Hydrographische Zeitschrift, 25: 179–189.

Battjes, J., and van Vledder, G., 1984. Verification of Kimura's Theory for wave group statistics. Proceedings of the 19th International Conference on Coastal Engineering, ASCE, pp. 642–648.

Bitner, E.M., 1980. Non-linear effects of the statistical model of shallow-water wind waves. Applied Ocean Research, 2 (2): 63–73.

Bitner-Gregersen, E.M., and Guedes Soares, C., 1997. Overview of Probabilistic models of the wave environment for reliability assessment of offshore structures. In: Guedes Soares, C. (Editor), Advances in Safety and Reliability. New York: Pergamon, pp. 1445–1456.

Bitner-Gregersen, E.M., Guedes Soares, C., Machado, U., and Cavaco, P., 1998. Comparison of different approaches to joint environmental modelling. Proceedings of the 17th International Conference on Offshore Mechanics and Arctic Engineering, ASME, New York, Vol. II.

Bitner-Gregersen, E.M., and Hagen, O., 1990. Uncertainties in data for the offshore environment. Structural Safety, 7: 11–34.

Bitner-Gregersen, E.M., and Hagen, O., 1999. Extreme value analysis of wave steepness and crest using joint environmental description. Proceedings of the 18th International Conference on Offshore Mechanics and Arctic Engineering, ASME, Paper OMAE99-6033.

Bitner-Gregersen, E.M., and Haver, S., 1989. Joint long term description of environmental parameters for structural response calculation. Proceedings of the 2nd International Workshop on Wave Hindcasting and Forecasting.

Borgman, L.E., 1963. Risk criteria. Journal of the Waterways and Harbors Division, ASCE, 89 (WW3): 1–35.

Bouws, E., Günther, H., Rosenthal, W., and Vincent, C.L., 1985. Similarity of the wind wave spectrum in finite depth water 1. Spectral form. Journal of Geophysical Research, 90 (C1): 975–986.

Box, G.E.P., and Cox, D.R., 1964. An analysis of transformations. Journal of the Royal Statistical Society, 26, Series B: 211–252.

Carter, D.J.T., and Challenor, P.G., 1983. Methods of fitting the Fisher-Tippett Type 1 extreme value distribution. Ocean Engineering, 10: 191–199.

Cartwright, D.E., and Longuet-Higgins, M.S., 1956. The statistical distribution of the maxima of a random function. Proceedings of the Royal Society London, 237, Series A: 212–232.

Cavanié, A.G., Arhan, M.F., and Ezraty, R.S., 1976. A statistical relationship between individual heights and periods of storm waves. Proceedings of the BOSS'76 Conference, Norwegian Institute of Technology, Trondheim, pp. 354–360.

Chakrabarti, S.K., and Cooley, R.P., 1977. Statistical distribution of periods and heights of ocean waves. Journal of Geophysical Research, 82 (9): 1363–1368.

Cherneva, Z., and Guedes Soares, C., 2001. Local non-stationary properties of the wind wave groups. Proceedings of the Conference on Design and Operation for Abnormal Conditions II (RINA), London, pp. 137–145.

Cherneva, Z., and Velcheva, A., 1993. Wave group analyses based on phase properties. 1st International Conference on the Mediterranean Coastal Environment (MEDCOAST 93), pp. 1213–1220.

Cieslikiewicz, W., 1990. Determination of the probability distribution of wind waves using the maximum-entropy principle. In: Torum, A., and Gudmestad, O.T. (Editors), Water Wave Kinematics, pp. 345–348. The Netherlands: Kluwer Academic Publishers.

Cieslikiewicz, W., 1998. Maximum-entropy probability distribution of free-surface elevations of wind-generated coastal waves. Proceedings of the 26th International Conference on Coastal Engineering, ASCE, pp. 1155–1168.

Cunha, C., and Guedes Soares, C., 1999. On the choice of data transformation for modelling time series of significant wave height. Ocean Engineering, 26: 489–506.

Dally, W.R., 1992. Random breaking waves: Field verification of a wave-by-wave algorithm for engineering application. Coastal Engineering, 16: 369–397.

Davison, A.C., and Smith, R.L., 1990. Models for exceedances over high thresholds. Journal of the Royal Statistical Society, 52 (3), Series B: 393–442.

Dawson, T.H., Kriebel, D.L., and Wallendorf, L.A., 1991. Experimental study of wave groups in deep-water random waves. Applied Ocean Research, 13 (3): 116–131.

Der Kiureghian, A., and Liu, P.L., 1986. Structural reliability under incomplete reliability calculations. Journal of Engineering Mechanics, 112 (1): 85–104.

Doering, J.C., and Donelan, M.A., 1993. The joint distribution of heights and periods of shoaling waves. Journal of Geophysical Research, 98 (7): 12,543–12,555.

Donelan, M.A., Hamilton, J., and Hui, W.H., 1985. Directional spectra of wind-gathered waves. Philosophical Transactions of the Royal Society, London, A-315: 509–562.

Earle, M.D., and Baer, L., 1982. Effects of uncertainties on extreme wave heights. Journal of Waterway, Port, Coastal and Ocean Engineering, 108 (WW4): 456–478.

Earle, M.D., Ebbesmeyer, C.C., and Evans, D.J., 1974. Height-period joint probabilities in Hurricane Camille. Journal of the Waterway, Harbors and Coastal Engineering Division, 100 (WW3): 257–265.

Elgar, S., Guza, R., and Seymour, R., 1984. Groups of waves in shallow water. Journal of Geophysical Research, 89 (3): 3623–3634.

Elsinghorst, C., Groeneboom, P., Jonathan, P., Smulders, L., and Taylor, P.H., 1998. Extreme value analysis of North Sea storm severity. Journal of Offshore Mechanics and Arctic Engineering, 120: 177–183.

Ewans, K.C., and Kibblewhite, A.C., 1990. An examination of fetch-limited wave growth off the west coast of New Zealand by a comparison with the JONSWAP results. Journal of Physical Oceanography, 20 (9): 1278–1296.

Ferreira, J.A., and Guedes Soares, C., 1998. An application of the peaks over threshold method to predict extremes of significant wave height. Journal of Offshore Mechanics and Arctic Engineering, 120 (3): 165–176.

Ferreira, J.A., and Guedes Soares, C., 1999. Modelling the long-term distribution of significant wave height with the Beta and Gamma models. Ocean Engineering, 26: 713–725.

Ferreira, J.A., and Guedes Soares, C., 2000. Modelling distributions of significant wave height. Coastal Engineering, 40: 361–374.

Ferreira, J.A., and Guedes Soares, C., 2002. Modelling bivariate distributions of significant wave height and mean wave period. Applied Ocean Research, 24 (1): 31–45.

Forristall, G.Z., 1978. On the statistical distribution of wave heights in a storm. Journal of Geophysical Research, 83 (C5): 2353–2358.

Forristall, G.Z., 1981. Measurements of a saturated range in ocean wave spectra. Journal of Geophysical Research, 86: 8075–8084.

Forristall, G.Z., 1984. The distribution of measured and simulated wave heights as a function of spectral shape. Journal of Geophysical Research, 89 (C6): 10,547–10,552.

Gentile, R., Lando, L.R., and Scarsi, G., 1994. Design wave on finite depth: A re-analysis of the TMA model. Proceedings of the 13th International Conference on Offshore Mechanics and Arctic Engineering, ASME, 2, pp. 49–56.

Goda, Y., 1970. Numerical experiments on wave statistics with spectral simulation. Report of Research Institute of Port and Harbor, Japan, 9: 3–57.

Goda, Y., 1975. Irregular wave deformation in the surf zone. Coastal Engineering, Japan, 18: 13–26.

Goda, Y., 1978. The observed joint distribution of periods and heights of sea waves. Proceedings of the 16th International Conference on Coastal Engineering, ASCE, New York, pp. 227–246.

Goda, Y., 1983. Analysis of wave grouping and spectra of long-travelled swell. Report of Research Institute of Port and Harbor, Japan, 22: 3–41.

Goda, Y., Konagaya, O., Takeshita, N., Hitomi, H., and Nagai, T., 2000. Population distribution of extreme wave heights estimated through regional analysis. Proceedings of the 27th International Conference on Coastal Engineering, ASCE, pp. 1078–1091.

Guedes Soares, C., 1984. Representation of double-peaked sea wave spectra. Ocean Engineering, 11: 185–207.

Guedes Soares, C., 1986. Assessment of the uncertainty in visual observations of wave height. Ocean Engineering, 13 (1): 37–56.

Guedes Soares, C., 1989. Bayesian prediction of design wave heights. In: Thoft-Christensen, P. (Editor), Reliability and Optimization of Structural Systems'88, pp. 311–323. New York: Springer-Verlag.

Guedes Soares, C., 1991. On the occurrence of double peaked wave spectra. Ocean Engineering, 18 (1/2): 167–171.

Guedes Soares, C., and Caires, S., 1995. Changes in spectral shape due to the effect of finite water depth. Proceedings of the 14th International Conference on Offshore Mechanics and Arctic Engineering, ASME, pp. 547–556.

Guedes Soares, C., and Carvalho, A.N., 2001. Probability distributions of wave heights and periods in measured two-peaked spectra from the Portuguese coast. Proceedings of the 20th International Conference on Offshore Mechanics and Arctic Engineering, ASME, Paper OMAE2001/S&R-2178.

Guedes Soares, C., and Cunha, C., 2000. Bivariate autoregressive models for the time series of significant wave height and mean period. Coastal Engineering, 40: 297–311.

Guedes Soares, C., and Ferreira, A.M., 1995a. Analysis of the seasonality in non-stationary time series of significant wave height. In: Spanos, P.D. (Editor), Computational Stochastic Mechanics, pp. 559–578. The Netherlands: A.A. Balkema.

Guedes Soares, C., and Ferreira, J.A., 1995b. Modelling long-term distributions of significant wave height. Proceedings of the 14th International Conference on Offshore Mechanics and Arctic Engineering, ASME, New York, pp. 51–61.

Guedes Soares, C., Ferreira, A.M., and Cunha, C., 1994. Auto-Regressive model for the long term series of significant wave height in the Portuguese Coast. In: Seabra, F.J., and Temperville, A. (Editors), Modelling of Coastal and Estuarine Processes, pp. 59–70. Coimbra.

Guedes Soares, C., Ferreira, A.M., and Cunha, C., 1996. Linear models of the time series of significant wave height in the southwest coast of Portugal. Coastal Engineering, 29: 149–167.

Guedes Soares, C., and Henriques, A.C., 1994. Long term predictions of significant wave heights at Sines and Faro. Proceedings of the LITTORAL'94 Conference, pp. 343–356.

Guedes Soares, C., and Henriques, A.C., 1996. Statistical uncertainty in long-term distributions of significant wave height. Journal of Offshore Mechanics and Arctic Engineering, 11: 284–291.

Guedes Soares, C., Lopes, L.C., and Costa, M., 1988. Wave climate modelling for engineering purposes. In: Schrefer and Zienkiewicz (Editors), Computer Modelling in Ocean Engineering, pp. 169–175. The Netherlands: A.A. Balkema Publishers.

Guedes Soares, C., and Nolasco, M.C., 1992. Spectral modelling of sea states with multiple wave systems. Journal of Offshore Mechanics and Arctic Engineering, 114: 278–284.

Guedes Soares, C., Rodriguez, G.R., Cavaco, P., and Ferrer, L., 2000. Experimental study on the interaction of wave spectra and currents. Proceedings of the 19th International Conference on Offshore Mechanics and Arctic Engineering, ASME, New York, Paper OMAE2000/S&R - 6133.

Guedes Soares, C., and Scotto, M.G., 2001. Modelling uncertainty in long-term predictions of significant wave height. Ocean Engineering, 28: 329–342.

Guedes Soares, C., and Trovão, M.F.S., 1991. Influence of wave climate modelling on the long term prediction of wave induced responses of ship structures. In: Price, W.C., and Memarel, P. (Editors), Dynamics of Marine Vehicles and Structures in Waves, pp. 1–10. Amsterdam, The Netherlands: Elsevier Science Publishers.

Guedes Soares, C., and Viana, P.C., 1988. Sensitivity of the response of marine structures to wave climatology. In: Schrefer and Zienkiewicz (Editors), Computer Modelling in Ocean Engineering, pp. 487–492. The Netherlands: A.A. Balkema Publishers.

Hansen, C., Katsaros, K.B., Kitaigorodskii, S.A., and Larsen, S.E., 1990. The dissipation range of wind-wave spectra observed on a lake. Journal of Physical Oceanography, 20: 1264–1277.

Hasselmann, K., Barnett, T.P., Bouws, E., Carlson, H., Cartwright, D.E., Enke, K., Ewing, J.A., Gienapp, H., Hasselmann, D.E., Kruseman, P., Meerburg, A., Müller, P., Olbers, D.J., Richter, K., Sell, W., and Walden, H , 1973. Measurements of wind-wave growth and swell decay during the joint North Sea wave project (JONSWAP). Deutsche Hydrographische Zeitschrift, A12: 1–95.

Haver, S., 1985. Wave climate off northern Norway. Applied Ocean Research, 7 (2): 85–92.

Hedges, T.S., Anastasiou, K., and Gabriel, D., 1985. Interaction of random waves and currents. Journal of Waterway, Port, Coastal and Ocean Engineering, 111 (6): 275–288.

Hidalgo, O.S., Nieto Borge, J.C., Cunha, C., and Guedes Soares, C., 1995. Filling missing observations in time series of significant wave height. Proceedings of the 14th International Conference on Offshore Mechanics and Arctic Engineering, ASME, pp. 9–17.

Hosking, J.R.M., and Wallis, J.R., 1997. Regional Frequency Analysis: An Approach Based on L-Moments. Cambridge, UK: Cambridge University Press.

Huang, N.E., Chen, D.T., Tung, C.C., and Smith, J.R., 1972. Interactions between steady non-uniform currents and gravity waves with application for current instruments. Journal of Physical Oceanography, 2: 420–431.

Huang, N.E., Long, S.R., Tung, C.-C., Yuan, Y., and Bliven, L.F., 1981. A unified two-parameter wave spectral model for a general sea state. Journal of Fluid Mechanics, 112: 203–224.

Huang, N.E., Long, S.R., Tung, C.-C., Yuan, Y., and Bliven, L.F., 1983. A non-Gaussian statistical model for surface elevation of nonlinear random wave fields. Journal of Geophysical Research, 88 (C12): 7597–7606.

Hudspeth, R.T., and Medina, J.R., 1988. Wave groups analyses by the Hilbert transform. Proceedings of the 21st International Conference on Coastal Engineering, ASCE, pp. 884–898.

Hughes, S.A., and Borgman, L.E., 1987. Beta-Rayleigh distribution for shallow water wave heights. Proceedings of the ASCE Special Conference on Coastal Hydrodynamics, pp. 1211–1231.

Isaacson, M., and Mackenzie, N.G., 1981. Long-term distributions of ocean waves: A review. Journal of Waterway, Port, Coastal and Ocean Engineering, 107 (WW2): 93–109.

Isobe, M., 1985. Calculation and application of first-order Cnoidal wave theory. Coastal Engineering, 9: 309–325.

Jahns, H.O., and Wheeler, J.D., 1972. Long-term wave probabilities based on hindcasting of severe storms. Proceedings of the Offshore Technology Conference, pp. 739–756.

Jasper, N.H., 1956. Statistical distribution patterns of ocean waves and of wave-induced ship stresses and motions, with engineering applications. Transactions of the Society of Naval Architects and Marine Engineers, pp. 375–432.

Kamphuis, J.W., 1994. Wave height from deep water through breaking zone. Journal of Waterway, Port, Coastal and Ocean Engineering, 120 (4): 347–367.

Kerstens, J.G.M., Pacheco, L.A., and Edwards, G., 1988. A Bayesian method for the estimation of return values of wave heights. Ocean Engineering, 15 (2): 153–170.

Kimura, A., 1980. Statistical properties of random wave groups. Proceedings of the 17th International Conference on Coastal Engineering, ASCE, pp. 2955–2973.

Kitaigorodskii, S.A., 1983. On the theory of the equilibrium range in the spectrum of wind-generated gravity waves. Journal of Physical Oceanography, 13: 816–827.

Kitaigorodskii, S.A., Krasitski, V.P., and Zaslavski, M.M., 1975. On Phillips theory of equilibrium range in the spectra of wind-generated gravity waves. Journal of Physical Oceanography, 5: 410–420.

Kuo, C.T., and Kuo, S.J., 1975. Effect of wave breaking on statistical distribution of wave heights. Proceedings of Civil Engineering in the Oceans Conference, ASCE, pp. 1211–1231.

Langley, R.S., 1987. A statistical analysis of non-linear random waves. Ocean Engineering, 14 (5): 389–407.

Lindgren, G., and Rychlik, I., 1982. Wave characteristic distributions for Gaussian Waves—Wavelength, amplitude and steepness. Ocean Engineering: 411–432.

Longuet-Higgins, M.S., 1952. On the statistical distribution of the heights of sea waves. Journal of Marine Research, XI (3): 245–266.

Longuet-Higgins, M.S., 1963. The effect of non-linearities on statistical distributions in the theory of sea waves. Journal of Fluid Mechanics, 17 (3): 459–480.

Longuet-Higgins, M.S., 1975. On the joint distribution of the periods and amplitudes of sea waves. Journal of Geophysical Research, 80 (18): 2688–2694.

Longuet-Higgins, M.S., 1980. On the distribution of the heights of sea waves: Some effects of non-linearity and finite band width. Journal of Geophysical Research, 85 (C3): 1519–1523.

Longuet-Higgins, M.S., 1983. On the joint distribution of wave periods and amplitudes in a random wave field. Proceedings of the Royal Society London, 389, Series A: 241–258.

Longuet-Higgins, M.S., 1984. Statistical properties of wave groups in a random sea state. Philosophical Transactions of the Royal Society, London, 312, Series A: 219–250.

Longuet-Higgins, M.S., and Stewart, R.W., 1962. Radiation stress and mass transport in gravity waves with application to surf beats. Journal of Fluid Mechanics, 13: 481–504.

Marthisen, T., and Winterstein, S.R., 1992. On the skewness of random surface waves. Proceedings of the 2nd International Offshore and Polar Engineering Conference, pp. 472–478.

Mase, H., 1989. Groupiness factor and wave height distribution. Journal of Waterway, Port, Coastal and Ocean Engineering, 115 (1): 105–124.

Mase, H., and Iwagaki, Y., 1982. Wave height distributions and wave grouping in surf zone. Proceedings of the 18th International Conference on Coastal Engineering, ASCE, pp. 58–67.

Massel, S.R., and Sobey, R.J., 2000. Distribution of the highest wave in a record. Coastal Engineering Journal, 42 (2): 153–173.

Medina, J.R., and Hudspeth, R.T., 1987. Sea states defined by wave height and period functions. Proceedings of the 22nd IAHR Congress—IAHR Seminar Wave Analysis and Generation in Laboratory Basins.

Medina, J.R., and Hudspeth, R.T., 1990. A review of the analyses of ocean wave groups. Coastal Engineering, 14: 515–542.

Melville, W.K., 1983. Wave modulation and breakdown. Journal of Fluid Mechanics, 128: 489–506.

Memos, C.D., 1994. On the theory of the joint probability of heights and periods of sea waves. Coastal Engineering, 22: 201–215.

Memos, C.D., and Tzanis, K., 2000. Joint distribution of wave heights and periods in waters of any depth. Journal of Waterway, Port, Coastal and Ocean Engineering, 126 (3): 162–172.

Mitsuyasu, H., Tasai, F., Suhara, T., Mizuno, S., Ohkusu, M., Honda, T., and Rikiishi, K., 1980. Observation of the power spectrum of ocean waves using a cloverleaf buoy. Journal of Physical Oceanography, 10: 286–296.

Muir Langley, R., and El-Shaarawi, A.H., 1986. On the calculation of extreme wave heights: A review. Ocean Engineering, 13 (1): 93–118.

Myrhaug, D., and Kjeldsen, S.P., 1986. Steepness and asymmetry of extreme waves and the highest waves in deep water. Ocean Engineering, 13 (6): 549–568.

Myrhaug, D., and Rue, H., 1998. Joint distribution of successive wave periods revisited. Journal of Ship Research, 42 (3): 199–206.

Myrhaug, D., and Slaattelid, O.H., 1999. Statistical properties of successive wave periods. Journal of Offshore Mechanics and Arctic Engineering, 121 (3): 166–171.

Naess, A., 1984. The effect of the Markov chain condition on the prediction of extreme values. Journal of Sound Vibration, 94: 87–103.

Naess, A., 1985. On the distribution of crest to trough wave heights. Ocean Engineering, 12 (3): 221–234.

Nolte, K.G., 1973. Statistical methods for determining extreme sea states. Proceedings of the 2nd International Conference on Port and Ocean Engineering under Arctic Conditions, pp. 705–742.

Nolte, K.G., and Hsu, F.H., 1972. Statistics of ocean wave groups. Proceedings of the Offshore Technology Conference, pp. 637–643.

Nolte, K.G., and Hsu, F.H., 1979. Statistics of larger waves in a sea state. Journal of Waterway, Port, Coastal and Ocean Engineering, 105 (4): 389–404.

Nwogu, O., 1993. Effect of steady currents on directional wave spectra. Proceedings of the 12th International Conference on Offshore Mechanics and Arctic Engineering, Vol. 1, pp. 25–32.

Ochi, M.K., 1978. Wave statistics for the design of ships and ocean structures. Transactions of the Society of Naval Architects and Marine Engineers, 86: 47–76.

Ochi, M.K., 1986. Non-Gaussian random processes in ocean engineering. Probabilistic Engineering Mechanics, 1: 28–39.

Ochi, M.K., 1992. New approach for estimating the severest sea state from statistical data. Proceedings of the 23rd International Conference on Coastal Engineering, ASCE, pp. 512–525.

Ochi, M.K., 1998a. Probability distribution of wave height in finite water depth. Proceedings of the 26th International Conference on Coastal Engineering, ASCE, pp. 958–971.

Ochi, M.K., 1998b. Probability distributions of peaks and troughs of non-Gaussian random processes. Probabilistic Engineering Mechanics, 13 (4): 291–298.

Ochi, M.K., and Hubble, E.N., 1976. Six-parameter wave spectra. Coastal Engineering, pp. 301–328.

Ochi, M.K., and Sahinoglou, I.I., 1989a. Stochastic characteristics of wave group in random seas. Part I: Time duration of and number of waves in a wave group. Applied Ocean Research, 11 (1): 39–50.

Ochi, M.K., and Sahinoglou, I.I., 1989b. Stochastic characteristics of wave group in random seas. Part II: Frequency of occurrence of wave groups. Applied Ocean Research, 11 (2): 89–99.

Ochi, M.K., and Wang, W.C., 1984. Non-Gaussian characteristics of coastal waves. Proceedings of the 19th International Conference on Coastal Engineering, ASCE, pp. 516–531.

Petruaskas, C., and Aagaard, P.M., 1970. Extrapolation of historical storm data for estimating design wave heights. Proceedings of the Offshore Technology Conference, pp. 409–420.

Phillips, O.M., 1958. The equilibrium range in the spectrum of wind-generated waves. Journal of Fluid Mechanics, 4: 426–434.

Phillips, O.M., 1985. Spectral and statistical properties of the equilibrium range in wind-generated gravity waves. Journal of Fluid Mechanics, 156: 505–531.

Pierson, W.J., and Moskowitz, L., 1964. A proposed spectral form for fully developed wind seas based on the similarity theory of S.A. Kitaigorodskii. Journal of Geophysical Research, 69 (24): 5181–5190.

Prevosto, M., Krogstad, H.E., Barstow, S.F., and Guedes Soares, C., 1996. Observations of the high frequency range of the wave spectrum. Journal of Offshore Mechanics and Arctic Engineering, 118.

Prince-Wright, R., 1995. Maximum likelihood models of joint environmental data for TLP design. Proceedings of the 14th International Conference on Offshore Mechanics and Arctic Engineering, Vol. 2, pp. 535.

Repko, A., Van Gelder, P.H.A.J.M., Voortman, H.G., and Vrijling, J.K., 2000. Bivariate statistical analysis of wave climates. Proceedings of the 27th International Conference on Coastal Engineering, ASCE, pp. 583–596.

Rice, S., 1945. The mathematical analysis of random noise. Bell Systems Technical Journal, 24: 46–156.

Rodriguez, G.R., and Guedes Soares, C., 1998. Uncertainty in the estimation of the slope of the high frequency tail of wave spectra. Applied Ocean Research, 21: 207–213.

Rodriguez, G.R., and Guedes Soares, C., 1999. The Bivariate distribution of wave heights and periods in mixed sea states. Journal of Offshore Mechanics and Arctic Engineering, 121 (2): 102–108.

Rodriguez, G.R., and Guedes Soares, C., 2000. Wave period distribution in mixed sea states. Proceedings of the 19th International Conference on Offshore Mechanics and Arctic Engineering, ASME, New York, Paper OMAE2000/S&R - 6132.

Rodriguez, G.R., and Guedes Soares, C., 2001. Correlation between successive wave heights and periods in mixed sea states. Ocean Engineering, 28 (8): 1009–1030.

Rodriguez, G.R., Guedes Soares, C., and Ferrer, L., 2000. Wave group statistics of numerically simulated mixed sea states. Journal of Offshore Mechanics and Arctic Engineering, 122: 282–288.

Rodriguez, G.R., Guedes Soares, C., and Ocampo-Torres, F.J., 1999. Experimental evidence of the transition between power law models in the high frequency range of the gravity wave spectrum. Coastal Engineering, 38: 249–259.

Rodriguez, G.R., Guedes Soares, C., Pacheco, M., and Pérez-Martell, E., 2002. Wave height distribution in mixed sea states. Journal of Offshore Mechanics and Arctic Engineering, 124 (1): 34–40.

Rye, H., 1974. Wave group formation among storm waves. Proceedings of the 14th International Conference on Coastal Engineering, ASCE.

Rye, H., 1982. Ocean Wave Groups. Report UR-82-18. Norway: Department of Marine Technology, Norwegian Institute of Technology.

Scheffner, N.W., and Borgman, L.E., 1992. Stochastic time-series representation of wave data. Journal of Waterway, Port, Coastal and Ocean Engineering, 118 (4): 337–351.

Scotto, M.G., and Guedes Soares, C., 2000. Modelling the long-term time series of significant wave height with non-linear threshold models. Coastal Engineering, 40: 313–327.

Sobey, R.J., 1992. The distribution of zero-crossing wave heights and periods in a stationary sea state. Ocean Engineering, 19: 101–118.

Sobey, R.J., 1996. Correlation between individual waves in a real sea state. Coastal Engineering, 27: 223–242.

Spanos, P.D., 1983. ARMA algorithms for ocean wave modeling. Journal of Energy Resources Technology, 105: 300–309.

Srokosz, M.A., and Challenor, P.G., 1987. Joint distributions of wave height and period: A critical comparison. Ocean Engineering, 14: 295–311.

Stefanakos, C.N., and Athanassoulis, G.A., 2001. A unified methodology for the analysis, completion and simulation of non stationary time series with missing values, with application to wave data. Journal of Geophysical Research, 23: 207–220.

Strekalov, S.S., Tsyploukhin, V.P., and Massel, S.R., 1972. Structure of sea wave frequency spectrum. Proceedings of the 13th International Conference on Coastal Engineering, ASCE, pp. 307–314.

Su, M.-Y., Bergin, M., Marler, P., and Myrick, R., 1982. Experiments on nonlinear instabilities and evolution of steep gravity-wave trains. Journal of Fluid Mechanics, 124: 45–72.

Suh, K.D., Oh, S.H., Thurston, S.W., and Hashimoto, N., 2000. Influence of currents on equilibrium range spectra of wind waves. Journal of Waterway, Port, Coastal and Ocean Engineering, 126: 79–87.

Tayfun, M.A., 1980. Narrow-band nonlinear sea waves. Journal of Geophysical Research, 85 (C3): 1548–1552.

Tayfun, M.A., 1981. Distribution of crest-to-trough wave heights. Journal of Waterway, Port, Coast and Ocean Engineering, 107: 149–158.

Tayfun, M.A., 1983. Frequency analysis of wave heights based on wave envelope. Journal of Geophysical Research, 88 (C12): 7573–7587.

Tayfun, M.A., 1990. Distribution of large wave heights. Journal of Waterway, Port, Coastal and Ocean Engineering, 116 (6): 686–707.

Thom, H.C.S., 1971. Asymptotic extreme-value distributions of wave heights in the open ocean. Journal of Marine Research, 29 (1): 19–27.

Toba, Y., 1973. Local balance in air-sea boundary processes. III: On the spectrum of wind waves. Journal of the Oceanographical Society of Japan, 28: 209–220.

Torsethaugen, K., 1993. A two peak wave spectrum model. Proceedings of the 12th International Conference on Offshore Mechanics and Arctic Engineering, pp. 175–180.

Van Gelder, P., de Ronde, J., Neykov, N.M., and Neytchev, P., 2000. Regional frequency analysis of extreme wave heights: Trading space for time. Proceedings of the 27th International Conference on Coastal Engineering, ASCE, pp. 1099–1112.

Van Gelder, P.H.A.J.M., Vrijling, J.K., and Neykov, N.M., 1999. Regional frequency analysis of extreme water levels along the north-sea coasts. European Geophysical Society, XXIV General Assembly.

Van Vledder, G., Goda, Y., Hawkes, P.J., Mansard, E., Martin, M., Mathiesen, M., Peltier, E., and Thompson, E.F., 1993. Case studies of extreme wave analysis—A comparative analysis. Proceedings of the Second International Symposium on Ocean Wave Measurement and Analysis, pp. 977–991.

Vrijling, J.K., and Bruinsma, J., 1980. Hydraulic boundary conditions. Proceedings of the Conference on Hydraulic Aspects of Coastal Structures—Developments in Hydraulic Engineering Related to the Design of the Oosterschelde Storm Surge Barrier in the Netherlands, pp. 109–133. Delft, The Netherlands: Delft University Press.

Wang, S., and Le Mehaute, B., 1983. Duration of measurements and long-term wave statistics. Journal of Waterway, Port, Coastal and Ocean Engineering, 109 (2): 236–249.

Winterstein, S.R., 1988. Nonlinear vibration models for extremes and fatigue. Journal of Engineering Mechanics, 114: 1772–1790.

Winterstein, S.R., Bitner-Gregersen, E.M., and Ronold, K.O., 1991. Statistical and physical models of nonlinear random waves. Proceedings of the 10th International Conference on Offshore Mechanics and Arctic Engineering, ASME, Vol. 1, pp. 23–31.

Young, I.R., and Verhagen, L.A., 1996. The growth of fetch limited waves in water of finite depth. Part 2: Spectral evolution. Coastal Engineering, 29: 79–99.

This Page Intentionally Left Blank

189

Chapter 7

Modeling the Effects of Permeable and Reflective Structures on Waves and Nearshore Flows

Inigo J. Losada

Ocean & Coastal Research Group, University of Cantabria, E.T.S.I. de Caminos, Canales y Puertos, Avda. de los Castros s/n, 39005 Santander, Spain

1. INTRODUCTION

Coastal structures are placed in a marine environment with several objectives. Preventing shoreline erosion or flooding, sheltering harbor basins or the stabilization of inlet entrances are some of the possible applications. Each of these functions may require a different type of structure. Coastal structures are usually exposed to waves, currents or the combined effect of waves and currents. It is quite obvious that the presence of the structure will change the flow pattern resulting in one or more phenomena with different space and time scales.

The formation of vortices in front of and behind the structure, the generation of turbulence or the occurrence of diffraction, reflection, transmission and wave breaking are some of the processes associated with wave and structure-interaction.

Traditionally, most of these processes have been modeled to analyze structure functionality or stability considering the structure to be impermeable. However, rubble-mound or berm breakwaters, submerged structures, outfall protections, artificial fishing reefs or armor layers for the protection of seawalls or vertical structures are porous and, therefore, additional processes associated with porous flow have to be considered. Some of the processes associated with wave and porous media interaction are wave transmission different from overtopping as a consequence of wave penetration, wave dissipation due to friction, partial reflection, combined transmission-diffraction, modification of the runup-rundown patterns, water level variations inside the structure, and different turbulence generation or wave breaking mechanisms. For instance, an increase in slope permeability reduces the flow velocities along the slope surface because a larger proportion of the flow takes place inside the structure causing a rise of the internal water level, leading to an increase in the mean pore pressure. Regarding runup, the storage capacity of the structure pores results in a maximum runup smaller than that for an equivalent structure with an impermeable core. Wave reflection from permeable walls may result in a spatial variation of partially standing nodes and antinodes whose magnitude and position depends on porous material characteristics. This will result in a different scouring pattern than for an equivalent vertical impermeable wall with perfect reflection.

It is obvious that these processes have to be modeled correctly since porous flow is clearly affecting the functional and stability characteristics of the structure as well as the wave climate and morphodynamics in the near field of the structure.

This chapter summarizes some of the most recent work available in the literature on the modeling of wave interaction with porous structures. In Section 2 the general governing equations for flow in porous media are derived and the general formulation of wave and porous structure interaction is presented. It will be shown that the study of wave interaction with permeable structures has evolved in parallel with wave theories in fluids.

The linearized problem is shown in Section 3 considering potential flow inside and outside the porous medium. The solutions are formulated in terms of eigenfunction expansions to analyze the

wave field in the presence of a vertical permeable structure. Furthermore, the derivation of an extended mild-slope equation for wave propagation on permeable layers is presented. The equation is applied to wave interaction with submerged permeable breakwaters including wave breaking. In order to extend the range of applicability Section 4 shows the most recent developments for shallow water equations. Based on Boussinesq-type equations wave diffraction and transmission by a permeable vertical breakwater are analyzed using a numerical model.

Finally, in Section 5 a model based on the Navier-Stokes equation is presented. This model, called COBRAS (COrnell BReAking wave and Structure) is able to simulate wave interaction with permeable structures including wave breaking and turbulence.

Section 6 is devoted to giving some conclusions on the state-of-the-art and to speculating on some future trends in the modeling of wave and porous structure interaction.

2. FORMULATION OF THE PROBLEM

A porous medium is a two-phase material in which the solid matrix, usually assumed to be rigid, constitutes one phase, and the interconnected voids or pores constitutes the other. One of the main characteristics of porous media is the irregular shape and size of its pores which are randomly distributed; considering the flow through this heterogeneous formation is very complex. Our interest will be to determine the flow through the porous formation, with typical length scales much larger than the characteristic pore size.

The complex internal geometry of a porous medium, artificial or natural, is difficult if not impossible to determine. Furthermore, in general, in the coastal and harbor engineering field there is a lack of interest in knowing the internal details of the structure or the microscopic flow. In fact, in most circumstances our interest will be in determining the characteristics of the flow in large portions of the porous structure under consideration, introducing an averaging process in the analysis of the flow. The averaging process has a smoothing effect, filtering out small-scale variations associated with the media heterogeneity and pore irregularities.

The modeling of wave and permeable natural or artificial structure interaction is based on the coupling of two models, one that describes the flow acting on the structure and one that describes spatially-averaged flow through the porous structures. The accuracy of the modeling will be limited by the hypotheses and simplifications formulated for the flow in the outer fluid region and by the validity and hypotheses of the porous flow model, usually relying on some constants depending on the flow, and finally on the matching conditions imposed.

2.1. Governing Equations

The flow in porous media can be described by the general Navier-Stokes equations

$$\frac{\partial u_i^*}{\partial x_i} = 0 \tag{1}$$

$$\frac{\partial u_i^*}{\partial t} + u_j^* \frac{\partial u_i^*}{\partial x_j} = -\frac{1}{\rho} \frac{\partial p^*}{\partial x_i} + \nu \frac{\partial^2 u_i^*}{\partial x_j \partial x_j} \tag{2}$$

where ν is the molecular viscosity, u_i^* is the i-th component of the instantaneous velocity in the pores and, p^* the instantaneous effective pressure. As already stated using the macroscopic approach, based on averaging over a small but finite volume with a representative length scale larger than the typical pore size but smaller than the characteristic length scale of the problem, perturbation in the field due to the presence of individual particles and pore irregularities can be ignored.

To replace the actual velocity with the seepage velocity, Sollitt and Cross (1972) resolved the local instantaneous velocity field, u_i^*, into three components

$$u_i^* = u_i + u_i^s + u_i^t \tag{3}$$

where u_i is the seepage velocity, that is, "the average velocity within a small but finite and uniformly distributed void spaces; u_i^s is the spatial perturbation accounting for local velocity components due to pore irregularities or boundary layers, and u_i^t is the time perturbation accounting for local transient fluctuations within the pores" (Sollitt and Cross, 1976, p. 23). Likewise, the pressure field may be split up into analogous components.

The effect of the transient or turbulent and spatial perturbations on the mean flow in the pore can be determined by substituting these definitions in the Navier-Stokes equations. Expanding the total derivative in the Navier-Stokes equations, substituting equation (3) and the analogous expression for the pressure field in this equation, and performing the time-averaging for a period much smaller than the time scale of the macroscopic unsteadiness yields

$$\frac{\partial}{\partial t}(u_i + u_i^s) + (u_i + u_i^s) \cdot \nabla(u_i + u_i^s) + \widehat{u_i^t \nabla u_i^t} =$$
$$-\frac{1}{\rho}(p + p^s + \gamma z) + \nu \nabla^2(u_i + u_i^s) \tag{4}$$

where $(\hat{\lambda})$ denotes time average in a period of time smaller than the wave period.

Proceeding in the same way in the continuity equations leads to

$$\nabla \cdot (u_i + u_i^s) = 0 \tag{5}$$

By integrating the equations of motion over a small but finite volume, the effect of spatial fluctuations within the pore may be isolated.

Finally, the following set of Reynolds Averaged Navier-Stokes equations (RANS) are obtained

$$\frac{\partial u_i}{\partial t} + u_i \nabla u_i + \underline{\widehat{u_i^t \cdot \nabla u_i^t}} + \underline{u_i^s \cdot \nabla u_i^s} = -\frac{1}{\rho}\nabla(p + \gamma z) + \nu \nabla^2 u_i$$

and
$$\tag{6}$$

$$\nabla u_i = 0$$

where $(\underline{\lambda})$ denotes spatial average. Due to the nonlinearity related to the convective terms, the terms associated with the spatial and turbulent fluctuations, $u_i^s \cdot \nabla u_i^s$ and $\widehat{u_i^t \cdot \nabla u_i^t}$, remain in the equations after the averaging process. Analogous to turbulence analysis these two terms may be interpreted as stresses with respect to the mean motion.

In order to solve the equations it is necessary to find closure equations. Based on the work by Ward (1964) for steady and nonconvective flow conditions Sollitt and Cross (1972) established the following equivalency

$$\nu \nabla^2 \overline{u_i} - \left[\underline{\widehat{u_i^t \cdot \nabla u_i^t}} + \underline{u_i^s \cdot \nabla u_i^s} \right] = -\left[\frac{\nu u_i^d}{K_p} + \frac{C_f}{\sqrt{K_p}} u_i^d \left| u_i^d \right| \right] \tag{7}$$

where $K_p \, [m^2]$ is the intrinsic permeability, C_f a dimensionless turbulent coefficient, and u_i^d the discharge velocity which is related to the seepage velocity by the following relationship: $u_i^d = n_e u_i$, where n_e is the porosity.

The following equation is obtained

$$s \frac{\partial u_i}{\partial t} = -\frac{1}{\rho} \nabla(p + \gamma z) - \left[\frac{\nu n_e u_i}{K_p} + \frac{C_f n_e^2}{\sqrt{K_p}} u_i |u_i| \right] \tag{8}$$

where the non-dimensional coefficient s is introduced as a co-factor in the local acceleration term to account for the added mass, and the following additional assumption has been made

$$u_i \nabla u_i \ll \underbrace{u_i^s \cdot \nabla u_i^s} + \widehat{u_i^t \cdot \nabla u_i^t} \tag{9}$$

Sollitt and Cross (1972; 1976) claimed this assumption to be valid for problems of practical importance, where wavelength is much greater than pore diameter. Note that the viscous terms in equation (6) have been included in the equivalency. One could have assumed this term to be negligible compared to the fluctuations.

Using a vertical-lattice type porous medium made of rectangular wooden sticks nailed together to produce uniform pores, Losada et al. (1995) performed a very comprehensive set of measurements inside and outside the structure including free surface, and water particle velocities, using Laser Doppler Velocimetry and pressure records.

Instantaneous measurements at 9 points at each pore were processed in order to calculate the instantaneous and spatial fluctuations, the time and space-averaged velocity, and the convective terms associated with each of the components.

The analysis points out two important results: 1) spatial fluctuations are always more important than temporal fluctuations since temporal fluctuations are confined by the pore size, and 2) even if under certain circumstances convective terms associated with fluctuations are more important than those associated with seepage flow, the latter should not be neglected. Therefore, even if Ward (1964) and consequently equation (8) is based on nonconvective conditions, it is recommended that the terms, $u_i \nabla u_i$, be retained in equation (8).

Furthermore, there is no unique way to decompose the instantaneous velocity. Liu et al. (1999; 2000), supported by the experimental results by Losada et al. (1995), considered dividing the fluid variables into two parts only, a spatially-averaged component and a spatially-fluctuating component, assuming the temporal fluctuations to be negligible. The resulting spatially-averaged Navier-Stokes equations are

$$\frac{1 + c_A}{n_e} \frac{\partial u_i^d}{\partial t} + \frac{u_i^d}{n_e^2} \frac{\partial u_i^d}{\partial x_j} = -\frac{1}{\rho} \frac{\partial p}{\partial x_i} + \frac{\nu}{n_e} \frac{\partial^2 u_i^d}{\partial x_j \partial x_j} - \frac{1}{n_e^2} \frac{\partial \overline{u_i^s u_j^s}}{\partial x_j} \tag{10}$$

$$\nabla u_i^d = 0$$

where u_i^d is the discharge velocity related to the seepage velocity by $u_i^d = n_e u_i$, $c_A = \gamma((1 - n_e)/n_e)$ is the added mass coefficient and, γ is a non-dimensional coefficient (see Section 2.3).

The correlation of spatial velocity fluctuations, the last term on the right-hand side of equation (10), is modeled by Liu et al. (1999) by a combination of linear and nonlinear frictional forces as follows

$$-\frac{1}{n_e^2} \frac{\partial \overline{u_i^s u_j^s}}{\partial x_j} = -g\, a_p\, u_i^d - g\, b_p\, u_c\, u_i^d \tag{11}$$

in which $u_c = \sqrt{u_i^d u_i^d}$ so that the first term on the right side represents the linear, viscous force, while the second term represents the nonlinear turbulent force. Both a_p and b_p are empirical co-

efficients, which are functions of Reynolds number and the geometric characteristics of the porous media. Further explanations regarding the empirical porous flow parameters can be found in Section 2.3.

Notice that equations (11) and (7) are similar. However, the second (viscous) term on the right-hand side in equation (6), generally much smaller than the third term for problems of engineering interest, is retained in Liu et al. (1999), since this term is responsible for transferring shear force, and may become increasingly important near the interface between porous media and outside flow for smaller scale problems.

2.2. Matching Conditions

Matching conditions are necessary to guarantee the continuity of the solution at the interface between the fluid and porous regions. In general, continuity of mass flux and pressure are the matching conditions considered.

For long wave models continuity of free surface, velocity and their derivatives are usually enforced. However, when the models in the fluid region or inside the porous structure include the modeling of turbulence or boundary layers, the matching at the interface has to be carried out using other nonconventional matching conditions.

2.3. Porous Flow Parameters

As shown, the success of modeling wave and porous structure interaction depends largely on the accuracy of the empirical formulae used to describe the frictional forces exerted by the porous media (see equations (8) and (11)). In this regard, most of the existing work is based on stationary flow. However, wave action on structures induces a non-stationary flow. Polubarinova-Kochina (1962) added a time-dependent term to the existing expressions for stationary flow. The resulting equation, including the inertia term accounting for the acceleration and added mass, is referred to as the extended Forchheimer equation

$$I = a_p u^d + b_p u^d \left| u^d \right| + c_p \frac{\partial u^d}{\partial t} \tag{12}$$

where I is the hydraulic gradient, and a_p, b_p, and c_p are empirical coefficients related to the porous flow. The coefficient a_p, with dimensions (s/m) takes into account the frictional force induced by laminar Darcy-type flow, and b_p, with dimensions (s^2/m^2) accounts for the frictional force induced by turbulence. Finally, the dimensional coefficient c_p (s^2/m) accounts for the added mass.

The concept of added mass is associated with the fact that in order to accelerate a certain volume of water a certain amount of momentum is needed. To accelerate the same volume of water in a porous medium, an additional amount of momentum is needed. This is called added mass since the extra amount of momentum suggests that a larger volume of fluid has to be accelerated.

Equation (12) does not include a possible resistance force due to the presence of a convective term. Such a resistance term, probably important for flow through porous media with considerable large-scale convective transport, could be incorporated in the b_p term, because it would be quadratic in the velocity (van Gent, 1991).

In order to determine the magnitude of the porous flow parameters a_p, b_p, and c_p Smith (1991), Hall et al. (1995), and van Gent (1993; 1995) carried out a limited set of experiments using oscillating or U-tube water tunnels for different stone and sphere sizes.

Based on the experimental results, new expressions for non-stationary porous flow friction coefficients were formulated. According to van Gent (1995), the friction coefficients for the extended Forchheimer equation should be expressed as

$$a_p = \alpha_p \frac{(1 - n_e)^2}{n_e^3} \frac{\nu}{g D_{50}^2}$$

$$b_p = \beta_p \left(1 + \frac{7.5}{KC}\right) \frac{1 - n_e}{n_e^3} \frac{1}{g D_{50}}, \quad \text{where } KC = \frac{u_c T}{n_e D_{50}}$$

$$c_p = \frac{1 + \gamma \dfrac{1 - n_e}{n_e}}{n_e g} = \frac{1 + c_A}{n_e g}, \quad \text{where } \gamma = 0.85 - \frac{0.015}{A_c} \tag{13}$$

and

$$A_c = \frac{u_c}{n_e g T} > \frac{0.015}{\dfrac{n_e}{1 - n_e} + 0.85}$$

where u_c is a characteristic velocity of the flow, T is the wave period, and D_{50} is the median grain size diameter. It is recommended that the maximum discharge velocity be taken as representative of the flow.

Although the coefficients α_p and β_p, may still depend on parameters like grading, shape, aspect ratio or orientation of the stones, the following values are recommended: $\alpha_p = 1000$, and $\beta_p = 1.1$.

The relationship between these coefficients and those used by Sollitt and Cross (1972; 1976) are

$$s = c_p n_e g$$

$$K_p = \frac{\nu}{g a_p} \tag{14}$$

$$C_f = b_p g \sqrt{K_p}$$

Further work on unsteady flow equations can be found in Burcharth and Andersen (1995).

Equation (13) represents a significant contribution to the modeling of wave interaction with permeable structures. However, the discrepancies appearing in the application of the formulae by other authors (see, Liu et al., 1999; Lynett et al., 2000), the limited range of existing experimental data, and the importance of an accurate prediction of the coefficients on the modeling of wave and structure interaction seem to be important reasons to do further research on this topic in the near future, especially if the modeling is to be applied to prototypes.

3. WAVE INTERACTION WITH STRUCTURES. LINEAR SOLUTIONS

3.1. Linearized Problem

Assuming simple harmonic wave of frequency, ω, equation (8) may be linearized on the basis of Lorentz's hypothesis of equivalent work (Sollitt and Cross, 1972; Madsen, 1974), replacing the

nonlinear terms in equation (8) by an equivalent linear term $f\omega u_i$, where f is a dimensionless friction coefficient. This yields a linearized form of the equation

$$is\omega u_i = -\nabla \cdot \left(\frac{p}{\rho} + gz\right) - \omega f u_i \tag{15}$$

Taking the curl of this equation shows that the flow in the porous medium is irrotational and, therefore, can be described by a potential $\Phi(x, y, z, t)$, that satisfies

$$u_i = \nabla\Phi \tag{16}$$

Substituting equation (16) into equation (15) results in a Bernoulli-type equation for unsteady flow within the porous medium

$$s\frac{\partial\Phi}{\partial t} + \frac{p}{\rho} + gz + f\omega\Phi = 0 \tag{17}$$

Finally, substituting equation (16) into the continuity equation (6) yields Laplace's equation

$$\nabla^2\Phi = 0 \tag{18}$$

At the free surface, η, the Bernoulli equation (17) can be combined with the linear kinematic free surface boundary condition

$$\frac{\partial\eta}{\partial t} = \frac{\partial\Phi}{\partial z} \text{ at } z = 0 \tag{19}$$

to yield

$$\frac{\partial\Phi}{\partial z} - \omega^2(s - if)\frac{\Phi}{g} = 0 \text{ at } z = 0 \tag{20}$$

Furthermore, the following linear complex dispersion relationship has to be satisfied by the waves propagating inside the porous medium

$$\omega^2(s - if) = g\Gamma \tanh\Gamma h \tag{21}$$

where Γ is a complex wave number.

Solutions to these equations depend on the values of the porous material parameters, s, n_e, K_p, C_f, equation (14) known for a given material, and the linearized friction coefficient, f. Therefore, an additional condition is required to evaluate this coefficient. Following Sollitt and Cross (1972) and Madsen (1974), f is evaluated from the following equation for a porous structure of volume V under a wave cycle of period T

$$f = \frac{1}{\omega}\frac{\displaystyle\int_0^T\!\!\int_V \left(\frac{n_e^2\nu}{K_p}|u_i|^2 + \frac{n_e^3 C_f}{\sqrt{K_p}}|u_i|^3\right)dt\,dV}{\displaystyle\int_0^T\!\!\int_V n_e|u_i|^2\,dt\,dV} \tag{22}$$

Note that u_i is taken to be the real part of the seepage velocity. An iterative procedure is needed to evaluate f. As it will be shown later, several authors have assumed the friction coefficient, f, to be a known constant parameter. However, this assumption may lead to unrealistic results.

3.2. Solutions for Simple Geometries Based on Eigenfunction Expansions

Based on this irrotational and linear approximation, Sollitt and Cross (1972) presented a model to analyze wave interaction with vertically sided porous structures. This work was later extended by Dalrymple et al. (1991) to include oblique incident waves, and by Requejo et al. (2002) to evaluate wave loads on the structure.

Dalrymple et al. (1991) considers the interaction of a gravity wave train with a single homogeneous, isotropic, porous structure of width b between two semi-infinite fluid regions of constant depth, h (Fig. 1). The wave field outside the structure can be specified by velocity potentials, $\Phi_1(x, y, z, t)$ in the seaward region, and $\Phi_3(x, y, z, t)$ in the leeward region of the breakwater, by specifying the well-known linear boundary-value problem for water waves in constant water depth. In the rigid porous medium, region 2, a boundary value problem can be defined using equations (18) to (21) and adding the kinematic bottom boundary condition $\partial \Phi_2 / \partial z = 0$ in $z = -h$.

Each of the boundary value problems is formulated in terms of linear homogeneous equations. Separation of variables leads to Sturm-Liouville problems where the potentials may be expressed in terms of an eigenfunction expansion. Since the solution in adjacent regions must be continuous at each interface, continuity of mass flux and pressure at $x = 0$ (interface between regions 1 and 2) and at $x = b$ (interface between regions 2 and 3) is required. These conditions may be expressed as

$$\Phi_{1_x} = n_e \Phi_{2_x}$$
$$\Phi_1 = (s - if)\Phi_2 \text{ at } x = 0$$

and   (23)

$$\Phi_{3_x} = n_e \Phi_{2_x}$$
$$\Phi_3 = (s - if)\Phi_2 \text{ at } x = b$$

where the continuity of pressure is derived from the Bernoulli equation (17).

Substituting the potentials into the matching conditions (equation (23)), a system of equations is obtained. Unknowns are the complex amplitudes of the progressive and evanescent modes in the potentials Φ_1, Φ_2, and Φ_3 that can be expressed in terms of the complex reflection coefficient, R in region 1, and of the complex transmission coefficient, T in region 3. Applying the orthogonality
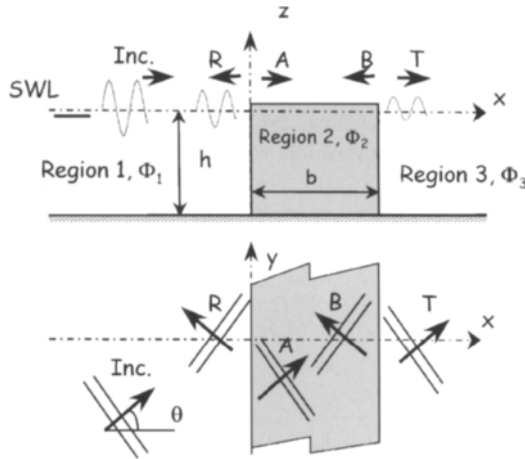
Figure 1. Schematic description of the vertical permeable structure problem.

of the eigenfunctions over the water depth in the 3 regions, results in a simpler system. Once the system of equations is solved together with equation (22), and the corresponding dispersion relationships in the fluid regions and porous region, (equation (21)), the potential, and therefore, the flow is completely defined.

Dalrymple et al. (1991) presents the variation of reflection and transmission coefficients for several rectangular geometries, finite, semi-infinite and infinite breakwater with an impermeable wall considering several relative water depths and analyzing the influence of wave incidence. They found that a minimum reflection coefficient occurs for different angles of incidence depending on the f value. However, they consider f to be a constant value, independent of the flow and porous media parameters. The eigenfunction approach has also been applied to crowned breakwaters (Losada et al., 1993), or extended to submerged porous steps (Losada et al., 1997a) for variable f.

The complex nature of the dispersion equation (21) leads to two particular difficulties when the Sollitt and Cross (1972) model is used in conjunction with the eigenfunction expansions technique. First, it is difficult to locate the complex roots of the dispersion relation by standard numerical methods. Secondly, the vertical eigenfunction problem is not self-adjoint and standard expansions theorems do not apply. These problems have been discussed by several authors (see Dalrymple et al., 1991). A solution to this problem is given in McIver (1998) who presents a method that allows the explicit calculation of the roots of the complex dispersion relation and uses the theory of non-self-adjoint differential operators to show how the formal construction of eigenfunction expansions can be carried out for the interaction of water waves with porous structures.

In order to consider different geometries, generalizing the theory of Sollitt and Cross (1972), Sulisz (1985; 1997) developed a boundary element method to investigate wave transmission and reflection from a multilayered breakwater with arbitrary shape.

Based on a linearized long wave theory, Massel and Mei (1977) and Massel and Butowski (1980) were the first to consider random wave interaction with permeable structures. Following Dalrymple et al. (1991), Losada et al. (1997b) considered the interaction of directional random waves with vertical permeable structures. Using an eigenfunction expansion Losada et al. (1997b) simulated the transformation of a given incident spectrum in the vicinity of the partially reflecting structures. The influence on the results of the structure's geometry, permeable material characteristics and incident wave spectrum is analyzed. In general, this method can be extended to any structure.

Based on the fact that linear wave theory may be used, Losada et al. (1997b) assumes the incident wave train to be a superposition of a large number of components. Therefore, a directional spectrum may be expressed as the product of a frequency spectrum, S_η, and a directional spreading function, $G(f, \theta)$. Discretizing, the incident frequency spectrum in conjunction with the directional spreading function is divided into a finite number of wave components characterized by a certain frequency, f_j, and direction, θ_j. Each discrete wave field may be represented by a velocity potential $\Phi_{jk}^{(i)}(x, y, z, t) = \mathrm{Re}\left\{\phi_{jk}^{(i)}(x, z) \exp\left[-i(\lambda_{jk} y - \omega_j t)\right]\right\}$, which satisfies the Laplace equation in every region, i, where $\lambda_{jk} = k_j \sin\theta_k$ and $\omega_j = 2\pi/f_j$, the first representing the longitudinal component of wave number in the fluid region, and the second the angular wave frequency, for wave component, $-j$. The reflected, S_R, and transmitted, S_T, wave spectra can be evaluated using the following expressions

$$S_R(f_j, \theta_k) = S_\eta(f_j) G(f_j, \theta_k) \left|R_{jk1}\right|^2 \tag{24}$$

$$S_T(f_j, \theta_k) = S_\eta(f_j) G(f_j, \theta_k) \left|T_{jk1}\right|^2 \tag{25}$$

Assuming the incident wave train to be of unit amplitude, the complex coefficients, R_{jk1} and T_{jk1}, are the reflection and transmission coefficients, respectively, for the spectral incident wave component of frequency, f_j, traveling at an angle, θ_k, with the x-direction. The resulting problem

can be solved for each discrete frequency and direction as explained in the previous section. Recall that the value of these coefficients depends on incident wave characteristics, relative water depth, structure geometry and porous material characteristics.

The analysis of the wave-induced flow or scour in front of a partially reflective and dissipative structure, requires the modeling of the evolution of the total spectrum, S_ζ (incident and reflected) and the associated horizontal bottom velocities. The total spectrum, S_ζ, in front of the structure is given by

$$S_\zeta(f, \theta, x) = |K_r(f, \theta, x)|^2 \, S_\eta(f, \theta, x) \tag{26}$$

where the modulus of the transfer function, K_r, for a horizontal bottom case is expressed as

$$|K_r(f, \theta, x)|^2 = 1 + |R(f, \theta)|^2 + 2|R(f, \theta)| \cos\left[2k_x(f)x + \xi(f, \theta)\right] \tag{27}$$

where $|R(f, \theta)| \equiv |R_{jk1}|$ for each of the frequency components, and ξ is the argument of the complex reflection coefficient, R_{jk1}. The root-mean-square wave height distribution in front of the reflective structure, can be obtained by calculating the zero-order moment of the total spectrum.

In order to analyze the scouring process in front of a structure, usually the root-mean-square horizontal velocity at the bottom, u_{rms}, is required. Based on previous derivations, the frequency spectral density of the horizontal water particle velocity at a given point (x, z) of the fluid domain is

$$S_u(f, x) = |H_u|^2 \, S_\eta(f, x) \tag{28}$$

where H_u is a transfer function that can be obtained from the velocity potentials (see Losada et al., 1997b, for details). Once S_u is calculated, the root-mean-square horizontal velocity may be evaluated using the following expression

$$u_{rms} = \sqrt{m_o} \tag{29}$$

To show the influence of structure permeability on bottom velocity in front of a structure, Fig. 2 presents the non-dimensional u_{rms} for three different vertical porous structures with identical geometry but varying porous material. An impermeable wall is also included for comparison. The incident
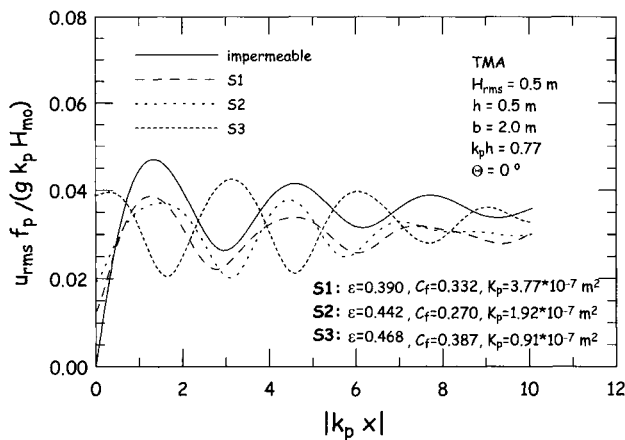
Figure 2. Effects of reflective vertical structures permeability on random wave kinematics. Non-dimensional u_{rms} at the bottom versus $|k_p x|$ for varying porous material. f_p and k_p stand for peak frequency and corresponding wave number. (From Losada et al., 1997b. Reproduced with permission of ASCE).

waves are modeled by a TMA spectrum. The plot shows that interaction with the impermeable structure is inducing the maximum bottom velocity. However, the porous breakwater with material S3 is inducing higher values at different locations. Analyzing the velocities at $x = 0$, it can be observed that the impermeable structure gives a zero value while the porous structures have nonzero values, with magnitudes depending on the porous material characteristics. Increasing porosity gives higher velocities at the breakwater face. Furthermore, the visible phase shift with respect to the impermeable case increases with increasing porosity.

This is due to the fact that for the permeable structures, reflection does not take place at $x = 0$ but somewhere inside the structure. Reflection location depends on material characteristics, structure geometry and incident wave conditions.

Further information regarding linear solutions for monochromatic waves and simple geometries can be found in Chwang and Chan (1998).

3.3. Solutions Based on the Mild-Slope Equation

Within the framework of linear wave theory, Berkhoff (1972) proposed a two-dimensional theory which can deal with large regions of refraction and diffraction. This new equation, the mild-slope equation, has been extensively used for wave propagation modeling.

In order to consider wave propagation on porous slopes and wave interaction with trapezoidal permeable submerged breakwaters, Rojanakamthorn et al. (1989), Losada et al. (1996a), and Mendez et al. (2001) present extended versions of the mild-slope equation (see Fig. 3). These formulations differ slightly in the definition of the vertical eigenfunctions, porous dispersion equations and the treatment of the wave breaking process.

The extension of the mild-slope equation for permeable layers is derived by multiplying the Laplace equation by its correspondent vertical eigenfunctions, $M_O(z)$ and $P_O(z)$, expressed in terms of the propagating mode only, Γ_o, neglecting evanescent modes and integrating over depth.

Following Losada et al. (1996a), the new governing equation is

$$\int_{-h+\alpha h}^{0} M_O(z) \left(\nabla_h^2 \Phi_2 + \frac{\partial^2 \Phi_2}{\partial z^2} \right) dz + n_e(s - if) \int_{-h}^{-h+\alpha h} P_O(z) \left(\nabla_h^2 \Phi_4 + \frac{\partial^2 \Phi_4}{\partial z^2} \right) dz = 0 \qquad (30)$$

where

$$\Phi_2 = \varphi(x, y) M_O(z) \quad \text{and} \quad \Phi_4 = \varphi(x, y) P_O(z) \qquad (31)$$

and Φ_2 is the velocity potential in the fluid region above the permeable layer or submerged breakwater, Φ_4 is the potential inside the permeable region, φ is the complex amplitude of the water surface, and $\nabla_h = (\partial/\partial x, \partial/\partial y)$.
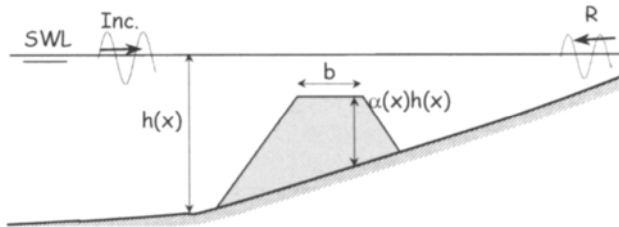
Figure 3. Schematic description of the submerged permeable structure geometry.

The boundary and matching conditions for variable depth are:

Combined free surface boundary condition

$$\frac{\partial \Phi_2}{\partial z} - \frac{\omega^2}{g} \Phi_2 = 0 \text{ at } z = 0 \tag{32}$$

Bottom boundary condition

$$\frac{\partial \Phi_4}{\partial z} + \nabla_h \cdot h \nabla \cdot \Phi_4 = 0 \text{ at } z = -h \tag{33}$$

Continuity of mass flux

$$\frac{\partial \Phi_2}{\partial z} + \nabla_h \cdot h \nabla_h \cdot \Phi_2 = n_e \left(\frac{\partial \Phi_4}{\partial z} + \nabla_h \cdot h \nabla_h \cdot \Phi_4 \right) \text{ at } z = -h + \alpha h \tag{34}$$

Continuity of pressure

$$\Phi_2 = (s - if)\Phi_4 \text{ at } z = -h + \alpha h \tag{35}$$

Integrating equation (30) using the boundary and matching conditions and finally the mild-slope assumption, the following equation is obtained

$$\nabla_h \cdot (\chi \nabla_h \cdot \varphi) + (\Gamma_o^2 \chi - i \omega \chi f_D) \varphi = 0 \tag{36}$$

where

$$\chi = \left(\frac{\omega}{ig} \right) \left[\int_{-h+\alpha h}^{0} M_o^2(z)\,dz + n_e(s - if) \int_{-h}^{-h+\alpha h} P_o^2(z)\,dz \right] \tag{37}$$

and, where the term $i\omega\chi f_D\varphi$ has been added to account for wave breaking, f_D being an energy dissipation function, g the acceleration of gravity, and i the imaginary unit. $M_o(z)$ and $P_o(z)$ are the vertical eigenfunctions. The expressions of the vertical eigenfunctions, dispersion equations and complete potentials can be found in Losada et al. (1996a), and Mendez et al. (2001).

The energy dissipation function due to wave breaking on a submerged permeable breakwater takes into account the processes of wave decay and recovery and is expressed by Rojanakamthorn et al. (1990) as

$$f_D = \frac{\Gamma_R}{\omega C_g} \alpha_D \tan \varsigma \sqrt{\frac{g}{h_{ef}}} \sqrt{\frac{\upsilon - \upsilon_r}{\upsilon_s - \upsilon_r}} \tag{38}$$

where, C_g is the group velocity, Γ_R is the real part of the wave number Γ_o, $\tan \zeta$ is the equivalent bottom slope at the breaking point which is defined as a mean slope in the distance $5h_{ef,b}$, offshore the breaking point, and

$$\upsilon = \frac{|\varphi|}{h_{ef}}$$

$$\upsilon_s = 0.4(0.57 + 5.3 \tan \zeta) \tag{39}$$

$$\upsilon_r = 0.4 \left. \frac{|\varphi|}{h_{ef}} \right|_b$$

where the subscript b means the value at the breaking point. Mendez et al. (2001) modified the initial formulation by Rojanakamthorn et al. (1990) by using h_{ef} instead of h in equation (39) to take into
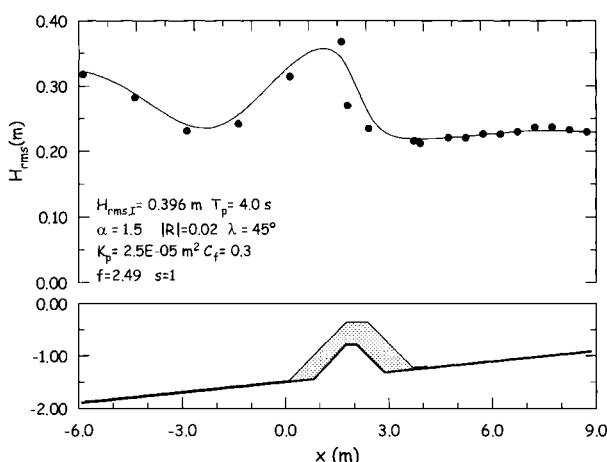
Figure 4. Wave transformation by a permeable submerged breakwater. Comparison of experimental and numerical results.

account empirically, the effect of permeable bottom layer on wave breaking. As defined in Losada et al. (1997a), h_{ef} is the effective water depth over the porous layer, and depends on the porous material characteristics and flow conditions.

To solve the problem a finite difference scheme and proper boundary conditions at the domain boundaries are used. The resulting system of equations including equation (22) can be simultaneously solved. Assuming a breaking criteria, f_D is calculated using the expression in Rojanakamthorn et al. (1990). In order to arrive at a solution an iterative procedure has to be carried out.

Losada et al. (1996b) extended the model to consider the interaction of directional random waves with submerged breakwaters. The influence of structure geometry, porous material properties and wave characteristics, including oblique incidence, on the kinematics and dynamics over and inside the breakwater is considered in Losada et al. (1996a; 1996b), and Mendez et al. (2001). Models are validated against experimental data.

Fig. 4 shows root-mean-square wave height, H_{rms}, evolution on a submerged permeable breakwater. The numerical model results obtained in Mendez et al. (2001) are compared with experimental data (Rivero et al., 1998). The submerged breakwater, with 1:1.5 slopes on both sides, has a crown width of 0.61 m and is constructed on an impermeable core and an armor layer of quarrystones with a mean weight of 25 kg. The structure is placed on a 1:15 rigid slope bottom. The incident irregular wave characteristics are given by $H_{rms,I} = 0.396$ m, and $T_p = 4$ s.

Applying equations (13) and (14) with $n_e = 0.4$, the rest of the permeable material characteristics are: $K_p = 2.5 \times 10^{-5}$ m^2, $C_f = 0.3$, $s = 1$. Using equation (22) the resulting linearized friction coefficient is $f = 2.49$.

Results show very good agreement even under breaking conditions. In front of the structure, wave reflection induces a modulation of the wave height. Wave breaking takes place on the crest. A modulation of the wave height is also visible leeward the submerged breakwater due to the reflection induced by the bottom slope.

Mase and Takeba (1994) extend the mild-slope equation, deriving time-dependent and time-independent wave equations for waves propagating over porous rippled beds. By using the time-independent equation, the Bragg scattering is examined in a one-dimensional case showing that energy dissipation in the porous layer contributes to smaller reflected and transmitted coefficients than those in the case of an impermeable rigid rippled bed. Recently, Silva et al. (2002), using Green's

second identity, extend the time-dependent and time-independent mild-slope equation for waves over a finite porous bed. The model is applied to analyze rippled beds and submerged structures.

3.4. Extension to Nonlinear Magnitudes Derivable from Linear Wave Theory and Applications

Based on linear wave theory presented in previous sections, Losada et al. (1998) and Mendez et al. (2001) provide general expressions correct to second-order of wave-averaged quantities such as mass transport, radiation stress and energy flux for wave propagation inside or above a porous layer in terms of some shape functions defined accordingly.

Using an approximation, Mendez et al. (2001) applied a simplified one-dimensional version of the time- and depth-averaged equations for porous media flow derived in Losada (1996) considering the forcing of the radiation stress of the seepage component in order to analyze the mean water level variations induced by the presence of a submerged permeable breakwater.

Fig. 5 presents numerical and experimental results of wave height and mean water level variation for a submerged permeable breakwater. A description of the experimental conditions can be found in Rivero et al. (1998). Results show a modulation of the mean water level in front of the structure imposed by reflection. A set-down can be clearly observed at the front slope or above the breakwater crest just before the maximum wave height is reached before breaking. After breaking a slightly modulated set-up is clearly observed leeward the structure in both the experimental and numerical results. Results point out that the set-up induced by a permeable submerged breakwater is due to radiation stress gradients induced by dissipation associated with both breaking and friction. In general,
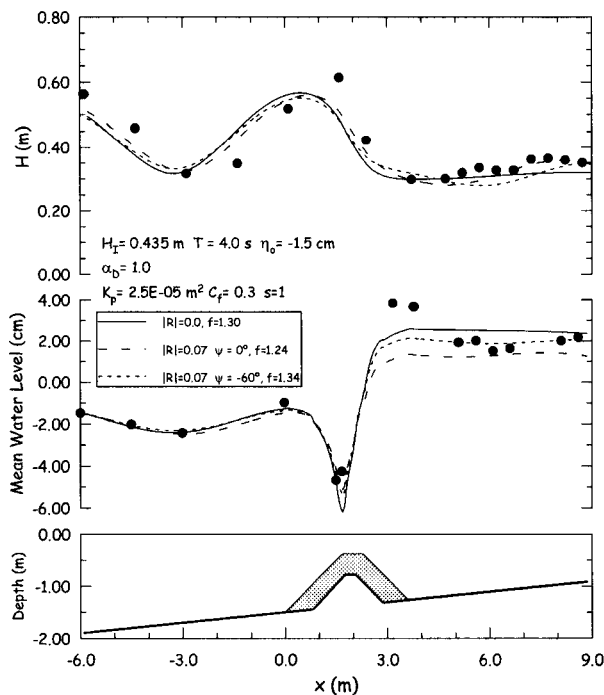
Figure 5. Wave height and mean water level variation in a submerged breakwater under breaking conditions. (From Mendez et al., 2001. Reproduced with permission of ASCE).

the set-up due to breaking is much more important than the one produced by the porous material (Mendez et al., 2001). However, the relative magnitude of the different contributions requires further exploration due to the lack of roller effects, flow separation or turbulent effects in this first approach to the problem.

3.5. Some Consequences of Including Porous Flow Modeling

The modeling of wave interaction with permeable structures shows how partial reflection, magnitude and phase, and consequently the position of partial nodes and antinodes are controlled by the incident wave conditions, structure geometry and porous material characteristics. This is clearly affecting the flow near the structure and is especially important in evaluating structure functionality, wave loads on the structure and the wave kinematics associated with scour.

The modeling has shown that the wave-averaged motion is also affected by the flow above or through the porous material. In fact, several analogies between a dissipative porous media and the surf zone can be drawn. Radiation stress variations due to dissipation in the porous media may induce mean water level variations or return flows inside or close to the structure in the absence of wave breaking (Mendez et al., 2001).

An additional example is given in Baquerizo and Losada (1998) where it is shown how dissipation inside an infinitely long vertical breakwater in a constant water depth generates an along-breakwater current inside the structure. For an obliquely incident wave train, dissipation of energy inside the pores produces a radiation stress gradient which is balanced by the frictional and diffusive terms in the time- and depth-integrated momentum equation for wave-induced porous flow. The current driven inside the porous medium is transferred by turbulent diffusion seaward and leeward the structure.

4. MODELS BASED ON SHALLOW WATER EQUATIONS

There are numerous situations where accurate computations of the wave field on permeable beaches or around permeable structures are not possible using the mathematical models presented in previous sections.

Nonlinearity is an important feature in the process on wave interaction with most coastal structures that are usually located between intermediate and shallow water depths. For example, in order to model the generation of higher harmonics on regions of abrupt depth variations, such as crowns of permeable submerged structures (Losada et al., 1997a), the mild-slope equation is limited by the use of linear theory. A review of shallow water models can be found in van Gent (1995).

4.1. Recent Developments

Using a perturbation method, Cruz et al. (1992) derived a set of time-dependent nonlinear equations for one-dimensional wave transformation on porous beds. Since these models include the leading order of nonlinearity, they are able to generate higher harmonics on the shallow water region. However, the inherent dispersivity is weak and, consequently, the frequency-dependent wave decomposition beyond submerged breakwaters cannot be reproduced. Following the approach by Madsen et al. (1991) for impermeable beds, Cruz et al. (1997) derived a set of Boussinesq equations over a porous bed of arbitrary thickness with an underlying solid bottom of arbitrary depth. After determining the governing equations and boundary conditions for the three-dimensional wave motion, assuming incompressible and irrotational flow in both the fluid and permeable layer, a set of time-dependent, vertically-integrated equations is derived containing the leading order of nonlinearity. The weak dispersivity of Boussinesq-type equations is corrected by adding dispersion terms to the basic momentum equations and matching the resulting dispersion relation with that of the appropriate theory.

The equations of motion inside the porous layer include resistance terms following the approach by Sollitt and Cross (1972). The permeable material parameters were extrapolated from values tabulated in Sollitt and Cross (1972). Numerical results are obtained for wave propagation on a horizontal bottom of uniform thickness with good agreement.

Liu and Wen (1997) derived a two-dimensional fully nonlinear, diffusive and weakly dispersive set of equations for long wave propagation in a shallow porous medium. Using analytical perturbation solutions as well as numerical solutions the one-dimensional equations are used to study the tide-induced free surface fluctuations in a porous region and the transmission and reflection of solitary waves by a rectangular porous breakwater. The last is calculated considering the Boussinesq approximation carrying out a linearization process inside the porous breakwater to convert the nonlinear resistance formula to a linear Darcy-type resistance. Numerical results are compared with experimental data (Vidal et al., 1988) observing an excellent agreement.

4.2. Diffraction and Transmission by Porous Structures

Diffraction of waves by a solid breakwater has received a considerable amount of attention. However, the role of breakwater porosity on the wave diffraction process has not been addressed until recently. Based on the linear potential wave theory, Yu (1995) developed a porous breakwater diffraction model. This model was extended to waves of arbitrary incidence (Yu and Togoshi, 1996; McIver, 1999), but requires the breakwater to be thin compared to the incident wavelength.

Lynett et al. (2000) presents a model based on depth-integrated equations suitable for weakly nonlinear, weakly dispersive transient waves propagating in both variable-depth open water and porous region. In this first work, the model is applied to analyze solitary wave interaction with vertically-walled porous structures in a horizontal bottom.

In the open water region the model employs the generalized Boussinesq equations presented originally by Wu (1981). The equations are expressed in terms of the free surface displacement, ζ, and the depth-averaged velocity potential, ϕ. In dimensional form, the equations are given as

$$\frac{\partial \zeta}{\partial t} + \nabla \cdot [(\zeta + h) \nabla \phi] = 0 \tag{40}$$

$$\frac{\partial \phi}{\partial t} + \frac{1}{2} (\nabla_h \phi)^2 + g\zeta - \frac{h}{2} \frac{\partial}{\partial t} \nabla_h \cdot (h \nabla_h \phi) + \frac{h^2}{6} \frac{\partial}{\partial t} \nabla^2 \phi = 0 \tag{41}$$

where h is the local water depth, g is gravity, and $\nabla_h = (\partial/\partial x, \partial/\partial y)$ the horizontal gradient. Using ϕ, the depth-averaged velocity, $\bar{u}$, can be calculated by

$$\bar{u} = \nabla_h \phi \tag{42}$$

These equations are valid only for weakly nonlinear and dispersive waves, limiting the application to waves satisfying $O(A/h) = O(kh) \ll 1$, where A/h is a nonlinearity parameter and $(kh)^2$ a dispersion parameter.

This model is coupled with a specific model for the porous region. In the porous region a truncated version of Liu and Wen's (1997) Boussinesq-type equations is used. Consistency with the water region model requires the truncation of the equations retaining only weakly nonlinear effects and depth averaging. Denoting ψ as the depth-averaged piezometric head, K as the hydraulic conductivity that can be written in terms of the porous parameters in Section 2.3, n_e as the effective porosity of the porous material, the governing equation can be expressed as

$$\frac{\partial \zeta}{\partial t} - \frac{K}{n_e} \nabla_h \left[(\zeta + h) . \nabla_h \zeta \right] - \frac{h^2}{3} \frac{\partial}{\partial t} \nabla^2 \zeta = 0 \tag{43}$$

$$\psi = \zeta - \frac{h^2}{3}\nabla^2 \zeta \tag{44}$$

Velocity in the porous region is given as

$$\overline{u} = -K\nabla_h \psi \tag{45}$$

The resolution of the problem requires reflective and radiation conditions at the exterior boundaries and matching conditions along the interface between the fluid and porous region.

The matching conditions are given as

$$\zeta|_+ = \zeta|_- \quad \overline{u}|_+ = \overline{u}|_- \tag{46}$$

$$\overline{n} \cdot \nabla \zeta|_+ = \overline{u} \cdot \nabla \zeta|_- \quad \nabla \cdot (\overline{n} \cdot \overline{u})|_+ = \nabla \cdot (\overline{n} \cdot \overline{u})|_- \tag{47}$$

where the sign denotes opposite sides of the interface and $\overline{n}$ is the unit normal vector. Velocities are evaluated using equations (44) and (45).

Using a high-order finite difference scheme, the numerical model is used for both one-dimensional and two-dimensional problems. Considering solitary wave interaction with a permeable vertical structure considerably simplifies our understanding of the wave diffraction-transmission process.

To validate the model and compare the different mechanisms, a comprehensive set of experiments was performed in a wave tank with a porous and impermeable breakwater perpendicular to solitary wave incidence. Water depth, wave height and gravel diameter were varied and free surface was recorded in a dense grid covering the region in front of the structure and in the shadow zone.

Results show that the model predicts wave height, wave form and arrival time excellently. Furthermore, the model and experimental results are useful for evaluating the differences between the wave field in the shadow zone comparing the porous breakwater case with the solid breakwater case. Fig. 6 presents the results of a numerical simulation of the interaction of a solitary wave passing a solid (left) and a porous (right) detached breakwater. The snapshots correspond to spatial profiles of a normally incident solitary wave with $A/h = 0.1$, interacting with a breakwater with a length of 5 water depths and a width of 80 water depths. For the porous breakwater the scaled rock size has the following characteristics: $D_{50}/h = 0.2$, $n_e = 0.5$, $\alpha_p = 1100$, and $\beta_p = 0.81$.

The first two snapshots (a) and (b) show the solitary wave approaching the detached breakwater. In Figs. 6c and d the wave height at the front face is at a maximum, while Figs. 6e and f show the reflected waves at the beginning of diffraction behind the breakwater. The analysis of the shadow zone in Figs. 6e, f, g and h shows that less energy is diffracting to form a wave with a circular crest line in the porous breakwater case than in the solid breakwater case. The main difference between both cases is that most of the energy that diffracts in the solid breakwater case to form this circular wave, diffracts into the transmitted wave front in the porous breakwater case. This is due to the fact that in the shadow zone of the porous breakwater, wave diffraction occurs in two ways. A wave with circular crest lines is created, since part of the wave energy is diffracting into the calm water behind the transmitted wave in the same form as diffraction occurs behind a solid breakwater. The second part of diffraction takes place because wave energy diffracts into the transmitted wave front from the incident wave front, due to the discontinuity of wave amplitude. The relative importance of each of the mechanisms will depend on the incident wave characteristics, breakwater geometry and permeable material characteristics.

4.3. Some Consequences of Including Porous Flow Modeling

The planform of an equilibrium bay-shaped beach is governed mainly by the wave-induced currents, the existing sediments and the boundaries which confine the beach that usually consist of
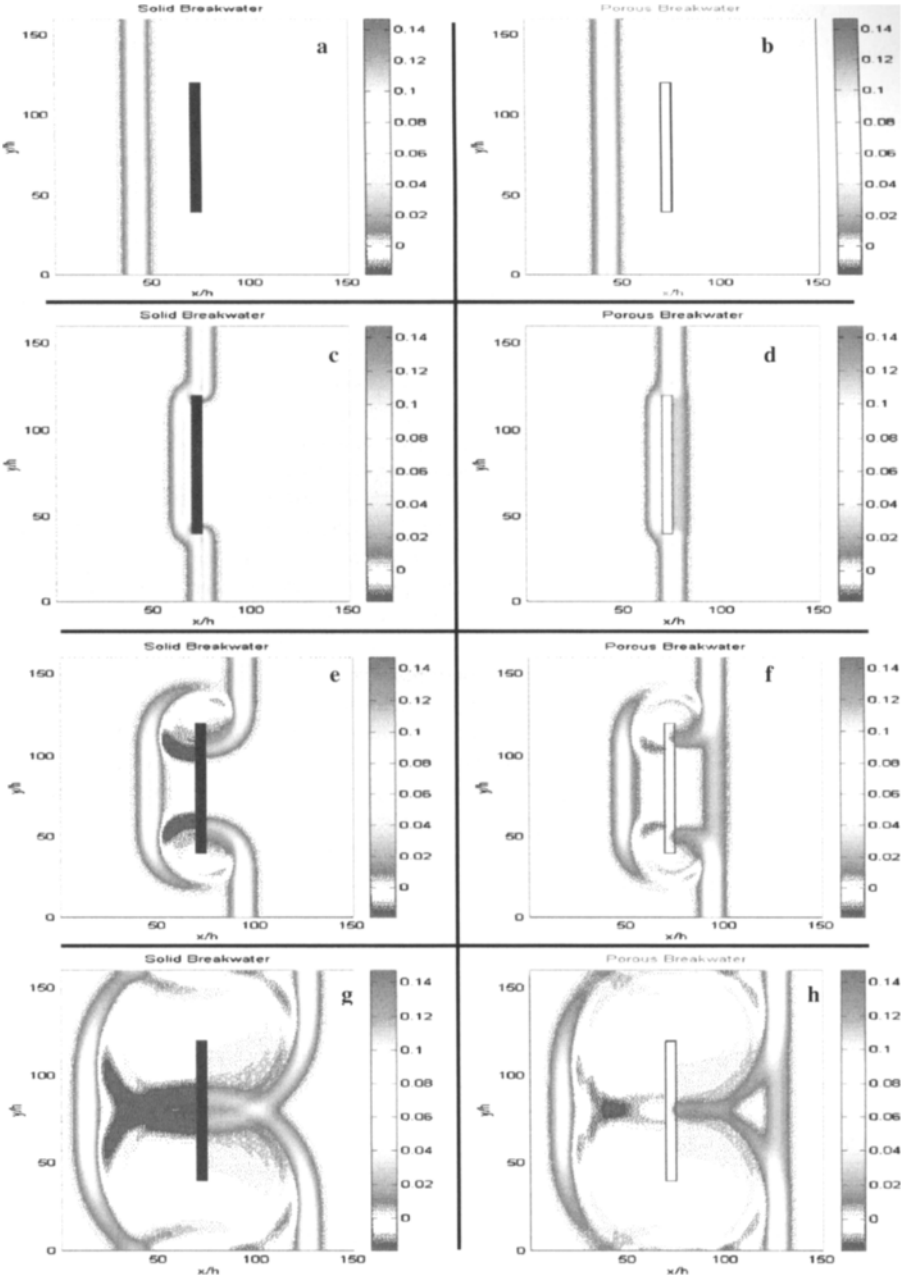
Figure 6. Numerical simulation of solitary wave interaction with detached impermeable and permeable break-waters.

permeable breakwaters. Both static or dynamic equilibrium shapes are controlled by the diffraction-refraction process and the associated wave fronts and wave height gradients (Gonzalez and Medina, 2001). Therefore, and according to the example shown that can be easily extended to periodic waves, it is clear that including the effect of structure permeability will partially modify wave fronts and wave height gradients, consequently affecting the final shape of the beach at least near the structure.

Equivalent reasoning can be applied to the formation of tombolos and salients as a response of the shoreline to the presence of detached porous breakwaters. Therefore, it can be stated that a correct morphodynamic modeling requires considering the modeling of porous flow when permeable structures are present since it might affect the final result.

5. MODELING BASED ON THE REYNOLDS-AVERAGED NAVIER-STOKES (RANS) EQUATIONS

In order to overcome most of the limitations associated with previous models, significant efforts have been made in the last few years to develop a tool capable of successfully simulating the free surface of breaking waves on permeable structures. Three examples of successful models are the models SKYLLA (van Gent, 1995), VOFbreak (Troch and de Rouck, 1998), and COBRAS (Liu et al., 1999; 2000), all based on two-dimensional Navier-Stokes equations for the fluid and porous regions, and making use of the VOF method to track the free surface.

COBRAS (COrnell BReAking wave and Structure) was initially developed to track the free surface movement, and to describe the turbulence generated by the wave breaking process on impermeable slopes (Lin and Liu, 1998a; 1998b).

5.1. Mathematical Formulation

The breaking waves numerical model is based on the Reynolds Averaged Navier-Stokes (RANS) equations. Although the model has only been applied to two-dimensional problems, the complete three-dimensional formulation will be given herein. For a turbulent flow in the fluid region, the velocity field and pressure field can be divided into two parts: the mean (ensemble average) velocity and pressure $\langle u_i \rangle$ and $\langle p \rangle$, and the turbulent velocity and pressure u_i' and p'. Thus,

$$u_i = \langle u_i \rangle + u_i', \quad p = \langle p \rangle + p' \tag{48}$$

in which $i = 1, 2, 3$ for a three-dimensional flow. If the fluid is assumed incompressible, the mean flow field is governed by the RANS equations

$$\frac{\partial \langle u_i \rangle}{\partial x_i} = 0 \tag{49}$$

$$\frac{\partial \langle u_i \rangle}{\partial t} + \langle u_j \rangle \frac{\partial \langle u_i \rangle}{\partial x_j} = -\frac{1}{\rho} \frac{\partial \langle p \rangle}{\partial x_i} + g_i + \frac{1}{\rho} \frac{\partial \langle \tau_{ij} \rangle}{\partial x_j} - \frac{\partial \langle u_i' u_j' \rangle}{\partial x_j} \tag{50}$$

in which ρ is the density of the fluid, g_i the i-th component of the gravitational acceleration, and the mean molecular stress tensor $\langle \tau_{ij} \rangle = 2\mu \langle \sigma_{ij} \rangle$ with μ being the molecular viscosity and $\langle \sigma_{ij} \rangle = (1/2) [(\partial \langle u_i \rangle /\partial x_j) + (\partial \langle u_j \rangle /\partial x_i)]$, the rate of strain tensor of the mean flow. In the momentum equation (50), the influence of the turbulent fluctuations on the mean flow field is represented by the Reynolds stress tensor $\rho \langle u_i' u_j' \rangle$. Many second-order turbulence closure models have been developed for different applications, which have been summarized in a recent review article (Jaw and Chen,

1998a; 1998b). In the present model, the Reynolds stress, $\rho\langle u_i' u_j'\rangle$, is expressed by a nonlinear algebraic stress model (Shih et al., 1996; Lin and Liu, 1998a; 1998b)

$$
\rho\left\langle u_i' u_j'\right\rangle = \frac{2}{3}\rho k\,\delta_{ij} - C_d\,\rho\,\frac{k^2}{\varepsilon}\left(\frac{\partial\langle u_i\rangle}{\partial x_j} + \frac{\partial\langle u_j\rangle}{\partial x_i}\right)
$$

$$
- \rho\,\frac{k^3}{\varepsilon^2}\left[C_1\left(\frac{\partial\langle u_i\rangle}{\partial x_l}\frac{\partial\langle u_l\rangle}{\partial x_j} + \frac{\partial\langle u_j\rangle}{\partial x_l}\frac{\partial\langle u_l\rangle}{\partial x_i} - \frac{2}{3}\frac{\partial\langle u_l\rangle}{\partial x_k}\frac{\partial\langle u_k\rangle}{\partial x_l}\delta_{ij}\right)\right.
\tag{51}
$$

$$
\left. + C_2\left(\frac{\partial\langle u_i\rangle}{\partial x_k}\frac{\partial\langle u_j\rangle}{\partial x_k} - \frac{1}{3}\frac{\partial\langle u_l\rangle}{\partial x_k}\frac{\partial\langle u_l\rangle}{\partial x_k}\delta_{ij}\right) + C_3\left(\frac{\partial\langle u_k\rangle}{\partial x_i}\frac{\partial\langle u_k\rangle}{\partial x_j} - \frac{1}{3}\frac{\partial\langle u_l\rangle}{\partial x_k}\frac{\partial\langle u_l\rangle}{\partial x_k}\delta_{ij}\right)\right]
$$

in which C_d, C_1, C_2, and C_3 are empirical coefficients, δ_{ij} the Kronecker delta, $k = (1/2) < u_i' u_i' >$ the turbulent kinetic energy, and $\varepsilon = \nu < (\partial u_i'/\partial x_j)^2 >$ the dissipation rate of turbulent kinetic energy, where $\nu = \mu/\rho$ is the molecular kinematic viscosity. It is noted that for the conventional eddy viscosity model $C_1 = C_2 = C_3 = 0$ in equation (51), and the eddy viscosity is then expressed as $\nu_t = C_d\,(k^2/\varepsilon)$. Compared with the conventional eddy viscosity model, the nonlinear Reynolds stress model (equation (51)) can be applied to general anisotropic turbulent flows.

Rodi (1980) and Lin and Liu (1998a; 1998b) modeled the governing equations for k and ε as

$$
\frac{\partial k}{\partial t} + \langle u_j\rangle\frac{\partial k}{\partial x_j} = \frac{\partial}{\partial x_j}\left[\left(\frac{\nu_t}{\sigma_k} + \nu\right)\frac{\partial k}{\partial x_j}\right] - \left\langle u_i' u_j'\right\rangle\frac{\partial\langle u_i\rangle}{\partial x_j} - \varepsilon
\tag{52}
$$

$$
\frac{\partial\varepsilon}{\partial t} + \langle u_j\rangle\frac{\partial\varepsilon}{\partial x_j} = \frac{\partial}{\partial x_j}\left[\left(\frac{\nu_t}{\sigma_\varepsilon} + \nu\right)\frac{\partial\varepsilon}{\partial x_j}\right]
$$

$$
+ C_{1\varepsilon}\frac{\varepsilon}{k}\,\nu_t\left(\frac{\partial\langle u_i\rangle}{\partial x_j} + \frac{\partial\langle u_j\rangle}{\partial x_i}\right)\frac{\partial\langle u_i\rangle}{\partial x_j} - C_{2\varepsilon}\frac{\varepsilon^2}{k}
\tag{53}
$$

in which σ_k, σ_ε, $C_{1\varepsilon}$ and $C_{2\varepsilon}$ are empirical coefficients. In the transport equation for the turbulent kinetic energy (equation (52)), the left-hand side term denotes the convection, while the first term on the right-hand side represents the diffusion. The second and the third term on the right-hand side of equation (52) are the production and the dissipation of turbulent kinetic energy, respectively.

The coefficients in equations (51) to (53) have been determined by performing many simple experiments and enforcing the physical realizability. Recommended values for these coefficients are given in Rodi (1980) and Lin and Liu (1998a; 1998b).

Appropriate boundary conditions need to be specified. For the mean flow field, the non-slip boundary condition is imposed on the solid boundary, and the zero-stress condition is required on the mean free surface by neglecting the effect of airflow. For the turbulent field, near the solid boundary, the log-law distribution of mean tangential velocity in the turbulent boundary layer is applied so that the values of k and ε can be expressed as functions of distance from the boundary and the mean tangential velocity outside the viscous sublayer. On the free surface, the zero-gradient boundary conditions are imposed for both k and ε (i.e., $(\partial k/\partial n) = (\partial\varepsilon/\partial n) = 0$). A low level of k for the initial and inflow boundary conditions is assumed. The justification for this approximation can be found in Lin and Liu (1998a; 1998b).

When it comes to model wave and porous structure interaction the flow in the porous domain is described using equations (10), (11) and (13).

In order to couple the flow inside and outside the permeable structure, Liu et al. (1999) apply continuity of the mean and averaged velocity and pressure across the interface of porous media

and outside flow. Strictly speaking, the outside mean (ensemble-averaged) flow is not equivalent to the spatially-averaged flow in porous media, since the latter may still contain turbulent fluctuations. However, and as previously explained, these turbulent fluctuations are, in general, negligible. It is important to note that the turbulence model is not solved in porous media. Therefore, the evaluation of the turbulence kinetic energy needs special treatment. For details, see Liu et al. (1999).

Finally, it has to be said that a new version of COBRAS, currently under development, includes volume-averaged equations for both the turbulent kinetic energy and turbulence dissipation rate in order to consider turbulence inside the porous media (Hsu et al., 2002).

Regarding the numerical algorithm, in the numerical model, the RANS equations are solved by the finite difference two-step projection method (Chorin, 1968). The forward time difference method is used to discretize the time derivative. The convection terms are discretized by the combination of the central difference method and upwind method. The central difference method is employed to discretize the pressure gradient terms and stress gradient terms. The VOF method is used to track the free surface (Hirt and Nichols, 1981). The transport equations for k and ε are solved with the similar method used in solving the momentum equations. Detailed information can be found in Kothe et al. (1991), Liu and Lin (1997), and Lin and Liu (1998a; 1998b).

5.2. Application Examples

The mathematical model described above has been verified by comparing numerical results with either experimental data or analytical solutions. The detailed descriptions of the numerical results and their comparison with experimental data for waves breaking on an impermeable slope can be found in Liu and Lin (1997), and Lin and Liu (1998a; 1998b). The overall agreement between numerical solutions and experimental data was very good.

The extension to the modeling of waves breaking on a permeable slope has been carried out by Lara and Losada (2002). Fig. 7 shows a spilling breaker on a 1:20 slope with a 11 cm porous layer made of $D_{50} = 3.7$ cm stones. Water depth is 40 cm and incident wave characteristics are wave period, $T = 2$ s and wave height, $H = 15$ cm.

The dashed line in Fig. 7 represents the upper interface of the permeable layer. In the plot the free surface evolution along the slope at a given instant can be seen. Lines and color shadings represent turbulent kinetic energy intensity. It can be observed that there are two mechanisms of turbulence generation. The wave breaking process introduces turbulence at the free surface while a second mechanism generates turbulence at the fluid and porous layer interface that is advected to both the fluid and porous regions.

Furthermore, the model is suitable to analyze wave interaction with emerged or submerged permeable or solid structures, both for breaking or non-breaking conditions.

Fig. 8 presents numerical results of wave-induced flow in a rubble mound breakwater with a crown wall (Martin et al., 2002). The prototype corresponds to a rubble mound breakwater with a 90 ton blocks core and an armor layer made of 120 ton blocks. Numerical results have been obtained for a physical model with a scale 1/18.4.
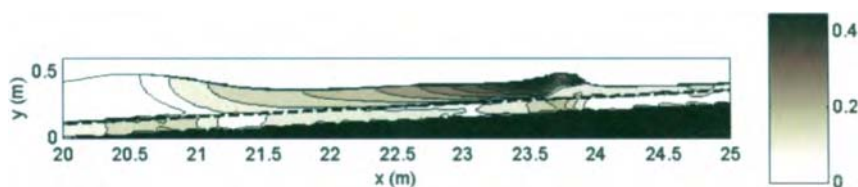
Figure 7. Spilling breaker on a 1:20 slope with a 10 cm permeable layer (Lara and Losada, 2002).
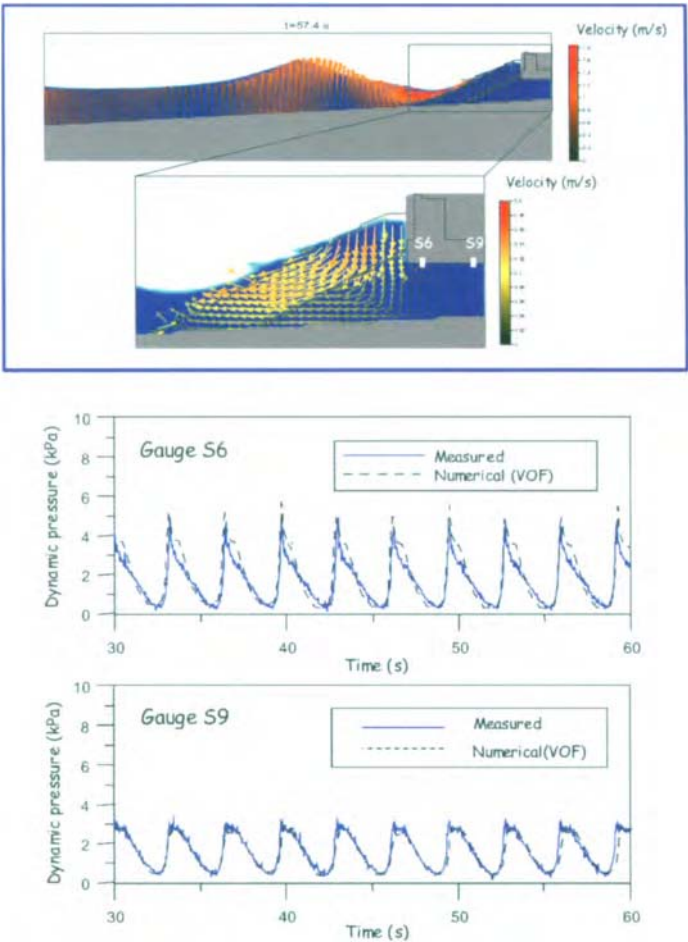
Figure 8. Numerical results of wave-induced flow in a rubble mound breakwater. Upper panel: Instantaneous velocity field in front and inside a rubble mound breakwater with a crown wall. Lower panels: Instantaneous dynamic pressure at the base of the crown: comparison between numerical and experimental results. (Martín et al., 2002)

The upper panel shows the instantaneous velocity field in front and inside the structure. Vectors visualize the flow induced by wave action in the proximity, and inside the armor and core layers. The rundown flow, infiltration in the porous layers and return flow are clearly visible in the graph. Lower panels present a comparison between numerical and experimental results. Dynamic pressure at gauges S6 and S9 located at different positions at the base of the crown is compared. First, it can be seen that there is an excellent matching in phase and magnitude of the numerical and experimental results. Wave attenuation inside the porous layers results in a decreasing dynamic pressure as we move toward the sheltered region. However, it is clearly visible that dynamic pressure at the base is not zero at the onshore side of the structure as assumed by most of the semi-empirical formulations to calculate the uplift force.

Another recent application can be found in Hsu et al. (2002), where the COBRAS is applied to the analysis of the wave motions and turbulence flows in front of a composite breakwater.

5.3. Some Consequences of Including Porous Flow Modeling

It is evident that including porous flow modeling in numerical models based on RANS equations has enormous potential. This kind of modeling allows the study of transient, breaking and non-breaking wave interaction with almost any kind of geometry, opening a broad range of possibilities. The analysis of internal flow, including turbulence, in a rubble-mound breakwater will result in a better functional and stability design. Furthermore, RANS modeling opens the possibility of addressing the problem of wave breaking on permeable structures and slopes. Therefore, it can be used as a tool to parameterize the effect of wave breaking on permeable layers and derive semi-empirical formulations that can be implemented in other propagation or morphodynamic models. It is clear that wave attenuation, internal flow, percolation, etc. may vary the location of the breaking point, wave breaking conditions and breaker type predicted considering impermeable bottom formulations.

Wave and porous structure interaction using RANS equations combined with a VOF solver may be an interesting complement to physical modeling. The combination of a numerical flume with a limited number of physical experiments may provide a more efficient and economic tool for the design of permeable structures and to evaluate their effects on the nearby area.

6. CONCLUSIONS AND FUTURE TRENDS

In this chapter it has been shown that, in the last decade, very important progress has been achieved in the field of modeling wave and permeable structure interaction. However, application by the engineering community is still limited. Models based on linear wave theory, modified Boussinesq equations or other kinds of shallow water equations and RANS equations are currently available. However, for any of these models the accuracy of the final results relies greatly on some parameters depending on the flow.

It has been shown that the consideration of structure permeability is important for structure functionality and stability and therefore, porous flow modeling should be considered in structure design. Future investigation could be oriented, for example, toward the modeling of the permeable structure deformation and the development of stability models as an alternative to current semi-empirical stability models.

Considering structure permeability modifies the flow in the nearby area, therefore having important consequences on scour and shoreline morphodynamics.

Porous flow should be implemented with care as part of morphodynamic modeling in coastal areas where permeable structures have been placed. Special attention has to be paid to considering the effects of wave transmission and combined diffraction-transmission leeward the structures, as well as the influence of structure permeability on wave breaking. The last may be implemented in standard Boussinesq or mild-slope equation-based wave propagation models using semi-empirical formulations.

Regarding the existing porous flow models, further research on the determination of predictive expressions for the porous flow parameters under oscillatory flow conditions is needed.

The validity of current porous flow models for rigid porous media with macroscopic pores, such as artificial block layers in rubble mound structures, should be analyzed.

The introduction of turbulence modeling in the porous region requires a careful exploration of the standard turbulence models as well as of the matching conditions at the water-porous medium interface, variable in time and space.

The extension of COBRAS to three-dimensions would imply a considerable improvement to the current modeling of wave and permeable structure interaction.

212

ACKNOWLEDGMENTS

LIST OF SYMBOLS

I	—	hydraulic gradient
ρ	—	fluid density
g	—	gravitational acceleration
$\overline{p}_o$	—	effective pressure
h_o	—	vertical distance from the selected datum
u^d	—	discharge velocity
$K = 1/a_p$ (m/s)	—	permeability coefficient
a_p	—	porous flow empirical coefficient
K_p (m^2)	—	intrinsic permeability
Re $= u_c D_c/v$	—	Critical Reynolds number
u_c	—	characteristic discharge velocity
D_C	—	characteristic length scale of the porous media
v	—	molecular viscosity
b_p	—	empirical coefficient with dimension (s^2/m^2)
n_e	—	porosity
α_p	—	non-dimensional coefficient
β_p	—	non-dimensional coefficient
$c_p(s^2/m)$	—	porous flow empirical coefficient
γ	—	non-dimensional coefficient accounting for the added mass
f_L	—	resistance force due to laminar flow
f_N	—	resistance force due to turbulent flow
f_I	—	resistance force due to inertia
KC	—	Keulegan-Carpenter number
u_i^*	—	i-th component of the instantaneous velocity in the pores
p^*	—	instantaneous effective pressure
u_i	—	i-th component of the seepage velocity
u_i^s	—	i-th component of the spatial perturbation
u_i^t	—	i-th component of time perturbation
C_f	—	dimensionless turbulent coefficient
s	—	co-factor accounting for added mass
f	—	linearized friction coefficient
ω	—	wave angular frequency
h	—	water depth
b	—	porous structure width
Φ	—	velocity potential
f_D	—	energy dissipation function associated with wave breaking
$\Gamma_o = \Gamma_R + i\Gamma_i$	—	complex wave number in the porous medium
ζ	—	free surface displacement
H_{rms}	—	mean-root-square wave height

T_p	—	peak period
h_{ef}	—	effective water depth
ϕ	—	depth-averaged potential
$\bar{u}$	—	depth-averaged velocity
ψ	—	depth-averaged piezometric head
δ_{ij}	—	Kronecker delta
k	—	turbulent kinetic energy
ε	—	dissipation rate of turbulent kinetic energy

REFERENCES

Baquerizo, A., and Losada, M.A., 1998. Longitudinal current induced by oblique waves along coastal structures. Coastal Engineering, 35: 211–230.

Berkhoff, J.C.W., 1972. Computation of combined refraction-diffraction. Proceedings of the 13th International Conference on Coastal Engineering, ASCE, pp. 471–490.

Burcharth, H.F., and Andersen, O.H., 1995. On the one-dimensional steady and unsteady porous flow equations. Coastal Engineering, 24: 233–257.

Chorin, A.J., 1968. Numerical solution of the Navier-Stokes equations. Mathematics of Computation, 22: 745–762.

Chwang, A.T., and Chan, A.T., 1998. Interaction between porous media and wave motion. Annual Review of Fluid Mechanics, 30: 53–84.

Cruz, E., Isobe, M., and Watanabe, A., 1992. Nonlinear wave transformation over a submerged permeable breakwater. Proceedings of the 23rd International Conference on Coastal Engineering, ASCE, pp. 1101–1114.

Cruz, E., Isobe, M., and Watanabe, A., 1997. Boussinesq equations for wave transformation on porous beds. Coastal Engineering, 30: 125–154.

Dalrymple, R.A., Losada, M.A., and Martin, P., 1991. Reflection and transmission from porous structures under oblique wave attack. Journal of Fluid Mechanics, 224: 625–644.

Gent, M.R.A., van 1991. Formulae to describe porous flow. Communications on Hydraulic and Geotechnical Engineering. Report 92–2. Delft, The Netherlands: Technical University, Delft. ISSN 0169-6548.

Gent, M.R.A., van 1993. Stationary and oscillatory flow through coarse porous media. Communications on Hydraulic and Geotechnical Engineering. Report 93–9. Delft, The Netherlands: Technical University, Delft. ISSN 0169-6548.

Gent, M.R.A., van 1995. Porous flow through rubble-mound material. Journal of Waterway, Port, Coastal, and Ocean Engineering, 121: 176–181.

Gonzalez, E.M., and Medina, R., 2001. On the application of static equilibrium bay formulations to natural and man-made beaches. Coastal Engineering, 43: 209–225.

Hall, K.R., Smith, G.M., and Turcke, D.J., 1995. Comparison of oscillatory flow and stationary flow through porous media. Coastal Engineering, 24: 217–232.

Hirt, C.W., and Nichols, B.D., 1981. Volume of Fluid (VOF) method for the dynamics of free boundaries. Journal of Computational Physics, 39: 201–225.

Hsu, T., Sakakiyama, T., and Liu, P.L.-F., 2002. A numerical model for wave motions and turbulence flows in front of a composite breakwater. Coastal Engineering, 46: 25–50.

Jaw, S.Y., and Chen, C.J., 1998a. Present status of second-order closure turbulence model. I: Overview. Journal of Engineering Mechanics, 124: 485–501.

Jaw, S.Y., and Chen, C.J., 1998b. Present status of second-order closure turbulence models. II: Application. Journal of Engineering Mechanics, 124: 502–512.

Kothe, D.B., Mjolsness, R.C., and Torrey, M.D., 1991. RIPPLE: A Computer Program for Incompressible Flows with Free Surfaces. LA-12007-MS. Los Alamos, NM: Los Alamos National Laboratory.

Lin, P., and Liu, P. L.-F., 1998a. A numerical study of breaking waves in the surf zone. Journal of Fluid Mechanics, 359: 239–264.

Lin, P., and Liu, P. L.-F., 1998b. Turbulence transport, vorticity dynamics, and solute mixing under plunging breaking waves in surf zone. Journal of Geophysical Research, 103: 15,677–15,694.

Liu, P.L.-F., and Lin, P., 1997. A Numerical Model for Breaking Wave: The Volume of Fluid Method. Research Report No. CACR-97-02. Newark, DE: Center for Applied Coastal Research, Ocean Engineering Laboratory, University of Delaware.

Liu, P.L.-F., and Wen, J., 1997. Nonlinear diffusive surface waves in porous media. Journal of Fluid Mechanics, 347: 119–139.

Liu, P.L.-F., Lin, P., Chang, K.-A., and Sakakiyama, T., 1999. Numerical modeling of wave interaction with porous structures. Journal of Waterway, Port, Coastal, and Ocean Engineering, 125: 322–329.

Liu, P.L.-F., Hsu, T.-J., Lin, P.-Z., Losada, I.J., Vidal, C., and Sakakiyama, T., 2000. The Cornell breaking wave and structure (COBRAS) model. In: Losada, I.J. (Editor), Proceedings of Coastal Structures '99. Vol. 1., pp. 169–175. Rotterdam: A.A. Balkema Publishers.

Lara, J.L., and Losada, I.J., 2002. Numerical modeling of wave breaking on a permeable porous slope. (in preparation).

Losada, I.J., 1996. Wave interaction with permeable structures. Ph.D. Thesis. Newark, DE: Department of Civil Engineering, University of Delaware. 230 pp.

Losada, I.J., Dalrymple, R.A., and Losada, M.A., 1993. Water waves on crown breakwaters. Journal of Waterway, Port, Coastal, and Ocean Engineering, 119 (4): 367–380.

Losada, I.J., Losada, M.A., and Martin, F.L., 1995. Experimental study of wave-induced flow in a porous structure. Coastal Engineering, 26 (1–2): 77–98.

Losada, I.J., Silva, R., and Losada, M.A., 1996a. 3-D non-breaking regular wave interaction with submerged breakwaters. Coastal Engineering, 28 (1–4): 229–248.

Losada, I.J., Silva, R., and Losada, M.A., 1996b. Interaction of non-breaking directional random waves with submerged breakwaters. Coastal Engineering, 28 (1–4): 248–265.

Losada, I.J., Patterson, M.D., and Losada, M.A., 1997a. Harmonic generation past a submerged porous step. Coastal Engineering, 31: 281–304.

Losada, I.J., Silva, R., and Losada, M.A., 1997b. Effects of reflective vertical structures permeability on random wave kinematics. Journal of Waterway, Port, Coastal, and Ocean Engineering, 123 (6): 347–353.

Losada, I.J., Dalrymple, R.A., and Losada, M.A., 1998. Wave-induced mean flows in vertical rubble mound structures. Coastal Engineering, 35: 251–281.

Lynett, P.J., Liu, P.L.-F., Losada, I.J., and Vidal, C., 2000. Solitary wave interaction with porous breakwaters. Journal of Waterway, Port, Coastal, and Ocean Engineering, 126 (6): 314–322.

Madsen, O.S., 1974. Wave transmission through porous structures. Journal of Waterways, Harbors, Coastal Engineering Division, ASCE, 100 (WW3): 168–188.

Madsen, P.A., Murray, R., and Sorensen, O.R., 1991. A new form of Boussinesq equations with improved linear dispersion characteristics. Coastal Engineering, 15: 371–388.

Martín, F.L., Martinez, C., Lomonaco, P., Vidal, C., 2002. A new procedure for the scaling of core material in rubble mound breakwaters model tests. Proceedings of the 28th International Conference on Coastal Engineering, ASCE, pp. 1594–1606.

Mase, H., and Takeba, K., 1994. Bragg scattering of waves over porous rippled bed. Proceedings of the 24th International Conference on Coastal Engineering, ASCE, pp. 635–649.

Massel, S.R., and Mei, C.C., 1977. Transmission of random wind waves through perforated or porous breakwaters. Coastal Engineering, 1 (1): 63-78.

Massel, S.R., and Butowski, P., 1980. Wind waves transmission through porous breakwaters. Proceedings of the 17th International Conference on Coastal Engineering, ASCE, pp. 333–346.

McIver, P., 1998. The dispersion relation and eigenfunction expansions for water waves in a porous structure. Journal of Engineering Mathematics, 34: 319–334.

McIver, P., 1999. Water wave diffraction by thin porous breakwater. Journal of Waterway, Port, Coastal, and Ocean Engineering, 125 (2): 66–70.

Mendez, F., Losada, I.J., and Losada, M.A., 2001. Wave-induced mean magnitudes in permeable submerged breakwaters. Journal of Waterway, Port, Coastal, and Ocean Engineering, 127 (1): 1–9.

Polubarinova-Kochina, P.Y., 1962. Theory of Groundwater Movement. Princeton, NJ: Princeton University Press.

Requejo, S., Vidal, C., and Losada, I.J., 2002. Modeling of wave loads and hydraulic performance of vertical permeable structures. Coastal Engineering, 46 (4): 249–276.

Rivero, F.J., Sanchez-Arcilla, A., Gironella, X., and Corrons, A., 1998. Large-scale hydrodynamic experiments in submerged breakwaters. Proceedings of Coastal Dynamics '97, pp. 754-762. Reston, VA: ASCE.

Rojanakamthorn, S., Isobe, M., and Watanabe, A., 1989. A mathematical model of wave transformation over a submerged breakwater. Coastal Engineering in Japan, JSCE, 32 (2): 209–234.

Rojanakamthorn, S., Isobe, M., and Watanabe, A., 1990. Modeling of wave transformation on submerged breakwater. Proceedings of the 22nd International Conference on Coastal Engineering, ASCE, pp. 1060-1073.

Rodi, W., 1980. Turbulence models and their application in hydraulics-a state-of-the-art review. IAHR Publication.

Shih, T.-H., Zhu, J., and Lumley, J.L., 1996. Calculation of wall-bounded complex flows and free shear flows. International Journal for Numerical Methods in Fluids, 23: 1133–1144.

Silva, R., Salles, P., and Palacio, A., 2002. Linear waves propagating over a rapidly varying finite porous bed. Coastal Engineering, 44: 239–260.

Smith, G., 1991. Comparison of stationary and oscillatory flow through porous media. M.Sc. Thesis. Kingston, ON: Queens University, Canada.

Sollitt, C.K., and Cross, R.H., 1972. Wave transmission through permeable breakwaters. Proceedings of the 13th International Conference on Coastal Engineering, ASCE, pp. 1827–1846.

Sollitt, C.K., and Cross, R.H., 1976. Wave Reflection and Transmission at Permeable Breakwaters. Technical Paper No. 76–8. Vicksburg, MS: Coastal Engineering Research Center.

Sulisz, W., 1985. Wave reflection and transmission at permeable breakwaters of arbitrary cross-section. Coastal Engineering, 9: 371–386.

Sulisz, W., 1997. Wave loads on caisson founded on multilayered rubble base. Journal of Waterway, Port, Coastal, and Ocean Engineering, 123 (3): 91–101.

Troch, P., and de Rouck, J., 1998. Development of a two-dimensional numerical wave flume for wave interaction with rubble mound breakwaters. Proceedings of the 26th International Conference on Coastal Engineering, ASCE, pp. 1638–1846.

Vidal, C., Losada, M.A., Medina, R., and Rubio, J., 1988. Solitary wave transmission through porous breakwater. Proceedings of the 21st International Conference on Coastal Engineering, ASCE, pp. 1073–1083.

Ward, J.C., 1964. Turbulent flow in porous medium. Journal of the Hydraulics Division, ASCE, 90 (HY5): 1–12.

Wu, T.Y., 1981. Long waves in ocean and coastal waters. Journal of the Engineering Mechanics Division, 107: 501–522.

Yu, X., 1995. Diffraction of water waves by porous breakwaters. Journal of Waterway, Port, Coastal, and Ocean Engineering, 121 (6): 275–282.

Yu, X., and Togoshi, H., 1996. Combined diffraction and transmission of water waves around a porous breakwater gap. Proceedings of the 25th International Conference on Coastal Engineering, ASCE, pp. 2063–2076.

Chapter 8

Perspective on Evolution in Sediment Modeling

Kerry Black

ASR Limited, P.O. Box 13048, Hamilton, New Zealand

1. INTRODUCTION

With good sediment transport forecasts, many coastal protection outcomes and environmental impacts could be foretold. But we must appear lame sometimes to the coastal manager...even to the point of letting a beach erode because some solutions have failed in the past. The science must precede the engineering, but just measuring the currents and waves, rather than doing a numerical prediction, is usually not adequate. To forecast an outcome, in relation to planned coastal construction for example, extrapolation to a "wide variety of conditions" will be needed, and so the numerical models cannot be ignored. But are accurate sediment transport predictions impossible to achieve?

One reason sediment flux predictions seem to be so difficult is because the forecast is at the bottom end of the "numerical chain". To obtain a good forecast, we need to accurately predict the hydrodynamics—waves, currents and turbulence before we can contemplate the sediment prediction. And the currents could result from processes at different time scales (for example, continental shelf waves, local winds) developed within different generating locations (remote, fairly local or immediate) and highly variable in space and time. The waves may be driving currents also, and they agitate the sea bed sediments through orbital motion. The whole system is three-dimensional. For sediment transport, we are mostly dealing with a boundary layer some 1–2 cm from the sea bed, but this thin zone lies within a "maxi-hydrodynamic environment".

There are other confounding issues at the sea bed (Fig. 1). Bedload versus suspended load ...everyone nods wisely, noting that the two are not the same, but there is still no full agreement over when one starts and the other stops within a few centimeters of the sea bed. Experienced graduate lecturers sometimes use this example so young students can start visualizing the processes, by introducing words like saltation, shear flow, bedload, pore pressure, intra-granular forces, near bed reference concentration, etc. These processes then occur in an environment that is very near the sea bed for a variety of grain sizes, and over plane beds, bedforms or undulations. The sum of these processes with turbulence (Savioli and Justesen, 1997; Bryan et al., 2002) determines instantaneous or time-averaged suspended sediment concentration in the water column. Evolution modeling is yet another extension of the modeler's capabilities, where sand body erosion/accretion depends on the input/output balance within regions over much longer time scales.

The essence of sediment transport knowledge is in the understanding of the micro-sphere at the sea bed when sand is first moved or suspended at instantaneous time scales (Black and Rosenberg, 1991; Ribberink and Al-Salem, 1992). This is where the latest research is being directed and the thrust will continue for a while yet. As computers become more powerful and the intuitive Lagrangian solutions (where each grain can be modeled as a particle) are continuing to evolve, the "ultimate" sediment transport model is beginning to appear. Better measurements have led to better theory and better computer simulations. Sediment transport remains challenging, and its complexity cannot be underestimated, but major advances in modeling approaches have been and are being made.

The discipline is feared by the non-specialist, needed by the planners and exciting to the aficionados and so an evolutionary perspective is presented on advanced capabilities in numerical modeling

Figure 1. Sediment suspension under waves with a barrage of recording instruments mounted on a mobile sled that is winched through the surf zone.

of waves, hydrodynamics and sediment dynamics in natural systems. Case studies from natural sites are used to initiate discussion about modeling strengths and weaknesses, the difficulties confronted by the modelers and ways to overcome them.

The chapter examines some of the author's research into physical processes and numerical models, leading to sand body evolution modeling. The voluminous body of general literature is not summarized because the objective is to highlight the lessons learned over a long period of practical sediment transport modeling by the author.

The chapter moves from large to micro-physical scales and from long to short time scales. The final section considers "evolution" modeling, i.e. migration of sand bodies on beaches and estuaries.

2. NUMERICAL MODELS

The numerical modeling is based on the "3DD Numerical Laboratory" (Fig. 2), a suite of coupled hydrodynamic, wave and dispersal models (Black, 2001a; 2001b), developed over 25 years of collaborative modeling research, since the first beach model in 1975 (Black, 1975).

The sediment transport forecasts use Model POL3DD, a multi-purpose dispersal model (pollution, oil spills, sediment transport, etc.). POL3DD is Lagrangian, i.e. for suspended sediment transport, particles are "lifted" into the water column from the sea bed each time step, with upward mass fluxes governed by an empirical prediction of near bed reference concentration (for example, Black et al., 1999). Once in the water column, the particles move under the action of gravity (fall velocity) and diffusion (random walk). The model is intuitive, indeed, simulating sediment grains using Lagrangian particles is a modeler's pleasure, because real grains and model particles can have a lot in common, like size, density, fall velocity and three-dimensional coordinates. The sediment model is described in the publication of Black et al. (1999) or in the user's manual (Black, 2001b).

The hydrodynamics is simulated with the well-known model 3DD (Black, 2001a), which has been used in more than 500 different research and consulting projects. In its modern form, 3DD is essentially five different simulations coupled into one fully-linked computer code dealing with:
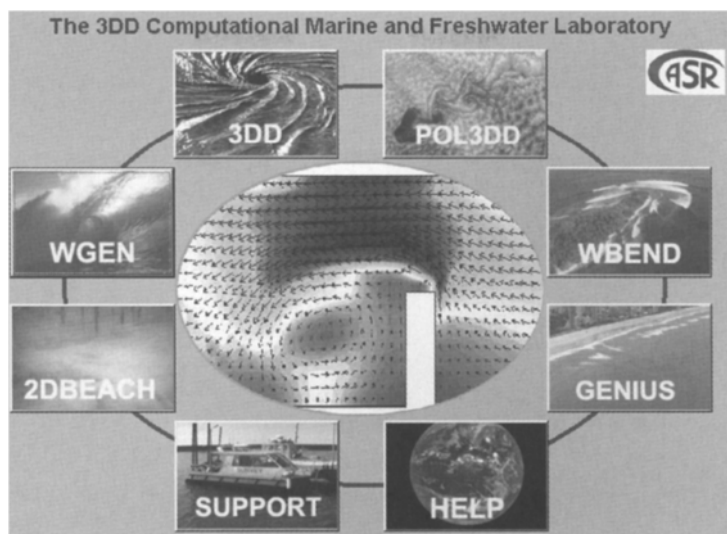
Figure 2. The 3DD suite of numerical models.

- Side-view, two-dimensional, three-dimensional homogeneous and three-dimensional stratified hydrodynamics
- Lagrangian and Eulerian dispersal, including buoyant plumes
- Ocean/Atmosphere heat transfers
- "Boussinesq" short waves
- Radiation stress wave-driven circulation

3. SEDIMENT TRANSPORT FORMULAE

A plethora of formula appeared in the 1970's and 1980's to predict the time-averaged sediment transport in rivers and estuaries. The objective was to get the best or simplest formula. Any consultant will confirm that "a technical argument amongst the experts leads to total confusion of the client". In this instance, even the scientists got perturbed and many publications appeared comparing, confirming or denying the many formulae.

While some highly technical data collection methods are now being applied, the early methodology was relatively straightforward. Bedload was associated with ripple migration rates and best results from my field data came after slightly modifying the Yalin formula (Black and Healy, 1982). For suspended load, water samples were pumped over several minutes with simultaneous current measurements at 1 m above the sea bed. The log of concentration versus currents or Shields stress (Shields, 1936) flushes out the current power dependence, while the intercept of the line may eventually become a modified empirical coefficient in the formula.

For time-averaged suspended load, the Engelund and Fredsoe formula (see Fredsoe and Deigaard, 1992) were proven accurate, but the "pre-moments" Bailard (1981) equations beneficially contain terms for sea bed gradient which are useful when modeling the slip face of migrating large bars on beaches. For example, Ranasinge et al. (under review) predicted the evolution of bars on beaches, as observed by an Argus time-lapse video at Palm Beach, Sydney with these equations. Such video

Figure 3. Time lapse image showing wave breaking positions at Palm Beach, Sydney (from the Argus Camera managed by G. Symonds).

systems provide exceptional insight into the bar evolution (Bogle et al., 1999; Brander, 1999) and are ideal for model calibration (Fig. 3).

In wave environments, the moments approach lends itself well to understanding the physics but research continues. For example, Green and Black (1999) questioned the Smith and McLean formula in relation to its functional form and efficacy. McComb and Black (2000) examined "black" sand (densities up to 5,500 $kg.m^{-3}$) and recommended a formula based on Shields stress to the power 1.5

The simple formula of Nielsen (1986) has become entrenched in the author's own investigations in wave environments (for example, Black and Rosenberg, 1991; Black et al., 1995; Black et al., 1997; Black and Vincent, 2001; Black et al., 2002b; Aagaard et al., 2002). Essentially, the near bed reference concentration is proportional to the Shields stress to the third power and instantaneous orbital motion to the sixth power! Understandably, Nielsen (personal communication) points out that the formula came from a few time-averaged concentration profiles in an Australian surf zone, and its widespread use and application to instantaneous time scales may be inapplicable. But nevertheless, it has been shown to work well in a wide variety of cases (see case studies below).

4. CAUSE AND EFFECT

Some of the confusion over wave-induced sediment transport formulae validated in field conditions arises:
(a) due to the lack of standards when defining single time-averaged statistics to describe a full time series of wave orbital currents, and
(b) simplifying a complex natural environment to a single empirical formula, without a numerical model for support.

With respect to the best statistic to describe an unsteady time series, "U_3" has been very successful (for example, Aagaard et al., 2002). It is a third moment of velocity (Black and Rosenberg, 1991), where

$$U_3 = 1.4 \left[\left(\sum_{j=i}^{N} |U_j|^3 / N \right) \right]^{1/3} \tag{1}$$

and U_j is the jth principal near bed orbital velocity measurement in a time series of N values. This statistical velocity is roughly equivalent to the 90th percentile of a time series of velocities, depending on the shape of the velocity distribution. Being one of the larger velocities in the time series, it reflects the nonlinearity of the relationship between current and suspended load.

Secondly, local field measurements (particularly at distances exceeding 1 m above the sea bed) will be contaminated by advected sand consisting of a variety of grain sizes. Over highly variable sea beds, a comprehensive numerical model is needed to cope with the rapid variations in near bed reference concentrations due to changes in sea bed character, factors of grain size fining with elevation, winnowing, etc.

4.1. Taranaki, Between a Rock and a Soft Black Place

Taranaki in west New Zealand features rock shelves interleaved by "black" sand, mostly a dense volcanic composite with titanomagnetites. The wave climate is moderate to large, with mean annual wave heights of 1.75 m. A major field program, spread over 4 years, was initiated for a port dredging permit. The study resulted in measurements of waves, currents, sediment settlement, grain sizes, fluorescent tracers, plus lots of repetition and variation in the physical conditions (McComb et al., 1999). A trial dredge mound of over 40,0000 m^3 was created and monitored over 18 months (McComb and Black, 2001).

From these comprehensive data, the search for the best suspended sediment transport equation led to a functional dependence that was different to the simple Nielsen formula. The conclusion proved to be inescapable, suggesting that black sands must behave differently to "white" quartzose sands.

The numerical modeling was, however, much more sophisticated than the empirical analysis. The modeling allowed for the spatial variation in sea bed grain size, the big rocky gaps between sandy patches, plus advection from distant sources, fining of grain size with elevation in the water column, etc. The site is very complex, with a series of islands, large sub-tidal reefs, irregular coastline and the patchy sand/rock sea bed. Some of the strongest currents inshore are wave-driven, while offshore the continental shelf waves and wind-driven flows dominate. Consequently, the modeling also included radiation-stress-driven currents and involved the coupling of a wave model (WBEND), with the hydrodynamic model 3DD and sediment model POL3DD.

With the numerical power underpinning the analysis using the models, it could be concluded that the Nielsen formula produced the strongest calibration (Black and McComb, 2000), not the authors' own black sand formula. A parallel program in southern India for a sand mining company, in collaboration with the Centre for Earth Science Studies in Kerala, reached the same conclusions (Black et al., 2002a).

4.2. Tauranga, Between Shell Lag and a Soft Place

In the clear Pacific waters of New Zealand's east coast, much of Tauranga Harbour is covered by an abundant detrital shell lag (Fig. 4). For example, in the fast-flowing entrance, there's no sand on the sea bed, only shell. But about 1 million m^3 of sand passes through annually in suspension, and settles in the shipping channels cut through the flood-tidal delta. When the port needed to consider environmental effects of dredging, an all-embracing field and numerical modeling study was undertaken. Waves, currents, suspended sediment load were measured while grain size analysis, side-scan

Figure 4. A detrital shell bed in the entrance to Tauranga Harbour, New Zealand. The scale is in 10 mm gradations.
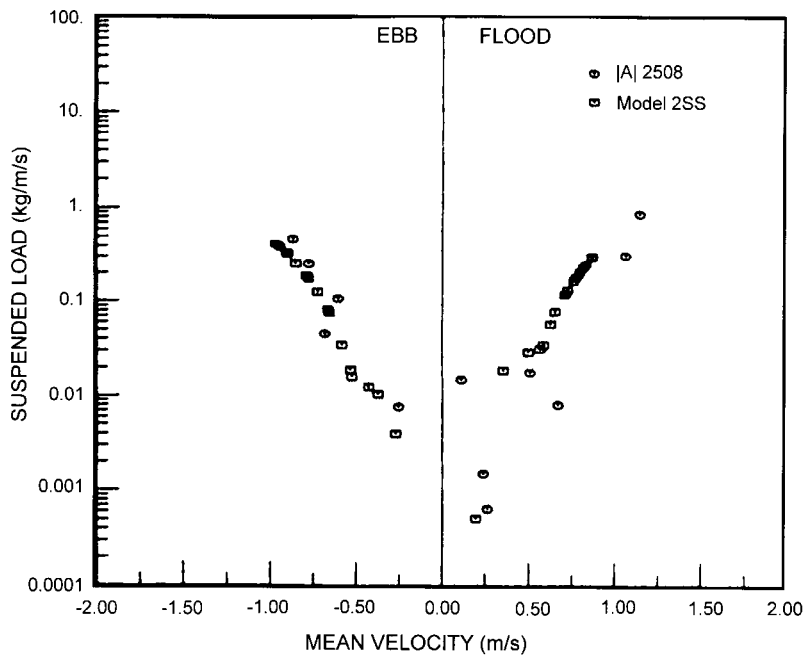
Figure 5. Ebb and flood suspended sediment concentration predictions by the model (square symbols) compared to measurements (circular symbols) in the shell-lagged entrance to Tauranga Harbour, New Zealand.

sonar, video and diving at some 300 sites gave a detailed view of the sea bed character. Full hydrodynamic and sediment models for multiple bed types were developed.

The model reproduced the sediment dynamics with great accuracy (Fig. 5), even over the shell lags where there was no local sea bed supply of sand (Black, 1987; Black and Barnett, 1988). The

success with the model was due in part to a novel feature of POL3DD coined "Sediment Availability". This is the thickness of erodible sediment in each cell, where shell lag has zero erodible thickness but settling sand can be re-suspended. Without the effect of the shell lag built into the simulation, the predictions in Tauranga Harbour were poor—for example, the dynamically-stable entrance was incorrectly predicted to erode rapidly. The sediment availability concept is an important component of a sediment model, relevant to all non-erodible surfaces such as natural reefs, geotextile bags on artificial surfing reefs, breakwaters, etc.

A general rule is that models must especially simulate the factors that lead to pseudo-equilibrium. For example, in most estuaries the infilling or erosion volumes are only a very small fraction of the total volume of sand that is mobilized each tide. Consequently, the pure sand assumption, which is often applied just because the model lacks sophistication or field data are not available, can be terminal. The high quality description of the estuarine sea bed and the model's capacity to accept these data, were ultimately essential for the accurate prediction of sediment concentrations in the compound environment of Tauranga Harbour.

With the confidence arising from these predictions, sand body evolution modeling was undertaken, and erosion/accretion rates in the harbor were successfully compared with natural changes, inferred from successive bathymetry surveys over periods of several years. The model was ultimately used for prediction of dredging impacts, port expansion and to develop an understanding of large sand bank evolution around the flood-tidal deltas (Fig. 6).

The modeling demonstrated that flow diversion between two main channels in the estuary resulted in a rotation of the ebb jet that strongly influenced ebb-tidal delta dynamics. Internally, flow patterns were responsive to the size of sand banks that blocked one of the two main channels. The sand bars forming the blockage migrated across the channel at decadal time scales and eventually welded onto a sand spit shoreline. Thus, the diversion of flow between the channels was cyclic and the estuary also went through synchronous cyclic evolution (Fig. 6). The evolution of the estuary was modeled and compared to a series of bathymetry surveys done every 10–30 years and dating back to 1852.

As a footnote, the correction that bandaged the Eulerian advection term in Black (1987) led the author to focus solely on Lagrangian schemes two decades ago. Quite simply, no matter how sophisticated the Eulerian finite difference approximations are, they can never accurately treat continuous fields of sources and sinks. Indeed, sediment transport modeling is a worst case where every cell is both a source and a sink and the sea bed may vary from muds, to sands, shells or rocks on a cell-by-cell basis.

4.3. Manukau, Somewhere in the Middle of Nowhere Over Mixed Sand Beds

So where does a curious sediment modeler with proven predictions in a complex estuary go next?—to the microcosm to shrink the perspective and to the beach to examine wave-induced transport, armed with high-tech equipment (Black and Rosenberg, 1991). A parallel thrust was simultaneously happening in the laboratories of Europe (Ribberink and Al-Salem, 1992).

When landing at Auckland airport, passengers pass over Manukau Harbour, some 10 km across and roundish. An important trial was conducted there and the reader is referred to Black et al. (1999) for details. A high-tech frame recorded waves, currents and suspended sediment concentrations (SSC) on an isolated inter-tidal sand bank, sitting somewhere near the middle of the estuary. The challenge was "to attempt to hindcast all parameters numerically over a mixed sand bed" ... wave generation, tidal and other currents, and bottom boundary layer sediment concentrations with near bed reference concentrations. The site experiences wave and tidal currents, but sediment transport is predominantly induced by waves.

Three numerical models from the 3DD Suite were utilized-wave generation (Model WGEN), hydrodynamic (Model 3DD) and sediment transport (Model POL3DD). The sediment prediction, of course, relied also on the accuracy of the other two models and on a series of empirical relationships

RESIDUAL FLOW   1902
1   20000.   10MM = 6000.00 M/S

metres   (1000's)

3   10   20   30

metres

0   500   1000

MOUNT
MAUNGANUI

MATAKANA
ISLAND

OTUMOETAI
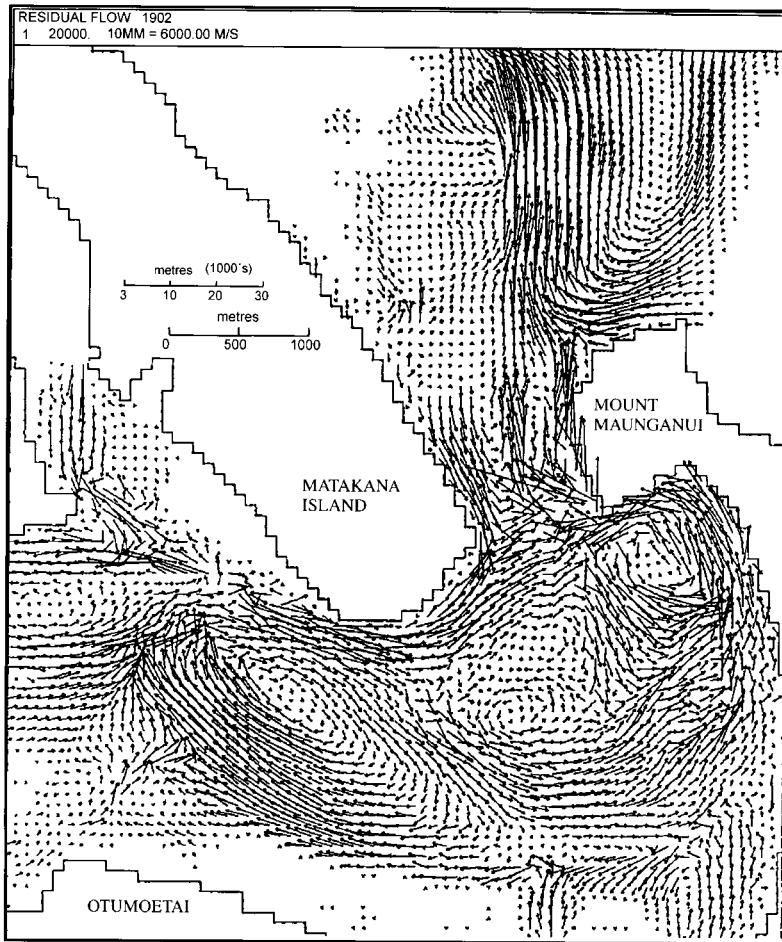
Figure 6. Tidally-averaged velocity vectors in Tauranga Harbour using bathymetry from the year 1902. The vectors infer the pathways of net sediment transport in the harbor and coincide with morphological interpretations and subsequent changes in the harbor.

that were tested. Examples were the relevance of linear theory for converting surface wave heights to near bed orbital velocities, the best single orbital motion statistic to describe a spectrum of waves when forecasting time-averaged SSC, bed friction formulae, etc.

The outcome was that the physical parameters could be accurately predicted. But why did it seem to work so well? For the hydrodynamics, the processes were mostly constricted to the estuary (i.e., tidal and local wind-driven), and the estuary was well-mixed. Generally, the most difficult hydrodynamic models to calibrate are on open coasts — remote forcing makes boundary conditions hard to formulate and water column stratification can vary rapidly over short vertical distances.

Good tidal prediction models have been highly successful for many years (for example, McDowell and O'Connor, 1977), although the author's experience of numerical models using the alternating-direction implicit (ADI) algorithm, particularly around eddies or wide inter-tidal zones, have been disappointing. The simpler explicit schemes offer many advantages, and computer speeds have im-

proved considerably since the demand in the late 1970's for longer time steps, the only known benefit of an ADI model. (This section has undoubtedly offended about three quarters of the readers and the agents for a couple of well-known commercial products).

Simple wave prediction theory is a mature science and the accuracy in the enclosed bay proved to be good, without any special new developments. Using the JONSWAP formula (Hasselmann et al., 1973), the key factors for wave prediction accuracy were bathymetry, inter-tidal flooding and drying, effective fetch, wave-induced bed friction, and breaking criteria. Subsequent tests showed that the simple methods adopted were more accurate than the SWAN and WAM models (see Chapter 5) in this small, enclosed environment, noting that WAM was not designed for small embayments. In the small bay (up to 10 km fetch), the wave heights responded quickly to the winds (within 1 hr), so the history of the sea state played a minor role. The "bathy, bathy, bathy" rule was dominant, i.e., the most important requirement was accurate depth along the wind fetch, which varied with the tide. The full spectrum was also needed as the water depths were intermediate above mid-tide for the short-period (2 s) local waves.

In the sediment model, treatment of the full grain size distribution was essential. The model was not accurate with a single grain size and so the investigation led to speculation about how the mixed sand/mud beds are suspended. Does the wave orbital motion indiscriminately strip off a layer of the bed, tossing all grains into the water column for subsequent suspension and settling, or does it selectively strip out the fine ones (Fig. 1)? It was inferred from the field measurements that each time a layer of bed material is suspended, the coarse sediments settle more quickly while finer sizes are winnowed out, leading to a subtle change in bed friction through time. The sediment model showed the same phenomenon. The inclusion of multiple grain sizes in the model also explained the observed fining of sediment with elevation above the bed and the distribution of mud plumes.

How the bed is suspended is fundamentally important to the way that the modeler formulates the computer code. The coding is different if (a) a burst of current (say under a wave crest) takes a whole layer of bed into suspension, or if (b) the wave preferentially lifts out of the mixed bed the grain fractions that are most easily suspended. The issue arises over all mixed grain beds, not only mud/sands. In practice, grain size distributions in the Lagrangian model are coded as individual particles, described by their size (fall velocity) and relative abundance in the grain size distribution. When the Shields stress is calculated, the near bed reference concentration can be calculated for each fraction individually as the Shields stress is grain size dependent. In this case, the amount suspended is not affected by the presence of the other fractions. This represents the case where the wave preferentially lifts the most easily suspended fractions. However, the alternative is to calculate near bed reference concentration using an effective grain (say the D_{50}), and then partitioning this concentration into fractions in accordance with their relative abundance on the sea bed. This represents the case where the wave strips off a layer of the bed indiscriminately and puts the entire size distribution into suspension.

A problem when trying to resolve this is that the commonly-used Optical Backscatter Sensors (OBS) are very responsive to muds, making it hard to "see" the sand in mixed sand/mud environments. On the contrary, the Acoustic Backscatter Sensor (ABS) is not able to resolve the muds well. So with electronic technology failing us, Beamsley et al. (2001) developed microscale pumps, with 5 inlets within 20 cm of the sea bed. Friction in the pipes restricted the hose lengths, and so Beamsley will recall diving at 4 m above the sea bed (in 10 m of water) operating the pumps on their short outlet hoses, with zero vision and substantial swell, over a variety of mixed sand/mud beds!

Of relevance to the above discussion, is that the mixed beds were apparently suspended as a unit, identified by a smooth transition in grain size from the bed into the water column. Even so, changes to the grain size distribution of the bottom sediments in the top several millimeters, as a wave event evolves, are inevitable, as fines are held longer in suspension. We conclude that the most effective way to model this is to use a representative grain size to calculate the near bed reference concentrations

(D_{50}) and suspend a whole layer of sea bed, while also evolving the changing grain size distributions in each model cell during the simulation as the coarser fractions resettle more rapidly.

5. COOKS BEACH, DOWNSCALE AND UPMARKET!

At averaged time scales exceeding 1–5 minutes, the case studies have demonstrated modeling capability in estuaries and on the open coast. Scientific curiosity then leads naturally to more detailed examination of modeling at instantaneous time scales within a couple of hundred millimeters of the sea bed.

Lagrangian modeling of SSC is fundamentally dependent on the pick-up function, which determines the mass of sand lifted off the bed. In turn, the pick-up function depends on current strength (i.e., orbital current under waves). The challenge to find out if modeling at these time and space scales could be done (i.e., to model instantaneous suspension at intra-wave time scales) is presented in four significant publications (Black and Rosenberg, 1991; Black et al., 1995; 1997; Black and Vincent, 2001).

The data sets had to be recorded with very high precision, as small differences in instrument elevation lead to large changes in concentration when measuring within 50 mm of the sea bed. A computer-controlled vertical profiler with 0.1 mm precision, instrumented sleds and bottom-mounted frames were developed (Radford et al., 1997; Black and Vincent, 2001), and the best data came from combinations of OBS, ABS and acoustic doppler velocimeters (ADV). The ADV is especially useful for the hydrodynamics, because it measures about 5 cm below the small sensor heads. Thus with care, the instrument can be placed to measure within a bedform trough or on a crest, under natural waves on a beach. On the white sandy shore of Cooks Beach on New Zealand's spectacular Coromandel peninsula, a "cast of thousands in a single rented house" did just this (Black et al., 1997; Osborne et al., 1997). They recorded the currents within bedform troughs, including the vortices that develop each wave cycle.

Interestingly, the idealized description, of a vortex forming in the bedform trough each wave cycle after peak orbital velocity, was not shown to be universally valid. Under random waves, the pressure gradients were not sinusoidal and so sometimes a small wave may produce a big vortex velocity and vice versa, while at other times no vortex would form at all. It depended on the relative intensity and time interval between accelerating and decelerating segments of the wave cycles.

Using the side-view capacity of Model 3DD and fine vertical grid spacing of 5 mm, the measured time series of surface waves were applied as boundary conditions (Black et al., 1997). The challenge was to simulate the complex flows and then the sediment suspension over bedforms at micro time and space scales. The test of the model was to determine if the velocities measured in the bedform trough could be reproduced.

The side-view hydrodynamic model reproduced much of this behavior (Black et al., 1997), demonstrating that currents responsible for microscale suspension within bedforms can be modeled at instantaneous time scales.

In relation to the sediment transport, the OBS (as used in the Cooks Beach experiment) cannot be brought closer than 50 mm from the sea bed, due to sand plumes induced by turbulence around the sensor. These were observed on underwater video. Also, the control of position relative to the bedform crest was not possible. Consequently, the sediment predictions were effective, but could not be used to examine the region within 50 mm of the bed. This had to wait until the ABS probed acoustically right to the sea bed (see below). Black et al. (1997) presented novel numerical demonstrations of sediment being ejected upwards by the vortex in the bedform trough—one of the causes of increased suspension over ripples (Fig. 7).
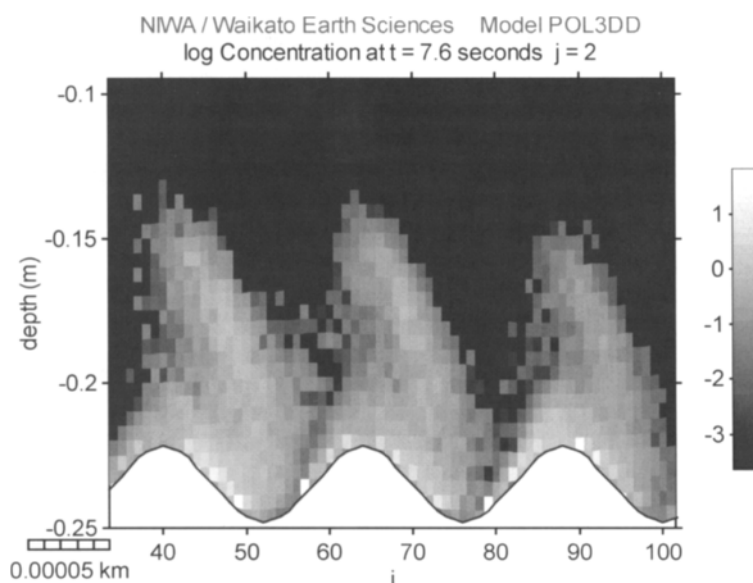
Figure 7. Instantaneous suspended sediment concentrations numerically predicted over ripples (25 mm high). The vortex in the trough leads to sediment ejection followed by horizontal advection of the sediment by the wave orbital motion.

The near bed reference concentration predicted by the model had to be increased by a calibration factor of about 20. After publishing the results, the author recalled what everyone else knew already—that a correction for near bed reference concentrations over bedforms had been presented by Du Toit and Sleath (1981)—and that the correction is about a factor of 20 for the bedforms at Cooks Beach! The same useful correction turned scattered data into a straight line in a more recent paper by Aagaard et al. (2002).

6. NAPIER, ART DECO AND POST-EARTHQUAKE

The Napier wine-growing district of New Zealand features unique art deco buildings, constructed after the earthquake flattened much of the town in the 1930's. It is also an ideal location for sediment transport measurements, with "clean" swell on a beach partially sheltered by a large headland (Black and Vincent, 2001). The experiment was a major offensive on microscale sediment transport—to capture high resolution SSC profiles (in 5 mm bins above the sea bed) at 12 Hz, armed with microscale video (PERVE), acoustic backscatter sensors (ABS) and acoustic doppler velocimeters (ADV). All equipment (including 2 ABS, an S4 vector-averaging current meter and an ADV on a high resolution computer-controlled profiler) was mounted on a frame and carried into the ocean. Output was cabled to shore for immediate digestion and quality checks in the shore base.

Years of preparation fell into place and all the best data were recorded over one day. Eventually simulations of only a couple of minutes of data were presented, but the results were astounding (Black and Vincent, 2001). For the first time, a sediment model was shown to be able to precisely reproduce the SSC time series at elevations within 120 mm of the sea bed, at intra-wave time scales (Fig. 8).
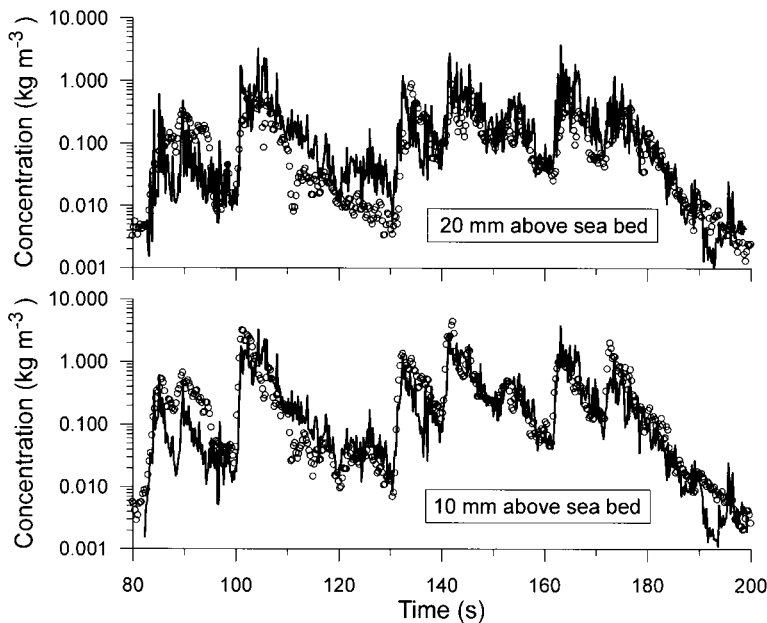
Figure 8. Measured (circles) and predicted (solid line) suspended sediment concentration at 10 mm and 20 mm above the sea bed at instantaneous time scales (see section of Figure previously presented in Black and Vincent, 2001).

Given the high quality field data, the research focused on model capability and on sediment ejection around flow reversal. The latter occurs when free stream orbital currents are zero and one might expect no suspension at this time. Discussed initially by Black and Rosenberg (1991), this phenomenon was later recorded more fully in a European laboratory (Ribberink and Al-Salem, 1992).

The Lagrangian model treats the processes with a close duplication of nature. Three key factors to consider when modeling are the near bed reference concentrations at instantaneous time scales, the vertical eddy diffusivity (which varies during the wave cycle), and the sea bed grain size distribution. Once again, the simple Nielsen formula proved best, the vertical eddy diffusivity could be inferred from the concentration profiles during the wave cycle and the sea bed grain sizes were determined with an automated fall velocity analyzer.

One problem for the modelers is the common assumption that eddy sizes diminish to zero adjacent to the bed, and that vertical eddy diffusivity is correspondingly zero (Simons et al., 1989). The most common laboratory measurements over smooth plates show eddy viscosity decreasing linearly to zero above the bed. This does not work in a diffusion-based sediment model, as sand cannot get off the sea bed if vertical eddy diffusivity is zero. Similarly, model tests of advection based ejection, by including the vertical orbital velocity (w), did not improve the predictions, particularly as w is also very small near bed level over plane beds. In a long series of case studies, the most appropriate assumption has been that eddy diffusivity goes to a finite value, rather than to zero near the bed in natural systems. Mostly, data have indicated that the best assumption is a profile of vertical diffusivity that is constant from the bed up to about 50 mm elevation.

A second problem for the modelers is the presence of suspension occurring at the time of flow reversal, even over plane beds (Black, 1994). When using the near bed reference pick-up function, concentration depends on currents, but orbital currents are zero at the time ... and so there should be

no suspension! But there was. The timing is such that the burst of sediment is ejected just before the trough, and so suspension around flow reversal mostly acts to transport sand offshore on beaches. This is opposite to, and may even balance, the well-known beach building mechanism of shoreward transport under the crest associated with wave asymmetry in swell conditions. As such, the issue is fundamentally important for accurate modeling of beach evolution.

The high resolution ABS measurements showed that vertical eddy diffusivity was maximum around flow reversal, at a time when flows very near the bed are opposite to the free stream due to the phase lag associated with frictional retardation of flow at bed level — coined "adverse shear". At this time, sediment penetrates higher into the water column.

Near bed reference concentration at the time of flow reversal could be predicted by substituting the zero current with the orbital current from the previous crest, while the duration of the SSC burst at flow reversal was associated with periods of "adverse shear" lasting up to about 0.3 s, which could be predicted numerically with the side-view hydrodynamic model. Adverse shear was shown with the model to become more pronounced as the wave asymmetry increased, in accordance with laboratory observations of higher suspension at flow reversal under asymmetric waves.

7. BEACH EVOLUTION, AND SUNTAN LOTION

If you surf waves, then beach research is definitely worth attempting. One aspect of surfing is that the processes are seen up close, particularly the changing sand bars and the processes around the breakpoint. (Remember the time it was necessary to deploy a frame in 3 m of water without a boat, Graham? We walked it out across the sea bed, dropping it every 15 s or so to get a breath and then back down to pick it up and run seaward.)

Personal observations suggest that things only exist if they evolve within a positive feedback loop, i.e. an ephemeral object like a breakpoint bar is subjected to a large amount of wave power and turbulence, and yet it exists in the midst of all this chaos. There must be a positive feedback such that the bar itself enhances bar formation, until some form of dynamic equilibrium is reached. Also, a breakpoint bar is not a subtle thing. Big waves break incredibly hard and the turbulence is sometimes life threatening on a surfboard. Thus, breakpoint bar formation is unlikely to be the result of the gentle blending of subtle steady processes, like infragravity wavelengths carefully matching the surf zone width, or a balance between bed-return flow (Masselink and Black, 1995) and wave asymmetry (Black, 1994). Such processes can play a modifying role but they are unlikely to be first-order processes responsible for the formation and evolution of breakpoint bars on beaches.

Black et al. (1995) recorded OBS and wave height data around the breakpoint at Apollo Bay in southern Victoria, including time series from just seaward of the breakpoint. At times, the infragravity and orbital motions combined to translate offshore (through the sensors) the highly-turbulent sediment-laden water from the breakpoint. The same phenomenon was happening in the shoreward direction. The medium sands were settling continuously, and so the process acted to move sand from the breakpoint, to be deposited both offshore and onshore.

The model was able to very closely predict these concentrations of SSC at instantaneous time scales (Black et al., 1995). Then the numerical simulations were used to demonstrate that this process can lead to bar formation at the breakpoint and predicted deposition rates were compatible with beach observations.

In relation to the evolution of bars, Black et al. (2002b) then expanded this mechanism throughout the surf zone. The orbital motion and turbulence is maximum at the breakpoint where the waves are largest. This leads to higher near bed reference concentrations and more sand in suspension. A basic law of diffusion (Ficks Law) is that material in suspension mixes "down" the concentration gradient (i.e., from high to low concentration).

The "diffusion" can be turbulent diffusion, or it can be enhanced by oscillating orbital currents that allow sand to be deposited away from the suspension location due to the back and forth motion. Infragravity oscillations can also act in the same way by oscillating the breakpoint SSC. The length scales of these oscillations are equivalent to the semi-orbital excursion and the numerical modeling showed that bars can be generated numerically by adding a horizontal diffusion term to the model with eddy diffusivity of order 0.1 to 1.0 m^2s^{-1}, and the bars were denoted as "diffusion" bars, in recognition of the formation mechanism.

Among the many features explained by this mechanism is the positive feedback discussed above. As the bar forms, the sea bed steepens and waves then break over a narrower region on the bar face. The mechanism is intensified at the one location and bar growth is enhanced. Similarly, bar growth is reduced if the spectrum is wide because the waves break at a variety of positions and the mechanism is diffused. The other common observation is for stronger bar formation on steeper beaches, and this can be similarly explained by the compression of the breakpoint into a narrower region on the steeper beach face.

Because the wave height gradient is strongest just shoreward of the breakpoint (when height is quickly lost by breaking), the near bed reference concentration gradient is also greatest shoreward of the breakpoint. Consequently, Ficks Law suggests that maximum transfer of sediment down the concentration gradient will be shoreward. The mechanism thereby explains the shoreward migration of bars under narrow band swell, a commonly-observed feature that has been missing from previous numerical simulations. Similarly, the offshore migration of a bar as it tracks wave height increases is also explained.

Perhaps best of all, the mechanism is entirely associated with individual breaking waves, which cause the concentration gradients and the diffusion. It requires no subtle coupling of different processes for the bar to form.

When modeling the evolution of the bar and its shoreward migration, the overall "equilibrium" beach profile (from the shore to beyond the breakpoint) that evolved in the model exhibited a convex "dome-like" character that is actually very common on beaches. The dome is common in the accretionary phase, while the exponential scoured shape (considered by Dean, 1977 among others) is more common in storms. In accordance with the evolution modeling, this dome-like convex profile can be explained by including horizontal diffusion in the model, and was accordingly called a "diffusion profile" by Black et al. (2002b).

In another category of evolution modeling, often superimposed on these profiles are large-scale bars and channels. Horizontal circulation around surf zones can lead to major (numerically predictable) transitions in these features also (Ranasinge et al., under review).

8. OFFSHORE COASTAL PROTECTION, WHERE IT ALL COMES TOGETHER

There has to be a reason for all this sediment dynamics research. For details of one application, the reader is referred to Special Issue No. 29 of the Journal of Coastal Research (Black, 2001c). It contains the first broad examination of amenity-based offshore coastal protection. Coined "artificial surfing reefs", the reefs give coastal protection while incorporating amenity (Black, 2001d; Mead and Black, 2001a; 2001b; 2001c). The application is a duplication of nature, copying the fact that offshore islands and reefs shelter the beach and lead to salient formation (Black and Andrews, 2001)—strictly not rocket science. But there is a benefit to our fragile coasts if the protection is offshore underwater, and the surfers, divers, wind surfers and fishermen are very supportive.

Computer design of these structures makes them more feasible, and very sophisticated shapes that incorporate world-class surfing can be achieved (Black, 1999; Black and Mead, 2001). At Noosa in southern Queensland, the shape that evolved incorporated wave rotation to realign the wave crests with the beach and thereby reduce longshore transport. The wave rotation concept is particularly beneficial in cases where expensive shoreline buildings prevent realignment of the coast, or large tidal ranges reduce the dissipation benefits of the reef. The theory is simply "if you can't rotate the coast, then rotate the waves". The structure at Noosa also creates set-up shoreward of the reef during storms, which leads to a reversal of the longshore currents that have been responsible for the erosion. At Noosa, the model was successfully validated against long-term measurements of the migration of a sand mound (placed by dredge near the breakpoint and monitored), while the desired surfing character was designed numerically in accordance with studies of actual surfing reefs (Black, 2001c).

The coastal protection capacity of the reefs was forecast after hundreds of numerical simulations of waves, currents and sediment evolution, individually considering the broad range of weather and wave conditions. One key modeling technique underpinning the sediment transport, is the hydrodynamic Boussinesq wave modeling within Model 3DD (Gorman and Black, 1997). The Boussinesq model shows the wave refraction and diffraction patterns, while also prescribing the instantaneous orbital velocities across the grid, which can be vital for accurate sediment modeling over complex topographies (Fig. 9).
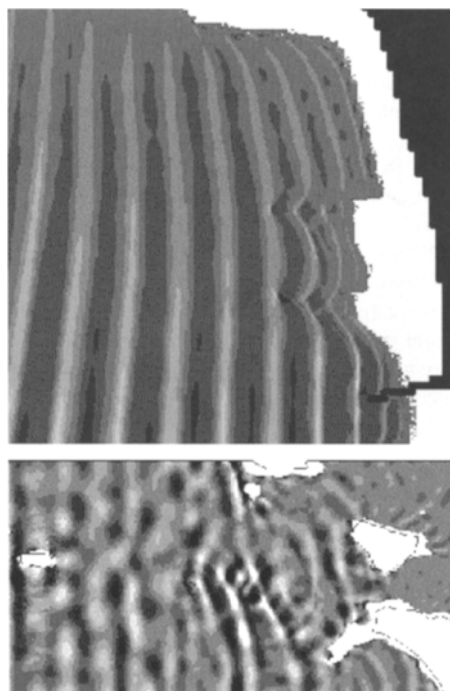
Figure 9. Simulation of waves around a proposed artificial reef for coastal protection and surfing at Noosa, Australia (upper panel) and in the Bay of Islands, New Zealand (lower panel). A Boussinesq model is an essential tool for examining wave refraction and diffraction over complex topographies.

9. DISCUSSION

Many applications over decades have demonstrated the ever-improving power of numerical simulations of sediment dynamics. Current capabilities for simulating wave-induced sediment transport within the bottom boundary layer were also presented, on open coast beaches and estuaries.

Throughout much of this work, the core of the sediment model has not fundamentally changed over nearly a decade. Indeed, the simplest case presented in Black and Vincent (2001) came from the first model simulation that was done for that investigation.

In all the case studies, sediment dynamics has always proved to be "predictable" and so the level of confidence is high ... perhaps this is contrary to the non-specialists' general opinion. All researchers have seen cases in the literature where the sediment prediction is said to be close—but inspection reveals order of magnitude agreement only. However, in the simulations presented from the various case studies above, the predictions are truly close. This includes models of bedforms at instantaneous time scales, where both the hydrodynamics and sediment dynamics were predicted.

Interestingly, evolution modeling in tidal conditions achieved a high degree of correlation some 15 years ago (Black, 1987) and so little has been done to advance this modeling over the last decade. The effort has been directed at wave environments for the modeling of sand bar evolution and sedimentation around structures. It was necessary to deal with the basics of suspended sediment prediction, before advancing to evolution. Even now, the confidence in evolution modeling over time scales longer than about 6 months has not been tested. But bar evolution over shorter time scales, often depicted by remote video systems (Bogle et al., 1999), has been successfully challenged and "equilibrium" beach states have been simulated.

The essence of the modeling presented here is that "direct" simulations are undertaken. That is, the models use the basic fluid and sediment dynamics equations at small space and time scales. They are not empirical models with many simplifying assumptions. By treating the problem directly, the model can break a system down into components for direct mathematical reproduction of the physical processes.

Some of the development of POL3DD did not come from sediment studies. The model has also been widely applied to larval transport, oil spills and outfalls (for example, Black and Parry, 1999; Jenkins et al., 1999). The variety of conditions to be simulated has led to breadth in the model's coding. Interestingly, POL3DD uses methodologies that represent broad physical processes, including fish larval behaviors, oil dissolution and evaporation, the Availability concept and associated advection over hard substrates, treatment of flow reversal, multiple and spatially-variable grain sizes, coupling with wave and current models, variable vertical eddy diffusivity at short time scales, spatial horizontal eddy diffusivity grids and a range of other spatially-varying variables. Given the wide range of environments that occur in nature, such versatility has proved to be an essential element of the modeling success.

10. CONCLUSIONS

Issues surrounding the numerical simulation of sediment dynamics, leading from site-specific modeling to bar evolution on beaches were considered. While there is a general fear about sediment modeling among the non-specialists and we cannot underestimate the complexity, major advances are being made. Lagrangian sediment transport modeling has systematically evolved to a high level of confidence, when the model is versatile and able to accept multiple inputs describing the natural system. The sediment model also relies on accurate modeling of waves and hydrodynamics.

Key aspects that make a sediment model suitable for a broad range of conditions are use of the Lagrangian technique, accurate pick-up functions for near bed reference concentration, the Availability concept and associated advection over hard substrates, treatment of flow reversal, multiple and

spatially-variable grain sizes, coupling with wave and current models, variable vertical eddy diffusivity at short time scales, spatial horizontal eddy diffusivity grids and a range of other spatially-varying variables.

One application of sediment evolution modeling is the development of better coastal protection measures. With good numerical simulations, the benefit/impacts of coastal protection structures can be predicted, including the more sophisticated offshore reef shapes that incorporate world-class surfing and other amenities.

ACKNOWLEDGMENTS

REFERENCES

Aagaard, T., Black, K.P., and Greenwood B., 2002. Cross-shore suspended sediment transport in the surf zone: A field-based parameterization. Marine Geology, 185: 283–302.

Bailard, J. A., 1981. An energetics total load sediment transport model for a plane sloping beach. Journal of Geophysical Research, 86 (C11): 10,938–10,954.

Beamsley, B., Black K.P., and Healy T.R., 2001. Micro-scale pumped measurements of suspended sediment over a mixed sand/mud bed: Profiles, grain sizes and sediment diffusivity. Journal of Coastal Research, Special Issue 34, ICS 2000): 342–356.

Black, K.P., 1975. Rip Currents. Bachelor of Science (Hons) thesis. Melbourne: University of Melbourne, 187p.

Black, K.P., 1987. A numerical sediment transport model for application to natural estuaries, harbours and rivers. In: Noye, J. (Editor), Numerical Modelling Applications to Marine Systems, Vol. 145, pp. 77–105. The Netherlands: North Holland/Elsevier, Mathematics Studies.

Black, K.P., 1994. Suspended sediment load during an asymmetric wave cycle over a plane bed. Coastal Engineering, 23: 95–114.

Black, K., 1999. Designing the shape of the Gold Coast Reef: Sediment dynamics. Proceedings of the Coasts & Ports '99 Conference, Perth, Australia. Vol. 1, pp. 58-63.

Black, K.P., 2001a. The Hydrodynamic Model 3DD. User's Manual. Hamilton, New Zealand: ASR Ltd., PO Box 13048, 120p.

Black, K.P., 2001b. The Lagrangian Model POL3DD. User's Manual. Hamilton, New Zealand: ASR Ltd., PO Box 13048, 115p.

Black, K. (Editor), 2001c. Natural and Artificial Reefs for Surfing and Coastal Protection. Journal of Coastal Research, Special Issue 29, 2001.

Black, K.P., 2001d. Artificial surfing reefs for erosion control and amenity. Theory and application. Journal of Coastal Research, Special Issue 34 (ICS 2000): 1–7.

Black, K., and Andrews, C., 2001. Sandy shoreline response to offshore obstacles, Part 1: Salient and tombolo geometry and shape. In: Black, K. (Editor), Natural and Artificial Reefs for Surfing and Coastal Protection. Journal of Coastal Research, Special Issue 29: 82–93.

Black, K.P., and Barnett, A.G., 1988. Sediment transport modelling under tidal flows with applications in a natural estuary. IAHR Symposium on Mathematical Modelling of Sediment Transport in the Coastal Zone, Copenhagen, Denmark, 9p.

Black, K.P., Gorman, R.M., and Bryan K.R., 2002b. Bars formed by horizontal diffusion of suspended sediment. Coastal Engineering, 47 (1): 53–75.

Black, K.P., Gorman, R.M., and Symonds, G., 1995. Sediment transport near the breakpoint associated with cross-shore gradients in vertical eddy diffusivity. Coastal Engineering, 26: 153–175.

Black, K., Green, M., Healy, T., Bell, R., Oldman, J., and Hume, T., 1999. Lagrangian modelling techniques simulating wave and sediment dynamics determining sand-body equilibria. In: Harff, J., Lemke, W., and Stattegger, K. (Editors), Computerized Modeling of Sedimentary Systems, Chapter 1, pp. 3–21.

Black, K.P., and Healy, T.R., 1982. Sediment transport investigations in New Zealand tidal inlet. Proceedings of the 18th International Conference on Coastal Engineering, ASCE, pp. 2436–2457.

Black, K.P., Mathew, J., Kurian, N.P., Prakash, T.N., and Thomas, K.V., 2002a. Heavy Mineral Budgeting and Management at Chavara. Volumes I and II. Prepared with Centre for Earth Science Studies, submitted to Indian Rare Earths Ltd, by ASR Limited April, 2002, Vol. I, 302p, Vol. II, 513p.

Black, K.P., and McComb, P.J., 2000. Port Taranaki Maintenance Dredging Consent Renewal Studies Report 2: Site Selection, Effects and Outcomes. Prepared for Westgate Transport Ltd., Port Taranaki, Department of Earth Sciences, University of Waikato, August 2000, 142 p.

Black, K.P., and Mead S., 2001. Design of the Gold Coast Artificial Surfing Reef: Surfing aspects. In: Black, K. (Editor), Natural and Artificial Reefs for Surfing and Coastal Protection. Journal of Coastal Research, Special Issue 29: 115–130.

Black, K.P., Osborne, P.D., Green, M.O., and Villard, P.V., 1997. Intra-wave suspended sediment concentrations over bedforms. Pacific Coasts and Ports '97 Conference, Christchurch, pp. 365–370.

Black, K.P., and Parry, G.D., 1999. Entrainment, dispersal and settlement of scallop dredge sediment plumes: Field measurements and numerical modelling. Canadian Journal of Fisheries and Aquatic Sciences, 56: 2271–2281.

Black, K.P., and Rosenberg, M.A., 1991. Suspended load at three time scales. Coastal Sediments '91. Waterway, Port, Coastal and Ocean Division (ASCE), Vol. 1, pp. 313–327.

Black, K.P., and Vincent, C.E., 2001. High-resolution field measurements and numerical modelling of intra-wave sediment suspension on plane beds under shoaling waves. Coastal Engineering, 42: 173–197.

Bogle, J.A., Bryan, K.R., Black, K.P., Hume, T.M., and Healy, T.R., 1999. Observations of geomorphic parameters using video images. Coasts and Ports '99. Institution of Engineers, Australia, pp. 70–75.

Brander, R. W., 1999. Field observations on the morphodynamic evolution of a low-energy rip current system. Marine Geology, 157: 199–217.

Bryan, K.R., Black, K.P., and Gorman, R.M., 2002. Spectral estimates of dissipation rate within and around the surf zone. Journal of Physical Oceanography. (in press).

Dean, R.G., 1977. Equilibrium Beach Profiles: U.S. Atlantic and Gulf Coasts. Newark, DE: Department of Civil Engineering, University of Delaware.

Du Toit, C.G., and Sleath, J.F.A., 1981. Velocity measurements close to rippled beds in oscillatory flow. Journal of Fluid Mechanics, 112: 71–96.

Fredsoe, J., and Deigaard, R., 1992. Mechanics of Coastal Sediment Transport. Singapore: World Scientific Publishing Co., 369p.

Gorman, R.M., and Black, K.P., 1997. Harbour wave studies with a hybrid explicit-implicit hydrodynamic model. Pacific Coasts and Ports '97 Conference, Christchurch, pp. 631-636.

Green, M.O., and Black, K.P., 1999. Suspended-sediment reference concentration under waves: Field observations and critical analysis of two predictive models. Coastal Engineering, 38: 115–141.

Hasselmann, K., Barnett, T.P., Bouws, E., Carlson, H., Cartwright, D.E., Enke, K., Ewing, J.I., Gienapp, H., Hasselmann, D.E., Kruseman, P., Meerbrug, A., Müller, P., Olbers, D.J., Richter, K., Sell, W., and Walden, H., 1973. Measurements of wind-wave growth and swell decay during the joint North Sea Wave Project (JONSWAP). Deutsche Hydrographische Zeitschrift, A8(12): 95p.

Jenkins, G.P., Black, K.P., and Keough, M.J., 1999. The role of passive transport and the influence of vertical migration on the pre-settlement distribution of a temperate, demersal fish: Numerical model predictions compared with field sampling. Marine Ecology Progress Series, 184: 259–271.

Masselink, G., and Black, K.P., 1995. Magnitude and cross-shore distribution of bed return flow measured on natural beaches. Coastal Engineering, 25: 165–190.

McComb, P., and Black, K., 2000. Port Taranaki Maintenance Dredging Consent Renewal Studies—Report 1: Field measurements. Volume 1: Text. Prepared for Westgate Transport Ltd, Port Taranaki, Department of Earth Sciences, University of Waikato, August 2000, 102p.

McComb, P.J., and Black, K.P., 2001. Dynamics of a nearshore dredged-sand mound on a rocky, high-energy coast. Journal of Coastal Research, Special Issue 34 (ICS 2000): 550–563.

McComb, P., Black, K., Healy, T., and Atkinson, P., 1999. Coastal and sediment dynamics at Port Taranaki, New Zealand: A large, multi-faceted, field experiment. Coastal Structures '99 Conference, Vol. 2, pp. 823–832. The Netherlands: A.A. Balkema Publishers.

McDowell, D.M., and O'Connor, B.A., 1977. Hydraulic Behaviour of Estuaries. New York: MacMillan Press Ltd, 292p.

Mead, S., and Black, K., 2001a. Functional components combinations controlling surfing wave quality and world-class surfing breaks. In: Black, K. (Editor), Natural and Artificial Reefs for Surfing and Coastal Protection. Journal of Coastal Research, Special Issue 29: 21–32.

Mead, S., and Black, K., 2001b. Predicting the breaking intensity of surfing waves. In: Black. K. (Editor), Natural and Artificial Reefs for Surfing and Coastal Protection. Journal of Coastal Research, Special Issue 29: 51–65.

Mead, S., and Black, K., 2001c. Field studies leading to the classification of world class surfing breaks. In: Black, K. (Editor), Natural and Artificial Reefs for Surfing and Coastal Protection. Journal of Coastal Research, Special Issue 29: 5–20.

Nielsen, P., 1986. Suspended sediment concentrations under waves. Coastal Engineering, 10: 1–21.

Osborne, P.D., Black, K., Villard, P.V., and Douglass, S., 1997. Field measurements of 3-D velocity structure and suspended sediments under locally generated waves and swell. Pacific Coasts and Ports '97 Conference, Christchurch, pp. 131–136.

Radford, J., Black, K., and Grant, D., 1997. Mobile instrument-support system for data collection within the surfzone: Rudolph experiments. Pacific Coasts and Ports '97 Conference, IPENZ, Christchurch, pp. 397–400.

Ranasinghe, R., Symonds, G., Black, K., and Holman, R., submitted. Morphodynamics of intermediate beaches. Coastal Engineering (submitted).

Ribberink, J.S., and Al-Salem, A.A., 1992. Time-dependent sediment transport phenomena in oscillatory boundary-layer flow under sheet flow conditions. Delft Hydraulics Data Report H840.20, Part VI. Delft, The Netherlands: Delft Hydraulics.

Savioli, J., and Justesen, P., 1997. Sediment in oscillatory flows over a plane bed. Journal of Hydraulic Research, 35 (N2), IAHR.

Shields, A., 1936. Anwendung der Ahnlichkeits Mechanik und der Turbulenzforschung auf die Geschiebe Bewegung. Berlin, Germany: Preuss. Versuchanstalt fur Wasserbau und Schiffbau.

Simons, R.R., Kyriacou, A.G., and Black, K.P., 1989. Predicting wave-current interactions at Mallacoota Bay. Proceedings of the 9th Australasian Coastal Engineering Conf., Adelaide, pp. 297–301.

This Page Intentionally Left Blank

Chapter 9

Large-Scale Finite Element Modeling and Parallel Computation of Sediment Transport in Coastal Areas

Onyx Wing-Hong Wai [a], Yu-Wu Jiang [a] and Qi-Miao Lu [b]

[a]Department of Civil and Structural Engineering, The Hong Kong Polytechnic University, Hung Hom, Kowloon, Hong Kong
[b]Baird and Associates, 627 Lyons Lane, Suite 200, Oakville, Ontario, Canada L6J 5Z7

1. INTRODUCTION

With more than half of the world's population residing near the coast, many coastal projects (for example, reclamation) and marine activities (for example, sediment dumping) of different sizes and scales are actively underway in nearshore zones. Numerical models are commonly used to predict and monitor the impact of these activities on the existing flow and sediment transport patterns to ensure that any potential adverse effects are within the shore protection and environmentally acceptable limits. Models that are built for coastal situations and equipped with the sediment-water coupling effect are, in general, three-dimensional (3-D) and highly complex. Thus, to achieve a meaningful coastal process simulation with such models, the problem set-up is usually large-scale with a large computational domain and long simulation period.

The quantum leap in the advancement of computer speed (computation and communication speed) in the last decade makes the implementation of parallel computation to investigate large-scale computational fluid dynamic problems attractive for many scientists and engineers. Parallel computation is a method for solving a problem using more than one computer or processor simultaneously. The implementation of this method needs the support of appropriate hardware and parallel computing algorithms. The main issues in parallel computation are: (1) problem partitioning so that each smaller partitioned component can be solved faster by a processor, and (2) result sharing between processors to produce the overall final result of the problem. However, one faces a dilemma of choosing between the parallel computation method, which can greatly shorten computation time, but requires the extra financial cost of obtaining additional hardware, and the conventional sequential method, which does not require effort in problem parallelization but requires a time cost that is at least several times that of parallel computation. The worthiness of implementing parallel computation can be evaluated by the efficiency and scalability of the overall parallel computation operation which is dependent on the hardware (speed of the CPU and communication cable), software (such as the parallel compiler, debugger and the communication library), and nature of the problem.

Wai and Lu (2000) developed a parallel model (WLPM) that can efficiently simulate hydrodynamic and sediment transport processes in coastal and estuary regions. The model utilized various parallel computational techniques to increase the computation efficiency as well as the model stability and accuracy. The efficiency is maximized in two steps. In the first step, a fully parallelizable hybrid operator splitting technique (Lu and Wai, 1998) was applied to discretize the governing equations of the model. Within one computation time step, the technique makes use of an explicit Eulerian-Lagrangian scheme to deal with the advection, a finite element method to handle the horizontal diffusion, and a finite difference method to handle the vertical diffusion. In the second step, the model parallelization is established according to a mixed strip/patch domain decomposition and

Master-Slave (M-S) communication approach. The stability is achieved by using an implicit discretization scheme for the continuity equation and the horizontal and vertical diffusion terms in the momentum and sediment transport equations. The 2nd order accurate, 9-node quadrilateral isoparametric finite elements are used in the horizontal layer to maintain the accuracy of the discretization scheme. The unstructured finite elements can be refined to better fit the irregular coastal boundary and to obtain a more detailed resolution at the area of interest. This results in a large amount of data on the nodes to be processed and stored in each time step. In the sequential computing method, two ways to speed-up a simulation are to enlarge the time step by enhancing the numerical stability and to increase the data processing speed by using a fast sparse matrix solver. Lu and Wai (1998) used an implicit discretization method to maintain the numerical stability of a finite element model, and the maximum time step was increased to one hour in an estuary simulation. A Gauss-Jacobi iteration method (GJI) was implemented in WLPM to solve the non-symmetrically linear equation system on an IBM SP2 parallel computer. It was found that if the number of nodes in each sub-domain (component) is within 80 to 85, the GJI method is efficient and takes about 0.5 s to complete the calculation of one time step. However, the efficiency of this method decreases steeply when the number of nodes increases. For example, when 8 sub-domains are used with 1000 nodes in each sub-domain, the GJI method takes about 315 s for each time step calculation.

This chapter describes a finite element parallel model that is largely based on WLPM. Because the GJI method used in WLPM is only for intermediate size problems, the preconditioned conjugate gradient method (PCG) is suggested for solving large-scale finite element linear systems. The performance of the parallel model running on a low-cost Beowulf distributed computer system (Hargrove et al., 2001) is discussed. Because parallel computing is still a relatively new science, the terminology used in this science may not be universal.

2. MODEL DESCRIPTIONS

2.1. Governing Equations

With the hydrostatic assumption, the standard governing equations for the flow field and sediment field in coastal waters in the σ topographic following coordinate system are given below. They are the continuity equation, the momentum equation, sediment transport equation and the bed deformation equation.

2.1.1. Continuity and Momentum Equations

$$\frac{\partial \zeta}{\partial t} + \frac{\partial H u_j}{\partial x_j} = 0 \tag{1}$$

$$\frac{d u_i}{dt} + f \beta_{ij} u_j + P_i^* + g \frac{\partial \zeta}{\partial x_i} = \frac{\partial}{\partial x_j} \left(\varepsilon_j \frac{\partial u_i}{\partial x_j} \right) \tag{2}$$

P_i^* is the baroclinic term with the Boussinesq assumption.

$$P_i^* = \frac{gH}{\rho_0} \int_\sigma^1 \frac{\partial \rho}{\partial x_i} \, d\sigma - \frac{g}{\rho_0} \frac{\partial H}{\partial x_i} \int_\sigma^1 (\sigma - 1) \frac{\partial \rho}{\partial \sigma} \, d\sigma \tag{3}$$

2.1.2. Sediment Transport and Bed Deformation Equations

$$\frac{d C_s}{dt} - \frac{\partial \omega_s C_s}{\partial x_3} = \frac{\partial}{\partial x_j} \left(\varepsilon_{s,j} \frac{\partial C_s}{\partial x_j} \right) \tag{4}$$

$$q_s = \omega_s C_s + \varepsilon_{s,3} \frac{\partial C_s}{\partial x_3} \tag{5}$$

where

$$u_j = \{u, v, \omega\} \ , \ \omega = \frac{1}{H} \left[w + (1 - x_3) \, u_i \, \frac{\partial h}{\partial x_i} - x_3 \left(\frac{\partial \zeta}{\partial t} + u_i \, \frac{\partial \zeta}{\partial x_i} \right) \right] ;$$

$$\varepsilon_j = \left[\varepsilon_x, \varepsilon_y, \varepsilon_z H^{-2} \right] ; \ \varepsilon_{s,j} = \left[\varepsilon_{s,x}, \varepsilon_{s,y}, \varepsilon_{s,z} H^{-2} \right] ;$$

$$x_j = \left[x, y, (z+h) \, H^{-1} \right] ; \ H = h + \zeta ;$$

$$\beta_{ij} = \begin{bmatrix} 0 & -1 & 0 \\ 1 & 0 & 0 \end{bmatrix} ; \ i = 1, 2; \ j = 1, 2, 3;$$

t is the time; h is the water depth relative to the mean sea level; ζ is the water fluctuation from the mean sea level; f is the Coriolis parameter; x_1, x_2, x_3 are the spatial coordinates with the σ transformation; u, v, ω are components of velocity of the x, y, z direction in σ coordinates, respectively; w is the vertical velocity in Cartesian coordinates; ρ is the bulk density of water-salinity; ρ_0 is the constant reference water density; ε_x, ε_y, ε_z are the eddy viscosity coefficients for water; C_s is the sediment concentration; $\varepsilon_{s,x}$, $\varepsilon_{s,y}$, $\varepsilon_{s,z}$ are the eddy diffusion coefficients for sediment; ω_s is the sediment settling velocity in σ coordinates; q_s is the sediment net flux in the vertical direction which is the difference between the downward sediment flux, $\omega_s C_s$, and the upward sediment flux, $\varepsilon_{s,3} \, \partial c_s / \partial x_3$. The parameters, such as the turbulence damping factor, near bed equilibrium reference and entrainment associated with the complex sediment dynamics are mentioned in detail by Wai et al. (1996). It should be noted that the advection term is included in the total time difference term, which will be solved by an Eulerian-Lagrangian method.

2.2. Sediment Settling Velocity

The settling velocity ω_s can be obtained from the balance between the gravitational and drag force. Yalin (1977) and van Rijn (1993) provided a formula for the settling velocity of a single non-spherical particle in static water

$$w_s = \begin{cases} \dfrac{g(\rho_P - \rho_w) D_P^2}{18 \, \rho_w \, v} & (1 < D_P < 100 \, \mu m) \\[3ex] \dfrac{10v}{D_P} \left(\sqrt{1 + \dfrac{0.01(\rho_P - \rho_w) g D_P^3}{\rho_w \, v^2}} - 1 \right) & (100 < D_P < 1000 \, \mu m) \\[3ex] 1.1 \sqrt{\dfrac{\rho_P - \rho_w}{\rho_w} g D_P} & (D_P > 1000 \, \mu m) \end{cases} \tag{6}$$

where w_s is the sediment settling velocity in Cartesian coordinates, ρ_P is the density of the initial grain, ρ_w is the density of water, D_P is the initial grain diameter. For higher sediment concentrations, the settling velocity will decrease due to the hindering effect caused by the fluid return flow induced by the other settling particles. Oliver (1961) suggested a formula for estimating this effect

$$w_{s,m} = (1 - 2.15 \, C_v) \left(1 - 0.75 \, C_v^{0.33} \right) w_s \tag{7}$$

where $w_{s,m}$ is the sediment settling velocity with the hindering effect and C_v is the sediment volumetric concentration, $C_v = C_s/\rho_P$.

Because cohesive sediment flocculates result in particle aggregation, this process may increase the settling velocity by several orders of magnitude. The settling velocity, including the hindering effect and flocculation, can be expressed as (Lick, 1982)

$$
w_{s,m} = \begin{cases} k\, C_v^m & \left(0 < C_v \leq \dfrac{10g/l}{\rho_P} \right) \\[3mm] w_f\, (1 - C_v)^r & \left(C_v > \dfrac{10g/l}{\rho_P} \right) \end{cases}
\tag{8}
$$

in which w_f is the settling velocity of individual flocs, m ($= 1\sim2$), r ($= 3\sim5$) and k is a coefficient.

2.3. Sediment Deposition and Entrainment Rate

The sediment deposition rate near the sea bed can be estimated by the formula given by Lick (1982)

$$
D_s = \alpha_s w_s C_s
\tag{9}
$$

where α_s ($= 0 \sim 1$) is the probability of sediment settling. For small particles (for example, size less than $1\,\mu m$) α_s is determined by the Brownian motion and turbulence. However, for larger particles, α_s can be set to 1.

The entrainment rate can be estimated by the following formula (van Rijn, 1986)

$$
E = \begin{cases} 0 & \left(\tau^b \leq \tau^{b,cr} \right) \\[2mm] w_s C_{a,e} & \left(\tau^b > \tau^{b,cr} \right) \end{cases}
\tag{10}
$$

where $C_{a,e}$ is the near bed equilibrium reference concentration; $\tau^{b,cr}$ is the critical erosion shear stress. Note that this formula is not suitable for fine cohesive sediment, for example, $D_P < 4\,\mu m$. Lick (1982) suggested another entrainment rate formula for fine sediment

$$
E = \begin{cases} 0 & \left(\tau^b \leq \tau^{b,cr} \right) \\[2mm] \alpha \left(\dfrac{\tau^b - \tau^{b,cr}}{\tau^{b,cr}} \right)^m & \left(\tau^b > \tau^{b,cr} \right) \end{cases}
\tag{11}
$$

where $a (= 8 \times 10^{-3})$ is the empirical parameter and m (≈ 2) is a constant.

3. NUMERICAL SPECIFICATIONS

3.1. Time Splitting for the Momentum Equations

An operator splitting method is used to discretize the momentum equation, equation (2), and the mass transport equation, equation (4). Taking the momentum equation (2) as an example, the equation is split into three subsystems that represent the advection, the horizontal diffusion and vertical diffusion

$$
\frac{u_i^{n+1/3} - u_i^n}{\Delta t} + u_j^n \frac{\partial u_i^n}{\partial x_j} + f\beta_{ij}\, u_j^{n+1/3} = 0; \quad i = 1, 2; \quad j = 1, 2, 3
\tag{12}
$$

$$\frac{u_i^{n+2/3} - u_i^{n+1/3}}{\Delta t} + P_i^{*n+1/3} = \frac{\partial}{\partial x_j}\left(\varepsilon_j \frac{\partial u_i^{n+2/3}}{\partial x_j}\right), \quad i = 1, 2; \quad j = 1, 2 \tag{13}$$

$$\frac{u_i^{n+1} - u_i^{n+2/3}}{\Delta t} + g\frac{\partial \zeta^n}{\partial x_i} = \frac{\partial}{\partial x_3}\left(\varepsilon_3 \frac{\partial u_i^{n+1}}{\partial x_3}\right), \quad i = 1, 2 \tag{14}$$

The continuity equation is integrated for the whole time step to ensure that the mass is conserved in an element. By integrating equation (1) from the sea bed to the water surface and employing the boundary condition, the continuity equation becomes

$$\frac{\partial \zeta}{\partial t} + \frac{\partial Q_i H}{\partial x_i} = 0 \quad i = 1, 2 \tag{15}$$

where Q_i is the vertical averaged velocity in the x_i direction. By substituting equation (14) into (15), the continuity equation can be combined as follows

$$\frac{\zeta^{n+1} - \zeta^n}{\Delta t} + \frac{\partial Q_i^{n+2/3} H^{n+1}}{\partial x_i} - \Delta t g \frac{\partial}{\partial x_i}\left(H^n \frac{\partial \zeta^{n+1}}{\partial x_i}\right) + \Delta t \frac{\partial}{\partial x_i}\left(\tau_i^w - \tau_i^b\right) = 0; \quad i = 1, 2 \tag{16}$$

where τ_i^w and τ_i^b are surface and bottom shear stress, respectively, in the x_i direction. Note that equations (13), (14) and (16) have to be implicitly solved.

3.2. Time Splitting for the Sediment Transport Equations

The sediment transport equation is different from the momentum equation in two ways: (1) the sediment transport equation does not include the pressure gradient term and the Coriolis term in which pressure is the principal force for shallow water flows, and (2) the sediment settling and re-suspension processes are the key sink/source terms in the sediment transport equation. Similar to the momentum equation, with the use of the splitting operator method, the sediment transport, equation (4), is split into three subsystems, the advection, the horizontal diffusion and vertical diffusion as follows

$$\frac{C_s^{n+1/3} - C_s^n}{\Delta t} + u_j^n \frac{\partial C_s^n}{\partial x_j} = 0; \quad j = 1, 2, 3 \tag{17}$$

$$\frac{C_s^{n+2/3} - C_s^{n+1/3}}{\Delta t} = \frac{\partial}{\partial x_j}\left(\varepsilon_{s,j} \frac{\partial C_s^{n+2/3}}{\partial x_j}\right), \quad j = 1, 2 \tag{18}$$

$$\frac{C_s^{n+1} - C_s^{n+2/3}}{\Delta t} = \frac{\partial}{\partial x_3}\left(\omega_s C_s^{n+1} + \varepsilon_{s,3} \frac{\partial C_s^{n+1}}{\partial x_3}\right) \tag{19}$$

3.3. Spatial Discretization for the Navier-Stokes Equations
3.3.1. Explicit Eulerian-Lagrangian Method for Advection

In the first fractional step (first subsystem), an explicit Eulerian-Lagrangian method is employed to solve the advection term. Equation (12) can be directly obtained from the following algebraic equations

$$u_i^{n+1/3} = A_{ij} u_{jp}^n \quad (i, j = 1, 2) \tag{20}$$

where

$$A_{ij} = \frac{1}{1 + (\Delta t\, f)^2} \begin{bmatrix} 1 & \Delta t f \\ -\Delta t f & 1 \end{bmatrix}$$

and u_{jp}^n is the velocity at the point P that is the location of a particle on the streamline. This particle will reach the point x_i over a time step, Δt.

3.3.2. Implicit Finite Element Method for Horizontal Diffusion

In the second fractional step, the standard Galerkin finite element method (FEM), with the 9-node isoparametric quadrilateral finite element, is employed to implicitly discretize the horizontal diffusion equation (13). There are a total of $L_{ayer} * N_c$ equations similar to equation (13), where L_{ayer} is the number of layers in the vertical direction, and N_c can be 3 if there are three variables (u_1, u_2, C_s). All these equations are solved in each step. In WLPM, equation (13) is discretized with a final form as shown below

$$u_i^{n+2/3} = \mathbf{D}^{-1}\mathbf{M} u_i^{n+1/3} \tag{21}$$

where $\mathbf{u}_i = [u_{i,1}, u_{i,2}, \ldots, u_{i,N}]^T$, N = number of nodes in a layer, $\mathbf{M}$ is the summation of the mass matrix and $\mathbf{D}$ is the stiffness matrix. The inverse of the coefficient matrix $\mathbf{D}^{-1}$ can be calculated in advance (before the time marching process) with the assumption that the eddy viscosity coefficient is constant. This approach has two shortcomings. First, the $\mathbf{D}^{-1}$ loses the sparse property, and at least N^2 multiplications are needed for calculating equation (13). Second, the eddy viscosity coefficient cannot be changed in the time marching process. As suggested by Mellor (1998), the eddy viscosity may vary with the current velocity and other parameters. Furthermore, there are two matrix inversion operations that must be done in advance (one for velocity and the other for sediment). This demands long computation time if the algorithm is not efficient.

It is important to maintain the symmetric, positive-definite matrix $\mathbf{D}$ in the linear equation system of equation (21), because the linear equations forming such matrices can be solved more efficiently than the non-symmetric or non-positive-definite matrix. Equation (13) can be transformed to equation (22) with the use of the 2nd order 9-node quadrilateral shape function $(\phi_j, j = 1, \ldots, 9)$ in the standard Galerkin FEM. With the baroclinic term ignored, the simplified case can be expressed as follows

$$\int_\Omega u_{i,j}^{n+2/3} \phi_j \phi_k \, d\Omega - \Delta t \int_\Omega \frac{\partial}{\partial x_i} \left(\varepsilon_i \frac{\partial u_{i,j}^{n+2/3} \phi_j}{\partial x_i} \right) \phi_k \, d\Omega = \int_\Omega u_{i,j}^{n+1/3} \phi_j \phi_k \, d\Omega \tag{22}$$

This equation can be transformed to the following equation using the divergence theorem

$$\mathbf{D} u_i^{n+2/3} = \mathbf{M} u_i^{n+1/3} \tag{23}$$

where

$$M_{j,k} = \int_\Omega \phi_j \phi_k \, d\Omega \tag{24}$$

$$D_{j,k} = M_{j,k} + \Delta t \int_\Omega \varepsilon_i \frac{\partial \phi_j}{\partial x_i} \frac{\partial \phi_k}{\partial x_i} \, d\Omega + \Delta t \oint_\Gamma \varepsilon_2 \phi_k \frac{\partial \phi_j}{\partial x_2} \, dx_1 - \varepsilon_1 \phi_k \frac{\partial \phi_j}{\partial x_1} \, dx_2 \tag{25}$$

and Γ is the boundary around the concerned domain Ω. The third term is generated by the velocity gradient normal to the boundary, which can be assumed to be zero, i.e., $\partial u_i / \partial n = 0$. That means,

in the horizontal direction, the current at the open and close boundaries will not affect the internal current via the eddy viscosity function. The assumption is acceptable because the velocity at the boundary should be prescribed manually in order to close the governing equations, for example, $u = 0$ can be the close boundary condition as can $\partial u_i / \partial n = 0$. With this assumption, the matrix $\mathbf{D}$ is symmetric in the linear equation that can be solved efficiently by an algorithm taking advantage of such characteristics as sparse, symmetric, and positive-definite matrix.

3.3.3. Implicit Finite Element Method for the Continuity Equation

Equation (16) is relatively complex. It is solved in the third fractional step. Applying the standard Galerkin FEM method gives

$$\mathbf{G}\,\zeta^{n+1} = z \tag{26}$$

where $\mathbf{G}$ is the coefficient matrix, and z is a known vector. This linear equation is more difficult to solve than equation (16) because the matrix $\mathbf{G}$ is not symmetric and positive. In Section 4.3, a more efficient algorithm is suggested and described in detail for equation (26).

3.3.4. Implicit Finite Difference Method for Vertical Diffusion Term

The last fractional step uses an implicit finite difference method (FDM) to discretize equation (14) in each vertical node column. With the central difference scheme and insertion of the bottom and surface conditions, the finite difference discretization of equation (14) can be written as

$$\mathbf{B}u_i^{n+1} = v_i \tag{27}$$

where $\mathbf{u}_i = \left[u_{i,1}, u_{i,2}, \ldots, u_{i,L}\right]^T$. Here, $u_{i,l}$ is the velocity at the l-th layer; L is the number of vertical layers; $\mathbf{B}$ is a triangular coefficient matrix, and v_i is a known vector. The gradient of the surface elevation in the horizontal direction can be calculated by the 1st-order elevation shape function φ as shown below

$$\left(\frac{\partial \zeta^{n+1}}{\partial x_i}\right)_j = \sum_{e=1}^{m_j} \int_\Omega \frac{\partial \varphi_k \zeta_k}{\partial x_i} \, d\Omega \bigg/ \sum_{e=1}^{m_j} \Omega \tag{28}$$

where m_j is the number of elements around the jth node. Equation (27) can be solved efficiently by the double sweep method. It is not necessary to parallelize this equation because the parallelization is achieved through the domain decomposition strategy in the horizontal direction discussed in Section 4.1.

3.4. Spatial Discretization for Sediment Transport Equations

The sediment transport equation is similar to the momentum equation except for the pressure gradient, Coriolis and sink/source terms. The detailed discretization procedures of the sediment transport equations are given below.

3.4.1. Explicit Eulerian-Lagrangian Method for Advection

The explicit Eulerian-Lagrangian method is used to handle the advection term in the transport equation in the first fractional step. Equation (17) can then be solved with the following algebraic equation

$$C_s^{n+1/3} = C_{s_{jp}}^n \tag{29}$$

where $C_{s_{jp}}^n$ is the sediment concentration at point P on a streamline. In the model, the time step is divided into a number of sub-steps (for example, $\Delta t = n \times \Delta t^*$, where $n = 10$), for improving the numerical stability.

3.4.2. Implicit Finite Element Method for Horizontal Diffusion

In the 2nd fractional step, the horizontal diffusion terms in equation (18) are now implicitly discretized by the standard 9-node Galerkin finite element method and the transformed equation is expressed as

$$C_s^{n+2/3} - C_s^{n+1/3} - \Delta t \frac{\partial}{\partial x_1} \left(\varepsilon_1 \frac{\partial C_s^{n+2/3}}{\partial x_1} \right) - \Delta t \frac{\partial}{\partial x_2} \left(\varepsilon_2 \frac{\partial C_s^{n+2/3}}{\partial x_2} \right) = 0 \tag{30}$$

The weak form of equation (30) can be obtained by multiplying the weighting function, ϕ_k, and then integrating the entire model domain.

$$\int_\Omega \left(C_s^{n+2/3} - C_s^{n+1/3} \right) \phi_k \, d\Omega -$$

$$\int_\Omega \left[\frac{\partial}{\partial x_1} \left(\varepsilon_1 \frac{\partial C_s^{n+2/3}}{\partial x_1} \right) + \frac{\partial}{\partial x_2} \left(\varepsilon_2 \frac{\partial C_s^{n+2/3}}{\partial x_2} \right) \right] \phi_k \Delta t \, d\Omega = 0 \tag{31}$$

With the use of the 9-node isoparametric shape function, $\phi_j, j = 1, \ldots, 9$, equation (31) can be written as follows

$$\int_\Omega \left(C_{s,j}^{n+2/3} - C_{s,j}^{n+1/3} \right) \phi_j \phi_k \, d\Omega -$$

$$\Delta t \, C_{s,j}^{n+2/3} \int_\Omega \left[\frac{\partial}{\partial x_1} \left(\varepsilon_1 \frac{\partial \phi_j}{\partial x_1} \right) + \frac{\partial}{\partial x_2} \left(\varepsilon_2 \frac{\partial \phi_j}{\partial x_2} \right) \right] \phi_k \, d\Omega = 0 \tag{32}$$

The second integration term can be transformed to

$$\int_\Omega \left\{ \frac{\partial}{\partial x_1} \left(\varepsilon_1 \frac{\partial \phi_j}{\partial x_1} \phi_k \right) + \frac{\partial}{\partial x_2} \left(\varepsilon_2 \frac{\partial \phi_j}{\partial x_2} \phi_k \right) \right\} d\Omega -$$

$$\int_\Omega \left\{ \varepsilon_1 \frac{\partial \phi_j}{\partial x_1} \frac{\partial \phi_k}{\partial x_1} + \varepsilon_2 \frac{\partial \phi_j}{\partial x_2} \frac{\partial \phi_k}{\partial x_2} \right\} d\Omega \tag{33}$$

Applying the divergence theorem, the first term of equation (33) is now expressed as

$$\oint_\Gamma \left\{ \varepsilon_1 \frac{\partial \phi_j}{\partial x_1} \phi_k \, dx_2 - \varepsilon_2 \frac{\partial \phi_j}{\partial x_2} \phi_k \, dx_1 \right\} \tag{34}$$

As discussed earlier, equation (34) can be set to zero and thus equation (18) can form a linear equation system as follows

$$\mathbf{D} C_s^{n+2/3} = \mathbf{M} C_s^{n+1/3} \tag{35}$$

where $\mathbf{D} = \mathbf{M} + \mathbf{F}$ and

$$M_{j,k} = \int_\Omega \phi_j \phi_k \, d\Omega \qquad F_{j,k} = \Delta t \int_\Omega \left\{ \varepsilon_1 \frac{\partial \phi_j}{\partial x_1} \frac{\partial \phi_k}{\partial x_1} + \varepsilon_2 \frac{\partial \phi_j}{\partial x_2} \frac{\partial \phi_k}{\partial x_2} \right\} d\Omega$$

Note that $\mathbf{D}$ is a sparse symmetric positive-definite matrix. An efficient solver for this kind of linear equation is described in Section 4.3.

3.4.3. Implicit Finite Difference Method for Vertical Diffusion Term

Similar to equation (14), the last fractional step uses an implicit finite difference method (FDM) to discretize equation (19) in the water column. The double sweep method is used to solve this equation efficiently. Details on the vertical discretization are given by Wai and Lu (2000). As mentioned, there is no need to parallelize this equation because equations in the vertical direction are not decomposed.

3.5. Boundary Conditions

In each sub-step, boundary conditions are prescribed. For the first and third fractional steps, the implementation of the boundary condition is relatively easy and the parameters of boundary nodes can be set directly. However, it is more difficult to prescribe boundary conditions in the second sub-step because the parameters in each node are related to the others through equation (35). The simplest way is to solve the equation first, and then set the parameters on the boundary nodes as boundary conditions. The shortcoming of this method is the exclusion of the boundary effect on the inner nodes. The present model makes use of a method described below.

$$
\begin{bmatrix} d_{11} & d_{12} & d_{13} & d_{14} \\ d_{21} & Gd_{22} & d_{23} & d_{24} \\ d_{31} & d_{32} & d_{33} & d_{34} \\ d_{41} & d_{42} & d_{43} & d_{44} \end{bmatrix} \begin{bmatrix} c_1 \\ c_2 \\ c_3 \\ c_4 \end{bmatrix} = \begin{bmatrix} b_1 \\ Gd_{22}c^* \\ b_3 \\ b_4 \end{bmatrix}
$$

In the above matrix, if the 2nd node is a boundary point, whose value can be obtained through the prescribed boundary condition (for example, $c_2 = c^*$), then d_{22} will be multiplied by a large value G (for example, $G = 10^{20}$), and the corresponding b_2 will be set to $Gd_{22}c^*$. If there is more than one boundary node, the corresponding d_{ii} and b_i will be revised accordingly. The advantage of this method is to maintain the sparse symmetric positive-definite characteristics of matrix **D**.

4. PARALLEL IMPLEMENTATION

WLMP developed by Wai and Lu (2000) was run on an MIMD structured parallel computer, IBM SP2 900, which consists of two frames, each has 16 processors, whose internode point to point communication bandwidth is 150 MB/s, and the communication latency is very short (the actual parameter is not available).

The parallel computer used to run the present model is a Beowulf distributed computer system. The cost of the Beowulf system is only a fraction of the IBM system. The system consists of 11 personal computers connected with a 100MB/s switcher. There are one master and 10 slave processors. The master processor has a 733 MHz Intel CPU, a 40GB hard disk and 4 GB memory. Each slave processor has a 733 MHz Intel CPU and 1 GB memory. The entire initial and computed data are stored on the master. The maximum communication bandwidth between each PC is around 80 MB/s, but the latency is not satisfactory. There will be about 0.1–0.2 s delay for the first communication operand passing when a serial of communication operands is performed. The operating system is Red Hat Linux 6.2, the Message Passing Interface (MPI) is LAM/MPI 6.5.2 provided by the University of Notre Dame, and the compiler is Layhey FORTRAN 95 Pro 6.0.

4.1. Domain Decomposition and Communication

Recent approaches for parallelizing sequential models are domain decomposition and functional decomposition. In this chapter, the domain decomposition method is used. This means that each processor is in charge of a sub-domain. Each sub-domain has the same quantity of nodes to balance

the workload among the processors. The decomposition method must be carefully selected to minimize the overhead due to any uneven amount of data transfer between processors. For a domain with irregular geometry, such as an estuary and a coast, the mixed strip/patch domain decomposition method is preferred (Wai and Lu, 2000). The M-S communication strategy is employed in the present numerical model for data transfer between adjacent processors. In the M-S strategy, communication only takes place between the master processor and other active processors assigned as slaves. The master plays the role of coordinator and the slaves play the roles of workers. The master gathers necessary data from the slaves and redistributes data to the targeted slaves. The master also controls the slave operations. The slaves mainly perform the computations of the sub-domain, and send the data needed by other slaves, to the master. Thus, the necessities for an efficient distributed computer system are a large memory for the master, a high performance processor for the slaves and a fast network connecting the master and the slaves.

4.2. Data Structures for Message Passing

As described by Wai and Lu (2000), the solution of a grid point depends on the values of the neighboring points sharing the same element. For a sub-domain, calculations at an interconnection point require the solutions at its adjacent points to be partly held by the neighboring processors. These adjacent points are called 'halo points' of the sub-domain. Inside a sub-domain, the values at the halo points are only for calculations and are not updated. Fig. 1 shows the halo points around a sub-domain with 4 x 4 9-nodal quadrilateral elements. The points denoted by 'x' and '⊗' are the calculation points in the sub-domain. The calculation points at the interconnections, symbolized by '⊗', are the halo points for neighboring sub-domains, the values of which are sent to neighboring processors. The halo points in the sub-domain consist of internal halo points denoted as '+' and external halo points as '⊕'. All values at the halo points are obtained and updated in the neighboring processors. The values at the external halo points are used for the Eulerian-Lagrangian scheme in the advection solver. To ensure efficient message passing without broken arrays, the node numbers are reordered starting from the interior points of the sub-domain, and then passed to the interconnection points, the internal halo points and finally to the external halo points in a contiguous array. The re-ordering of the array is shown in Fig. 2.

4.3. Matrix Solver

Two major types of large-scale linear equation systems are solved in the present model. One is from the horizontal diffusion equations, (equation (23) and equation (35)), and the other is from the continuity equation, (equation (26)). The procedures used in WLPM for solving the horizontal system are: (1) keeping the coefficient matrix $\mathbf{D}$ invariant in time, (2) inverting the $\mathbf{D}$ matrix, (3) storing the

×	Calculation points in interior area.
⊗	Calculation points on interconnects, which are halo points possessed by neighbor sub-domains.
+	Internal halo points for general computations.
⊕	External halo points.
··········	Boundary of each element
——	Boundary of a sub-domain
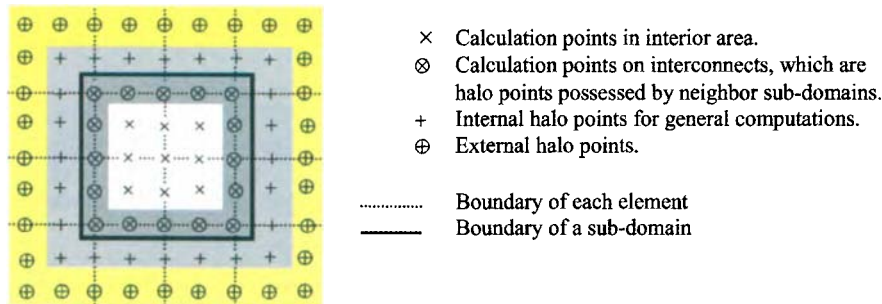
Figure 1. Definition of calculation points and halo points in sub-domains (after Wai and Lu, 2000).
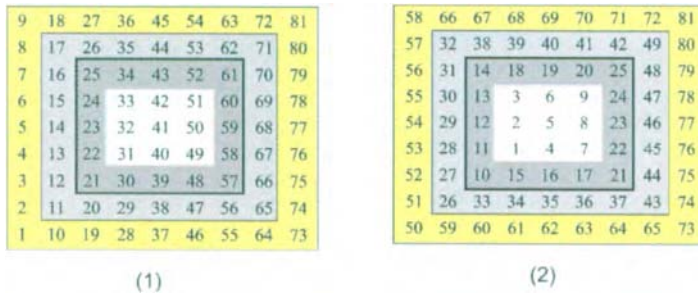
Figure 2. (1) Numbering scheme in global domain. (2) Numbering scheme in a sub-domain.

result before the time marching process, and then (4) calculating equation (23) and (35) for u, v, C_s on each layer for each time step. Although **D** is sparse, its inverse is dense and the operation of the inversed matrix in equations (23) and (35) would involve N^2 multiplications. This will lead to a heavy task for the processors. A Gauss-Jacobi iterative (GJI) method was used in WLPM for the continuity equation, equation (26). However, the cost of solving equation (26) by using the iterative method is still considerable. In the following paragraphs, the efficiency of two iterative methods, namely the preconditioned conjugate-gradient iteration method (PCG) and the preconditioned bi-conjugate gradient iteration method (PBiCG), for solving large linear systems is discussed in detail.

For Equation (23): $\mathbf{D}u_i^{n+2/3} = \mathbf{M}u_i^{n+1/3}$ *and Equation (35):* $\mathbf{D}C_s^{n+2/3} = \mathbf{M}C_s^{n+1/3}$

The right sides of equation (23) and equation (35) are known, so they can be expressed in a simple form as shown below.

$$\mathbf{A}x = b \tag{36}$$

The coefficient matrix **A** is a sparse, positive-definite matrix, x is an unknown vector, and b is a known vector. In this chapter, the PCG method is adopted to solve these equations. The PCG algorithm is one of the best-known iterative techniques for solving sparse symmetric positive definite linear systems. Discussion on the theory of this method can be found in Saad's (1996) work. The method proceeds by (1) generating vector sequences of iterates (i.e. successive approximations to the solution), (2) calculating residuals corresponding to the iterates, and (3) searching directions used in updating the iterates and residuals. Although the length of these sequences may become large, only a small number of vectors need to be kept in the memory. For every iteration, two inner products are produced in order to compute update values to make the sequences satisfy certain orthogonality conditions. On a symmetric positive definite linear system these orthogonality conditions imply that the distance to the true solution is minimized in some form (Barrett et al., 1994). The PCG algorithm is listed below:

compute $\quad r_1 = b - Ax_1, z_1 = Kr_1, p_1 = z_1$
Do $i = 1, 2, \ldots,$ *until* $\max(x_i - x_{i-1} \leqslant T_{olerance})$
$\quad \alpha_i = (r_i \cdot z_i)/(Ap_i \cdot p_i)$
$\quad x_{i+1} = x_i + \alpha_i \, p_i$
$\quad r_{i+1} = r_i - \alpha_i \, Ap_i$ $\qquad\qquad\qquad\qquad\qquad\qquad$ Algorithm (1)
$\quad z_{i+1} = Kr_{i+1}$
$\quad \beta_i = (r_{i+1} \cdot z_{i+1})/(r_i \cdot z_i)$
$\quad p_{i+1} = z_{i+1} + \beta_i \, p_i$
EndDo

where α is a constant parameter that minimizes the magnitude of residual vector r; β ensures that p_i and Ap_{i-1} (or equivalently r_i and r_{i-1}) are orthogonal, and p is the search direction vector. The iteration terminates when the maximum difference, x, between two sequential iteration steps is less than a tolerance ($T_{olerance}$) set to be 1.0×10^{-6}. $\mathbf{K}$ is the preconditioner, and x_1 is the initial guess of x. Fortunately, the value can be obtained from the previous advection calculation which is usually a good guess.

In general, a sound strategy is to focus on finding a good preconditioner instead of using a better accelerator (Saad, 1996). The rate of convergence varies with the iteration algorithm, the preconditioner, the initial data, and so forth. As a rough guide, the maximum iteration step $= N^{1/2}$ is often sufficient when $N \gg 1$. For elliptic second-order partial differential equations, the number of iterations is inversely proportional to the discretization element width, h^{-1} (Axelsson and Barker, 1984). Equations (23) and (35) converge quickly when the preconditioners align in the diagonal entries of $\mathbf{D}$. In a real life application in Xiamen Bay (described in detail in Section 5), equation (23) converges in 14 steps for the velocity calculation and equation (35) converges in 8 steps for the mass concentration calculation. Furthermore, the cost of this simple preconditioner is small because the cost of generating preconditioners can be neglected since it is the diagonal part of $\mathbf{D}$. The number of multiplications of $\mathbf{K}r_i$ in each time step of Algorithm (1) is N. For other preconditioners, such as the incomplete lower and upper triangular decomposition (ILU), the number is $N \times N_r$, where N_r is the number of nonzero entries in one row or column in the coefficient matrix $\mathbf{D}$. In FEM, N_r also means the number of nodes, which share the same element. Its value ranges from 9 to 33 for the 9-nodal quadrilateral FEM element according to the element's distribution, and the average value is 25. With this information, one can estimate N_r and the corresponding node label for each node before the time marching process. Thus, the number of multiplications of D and a vector, such as $\mathbf{A}p$, in Algorithm (1), is $N \times N_r$. Above all, the PCG method involves one matrix-vector product, four vector updates, and two inner products per iteration. The amount of multiplication for equation (23) can be estimated by the following equation

$$\tau_{pcg} = (N \times N_r + 5N) \times IT_{\max} \tag{37}$$

where $IT_{\max}$ is the maximum iteration step to convergence. As mentioned, the amount of multiplication will be N^2 for WLPM. Hence, the PCG method will be $N/(30 IT_{\max})$ times faster than the method used in WLPM, besides the inversion cost required by WLPM. In the application of Xiamen Bay, equation (13) is 12.40 times faster to solve.

For Equation (26): $\mathbf{G}\,\zeta^{n+1} = z$

Similarly, a simple form is considered

$$\mathbf{A}x = b \tag{38}$$

where $\mathbf{A} = \mathbf{G}$, $x = \zeta$, $b = z$.

The procedures of the GJI algorithm used in WLPM are described as follows. First, use the Gauss elimination method to diagonalize the coefficient matrix $\mathbf{A}$ and obtain the initial rough value of x in each sub-domain. Second, use the Jacobi iteration method to eliminate the error of x caused by the internal halo points. The total multiplication amount can be estimated by the following equation (Wai and Lu, 2000)

$$\tau_{Gj} = N_d \left[N_s^2 (N_s + N_h) + 4 \frac{N_h^2}{N_r} \frac{\alpha \ln(10)}{R(G)} \right] \tag{39}$$

where N_d is the sub-domain number; N_s is the node number in each sub-domain; N_h is the number of internal halo points in the sub-domain; the prescribed precision is $10^{-\alpha}$ (here the value is 10^{-16}),

and $R(G)$ is the convergence rate, the typical value of which can be set to 0.11. Here, the typical value of N_h is also set as $5N_s^{1/2}$, and H_r is set as 25 for a typical 9-node quadrilateral elements domain. For the case of equation (30), the equation can be simplified to

$$\tau_{Gj} = N_d \left[N_s^3 + 5N_s^{5/2} + 1340N \right] \tag{40}$$

If $N \gg 1$, the computational work will be three orders of the node number. This will be an unrealistic task when $N_s > 1000$. This indicates that the GJI method is only efficient for problems with moderate size.

The PCG adopted for solving equation (23) is not suitable for non-symmetric systems, such as equation (26), because the residual vectors cannot be made orthogonal with short recurrences (Vo-evodin, 1983). The method retains the orthogonality of the residuals by using long recurrences, at the cost of a larger storage demand (Saad, 1996). The Preconditioned BiConjugate Gradient method (PBiCG) uses another approach, replacing the orthogonal sequence of residuals with two mutually orthogonal ones, at the cost of eliminating the minimization process (Barrett et al., 1994). The updated relations for residuals in the PCG are augmented in the PBiCG by relations that are similar, but based on A^T instead of A. Thus, updating two sequences of residuals gives

$$r_i = r_{i-1} - \alpha_1 \mathbf{A} p_i, \quad \tilde{r}_i = \tilde{r}_{i-1} - \alpha_i \mathbf{A}^T \tilde{p}_i \tag{41}$$

and two sequences of search directions give

$$p_i = p_{i-1} + \beta_{i-1} \, p_{i-1}, \quad \tilde{p}_i = \tilde{r}_{i-1} + \beta_{i-1} \, \tilde{p}_{i-1} \tag{42}$$

To ensure the bi-orthogonality relations, the following relationships are used

$$\tilde{r}_i^T \cdot r_j = 0, \quad \tilde{p}_i^T \cdot A p_j = 0 \quad i \neq j \tag{43}$$

Using equations (41), (42) and (43), Algorithm (1) with the PBiCG method is modified to

$compute \quad r_1 = b - Ax_1, \tilde{r}_1 = r_1, z_1 = Kr_1, \tilde{z}_1 = K\tilde{r}_1, p_1 = z_1, \tilde{p}_1 = \tilde{z}_1$
$Do \; i = 1, 2, \ldots, until \; \max(x_i - x_{i-1} \leqslant T_{olerance})$
$\quad \alpha_i = (\tilde{r}_i \cdot z_i)/(Ap_i \cdot \tilde{p}_i)$
$\quad x_{i+1} = x_i + \alpha_i \, p_i$
$\quad r_{i+1} = r_i - \alpha_i \, Ap_i$
$\quad \tilde{r}_{i+1} = \tilde{r}_i - \alpha_i \, A^T \tilde{p}_i$ \hfill Algorithm (2)
$\quad z_{i+1} = Kr_{i+1}$
$\quad \tilde{z}_{i+1} = K\tilde{r}_{i+1}$
$\quad \beta_i = (\tilde{r}_{i+1} \cdot z_{i+1})/(\tilde{r}_i \cdot z_i)$
$\quad p_{i+1} = z_{i+1} + \beta_i \, p_i$
$\quad \tilde{p}_{i+1} = \tilde{z}_{i+1} + \beta_i \, \tilde{p}_i$
$EndDo$

The variables used in Algorithm (2) are the same as in Algorithm (1).

The PBiCG method involves four matrix-vector multiplication processes, seven vector updates, and two inner products per iteration. The amount of multiplication for equation (26) can be estimated by the following equation (not including the preconditioner process in priori)

$$\tau_{PBiCG} = (4N \times N_r + 7N) \times IT_{max} \tag{44}$$

IT_{max} is dependent on the convergence rate. Few theoretical results are known for the convergence of the PBiCG. For symmetric positive definite systems, the PBiCG delivers the same results as the PCG, but at twice the cost per iteration. In practice this is confirmed, but it is also observed that the PBiCG convergence behavior may be quite irregular. In the Xiamen Bay application, it also varies with the modeling time step. The maximum number of iterations is 45 for a 200 s time step and 98 for a 600 s time step.

4.3.1. Initial Value and Preconditioner

A good initial value which is close to the actual value will not only improve the convergence rate, but also reduce the chance of breakdown, such as $Ap_i \cdot \widetilde{p}_i = 0$ or $\widetilde{r} \cdot z = 0$. In the time marching process, the value of the last time step is a good initial variant value

$$\zeta^* = \zeta^{(1)} \tag{45}$$

where ζ^* is the initial value of water elevation, and $\zeta^{(1)}$ is the water elevation computed at the last time step. This choice of initial value is based on the assumption that the 1st order partition difference of the variable is zero ($\partial \zeta / \partial t = 0$), and better initial values can be obtained through setting higher-order partition differences of the variable to zero. After a series of sensitivity tests, the 2nd order form was selected, because the convergence step reduced 30 percent on average more than the zero order form (equation (45)). The 2nd order extrapolation formula is expressed as

$$\zeta^* = 3\zeta^{(1)} - 3\zeta^{(2)} + \zeta^{(3)} \tag{46}$$

where $\zeta^{(2)}$ and $\zeta^{(3)}$ are the water elevations computed at the last two and three time steps, respectively.

A preconditioner, **K**, is a matrix that affects such a transformation: $(\mathbf{KA})x = \mathbf{K}b$, where $\mathbf{KA} \approx 1$. The ILU preconditioner was used in the PBiCG iteration method to solve equation (26) in the present model.

In the ILU algorithm, the incomplete factorization produces no nonzero elements beyond the sparsity structure of the original matrix. This means that the ILU factorization process computes a sparse lower triangular matrix **L** and a sparse upper triangular matrix **U**, which fits with the equation: $A = LU + R$. Here, **A** is the original coefficient sparse matrix, **R** is the residual matrix, and both **L** and **U** have the same sparse structure as **A**. Hence, the process Kr in Algorithm (2) can be split into two steps: First, solving for vector y such that

$$\mathbf{L}y = r \tag{47}$$

and then solving for vector x

$$\mathbf{U}x = y \tag{48}$$

The amount of multiplication required for equation (47) and equation (48) is $N \times N_r$. Because **L** and **U** have the same sparse structures as **A**, the algorithm for zero fill in ILU [ILU(0)] is written as

$$
\begin{aligned}
&Do\ i = 1, \ldots, n - 1 \\
&\quad Do\ k = i + 1, \ldots, n\ and\ (i, k) \in NZ(A) \\
&\quad\quad a_{ik} = a_{ik}/a_{ii} \\
&\quad\quad Do\ j = k + 1, \ldots, n\ and\ (i, j) \in NZ(A) \qquad \text{Algorithm (3)} \\
&\quad\quad\quad a_{kj} = a_{kj} - a_{ik}a_{ij} \\
&\quad\quad EndDo \\
&\quad EndDo \\
&EndDo
\end{aligned}
$$

Here, a_{ij} is the element at row i and column j in matrix $\mathbf{A}$; $NZ(\mathbf{A})$ is the set of pairs (i, j), $1 \leqslant i, j \leqslant n$ and $a_{ij} \neq 0$.

The use of the PCG and the PBiCG solvers for the large-scale linear equation systems in the present model appears promising. The solvers take advantage of such properties as sparse positive-definite, and symmetric matrix. In addition, the choice of the 2nd order initial value estimation and the ILU preconditioner can further enhance the speed of the solvers.

4.3.2. Parallelization of the Linear Equation Solvers

Because the M-S communication strategy is employed in this model, the parallelization of the PCG algorithm uses the same symbols as in Fig. 1, where '$\otimes$' is the outer calculation points from which values are used by the neighboring sub-domain and '+' is the internal halo points from which values are obtained from the neighboring sub-domains. The parallelism of the PCG with the M-S communication strategy is shown in Fig. 3. It can be seen from the figure that almost all the computing tasks, such as matrix and vector multiplication, vector upgrade, are carried out on the slaves. The master decides whether the convergence is reached. In fact, few data need to be transferred. For a slave processor, the number of times that the data has to be sent and received in each iteration step are $N_0 + 3$ and $N_h + 3$, respectively. N_0 is the number of calculation points on interconnects at '$\otimes$', and
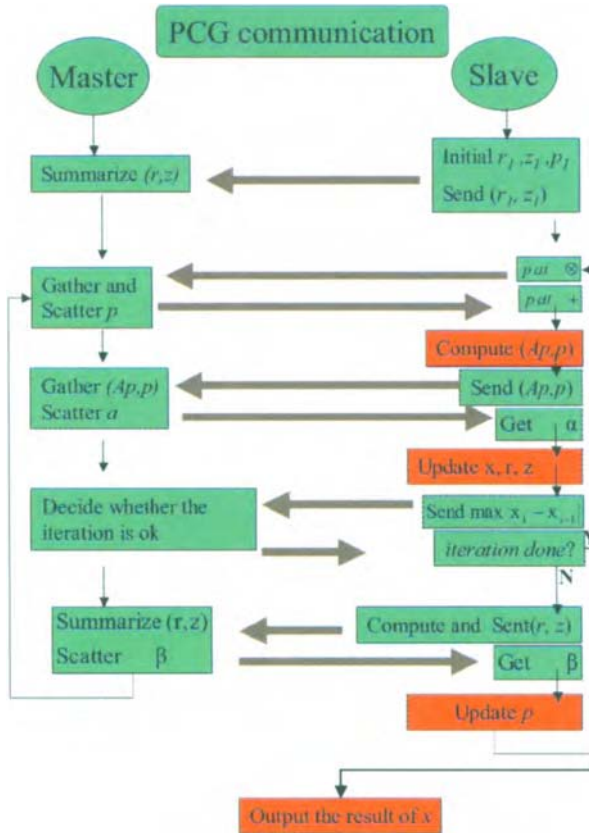
Figure 3. The parallelism of PCG method.

N_h is the number of internal halo points at '+'. Nevertheless, there are 8 communication processes in each iteration step and the cost of these 8 processes is high. The process takes about 33 percent of the time in the PCG solver. Thus, improving the bandwidth, especially cutting down the latency, is essential for a distributed computer. For a parallel computer with bottleneck latency, the parallelism strategy should be aimed at reducing the data communication time.

5. APPLICATION TO XIAMEN BAY, CHINA

5.1. General Description

To demonstrate the efficiency and accuracy of the present parallel model, a real life simulation of the flow and sediment transport situations after a typhoon event in Xiamen Bay, China has been conducted. Xiamen Bay is located in the west of Taiwan Strait, between the longitudes of $117°40'$ and $118°40'$, latitudes of $24°6'$ and $24°40'$ (see Fig. 4). In the west, the Jiulong River discharges into the bay. The net discharge of freshwater is 1.5×10^{10} m^3 per year, and the net discharge of sediment is 2.2×10^9 kg per year. In the south and east of the bay, Xiamen Bay connects with Taiwan Strait through the two seaward openings separated by Jinmen Island. The tides flow through the two openings to three parts of Xiamen Bay, i.e., Jiulong River estuary, Western seas and Eastern seas divided by a dike built in 1953. The water depth is relatively shallow in these three areas, and the three channels connect these three areas with the sea. The maximum depth of the channel between Xia Jinmen Island and Jinmen Island is 54 m. The tide of Xiamen Bay is a typical semidiurnal tide with a mean tidal range of 3.79 m and maximum range of 6.24 m. The tidal current is the predominant force in Xiamen Bay.

5.2. Model Establishment

The 9-node unstructured finite element mesh on the horizontal plane of the model area is shown in Fig. 5. There are a total of 1939 elements and 8480 nodes. The largest element size is 2.4 km^2 and the minimum is 0.035 km^2. There are 11 layers in the water column and each layer has the same depth of 1/11-th in the σ coordinate. The computation domain is decomposed into eight sub-domains, each of which has 1000–1100 nodes to achieve a well-balanced parallel computation.

5.3. Boundary Conditions

There are five open boundaries (Fig. 5). The open boundaries at a, b, and c are the outlets of Jiulong River. The other boundaries at d and e are sea boundaries. In this simulation, all the open boundaries are regulated by tidal variations. Errors in the boundary condition can be caused by unrealistic interpolation/extrapolation estimations of tidal elevations and the exclusion of the advection terms at the boundary. At the wall boundary, either the slip or no-slip boundary condition can be used. Based on the results of a number of sensitivity tests, the no-slip condition was adopted because it is able to better simulate an irregular boundary. The initial velocity was set to zero for a cold start simulation. The time step used in the application was 200 s.

5.4. Model Verification

On August 4th, 1996, just after a typhoon event, the Third Oceanography Institute, Xiamen, China, conducted a marine survey on several variables, such as, tidal elevation, velocity and sediment concentration. Fig. 5 depicts the 7 tidal stations and the 8 velocity and sediment concentration stations selected in this survey. The time series of tidal elevations at stations a, b, c, d_1 and e_1 are used as the boundary condition with the assumption that the water elevations at d and d_1, and at e and e_1 are comparable. The field measurements of Stations JC2, JM2, SG1 and XG2 are used to verify the model results.
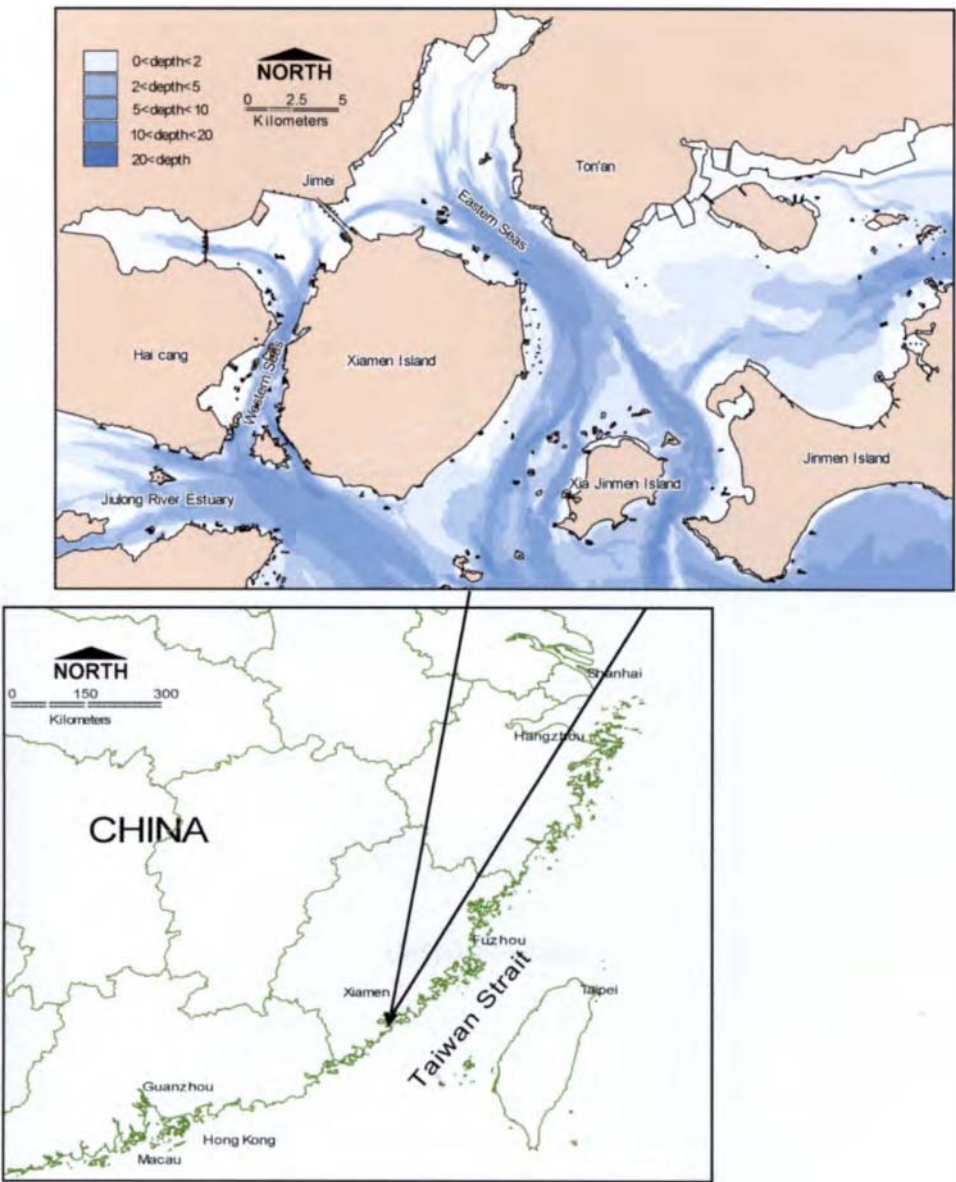
Figure 4. Map and location of Xiamen Bay, China.

Tidal elevation: Fig. 6 shows that the computed tidal elevations at the Dondu and Yzw stations agree well with the observed values. The averaged relative error at these two stations is less than 4%. The figure reveals that the tidal amplitude in the inner bay near the Dondu station is larger than that of the outer bay near Station Yzw.
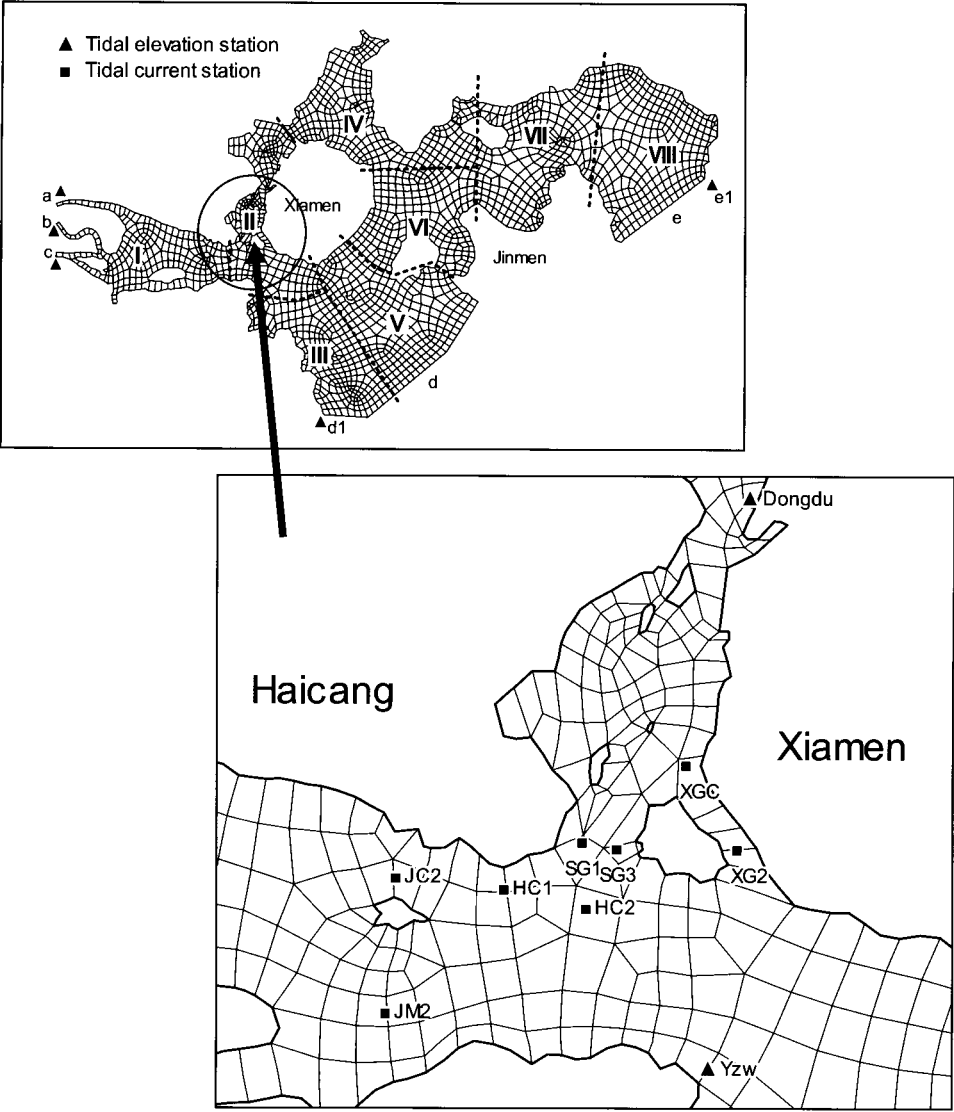
Figure 5. Element discretization, domain partitioning and survey station locations.

Tidal velocity: The computed vertically averaged velocities at Stations JC2, JM2, SG1 and XG2 are compared with the observed data as shown in Fig. 7. The averaged relative error calculated at all the stations, over a 28-hour period, is 16%. The largest errors are found at Station SG1. Such errors may be due to the highly irregular elements present in the region with a complex coastline boundary.

Fig. 8 shows the tidally averaged velocity profiles at the three stations, JC2, XGC and HC2. It appears that the model simulated the tidal velocity profiles well in the vertical direction, except at Station HC2 where the stratification is strong. The result accuracy in the vertical direction may be
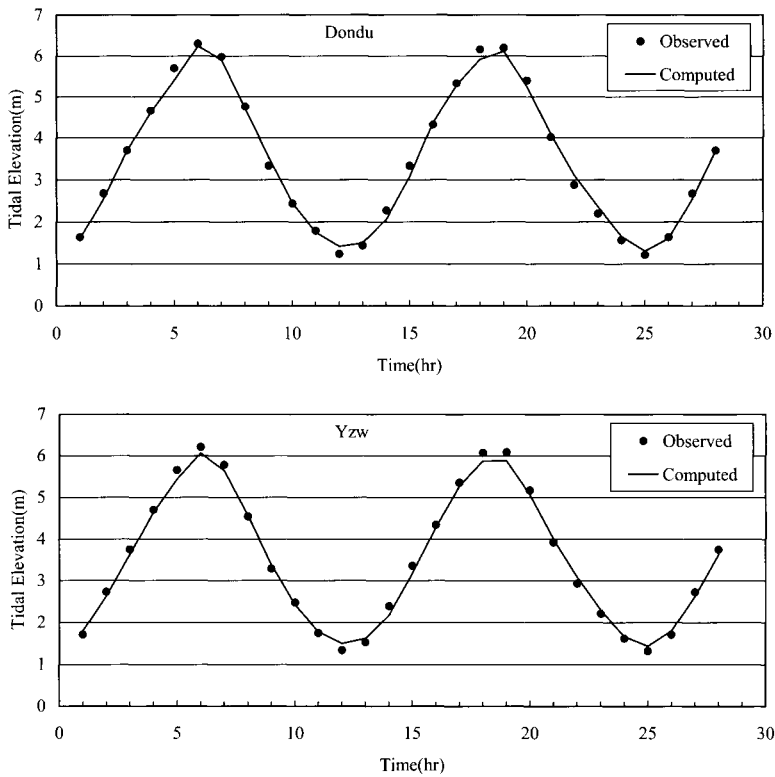
Figure 6. The computed and observed tidal elevations at Dondu and Yzw.

improved by including a baroclinic term and a sophisticated turbulence closure scheme, such as the scheme, $k - \varepsilon$ in the model.

Figs. 9 and 10 show the water surface flow patterns during the flood tide and ebb tide, respectively. The velocity at the surface is slightly larger than at the bottom. The maximum velocity occurs at the Jiulong River estuary at the ebb tide with a magnitude of 1.3 m/s. The high velocity is caused by the large freshwater influx from the Jiulong River. At the flood tide, the maximum velocity (1.0 m/s) is found in the channel between Xia Jinmen and Jinmen Island, where the flow depth is 54 m. At flood tide, the tides from the two open sea boundaries merge at the location between Ton'an and Jinmen Island. This is also the location where tidal currents split during ebb tides. The tidal current in this region is relatively slow with a shallow flow depth (< 2 m). In general, the simulated current pattern correlates well with the observed flow field reported by Zhang (1991).

5.5. Sediment Transport

Because there was no collected sediment data available at the open boundaries, estimated sediment concentration was used. At the river outlets, i.e., a, b and c, the vertical average concentration was set to 0.3 kg/m^3, and a concentration of 0.01 kg/m^3 was used at the sea boundaries. The initial concentration was set to 0.01 kg/m^3. The computed sediment concentration patterns in a tidal cycle are plotted in Fig. 11. In the left column, the plots depict the sediment concentration distribution at the bottom layer. The right column shows the concentration at the surface layer. The concentration at the bottom is one fold higher than at the surface. At ebb tide, sediment is transported from the Jiulong
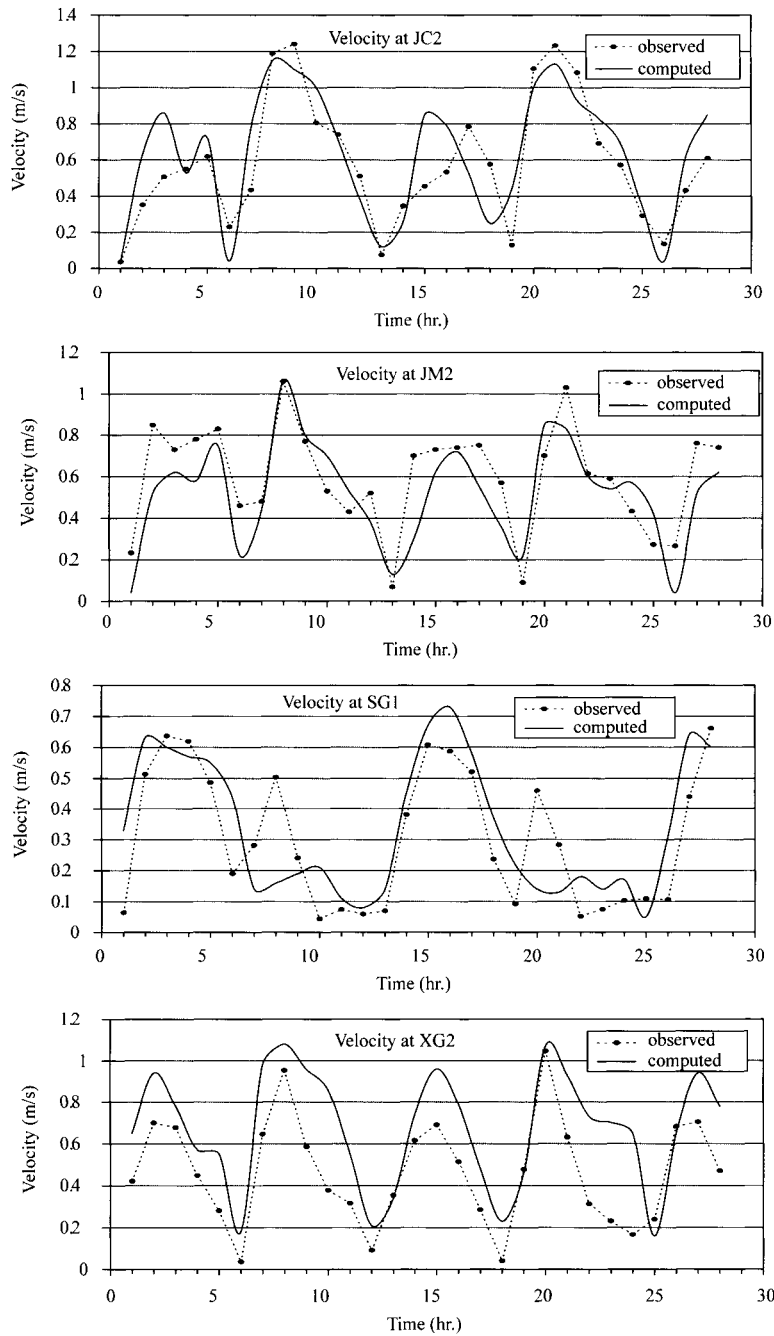
Figure 7. The computed vertically averaged velocity and the corresponding observed values.
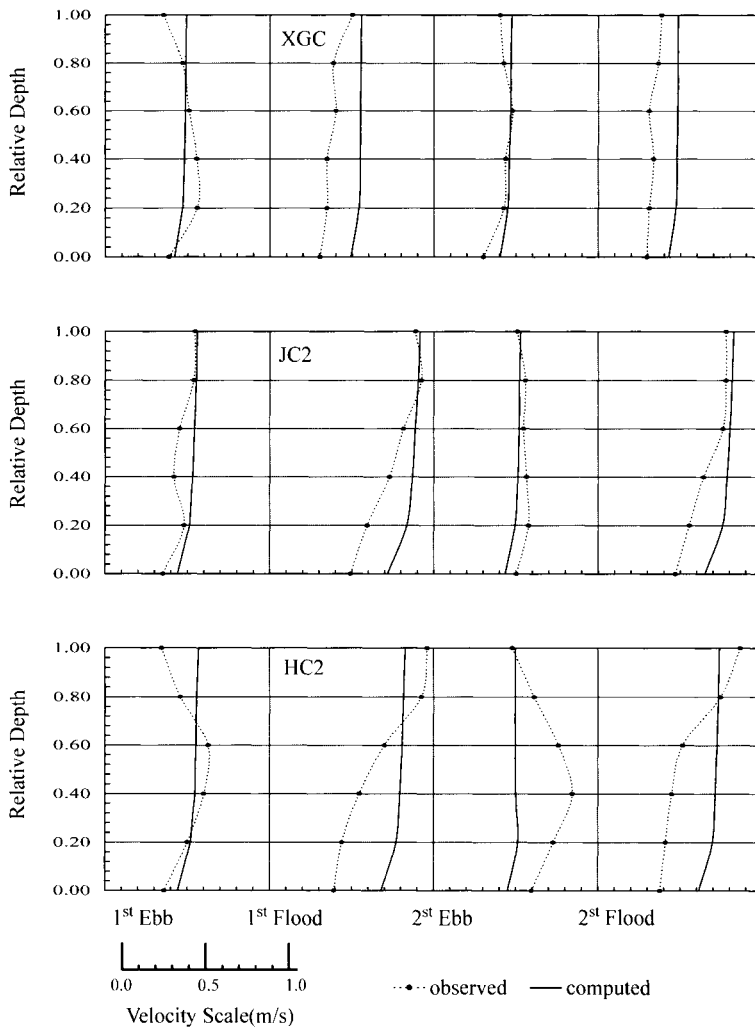
Figure 8. Comparison of the computed tidally averaged velocity profiles with the observations at JC2, XGC and HC2.

estuary to the open seas. At flood tide, part of the sediment which has been transported to the sea, is carried by the flood current to Western Seas, an important harbor in China. Some of this sediment may settle in the harbor and can cause siltation problems in the major navigation channels. In essence, the computed sediment patterns in Xiamen Bay agree with the observed patterns reported by Zhang and Liu (1995). The time series of the computed and observed vertically averaged sediment concentration at stations JC2, JM2, SG1 and XG2 are plotted in Fig. 12. Except at station XG2 where it is located at the flow confluent region, the computed concentration is in good agreement with the observed concentration. The persistently high suspended sediment concentration observed at XG2 may also be attributed to the high turbulence energy generated during the typhoon period. This energy re-suspended a large amount of mud from the sea bed and broke the mud into smaller particles that may
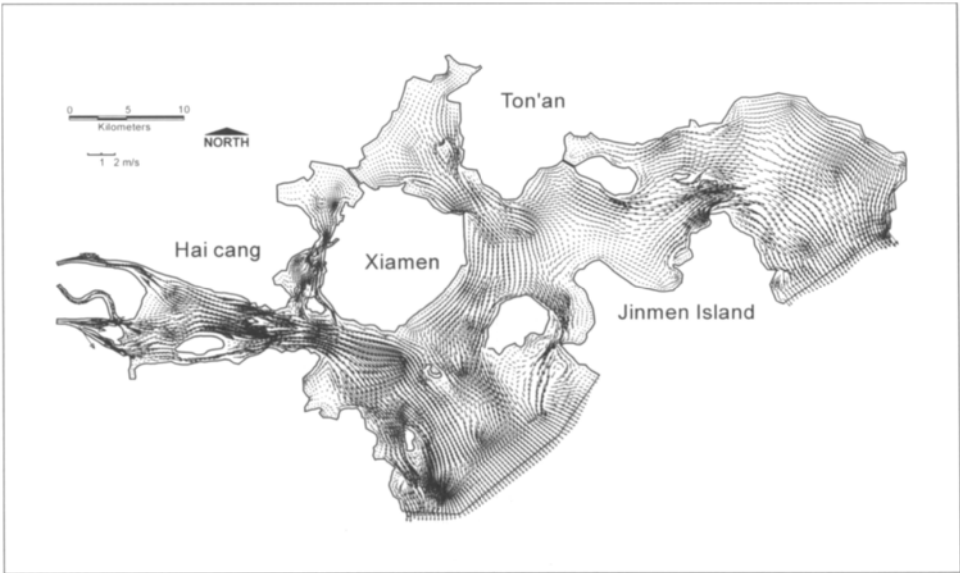
Figure 9. Ebbing flow field near water surface.
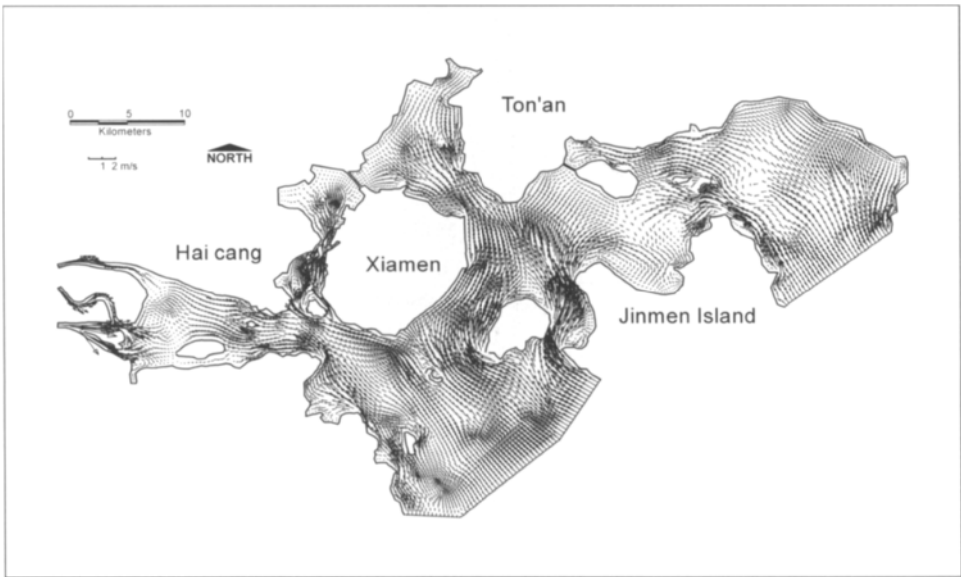
Figure 10. Flooding flow field near water surface.

stay in the water column for a long period of time. It should be noted that, due to lack of information on the net sediment flux (q_s) at the sediment-water interface, the net sediment flux was used as a tuning parameter in the simulation. This is a common engineering practice in dealing with this
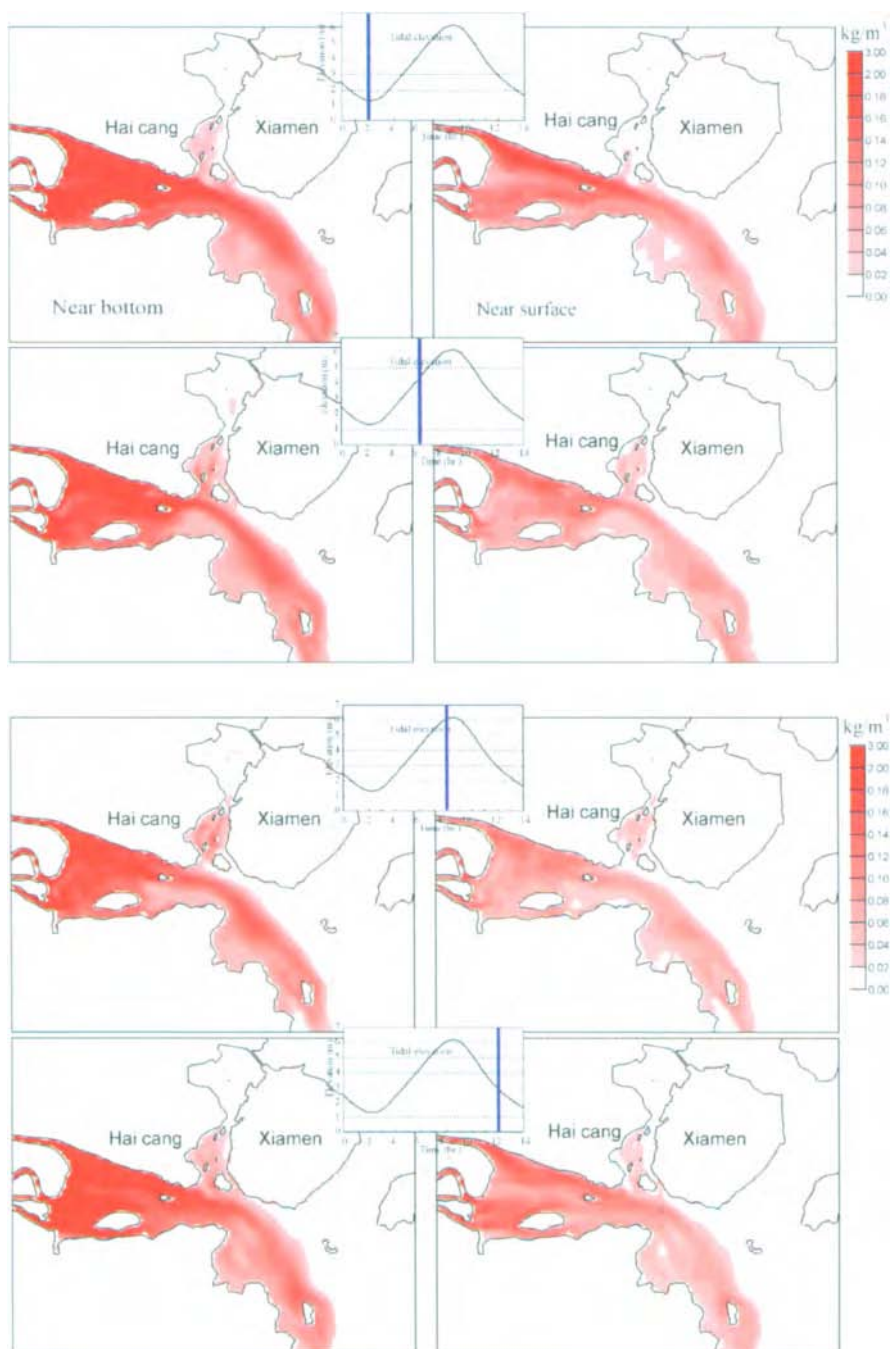
Figure 11. Sediment transport patterns in a tidal cycle. (The figures in the left column are concentration patterns at the bottom, and the right column represents patterns at the surface).
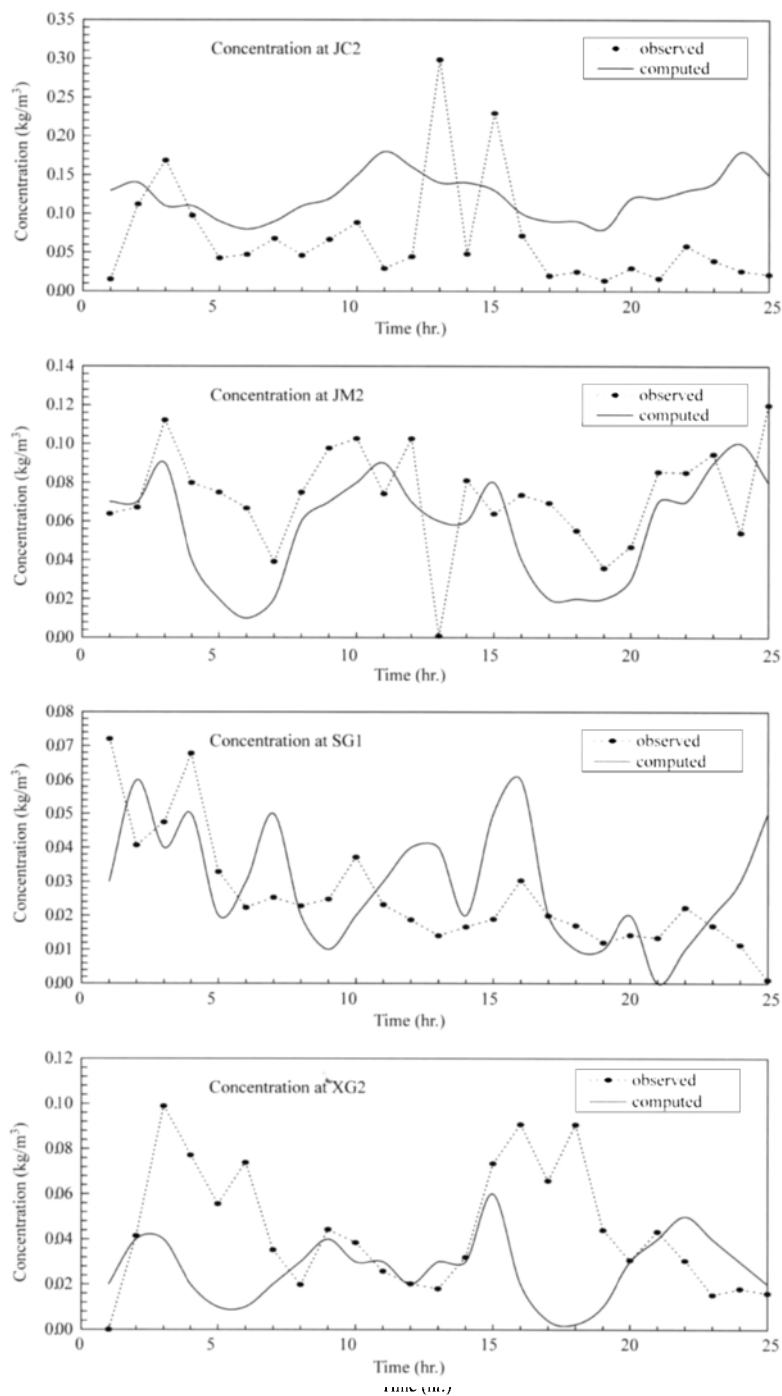
Figure 12. The computed vertically averaged concentration and the corresponding observed values.

source/sink term in sediment transport simulations. However, it is important for a modeler to have a good knowledge of the characteristics of sediment dynamics at the sediment-water interface in order to make a sensible judgment on the validity of this tuned parameter. In fact, this parameter represents the major source or sink of sediment in the water. It is highly recommended that, before carrying out a sediment transport simulation, good quality field observations and laboratory experiments must be conducted to obtain the sediment properties that include cohesiveness, bulk density, settling velocity, critical re-suspension shear stresses in different sea bed consolidation history, etc. for the model parameters.

5.6. Computation Speed-Up

Two matrix solving techniques have been discussed and used to speed-up the present model. The first is the PCG iterative method for solving the horizontal diffusion terms, and the second is the PBiCG method for solving the continuity equation. Based on the error tolerance of 10^{-8} m for the water elevation calculation, the time cost for using the PCG method and the GJI method in each computation sub-process is compared and tabulated in Table 1. It can be clearly seen that the PCG method speeds up in three processes. Firstly, the matrix inversion in the PCG method is not necessary, thus saving more than 8 hours of eight 733 MHz CPU time (for matrix inversion required in WLPM) before the time marching process. Secondly, the PCG method re-discretizes the horizontal diffusion term and forms a linear equation system with a symmetric coefficient matrix. This matrix can be solved efficiently by the PCG iterative method. In the Xiamen Bay application, the PCG converged in 14 and 8 steps for the velocity and sediment concentration calculations, respectively. In addition, specifying the preconditoners, which are the diagonal entries of the matrix, do not require any additional time cost. As a consequence, the cost of solving the horizontal diffusion term was reduced from 38.69 s to 3.11 s (a more than 12 times reduction). Thirdly, the PBiCG iterative method with the ILU(0) preconditioner adopted to solve the continuity equation was 245 times faster than the GJI method (the time cost reduced from 274.92 s to 1.12 s).

Above all, the present model required 112.3 s of computer run time for every hour of simulation in the Xiamen Bay application. This is a 50 times speed-up compared with the WLPM performance. It also eliminates the huge time cost on the matrix inversion before the time marching process. Without the inversion in priori, some parameters, such as the horizontal diffusion coefficient, can be updated during the time marching process. This is also beneficial if one wants to include, for example, the large eddy simulation technique in the horizontal plane. In this application using 8 sub-domains, the speed-up due to extra processors used is shown in Fig. 13. The reason that the number of times of speed-up is larger than the number of processors being used is because of the increase in the cache memory contributed by each involved processor.

6. CONCLUDING REMARKS

This chapter describes a finite element parallel model that is developed for large-scale simulations of flow and sediment transport processes in coastal waters. The domain decomposition method has been implemented to decompose a large modeled area into smaller sub-domains so that calculations involved in each sub-domain can be carried out quickly and efficiently by a separate processor. With a low-cost PC-based Beowulf MIMD machine, the master processor is responsible to read the initial grids and boundary information and to partition the entire modeled area (the global domain) into a number of sub-domains. The sub-domain information is sent to each slave processor to perform the computation. The performance of two types of matrix solvers has been compared. The GJI method is an efficient method for moderate size finite element systems or when the node number in each sub-domain is less than 200. However, the cost of GJI is proportional to the third power of the node

Table 1

The time cost comparison between WLPM and the model described in the chapter (8480 nodes, 11 layers, 8 sub-domains, 200 s time step).

Process	Time need in WLPM (second)	Time need in model of this paper (second)	Speed up times
Inverse of matrix D^{-1}		0	
Two inverses are needed,	$2 \times 4.2 \times 3600$		Null
One for velocity the other for sediment.		PCG method do not need inverse	
Do	Time marching process begin		
Explicit Eulerian-Largangian method for **advection term**	1.61	1.61	1.00
Implicit FEM for **horizontal diffusion term**		3.11	
Total $11(layer) \times 3(u_1, u_2, c_s) = 33$	38.69	14 iterations for u_1, u_2	12.40
Linear equations shall be solved.		8 iterations for c_s (PCG method)	
Implicit FEM for **continuity equation**	274.92	1.12	
Elevation tolerance=10^{-8} m/s,	Gauss eliminate uses 84%,	45 iterations need for	245.46
One non-symmetric linear equation shall be solved.	Jacobi iteration uses 16%	convergence (PBiCG method)	
Implicit FDM for **vertical diffusion term**	0.27	0.27	1.00
Total cost for one time step			
There are other processes such as combining matrix, computing w etc.	315.62	6.24	50.58
EndDO	Time marching process end		
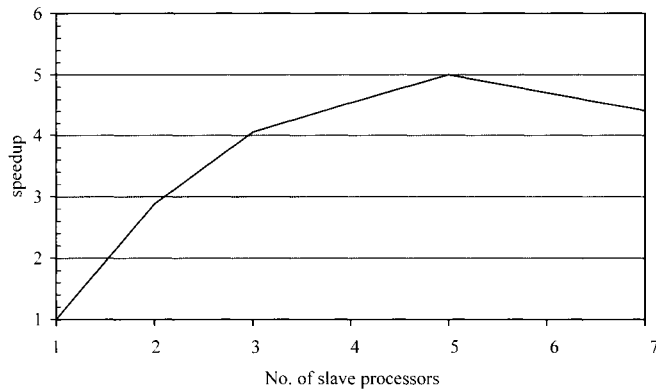
Figure 13. Overall speed-up versus number of slave processors implemented.

number in each sub-domain, thus this method becomes inefficient for large size problems. In the present model, the parallel PCG method with effective preconditioners has replaced the GJI method to solve the horizontal diffusion and the fully implicit continuity equation. The Xiamen Bay application indicates that the present model with the PCG method is accurate and performs 50 times faster than WLPM. This is a successful case of using an affordable Beowulf distributed computer system in a real life application. The additional computing power provided by the distributed computer system allows engineers and scientists to investigate more complex real life problems, and sophisticated turbulence schemes that may lead to a better understanding of the fate and transport of sediment in the coastal waters.

ACKNOWLEDGMENTS

LIST OF SYMBOLS

$C_{a,e}$	—	near bed equilibrium reference concentration
C_s	—	sediment concentration
C_v	—	sediment volumetric concentration
D_P	—	initial grain diameter
f	—	Coriolis parameter
g	—	acceleration of gravity
h	—	water depth relative to the mean sea level
IT_{max}	—	maximum iteration step to convergence in PCG or PBiCG Method
N	—	node number in one layer
N_d	—	sub-domain number
N_h	—	number of internal halo points at '+'
N_0	—	number of calculation points on interconnects at '⊗'
N_r	—	number of nonzero entries in one row or column in coefficient matrix

N_s	—	node number in each sub-domain
P_i^*	—	baroclinic term with Boussinesq assumption in x_i direction
Q_i	—	vertical averaged velocity in x_i direction
$R(G)$	—	convergence rate
t	—	time
$T_{olerance}$	—	tolerance of the convergence
u_j	—	velocity in x_j direction
u_{jp}^n	—	velocity at the point P at n time step in x_j direction
V_0	—	characteristic velocity
w	—	vertical velocity in Cartesian coordinates
w_f	—	settling velocity of individual flocs in Cartesian coordinates
w_s	—	sediment settling velocity in Cartesian coordinates
$w_{s,m}$	—	sediment settling velocity with the hindering effect
x_i	—	coordinate in i direction
a_s	—	probability of the sediment settling
Γ	—	boundary around the interested domain
ε_j	—	eddy viscosity coefficients for water in j direction
$\varepsilon_{s,j}$	—	sediment diffusivity coefficient in j direction
$\varepsilon_{s,w}$	—	sediment-water diffusion mass-transfer coefficient
ζ	—	water level from the mean sea level
ζ^*	—	initial value of water elevation
$\zeta^{(1)}$	—	water elevation computed at last one time step
$\zeta^{(2)}$	—	water elevation computed at last two time step
$\zeta^{(3)}$	—	water elevation computed at last three time step
ν	—	kinematic viscosity
ρ	—	bulk density of water-salinity
ρ_0	—	constant reference water density
ρ_P	—	density of initial grain
ρ_w	—	density of water
τ_i^b	—	bottom shear stress in i direction
$\tau^{b,cr}$	—	critical erosion bed shear stress
τ_i^w	—	surface shear stress in i direction
ϕ_j	—	shape function
Ω	—	area of interested domain
ω	—	vertical velocity in sigma coordinates
ω_s	—	sediment settling velocity in sigma coordinates
$\mathbf{D}$	—	stiffness matrix
$\mathbf{K}$	—	preconditioner matrix
$\mathbf{L}$	—	lower triangular matrix
$\mathbf{M}$	—	summation of mass matrix
p	—	searching direction vector
$\mathbf{R}$	—	residual matrix
r	—	residual vector
$\mathbf{U}$	—	upper triangular matrix
$\mathbf{u}_i$	—	velocity vector in x_i direction
PCG	—	preconditioned conjugate gradient method
PBiCG	—	preconditioned bi-conjugate gradient method
MPI	—	message passing interface

WLPM	—	efficient parallel model developed by Wai and Lu (2000)
GAS	—	gradient-adaptive-sigma
GJI	—	Gauss-Jacobi iteration method
M-S	—	master-slave
FDM	—	finite difference method
FEM	—	finite element method
ILU	—	incomplete lower and upper triangular decomposition
ILU(0)	—	zero fill in ILU
MIMD	—	multiple instruction multiple data

REFERENCES

Axelsson, O., and Barker, V.A., 1984. Finite Element Solution of Boundary Value Problems-Theory and Computations. London: Academic Press.

Barrett, R., Berry, M., Chan, T.F., Demmel, J., Donato, J., Dongarra, J., Eijkhout, V., Pozo, R., Romine, C., and Van der Vorst, H., 1994. Templates for the Solution of Linear Systems: Building Blocks for Iterative Methods. 2nd Edition. Philadelphia, PA: SIAM Co.

Hargrove, W.W., Hoffman, F.M., and Sterling, T., 2001. The do-it-yourself supercomputer. Scientific American, August 2001.

Lick, W., 1982. Entrainment, deposition and transport of fine-grained sediments in lakes. Hydrobiologia, 91: 31–40.

Lu, Q., and Wai, O., 1998. Three-dimensional coastal hydrodynamic computations with an efficient splitting method. International Journal of Numerical Methods in Fluids, 26: 771–789.

Mellor, G.L., 1998. User Guide for a Three-dimensional, Primitive Equation, Numerical Ocean Model. Princeton, NJ: Princeton University.

Oliver, D.R., 1961. The sedimentation suspension of closely-sized spherical particles. Chemical Engineering Science, 15: 230–242.

Saad, Y., 1996. Iterative Methods for Sparse Linear Systems. Boston, MA: PWS Publishing Company.

Van Rijn, L.C., 1986. Mathematical modeling of suspended sediment in nonuniform flows. Journal of Hydraulic Engineering, ASCE, 112 (6): 433–455.

Van Rijn, L.C., 1993. Principles of Sediment Transport in River, Estuaries and Coastal Seas. Amsterdam, The Netherlands: AQUA Publications.

Voevodin, V., 1983. The problem of non-self-adjoint generalization of the conjugate gradient method is closed. Computational Mathematics and Mathematical Physics, 23: 143–144.

Wai, O., and Lu, Q., 2000. An efficient parallel model for coastal transport process simulation. Advances in Water Resources, 23 (7): 747–764.

Wai, O., Lu, Q., and Li, Y.S., 1996. Multi-layer modeling of three dimensional hydrodynamic transport processes. Journal of Hydraulic Research, IAHR, 34 (5): 76–93.

Yalin, M.S., 1977. Mechanics of Sediment Transport. Oxford: Pergamon Press.

Zhang, J.C., 1991. Sediment Deposition in Xiamen Bay: Now and Future. NHRI Technical Report, NanJing. (in Chinese).

Zhang, J.C., and Liu, J.J., 1995. The Overall Arrangement and Environment Protection in Western Seas of Xiamen. NHRI Technical Report, NanJing (in Chinese).

This Page Intentionally Left Blank

Chapter 10

Nonlinear Wave Modeling and Sediment Transport in the Surf and Swash Zone

Theophanis V. Karambas

Technological Education Institute of Serres, Department of Civil Engineering, Terma Magnesias, 621 24, Serres, Greece

1. INTRODUCTION

Sediment transport prediction in the nearshore region requires the use of a wave and a wave-induced current model. Usually phase-averaged linear wave models are adopted where the effect of long waves and wave asymmetry can only be included in an approximate manner. The development of nonlinear breaking and non-breaking wave propagation models based on the Boussinesq equations, led to the combination of these models with a sediment transport model (Karambas et al., 1995; Watanabe and Dibajnia, 1996; Rakha et al., 1997; Karambas, 1998; Rakha, 1998). The main advantages of the use of a Boussinesq type nonlinear wave model, instead of a linear one, are:

(a) Only a unified model can be used for an accurate description of nonlinear irregular wave refraction, shoaling, diffraction, nonlinear wave-wave interactions, reflection (presence of structures), breaking, and dissipation after breaking (without the assumption of progressive waves).
(b) Breaking wave-induced current is automatically reproduced. Thus, there is no need for an additional current model (i.e., coupling of two models).
(c) The effect of long waves and wave asymmetry in the calculation of the sediment transport rates are included.
(d) three-dimensional effects are present (a 'mean' undertow is automatically reproduced).
(e) Wave runup and rundown on a beach can be included.

In this chapter a phase-resolving nonlinear wave module is combined with two sediment transport modules (based on a detailed and on an energetics approach) to study the process of sediment transport and morphological evolution in the nearshore area both inside and outside the surf zone. Application of the model to cross-shore and longshore transport are also given. Finally, the influence of swash infiltration-exfiltration on beach face sediment transport is studied.

2. WAVE TRANSFORMATION MODULE

2.1. Boussinesq Type Equations for Breaking and Non-Breaking Waves

Boussinesq type of equations are widely used for the description of the nonlinear breaking and non-breaking wave propagation in the nearshore region (Schäffer et al., 1993; Karambas, 1996; Madsen and Schäffer, 1998; Karambas, 1999; Veeramony and Svendsen, 2000). The models are usually based on the standard Boussinesq equations with improved linear dispersion characteristics (Madsen et al., 1997; Veeramony and Svendsen, 2000). However, in the shoaling region, Boussinesq-type of equations with additional higher-order nonlinear terms can provide better results in comparison with standard Boussinesq equations (Brocchini et al., 1992). In addition, according to Sobey (1993) standard Boussinesq equations do not satisfy the appropriate conservation laws even in shallow water. Sobey also concluded that much better results can be obtained using higher-order Boussinesq-type equations. Thus, in this chapter, higher-order Boussinesq type of equations are applied.
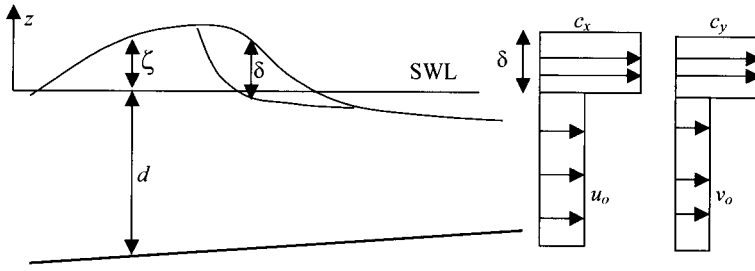
Figure 1. Cross-section of a breaking wave and assumed vertical profile of the horizontal velocity in the wave model.

Wave energy dissipation due to wave breaking is usually based on a significant characteristic of a breaker: the presence of the surface roller, i.e., a passive bulk of water transported with the wave celerity (Svendsen, 1984). Dissipation due to the roller can be introduced either as an excess momentum term due to the non-uniform velocity distribution (Schäffer et al., 1993) or as an additional pressure term due to its weight (Deigaard, 1989). Schäffer et al. (1993) are based on a simplified velocity profile where the surface roller is being transported with the wave celerity $c = (c_x, c_y)$ (in which c_x, and c_y are the wave celerities in the x and y directions). The velocity profile is (see Fig. 1)

$$
\begin{aligned}
u = c_x, \ v = c_y \text{ for } \ \zeta - \delta \leqslant z \leqslant \zeta \\
u = u_o, \ v = v_o \text{ for } -d \leqslant z \leqslant \zeta - \delta
\end{aligned}
\tag{1}
$$

where u_o and v_o are the bottom velocities in the x and y directions.

Based on the above velocity profile, the following higher-order Boussinesq-type equations for breaking and non-breaking waves can be derived (Zou, 1999; Karambas and Koutitas, 2002)

$$
\zeta_t + \nabla(h\mathbf{U}) = 0
$$

$$
\begin{aligned}
\mathbf{U}_t + \frac{1}{h}\nabla M_{\mathbf{u}} - \frac{1}{h}\mathbf{U}\nabla(\mathbf{U}h) + g\nabla\zeta + G = \frac{1}{2}h\nabla[\nabla\cdot(d\mathbf{U}_t)] - \frac{1}{6}h^2\nabla[\nabla\cdot\mathbf{U}_t] + \\
+ \frac{1}{30}d^2\nabla[\nabla\cdot(\mathbf{U}_t + g\nabla\zeta)] + \frac{1}{30}\nabla[\nabla\cdot(d^2\mathbf{U}_t + gd^2\nabla\zeta)] \\
- d\nabla(\delta\nabla\cdot\mathbf{U})_t - \frac{\tau_b}{h} + \mathbf{E}
\end{aligned}
\tag{2}
$$

$$
G = \frac{1}{3}\nabla\left\{d^2\left[(\nabla\cdot\mathbf{U})^2 - \mathbf{U}\cdot\nabla^2\mathbf{U} - \frac{1}{10}\nabla^2(\mathbf{U}\cdot\mathbf{U})\right]\right\} - \frac{1}{2}\zeta\nabla[\nabla\cdot(d\mathbf{U}_t)]
$$

where the subscript t denotes differentiation with respect to time, d is the still water depth, U is the horizontal velocity vector, $U = (U, V)$, where U and V are the depth-averaged horizontal velocities in directions x (cross-shore) and y (along-shore), ζ is the surface elevation, h is the total depth, $h = d + \zeta$, g is the gravitational acceleration, $M_{\mathbf{u}} = (d + \zeta)\mathbf{u}_0^2 + \delta(\mathbf{c}^2 - \mathbf{u}_0^2)$, in which $\mathbf{u}_0 = (u_o, v_o)$, $\tau_b = (\tau_{bx}, \tau_{by})$ is the bottom friction term, and $\mathbf{E} = (E_x, E_y)$ is the eddy viscosity term.

In the one-dimensional (1-D) model described by Schäffer et al. (1993) the roller region and the roller thickness δ, are determined geometrically. They assumed that for a non-breaking wave the local gradient of the wave front has a maximum $\tan\varphi$. When this gradient is exceeded the wave breaking initiates. The toe of the roller is defined as the location where the wave steepness is identical to $\tan\varphi$. The geometry of the roller can be approximated by using the tangent of slope $\tan\varphi$, starting at the toe and pointing in the direction opposite to the direction of wave propagation. The water above

this tangent belongs to the roller. Thus both the position of the roller and the roller thickness δ is determined. The roller thickness δ is multiplied by the roller shape function f_δ prior to inclusion in the governing equations. A breaking event begins using $\varphi = \varphi_B$, but as breaking develops, φ gradually changes to the smaller terminal value $\varphi = \varphi_o$. An exponential decay of $\tan\varphi$ has been chosen

$$\tan\varphi = \tan\varphi_o + (\tan\varphi_B - \tan\varphi_o)\exp\left[-\ln 2\,\frac{t - t_B}{t_{1/2}}\right] \tag{3}$$

where t_B is the time that breaking was initiated and $t_{1/2}$ is the time scale for the development of the roller. The values $\varphi_B = 20^0$, $\varphi_o = 10^0$, $f_\delta = 1.5$, and $t_{1/2} = T_p/5$ (T_p is the peak period of the incident spectrum) can be adopted as default values (Rakha et al., 1997).

In the two horizontal dimensions (2DH), the toe of the roller becomes a curve instead of a single point and the tangent becomes a tangential surface separating the roller from the rest of the flow. The roller toe curve is defined as the points satisfying the condition that the absolute value of the gradient equals the instantaneous local value of $\tan\varphi$ and the gradient in the direction of the wave propagation is negative (Sørensen et al., 1998).

The bottom velocity $\mathbf{u_0}$ is estimated using the definition of the depth-averaged velocity $\mathbf{U}$

$$\mathbf{U} = \frac{1}{h}\int_{-d}^{\zeta}\mathbf{u}\,dx$$

$$\mathbf{u_0} = \mathbf{U}\,\frac{h}{h-\delta} - \mathbf{c}\,\frac{\delta}{h-\delta} \tag{4}$$

$h = d + \zeta$. The roller celerity $\mathbf{c} = (c_x, c_y)$ is computed by using (Sørensen et al., 1998)

$$c_x = \frac{\partial\zeta}{\partial x}\,\frac{1.3\sqrt{gd}}{\sqrt{\left(\frac{\partial\zeta}{\partial x}\right)^2 + \left(\frac{\partial\zeta}{\partial y}\right)^2}} \qquad c_y = \frac{\partial\zeta}{\partial y}\,\frac{1.3\sqrt{gd}}{\sqrt{\left(\frac{\partial\zeta}{\partial x}\right)^2 + \left(\frac{\partial\zeta}{\partial y}\right)^2}} \tag{5}$$

2.2. Bottom Friction

The instantaneous bottom shear stresses can be approximated by the use of quadratic law

$$\tau_{bx} = \frac{1}{2}\,f_{cw}u_o\,|\mathbf{u_0}| \qquad \tau_{by} = \frac{1}{2}\,f_{cw}v_o\,|\mathbf{u_0}| \tag{6}$$

where $|\mathbf{u_0}| = \sqrt{u_o^2 + v_o^2}$ and f_{cw} is the wave-current bottom friction factor (Bosboom et al., 1997; Ribberink, 1998)

$$f_{cw} = \left(\frac{|\mathbf{U_c}|}{|\mathbf{U_c}| + u_{ow-\max}}\right)f_c + \left(1 - \frac{|\mathbf{U_c}|}{|\mathbf{U_c}| + u_{ow-\max}}\right)f_w \tag{7}$$

where f_w is the wave friction factor and f_c the current friction factor, $u_{ow-\max}$ is the amplitude of the oscillatory component of the near bottom velocity $\mathbf{u_{ow}} = (u_{ow}, v_{ow})$, $|\mathbf{U_c}| = \sqrt{U_c^2 + V_c^2}$, U_c and V_c are the velocity components if the time-average current field, obtained by averaging the

instantaneous velocities

$$U_c = \overline{U} \qquad V_c = \overline{V} \tag{8}$$

where the overbar denotes time-averaging between time t_1 and t_2: $\overline{*} = \dfrac{1}{t_2 - t_1} \displaystyle\int_{t_1}^{t_2} * \, dt.$

For irregular waves, the current velocities U_c and V_c, as well as all the time mean values of the parameters, can be obtained following the procedure proposed by Rakha et al. (1997). The time series of the instantaneous velocities U and V calculated by the wave model are divided into a number of cycles N_c each consisting of N time steps. All calculations described below are performed for each cycle separately. For each cycle the values of the instantaneous velocities U and V are time-averaged over N time steps to obtain automatically the current velocities U_c and V_c. The length of the cycles is the result of the compromise. Very short cycles result in an unrealistic, instantaneous response of the hydrodynamics to the individual waves. Very long cycles average out the variation in the (wave period averaged) forcing of an irregular wave train. Typically, a cycle has a duration of 20–30 times the mean wave period. The results are not very sensitive to the duration of the cycles (Rakha et al., 1997). The final values are calculated by averaging the current velocities for N_c cycles (usually $N_c = 2$–6). For periodic waves U_c and V_c are obtained by averaging the instantaneous velocities U and V over three wave periods.

For non-breaking waves the bottom velocity can be given by (Dingemans, 1997)

$$u_o = U + \left(\frac{d}{2}\right) \frac{\partial^2 (dU)}{\partial x^2} - \left(\frac{d^2}{3}\right) \frac{\partial^2 U}{\partial x^2} \quad v_o = V + \left(\frac{d}{2}\right) \frac{\partial^2 (dV)}{\partial y^2} - \left(\frac{d^2}{3}\right) \frac{\partial^2 V}{\partial y^2} \tag{9}$$

The oscillatory component of the near bottom velocities u_{ow} and v_{ow} are calculated from the near bottom velocities u_o and v_o after the subtraction of the mean currents $\overline{u}_o$ and $\overline{v}_o$ under the roller

$$u_{ow} = u_o - \overline{u}_o \quad v_{ow} = v_o - \overline{v}_o \tag{10}$$

The wave friction factor is calculated with the following formula, which is based on an implicit relation of Jonsson (1966)

$$
\begin{aligned}
f_w &= \exp\left[-5.977 + 5.213 \left(\frac{K_N}{A_b}\right)^{0.194} \right] & \text{for:} \quad & \frac{K_N}{A_b} < 0.63 \\
f_w &= 0.3 & \text{for:} \quad & \frac{K_N}{A_b} \geqslant 0.63
\end{aligned}
\tag{11}
$$

where A_b is the water particle amplitude of the oscillation, and K_N is the bed roughness which is a function of the Shields parameter, median grain diameter d_{50}, ripple height η_r and length λ_r (Nielsen, 1992)

$$K_N = 170 \sqrt{\theta_{2.5} - 0.05} \, d_{50} + 8 \eta_r^2 / \lambda_r \tag{12}$$

where $\theta_{2.5}$ is the Shields parameter based on $K_N = 2.5 \, d_{50}$

$$\theta_{2.5} = \frac{1}{2} f_{2.5} \, \psi \tag{13}$$

and ψ is the mobility number

$$\psi = \frac{u_{ow-max}^2}{(s-1) \, g \, d_{50}} \tag{14}$$

where s is the specific density of the sediment, $s = (\rho_s - \rho)/\rho$, in which ρ and ρ_s are the densities of the water and sediment, respectively.

The ripple height η_r and the ripple steepness η_r/λ_r are calculated from the following formulae suggested by Nielsen (1992) for irregular waves

$$\eta_r = 21\, A_b\, \psi^{-1.85} \quad \text{for } \psi > 10 \text{ and } \frac{\eta_r}{\lambda_r} = 0.342 - 0.34\sqrt[4]{\theta_{2.5}} \tag{15}$$

The current friction factor f_c is calculated from (Bosboom et al., 1997; Ribberink, 1998)

$$f_c = 0.24 \left(\log \frac{12\,(d + \bar{\zeta})}{K_N} \right)^{-2} \tag{16}$$

2.3. Subgrid Turbulent Mixing

In two horizontal dimensions the effects of subgrid turbulent processes can be taken into account by using the Smagorinsky-type subgrid model.

The terms E_x and E_y in the momentum equation are written

$$E_x = \frac{1}{d + \zeta} \left[\frac{\partial}{\partial x} \left(\nu_{sg} \frac{\partial ((d + \zeta)U)}{\partial x} \right) + \frac{1}{2} \frac{\partial}{\partial y} \left(\nu_{sg} \frac{\partial ((d + \zeta)U)}{\partial y} + \nu_{sg} \frac{\partial ((d + \zeta)V)}{\partial x} \right) \right]$$

$$E_y = \frac{1}{d + \zeta} \left[\frac{\partial}{\partial y} \left(\nu_{sg} \frac{\partial ((d + \zeta)V)}{\partial y} \right) + \frac{1}{2} \frac{\partial}{\partial x} \left(\nu_{sg} \frac{\partial ((d + \zeta)U)}{\partial x} + \nu_{sg} \frac{\partial ((d + \zeta)V)}{\partial y} \right) \right] \tag{17}$$

where ν_{sg} is the eddy viscosity due to subgrid turbulence given by

$$\nu_{sg} = (0.5\,dx)^2 \left[\left(\frac{\partial U_c}{\partial x} \right)^2 + \left(\frac{\partial V_c}{\partial y} \right)^2 + \frac{1}{2} \left(\frac{\partial U_c}{\partial y} + \frac{\partial V_c}{\partial x} \right)^2 \right]^{1/2} \tag{18}$$

where dx is the grid spacing.

2.4. Hydrodynamics in the Swash Zone

The surface roller concept is valid only inside the surf zone (in the inner region) where unsteady bores are formed and propagate over a sloping bottom. In the swash zone the bore collapses at the shore, surface rollers are not present and consequently the velocity distribution given by equation (1) is not valid.

In order to simulate the dissipation due to turbulence in the swash zone the eddy viscosity concept can be adopted. Zelt (1991) obtained good results using this concept to simulate runup of breaking solitary waves. The swash zone eddy viscosity coefficient ν_s can be estimated from (Zelt, 1991)

$$\nu_s = \ell_s^2 \left[\left(\frac{\partial U}{\partial x} \right)^2 + \left(\frac{\partial V}{\partial y} \right)^2 + \frac{1}{2} \left(\frac{\partial U}{\partial y} + \frac{\partial V}{\partial x} \right)^2 \right]^{1/2} \tag{19}$$

where ℓ_s is a length scale related to the total water depth $(d + \zeta)$ through $\ell_s = 2(d + \zeta)$.

Near the shore, where ℓ_s is less than one node spacing, ℓ_s is taken equal to $\ell_s = 2\,dx$, where dx is the grid size. The above artificial viscosity technique is applied in the front side of the broken wave and the eddy viscosity coefficient ν_s is added to the eddy viscosity coefficient due to subgrid turbulence ν_{sg}.

The 'dry bed' boundary condition can be used to simulate runup (Karambas, 1998). The condition, at the point i of the swash zone, is written

$$
\begin{aligned}
&\text{if} \quad (d+\zeta)_{i-1} < 0.0001\,\text{m} \text{ and } U_i > 0 \text{ then } \zeta_i = -d \text{ and } U_i = 0 \\
&\text{and} \\
&\text{if} \quad (d+\zeta)_i < 0.0001\,\text{m} \text{ and } U_i < 0 \quad \text{then } \zeta_i = -d \text{ and } U_i = 0
\end{aligned}
\tag{20}
$$

which can be easily incorporated in a nonlinear model.

2.5. Numerical Scheme and Boundary Conditions

The numerical solution of the Boussinesq-type equations can be based on an accurate higher-order numerical scheme, which has been developed by Wei and Kirby (1995). They used a fourth-order predictor-corrector scheme for time stepping and discretize the first-order spatial derivatives to fourth-order accuracy. This discretization automatically eliminates error terms that would be of the same form as the dispersive terms, and which must, therefore, be corrected for if lower order schemes are used.

Waves propagating out of the domain are artificially absorbed using the flow relaxation scheme. The technique is applied on the prognostic variables within a specified relaxation zone at the open boundaries. The relaxation scheme updates the prognostic variables (ζ, U, V) in the zones by the equations (Martinsen and Engedahl, 1987)

$$
\begin{aligned}
\zeta &= r\,\widehat{\zeta} + (1-r)\,\widetilde{\zeta} \\
U &= r\,\widehat{U} + (1-r)\,\widetilde{U} \\
V &= r\,\widehat{V} + (1-r)\,\widetilde{V}
\end{aligned}
\tag{21}
$$

where the variables marked by the tilde ($\widetilde{}$) contain unrelaxed values, the variables marked by the hat ($\widehat{}$) are the specified external solutions and r is a relaxation parameter which varies from 0 to 1 within the specified relaxation zone. It is equal to 1 at the outer edges of the zones, and decreases down to zero at the edges facing the model domain

$$
r = 1 - \tanh\left(\frac{i-1}{2}\right) \quad i = 1, 2, 3, \ldots, \text{NN}
\tag{22}
$$

where NN is the number of grid elements in the relaxation zone.

The success of the method will depend on how well the external solutions are known. In the case where the external solutions are 'correct' in the way that they coincide with the solutions that the model would have produced, the technique will work perfectly. For regular waves approaching a straight shoreline at an oblique angle, the external solution for the longshore current V_{es} can be obtained from the model itself across the line $y = y_m$

$$
V_{es} = V_c\,(x, y = y_m)
\tag{23}
$$

where x is the coordinate normal to the shoreline, y is the coordinate parallel to the shoreline and $y = y_m$ is a line in the middle of the model domain.

For irregular waves the external solution is not known, and in this case, in order to absorb wave energy, the following artificial damping terms F and G are added to the right-hand side of the momentum equations in the x and y directions respectively (Wei and Kirby, 1995)

$$
\begin{aligned}
F &= -\alpha_r\,r\,\omega\,U \\
G &= -\alpha_r\,r\,\omega\,V
\end{aligned}
\tag{24}
$$

where α_r is the constant to be determined for the specific run and ω is the radian frequency of the wave.

The above damping layer is applied together with a radiation boundary condition. For wave propagation with the principal propagation direction close to the x-axis, the radiation boundary condition is written (Wei and Kirby, 1995)

$$\frac{\partial^2 \zeta}{\partial t^2} + c_l \frac{\partial^2 \zeta}{\partial t \partial x} - \frac{c_l^2}{2} \frac{\partial^2 \zeta}{\partial y^2} = 0 \tag{25}$$

where c_l is the phase speed specified by the long-wave limit $c_l = \sqrt{gd}$.

Numerical experiments show that the addition of the damping layer combined with radiation boundary conditions works very well. Using damping layers near the boundaries rules out the possibility of any type of wave generation at the boundary. Therefore, a source term, inside the domain, is introduced to generate the desired waves. The term is added to the right-hand side of the continuity equation (3). In order to avoid spurious noise appearing around the source point, it is necessary to distribute the source function around a certain neighborhood of the source (Wei et al., 1999). The source function is written

$$f_s(x, t) = D_s \exp\left[-\beta_s (x - x_s)^2\right] \sin(ky \sin(\theta_s) - \omega t) \tag{26}$$

where x_s is the central location of the source in the x direction, for a source oriented parallel to the y axis, β_s is the shape coefficient for the source function ($\beta_s \approx 80/L^2$, L = wavelength), D_s is the magnitude of the source function (which is related to the desired wave amplitude, Wei at al., 1999), k is the wave number, and θ_s is the angle between the propagation direction of the wave and the x-axis.

2.6. Undertow and Eddy Viscosity Calculations

2.6.1. Undertow Calculations

The mean undertow $\bar{u}_o$ can be obtained by averaging the instantaneous bottom velocities u_o, following the procedure already described in Section 2.2. The above method cannot predict the near bed shoreward drift (steady streaming) generated by the phase shift in orbital motions due to bottom boundary layer mechanisms (viscosity effects). Inside the surf zone the phase shift mechanism is suppressed by both the developing turbulence and the undertow acting in the middle layer, and so the resulting near bed mass transport should be directed offshore. The above mechanisms can be incorporated in a Boussinesq model by calculating the undertow velocity U_{und}, from the analytical expression proposed by Putrevu and Svendsen (1993) which is valid inside and outside the surf zone

$$U_{und}(x, z) = \frac{a_1}{2 \, v_{br}} (d + z)^2 + \frac{\overline{\tau}_{bx} - \tau_{sb}}{\rho \, v_{br}} (d + z) + U_b \tag{27}$$

with

$$\frac{U_b}{\sqrt{g(d + \overline{\zeta})}} = \left(\frac{\bar{u}_o}{\sqrt{g(d + \overline{\zeta})}} - \frac{A}{6} + \frac{\tau_{sb}(d + \overline{\zeta})}{2 \rho \, v_{br} \sqrt{g(d + \overline{\zeta})}} \right) (1 + R_1)^{-1} \tag{28}$$

where x is the coordinate normal to the shoreline, U_b is the undertow bottom velocity, $\overline{\zeta}$ is the mean water level (set-up), $\overline{\tau}_{bx}$ is the time-averaged bed shear stress in the x direction, τ_{sb} is the steady streaming term, v_{br} is the depth-averaged value of the time-averaged eddy viscosity coefficient due to wave breaking, and a_1, A, R_1 are coefficients given by Putrevu and Svendsen (1993) (see also Karambas and Koutitas, 2002)

$$\tau_{sb} = \frac{1}{2} \rho \, v_{tg} \sqrt{\frac{\omega}{2 \, v_{tg}}} \frac{u_{ow-max}^2}{c} \tag{29}$$

and

$$a_1 = g \frac{\partial \overline{\zeta}}{\partial x} + \frac{1}{2} \frac{\partial \overline{u}_{ow}^2}{\partial x}, \quad A = \frac{a_1 \left(d + \overline{\zeta}\right)^2}{\nu_{br}\sqrt{g\left(d + \overline{\zeta}\right)}}, \quad R_1 = \frac{f_w u_{ow-\max}(d + \overline{\zeta})}{\pi \nu_{br}} \tag{30}$$

where ν_{tg} is the eddy viscosity coefficient inside the bottom boundary layer and c is the wave celerity. Outside the surf zone ν_{br} is taken as equal to ν_{tg}, $\nu_{br} = \nu_{tg}$.

2.6.2. Eddy Viscosity Calculations

The instantaneous eddy viscosity coefficient due to wave breaking ν_z can be calculated from the turbulent kinetic energy

$$\nu_z = \ell\sqrt{k_t} \tag{31}$$

where ℓ is the length scale of turbulence and k_t is the turbulent kinetic energy induced by wave breaking.

The transport equation for turbulent kinetic energy is given by (Deigaard et al., 1986)

$$\frac{\partial k_t}{\partial t} = \frac{\partial}{\partial z}\left(\nu_z \frac{\partial k_t}{\partial z}\right) + \frac{\text{PROD}}{\rho} - c_d \frac{k_t^{3/2}}{\ell} \tag{32}$$

in which c_d is a constant, $c_d = 0.08$ and PROD stands for the production of turbulent energy. The energy lost from the waves due to breaking is the source of turbulence in the turbulence model. The instantaneous production of turbulence is calculated from (Rakha et al., 1997, Rakha, 1998)

$$\text{PROD} = 0.33 \, \rho \, g \, c \, \delta \tan 10^o \tag{33}$$

The variation in PROD with depth is assumed to be parabolic over a distance of half the wave height $(H/2)$ below the water surface (Deigaard et al., 1986; Rakha et al., 1997). The turbulent length scale ℓ is determined from Deigaard et al. (1991)

$$\ell = c_d^{1/4}\kappa \, (d + z) \quad d + z \leq \frac{0.1\,d}{c_d^{1/4}\kappa}$$

$$\ell = 0.1\,d \qquad d + z > \frac{0.1\,d}{c_d^{1/4}\kappa} \tag{34}$$

where κ is the von Karman's constant ($\kappa = 0.4$).

The transport equation can be solved by numerical integration with two boundary conditions

$$k_t = 0 \text{ at } z = -d \tag{35}$$

corresponding to k_t decreasing to zero at the bed, and

$$\frac{\partial k_t}{\partial z} = 0 \text{ at } z = 0 \tag{36}$$

corresponding to no energy flux through the water surface.

Equation (32) is solved numerically by application of the finite difference method. The depth-averaged value ν_{br} of the time-averaged eddy viscosity coefficient due to wave breaking is computed from the depth integration of $\overline{\nu}_z$, according to $\nu_{br} = \frac{1}{d} \int_{-d}^{0} \overline{\nu}_z \, dz$.

The eddy viscosity coefficient inside the bottom boundary layer v_{tg} is given by Staub et al. (1996), assuming an average value over the wave boundary layer

$$v_{tg} = \frac{1}{6} \kappa u_* \delta_w \tag{37}$$

where δ_w is the wave boundary layer thickness (Jonsson and Carlsen, 1976) and u_* is the friction velocity (Staub et al., 1996)

$$\frac{30\,\delta_w}{K_N} \log \frac{30\,\delta_w}{K_N} = 1.2 \frac{A_b}{K_N} \quad u_* = \frac{2}{\pi} \sqrt{\frac{f_w}{2}} u_{ow-\max} \tag{38}$$

3. SEDIMENT TRANSPORT MODULE

The mode of nearshore sediment movement is usually divided into bedload, suspended load and sheet flow. As the magnitude of the wave orbital velocity on the sea bed increases, one observes: (1) bedload movement, (2) sediment suspension in the vicinity of ripples, and (3) sheet flow movement in this order as the waves approach the breaker line. In the surf zone, strong agitation of the water due to wave breaking causes intense sediment suspension. The high shear stresses in the swash zone prescribe that sediment transport in the swash zone is performed predominantly by sheet flow, which consists of a mixture of bedload and suspended load (Masselink and Hughes, 1998). Especially during uprush, the bore generated turbulence directly influences local sediment transport (Puleo et al., 2000). Fig. 2 schematically illustrates the sediment transport modes in the zones on a natural beach.

There exist two main approaches for calculating the above sediment transport modes in the coastal zone: the process-based (or detailed) and the energetics approach. The detailed approach consists of calculating the three-dimensional velocity field and the sediment concentration profiles independently over the study area (Deigaard et al., 1986; Katopodi and Ribberink 1992; Briad and Kamphuis, 1993; Rakha, 1998). The energetics approach is based on the idea that the sediment transport is related to the rate of energy dissipation of the flow (Bailard 1981; Roelvink and Stive, 1989). Both approaches can be combined with a phase-resolving wave transformation module.
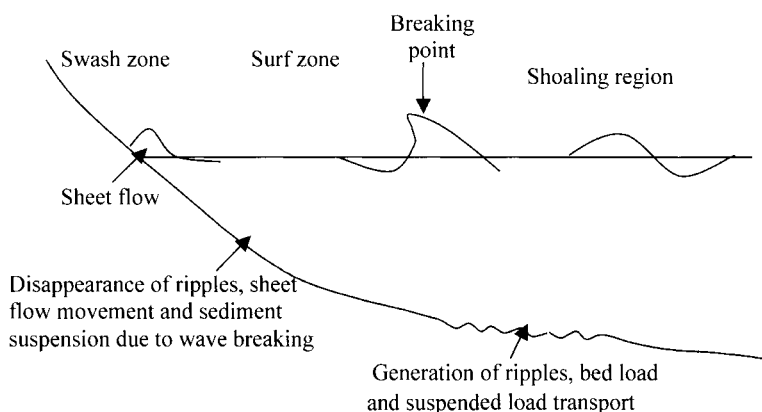
Figure 2. Cross-shore variation of sediment transport modes.

3.1. Process-Based Approach

The total time-averaged sediment transport rate (including pores) $\mathbf{q_t}$ ($\mathbf{q_t} = (q_{tx}, q_{ty})$), is estimated from by

$$\mathbf{q_t} = \bar{\mathbf{q}}_\mathbf{b} + \mathbf{q_s} \tag{39}$$

where, q_{tx} and q_{ty} are the transport rates in directions x and y, $\mathbf{q_b}$ ($\mathbf{q_b} = (q_{bx}, q_{by})$) is the bedload transport and $\mathbf{q_s}$ ($\mathbf{q_s} = (q_{sx}, q_{sy})$) is the time-averaged suspended load under broken waves. Sheet flow and suspended load over ripples are considered as being part of the bedload transport.

3.1.1. Sheet Flow Transport, Suspended Load Transport Over Ripples and Bedload Transport

A new transport rate formula involving unsteady aspects of the sand transport phenomenon has been presented by Dibajnia and Watanabe (1992). The formula estimates the sheet flow sand transport rates, and has been generalized by them for the bedload as well as for the suspended load over ripples (Watanabe and Dibajnia, 1996). Dibajnia and Watanabe (1996) also extended the formula for mixed-size sands, while in Dibajnia and Watanabe (1998) and Dibajnia et al. (2001) the formula has been modified to estimate the sand transport rate under irregular sheet flow conditions. The cross-shore sheet flow transport rate formula for irregular waves is written as (Dibajnia et al., 2001)

$$\frac{q_{bx}}{w_s\, d_{50}} = 0.0038\, \frac{u_c\, T_c\left(\Omega_c + \Omega_t'\right) - u_t\, T_t\left(\Omega_t + \Omega_c'\right)}{(T_c + T_t)\sqrt{s\, g\, d_{50}}} \tag{40}$$

where w_s is the sediment fall velocity, and u_c and u_t are the equivalent root-mean-square velocity amplitudes for the positive (crest) and negative (trough) portions of the velocity profile (Fig. 3), with T_c and T_t being the corresponding durations respectively. They are defined as

$$u_c^2 = \frac{2}{T_c} \int\limits_{t_0}^{t_0+T_c} u_{ou}^2\, dt, \quad u_t^2 = \frac{2}{T_t} \int\limits_{t_0+T_c}^{t_0+T} u_{ou}^2\, dt \tag{41}$$

where $T = T_c + T_t$, and u_{ou} is the bottom velocity where $u_{ou} = u_{ow} + U_b$ (as already defined, u_{ow} is the oscillatory component of the near bottom velocity where $u_{ow} = u_o - \bar{u}_o$, and U_b is the undertow velocity near the bottom).
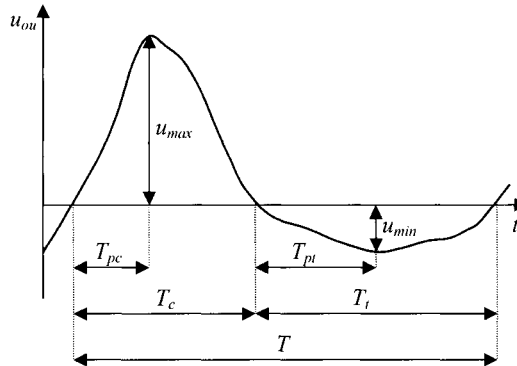
Figure 3. Definitions of velocity parameters. In general, u_{ou} may include low frequency components and steady current.

Values of Ω_j are determined as follows

if $\omega_j \leqslant \omega_{cr}$ $\Omega_j = \omega_j T_j \sqrt{\dfrac{s\,g}{d_{50}}}\,,$ $\Omega'_j = 0$

$$\text{if } \omega_j > \omega_{cr}\ \ \Omega_j = \left[\omega_{cr} + (1-\gamma_j)(\omega_j - \omega_{cr})\right]T_j\sqrt{\frac{s\,g}{d_{50}}},\ \ \Omega'_j = \gamma_j\,(\omega_j - \omega_{cr})\,T_j\sqrt{\frac{s\,g}{d_{50}}}$$

(42)

with the condition for Ω_j (and not Ω'_j) that

$$\text{if } \theta_j < \theta_{sheet}:\ \ \Omega_j = \left(\frac{\theta_j - \theta_{cr}}{\theta_{sheet} - \theta_{cr}}\right)^3 \Omega_j \tag{43}$$

where θ_j is the Shields number, $\theta_j = f_w\,u_j^2/(2\,s\,g\,d_{50})$, and

$$\omega_j = \left(\frac{1}{2}\frac{u_j^2}{s\,g\,d_{50}} - 5\right)\frac{d_{50}}{w_s T_j} \tag{44}$$

$$\gamma_j = \beta_j^* \cdot \beta'_j \tag{45}$$

in which

$$\begin{cases} \beta'_c = 1 & \text{if } \dfrac{u_t}{u_c} \geq \dfrac{1}{4} \\[2mm] \beta'_c = 4\dfrac{u_t}{u_c} & \text{if } \dfrac{u_t}{u_c} < \dfrac{1}{4} \end{cases} \quad , \quad \begin{cases} \beta'_t = 1 & \text{if } \dfrac{u_c}{u_t} \geq \dfrac{1}{4} \\[2mm] \beta'_t = 4\dfrac{u_c}{u_t} & \text{if } \dfrac{u_c}{u_t} < \dfrac{1}{4} \end{cases} \tag{46}$$

and

$$\begin{cases} \beta_j^* = 1 & \text{if } \dfrac{T_{pj}}{T_j} \geq \dfrac{1}{2} \\[3mm] \beta_j^* = \dfrac{6T_{pj}}{T_j} - 2 & \text{if } \dfrac{1}{3} < \dfrac{T_{pj}}{T_j} < \dfrac{1}{2} \\[3mm] \beta_j^* = 0 & \text{if } \dfrac{T_{pj}}{T_j} \leq \dfrac{1}{3} \end{cases} \tag{47}$$

In the above relations, θ_{sheet} is the critical Shields number for initiation of sheet flow, $\theta_{sheet} = 0.8$, and θ_{cr} is the critical Shields number for initiation of motion, $\theta_{cr} = 0.05$, $\omega_{cr} = 1.2$ for sheet flow, and subscript j should be replaced by either c or t (i.e., crest or trough).

The above relations are derived to predict the net transport rate under sheet flow conditions. Experiments indicate that especially for highly asymmetric waves the sand which had been entrained during the positive cycle, was brought back into the negative direction by the successive negative cycle. This mechanism, in some cases, is strong enough to make the net transport occur in the negative direction. The Dibajnia and Watanabe formula takes into account the above mechanism. Ω_c and Ω_t indicate those amounts of sand which are entrained and carried directly by the positive cycle and negative half-cycle respectively. On the other hand, Ω'_c represents the amount of suspended sand remaining after the positive half-cycle, to be carried by the negative velocity. Similarly, Ω'_t stands for the amount of sand still in suspension after the negative half-cycle of the previous wave that will be

transported in the positive direction. ω is the ratio of the fall time of the particles (determined by their fall velocity and the height to which the particles are suspended) and the period of the corresponding half wave cycle. The parameter β^* accounts for the effect of wave asymmetry, and β' considers whether the velocity in the next half-cycle is high enough to carry the suspended sand delivered by the half-cycle or not. For details the reader is referred to Dibajnia and Watanabe (1992; 1998) and Dibajnia et al. (2001).

The suspended load over ripples and the bedload transport will also be taken into account if the critical value of ω is set equal to 0.03, i.e., $\omega_{cr} = 0.03$ (Dibajnia, 1995). In the transition region between the rippled bottom of suspended load and the flat bed of sheet flow, we can assume that ω_{cr} should gradually change from 0.03 to 1.2 in a parabolic manner (Dibajnia, 1995)

$$\omega_{cr} = 1.2 - 1.17\sqrt{\Lambda} \tag{48}$$

in which

$$\begin{aligned}
\Lambda &= 0 & &\text{for } \theta > \theta_{sheet} \\
\Lambda &= \left[\min(1, 2\lambda_r/A_b)\right] & &\text{for } \theta < 0.5, \text{ and} \\
\Lambda &= \left\{1 - \left[(\theta - 0.5)/0.3\right]^2\right\} \left[\min(1, 2\lambda_r/A_b)\right] & &\text{for } 0.5 \geqslant \theta \geqslant 0.8
\end{aligned} \tag{49}$$

where θ is the Shields number estimated in terms of u_c, and λ_r is the length of ripples if any (equation (15)).

In a 2DH wave-current coexisting field the total velocity field can be represented by the vector $\mathbf{u_c}$ which lasts for an interval of T_c, followed by the vector $\mathbf{u_t}$ which lasts for an interval of T_t. The sediment transport vector $\mathbf{q_b}$ is now estimated by (Dibajnia, 1995; Dibajnia et al., 2001)

$$\frac{\mathbf{q_b}}{w_s d_{50}} = 0.0038 \frac{\mathbf{u_c} T_c \left(\Omega_c + \Omega_t'\right) + \mathbf{u_t} T_t \left(\Omega_t + \Omega_c'\right)}{(T_c + T_t)\sqrt{s g d_{50}}} \tag{50}$$

The parameter γ is now defined as (Dibajnia, 2002)

$$\gamma_j = \beta_j^* \cdot \beta_j' \cdot \beta_j'' \tag{51}$$

where

$$\beta_j'' = (\Delta\alpha/\pi)^2, \ \Delta\alpha = |\alpha_c - \alpha_t| \tag{52}$$

in which β_j'' is an additional correction factor for sediment exchange between the two half-cycles, and α_c and α_t are the angles for $\mathbf{u_c}$ and $\mathbf{u_t}$ velocity vectors.

3.1.2. Suspended Sediment Transport Under Broken Waves

Since the aforementioned Dibajnia and Watanabe sheet flow formula also covers wave-induced suspended load over ripples as well as bedload transport, in order to estimate the total load only the suspended load due to wave breaking has to be included.

Inside the surf zone we can use a simple time-averaged approach to estimate suspended sediment concentration (Briad and Kamphuis, 1993). Experimental results (Smith et al., 1995) also indicated the suitability of wave-averaged modeling of the suspended load at the inner surf zone, because of the fairly random distribution of sediment suspension events throughout the wave cycle. The time-averaged suspended load $\mathbf{q_s}$ can be estimated from

$$\mathbf{q_s} = \frac{1}{1 - \lambda} \int_{-d}^{0} \mathbf{U_{tc}} C \, dz \tag{53}$$

where λ is the sediment porosity, $C = C(z)$ is the time-averaged concentration, and $\mathbf{U_{tc}}$ is the current velocity including the undertow contribution

$$\mathbf{U_{tc}} = (U_{tc}, V_{tc})$$ (54)

where

$$U_{tc} = U_c + U_{und} \text{ and } V_{tc} = V_c$$ (55)

For the current velocity $\mathbf{U_{tc}}$ a uniform depth distribution is assumed.

The time-averaged concentration C is calculated from the diffusion equation which describes the suspension of solids in a fluid

$$\frac{\partial C}{\partial t} = w_s \frac{\partial C}{\partial z} + \frac{\partial}{\partial z} \left(\varepsilon_{sb} \frac{\partial C}{\partial z} \right)$$ (56)

where ε_{sb} is time-averaged vertical diffusion coefficient (taken equal to the flow eddy viscosity $\bar{v}_z$, $\varepsilon_{sb} = \bar{v}_z$).

In equation (56) the horizontal diffusion coefficients are neglected as these, relative to the vertical gradients, are irrelevant. For the present case, namely, the description of time-averaged concentrations, the time derivative $\partial C / \partial t$ should equal zero. In addition, inside the inner surf zone we assume that a local equilibrium between the upward mixing-related and downward gravity-related transport occurs (Steetzel, 1993). From this, a general expression describing the vertical profile of the time-averaged sediment concentration can be derived (Steetzel, 1993)

$$C(z) = C_b \exp \left[-\int_{-d}^{z} \frac{w_s}{\varepsilon_{sb}} dz \right]$$ (57)

where C_b is the bed concentration (Sawaragi, 1995, p. 194)

$$C_b = 0.49 \theta^{1.77} \left(\frac{d_{50}}{w_s T f_w} \right)^{1.77}$$ (58)

where θ is the Shields parameter and T is the wave period.

The above adopted exponential form for $C(z)$ has been confirmed in many series of field and laboratory experiments.

3.1.3. Morphology Module and Applications

In the present section the model is applied to simulate beach erosion and accretion. The Boussinesq model is used to predict cross-shore transport rates. The sediment transport rate in the swash zone is calculated as in the submerged part using only the Dibajnia and Watanabe formula, after the assumption that the primary sediment transport mechanism in this zone is the sheet flow (although a different approach is adopted in Section 4). The estimated q_t is the input of the morphology model to the prediction of the bathymetry changes. The morphology model is applied for N_m time steps. Then, the Boussinesq model is applied again with the updated morphology to obtain the new transport rates. The above process is repeated as many times as it is required to reach the final time.

The time step of the Boussinesq model dt is different from the time step dt_m of the morphology model. The spatial steps dx are the same. In the next applications the spatial grid spacing is $dx = 0.5$ m. A time step of $dt = 0.00625$ s is used for the Boussinesq model, while for the morphology model $dt_m = 18$ s. The morphology model is applied for $N_m = 250$ time steps.

Changes in the cross-shore beach profile are computed from the numerical solution of the conservation equation of the sediment mass

$$\frac{\partial z_b}{\partial t} = -\frac{\partial}{\partial x}\left(q_{tx} - \varepsilon_m \left|q_{tx}\right| \frac{\partial z_b}{\partial x}\right) - \frac{\partial}{\partial y}\left(q_{ty} - \varepsilon_m \left|q_{ty}\right| \frac{\partial z_b}{\partial y}\right)$$ (59)

where z_b is the bottom elevation, and the value of coefficient ε_m is set equal to 2.0. The diffusion term is an additional gravitational term which reflects the effect of local bottom slope on the sediment transport (Horikawa, 1988, p. 301). Sediment transport is influenced by the bottom slope as downslope reduces resistance and upslope increases resistance. The down-slope gravitational transport is the most important mechanism to keep the bed from growing indefinitely, and to enable the coastal profile to reach a dynamic equilibrium state (Kim and Wang, 1996).

In the following, the model is applied to predict erosional and accretional profiles under periodic wave action. The purpose of this numerical experiment is to check the ability of the model in predicting erosion or accretion under specific conditions.

The erosion/accretion criterion used in the present application is that proposed by Hands et al. (1996) and Ahrens and Hands (1998). Based on field and experimental data, Hands et al. (1996) parameterized beach erosion and accretion processes on the basis of the ratio U_T of the near bed peak orbital wave velocity $u_{\max -t}$ under the trough, to the grain threshold speed u_{crit} required to initiate sediment movement, where $U_T = u_{\max -t}/u_{crit}$. The bottom velocity $u_{\max -t}$ is estimated at the breaking point using stream function theory. The breaking wave height and depth are obtained using the expressions proposed by Hands et al. (1996). The critical velocity u_{crit} is defined as

$$u_{crit} = \sqrt{8sgd_{50}}$$ (60)

Hands et al. (1996) and Ahrens and Hands (1998) applied parameter U_T to a number of field and experimental data and concluded that U_T discriminates well between erosional and accretional profiles at a value around -2. If $U_T < -2$, erosional profiles occur. The above criterion is not universally applicable. It is only adopted here to distinguish accretionary and erosional cases.

The conditions of the numerical experiment are summarized in Table 1. The beach slope is 1:20. Case 0 corresponds to the value $U_T = -2$, i.e., the value that separates accretion and erosion. By changing median grain diameter d_{50} we obtained two different conditions: an accretive, Case A, with $d_{50} = 0.47$ mm and $U_T = -1.65$, and an erosive, Case E, with $d_{50} = 0.2$ mm and $U_T = -2.50$. Based again on Case 0 and changing the wave steepness H_o/L_o, we obtained another pair of accretive and erosive conditions. Case A1 is obtained by increasing the wave period and decreasing the wave height while Case E1 is obtained by decreasing the wave period and increasing the wave height. The two accretive (A and A1) and the two erosive (E and E1) conditions have the same value of U_T. The above conditions cannot be considered highly erosive and highly accretive respectively.

Table 1
Conditions and test cases of the numerical experiment.

CASE	Wave Height H_o (m)	Wave Period T (s)	Median Diameter d_{50} (mm)	U_T
0	1.05	6.0	0.30	−2.00
A	1.05	6.0	0.47	−1.65
A1	0.96	9.0	0.30	−1.65
E	1.05	6.0	0.20	−2.50
E1	1.25	5.0	0.30	−2.50
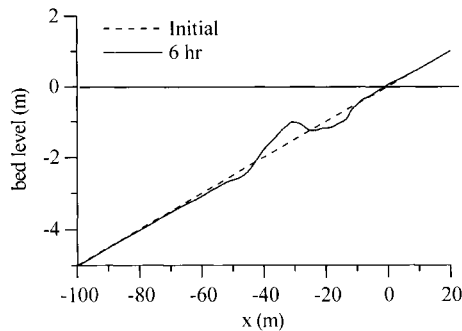
Figure 4. Beach profile change for Case 0 after 6 hours; $H_o = 1.05$, $T = 6.0$ s, $d_{50} = 30$ mm, $U_T = -2.0$.
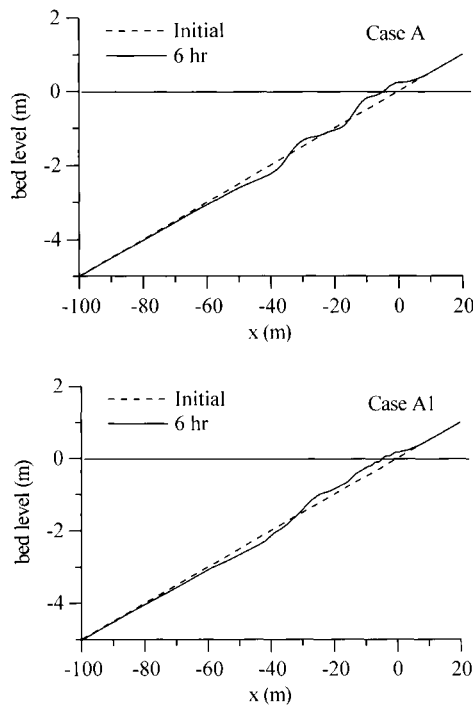
Figure 5. Beach profile change for accretive Cases A and A1 after 6 hours; Case A: $H_o = 1.05$, $T = 6.0$ s, $d_{50} = 0.47$ mm, $U_T = -1.65$, and Case A1: $H_o = 0.96$, $T = 9.0$ s, $d_{50} = 0.30$ mm, $U_T = -1.65$.

Figs. 4 to 6 present the resulting beach profiles after 6 hours of wave action. The model predicts accretion for $U_T > -2$ (Cases A and A1, Fig. 5) and erosion for $U_T < -2$ (Cases E and E1, Fig. 6). For $U_T = -2$, the transition from erosion to accretion, the depth near the shoreline remains unchanged (Case 0 in Fig. 4). The model performs well in predicting beach erosion and accretion without the need of a criterion to distinguish accretionary and erosional waves as it is required in
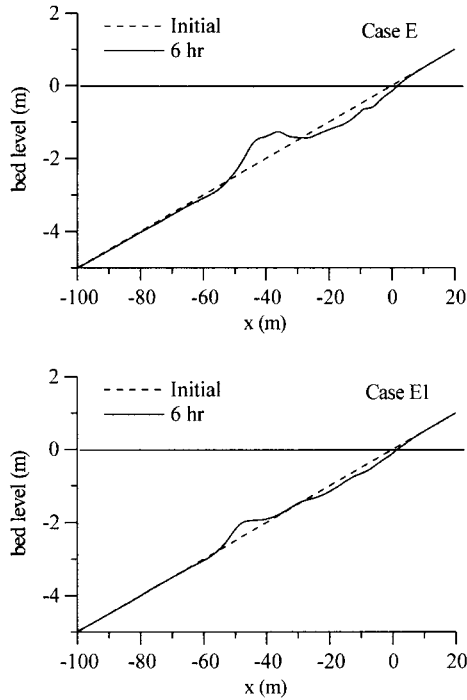
Figure 6. Beach profile change for erosive Cases E and E1 after 6 hours; $H_o = 1.05$, $T = 6.0$ s, $d_{50} = 0.20$ mm, $U_T = -2.50$. Case E1: $H_o = 1.25$, $T = 5.0$ s, $d_{50} = 0.30$ mm, $U_T = -2.50$.

some beach profile models (Larson, 1996, Leont'yev, 1996). The predictions also agree with the Hands et al. (1996) criterion.

Karambas and Koutitas (2002) concluded that the use of the Dibajnia and Watanabe formula provides a model with the ability to reproduce accretion and erosion (this ability is also reported by Dibajnia et al., 2001).

The Delta flume tests, performed at Delft Hydraulics in 1993, are also reproduced (Roelvink and Reniers, 1995). The mean grain size was $d_{50} = 0.2$ mm. Narrow-banded, random waves were chosen such that the wave steepness in combination with the water level were expected to result in a stable, erosive and accretive beach, consecutively. Two tests are reproduced: 1b (highly erosive wave conditions) and 1c (strongly accretive wave conditions). For the 1b test the conditions were: $H_{mo} = 1.4$ m, $T_p = 5$ s, duration 18h, while for the 1c test: $H_{mo} = 0.6$ m, $T_p = 8$ s, duration 13h. The initial beach geometry for the 1b test was the results of the 1a test (the resulting geometry of a Dean-type beach after 12h of the following wave conditions: $H_{mo} = 0.9$ m, $T_p = 5$ s). The initial geometry for the 1c test was the results of the 1b test. In Fig. 7 the comparisons of calculated and measured cross-shore transport rates are shown for tests 1b and 1c. Predicted transport rates in the surf and swash zone agree well with measurements.

Finally, the model is applied to predict the total longshore transport rate due to irregular waves and longshore current. The following computational conditions are assumed: peak wave period of the incident spectrum $T_p = 8$ s, uniform slope $\tan \beta = 1/30$ and deep water incident angle $\theta_s = 25^0$. The volumetric total longshore transport rate Q_y, from the swash zone across the surf zone to deep water, is calculated by the cross-shore integration of q_{ly}. In Fig. 8 the predicted longshore transport
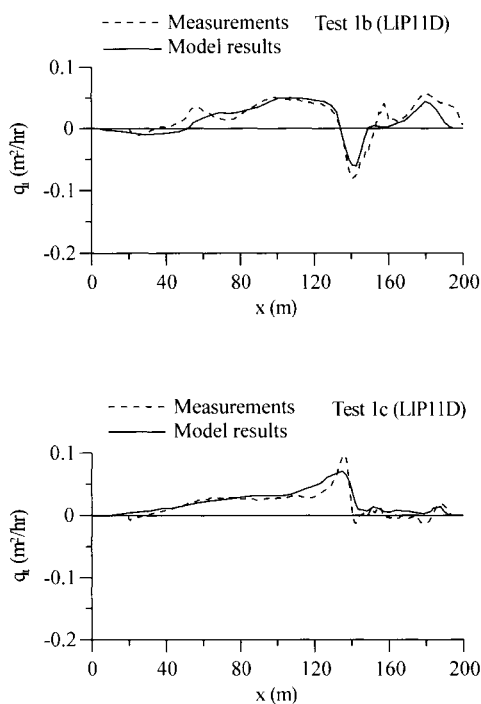
Figure 7. Comparison between calculated and measured cross-shore transport rate for LIP11D tests 1b and 1c.
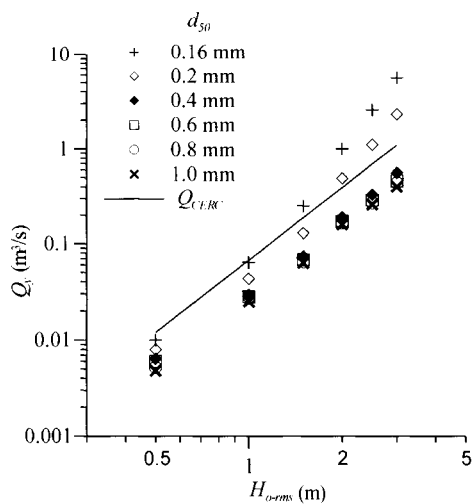
Figure 8. Comparison between calculated longshore transport rate and CERC formula. The numerical prediction is based on the process-based approach.

rates for different grain sizes are plotted against deep water wave height H_{o-rms}. The CERC formula for Q_y, Q_{CERC}, is also shown

$$Q_{CERC} = \frac{1}{(1-\lambda)} \frac{0.7\, E_{fb}\, \cos(\theta_b)\, \sin(\theta_b)}{\rho\, g\, (s-1)} \tag{61}$$

where E_{fb} is the wave energy flux (calculated from the Boussinesq model results on the basis of H_{rms}) and θ_b is the wave angle at the point of breaking.

Assuming that the CERC formula describes the longshore transport fairly well, the mathematical model seems rather sensitive to variation in the incident wave height, especially for small grain sizes. For high activity wave conditions, the model is also sensitive to variation in the small grain size, which does not even enter the basic formulation of the CERC formula. The sediment transport rate might not be very sensitive to modest changes in grain size but since the grain size can vary by one order of magnitude (from 0.16 mm to 1 mm) the grain dependency can be important. The grain size dependence of the longshore transport rate is also justified by field measurements (Del Valle et al., 1993). It was concluded that the values of the proportionality coefficient (which is taken constant and equal to 0.7 in equation (61)) decrease with increasing d_{50}.

3.2. Energetics Approach

Karambas et al. (1995) combined a Boussinesq breaking wave model with the Bailard formula in order to estimate the on-offshore sediment transport rate outside and inside the surf zone. In Karambas (1998) the model was extended in 2DH conditions. The energetics approach is based on Bagnold's original idea that the sediment transport load is proportional to the time-averaging energy dissipation of the stream (Bailard, 1981).

The submerged weight transport rate $\mathbf{i_f} = (i_{fx}, i_{fy})$ is given by Bailard (1981)

$$\mathbf{i_f} = \rho\, C_f \frac{\varepsilon_b}{\tan\phi} \left[|\mathbf{u_{ou}}|^2\, \mathbf{u_{ou}} - \frac{\tan\beta}{\tan\phi} |\mathbf{u_{ou}}|^3\, \widehat{\mathbf{i}} \right] + \rho\, C_f \frac{\varepsilon_s}{w_s} \left[|\mathbf{u_{ou}}|^3\, \mathbf{u_{ou}} - \frac{\varepsilon_s}{w_s} \tan\beta\, |\mathbf{u_{ou}}|^5\, \widehat{\mathbf{i}} \right] \tag{62}$$

where $\mathbf{u_{ou}} = (u_{ou}, v_o)$, in which $u_{ou} = u_{ow} + U_b$, $|\mathbf{u_{ou}}| = \sqrt{u_{ou}^2 + v_o^2}$, C_f is a friction coefficient, $C_f = f_w/2$, ϕ is the angle of internal friction (about 30 degrees), $\tan\beta$ is the local beach slope (the x axis is directed upslope), $\widehat{\mathbf{i}}$ is the unit vector, and ε_b and ε_s are the bed and suspended load efficiency factors respectively.

The above formulation ignores an obvious effect, namely, the additional stirring of sediment by the surface breaking-induced turbulence which penetrates toward the bottom. This additional stirring is simulated adopting the Bailard formula after the consideration that the dissipation mechanism is the wave breaking. As already mentioned we can assume a time-averaged approach for the estimation of the suspended load induced by wave breaking. Thus, the total submerged weight transport rate can be estimated from (Roelvink and Stive, 1989)

$$\mathbf{i_t} = \mathbf{i_f} + \frac{\varepsilon_s\, \rho\, \overline{k}_b^{3/2}\, \overline{\mathbf{u}}_{ou}}{w_s} \tag{63}$$

where k_b is the near bed magnitude of the turbulent kinetic energy k_t (obtained from equation (32)).

Since the present module is based on a nonlinear model, the approach uses the original energetics formula without simplifications concerning the decomposition of the moments, as in most of the previous works based on period-mean approaches. The use of a nonlinear theory to incorporate the effects of the wave asymmetry is also avoided.

According to the original Bagnold estimations (from river data) the bed and suspended load efficiency factors ε_b and ε_s take the values $\varepsilon_b = 0.13$ and $\varepsilon_s = 0.01$. Bailard (1981) first calibrated the energetics approach based on laboratory and field measurements. Least square estimates of ε_b and ε_s resulted in values 0.21 and 0.025 respectively. However, Bailard's value of ε_s had to compensate for increased turbulence due to breaking in the surf zone. Since the breaking wave-induced dissipation has already been incorporated, the values $\varepsilon_s = 0.015$ and $\varepsilon_b = 0.15$ are used.

The total time-averaged volumetric sediment transport rate is given by

$$\overline{q}_t = \frac{\overline{i}_t}{(\rho_s - \rho)\,g\,(1 - \lambda)} \tag{64}$$

The energetics approach is based on the assumption of quasi-steadiness and, hence, the formula is not able to predict 'unsteady effects'. These 'unsteady effects' are caused by a time lag between velocity and concentration, resulting in negative wave-related transport rates and therefore smaller (and, in some cases, negative) total net transport rates than without these effects. Experimental investigations (Janssen and Ribberink, 1996; Bosboom et al., 1997) indicated that Bailard's formula fails to predict correctly the net sediment transport rate in oscillatory sheet flow while the Dibajnia and Watanabe formula gives much better results. Thus, the energetics approach is recommended for use to predict the sediment transport rate in the longshore direction, where the transport rate due to longshore currents is more significant than the longshore transport rate from the direct action of waves.

In Fig. 9 the predicted longshore transport rates based on the energetics approach are plotted against deep water wave height H_{o-rms}. The comparison between model results based on the energetics approach, and the CERC formula shows close agreement. The results are not very sensitive to variations in the wave height and the grain size compared with the results obtained by using the process-based approach. In addition, a linear relation between Q_y and Q_{CERC} is observed.
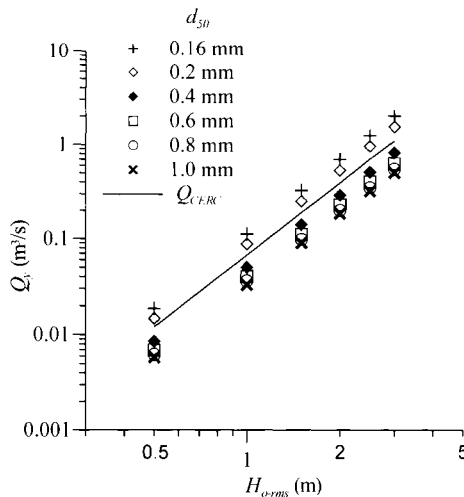
Figure 9. Comparison between calculated longshore transport rate and CERC formula. The numerical prediction is based on the energetics approach.

4. EFFECTS OF INFILTRATION-EXFILTRATION ON CROSS-SHORE SEDIMENT TRANSPORT IN THE SWASH ZONE

The influence of the vertical flow of the water into and out of the porous bed (infiltration-exfiltration, Figs. 10 and 11) on sediment mobility in the swash zone can be taken into consideration in a phase-resolving wave model.

Two mechanisms are expected to be important in altering the uprush and backwash sediment transport: sediment stabilization and boundary layer thinning due to infiltration on the uprush, and sediment destabilization and boundary layer thickening due to exfiltration on the backwash (Butt et al., 2001).

On the uprush, downwards-directed piezometric head gradients (infiltration) will increase the effective weight of sediment (i.e., bed stabilization), thereby decreasing the potential for sediment transport. On the backwash, the upwards-directed piezometric head gradients (exfiltration) may lead to rapid groundwater outflow and hence fluidization. This might considerably increase the sediment transport since the fluidized layer would quickly become entrained by the seaward flow in the backwash. Even if the upwards-directed piezometric head gradients are too small to produce fluidization, this may still increase sediment transport by reducing the effective weight of the sediment (i.e., 'destabilize' the bed). Therefore, the net effect of the stabilization-destabilization process would be to bias the transport in the offshore direction.
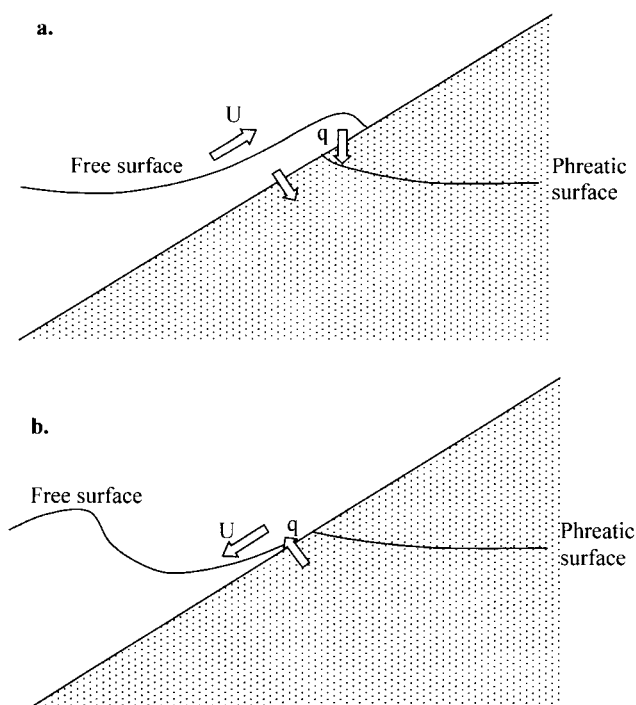
Figure 10. Schematic illustrating hydraulic conditions during: (a) uprush (situation with infiltration), and (b) backwash (situation with exfiltration).
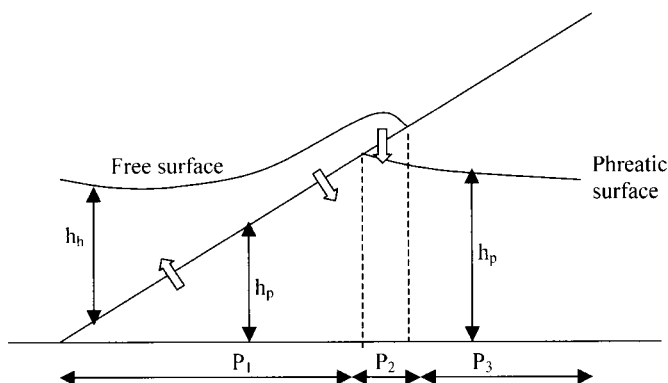
Figure 11. Areas with different treatment for the coupling of the hydraulic model to the porous flow model.

On the other hand the thickness of the boundary layer is reduced by infiltration increasing the potential for sediment transport, and increased by exfiltration decreasing the potential for sediment transport.

The effects of the above processes can be introduced in a simple and well-proven sediment transport formula (different from that used in the previous section) by introducing the effects of the vertical velocity on the Shields parameter (Nielsen, 1997; Turner and Masselink, 1998; Butt et al., 2001). The calculation of the vertical velocity requires the use of a porous flow model which is described in Section 4.1.

4.1. Coupling of a Boussinesq Model to a Porous Flow Model

A combined model with interaction between the external and internal wave motion is developed here. The model is composed in such a way that an external layer of water overlaps a layer of water governed by the equations for porous media flow. The external wave motion causes pressure differences resulting in a flow between the external volume of water and the volume in the permeable bed. Both the volume flux of this exchange and the momentum of this flow are incorporated in the basic equations as source terms.

For the external wave motion two extra terms S_c and S_m are introduced on the right-hand side of the momentum and continuity equations (van Gent, 1994; 1995)

$$S_c = q \qquad \text{in the right-hand side of the continuity equation (3)} \qquad (65)$$

$$S_m = \frac{q\, q_x}{d + \zeta} \qquad \text{in the right-hand side of the momentum equation (3)} \qquad (66)$$

where q (m/s) is the volume flux of the flow between both layers and q_x is the horizontal component of the velocity of this flow which is obtained by assuming that this flow is perpendicular to the slope.

The following long wave equations are used for the porous flow model (van Gent, 1994; 1995)

$$(1 + c_A)\frac{\partial h_p u_p}{\partial t} - c_A u_p \frac{\partial h_p}{\partial t} + \frac{1}{\lambda}\frac{\partial h_p u_p^2}{\partial x} + \lambda g \frac{\partial 1/2 h_p^2}{\partial x} + \lambda g h_p (a u_p + b u_p |u_p|) = -\frac{q\, q_x}{\lambda}$$

$$\frac{\partial h_p}{\partial t} + \frac{1}{\lambda}\frac{\partial h_p u_p}{\partial x} = -\frac{q}{\lambda}$$

$$(67)$$

where h_p is the thickness of the water layer in the porous medium, u_p is the depth-averaged filter/discharge velocity in this layer, a, b are the Forchheimer coefficients, c_A is the coefficient for added mass ($c_A = 0$, Cruz et al., 1997) and λ is the porosity.

For the coupling of the hydraulic model to the porous flow model the internal area of the swash zone is subdivided into three areas with different treatment (Fig. 11).

The part of the porous medium that is overlapped by the hydraulic model is area P_1 in which the thickness of the porous layer h_p is time-independent and consequently $\partial h_p/dt = 0$. In this area (P_1) the term $\lambda g\,\partial(1/2\,h_p^2)/\partial x$ becomes $\lambda g\,\partial(1/2\,(h_h+h_p)^2)/\partial x$, where h_h is the thickness of the hydraulic layer, $h_h = d + \zeta$ (Fig. 11). In area P_2 infiltration q through a partially saturation area appears. In area P_3 there is no infiltration or direct flow from the hydraulic model and consequently $q = 0$.

The calculated downward vertical velocity of the phreatic surface has a maximum. If the maximum would be exceeded, the gradients of the pressure ($I = -1/\rho\,g\,\partial p/\partial z$) would be greater than one. This means that the water would flow quicker than the 'free seepage velocity' which is not possible (Van Gent, 1994; 1995). The upward velocity has a maximum as well. This velocity is of the same order of magnitude as the maximum downward velocity. In the numerical model the maximum vertical velocity $w_{\max}$ is computed from the expression (Van Gent, 1992)

$$|w_{\max}| = -\frac{a}{2b} + \frac{1}{2}\sqrt{\left(\frac{a}{b}\right)^2 + \frac{4}{b}} \tag{68}$$

For w, $\lambda(\partial h_p/\partial t)$ is taken.

In area P_2 the velocity of the infiltrated water is computed using the maximum seepage velocity $w_{\max}$. In area P_3 a different phenomenon, seepage, appears in the case where the phreatic level reaches the slope while no (external) layer of water is present there. If the new phreatic surface appears to be above the slope of the bed, the volume above this boundary is assumed to be the flow outward from the porous bed.

Expressions for a and b can be estimated from

$$a = \alpha_p \frac{(1-\lambda)^2}{\lambda^3}\,\frac{\nu}{g\,d_{50}^2} \quad b = \beta_p \frac{1-\lambda}{\lambda^3}\,\frac{1}{g\,d_{50}} \tag{69}$$

where ν is the kinematic viscosity and α_p and β_p are non-dimensional parameters. For the parameters α_p and β_p, the values $\alpha_p = 180$ (Butt et al., 2001), and $\beta_p = 1.8$ are used.

More details of the coupling are found in Van Gent (1994; 1995) and Karambas (2003).

4.2. Revised Sediment Transport Formula

The influence of swash infiltration-exfiltration on sediment transport is introduced in a simple and well-proven sediment transport formula by using a new modified Shields parameter θ, which is derived after the modification of the shear stress and the immersed sediment weight W (Nielsen, 1997; Turner and Masselink, 1998; Butt et al., 2001).

The non-dimensional sediment transport rate Q is considered proportional to $\theta^{3/2}$ and can be estimated from a slightly modified Meyer-Peter and Müller formula (Meyer-Peter and Müller, 1948;

Ribberink, 1998; Butt et al., 2001; Larson et al., 2001)

$$Q_w = \frac{q_{bw}(1-\lambda)}{\sqrt{(s-1)\,g\,d_{50}^3}} = \frac{C}{1+\dfrac{\tan\beta}{\tan\phi}}\;\theta_w^{3/2}\,\frac{U}{|U|}$$

$$Q_o = \frac{q_{bo}(1-\lambda)}{\sqrt{(s-1)g\,d_{50}^3}} = \frac{C}{1+\dfrac{\tan\beta}{\tan\phi}}\;\theta_o^{3/2}\,\frac{U}{|U|}$$

(70)

where the suffix 'w' means that this parameter contains extra terms to account for through bed flow while the suffix 'o' refers to the case of no through bed flow, C is a multiplier, ϕ is the angle of internal friction (about 30 degrees), $\tan\beta$ is the local beach slope (positive during the uprush phase and negative during the backwash phase) and θ is the Shields parameter

$$\theta_w = \frac{\tau_w}{W_w} \quad \theta_o = \frac{\tau_o}{W_o}$$

(71)

where τ is the bed shear stress and W is the immersed sediment weight per unit volume of the bed, $W = W_o = \rho\,g\,d_{50}(s-1)$.

The multiplier C needs to have different values for uprush and downrush (Hughes et al., 1997; Nielsen, 2002). Masselink and Hughes (1998) show that sediment transport rates for a given $U(t)$ are of the order twice as large during uprush than during downrush. The observed higher transporting efficiency of the uprush is due, in some part, to the presence of pre-suspended sediment from the bore collapse (Puleo et al., 2000). In addition, in Nielsen's (2002) work, it has been shown that part of the different transporting efficiencies can be explained in terms of differences in bed shear stress for a given free stream velocity. That is, in a rapidly accelerating uprush, the same velocity generates a stronger bed shear stress than in a more gradually accelerated downrush. Nevertheless, the calculation procedure based on equation (70) should not be seen as a detailed representation of all physical details of the swash (Nielsen, 2002). Perhaps it is merely a method of getting the right total transport rates in a way consistent with sediment transport calculations in other flow types.

The following values for C, suggested by Nielsen (2002), are used here: $C_{uprush} = 20$ and $C_{downrush} = 9$. The immersed sediment weight W_w is adjusted for infiltration-exfiltration by simply adding the weight loss or gain caused by seepage (Nielsen, 1997)

$$W_w = W_o - 0.5\,\rho\,g\,d_{50}\,\frac{w}{K} = \rho\,g\,d_{50}\,(s-1) - 0.5\,\rho\,g\,d_{50}\,\frac{w}{K}$$

(72)

where w is the vertical velocity in the bed (positive upwards) and K is the hydraulic conductivity (m/s)

$$K = \left(\frac{1}{180}\right)\frac{\lambda^3}{(1-\lambda)^2}\left(\frac{g\,d_{50}^2}{\nu}\right)$$

(73)

Nielsen (1997) assumed a linear relation between shear stress and the relative vertical velocity (w/U), given by equation (1). Turner and Masselink (1998) derived an alternative form for the modified numerator of equation (1). The numerator, unlike Nielsen's, does not assume a linear relation between shear stress and infiltration velocity. The modified shear stress is defined as follows (Turner and Masselink, 1998; Butt et al., 2001)

$$\tau_w = \tau_o\left(\frac{\Phi}{e^\Phi - 1}\right)$$

(74)

where

$$\tau_o = 0.125 \rho f U^2 \tag{75}$$

and

$$\Phi = \frac{2}{f} \frac{w}{|U|} \tag{76}$$

where f is the friction factor.

The friction factor f is estimated using a formula for steady flow, since it is preferred to treat the flow in the swash zone as quasi-steady, and the use of the formula for orbital flow (equation (11)), is considered inappropriate (Butt et al., 2001)

$$f = 1.28 \left(\log \frac{12 h}{K_N} \right)^{-2} \tag{77}$$

To obtain a new (and different from equation (12)) value for K_N, it will be assumed that the bed is approximately flat, and any bedforms are negligible. Ribberink (1998) suggested the following for high Shields numbers

$$K_N = d_{50}[1 + 6(\theta - 1)] \quad \text{for } \theta > 1 \tag{78}$$

In the following numerical experiment the present model is applied to predict sediment transport rates with and without infiltration-exfiltration effects. The wave height is assumed to be $H = 1.8$ m, the wave period $T = 8$ s and the beach slope 1/30. In Figs. 12 and 13 comparisons of the transport with (Q_w) and without (Q_o) infiltration-exfiltration are shown over a single swash cycle at a point in the mid-swash zone. Two different median grain sizes are used: $d_{50} = 0.1$ mm and $d_{50} = 1$ mm. For $d_{50} = 0.1$ mm (Fig. 12) decrease in transport on the uprush and the (smaller) increase in transport on the backwash can clearly be seen. For $d_{50} = 1$ mm (Fig. 13) increase in transport on the uprush and the (smaller) decrease in transport on the backwash are observed.

The difference Q_{inf} between Q_w and Q_o ($Q_{inf} = Q_w - Q_o$) will isolate that part of the dimensionless sediment transport due to infiltration-exfiltration. In order to examine the grain size dependency of the transport due to infiltration-exfiltration the time-averaged $\overline{Q}_{inf}$, is calculated for different values of d_{50} and the same wave conditions (Butt et al., 2001). Fig. 14 shows that the direction of
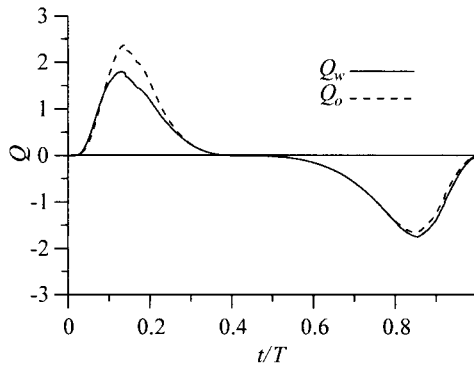
Figure 12. Comparison of sediment transport with (Q_w) and without (Q_o) infiltration-exfiltration, over a single cycle, at a point near the maximum set-up point ($d_{50} = 0.1$ mm).
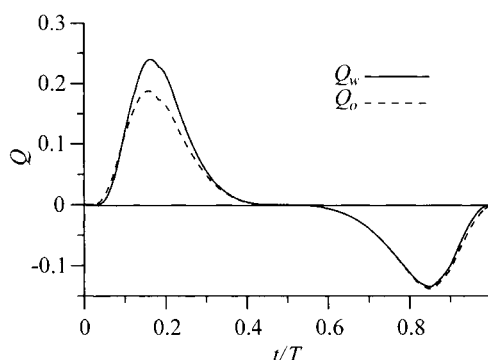
Figure 13. Comparison of sediment transport with (Q_w) and without (Q_o) infiltration-exfiltration, over a single cycle, at a point near the maximum set-up point ($d_{50} = 1$ mm).
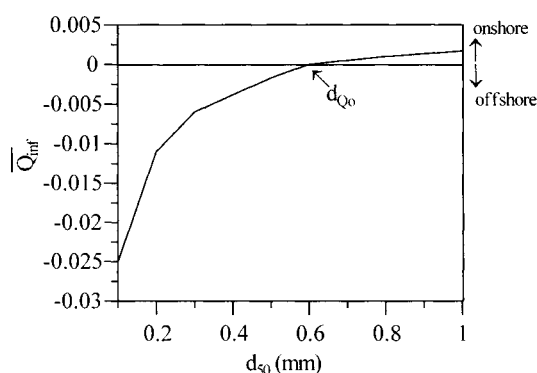
Figure 14. Grain size dependency of the transport due to infiltration (Q_{inf}).

$\overline{Q}_{inf}$ becomes more onshore with increasing grain size. The grain size at which the balance changes (the 'crossover' point d_{Qo}) is at about 0.6 mm. Above it the effects of infiltration-exfiltration change from biasing the transport offshore to onshore, indicating a dominance of stabilization-destabilization to a dominance of boundary layer effects. This is in general accordance with nature where coarser sediments are associated with beaches exhibiting steeper beach face gradients. Nielsen (1997) suggested that boundary layer effects are only likely to dominate at grain sizes above approximately $d_{Qo} = 0.58$ mm which is very close to the present model results. Similar results have been obtained by Butt et al. (2001), based on field measurements of cross-shore and vertical velocities and on a sediment transport formula similar to equation (70). They suggested that the grain size at which the balance changes is roughly $d_{Qo} = 0.55$ mm. Their measurements were conducted at Perranporth Beach (U.K.) with median grain size $d_{50} = 0.24$ mm and significant wave height and period 2.0 m and 8 s, respectively.

However, Turner and Masselink (1998) concluded that the role of infiltration-exfiltration in the swash zone is generally to enhance uprush transport. Their conclusion was derived based on field experiments at Duck (U.S.A.) with moderate grain size $d_{50} = 0.5$ mm. This appears to conflict with the above results (Fig. 14) and the results of Butt et al. (2001), since the grain size is smaller than d_{Qo}. Turner and Masselink used, in their analysis, a constant friction factor $f = 0.01$, instead of equation (77) which has been used by Butt et al. (2001). Butt et al. also concluded that small changes

in the estimation of f might change the direction of the apparent influence of infiltration-exfiltration. This conclusion can also be derived considering the following Nielsen et al. (2001) rule: Infiltration enhances sediment mobility for dense, coarse sediment with $16(s-1) > 0.4(u_*/K)$, and impedes sediment motion for fine, light sediment with $16(s-1) < 0.4(u_*/K)$. The important role of the shear velocity u_* (and consequently of the friction factor f) is clear.

It would, therefore, seem appropriate to use a different formula for the friction factor f and observe the behavior of the present model. Nielsen (2002) used equation (11) (with $K_N = 2.5\,d_{50}$) for orbital flow, instead of equation (77), in order to calculate the friction factor f.

The above numerical experiment is repeated by using equation (11) and adopting $K_N = 2.5\,d_{50}$. The new grain size at which the balance changes, the new 'crossover' point d_{Q_o-N}, is estimated to be about $d_{Q_o-N} = 0.4$ mm. The grain size in Turner and Masselink's field measurements was $d_{50} = 0.5$ mm, which is larger than d_{Q_o-N}, confirming their findings of onshore transport dominance. The grain size in Butt et al. ($d_{50} = 0.24$ mm) was smaller than d_{Q_o-N}, suggesting offshore dominance, which has also been confirmed by their field measurements. Thus, using another formula for the friction factor f, present model results are in agreement with both field measurements.

5. CONCLUSIONS

A nonlinear breaking wave model based on the higher-order Boussinesq-type equations can be combined with a sediment transport and morphology model. The wave model provides the sediment transport module with the required hydrodynamic information such as the bottom velocity, undertow and wave energy dissipation due to breaking.

The (process-based) Dibajnia and Watanabe transport rate formula involving unsteady aspects of the sand transport phenomenon can be adopted for estimating the sheet flow sediment transport rates as well as the bedload and suspended load over ripples. For the calculation of the suspended load induced by wave breaking a time-averaged approach can be adopted.

Swash zone sediment transport can be calculated as in the submerged part, after the assumption that the primary sediment transport mechanism in this zone is the sheet flow.

Model results, in the cross-shore direction, indicate that not only erosion and formation of a bar but also the recession of the shoreline can be reproduced. The applications of the model confirm the criterion proposed by Hands et al. (1996) and Ahrens and Hands (1998) for discriminating between erosive and accretive conditions.

The comparison of longshore transport rates between the present model and the energetics approach and the CERC formula shows close agreement. The process-based approach is more sensitive to variations in the wave height and the grain size.

The importance of the inclusion of a seepage process in the mass of the beach sand is also investigated. By allowing the grain size to vary in the computations, it was found that, above a particular critical grain size, the effects of infiltration-exfiltration change from biasing the transport offshore to onshore. This indicates a shift from a dominance of stabilization-destabilization to a dominance of boundary layer effects.

LIST OF SYMBOLS

A_b —   water particle amplitude of the oscillation
a —   Forchheimer friction coefficient
b —   Forchheimer friction coefficient
B —   dispersion coefficient, $B = 1/15$
c —   wave celerity vector

C	—	time-averaged concentration
c_A	—	coefficient for added mass
C_b	—	bed concentration
C_f	—	friction coefficient, $C_f = f_w/2$
c_l	—	phase speed, specified by the long-wave limit
d	—	still water depth
d_{50}	—	median grain diameter
dx	—	grid spacing
dt	—	time step (wave module)
dt_m	—	time step (morphology module)
D_s	—	magnitude of the source function
$\mathbf{E}$	—	eddy viscosity term, $\mathbf{E}=(E_x, E_y)$
E_{fb}	—	wave energy flux
f	—	friction factor in the swash zone
f_δ	—	roller shape function
f_{cw}	—	wave-current bottom friction factor
f_c	—	current friction factor
f_s	—	source function
f_w	—	wave friction factor
F	—	artificial damping term
g	—	acceleration of gravity
G	—	artificial damping term
H	—	wave height
H_{o-rms}	—	deep water wave height
h_p	—	thickness of the water layer in porous medium
$\mathbf{i_f}$	—	submerged weight transport rate
$\hat{\mathbf{i}}$	—	unit vector
K	—	hydraulic conductivity
K_N	—	bed roughness
k	—	wave number
k_t	—	turbulent kinetic energy induced by wave breaking
k_b	—	near bed magnitude of the turbulent kinetic energy k_t
ℓ_s	—	length scale in the swash zone
ℓ	—	length scale of turbulence in the surf zone
$\mathbf{q_t}$	—	total time-averaged sediment transport rate $\mathbf{q_t} = (q_{tx}, q_{ty})$, q_{tx}, q_{ty} are the transport rates in the directions x and y
$\mathbf{q_b}$	—	bedload transport $\mathbf{q_b} = (q_{bx}, q_{by})$
$\mathbf{q_s}$	—	time-averaged suspended load under broken waves, $\mathbf{q_s} = (q_{sx}, q_{sy})$
PROD	—	production of turbulent energy
Q	—	swash zone non-dimensional sediment transport rate
Q_{CERC}	—	longshore transport rate predicted by the CERC formula
Q_y	—	volumetric total longshore transport rate
q	—	volume flux of the flow between external and media flow layers
q_x	—	horizontal component of q
r	—	relaxation parameter
s	—	specific density of sediment
t	—	time
T	—	wave period
T_c	—	duration of positive portion of the velocity profile

T_t	—	duration of negative portion of the velocity profile
$\mathbf{U}$	—	horizontal velocity vector, $\mathbf{U} = (U, V)$, U, V are the depth-averaged horizontal velocities in the x and y directions
$\mathbf{u_0}$	—	bottom velocity vector, $\mathbf{u_0}(u_o, v_o)$
u_{ow}	—	oscillatory component of the near bottom velocity u_o
u_{ow-max}	—	amplitude of the oscillatory component of the near bottom velocity u_{ow}
$\mathbf{U_c}$	—	current velocity vector $\mathbf{U_c} = (U_c, V_c)$
u_c	—	equivalent root-mean-square velocity amplitudes for the positive (crest) portion of the velocity profile
u_t	—	equivalent root-mean-square velocity amplitudes for the negative (trough) portion of the velocity profile
u_{ou}	—	bottom velocity ($u_{ou} = u_{ow} + U_b$)
u_p	—	depth-averaged filter/discharge velocity in the porous layer
u_{crit}	—	grain threshold speed
u_{max-t}	—	near bed peak orbital wave velocity under the trough
U_{und}	—	undertow velocity
U_b	—	undertow velocity at the bottom
u_*	—	friction velocity
V_{es}	—	external solution for the longshore current
v_{ow}	—	oscillatory component of the near bottom velocity v_o
W	—	immersed sediment weight per unit volume of the bed
w	—	vertical velocity in the bed (positive upwards)
w_{max}	—	maximum vertical velocity in the porous layer
x	—	onshore direction
x_s	—	central location of the source function
y	—	longshore direction
z_b	—	bottom elevation
α_p	—	non-dimensional parameter of the Forchheimer coefficient a
β_p	—	non-dimensional parameter of the Forchheimer coefficient b
β	—	bottom slope
β_s	—	shape coefficient for the source function
δ	—	roller thickness
δ_w	—	wave boundary layer thickness
ε_b	—	bedload efficiency factor
ε_s	—	suspended load efficiency factor
ε_{sb}	—	time-averaged vertical diffusion coefficient
ζ	—	surface elevation
$\overline{\zeta}$	—	mean water level (set-up)
η_r	—	ripple height
θ	—	Shields parameter
θ_b	—	wave angle at the point of breaking
θ_s	—	angle between the propagation direction of the wave and the x-axis
θ_{sheet}	—	critical Shields number for initiation of sheet flow
θ_{cr}	—	critical Shields number for initiation of motion
λ_r	—	ripple length
λ	—	sediment porosity
ν	—	kinematic viscosity
ν_s	—	swash zone eddy viscosity coefficient
ν_{sg}	—	eddy viscosity coefficient due to subgrid turbulence

ν_{tg}	—	eddy viscosity coefficient inside the bottom boundary layer
ν_z	—	instantaneous eddy viscosity coefficient outside the bottom boundary layer
ν_{br}	—	depth-averaged value of $\bar{\nu}_z$
ρ	—	density of water
ρ_s	—	density of sediment
$\boldsymbol{\tau}_b$	—	bottom friction term, $\boldsymbol{\tau}_b = (\tau_{bx}, \tau_{by})$
ϕ	—	angle of internal friction
φ_B	—	maximum non-breaking water surface slope
φ_o	—	terminal slope of lower surface of roller
ψ	—	mobility number
ω	—	radian frequency

REFERENCES

Ahrens, J.P., and Hands, E.B., 1998. Velocity parameters for prediction of cross-shore sediment transport. Journal of Waterway, Port, Coastal, and Ocean Engineering, 124 (1): 16–20.

Bailard, J.A., 1981. An energetics total sediment transport model for a plane sloping beach. Journal of Geophysical Research, 86, (C11): 10,938–10,954.

Bosboom, J., Aarninkhof, S.G.J., Reniers, A.J.H.M., Roelvink, J.A., and Walstra, D.J.R., 1997. Unibest-TC. Overview of Model Formulations. H2305.42, Delft Hydraulics, The Netherlands.

Briad, M-H.G., and Kamphuis, J.W., 1993. Sediment transport in the surf zine: A quasi 3-D numerical model. Coastal Engineering, 20: 135–156.

Brocchini, M., Drago, M., and Iovenitti, L., 1992. The modelling of short waves in shallow waters. Comparison of numerical models based on Boussinesq and Serre equations. Proceedings of the 23rd International Conference on Coastal Engineering, ASCE, pp. 76–89.

Butt, T., Russell, P., and Turner, I., 2001. The influence of swash infiltration-exfiltration on beach face sediment transport: Onshore or offshore? Coastal Engineering, 42: 35–52.

Cruz, E.C., Isobe, M., and Watanabe, A., 1997. Boussinesq equations for wave transformation on porous beds. Coastal Engineering, 30: 125–156.

Deigaard, R., 1989. Mathematical modelling of waves in the surf zone. Prog. Rep. 69: 47–59. ISVA, Technical University of Denmark, Lyngby.

Deigaard, R., Fredsoe, J., and Broker Hedegaard, I., 1986. Suspended sediment in the surf zone. Journal of Waterway, Port, Coastal, and Ocean Engineering, 112 (1): 115–128.

Deigaard, R., Justesen, P., and Fredsoe, J., 1991. Modelling of undertow by one-equation turbulence model. Coastal Engineering, 15: 431–458.

Del Valle, R., Medina, R., and Losada, M.A., 1993. Dependence of coefficient K on grain size. Journal of Waterway, Port, Coastal, and Ocean Engineering, 119 (5): 568–574.

Dibajnia, M., 1995. Sheet flow transport formula extended and applied to horizontal plane problems. Coastal Engineering in Japan, 38 (2): 179–194.

Dibajnia, M., 2002. Personal communication.

Dibajnia, M., Moriya, T., and Watanabe, A., 2001. A representative wave model for estimation of nearshore local transport rate. Coastal Engineering, 43 (1): 1–38.

Dibajnia, M., and Watanabe, A., 1992. Sheet flow under nonlinear waves and currents. Proceedings of the 23rd International Conference on Coastal Engineering, ASCE, pp. 2015–2028.

Dibajnia, M., and Watanabe, A., 1996. A transport rate formula for mixed sands. Proceedings of the 25th International Conference on Coastal Engineering, ASCE, pp. 3791–3804.

Dibajnia, M., and Watanabe, A., 1998. Transport rate under irregular sheet flow conditions. Coastal Engineering, 35: 167–183.

Dingemans, M.W., 1997. Water wave propagation over uneven bottoms: 2. Non-linear wave propagation. Advanced Series on Ocean Engineering, Vol. 13. Singapore: World Scientific Publishing Co.

Hands, E.B., Ahrens, J.P., and Resio, D.T., 1996. Predicting large-scale, cross-shore sediment movement from orbital speeds. Proceedings of the 25th International Conference on Coastal Engineering, ASCE, pp. 3379–3390.

Horikawa, K., 1988. Nearshore Dynamics and Coastal Processes. Tokyo: University Tokyo Press, 522p.

Hughes, M.G., Masselink, G., and Brander, R.W., 1997. Flow velocity and sediment transport in the swash zone of a steep beach. Marine Geology, 138: 91–103.

Janssen, C.M., and Ribberink, J.S., 1996. Grain-size influence on sand transport in oscillatory sheet flow. Proceedings of the 25th International Conference on Coastal Engineering, ASCE, pp. 4779–4792.

Jonsson, I.G., 1966. Wave boundary layers and friction factors. Proceedings of the 10th International Conference on Coastal Engineering, ASCE, pp. 127–148.

Jonsson, I.G., and Carlsen, N.A., 1976. Experimental and theoretical investigations in an oscillatory turbulent boundary layer. Journal of Hydraulics Research, 14 (1): 45–60.

Karambas, Th.V., 1996. Nonlinear wave energy modelling in the surf zone. Nonlinear Processes in Geophysics, 3: 127–134.

Karambas, Th.V., 1998. 2DH nonlinear dispersive wave modelling and sediment transport in the nearshore zone. Proceedings of the 26th International Conference on Coastal Engineering, ASCE, pp. 2940–2953.

Karambas, Th.V., 1999. A unified model for periodic nonlinear dispersive wave in intermediate and shallow water. Journal of Coastal Research, 15 (1): 128–139.

Karambas, Th.V., 2003. Modelling of infiltration-exfiltration effects of cross-shore sediment transport in the swash zone. Coastal Engineering Journal, March 2003 (in press).

Karambas, Th.V., and Koutitas, C., 2002. Surf and swash zone morphology evolution induced by nonlinear waves. Journal of Waterway, Port, Coastal, and Ocean Engineering, 128 (3): 102–113.

Karambas, Th.V., Southgate, H.N., and Koutitas, C., 1995. A Boussinesq model for inshore zone sediment transport using an energetics approach. Coastal Dynamics '95, pp. 841–849.

Katopodi, I., and Ribberink, J.S., 1992. Quasi-3D modelling of suspended sediment transport by currents and waves. Coastal Engineering, 18: 83–110.

Kim, T., and Wang, H., 1996. Numerical modeling of nearshore morphological changes under a current-wave field. Proceedings of the 25th International Conference on Coastal Engineering, ASCE, pp. 3830–3845.

Larson, M., 1996. Model of beach profile change under random waves. Journal of Waterway, Port, Coastal, and Ocean Engineering, 122 (4): 172–181.

Larson, M., Kubota, S., and Erikson, L., 2001. A model of sediment transport and profile evolution in the swash zone. Coastal Dynamics '01, ASCE, pp. 908–917.

Leont'yev, I.O., 1996. Numerical modelling of beach erosion during storm event. Coastal Engineering, 29: 187–200.

Madsen, P.A., and Schäffer, H.A., 1998. Higher-order Boussinesq-type equations for surface gravity waves: Derivation and analysis. Philosophical Transactions of the Royal Society London, 356: 3123–3184.

Madsen, P., Sorensen, O., and Schäffer, H., 1997. Surf zone dynamics simulated by a Boussinesq type model. Part I. Model description and cross-shore motion of regular waves. Coastal Engineering, 32: 255–287.

Martinsen, E.A., and Engedahl, H., 1987. Implementation and testing of a lateral boundary scheme as an open boundary condition in a barotropic ocean model. Coastal Engineering, 11: 603–627.

Masselink, G., and Hughes, M.G., 1998. Field investigation of sediment transport in the swash zone. Continental Shelf Research, 18: 1179–1199.

Meyer-Peter, E., and Müller, R., 1948. Formulas for bedload transport. Proceedings of the 2nd Congress of the International Association for Hydraulics Structures Research, Stockholm, Sweden.

Nielsen, P., 1992. Coastal Bottom Boundary Layers and Sediment Transport. Advanced Series on Ocean Engineering, Vol. 4. Singapore: Word Scientific Publishing Co., 324p.

Nielsen, P., 1997. Coastal groundwater dynamics. Proceedings, Coastal Dynamics '97, ASCE, pp. 546–555.

Nielsen, P., 2002. Shear stress and sediment transport calculations for swash zone modeling. Coastal Engineering, 45: 53–60.

Nielsen, P., Robert, S., Moeller-Christiansen, B., and Oliva, P., 2001. Infiltration effects on sediment mobility under waves. Coastal Engineering, 42 (2): 105–114.

Puleo, J.A., Beach, R.A., Holman, R.A., and Allen, J.S., 2000. Swash zone sediment suspension and transport and the importance of bore generated turbulence. Journal of Geophysical Research, 105 (C7): 17,021–17,044.

Putrevu, U., and Svendsen, I.A., 1993. Vertical structure of the undertow outside the surf zone. Journal of Geophysical Research, 98 (C12): 22,707–22,716.

Rakha, K.A., 1998. A Quasi-3D phase-resolving hydrodynamic and sediment transport model. Coastal Engineering, 34: 277–311.

Rakha, K.A., Deigaard, R., and Broker I., 1997. A phase-resolving cross shore transport model for beach evolution. Coastal Engineering, 31: 231–261.

Ribberink, J.S., 1998. Bedload transport for steady flows and unsteady oscillatory flows. Coastal Engineering, 34: 59–82.

Roelvink, J.A., and Reniers, A.J.H.M., 1995. LIP 11D Delta Flume experiments. Delft Hydraulics, Delta, Data Report H 2130. Delft, The Netherlands: Delft Hydraulics.

Roelvink, J.A., and Stive, M.J.F., 1989. Bar-generating cross-shore flow mechanics on a beach. Journal of Geophysical Research, 94 (C4): 4785–4800.

Sawaragi, T., 1995. Coastal Engineering—Waves, Beaches, Wave-Structure Interactions. Amsterdam, The Netherlands: Elsevier Science, 479p.

Schäffer, H.A., Madsen, P.A., and Deigaard, R., 1993. A Boussinesq model for waves breaking in shallow water. Coastal Engineering, 20: 185–202.

Smith, G., Mocke, G., and Engelbrecht, L., 1995. Sediment transport fluxes as determined from wave breaker induced suspended sediment and flow fields. In: Dally, W.R., and Zeidler, R.B. (Editors), Coastal Dynamic '95, pp. 783–794.

Sobey, R.J., 1993. Conservation properties of the mild slope and Boussinesq equations. Waves '93, pp. 135–149.

Sørensen, O.R., Schäffer, H.A., and Madsen, P.A., 1998. Surf zone dynamics simulated by a Boussinesq type model. Part III. Wave-induced horizontal nearshore circulations. Coastal Engineering, 33: 155–176.

Staub, C., Jonsson, I.G., and Svendsen, I.A., 1996. Sediment suspension in oscillatory flow: Measurements of instantaneous concentration at high shear. Coastal Engineering, 27: 67–96.

Steetzel, H.J., 1993. Cross-shore sediment transport during storm surges. Ph.D. Thesis. Delft, The Netherlands: Technical University.

Svendsen, I.A., 1984. Wave heights and setup in a surf zone. Coastal Engineering, 8: 303–329.

Turner, I.L., and Masselink, G., 1998. Swash infiltration-exfiltration and sediment transport. Journal of Geophysical Research, 103: 30,813–30,824.

Van Gent, M.R.A., 1992. The coupling of a hydraulic model to a porous flow model. MAST-G6S Report. Delft, The Netherlands: Technical University, 85p.

Van Gent, M.R.A., 1994. The modeling of wave action on and in coastal structures. Coastal Engineering, 22: 311–339.

Van Gent, M.R.A., 1995. Wave Interaction with Permeable Coastal Structures. Ph.D. Thesis. Delft, The Netherlands: Delft University of Technology.

Veeramony, J., and Svendsen, I.A., 2000. The flow in surf-zone waves. Coastal Engineering, 39: 93–122.

Watanabe, A., and Dibajnia, M., 1996. Mathematical models for waves and beach profiles in surf and swash zones. Proceedings of the 25th International Conference on Coastal Engineering, ASCE, pp. 3105–3114.

Wei, G., and Kirby, T., 1995. Time-dependent numerical code for extended Boussinesq equations. Journal of Waterway, Port, Coastal, and Ocean Engineering, 121 (5): 251–261.

Wei, G., Kirby, J.T., and Sinha, A., 1999. Generation of waves in Boussinesq models using a source function method. Coastal Engineering, 36: 271–299.

Zelt, J.A., 1991. The runup of nonbreaking and breaking solitary waves. Coastal Engineering, 15: 205–246.

Zou, Z.L., 1999. Higher order Boussinesq equations. Ocean Engineering, 26: 767–792.

Chapter 11

Modeling the Morphological Response in a Coastal Zone for Different Temporal Scales

Igor O. Leont'yev

Russian Academy of Sciences, P.P. Shirshov Institute of Oceanology, Nakhimov Prospect, 36, Moscow 117851, Russian Federation

1. GENERAL PROPERTIES AND BEHAVIOR OF A NEARSHORE MORPHODYNAMIC SYSTEM

A coastal region may be regarded as a morphodynamic system consisting of a number of interrelated elements and possessing a series of inherent properties (Cowell and Thom, 1995). Coastal evolution is a result of several morphodynamic processes of different temporal and spatial scales with consequent adjustments to bottom topography by waves and currents that generate sediment movement over the underlying sea bed. Changes in bed relief, in turn, interact with waves and currents, thereby further affecting variations in sediment transport, and eventually changes to bed morphology.

Therefore, the morphodynamic system represents a chain of interactions (waves—currents—sediment transport—bed relief) with a feedback, which may be either positive or negative. Negative feedback is a mechanism that acts against departure from a given state. It is a stabilizing mechanism causing an auto-regulation of the system and maintaining its equilibrium. In contrast, positive feedback causes the self-forcing process of the morphodynamic processes. This mechanism is responsible for an auto-organization of the system as it approaches the limit of some threshold conditions, and then reaches a new equilibrium state.

Coastal evolution is a cumulative process requiring morphological data from a preceding state that serves as input for the next step of its evolution. Nonlinearity is an important property of morphodynamic systems. "Non-linearity means that the act of playing the game has a way of changing the rules ... Morphological changes in coastal evolution therefore cannot be explained simply by studying the inputs individually, since morphodynamic processes themselves vary according to the antecedent system state" (Cowell and Thom, 1995, p. 52).

The state-dependent behavior of the coastal system is accompanied by stochastic variation in external inputs, therefore, coastal evolution may be treated as a Markovian process. The morphological state of any given evolutionary stage of the coast is only one state in a set of possible states. The determination of a new state depends on the stochastic input data that are characterized by a given probability distribution. Even if the initial external forcing conditions are cyclic, the coastal system does not necessarily return to its initial state. It shows that the process of coastal evolution may be characterized by hysteresis of a complex nonlinear system.

The response of bed morphology to variations in forcing conditions is not instantaneous. A period of time is required to set in motion and redistribute the sediment volumes. In other words, a time lag exists relative to external impacts, and a relaxation time is necessary to attain a new quasi-equilibrium state of the system. Relaxation time depends on the dimensions of the sediment body and on the rate of morphological changes.

Coastal evolution modeling can be successful only if the modeling procedure reproduces the main properties of the morphodynamic system. A number of recent models already satisfy this requirement

to some extent. These models describe the feedback chains including nonlinearity, hysteresis, the dependence of the results on consecutive preceding states, and bed topography tending toward a certain equilibrium state. However, the challenge is to incorporate Markovian inheritance, as most models are essentially deterministic.

Morphodynamic processes are characterized by different temporal scales. Practical applications focus on morphological changes due to storm events (short-term or event scale), and on coastal evolution over several years or decades (long-term or engineering scale). In the event-scale, the storm impact results in coastal or shoreline deformations, which can be smoothed during the next storm event. In the engineering scale, the general trend in morphological response is examined over time spans coinciding with a designed period of life for coastal structures installed in the study area (De Vriend, 1997). In addition, the instantaneous and the geological scales of the morphodynamic evolution are selected. The first of these refers to a time scale of process such as bed ripples formation (tens of wave periods) while the second one involves the coastal evolution spanning millennia. However, the present analysis considers only the first two temporal scales.

The modeling procedures describing short-term and long-term coastal evolution vary essentially because of the differences in the main mechanisms controlling the related morphodynamic processes. Waves and wave-driven currents induce the deformations of a bed profile, or a coastline during a storm. By contrast, over decades the perturbations due to single storm events look like high frequency oscillations around a long-term mean trend. This trend depends on factors which are almost invisible at small temporal scales. For instance, a gradual change in a bottom slope, a variation of the mean sea level or a variation in the wave climate does not influence the sediment transport during a single storm event. These phenomena determine the morphological evolution in a long-term sense.

The quantitative basis of the majority of morphodynamic models is the continuity (or mass conservation) equation for sediment transport given in the following form

$$\frac{\partial d}{\partial t} = \frac{\partial q_x}{\partial x} + \frac{\partial q_y}{\partial y} \tag{1}$$

where d is the water depth measured from the level at rest, t denotes time, q_x and q_y are the cross-shore and longshore volumetric sediment fluxes (per unit width in the direction normal to the sediment flux component), and the coordinate axes OX and OY are shore normal and shore parallel respectively. In equation (1), temporal changes in the local depths are determined by spatial gradients of the sediment flux. The contribution of the cross-shore (q_x) and longshore (q_y) components depends, among others, on the choice of the temporal scale of the considered process. For instance, the long-term evolution of a coastal zone with groin-type structures is mainly influenced by gradients of the longshore sediment flux. By contrast, the shoreline displacement and evolution of a coastal profile during a storm event depends mainly on the gradients of the cross-shore sediment transport flux.

The first part of the presented analysis is dedicated to models describing short-term storm-induced deformations of nearshore morphology, and is followed by modeling of long-term coastal evolution.

2. MODELING A SHORT-TERM MORPHOLOGICAL RESPONSE TO EXTERNAL FORCING OF GOVERNING EQUATIONS

2.1. Composition of the Morphodynamic Model

In order to integrate equation (1) the depth at a given time step has to be calculated. This depth can serve as initial input data for the next step of calculations. From a mathematical viewpoint, the system of differential equations describing the bed evolution of the coastal system is to a large extent a hyperbolic one, in which the information propagates along with the sediment transport (De Vriend
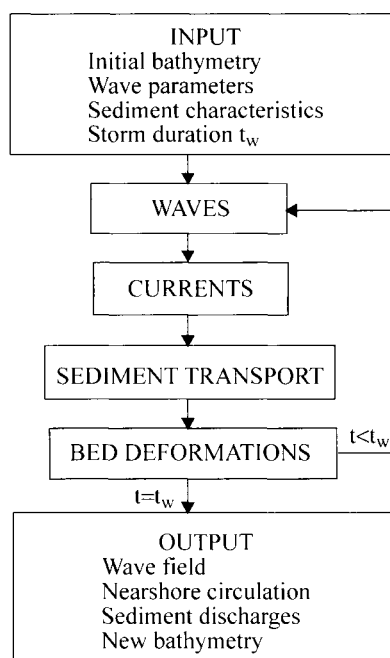
Figure 1. Structure of the process-based morphodynamic model.

et al., 1993b). At each boundary of the model domain the morphological and transport conditions should be specified.

A typical structure for the process-based morphodynamic model is depicted in Fig. 1. It consists of several linked modules describing the constituents of the individual processes responsible for the evolution in coastal morphology. In the model, the following input data have been specified:

1. initial water depths taken from a bathymetric record of the study area,
2. wave parameters at the boundary (wave height, wave period, angle of wave incidence),
3. sediment characteristics (density, porosity, mean size),
4. duration of the storm event, and
5. the mean water level (changes in position of the water surface due to storm surge, tide or another dynamical factor).

At each time step, wave shoaling, refraction and energy dissipation are computed. Calculations of wave diffraction induced by existing structures may also be included in the calculation. Then, characteristics of storm-driven horizontal currents and near bed mass transport are computed, and finally the sediment transport rates and new water depths are predicted by solving equation (1). If the actual time t is less than the given storm duration t_w, then the described numerical procedure is repeated for a next time step using the new water depths (Fig. 1).

The governing equations (energy, momentum and mass balance) are solved numerically using a finite-difference scheme with a spatial grid covering the entire nearshore area (Fig. 2). Cell dimensions depend on the required resolution for the bottom relief and usually they are in the order of $10^0 - 10^2$ m.
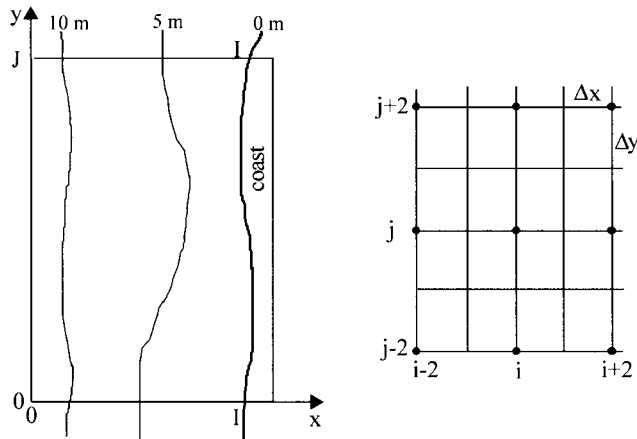
Figure 2. Spatial grid used for calculations.

The predicted sediment balance equation (1) is integrated using the Lax-Wendroff numerical scheme where each morphological time step n splits into two iterations. At first, an intermediate depth file is defined corresponding to a temporal level $n + 1/2$

$$d_{ij}^{n+1/2} = \frac{1}{2} d_{ij}^n + \frac{1}{4}\left(d_{i+1,j}^n + d_{i,j+1}^n\right) + \frac{1}{2}\frac{\Delta t}{\Delta x}\left(q_{xi+1,j}^n - q_{xi,j}^n\right) + \frac{1}{2}\frac{\Delta t}{\Delta y}\left(q_{yi,j+1}^n - q_{yi,j}^n\right)$$

(2)

At the next iteration the respective sediment discharges are computed for the level $n + 1/2$ and then the depth file for the step $n + 1$ is calculated

$$d_{i+1,j+1}^{n+1} = d_{i+1,j+1}^n + \frac{\Delta t}{\Delta x}\left(q_{xi+1,j+1}^{n+1/2} - q_{xi,j+1}^{n+1/2}\right) + \frac{\Delta t}{\Delta y}\left(q_{yi+1,j+1}^{n+1/2} - q_{yi+1,j}^{n+1/2}\right)$$

(3)

Such a scheme provides a high stability for the numerical procedure even for locally uneven bottom topographies. The depth, d_{0j}, is given by the boundary condition. If the outer boundary of the model domain is located outside of the active sediment motion area, the depth, d_{0j}, is considered constant during the entire calculation. In a typical case, noticeable deformations of a sandy coastal slope during a storm are concentrated over the area of depths not exceeding approximately five incident wave heights. Based on investigations by Leont'yev (2001) the length of the time step Δt is estimated as

$$\frac{\Delta t}{T} < \frac{10}{\beta^2}\sqrt{\frac{d_s}{H_{rms0}}}$$

(4)

where β is the mean beach slope, d_s is the mean diameter of sediment grain, H_{rms0} and T are the deep water root-mean square wave height and spectral peak period. For gentle slopes $10^{-3} - 10^{-2}$ the magnitude of Δt is of the order of $(10^1 - 10^2)\,T$, while in the case of a steep beach it may by close to the value of the wave period T.

In the calculation procedure, the local bed slope may reach or exceed the threshold value β' limiting the slope stability, causing avalanching. The way to model such a situation was suggested by Larson and Kraus (1989) and Leont'yev (1996).

2.2. Sediment Transport Module

The sediment transport module is the main element in a morphodynamic model. A reliable assessment of the morphological response of the bed to wave and current forcing is possible with adequately parameterized sediment discharges q_x and q_y.

Numerous studies concentrate on sediment transport modeling. In the present analysis, three major groups were selected. The first group of models involves a series of elementary physical processes that are thought to be responsible for sediment motion in a fluid flow. In most advanced models of this kind sediment discharges are obtained from complicated calculations of the detailed structure of the mean flow including turbulence and related sediment concentrations in the water column (Fredsøe et al., 1985; Brøker et al., 1991; Briand and Kamphuis, 1993).

In the second group of models the transport mechanisms are represented in a more highly integrated form. Typically, the concept of these models relies on the energetic approach (Bagnold, 1963; Bailard, 1981; Roelvink and Stive, 1989; Ohnaka and Watanabe, 1990; Roelvink and Brøker, 1993; Leont'yev, 1999; 2001).

The third group of models applies the equilibrium concept of the coastal profile. Herein, transporting mechanisms are not considered at all, and sediment discharges are assumed to depend on the deviation of the current bed profile from its equilibrium shape. According to Kriebel and Dean (1985) and Larson and Kraus (1989), the cross-shore sediment transport rates are proportional to the difference between the energy dissipation rate over the current bed profile when compared to those over the corresponding equilibrium profile.

The choice of the modeling approach depends on the problem to be solved. A higher level of parameterization implies more detail and should provide more accurate results describing the studied process. However, inaccuracies existing in each parameter tend to accumulate when integrating them into the model. Therefore, the advantages of a more complicated representation could be lost. Thus, a compromise is always necessary between the level of parameterization and the possible reliability of model predictions. An important issue is also the computational efficiency of a model required in practical applications.

An example of such a compromise is shown using Leont'yev's (1996; 1999; 2001) results. The presented analysis uses the energetic approach, and so refers to the second group of models presented above.

Two sediment transport rates are estimated in the nearshore region (Fig. 3): the rate q_W generated by the action of wave and currents induced by wave shoaling and breaking in the surf zone, and the rate q_R due to runup in the swash zone. The limit separating the swash and surf zones X_W, as shown in Fig. 3, is set at a water depth equal to the incident root mean square wave height H_{sms0} for the irregular waves considered in the model. The coordinates, X_C and X_R, are the position of the coastline and of the upper limit of runup, respectively. Symbols X_B and d_B in Fig. 3 designate the breakpoint position and corresponding breaking depth, respectively. The general expressions for sediment transport rates are given by

$$
q_x, q_y = \begin{cases} q_{Wx}, q_{Wy}, & x < X_W \\ q_{Wx} + q_{Rx}, q_{Wy} + q_{Ry}, & X_W \leqslant x \leqslant X_C \\ q_{Rx}, q_{Ry}, & X_C \leqslant x \leqslant X_R \end{cases} \tag{5}
$$
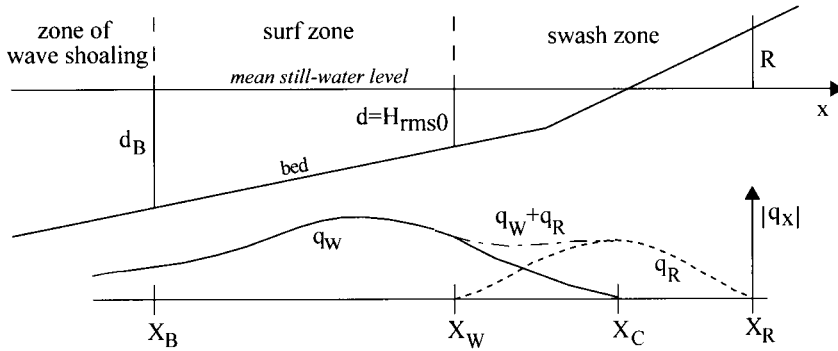
Figure 3. Scheme of the nearshore zone.

in which

$$
q_W = \begin{cases} q_W^0 - 2s\sqrt{q_{Wx}^0{}^2 + q_{Wy}^0{}^2} & x \leqslant X_W \\[2mm] q_W(X_W)\left[\dfrac{x - X_W}{X_C - X_W}\right]^{1.5} & X_W \leqslant x \leqslant X_C \end{cases}
\tag{6}
$$

and

$$
q_R = \begin{cases} \hat{q}_R\left[\dfrac{x - X_W}{X_C - X_W}\right]^{0.5} & X_W \leqslant x \leqslant X_C \\[2mm] \hat{q}_R\left[\dfrac{X_R - x}{X_R - X_C}\right] & X_C \leqslant x \leqslant X_R \end{cases}
\tag{7}
$$

where $q_W = (q_{Wx}, q_{Wy})$, $q_R = (q_{Rx}, q_{Ry})$, and $s = (s_x, s_y)$.

The quantities q_{Wx}^0 and q_{Wy}^0 are the cross-shore and longshore sediment discharges over a horizontal bed (with slopes $s_x = -\partial d/\partial x$ and $s_y = -\partial d/\partial y$ equal to zero), and

$$
q_{Wx}^0 = GU, \qquad q_{Wy}^0 = GV
\tag{8}
$$

Here G denotes the immersed weight of sediment grains per unit area

$$
G = \frac{9\pi}{8}\,\frac{\varepsilon_b}{\tan\Phi}\,\frac{F}{u_m} + \frac{\varepsilon_s}{W_s}\,(4F + B)
\tag{9}
$$

where ε_b and ε_s are the bedload and suspended load efficiency factors, $\tan\Phi$ is the grain-to-grain friction coefficient, W_s is the fall velocity, u_m is the horizontal orbital wave velocity amplitude at the bed, and F and B are the dissipation rates due to bed friction and near bed turbulence generated by breakers, respectively.

The mean flow velocity near the bed (at the edge of wave boundary layer) U and V include the contribution of the wave-induced boundary layer mass transport velocity (U_W^B, V_W^B), the horizontal circulation velocity components (U_C^B, V_C^B), and additional currents such as those generated by wind (U_{wind}^B, V_{wind}^B)

$$
U = U_W^B + U_C^B + U_C^B + U_{wind}^B, \qquad V = V_W^B + V_C^B + V_{wind}^B
\tag{10}
$$

The near bed mass transport velocities are given by the following set of equations

$$\left(U_W^B, V_W^B\right) = \alpha \, \frac{D^* - D}{D^*} \, \frac{u_m^2}{C} \, (\cos\Theta, \sin\Theta) \tag{11}$$

where

$$D = -\frac{\partial}{\partial x}\left(EC_g\right), \qquad D^* = \frac{EC_g \cos\Theta}{X}, \qquad E = \frac{1}{8}\rho\, g\, H_{\text{rms}}^2 \tag{12}$$

$$\alpha = \begin{cases} 1, & \Psi \geqslant 0.5 \\ -0.2, & \Psi < 0.5 \end{cases} \tag{13}$$

In equations (11) and (12), D is the energy dissipation rate due to wave breaking and D^* is a threshold value that may induce reversal of transport from positive to negative (due to the influence of undertow). E is the wave energy, C and C_g are the wave phase and group wave velocities, $X = X_C - x$ is the distance from the shoreline to a given location, Θ is the angle of wave incidence, ρ is the water density and g is the gravity constant. The coefficient α depends on the bed roughness and is negative for a rippled bed (for small values of the Shields parameter Ψ). In the absence of dissipation ($D \to 0$) over a non-rippled bed ($\Psi > 0.5$), equation (11) is the well-known expression given by Longuet-Higgins (1953).

The bottom velocities of the wave-driven horizontal circulation U_C^B, V_C^B are calculated using the depth-averaged momentum and mass balance equations, and by using these values in an assumed logarithmic velocity profile.

The onshore steady wind creates shear stress, which is balanced by a pressure gradient due to the mean sea level rise η. Consequently, the mean flow directed offshore is generated in the lower part of the water column. The near bed velocity of this flow can be estimated by the following expression (Leont'yev, 2001)

$$U_{\text{wind}}^B \cong -0.0007 \, \frac{W^2}{\sqrt{g\,(d + \eta)}} \, \cos\Theta_{\text{wind}} \tag{14}$$

where W is the wind speed, and Θ_{wind} is the angle of the wind direction with the shore normal. Under certain weather conditions, the velocity U_{wind}^B may be comparable with wave and current induced contributions to the total cross-shore transport velocity. By contrast, the longshore component of the wind-driven depth-averaged velocity is of order $0.01\, W\sqrt{\sin\Theta_{\text{wind}}}$ and it is usually small when compared with the wave-generated longshore current.

The model also takes into account the wave set-up ζ and so the total local depth is actually considered as a sum $d + \eta + \zeta$.

The maximal cross-shore and longshore sediment discharges in the swash zone ($\hat{q}_{Rx}$ and $\hat{q}_{Ry}$ in equation (7)) are expressed by

$$\hat{q}_{Rx} = K_R\,\rho\,u_R^3\left(\beta_{eq} - \beta\right), \qquad \hat{q}_{Ry} = 0.1\,K_R\,\rho\,u_R^2\,\frac{R}{T}\,\frac{\tan\Theta_W}{\beta} \tag{15}$$

where K_R and u_R are the scaling coefficient and the amplitude of the runup flow defined as follows

$$K_R = 0.5 \cdot 10^{-7}\,\frac{T\sqrt{g\,H_{\text{rms0}}}}{d_s}, \qquad u_R = \sqrt{2\,g\,R}, \qquad R = \beta\sqrt{H_{s0}\,L_0}, \tag{16}$$

Θ_W is the angle of wave incidence measured at $x = X_W$ (Fig. 3), R is the height of runup estimated from Hunt's (1959) formula, and H_{s0} and L_0 are the deep water significant wave height and wavelength, respectively. The actual and equilibrium beach slopes β and β_{eq} are defined by

$$\beta = \frac{H_{rms0} + R}{X_R - X_W}, \qquad \beta_{eq} = 0.15 \sqrt{\frac{W_s T}{H_{rms0}}} \tag{17}$$

where β_{eq} was established by Kriebel et al. (1991).

The volumetric sediment discharges used in equation (1) are obtained by dividing q_x and q_y (equations (5)–(17)) by $g(\rho_s - \rho)(1 - \sigma)$, where ρ_s and σ denote the density and porosity of the sediment, respectively.

2.3. Coastal Profile Modeling

Modeling of short-term changes in a coastal profile requires an additional assumption about the longshore uniformity ($\partial/\partial y = 0$), that simplifies the calculation. In particular, in such a case the horizontal component of nearshore circulation equals zero, or it transforms into a uniform longshore current. Different aspects of the profile modeling were discussed in detail by Nairn and Southgate (1993). Herein, several predictions of the evolution of the coastal profile are presented using the model described above.

Predictions are compared with laboratory data. Sediment properties (mean diameter d_s, fall velocity W_s) and wave conditions (rms height H_{rms0}, spectral peak period T and duration of wave action t_w) in these experiments are given in Table 1. Incident water depths are in the approximate range of 0.5 to 5 m.

The observed and predicted profiles are shown in Figs. 4, 5 and 6 with distributions of cross-shore sediment discharges for the initial and final stages of profile evolution. The test numbers in Table 1, and the profile numbers in Figs. 4, 5 and 6 are identical.

Fig. 4 presents the evolution of bed profiles from various initial shapes. In the process of wave action all initially different profiles tend to be similar, with nearly uniform shape. In both observation and prediction, the nearshore section of the bed profile is represented by a concave curve. In the offshore part, the profile is convex with a bar formed in cases 1 and 3. Predictions and observations show an overall agreement; however, the model does not reproduce the bar in case 3. This is the most visible discrepancy, which is not manifested in the other cases and is difficult to explain.

Table 1
Laboratory test conditions.

No.	Reference	d_s (mm)	W_s (m/s)	H_{rms0} (m)	T (s)	t_w (h)
1	Roelvink and Stive, 1989	0.10	0.008	0.123	2.0	12
2	Brøker et al., 1992	0.22	0.027	1.1	6.0	6.3
3	Larson, 1994	0.22	0.027	0.57	3.0	6.7
4	Larson, 1994	0.22	0.027	0.49	3.0	0.8
5	Uliczka, 1987	0.22	0.027	1.1	6.0	3.5
6	Uliczka, 1987	0.33	0.044	1.1	6.0	3.5
7	Karmabas et al., 1997	0.10	0.010	0.085	1.55	7.5
8	Rakha and Kamphuis, 1995	0.12	0.012	0.057	1.15	12
9	Wu et al., 1994	0.22	0.027	0.85	10.0	10.5
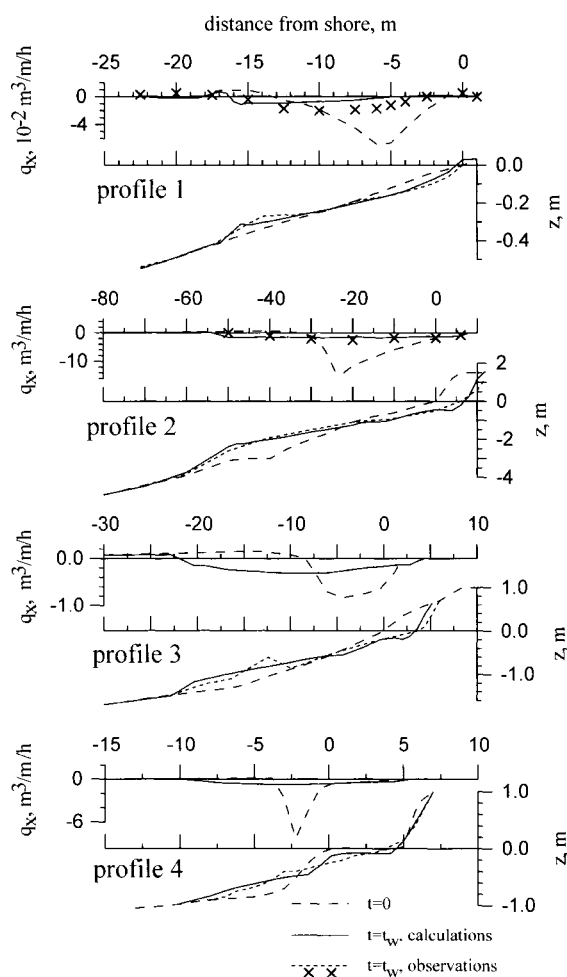
Figure 4. Cross-shore sediment transport rates and changes in beach profiles as observed in the laboratory tests and obtained from calculations. Test conditions are given in Table 1.

In the early stages of the experiments, the peak of sediment transport is located near the boundary of the swash zone. At the final stage of profile evolution, the sediment discharges decrease significantly when compared with initial values, and the overall distributions become nearly uniform.

Prototype-scale tests 5 and 6 illustrated in Fig. 5, simulate the erosion of dunes during a storm for a relatively gentle (a) and very steep (b) beach profile. In both cases, a wide terrace is formed in front of the dune foot, resulting in a gradual decay of coastal recession due to a weakening wave impact on the beach. The sediment discharge is at a maximum in the swash zone (more than 50 m³/m/h). In the initial stage of the experiment, transport decreases rapidly, and its peak is displaced from the shore.

In test 6 (Fig. 5b) waves are reflected from the steeply sloping bed ($s = 0.25$). Reflection is not included in the model. However, agreement of predictions and observations indicate that reflection is of secondary importance in profile deformation. In principle, standing waves induced by the reflection
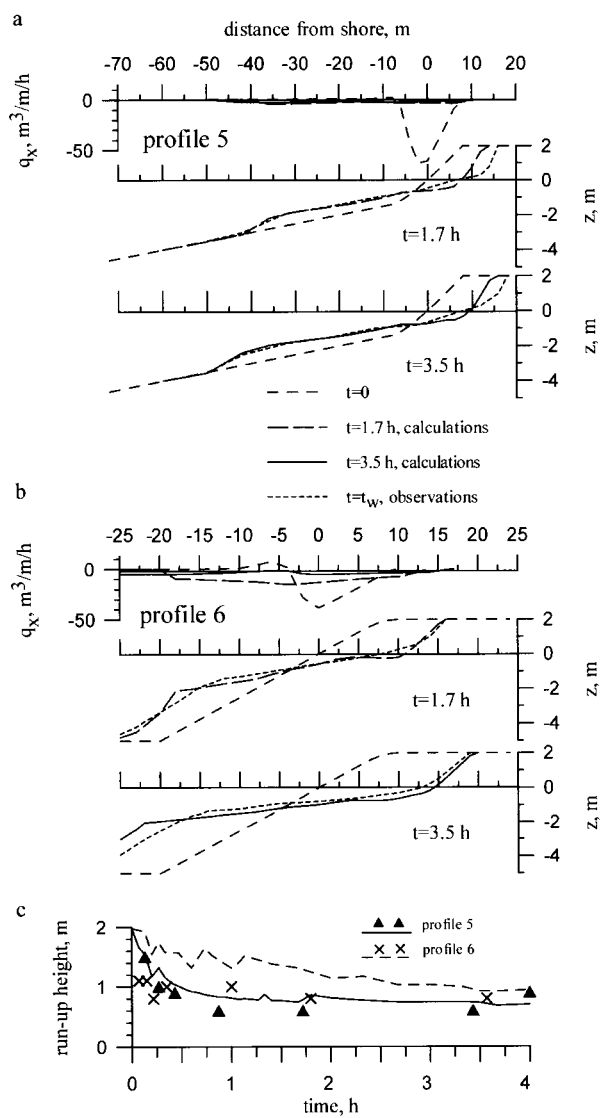
Figure 5. Erosion of dunes with gentle (a), and steep foreshore (b), and also temporal changes in the runup height during a wave attack (c). Test conditions are given in Table 1.

can change the cross-shore transport distribution, as those tend to create the alternating convergence and divergence in the near bed mean flow. This influence is most visible if the waves are reflected from the vertical wall without breaking. But in the case considered the energy dissipation effect is significant, and seems to be a central factor controlling the sediment transport regime.

Fig. 5c shows how the runup heights R vary during the evolution of profiles 5 and 6. Both the observed and computed values decrease.

In Fig. 6a, the results of tests are depicted, in which the Shields parameter was relatively small (approximately 0.3–0.4), and therefore, well-developed bed ripples could be formed during the ex-
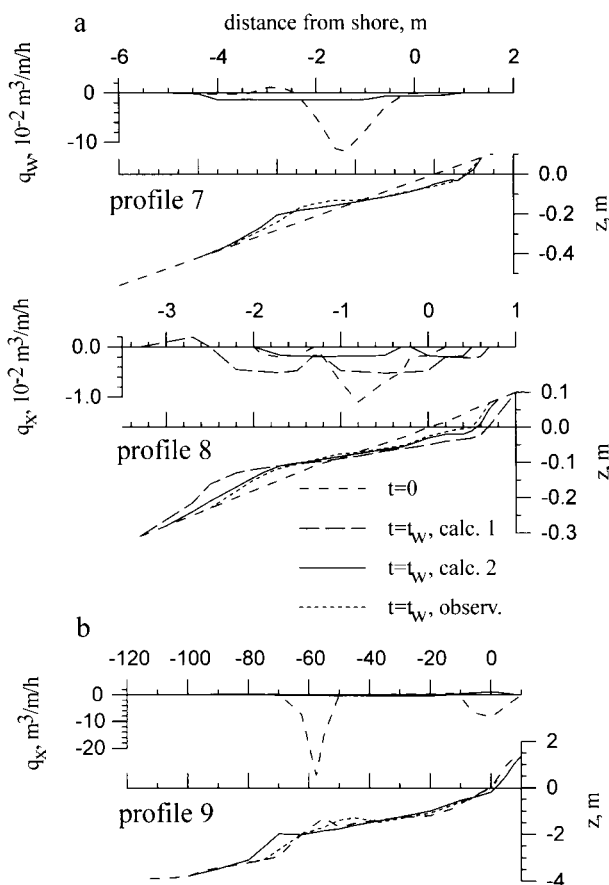
Figure 6. Cross-shore sediment transport rates and changes in beach profiles under conditions of small Shields parameter magnitudes (a), and in the case of long-period swell (b). Test conditions are given in Table 1.

periment. Consequently, the ripples affect the mass transport velocity at the bed and the related morphodynamic processes. The latter is shown for profile 8, where calculations 1 and 2 were performed without and with the effect of ripples, respectively. In the first case, the predicted bed deformation is overestimated, while calculation 2 provides more realistic results. In the model, the presence of ripples in the offshore portion of the profile also affects the sediment transport in the swash zone as shown in the distribution of sediment discharges over the profile 8 (see Fig. 6).

Test 9 simulates the action of long period swell, and the resulting bed profile evolution in Fig. 6b shows accretion. The initial bed profile includes a bar, which is smoothed during the experiment and displaced toward the shoreline. The model, however, predicts erosion of the bar associated with offshore sand movement. The calculations reproduce correctly part of the bed profile and its stability. In the final stages of the calculation, a quasi-equilibrium bed profile is obtained with an almost zero sediment discharge over the entire underwater beach.

When modeling evolution of natural coastal profiles, one should take into consideration changes in mean sea level and in wave parameters over the period of observations. In addition, the morpho-

310
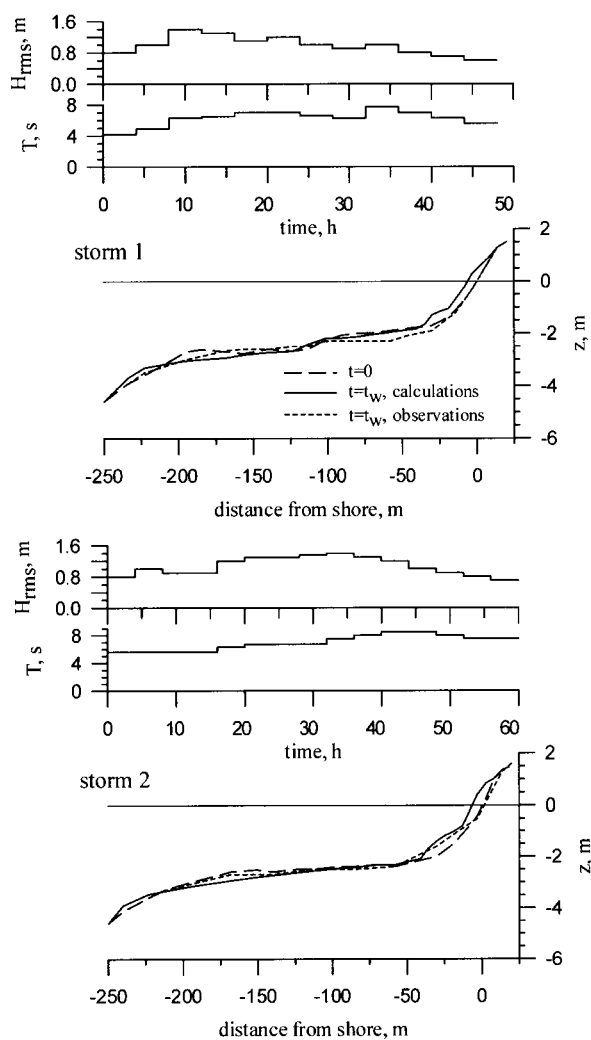
Figure 7. Observed and computed changes in coastal profile at Kamchya (Bulgarian coast of the Black Sea) caused by successive storm event 1 and 2. Data from Antsyferov et al. (1990).

dynamics in the natural environment are also influenced by non-uniformity of bed relief along the shore and changes in sediment properties over the coastal slope.

Fig. 7 shows morphological changes induced by two successive storm events on a coastal profile located on the Bulgarian coast of the Black Sea (site Kamchya, Antsyferov et al., 1990). The time history of these storms is also depicted in Fig. 7. In the calculation, the duration of the storm was divided into 4-hour intervals, with constant wave conditions. The grain diameter of 0.4 mm was taken into account for the whole length of the profile.

Observed changes in both bed profiles are insignificant. The model reproduces correctly the observed bed deformation. The model does not predict the erosion observed near the shoreline during
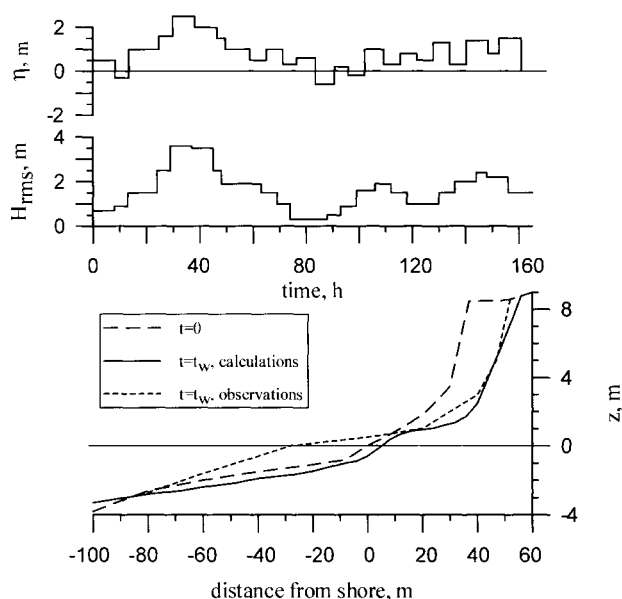
Figure 8. Beach erosion during a storm on the Island of Sylt (the North Sea). Data from Newe and Dette (1995).

the first storm. By contrast, the model reproduces sand accumulation at the foot of the beach observed during the second storm.

Fig. 8 presents erosion of a coastal dune at the island of Sylt (North Sea) induced by an extreme storm event accompanied by a large storm surge (observed in the autumn of 1985). The data used in Fig. 8 are from the work by Newe and Dette (1995). Temporal changes in the mean sea level η and in wave heights documented during the storm are shown in the upper panels of Fig. 8. The storm surge superimposed on the tidal elevation reached a maximum of 2.7 m above the mean water level. In the calculations, the mean water level was averaged during 4–8-hour intervals. In the calculation, wave periods varied in the interval of 6–9 s and the mean sand diameter was taken to be equal to 0.35 mm.

Comparisons presented in Fig. 8 show that the model reproduces correctly the actual recession of the dune. Computed and observed erosion volumes are nearly equal. According to observations the eroded material accumulates near the dune foot. However, the model predicts the deposition in the deeper area, and this trend is in agreement with the test data shown in Figs. 5 and 6. Such a discrepancy in the given case may be due to the process of beach restoration after a storm under the action of weak swell and tidal currents.

Fig. 9 represents the evolution of the beach profile at Duck situated on the Atlantic coast of the United States in response to moderate storm conditions (Larson and Kraus, 1989). The storm surge is superimposed on the tidal elevation (amplitude of about 1 m). As in the former calculation, the mean water level oscillations were simulated by a succession of time steps shown in the upper panels of Fig. 9.

The mean sand diameter observed over the major part of the bed profile is about 0.16 mm. Near the shoreline the mean diameter increases to 0.4–0.5 mm. To prove the influence of the non-uniform grain size distribution, the predictions are shown for both a uniform sediment distribution (0.16 mm), and for a case where the coarser sediment (0.4 mm) is taken into account in the swash zone. The results of the calculations are different for both cases. In the first case, the predicted beach slope is
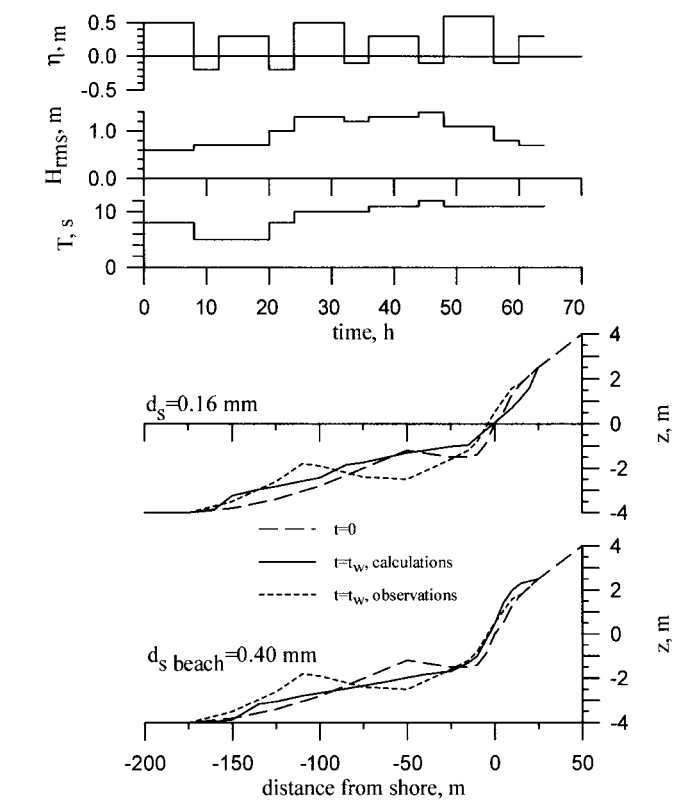
Figure 9. Deformations of beach profile during a storm at Duck (Atlantic coast, USA). Calculations were performed with uniform grain size 0.16 mm over the whole profile and increased to 0.4 mm grain size on a beach.

underestimated, while in the second case, the nearshore section of the profile is in close agreement with observations. The model does not reproduce the evolution of the longshore bar during the storm.

Several models explain the formation of the nearshore bar. Bars are shown to be formed by edge waves (Bowen and Inman, 1971; Holman and Bowen, 1982; Bowen and Huntley, 1984) or by groups of short-waves (O'Hare and Huntley, 1994). Long period waves reflected from the beach induce standing oscillations (surf beats) which create alternating zones of flow convergence or divergence over the bed and the generation of a bar crest or a bar trough.

Another model considers nonlinear properties of shallow water waves (Boczar-Karakiewicz and Davidson-Arnott, 1987; Boczar-Karakiewicz et al., 1987; Chapalain and Boczar-Karakiewicz, 1992; Boczar-Karakiewicz et al., 1995; 1998; Romanczyk et al., 1999). Spatial changes in wave asymmetry can result in variations of sediment discharges accompanied by accretion or erosion in a certain length-scale pattern. Calculations predict decreasing distances between bar crests when moving in the onshore direction. The predicted trend is in agreement with field data.

The "classical" concept explains the formation of bars by breaking waves (Larson and Kraus, 1989). The offshore-directed sediment flux decays, and the deposited material forms an accretionary sediment body. The latter mechanism of bar growth is applied in the majority of morphodynamic models (including the model discussed here). According to this mechanism, a multiple-bar system may be formed by a series of typical storms with wave breaking at various distances from the shore-

line, or during a storm, when waves break at several locations simultaneously. The latter situation is observed on gently sloping beaches.

Zhang and Sunamura (1994) described a multiple-bar system with a series of eddies generated by breaking waves. The distribution of evolving eddies in a wave tank experiment was observed to be determined by incident wave conditions and by the geometry of the bed profile. Eddies interact with the flux of suspended sediments and they enhance the undertow. Somewhat farther down-slope, the undertow velocity sharply decays and a suspended cloud of sediment is deposited causing the growth of an accretionary body. In the laboratory tests, three bars were formed simultaneously. These bars, however, were much lower than observed bars located at the breakpoint.

2.4. Equilibrium Profile

Results presented show that waves rework the coastal profile, and eventually form an equilibrium profile. Results of extensive field observations (Bruun, 1954) suggested a following approximation for the equilibrium profile

$$d = A X^{2/3} \tag{18}$$

where $X = X_C - x$ is the distance from the shoreline, and A is a shape parameter on the order of $0.1 \text{ m}^{1/3}$. Using field data, Kriebel et al. (1991) also showed that the parameter A depends on the sediment fall velocity W_s

$$A = 2.25 \left(\frac{W_s^2}{g} \right)^{1/3} \tag{19}$$

Dean (1991) proposed a hypothesis that the equilibrium profile is a response to a uniform rate of wave energy dissipation per unit volume, therefore

$$\frac{D}{d} = \text{const} \tag{20}$$

Dean's ideas were further developed by Creed et al. (1992), Gonzalez et al. (1997), and also by Kraus (2001). In the study by Gonzalez et al. (1997), the effect of wave refraction was shown to result in steeping of the bed profile in sheltered bays and inlets.

Longuinov (1963) proposed a concept of the bed equilibrium profile resulting from a uniform wave energy flux per unit volume over the wave breaking region. This concept is described by a constant ratio

$$\frac{E}{d} = \text{const} \tag{21}$$

An alternative equilibrium profile concept is based on mass conservation (equation (1)). The criterion of profile stability ($\partial d / \partial t = 0$ in equation (1)) is equivalent to zero sediment discharge gradients over the whole nearshore zone ($\partial q_x / \partial x = \partial q_y / \partial y = 0$). The condition $\partial q_x / \partial x = 0$, in turn, implies the disappearance of cross-shore discharges over the whole bed profile, therefore

$$q_x = 0 \tag{22}$$

The models using equation (22) were proposed by Bowen (1980), Leont'yev (1985), and Creed et al. (1992).

Considering the transport concept given by equations (5)–(8), and assuming the absence of wind and horizontal circulation, the cross-shore discharge outside of the swash zone equals $q_x = G U_W^B$.

In order to satisfy equation (22), the mass transport velocity at the bed, U_W^B, equals zero. In such a case we have from equation (11)

$$D = D^* \quad \text{or} \quad -\frac{d}{dx}\left(EC_g\right) = \frac{EC_g}{X_C - x} \tag{23}$$

(the angle Θ of wave incidence is assumed to equal zero), and

$$\frac{EC_g}{(EC_g)_B} = \frac{X_C - x}{X_C - X_B} \tag{24}$$

where the index B refers to the breakpoint location (Fig. 3). Using both the shallow water approximation, $C_g \cong \sqrt{gd}$, and the hypothesis of Longuinov (equation (21)) we have

$$\frac{d}{d_B} = \left(\frac{X}{l_{br}}\right)^{2/3} \quad \text{or} \quad d = A X^{2/3}, \quad A = d_B^{1/3} s_{eq}^{2/3} \tag{25}$$

where $X = X_C - x$ is the distance from shore, $l_{br} = X_C - X_B$ is the surf zone width and $s_{eq} = d_B/l_{br}$ is the mean slope of the equilibrium profile in the surf zone. The obtained equation (25) is identical with the equilibrium profile equation (equation (18)) proposed by Bruun.

In Fig. 10 the equilibrium profile described by equation (25) (or equation (18)) is compared with profile 1. Herein, the successive stages of evolution of profile 1 are shown (computations are based on data from Table 1). After stabilization ($t > 6$ hours), the form of the observed profile within the dissipation region (nearshore section) is very close to the predicted equilibrium profile.

The mean surf zone equilibrium slope, s_{eq}, in equation (25) can be estimated using the previously defined parameter A (equation (19)). This yields

$$s_{eq} = 3.38 \frac{W_s}{\sqrt{g\, d_B}} \tag{26}$$

Using the result given by equation (26), for a case of wave height $H_{rms} = 1$ m, the mean slope, s_{eq}, for a 0.22 mm sand diameter equals 0.018, while for a diameter of 0.33 mm s_{eq} increases to 0.029.

An estimate of a temporal scale of profile stabilization is proposed by Leont'yev (2001). It is assumed that the stabilization time, t_{eq}, is given by a time in which the value of maximal sediment
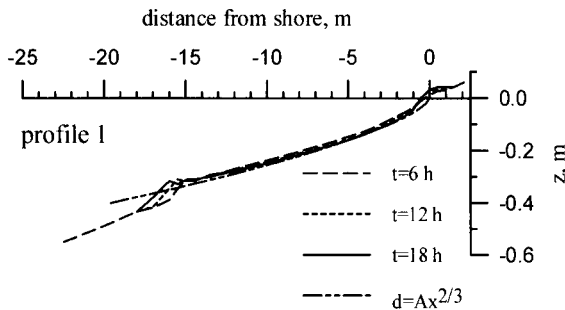
Figure 10. Comparison of equilibrium profile described by equation(25) with typical coastal profile at different stages of its evolution. Calculations are based on data for profile 1 (see Table 1).

discharge decreases by one order of magnitude. Based on experimental data from Larson and Kraus (1989), Leont'yev (2001) proposes the value of t_{eq} to be given by

$$t_{eq} \approx 500 \left(\frac{d_s \, l_{br}}{g^2 \, T} \right)^{1/3} \tag{27}$$

where t_{eq} is measured in hours, and the surf zone width l_{br} is defined for the initial profile (using any breaking criterion). The stabilization time obtained from equation (27) for the data presented for profiles 1–9 (see Table 1) varies from 6 to 12 hours. For profiles in Kamchya (Fig. 8) and in Duck (Fig. 9), t_{eq} is about 20 and 14 hours respectively. All these values are comparable with duration of the storms observed at these sites.

2.5. Modeling the Evolution of a Coastal Area in Three Spatial Dimensions

In the last decade, several coastal area (3-D) models were developed by the Danish Hydraulic Institute (DHI) (Brøker, 1995), by Delft Hydraulics (DH) (Roelvink et al., 1995), by the University of Liverpool (UL), by HR Wallingford (HR) (Price et al., 1995), by Florida University (Wang et al., 1992), and by the Moscow Institute of Oceanology (IO) (Leont'yev, 1999; 2001). The general scheme of these models is similar (see Fig. 1) with different components. For example, the DHI model contains a rather complicated sediment transport description that takes into account almost instantaneous (intra-wave period) changes in sediment concentration (Brøker et al., 1991). In the UL model an empirical transport description is used, and HR and IO models are based on Bagnold's energetic concept.

To save computational time, the calculations of the wave-driven horizontal circulation are usually performed with a relatively long time step, which is at least one order larger than the morphological time step. (The order of magnitude of the latter quantity may be estimated from the empirical relationship expressed by equation (4)). At intermediate stages of the calculation, a "continuity correction" for the mean flow velocities is applied assuming the conservation of total water discharge (De Vriend et al., 1993b). As the waves are almost insensitive to small changes in the bed, the sediment transport on the morphological time scale is a function of the local depth. Using this property, Roelvink et al. (2001) proposed a method of calculation leading to a significant reduction of simulation time.

Comparisons of three-dimensional (3-D) coastal morphological models carried out by De Vriend et al. (1993b) and Nicholson et al. (1997) showed the capability of these models to reproduce the observed trends of morphological changes, at least in a qualitative sense. It was also shown that the simulated two-dimensional bottom topography also tends to equilibrium. However, this process takes much more time to simulate than the case of a one-dimensional coastal profile. Additional computational time is needed to adjust the neighboring bed profiles.

It should be noted that experimental verification of a 3-D coastal model against available field data is still quite limited. A lack of relevant data is due to difficulties in carrying out accurate depth measurements over a period of time over an entire nearshore area.

An example given below illustrates the application of the IO model (Leont'yev, 1999; 2001) to a stretch of sandy beach at a Baltic Sea site (Lubyatowo, Poland) with a system of multiple longshore bars. Depth contours in the modeling domain are depicted in the upper panel of Fig. 11. The mean sand diameter in the Lubyatowo region is about 0.2 mm. The input data used in the model were obtained from measurements carried out during the field experiment "Lubyatowo'76" (Gizhevsky et al., 1978).

Within the period of observations, three successive storm events were observed (see the time histories presented in Fig. 11). During the first and second storm, waves arrived from two opposite directions, namely from the West and from the East, respectively. The duration of both storms was
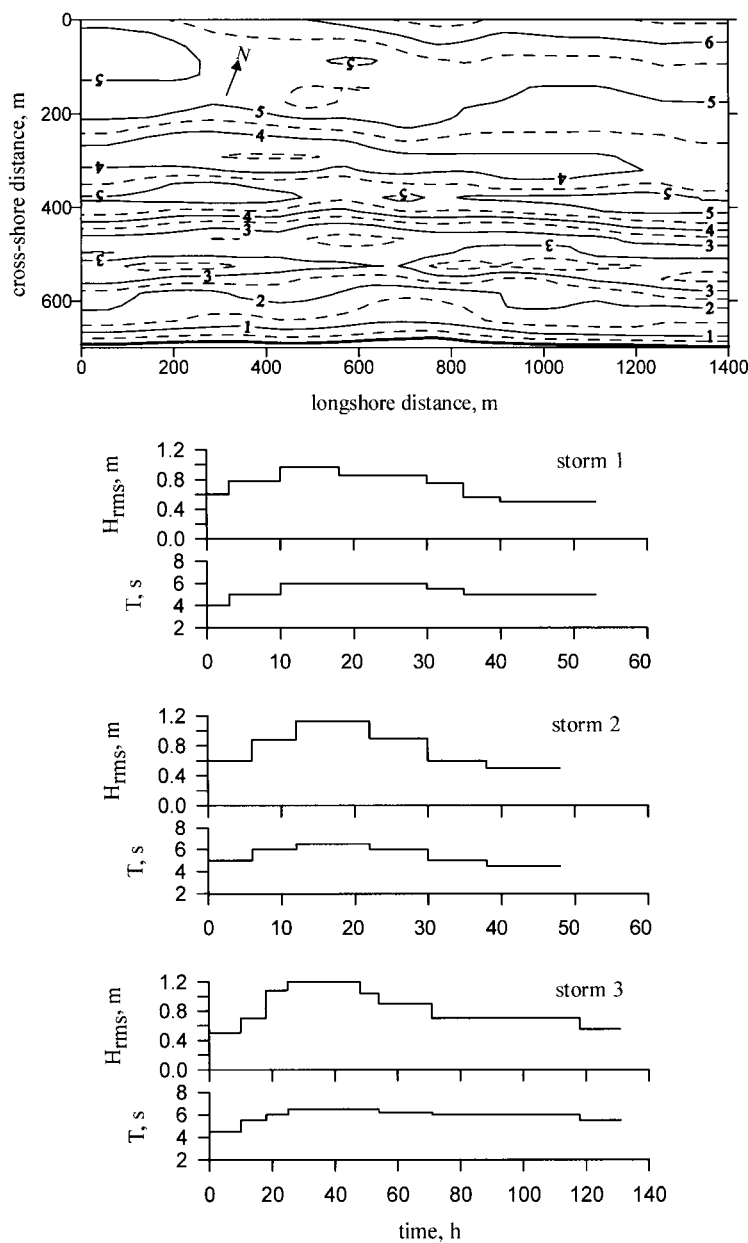
Figure 11. Bottom contours at Lubyatowo (the Baltic Sea) and history of successive storm events registered in the autumn of 1976. Data from Gizhevsky et al. (1978).

about 2 days, with a maximal H_{rms} wave height that did not exceed 1 m. The strongest third storm arrived from the north-west and lasted almost a week. Waves higher than 1 m were observed during 30 hours. Observed changes in the sea level did not exceed 0.3 m.

Prior to the field experiment and after each storm event, the bathymetry in the experimental zone was measured along several chosen profiles by using an echo sounder. The amplitudes of observed bed deformations Δz_b measured before and after the storm indicated either accretion (if $\Delta z_b > 0$) or erosion ($\Delta z_b < 0$). Deformation distributions obtained for each storm are presented in Fig. 12, where the numbers indicate mean amplitudes of bed deformations in meters. Within area sections that are white, deformation amplitudes are less than 0.1 m. Measurements near the shoreline were not available. The positions of two large longshore bars are also shown in Fig. 12.

Fig. 13 represents the results of simulations for each successive storm. The initial bed topography for the first calculation is depicted in Fig. 11. The final topography served as input to the second simulation and so on. A value of 0.01 m is taken as the minimum mean level of computed deformations. Referring to the area of a cell in the spatial grid (7×14 m^2) used in the simulation, the mean level corresponds to a change in sediment volume of about 1 m^3.

In Figs. 12 and 13, it can be seen that the computed and observed deformations are of the same order of magnitude. Significant changes in the initial water depths occur near the shore and over the second bar located closest to the shoreline. Maximal bed deformations are caused by the third storm.

In both observed and computed patterns of bed deformations the zones of accretion and erosion alternate in the cross-shore direction. The observed and computed locations of these zones sometime coincide, but in some cases they evidently disagree. For instance, predicted changes in longshore bars consist mainly of erosion of the crests, and accretion of the area between the crests and troughs. The measurements, however, only partly confirm the predicted trends. Within a trough situated between two bars, calculations predict accretion alternating with erosion over some sections of the bed, and this behavior is in agreement with observations. It may be mentioned that computed bed changes are underestimated in the outer part of the nearshore region, where mechanisms not accounted for in the model may play an important role in the erosion or accretion of the sea bed.

The interest in 3-D coastal models is due to their capacities to predict morphological changes in areas with coastal structures, and to estimate the morphological response to beach nourishment. The effects of groins and breakwaters were studied in the European program MAST (Brøker, 1995; Brøker et al., 1995; Roelvink et al., 1995). The influence of coastal structures was also discussed by Leont'yev (1999; 2001). Morphological changes in a region of shoreface nourishment were simulated recently by Johnson et al. (2001).

Fig. 14 presents measured morphological changes near a groin. The bathymetry data were obtained from a laboratory test by Badiei et al. (1994). In the experiment, the initially planar sandy beach (bed slope $= 0.1$, sand diameter $= 0.12$ mm) was exposed to obliquely incident irregular waves ($H_{rms} = 0.057$ m, $T = 1.15$ s, $\Theta = -10^0$). A groin was installed after a period of 4 hours of wave action when a typical quasi-stable coastal profile was formed (concave near the shore and convex in the outer section; see for example profile 7 or 8 in Fig. 6). A quasi-stable state of the profile was also indicated by stabilization of the longshore sediment discharge. The final bottom contours observed after 12-hours of wave action are shown in Fig. 14a (in a smoothed form to simplify the comparison). The results of computations based on the IO model are shown in Fig. 14b which represents the evolution of bottom topography at three successive stages of wave action. In the numerical test the Shields parameter was low ($\Psi < 0.4$) allowing the formation of well-developed sand ripples. The effect of ripples was taken into account in the sediment transport calculation (see equations (11) and (13)).

The model predictions slightly exaggerate the updrift accretion and an associated scour at the groin head that occurs in the downdrift area. However, the observed and predicted displacements of the shoreline show a satisfactory agreement. At the updrift side of the structure, the shoreline advances, and it retreats at the down-stream side of the groin. After 12 hours in the experiment, the bottom topography tended to a quasi-stable state (Badiei et al., 1994).

318
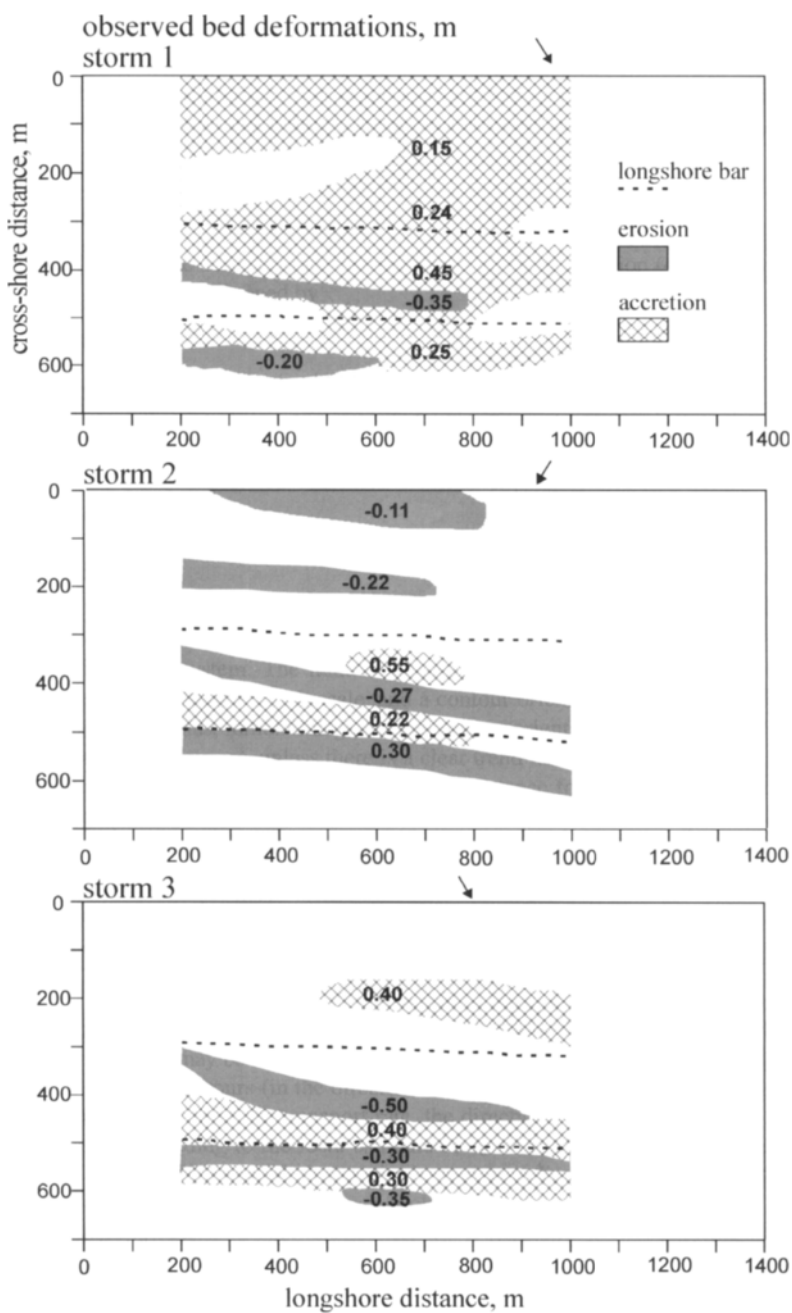
Figure 12. Bed deformations observed after each storm event at Lubyatowo. Averaged magnitudes are given in meters.

computed bed deformations, m

storm 1

storm 2

storm 3

longshore distance, m
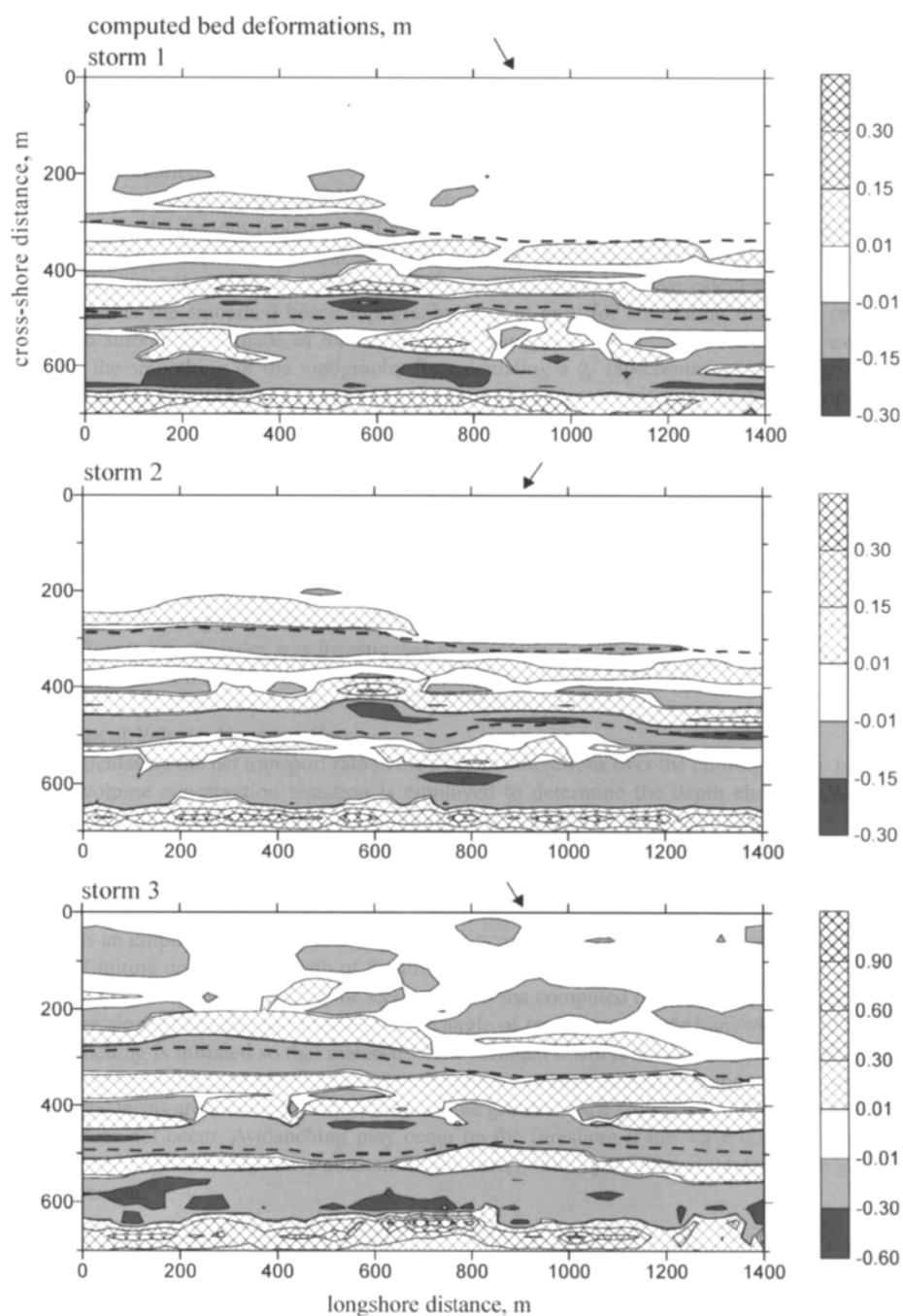
Figure 13. Computed changes in depths at Lubyatowo based on the Moscow Institute of Oceanology (IO) coastal area model. Magnitudes are given in meters.
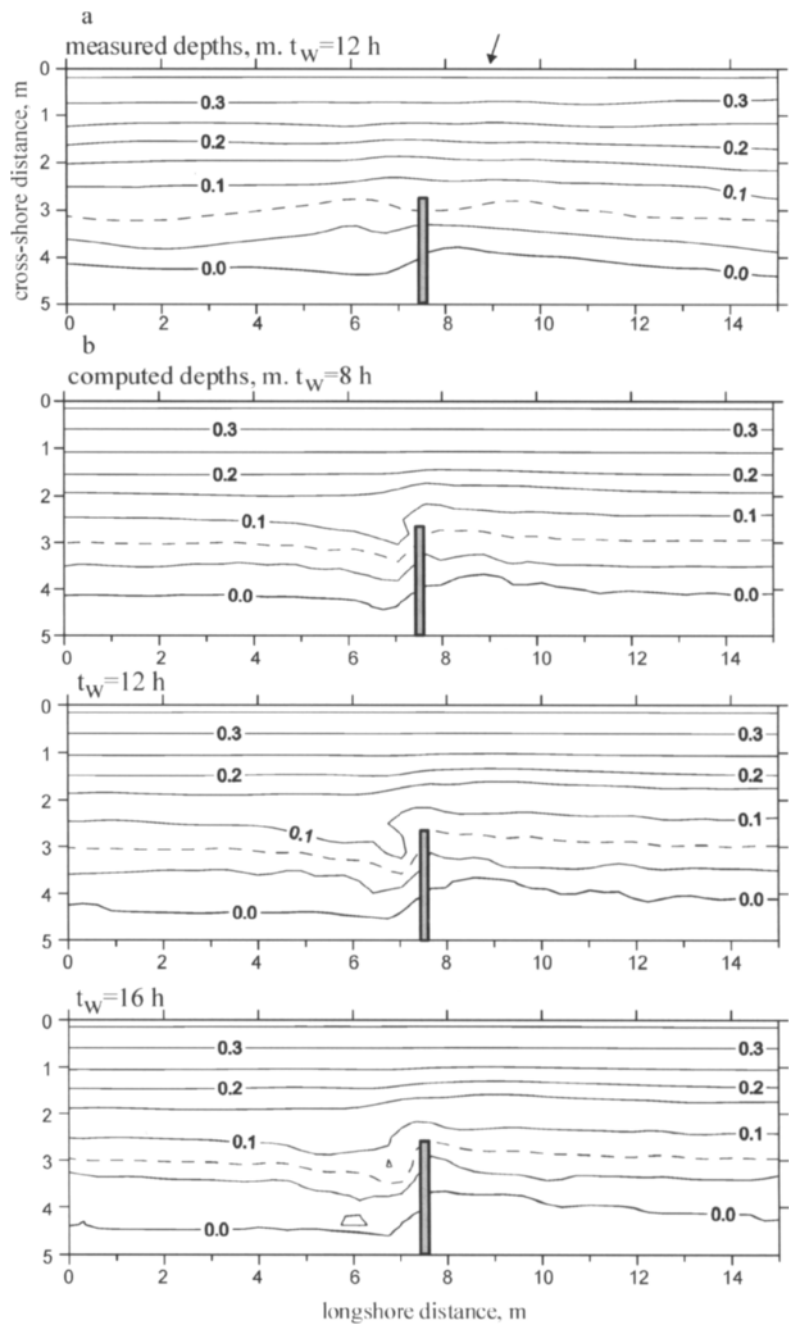
Figure 14. Bottom contours near a groin after wave attack: (a) observed in a wave basin (Badiei et al., 1994); (b) computed from IO model for a few successive moments of time. Initial wave rms height = 0.057 m, period = 1.15 s. Mean sand size = 0.12 mm.
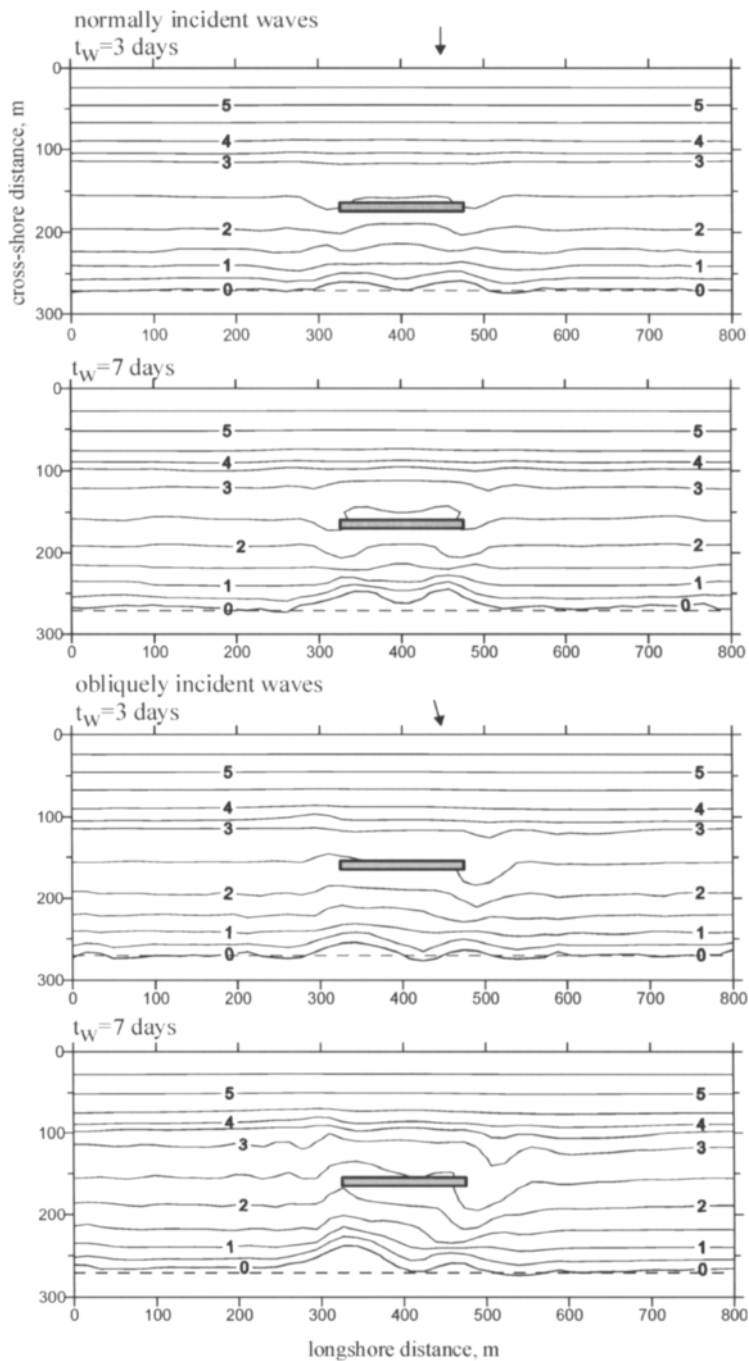
Figure 15. Bottom contours near a breakwater computed from IO model for normally (a), and obliquely incident waves (b). Initial wave rms height = 1 m, period = 6 s. Mean sand size = 0.25 mm.

initial depths, m
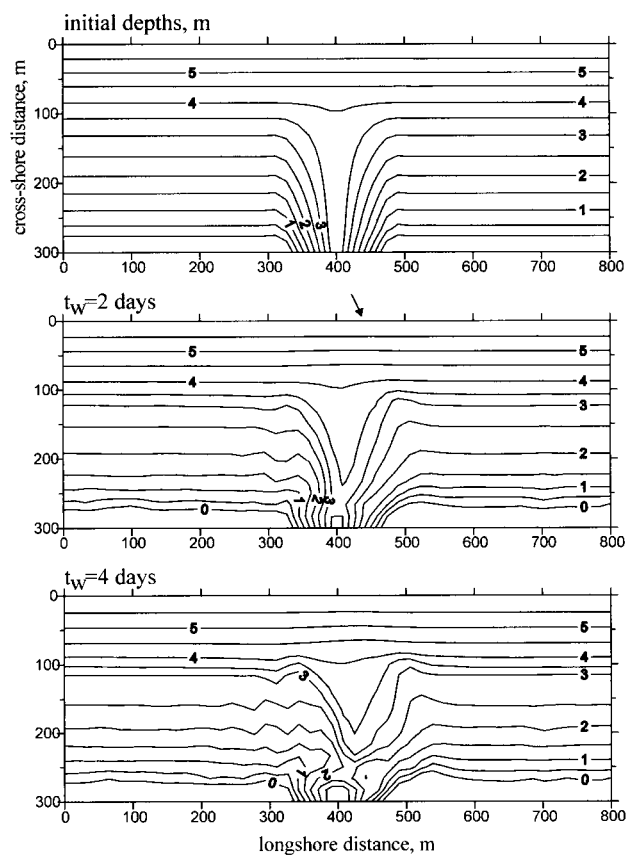
Figure 16. Deformations of a navigable channel exposed to waves with rms height = 1 m, period = 6 s, and incidence angle = 15^0. Mean sand size = 0.25 mm.

Fig. 15 represents the results of a numerical simulation of a morphological evolution of a nearshore zone in the vicinity of a detached breakwater (IO model). The initially uniformly sloping sandy beach ($d_s = 0.2$ mm) is exposed to: (a) shore normal, and (b) obliquely incident random waves ($H_{rms} = 1$ m, $T = 6$ s) over a period of 7 days. Shore normal waves cause an advance of the shoreline against the ends of the structure, while in the case of oblique waves the coastline prominence develops mainly against the updrift end of the structure. The model reproduces the initial stage of the formation of a tombolo, which would eventually connect the coastline with the structure.

Fig. 16 presents the results of a numerical computation of the evolution of a sandy bed (based on the IO model) of an initially symmetrical navigation channel. The obliquely incident waves ($H_{rms} = 1$ m, $T = 6$ s, $\Theta = 15^0$) deform the sea bed: the updrift and downdrift slopes become gentler and steeper, respectively. The axis of the channel is distorted and shifts down-stream. The channel is eventually filled by sand and the sea bed surface becomes more uniform.

The presented examples of short-term morphodynamic modeling show fields of application in solving practical problems. However, model testing with field data is still insufficient. Further improvements to the models will depend on the availability of reliable data from field studies in coastal areas.

3. MODELING THE LONG-TERM MORPHOLOGICAL EVOLUTION OF THE NEARSHORE ZONE

3.1. Coastline Evolution

Prediction of long-term coastal behavior is, in most cases, based on simplifications of the description of constituent processes. This implies that the effects of the primary mechanisms relating to long-term coastal behavior will be included in the model in a highly aggregated form. This is so-called "behavior-oriented modeling" relying on available knowledge and data, but not, formally, on small-scale process-description (De Vriend, 1997). A typical example of such an approach is a one-line model that simulates coastline evolution due to changes in net longshore sediment flux under the influence of any obstacle. A key assumption of the one-line model is that the evolving coastal profile always remains close to its dynamical equilibrium, and so only shifts as a whole in the shore normal direction. The assumption allows the transformation of the equation of mass conservation (equation (1)) to the equation of coastline evolution

$$\frac{\partial X_C}{\partial t} = (d_* + R)^{-1} \frac{\partial Q_y}{\partial y} \tag{28}$$

In equation (28), X_C is the coastline position, d_* is the closure depth limiting the zone of pronounced morphological changes, R is the mean runup height, and Q_y is the total longshore sediment discharge (in m^3/year).

An analytical solution of the problem was first derived by Pelnard-Consideré (1956). Introducing several additional assumptions he transformed equation (28) into a diffusion equation

$$\frac{\partial X_C}{\partial t} = K \frac{\partial^2 X_C}{\partial y^2}, \quad K = \frac{2 Q_m}{d_* + R}, \quad Q_y = Q_m \sin 2\Theta_0 \tag{29}$$

where the diffusion coefficient K characterizes the rate of the morphological response to the variability of the external forcing conditions. The rate increases with the increasing sediment flux amplitude, Q_m, and with the decreasing water depth.

Consider a cross-shore obstacle of length l_g to be located at $y = 0$ of an initially straight coastline (X_C^0 = const) (see Fig. 17). The incident waves approach the shore with a small constant angle Θ_0.
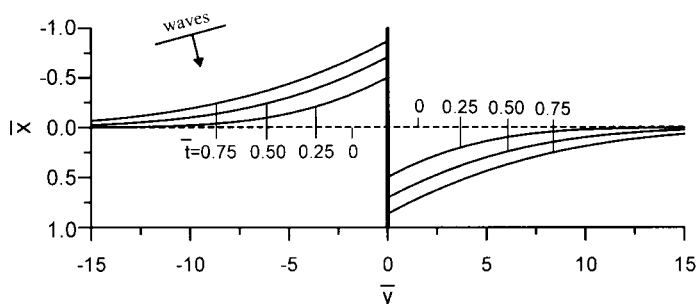
Figure 17. Evolution of shoreline contour in the vicinity of cross-shore structure (theory of Pelnard-Consideré, 1956).

It is assumed that at $y = 0$, $\partial X_C/\partial y = \pm t\,g\,\Theta_0$ (the negative sign refers to the updrift side of the obstacle), and for $y \to \pm\infty$, $\partial X_C/\partial y \to 0$. The solution of equation (29) is given by

$$X_C - X_C^0 = \pm \frac{t\,g\,\Theta_0}{\sqrt{\pi}}\left(\sqrt{4Kt}\,e^{-u^2} - 2|y|\int_u^\infty e^{-u^2}\,du\right), \quad u = \frac{|y|}{\sqrt{4Kt}} \tag{30}$$

The results of calculations for $\Theta_0 = 6^0$ in non-dimensional coordinates $\bar{x} = (X_C - X_C^0)/l_g$, $\bar{y} = y/l_g$ and $\bar{t} = t/t_g$ are shown in Fig. 17, where t_g denotes the time when the coastline position (on the updrift side) reaches the end of the obstacle ($t = \pi\,l_g^2/(4K\tan^2\Theta_0)$). The predicted long-term coastal changes are similar to those induced by earlier described short-term processes (see Fig. 14). Additional simplifying assumptions introduced into the model allow the description of larger spatial and temporal scales. For instance, if $\Theta_0 = 6^0$, $Q_m = 10^5$ m^3/year, $d_* + R = 10$ m and $l_g = 100$ m the predicted time lapse, t_g, is in the order of some 40 years.

A version of a one-line model proposed by Hanson (1989) is often used in practical applications. This model is based on equation (28), and uses the CERC-formula to estimate the longshore sediment flux. The coastal profile is considered to be in an equilibrium state as given by Bruun (see equation (18)). Sediment volumes trapped by a coastal structure are determined from an empirical formula. An advantage of Hanson's model is that it can be applied to complicated situations comprising several structures of different kind (seawalls, series of groins or breakwaters). The recent version of this model (Hanson et al., 2001) takes into account the influence of tidal currents and the longshore non-uniformity of the bed topography.

In Leont'yev's (1997) model, the total sediment discharges, Q_y, are calculated by integrating the local sediment transport rates q_y, which, in turn, are computed for a given coastal profile. However, the discharge gradients, $\partial Q_y/\partial y$, in front of and behind the structure are approximated by empirical formulae. A comparison of various one-line models was recently done by Szmytkiewicz et al. (2000).

A prediction of long-term coastline evolution can also be based on an alternative approach using a combination of equation (28), completed by more detailed process-based models. The latter ones allow a more accurate prediction of the longshore sediment discharge over a realistic bottom topography (comprising the presence of coastal structures), and it avoids the use of additional assumptions that are needed in aggregated models. By summing the shoreline changes computed for typical wave conditions one may assess the net displacements of the coastline over several years or decades.

An example of the described approach is given below. The model calculation predicts the shoreline evolution during 50 years in the vicinity of a solid pier located on the Sakhalin coast of the Okhotsk Sea. The pier position and the bottom contours are shown in Fig. 18a. The observed slope of the sea bed in the coastal region is gentle and the beach is composed of sand with a mean diameter of approximately 0.25 mm. The observed coastal evolution is induced by two opposite longshore sediment fluxes that are generated by southern and northern storms. Waves arriving from the North are higher, but the total duration of the northern storms is shorter when compared to southern storms. However, due to ambient currents from the North (approximately 0.1 m/s) the net sediment flux at the site is directed to the south.

Fig. 18b represents the computed 1-year displacements of the coastline, and also shows the contributions of southern and northern storms (with superimposed ambient current). In the vicinity of the structure the shoreline advances (up to 35 m/year), while at a distance from the pier (see Fig. 18b) erosion occurs with a shoreline retreat up to −10 m/year.

A linear extrapolation of the 1-year result to 50-years does not provide a realistic prediction. Observed morphological variability decreases with time as a consequence of reaching a new equilibrium state. The theory of Pelnard-Consideré (1956) predicts coastline deformation growth to be proportional to $\sqrt{t}$. Based on this result, it can be assumed that the total coastal change over a period of
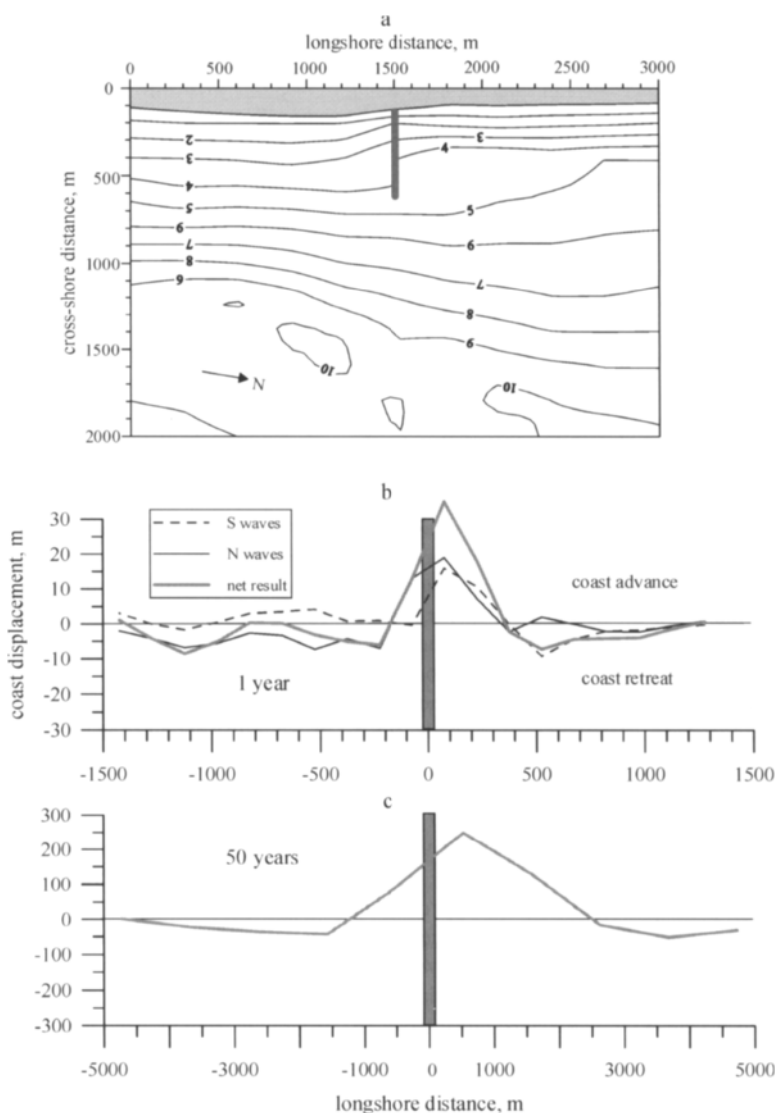
Figure 18. Forecast of coastline changes due to a pier designed at the Sakhalin coast (the Okhotsk Sea): (a) recent bathymetry; (b) coastline displacements after 1 year; (c) coastline changes after 50 years.

N-years can be estimated by increasing the 1-year displacements $\sqrt{N}$ times (some 7 times in the given case). The longshore extension of the shoreline perturbations is also assumed to increase in proportion to $\sqrt{t}$.

The predicted changes of the coastline after 50 years are shown in Fig. 18c. The shoreline advances some 250 m and arrives at about half the pier length. The extension of an accretion zone around the pier is about 3 km. The recession of the shoreline reaches some 50–70 m and the erosion zones also extend over a longer stretch of the coast.

3.2. Evolution of the Coastal Profile

The morphodynamic evolution of a coastal area is strongly influenced by long-term changes in the mean sea level. Bruun's (1988) field studies show that the coastal profile shifts in response to sea level rise or falls without a visible change in the shape of the initial profile. In conclusion, the evolution of the coastal profile is controlled by the so-called Bruun rule implying that shore displacement, ΔX_C, is proportional to the rate of sea level change $\overline{\Delta z_0} = w \Delta t$ (where w is the rate of sea level change), and inversely proportional to mean sea bed slope $\overline{s}$ estimated over the active profile section

$$\Delta X_C = \frac{w \, \Delta t}{\overline{s}} \tag{31}$$

Material eroded from the beach during the period of sea level rise is supposed to accumulate in the deeper part of the nearshore zone. However, in reality the observed profile behavior often deviates from following Bruun's rule because of numerous additional factors not taken into account. In particular, sea level rise can result in sediment movement toward the shore and in the formation of a beach barrier (Cowell et al., 1995).

The recent models include a greater number of factors providing a better forecast (or hindcast) of long-term coastal evolution. Certain progress in long-term modeling is achieved using a "hinged-panel approach" developed by Stive and De Vriend (1995). This approach proposes the representation of coastal profile evolution using a set of linked panels (Fig. 19). The upper panel represents the dune face and the upper shoreface dominated by waves. The lower panel contains the lower shoreface dominated by other dynamic factors (for example, ambient currents). The lower boundary of the lower panel represents the limit of the inner shelf. A transition panel covers the middle shoreface.

In the adopted scheme of the coastal zone the horizontal displacements, Δx, of the centers and edges of each panel are related by simple geometric rules. Related temporal changes in the volumes, $\Delta \Omega$, (per unit length of the coast) in each zone are described by the mass conservation equations. These incorporate changes in sea level, gradients of the total longshore sediment flux and also the cross-shore sediment discharges across the upper and lower boundaries of the shoreface area (in particular, the aeolian transport over the dune face). In the case of a predominant influence of sea level changes, the mass conservation in the upper panel may be treated as a generalized Bruun rule

$$\frac{d(\Delta \Omega_A)}{dt} = \frac{\Delta \Omega_A}{\tau} - \frac{x_T \, h_U}{h_U + (1/2) h_T} w \tag{32}$$
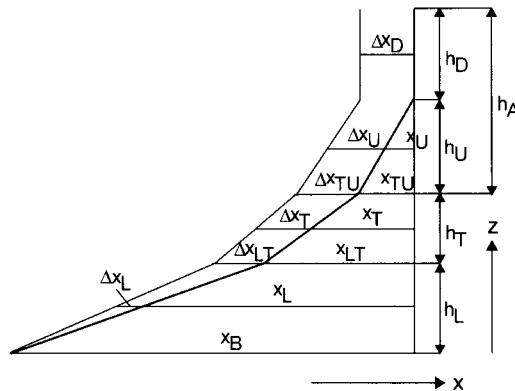
Figure 19. Scheme of coastal profile in hinged-panel approach of Stive and De Vriend (1995).

where τ is the relaxation time (in the order 10^4 years) and other symbols are explained in Fig. 19. The first term on the right-hand side of equation (32) describes the sediment exchange between the middle and upper panels and damps the reaction of the upper shoreface to sea level change. Therefore, the profile evolution is slower than predicted by Bruun's rule, especially over large time scales (for example, over millennia).

Based on available field data of coastal morphology and sediment stratigraphy, Stive and De Vriend applied their model to reproduce successfully the morphological evolution of the Central Coast of the Netherlands over the last century, and also over the period 5000–2000 years B.P.

The models describing long-term coastal profile evolution operate with integral properties of physical mechanisms applied to large morphological units while the contributions of short-term mechanisms are incorporated in highly aggregated form (De Vriend et al., 1993a; Stive and De Vriend, 1995; Cowell et al., 1995). These models may be complemented using an alternative approach involving the technique of short-term process-based modeling in the overall simulation process thereby resulting in a more detailed description of profile behavior.

Such an approach is used by Leont'yev (2001) using the mass conservation equation, in which the short- and long-term model constituents contribute in the following manner

$$\frac{\partial d}{\partial t} = \frac{\partial q_x}{\partial x} + \frac{q_{\text{AEOL}} + \partial Q_y/\partial y - q_* + S}{l_*} + w \tag{33}$$

During a given storm event, the principal components of the mass balance in a shoreface profile are the cross-shore gradients $\partial q_x/\partial x$ of sediment transport rates, induced by waves and currents. The sediment balance in temporal scales of years and decades is mainly controlled by the longshore gradients of gross shore parallel sediment flux $\partial Q_y/\partial y$, and by the contribution of the aeolian transport q_{AEOL} and q_* that provide the long-term sediment discharges across the upper and lower limits of the active zone, respectively. If necessary, the contribution of other existing sources or sinks of sediments, S, may be included in the calculation. All long-term contributions are averaged over the length of the width of the active zone l_* where the bed deformations are most pronounced. In equation (33), the rate w characterizes the long-term variations in sea level due to climate changes or tectonic motions.

The contribution of long-term factors result in a gradual change in the mean elevation of the water surface $\overline{z_0}$ and in the evolution of the position of the underlying bed $\overline{z_b}$

$$\frac{\overline{\Delta z_0}}{\Delta t} = w, \qquad \frac{\overline{\Delta z_b}}{\Delta t} = -\frac{q_{\text{AEOL}} + \partial Q_y/\partial y - q_* + S}{l_*} \tag{34}$$

The symbol $\overline{z_b}$ denotes the averaged thickness of the sediment layer deposited (positive values) or eroded (negative values) during a time lapse Δt. The time step Δt in equation (34) may be chosen arbitrarily (for example, 1 year).

A flow chart of the model is shown in Fig. 20. The numerical procedure includes two cycles providing the calculations of short- and long-term morphological changes. Within the inner cycle the process-based morphodynamic model is employed to simulate the development of the coastal profile under the once-per-year storm conditions (also taking into account the corresponding height of the surge). These conditions are assumed to be adequate to determine the principal shoreface profile geometry. Consequences of more frequent weak storms are supposed to be mainly the shoreline oscillations and migrations of longshore bars (if those exist). Calculations continue until the coastal profile stabilized (time t_e needed to form a quasi-equilibrium beach profile is estimated from the equation (27)).

Within the outer cycle of numerical procedure computed depths are adjusted in response to long-term influence by inclusion of quantities $\overline{\Delta z_0}$ and $\overline{\Delta z_b}$. The obtained sea bed profile constitutes the input to the next step of the calculation. The period of interest, T_E, may be of the order of decades.
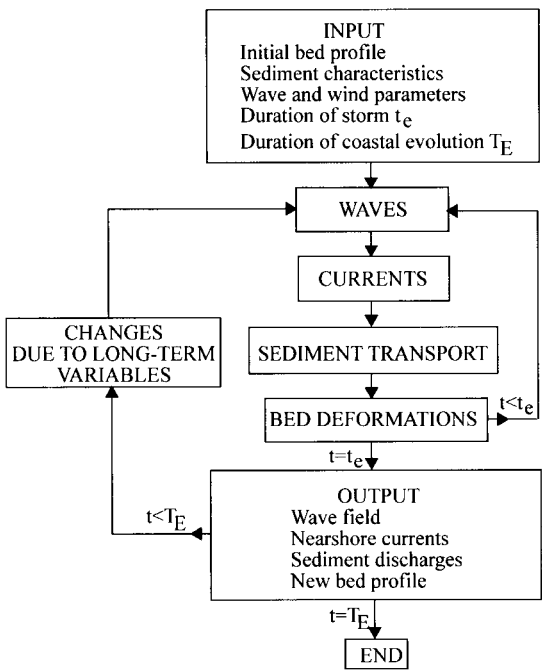
Figure 20. Flow chart of the model simulating the long-term evolution of coastal profile.

The presented model was applied to predict the coastal evolution of the same section of the Central Coast of the Netherlands considered earlier by Stive and De Vriend (1995). Based on field data, it was assumed that: $q_* = S = 0$, $q_{AEOL} \approx -\partial Q_y/\partial y$, and $w = 0.0015$ m/year. Observations indicate that from 1896 to 1975 the shoreline advanced some 30 ± 10 m, while the 7 m depth contour approached the coast some 25 ± 15 m. Predictions of these changes are 40 and 20 m, respectively.

In the following example, the IO model is applied to predict the long-term coastal evolution in the region of Varandey situated in the southeastern part of the Barents Sea. The coast in this region consists of an accretionary marine terrace situated 3–10 m above mean sea level. Recently, the escarpment of the terrace retreated over the entire stretch of the coast with rates of 1–4 m/year.

The bed slopes vary gently, and the water depths over the adjacent shelf area are shallow. The bottom topography is uniform in the longshore direction (Fig. 21a). The incident low energy waves (the once-per-year H_{rms} heights are about 1.3–1.5 m at 10 m depth) are accompanied by a high storm surge (some 1.5 m). The wave-induced longshore sediment flux is nearly uniform (Fig. 21b). The longshore gradients $\partial Q_y/\partial y$ do not contribute significantly to the coastal dynamics at the site. The recession of the coastline is, therefore, related to the remaining long-term factors of the sediment balance given by equation (33). These are the fluxes q_{AEOL} and q_* carrying sand material landward and offshore, respectively. The erosion due to aeolian deflation is important in the area with numerous observed interruptions of the coastal vegetation. The offshore sediment flux, q_*, is generated mainly by local storm surges (see Section 2.2).

Since the total sediment discharge $q_{AEOL} - q_*$ is a priori unknown the model was calibrated by using available field data documenting observed changes in the coastal profile V-5 over a period of 12 years (Fig. 22a). Calibration provided the optimal quantity $q_{AEOL} - q_*$ giving an agreement of predicted and measured morphological variability. Calculations were performed for typical storm
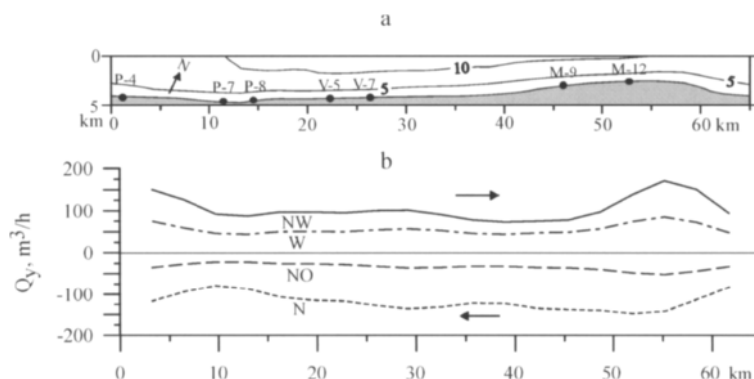
Figure 21. Bottom contours at site Varandey in the Barents Sea (a), and distributions of total longshore sediment discharges during the once-per-year storms of major directions (b).

conditions (wind speed = 20 m/s, rms wave height = 1.4 m at 10 m depth, wave period = 5.1 s and storm surge elevation = 1.5 m). The model calculation provided an estimate of the volume of sediment deficit of some 10 m^3/m/year. The evolution of predicted profile 1 is shown in Fig. 22a.

The most active morphological changes are observed in the profile situated above the mean water level. From this observation, the estimate of the linear scale l_* in equation (33) is taken to be equal to the width of the swash zone during a storm surge. This width is on average about 30 m (but oscillates from step to step in the course of the numerical procedure). Hence, the resultant volume of sediment deficit leads to erosion, which is $\overline{\Delta z_b}/\Delta t = -(q_{AEOL} - q_*)/l_* \approx -0.3$ m/year.

The predicted profile 2 in Fig. 22a represents the result of a calculation without the contribution of the wind-driven flow to the transport rates q_x (i.e., $U_{wind}^B = 0$). The calculated profile shows a significant underestimation of the observed coastal recession. Thus, the offshore mean flow noticeably enhances the wave erosion capability (especially, in the case of short-period waves observed at the site), and provides additional destructive effects on the coastal environment.

The evolution of the coastal profile V-5 over the next 100 years was simulated with the previously calculated value $q_{AEOL} - q_* = 10$ m^3/m/year. To assess the influence of relative sea level rise, the calculations were performed with two different rates 0.01 and 0.005 m/year, in addition to a constant sea level. The results obtained are shown in Figs. 22b, c and d. Initial profile shapes remain almost unchanged in the course of the evolution. With higher rates of water level rise the coast retreats more rapidly, but this difference is not large in general. It means that under given environmental conditions sea level changes play a secondary role as compared with other factors involved.

It can be also seen from Figs. 22b, c and d that in all cases the recession of the coast is slightly retarded with time. The possible reason is a gradual decrease in the foreshore slope and accompanied lowering of waves attacking the escarpment (since the wave energy is dissipated over a greater extension). Such a trend in modeling coastal evolution is more clearly manifested in cases when the sediment deficit on the coast is not large ($q_{AEOL} - q_*$ is small). This gives the evidence that the eroded coastal system may tend to a new morphodynamic quasi-equilibrium state.

4. CONCLUDING REMARKS

Based on the above considerations one can conclude that short-term morphodynamic modeling, at the present time, has achieved a higher rate of progress than the modeling of long-term coastal
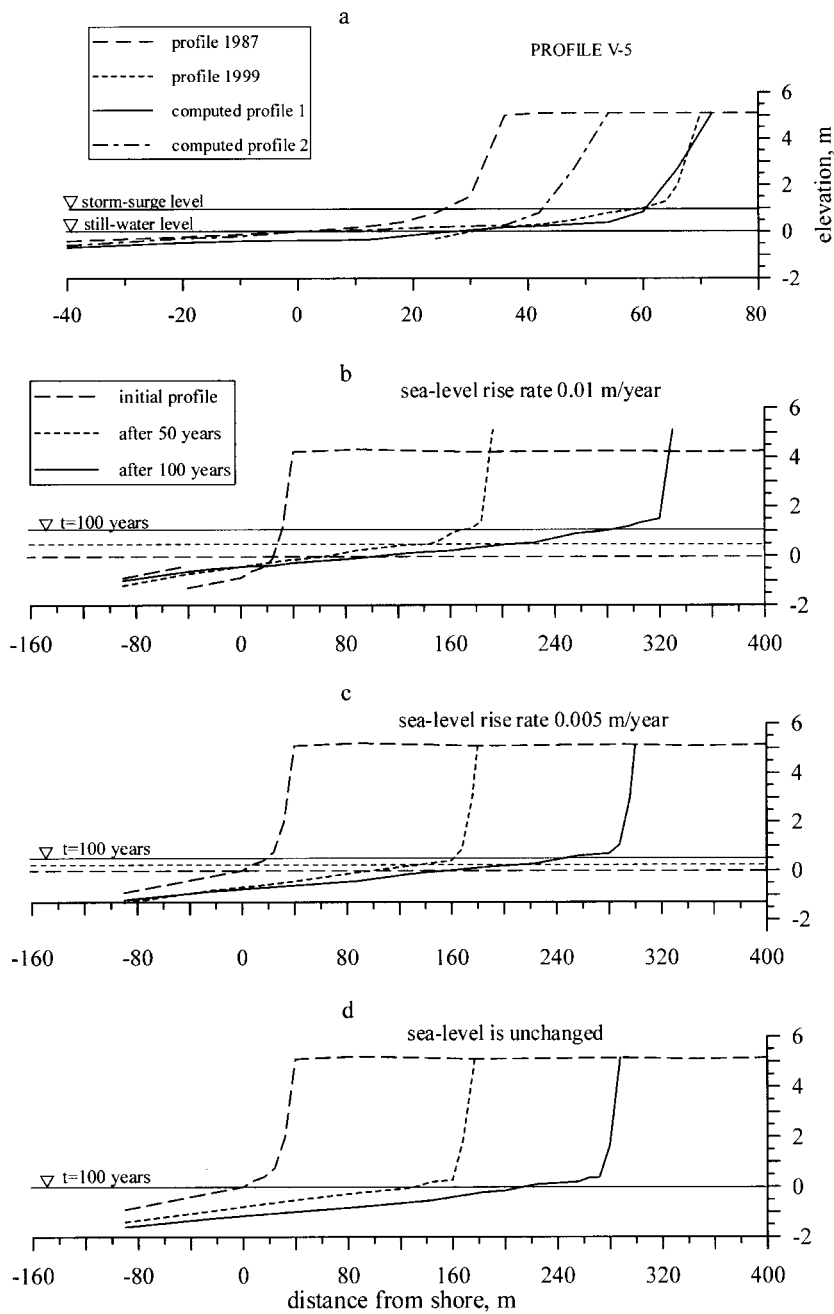
Figure 22. Recent dynamic and predicted evolution of profile V-5 at site Varandey: (a) comparison of observed changes and computations with sediment deficiency volume 10 m³/m/year; profiles 1 and 2 are predicted with inclusion and exclusion of wind-driven outflow, respectively. (b), (c) and (d) profile behavior over the next 100 years for different rates of sea level rise (0.01 and 0.005 m/year) and also for constant sea level.

evolution. This may be explained by the fact that the short-term processes are manifested in more direct mode, and that most of those can be investigated in laboratory conditions, and so parameterized accurately enough to be included in morphodynamic modeling systems. Nevertheless, satisfactory solutions for many problems are still outstanding. The significant fact is that a number of concepts on the nature of bar formation exist, but consensus has not yet been reached. It should be noted, however, that the bar system may be treated as a secondary form of bottom relief in relation to the principal coastal profile geometry. The latter one characterizing large-scale morphological features of specific dynamic zones (for example, surf or swash zones) is in many cases adequately reproduced by existing models. Further progress in short-term morphodynamic modeling seems to be determined to a greater extent by the deepening of knowledge on sediment transport processes.

As to the modeling of long-term coastal evolution it can be developed in three main ways. The first one employs a traditional "integral" approach operating with sediment balance within the large-scale units of coastal morphology and leaving the detailed analyses of acting transport mechanisms out of the discussion.

In contrast, the "local" approach tends to describe the long-term morphological changes as a cumulative result of the primary short-term processes proceeding against a given environmental background. Recently, Roelvink et al. (2001) carried out a hindcast of morphological changes in a complex estuary area over a period of 40 years by using fully process-based simulations, in which the new method for rapid assessment of morphology evolution was incorporated. The results which have been obtained are promising.

Finally, the third way combines the "integral" and "local" approaches resulting in a "hybrid-type" model of coastal profile evolution. By means of two numerical cycles such a model takes into account cumulative effects of both the short- and long-term mechanisms. With relatively low consumption of computational time it provides rather detailed information on profile changes.

The forecast of coastal evolution over the next few decades is of great practical interest. To use morphodynamic modeling for long-term predictions, realistic scenarios of future behavior of long-term variables should be elaborated. It may be expected that investigations into this problem will be intensified, especially in relation to global climate change.

LIST OF SYMBOLS

A	—	shape parameter in equilibrium profile equation
B	—	rate of energy dissipation due to excess near bed turbulence generated by breaking waves
C	—	wave speed
C_g	—	wave group velocity
D	—	total rate of energy dissipation due to wave breaking
d	—	water depth from still water level
d_s	—	mean size of sediment grains
E	—	wave energy per unit area
F	—	rate of energy dissipation due to bed friction
g	—	gravity acceleration
H	—	wave height
$i j$	—	numbers of cells in spatial grid
l_*	—	length of active profile zone
l_{br}	—	surf zone width
n	—	number of temporal level in numerical procedure
Q_y	—	total longshore sediment flux

q_x, q_y	—	cross-shore and longshore sediment transport rates or local sediment discharges per unit width
q_W, q_R	—	local sediment discharges in wave shoaling/breaking region and in swash zone
R	—	runup height
s_x, s_y	—	bed slopes in cross-shore and longshore directions
T	—	wave period
t	—	time
t_w	—	duration of wave attack
t_{eq}	—	time needed to form quasi-equilibrium profile
U, V	—	cross-shore and longshore mean flow velocity components
u_m, u_R	—	wave orbital and runup velocities amplitudes
W	—	wind speed
W_s	—	grain fall velocity
w	—	rate of changes in mean sea level
x, y, z	—	cross-shore, longshore and vertical coordinates
X	—	distance from shore
X_B	—	breakpoint position
X_C	—	shoreline position
X_R	—	runup limit position
β	—	mean beach slope
$\varepsilon_b, \varepsilon_s$	—	bedload and suspended load transport efficiency coefficients
Φ	—	angle of internal friction in sediment layer
η	—	change in mean sea level
$\Theta, \Theta_{\text{wind}}$	—	wave and wind angles relative to shore normal
Ψ	—	Shields parameter

REFERENCES

Antsyferov, S.M., Pykhov, N.V., and Dachev, V.Zh., 1990. Dynamics of suspended sediments. In: Dynamical Processes in Coastal Regions, pp. 127–177. Sofia: Publication of the Bulgarian Academy of Sciences.

Badiei, P., Kamphuis, J.W., and Hamilton, D.G., 1994. Physical experiments on the effects of groins on shore morphology. Proceedings of the 24th International Conference on Coastal Engineering, ASCE, pp. 1782–1796.

Bagnold, R.A., 1963. Mechanics of marine sedimentation. In: The Sea. Vol. 3, pp. 507–528. New York: J. Wiley.

Bailard, J.A., 1981. An energetics total load sediment transport model for a plane sloping beach. Journal of Geophysical Research, 86 (C11): 10,938–10,954.

Boczar-Karakiewicz, B., and Davidson-Arnott, R.G.D., 1987. Nearshore bar formation by non-linear wave process—a comparison of model results and field data. Marine Geology, 77: 287–304.

Boczar-Karakiewicz, B., Bona, J.L., and Cohen, D.L., 1987. Interaction of shallow-water waves and bottom topography. In: Bona, J.L., Dafermos, C., Erikson, J., and Kinderlehrer, D. (Editors), Dynamical Problems in Continuum Physics, Vol. 4, pp. 131–176. New York: Springer-Verlag, IMA Series in Mathematics and its Applications.

Boczar-Karakiewicz, B., Forbes, D.L., and Drapeau, G., 1995. Nearshore bar development in the Southern Gulf of St. Lawrence. Journal of Waterway, Port, Coastal, and Ocean Engineering, 121 (1): 49–60.

Boczar-Karakiewicz, B., Romanczyk, W., Bona, J.L., and Thornton, E.B., 1998. Modeling the dynamics of the bar system at Duck, NC, USA. Proceedings of the 26th International Conference on Coastal Engineering, ASCE, pp. 2877–2887.

Bowen, A.J., 1980. Simple models of nearshore sedimentation; beach profiles and longshore bars. Coastline of Canada, pp. 1–11. Halifax, NS: Geological Survey of Canada.

Bowen, A.J., and Inman, D.L., 1971. Edge waves and crescentic bars. Journal of Geophysical Research, 76 (30): 8662–8671.

Bowen, A.J., and Huntley, D.A., 1984. Waves, long waves and nearshore topography. Marine Geology, 60: 1–13.

Briand, M.H.G., and Kamphuis, J.W., 1993. Sediment transport in the surf zone: Quasi 3-D numerical model. Coastal Engineering, 20: 135–156

Brøker, I., 1995. Coastal area modelling. MAST 68-M Final Workshop, Gdansk, pp. 2–86 – 2–90.

Brøker, I., Deigaard, R., and Fredsøe, J., 1991. Onshore/offshore sediment transport and morphological modelling of coastal profiles. Proceedings of Coastal Sediments '91, Seattle, pp. 643–657.

Brøker, H.I., Roelvink, J.A., Southgate, H., Pechon, P., Nicholson, J., Hamm, L., 1992. Intercomparison of coastal profile models. Proceedings of the 23rd International Conference on Coastal Engineering, ASCE, pp. 2108–2121.

Brøker, I., Johnson, H.K., Zyserman, J.A., Ronberg, J.K., Pedersen, C., Deigaard, R., and Fredsøe, J., 1995. Coastal profile and coastal area morphodynamic modelling. MAST 68-M Final Workshop, Gdansk, pp. 7–12 – 7–16.

Bruun, P., 1954. Coast erosion and the development of beach profiles. TM-44. Washington: US Army Corps of Engineers, Beach Erosion Board.

Bruun, P., 1988. The Bruun rule of erosion by sea-level rise: A discussion on large-scale two- and three-dimensional usages. Journal of Coastal Research, 4 (4): 627–648.

Chapalain, G., and Boczar-Karakiewicz, B., 1992. Modeling of hydrodynamics and sedimentary processes related to unbroken progressive shallow water waves. Journal of Coastal Research, 8 (2): 419–441.

Cowell, P.J., Roy, P.S., and Jones R.A., 1995. Simulation of large-scale coastal change using a morphological behaviour model. Marine Geology, 126: 45–61.

Cowell, P.J., and Thom, B.G., 1995. Morphodynamics of coastal evolution. In: Carter, R.G.W., and Woodroffe, C.D. (Editors), Coastal Evolution: Late Quarternary Shoreline Morphodynamics, pp. 33–86. Cambridge: Cambridge University Press.

Creed, G.C., Dalrymple, R.A., Kriebel, D.L., and Kaihatu J.M., 1992. Equilibrium beach profiles with random seas. Proceedings of the 23rd International Conference on Coastal Engineering, ASCE, pp. 1973–1986.

Dean, R.G., 1991. Equilibrium beach profiles. Characteristics and applications. Journal of Coastal Research, 7 (1): 53–84.

De Vriend, H.J., 1997. Prediction of aggregated-scale coastal evolution. Proceedings, Coastal Dynamics '97, Plymouth, pp. 644–653.

De Vriend, H.J., Capobianco, M., Chesher, T., de Swart, H.E., Latteux, B., and Stive, M.J.F., 1993a. Approaches to long-term modelling of coastal morphology: A review. Coastal Engineering, 21: 225–269.

De Vriend, H.J., Zyserman, J., Nicholson, J., Roelvink, J.A., Pechon, P., and Southgate, H.N., 1993b. Medium-term 2DH coastal area modelling. Coastal Engineering, 21: 193–224.

Fredsøe, J., Andersen, O.H., and Silberg, S., 1985. Distribution of suspended sediment in large waves. Journal of Waterway, Port, Coastal and Ocean Engineering, 111: 1041–1059.

Gizhevsky, E., Melcharsky, A., Nicholov, H., Ronevich, P., Rudovsky, S., and Semrau, I., 1978. Composition and short-term changes in the beach slope. In: Coastal processes in a non-tidal sea

(Lubyatowo-76), pp. 337–350. Gdansk, Poland: Polska Academia Nauk. Institutu Budownocntwa Wodnego (in-Russian).

Gonzalez, M., Medina, R., and Losada, M.A., 1997. Equilibrium beach profiles: Effects of refraction. Proceedings, Coastal Dynamics '97, Plymouth, pp. 933–941.

Hanson, H., 1989. GENESIS: A generalized shoreline change numerical model. Journal of Coastal Research, 5 (1): 1–27.

Hanson, H., Larson, M., and Kraus, N.C., 2001. A new approach to represent tidal currents and bathymetric features in the one-line model concept. Proceedings, Coastal Dynamics '01, Lund, Sweden, pp. 172–181.

Holman, R.A., and Bowen, A.J., 1982. Bars, bumps and holes: Models for the generation of complex beach topography. Journal of Geophysical Research, 87 (C1): 457–468.

Hunt, I.A., 1959. Design of seawalls and breakwaters. Journal of Waterway and Harbors Division, ASCE, 85: 123–152.

Johnson, H.K., Appendini, C.M., Soldati, M., Elfrink, B., and Sorensen, P., 2001. Numerical modelling of morphological changes due to shoreface nourishment. Proceedings, Coastal Dynamics '01, Lund, Sweden, pp. 878–887.

Karambas, Th.V., Prinos, P., and Kriezi, E.E., 1997. Modelling of hydrodynamic and morphological effects of submerged breakwaters on the nearshore region. Proceedings, Coastal Dynamics '97, Plymouth, pp. 764–773.

Kraus, N.C., 2001. On equilibrium properties in predictive modeling of coastal morphology change. Proceedings, Coastal Dynamics '01, Lund, Sweden, pp. 1–15.

Kriebel, D.L., and Dean, R.G., 1985. Numerical simulation of time-dependent beach and dune erosion. Coastal Engineering, 9: 221–245.

Kriebel, D.L., Kraus, N.C., and Larson, M., 1991. Engineering methods for predicting beach profile response. Proceedings, Coastal Sediments '91, Seattle, pp. 557–571.

Larson, M., 1994. Prediction of beach profile change at mesoscale under random waves. Proceedings of the 24th International Conference on Coastal Engineering, ASCE, pp. 2252–2266.

Larson, M., and Kraus, N.C., 1989. SBEACH: Numerical model for simulating storm-induced beach change. Tech. Rep. CERC-89-9. Vicksburg, MS: US Army Engineers Waterways Experiment Station. Coastal Engineering Research Center.

Leont'yev, I.O., 1985. Sediment transport and beach equilibrium profile. Coastal Engineering, 9: 277–291.

Leont'yev, I.O., 1996. Numerical modelling of beach erosion during storm event. Coastal Engineering, 29: 187–200.

Leont'yev, I.O., 1997. Short-term shoreline changes due to cross-shore structures: A one-line numerical model. Coastal Engineering, 31: 59–75.

Leont'yev, I.O., 1999. Modelling of morphological changes due to coastal structures. Coastal Engineering, 38: 143–166.

Leont'yev, I.O., 2001. Coastal dynamics: Waves, currents, sediment transport. Moscow: GEOS, 272p. (in-Russian).

Longuet-Higgins, M.S., 1953. Mass transport in water waves. Philosophical Transactions of the Royal Society London, Series A, 245 (903): 535–581.

Longuinov, V.V., 1963. Dynamics of coastal-zone in a non-tidal sea. Moscow, USSR Academy of Sciences, 379p. (in-Russian)

Nairn, R.B., and Southgate, H.N., 1993. Deterministic profile modeling of nearshore processes. Part 2. Sediment transport and beach profile development. Coastal Engineering, 19: 57–96.

Newe, J., and Dette, H., 1995. Simulation of dune and nourished berm erosion during storm surges. Proceedings, Coastal Dynamics '95, Gdansk, pp. 850–861.

Nicholson, J., Brøker, I., Roelvink, J.A., Price, D., Tanguy, J.M., and Moreno, L., 1997. Intercomparison of coastal area morphodynamic models. Coastal Engineering, 31: 97–123.

O'Hare, T.J., and Huntley, D.A., 1994. Bar formation due to wave groups and associated long waves. Marine Geology, 116: 313–325.

Ohnaka, S., and Watanabe, A., 1990. Modelling of wave-current interaction and beach change. Proceedings of the 22nd International Conference on Coastal Engineering, ASCE, pp. 2443–2456.

Pelnard-Consideré, R., 1956. Essai de theorie de l'evolution des formes de rivage en plages de sable et de galets. Quatr. J. hydraulique, Question 3, Rapp. No. 1, Paris.

Price, D.M., Chesher, T.J., and Southgate, H.N., 1995. PISCES. A morphological coastal area model. HR Wallingford, Report SR 411. Wallingford, UK: HR Wallingford.

Rakha, K.A., and Kamphuis, J.W., 1995. A morphology model to predict erosion near a seawall. Proceedings, Coastal Dynamics'95, Gdansk, pp. 879–890.

Roelvink, J.A., and Brøker, I., 1993. Cross-shore profile models. Coastal Engineering, 95: 163–191.

Roelvink, J.A., Jeuken, M.C.J.L., Van Holland, G., Aarninkhov, S.G.J., and Stam, J.M.T., 2001. Long-term, process-based modelling of complex areas. Proceedings, Coastal Dynamics '01, Lund, Sweden, pp. 383–392.

Roelvink, J.A., Reniers, A.J.H.M., and Walstra, D.J.R., 1995. Medium-term morphodynamic modelling. MAST 68-M Final Workshop, Gdansk, pp. 7–3 – 7–6.

Roelvink, J.A., and Stive, M.J.F., 1989. Bar-generating cross-shore flow mechanisms on a beach. Journal of Geophysical Research, 94 (C4): 4785–4800.

Romanczyk, W., Boczar-Karakiewicz, B., Thornton, E.B., and Bona, J.L., 1999. Sand bars at Duck, NC, USA. Observations and model predictions. Proceedings, Coastal Sediments '99, ASCE, pp. 491–594.

Stive, M.J.F., and De Vriend, H.J., 1995. Modelling shoreface profile evolution. Marine Geology, 126: 235–248.

Szmytkiewicz, M., Biegowski, J., Kaczmarek, L.M., Okroj, T., Ostrowski, R., Pruszak, Z., Rosynsky, G., and Skaja, M. 2000. Coastline changes nearby harbour structures: Comparative analyses of one-line models versus field data. Coastal Engineering, 40: 119–139.

Uliczka, K., 1987. Wave runup on dunes with and without foreshore at a prototype scale. Leichtweiss-Inst. Wasserbau Tech. Univ. Braunschweig Mitt., 98: 67–88.

Wang, H., Miao, G., and Lin, L.-H., 1992. A time-dependent nearshore morphological response model. Proceedings of the 23rd International Conference on Coastal Engineering, ASCE, pp. 2513–2527.

Wu, Y., Dette, H., and Wang, H., 1994. Cross-shore profile modelling under random waves. Proceedings of the 24th International Conference on Coastal Engineering, ASCE, pp. 2843–2855.

Zhang, D.P., and Sunamura, T., 1994. Multiple bar formation by breaker-induced vorticies: A laboratory approach. Proceedings of the 24th International Conference on Coastal Engineering, ASCE, pp. 2856–2870.

This Page Intentionally Left Blank

337

Chapter 12

Numerical Modeling of Beach Topography Change

Magnus Larson [a], Hans Hanson [a] and Nicholas C. Kraus [b]

[a]Department of Water Resources Engineering, Lund University, Box 118, S-221 00 Lund, Sweden
[b]Coastal and Hydraulics Laboratory, US Army Engineer Research and Development Center, 3909
 Halls Ferry Road, Vicksburg, MS 39180–6199, USA

1. INTRODUCTION

1.1. Background
Numerical models of beach topography change are commonly used tools in engineering projects. However, at present these models typically focus on simulating a limited set of processes characterized by certain time and space scales. For example, shoreline evolution models, which were the first types of models to be used in engineering studies, describe changes in the shoreline location due to gradients in the longshore transport. These models typically simulate shoreline evolution over decades with limited resolution of the response on the intra-annual scale. On the other hand, profile evolution models compute changes in the profile shape due to cross-shore transport only. Such models have traditionally been used to estimate the impact of storms, implying a characteristic scale for the processes on the order of days.

Since the beginning of the 1990s, efforts have been made to develop more general numerical models of beach change that could include the whole topography, not only the shoreline or a specific profile. However, these models are complicated to apply and often yield results that are neither reliable nor robust. Nevertheless, models of beach topography change have to include both longshore and cross-shore transport, which make it possible to simulate processes over a wider scale range. Thus, responses in the topography from an hourly scale up to an annual scale might be simulated. Although models simulating the response of the entire topography by necessity cover more scales than shoreline and beach profile evolution models, it is not expected that they can be employed to compute the evolution at all scales. Because of limited process knowledge and collective movement of sediment at different scales, it is anticipated that a suite of models are needed in engineering studies in a foreseeable future where each model has its characteristic scale(s).

In developing numerical models of beach topography change various simplifying approaches have been taken in the past to make the models robust and reliable. Examples of such simplifications, further discussed below, are decoupling of certain calculations (i.e., some calculations are made in one instead of in two-dimensions), and limited updating of the hydrodynamic and transport fields. In this chapter, a numerical model of beach topography change is presented for utilization in engineering projects. Decoupling of the computations of cross-shore and longshore processes was employed in the model development to speed-up model execution and improve robustness. The emphasis in the modeling is on surf zone processes where breaking waves are assumed to be the main agent for mobilizing and transporting sand.

1.2. Objectives
The main objective of this study was to develop a beach topography change model, describing both the effects of longshore and cross-shore sediment transport, to be used in engineering projects where time scales from individual storms to seasonal variations are included. Emphasis in the model

development was on robustness and execution speed, implying that a number of simplifications were introduced during the development. Breaking waves and related surf zone processes were assumed to be the main agents for transporting sediment and inducing beach change.

1.3. Procedure

A two-dimensional (2-D) model for random waves was derived based on the mild-slope equation. In the derivation of the wave model diffraction was neglected and a sink term was added to quantify wave breaking. The randomness of the waves is described through the probability density function (pdf) for the wave height, whereas the wave period and incident wave angle are assumed constant during a specific time step when the wave field is determined. The wave model allows for wave shoaling, refraction, breaking, and reforming. Mean water elevation is obtained from a simplified momentum equation, neglecting convective terms and lateral mixing. In the sediment transport calculations, cross-shore and longshore transport are computed independently with respect to the local orientation of the contour line defined over a representative length scale. The cross-shore sediment transport is mainly a function of the wave energy dissipation per unit water volume, and the longshore transport is determined by the longshore current and dissipation. For the swash zone a transport relationship is used where the rate is parameterized in terms of the local bore front velocity and slope. The change in beach elevation is determined from the sediment volume conservation equation.

First, a short review is given of different kinds of beach change models to bring the present modeling effort into perspective. The theoretical foundation for the model is then summarized with respect to the different components, that is, waves, mean water elevation, currents, cross-shore transport, longshore transport, and swash zone transport. Finally, selected simulation results are presented both concerning hypothetical situations and cases where detailed field data were collected in engineering projects. The latter cases involved major beach nourishment projects in the United States and Germany.

2. OVERVIEW OF NUMERICAL BEACH CHANGE MODELING

Numerical models of beach change can be classified into three broad types: (1) profile evolution models, which simulate cross-shore processes, but neglect longshore processes; (2) contour line models, which mainly simulate beach change caused by gradients in the longshore sediment transport rate, and (3) three-dimensional (3-D) models, in which both cross-shore and longshore processes are described. Profile change models have mostly been employed to simulate the impact of single storm events, whereas contour line models have been used to predict the long-term shoreline evolution. However, in applications where both short- and long-term effects must be simulated, 3-D models that simultaneously include cross-shore and longshore processes are needed. Profile change and contour line models are routinely employed in engineering projects, whereas reliable and robust 3-D models are still lacking to a large degree.

2.1. Profile Evolution Models

During the past fifteen years, considerable efforts have been put into the development of numerical models for calculating beach profile change due to cross-shore sediment transport (Kriebel and Dean, 1985; Watanabe and Dibajnia, 1988; Larson and Kraus, 1989; Roelvink and Stive, 1989; Steetzel, 1990; Brøker-Hedegaard et al., 1991; Nairn and Southgate, 1993). These models have mainly been developed to determine the profile response on a time scale of days to describe dune and foreshore erosion during storms, and longshore bar formation and movement. Although some of the models could be used for predicting profile evolution at longer time scales, sufficient validation is often lacking to prove the model capabilities for such long-term simulations. The necessity of specifying

the input forcing with a resolution that corresponds to the description of the physical processes makes long-term predictions difficult in most models (Larson and Kraus, 1995).

Numerical models of beach profile change may be classified according to the characteristic scale employed in resolving the fluid and sediment motion. Models which attempt to describe scales of motion in time (t) and space (s) compatible with individual waves belong to the class of microscale models (for example, $t = 10^{-1} - 10^{0}T$ and $s = 10^{-4} - 10^{-3}L$, where T is the wave period and L the wavelength), whereas mesoscale models (for example, $t = 10^{1} - 10^{2}T$ and $s = 10^{-2} - 10^{-1}L$) focus on resolving scales of motion that are the result of many waves (Larson and Kraus, 1995). The numerical models by Kriebel and Dean (1985) and Larson and Kraus (1989) are examples of models that mainly adopt a mesoscale process description; the local cross-shore flow pattern is not computed, and the net transport rate is derived directly from the variation in wave properties across shore. Most other numerical cross-shore models (Roelvink and Stive, 1989; Steetzel, 1990; Brøker-Hedegaard et al., 1991; Nairn and Southgate, 1993) involve both elements of micro- and mesoscale descriptions. These models typically calculate local flow velocities and transport rates characteristic for a microscale approach but employ input wave conditions that are averaged at the mesoscale.

2.2. Contour Line Evolution Models

The earliest type of beach change model focused on predicting the shoreline response to gradients in the longshore transport generated by obliquely incident waves. Pelnard-Considère (1956) originated the mathematical theory of shoreline response to wave action under the assumption that the beach profile moves parallel to itself, i.e., that it translates shoreward and seaward without changing shape in the course of eroding and accreting. He also verified his mathematical model by comparison to beach change produced by waves obliquely incident to a beach with a groin installed in a movable-bed physical model. Mathematical modeling of shoreline change is a powerful and flexible engineering technique for understanding and predicting the long-term evolution of the plan shape of sandy beaches. For example, Hanson et al. (1988) give several applications. Mathematical models provide a concise, quantitative means of describing systematic trends in shoreline evolution commonly observed at groins, jetties, and detached breakwaters.

If the profile shape does not change, any point on it is sufficient to specify the location of the entire profile with respect to a baseline. Thus, one contour line can be used to describe change in the beach plan shape and volume as the beach erodes and accretes. This contour line is conveniently taken as the readily observed shoreline, and the model is therefore called a "shoreline change" or "shoreline response" model. Sometimes the terminology "one-line" model, a shortening of the phrase "one-contour line" model, is used with reference to the single contour line. The one-line theory was numerically first implemented by Price et al. (1972), followed by many others. Willis (1977) applied a one-line model to prototype conditions, evaluating different formulae for the longshore transport, and Perlin (1979) simulated the shoreline evolution around detached breakwaters. Kraus et al. (1984) and Hanson and Kraus (1986) developed a one-line model with the overall aim to arrive at a model that could be used as an engineering tool (Hanson, 1989).

If the response of two contours along the beach is described, a two-line model is obtained (Bakker, 1968). Similarly, a generalization to N contour lines yields an N-line model (Perlin and Dean, 1983; Steetzel et al., 1998; Hanson and Larson, 1999; 2000). In contrast to the one-line model that assumes a constant profile shape N-line models simulate changes in the profile by introducing cross-shore transport relationships. These relationships are typically expressed in terms of beach slope, or, equivalently, distance between the contours (Swart, 1974). The main disadvantage with N-line models is that only profiles where the depth is monotonically increasing with distance offshore may be represented. Thus, morphological features such as longshore bars cannot be reproduced.

2.3. Three-Dimensional Models

Fully combining cross-shore and longshore sediment transport yields a model that can predict the evolution of the complete topography. In the general terminology such a model is known as a 3-D model since it includes three spatial coordinates, even though one coordinate (depth) is a dependent variable to be solved. Significant progress has been made in recent years concerning 3-D modeling, but still very few examples exist where these models have been successfully used in engineering studies (Watanabe, 1982). The interaction between the waves, currents, sediment transport, and morphological evolution is difficult to simulate in a stable and robust manner.

Because of the complexity involved in 3-D modeling, and, to some degree the computational efforts needed, several simplifying approaches have been developed. In this respect, the N-line formulation may be interpreted as a simplified three-dimensional approach where selected contour lines are modeled. Another option is to decouple cross-shore and longshore processes during some portion of the calculations assuming that certain gradients are small and may be neglected (Larson et al., 1990). Finally, the interaction between the hydrodynamic fields and the bottom topography may be relaxed by only updating these fields at certain intervals (Roelvink et al., 1994). Thus, even if the bottom topography changes the hydrodynamic field and associated transport field are not recalculated until some specified criterion is satisfied (for example, a certain time interval or bottom change is exceeded). Roelvink et al. (1998) employed an even more schematic approach where the long-term bathymetric changes were based only on an initial transport field obtained from a detailed process model.

3. A NUMERICAL MODEL OF TOPOGRAPHIC EVOLUTION

3.1. Model Overview

The beach topography change model presented here represents a generalization and extension of the model developed by Larson et al. (1990). The new model involves a more consistent approach to treat random waves (Larson, 1995; 1996), and there is no decoupling of profile lines in the calculations of the wave field. Also, a newly proposed sediment transport formula was utilized to compute the longshore sediment transport rate. The numerical model encompasses major modules to calculate the following (in order): (1) wave transformation, including shoaling, refraction, breaking, and reforming, (2) mean water level (wave set-up and set-down), (3) longshore current and transport rate, (4) cross-shore transport rate, (5) swash zone transport rate, (6) bottom contour orientation, and (7) topographic change. A brief review of each of these modules is provided.

3.2. Wave Transformation

The mild-slope equation is often employed to describe the transformation of linear water waves according to Berkhoff (1972), and Berkhoff et al. (1982)

$$\frac{\partial}{\partial x}\left(CC_g\frac{\partial \Phi}{\partial x}\right) + \frac{\partial}{\partial y}\left(CC_g\frac{\partial \Phi}{\partial y}\right) + \sigma^2\frac{C_g}{C}\Phi = 0 \tag{1}$$

where C is the phase speed, C_g the group speed, Φ a two-dimensional complex wave potential function, σ the angular frequency, and x and y coordinates in a rectangular system. In the present application the coordinate system is oriented in such a way that the y-axis extends along the main orientation of the bottom contours. Thus, for straight and parallel contours the x-coordinate would denote the cross-shore direction and the y-coordinate the longshore direction. However, for more complex topographies this is not the case, as will be discussed later.

Equation (1) may be rewritten by introducing the following expression for Φ

$$\Phi = ae^{iS} \tag{2}$$

where a is the wave amplitude and S a phase function. Substituting equation (2) into equation (1) and separating the real and imaginary parts yields one equation that represents the conservation of wave energy flux and one equation that describes the evolution of the phase function (Ebersole et al., 1986). The equation for the conservation of wave energy flux is

$$\frac{\partial}{\partial x}\left(CC_g\, a^2\, \frac{\partial S}{\partial x}\right) + \frac{\partial}{\partial y}\left(CC_g\, a^2\, \frac{\partial S}{\partial y}\right) = 0 \tag{3}$$

whereas the other equation becomes

$$\frac{1}{aCC_g}\left[\frac{\partial}{\partial x}\left(CC_g\, \frac{\partial a}{\partial x}\right) + \frac{\partial}{\partial y}\left(CC_g\, \frac{\partial a}{\partial y}\right)\right] + \left(\frac{\partial S}{\partial x}\right)^2 + \left(\frac{\partial S}{\partial y}\right)^2 - k^2 = 0 \tag{4}$$

in which k is the wave number.

The main problems with employing the mild-slope equation in a model to predict beach topography evolution are that the equation requires considerable computational effort to solve at each time step, energy dissipation due to wave breaking is not included, and random waves are not described. Thus, the equation will be modified to overcome these problems. It is straightforward to add sink terms in the wave energy flux conservation equation based on empirical considerations (Dally et al., 1985; Ebersole et al., 1986) that take into account the effects of wave breaking and bottom friction. Using the expression proposed by Dally et al. (1985) to determine the energy dissipation due to depth-limited wave breaking (neglecting bottom friction), equation (3) takes the form

$$\frac{\partial}{\partial x}\left(F\, \frac{1}{k}\, \frac{\partial S}{\partial x}\right) + \frac{\partial}{\partial y}\left(F\, \frac{1}{k}\, \frac{\partial S}{\partial y}\right) = \frac{\kappa}{d}\, (F - F_s) \tag{5}$$

where κ is an empirical coefficient $(= 0.15)$, d the total water depth, and F is the wave energy flux given by

$$F = \frac{1}{8}\, \rho\, g\, H^2\, C_g \tag{6}$$

where H is the wave height, ρ the water density, and g the acceleration of gravity. The stable wave energy flux is given by $F_s = 1/8\, \rho\, g\, (\Gamma d)^2\, C_g$, where Γ is an empirical coefficient $(= 0.4)$.

The most time consuming aspect of solving the mild-slope equation arises from the coupled system of equations for the wave amplitude and phase (equations (3) and (4)). Solving equation (4) especially requires substantial computational effort. However, if diffraction effects are negligible, equation (4) reduces to

$$\left(\frac{\partial S}{\partial x}\right)^2 + \left(\frac{\partial S}{\partial y}\right)^2 - k^2 = 0 \tag{7}$$

Equation (7) states that the magnitude of the wave phase gradient is equal to the wave number. This implies that the phase function may be derived from the wave number conservation equation describing pure refraction. Equation (5) may in this case be written as

$$\frac{\partial}{\partial x}\, (F\cos\theta) + \frac{\partial}{\partial y}\, (F\sin\theta) = \frac{\kappa}{d}(F - F_s) \tag{8}$$

where θ is the local wave angle given by the wave number conservation equation (see below).

In order to realistically describe the wave field on a real beach, the randomness of the waves must be taken into account. If a random sea is narrow-banded in frequency and direction, the randomness

enters mainly through the variation in the wave height H, and the probability density function (pdf) for H uniquely specifies the conditions. A Rayleigh pdf has been shown to give a good description of the variation in wave height in deeper water where depth-limited breaking is absent. The root-mean-square (rms) wave height H_{rmso} is the only shape parameter in the Rayleigh pdf. In areas where depth-limited breaking occurs, however, it has been shown that a Rayleigh pdf only approximately describes the variation in H (Hughes and Borgman, 1987; Dally, 1990; 1992).

One method that has been successfully employed to describe the transformation of random waves in the surf zone is the wave-by-wave approach (Dally, 1990; Larson and Kraus, 1991; Dally, 1992). This method is based on the assumption that properties of the random wave field may be derived by transforming a large number of individual waves that represent the appropriate pdf in the offshore. The statistical properties of the wave field at each location are obtained by linearly adding up the contribution from each single wave. Larson (1995) employed this technique to develop a rapid method to calculate the transformation of random waves. This method transforms only one wave height across shore, the rms wave height for breaking and non-breaking waves H_{rms}, and several characteristic average quantities of the wave field are predicted such as the mean energy dissipation and the mean ratio of breaking waves.

Generalizing the method used by Larson (1995), equation (5) may be developed to describe the transformation of random waves

$$\frac{\partial}{\partial x}\left(F_{rms}\frac{1}{k}\frac{\partial S}{\partial x}\right) + \frac{\partial}{\partial y}\left(F_{rms}\frac{1}{k}\frac{\partial S}{\partial y}\right) = \frac{\kappa}{d}\left(F_{rms} - F_{stab}\right) \tag{9}$$

where F_{rms} is the wave energy flux based on H_{rms}, and the equivalent stable wave energy flux for random waves is defined as

$$F_{stab} = \beta F_m + \mu F_r + \alpha \left(\frac{\Gamma}{\gamma}\right)^2 F_b \tag{10}$$

where α, β, and μ is the ratio of breaking, unbroken, and reformed waves, respectively, and F_m and F_r are the wave energy flux based on the rms wave height for the unbroken and reformed waves, respectively. The energy flux, F_b, refers to the wave height that corresponds to incipient breaking at the specific depth given by $H_b = \gamma d$, where γ is the breaker depth index. In equation (9), F_{rms} is the primary unknown that should be solved, implying that α, β, μ, F_m, F_r, and F_b must be supplied in the calculation. Once F_{rms} has been determined everywhere the average energy dissipation per unit surface area is given by $P = \kappa/d\,(F_{rms} - F_{stab})$, which is used to compute the cross-shore sediment transport rate.

For a beach where the depth is decreasing monotonically in the direction of the approaching local wave, the ratio of breaking waves is determined directly from the truncated Rayleigh pdf through

$$\alpha = e^{-F_b/F_x} \tag{11}$$

where F_x is the local rms wave height neglecting wave breaking, and $F_b = 1/8\rho g(\gamma d)^2 C_g$. In order to calculate α, F_x has to be obtained everywhere which is done by solving the wave energy flux equation (equation (5)) without including energy dissipation due to breaking. Thus, in the solution procedure for the wave field two wave transformation equations have to be solved simultaneously, one with and one without energy dissipation. Wave reforming may occur if the beach topography is complex with sections of non-monotonic depth changes. In this case α can not be predicted directly from equation (11), but α is determined based on how the wave reforming is modeled (discussed below).

The ratio of unbroken waves (waves that have never broken) is given by

$$\beta = 1 - e^{-F_b/F_x} \tag{12}$$

if the beach is monotonic in the direction of the local wave. The ratio β can never increase along a wave ray (once a wave breaks it can never become unbroken, only reform), and this requirement may be expressed as

$$\frac{\partial \beta}{\partial x} \geq -\frac{\partial \beta}{\partial y} \tan \theta \tag{13}$$

where θ is the local wave angle, as before. If wave reforming takes place, the energy fluxes employed in equation (12) should refer to the smallest depth the waves passing through a specific point have encountered seaward of this point. However, if this condition is enforced the calculations become exceedingly complex because it will be necessary to keep track of all individual wave rays over the entire grid. Instead, the assumption is made in the model that $\partial \beta / \partial y$ is small, implying that the minimum seaward depth for a non-monotonic beach approximately occurs along the x-line.

The energy flux of the unbroken waves may be calculated from the truncated local Rayleigh pdf according to

$$F_m = \frac{1}{\beta} \left[F_x - (1 - \beta)(F_x + F_b) \right] \tag{14}$$

The energy flux F_m is based on the rms wave height for the unbroken waves. If the waves passing a specific point are reforming at some seaward location the smallest seaward depth should be employed in equation (14) analogous with the case in equation (12). However, the same approximation as discussed above for β is employed in determining F_m after wave reforming: F_m is calculated from transforming the truncated pdf from the minimum depth along the x-line.

In comparison with the model by Larson (1995), a simplified modeling of wave reforming is used. Larson (1995) included a gradual decrease in the ratio of breaking waves along beach sections that were negatively sloping and the entire empirical pdf of the reformed waves were transformed onshore. This technique is rather time consuming, and in the two-dimensional wave model a simpler approach is utilized to achieve a rapid solution of the wave field. Wave reforming is assumed to occur if the beach is negatively sloping and $F_{rms} < F_{stab}$. Furthermore, all waves that are breaking are made to reform instantaneously instead of gradually along the beach as in Larson (1995). The present modifications of the wave reforming were evaluated by comparison with the more detailed model by Larson (1995) for the one-dimensional case. The predicted H_{rms} and average energy dissipation differed only to a small degree for several cases tested using SUPERTANK data (Kraus et al., 1992).

The condition that $F_{rms} < F_{stab}$ may be rewritten as

$$F_{rms} < \beta F_m + \mu F_r + \alpha \left(\frac{\Gamma}{\gamma} \right)^2 F_b \tag{15}$$

The requirement that the slope must be negative if wave reforming occurs should be formulated in terms of the slope along the local direction of the wave propagation. Waves propagating at constant depth (i.e., zero bottom slope) imply a gradual dissipation toward the stable wave height with no reforming. A negative slope in the direction of the waves results in the following condition (compare equation (13))

$$\frac{\partial d}{\partial x} < -\frac{\partial d}{\partial y} \tan \theta \tag{16}$$

As before, in order to simplify the calculations the assumption is made that $\partial d / \partial y$ is small enough to be neglected; thus, the slope along an x-line controls the wave reforming. The energy flux based on the reformed wave height is given by $F_r = 1/8 \rho g (\Gamma d)^2 C_g$. If the reformed waves break again inshore, (that is, $F_r > F_b$) all the reformed waves become breaking waves instantaneously.

If diffraction is neglected the phase function may be determined from equation (7) once the wave number k is known everywhere. For linear water waves the wave number is uniquely given by the wave period and water depth, and k (or the wavelength L) may be calculated directly from the dispersion relationship. Using the observation that the wave number is the magnitude of the wave phase gradient the irrotationality conditions for water waves may be developed to yield the wave number conservation equation according to

$$\frac{\partial}{\partial x}(k\sin\theta) - \frac{\partial}{\partial y}(k\cos\theta) = 0 \tag{17}$$

Thus, after solving equation (17) over the entire grid yielding the local wave angle, equation (9) is employed for determining F_{rms} (note that $\partial S/\partial x = k\cos\theta$ and $\partial S/\partial y = k\sin\theta$ for the case of refraction only). Once F_{rms} is known other quantities needed in the model calculations can easily be derived.

In the numerical solution, equation (17) was rewritten in a slightly different form. Defining a variable $\chi = \sin\theta/C$ (where $C = L/T$), equation (17) may be expressed as

$$\frac{\partial\chi}{\partial x} = \frac{\partial}{\partial y}\left(\sqrt{\frac{1}{C^2} - \chi^2}\right) \tag{18}$$

where $-\pi/2 < \theta < \pi/2$. Solving the wave number conservation equation in terms of χ will be faster than computing θ directly from equation (17). Because the coordinate system should be located so that the y-axis approximately points along the main trend of the bottom contours, it is expected that the change in quantities in the y-direction is considerably smaller than in the x-direction. As will be discussed in Section 3.9, equation (17) is discretized so that the term on the right-hand side somewhat lags the $\partial\chi/\partial x$ term to allow for a rapid and efficient solution scheme. This technique works well for reasonable changes in the contour orientation along the y-axis. However, for complex topographies with large gradients in the y-direction this method may not be accurate enough to yield a robust solution.

3.3. Mean Water Elevation

The steady state momentum equation in the x-direction may be written (Horikawa, 1988) as

$$U\frac{\partial U}{\partial x} + V\frac{\partial U}{\partial y} + F_x - M_x + R_x + g\frac{\partial\eta}{\partial x} = 0 \tag{19}$$

where U and V are the depth-integrated mean velocity components in the x- and y-direction, respectively, F_x the bottom friction term, M_x the lateral mixing term, R_x the wave radiation stress (driving force term), and η the wave set-up (set-down). In the case of bottom contours that run primarily parallel to the y-axis, the mean velocity component U may be neglected (the circulation pattern in the x-direction produces a depth-integrated current that is close to zero), and the convective terms in equation (19) could be dropped. Furthermore, assuming that the bottom friction and lateral mixing is small in the x-direction compared to the other terms, η may be solved for directly in equation (19) if the wave radiation stresses are known.

With the above simplifications, and introducing the expressions for the radiation stresses equation (19) reduces to

$$g\frac{\partial\eta}{\partial x} = -\frac{1}{\rho d}\left(\frac{\partial S_{xx}}{\partial x} + \frac{\partial S_{xy}}{\partial y}\right) \tag{20}$$

where $d = h + \eta$, h is the still water depth, and S_{xx} and S_{xy} are the radiation stresses, defined below. For the case of random waves the average radiation stresses should be employed and these stresses

may be derived by computing the average for a large number of individual waves. The following expressions are obtained for the average radiation stresses

$$S_{xx} = F_{rms} \left(\frac{\cos^2 \theta + 1}{C} - \frac{1}{2C_g} \right) \tag{21}$$

$$S_{xy} = \frac{1}{2} F_{rms} \frac{\sin \theta}{C} \tag{22}$$

In the case of bottom contours that curve significantly along the y-axis, causing a marked net current U in the x-direction, the above simplifications of the momentum equation give a less accurate description of η. Solving for the entire current field would be extremely time consuming and involves the coupled system of two momentum equations (x- and y-direction) and the continuity equation. Thus, the assumption is made that U is sufficiently small to be neglected in equation (19) and η may be calculated by employing the x-momentum equation only.

3.4. Sediment Transport

The concept of cross-shore and longshore sediment transport are well-established and are often employed in engineering numerical models of beach change at the mesoscale (Larson and Kraus, 1995). Cross-shore transport typically refers to the movement of material that takes place perpendicular to the main trend of the bottom contours, where undertow and mass transport by the waves are two important mechanisms controlling the sediment transport. Longshore transport refers to the movement of material along the depth contours, where the longshore current is the main agent for the transport. In general, different predictive equations are employed at the mesoscale for cross-shore and longshore transport depending on the different governing mechanisms. In the ideal case, one equation would be sufficient to describe the transport at each point and from a computational point of view there would be no distinction between cross-shore and longshore transport. Besides the lack of a unifying equation for the sediment transport, such an approach must necessarily rely on microscale quantities (for example, the local velocity, shear stress, and concentration), which would be computationally inefficient to predict in an engineering model. Also, the possibility of obtaining robust estimates of such quantities over longer time periods, at our present state of knowledge of surf zone processes, seems small.

Thus, the technique of calculating cross-shore and longshore transport separately seems justified in engineering models at the mesoscale. However, for a complex bottom topography with markedly curved bottom contours the separation of these two types of transport may not be trivial. In the present model the general contour orientation is determined from a smoothed bottom topography (see Section 3.7) and it is assumed that the cross-shore and longshore transport occurs perpendicular and parallel to the contours, respectively. Before applying the sediment conservation equation to determine depth changes induced by the transport gradients, the transport rates must be transformed into the rectangular x-y coordinate system.

3.4.1. Cross-Shore Sediment Transport

A slightly modified version of the model for the cross-shore transport rate under random waves developed by Larson (1996) is used in the present model. The criterion developed by Larson and Kraus (1989) to distinguish between erosional and accretionary waves under monochromatic waves may be generalized to random waves to predict the direction of transport, and to weigh the influence

of constructive and destructive waves in the Rayleigh pdf. The smallest deep water wave height H_{oc} that causes erosion according to this criterion is

$$H_{oc} = \sqrt{\frac{1}{M} \frac{(wT)^3}{L_o}} \qquad (23)$$

where w is the sediment fall speed, L_o the deep water wavelength, and M an empirical coefficient ($= 0.00070$). Thus, for all waves with $H_o > H_{oc}$ in the deep water Rayleigh pdf erosion is predicted. It is also possible to express H_{oc} with energy fluxes through $F_{oc} = 1/8 \, \rho \, g \, H_{oc}^2 \, C_g$.

A transport function ξ may be defined that sums up the effect on the transport of all individual waves making up the Rayleigh pdf

$$\xi = 2 \frac{e^{-F_{oc}/F_{rmso}}}{\alpha} - 1 \qquad -1 \le \xi \le 1 \qquad (24)$$

where F_{rmso} is the energy flux in deep water. Equation (24) results if the ratio of the accretional/erosional breaking waves is determined, giving the waves equal weight in their contribution to the overall transport. Although equation (24) predicts the direction of transport ($\xi > 0$ implies offshore transport), the magnitude of the transport is not obtained.

Based on the work by Kriebel and Dean (1985) and Larson and Kraus (1989) on the net cross-shore transport rate for monochromatic waves, a predictive equation for random waves was developed by Larson (1996)

$$q_c = K_c \xi \left[D - \alpha \left(D_{eq} - \frac{\varepsilon}{K} \frac{\partial h}{\partial n} \right) \right] \qquad (25)$$

where q_c is the average net cross-shore transport rate, D the average energy dissipation per unit water volume (P/d) and D_{eq} its equilibrium value as defined by Dean (1977), K_c and ε empirical transport coefficients, n a coordinate perpendicular to the bottom contours, and $\partial h/\partial n$ the bottom slope in the n-direction. Equation (25) was derived by linearly superimposing the transport contribution from a large number of individual waves. Seaward of the breakpoint it is assumed that the transport rate decays exponentially with distance offshore from the breakpoint, where the decay rate is a function of the grain size and breaking wave height (Larson and Kraus, 1989). Integration is carried out across the profile to take into account that random waves may imply incipient breaking at any point on the profile (Larson, 1996).

3.5. Longshore Sediment Transport

It is assumed that the longshore current is flowing along the main orientation of the bottom contours and that V may be estimated from a balance between the linearized bottom friction and the driving force along the local contour according to

$$V = \frac{\pi}{2\rho \, c_f \, u_{rms}} \frac{\partial S_{xys}}{\partial s} \qquad (26)$$

where u_{rms} is the amplitude of the horizontal bottom orbital velocity based on H_{rms}, S_{xys} the average radiation stress along the bottom contour, s the coordinate along the contour, and c_f the bottom friction coefficient. Although cross-shore exchange of momentum will occur if there are cross-shore gradients in the mean current, lateral mixing is neglected in the model. Thus, it is assumed that the randomness of the wave field is more important in determining the cross-shore current distribution than any momentum exchange due to current shear. No attempt is made to include the momentum exchange that occurs because of surface rollers (Smith et al., 1993). Because the wave model provides

the mean radiation stress in the x-y system and not with reference to the bottom contour orientation θ_c, a tensor transformation is employed to derive S_{xys}

$$S_{xys} = S_{xy} \left(\cos^2 \theta_c - \sin^2 \theta_c \right) + \left(S_{yy} - S_{xx} \right) \sin \theta_c \cos \theta_c \tag{27}$$

where S_{xx} and S_{xy} are given by equations (21) and (22), respectively, and

$$S_{yy} = F_{rms} \left(\frac{\sin^2 \theta + 1}{C} - \frac{1}{2C_g} \right) \tag{28}$$

The current calculated from equation (26), directed along the main trend of the bottom contours, is used to predict the longshore sediment transport rate. A transport relationship derived by Larson and Hanson (1996) and further developed by Larson and Bayram (2003) is used in the model. A brief derivation of this relationship is given in the following.

It is assumed that the breaking waves generate a steady state vertical concentration profile $c(x, z)$ that is self-similar through the surf zone according to

$$c(x, z) = c_b(x) \, \Psi(z/h) \tag{29}$$

where c_b is a reference concentration taken at $z = -h$ (z originates at the still water level), and Ψ is a shape function. The concentration, c, is taken as the local mass of sediment particles per unit water volume which may be written as

$$c = \frac{dm_s}{dV_{tot}} = \frac{dm_s}{dV + dV_s} \tag{30}$$

where dm_s is the local mass of sediment particles, dV_s the volume of particles, and dV the water volume ($dV_{tot} = dV + dV_s$).

The steady state concentration profile represents a balance between particles that settle and particles that are lifted up by the turbulence created by the breaking waves. Thus, the work done by the fluid on the particles against gravity at a certain level to counteract the settling of particles is

$$dW_s = (\rho_s - \rho) dV_s \, g \, w \tag{31}$$

where ρ_s is the density of the particles. Equation (31) may be rewritten in terms of c

$$dW_s = c \, \frac{\rho_s - \rho}{\rho_s} \, g \, w A dz \tag{32}$$

where equation (30), $dm_s = \rho_s \, dV_s$, and $dV_{tot} = A dz$ were used. Thus, keeping all particles in suspension through the water column requires the total work per unit area and time of

$$W_s = \int_{-h}^{0} c \, \frac{\rho_s - \rho}{\rho_s} \, g \, w \, dz \tag{33}$$

Introducing the expression for c in equation (29) into equation (33) will yield

$$W_s = A_c \, \frac{\rho_s - \rho}{\rho_s} \, g \, w \, c_b \, h \tag{34}$$

where

$$A_c = \int_{-1}^{0} \Psi(z/h)\, d(z/h) \tag{35}$$

Following Kraus et al. (1991), it is assumed that a certain ratio ε_c of the wave energy dissipation P is used for keeping the particles in suspension

$$\varepsilon_c P = A_c \frac{\rho_s - \rho}{\rho_s} g\, w\, c_b\, h \tag{36}$$

Equation (36) yields the following expression for c_b

$$c_b = \frac{\varepsilon_c}{A_c} \frac{\rho_s}{\rho_s - \rho} \frac{1}{g\, w} \frac{P}{h} \tag{37}$$

The local longshore mass transport rate is given as the product between the time-averaged concentration and the longshore current V, which is taken as constant over the water depth

$$\dot{m} = \int_{-h}^{0} V c_b \Psi(z/h)\, dz = A_c\, V c_b\, h \tag{38}$$

where A_c is given by equation (35) and the transport is in mass per unit beach width and time. In order to convert to the volumetric transport q_l

$$q_l = \frac{\dot{m}}{\rho_s} \frac{1}{1-a} \tag{39}$$

where a is the porosity of the sediment.

Combining equations (36), (38), and (39) yields

$$q_l = \frac{\varepsilon_c}{1-a} \frac{1}{\rho_s - \rho} \frac{1}{g\, w} V P \tag{40}$$

As seen from equation (40) the shape function A_c disappears and knowledge of A_c is not needed for calculating the total transport. The expression for the longshore transport resembles the formula by Inman and Bagnold (1963) in the sense that the equation contains a stirring (P) and a transporting part (V). Equation (40) could probably be applied directly for a random wave field as a good approximation. Integrating q_l over the surf zone yields the total longshore transport, and comparison with the CERC formula, assuming a constant V, produces an approximate relationship between ε_c and the transport coefficient K in the CERC formula according to $\varepsilon_c = 0.77 c_f K$. This gives some guidance on how to select the value on ε_c when calculating q_l, although for complex distributions on V, calibration against data might be warranted.

3.6. Swash Zone Sediment Transport

Larson (1996) developed a heuristic equation for calculating the net transport in the swash zone based on the local shear stress and bottom slope. This equation was then generalized to random waves by superimposing a large number of individual swash waves to yield an average transport. Each single wave has a different runup height R, and the pdf for R determines what ratio of the waves that run up passed a specific point on the foreshore. The transport at a point on the foreshore will be a function

of this ratio, since it is only waves passing the point that may contribute to the transport. This method for computing the swash zone transport q_s is, however, fairly time consuming, and a simpler model was developed to allow for rapid computation of q_s.

Assuming that the runup height for an individual wave is related to the surf similarity parameter, the distribution function for the runup height $F(R)$ may be obtained from a transformation of the Rayleigh wave height pdf in the offshore

$$F(R) = 1 - e^{(R/R_{rms})^{2/(1-b/2)}} \tag{41}$$

where

$$R_{rms} = a \left(\tan \beta_s \sqrt{L_o} \right)^b H_{rms}^{1-b/2} \tag{42}$$

where a and b are empirical coefficients, and β_s the foreshore slope. If the runup formula by Hunt (1959) is employed $a = 1$ and $b = 1$, whereas Larson and Kraus (1989) arrived at $a = 1.47$ and $b = 0.79$ from studying the effect of wave runup on beach profiles in large wave tank experiments. Thus, for a selected probability p the corresponding runup height R_p that is exceeded with this probability may be determined from

$$R_p = R_{rms} \left[\ln(1/p) \right]^{(1-b/2)/2} \tag{43}$$

A foreshore slope β_s must be determined before a characteristic runup height is calculated. Here, an average slope is calculated over a predefined stretch of the foreshore; at present, the slope is arbitrarily based on an average taken over a vertical distance of one significant wave height centered around the still water level. The coefficient values for a and b as given by Larson and Kraus (1989) are used. As a representative probability for the runup height $p = 0.10$ is selected, implying that 10% of the waves runup passed this elevation.

Instead of using the more complex expression for the transport on the foreshore that involves summing the contributions at each location from all waves with runup that passed that location, a simplified equation is used that produces a transport rate distribution corresponding to a single representative wave. Larson (1996) derived the following equation for the transport in the swash q_s due to monochromatic waves

$$\frac{q_s}{q_{so}} = \left(1 - \frac{\Delta h}{R} \right)^{3/2} \frac{\tan \beta_s}{\tan \beta_{so}} \tag{44}$$

where q_{so} is the transport rate at the seaward end of the swash zone located at x_{so}, Δh is the elevation at a specific point x_s in the swash zone above x_{so}, β_s is the local slope at x_s, and β_{so} is the local slope at x_{so}. The transport q_{so} is given by the conditions in the surf zone; thus, the derivation of the transport relationship in the swash only gives the shape of the transport rate distribution, and the magnitude is determined by the wave energy dissipation at the shoreward end of the surf zone. For a plane-sloping foreshore equation (44) may be reduced to

$$\frac{q_s}{q_{so}} = \left(\frac{x_s - x_r}{x_{so} - x_r} \right)^{3/2} \tag{45}$$

where x_r is the location of the runup height (determined from equation (43)).

The model employs equation (45) to determine the distribution of the net transport rate in the swash zone, implying that the average foreshore slope rather than the local slope is used to determine the transport rate q_s. Although the simplified method to compute q_s yields the shape of the transport rate distribution for a monochromatic (representative) wave, the magnitude of the transport rate is

given by the conditions in the surf zone that are determined by a random model. Thus, the randomness of the wave field is also reflected in the swash zone transport rate even though the shape of the distribution is derived through a simplified approach.

The magnitude of the net transport rate at the seaward end of the swash zone q_{so} is calculated from the transport rate in the x- and y-directions at the shoreward end of the surf zone (q_{xs} and q_{ys}, respectively)

$$q_{so} = \sqrt{q_{xs}^2 + q_{ys}^2} \tag{46}$$

The shape of the swash zone transport rate distribution as given by equation (45) is assumed to give the transport rate in a direction defined by

$$\theta_{qs} = \arctan(q_{ys}/q_{xs}) \tag{47}$$

Thus, before the swash zone transport can be employed to compute depth changes on the foreshore through the sediment volume conservation q_s must be transformed to the x-y system according to

$$q_{sx} = q_s \cos\theta_{qs} \tag{48}$$

$$q_{sy} = q_s \sin\theta_{qs} \tag{49}$$

3.7. Contour Orientation

As previously discussed the cross-shore and longshore transport rates are computed with respect to the main contour orientation, after which a coordinate transformation is performed to obtain the transport in the fixed x-y system. The main assumption is that the current responds to the morphology over some representative length scale, and a contour orientation should be determined that corresponds to this scale. Thus, minor changes in the contour orientation are not expected to significantly alter the flow of the current, unless there is a clear trend in the orientation. Selecting a robust method for determining the contour orientation is of importance for obtaining a realistic feedback between the waves and the bottom topography. If the interaction between the waves and the bottom is not correctly modeled, the evolution of the topography will not be realistic.

The orientation of the bottom contour at a specific depth is defined by

$$\theta_c = \arctan\left(\frac{\partial h/\partial y}{\partial h/\partial x}\right) \tag{50}$$

where θ_c is the angle between the x-axis and the normal to the bottom contour. This angle is used in equation (27) to obtain the radiation stress along the local contour from which the longshore current and the sediment transport may be computed. Also, the direction of the cross-shore transport is taken to be perpendicular to the contours (in the direction of the normal). If the actual bottom topography is employed in the calculation of the transport rate, the directions of the cross-shore and longshore transport will change according to the local estimate of θ_c. For a complex bottom topography, the local values of θ_c may produce spatial changes in the transport direction at a high rate that are non-physical and that will cause an unrealistic beach evolution.

A more realistic approach is to smooth or filter the topography so that only the main features remain in determining the contour orientation (still using equation (50)). The question then arises over which length scale smoothing should be performed. Because the computed contour orientation should be representative for the main direction of the current, it is the tendency for the current to respond to the topography that determines the appropriate length scale for the smoothing. Typically the length step in the model in the y-direction is much larger than in the x-direction, since changes in the topography along the y-axis (the main trend of the bottom contours) occur at a much lower rate

than along the x-axis. In computing θ_c equation (50) is discretized based on the model length step (Δx and Δy in the x- and y-directions, respectively), and since Δy often is of a magnitude compatible to the length scale of the alongshore current, smoothing in the y-direction is not necessary. In the x-direction, however, a small Δx may resolve morphological features of interest that have little influence on the overall current direction. In this case, smoothing of the topography before calculating the contour orientation is necessary.

The wave calculation is performed for a smoothed topography to achieve a more realistic response of the waves to the bottom topography. Larson and Kraus (1989) used a moving average scheme to determine the smoothed topography by averaging the depth over a number of calculation cells corresponding to $3H_b$. Here, a similar scheme is employed in the wave calculation. It should be pointed out that the smoothed beach topography is used only for computing the wave properties and that no smoothing is made of the original topography when determining the beach evolution. Regarding the smoothing of the topography for calculating a θ_c representative of the current, it is expected that the direction of the generated current would be less sensitive to the bottom topography than the waves, and thus the smoothing should be carried out over a larger number of cells than for the waves. The waves passing over the local topography are expected to respond to features such as longshore bars, whereas the direction of the current is expected to be relatively unaffected by any local bottom slopes that appear as a result of features of that scale. The magnitude and distribution of the current is to a large degree determined by the waves, and thus by the topography smoothed at the scale of the waves, but the direction of the current is a function of the topography at a larger scale.

The contour orientation is computed based on a topography that is smoothed over about $20H_{rmso}$, which corresponds to approximately 1/4–1/2 of the most active part of the surf zone. Smoothing over several different length scales was investigated in the model, and this criterion seemed to provide a stable beach evolution for the cases studied.

3.8. Sediment Volume Conservation

After calculating the net transport rate in the x- and y-directions over the entire grid, the following sediment volume conservation equation is employed to determine the depth changes (Watanabe, 1982)

$$\frac{\partial h}{\partial t} = \frac{\partial}{\partial x}\left(q_x - \varepsilon_s \,|q_x|\,\frac{\partial h}{\partial x}\right) + \frac{\partial}{\partial y}\left(q_y - \varepsilon_s \,|q_y|\,\frac{\partial h}{\partial y}\right) \tag{51}$$

where ε_s is an empirical coefficient. This equation incorporates the effects of slope on the sediment transport, limiting unrealistic growth of features that could occur under certain conditions. The bottom topography is updated at each time step based on the computed depth changes. A check is also made of the slopes over the grid to detect if the angle of repose is exceeded anywhere; if this is the case avalanching is initiated so that material is redistributed down to a lower stable slope. However, since the forcing is more evenly distributed under random waves compared to monochromatic waves and the slope terms are included in equation (51), the growth of the slopes is limited and avalanching typically does not occur. Avalanching may occur on the foreshore if the wave conditions are such that the runup height remains fairly constant (shoreward boundary fixed) and the foreshore gradually becomes steeper.

3.9. Numerical Solution Scheme

The governing equations are written in finite-difference form and solved through an explicit method. Although an implicit method would allow larger length step and be unconditionally stable, the wave transformation model is more easily solved using an explicit technique. The calculation proceeds to different shoreward locations for different x-lines depending on the intersection between the foreshore topography and the set-up, which would be difficult to handle in a straightforward manner

in an implicit scheme. Furthermore, wave reforming would require iteration at a specific y-line until obtaining a solution where the grid points of wave reforming were determined. Another problem is that some equations, such as the wave number conservation equation, are nonlinear in the dependent variable and will not be easily solved using an implicit technique, unless they are approximated by linear expressions.

The explicit solution method employed starts at the seaward end of the grid where boundary values are provided and proceeds onshore, solving for the unknown quantities at a certain y-line based on the known values at the last line. All derivatives in the y-direction are taken at the previous y-line and thus lag the x-derivatives by $\Delta x/2$ in the seaward direction. The explicit method only makes it necessary to store the calculated quantities at two y-lines saving a considerable amount of computer storage. The only quantities that are stored for every grid point during the calculations are q_x, q_y, and h. All major quantities are calculated in the middle of a cell except q_x and q_y that are obtained at the boundary between the calculation cells.

The main disadvantage of the explicit scheme is that it cannot accommodate gradients in the y-direction that vary greatly in the x-direction because of the spatial lag introduced in the discretization. However, because some portions of the model still rely on changes in the y-direction to occur with a fairly mild gradient, the explicit scheme does not constitute a serious restriction to the use of the model. Furthermore, for complex bottom topographies with strong gradients perpendicular to the wave propagation, it is more important to include diffraction effects than to improve the numerical solution scheme of the wave transformation equations.

In the numerical solution strategy, the wave number conservation equation (equation (18)) is first solved yielding the angles at the next (shoreward) y-line. The average wave energy flux F_{rms} is then obtained from equation (9). In order to determine the ratio of breaking waves (α), equation (9) is also solved without the energy dissipation term and α is calculated from equation (11). Since α is needed in computing F_{rms}, the calculation of the energy flux neglecting wave breaking has to precede the solution of equation (9). A check is made for wave reforming at each grid point using the criterion according to equation (15) and the condition that the slope must be negative, and if this is the case all breaking waves are made to reform at this point. The mean water elevation d $(= h + \eta)$ used in the calculation of the wave properties on the next y-line involves the set-up (η) from the preceding y-line to avoid iteration between the two lines. Under random waves the set-up tends to vary rather slowly over the topography, and this approximation will in general be sufficient. Thus, the x-momentum equation (equation (20)) is solved for the next line to yield η after equation (9) has been solved.

Several different wave-related quantities that are needed in the sediment transport calculations, such as the radiation stresses and the energy dissipation, are computed on the next line after equation (9) has been solved. The net cross-shore transport rate is determined from equation (25), where the average energy dissipation per unit water volume is calculated from $D = \kappa/d^2(F_{rms} - F_{stab})$. The slope-dependent term in equation (25) is determined from the gradient in the direction perpendicular to the bottom contours. Before calculating the longshore transport from equation (40) the longshore current is determined from equation (26), where the driving term is obtained through the tensor transformation given by equation (27). Because the cross-shore and longshore transport are assumed to be directed perpendicular and parallel, respectively, to the main orientation of the bottom contours, a transformation to the fixed x-y system is needed before the sediment volume conservation equation is employed to calculate depth changes. Equation (50) is used to compute the main orientation of the bottom contours for a topography smoothed over about $20 H_{rmso}$.

As input to the model, a time series of H_{rms}, T, θ, and Δh (deviation from the mean still water level) should be provided at some offshore point where a Rayleigh pdf is a good description of the variation in wave height. The boundary values at the seaward end of the grid are obtained by transforming the waves from the offshore point assuming plane and parallel bottom contours seaward of the grid and neglecting wave breaking. At the lateral boundaries, the local bottom contours are

extrapolated based on the orientation of the contours adjacent to the boundary. This procedure determines the wave angles at the boundaries through the wave number conservation equation. In the wave energy flux conservation equation it is assumed that $\partial(F_{rms} \sin\theta)/\partial y = 0$ at the lateral boundaries; this implies that wave energy can freely flow in and out over the lateral boundaries. However, for the case of a groin at the boundary it means that all energy transported along the y-axis toward the groin is completely dissipated and no energy is reflected back into the grid. As previously mentioned, the location of the shoreward boundary is determined by the intersection between the set-up and the local foreshore topography. In the case that the calculation has stopped at a neighboring x-line the derivatives in the governing equations must be discretized right- or left-adjusted. If the calculation has stopped at both neighboring x-lines plane and parallel bottom contours are assumed, that is, the y-derivatives are set to zero in the equations.

In the sediment transport and depth change calculations it is assumed that the transport is zero at the shoreward and seaward boundary. If the grid extends into deep enough water with respect to the wave conditions, the transport should decay down to zero before reaching the seaward end of the grid. At the lateral boundaries two different conditions may be specified regarding the transport rate q_y in the y-direction, that is, $q_y = $ constant for an open coast, and $q_y = 0$ for an impermeable groin. In the latter case the length of the groin must be specified, and if the groin does not extend to the end of the grid the transport seaward of the groin tip will bypass the groin. The material is free to move in the x-direction at the lateral boundaries.

4. MODEL SIMULATIONS

The theoretical formulations of the various components in the model have been validated toward laboratory and field data in several previous studies, although in most cases the validation was carried out for one-dimensional situations. For example, the random wave model was investigated by Larson (1996); the current model by Larson and Kraus (1991) and Smith et al. (1993); the cross-shore transport model by Larson and Kraus (1989), Larson (1996), and Wise et al. (1996); and the longshore transport model by Larson and Bayram (2003). However, since most of the modules were not validated for the two-dimensional case or for simulations when the modules are functioning together, additional validation was needed.

High-quality data on topographic change are scarce, so initially the model was tested for a wide range of hypothetical cases to check if model performance qualitatively was in accordance with the expected behavior. Here, an example concerning the accumulation updrift a groin or jetty is discussed. Furthermore, two data sets obtained in connection with beach fill projects at Ocean City, Maryland, and Sylt Island, Germany, were used for model validation. Detailed beach profile surveys together with wave and water level data were available from these sites. The results of the model simulations are briefly summarized as well as some background information about the sites and the fill projects.

4.1. Accumulation Updrift a Jetty

The numerical model was employed to calculate the beach topography evolution updrift a groin or jetty that completely blocks the alongshore transport (i.e., the groin/jetty is infinitely long). A hypothetical case was selected since no actual data were available. An initial, uniform topography was generated by using the starting profile from a SUPERTANK Project run (Test ST10; see Kraus and Smith, 1994). The computational grid encompassed 69 x 10 points with a cell size of 1 x 10 m (x- and y-direction, respectively), and the jetty was located immediately downdrift the first profile line ($y = 0$). A constant wave input was used with $H_{rms} = 0.57$ m and $T = 3.0$ s (in 3 m water depth) and the median grain size was 0.22 mm. The incident wave angle was set to 45 degrees, which

produced transport toward the jetty and significant accumulation in this area. The jetty boundary condition implies $q_y = 0$ along the boundary cells, whereas exchange of material may still occur in the x-direction. Model calculations were made with the same coefficient values as for the Ocean City simulations (discussed in Section 4.2.1).

Fig. 1 shows the calculated bottom topography after 600 time steps ($\Delta t = 20$ min). The accumulation at the jetty is marked, and the blocking effect propagates updrift producing contour lines that curve offshore approaching the jetty. Above the still water level a plateau is built up, and outside the surf zone the profile depths increase at a high rate along the jetty. The slope in this latter region becomes quite steep due to the constant wave input. There is an indication of a longshore bar, although the accumulation due to the gradients alongshore smooths the topography. Fig. 2 is a contour plot of the topography displayed in Fig. 1 where the transport vectors are shown. The transport follows the local contour orientation and the highest magnitudes are found adjacent to the jetty where the surf zone is most narrow due to the profile shape (note that the jetty is located immediately downdrift
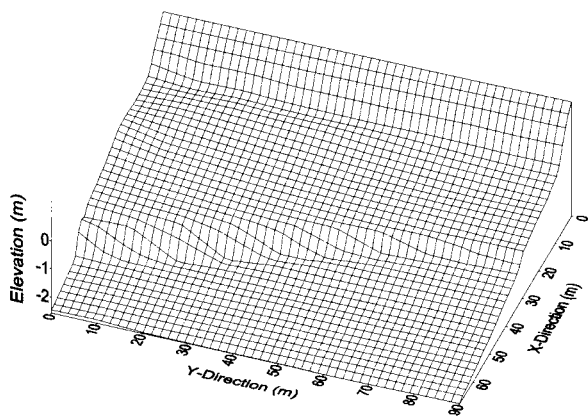
Figure 1. Calculated topography updrift a jetty (infinite jetty located on the left side; transport from right to left).
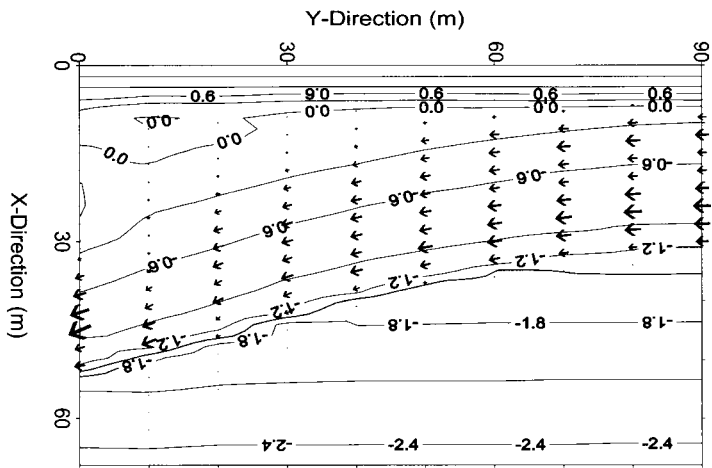
Figure 2. Calculated bottom contours and transport vectors updrift a jetty.

$y = 0$). The cross-shore transport at the updrift end of the grid ($y = 90$) is close to zero across the profile since near equilibrium conditions have developed. Closer to the jetty, accumulation of sand occurs due to the decrease in the longshore transport rate approaching the jetty. This accumulation causes changes in the profile shape that implies marked cross-shore transport as the profile continuously strives toward equilibrium.

4.2. Responses of Beach Fill

4.2.1. Ocean City, Maryland

In order to provide beach erosion control along the northern Atlantic Coast of Maryland and to protect the town of Ocean City, a large beach nourishment project was jointly undertaken by the State of Maryland and the US Army Corps of Engineers (CE) in the late 1980's (Stauble et al., 1993). The project was carried out as two separate beach fill operations: the State of Maryland placed one fill during the summer of 1988 (state fill) and the other fill was placed by the CE during the summer of 1990 (federal fill). The state fill consisted of about $2 \cdot 10^6 \, \mathrm{m}^3$ of sand and the federal fill of almost 3 $10^6 \, \mathrm{m}^3$. Approximately 13 km of beach were nourished involving an area from just north of Ocean City Inlet to the Maryland-Delaware state line (see Fig. 3).

The long-term shoreline recession in the area is related to a divergence in the longshore transport in the vicinity of Bethany Beach (north of the fill area) on Fenwick Island, where there is a change in the orientation of the coast, and the net transport to the south causes an impoundment on the north jetty at Ocean City Inlet (Dean and Perlin, 1977). Stauble et al. (1993) reported an average shoreline recession rate for Fenwick Island from Ocean City Inlet to the state line of 0.6 m/year, ranging between 0 and 1.2 m/year. The sediment trapping capacity of the north jetty has effectively

(a)   (b)
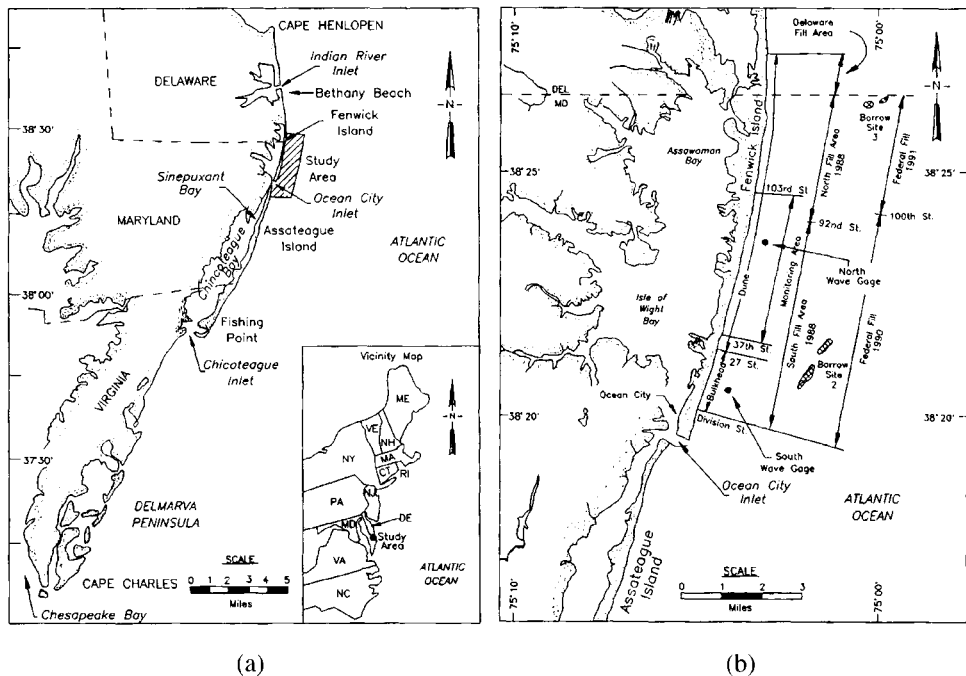
Figure 3. Schematic maps of the Ocean City area showing: (a) the location of the nourishments, and (b) a detail of the nourishment site (from Stauble et al., 1993).

reached its maximum, and most of the sediment transported southward is presently bypassing the jetty (Stauble et al., 1993). This sediment deposits in the entrance channel of the inlet, settles on the ebb-tidal shoal, or bypasses the inlet and supplies northern Assateague Island with material. Sediment periodically dredged from the entrance channel are placed on the northern end of Assateague Island. Previous studies indicated that the annual net longshore transport rate to the south varies between 100,000 and 250,000 m^3.

The State of Maryland, the U.S. Army District in Baltimore, and the Coastal Engineering Research Center (CERC) of the CE carried out a detailed monitoring program in connection with the placement of the two beach fills. The monitoring program encompassed beach profile measurements, sediment sampling, and wave and tide data collection. Profile surveying using a towable sled started in June 1988 immediately before the state fill was placed and continued until July of 1993. For the numerical modeling study a subset of the survey data from the center of the fill area was used consisting of 10 lines spaced approximately 500 m apart. Material to the fills was taken from two borrow areas located off the coast; the representative grain sizes for the two areas were 0.25 mm and 0.35 mm. Anders and Hansen (1990) developed a composite grain size for the native beach of 0.37 mm. During the measurement period several major storms passed through the Ocean City area (Dolan et al., 1990; Kraus, 1993), providing an excellent opportunity to evaluate the response of the fills during storm conditions.

The data from Ocean City were employed to evaluate the performance of the numerical model regarding the topographic response of a beach fill. Between January and April of 1989 several large storms occurred in the area causing severe beach erosion with a marked shift of material toward the offshore. Fig. 4 shows the difference in elevation between the measured April and January topographies, where a negative value (shaded area) denotes erosion. This period was selected for testing with the numerical model.

The numerical model was employed using 61 x 15 grid points with a cell size of 5 x 410 m (in the x- and y-direction, respectively). A time step Δt of 20 min was used in the calculations and a representative grain size of 0.26 mm was selected. The main model parameters were set to their standard values as determined from applications in previous cross- and longshore modeling (Larson and Hanson, 1996; Larson, 1996; Larson and Bayram, 2003), and no specific calibration was performed. The measured time series of wave height and period was used as input (in 10 m water depth). However, no water level data were available and only limited information on the incident wave angle. Synthetic water level data were generated from information about the tide at Ocean City
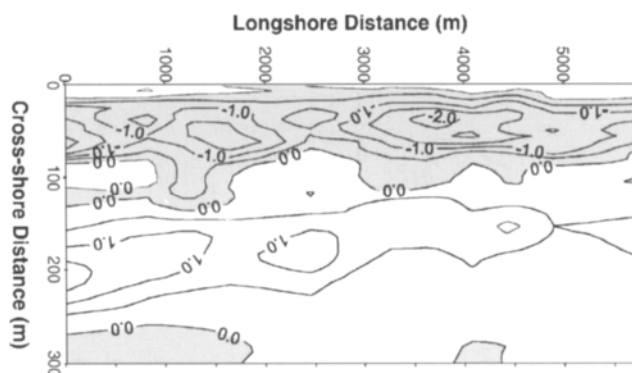
Figure 4. Measured difference in elevation for the studied area at Ocean City, MD between January and April 1989 (shaded areas denote negative changes).

Longshore Distance (m)
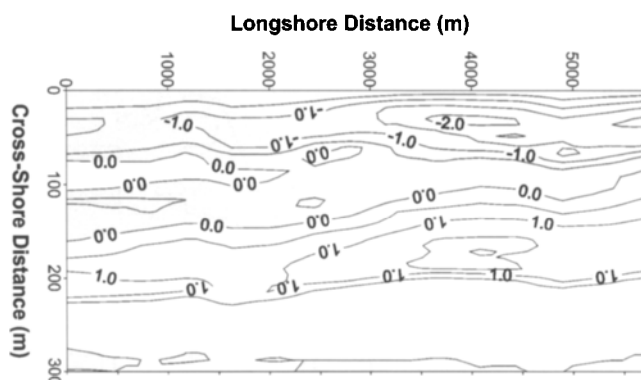
Figure 5. Calculated difference in elevation for the studied area at Ocean City, MD between January and April 1989 (shaded areas denote negative changes).

and using an empirical equation to relate storm surge level to wave height. A mean incident wave angle of 10 degrees with respect to shore normal was used to simulate the longshore transport.

Fig. 5 displays the calculated difference in elevation between the April and January topographies. The general shift of the material from the nearshore to the offshore is well captured, both qualitatively and quantitatively, although the numerical model tends to produce less alongshore variation in the profile response. The tendency for the model to smooth the topography more than what actually occurred is primarily caused by the fact that transport rates are based on the main features of the topography and that the rates are not overly sensitive to local variations. Another reason for the discrepancy between the measurements and the model predictions is limitations in the model to describe the effects of an offshore shoal (Stauble et al., 1993) that attaches to the shoreface in the model area.

4.2.2. Sylt Island, Germany

The Island of Sylt is a well-known beach resort on the German North Sea coast that has suffered severe erosion at least since the middle of the last century (Dette, 1977; Dette and Gärtner, 1987). Storms with large waves in combination with high water levels are causing erosion and retreat of the dunes. The eroded material is temporarily deposited in the nearshore after which the material is transported by longshore currents toward the ends of the island. Based on the mean yearly dune recession rates (1952 to 1984) the annual sand losses over ends of the island by longshore transport were estimated to be 1.0 million and 0.5 million m^3 at the northern and southern ends, respectively (Dette and Newe, 1997). Over the last hundred years the coastline has receded about 1 m/year on the average (Dette, 1977). The coastline retreat has been larger toward the ends of the island, and it has increased in recent years due to an increased frequency of high-water events (Dette and Newe, 1997).

Different types of structural solutions (seawalls, revetments, groins, etc.) have been applied at Sylt to prevent the erosion, but most measures were not successful (Dette, 1977). In the beginning of the 1980's it was decided to halt further erosion of the dunes and high cliffs by exclusively using beach nourishment. In order to implement this policy beach fills have been placed along selected stretches of the island. Two such locations where fills were placed are Kampen/Wenningstedt in the northern part of the island and Rantum in the southern part (see Fig. 6). At these sites detailed topographic surveys were undertaken in connection with the fill placements making it possible to determine the fill response at different scales in time and space (Larson et al., 1999). The material used for the fills
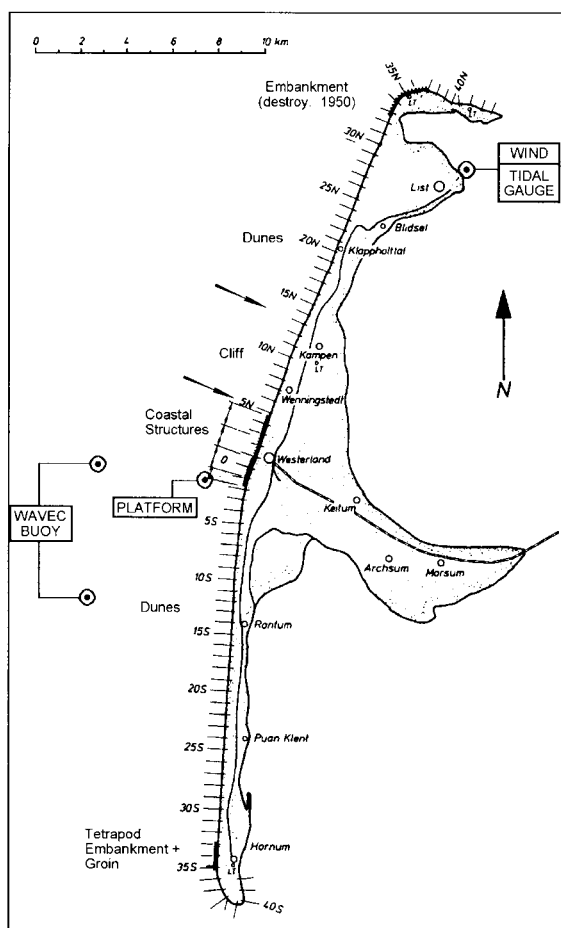
Figure 6. Schematic map of the Island of Sylt located on the German North Sea Coast where several nourishment projects have been performed (after Dette and Newe, 1997).

was taken offshore the island in about 20 m water depth. The grain size varies substantially in the area, both in the cross-shore and longshore direction, with typical median grain sizes in the range 0.30 to 0.50 mm.

In 1985 the beach at Kampen was nourished with about $2 \cdot 10^6$ m^3 of sand along a 4.5 km stretch of the coast. The material had a median grain size of 0.53 mm and it was placed as a beach depot fill in front of the cliff (Führböter and Dette, 1992). Profile surveys using an echosounder were made at a high spatial resolution before the fill placement and at six dates after the fill placement, in total spanning a time period of about six years. In this study a data subset encompassing 43 survey lines in the northern part of the fill area was employed for the numerical modeling. A smaller fill was also added at the end of the cliff in 1987 encompassing about $0.3 \cdot 10^6$ m^3 along 0.6 km of the coast.

Shortly after the placement of the fill at Kampen several storms eroded away a large portion of the fill, and in the beginning of 1990 another series of storms eroded the remaining portion of the fill. A detailed data set exists from these latter storms and this set was employed to further test the

Longshore Distance (m)
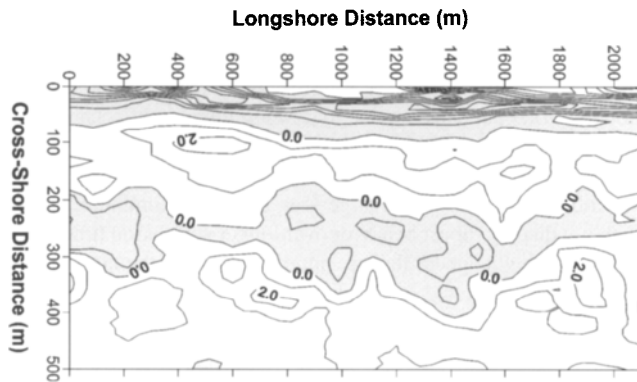
Figure 7. Measured difference in elevation for the studied area at Sylt Island between September 1989 and May 1990 (shaded areas denote negative changes).

Longshore Distance (m)
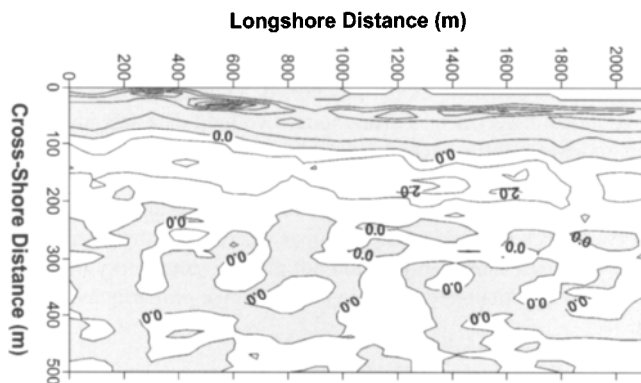
Figure 8. Calculated difference in elevation for the studied area at Sylt Island between September 1989 and May 1990 (shaded areas denote negative changes).

numerical model. Topographic surveys made in September 1989 and May 1990 were used as input and for comparison with calculation results, respectively. Wave and water level data were available on an hourly basis. The grid consisted of 149 x 22 grid points with a cell size of 5 x 100 m (in the x- and y-directions, respectively), and the calculation time step was set to 30 min. A representative grain size of 0.25 mm was selected and the same model parameter values as for the Ocean City simulations were employed.

Fig. 7 displays the measured change in bottom elevation between May and September, and Fig. 8 shows the corresponding calculated change. Overall, the result exhibits the same characteristics as the Ocean City simulations: the erosion of the foreshore and dune regions are fairly well reproduced together with the associated deposition in shallow water. Changes in the offshore and effects related to alongshore variations in morphological features are not described by the model. At Sylt rhythmic features of varying spatial scales are often present, which affects the patterns of erosion and deposition.

5. CONCLUDING REMARKS

Shoreline and profile evolution models have routinely been applied in engineering projects for the last ten years. Although efforts have been made to develop topographic change models that include both the evolution of the shoreline and the profile, many of these models have their limitations. The models are often complicated to run (expert knowledge is needed), require extensive computational resources (fully 3-D models applied over a large area and long simulation time are computationally intensive), and do not display robust behavior over longer simulation times (instabilities develop and morphological features might appear that are purely artifacts of the numerical solution scheme). Here, a numerical model was presented to simulate the topographic evolution without some of the drawbacks associated with previous modeling efforts. Thus, the model is fast to run, robust in describing the beach evolution, and does not require significant expertise to apply.

The model consists of sub-modules to calculate waves, mean water elevation, longshore current, cross-shore transport, longshore transport, swash zone transport, and beach change. Cross-shore and longshore transport are computed separately based on the local orientation of the contour lines defined over a certain length scale. This approach implies a decoupling of cross-shore and longshore processes. However, it significantly decreases the time required for computations and improves model robustness.

All the sub-modules have previously been validated with laboratory and field data, although in most cases for the one-dimensional situation. In order to further test and validate the sub-modules, as well as investigating how the complete model functioned, a number of hypothetical cases were simulated for qualitative model assessment. Furthermore, two field data sets involving the response of beach nourishments to severe storms were employed for quantitative comparison. The hypothetical cases showed that the model could reproduce the main features of the topographic evolution updrift a jetty or groin. Comparisons for the field data sets indicated that the model yielded accurate predictions of the observed beach changes, except in areas where some rhythmic features were present. However, the open coast cases simulated here did not provide satisfactory means for evaluating the capability of the model to quantitatively simulate beach change primarily associated with longshore sediment transport.

ACKNOWLEDGMENTS

LIST OF SYMBOLS

a — wave amplitude (m) (also porosity)
b — empirical coefficient in runup height formula
A — area (m^2)
A_c — integral of shape function
c — suspended sediment concentration (kg/m^3)

c_b	—	reference concentration (kg/m^3)
c_f	—	bottom friction coefficient
C	—	phase speed (m/s)
C_g	—	group speed (m/s)
d	—	water depth (m)
D	—	energy dissipation due to wave breaking per unit water volume (Nm/m^{3}s)
D_{eq}	—	equilibrium value of D (Nm/m^{3}s)
F	—	wave energy flux (Nm/ms)
F_b	—	wave energy flux based on H_b (Nm/ms)
F_m	—	wave energy flux based on rms wave height for unbroken waves (Nm/ms)
F_{oc}	—	wave energy flux based on H_{oc} (Nm/ms)
F_r	—	wave energy flux based on rms wave height for reformed waves (Nm/ms)
F_{rms}	—	wave energy flux based on H_{rms} (Nm/ms)
F_{rmso}	—	wave energy flux based on H_{rmso} (Nm/ms)
F_s	—	stable wave energy flux (Nm/ms)
F_{stab}	—	stable wave energy flux for random waves (Nm/ms)
F_x	—	wave energy flux neglecting wave breaking (Nm/ms) (also bottom friction term; m/s^2)
g	—	acceleration of gravity (m/s^2)
h	—	still water depth (m)
H	—	wave height (m)
H_b	—	wave height at incipient breaking (m)
H_o	—	deep water wave height (m)
H_{oc}	—	smallest deep water wave height to cause erosion (m)
H_{rms}	—	rms wave height (m)
H_{rmso}	—	rms wave height in deep water (m)
k	—	wave number (m^{-1})
K	—	empirical longshore transport rate coefficient (from the CERC formula)
K_c	—	empirical cross-shore transport rate coefficient
L	—	wavelength (m)
L_o	—	deep water wavelength (m)
m_s	—	mass of sediment particles (kg)
M	—	empirical coefficient for transport direction
M_x	—	lateral mixing term (m/s^2)
n	—	coordinate perpendicular to the bottom contours (m)
p	—	probability
P	—	wave energy dissipation due to breaking (Nm/m^{2}s)
q_c	—	cross-shore sediment transport rate (m^3/ms)
q_l	—	longshore sediment transport rate (m^3/ms)
q_s	—	swash zone sediment transport rate (m^3/ms)
q_{so}	—	sediment transport rate at the seaward end of the swash zone (m^3/ms)
q_x	—	sediment transport rate in the x-direction (m^3/ms)
q_y	—	sediment transport rate in the y-direction (m^3/ms)
R	—	runup height (m)
R_p	—	runup height exceeded with a probability p (m)
R_{rms}	—	runup height determined based on H_{rms} (m)
R_x	—	wave radiation stress term (m/s^2)
s	—	length (m) (also coordinate parallel to the bottom contours; m)

S	—	phase function
S_{xx}	—	radiation stress (N/m)
S_{xy}	—	radiation stress (N/m)
S_{xys}	—	radiation stress (directed parallel to the bottom contours) (N/m)
S_{yy}	—	radiation stress (N/m)
t	—	time (s)
T	—	wave period (s)
u_{rms}	—	amplitude of horizontal bottom orbital velocity (m/s)
U	—	mean velocity in the x-direction (m/s)
V	—	mean velocity in the y-direction (also mean longshore current velocity) (m/s)
V_s	—	volume of sediment particles (m^3)
V_{tot}	—	total volume of water and sediment particles (m^3)
w	—	sediment fall speed (m/s)
W_s	—	work required to keep sediment particles in suspension (Nm/m^2s)
x	—	coordinate in a rectangular system (m)
x_s	—	coordinate in the swash zone (m)
x_{so}	—	location of the seaward end of the swash zone (m)
x_r	—	location of the runup height (m)
y	—	coordinate in a rectangular system (m)
z	—	vertical coordinate (m)
α	—	ratio of breaking waves
β	—	ratio of unbroken waves
β_s	—	foreshore slope
β_{so}	—	foreshore slope at the seaward end of the swash zone
γ	—	breaker depth index
ε	—	empirical slope-related transport coefficient
ε_c	—	empirical longshore transport coefficient
ε_s	—	empirical coefficient describing the effects of slope on sediment transport
η	—	wave set-up (set-down) (m)
χ	—	$\sin\theta/C$ (s/m)
Φ	—	complex wave potential function (m)
Γ	—	empirical stable wave height coefficient
κ	—	empirical wave decay coefficient
μ	—	ratio of reformed waves
ρ	—	water density (kg/m^3)
ρ_s	—	sediment density (kg/m^3)
σ	—	angular frequency (s^{-1})
ξ	—	cross-shore transport function
θ	—	local wave angle
θ_c	—	bottom contour orientation
θ_{qs}	—	transport direction in the swash zone
Ψ	—	shape function for suspended sediment concentration

REFERENCES

Anders, F., and Hansen, M., 1990. Beach and borrow site sediment investigation for a beach nourishment at Ocean City. Technical Report CERC-90-5. Vicksburg, MS: US Army Engineer Waterways Experiment Station, Coastal Engineering Research Center.

Bakker, W.T., 1968. The dynamics of a coast with a groin system. Proceedings of the 11th International Conference on Coastal Engineering, ASCE, pp. 492–517.

Berkhoff, J.C.W., 1972. Computation of combined refraction-diffraction. Proceedings of the 16th International Conference on Coastal Engineering, ASCE, pp. 471–490.

Berkhoff, J.C.W., Booy, N., and Radder, A.C., 1982. Verification of numerical wave propagation models for simple harmonic linear water waves. Coastal Engineering, 6: 255–279.

Brøker-Hedegaard, I., Deigaard, R., and Fredsøe, J., 1991. Onshore/offshore sediment transport and morphological modelling of coastal profiles. Proceedings of Coastal Sediments '91, ASCE, pp. 15–27.

Dally, W.R., 1990. Random breaking waves: A closed-form solution for planar beaches. Coastal Engineering, 14: 233–263.

Dally, W.R., 1992. Random breaking waves: Field verification of a wave-by-wave algorithm for engineering application. Coastal Engineering, 16: 369–397.

Dally, W.R., Dean, R.G., and Dalrymple, R.A., 1985. Wave height variation across beaches of arbitrary profile. Journal of Geophysical Research, 90 (C6): 11,917–11,927.

Dean, R.G., 1977. Equilibrium beach profiles: U.S. Atlantic and the Gulf Coasts. Newark, DE: Department of Civil Engineering, Ocean Engineering Report No. 12, University of Delaware.

Dean, R.G. and Perlin, M., 1977. Coastal engineering study of Ocean City Inlet, Maryland. Proceedings of Coastal Sediments '77, ASCE, pp. 520–542.

Dette, H.H., 1977. Effectiveness of beach deposit nourishment. Proceedings of Coastal Sediments '77, ASCE, pp. 211–227.

Dette, H.H., and Gärtner, J., 1987. Time history of a seawall on the Island of Sylt. Proceedings of Coastal Sediments '87, ASCE, pp. 1006–1022.

Dette, H.H., and Newe, J., 1997. Depot beach fill in front of a cliff. Monitoring of a nourishment site on the Island of Sylt 1984–1994. Draft Report. Braunschweig, Germany: Leichtweiss Institute, Technical University of Braunschweig.

Dolan, R., Inman, D.L., and Hayden, B., 1990. The Atlantic Coast storm of March 1989. Journal of Coastal Research, 6 (3): 721–725.

Führböter, A., and Dette, H.H., 1992. Strandvorspülungen vor der Westküste von Sylt. Die Küste, Archiv für Forschung und Technik an der Nord- und Ostsee, Heft 53, pp. 51–126.

Ebersole, B.A., Cialone, M.A., and Prater, M.D., 1986. Regional coastal processes numerical modeling system. Technical Report CERC-86-4. Vicksburg, MS: Coastal Engineering Research Center, Waterways Experiment Station.

Hanson, H., 1989. Genesis—A generalized shoreline change numerical model. Journal of Coastal Research, 5 (1): 1–27.

Hanson, H., Gravens, M., and Kraus, N.C., 1988. Prototype applications of a generalized shoreline change numerical model. Proceedings of the 21st International Conference on Coastal Engineering, ASCE, pp. 1265–1279.

Hanson, H., and Kraus, N.C., 1986. Forecast of shoreline change behind multiple coastal structures. Coastal Engineering in Japan, 29: 195–213.

Hanson, H., and Larson, M., 1999. Extension of GENESIS into the cross-shore dimension. From 1-Line to N-Line. Proceedings of the 5th International Conference on Coastal and Port Engineering in Developing Countries (COPEDEC), pp. 312–323.

Hanson, H., and Larson, M., 2000. Simulating shoreline evolution using a new type of N-Line model. Proceedings of the 27th International Conference on Coastal Engineering, ASCE, pp. 2808–2821.

Horikawa, K. (ed.), 1988. Nearshore Dynamics and Coastal Processes. Theory, Measurement, and Predictive Tools. Tokyo, Japan: University of Tokyo Press.

Hughes, S.A., and Borgman, L.E., 1987. Beta-Rayleigh distribution for shallow water waves. Proceedings of Coastal Hydrodynamics '87, ASCE, pp. 17–31.

Hunt, I.A., 1959. Design of seawalls and breakwaters. Journal of Waterways and Harbors Division, 85: 123–152.

Inman, D.L., and Bagnold, R.A., 1963. Littoral processes. In: Hill, M.N. (Editor), The Sea, pp. 529–553. New York: Wiley-Interscience.

Kraus, N.C. (Editor), 1993. The January 4, 1992 storm at Ocean City, Maryland. Shore and Beach, 61 (1).

Kraus, N.C., Hanson, H., and Harikai, S., 1984. Shoreline change at Oarai Beach: Past, present, and future. Proceedings of the 19th International Conference on Coastal Engineering, ASCE, pp. 2107–2123.

Kraus, N.C., Larson, M., and Kriebel, D.L., 1991. Evaluation of beach erosion and accretion predictors. Proceedings of Coastal Sediments '91, ASCE, pp. 572–587.

Kraus, N.C., and Smith, J.M., 1994. SUPERTANK laboratory data collection project. Vol. I: Main text. Technical Report CERC-94-3. Vicksburg, MS: US Army Engineer Waterways Experiment Station, Coastal Engineering Research Center.

Kraus, N.C., Smith, J.M., and Sollitt, C.K., 1992. SUPERTANK laboratory data collection project. Proceedings of the 23rd International Conference on Coastal Engineering, ASCE, pp. 2191–2204.

Kriebel, D.L., and Dean, R.G., 1985. Numerical simulation of time-dependent beach and dune erosion. Coastal Engineering, 9: 221–245.

Larson, M., 1995. Model for decay of random waves in the surf zone. Journal of Waterway, Port, Coastal, and Ocean Engineering, 121 (1): 1–12.

Larson, M., 1996. A model of beach profile change under random waves. Journal of Waterway, Port, Coastal, and Ocean Engineering, 122 (4): 172–181.

Larson, M., and Bayram, A., 2003. Calculating Cross-Shore Distribution of Longshore Sediment Transport. In: Bruun, P. (Editor), Port Engineering. Butterworth-Heinemann.

Larson, M., and Hanson, H., 1996. Schematized numerical model of three-dimensional beach change. 10th Congress of the Asia and Pacific Division, International Association for Hydraulic Research, Langkawi, Malaysia, Vol. 2, pp. 325–332.

Larson, M., Hanson, H., Kraus, N.C., and Newe, J., 1999. Short- and long-term responses of beach fills determined by EOF analysis. Journal of Waterway, Port, Coastal, and Ocean Engineering, 125 (6): 285–293.

Larson, M., and Kraus, N.C., 1989. SBEACH: Numerical model for simulating storm-induced beach change, Report 1: Empirical foundation and model development. Technical Report CERC-89-9. Vicksburg, MS: US Army Engineer Waterways Experiment Station, Coastal Engineering Research Center.

Larson, M., and Kraus, N.C., 1991. Numerical model of longshore current for bar and trough beaches. Journal of Waterways, Port, Coastal, and Ocean Engineering, 117 (4): 326–347.

Larson, M., and Kraus, N.C., 1995. Prediction of cross-shore sediment transport at different spatial and temporal scales. Marine Geology, 126 (1/4): 111–127.

Larson, M., Kraus, N.C, and Hanson, H., 1990. Decoupled numerical model of three-dimensional beach change. Proceedings of the 22nd International Conference on Coastal Engineering, ASCE, pp. 2173–2185.

Nairn, R.B., and Southgate, H.N., 1993. Deterministic profile modeling of nearshore processes. Part 2. Sediment transport and beach profile development. Coastal Engineering, 19 (1/2): 57–96.

Pelnard-Considère, R., 1956. Essai de théorie de l'evolution des forms de rivages en plage de sable et de galets. 4th Journées de l'Hydraulique, les Energies de la Mer, Question III, Rapport No. 1, pp. 289–298.

Perlin, M., 1979. Prediction of beach planforms in the lee of a breakwater. Proceedings of Coastal Structures '79, ASCE, pp. 792–808.

Perlin, M., and Dean R.G., 1983. A numerical model to simulate sediment transport in the vicinity of coastal structures. Miscellaneous Report No. 83-10. Vicksburg, MS: Coastal Engineering Research Center.

Price, W.A., Tomlinson, D.W., and Willis, D.H., 1972. Predicting changes in the plan shape of beaches. Proceedings of the 13th International Conference on Coastal Engineering, ASCE, pp. 1321–1329.

Roelvink, D., Boutmy, A., and Stam, J.-M., 1998. A simple method to predict long-term morphological changes. Proceedings of the 26th International Conference on Coastal Engineering, ASCE, pp. 3224–3237.

Roelvink, J.A., and Stive, M.J.F., 1989. Bar-generating cross-shore flow mechanisms on a beach. Journal of Geophysical Research, 94 (C4): 4785–4800.

Roelvink, J.A., Walstra, D.J.R., and Chen, Z., 1994. Morphological modeling of Keta Lagoon case. Proceedings of the 24th International Conference on Coastal Engineering, ASCE, pp. 3223–3236.

Smith, J.M., Larson, M., and Kraus N.C., 1993. Longshore current on a barred beach: Field measurements and calculation. Journal of Geophysical Research, 98, (C12): 22,717–22,731.

Stauble, D.K., Garcia, A.W., Kraus, N.C., Grosskopf, W.G., and Bass, G.P., 1993. Beach nourishment project response and design evaluation: Ocean City, Maryland. Report 1. 1988–1992. Technical Report CERC-93-13. Vicksburg, MS: US Army Engineer Waterways Experiment Station, Coastal Engineering Research Center.

Steetzel, H.J., 1990. Cross-shore transport during storm surges. Proceedings of the 22nd International Conference on Coastal Engineering, ASCE, pp. 1922–1934.

Steetzel, H., De Vroeg, H., Van Rijn, L.C., and Stam, J.-M., 1998. Morphological modelling using a modified multilayer approach. Proceedings of the 26th International Conference on Coastal Engineering, ASCE, pp. 2368–2381.

Swart, D.H., 1974. A schematization of onshore-offshore transport. Proceedings of the 14th International Conference on Coastal Engineering, ASCE, pp. 884–900.

Watanabe, A., 1982. Numerical models of nearshore currents and beach deformation. Coastal Engineering in Japan, 25: 147–161.

Watanabe, A., and Dibajnia, M., 1988. Numerical modeling of nearshore waves, cross-shore sediment transport and beach profile change. Proceedings of the IAHR Symposium on Mathematical Modeling of Sediment Transport in the Coastal Zone, Copenhagen, pp. 166–174.

Willis, D.H. ,1977. Evaluation of alongshore transport models. Proceedings of Coastal Sediments '77, ASCE, pp. 350–365.

Wise, R.A., Smith, S.J., and Larson, M., 1996. SBEACH: Numerical model for simulating storm-induced beach change, Report 4: Cross-shore transport under random waves and model validation with SUPERTANK and field data. Technical Report CERC-89-9. Vicksburg, MS: US Army Engineer Waterways Experiment Station, Coastal Engineering Research Center.

This Page Intentionally Left Blank

367

Chapter 13

Morphodynamic Modeling of Tidal Basins and Coastal Inlets

Marcel J.F. Stive and Z.B. Wang*

Faculty of Civil Engineering and Geosciences, Delft University of Technology, Delft,
The Netherlands

1. INTRODUCTION

Tidal lagoons and estuaries, collectively named tidal basins hereafter, interrupt a large part of the world's shorelines with their associated coastal inlets. Compared to the morphodynamic behavior of uninterrupted coastlines and of rivers, the morphodynamic behavior of tidal basins is a degree more complex and less well understood. These systems are important for both ecological (for example, for marine life, birds) and for socio-economic reasons (harbors, inland waterways, recreation, resource exploitation, etc.). Also, there are strong indications (Stive et al., 1990) that the morphological response of tidal basins to natural and human interventions has an impact on the coastal sediment budget which is large compared to that of interventions along an uninterrupted coast. As an example consider the impact of sea level rise on a coast adjacent to a tidal basin compared to that on an uninterrupted coast. Under the assumption that a tidal basin establishes morphodynamic equilibrium in following the rate of sea level rise (see Section 4.4), shoreline recession of the adjacent coast can be expressed as follows (extended from Cowell et al., 2003)

$$c_{pr} = \frac{\partial \zeta}{\partial t} \frac{L_p}{H_p} + \frac{\partial \zeta}{\partial t} \frac{A_b}{H_p L_{ac}} \qquad (1)$$

where c_{pr} is the rate of profile recession, $\partial \zeta / \partial t$ is the rate of sea level rise, L_p is the active cross-shore profile length, H_p is the depth of the active cross-shore profile, A_b is the tidal basin area, and L_{ac} is the length of the adjacent coast impacted.

In equation (1) the first term on the right-hand side expresses the Bruun effect (Bruun, 1962), and the second term expresses the basin effect. The Bruun effect is exceeded by the basin effect as soon as

$$A_b > L_p L_{ac} \qquad (2)$$

Typical orders of magnitude for L_p and L_{ac} are 1 km and 10 km respectively, so that basin areas larger than 0 (10 km^2) cause an impact on shoreline recession rates which exceeds the direct impact due to the Bruun effect.

We would therefore argue that the interest into the morphodynamic behavior of tidal basins is not only motivated by their intrinsic characteristics, but also by their extrinsic impacts on adjacent coasts. Hindcasting and forecasting the impact of natural and human interventions in tidal basins, based on physical insight, is therefore of utmost importance.

In considering morphodynamic processes it is essential to distinguish spatial and associated temporal scales (see De Vriend, 1998). On the microscale we encounter bedforms, which are a result of interaction between local bed properties and local flow conditions. On the mesoscale we focus on

---

*Delft Hydraulics, Delft, The Netherlands

alternating bars or flats and curved channels, which may be the result of a feedback between secondary currents due to centrifugal and coriolis effects and basin geometry. On the macroscale we focus on the macro-inlet elements, such as flats, channels, inlet gorge and ebb-tidal delta, the aggregated properties of which may be the result of an interaction between sea, swell and tidal wave properties and the elements' geometric properties. The megascale concerns the interaction between adjacent basins and adjacent coasts including the shoreface on time scales of centuries to millenia, which has importance on a geological scale (Beets et al., 1992).

In this chapter we limit ourselves to the meso- and the macroscales, which play a role on human and/or engineering time scales. Microscale processes concern the interaction between flow and sea bed resulting in a variety of bedforms which in turn influence the flow. We assume though that these are of secondary importance in the context of our work. The megascale interactions play a role on geological scales and are considered beyond the scope of this chapter.

The organization of this chapter is broadly divided into a description of mesoscale dynamic process, and of macroscale aggregated process knowledge. First, mesoscale properties of macroscale elements are discussed. Despite the progress in process knowledge we conclude that this knowledge is insufficient to predict the evolution of tidal basins and their interaction with the coast on time scales much longer than the process scale. We subsequently discuss the morphodynamic interaction between tidal wave propagation and basin geometry, through which we establish a macroscale relation between tidal propagation and geometry that leads to morphodynamic equilibrium. These findings are used in a macroscale aggregated model approach, which is based on the concept of looking for morphodynamic responses when macroscale elements are out-of-equilibrium. It is shown that the process-aggregated approach enables us to at least hindcast, and possibly forecast, the morphodynamic behavior of tidal basins to human and natural impacts on engineering time scales.

2. CHARACTERISTIC PROCESSES OF TIDAL BASINS AND COASTAL INLETS

In this section we introduce and discuss a number of observations and interpretations of characteristic processes in tidal basins and coastal inlets. In doing so we also use sketches and observations as originally made by Van Veen[1] (1950). We distinguish two typical morphologically near-equilibrium modes of Dutch tidal basins, namely near square, rectangular tidal lagoons, characteristic of the Wadden Sea basins, and funnel-shaped estuaries, characteristic of the Scheldt basins (Fig. 1a and 1b). Obviously, these two modes are not representative of the whole variety of basin modes that may be encountered world-wide, but they should be considered representative for two important end-modes.

In principle, tidal lagoons (i.e., the idealized mode of a rectangular basin which is short relative to the tidal wavelength), and their associated coastal inlets consist of two major macroscale morphological entities, that is to say, the ebb- and flood-tidal deltas, connected by the inlet entrance. A large number of different modes of tidal basins are determined by the extent to which the flood-tidal delta is developed over the basin. In the Dutch case the current basins all display a well-developed, equilibrium flood-tidal delta, as sketched in Van Veen's characterization of a Wadden Sea lagoon (Fig. 2). This could be attributed to the combination of moderate sea level rise and availability of sediment from the adjacent barrier coasts (Van Goor, 2001). An example of an underdeveloped flood-tidal delta is Red Fish Pass, Florida, displayed in Fig. 3. Both deltas are characterized by channels and adjacent flats, which are counterparts in the same system.

An analysis of the well-developed flood-tidal deltas of the Wadden Sea lagoons indicates that the branching behavior is of a fractal nature (Cleveringa and Oost, 1999). This is probably due to an instability mechanism leading to self-organization. Based on a strongly simplified linear stability analysis, using a linear bottom (with decreasing depth from sea to land) as equilibrium (zero order
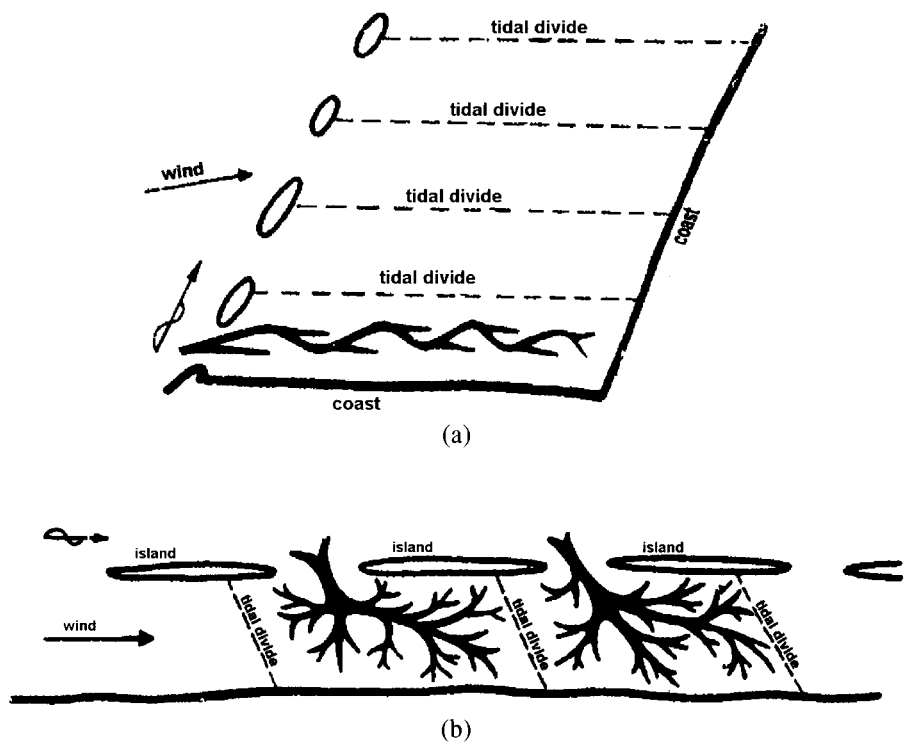
Figure 1. Two typical, morphologically near-equilibrium modes of Dutch tidal basins, namely near square, rectangular tidal lagoons (b), characteristic for the Wadden Sea basins, and funnel-shaped estuaries (a), characteristic for the Scheldt basins (after Van Veen, 1950).
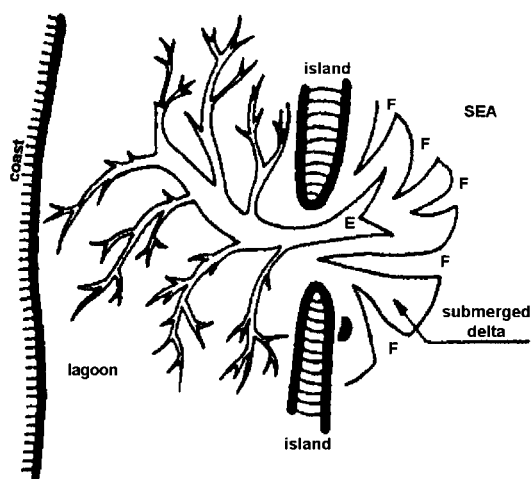
Figure 2. Well-developed, equilibrium flood-tidal delta, as sketched in Van Veen's (1950) characterization of a Wadden Sea lagoon.

Figure 3. Example of an underdeveloped flood-tidal delta: Red Fish Pass, Florida, USA (source: Website CERC-WES Coastal Inlet Research Project).

solution), Wang (1992) derived the following relation for the most stable mode of channels for tidal lagoons like the Wadden Sea

$$\left(k_y\, h_0\right)^2 = \frac{I\, f_s\, \theta}{2} \tag{3}$$

where, k_y is the wave number in the lateral direction, h_0 is the equilibrium water depth, I is the bottom slope in the longitudinal direction, f_s is a shape factor for sediment grains, and θ is the Shields parameter.

This relation suggests that:
- The larger the slope the smaller and the closer spaced the channels,
- The more active (morphologically) the region, the smaller and closer spaced the channels, and
- The larger the water depth, the larger and the wider spaced the channels.

It should be noted that in a certain area the water depth could vary continuously in space, whereas the wave number cannot. Every time a bifurcation occurs the wave number is doubled. According to equation (3) doubling of the wave number can happen if the water depth is halved. For an area with constant slope this also implies that a channel after a bifurcation will have half the length of the original channel. With this rule a fractal structure (Cantor's tree) of the channels can be constructed (Fig. 4). Field data of the Dutch Wadden Sea appear to substantiate this rule. Especially, the rule that channels after a bifurcation become half as deep is well verified by data (Fokkink, 1993).

For estuaries the above-mentioned self-organization concept is becoming even better understood. In estuaries we observe the existence of both channels and bars or flats in the case where an estuary
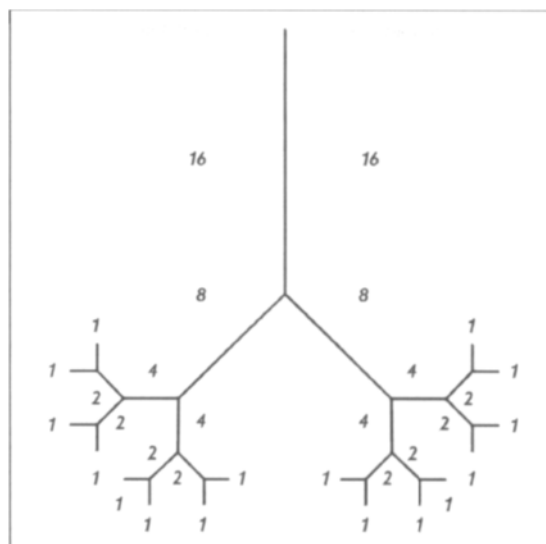
Figure 4. Theoretical tree-structure of channels in Wadden Sea (after Wang, 1992).

exceeds a certain width. Observations in the Western Scheldt estuary suggest that there seems to be a maximum size of the channels, above which a channel will bifurcate into additional channels (Allersma, 1992, see Fig. 5). However, by analyzing data of more estuaries in the world, Allersma (1994) later concluded that this maximum size is not a universal constant, but seems to be dependent on the size of the estuary and type of sediment in the estuary. The larger the size of the estuary and the finer the sediment the larger the maximum size of the channels (see legend box of Fig. 6). Fig. 6 shows that the number of channels in a cross-section is determined by the width to depth ratio of the estuary.

Recent analytical stability studies such as those by Seminara and Tubino (1998), Schuttelaars and de Swart (1999; 2000), and Seminara and Tubino (2001) seem to explain the above observations to a certain extent. These studies indicate that when the width scale exceeds a certain tidal length scale, instability mechanisms trigger the existence of alternating bars and channels. Hibma et al. (2001) has used a process-based approach to investigate whether the full nonlinear equations confirm such findings. Indeed, it is found that process-based models of the 2DH long wave equations, when seeded with small two-dimensional periodic or random perturbations, predict the development of alternating channels and bars (Figs. 7a, and 7b).

Feedback between secondary flow effects and basin geometry might well explain the existence of both channels and flats as counterparts in many tidal basins and ebb-tidal deltas. In this context we mention the effect of channel curvature in an idealized situation of alternating flats and channels as sketched in Fig. 8, yielding a spiral flow pattern. The momentum equation in the direction normal to the flow streamline requires that the centrifugal force be balanced by a water level gradient

$$\int_{depth} \left(\frac{u_t^2}{R} + \frac{1}{\rho} \frac{\partial p}{\partial n} \right) \, dz = 0 \tag{4}$$

where u_t is the tangential flow velocity, R the bend radius, and p the hydrostatic pressure.
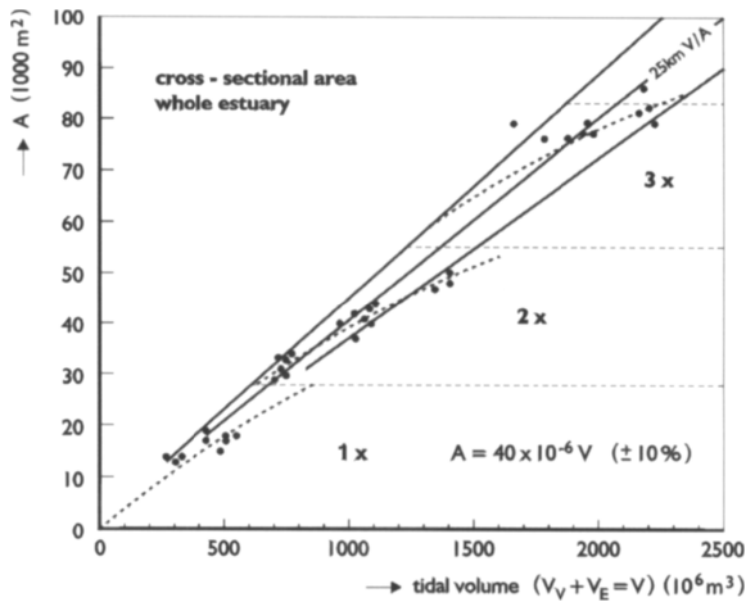
Figure 5. Cross-sectional area and number of channels as a function of tidal volume, Western Scheldt, The Netherlands (after Allersma, 1992).
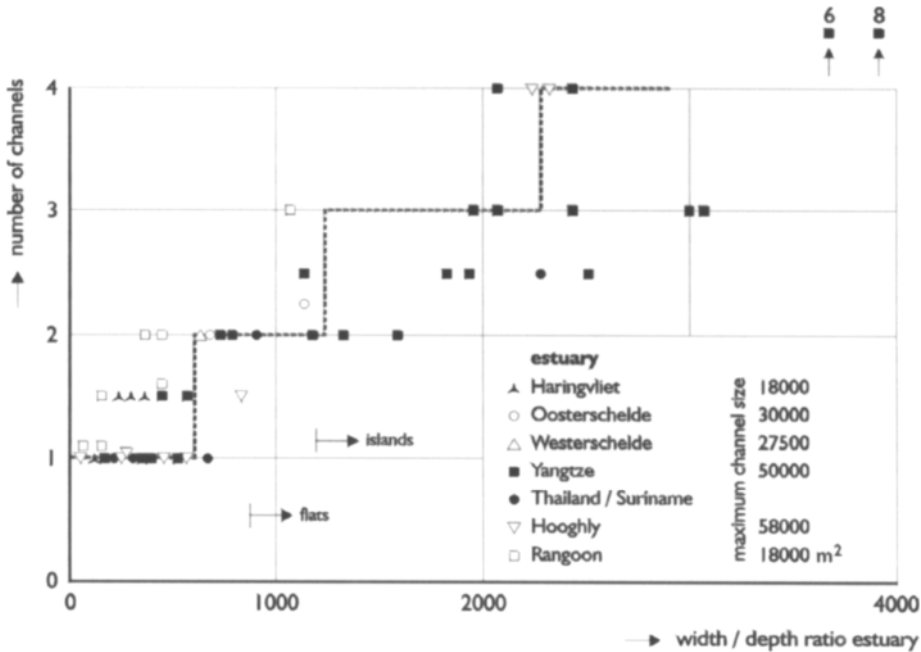
Figure 6. Number of channels as a function of width to depth ratio (after Allersma, 1994).
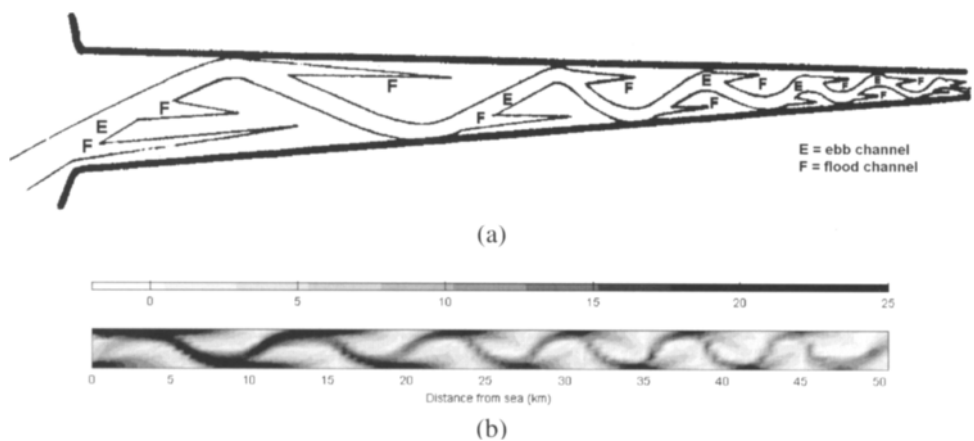
Figure 7. Nonlinear stability results (b) of a process-based model (Hibma et al., 2001) compared to Van Veen's sketch (a) of ebb- and flood-channel systems in estuaries.
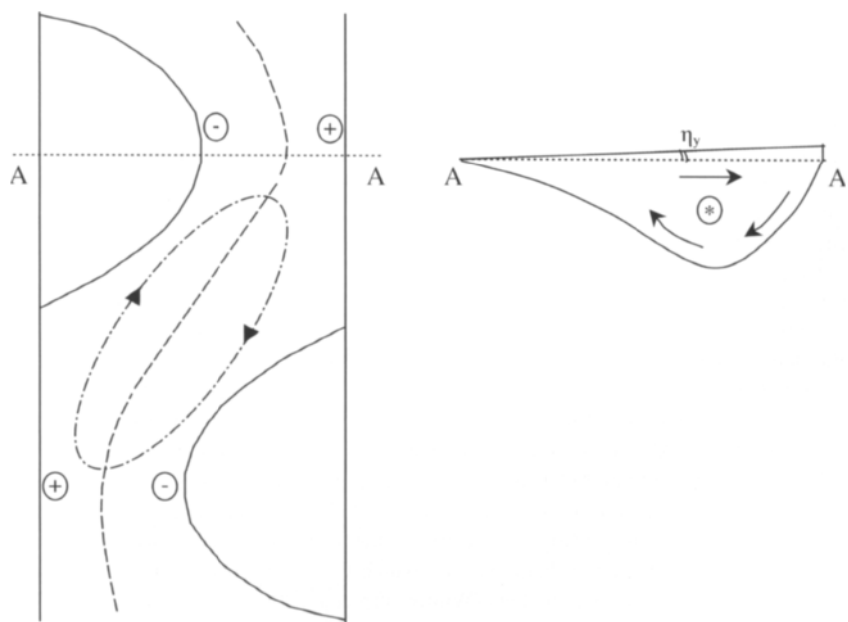
Figure 8. Idealized situation of alternating flats and channels, while horizontal secondary flows are induced by the water level set-up and set-down pattern.

While the depth-integrated momentum balance is satisfied by the creation of a water level gradient, there exists a secondary effect due to the imbalance in the vertical caused by the vertical distribution of the centrifugal force, which is caused by the logarithmic distribution of the main channel flow. As

sill = evasion of flood and ebb channel

(a)

(b)
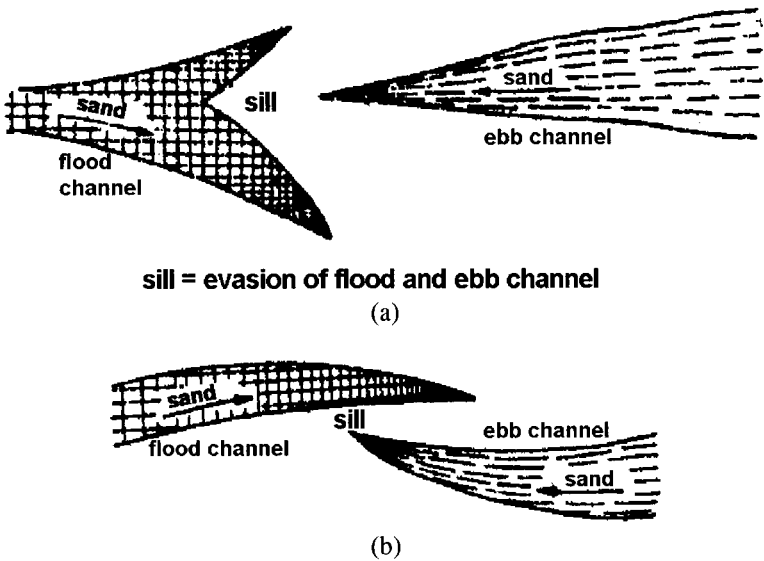
Figure 9. Flanking (b) and forking (a) behavior of ebb- and flood-channels according to Van Veen (1950).

a result, a secondary flow is induced in the channel-normal direction which favors the build up of the flat in the inner bend (Fig. 8). Moreover, a 2DH water level set-up and set-down pattern evolves (Fig. 8), which induces horizontal circulation currents with a similar effect. When the bend radius exceeds a value that depends on the latitude the coriolis effect may be of similar magnitude and may act in concert or counteract the centrifugal effect, depending on whether we are on the Northern or Southern Hemisphere. Since the centrifugal effect is independent of the flow direction it is generally of greater importance.

From the work by Hibma et al. (2001) and the striking similarity with Van Veen's sketch of the idealized ebb- and flood-channel pattern (Figs. 7a, 7b) one observes the existence of sills at the end of the flood-channels. Van Veen generalized his observations of the meeting of ebb- and flood-channels and sketches two possible modes (Figs. 9a, 9b). He distinguished the so-called forking and side attack, and referred to this as the "battle between their deltas". Indeed, in many of the systems analyzed by Van Veen one encounters such patterns. The residual sediment transport patterns associated with the ebb- and flood-channel systems are often of a circulating nature (Fig. 10), which implies that the gross sediment transport is often an order-of-magnitude larger than the net residual sediment transport. As an example (Fig. 11) we present the result of a process-based analysis of gross sediment transport in the Western Scheldt estuary, which yields an order-of-magnitude larger gross numbers than known to exist as net numbers (Winterwerp et al., 2001). These process-based studies, however, have shown their relevance on smaller time scales, but have not proven to be of importance in longer-term development and prediction of tidal basins.

Van Veen (1950) pointed at the typical development of ebb-tidal deltas in different regions. However, it was not until Sha and Van den Berg (1993) that the importance of both the phase of the tide in the gorge relative to that at sea and of the dominant wave direction were identified as main factors. Over the last decade good progress has also been made with process-based modeling of ebb-tidal deltas. However, prediction horizons have proven to be quite moderate (see De Vriend and Ribberink, 1996).
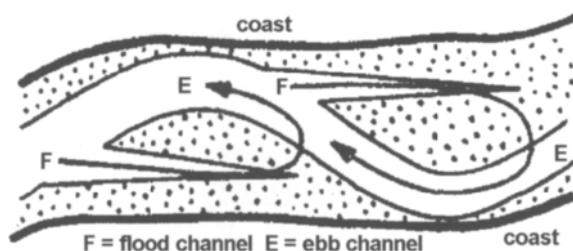
Figure 10. Circulating sediment transport pattern in a flood- and ebb-channel system (Van Veen, 1950).
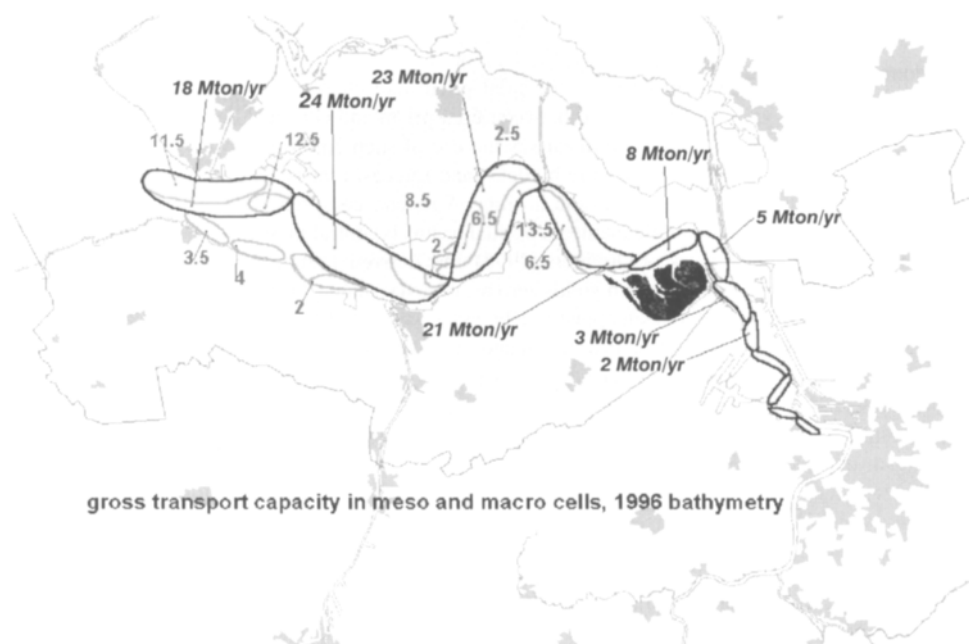
Figure 11. Process-based analysis of gross sediment transport in the Western Scheldt estuary, which yields an order-of-magnitude larger gross numbers than known to exist as net numbers (Winterwerp et al., 2001).

In conclusion, we have a rich description of processes in tidal basins and an initial insight into the complex feedback between local processes and morphology. We lack sufficient knowledge to predict the evolution of tidal basins and their interaction with the coast on time scales much longer than the process scale.

3. MACROSCALE INTERACTION BETWEEN TIDAL PROPAGATION AND BASIN GEOMETRY

Because of the insufficient capabilities of process-based modeling to predict behavior of longer-term development of tidal basins and coastal inlets, one often relies on empirical observations. As
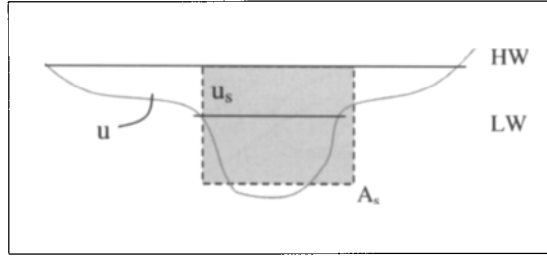
Figure 12. The basin's cross-section is schematized as in a tidal river with an approximate uniform velocity, u_s, in the flow dominant cross-section, A_s, and approximate zero velocity, u, in the alongside inter-tidal storage cross-section.

examples, consider the relation between the tidal prism and channel cross-section (see O'Brien, 1969; Eysink, 1990; see also Fig. 5), and between tidal prism and ebb-tidal delta volume (see Dean and Walton, 1975). De Vriend (1996) discusses the use of such empirical observations in process-aggregated models, which may be used to hindcast and forecast morphodynamic evolution of near-equilibrium basins when forced out-of-equilibrium. A recent, comprehensive model based on this approach and applied to macroscale elements of tidal basins is central in Section 4. Before presenting this, we first introduce the work of Dronkers (1998) who derived a relation between basin geometry and tidal propagation properties which yields zero asymmetry-induced transport for sand. The role of the inter-tidal areas in the tidal basin appears to be essential here. This is also found in other studies dealing with the interaction between tidal asymmetry and morphology of tidal basins (Friedrichs and Aubrey, 1988; Van de Kreeke and Dunsbergen, 1998).

Dronkers (1998) considers the one-dimensional tidal equations for rectangular, uniform basins and for funnel-shaped basins. It is assumed that the tide propagates along the main channel(s) of the basin, such that the large-scale geometry rather than local variations determine its properties. The basin's cross-section is schematized as in a tidal river with an approximate uniform velocity, u_s, in the flow dominant cross-section, A_s, and approximate zero velocity, u, in the adjacent inter-tidal storage cross-section (Fig. 12). In contrast to tidal rivers, the flow-dominant cross-sectional width of tidal basins is generally much smaller than the total cross-sectional storage width, b_k, certainly at high-water. The apparent depth $H_k \equiv A_s/b_k \equiv H b_s/b_k$ is generally smaller at HW than at LW. In this case the one-dimensional tidal balance equations for mass and momentum read

$$H_k \frac{\partial u_s}{\partial x} + \frac{\partial \eta}{\partial t} = 0 \tag{5}$$

$$\frac{\partial u_s}{\partial t} + g \frac{\partial \eta}{\partial x} + C_D \frac{|u_s| u_s}{H} = 0 \tag{6}$$

where η is the water surface level, and C_D is a friction coefficient. In these equations the terms $H_k u_s \partial \eta / \partial x / H$, and $u \partial u_s / \partial x$ respectively have been neglected, since solutions are sought for HW and LW.

Resolving these equations for a short rectangular basin and for a funnel-shaped basin forced by a harmonic boundary condition, Dronkers (1998) derives expressions for ebb and flood duration in terms of cross-sectional variables. In both cases the difference in ebb and flood duration, $t_e - t_f$ can be expressed as

$$t_e - t_f \approx H_k^+ H^+ - H_k^- H^- \tag{7}$$

where the superscripts $+$ and $-$ indicate HW and LW levels, respectively.
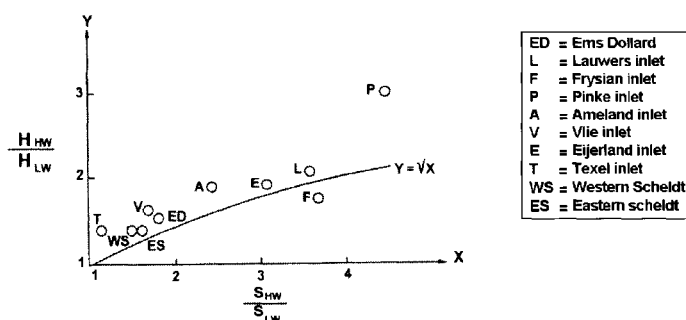
Figure 13. Indicates that for all Dutch tidal basins, either funnel-shaped estuaries or rectangular lagoons, the mean cross-sectional geometry satisfies equation (10) approximately.

In the case where ebb and flood duration are equal we may expect virtual zero asymmetry-induced transport when assuming sand transport to be proportional to a power higher than one of the tidal current speed. This requires that the basin geometry satisfies

$$H_k^+ H^+ \approx H_k^- H^- \tag{8}$$

or

$$H^+/H^- \approx \sqrt{b_k^+/b_k^-} \ \sqrt{b_s^-/b_s^+} \tag{9}$$

In many tidal basins the flow-dominant cross-section at HW does not differ much from the flow-dominant cross-section at LW, implying that

$$\alpha = \frac{H^+/H^-}{\sqrt{b_k^+/b_k^-}} \approx 1 \tag{10}$$

In the case where α is greater than one, the basin is importing, since the basin is shallower than would be necessary for morphologic equilibrium. In contrast, when α is less than one, the basin is exporting. Fig. 13 indicates that for all Dutch tidal basins, be it funnel-shaped estuaries or rectangular lagoons, the mean cross-sectional geometry satisfies equation (10) approximately. This implies that ebb-induced and flood-induced sand transports are in near-equilibrium. The factor α appears to be somewhat larger than one, which might be due to two factors:
- Adaptation of tidal basins to sea level rise requiring a net sand import, and
- Compensation of the Stokes' drift, which is a result of the phase difference between vertical and horizontal tide, favoring ebb-dominance.

We adopt the above elegant and validated interaction between tidal propagation and basin geometry as a confirmation that, under the condition that the adjacent coast is an unlimited source or sink of sediment, tidal basins can achieve equilibrium under constant forcing conditions.

4. MACROSCALE AGGREGATED MODELING OF TIDAL BASINS

A major objective of the chapter is to discuss a process-aggregated approach to handle macroscale morphodynamic evolution, and explore the application of such an approach to hindcast and forecast the morphodynamic evolution of tidal basins in the light of natural and human forcing. This
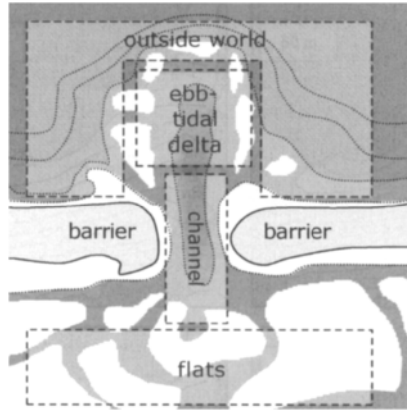
Figure 14. Basic macroscale elements of a tidal basin.

approach, embedded in the ASMITA (Aggregated Scale Morphological Interaction between a Tidal basin and the Adjacent coast) model, has recently been introduced by Stive et al. (1998) and others (for example, Kragtwijk, 2002; Van Goor et al., 2002). The approach depends heavily on the concept of the existence of morphodynamic equilibrium in the case of constant forcing based on the afore-mentioned discussion, and also, to a certain degree, on explained observations. These findings are used to study morphodynamic evolution of near-equilibrium basins when forced out-of-equilibrium.

4.1. Model Concept

The basic idea of the approach is that a tidal inlet can be schematized into a number of morphological elements. For each element a volume can be defined acting as an integral state variable. The level of schematization is similar to that of the ebb-tidal delta by Dean and Walton (1975). As shown in Fig. 14, a tidal inlet is thus schematized into:

- the ebb-tidal delta (state variable = integral excess sediment volume relative to an undisturbed coastal bed profile, V_d),
- the inter-tidal flat area in the tidal basin (state variable = integral sediment volume between MLW and MHW, V_f), and
- the total channel volume in the tidal basin (state variable = integral water volume below MLW, V_c).

Following this schematization the adjacent coastal stretches are considered as an external boundary—"the outside world"—which can exchange sediment with the inlet system.

As mentioned before, the important hypothesis used in the model concept is that a morphological equilibrium can be defined for each element depending on the hydrodynamic conditions (for example, tidal prism, tidal range) and morphometric conditions (for example, basin area). Theoretical arguments for the existence of such equilibrium were given by Dronkers (1998), but it is also supported by various field investigations, which have resulted in empirical relations between state variables and parameters of the governing hydrodynamic and morphometric conditions (Eysink, 1990). In general, the (dry or wet) volume V_{ne} [m^3] of an arbitrary element (n) in a state of morphodynamic equilibrium, appears to be highly correlated to the tidal range H_{tide} [m], the tidal prism P [m^3], and the basin area A_b [m^2]

$$V_{ne} = V_{ne} (P, H_{tide}, A_b) \tag{11}$$

According to this hypothesis no morphological change takes place when all elements in the system are in equilibrium. When one or more elements are out of equilibrium morphological changes will take place tending to restore the system to (a possibly new) equilibrium.

Obviously, sediment transport must accompany morphological changes. It is assumed that suspended load is representative for the transport mode (Di Silvio, 1989). The sediment transport formulation is basically the same as for any other suspended sediment transport model. However, unlike process-based models describing flow and sediment transport within tidal cycles residual sediment transport T is directly modeled here. This means that the long-term (time scale much larger than tidal period) mass-balance is considered for every morphological element

$$\pm \frac{dV_n}{dt} = \sum_i T_{ni} \tag{12}$$

The left-hand side of this equation represents the erosion rate within the element. Its sign is positive for a wet volume and negative for a dry volume. The right-hand side represents the sum of the transports leaving the element via all connections to other elements including the outside world. The erosion rate is assumed to be proportional to the difference between the local equilibrium concentration and the actual concentration such as the depth-averaged model for suspended sediment transport of Gallappatti and Vreugdenhil (1985)

$$\pm \frac{dV_n}{dt} = w_s \cdot A_n \cdot (c_{ne} - c_n) \tag{13}$$

where, w_s [m/s] is the vertical exchange rate, and A_n [m^2] is the horizontal area of the element. Erosion occurs when the actual sediment concentration c_n is smaller than the equilibrium concentration c_{ne}. Sedimentation occurs when the actual sediment concentration is larger than the equilibrium concentration. Also, as in any suspended sediment transport model the (long-term residual) sediment transport between two elements is assumed to be of the advective-diffusive type

$$T_{ni} = Q_{ni} \frac{c_n + c_i}{2} + \delta_{ni} (c_n - c_i) \tag{14}$$

where Q [m^3/s] is the residual flow rate, δ [m^3/s] the diffusion exchange rate between the two elements, and c_i the sediment concentration in the adjacent element.

Substituting equations (13) and (14) into equation (12) yields an equation for the sediment concentration for each element. In this way a system of coupled equations for the sediment concentrations in all elements is established. It can readily be solved if the local equilibrium concentration is known. Equilibrium sediment concentration, according to most sediment transport theories, can be considered as proportional to a certain power of the flow velocity. In an aggregated-scale model as considered here, flow velocity is not an available hydrodynamic parameter. However, the ratio between the equilibrium volume and the actual volume of, for example, the channel can be considered as the ratio between the flow velocity and the velocity under the equilibrium condition. Therefore, the following formulation is used

$$c_{ne} = c_E \cdot \left(\frac{V_{ne}}{V_n} \right)^r \tag{15}$$

The magnitude of power r is larger than one, commonly taken as 2 in compliance with a third power for the sediment transport as a nonlinear function of the mean flow velocity. Its sign depends on the definition of the element volume, V_n, positive for wet volume and negative for dry volume.

The parameter c_E has the dimension of sediment concentration. When the whole system is in equilibrium the sediment concentration in all elements will be the same and equal to c_E. Therefore,

it is called the overall equilibrium concentration. It is usually prescribed at the outside world as a boundary condition if the outside world can be considered in equilibrium, which physically means that there is no limitation for supply or accommodation of sediment adjacent to the system under consideration. In the cases described this is proven to be valid. However, in the case where the adjacent coast is protected, constrained by headlands, or in general insufficiently dynamic this assumption may not hold. In this case the adjacent coast needs to be introduced as an intrinsic morphological element to the system.

4.2. Morphological Time Scales

In order to obtain insight into the behavior of the model, we first demonstrate how the system reacts to a disturbance of the morphological equilibrium. To do this we first introduce a model with only one morphological element, for example, the channel volume within the basin. In this case, there is only one connection for diffusive sediment transport, i.e., the connection to the outside world. From the formulation described in Section 4.1, the following equation can be derived for the channel volume

$$\frac{dV_c}{dt} = \frac{\delta_{co} \cdot w_s \cdot A_c \cdot c_E}{\delta_{co} + w_s \cdot A_c} \left[\left(\frac{V_{ce}}{V_c} \right)^r - 1 \right] \tag{16}$$

Obviously, V_c will increase if it is smaller than its equilibrium value and vice versa. In other words, a disturbance always tends to be damped out and the equilibrium can be restored. For small disturbances equation (16) can be linearized

$$\frac{dV_c'}{dt} = -\frac{w_s \cdot A_c \cdot \delta_{co} \cdot c_E \cdot r}{(\delta_{co} + w_s \cdot A_c) \cdot V_{ce}} \cdot V_c' \tag{17}$$

with $V_c' = V_c - V_{ce}$ expressing the disturbance. The solution of this differential equation is an exponential function

$$V_c'(t) = V_{co}' \cdot \exp\left(\frac{-t}{\tau} \right) \tag{18}$$

where V_{co}' is the initial disturbance $V_{co} - V_{ce}$, and

$$\tau = \frac{1}{c_E \cdot r} \left(\frac{V_{ce}}{w_s \cdot A_c} + \frac{V_{ce}}{\delta_{co}} \right) \tag{19}$$

The exponential decay of a disturbance from morphological equilibrium has been suggested before (see for example, Eysink, 1990). However, there are a number of differences between the model described here and the earlier suggestions. First, according to the present model the exponential decay only applies to small disturbances whereas Eysink (1990) applies the exponential decay function to an arbitrary disturbance. Second, the time scale for the decay in the model of Eysink is an empirical input parameter, whereas equation (19) relates this time scale to a number of physical characteristics of the system. Equation (19) actually shows that the time scale consists of two parts, one for the vertical sediment exchange (first term within the bracket), and the other for the horizontal sediment exchange (second term within the bracket). Furthermore, the time scale is found to be inversely proportional to the overall equilibrium concentration and the power r, in agreement with the process-based models.

The most important difference with the classic empirical models can readily be made clear when two morphological elements are considered in the model, take for example, the inter-tidal flat volume, V_f, and the channel volume, V_c, in a tidal basin as state variables. Without going into the

mathematical details, the equations for the morphological evolution can be written in the following general form

$$\frac{dV_f}{dt} = F_1\left(V_f,\ V_c\right)$$

$$\frac{dV_c}{dt} = F_2\left(V_f,\ V_c\right)$$

(20)

This is a system of coupled first-order nonlinear differential equations. Linearization of the system yields

$$\frac{d}{dt}\begin{pmatrix} V_f' \\ V_c' \end{pmatrix} = \left.\begin{pmatrix} \dfrac{\partial F_1}{\partial V_f} & \dfrac{\partial F_1}{\partial V_c} \\[2ex] \dfrac{\partial F_2}{\partial V_f} & \dfrac{\partial F_2}{\partial V_c} \end{pmatrix}\right|_E \begin{pmatrix} V_f' \\ V_c' \end{pmatrix}$$

(21)

The solution of this system is

$$\begin{pmatrix} V_f'(t) \\ V_c'(t) \end{pmatrix} = C_1 \cdot \begin{pmatrix} Q_{11} \\ Q_{12} \end{pmatrix} e^{\lambda_1 \cdot t} + C_2 \cdot \begin{pmatrix} Q_{21} \\ Q_{22} \end{pmatrix} e^{\lambda_2 \cdot t}$$

(22)

Herein λ_1 and λ_2 are the eigenvalues of the Jacobian matrix in equation (21) with the corresponding eigenvectors Q_1 and Q_2. The constants C_1 and C_2 depend on the imposed disturbances (initial condition). The result is that the morphological behavior is determined by two morphological time scales, which are equal to the inverse of the eigenvalues ($T_1 = -1/\lambda_1$ and $T_2 = -1/\lambda_2$). These are time scales, not of the individual elements, but of the system and they depend on geometric and exchange parameters (input parameters ASMITA). The larger time scale is related to the situation when both elements have a sediment demand or sediment surplus. The smaller time scale is related to the situation when one element has a sediment surplus while the other one has a sediment demand. An arbitrary disturbance is damped out by a combination of two exponential functions with two time scales.

If the system is given sufficient time to respond to a disturbance, it will always evolve toward an equilibrium state. This evolution is not necessarily monotonous. Depending on the combination of the disturbances, the initial response of an element may be away from its equilibrium (this type of behavior is referred as 'bump' behavior). It is also possible that an element overshoots its equilibrium. These two contrasting situations are illustrated in Figs. 15a, and 15b. Physically it means that sedimentation does not necessarily occur in an element when it has a sediment demand, but that this depends on the situation in the surrounding elements. In fact sediment transport within the system is in the direction of the gradient of sediment demand.

For the general case, if N morphological elements are included in the model there will be N morphological time scales. All the time scales are system time scales related to different type of disturbances represented by the corresponding eigenvectors. None of the time scales can be related to an individual element in the system.

Kragtwijk (2002) analyzed the morphological time scales of five tidal inlets in the Dutch Wadden Sea (Fig. 16). In this analysis each tidal inlet is schematized into three morphological elements, i.e., the ebb-tidal delta, the channel in the basin, and the inter-tidal flat in the basin. Therefore, three morphological time scales are found for each inlet as presented in Table 1.

From this table, we can conclude that the Wadden inlets can be characterized by two comparatively small time scales and one larger time scale. The main differences between the inlets are present in
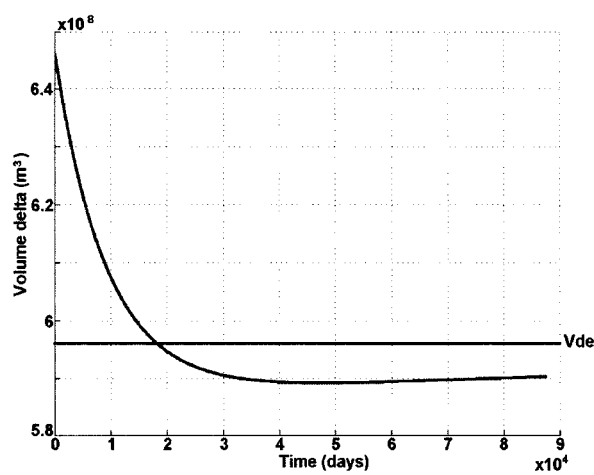
(a)
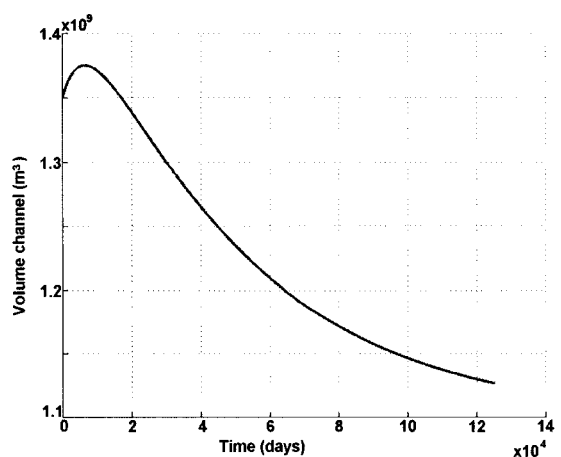
(b)

Figure 15. Characteristic morphological development; (a) overshoot, (b) bump (after Kragtwijk, 2002).
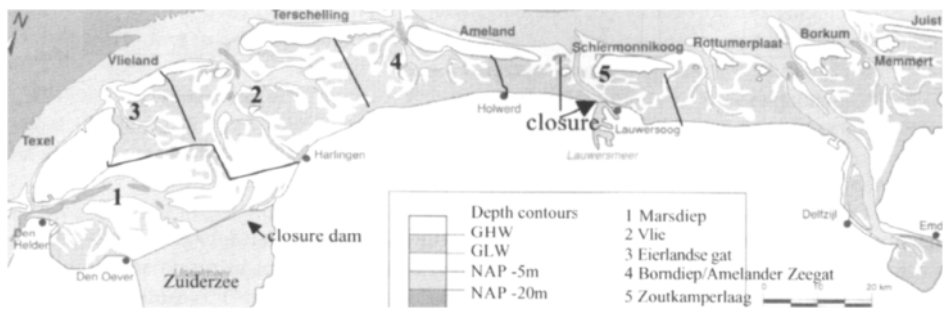
Figure 16. Overview of tidal inlets, Western Wadden Sea (with approximate tidal divides).

Table 1
System time scales for various Wadden inlets (after Kragtwijk, 2002).

Inlet	T_1 (years)	T_2 (years)	T_3 (years)
Marsdiep	3	12	198
Eierlandse Gat	3	7	38
Vlie	8	11	130
Borndiep	6	8	69
Zoutkamperlaag	5	8	48

the largest time scales, which characterize the overall development of the tidal inlet. For a relatively large tidal inlet like the Marsdiep system time scale, T_3 (see Table 1) is considerably larger than for a small inlet like the Eierlandse Gat. This means that a tidal inlet consisting of large morphological elements, has a comparatively larger adaptation time.

Since the derived time scales are system time scales and not intervention related, we emphasize that these findings are generic for tidal basins of similar size.

4.3. Response to Human Interference

There have been two major human interferences in the Dutch Wadden Sea in the last century, the closure of the Zuiderzee (IJssel Lake presently) in 1932, and the closure of the Lauwerszee (Lauwers Lake presently) in 1969. The former closure has impacted the morphological development of the Marsdiep and the Vlie (Figs. 17a, 17b, and 17c), and the latter has impacted the development of the Zoutkamperlaag (Fig. 18). The effects of both closures have been monitored, although the early years' data concerning the first closure are less extensive and less accurate. The effect of the closure of Zuiderzee has been simulated by Kragtwijk (2002) using the ASMITA model with three elements as described above. Figs. 17a, 17b, and 17c shows the computed and observed development of the Vlie. Fig. 18 shows the hindcast simulation of the development of the Zoutkamperlaag after the closure of the Lauwerszee (Van Goor et al., 2002).

Both cases show a satisfactory agreement between the computed development and the observations. More important, the experiences with the parameter setting of the model can be used for other applications of the model, for instance, studying the impact of sea level rise.

4.4. Response to Sea Level Rise

Sea level rise (SLR) induces a special kind of disturbance or forcing for the morphological development. The volume of a morphological element will then not only change due to sedimentation or erosion but also due to the change of the mean sea level. This can be implemented into the model by adding a term to equation (13)

$$\pm \frac{dV_n}{dt} = w_s \cdot A_n \cdot (c_{ne} - c_n) + A_n \frac{d\zeta}{dt} \tag{23}$$

where ζ is the mean sea level. For the model with a single element the equation for the morphological evolution (equation (16)) becomes

$$\frac{dV_c}{dt} = \frac{w_s \cdot A_c \cdot \delta_{oc} \cdot c_E}{\delta_{oc} + w_s \cdot A_c} \left(\left(\frac{V_{ce}}{V_c} \right)^r - 1 \right) + A_c \cdot \frac{d\zeta}{dt} \tag{24}$$

(a)

(b)

(c)
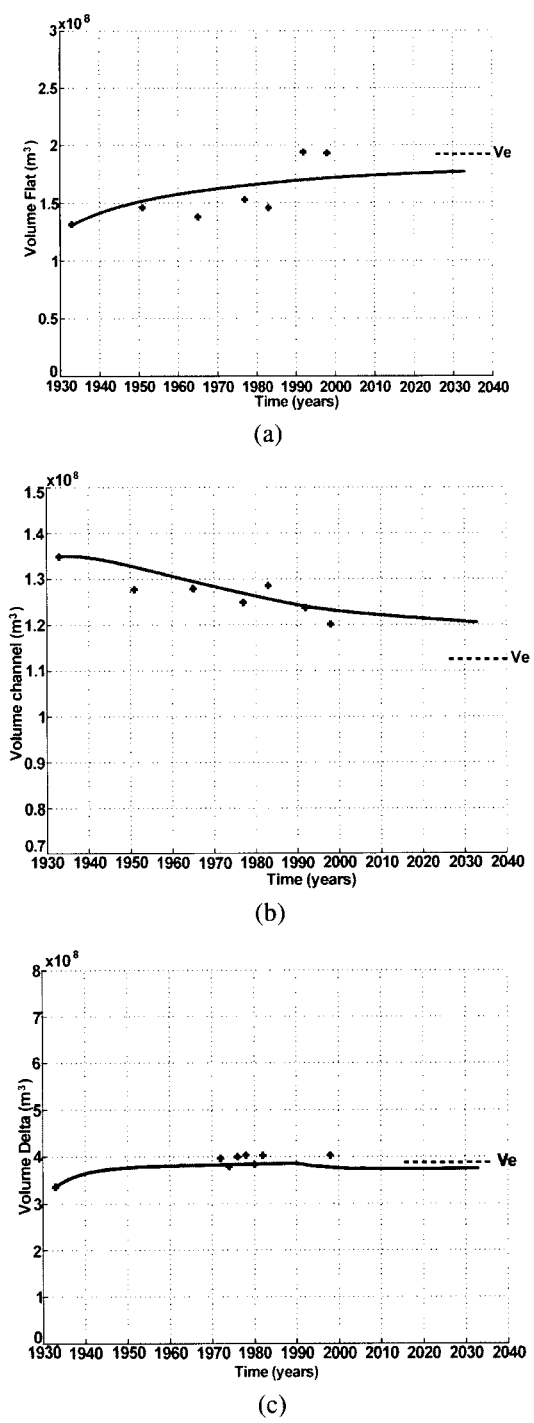
Figure 17. Model results for Vlie inlet (after Kragtwijk, 2002).
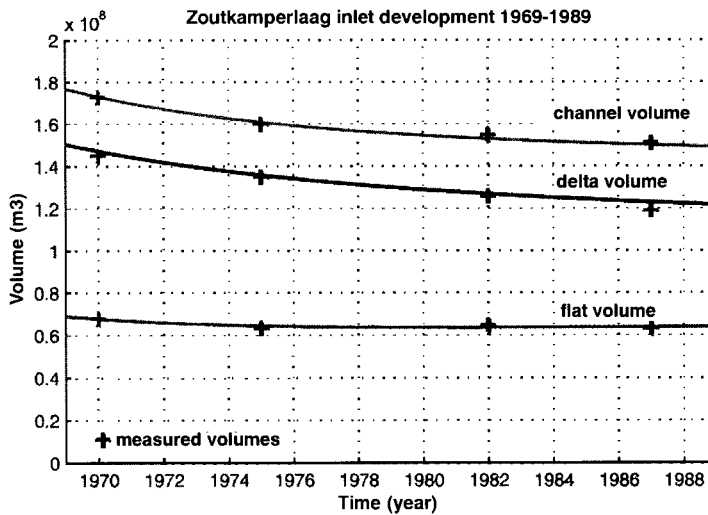
Figure 18. Simulation of volume development of Zoutkamperlaag inlet after closure of Lauwerszee in 1969 (after Van Goor et al., 2002).

The volume of the channel V_C will now still be changing in time if it is equal to its equilibrium value. When sea level rise rate is constant a dynamic equilibrium can be established and the equation becomes

$$V_{ce}^* = V_c|_{\frac{dV_c}{dt}=0} = \frac{V_{ce}}{\left(1 - \frac{d\zeta}{dt} \cdot \frac{\delta_{oc} + w_s \cdot A_c}{w_s \cdot \delta_{oc} \cdot c_E}\right)^{\frac{1}{r}}} \tag{25}$$

Equation (25) gives the channel volume in case of a dynamic equilibrium under external forcing of a constant sea level rise. In the case of no sea level rise $(d\zeta/dt = 0)$ equation (25) reduces to $V_{ce}^* = V_{ce}$. However, in case of a constant rate sea level rise $(d\zeta/dt > 0)$ equation (25) gives a 'new' dynamic equilibrium volume which is larger than the original equilibrium volume $(V_{ce}^* > V_{ce})$. Apparently there is a permanent difference between the equilibrium volume with SLR (V_{ce}^*) and the equilibrium volume without SLR (V_{ce}). This difference in equilibrium volume is necessary to maintain the demand of sediment that drives sediment imports into the system to such an extent that the system does not drown. Equation (25) also shows that the equilibrium volume V_{ce}^* becomes infinitely large when

$$\frac{d\zeta}{dt} = \frac{w_s \cdot \delta_{oc} \cdot c_E}{\delta_{oc} + w_s \cdot A_c} \tag{26}$$

Apparently, there is a maximum SLR rate an inlet can keep pace with. It is referred to as critical sea level rise rate as it indicates the transition between preservation and degeneration of the inlet. The dynamic equilibrium volume (relative to the equilibrium value) as a function of the sea level rise rate (relative to the critical value) is shown in Fig. 19.

That there is a critical value of the sea level rise rate at which a tidal inlet will drown can also be found if the system is divided into more morphological elements. Van Goor et al. (2002) applied the three-elements model as described above to investigate the impact of sea level rise on two tidal inlets in the Dutch Wadden Sea, the 'Amelander Zeegat' and the 'Eierlandse Gat' (see Figs. 20a, and 20b).
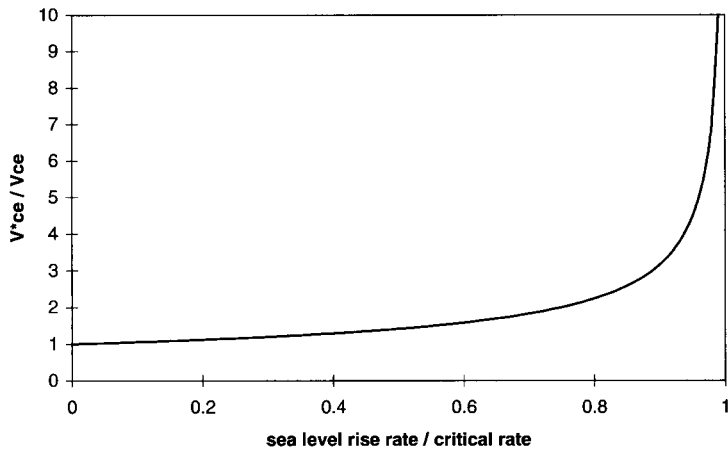
Figure 19. Dynamic equilibrium volume under the influence of sea level rise ($r = 2$).

In this figure the dynamic equilibrium volumes of the inlet elements are plotted as a function of sea level rise rates. The vertical line represents the current state of dynamic equilibrium under the present rate of SLR. With a larger rate of SLR (moving to the right in the figures) we see that the dynamic equilibrium volume of the channel element increases (wet volume), and that the dynamic equilibrium volumes of the flat and ebb-tidal delta element decreases (sediment volume).

As shown, the faster the sea level rises, the more the element volumes have to deviate from the equilibrium volumes (V_{ne}) belonging to a constant sea level ($d\zeta/dt = 0$). This deepening of the basin stimulates the system to follow the rising sea level. For the Amelander Zeegat case, Fig. 20 shows that the critical sea level rise rate is 105 cm per century. For the Eierlandse Gat the critical sea level rise rate is 180 cm per century. As the sediment demand of a smaller basin is less, the latter inlet finds it easier to adapt to a higher rate of sea level rise.

In order to cope with the uncertainties in the input parameters for calculating the critical sea level rise rate Van Goor et al. (2002) employed a probabilistic approach. The ASMITA model is especially suited for such an approach because of its simplicity. The end result is the probability that a tidal inlet can no longer follow the rise of sea level as a function of the sea level rise rate, as shown in Fig. 21a and 21b. The three different lines in Fig. 21 indicate three different methods for determining the overall equilibrium sediment concentration.

Validation of these findings is difficult since morphological observations of tidal basins under increasing rates of sea level rise are, to the authors' knowledge, nonexistent. From geological reconstruction of the Holland coast (Beets et al., 1992), however, validation in a reverse manner is to a certain extent confirmed. When sea level rise rates decreased to less than about 1 m/century the central Holland tidal basins changed from drowned systems to well-developed inter-tidal basins.

5. DISCUSSION AND CONCLUSIONS

Morphodynamic evolution of tidal basins and coastal inlets is a complex issue. Probably due to this complexity scientific attention has been less than that spent on uninterrupted coasts and rivers. Ecologically and socio-economically tidal basins and coastal inlets are of high importance. This in combination with the highly dynamic nature of tidal basins and coastal inlets and the associated im-

x 10⁸

Stability analysis Amelander Zeegat inlet

(a)

x 10⁸

Equilibrium volumes Eierlandse gat inlet

(b)
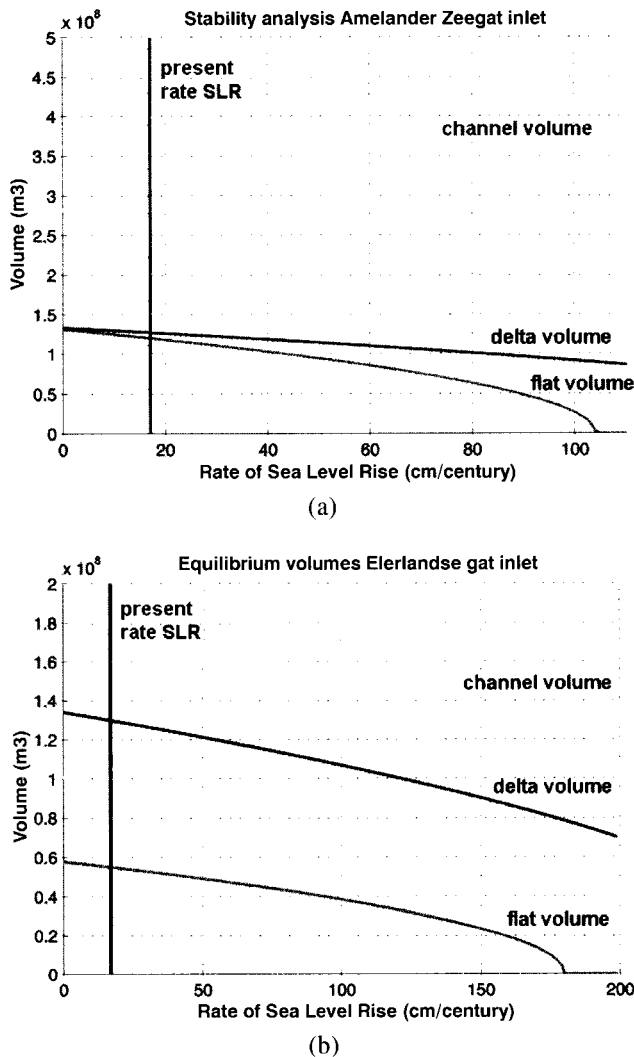
Figure 20. Dynamic equilibrium volumes and stability limit of the Amelander Zeegat and Eierlandse Gat (after Van Goor et al., 2002).

pact on the adjacent coast justifies that scientific attention be focused on these systems. This chapter aims to make a contribution in this respect.

We began this chapter by describing observations and modeling capabilities of morphodynamic evolution on the process-scale. Note that our descriptions are limited to tidal basins with little to no freshwater runoff, and that we assume sediment transport as related to morphological evolution to be dominated by sand fractions rather than silt fractions. It is shown that we have an extensive description of process-scale phenomena. For instance, we have shown that process-based modeling of the interaction between tidal wave propagation and bottom evolution in an estuary is now capable of mimicking the emergence of channels and flats. However, this knowledge has not allowed us
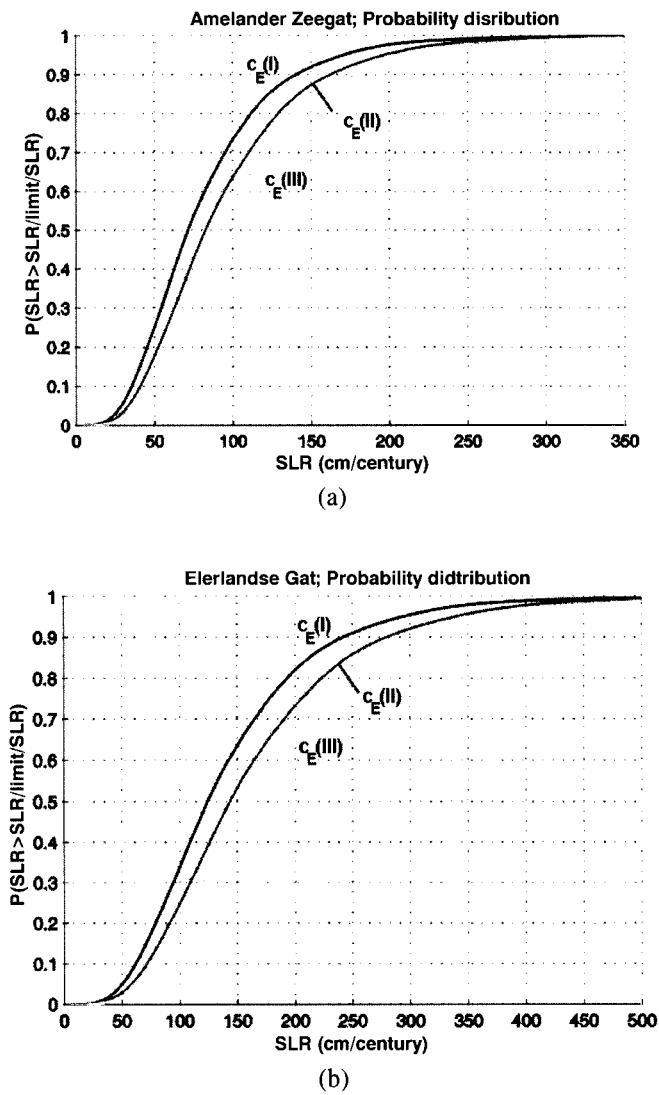
Figure 21. Probability distribution (2D) of Amelander Zeegat and Eierlandse Gat for present (II) and changed (I, III) wave climate scenarios (after Van Goor et al., 2002).

to hindcast or predict the evolution of tidal basins and coastal inlets on time scales of decades or centuries.

The value of empirical observations has been established even before insights have emerged on process-based mimicking of channel-flat development. For instance, the relations between tidal prism and channel cross-section and between tidal prism and ebb-tidal delta volume are well-known. Using these relations one may determine the aggregated sediment balance in the case of, for example, a tidal basin closure in the sense that required sediment volumes for each of these units may be assessed. As a result, the sediment source or sink magnitude of the adjacent coast results. However, what is lacking

is the assessment of the time scales involved with the adaptations of the macroscale elements. Before resolving the latter imperfection, in Section 3 of the present chapter we introduced the elegant and validated derivation by Dronkers (1998) explaining the relation between tidal propagation and basin geometry. The derivation explains that tidal basins with relatively shallow channels require relatively wide flats, and that tidal basins with relatively deep channels require relatively narrow flats to create zero asymmetry-induced sand transport, thus promoting dynamic equilibrium.

By accepting these semi-empirical observations of dynamic equilibrium we have expanded on an aggregated-scale model with which we are able to assess the macroscale response of tidal basins and ebb-tidal deltas to natural and human forcing. An essential generic conclusion is that the morphodynamic response of tidal basins consists of a complex mix of several time scales, which may differ an order-of-magnitude.

ACKNOWLEDGMENTS

ENDNOTES

1. Van Veen (1950) refers to a publication in Dutch, which has recently been translated in English. In the Netherlands the article is considered of value as a good account of lagoon and estuarine behavior. It can be downloaded from http://www.waterbouw. tudelft.nl/.

LIST OF SYMBOLS

A_b — basin area (m^2)
A_n — horizontal area of element n (m^2)
A_s — flow dominant cross-section (m^2)
b_k — channel storage width (m)
b_s — flow dominant cross-section width (m)
c_{pr} — horizontal propagation speed coastal profile (m/s)
c_e — local equilibrium concentration (-)
c_E — overall equilibrium concentration (-)
c_n — concentration in element n (-)
c_{ne} — equilibrium concentration in element n (-)
$C_{1,2}$ — constant coefficients (-)
C_D — friction coefficient (-)
f_s — shape factor for sediment grains (-)
$F_{1,2}$ — non-dimensional functions (-)
g — acceleration of gravity (m/s^2)
h — depth (m)
h_0 — equilibrium water depth (m)
H — depth (m)
H_{tide} — tidal range (m)

H^+	—	depth at High Water (m)
H^-	—	depth at Low Water (m)
H_k	—	mean depth channel storage cross-section (m)
H_p	—	depth of active cross-shore profile (m)
I	—	longitudinal channel slope (-)
k_y	—	wave number in lateral direction (-)
L_{ac}	—	length of impacted adjacent coast (m)
L_p	—	length of active cross-shore profile (m)
n	—	co-ordinate normal to streamline (-)
p	—	hydrostatic pressure (N/m^2)
P	—	tidal prism (m^3)
Q	—	residual flow rate (m^3/s)
$Q_{1,2}$	—	eigenvectors (m^3)
r	—	transport related power (-)
R	—	channel bend radius (m)
t	—	time (s)
t_e	—	ebb duration (s)
t_f	—	flood duration (s)
T	—	residual transport (m^3/s)
$T_{1,2,3}$	—	time scales (yr)
u	—	longitudinal flow velocity (m/s)
u_s	—	longitudinal flow velocity flow-dominant cross-section (m/s)
u_t	—	tangential flow velocity (m/s)
V_d	—	excess sediment volume relative to undisturbed coastal profile (m^3)
V_f	—	integral sediment volume between MLW and MHW (m^3)
V_c	—	integral water volume below MLW (m^3)
V_n	—	volume of element n (m^3)
V_{ne}	—	equilibrium volume of element n (m^3)
w_s	—	vertical exchange rate (m/s)
x	—	longitudinal co-ordinate (-)
z	—	vertical co-ordinate (-)
α	—	parameter indicating flood or ebb dominance (-)
δ	—	diffusion exchange rate between elements (m^3/s)
η	—	water surface level (m)
θ	—	Shields parameter (-)
$\lambda_{1,2}$	—	eigenvalues Jacobian matrix (s)
ρ	—	water density (kg/m^3)
τ	—	characteristic time scale (s)
ζ	—	Mean Water Level (m)

REFERENCES

Allersma, E., 1992. Management Study of the Eastern Part of the Western Scheldt; Analysis of the Physical System. Report Z368. Delft, The Netherlands: WL | Delft Hydraulics.

Allersma, E., 1994. Channels in Estuaries; 1-D Modelling of Parallel Channels. Report H1828. Delft, The Netherlands: WL | Delft Hydraulics.

Beets, D.J., Van der Valk, L., and Stive, M.J.F., 1992. Holocene evolution of the coast of Holland. Marine Geology, 103: 423–443.

Bruun, P., 1962. Sea-level rise as a cause of shore erosion. Journal of Waterways Harbors Division, ASCE, 88: 117–130.

Cleveringa, J., and Oost, A.P., 1999. The fractal geometry of tidal-channel systems in the Dutch Wadden sea. Geologie en Mijnbouw, 78: 21–30.

Cowell, P.J., Stive, M.J.F., Niedoroda, A.W., Swift, D.J.P., De Vriend, D.J., Buijsman, M.C., Nicholls, R.J., Roy, P.S., Kaminsky, G.M., Cleveringa, J., Reed, C.W., and De Boer, P.L., 2003. The Coastal-Tract (Part 2): Applications of aggregated modeling to lower-order coastal change. Journal of Coastal Research (in press).

De Vriend, H.J., 1996. Mathematical modelling of meso-tidal barrier island coasts, Part I: Empirical and semi-empirical models. In: Liu, P.L.-F. (Editor), Advances in Coastal and Ocean Engineering, Vol. 2, pp. 115–149. Singapore: World Scientific Publishing Co.

De Vriend, H.J., 1998. On the Predictability of Coastal Morphology. Proceedings of the 3rd Marine Science and Technology Conference, Lisbon, Portugal.

De Vriend, H.J., and Ribberink, J.S., 1996. Mathematical modelling of meso-tidal barrier island coasts, Part II: Process-based simulation models, In: Liu, P.L.-F. (Editor), Advances in Coastal and Ocean Engineering, Vol. 2, pp. 150–168. Singapore: World Scientific Publishing Co.

Dean, R.G., and Walton, T.L., 1975. Sediment transport processes in the vicinity of inlets with special reference to sand trapping. In: Cronin, L.E. (Editor), Estuarine Research, Vol. 2, pp. 129–150. New York: Academic Press.

Di Silvio, G., 1989. Modelling the morphological evolution of tidal lagoons and their equilibrium configurations. XXII Congress of the IAHR, Ottawa, Canada.

Dronkers, J., 1998. Morphodynamics of the Dutch Delta. In: Dronkers, J., and Scheffers, M. (Editors), Physics of Estuaries and Coastal Seas, pp. 297–304. Rotterdam: Balkema.

Eysink, W.D., 1990. Morphological response of tidal basins to change. Proceedings of the 22nd International Conference on Coastal Engineering, ASCE, Vol. 2, pp. 1948–1961.

Fokkink, R.J., 1993. Verification of a Relation for Sizes of Channels in Tidal Basins. Report Z331. Delft, The Netherlands: WL | Delft Hydraulics.

Friedrichs, C.T., and Aubrey, D.G., 1988. Non-linear tidal distortion in shallow well-mixed estuaries: A synthesis. Estuarine, Coastal and Shelf Science, 27: 521–545.

Gallappatti, R., and Vreugdenhil, C.B., 1985. A depth-integrated model for suspended sediment transport. Journal of Hydraulic Research, 23 (4): 359–377.

Hibma, A., De Vriend, H.J., and Stive, M.J.F., 2001. Channel and shoal formation in estuaries. Proceedings of the 2nd IAHR Symposium on River, Coastal and Estuarine Morphodynamics, Obihiro, Japan.

Kragtwijk, N.G., 2002. Aggregated Scale Modelling of Tidal Inlets of the Wadden Sea. Report Z2822/DC03.01.03b. Delft, The Netherlands: WL | Delft Hydraulics/ Delft Cluster.

O'Brien, M.P., 1969. Equilibrium flow areas of inlets on sandy coasts. Journal of the Waterways and Harbor Division, ASCE, 95 (WW1): 43–52.

Schuttelaars, H.M., and de Swart, H.E., 1999. Initial formation of channels and shoals in a short tidal embayment. Journal of Fluid Mechanics, 386: 15–42.

Schuttelaars, H.M., and de Swart, H.E., 2000. Multiple morphodynamic equilibria in tidal embayments. Journal of Geophysical Research, 105 (C10): 24,105–24,118.

Seminara, G., and Tubino, M., 1998. On the formation of estuarine free bars. In: Dronkers, J., and Scheffers, M. (Editors), Physics of Estuaries and Coastal Seas, pp. 345–353. Rotterdam: Balkema.

Seminara, G., and Tubino, M., 2001. Sand bars in tidal channels. Part one: Free bars. Journal of Fluid Mechanics, 440: 49–74.

Sha, L.P., and Van den Berg, J.H., 1993. Variation in ebb-tidal delta geometry along the coast of the Netherlands and the German Bight. Journal of Coastal Research, 9 (3): 730–746.

Stive, M.J.F., Capobianco, M., Wang, Z.B., Ruol, P., and Buijsman, M.C., 1998. Morphodynamics of a tidal lagoon and the adjacent coast. In: Dronkers, J., and Scheffers, M. (Editors), Physics of Estuaries and Coastal Seas, pp. 397–407. Rotterdam: Balkema.

Stive, M.J.F., Roelvink, D.J.A., and De Vriend, H.J., 1990. Large-scale coastal evolution concept. Proceedings of the 22nd International Conference on Coastal Engineering, ASCE, pp. 1962–1974.

Van de Kreeke, J., and Dunsbergen, D.W., 1998. Tidal asymmetry and sediment transport in the Frisian Inlet. In: Yanagi, T. (Editor), Interactions Between Estuaries Coastal Seas and Shelf Seas, pp. 139–159. Tokyo: Terra Scientific Publishing Company.

Van Goor, M.A., 2001. Influence of Relative Sea Level Rise on Coastal Inlets and Tidal Basins. Report Z2822/DC03.01.03a. Delft, The Netherlands: WL I Delft Hydraulics/Delft Cluster.

Van Goor, M.A., Stive, M.J.F., Wang, Z.B., and Zitman, T.J., 2002. Influence of relative sea level rise on coastal inlets and tidal basins. Proceedings, Coastal Dynamics '01, ASCE, Lund, Sweden, pp. 242–252.

Van Veen, J., 1950. Ebb and flood channel systems in the Netherlands tidal waters. Journal of the Royal Dutch Geographical Society, 67: 303–325.

Wang, Z.B., 1992. Fundamental Considerations on Morphodynamic Modelling in Tidal Regions, Part I: Theoretical Analysis and 1-D Test Computations. Report Z331. Delft, The Netherlands: WL I Delft Hydraulics.

Winterwerp, J.C., Wang, Z.B., Stive, M.J.F., Arends, A., Jeuken, C., Kuijper, C., and Thoolen, P.M.C., 2001. A new morphological schematisation of the Western Scheldt estuary, The Netherlands. Proceedings of the 2nd IAHR Symposium on River, Coastal and Estuarine Morphodynamics, Obihiro, Japan.

Chapter 14

Modeling Shore Platforms: Present Status and Future Developments

Alan S. Trenhaile

Department of Earth Sciences, University of Windsor, Windsor, Ontario, Canada, N9B 3P4

1. INTRODUCTION

A high proportion of the world's coasts are rocky, and much of it consists of cliffs with gently sloping shore platforms at their base. Most coastal research is presently concerned with beaches and other depositional features that change fairly quickly, and are vulnerable to rising sea level. Shore platforms, and the cliffs behind them, are an important source of sediment for estuaries and beaches, however, and the platforms are frequently covered by sandy or stony beaches, whose initiation, stability, and form are, in part, controlled by the morphology of their rocky foundations. We need to understand the dynamics and mode of evolution of cliffs and shore platforms to predict patterns and rates of erosion, to manage increasing levels of human activity, including housing, transportation, and recreation in coastal regions, and to determine how cliffs and shore platforms, and the beaches associated with them, will adjust to future rises in sea level. This chapter discusses a recent attempt to model shore platform evolution, and the modifications that need to be made to increase its general utility.

2. SHORE PLATFORM MODELING

Models have been frequently employed to predict rates of sediment transport by waves, wind, and tidal and other currents in the coastal environment, and to study the development and dynamics of beaches, dunes, barrier spits, deltas, and other coastal features. Modeling provides a particularly important means of investigating the long-term development of slowly changing rock coasts. The inherent complexity of these coasts makes it difficult, however, to adequately consider and represent all the variables that play a role in their development. For example, whereas there are only limited variations in the substrates of beaches, salt marshes, and sand dunes, there are enormous differences in the physical resistance of rocks, according to their chemical composition, the dip, strike, and thickness of the beds, joint density and orientation, the degree of weathering, the effect of biological activity, and many other factors. The morphology and dynamics of sandy beaches are largely controlled by waves and tides, salt marshes by tidal currents, and sand dunes by wind, but rock coasts are affected by waves, tidal variations, bioerosion, frost, chemical and salt weathering, wetting and drying, mass movements, and many other mechanisms. The relative and absolute importance of these mechanisms have also varied through time, with changes in climate and sea level, and with the characteristics of the rocks that are being eroded.

The earliest shore platform models were qualitative, and the platforms were considered in the context of an evolutionary cycle of erosion (Davis, 1896; Johnson, 1919; Challinor, 1949). Although a number of mathematical models have subsequently been developed, most have been concerned with erosion in tideless seas (Flemming, 1965; Horikawa and Sunamura, 1967; Scheidegger, 1970; Sunamura, 1976; 1977; 1978a). Japanese workers have developed mathematical models based on

field data on wave height at the cliff base, and the compressive and impact strength of the rocks. Horikawa and Sunamura (1967) found that

$$\frac{dx}{dt} = C_R \cdot f \tag{1}$$

where dx is the eroded cliff distance in time dt, C_R is a coefficient representing the erodibility of the rocks, and f is the erosive force of the waves. This equation was modified using laboratory and field data from Japan (Sunamura, 1977)

$$\frac{dx}{dt} \propto \ln\left(\frac{f_w}{f_r}\right) \tag{2}$$

where dx/dt is the mean cliff erosion rate, f_w is the assailing force of the waves, and f_r is the resisting force of the rocks. Sunamura found that the ratio f_w/f_r can be approximated by $(\rho g H/S_c) + C$, where ρ is the density of sea water, g is the acceleration due to gravity, H is the wave height at the cliff base, S_c is the compressive strength of the rock, and C is a dimensionless constant. According to Sunamura (1982; 1992), the minimum height of a wave capable of eroding the base of a cliff (H_{crit}) is given by

$$H_{crit} = \left(\frac{S_c}{\rho g}\right) e^{-\Gamma} \tag{3}$$

where Γ, a non-dimensional constant, is equal to $\ln(A/B)$. The value of A may reflect the abrasive effects of beach sediments, and B of discontinuities in the cliff material. Tsujimoto (1987) proposed that the assailing force of the waves equals Ap, where A is a non-dimensional constant representing abrasion, and p is the wave pressure. He suggested that the resisting force of the rocks equals BS_c^*, where B is a non-dimensional constant representing the effects of weathering, and $S_c^* = S_c(V_{pf}/V_{pc})$, where V_{pf}/V_{pc} is Suzuki's (1982) discontinuity index, the ratio of the longitudinal sound wave velocity measured in the rock body *in situ* and in cylindrical specimens without visible cracks in the laboratory, respectively. These Japanese studies have used variables that can be measured in the field, but although they have made valuable contributions to our understanding of rock coast processes, a myriad of other factors also need to be considered. They include the effect of tidal variations, the dip and strike of the rock, and the presence, mobility and quantity of the cliff-foot deposits and whether they function as a protective or erosive agent. It may be impractical at this time to use mathematical equations to represent the effect of many of these factors, and platform models may therefore have to rely, at least in part, upon empirical data.

Field evidence strongly suggests that most mechanical wave erosion occurs through processes that are closely associated with the water surface (Sanders, 1968; Robinson, 1977a; Trenhaile, 1987). Trenhaile (1983; 1989) and Trenhaile and Byrne (1986) modeled the evolution of shore platforms using expressions that represented erosion rates at the high and low tidal levels; this model did not, however, consider erosion rates at intermediate elevations. A previous attempt has been made to model inter-tidal wave erosion (Trenhaile and Layzell, 1981). This model was based on a limited number of variables, but it was the first to use tidal duration values, the total time each year that the water surface spends at each inter-tidal elevation, to calculate rates of erosion in macro- to microtidal environments.

Shore platforms and other elements of rock coasts develop very slowly, but although there have been marked variations in Quaternary sea level, most models have been concerned with the development of shore platforms and erosional continental shelves under stable sea level conditions. Only a few workers have considered the effects of changing sea level. They include Scheidegger (1962; 1970) and King (1963), who modeled the effect of a steady rise and fall in sea level on steep rock

coasts; Sunamura (1978b), who modeled the development of erosional continental shelves, albeit in a tideless sea, during the Holocene transgression; and Trenhaile and Byrne (1986), who studied the effect of Holocene changes in relative sea level on the development of inter-tidal shore platforms. This latter model was also used to investigate the formation of continental shelves and coastal terraces with changing sea level over five glacial-interglacial cycles during the middle and upper Quaternary (Trenhaile, 1989). There have also been few attempts to investigate the effect of changes in the elevation of the land. Cinque et al. (1995) and Anderson et al. (1999) modeled the formation of erosional marine terraces on tectonically mobile coasts with Quaternary changes in sea level, but these models did not consider how wave energy is expended within the inter-tidal zone.

3. A TIDAL WAVE EROSIONAL MODEL

Basic wave equations are used in models that attempt to predict longshore and cross-shore sediment transport and beach profile evolution (Komar, 1976; Coastal Engineering Research Center, 1984; Horikawa, 1988; Trenhaile, 1997), but there has been little attempt to use them to investigate the long-term development of rock coasts. Therefore, although there have been significant improvements in our ability to model the evolution of shore platforms, until recently no models have considered the effect of such variables as breaker wave height and depth, the distance of the breaker zone from the shoreline and the minimum or threshold wave force capable of causing rock erosion.

A wave erosional model has recently been developed that uses basic wave equations to explore the interaction between wave dynamics, tides, coastal morphology, and rock erosion at the shoreline. The model has been used to study: the development of shore platforms under stable sea level conditions (Trenhaile, 2000); the contribution of weathering to platform evolution (Trenhaile, 2001a); the effect of variable sea level elevations in the last two interglacial stages on contemporary inter-tidal shore platforms (Trenhaile, 2001b); the evolution of shore platforms and erosional continental shelves on stable coasts during the Quaternary (Trenhaile, 2001c); and the formation of subaerial and submarine terraces in the Quaternary on tectonically mobile coasts (Trenhaile, 2002a). To avoid unnecessary repetition, only a fairly brief overview of the derivation and assumptions of this model are presented here: the reader is referred to Trenhaile (2000) for a more detailed discussion.

The most effective mechanical wave erosional processes are generally considered to be water hammer, abrasion, and especially air compression in joints, bedding planes, and other rock crevices (Everard et al., 1964; Sunamura, 1978c; Trenhaile, 1987; Sunamura, 1992). With the exception of abrasion, these processes are active in a narrow zone associated with the fluctuating waterline, where there are alternations of air and water. Abrasion by pebbles, sand or other coarse material can occur well below the water surface, but it is most effective in shallow water, and its efficacy rapidly decreases with decreasing agitation of the water at greater depths (Robinson, 1977b; Trenhaile, 1987; 1997). Large, unbroken waves can only attack cliffs that are standing in fairly deep water, and very few waves generate high shock pressures by breaking against steep, natural surfaces. Most mechanical wave erosion on gently sloping shore platforms is therefore accomplished by broken waves, and it is assumed that most of this erosion occurs at the water surface, at the surf-rock interface.

The elevation of the water surface, and therefore the level of most effective wave erosion, varies with the tide. The long-term elevation-frequency distribution of the mean water surface is bimodal, with maxima at, or close to, the mean high and low water neap tidal levels. Frequencies are roughly one-third lower at the mid-tidal level, and they decrease very rapidly from the neap maxima to the spring high and low tidal levels. As the tidal range decreases, the occurrence of the mean water surface becomes increasing concentrated between the neap tidal maxima (Carr and Graff, 1982; Trenhaile, 1987) (Fig. 1).
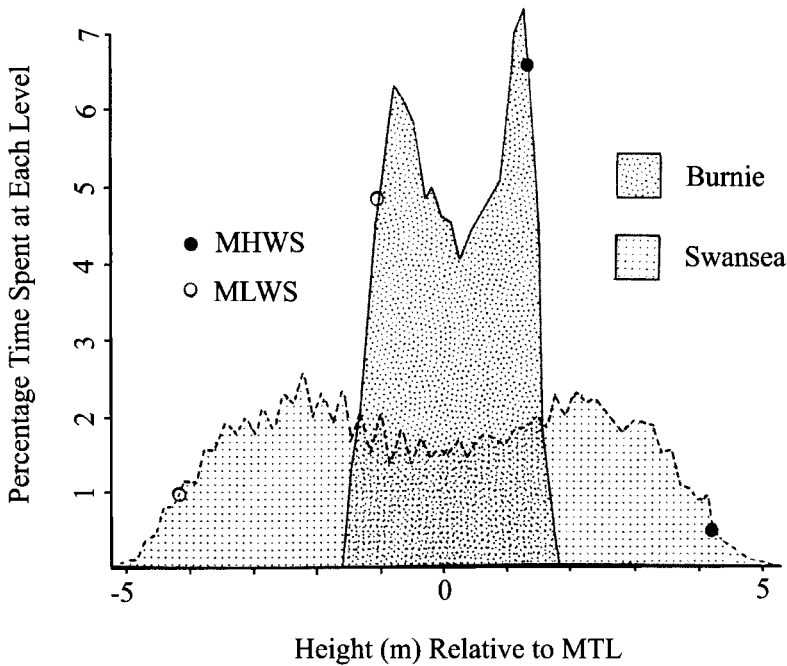
Figure 1. Tidal duration values (as a percentage of the time at each level) for a high (Swansea) and low (Burnie) tidal range environment (Carr and Graff, 1982). MHWS and MLWS refer to the mean high and mean low water spring tides, respectively.

The wave force (kg m^{-2}) generated at the breakers (F_b) is given by (Coastal Engineering Research Center, 1984)

$$F_b = 0.5 \rho_w h_b \qquad (4)$$

where ρ_w (1025 kg m^{-3}) is the unit weight of water and h_b is the breaker depth. Waves break when (Balsillie and Tanner, 2000)

$$H_b = 0.78 h_b \qquad (5)$$

Therefore, from equations (4) and (5)

$$F_b = 0.5 \rho_w \left(\frac{H_b}{0.78} \right) \qquad (6)$$

where H_b is the breaker height (m). A decay function was used to represent surf attenuation

$$S_f = 0.5 \rho_w \left(\frac{H_b}{0.78} \right) e^{-kW_s} \qquad (7)$$

where S_f is the force of the surf at the waterline (kg m^{-2}), k is a surf attenuation constant, and W_s is the width of the surf zone (m). Deep water wave characteristics can be used to determine breaker height (m) using the expression (Komar and Gaughan, 1972)

$$H_b = 0.39 g^{0.2} (T H_o^2)^{0.4} \qquad (8)$$

where g is the acceleration due to gravity, and T and H_o are the period (s) and deep water height (m) of the waves, respectively. For each broken wave, the excess surf force that is available for erosion is equal to

$$0.5\rho_w \left(\frac{H_b}{0.78} \right) e^{-kW_s} - S_{\text{fmin}} \tag{9}$$

where S_{fmin} (kg m^{-2}) is the minimum or threshold surf force capable of rock erosion. With the addition of the tidal duration value (T_d hrs a^{-1}) and the number of waves over the iteration interval, the required equation for inter-tidal erosion at the waterline, at the head of the surf zone (E_y) is

$$E_y = M \sum_{W=1}^{N} \left(T_d\ W \left(512.61 \left(\frac{H_b}{0.78} \right) e^{-kW_s} - S_{\text{fmin}} \right) \right) \tag{10}$$

where $0.5\rho_w = 512.61$ kg m^{-3}, M is a scaling coefficient (m^3 kg^{-1}), W is the hourly number of waves in each of N deep water height categories in the wave set, and E_y is the total erosion (m) accomplished by all the waves in the wave set at a specific inter-tidal level. This calculation must be repeated at the end of each iteration for each of the specified inter-tidal levels (for example, the mean high and low neap and spring tidal levels and mid-tide).

A decay function was used to represent slower rates of submarine erosion (E_s), which can occur in the upper portion of the inter-tidal zone during high tide, down to a depth equal to half the wavelength of the wave—the greatest depth at which significant interaction between a wave and the bottom is generally considered to take place

$$E_s = E_y\, e^{sh} \tag{11}$$

where s (m^{-1}) is a depth decay constant and h is the water depth.

The model requires tidal duration values for the study area for each of the required inter-tidal levels; these can be calculated from published tide tables (Smart and Hale, 1987). The initial surface could be either a simple linear surface with a specified gradient or a representation of an actual platform surface, depending on whether the intent is to model the long-term development of a rock coast or to predict how an existing platform might evolve in the future. The deep water height and period also have to be specified; this can be for a single wave or for a number of waves (a wave set) representing different portions of a wave spectrum. The degree to which erosion at the cliff base is reduced according to the amount and persistence of the cliff foot debris can be varied by multiplying the erosion that would occur at an unprotected cliff foot by a constant (<1), or by a variable related to cliff height and debris mobility. To consider the long-term development of rock coasts it is also necessary to include changes in sea level and possibly, depending upon the area of interest, changes in the elevation of the land (Trenhaile, 2001c; 2002a)

The derivation of the values for the various constants used in the model has been discussed elsewhere (Trenhaile, 2000; 2001b; 2001c), and will not be repeated at length here. In general, because of a lack of relevant field data, it was considered important to use a wide range of reasonable values. For example, surf forces generated at the shoreline for different k-values and surf zone widths (equation (7)) suggested that with S_{fmin} values between 20 and 1000 kg m^{-2}, erosion of the most resistant rocks would only occur with the highest breakers and the steepest and narrowest surf zones, whereas erosion of the weakest rocks would occur for all but the lowest breakers and the widest surf zones. Suitable k-values were calculated in a similar way, using equation (7) to determine the proportion of the breaker wave force reaching the surf-rock interface for a range of surf zone widths and k values. It was concluded that k-values of 0.1 and 0.01 could represent high rates of attenuation in very irregular surf zones and low attenuation rates over smooth and even surf zones, respectively.

Erosion rates per model iteration, as calculated by equation (10), are consistent with annual erosion rates measured in the field (tabulated, for example, by Sunamura, 1973; Kirk, 1977; Sunamura, 1992). Nevertheless, although each iteration appears to be roughly equivalent to one year, uncertainty over the value of the constants M, k and S_{fmin} requires caution in converting model iterations into real time units. Therefore, until reliable field data are available for model calibration, a range of values should be used for each variable to compensate for the effect of over- or underestimation of the annual rate of erosion, as well as to represent a wide range of natural environments.

3.1. Future Developments

The model has reproduced the morphology of contemporary shore platforms and erosional continental shelves, and replicated the relationships that exist in the field between tidal range and platform gradient and between other morphological and morphogenic variables (Trenhaile, 1978; 1987; 1999). To use the model to predict rates of cliff and platform erosion over fairly short time scales, however, as opposed to the very long time scales appropriate to geological investigations, would require the constants to be determined in the field. For example, because we lack an acceptable theory to describe water movement in the surf zone, k-values, which describe the relationship between surf attenuation rates and the roughness of bottom, will have to be determined from field data. The data should encompass a variety of geological conditions, ranging from horizontally bedded to steeply dipping rocks of variable resistance to erosion, striking parallel or perpendicularly to the shore.

The model is based on the assumption that the amount of erosion that occurs at each elevation is a function of the tidal duration distribution, the total time that the water surface spends at each elevation per year. There is also a relationship between wave energy and the elevation of the water surface, however, the most energetic waves occurring during storms, when the sea is raised above its tidal level. To incorporate this factor in the model requires analysis of the relationship between wave height and differences in predicted and recorded sea levels.

Many rocky coasts are irregular, consisting of a series of headlands and embayments, and because of wave refraction there are marked longshore variations in the energy reaching the coast. Theoretical considerations suggest that the plan shape of irregular rock coasts may ultimately attain a quasi-equilibrium state, when the erosion by refracted waves on the harder rocks of the exposed headlands becomes equal to the erosion by weaker waves operating on the less resistant rocks in the sheltered bays; this has important implications for the prediction and explanation of spatial and temporal patterns of cliff recession on rocky coasts. A three-dimensional version of the model, incorporating a wave refraction/diffraction subroutine, is needed to investigate this possibility, and whether there has been enough time during Quaternary interglacial stages to accomplish it (Trenhaile, 2002b).

3.1.1. Downwearing

The model is based on the assumption that cliffs and shore platforms develop through horizontal erosion, or backwearing, caused by mechanical wave erosional processes that are closely associated with the water surface. Annual rates of vertical erosion, or downwearing, ranging from about a tenth of a millimeter up to tens of millimeters, suggest that weathering and bioerosion, as well as abrasion where there is a beach at the cliff foot, are also important erosional processes. Downwearing can probably be ignored in attempting to predict the effect of rising sea level on cliffs and shore platforms over the next few decades, but it has serious implications for modeling their long-term evolution. Several workers have suggested that the negative feedback relationship between wave attenuation and the gradient of the bottom implies that shore platforms must ultimately develop a constant or equilibrium gradient and width (Edwards, 1941; Bird, 1968; Trenhaile, 1972), and this has been supported by the results of several wave erosional models under constant and oscillating sea level conditions (Sunamura, 1978a; Trenhaile and Layzell, 1981; Trenhaile, 1983; 2000; 2001c). The role of downwearing on platform evolution and equilibrium must be considered in future modeling,

however, not only because of its direct effect on platform morphology, but also because of its indirect influence on wave attenuation rates and patterns.

Most precise measurements of platform downwearing have been obtained using micro-erosion meters—an instrument which consists, in its simplest form, of an engineer's dial gauge that records the downward extension of a probe, mounted on a low, triangular frame. In use, the meter sits on three bolts embedded in the rock surface (High and Hanna, 1970; Stephenson, 1997a). Micro-erosion meters cannot record wave quarrying or frost riving of large rock fragments and joint blocks, and although they can measure small amounts of platform lowering, the responsible processes must be inferred from the spatial and temporal characteristics of the erosional data. In several studies, the occurrence of faster downwearing rates in the summer when air temperatures are higher and wave action is generally weaker than in winter, has suggested that weathering rather than wave action is responsible for platform lowering (Robinson, 1977a; Mottershead, 1989; Stephenson and Kirk, 1998). Mechanical wave erosion is most effective on platforms where there are scarps in horizontal or gently dipping rocks, or upstanding strata in steeply dipping rocks, which facilitate air compression in bedding planes, joints, and other rock crevices. Conversely, broken waves crossing smooth, gently sloping profiles that lack pronounced irregularities may be ineffective erosional agents. Shear stresses and dynamic forces under broken waves on a platform in New Zealand, for example, did not exceed the compressive strength of the rock (Stephenson and Kirk, 2000a). It is unlikely, therefore, that platform downwearing measured by micro-erosion meters can be ascribed to wave action, unless there are abrasives present.

Robinson (1977a) obtained a mean erosion rate of 1 mm yr^{-1} on a gently sloping shale platform in northeastern England, which he attributed to dessication of the shale in summer and subsequent removal of the loose fragments by waves. Abrasion is important on the more steeply sloping ramp at the cliff foot, where there is a sand and pebble beach, and it is most active in winter when the waves are largest. Ramp erosion rates, which vary from 1 to 30 mm yr^{-1}, are strongly influenced by the depth of the deposit and possibly by grain size. In southwestern England, a seven year record indicated that greenschist in the supratidal zone is being lowered at a mean rate of 0.625 mm yr^{-1}. Rates are much faster in summer than in winter, which suggests that the main erosive processes are crystallization and thermal expansion of halite from spray (Mottershead, 1989). Micro-erosion meters have been employed recently in the ESPED (European Shore Platform Erosion Dynamics) project, a multi-institutional, multidisciplinary study of European rock coasts. Although much of the data are not yet publically available, Foote et al. (2001) reported that there are considerable variations in the average rates of downwearing on the chalk platforms of southern England and northern France, ranging from 8.83 to 0.68 mm yr^{-1}. In southern Australia, Gill and Lang (1983) found that the average downwearing rate on primarily greywacke platforms is 0.37 mm yr^{-1}, compared with a mean backwearing rate, which is fastest at the cliff base, of 9 mm yr^{-1}. The 20 year record of Stephenson and Kirk (1996) indicated that the mainly mudstone platforms of the Kaikoura Peninsula in New Zealand are being lowered at a mean rate of 1.43 mm yr^{-1}.

Differences in tidal duration values and bottom gradients account for spatial variations in the efficacy of mechanical wave erosion in the model, whereas changes in such factors as breaker depth and height and the width of the surf zone, which vary with bottom gradients, are responsible for temporal variations. To model downwearing by abrasion and weathering we need to determine if there are any spatial and temporal patterns in its occurrence. Only a few investigations have employed sufficient micro-erosion meter sites along shore-normal profiles to compare rates of downwearing with elevation, relative to the tides. Robinson (1977b) found that downwearing is fastest on the highest, most landward part of the shore platform in northeastern England, and it also increases landwards on the ramp at the cliff base. Foote et al. (2001) found a persistent bi-modal distribution on the chalk platforms of southern England and northern France, with a downwearing maximum in the abrasion zone near the cliff foot, and a secondary maximum on the central portion of the

platforms. Kirk (1977) reported that downwearing rates are higher on the inner and outer margins of platforms on the Kaikoura Peninsula in southern New Zealand, but Stephenson and Kirk (1996), using a much longer record, found that rates are generally higher in the inner landward areas and decrease seaward.

Plotting downwearing rates, using data from a number of studies, failed to reveal any relationships with elevation (Fig. 2). Rates are higher along some profiles near the base of the cliff, but there is little evidence in these studies of any persistent trend down the platform with decreasing elevation. Most of the data in each of the studies were obtained from platforms with similar morphology and rock type: Gill and Lang's (1983) data were almost entirely from horizontal, supratidal greywacke platforms; Foote et al.'s (2001) from sloping chalk platforms; and Robinson's (1977b) from sloping shale platforms. On the Kaikoura Peninsula, however, the data were from mudstone platforms that either slope gently into the sea, or terminate abruptly seaward in a low tide cliff, the former having lower compressive strengths than the latter, or from gently sloping platforms in limestones. Stephenson (1997b) identified several significant relationships by correlating downwearing rates against elevation, the frequency of tidal wetting and drying cycles, and cross-shore location for each of the three morphological and lithological categories (Table 1). Multiple regression demonstrated that elevation was the significant variable for both types of mudstone platform ($R = 0.72$ for platforms that slope into the sea, and $R = 0.6$ for platforms with low tide cliffs), although distance from the seaward edge was the significant variable for the sloping limestone platforms ($R = 0.57$). Although much of the variance was unexplained by elevation, the Kaikoura data suggest that downwearing rates in platform models should be a function of the elevation of the site. Stephenson's (1997b) data also suggest that the decline in inter-tidal downwearing rates with elevation, and consequently with the number of wetting and drying cycles, is about three times greater on the mechanically weaker (sloping platforms) than on the mechanically stronger (horizontal platforms) mudstones. Mudstones are particularly susceptible to alternate wetting and drying, however, and it remains to be determined whether the same relationship occurs in other types of rock, or where other downwearing processes are dominant; the lack of a relationship between downwearing rates and elevation in other studies, as well as on the limestones at Kaikoura, suggests that it may not.

Although high values from abrasion are to be expected at the rear of some platforms, one would also expect to find that downwearing rates vary down a platform according to changes in the frequency and duration of tidal inundation events; this would also imply that these rates vary through time, as the surface is lowered. The lack of strong relationships between downwearing rates and site elevation and time is therefore surprising. If platforms are lowered at a constant rate, with typical downwearing rates of 0.5 to 1 mm yr^{-1}, they would have been reduced by 1.5 m to 3 m in the approximately 3,000 years since the sea reached its present level in much of the northern hemisphere, and 3 m to 6 m in much of the southern hemisphere, where sea level reached its present level about 6,000 years ago. It is difficult to accept that this degree of downwearing has actual taken place. Rapid downwearing cannot be reconciled with the occurrence of last interglacial beach deposits (probably 120,000 to 130,000 years in age) on the landward portions of shore platforms in Galicia, northwestern Spain (Trenhaile et al., 1999), or with inherited shore platforms of last interglacial age in southern Australia (Bryant et al., 1990; Young and Bryant, 1993; Brooke et al., 1994). This paradox is unlikely to be resolved, however, until we have a much larger body of downwearing data, collected from a greater variety of sites and over much longer periods of time than is presently available.

It is even more difficult to determine mean rates of erosion and the spatial and temporal effects of microflora and a host of grazing and boring marine organisms in different environments. Much of the available data are simply estimates; some refer to the erosion rates of single organisms, some to the total bioerosion accomplished by all organisms, and some to all the erosion accomplished by all agencies including marine organisms. The distribution of organisms in the vertical plane is of crucial importance. Tides determine the availability of water, and the time that each part of a
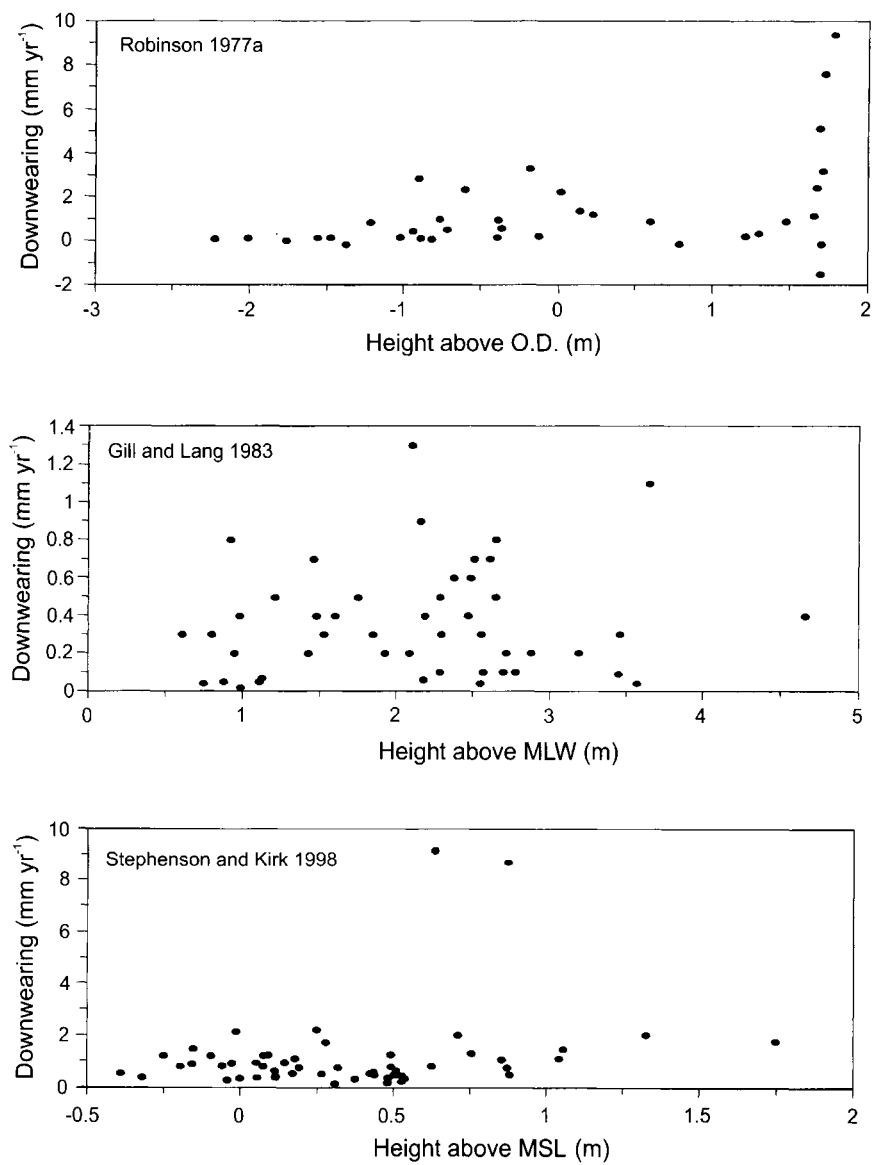
Figure 2. Micro-erosion meter downwearing rates and elevation. Elevations are expressed according to the data used by the authors. Because the datum of Gill and Lang corresponded to a biological horizon in the field, and therefore was poorly defined, and also because no direct comparisons were made between the three studies, no attempt was made to standardize the data. O.D. refers to ordnance datum, MLW to mean low water, and MSL to mean sea level.

Table 1
Correlation coefficients between downwearing rates and elevation, wetting and drying frequency, and location on the shore platforms of the Kaikoura Peninsula, New Zealand (Stephenson, 1997b).

Platform Lithological and Type	Number of Profiles[2]	Number of MEM[3] Stations	Elevation Above Mean Sea Level	Number of Wetting and Drying Cycles	Distance from Seaward Edge
Mudstone 1[4]	2	17	0.721[1]	0.621[1]	0.691[1]
Mudstone 2[4]	3	24	-0.23	0.601[1]	0.411[1]
Sloping, Limestone	2	14	-0.27	0.32	0.541[1]

[1] Significant at the 0.05 level

[2] Shore normal profiles from the cliff to the seaward edge

[3] Micro-erosion meter

[4] Mudstone 1 platforms slope into the sea whereas Mudstone 2 platforms terminate abruptly seaward in a low tide cliff. Mudstone 1 also have lower compressive strengths than Mudstone 2.

platform is inundated or exposed to dessication, and they play a crucial role in determining zonation and species composition. Wave intensity and the nature of the substrate also determine the occurrence and efficacy of erosive organisms. In general, biological activity is probably most active in the lower inter-tidal and sub-tidal zones, particularly where dessication occurs for long periods in the upper inter-tidal and supratidal zones of areas with a significant tidal range. It is generally considered to be most effective on tropical calcareous rocks, however, which appear to be eroding at rates of about 1 mm yr^{-1}, possibly reflecting the boring rate of endolithic microflora (Schneider and Torunski, 1983), and it does not appear to be a dominant factor on shore platforms in cooler, more vigorous wave environments at higher latitudes.

4. DISCUSSION

Loose blocks of rock and fresh erosional scars often testify to the importance of backwearing by wave quarrying during high intensity, low frequency events. Because we are only able to measure and document small amounts of platform downwearing with micro-erosion meters, however, there is a danger that downwearing will be assumed to be more important than backwearing on shore platforms today. Most micro-erosion meter data suggest that in the absence of abrasion, downwearing rates generally range up to about 1 mm yr^{-1}. For a 150 m wide platform, this maximum figure is equivalent to removal of 0.15 m^2 yr^{-1}, which would be matched by annual removal of a joint block along the shore-normal profile, 38.7 cm by 37.7 cm in size. Whether this takes place depends upon the morphogenic and geological environment. Backwearing is more important than downwearing in wave-dominated environments if there are favorable geological conditions. In the Vale of Glamorgan in southern Wales, for example, downwearing processes fail to penetrate the horizontally bedded limestones before the rock is removed by backwearing of the scarps (Trenhaile, 1972). Conversely, wave quarrying and backwearing are secondary to downwearing processes on the mudstone platforms of the Kaikoura Peninsula in New Zealand, where the waves are highly attenuated and pronounced rock scarps are generally absent (Stephenson and Kirk, 1998; 2000a; 2000b).

The roles of backwearing and downwearing in the development of shore platforms vary both spatially and temporally. Many factors determine their relative and absolute importance, including: the stage of platform development, equilibrium morphology; bed dip and thickness; offshore slope; the chemical and physical composition of the rock; the orientation of discontinuities, bed thickness, joint density; wave and tidal environments; and climate. Although we do not really understand how such factors as slope gradients or tidal inundation/exposure ratios influence the efficacy of downwearing mechanisms, it is possible to speculate on how they might vary through time. Mathematical models suggest that shore platforms become progressively wider and more gently sloping as they evolve, at least until they attain an equilibrium morphology (Sunamura, 1978a; Trenhaile, 2000; 2001c). During the early stages of development, higher gradients would facilitate mechanical wave erosion because of low wave attenuation, higher wave pressures generated against steep structures, and air compression in bedding planes and joints that face, and are accessible to, the approaching surf front. Steep surfaces also drain quite rapidly, and downwearing may not be rapid enough at this time to penetrate strata before they are removed by wave quarrying and backwearing. As gradients become progressively gentler, increasing wave attenuation and less accessible rock crevices reduce the efficacy of the waves, and downwearing must become relatively, and in some cases absolutely, more important. The roughness of the surface must also be considered. Uneven platforms, which generally reflect the occurrence of horizontal or dipping beds of variable resistance to erosion, allow waves to exert high forces in crevices and against scarps and upstanding beds of rock, although there may also be effective bioerosion in pools of standing water in the intervening troughs. Smooth platform surfaces generally develop in rocks that are weak and thinly bedded, or in fairly homogeneous rocks that lack marked variations in their erosive resistance. Mechanical wave erosion can operate on smooth platforms in well jointed rocks when they are still steep, but downwearing is likely to become progressively more dominant as gradients decrease through time.

The model primarily attributes platform development to the distribution of wave energy within the inter-tidal zone, and it is therefore suitable for environments dominated by wave quarrying of coarse, weathered or unweathered, material (Trenhaile, 2000; 2001a). It cannot be used, however, if the role of the waves is limited to washing away fine-grained, weathered material. Stephenson and Kirk (2000b) proposed that the mainly mudstone platforms at Kaikoura in southern New Zealand have developed in the vertical zone where tidal wetting and drying operate most frequently, and this is supported by the moderately strong relationship that exists in this area between downwearing rates and elevation (Stephenson 1997b). A program was written to calculate the annual number of wetting and drying cycles from predicted high and low tidal levels, in mainly semidiurnal tidal environments. The frequency distributions are single modal, with flat summits representing the zone of most frequent wetting and drying, which extends from the lowest of the neap high tidal levels to the highest of the neap low tidal levels, with the ratio of the period of drying to the period of wetting increasing with elevation within this zone. The maximum value is essentially constant for semidiurnal tidal regimes (2 cycles per day), although it is lower for mixed, and especially for diurnal regimes. The vertical extent of the zone of most frequent wetting and drying increases with the tidal range, and frequencies decrease very rapidly at higher and lower elevations, (Fig. 3). The relationship between tidal duration and wetting and drying frequency distributions and tidal range therefore provides a possible explanation for the global relationship between mean regional platform gradient and tidal range (Trenhaile, 1978; 1987; 1999), irrespective of whether the platforms are dominated by wave quarrying or by weathering (Fig. 4). Assuming that alternate wetting and drying of argillaceous rocks can undercut cliffs and produce shore platforms, as opposed to lowering and otherwise modifying wave-cut platforms, their development can be modeled by substituting tidal wetting and drying frequency distributions for tidal duration distributions.

There is a fundamental problem with all theories that attribute platform formation to subaerial (Bartrum, 1916) or inter-tidal (Stephenson and Kirk, 2000b) weathering, while relegating the role of
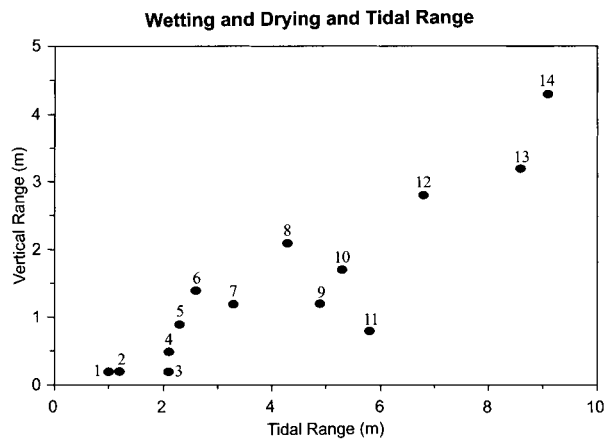
Figure 3. The relationship between the vertical extent of the zone of maximum wetting and drying frequency and spring tidal range for: (1) Apia, Samoa; (2) Bergen, Norway; (3) Kuantan, eastern Malaysia; (4) Halifax, eastern Canada; (5) Taku, northern China; (6) Mersey River, Tasmania; (7) Lisbon, Portugal; (8) Margate, southeastern England; (9) Mackay, northeastern Australia; (10) Prince Rupert, western Canada; (11) Port Hedland, northwestern Australia; (12) Le Havre, northern France; (13) Swansea, south Wales, UK; and (14) St. John, eastern Canada. All sites have semidiurnal tidal regimes, with the exception of Kuantan, which is mixed.
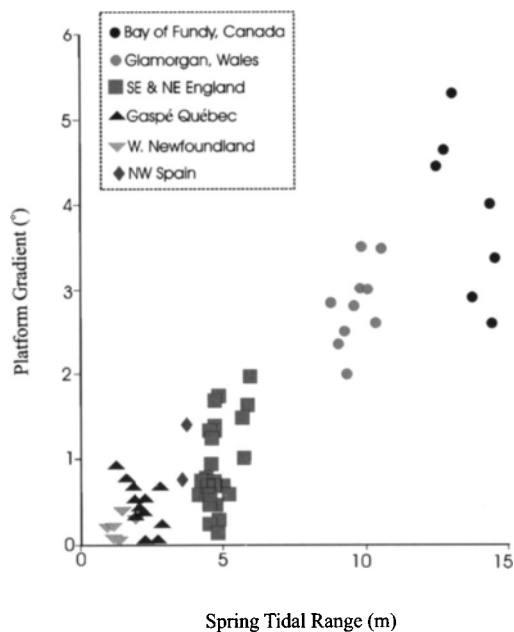
Figure 4. Regional mean shore platform gradient and spring tidal range. Each data point represents the mean of a large number of surveyed profiles.

the waves to removal of the fine-grained debris. This is concerned, in the absence of a role for wave strength and attenuation, with the apparent lack of a mechanism responsible for determining maximum platform width. Whereas wetting and drying produces fine-grained material that can be washed away by weak waves, however, cliff undercutting can bring much coarser, unweathered material down to the back of the platform. Platform width may therefore be limited by the eventual inability of attenuated waves to remove this debris. Modeling the development of platforms dominated by alternate wetting and drying would therefore require both a modified version of equation (10), to determine rates of debris removal according to the strength of the broken, attenuated waves, and a downwearing equation based on tidal wetting and drying frequency distributions and downwearing-elevation relationships to determine rates of cliff erosion and platform lowering.

Other types of downwearing mechanisms probably have different spatial and temporal relationships from wetting and drying, and would therefore have to be represented in a different way in the model (Trenhaile, 2001a). Tidally induced frost action occurs when inter-tidal rocks freeze in air during low tide and thaw in water during high tide. Theory, and field and laboratory experimentation, have suggested that this mechanism is most effective in the upper inter-tidal zone, which experiences the longest periods of exposure during tidal cycles (Robinson and Jerwood, 1987a; 1987b). Salt weathering, by hydration and crystallization, is also dependent on the degree of exposure of the platform surface, and is therefore probably most effective in the upper inter-tidal zone, where there is the greatest variation in temperature and moisture content. Bartrum (1916) first proposed that shore platforms in sheltered locations are formed by weak waves washing away weathered material above an inter-tidal level of permanent sea water saturation. More recent field and laboratory investigations have shown that the water content in surface rocks gradually decreases from the high to the low tidal level, however, which suggests that there is a corresponding decrease in the intensity of chemical weathering down the inter-tidal zone (Trenhaile and Mercan, 1984).

5. CONCLUSIONS

Platform models must consider erosive conditions within the inter-tidal zone, and they must also be flexible enough to encompass the wide range of wave, tidal, and geological conditions that occur in the field, as well as changes in sea level and climate. The model described in this chapter is the first to use basic wave equations to simulate the erosion of rock coasts in the inter-tidal zone. In its present form it can be used to study the long-term evolution of wave-dominated coasts with geological conditions that facilitate the formation of seaward-facing scarps or other upstanding irregularities. Field calibration of the constants in the model would also permit its use to predict platform and cliff erosion in specific areas with rising sea level, over much shorter time scales.

Although there have been several attempts to model shore platforms, they are all based on the assumption that platforms develop through wave erosion operating in the horizontal plane. The model in its present form does not consider the effect of bioerosion, weathering, or other downwearing mechanisms, although micro-erosion meter data suggest that they are important and in some cases dominant factors on some platforms today. The model can be modified fairly simply to allow downwearing processes to operate in conjunction with wave generated backwearing, but although we have a growing body of data on downwearing rates in different environments, it is unclear at present how spatial and temporal variations with changing elevation should be represented.

LIST OF SYMBOLS

E_s	—	amount of submarine erosion each year (m)
E_y	—	amount of inter-tidal erosion each year (m)
F_b	—	wave force at the breakers (kg m^{-2})
g	—	acceleration due to gravity (m s^{-2})
h	—	water depth (m)
h_b	—	breaker depth (m)
H_b	—	breaker height (m)
k	—	surf attenuation factor related to bottom roughness
M	—	coefficient (6.5 x 10^{-10} to 3.25 x 10^{-8} m^3 kg^{-1}) to convert the excess surf force into the amount of inter-tidal erosion during each model iteration
MHWS	—	mean high water spring tidal level
MLW	—	mean low water
MLWS	—	mean low water spring tidal level
MSL	—	mean sea level
MTL	—	mean tidal level
N	—	number of deep water wave categories used to represent the spectrum
O.D.	—	ordnance datum
p	—	wave pressure
s	—	submarine erosion depth decay constant (m^{-1})
S_f	—	surf force at the waterline (kg m^{-2})
S_{fmin}	—	threshold erosional strength of the rocks (kg m^{-2})
T	—	wave period (s)
T_d	—	tidal duration value, the time each year that the water level occupies each inter-tidal elevation (hr yr^{-1})
W	—	hourly number of waves of each of the five deep water heights gradient of the bottom extending from the breakers to the waterline
W_s	—	surf zone width (m)
ρ_w	—	unit weight of sea water (1025 kg m^{-3})

REFERENCES

Anderson, R.S., Densmore, A.L., and Ellis, M.A., 1999. The generation and degradation of marine terraces. Basin Research, 11: 7–19.

Balsillie, J.H., and Tanner, W.F., 2000. Red flags on the beach, Part II. Journal of Coastal Research, 16: iii–x.

Bartrum, J.A., 1916. High water rock platforms: A phase of shoreline erosion. Transactions of the New Zealand Institute, 48: 132–134.

Bird, E.C.F., 1968. Coasts. Canberra: Australian National University Press, 246 p.

Brooke, B.P., Young, R.W., Bryant, E.A., Murray-Wallace, C.B., and Price, D.M., 1994. A Pleistocene origin for shore platforms along the northern Illawarra coast, New South Wales. Australian Geographer, 25: 178–185.

Bryant, E.A., Young, R.W., Price, D.M., and Short, S.A., 1990. Thermoluminescence and uranium-thorium chronologies of Pleistocene coastal landforms of the Illawarra Region, New South Wales. Australian Geographer, 21: 101–111.

Carr, A.P., and Graff, J., 1982. The tidal immersion factor and shore platform development. Transactions of the Institute of British Geographers, 7: 240–245.

Coastal Engineering Research Center, 1984. Shore Protection Manual. Fourth Edition. Washington DC: U.S. Army Corps of Engineers.

Challinor, J., 1949. A principle in coastal geomorphology. Geography, 34: 212–215.

Cinque, A., De Pippo, T., and Romano, P., 1995. Coastal slope terracing and relative sea-level changes: Deductions based on computer simulations. Earth Surface Processes and Landforms, 20: 87–103.

Davis, W.M., 1896. Plains of marine and subaerial denudation. Geological Society of America Bulletin, 7: 377–398.

Edwards, A.B., 1941. Storm wave platforms. Journal of Geomorphology, 4: 223–236.

Everard, C.E., Lawrence, R.H., Witherick, M.E., and Wright, L.W., 1964. Raised beaches and marine geomorphology. In: Hosking, K.F.G., and Shrimpton, G.J. (Editor), Present Views on Some Aspects of the Geology of Cornwall and Devon, pp. 283–310. Truro, Cornwall: Royal Geological Society of Cornwall.

Flemming, N.C., 1965. Form and relation to present sea level of Pleistocene marine erosion features. Journal of Geology, 73: 799–811.

Foote, Y., Plessis, E., and Robinson, D., 2001. Rates and patterns of cliff erosion and downwearing of chalk shore platforms: Comparisons between France and England. Abstracts of the European Rock Coasts 2001 Conference, Brighton, England, December 17th–18th, 2001, pp. 24–25.

Gill, E.D., and Lang, J.G., 1983. Microerosion meter measurements of rock wear on the Otway Coast of southeast Australia. Marine Geology, 52: 141–156.

High, C.J., and Hanna, F.K., 1970. A method for the direct measurement of erosion on rock surfaces. British Geomorphological Research Group Technical Bulletin, 5: 1–25.

Horikawa, K., 1988 (Editor). Nearshore Dynamics and Coastal Processes: Theory, Measurement, and Predictive Models. Tokyo: University of Tokyo Press, 522 p.

Horikawa, K., and Sunamura, T., 1967. A study on erosion of coastal cliffs by using aerial photographs. Coastal Engineering in Japan, 10: 67–83.

Johnson, D.W., 1919. Shore Processes and Shoreline Development. New York: Wiley, 584p.

King, C.A.M., 1963. Some problems concerning marine planation and the formation of erosion surfaces. Transactions of the Institute of British Geographers, 33: 29–43.

Kirk, R.M., 1977. Rates and forms of erosion on the tidal platforms at Kaikoura Peninsula, South Island, New Zealand. New Zealand Journal of Geology and Geophysics, 20: 571–613.

Komar, P.D., 1976. Beach Processes and Sedimentation. Englewood Cliffs, New Jersey: Prentice-Hall, 429p.

Komar, P.D., and Gaughan, M.K., 1972. Airy wave theory and breaker height prediction. Proceedings of the 13th International Conference on Coastal Engineering, ASCE, pp. 405–418.

Mottershead, D.N., 1989. Rates and patterns of bedrock denudation by coastal salt spray weathering: A seven-year record. Earth Surface Processes and Landforms, 14: 383–398.

Robinson, D.A., and Jerwood, L.C., 1987a. Frost and salt weathering of chalk shore platforms near Brighton, Sussex, U.K. Transactions of the Institute of British Geographers, 12: 217–226.

Robinson, D.A., and Jerwood, L.C., 1987b. Sub-aerial weathering of chalk shore platforms during harsh winters in southeast England. Marine Geology, 77: 1–14.

Robinson, L.A., 1977a. Erosive processes on the shore platform of northeast Yorkshire, England. Marine Geology, 23: 339–361.

Robinson, L.A., 1977b. The morphology and development of the northeast Yorkshire shore platform. Marine Geology, 23: 237–255.

Sanders, N.K., 1968. The Development of Tasmanian Shore Platforms. Unpublished Ph.D. thesis. Hobart: University of Tasmania.

Scheidegger, A.E., 1962. Marine terraces. Pure and Applied Geophysics, 52: 69–82.

Scheidegger, A.E., 1970. Theoretical Geomorphology. New York: Springer-Verlag, 435p.

Schneider, J., and Torunski, H. 1983. Biokarst on limestone coasts, morphogenesis and sediment production. Marine Ecology, 4: 45–63.

Smart, C.C., and Hale, P.B., 1987. Exposure and inundation statistics from published tide tables. Computers and Geosciences, 13: 357–368.

Stephenson, W.J., 1997a. Improving the traversing micro-erosion meter. Journal of Coastal Research, 13: 236–241.

Stephenson, W.J., 1997b. The development of shore platforms on Kaikoura Peninsula, South Island, New Zealand. Unpublished PhD. thesis. Christchurch, New Zealand: University of Canterbury.

Stephenson, W.J., and Kirk, R.M., 1996. Measuring erosion rates using the micro-erosion meter: 20 years of data from shore platforms, Kaikoura Peninsula, South Island, New Zealand. Marine Geology, 131: 209–218.

Stephenson, W.J., and Kirk, R.M., 1998. Rates and patterns of erosion on inter-tidal shore platforms, Kaikoura Peninsula, South Island, New Zealand. Earth Surface Processes and Landforms, 23: 1071–1085.

Stephenson, W.J., and Kirk, R.M., 2000a. Development of shore platforms on Kaikoura Peninsula, South Island, New Zealand. Part One: The role of waves. Geomorphology, 32: 21–41.

Stephenson, W.J., and Kirk, R.M., 2000b. Development of shore platforms on Kaikoura Peninsula, South Island, New Zealand. II: The role of subaerial weathering. Geomorphology, 32: 43–56.

Sunamura, T., 1973. Coastal cliff erosion due to waves—field investigations and laboratory experiments. Journal of the Faculty of Engineering of the University of Tokyo, 32: 1–86.

Sunamura, T., 1976. Feedback relationship in wave erosion of laboratory rocky coast. Journal of Geology, 84: 427–437.

Sunamura, T., 1977. A relationship between wave-induced cliff erosion and erosive force of wave. Journal of Geology, 85: 613–618.

Sunamura, T., 1978a. A mathematical model of submarine platform development. Mathematical Geology, 10: 53–58.

Sunamura, T., 1978b. A model of the development of continental shelves having erosional origin. Geological Society of America Bulletin, 89: 504–510.

Sunamura, T., 1978c. Mechanisms of shore platform formation on the southeastern coast of the Izu Peninsula, Japan. Journal of Geology, 86: 211–222.

Sunamura, T., 1982. A predictive model for wave-induced erosion, with application to Pacific coasts of Japan. Journal of Geology, 90: 167–178.

Sunamura, T., 1992. Geomorphology of Rocky Coasts. Chichester, UK: John Wiley, 302p.

Suzuki, T., 1982. Rate of lateral planation by Iwaki River, Japan. Transactions of the Japanese Geomorphological Union, 3: 1–24.

Trenhaile, A.S., 1972. The shore platforms of the Vale of Glamorgan, Wales. Transactions of the Institute of British Geographers, 56: 127–144.

Trenhaile, A.S., 1978. The shore platforms of Gaspé, Québec. Annals of the Association of American Geographers, 68: 95–114.

Trenhaile, A.S., 1983. The width of shore platforms; a theoretical approach. Geografiska Annaler, 65A: 147–158.

Trenhaile, A.S., 1987. The Geomorphology of Rock Coasts. Oxford: Oxford University Press, 384p.

Trenhaile, A.S., 1989. Sea level oscillations and the development of rock coasts. In: Lakhan, V.C., and Trenhaile, A.S. (Editors), Applications in Coastal Modeling, pp. 271–295. Amsterdam, The Netherlands: Elsevier Science Publishers.

Trenhaile, A.S., 1997. Coastal Dynamics and Landforms. Oxford: Oxford University Press, 366p.

Trenhaile, A.S., 1999. The width of shore platforms in Britain, Canada, and Japan. Journal of Coastal Research, 15: 355–364.

Trenhaile, A.S., 2000. Modeling the development of wave-cut shore platforms. Marine Geology, 166: 163–178.

Trenhaile, A.S., 2001a. Modeling the effect of weathering on the evolution and morphology of shore platforms. Journal of Coastal Research, 17: 398–406.

Trenhaile, A.S., 2001b. Modeling the effect of late Quaternary interglacial sea levels on wave-cut shore platforms. Marine Geology, 172: 205–223.

Trenhaile, A.S., 2001c. Modeling the Quaternary evolution of shore platforms and erosional continental shelves. Earth Surface Processes and Landforms, 26: 1103–1128.

Trenhaile, A.S., 2002a. Modeling the development of sloping marine terraces on tectonically mobile rock coasts. Marine Geology, 185: 341–361.

Trenhaile, A.S., 2002b. Rocky coasts, with particular emphasis on shore platforms. Geomorphology, 48: 7–22.

Trenhaile, A.S., and Byrne, M.L., 1986. A theoretical investigation of rock coasts, with particular reference to shore platforms. Geografiska Annaler, 68A: 1–14.

Trenhaile, A.S., and Layzell, M.G.J., 1981. Shore platforms morphology and the tidal duration factor. Transactions of the Institute of British Geomorphologists, 6: 82–102.

Trenhaile, A.S., and Mercan, D.W., 1984. Frost weathering and the saturation of coastal rocks. Earth Surface Processes and Landforms, 9: 321–331.

Trenhaile, A.S., Pérez Alberti, A., Martínez Cortizas, A., Costa Casais, M., and Blanco Chao, R., 1999. Rock coast inheritance: An example from Galicia, northwestern Spain. Earth Surface Processes and Landforms, 24: 605–621.

Tsujimoto, H., 1987. Dynamic conditions for shore platform initiation. Science Report of the Institute of Geoscience, University of Tsukuba, A 8, pp. 45–93.

Young, R.W., and Bryant, E.A., 1993. Coastal rock platforms and ramps of Pleistocene and Tertiary age in southern New South Wales, Australia. Zeitschrift fur Geomorphologie, 37: 257–272.

This Page Intentionally Left Blank

Chapter 15

Merging Scales in Models of Water Circulation: Perspectives from the Great Barrier Reef

Eric Wolanski [a], Richard Brinkman [a], Simon Spagnol [a], Felicity McAllister [a], Craig Steinberg [a], William Skirving [a] and Eric Deleersnijder [b]

[a] Australian Institute of Marine Science, PMB No. 3, Townsville MC, Queensland 4810 Australia
[b] Institut d'Astronomie et de Geophysique G. Lemaitre, Universite Catholique de Louvain, 2 Chemin du Cyclotron, B-1348 Louvain-La-Neuve, Belgium

1. INTRODUCTION

Several challenges exist in modeling ocean circulation across a range of spatial and temporal scales. By focusing on the domain of the Great Barrier Reef this chapter emphasizes that a better understanding of large-scale water circulation can be obtained by merging scales to allow for feedbacks between smaller scale and coarser scale models. The Great Barrier Reef (GBR) (Fig. 1a) comprises more than 2800 individual reefs that are spread over a 2600 km length of Australia's north-eastern continental shelf, at the western margin of the Coral Sea. The topography is highly complex, with individual reefs ranging in area from 0.01 to 100 km^2. In some regions the reefs form a ribbon separated by narrow passages (Fig. 1b), and occupy approximately 90% of the along-shelf length, thus providing a significant barrier to the water circulation (Pickard et al., 1977). In other regions the reefs are widely scattered, separated by wide passages and occupy only about 10% of the along-shelf length (Fig. 1c). The continental shelf water depth tends to gently slope to around 100 m at the shelf break. The interaction of this complex topography, the wind, the tides, and the circulation in the adjoining Coral Sea all serve to strongly influence the circulation on the GBR shelf (Wolanski, 1994). This circulation plays a crucial role in a number of important biological processes, including the: (a) flushing of Great Barrier Reef waters by Coral Sea waters, (b) connectivity of reef populations as a result of the transport of water-borne larvae between reefs, (c) transport of nutrients and pollutants by water currents, (d) retention of fish larvae behind salient topographic features, (e) reef-induced upwelling controlling plankton dynamics, coral health, the location of meadows of the alga *Halimeda*, and (f) role of reef-induced temperature mixing in inhibiting coral bleaching (Andrews, 1983; Andrews and Furnas, 1986; Wolanski and Hamner, 1988; Wolanski et al., 1988; Oliver et al., 1992; Hughes, 1993; Sammarco and Heron, 1994; Wolanski, 1994; Wolanski et al., 1997; Hoegh-Guldberg, 1999; Skirving and Guinotte, 2001; Wolanski, 2001; Brinkman et al., 2002).

With operational processes occurring over a wide range of scales in both space and time, ranging from meters to hundreds of kilometers, and from minutes to years, it is not possible to model the whole GBR domain, including the adjoining western Coral Sea, using a fine-grid, three-dimensional (3-D) model at present. Instead, different two-dimensional (2-D) and 3-D models are used at different scales to study different processes. The merging of these scales and processes remains an art, and examples of such merging will be shown in this chapter. This chapter begins with a description of the technique chosen to include the effect of the oceanic circulation in a 2-D model of the large-scale circulation on the continental shelf. This circulation, however, is found to be modulated at an intermediate spatial scale by the interaction of the tidal circulation with individual reefs, and this process is modeled by merging large-scale and reef-scale 2-D circulation models. To further investigate the
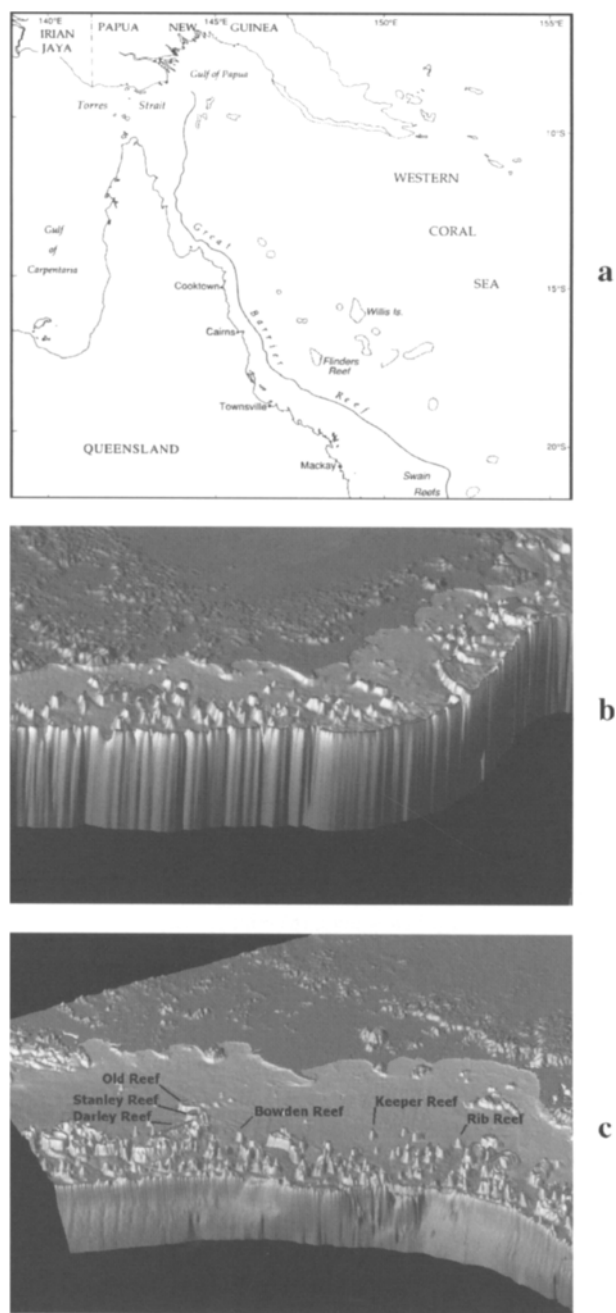
Figure 1. (a) General location map of the Great Barrier Reef. Three-dimensional rendering of the topography of the Great Barrier Reef (b) in the northern region where reefs form a ribbon-like structure, and (c) in the central region where reefs are more widely scattered. Note that the vertical scale of bathymetry has been exaggerated.

circulation around reefs, the reef-scale circulation (the island wake) around one reef in well-mixed coastal waters is studied using 2-D and 3-D models. It is shown that the horizontal properties of the island wake are well reproduced by 2-D models, and that the three-dimensional processes, including upwelling and downwelling, cannot be reliably captured by 3-D modeling except if subgrid scale processes are parameterized. The tidal jet is another reef-scale process generated by strong tidal flows in a reef passage, and this is also investigated using a 3-D model. Finally, a brief discussion is presented of the use of these models to calculate the vertical profiles of temperature in the waters near reefs.

2. THE INFLUENCE OF THE OCEANIC CIRCULATION ON THE GBR SHELF

The circulation in the Coral Sea acts in union with mesoscale wind events and tidal forcing to control the circulation on the GBR shelf (Church, 1987; Andrews and Clegg, 1989; Wolanski, 1994; Brinkman et al., 2002). In the Coral Sea, a westward flowing jet bifurcates as it approaches the Australian continental margin (Fig. 2). This results in two currents along the edge of the shelf; namely the Coral Sea Coastal Current that flows northward from the bifurcation point, and the East Australian Current that flows southward of the bifurcation point (Andrews and Clegg, 1989; Wolanski, 1994). The East Australian Current has a typical speed of 0.3 m s^{-1} in the upper 200 m of shelf break waters of the central GBR (Church and Boland, 1983); the current is halved at a depth of 100 m (Wolanski, 1994). Long-term studies have not been done on the strength and location of the oceanic jet in the Coral Sea creating this circulation. However, data from long-term moorings on the GBR outer continental shelf are available. These data suggest that the location of the bifurcation point varies seasonally and inter-annually.

The Coral Sea circulation is thus expected to generate both a cross-shelf and a longshore regional sea level gradient on the GBR shelf (Middleton, 1987). To the south of the bifurcation point the
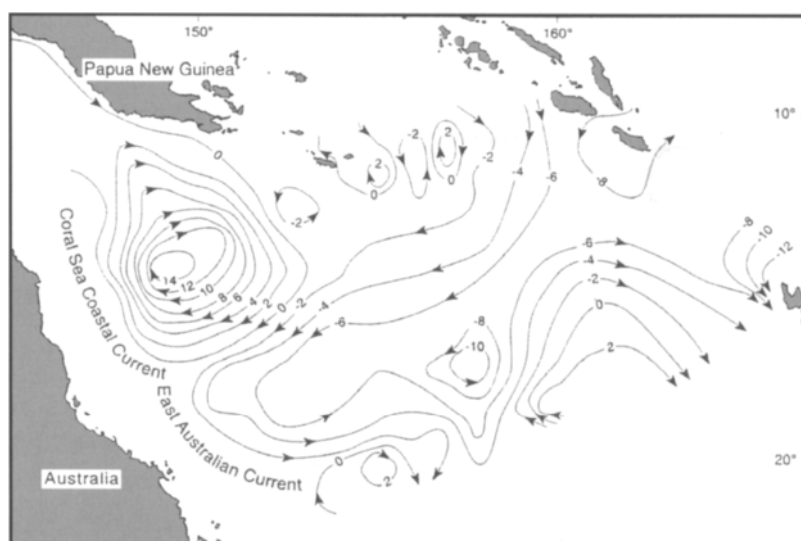
Figure 2. Contours of volume transport (in Sv) for the top 1000 m at 2.4 Sv intervals for the Western Coral Sea. Adapted from Andrews and Clegg (1989).

longshore surface slope induces a southward net flow on the GBR shelf, which displays strong inter-annual and seasonal fluctuations due to variability in the circulation in the Coral Sea (Wolanski, 1994). Similarly, north of the bifurcation point a net northward longshore flow exists on the GBR shelf (Brinkman et al., 2002). Analysis of long-term current meter records from moorings at various locations along the length of the central GBR region reveals the magnitude of these persistent, but variable net currents. The observed change of direction of the longshore net current between southern and northern mooring locations indicated that an oceanic inflow had occurred between these mooring sites, at latitudes 14.7°S and 16.75°S respectively. This cross-shelf component of the circulation is biologically important as it controls the flushing of the GBR by the Coral Sea, and hence the residence time of water on the GBR shelf.

3. MODEL PARAMETERIZATION

To model the influence of regional sea surface gradients on the circulation on the GBR shelf, a 2-D model was considered appropriate as the shelf waters are generally well-mixed throughout the year and flow is primarily horizontal (Wolanski, 1994). Regional sea surface gradients were parameterized in the model by defining the instantaneous sea surface elevation above mean sea level, η, as being composed of a mean elevation, $\bar{\eta}$, plus a time varying fluctuation, η', about this mean

$$\eta = \bar{\eta} + \eta' \tag{1}$$

Decomposition of the sea surface elevation into mean and fluctuating components allowed η' to be used as the prognostic variable for sea surface elevation, and presented an opportunity for regional sea level gradients, $\partial \bar{\eta}/\partial x$ and $\partial \bar{\eta}/\partial y$, to be additional model forcing parameters prescribed as inde-pendent values at each computational point and not just at the open boundaries.

The model domain covered a 500 km stretch of the continental shelf from Bowen, in the south, to Lizard Island in the north, and extended into the western Coral Sea. The computational grid for the model was a mesh of 2.0 x 2.0 km spatial resolution, and total grid dimensions of 343 x 138 computational points. The mesh size was sufficiently small to resolve the topographical influence of the reefs in the study region. Localized, reef-induced three-dimensional circulation features known to occur at much smaller scales ($\approx$ 10–500 m) (see Wolanski and Hamner, 1988; Deleersnijder et al., 1992; Wolanski et al., 1996) were not resolved by this model.

The open model boundaries to the northwest, northeast and southeast were forced by sea surface elevation, η, from long-term tide gauge moorings. At the closed coastal boundary and at island and emergent reef boundaries in the interior of the domain, zero transport perpendicular to the boundary was specified. Data from a weather station within the model domain prescribed the wind forcing. Regional sea level gradients, however, were not known explicitly. Such gradients are difficult to measure due to their large spatial and temporal variability. Instead, these slopes were inferred from the analysis of the observed low-frequency longshore currents, which identified a northward net flow in the northern region of the model domain, and a southward net flow in the southern region of the model domain. The region with zero sea surface gradients on the shelf represented the area immediately inshore of the bifurcation point on the continental slope, and defined a zone of inflow from the Coral Sea. Forcing by regional sea surface gradients was only applied on the shelf where bottom friction maintains numerical stability. The absolute values of the gradients were determined by adjusting the magnitude, extent and location of the regional gradients until there was adequate agreement between predicted and observed low frequency currents at the mooring sites.

3.1. Model Execution and Results

The model was run for a 100-day period coincident with the long-term current observations. With the inclusion of the regional sea surface gradient parameterization, computed low frequency long-shore currents at the mooring sites compared well with observations (see Fig. 3). The predicted net circulation (Fig. 4a) shows an inflow from the Coral Sea, the Coral Sea Coastal Current, and the East Australian Current. In the absence of the regional slope parameterization in the model, the observed southward flow in the southern region was significantly underpredicted (Fig. 3), and the computed synoptic distribution of the net current averaged over the 100-day run shows an unrealistic, northward flow over the entire shelf (Fig. 4b).

The topographical influence on the inflow onto the GBR is clearly evident in the spatial distribution of the transport across the shelf edge. The largest inflow, representing more than 50% of the total estimated volume, occurred in a region where the density of coral reefs on the outer shelf is sparse, and thus there is little topographical impediment to oceanic inflow. The predicted volume transport from the Coral Sea into the central region of the GBR represented by the model was estimated to be ~ 0.58 Sv. When regional forcing was neglected, the predicted cross-shelf transport was negligible (~ 0.008 Sv).

The oceanic inflow onto the central GBR and its spatial variability predicted by the model with parameterization of regional sea surface gradients is confirmed by a satellite image of the chlorophyll concentration in this region at 01:43:51, July 14, 2000 GTM (Fig. 5). In the northern region of the central GBR, north of approximately $16°$S, inflows are limited to very distinct channels between the otherwise highly dense reef matrices. South of $16°$S, where the spatial density of the reef matrix decreases, oceanic inflows become more spatially frequent, with a major zone of inflow evident between Rib Reef and Bowden Reef. Further south from Bowden Reef there is minimal inflow across the outer shelf inflow due to the presence of the dense reef matrix on the outer shelf. On the mid-shelf, however, oceanic water originating from inflows further north appears as a dark plume with distinct frontal features. This image also suggests that there can exist quite distinct cross-shelf fronts between coastal waters and waters of oceanic origin. A subsequent image collected at 02:06:10, July 15, 2000 GMT (not shown) revealed that the oceanic/coastal-water front south of Bowden Reef had
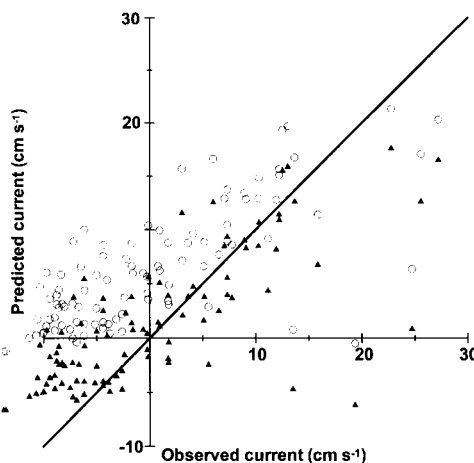
Figure 3. Scatter plots of observed and predicted daily mean currents at the Cape Upstart mooring site for ($\circ$) no forcing and ($\blacktriangle$) forcing by regional sea surface gradients.
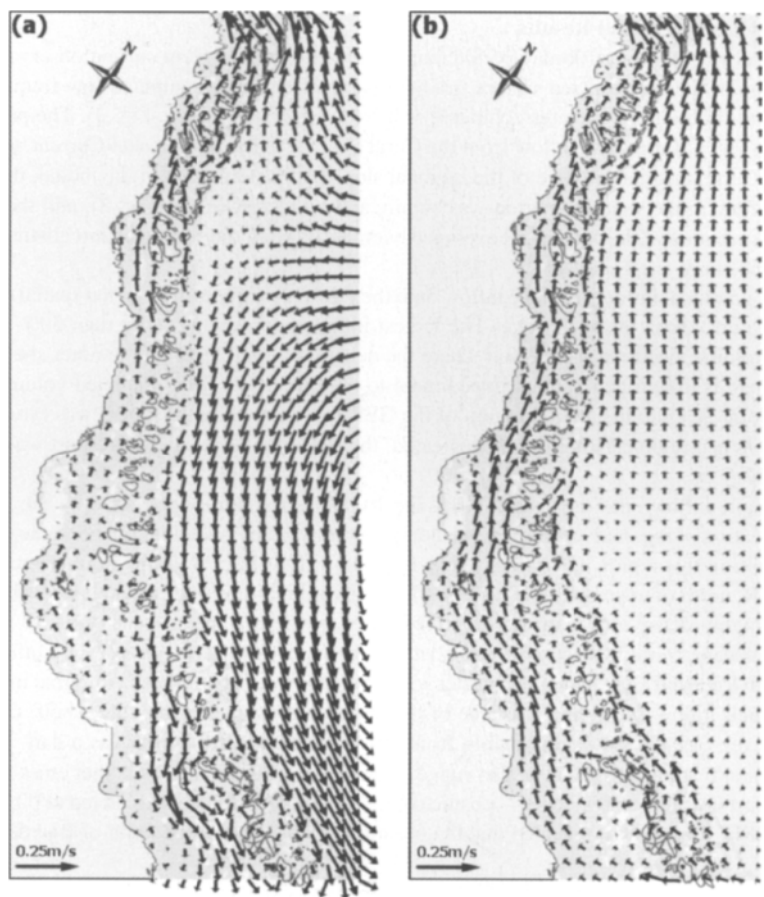
Figure 4. Synoptic views of mean currents over the 100 days of the model run in the austral winter of 1981 under the influence of wind and tides, and (a) forcing by regional sea surface gradients, and (b) no forcing by regional sea surface gradients.

penetrated approximately 16.5 km further southwards with an average speed of approximately 0.18 m s^{-1}.

4. FLOW AROUND OBSTACLES: AN ARCHIPELAGO

The southward flowing East Australian Current meets a system of reefs including Old, Stanley and Darley Reefs (Fig. 1c). This matrix includes a few narrow passages, typically 0.5–2 km in width. Data from current meter moorings have shown that the East Australian Current flows through such passages at neap tides (tidal range $\approx$ 2 m) and water in the reef matrix is rapidly flushed. However, at spring tides (tidal range $\approx$ 4 m), the East Australian Current is deflected sideways around the reef matrix and does not flow through the reef passages. In such cases the water inside the reef matrix is essentially trapped (Wolanski and Spagnol, 2000; Spagnol et al., 2001).
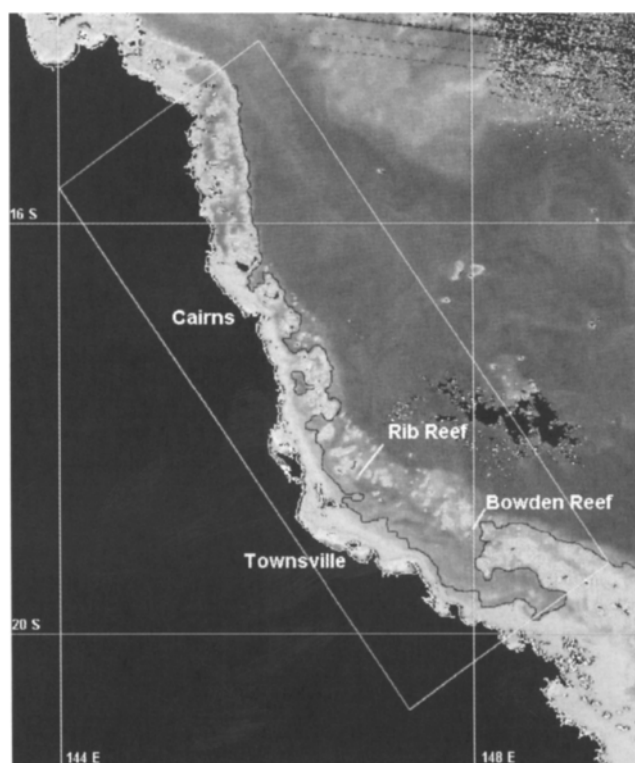
Figure 5. SeaWiFS satellite image of chlorophyll a concentrations in the central Great Barrier Reef, at 01:43:51, July 14, 2000 GMT. Darker areas indicate water of oceanic origin with low chlorophyll concentrations. Lighter areas are either chlorophyll rich shelf waters or turbid coastal water. The solid black contour line delineates waters of coastal and oceanic origin. Black areas are land or cloud. The model domain of the present study is indicated by the enclosed rectangle. The image was received and processed by the Australian Institute of Marine Science, courtesy of Orbimage. Adapted from Brinkman et al. (2002).

To model this process, the general circulation model including the regional slope parameterization (see Section 3) was used to force a 2-D model with a horizontal scale of 500 m. The model was run separately for neap and spring tides. At neap tides, tidal and mean currents are of similar magnitude and the East Australian Current is able to filter through the reef passages (Fig. 6). At spring tides the water entering the reef passage originates from a narrow band around the reef. Outside of this band, the water is deflected around the reef and the reef matrix is thus impermeable to the bulk of the water upstream.

This deflection is made obvious by the evolution of a plume of passive tracers released upstream from this reef matrix. As shown in Fig. 7, at neap tides a fraction of the plume spreads and diffuses through the reef matrix. At spring tides, however, the whole plume is deflected around the reef matrix. This has important biological implications in that the connectivity between reefs for water-borne larvae (including coral and fish) is quite different at spring and neap tides.

The reason for this process appears to be the high dissipation of energy and the resulting high tidal friction at spring tides as a result of the flow around and through the reef matrix. Satellite imagery (Fig. 8) shows island wakes and tidal jets in the lee of reefs, and Sections 5 and 6 describe models of
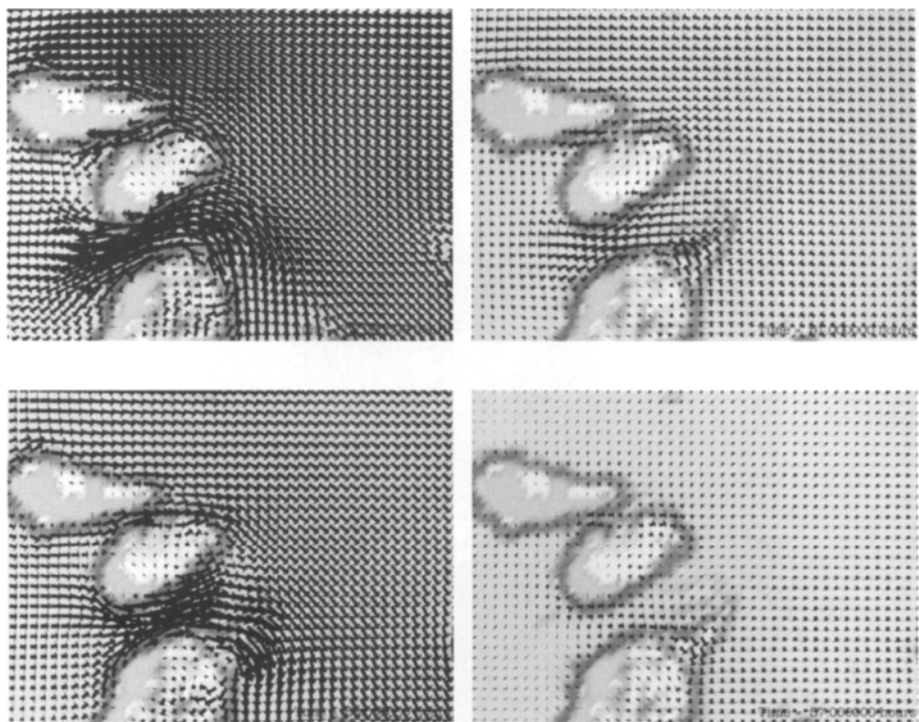
Figure 6. Predicted synoptic distribution of the velocity field on a windless day around Old, Stanley and Darley Reefs (see a location map in Fig. 1c) at (top) peak flood tide and (bottom) peak ebb tide for (left) spring tides and (right) neap tides, for the same regional sea level gradient forced by the Coral Sea. North is to the right. Adapted from Spagnol et al. (2001).

these phenomena. The dissipation of energy in forming an island wake is found to vary nonlinearly with the square of the water current speed. This suggests that four times more energy is dissipated in driving the East Australian Current through the reef matrix at spring tides, than at neap tides.

5. FLOW AROUND OBSTACLES: ONE REEF

The flow around a single reef appears two-dimensional because a reef is typically a few kilometers in size while water depth is typically 20–50 m. Little was known of the dynamics of such flows until a detailed field study was carried out at Rattray Island situated 20°S (Wolanski, 1994). This island is 1.5 km long and 300 m wide and lies in well-mixed coastal waters 20 to 30 m deep. Its long axis is oriented at about 60° to the direction of the dominant semidiurnal flood-tidal current. Flood-tidal currents generate an island wake in the lee of the island. This wake, measured using 26 moored current meters (Fig. 9a), takes the shape of a well-organized eddy growing in time to up to twice the island's width. This wake differs from that expected from laboratory experiments of flows around obstacles because the apparent Reynolds number (assuming a horizontal eddy viscosity of 1.5 m^2 s^{-1}) (see Okubo, 1974; Fischer et al., 1979) is about 400, which in laboratory experiments
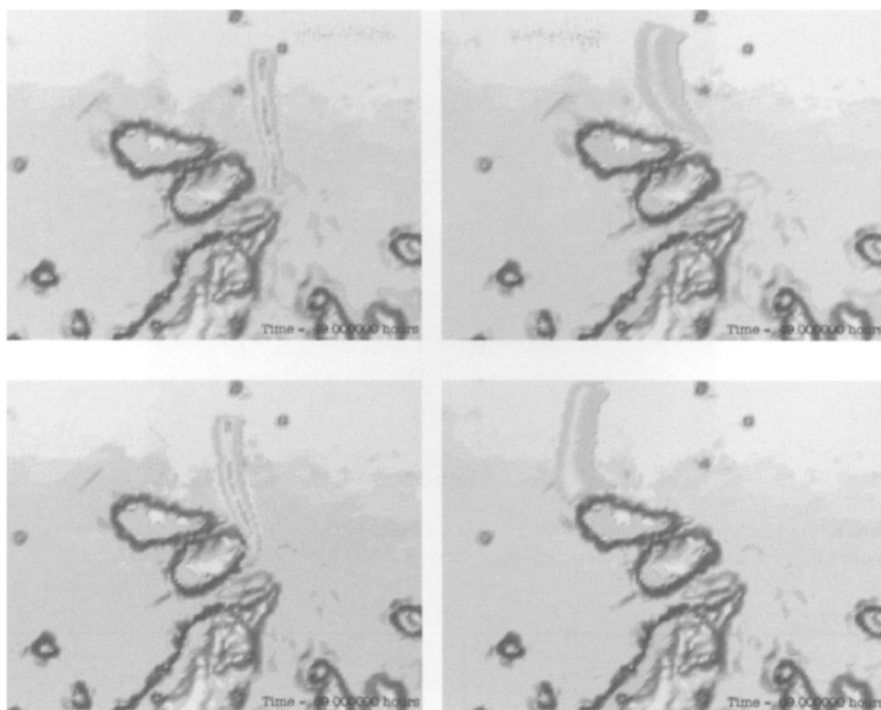
Figure 7. Predicted synoptic distribution of a passive tracer released upstream from Old, Stanley and Darley Reefs under no wind conditions, for (left) neap tides and (right) spring tides, at (top) time=0 and (bottom) time=20 hours, for the same regional sea level gradient forced by the Coral Sea. North is to the right. Note that part of the plume is advected through the reef passages at neap tides only, and that the whole plume is deflected sideways at spring tides. Adapted from Spagnol et al. (2001).

implies a long turbulent wake. In laboratory experiments a distinct eddy of a shape similar to that at Rattray Island forms for a Reynolds number of about 1–20.

A further difference between the eddy at Rattray Island and that in laboratory experiments is found in the different values of the ratio u/U, where u is the maximum velocity in the eddy, and U is the maximum velocity of the prevailing mean flow. At Rattray Island, $u/U = 0.75$, whereas in laboratory experiments $u/U \approx 0.01$. This observation suggests that the aspect ratio W/H is important, where W is the width of the island (the obstacle) and H is the depth. At Rattray Island, $W/H \gg 1$, while in laboratory experiments $W/H \ll 1$. This finding suggests that bottom friction is important for flows around coral reefs.

Depth-averaged, finite-difference 2-D models are able to reproduce quite accurately the horizontal velocity field (Fig. 9b). Discrete vortex models are also quite successful (not shown, see Furukawa and Wolanski, 1998).

Further, visual observations reveal that the eddies are also strongly three-dimensional because bottom mud is brought to the surface in the eddy center within one hour of eddy formation in water depth of 25 m, implying a vertical upward velocity of 5.5 mm/s. Visual observations also reveal that such eddies trap floating matter (for example, coral eggs) along their outer boundaries, implying a downward velocity near the outer edges of the eddy (Wolanski, 1994). Wolanski et al. (1996) carried out laboratory experiments on island wakes where the aspect ratio $W/H \ll 1$. They found a

420
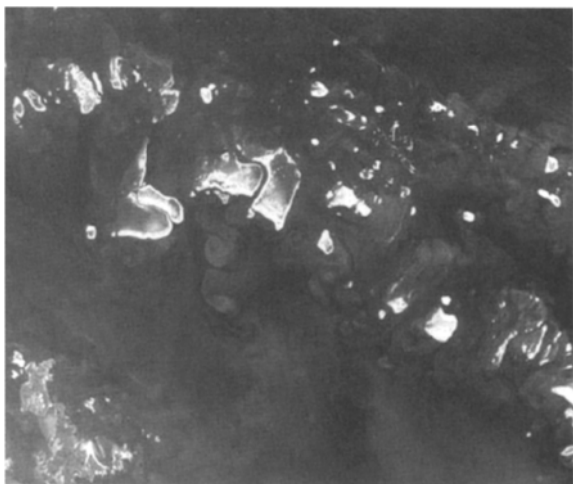
Figure 8. Satellite image of the Great Barrier Reef off the Whitsunday Islands (20°S). Note the vortices are streaming between narrow reef passages. Image courtesy of NASA/GSFC/LaRC/JPL MISR Team.
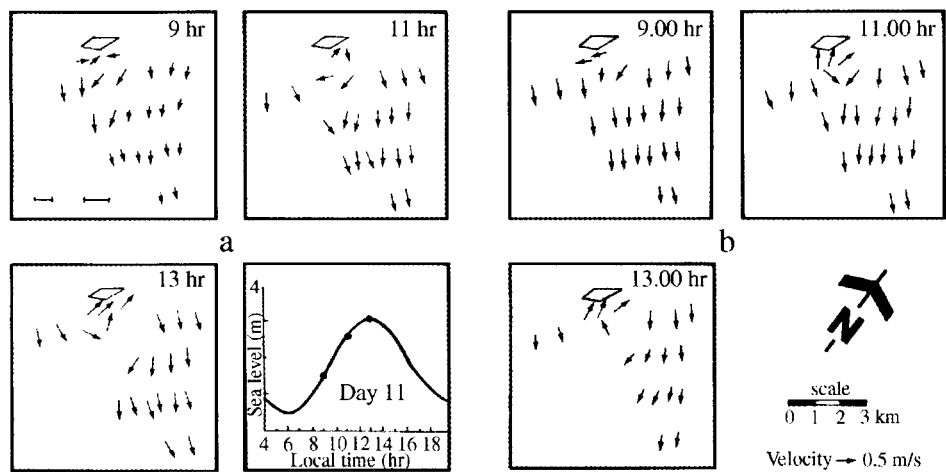
Figure 9. (a) Observed distribution of currents around Rattray Island at flood tide, at current meter mooring sites. (b) Predicted distribution at the same sites, from a depth-averaged 2-D model. Adapted from Wolanski (1994).

strong upwelling in the eddy center and an even stronger downwelling along the edges of the eddy. To calculate this three-dimensional circulation and to compare the ability of various 3-D models to reproduce such flows, five different 3-D models were used to model the island wake at Rattray Island. These models used the same bathymetry, horizontal grid size (200 m) and open boundary forcing (currents on the northern open boundary and tidal elevation on the southern open boundary) taken directly from the field data on currents and tides. The 3-D models were the Princeton Ocean Model (POM) (Blumberg and Mellor, 1987), the AIMS-GHER model (Deleersnijder et al., 1992),

Table 1
Summary of five 3-D model simulations and results for the wake behind Rattray Island.

Model	Vertical Coordinate	L/L_0	u/U
POM	σ	0.5	0.5
AIMS-GHER	σ	0.6	0.6
MECCA	σ	No eddy	No eddy
HAMSOM	z	0.2	0.2
MECO (a)	z	No eddy	No eddy
MECO (b)	z	0.8	0.4

L = predicted maximum eddy size. L_0 = observed maximum eddy size. u = predicted maximum velocity in the eddy. U = observed maximum velocity in the field. In the field, $u/U = 0.75$. Results from the first four models are adapted from Galloway et al. (1996). (a) Result when the model and prototype eddies are compared at the same time; (b) result when the model is allowed to run an extra hour.

the MECCA model (Hess, 1989), the HAMSON model (Stronach et al., 1993) and the MECO model (Walker and Waring, 1998).

The ability of the models to reproduce the observations was estimated by comparing the maximum predicted (L) and measured (L_0) eddy size, and the maximum predicted (u) and measured (U) velocity in the eddy. As summarized in Table 1, it is apparent that while those 3-D models differ in their ability to reproduce the observations, they all significantly under-estimate by at least 40% the horizontal eddy size as well as the circulation in the eddy. Since the 2-D models do not appear to suffer from this problem (Fig. 9), this observation suggests that the parameterization of processes in 3-D models near a salient bathymetry may need improvements. Indeed, while the models predicted an upwelling in the eddy center, the upward velocity was significantly underpredicted (≈ 0.5 mm/s as opposed to 5 mm/s in the field). Further, none of the models predicted a downwelling along the outer edges of the eddy.

To improve the ability of 3-D models to reproduce island wakes, Wolanski et al. (1996) explicitly parameterized, in the AIMS-GHER 3-D model, the intense turbulence present in the free shear layer downstream of the separation points at the tips of the island. This free shear layer was too thin to be resolved by the 200 m horizontal grid. This parameterization locally enhanced the value of the vertical eddy diffusivity in the subgrid scale free shear layer. The results were encouraging, in that the AIMS-GHER 3-D model predicted both downwelling along the eddy edges and upwelling at the eddy center (Fig. 10), although their magnitudes were still underpredicted by 50%. However, this parameterization of the free shear layer resulted in a more realistic representation of the horizontal properties of the eddy. Indeed, with this parameterization, $L/L_0 \approx 0.9$, as opposed to ≈ 0.6 without this parameterization (see Table 1). Similarly, $u/U \approx 0.9$, as opposed to ≈ 0.6, with and without this parameterization, respectively. The reason appears to be that the high eddy viscosity in the free shear layer effectively prevents eddy water, containing vorticity generated at the separation point, from escaping the eddy at the surface and vorticity-free oceanic water from entering the eddy near the bottom. Since vorticity is retained, the eddy spins up faster.

Two-dimensional, depth-averaged models do not suffer from the problem of the vertical shear of velocity advecting vorticity away since they do not allow shear flows with opposite directions at the surface and at the bottom, therefore such models are better able than 3-D models (without free shear layer parameterization) to reproduce the eddy.

Three-dimensional models underpredict the upwelling in island wakes, by 90% without free-shear layer parameterization, and by 50% with this parameterization. It is, however, these vertical motions which are of most interest to biologists. It remains unclear how to improve the models to make them perform more realistically. At present, the vertical eddy diffusion coefficient is calculated from
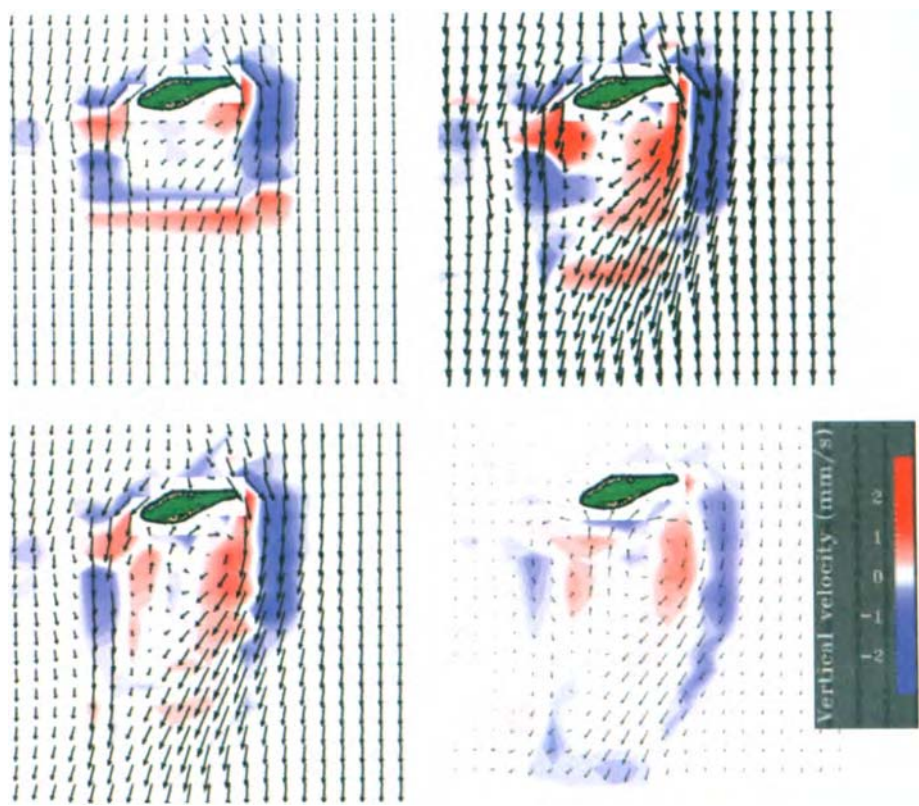
Figure 10. Clockwise starting from top left, synoptic distribution at two-hourly intervals of the predicted 3-D circulation around Rattray Island at flood tide, using the AIMS-GHER model when the free shear layer was explicitly parameterized. The horizontal velocity field at mid-depth is shown by arrows (maximum current ≈ 0.7 m/s, the vertical distribution by shading (a positive value = upwelling, negative value = downwelling; the maximum value ≈ 2 mm/s).

classical, open-channel flow theory. Laboratory experiments where the aspect ratio was conserved (Wolanski et al., 1996) tentatively suggest that bottom-induced turbulence may be reduced in island wakes. This suggests that models could possibly be improved by modifying the parameterization of the vertical eddy viscosity in island wakes. However, this has not been attempted yet, and the models still underperform, because supporting field data are not available. Modeling island wakes remains a rich area of research.

6. FLOW AROUND OBSTACLES: TWO REEFS

Tidal flow through reef passages generates unsteady tidal jets. These systems comprise an inertial jet entraining surrounding water into the jet, and an eddy pair at the leading edge (Wolanski, 1994). In aerial and satellite pictures (Fig. 8) these jets superficially look like mushroom shaped circulation patterns. Like island wakes, these systems also appear two-dimensional because they have an aspect ratio $W/H \gg 1$. As a result, the large-scale dynamics of these systems are successfully reproduced
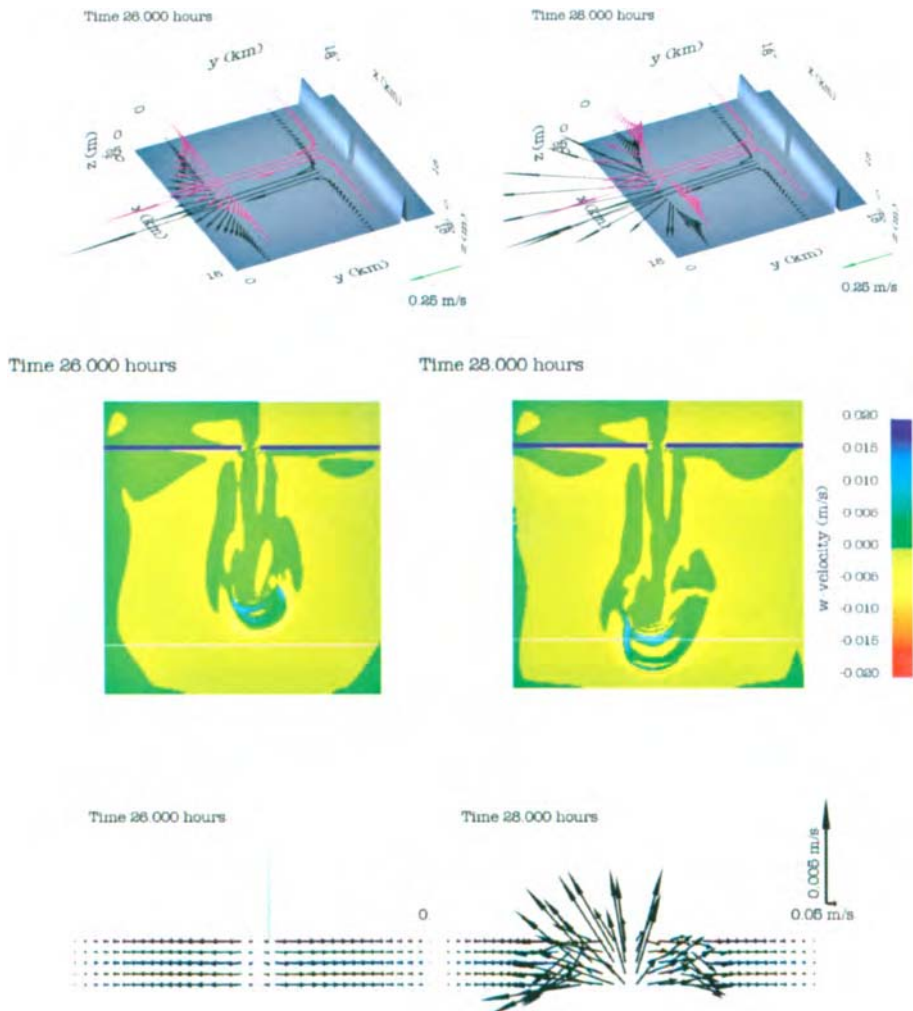
Figure 11. Two synoptic distributions, two hours apart, of the predicted, 3-D velocity field in a tidal jet emanating from the reef passage shown in the top figure in a 3-D rendering of the bathymetry. The top figures show in 3-D at two cross-sections the horizontal velocity field near the surface, and near the bottom. The middle figures show the vertical velocity distribution at mid-depth; the scale is shown by the bar on the far right. The bottom figures show the velocity field in a cross-section shown as the thin line in the middle figure. Thus, the figure on the left shows the velocity field upstream of the incoming tidal jet, and the figure on the right shows the velocity field in the upwelling core of the eddy pair at the leading edge of the tidal jet. In the bottom figures, the vertical velocity scale is much larger than the horizontal one.

by two-dimensional, depth-averaged models (Wolanski et al., 1988). However, the key biological process that oceanographers must understand for tidal jets remains the vertical motions which 2-D models do not resolve. Upwelling motions are strong (several mm/s to cm/s) and appear localized at two sites, namely the free-shear layer of the tidal jet and the center of the eddy, as revealed by

visual observations that these jets are turbid, and by CTD and laboratory studies (Onishi, 1984; van Senden and Imberger, 1990; Wolanski, 1994). To attempt to reproduce such flows, the AIMS-GHER 3-D model was used to model the tidal jet resulting from a tidal current peaking at 1 m s^{-1} through a 1 km wide channel facing a shelf sea 25 m deep. The model domain, shown in Fig. 11, was 18 x 18 km wide and the horizontal grid size was 100 m. The model predicted the formation of an unsteady eddy pair tidal jet system (Fig. 11). The jet entrained surrounding oceanic water and grew in width with increasing distance from the reef passage. At its leading edge a vortex pair was generated. Probably because of bottom friction, the jet tended to slide over the oceanic water and generated two weak vortices upstream of the jet and on either side of the jet axis, with a downwelling peaking at a few mm/s. Within the eddy pair, a very strong upwelling was predicted, peaking at 15 mm/s. This upwelled water would then reach the surface in only half an hour, suggesting that upwelled nutrients may quickly become available to plankton. The model predicts that some of this water downwells (sinks) on the fringes of the eddy and that the rest of the water spreads radially away. Interestingly, the model predicts that within the tidal jet itself there is a weak downwelling that will help to trap on the bottom nutrient-rich, cold water upwelled by the Bernoulli effect on the oceanic side of a reef passage. This nutrient-rich water then would become available to *Halimeda* algae on the bottom. Because of the important biological implications of such motions, field studies are needed.

7. TEMPERATURE DISTRIBUTION

The preceding sections have demonstrated that the complex three-dimensional circulation around coral reefs controls vertical and horizontal mixing and advection. Reef-induced mixing thus controls the horizontal and vertical distribution of temperature throughout the water column, as cooler sub-surface water is upwelled to the surface where it mixes with heated surface water. The importance of this key process was highlighted by the 1998 coral bleaching event. Bleaching means that corals (both hard and soft), as well as giant clams and some other animals like sponges, lose their symbiotic algae *zooxanthellae* and/or the pigments of those algae, such that the coral appears pale to stark white (Yonge and Nicholls, 1931). The algae are expelled when put under stress due to heat or intense solar radiation. The threshold temperature for bleaching may be as little as 1–2°C above the mean monthly summer values (Berkelmans and Willis, 1999). Frequently many corals recover from bleaching, but death may result if the stress is extreme or prolonged (Wilkinson, 2000). The coral bleaching of 1998 was the most geographically widespread ever recorded, and probably the most severe in recorded history. On the GBR mass bleaching occurred in the summer of 1998 during a period of neap tides, low winds and cloud-free skies, conditions optimal for coral bleaching (Skirving and Guinotte, 2001).

Sea surface temperatures sensed from NOAA AVHRR imagery provide evidence for enhanced mixing around reefs. Sea surface temperature was colder within two reef matrices, the Pompey and Swain systems (Fig. 12), and coral bleaching was correspondingly lesser in these regions during the 1998 bleaching event. The three-dimensional baroclinic model MECO (Walker and Waring, 1998) is being used to examine these processes. The solar heating of the water column was modeled for Keeper Reef located in the central GBR (Fig. 1c). The model was forced by short wave radiation data observed at the reef, and data from two temperature loggers deployed at different depths on the reef were used to initialize and verify the development of temperature stratification. The initial observed temperature profile on the 24th of January 1998 (Fig. 13) is well-mixed to approximately 28.3°C. Two weeks later on the 6th of February 1998, at the time of the 1998 bleaching event, the observed profile had developed a stratified structure, with a temperature of 30.75°C at 2 m below the surface, decreasing to 29.2°C at a 10 m depth. The model was run for this 2-week period prior
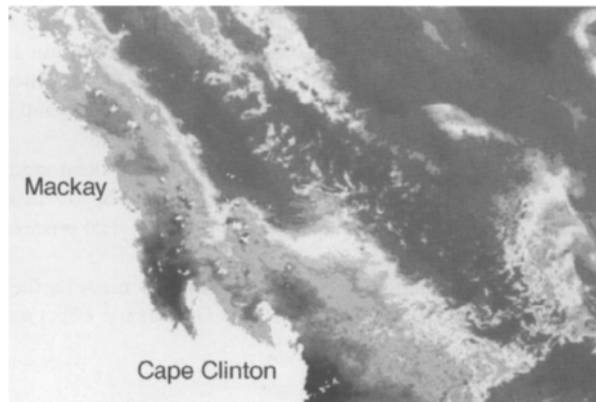
Figure 12. Sea Surface Temperature (SST) image of the Southern GBR from NASA AVHRR satellite during the 1998 coral bleaching event. Offshore between Mackay (21°S) and Cape Clinton (22.5°S) are the Pompey and Swains coral reef systems. These systems are dense reef matrices, their thermal signatures are evident by the patchy nature of the SST, which is colder than surrounding waters. Colder waters were found inshore and within reef matrices.
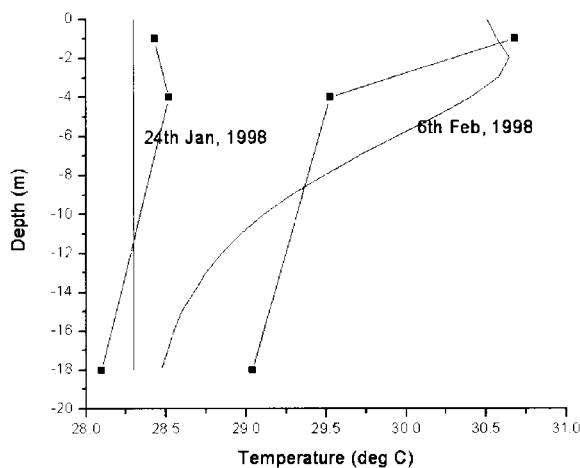
Figure 13. Modeled (smooth lines) and observed (straight lines through filled squares) temperature profile at Keeper Reef (location map in Fig. 1c) during the mass bleaching event in 1998. Temperature data from loggers deployed by the Great Barrier Reef Marine Park Authority.

to the bleaching event, and the predicted final temperature profile compared well with observations (Fig. 13). The predicted profile shows cooler water above the maximum: an effect caused by latent heat loss due to evaporation at the surface. Winds were light and, hence, there occurred little wind-driven mixing in the vertical. The predicted profile is consistent with observations that suggest that approximately three quarters of the total incoming short wave radiation is absorbed within the first 5 m of the ocean (Mann and Lazier, 1996).

It is also important to consider the effect of heating on reef flats. Reef flats are much shallower than the surrounding waters and are generally exposed at low tide. The incoming solar energy is thus partially absorbed in the shallow water and then absorbed, re-radiated and reflected by the reef flat back through the water column. This can significantly increase temperatures and is partly responsible for the elevated temperatures seen in Fig. 13.

Models thus appear effective in predicting the temperature profiles near coral reefs. The predictions are very sensitive to the bathymetry. A key parameter appears to be the density of reef coverage on the shelf—and this varies spatially on the GBR. The two key physical processes are reef-induced turbulence and three-dimensional flows.

It is hoped that models can be used to predict coral bleaching risk maps for the Great Barrier Reef, a tool of increasing need in view of the threat the enhanced Greenhouse effect may pose to the Great Barrier Reef (Hoegh-Guldberg, 1999).

8. DISCUSSIONS

The oceanography of the GBR is made particularly complex by the extraordinary complex bathymetry. The bathymetry interacts with the prevailing circulation at all scales (Fig. 14). As for any other continental shelf, the circulation in the adjoining ocean influences the circulation over the GBR shelf, generating zones of oceanic inflow and longshore currents. In the GBR, however, the obstruction of the flow by the presence of reefs steers and modifies, even at these large scales, the oceanic inflow and the longshore currents. Obstruction by large reefs or a reef matrix steers prevailing currents toward areas of low reef density. This provides the modeler the challenge to merge the large-scale (≈ 1000 km) oceanic circulation with the shelf-scale (≈ 100 km) general distribution of reefs over the shelf. The resulting currents through a reef matrix, and the deflection of the prevailing currents around a reef matrix, are modulated by the tides. This is a process dependent on the bathymetry of passages between reefs, and it presents the modeler yet another challenge to merge the shelf-scale circulation (≈ 100 km) with flow processes in reef passages at horizontal scales of 1.0–0.5 km. While larger scale model grids have spatial resolution (1–2 km) sufficient to adequately describe the majority of the topography, including small islands, reefs and reef passages, these models are not able to accurately reproduce the smaller scale processes that accompany the topography. For example, island wakes and tidal jets alter the friction, which in turn alters the large-scale processes (Fig. 14). The difficulty lies in identifying the small-scale processes that are relevant at larger scales, and then parameterizing these processes in the larger scale models.

The fate of nutrients and larvae is a key biological question that oceanographers must address. This is dependent on details of the currents around individual reefs, which requires the modeler to quantify currents at horizontal scales of the order of 100 m while the prevailing current field varies at horizontal scales of 0.5–2 km. To correctly quantify these three-dimensional processes at horizontal scales of 100 m, the oceanographer, however, has to take into account small-scale processes, such as free-shear layer dynamics, at horizontal scales of meters to tens of meters. All these processes influence the horizontal and vertical distribution of temperature near coral reefs, a key process for the biology as it controls coral survival and health.

A fundamental lesson that has emerged is the need for detailed field studies, occasionally complemented by laboratory studies, of key processes and phenomena. These studies not only provide data for model calibration, they also provide an understanding of key processes that must be incorporated in models, if those models are to successfully reproduce the observed phenomenon. Because of the complex bathymetry, these local physical processes operate at all scales, from subgrid through to scales comparable to the full domain that the modeler attempts to study, while other processes occur at large-scales, such as the oceanic circulation about which field data are not available. Field

time-space scales of GBR hydrodynamics
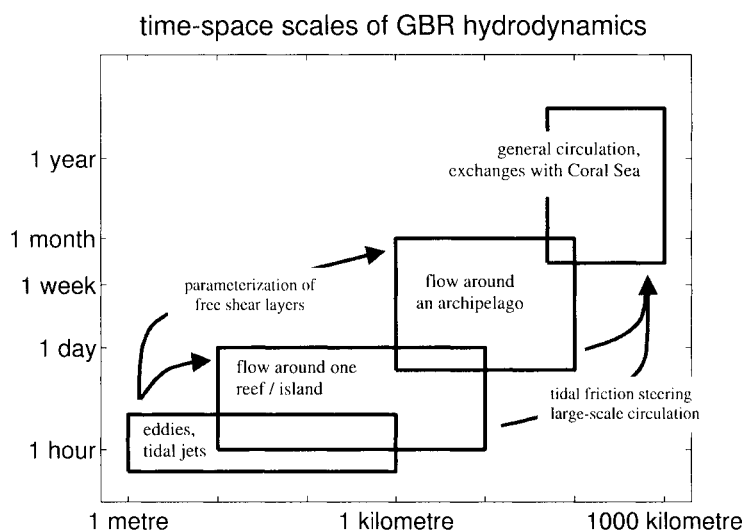
Figure 14. A sketch of the spatial and temporal scales of the dominant processes controlling the circulation in the GBR. The arrows indicate feedback processes.

studies provide an insight on how processes operating at very different spatial and temporal scales interact. They enable the wise modeler to advance their knowledge of the water circulation around the GBR. Modelers focusing on the GBR have become aware that a feedback exists between scales, meaning that small-scale processes have an effect at larger scales. The GBR modeler cannot just perform a one-way "zoom-in" by nesting models of increasingly smaller grid sizes and relying on the coarser models to provide accurate open boundary conditions for smaller scale problems. Instead, the modeler must merge scales judiciously by allowing feedbacks to occur between them (Fig. 14).

Most marine models address a range of time-space scales of motion that is relatively small compared with the complete range of the scales characterizing processes taking place in the sea. For instance, the order of magnitude of the ratio of the largest scale to the smallest one resolved by a model rarely exceeds 100. To broaden the range of space scales simulated numerically, one can have recourse to a variable-resolution grid, which is fine in the regions where it is necessary and is coarser otherwise. Another option is to implement a nested-grid model. However, none of these approaches alleviates the need for appropriate parameterization of subgrid-scale processes. Clearly, the latter depends on the nature of the subgrid-scale phenomena and technical aspects of the modeling of the resolved processes. There are processes that are so peculiar that it is difficult to parameterize them satisfactorily. The broad space-time variability of the GBR provides examples relevant to the present discussion, however, modeling this environment remains nearly an art.

ACKNOWLEDGMENTS

428

REFERENCES

Andrews, J.C., 1983. Water masses, nutrient levels and seasonal drift on the Outer Central Queensland Shelf (Great Barrier Reef). Australian Journal of Marine and Freshwater Research, 34: 821–834.

Andrews, J.C., and Clegg, S., 1989. Coral Sea circulation and transport from modal information models. Deep-Sea Research, 36: 957–974.

Andrews, J.C., and Furnas, M.J., 1986. Subsurface intrusions of Coral Sea water into the central Great Barrier Reef—I. Structures and shelf-scale dynamics. Continental Shelf Research, 6: 491–514.

Berkelmans, R., and Willis, B.L., 1999. Seasonal and local spatial patterns in the upper thermal limits of corals on the inshore Central Great Barrier Reef. Coral Reefs, 18: 219–228.

Blumberg, A.F., and Mellor, G.L., 1987. A description of the three-dimensional coastal ocean circulation model. In: Heaps, N. (Editor), Three-Dimensional Coastal Ocean Models, pp. 1–16. Washington, D.C.: American Geophysical Union.

Brinkman, R., Wolanski, E., Deleersnijder, E., McAllister, F., and Skirving, W., 2002. Oceanic inflow from the Coral Sea into the Great Barrier Reef. Estuarine, Coastal and Shelf Science, 54: 655–668.

Church, J.A., 1987. East Australian Current adjacent to the Great Barrier Reef. Australian Journal of Marine and Freshwater Research, 38: 671–683.

Church, J.A., and Boland, F.M., 1983. A permanent under current adjacent to the Great Barrier Reef. Journal of Physical Oceanography, 13: 1747–1749.

Deleersnijder, E., Norro, A., and Wolanski, E., 1992. A three-dimensional model of the water circulation around an island in shallow water. Continental Shelf Research, 12: 891–906.

Fischer, H.B.E., List, E.Y., Koh, R.C.Y., Imberger, J., and Brooks, N.H. , 1979. Mixing in Inland and Coastal Waters. New York: Academic Press, 483p.

Furukawa, K., and Wolanski, E., 1998. Shallow-water frictional effects in island wakes. Estuarine, Coastal and Shelf Science, 46: 599–608.

Galloway, D., Wolanski, E., and King, B., 1996. Modelling eddy formation in coastal waters: A comparison between model capabilities. In: Spaulding, M., and Cheng, R.T. (Editors), Estuarine and Coastal Modelling, pp. 13–25. Reston, VA: American Society Civil Engineers.

Hess, K.W., 1989. MECCA Programs Documentation. NOAA Technical Report NESDIS, 46.

Hoegh-Guldberg, O., 1999. Climate change, coral bleaching and the future of the world's coral reefs. Marine and Freshwater Research, 50: 839–866.

Hughes, R.D., 1993. An Investigation of the Coral Sea with an Ocean General Circulation Model. Ph.D. Thesis. James Cook University of North Queensland, Department of Civil and Systems Engineering, 290p.

Mann, K.H., and Lazier, J.R.N., 1996. Dynamics of Marine Ecosystems, Biological-Physical Interactions in the Oceans. Second Edition. Massachusetts: Blackwell Science, 394p.

Middleton, J.H., 1987. Steady coastal circulation due to oceanic longshore pressure gradients. Journal of Physical Oceanography, 17: 604–612.

Okubo, A., 1974. Effects of shoreline irregularities on streamwise dispersion in estuaries and other embayments. Netherlands Journal of Sea Research, 6: 213–224.

Oliver, J., King, B., Willis, B., Babcock, R., and Wolanski, E., 1992. Dispersal of coral larvae from a coral reef. Comparison between model predictions and observed concentrations. Continental Shelf Research, 12: 873–891.

Onishi, S., 1984. Study of vortex structure in water surface jets by means of remote-sensing. In: Nihoul, J.C.J. (Editor), Remote Sensing of Shelf Seas Hydrodynamics, pp. 107–132. Amsterdam, The Netherlands: Elsevier Science Publishers.

Pickard, G.L., Donguy, J.R., Hennin, C., and Rougerie, F., 1977. A Review of the Physical Oceanography of the Great Barrier Reef and Western Coral Sea. Monograph Series 2. Townsville: Australian Institute of Marine Science, 134p.

Sammarco, P.W., and Heron, M.L. (Editors), 1994. The Bio-Physics of Marine Larval Dispersal, Coastal and Estuarine Studies, Vol. 45. Washington, D.C.: American Geophysical Union, 352p.

Skirving, W., and Guinotte, J., 2001. The sea surface temperature story on the Great Barrier Reef during the coral bleaching event of 1998. In: Wolanski, E. (Editor), Oceanographic Processes of Coral Reefs: Physical and Biological Links in the Great Barrier Reef, pp. 301–313. Boca Raton, FL: CRC Press.

Spagnol, S., Wolanski, E., and Deleersnijder, E., 2001. Steering by Coral Reef assemblages. In: Wolanski, E. (Editor), Oceanographic Processes of Coral Reefs: Physical and Biological Links in the Great Barrier Reef, pp. 231–236. Boca Raton, FL: CRC Press.

Stronach, J.A., Backhaus, J.O., and Murty, T.S., 1993. An update on the numerical simulation of oceanographic processes in waters between Vancouver Island and the mainland: The GF8 model. Oceanography and Marine Biology Annual Review, 31: 1–86.

van Senden, D., and Imberger, J., 1990. Effects of initial condition and Ekman suction on tidal outflows from inlets. Journal of Geophysical Research, 95: 13,373–12,291.

Walker, S.J., and Waring, J.R., 1998. Model for Estuaries and Coastal Oceans. CSIRO Internal Report No. OMR-118/120, 77p.

Wilkinson, C.R., 2000. Status of Coral Reefs of the World: 2000. Townsville: Australian Institute of Marine Science, 363p.

Wolanski, E., 1994. Physical Oceanographic Processes of the Great Barrier Reef. Boca Raton, FL: CRC Press, 194p.

Wolanski, E. (Editor), 2001. Oceanographic Processes on Coral Reefs: Physical and Biological Links in the Great Barrier Reef. Boca Raton, FL: CRC Press, 356p.

Wolanski, E., Asaeda, T., Tanaka, A., and Deleersnijder, E., 1996. Three-dimensional island wakes in the field, laboratory and numerical models. Continental Shelf Research, 16: 1437–1452.

Wolanski, E., Doherty, P., and Carleton, J., 1997. Directional swimming of fish larvae determines connectivity of fish populations on the Great Barrier Reef. Naturwissenschaften, 84: 262–268.

Wolanski, E., Drew, E., Abel, K., and O'Brien, J., 1988. Tidal jets, nutrient upwelling and their influence on the productivity of the algal *Halimeda* in the Ribbon Reefs, Great Barrier Reef. Estuarine, Coastal and Shelf Science, 26: 169–201.

Wolanski, E., and Hamner, W.M., 1988. Topographically controlled fronts in the ocean and their biological influence. Science, 241: 177–181.

Wolanski, E., and Spagnol, S., 2000. Sticky waters in the Great Barrier Reef. Estuarine, Coastal and Shelf Science, 50: 27–32.

Yonge, C.M., and Nicholls, A.G., 1931. Studies on the physiology of the *zooxanthellae*. Science Report, Great Barrier Reef Expedition (1928–1929), Vol. 1, pp. 135–176.

This Page Intentionally Left Blank

Chapter 16

A Numerical Simulation of Japan/East Sea (JES) Thermohaline Structure and Circulation

Peter C. Chu [a], Shihua Lu [a], Chenwu Fan [a] and Chang S. Kim [b]

[a]Department of Oceanography, Naval Postgraduate School, Monterey, CA 93943
[b]Korea Ocean R&D Institute, Ansan 425–170, South Korea

1. INTRODUCTION

The Japan Sea, known as the East Sea in Korea, has a steep bottom topography (Fig. 1) that makes it a unique semi-enclosed ocean basin overlaid by a pronounced monsoon surface wind. The Japan/East Sea, hereafter referred to as JES, covers an area of 10^6 km^2. It has a maximum depth in excess of 3,700 m, and is isolated from open oceans except for small (narrow and shallow) straits, which connect the JES with the North Pacific through the Korea/Tsushima and Tsugaru Straits and
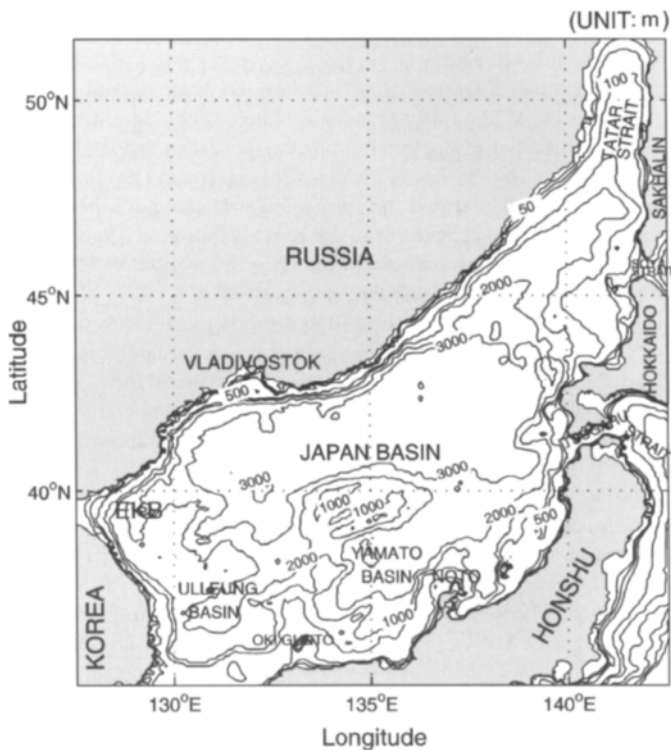
Figure 1. The bottom topography (m) of the Japan/East Sea (JES).

with the Okhotsk Sea through the Soya and Tatar Straits. The JES contains three major basins called the Japan Basin (JB), Ulleung/Tsushima Basin (UTB), and Yamato Basin (YB), and has a high central plateau called the Yamato Rise (YR). The JES has great scientific interest as a miniature prototype ocean. Its basin-wide circulation pattern, boundary currents, Subpolar Front (SPF), mesoscale eddy activities and deep water formation are similar to those in a large ocean.

The JES thermohaline structure and general circulation have been investigated for several decades. The Tsushima Warm Current (TWC), dominating the surface layer, flows in from the Tsushima Strait, and carries warm water from the south up to 40°N where a polar front forms (Seung and Yoon, 1995). Most of the nearly homogeneous water in the deep part of the basin is called the Japan Sea Proper Water (Moriyasu, 1972), and is of low temperature and low salinity. Above the Proper Water, warm and saline water flows in through the Tsushima Strait, transports northeastward, and flows out through the Tsugaru and Soya Strait.

The TWC separates north of 35°N into western and eastern channels (Uda, 1934; Kawabe, 1982a; 1982b; Hase et al., 1999; Senjyu, 1999). The flow through the western channel closely follows the Korean coast [called the East Korean Warm Current (EKWC)] until it bifurcates into two branches near 37°N. The eastern branch follows the SPF to the western coast of Hokkaido Island, and the western branch moves northward and forms a cyclonic eddy at the Eastern Korean Bay (EKB). The EKWC meets the southward coastal current, the North Korean Cold Current (NKCC), at about 38°N with some seasonal meridional migration. After separation from the coast, the EKWC and the NKCC converge and form a strong front (i.e., SPF) that stretches in a west-east direction across the basin. The NKCC makes a cyclonic recirculation gyre in the north but most of the EKWC flows out through the outlets (Uda, 1934). The formation of the NKCC and the separation of the EKWC are due to a local forcing by wind and buoyancy flux (Seung, 1992). Large meanders develop along the front and are associated with warm and cold eddies.

Seasonal variability of the JES thermohaline structure has been studied by many investigators (Gong and Park, 1969; Isoda et al., 1991; Isoda and Saitoh, 1993; Maizuru Marine Observatory, 1997) using limited data sets. For example, after analyzing satellite infrared (IR) images and routine hydrographic survey data (by the Korea Fisheries Research and Development Agency) for the western part of the JES in the winter and the spring 1987, Isoda and Saitoh (1993) found that a small meander of a thermal front originates from the Korean/Tsushima Strait near the Korean coast and gradually grows into an isolated warm eddy with a horizontal scale of 100 km. The warm eddy moves slowly northward from spring to summer.

Although the seasonal thermal variability on 150 m depth is weaker than on the surface, SPF still occurs at around 40°N all the time throughout the year and is located at almost the same location as at the surface. It divides the water masses with different characteristics. North of the SPF, temperature is uniformly cold (1°–3°C) throughout the year. South of the SPF, temperature changes from 5°C to 9°C. The SPF meandering at 131°E, 134°E, and 138°E forms several mesoscale eddies (Chu et al., 2001a; 2001b). The SPF meandering near Okin Gunto (134°E) in spring was previously reported by Isoda and Saitoh (1993).

With limited data, Miyazaki (1953) found a low salinity layer in the SPF region. Later on Kim and Chung (1984) found a very similar property in UTB and called it the JES Intermediate Water (JIW). After analyzing the comprehensive hydrographic data for the whole JES collected by the Japan Meteorological Agency, the Maizuru Marine Observatory, and the Hydrographic Department of the Japan Maritime Safety Agency, Senjyu (1999) showed the existence of a salinity minimum (SMIN) layer (i.e., JIW) between the TWC Water and the JES Proper Water. The southwestern JES west of 132°E is the upstream region of JIW. The lowest salinity and the highest oxygen concentration are found in the 38°–40°N areas west of 132°E. The JIW takes two flow paths: an eastward flow along the SPF and a southward flow parallel with the Korean coast in the region west of 132°E. Analyzing the hydrographic collected from an international program, Circulation Research of the East Asian

Marginal Seas (CREAMS), Kim and Kim (1999) found the high salinity water with high oxygen in the eastern JB (i.e., north of SPF) and named the water the High Salinity Intermediate Water (HSIW).

Recently, Chu et al. (1998; 1999a) reported the seasonal occurrence of JES eddies from the composite analysis of the U.S. National Center for Environmental Prediction (NCEP)'s monthly SST fields (1981–1994). For example, they identified a warm center appearing in late spring in the East Korean Bay. Chu et al. (2001a; 2001b; 2002) further reported the seasonal variation of the thermohaline structure and inverted circulation from the Navy's unclassified Generalized Digital Environmental Model (GDEM) temperature and salinity data on a $0.5° × 0.5°$ grid using the P-vector method (Chu, 1995). The GDEM for the JES was built on 136,509 temperature and 52,572 salinity (1930–1997) historical profiles. A three-dimensional estimate of the absolute geostrophic velocity field was obtained from the GDEM temperature and salinity fields using the P-vector method. The climatological mean and seasonal variabilities of the thermohaline structure and the inverted currents such as the SPF, the mid-level (50 to 200 m) salty tongue, the Tsushima Warm Current (TWC) and its bifurcation were identified. Using the data collected from Conductivity-Temperature-Depth (CTD) and Acoustic Doppler Current Profilers (ADCP) measurements in the southwestern JES from March to June 1992, Shin et al. (1995; 1996) found a dipole structure of gyres with an anticyclonic eddy near the Korean coast and a cyclonic eddy in the UTB.

Numerical studies of the JES circulation started in the early 1980s. Various types of models were used such as the multilayered model (Sekine, 1991; Kawabe, 1982a; 1982b; Yoon, 1982a; 1982b; Seung and Nam, 1992; Seung and Kim, 1995), the Modular Ocean Model (MOM) (Kim and Yoon, 1994; Holloway et al., 1995; Kim and Yoon, 1999; Yoshikawa et al., 1999), rigid-lid z-level model (Yoshikawa et al., 1999), the Miami Isopycnal Coordinate Model (MICOM) (Seung and Kim, 1993; Kim and Yoon, 1996) and the Princeton Ocean Model (POM) (Mooers and Kang, 1995; Chu et al., 1999b; 2000). Most of the numerical efforts are concentrated on simulating the basin-wide circulation, the TWC bifurcation, and formation of the intermediate waters using idealized or restoring-type surface thermal forcing. To date, most modelers (except Kim and Yoon, (1999)) used the restoring-type surface thermal forcing.

Kim and Yoon (1999) simulated seasonal variations of JES circulation and thermohaline structure using MOM with rigid-lid, 19 z-levels, and $(1/6)° × (1/6)°$ horizontal resolution. The model was forced by the monthly mean wind stress (Na et al., 1992), reconstructed Haney-type surface heat flux (Haney, 1971) using climatological data (Hirose et al., 1996), and Newtonian type salinity restoring condition using observed monthly mean surface salinity. The model successfully simulates seasonal variation of the surface circulation pattern (Fig. 2), the meandering and eddy formation, and the thermohaline structure, especially the salinity minimum layer under the East Korean Warm Water (EKWC). However, the model is not able to simulate the dual gyres with an anticyclonic eddy near the Korean coast and a cyclonic eddy in UTB as observed by Shin et al. (1995; 1996). Two approaches might be useful for simulating such a dipole structure near the Korean coast: (a) implementation of a model to a realistic bottom topography, and (b) increase of the horizontal resolution. Besides, the effect of surface salinity flux (evaporation minus precipitation) on the haline structure especially the salinity minimum layer should also be studied. Hogan and Hurlbert (1999a; 1999b; 2000a; 2000b) implemented the Naval Research Laboratory Layered Ocean Model (NLOM) to JES with various horizontal resolution (up to 1/64°) under different wind forcing. Their results demonstrate that at least 1/32° (3.5 km) grid is necessary to generate sufficient baroclinic instability to produce eddy-driven cyclonic deep mean flows and to obtain a realistic separation latitude of the EKWC from the Korean coast when Hellerman-Rosenstein monthly climatological wind stress forcing is used.

In this study, POM with realistic topography and flux-type surface forcing is used to simulate the seasonal variabilities of the JES circulation, and thermohaline structure including the dual gyres with an anticyclonic eddy near the Korean coast and a cyclonic eddy in UTB, the meandering SPF and eddies, the TWC bifurcation, the retroflection and dipole gyres of EKWC, the Liman Cold Current
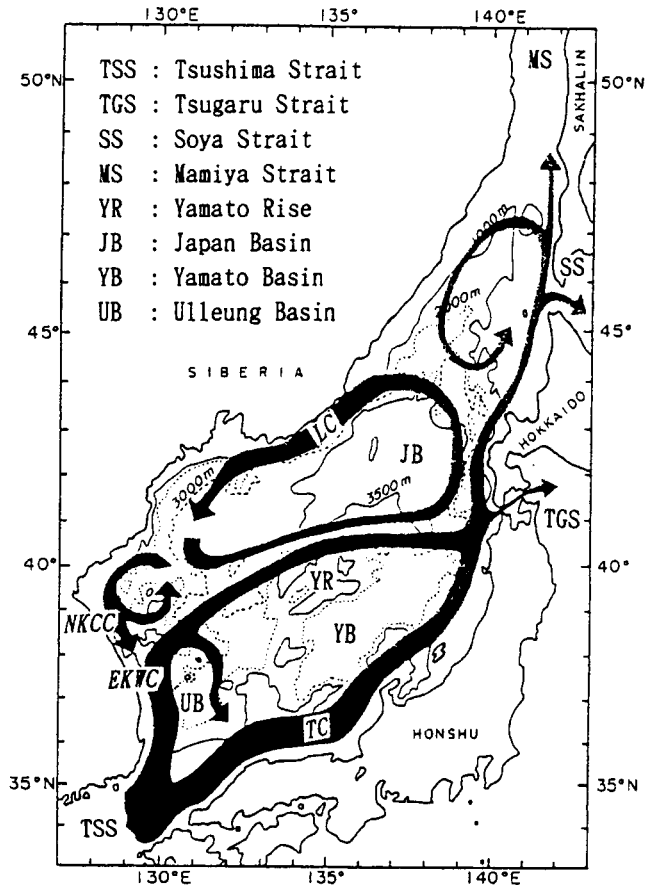
Figure 2. Schematic map of surface current systems (after Senjyu, 1999).

(LCC) and its penetration into the southwestern waters along the Korean coast, deep convection and salinity minimum layers near the SPF. These features were identified in the first part of this chapter using the Navy's GDEM data.

The outline of this chapter is as follows: A description of the JES current systems is given in Section 2. A depiction of the seasonal variation of atmospheric forcing is given in Section 3. The numerical ocean model and integration are depicted in Section 4. The simulated seasonal variability of temperature, salinity, and circulation are discussed in Sections 5, 6, and 7, respectively. In Section 8 conclusions are presented.

2. JES CURRENT SYSTEMS

Most of the nearly homogeneous water in the deep part of the basin is called the Japan Sea Proper Water (Moriyasu, 1972) and is of low temperature and low salinity. Above the Proper Water, the TWC, dominating the surface layer, flows in from the East China Sea through the Korea/Tsushima Strait and carries warm water from the south. The LCC carries cool fresh surface water from the north

and northeast (Seung and Kim, 1989; Holloway et al., 1995). The properties of this surface water are generally believed to be determined by the strong wintertime cooling coupled with freshwater input from the Amur River and the melting sea ice in Tatar Strait (Martin and Kawase, 1998). The LCC flows southward along the Russian coast, beginning at latitude slightly north of Soya Strait, terminating off Vladivostok (Fig. 2), and becoming the North Korean Cold Current (NKCC) after reaching the North Korean coast (Yoon, 1982a).

The TWC separates into two branches, which flow through the western and eastern channels of the Korea/Tsushima Strait (Kawabe, 1982a; 1982b; Hase et al., 1999). The flow through the eastern channel closely follows the Japanese Coast and is called the Nearshore Branch (Yoon, 1982c) or the first branch of TWC (FBTWC) (Hase et al., 1999). The flow through the western channel is called the EKWC, which closely follows the Korean coast until it separates near 37°N into two sub-branches. The western sub-branch moves northward and forms a cyclonic eddy over UTB off the eastern Korean coast. The eastern sub-branch flows eastward to the western coast of Hokkaido Island, and becomes the second branch of the TWC (SBTWC).

The NKCC meets the EKWC at about 38°N with some seasonal meridional migration. After separation from the coast, the NKCC and the EKWC converge and form a strong front that stretches in the zonal direction across the basin. The NKCC makes a cyclonic recirculation gyre in the north but most of the EKWC flows out through the Tsugaru and Soya Straits (Uda, 1934). The formation of NKCC and separation of EKWC are due to local forcing by wind and buoyancy flux (Seung, 1992). Large meanders develop along the front and are associated with warm and cool eddies.

Recent observation by Shin et al. (1995) shows the existence of an anticyclonic warm eddy during March to June near the Korean coast around 38°N. The length scale was approximately 150 km in surface and deepens down to about 200 m that are similar depth of the EKWC.

The surface current of the eddy reaches up to 65 cm/s while the maximum speed of the observed EKWC in June was reported as approximately 70 cm/s.

Seung (1992) identified major features of the volume transport from earlier numerical modeling results. The transport pattern is largely determined by the upper layer circulation and characterized by a large-scale cyclonic recirculation gyre, in which the EKWC and the Nearshore Branch take part as the inflow-outflow system, and also includes the NKCC. A few hundred kilometers from the separation point, the EKWC forms an anticyclonic gyre. The gyre becomes stronger as the EKWC develops. On the other hand, the northern cyclonic gyre is very deep and is most significant in winter when strengthened by the wind and buoyancy flux. It is usually called the JB gyre. The gyre, or the southward coastal current (NKCC) related to it, is deep enough to intrude southward beneath the EKWC most of the time. Seung (1992) also confirmed the summertime presence of a countercurrent beneath the Nearshore Branch.

3. SEASONAL VARIATION OF ATMOSPHERIC FORCING

3.1. General Description

The Asian monsoon strongly affects the thermal structure of the JES. During the winter monsoon season, a very cold northwest wind blows over the JES (Fig. 3a) as a result of the Siberian High Pressure System with a mean surface wind speed between 10 and 15 ms^{-1}. By late April, numerous frontally generated events occur making late April and May highly variable in terms of wind speeds and amount of clouds. During this period storms originating in Mongolia may cause strong, warm westerlies (Fig. 3b). By late May and early June, a summer surface atmospheric low pressure system begins to form over Asia. Initially this low pressure system is centered north of the Yellow Sea producing westerly winds. In late June, this low begins to migrate to the west setting up the southwest monsoon that dominates the summer months. The winds remain variable through June until the
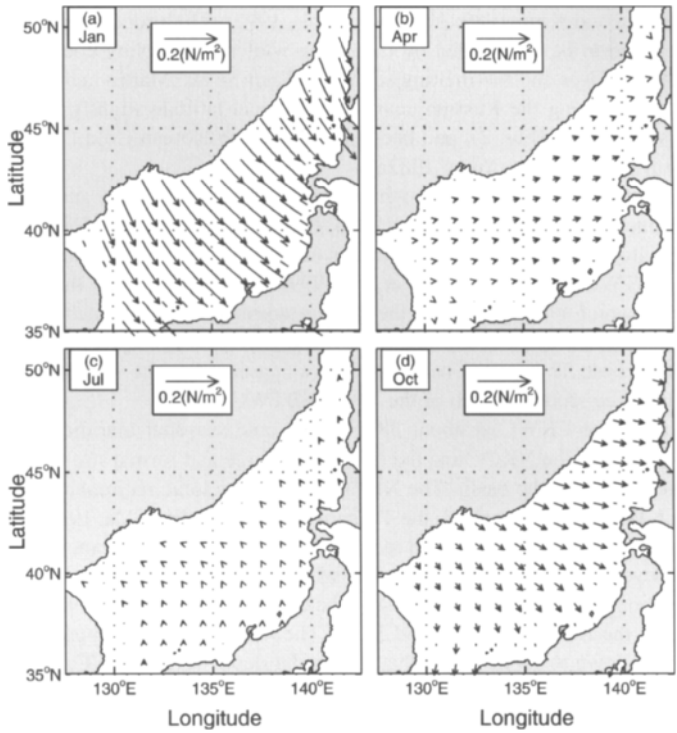
Figure 3. Climatological monthly mean wind stress for: (a) January, (b) April, (c) July, and (d) October, using the COADS data.

Manchurian Low Pressure System strengthens. Despite the very active weather systems, the mean surface wind speed over the JES in summer (Fig. 3c) is between 3 and 4 m/s, much weaker than in winter (Fig. 3a). By July, however, high pressure (the Bonin High) to the south and the low pressure over Manchuria produce southerly winds carrying warm, moist air over the East China Sea/Yellow Sea. In summer, warm air and strong downward net radiation stabilize the upper layer of the JES and causes the surface mixed layer to shoal. October (Fig. 3d) is the beginning of the transition to winter conditions. The southerly winds weaken and the sea surface slope establishes its winter pattern.

Here, a climatological description of the surface net heat and freshwater fluxes over the JES is presented. The data sets used were the objectively analyzed fields of surface marine climatology and anomalies of fluxes of heat, momentum, and freshwater. The fields are derived from individual observations in the Comprehensive Ocean-Atmosphere Data Set (COADS) from 1945 to December 1989 and are analyzed on a 1° by 1° grid (da Silva et al., 1994).

3.2. Net Surface Heat Flux
Net surface heat flux is computed by

$$Q_{Net} = R_S - (R_L + Q_S + Q_L) \tag{1}$$

where R_S is the net downward shortwave radiation, R_L the net upward longwave radiation, Q_S the sensible heat flux, and Q_L the latent heat flux. Positive (negative) values of Q_{Net} indicate net heat
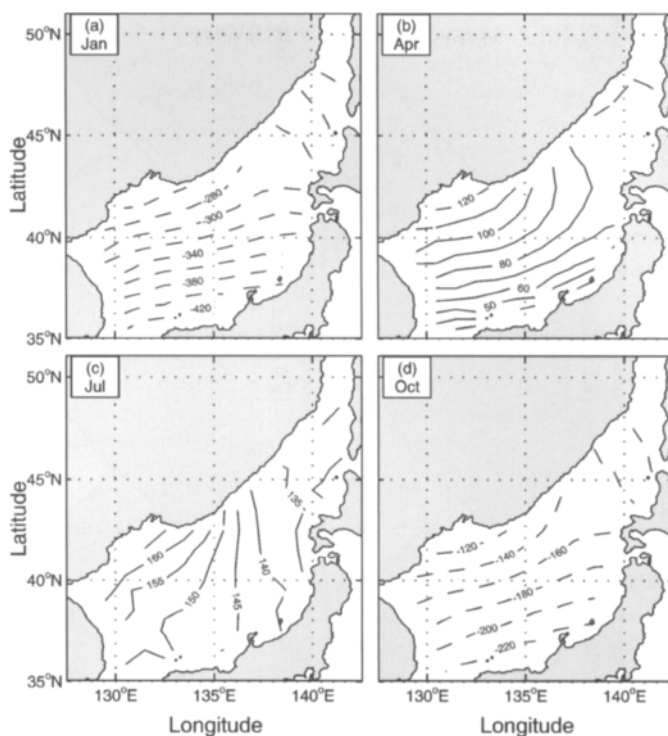
Figure 4. Climatological monthly mean net heat flux ($W m^{-2}$) for: (a) January, (b) April, (c) July, and (d) October, using the COADS data.

gain (loss) of the ocean at the surface. The summer field is relatively homogeneous (140 to 160 $W m^{-2}$) throughout the JES, whereas a significant horizontal gradient increasing from the southeast (Japan coast) to the northwest (Russian coast) exists for the other seasons (Fig. 4). The ocean surface near Korea/Tsushima Strait has a maximum heat loss of 400 $W m^{-2}$ in the winter (January) and a minimum heat gain of 60 $W m^{-2}$ in the spring (April). This range of values is consistent with earlier studies (Hirose et al., 1996; Seo, 1998). This long-term net surface heat loss will be compensated by the advection of warm waters from the East China Sea.

3.3. Surface Freshwater Flux

The surface freshwater flux is the difference between precipitation rate (P) and evaporation rate (E)

$$F = P - E \tag{2}$$

Positive values of F indicate net water mass gain at the sea surface. The surface freshwater flux exhibits a distinct four-season pattern. The winter is characterized by freshwater gain (2 to 6 cm/month) in the northern and northeastern JES, and freshwater loss (2 to 10 cm/month) in the southern and southwestern JES. A strong horizontal F-gradient monotonically decreases from northeast to southwest. The spring (Fig. 5b) and summer (Fig. 5c) are both characterized by freshwater gain in the whole JES with different horizontal F-gradients: decreasing (increasing) from 4 cm/month
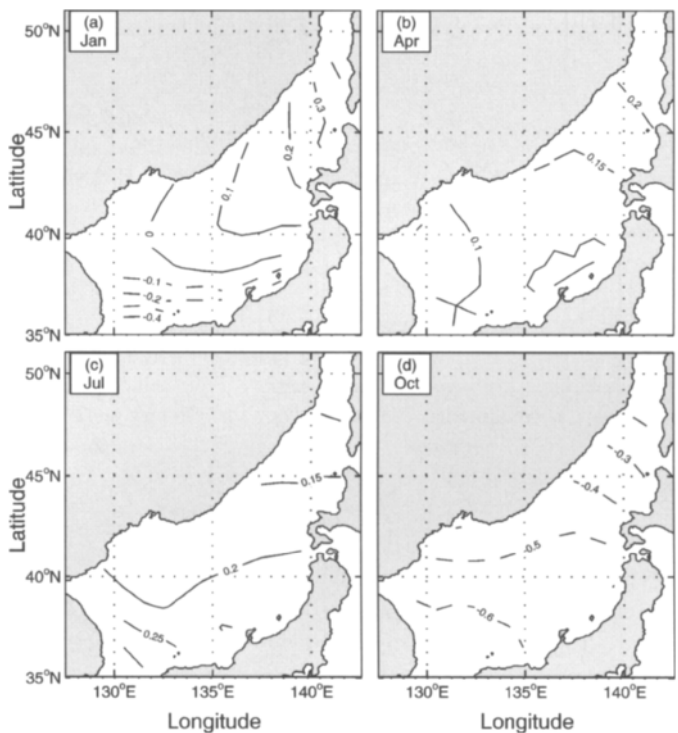
Figure 5. Climatological monthly mean precipitation minus evaporation [mm $(3 \text{ hr})^{-1}$] for: (a) January, (b) April, (c) July, and (d) October, using the COADS data.

(4 cm/month) in the northeast JES to 2 cm/month (6 cm/month) in the southwest JES in the spring (summer). The autumn (Fig. 5d) is characterized by freshwater loss in the whole JES (4 to 16 cm/month) with a maximum loss of 16 cm/month near Korea/Tsushima Strait.

4. NUMERICAL OCEAN MODEL

4.1. Model Description

Coastal oceans and semi-enclosed seas are marked by extremely high spatial and temporal variability that challenges the existing predictive capabilities of numerical simulations. POM is a time-dependent, primitive equation circulation model rendered on a three-dimensional grid that includes realistic topography and a free surface (Blumberg and Mellor, 1987). Tidal forcing was not included in this application of the model, since high frequency variability of the circulation is not considered. River outflow is also not included. However, the seasonal variation in sea surface height, temperature, salinity, circulation, and transport are represented by the model. From a series of numerical experiments, the qualitative and quantitative effects of nonlinearity, wind forcing, and lateral boundary transport on the JES is analyzed, yielding considerable insight into the external factors affecting the regional oceanography.

Consequently, the model contains $181 \times 199 \times 23$ fixed grid points. The horizontal spacing is $5'$ latitude and longitude (approximately 5.77 to 7.59 km in the zonal direction and 9.265 km in

the meridional direction) and there are 23 sigma levels in vertical coordinate. The model domain extends from 35.0°N to 51.0°N, and from 127.0°E to 142.0°E. The bottom topography (Fig. 1) is obtained from the Naval Oceanographic Office's Digital Bathymetry Data Base $5' \times 5'$ resolution (DBDB5). The horizontal friction and mixing are modeled using the Smagorinsky (1963) form with the coefficient chosen to be 0.2 for this application. The bottom stress τ_b is assumed to follow a quadratic law

$$\tau_b = \rho_0 |V_b| V_b \tag{3}$$

where ρ_0 (= 1025 kg/m^3) is the characteristic density of the sea water, V_b is the horizontal component of the bottom velocity, and C_D is the drag coefficient which is specified as 0.0025 (Blumberg and Mellor, 1987), which is similar to the value (0.002) used by Hogan and Hurlburt (2000a).

4.2. Surface Forcing Functions

The atmospheric forcing for the JES application of POM includes mechanical and thermohaline forcing. The wind forcing is depicted by

$$\rho_0 K_M \left(\frac{\partial u}{\partial z}, \frac{\partial v}{\partial z} \right)_{z=0} = \left(\tau_{0x}, \tau_{0y} \right) \tag{4}$$

where K_M is the vertical mixing coefficient for momentum, (u, v) and (τ_{0x}, τ_{0y}) are the two components of the water velocity and wind stress vectors, respectively. The wind stress at each time step is interpolated from monthly mean climatological wind stress from COADS (1945–1989), with a resolution of $1° \times 1°$. The COADS wind stress was interpolated into the model grid with a resolution of $5'$.

Surface thermal forcing is depicted by

$$K_H \frac{\partial \theta}{\partial z} = \alpha_1 \left(\frac{Q_H}{\rho C_p} \right) + \alpha_2 C \left(\theta_{OBS} - \theta \right) \tag{5}$$

$$K_S = \frac{\partial S}{\partial z} = -\alpha_1 FS + \alpha_2 C \left(S_{OBS} - S \right) \tag{6}$$

where K_H and K_S are the vertical mixing coefficients for heat and salt, (θ, S) and (θ_{OBS}, S_{OBS}) are modeled and observed potential temperature and salinity, and c_p is the specific heat. The relaxation coefficient C is the reciprocal of the restoring time period for a unit volume of water. The parameters (α_1, α_2) are (0, 1) switches: $\alpha_1 = 1$, $\alpha_2 = 0$, would specify only flux forcing is applied. The flux forcing is used in this study.

4.3. Lateral Boundary Forcing

Boundary conditions for closed lateral boundaries, (i.e., the modeled ocean) bordered by land, were defined using a free-slip condition for velocity and a zero gradient condition for temperature and salinity. Thus, no advective or diffusive heat, salt or velocity fluxes occur through these boundaries.

At open boundaries, the numerical grid terminates but the fluid motion is unrestricted. Uncertainty at open boundaries makes marginal sea modeling difficult. Three approaches, local-type, inverse-type, and nested-basin/coastal modeling, are available for determining the open boundary condition. Here, we take the local-type approach; i.e., use the radiation boundary condition with specified volume transport. When the water flows into the model domain, temperature and salinity at the open boundary are prescribed from observational data. When water flows out of the domain, the radiation condition was applied

$$\frac{\partial}{\partial t} (\theta, S) + U_n \frac{\partial}{\partial n} (\theta, S) = 0 \tag{7}$$
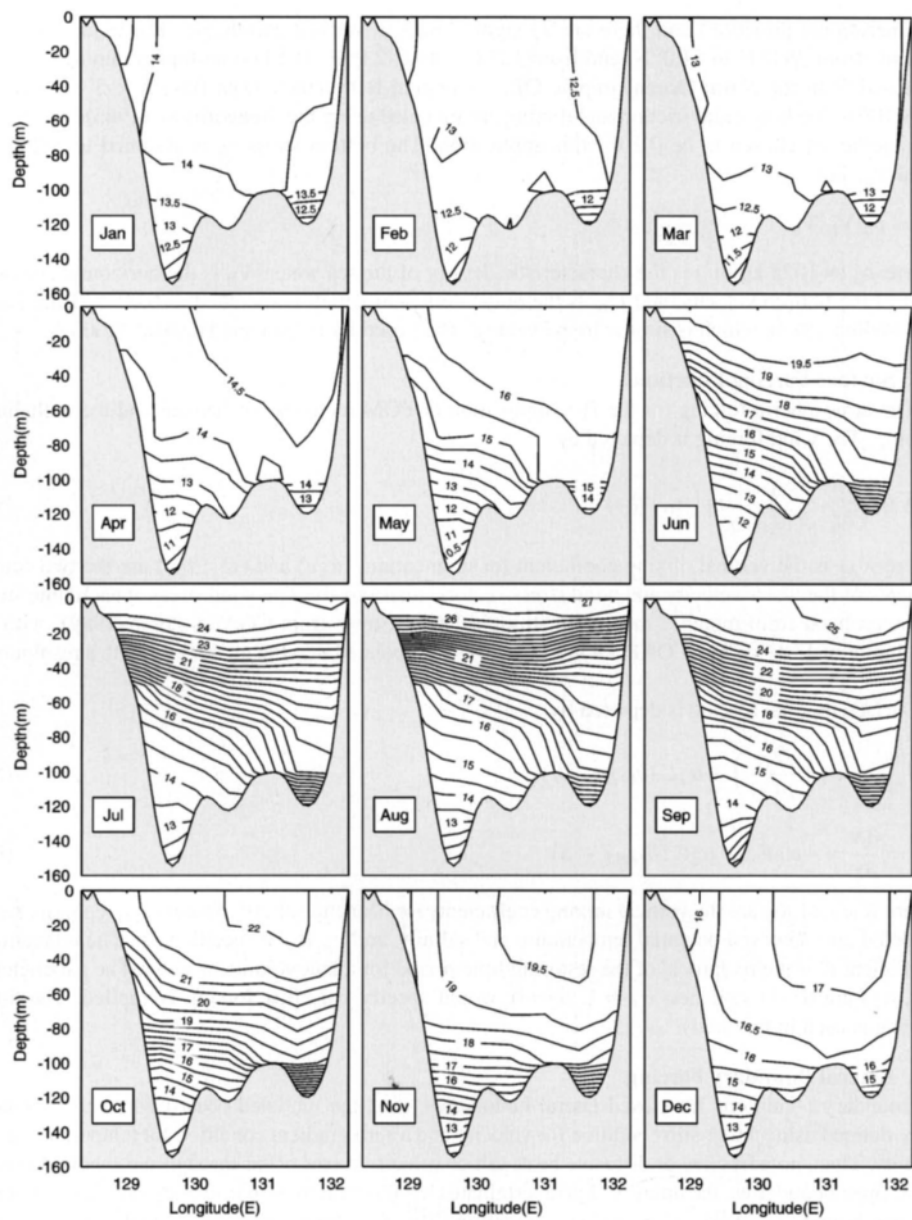
Figure 6. (a) Vertical cross-sections of monthly mean temperature (°C) at the Tsushima/Korea Strait.

where the subscript n denotes the direction normal to the boundary.

The temperature and salinity values at the open boundaries can be either obtained from historical data such as the Navy's Master Oceanographic Observational Data Set (MOODS), or monthly mean climatological data such as the Navy's Generalized Digital Environmental Model (GDEM) data (Chu
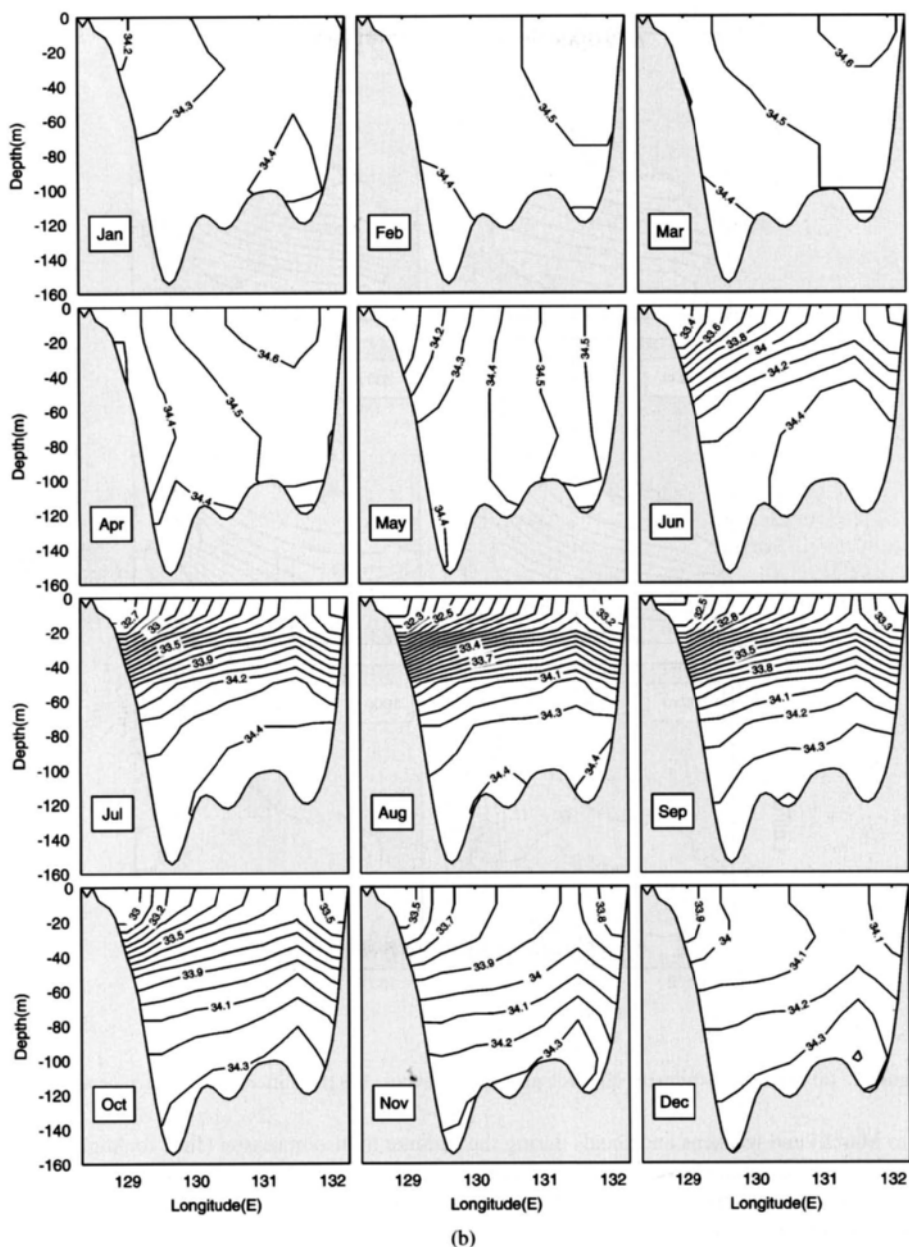
Figure 6. (b) Vertical cross-sections of monthly mean salinity (ppt) at the Tsushima/Korea Strait.

et al., 2000). For simulating the seasonal variability, we use the GDEM T, S data at the open boundaries. Vertical cross-sections of monthly mean temperature (Fig. 6a) and salinity (Fig. 6b) at the Korea/Tsushima Strait show the seasonal variability of a warm-core and a salt-core. The warm-core occupies a large portion of the Korea/Tsushima Strait during the winter monsoon season (Novem-
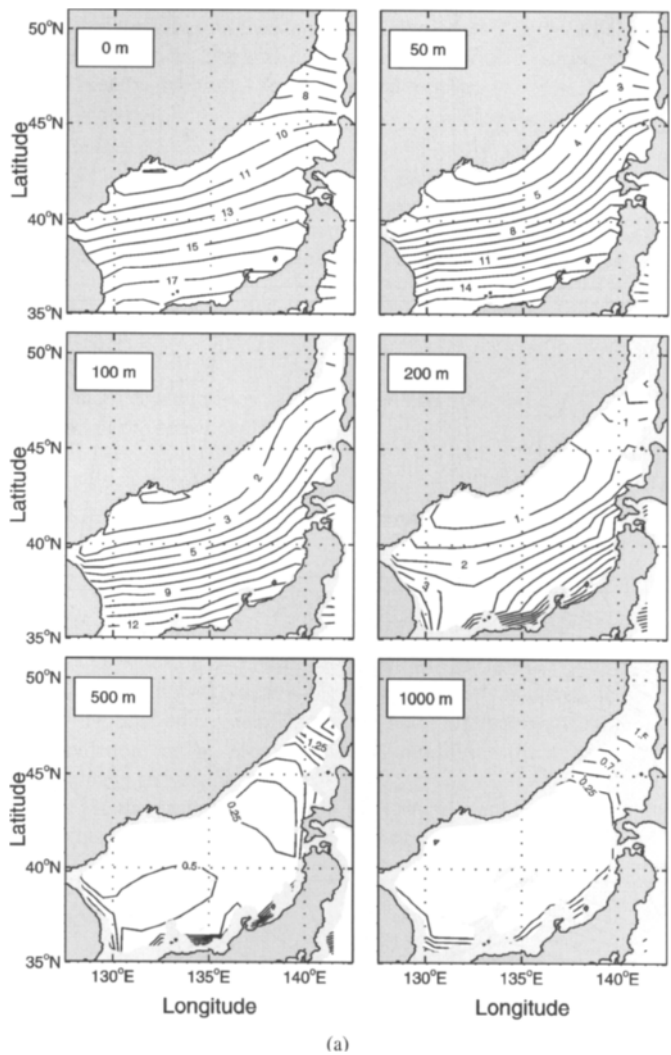
Figure 7. (a) Initial fields from the climatological data (Levitus, 1982) at different depths: temperature (°C).

ber to March) and weakens and shoals during the summer monsoon season (June to August). In the summer, the water at the Korea/Tsushima Strait is strongly stratified (Figs. 7a and 7b).

The volume transports at open boundaries are specified from historical data. Positive (negative) values are referred to inflow (outflow). Warm water enters the JES through the Korea/Tsushima Strait with the TWC from the East China Sea and exits the JES through the Tsugaru and Soya straits. There is no evident volume transport through the Tatar Strait (Martin and Kawase, 1998), which was taken as zero in this study. Recent estimates of the monthly mean volume transport, reported by Yi (1966), through the Korea/Tsushima Strait with the annual average of 1.3 Sv, a maximum of 2.2 Sv in October, and a minimum of 0.3 Sv in February. Bang et al. (1996) used the maximum inflow transport of about 3.5 Sv in August and minimum of 1.6 Sv in February, while Kim and Yoon (1999) used the mean value of 2.2 Sv with ± 0.35 Sv with the maximum in mid-September and the
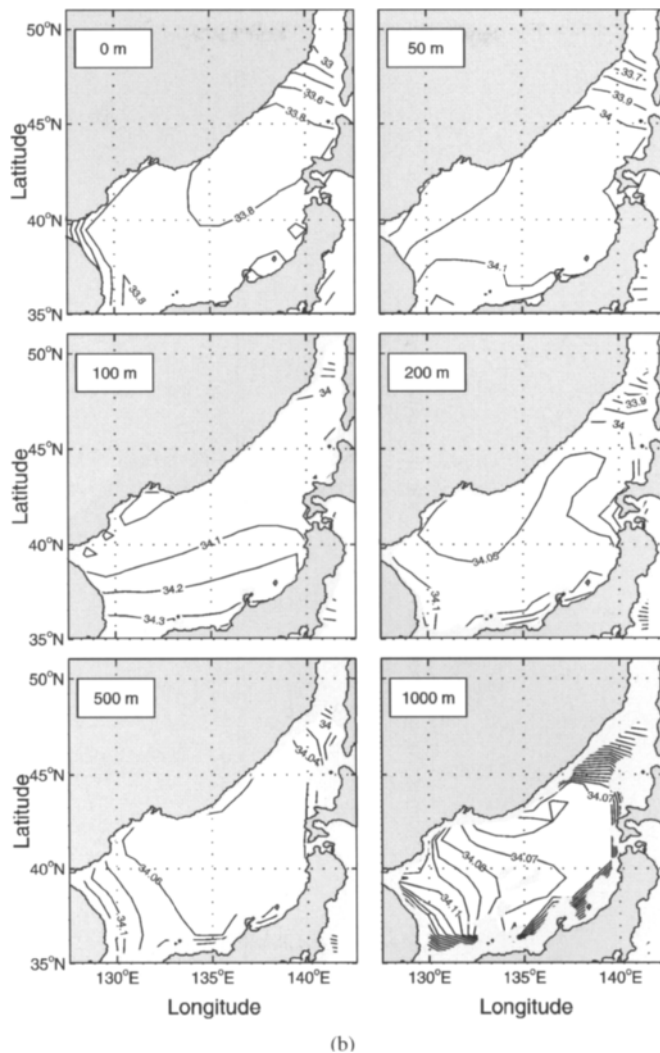
Figure 7. (b) Initial fields from the climatological data (Levitus, 1982) at different depths: salinity (ppt).

minimum in mid-March. The total inflow transport through Korea/Tsushima Straits should be the same as the total outflow transport through the Tsugaru and Soya Straits. We assume that 75% (80% in Bang et al., 1996) of the total inflow transport should flow out of the JES through the Tsugaru Strait, and 25% (20% in Bang et al., 1996) through the Soya Strait. This ratio is adopted from the maximum volume transport through the Tsugaru Strait estimated by Toba et al. (1982), and through the Soya Strait estimated by Preller and Hogan (1998). The monthly volume transports through open boundaries are listed in Table 1.

4.4. Mode Splitting

For computational efficiency, the mode splitting technique (Blumberg and Mellor, 1987) is applied with a barotropic time step of 25 seconds, based on the Courant-Friederichs-Levy computational

Table 1

Monthly values of volume transport (Sv) through the lateral open boundaries. The positive/negative values mean inflow/outflow.

Month	Jan	Feb	Mar	Apr	May	Jun	Jul	Aug	Sep	Oct	Nov	Dec
Soya	-0.2	- 0.08	- 0.08	- 0.13	- 0.23	- 0.33	- 0.43	- 0.53	- 0.55	- 0.53	- 0.48	- 0.35
Tatar	0.0	0.0	0.0	0.0	0.0	0.0	0.0	0.0	0.0	0.0	0.0	0.0
Tsugaru	- 0.6	- 0.22	- 0.22	- 0.37	- 0.67	- 0.97	- 1.27	- 1.57	- 1.65	- 1.57	- 1.42	- 1.05
Tsushima	0.8	0.3	0.3	0.5	0.9	1.3	1.7	2.1	2.2	2.1	1.9	1.4
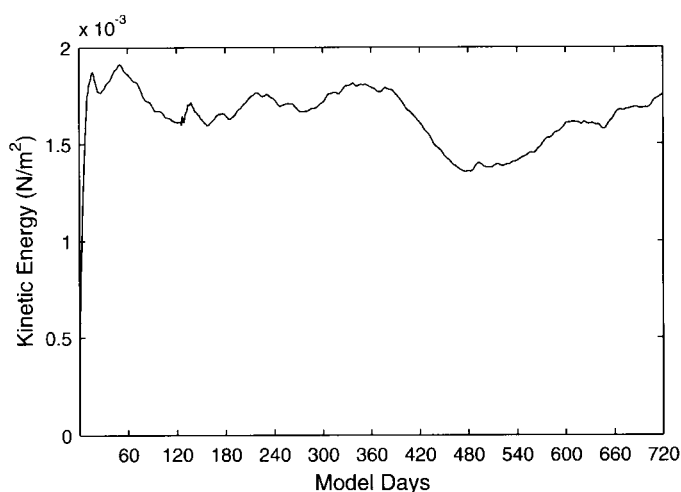
Figure 8. Temporal variation of kinetic energy per unit volume (N m^{-2}) during the model initialization.

stability (CFL) condition and the external wave speed; and a baroclinic time step of 900 seconds, based on the CFL condition and the internal wave speed.

4.5. Two-Step Initialization

Two steps are used to initialize POM. During the first step (restoring run), POM is integrated for two years from zero velocity and climatological temperature (Fig. 7a) and salinity (Fig. 7b) fields (Levitus, 1982) with climatological monthly mean surface wind stress from the COADS data and restoring-type surface thermohaline forcing ($\alpha_1 = 0$, $\alpha_2 = 1$) which are relaxed to surface monthly mean values. The climatological monthly mean field (Fig. 7a) shows that the horizontal temperature gradient is quite uniform in the JES basin (i.e., SPF is not evident).

It was found that 90 days were sufficient for the model kinetic energy to reach quasi-steady state under the imposed conditions (Fig. 8). The final states of the restoring run are taken as initial conditions for the second step (simulation run). During the simulation run, POM is integrated again for two more years with climatological monthly mean surface wind stress, net heat flux, and freshwater flux ($\alpha_1 = 1$, $\alpha_2 = 0$) from the COADS data. The simulated temperature and salinity fields are consistent with observational studies reported in Section 1 of this chapter.

5. TEMPERATURE

5.1. Sea Surface Temperature

The simulated monthly sea surface temperature (SST) is examined (Fig. 9). Comparing to the initial temperature field (Fig. 7a), the model simulated the formation of the Sub-Polar Front (SPF). Although SST field (Fig. 9) shows an evident seasonal variation, the SPF exists at all times throughout the year with mean latitude around 41°N. Its position is quite stationary, but its intensity strengthens in the winter and weakens in the summer. Such a pattern is similar to earlier descriptions (Maizuru Marine Observatory, 1997; Chu et al., 2001a). The location of the SPF in spring is quite consistent with Isoda and Saitoh's (1993) estimations using ten NOAA-8 satellite Advanced Very High Resolution Radiometer (AVHRR) images in spring 1984.
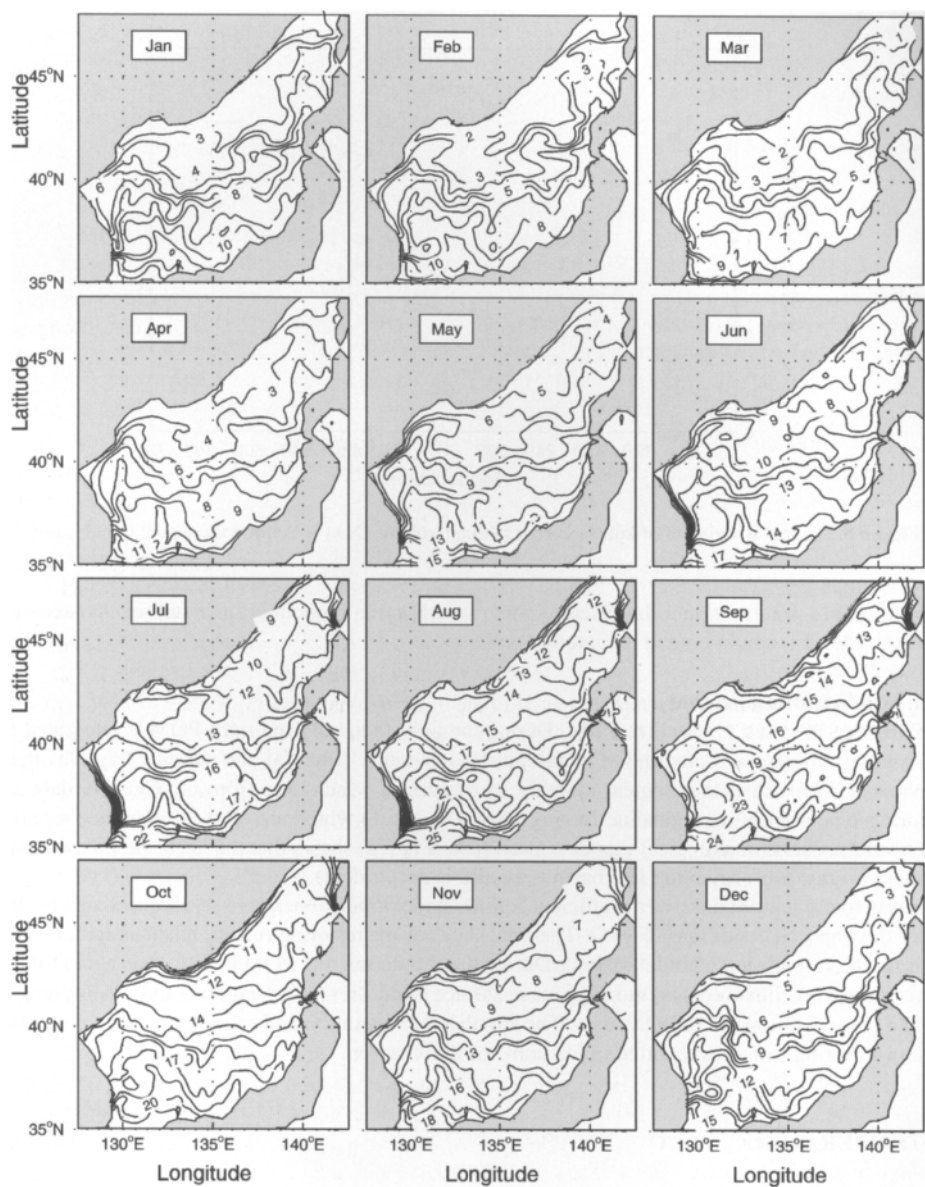
Figure 9. Simulated monthly mean sea surface temperature (°C) field.

In the simulation of Kim and Yoon (1999), the Location of the SPF was about 1° northward compared to the observed temperature field (Fig. 2 in their paper), and the water temperatures in the SPF area were 2–3°C higher than the observation. Comparison of Fig. 9 with Fig. 2 in Kim and Yoon (1999) signifies improvement of model performance in predicting the SPF location and the temperature field especially in winter.

The SST is always found higher in the UTB than in the YB, which is consistent with Kim and Kim's (1999) observational studies. The SST gradient across the SPF is twice as strong in the winter as in the summer. The weakening of the SPF in the summer is caused by the faster warming of the waters north of SPF than that of the waters south of it in the spring. North of the SPF a second front occurs (bi-frontal structure) during the fall-to-winter transition season, especially in November and December. This front parallels the Russian coast with the maximum SST gradient around $4°C/100$ km in November.

5.2. Zonal Cross-Sections (37° and 43°N)

The zonal cross-sections (37° and 43°N) of the simulated monthly mean temperature show a strong seasonal/permanent thermocline structure south of the SPF (Fig. 10a) and a strong seasonal/weak permanent thermocline structure north of the SPF (Fig. 10b).

South of the SPF at 37°N (Fig. 10a), the permanent thermocline is located at 80 to 250 m and appears throughout the year with the maximum strength ($0.08°C\ m^{-1}$) in August. Above it, the seasonal thermocline occurs from the surface to 50 m depth in June ($0.15°C\ m^{-1}$), intensifies during the summer monsoon season to a maximum value of around $0.36°C\ m^{-1}$ in August, and weakens in September. In October, the seasonal thermocline erodes and the ocean mixed layer (OML) starts to occur. In November, the OML is well-established with the temperature near $14°C$ and the depth around 75 m. During the prevailing winter monsoon season (December to March), the OML deepens to 80–100 m with a westward uplift of the OML depth: 50 m near the Korean coast and 130 m near the Japanese coast. The OML starts to warm in March, and its depth shoals rapidly. The OML depth decreases from 50–100 m in March to less than 10 m in April. This process (OML warming and shoaling) continues during the summer monsoon season (June-August). The OML shoaling simulated using POM is a month earlier compared to the observational data (Section 1 of this chapter).

North of SPF at 43°N (Fig. 10b), the permanent thermocline is quite weak. The seasonal thermocline occurs from the surface to 50 m depth in May ($\sim 0.08°C\ m^{-1}$), intensifies during the summer monsoon season to a maximum value of around $0.5°C\ m^{-1}$ in August and September, and weakens in October. In November, the seasonal thermocline erodes and becomes the part of the permanent thermocline, which weakens during the prevailing winter monsoon season. In February, the permanent thermocline is so weak that the water column is almost uniformly cold ($1°C$) west of 136°E, and weakly stratified ($\leqslant 0.01°C\ m^{-1}$) east of 136°E.

5.3. Meridional Cross-Section (135°E)

The strong north-south thermal asymmetry across the SPF is also seen from the meridional cross-section (135°E) of the monthly mean temperature (Fig. 11). North of the SPF, the seasonal thermocline occurs near the surface in April and May, enhances in summer, and is still quite strong with a vertical gradient of $0.12°C\ m^{-1}$ in October. It weakens drastically in November. South of the SPF, the seasonal thermocline occurs in summer monsoon season, weakens in early fall, and disappears in November. The winter convection (December to March) is very evident north of the SPF ($\sim 41°N$). This is consistent with the observational study reported by Seung and Yoon (1995).

During the prevailing winter monsoon season (December to March), the simulated permanent thermocline is identified at 100 to 300 m deep south of the SPF with a vertical temperature gradient weakening from December (near $0.05°C\ m^{-1}$) to March (near $0.025°C\ m^{-1}$). The simulated permanent thermocline is much weaker north of the SPF. From January to March, there is almost no evident thermocline north of the SPF.

During the prevailing summer monsoon season (June to August), a shallow seasonal thermocline occurs with a much greater strength north of the SPF than south of the SPF; and overlays relatively uniform water north of the SPF and stratified water (the permanent thermocline) south of the SPF. North of the SPF a seasonal thermocline appears near the surface (above 50 m depth) with a vertical
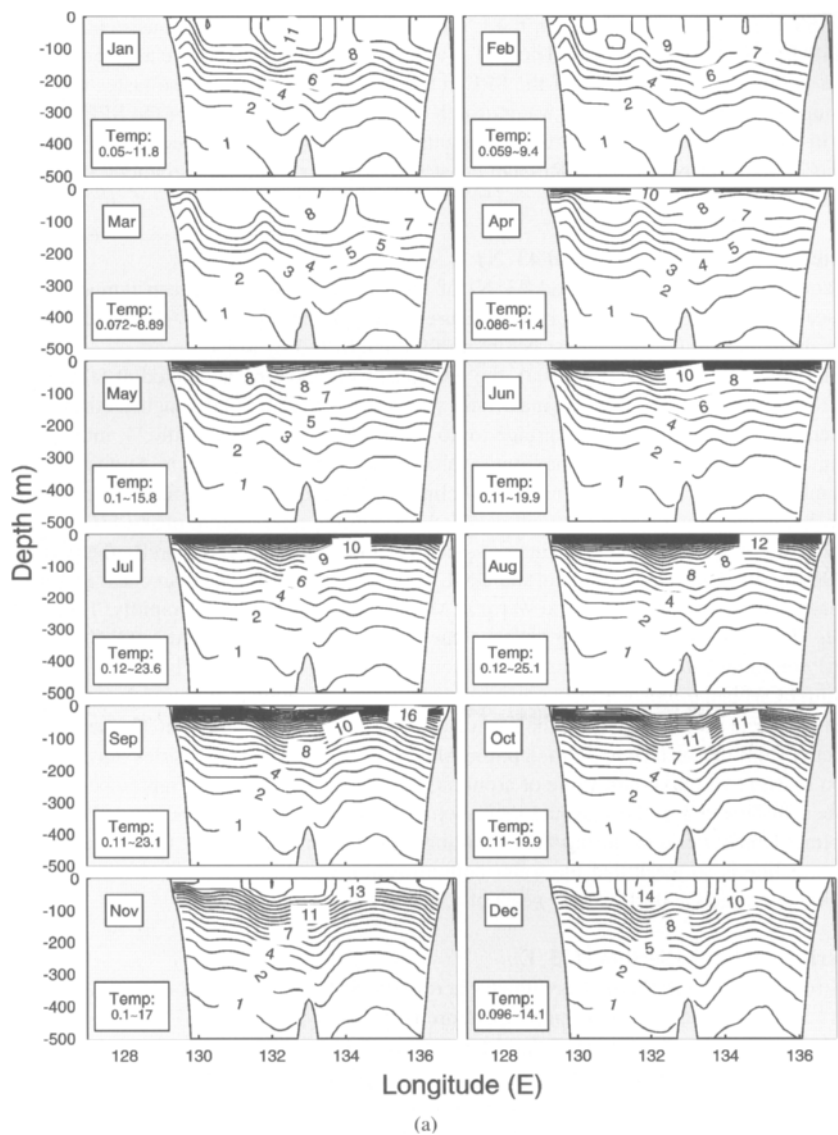
Figure 10. (a) Simulated zonal cross-section of the monthly mean temperature (°C): 37°N.

gradient enhancing from 0.25°C m^{-1} in June to 0.36°C m^{-1} in August. This strong and shallow thermocline isolates the exchange of the seawater below the thermocline from the atmospheric forcing and makes this water (north of the SPF under the thermocline) quite uniform. South of the SPF, the seasonal thermocline is wider (25 to 100 m deep) and weaker with a vertical gradient around 0.13°C m^{-1}. Such a north-south asymmetric pattern was previously presented by Kim and Kim (1999) using the Circulation Research of the East Asian Marginal Seas (CREAMS) data taken mainly in July 1995, and by Chu et al. (2000) using the GDEM data.
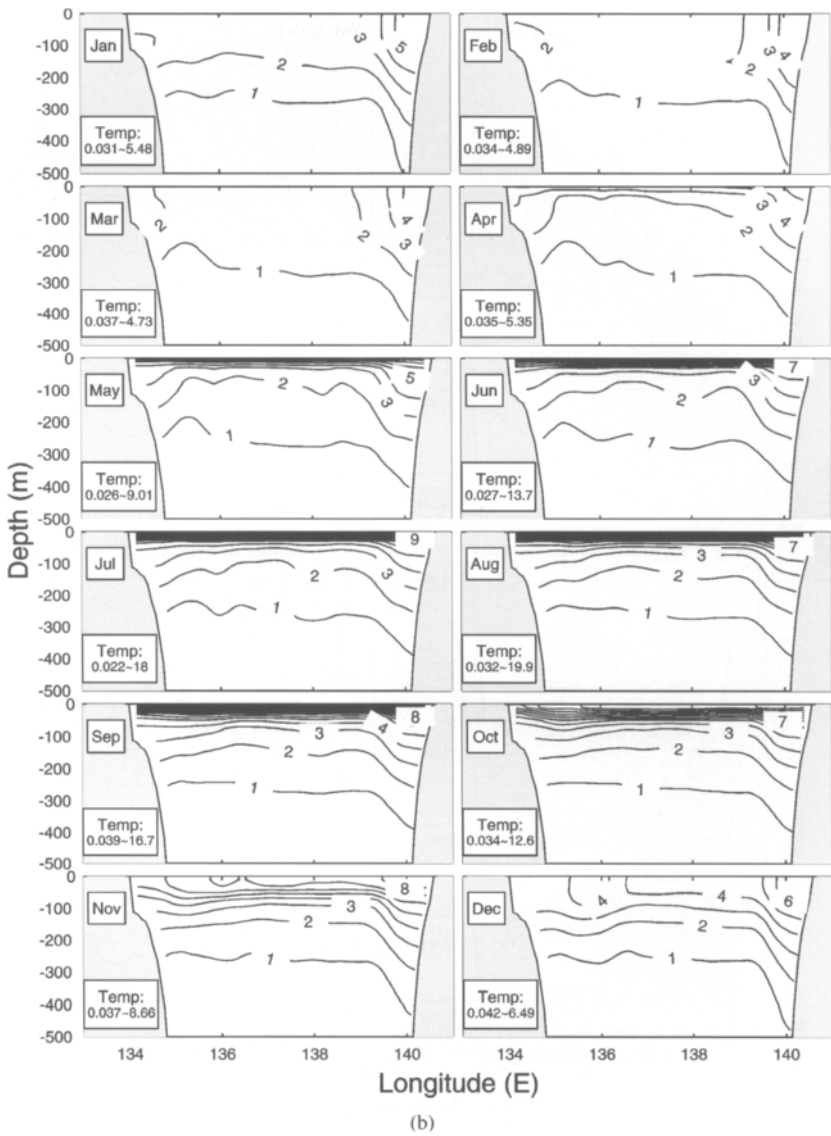
Figure 10. (b) Simulated zonal cross-section of the monthly mean temperature: 43°N.

6. SALINITY

6.1. Sea Surface

The most striking feature of the simulated monthly sea surface salinity (SSS) field (Fig. 12) is the existence of a strong salinity gradient in the far north of JES with low salinity waters along the continental coastal area. For the JES basin, the saline Kuroshio water enters the JES through the Korea/Tsushima Strait and forms two permanent salty centers located in the northern JB (west of Hokkaido Island), with the salinity higher than 34.0 ppt, and the area between UTB and YB with
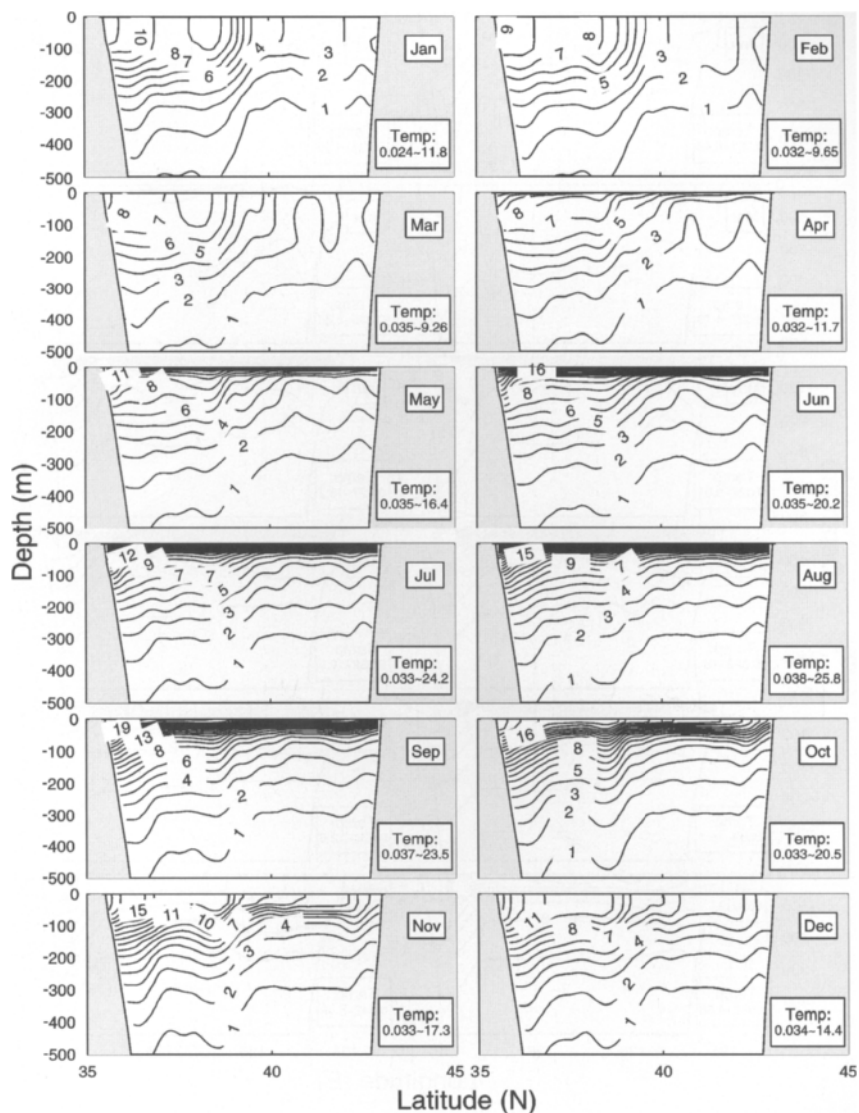
Figure 11. Simulated latitudinal cross-section (135°E) of the monthly mean temperature (°C) along 135°E.

the maximum salinity of 34.3 ppt in August-September, respectively. The northern JB salty center has less seasonal variation than the UTB/YB salty center. Around the UTB/YB salty center, there are several fresh centers occurring largely from late summer to fall-early winter. The simulated winter (February) field (Fig. 12) is consistent with that reported by Kim and Kim (1999, Fig. 9 in their paper) using the data set of the Japan Oceanographic Data Center from 1930 to 1990.
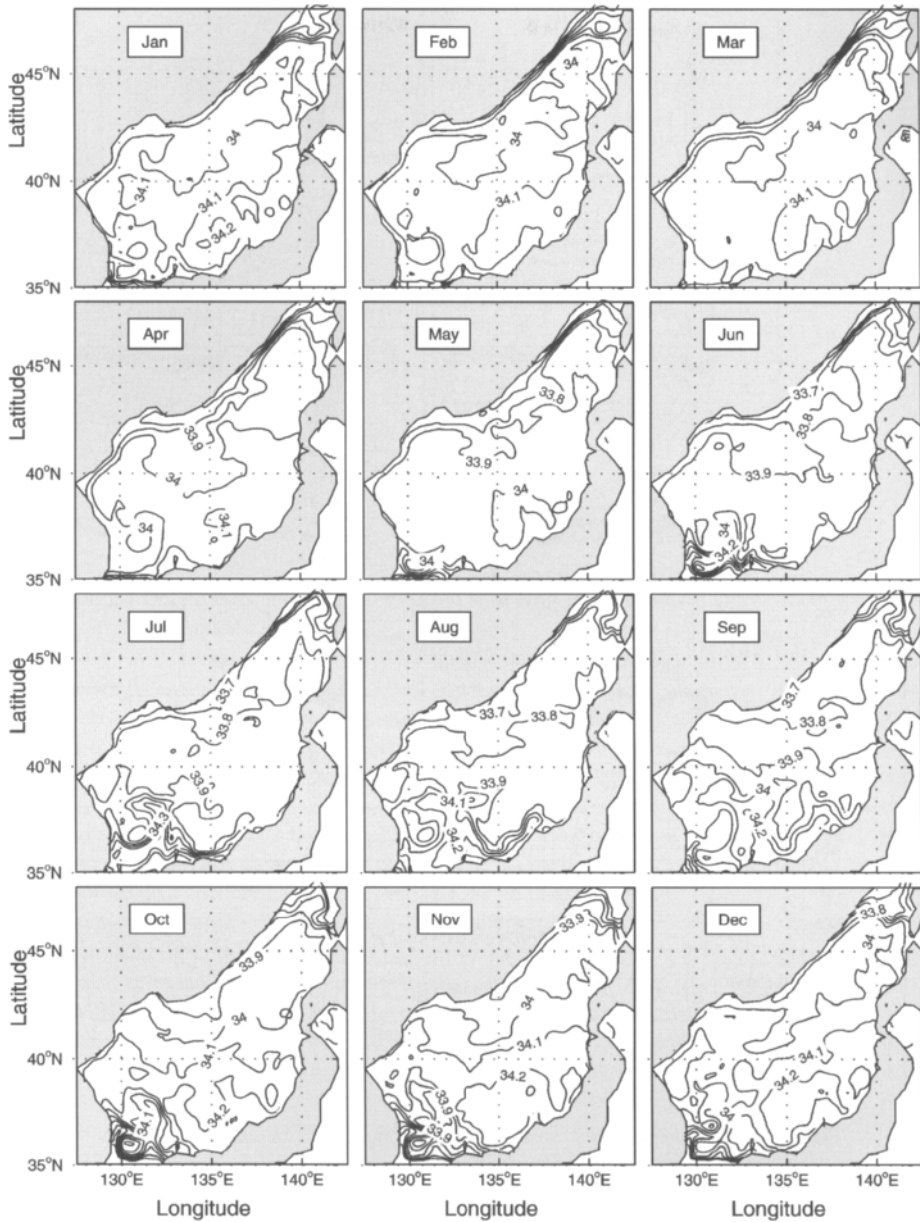
Figure 12. Simulated monthly mean sea surface salinity (ppt) field.

6.2. Zonal Cross-Sections (37° and 43°N)

The zonal cross-sections (37° and 43°N) of the simulated monthly mean salinity show an evident sublayer (200 to 300 m) SMIN south of the SPF (Fig. 13a) and absence of a SMIN north of the SPF
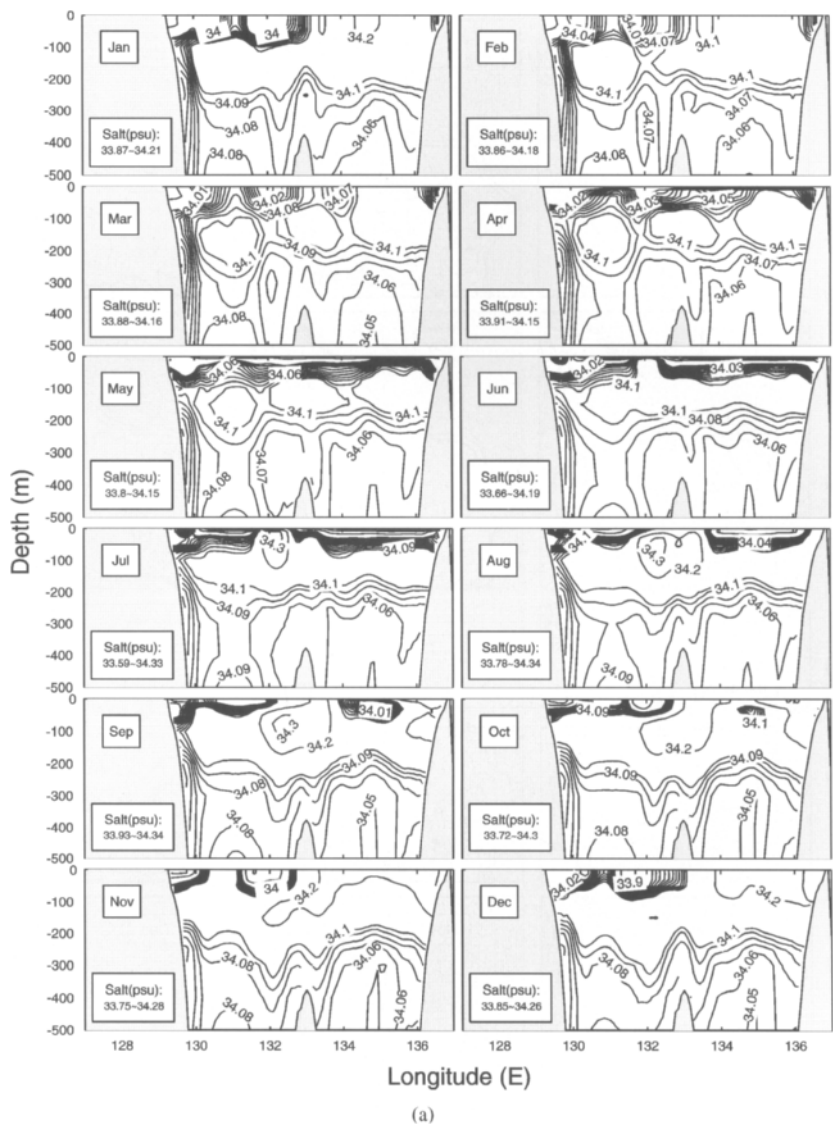
Figure 13. (a) Simulated zonal cross-section of the monthly mean salinity (ppt): 37°N.

(Fig. 13b). The water with salinity of about 34.08 ppt in the eastside of 134°E around the depth of about 200 m are located under more saline water in the surface layer that has the characteristics of the TWC. The low saline water throughout the water column in high latitude (Fig. 13b) is the typical coastal water that advects to southward under the TWC, and forms the SMIN (Kim and Kim, 1999; Kim and Yoon, 1999). This is consistent with many earlier studies such as Miyazaki (1952, 1953), Kim and Chung (1984), Senjyu (1999), and Chu et al. (2000).

South of the SPF at 37°N (Fig. 13a), a strong seasonal halocline occurs from the surface to 30 m depth in June (0.01 ppt m^{-1}), intensifies during the summer monsoon season to a maximum value of
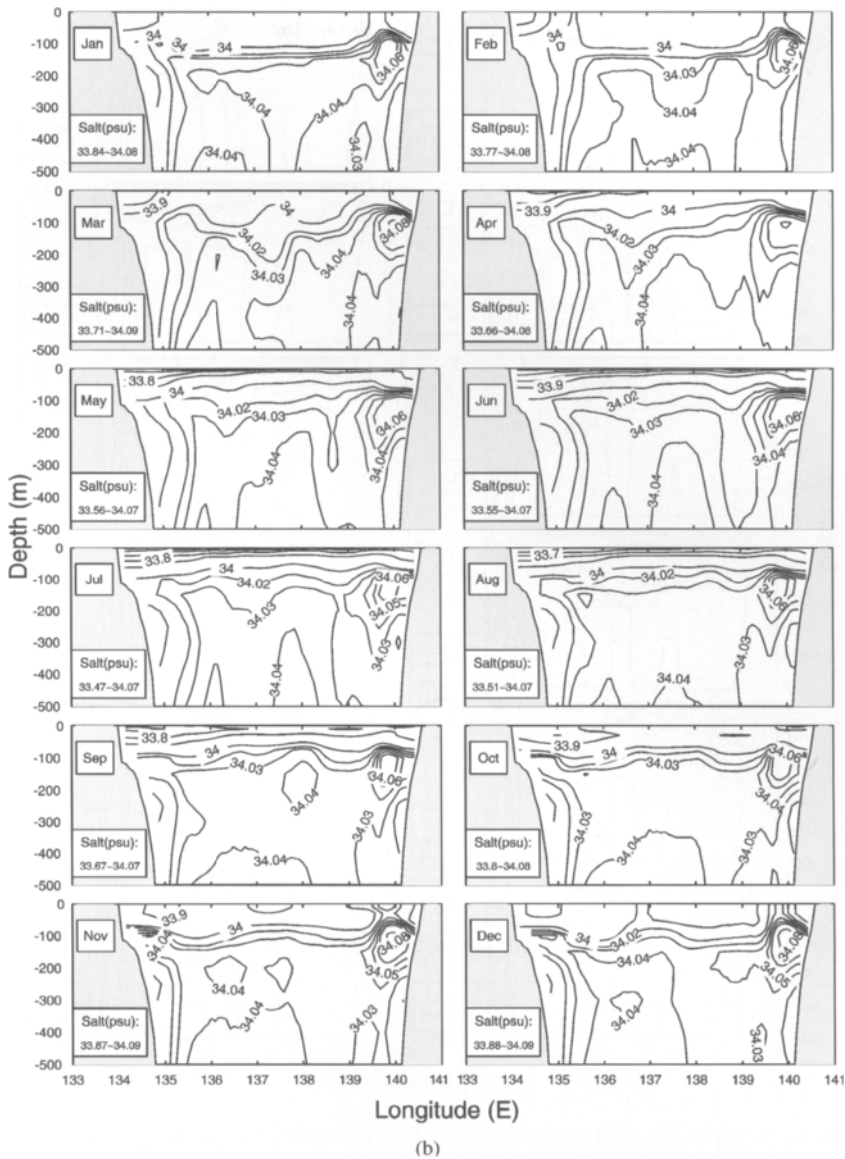
Figure 13. (b) Simulated zonal cross-section of the monthly mean salinity (ppt): 43°N.

around 0.02 ppt m^{-1} in August, and weakens from September to December. In January, the seasonal halocline erodes and disappears. A horizontally oriented salinity maximum (SMAX) ($S > 34.1$ ppt) usually broken into several salty parts appears in winter and spring above the SMIN with the interface at 200 to 300 m depths.

North of the SPF at 43°N (Fig. 13b), the SMIN shows up in the upper layer (above 100 m) of the western JB (west of 136°E) throughout the year. This is consistent with Kim and Kim's (1999)
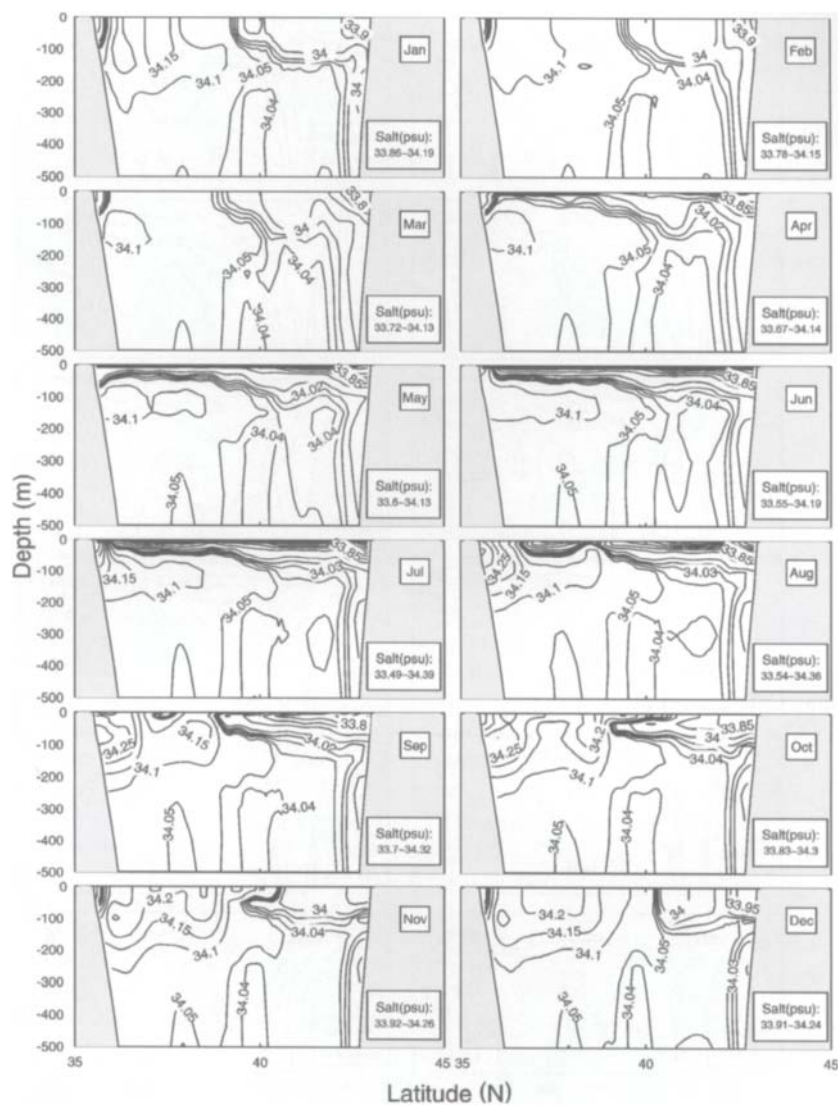
Figure 14. Simulated latitudinal cross-section (135°E) of the monthly mean salinity (ppt) along 135°E.

identification that the JIW in the western JB is characterized by a low salinity ($S < 34.00$), and the HSIW in the eastern (139°–140°E) JB is featured by high salinity ($S > 34.05$ ppt).

6.3. Meridional Cross-Section (135°E)

The strong north-south haline asymmetry across the SPF is also simulated from the meridional cross-section (135°E) of the monthly mean salinity; the appearance (disappearance) of the SMIN south (north) of the SPF (Fig. 14).

From the surface layer in high latitudes the low saline water penetrates into the intermediate depth of about 200 to 300 m during the summer monsoon season (July-October) underneath tongue-shaped saline water of the TWC. The SMAX with a salty core ($S > 34.05$ ppt) is simulated below the SMIN layer north of SPF.

The SMAX with a salty core ($S = 34.3$ ppt) was observed in October 1969 when a hydrographic survey for the whole JES basin was carried out by the Japan Meteorological Agency (Kim and Kim, 1999). The interface between the SMIN and the SMAX is located at 100 to 200 m deep. During the winter monsoon season, the SMIN is not evidently shown.

7. CIRCULATION

7.1. General Description

The simulated surface velocity field (Fig. 15) coincides with earlier description of JES circulation presented in Section 2. The TWC separates at the Korea/Tsushima Strait into two branches through a western and an eastern channel. Flow through the western channel (i.e., EKWC) closely follows the Korean coast until it separates near 38°N into two branches. The eastern branch follows the SPF to the west coast of Japan, and the western branch, flows northward and forms a cyclonic eddy in the southern UTB. The LCC carries fresh and cool water along the Russian coast and becomes the NKCC at the North Korean coast. The NKCC meets the EKWC at about 38°N. After separation from the coast, the NKCC and the EKWC converge to form a strong zonal jet across the basin.

7.2. Liman Cold Current

The LCC is a southwestward current following along the Russian coast. It bifurcates into two branches near Vladivostok: the western branch flows along the Russian-Korean coast and becomes the NKCC. The eastern branch flows southeastward, then turns eastward at 41.5°N, and becomes the southern flank of the JB gyre. The LCC has a strong seasonal variation with a maximum speed in winter and a minimum speed in the summer (Fig. 15).

Zonal cross-sections of the meridional velocity at 46°N for January (winter), April (spring), July (summer), and October (fall) indicate seasonal and spatial variabilities of the LCC. It has a maximum southward component (0.32 m/s), occurring near the surface in winter (Fig. 16 Jan) with a width of 100 km and the depth of 1500 m. The core of the LCC is close to the coast and near the surface. In the spring, it weakens to 0.20 m/s (Fig. 16 Apr), but the width and depth are almost unchanged. It further weakens to a minimum of 0.08 m/s in summer (Fig. 16 Jul) and fall (Fig. 16 Oct). The simulated LCC in spring (Fig. 16 Apr) is qualitatively consistent with a recent geostrophic calculation relative to the sea floor based on CTD measurements. Moreover, there is a very weak (0.01–0.04 m/s) northward return flow on the continental shelf underneath the LCC, with a width of 30 km between 100 and 250 m deep.

7.3. North Korean Cold Current

The NKCC is the continuation of LCC, flowing southward along the Korean coast. To present its seasonal variability, we plot the simulated bi-weekly surface current vectors (Fig. 17) in the southwest JES (127°– 133°E, 35°– 42°N). The NKCC is evident in winter and weakens in summer.

Zonal cross-sections of the meridional velocity at 40°N for January (winter), April (spring), July (summer), and October (fall) indicate seasonal and spatial variabilities of the NKCC. It flows along the continental slope with a maximum southward component (0.1 m/s) in winter and spring. The core of the NKCC is subsurface and close to the shelf break with a width of 100 km and depth of 1500 m (Fig. 18 Jan). The NKCC weakens in summer (Fig. 18 Jul) and fall (Fig. 18 Oct).
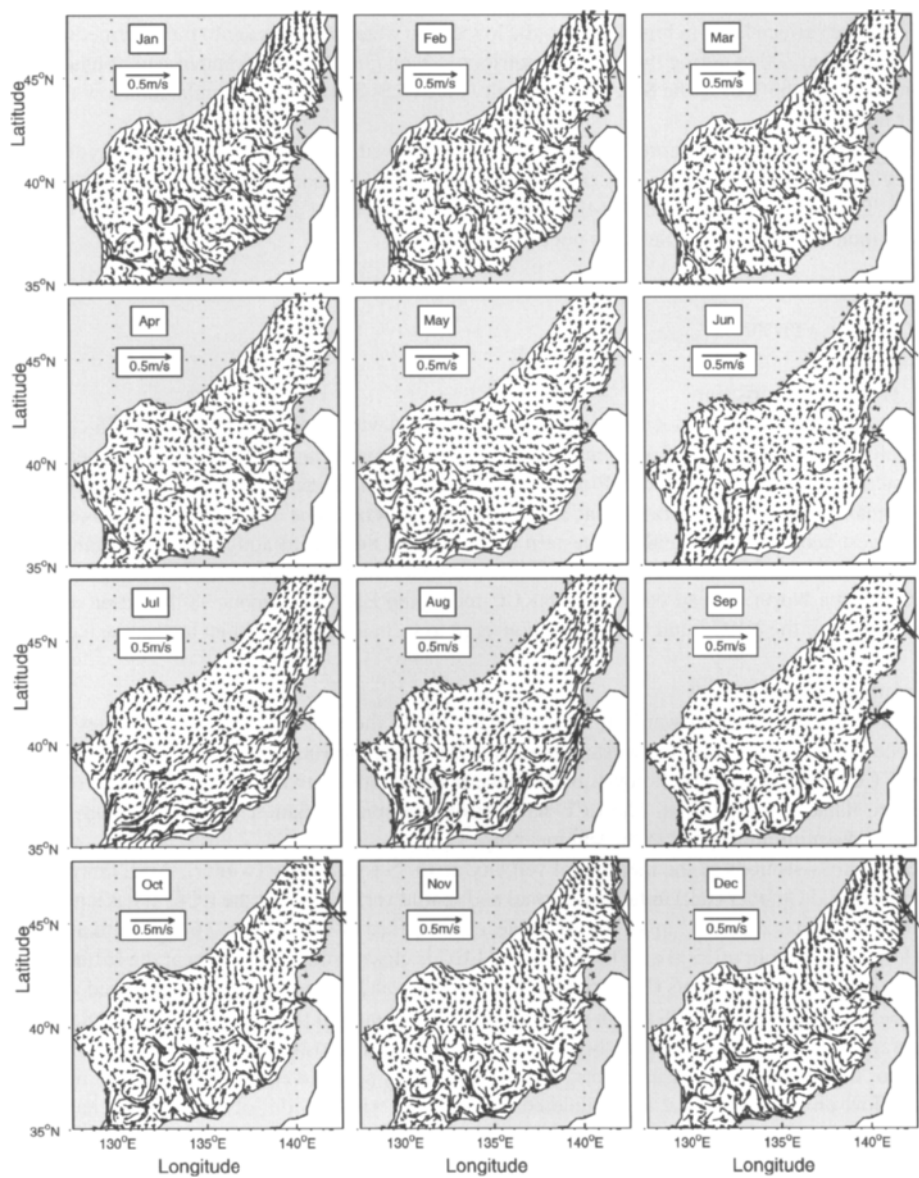
Figure 15. Simulated monthly mean surface velocity vector field.

7.4. Tsushima Warm Current Bifurcation

The TWC enters the JES through the western and eastern channels of the Korea/Tsushima Strait. The simulated bi-weekly velocity vector fields at 10 m depth (Fig. 17) show a branching pattern. This is the result of the boundary specification. The currents through the eastern channel flow along the Japanese coast and form the FBTWC. The flow through the western channel becomes
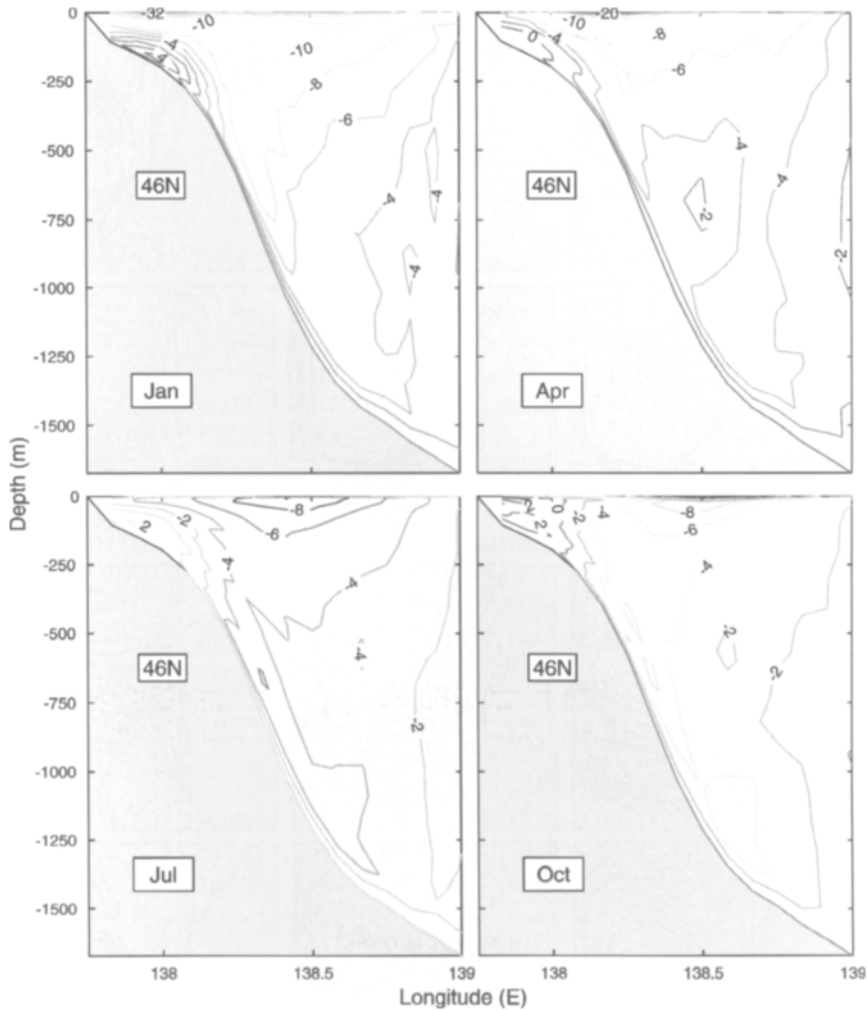
Figure 16. Simulated monthly mean meridional velocity (cm s^{-1}) along 46°N.

the EKWC, which closely follows the Korean coast until it separates near 37°N into northern and eastern branches (first bifurcation). The eastern branch after the first bifurcation flows eastward until 132°E and further separates (second bifurcation) into eastern and northern branches. The eastern branch after the second bifurcation continues to flow eastward and becomes the SBTWC. The northern branch after the second bifurcation flows northward and recirculates near 38°N as the northern flank of a cyclonic eddy located at (130°– 132°E, 36°– 38°N) in the southern UTB.

7.5. Dual Eddies Near Korean Coast

Meanders and eddies are simulated along the four major current systems north of Korea/Tsushima Strait (EKWC, NKCC, FBTWC, and SBTWC): an evident cyclonic eddy in the southern UTB as noted above and an anticyclonic eddy near the Korean coast. The southern UTB cyclonic eddy has
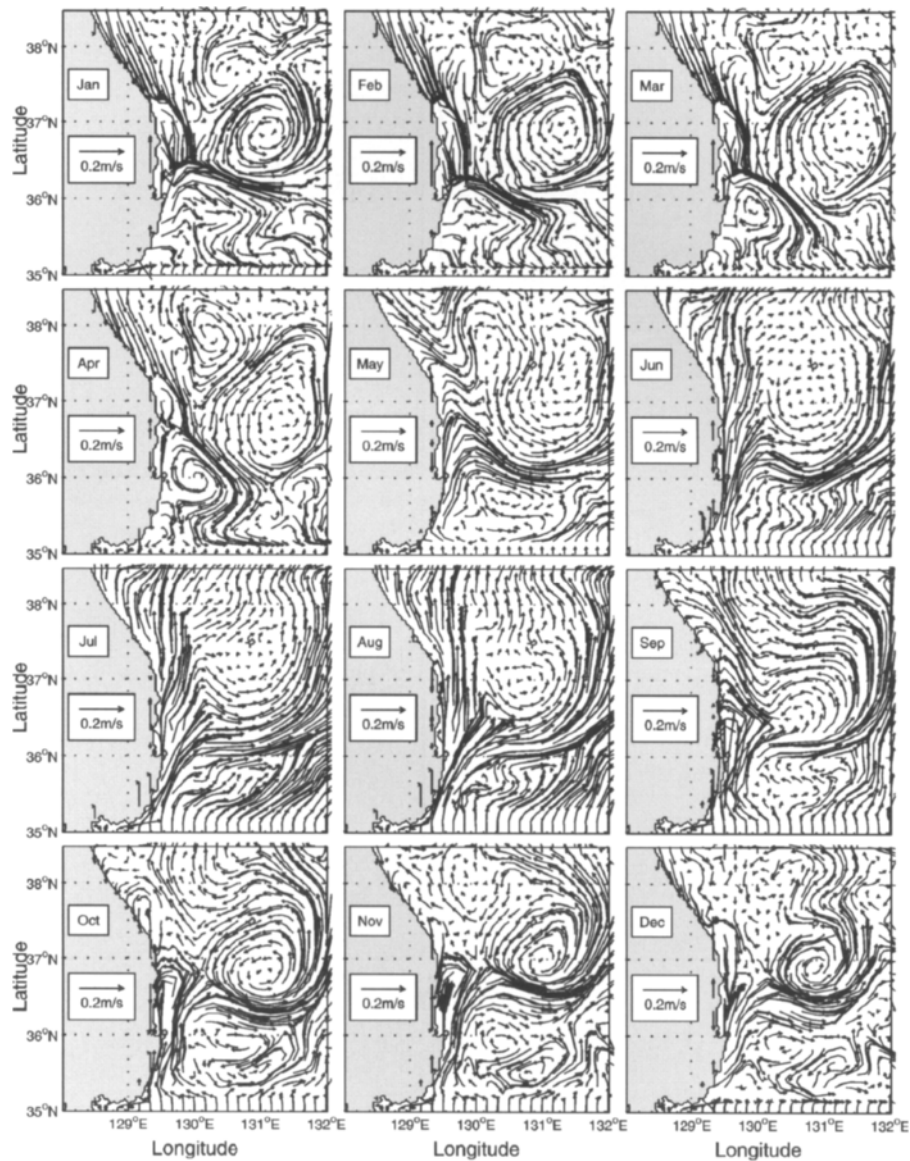
Figure 17. Simulated bi-weekly surface velocity vector field in the Ulleung/Tsushima Basin.

pronounced feature in winter, while the northwestern flank (westward flow) of this eddy weakens throughout summer showing strong EKWC heading toward the interior of the JES.

Such a dipole structure of gyres with an anticyclonic eddy near the Korean coast and a cyclonic eddy in UTB was reported by Shin et al. (1995; 1996) using the data collected from CTD and ADCP measurements in the southwestern JES from March to June 1992.
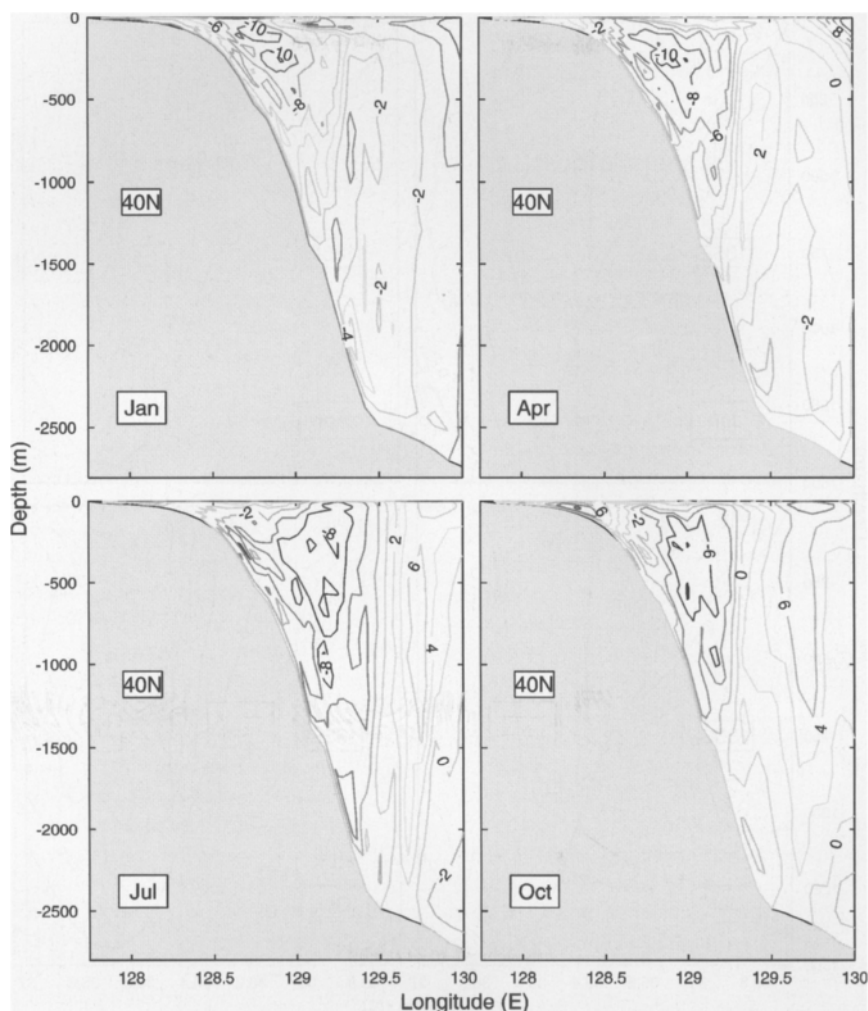
Figure 18. Simulated monthly mean meridional velocity (cm s^{-1}) along 40°N.

7.6. Two Tsushima Warm Current Branches Along the Japanese Coast

The TWC along the Japanese coast is characterized by strong variabilities in connection with many meanders and eddies (Fig. 15). Hase et al. (1999) identified the two main branches of the TWC along the Japanese coast using ADCP and CTD measurements conducted east of Oki Islands every early summer of 1995-1998, and used an analysis of temperature distribution at 100 m depth and the tracks of surface drifters.

The two TWC branches along the Japanese coast are simulated in the model (Fig. 15). To present such a feature more clearly, we plotted the meridional cross-sections of the zonal velocity (Fig. 19) along 135°E for January (winter), April (spring), July (summer), and October (fall). The FBTWC exists throughout the year. It starts from the eastern channel of Korea/Tsushima Strait, flows along the Japanese coast, and flows out of the JES through Tsugaru Strait (Fig. 15). The FBTWC exists
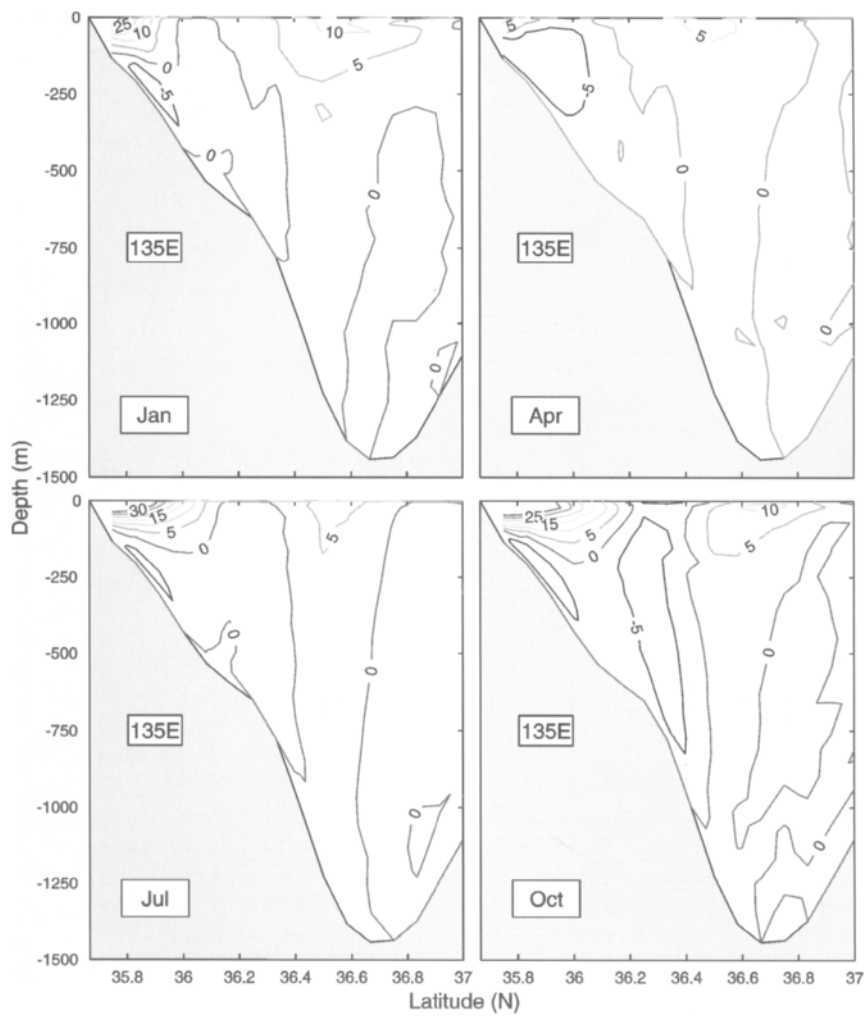
Figure 19. Simulated monthly mean zonal velocity (cm s^{-1}) along 135°E.

throughout the year and flows inshore of the 500 m isobath with a maximum strength (0.3 m/s) and spatial extent (0 to 200 m deep and 50 km wide) in July and October, and a minimum strength (0.1 m/s) and spatial extent (0 to 50 m deep and 20 km wide) in April. The current flowing through the western channel of the Korea/Tsushima Strait feeds the SBTWC, which is weaker than the FBTWC west of the Oki Islands (Fig. 18). The simulated SBTWC also exists throughout the year with a maximum strength (0.1 m/s) in October and January, and a minimum strength (0.05 m/s) in April and July. The simulated TWC branching qualitatively coincides with recent observational studies (Hase et al., 1999). A westward flowing under-current is also simulated below the FBTWC with a speed of 0.05 m/s (Fig. 19), which coincides with Seung and Yoon's (1995) observational study.
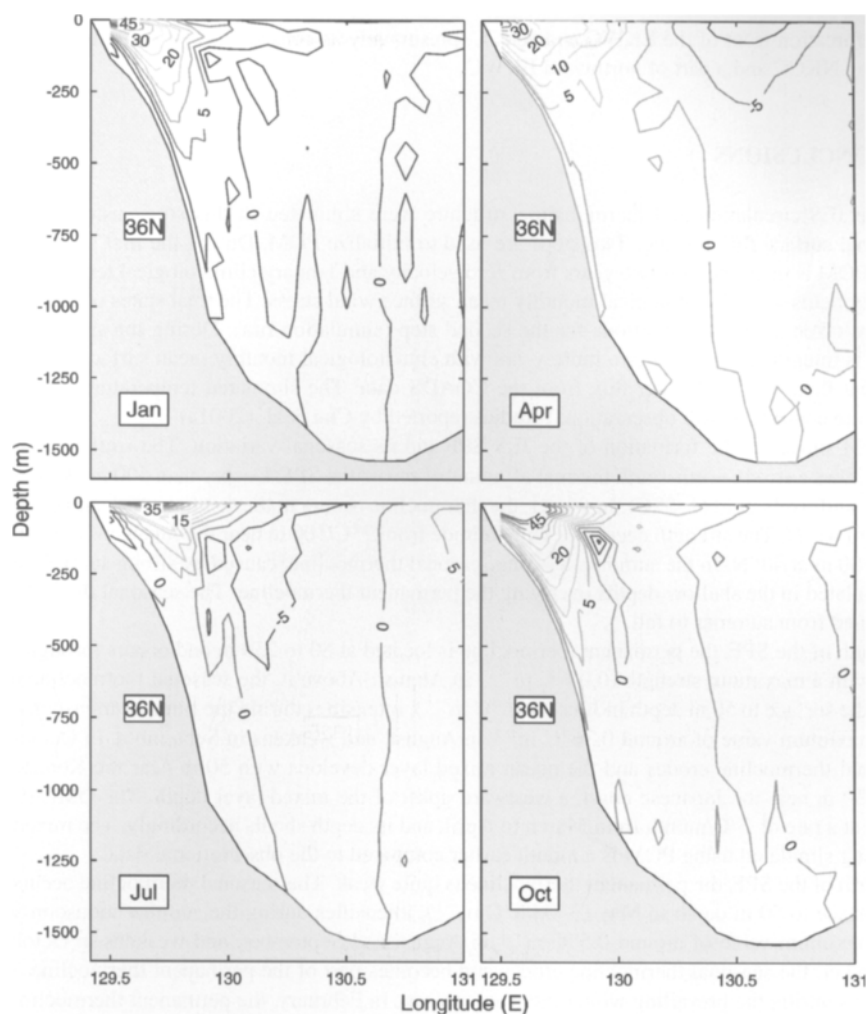
Figure 20. Simulated monthly mean meridional velocity (cm s^{-1}) along 36°N.

7.7. East Korean Warm Current

Zonal cross-sections of the meridional velocity at 36°N for January (winter), April (spring), July (summer), and October (fall) indicate seasonal and spatial variabilities of the EKWC (Fig. 20). It has a maximum northward component (0.65 m/s), occurring near the surface in summer with a width of 80 km and a depth of 200 m. The core of the EKWC is close to the coast and near the surface. In winter, it weakens to a narrow and shallow current with speed of about 0.3 m/s. These features are consistent with local observations off the Korean coast (Shin et al., 1995; 1996). The simulated seasonal variability of EKWC is also consistent with the observational analysis reported by Chu et al. (2001a).

This model simulates the anticyclonic eddy off Korean coast around 38°N during March and April as observed by Shin et al. (1995). The relatively small-scale eddy was found on the inner shelf of

the bifurcation front of the EKWC and KNCC, presumably as consequence of entrainment of south flowing NKCC and a part of northward EKWC.

8. CONCLUSIONS

The JES circulation and thermohaline structure were simulated in this study using POM with seasonal surface flux forcing. Two steps are used to initialize POM. During the first step (restoring run), POM is integrated for two years from zero velocity and January climatological temperature and salinity fields with climatological monthly mean surface wind stress. The final states of the restoring run are taken as initial conditions for the second step (simulation run). During the simulation run, POM is integrated again for two more years with climatological monthly mean surface wind stress, net heat flux, and freshwater flux from the COADS data. The simulated temperature and salinity fields are consistent with observational studies reported by Chu et al. (2001a).

POM simulates the formation of the JES SPF and its seasonal variation. The simulated thermal field shows a strong north-south thermal asymmetry across the SPF. Deeper than 500 m, the temperature is uniformly cold ($1–2°C$). In winter, the thermocline occurs in the southern JES, and disappears north of $41°N$. The strength decreases with latitude from $7°C/100$ m near the Japan coast to less than $1°C/100$ m at $40°N$. In the summer, a strong seasonal thermocline, caused by strong surface heating, is simulated in the shallow depths overlying the permanent thermocline. The seasonal thermocline is sustained from summer to fall.

South of the SPF, the permanent thermocline is located at 80 to 250 m and occurs throughout the year with a maximum strength ($0.08°C$ m^{-1}) in August. Above it, the seasonal thermocline occurs from the surface to 50 m depth in June ($0.15°C$ m^{-1}), intensifies during the summer monsoon season to a maximum value of around $0.36°C$ m^{-1} in August, and weakens in September. In October, the seasonal thermocline erodes and the ocean mixed layer develops with 50 m near the Korean coast and 130 m near the Japanese coast, a westward uplift of the mixed layer depth. The OML starts to warm at a rate of $2°C$/month from March to April, and its depth shoals accordingly. The mixed layer shoaling simulated using POM is a month earlier compared to the observational data.

North of the SPF, the permanent thermocline is quite weak. The seasonal thermocline occurs from the surface to 50 m depth in May ($\sim 0.08°C$ m^{-1}), intensifies during the summer monsoon season to a maximum value of around $0.5°C$ m^{-1} in August and September, and weakens in October. In November, the seasonal thermocline erodes and becomes part of the permanent thermocline, which weakens during the prevailing winter monsoon season. In February, the permanent thermocline is so weak that the water column is almost uniformly cold ($1°C$) west of $136°E$ and weakly stratified ($\leqslant$ $0.01°C$ m^{-1}) east of $136°E$.

POM simulates the surface salinity field reasonably well with surface field characterized by stronger seasonal variability south of the SPF than north of it. The model also simulates a strong north-south salinity asymmetry across the SPF with a salty tongue (> 34.1 ppt) appearing only south of the SPF. The shallow and strong halocline associated with strong thermocline makes the subsurface waters north of the SPF hydrostatically stable. The mid-level salty tongue associated with the weak and thick thermocline makes the water mass hydrostatically less stable south of the SPF.

POM simulates the strong north-south asymmetry of the seasonal halocline with an evident salinity minimum south of the SPF and absence of a salinity minimum north of the SPF. South of the SPF, the SMIN ($S < 34.08$ ppt) occurs during the summer monsoon season (July-October) underneath a horizontally oriented SMAX with a salty core ($S > 34.3$ ppt) at 100 m depth. The interface between the SMIN and the SMAX is located at 100 to 200 m depth. During the winter monsoon season, the SMIN is not evident. North of the SPF, the high salinity water ($S > 34.05$ ppt) of the HSIW appears in the eastern JB ($40°– 43°N$).

POM simulates the JES circulation reasonably well, especially the Tsushima Current and its bifurcation. The Tsushima Current bifurcates into a western and an eastern branch north of the Korea/Tsushima Strait. The flow through the eastern channel continues along the Japanese coast and forms the first branch of TWC (FBTWC). The flow through the western channel becomes the EKWC, which closely follows the Korean coast until it separates near 37°N into northern and eastern branches (first bifurcation). The eastern branch after the first bifurcation flows eastward until 132°E and further separates (second bifurcation) into eastern and northern branches. The eastern branch after the second bifurcation continues to flow eastward and becomes the second branch of the TWC (SBTWC). The FBTWC exists throughout the year and flows inshore of the 500 m isobath with a maximum strength (0.3 m/s) and spatial extent (0 to 200 m deep and 50 km wide) in July and October, and a minimum strength (0.1 m/s) and spatial extension (0 to 50 m deep and 20 km wide) in April. The simulated SBTWC also exists throughout the year and flows parallel to the continental margin with a maximum strength (0.1 m/s) in October and January, and a minimum strength (0.05 m/s) in April and July.

The other currents such as the LCC, EKWC, and NKCC are simulated reasonably well. The simulated LCC has a maximum southward component (0.32 m/s), occurring near the surface in winter with a width of 100 km and extending to a depth of 800 m. It weakens to a minimum of 0.08 m/s in summer and fall, and shrinks in size to a width of 60 km and depth of 400 m. The simulated EKWC varies from 0.65 m/s (summer) to 0.30 m/s (winter). The EKWC has a width of 80 to 100 km and a depth of about 200 m throughout the year. The northward branch (overshoot) of EKWC leaves the Korean coast and converges with the southward flowing NKCC, and forms a current meandering eastward along the SPF. The simulated NKCC flows along the continental slope with a maximum southward component (0.1 m/s) in winter and spring. The core of the NKCC is close to the shelf break with a width of 100 km and depth of 1500 m.

Using realistic bottom topography, POM successfully simulates the dipole structure of gyres in the southern JES with an anticyclonic eddy near the Korean coast and a cyclonic eddy in UTB as reported by Shin et al. (1995; 1996). The southern UTB cyclonic eddy has a pronounced feature in winter, while the northwestern flank (westward flow) of this eddy weakens throughout summer showing strong EKWC heading toward the interior of the JES.

Although POM adequately simulated the seasonal JES circulation and thermohaline structure, much more modeling work is required. Three-dimensional observations of ocean temperature, salinity and velocity fields would allow initialization of the model with a more realistic dynamic and thermodynamic structure. Atmospheric forcing could also be made more realistic by utilizing a coupled Ocean/Atmosphere model, such as the Coupled Atmosphere and Ocean Coastal System (CAOCS) under development by the Naval Postgraduate School (Chu et al., 1999a). Use of such a system would provide more accurate wind stress forcing, through modifications of the wind field by surface frictional effects, inclusion of ocean wave effects, and improved ocean/atmosphere thermal and salinity fluxes.

Future studies should concentrate on less simplistic scenarios. Realistic inflow transport should be included, and the use of interpolated climatological winds needs to be upgraded to incorporate synoptic winds to improve realism.

ACKNOWLEDGMENTS

REFERENCES

Bang, I., Choi, J.-K., Kantha, C., Horton, C., Cliford, M., Suk, M-S., Chang, K-I., Nam, S.Y., Lie, H-J., 1996. A hindcast experiment in the East Sea (Sea of Japan). La Mer, 34: 108–130.

Blumberg, A., and Mellor, G., 1987. A description of a three dimensional coastal ocean circulation model. In: Heaps, N.S. (Editor), Three-Dimensional Coastal Ocean Models, pp. 1–16. Washington, DC: American Geophysics Union.

Chu, P.C., 1995. P-vector method for determining absolute velocity from hydrographic data. Marine Technology Society Journal, 29 (3): 3–14.

Chu, P.C., Chen, Y.C., and Lu, S.H., 1998. Temporal and spatial variabilities of Japan Sea surface temperature and atmospheric forcings. Journal of Oceanography, 54: 273–284.

Chu P. C., Chen, Y., and Lu, S.,1999a. Japan/East Sea (JES). Subpolar front meandering and eddy shedding in May 1995. Proceedings of the CREAMS'99 International Symposium, Fukuoka, Japan, pp. 11–13.

Chu, P.C., Lan, J., and Fan, C.W., 2001a. Japan Sea thermohaline structure and circulation, Part 1. Climatology. Journal of Physical Oceanography, 31: 244–271.

Chu, P.C., Lan, J., and Fan, C.W., 2001b. Japan Sea thermohaline structure and circulation, Part 2. A variational P-vector method. Journal of Physical Oceanography, 31: 2886–2902.

Chu, P.C., Lan, J., and Strauhs, H., 2000. A numerical simulation of Japan/East Sea (JES) seasonal circulation. In: Spaulding, M.L., and Butler, H.L. (Editor), Estuarine and Coastal Modeling, pp. 94–113. New York: American Society of Civil Engineers.

Chu, P.C., Lu, S.H., and Chen, Y.C., 1999b. Circulation and thermohaline structures of the Japan/East Sea (JES) and adjacent seas simulated by a nested basin/coastal model. Proceedings of the CREAMS'99 International Symposium, Fukuoka, Japan, pp. 108–111.

Chu, P.C., Wang, G.H., and Chen, Y.C., 2002. Japan Sea thermohaline structure and circulation, Part 3. Autocorrelation functions. Journal of Physical Oceanography, 32: 3596–3615.

da Silva, A.M., Young, C.C., and Levitus, S., 1994. Atlas of Surface Marine Data 1994. Technical Report Geoscience, 94. Milwaukee, WI: University of Wisconsin-Milwaukee, 83p.

Gong, Y., and Park, C.G., 1969. On the oceanographical character of the low temperature region in the eastern sea of Korea. Bulletin Fisheries Research Development Agency, Korea, 4: 69–91.

Haney, L.R., 1971. Surface boundary condition for ocean circulation models. Journal of Physical Oceanography, 1: 241–248.

Hase, H., Yoon, J.-H., and Koterayama, W., 1999. The branching of the Tsushima Warm Current along the Japanese coast. Proceedings of the CREAMS'99 International Symposium, Fukuoka, Japan, pp. 19-22.

Hirose, N., Kim, C.H., and Yoon, J.H., 1996. Heat budget in the Japan Sea. Journal of Oceanography, Society of Japan, 52: 553–574.

Hogan, P.J., and Hurlburt, H.E., 1999a. A possible mechanism for the formation of the boundary current along the coast of Honshu in Japan/East Sea. Proceedings of the 10th PAMS/JECSS Workshop, Kagoshima, Japan, pp. 6.8–6.11.

Hogan, P.J., and Hurlburt, H.E., 1999b. Impact of different wind forcing on Japan/East Sea circulation. Proceedings of the CREAMS'99 International Symposium, Fukuoka, Japan, pp. 124–127.

Hogan, P.J., and Hurlburt, H.E., 2000a. Impact of upper ocean topographical coupling and isopycnal outcropping in Japan/East Sea models with 1/8 to 1/64 resolution. Journal of Physical Oceanography, 30: 2535–2561.

Hogan, P.J., and Hurlburt, H.E., 2000b. Modeled surface circulation in the Japan/East Sea: Impact of using different climatological wind forcing sets. Proceedings of the International Conference on Coastal Ocean and Semi-Enclosed Seas: Circulation and Ecology Modeling and Monitoring, Moscow, Russia, pp. 57-60.

Holloway, G., Sou, T., and Eby, M., 1995. Dynamics of circulation of the Japan Sea. Journal of Marine Research, 53: 539–569.

Isoda, Y., and Saitoh, S., 1993. The northward intruding eddy along the east coast of Korea. Journal of Oceanography, 17: 265–276.

Isoda, Y., Saitoh, S., and Mihara, M., 1991. SST structure of the Polar Front in the Japan Sea. In: Yakano, K. (Editor), Oceanography of Asian Marginal Seas, pp. 103–112. Amsterdam, The Netherlands: Elsevier Science.

Kawabe, M., 1982a. Branching of the Tsushima Current in the Japan Sea, Part I. Data analysis. Journal of Oceanographical Society of Japan, 38: 95–107.

Kawabe, M., 1982b. Branching of the Tsushima Current in the Japan Sea, Part II. Numerical experiment. Journal of Oceanographical Society of Japan, 38: 183–192.

Kim, K., and Chung, J.Y., 1984. On the salinity-minimum layer and dissolved oxygen-maximum layer in the East Sea (Japan Sea). In: Ichiye, T. (Editor), Ocean Hydrodynamics of the Japan and East China Sea, pp. 55–65. Amsterdam, The Netherlands: Elsevier Science.

Kim, Y.G., and Kim, K.K., 1999. Intermediate waters in the East/Japan Sea. Journal of Oceanography, 55: 123–231.

Kim, C.-H., and Yoon, J.-H.,1994. A numerical study on the seasonal variation of the Tsushima Warm Current along the coast of Japan. Proceedings of the CREAMS Third Workshop. Seoul, Korea, pp. 73–79.

Kim, C.-H., and Yoon, J.-H., 1996. Modeling of the wind-driven circulation in the Japan Sea using a reduced gravity model. Journal of Oceanography, 52: 359–373.

Kim, C.-H., and Yoon, J.-H., 1999. A numerical modeling of the upper and the intermediate layer circulation in the East Sea. Journal of Oceanography, 55: 327–345.

Levitus, S., 1982. Climatological atlas of the World Ocean. NOAA Professional Paper 13. Washington DC: National Ocean and Atmospheric Administration.

Maizuru Marine Observatory, 1997. Bulletin of the Maizuru Marine Observatory.

Martin, S., and Kawase, M., 1998. The southern flux of sea ice in the Tatarskiy Strait, Japan Sea and the generation of the Liman Current. Journal of Marine Research, 56: 141–155.

Miyazaki, M., 1952. The heat budget of the Japan Sea. Bulletin of Hokkaido Reg. Fisheries Research Laboratory, 4: 1–54 (in Japanese with English abstract).

Miyazaki, M., 1953. On the water masses of the Japan Sea. Bulletin of Hokkaido Reg. Fisheries Research Laboratory, 7: 1–65 (in Japanese with English abstract).

Mooers, C. N.K., and Kang, H.-S., 1995. Initial spin-up of a Sea of Japan numerical circulation model. In: Alekseev, A.S., and Bakhvalov, N.S. (Editors), Advanced Mathematics: Computations and Applications, pp. 350–357. Novosibirsk: NCC Publisher.

Moriyasu, S., 1972. The Tsushima Current. In: Stommel, H., and Yoshida, K. (Editors), Kuroshio-Its Physical Aspects, pp. 353–369. Tokyo: University of Tokyo Press.

Na, J.-Y., Seo, J.-W., and Han, S.-K., 1992. Monthly mean sea surface winds over the adjacent seas of the Korean Peninsula. Journal of Oceanology Society Korea, 27: 1–10.

Preller, R.H., and Hogan, P.J., 1998. Oceanography of the Sea of Okhotsk and the Japan/East Seas. In: Robinson, A.R., and Brink, K.K. (Editors), The Sea, pp. 429–481. New York: John Wiley and Sons, Inc.

Sekine, Y., 1991. Wind-driven circulation in the Japan Sea and its influence on the branching of the Tsushima Current. Progress in Oceanography, 17: 297–312.

Senjyu, T., 1999. The Japan Sea Intermediate Water: Its characteristics and circulation. Journal of Oceanography, 55: 111–122.

Seo, J. W., 1998. Research on the sea surface winds and heat flux in the East Asian Marginal Seas. Ph.D. Thesis. China: Hanyang University.

Seung, Y.H., 1992. A simple model for separation of East Korean Warm Current and formation of the North Korean Cold Current. Journal of Oceanology Society Korea, 27: 189–196.

Seung, Y.H., and Kim, K., 1989. On the possible role of local thermal forcing on the Japan Sea circulation. Journal of Oceanology Society Korea, 24: 1–14.

Seung, Y.H., and Kim, K., 1993. A numerical modeling of the East Sea circulation. Journal of Oceanology Society Korea, 28: 292–304.

Seung, Y.H., and Kim, K.J., 1995. A multilayer model for dynamics of upper and intermediate layer circulation of the East Sea. Journal of Oceanology Society Korea, 30: 227–236.

Seung, Y.H., and Nam, S.Y., 1992. A numerical study on the barotropic transport of the Tsushima Warm Current. La Mer, 30: 139–147.

Seung, Y.H., and Yoon, J.-H., 1995. Some features of winter convection in the Japan Sea. Journal of Oceanography, 51: 61–73.

Shin, H.-R., Byun, S.-K., and Kim, C., 1995. The characteristics of structure of warm eddy observed to the northwest of Ulleungdo in 1992. Journal of Oceanology Society Korea, 30: 39–56 (in Korean with English abstract).

Shin, C.W., Byun, S.K., and Kim, C.S., 1996. Comparison between geostrophic currents in the southwestern part of the East Sea. Journal of Oceanology Society Korea, 31: 89–96.

Smagorinsky, J., 1963. General circulation experiments with the primitive equations, I. The basic experiment. Monthly Weather Review, 91: 99–164.

Toba, Y., Tomizawa, K., Kurasawa, Y., and Hanawa, K., 1982. Seasonal and year-to-year variability of the Tsushima-Tsugaru Warm Current system with its possible cause. La Mer, 20: 41–51.

Uda, M., 1934. The results of simultaneous oceanographic investigations in the Japan Sea and its adjacent waters in May and June. Journal Imp. Fish. Exp. Sta., 5: 57–190 (in Japanese).

Yi, S.U., 1966. Seasonal and secular variations of the water volume transport across the Korea Strait. Journal of Oceanography Society Korea, 1: 7–13.

Yoon, J.-H., 1982a. Numerical experiment on the circulation in the Japan Sea, Part I. Formation of the East Korean Warm Current. Journal of Oceanography Society Japan, 38: 43–51.

Yoon, J.-H., 1982b. Numerical experiment on the circulation in the Japan Sea, Part II. Influence of seasonal variations in atmospheric conditions on the Tsushima Current. Journal of Oceanography Society Japan, 38: 81–94.

Yoon, J.-H., 1982c. Numerical experiment on the circulation in the Japan Sea Part, III. Mechanism of the nearshore branch of the Tsushima Current. Journal Oceanography Society Japan, 38: 125–130.

Yoshikawa, Y., Awaji, T., and Akitomo, K., 1999. Formation and circulation processes of intermediate water in the Japan Sea. Journal of Physical Oceanography, 29: 1701–1722.

Chapter 17

Analytical Modeling of Pollution Flushing in Well-Mixed Tidal Embayments

Robert W. Barber

Computational Engineering Group, CLRC Daresbury Laboratory, Daresbury,
Warrington WA4 4AD, United Kingdom

1. INTRODUCTION

Over the last decade there has been an overwhelming increase in public awareness of environmental issues which in turn has led to growing demands for major improvements in the levels of air and water quality in densely populated areas. The general public nowadays places a much greater emphasis on the cleanliness and visual appeal of their surroundings and demands far tighter regulation on the discharge of pollution into the environment. One of the reasons for society's growing concern over environmental water pollution can possibly be attributed to the increasing use of river, estuary and coastal waters for recreational activities and the widespread increase in tourism.

Throughout the world there has been a significant growth in the demand for harbor and marina facilities to meet the requirements of a steadily increasing number of pleasure craft. For example, Rajar and Sajovic (1995) estimated that in the United States of America there is one pleasure boat for every 15 people, amounting to approximately 15 million boats. Lacey (1992) estimated a somewhat smaller number of 3.3 million boats in the USA requiring permanent moorings in one of 10,000 marinas while similar levels of ownership per capita are reported in Canada and Europe. In addition, the growth in popularity of jet-skiing and wind-surfing has opened up water based recreational pursuits to a much larger cross-section of the population further increasing the demand for pollution-free coastal waters.

The determination of the flushing characteristics of small tidal embayments and the associated water quality implications are particularly important when conducting environmental impact assessments. The water quality of a coastal embayment and the health of the fauna and flora within the basin can be adversely affected by excessive discharges of chemical and biological pollutants. One of the most important criteria when assessing the release of any pollutant into a semi-enclosed tidal embayment is to ensure there is adequate flushing between the basin and sea in order to prevent excessive deterioration of the water quality beyond predefined limits such as those laid down in the European Community (EC) bathing water directive (European Community, 1976).

In recent years, there has been a significant increase in the use of two- and three-dimensional hydrodynamic and species transport models for assessing the circulation patterns and pollution flushing characteristics of tidal embayments. Examples include the numerical models developed by Chiang and Lee (1982), Blumberg and Mellor (1987), Koutitas (1988), Casulli and Cheng (1992), Falconer (1993), Wu and Tsanis (1994), Li and Falconer (1995), Dias et al. (1996), Lin and Falconer (1996), Rajar and Sirca (1996), Rajar (1997) and Fuentes et al. (1999). Multi-dimensional approaches can often include additional modules to account for complex physical processes such as turbulence, cohesive sediment transport and biochemical interactions such as the nitrification cycle. While the implementation of such models undoubtedly provides increasingly accurate predictions, they are often time consuming to develop and may require high spatial resolution and small time steps for stability. Furthermore, advanced numerical modeling techniques can sometimes be unnecessarily complicated

for the estimation of the pollution flushing characteristics of small, relatively simple tidal basins. For this reason, alternative numerical techniques employing simplified mathematical formulations often provide a more practical method of assessing the dispersion of pollution from a tidal embayment (DiLorenzo et al., 1989).

One of the most popular methods of simplifying the complexity of the flow problem is to adopt a 'zero-dimensional' (i.e., spatially uniform) mathematical approach based on the concept of repeated exchange of the inter-tidal volume. Zero-dimensional or tidal prism models have been used for many years to determine the pollution levels in tidal systems. For example, Harleman (1966) referred to 'classical tidal prism theory' while Dyer (1973) presented the method without further references, inferring general familiarity with the technique. Callaway (1981), van de Kreeke (1983) and Ozhan (1989) proposed similar concepts for estimating the residence time of marinas while Hinwood and McLean (1996) have proposed a method of simulating complex estuaries using a cost-effective parametric modeling technique. A primary consideration when applying a tidal prism model is to ensure that the basin exhibits strong internal mixing to induce a uniform concentration of pollutant throughout the tidal cycle. Although this assumption may not be valid in large tidal embayments, well-mixed conditions can usually be assumed if the characteristic length of the basin does not exceed one tidal excursion (DiLorenzo et al., 1994). Consequently, the maximum size of embayment that can be analyzed using tidal prism theory is generally considered to be of the order of a few kilometers. A second but usually less restrictive constraint on the size of the basin arises from the fact that the tidal embayment is assumed to exhibit a spatially uniform sea level response.

The most predictable mechanism governing the flushing of pollution from a tidal basin is the periodic rise and fall of the tide, although other factors such as wind, wave and density-driven circulation patterns also play an important role. For example, the wind acting on the water surface can force a three-dimensional circulation pattern within the embayment, or it can act on a larger scale by raising or lowering the coastal sea level beyond that of the normal astronomical tide. In addition, freshwater may enter the tidal basin from the land as either direct surface runoff or groundwater seepage. To simplify the formulation so that the water quality response can be predicted using an analytical technique, the present model considers the tide-induced and freshwater flushing effects in isolation. Although this assumption appears to be a serious omission, the mathematical model should underestimate the flushing capabilities of real situations and consequently overestimate the predicted pollution levels. In other words, the proposed analytical solution technique is likely to err 'safely' on the conservative side.

The analytical models described in the present chapter are based upon the Simplified Tidal Embayment Assessment Model (STEAM) developed by DiLorenzo et al. (1989, 1994) for predicting the water quality response and pollution susceptibility of small tidal basins. The mathematical model proposed by DiLorenzo and his co-workers was developed from an earlier tidal prism formulation presented by Isaji and Spaulding (1981). Subsequently DiLorenzo et al. (1995) improved the tidal prism method by including a return-flow factor to account for the pollution that leaves the basin on an ebb tide but returns on the subsequent flood tide. In addition, a novel extension to the tidal prism formulation has recently been proposed by Wearing and Barber (1999) to estimate the water quality response of embayments which are subjected to a continuous release of pollution throughout the tidal cycle.

The STEAM formulation uses an analytical solution to the water quality equations thereby allowing the pollutant concentrations to be found by direct analytical expressions at the end of every tidal cycle. To increase the flexibility of the tidal prism method, Rajar and Sajovic (1995) developed an alternative approach which takes into account a variety of additional features including first-order pollution decay, background pollution levels in the exterior water body and discharges of polluted water from the surrounding land. The scheme proposed by Rajar and Sajovic (1995) essentially uses the

same fundamental water quality equations as the STEAM formulation, but employs a time-marching finite-difference solution procedure instead of an analytical technique to increase the flexibility of the water quality simulations. By definition, the analytical procedures adopted in the present work are clearly less flexible than Rajar and Sajovic's (1995) approach. Nevertheless, analytical methods provide a unique opportunity to study the interrelationship between the main physical parameters which govern the flushing of pollution from a tidal embayment; a feature which is absent in numerical approaches. Furthermore, analytical methods can readily be extended to provide a set of 'engineering design guidelines' for conducting preliminary environmental impact assessments. Such design guidelines could be used to provide a rapid and cost-effective estimate of the water quality response of a tidal inlet system and to decide whether a more sophisticated multi-dimensional model study should be conducted. Furthermore, the proposed model could be used as an emergency response tool in the event of a major contaminant spillage. The results from the analytical model could be obtained within minutes of a spillage, providing reliable estimates of the residence time of the basin and the expected pollution dispersal rate. This information would be invaluable in helping environmental consultants make decisions on possible evacuation or clean-up operations.

2. MODEL FORMULATION

The water quality response of a tidal embayment can be found by solving a set of interrelated time-dependent equations for the volume of water and pollutant conservation on both the flood and ebb tides. As previously described in Section 1, tidal prism models should only be applied to small, well-mixed embayments having length scales less than one tidal excursion. Following DiLorenzo et al. (1995), the main assumptions in formulating the governing water quality equations can be listed as follows:
1. complete internal mixing of the contaminant in each tidal cycle,
2. zero pollution in the exterior water body,
3. no vertical stratification in the basin due to thermal or density effects,
4. the pollutant is conservative,
5. the freshwater from the land is constant with time, and
6. the initial pollutant distribution is uniform throughout the embayment.

The governing water quality equations for the flood and ebb tides are generated separately and then combined to give an overall equation for the pollutant concentration after n complete tidal cycles. In order to obtain a tractable set of equations that can be solved analytically, the basin is assumed to experience repetitive sinusoidal tides of constant amplitude. Thus, the volume of water within the basin, V, is given by

$$V = V_m + V_t \cos(\omega t) \tag{1}$$

where V_m is the mean volume of the basin, V_t is the amplitude of the oscillatory component of the tidal volume, t is the time and ω is the tidal angular frequency given by $\omega = 2\pi/T$ where T is the period of the tide. Equation (1) assumes that the mathematical model commences from high water at $t = 0$ although it is a trivial task to reformulate the analysis to start from low water. The inter-tidal volume or tidal prism, P, is defined as

$$P = 2V_t = HA \tag{2}$$

where H is the tidal range and A is the average surface area of the basin. The mathematical model first considers the scenario where the tidal embayment is subjected to an instantaneous release of contaminant close to the time of high water. The objective of the analysis is to determine the flushing

rate of the embayment as the contaminant is gradually diluted with unpolluted water from the open sea.

2.1. Pollution Flushing Model

The mixing processes within the basin are markedly different during the flood and ebb cycles and therefore the analysis is partitioned into separate intervals depending upon the direction of the tide. To obtain an analytical solution, the freshwater discharge from the surrounding land is assumed to be sufficiently small to have little effect on the duration of the flood and ebb tides. Since the mathematical model is considered to start from high water, the analysis first considers the pollution flux balance on the ebb tide.

2.1.1. Ebb Tide Interval: $2\pi(n-1) < \omega t < \pi + 2\pi(n-1)$

During the ebb tide, polluted water is exported to the open sea at a rate dependent upon the flow through the entrance. Thus the pollutant concentration, C, and volume of water, V, inside the basin satisfy the following equations

$$\frac{d}{dt}(CV) = C\frac{dV}{dt} + V\frac{dC}{dt} = QC \tag{3}$$

and

$$\frac{dV}{dt} = Q + Q_f \tag{4}$$

where Q is the discharge through the entrance (+ve for the flood tide), and Q_f is the steady freshwater inflow from the surrounding land. Combining equations (3) and (4) leads to the following differential equation governing the water quality response on the ebb tide

$$\frac{dC}{dt} = -\frac{C Q_f}{V} \tag{5}$$

In the present formulation, the freshwater inflow from the land, Q_f, is assumed constant with time. Substituting for the volume of the tidal basin, V, from equation (1) and integrating over the first ebb-tidal interval leads to

$$\int_{C_0}^{C_{e(1)}} \frac{dC}{C} = -Q_f \int_0^{\pi/\omega} \frac{dt}{V_m + V_t \cos(\omega t)} \tag{6}$$

where C_0 is the initial concentration at the start of the simulation ($t = 0$), and $C_{e(1)}$ is the concentration at the end of the first ebb tide. It can readily be shown that

$$\int_0^{\pi/\omega} \frac{dt}{V_m + V_t \cos(\omega t)} = \frac{\pi}{\omega\sqrt{V_m^2 - V_t^2}} \tag{7}$$

and therefore equation (6) can be integrated and rearranged to give

$$C_{e(1)} = C_0 \exp\left\{ \frac{-\pi Q_f}{\omega\sqrt{V_m^2 - V_t^2}} \right\} \tag{8}$$

Since the tidal basin is assumed to experience repetitive harmonic tides of constant amplitude, equation (8) can be rewritten for the more generalized case after n tidal cycles as

$$C_{e(n)} = C_{f(n-1)} \exp \left\{ \frac{-\pi Q_f}{\omega \sqrt{V_m^2 - V_t^2}} \right\} \tag{9}$$

where $C_{e(n)}$ is the pollutant concentration at the end of n ebb tides and $C_{f(n-1)}$ is the corresponding concentration at the end of the previous flood cycle.

2.1.2. Flood Tide Interval: $\pi + 2\pi(n-1) < \omega t < 2\pi n$

Similarly during the flood tide the pollutant concentration and volume of water inside the basin satisfy the following equations

$$\frac{d}{dt}(CV) = C \frac{dV}{dt} + V \frac{dC}{dt} = b Q C \tag{10}$$

and

$$\frac{dV}{dt} = Q + Q_f \tag{11}$$

where b is a parameter between 0 and 1 defining the proportion of pollutant which leaves the basin on an ebb cycle and returns on the subsequent flood tide. The 'return-flow' parameter therefore expresses the fate of the tidal prism after it leaves the embayment, and its value depends upon the level of mixing between the effluent plume and the surrounding coastal waters. Under idealized conditions the return-flow factor can be evaluated theoretically (Sanford et al., 1992) although in more realistic situations the value has to be found by calibrating the analytical model against observed pollution data.

The volume of water in the basin at low tide is $V_m - V_t$ while the corresponding volume at high tide is $V_m + V_t$. Consequently, equations (1), (10) and (11) can be combined on the first flood interval to give

$$\int_{C_{e(1)}}^{C_{f(1)}} \frac{dC}{C} = (b-1) \int_{V_m-V_t}^{V_m+V_t} \frac{dV}{V} - b Q_f \int_{\pi/\omega}^{2\pi/\omega} \frac{dt}{V_m + V_t \cos(\omega t)} \tag{12}$$

where $C_{f(1)}$ is the concentration at the end of the first flood tide. Integrating and rearranging leads to

$$C_{f(1)} = C_{e(1)} \left[\frac{V_m - V_t}{V_m + V_t} \right]^{(1-b)} \exp \left\{ \frac{-\pi b Q_f}{\omega \sqrt{V_m^2 - V_t^2}} \right\} \tag{13}$$

and generalizing the result for the nth flood tide gives

$$C_{f(n)} = C_{e(n)} \left[\frac{V_m - V_t}{V_m + V_t} \right]^{(1-b)} \exp \left\{ \frac{-\pi b Q_f}{\omega \sqrt{V_m^2 - V_t^2}} \right\} \tag{14}$$

Substituting for $C_{e(n)}$ from equation (9) leads to an expression for the pollutant concentration after n complete tidal cycles

$$C_{f(n)} = C_{f(n-1)} \left[\frac{V_m - V_t}{V_m + V_t} \right]^{(1-b)} \exp \left\{ \frac{-\pi \, Q_f \, (1+b)}{\omega \sqrt{V_m^2 - V_t^2}} \right\}$$

(15)

Repeated application of equation (15) from the starting conditions yields the pollutant concentration after n tidal cycles in terms of the initial concentration, C_0

$$C_{f(n)} = C_0 \prod_{i=1}^{n} \left[\frac{V_m - V_t}{V_m + V_t} \right]^{(1-b)} \exp \left\{ \frac{-\pi \, Q_f \, (1+b)}{\omega \sqrt{V_m^2 - V_t^2}} \right\}$$

(16)

which may be rewritten as

$$C_{f(n)} = C_0 \left[\frac{V_m - V_t}{V_m + V_t} \right]^{n(1-b)} \exp \left\{ \frac{-\pi \, Q_f \, n(1+b)}{\omega \sqrt{V_m^2 - V_t^2}} \right\}$$

(17)

The pollutant concentration at the end of the nth ebb tide can then be obtained by substituting $C_{f(n-1)}$ into equation (9)

$$C_{e(n)} = C_0 \left[\frac{V_m - V_t}{V_m + V_t} \right]^{(n-1)(1-b)} \exp \left\{ \frac{-\pi \, Q_f \, [n(1+b) - b]}{\omega \sqrt{V_m^2 - V_t^2}} \right\}$$

(18)

2.1.3. Pollution Exchange Coefficient

The efficiency of the tidal flushing can be expressed in terms of the pollution exchange coefficient, E, which measures the proportion of water exchanged with the sea each tidal cycle. Specifically, Falconer and Yu (1991) chose to define the pollution exchange coefficient as the fraction of water removed during a tidal cycle and replaced by unpolluted water. The coefficient can thus be expressed in generalized form after n complete tidal cycles as

$$E = 1 - \left(\frac{C_{f(n)}}{C_0} \right)^{1/n}, \quad n \to \infty$$

(19)

where C_0 is the initial concentration, $C_{f(n)}$ is the average basin concentration at the end of the nth flood tide and n is the integer number of tidal cycles from the start time ($t = 0$). Substituting $C_{f(n)}$ from equation (17) into equation (19) and simplifying yields

$$E = 1 - \left[\frac{V_m - V_t}{V_m + V_t} \right]^{(1-b)} \exp \left\{ \frac{-\pi \, Q_f \, (1+b)}{\omega \sqrt{V_m^2 - V_t^2}} \right\}$$

(20)

In the absence of freshwater flushing ($Q_f = 0$), the pollution exchange coefficient, E, and the return-flow factor, b, are interrelated via

$$E = 1 - \left[\frac{V_m - V_t}{V_m + V_t} \right]^{(1-b)}$$

(21)

High values of pollution exchange coefficient are indicative of efficient tidal flushing. The analytical model therefore demonstrates that the flushing rate of a tidal embayment depends crucially on the ratio of the volume of water in the basin at low tide to the volume of water at high tide, $(V_m - V_t)/(V_m + V_t)$. Small values of this ratio lead to high pollution exchange coefficients and rapid flushing. Conversely, values of $(V_m - V_t)/(V_m + V_t)$ which approach unity suggest that the basin may be at risk from water quality problems. As an aside, it should be noted that high values of the pollution-return parameter, b, will also have an adverse affect on the efficiency of the tidal flushing.

2.2. Pollution Discharge Model

The second analytical model provides a novel extension of the tidal prism approach for predicting the water quality response of embayments that are subjected to a continuous release of pollution throughout the tidal cycle. These improvements were first proposed by Wearing and Barber (1999) and allow an estimate to be made of the maximum pollutant concentrations that are likely to occur for a given pollution loading rate. There are essentially two main objectives for the analysis; the determination of the water quality response of the embayment from known starting conditions, and the estimation of the limit-cycle pollutant concentration after a large number of tidal cycles.

To obtain a tractable set of equations that can be solved analytically, the present formulation has to make the assumption that the freshwater discharge from the surrounding land, Q_f, is negligible in comparison to the tidal discharge through the entrance. As in the case of the pollution flushing model (Section 2.1), the mixing processes in the embayment are markedly different during the flood and ebb cycles and therefore the analysis is partitioned into separate intervals depending upon the direction of the tide. The mathematical model is assumed to start from high water and therefore the analysis first considers the pollution flux balance on the ebb tide.

2.2.1. Ebb Tide Interval: $2\pi(n-1) < \omega t < \pi + 2\pi(n-1)$

During the ebb tide interval, the pollutant concentration, C, and volume of water, V, inside the basin satisfy the following equations

$$\frac{d}{dt}(CV) = C\frac{dV}{dt} + V\frac{dC}{dt} = QC + k \tag{22}$$

and

$$\frac{dV}{dt} = Q \tag{23}$$

where Q is the discharge through the entrance and k is the internal pollution loading rate (measured as a mass per unit time). It should be noted that equations (22) and (23) are strictly only valid for situations where $Q_f C \ll k$. In other words, the term accounting for the freshwater inflow can only be omitted from equation (23) if Q_f has a negligible contribution in the pollutant mass balance equation resulting from combining equations (22) and (23).

Substituting equation (23) into (22) and rearranging leads to the following differential equation governing the water quality response on the ebb tide

$$\frac{dC}{dt} = \frac{k}{V} \tag{24}$$

Substituting the volume of water in the tidal basin, V, from equation (1) and integrating over the first ebb interval leads to

$$\int_{C_0}^{C_{e(1)}} dC = \int_0^{\pi/\omega} \frac{k\,dt}{V_m + V_t\cos(\omega t)} \tag{25}$$

where C_0 is the initial concentration at the start of the simulation ($t = 0$) and $C_{e(1)}$ is the concentration at the end of the first ebb tide. The pollution loading rate, k, is assumed constant with time and therefore equation (25) can be integrated and rearranged to give

$$C_{e(1)} = C_0 + \frac{k\pi}{\omega\sqrt{V_m^2 - V_t^2}} \tag{26}$$

Since the embayment is considered to experience repetitive harmonic tides of constant amplitude, equation (26) can be rewritten for the more generalized case after n tidal cycles as

$$C_{e(n)} = C_{f(n-1)} + \frac{k\pi}{\omega\sqrt{V_m^2 - V_t^2}} \tag{27}$$

where $C_{e(n)}$ is the pollutant concentration at the end of n ebb tides and $C_{f(n-1)}$ is the corresponding concentration at the end of the previous flood cycle.

2.2.2. Flood Tide Interval: $\pi + 2\pi(n-1) < \omega t < 2\pi n$

Similarly during the flood interval the pollutant concentration and volume of water inside the basin satisfy the following equation

$$\frac{d}{dt}(CV) = k \tag{28}$$

It should be noted that the inclusion of a return-flow factor in the above pollution flux balance equation would prevent the use of an analytical solution technique. It is therefore necessary to assume that the water entering the tidal embayment during the flood interval is uncontaminated. Instead, the pollution return phenomenon can be approximated by modifying the amplitude of the oscillatory tidal prism as described later in Section 2.2.4.

The volume of water in the basin at low tide is $V_m - V_t$ while the corresponding volume at high tide is $V_m + V_t$. Consequently, equation (28) can be integrated on the first flood tide to give

$$\int_{C_{e(1)}(V_m - V_t)}^{C_{f(1)}(V_m + V_t)} d(CV) = \int_{\pi/\omega}^{2\pi/\omega} k\,dt \tag{29}$$

where $C_{f(1)}$ is the concentration at the end of the first flood cycle. Integrating and rearranging leads to

$$C_{f(1)} = \left(\frac{V_m - V_t}{V_m + V_t}\right)\left(C_{e(1)} + \frac{k\pi}{\omega(V_m - V_t)}\right) \tag{30}$$

and generalizing the result for the nth flood tide gives

$$C_{f(n)} = \left(\frac{V_m - V_t}{V_m + V_t}\right)\left(C_{e(n)} + \frac{k\pi}{\omega(V_m - V_t)}\right) \tag{31}$$

Substituting for $C_{e(n)}$ from equation (27) enables the water quality response of the tidal embayment to be determined using a recurrence relationship

$$C_{f(n)} = \left(\frac{V_m - V_t}{V_m + V_t}\right)\left(C_{f(n-1)} + \frac{k\pi}{\omega\sqrt{V_m^2 - V_t^2}} + \frac{k\pi}{\omega(V_m - V_t)}\right) \tag{32}$$

To obtain a generalized expression in terms of the initial pollutant concentration, C_0, the equation can be rewritten as

$$C_{f(n)} = \alpha \left(C_{f(n-1)} + \beta \right) \tag{33}$$

where

$$\alpha = \left(\frac{V_m - V_t}{V_m + V_t} \right) \tag{34}$$

and

$$\beta = \frac{k\pi}{\omega\sqrt{V_m^2 - V_t^2}} + \frac{k\pi}{\omega(V_m - V_t)} \tag{35}$$

Repeated application of equation (33) from the starting conditions at $t = 0$ allows the pollutant concentration after each flood tide to be written in terms of the initial concentration, C_0, i.e.

$$C_{f(1)} = \alpha \left(C_0 + \beta \right) \tag{36}$$

$$C_{f(2)} = \alpha^2 C_0 + \beta \left(\alpha + \alpha^2 \right) \tag{37}$$

$$C_{f(3)} = \alpha^3 C_0 + \beta \left(\alpha + \alpha^2 + \alpha^3 \right) \tag{38}$$

Generalizing the result for the nth flood tide yields

$$C_{f(n)} = \alpha^n C_0 + \beta \left(\alpha + \alpha^2 + \alpha^3 + \ldots + \alpha^n \right) \tag{39}$$

which can be rewritten as

$$C_{f(n)} = \alpha^n C_0 + \beta \sum_{i=1}^{n} \alpha^i \tag{40}$$

The pollutant concentration in the embayment after n flood tides can therefore be expressed as

$$C_{f(n)} = C_0 \left(\frac{V_m - V_t}{V_m + V_t} \right)^n + \left(\frac{k\pi}{\omega\sqrt{V_m^2 - V_t^2}} + \frac{k\pi}{\omega(V_m - V_t)} \right) \sum_{i=1}^{n} \left(\frac{V_m - V_t}{V_m + V_t} \right)^i \tag{41}$$

while substitution of $C_{f(n-1)}$ into equation (27) yields the pollutant concentration after n ebb tides

$$C_{e(n)} = C_0 \left(\frac{V_m - V_t}{V_m + V_t} \right)^{n-1} + \left(\frac{k\pi}{\omega\sqrt{V_m^2 - V_t^2}} + \frac{k\pi}{\omega(V_m - V_t)} \right) \sum_{i=1}^{n-1} \left(\frac{V_m - V_t}{V_m + V_t} \right)^i +$$

$$\frac{k\pi}{\omega\sqrt{V_m^2 - V_t^2}} \tag{42}$$

2.2.3. Determination of Limit-Cycle Pollutant Concentrations

After a large number of tidal cycles, the pollutant concentration in the embayment will eventually settle to a level where the average rate of removal of contaminant due to tidal flushing balances the pollution loading rate, k. The equilibrium or limit-cycle conditions can readily be found by considering the values of $C_{f(n)}$ and $C_{e(n)}$ as the number of tidal cycles, n tends to infinity. By definition

$$\left(\frac{V_m - V_t}{V_m + V_t} \right) < 1 \tag{43}$$

and therefore the influence of the initial concentration, C_0, becomes less significant as the number of tidal cycles increases. In addition, using geometric series it can be shown that

$$\lim_{n \to \infty} \sum_{i=1}^{n} \left(\frac{V_m - V_t}{V_m + V_t} \right)^i = \frac{(V_m - V_t)}{2 V_t} \tag{44}$$

Therefore, the limit-cycle concentrations at the end of the flood and ebb cycles are given by

$$\lim_{n \to \infty} C_{f(n)} = \left(\frac{k \pi}{\omega \sqrt{V_m^2 - V_t^2}} + \frac{k \pi}{\omega (V_m - V_t)} \right) \left(\frac{V_m - V_t}{2 V_t} \right) \tag{45}$$

and

$$\lim_{n \to \infty} C_{e(n)} = \left(\frac{k \pi}{\omega \sqrt{V_m^2 - V_t^2}} + \frac{k \pi}{\omega (V_m - V_t)} \right) \left(\frac{V_m - V_t}{2 V_t} \right) + \frac{k \pi}{\omega \sqrt{V_m^2 - V_t^2}} \tag{46}$$

The above pollutant concentrations provide a useful analytical formulation for predicting the long-term water quality response of a tidal embayment. Alternatively, the expressions could be recast to provide an estimate of the maximum permitted pollution loading rate to prevent the water quality from deteriorating beyond predefined acceptable limits. This could be especially useful when establishing pollution discharge consent levels for industries surrounding the embayment.

2.2.4. Pollution Return-Flow Factor

It is usually necessary to adjust the concentration predictions to account for pollution that leaves the embayment on an ebb tide and returns on the subsequent flood tide—the so-called 'return-flow' effect. However, as previously explained in Section 2.2.2, the pollution discharge model is unable to consider this phenomenon in the water quality equations since the inclusion of a return-flow parameter would preclude the implementation of an analytical solution technique. Instead, a convenient (although approximate) method of accounting for the return flow is to reduce the amplitude of the oscillatory tidal prism. Thus, the effective amplitude of the oscillatory tidal volume can be expressed as

$$V_t' = (1 - b) V_t \tag{47}$$

where b is the pollution-return parameter between 0 and 1. The reduced oscillatory tidal volume, V_t', is therefore invoked in the pollution discharge model instead of the theoretical oscillatory tidal volume, V_t. As noted earlier, the pollution return-flow factor can sometimes be evaluated theoretically (Sanford et al., 1992), although in most situations the value has to be found by calibrating the analytical formulation against observed pollution data.

3. EXPERIMENTAL VALIDATION

Field data from estuaries and tidal embayments have been reported widely in the literature yet accurate and concurrent measurements of tidal levels, contaminant discharge rates and pollutant distributions suitable for the validation of a mathematical model are extremely rare. DiLorenzo et al. (1995) reported the results of a field experiment carried out in Centreport Harbor in the Huntington Bay Complex near New York, USA. Tidal elevations in the embayment were measured continuously while an instantaneous dye-release experiment was performed by injecting rhodamine WT dye into the upstream tributary at high tide. The resultant spatial distributions of the tracer-dye were sampled until the concentration approached the limit of detection (approximately two tidal cycles after the initial release). DiLorenzo et al. (1995) were able to demonstrate that the Simplified Tidal Embayment Assessment Model (STEAM) could predict the observed flushing rate of Centreport Harbor to an acceptable level of accuracy.

In the present work, the tidal prism models have been validated by comparing predictions against experimentally observed pollution data from a laboratory model of a generic tidal basin. The laboratory experiments were conducted in a 7.5 m x 3.5 m tidal testing facility at the University of Salford as detailed by Barber and Wearing (2000) and Wearing (2000). Conducting the pollution flushing experiments in a laboratory model offered greater flexibility than field experiments and enabled identical tests to be repeated several times to ensure the reproducibility of the experimental data.

The laboratory tests were conducted on a vertically distorted model of an idealized flat-bottomed prototype harbor having a square planform area of 432 m x 432 m (18.7 hectares), a single asymmetric entrance 48 m wide and vertical side walls. These dimensions are representative of small to medium sized marinas in the USA and larger marinas in the UK (Nece and Falconer, 1989; Falconer and Yu, 1991). The model harbor was scaled according to Froude number similarity and was constructed at a horizontal scale of 1:400. The model tidal basin was therefore 1.08 m x 1.08 m in plan with an entrance 0.12 m wide. Three sets of vertical scale ratios (Table 1) were used in the preliminary tests to investigate the effect of vertical distortion. However, the experiments soon revealed that the flushing characteristics of the laboratory embayment were only marginally affected by vertical distortion and therefore all the results presented in this chapter relate to the experiments conducted at a vertical scale of 1:40.

Sinusoidal water level variations in the testing facility were generated using a computer controlled constant-inflow, controlled-outflow tidal generator. Water was supplied to the testing facility at a constant rate with the level being determined by a computer-controlled movable weir which allowed excess water to flow back to a collecting sump. The system avoided the use of complex feedback control and was able to deliver tidal levels to within an accuracy of ± 0.5 mm.

The initial experiments considered a generic square tidal embayment. To ensure that this simplistic geometry was not affecting the validity of the results, various other rectangular-shaped embayments

Table 1

Summary of scaling data used in laboratory tests (after Falconer and Yu, 1991).

Horizontal scale	Vertical scale	Distortion ratio	Model period (s)
1:400	1:33.3	12:1	646
1:400	1:40	10:1	708
1:400	1:64	6.25:1	894

with different aspect ratios of length and breadth were also tested. All geometries showed remarkably consistent pollution dispersal characteristics compared with the results from the square basin.

Pollution levels in the tidal basin were measured using sodium fluorescein dye and a luminescence spectrometer. The experiments were conducted in two distinct phases to validate the pollution flushing and pollution discharge models. The initial tests replicated an instantaneous release of contaminant at high water in a similar manner to DiLorenzo et al.'s (1995) field experiments. In each test, the harbor entrance was temporarily sealed and a small quantity of sodium fluorescein dye thoroughly mixed with the water inside the basin. A distributed water quality sample was then taken to determine the initial pollutant concentration, C_0. Once the turbulence created by the mixing had decayed, the barrier across the mouth of the basin was removed and the tidal generator started. Sampling of the water quality took place at nine equally spaced points within the model harbor to give an accurate measurement of the overall average concentration of dye within the basin. A special frame was constructed so that instantaneous water quality observations could be carried out at the nine points with minimal disturbance to the tidal circulation. Sampling was carried out every high tide for six complete tidal cycles. At the end of the tests the water samples were analyzed using a Perkin-Elmer LS-5B luminescence spectrometer to determine the pollution flushing characteristics of the embayment.

In the second series of tests, the tidal basin was subjected to a known discharge of sodium fluorescein dye flowing from a constant head Mariotte vessel to simulate a continuous release of pollution. The sodium fluorescein was fed into the laboratory model at the corner diametrically opposite the entrance. All tests were started at high water from initially unpolluted conditions ($C_0 = 0$), and once a predetermined number of complete tidal cycles had been reached, the flow of dye from the Mariotte vessel was halted and a temporary barrier placed across the entrance. The sodium fluorescein within the model was then thoroughly mixed so that a spatially-averaged pollutant concentration could be sampled. The procedure was carried out for 1, 3, 5, 9 and 12 tidal cycles in order to obtain a representative set of pollution data spanning the approach to limit-cycle conditions. In addition, a calibration test was performed to determine, k, the pollution loading rate. This was achieved by measuring the linear increase in spatially-averaged pollutant concentration in the absence of tidal flushing. At the end of the tests the water samples were analyzed using a luminescence spectrometer to determine the water quality response. It should be noted that the nine-point sampling method was abandoned in the second series of tests and instead the spatially-averaged pollutant concentration was determined by thorough mixing of the sodium fluorescein dye in the model harbor after each test. This was deemed necessary since the local increase in dye concentration in the vicinity of the Mariotte vessel may not have been detected by the nine-point sampling method leading to possible errors in the measured pollutant concentrations.

4. LABORATORY RESULTS

The first set of validation tests (Fig. 1 and 2) assessed the pollution flushing characteristics of the basin under a variety of tidal and freshwater discharges. The tests employed repetitive sinusoidal tides having a prototypical semidiurnal period of 12.42 hours (44,712 s), a maximum water depth of 8 m, and tidal ranges of 2, 4 and 6 m respectively. These values can be considered representative of conditions found in tidal harbors around the coast of the United Kingdom. The corresponding tidal regime in the laboratory model had a period of 708 s, a maximum water depth at high tide of 200 mm and tidal ranges of 50, 100 and 150 mm. Initially, the tidal flushing characteristics were considered in isolation and so the freshwater inflow, Q_f, was set to zero. The pollution-return parameter, b, was estimated by applying a least-squares analysis to the observed water quality data. In this particular study, the return-flow factor was found to equal 0.135 which is relatively low and indicates efficient
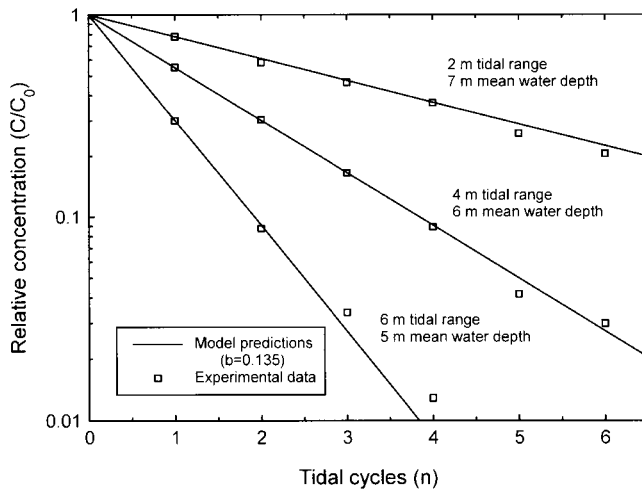
Figure 1. Experimental validation of proposed pollution flushing model (varying tidal ranges).
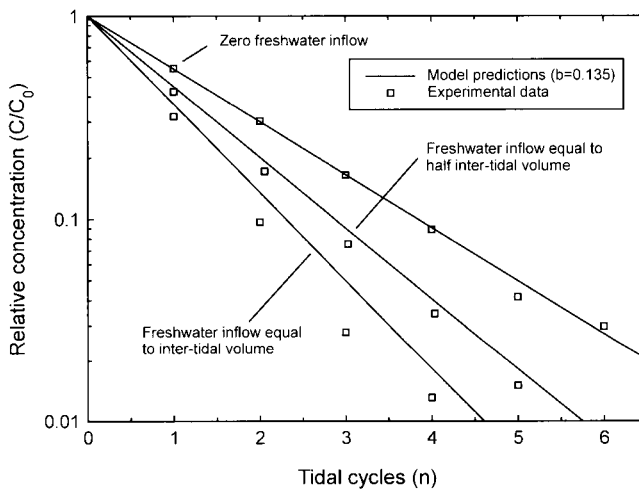
Figure 2. Experimental validation of proposed pollution flushing model (varying freshwater inflows).

mixing between the effluent plume and surrounding water just outside the harbor. Fig. 1 details the results of the various tidal ranges and shows good correlation between the analytical predictions and the observed flushing characteristics. It should be noted that the pollution flushing data have been non-dimensionalized and presented as graphs of relative concentration (C/C_0) against the number of tidal cycles (n). The laboratory tests reveal that the pollution flushing can be predicted using a single return-flow parameter, b, in spite of the variation in tidal range.

The analytical formulation was found to be quite sensitive to the chosen value of the return-flow parameter, b. Early tidal flushing models (for example, Dyer, 1973; Callaway, 1981) often ignored the return-flow factor completely, while other studies have suggested that the factor should be taken

as 0.5 in the absence of further information (U.S. EPA, 1985). The present study using a pollution-return parameter of 0.135 indicates that both these previous scenarios would yield erroneous pollution flushing characteristics.

A second set of pollution flushing experiments (Fig. 2) assessed the accuracy of the analytical technique when simulating the combined effect of tide-induced and freshwater flushing. In this case a prototypical tidal range of 4 m was considered which corresponds to a tidal range of 100 mm in the laboratory model (equivalent to the middle regime of the previous validation test). The freshwater was fed into the tidal embayment at the corner diametrically opposite the entrance and was varied from zero up to a maximum discharge of P/T where P is the volume of the inter-tidal prism and T is the tidal period. The freshwater inflow was non-dimensionalized with respect to the inter-tidal volume to assist in the interpretation of the results. In the laboratory tests the volume of the inter-tidal prism $P = 0.1166$ m^3 and the tidal period $T = 708$ s giving a maximum freshwater inflow of $Q_f = 0.165$ l/s (equivalent to 16.7 m^3/s in the prototype).

The water quality predictions were computed using the same pollution-return parameter as the initial study ($b = 0.135$) even though the higher discharge rates through the entrance may lead to increased mixing of the effluent plume and produce a lower value of b. Fig. 2 compares the predicted and observed flushing characteristics for freshwater inflows of 0, 0.5 P/T and P/T and again shows good correlation between the analytical and observed pollution data. It can be seen that the accuracy of the mathematical model is reduced as the freshwater discharge is increased, but this is to be expected since the analytical solution is derived from a basic assumption that the flood and ebb tides are of the same duration. As the freshwater discharge is increased, the duration of the flood tide is shortened while the duration of the ebb tide is lengthened. As a consequence, large freshwater inflow rates invalidate the assumption of partitioning the tidal cycle into equal intervals of $0.5\,T$ and reduce the accuracy of the analytical solution.

To demonstrate the overall effectiveness of the pollution flushing model, Table 2 compares the observed and predicted pollution exchange coefficients for each validation test. Following Falconer and Yu (1991), the experimental pollution exchange coefficients were determined by applying equation (19) over four complete tidal cycles while the predicted pollution exchange coefficients were evaluated using equation (20) with a constant return-flow parameter of $b = 0.135$. Table 2 demonstrates that the proposed analytical model offers a viable and accurate method for predicting the pollution exchange coefficient under a variety of tidal fluxes and freshwater discharges.

In the second series of validation tests, the tidal basin was subjected to a constant release of sodium fluorescein dye. The laboratory experiments considered the same prototype basin used for the pollution flushing tests, namely, a square planform area of 432 m x 432 m (18.7 hectares) and an asymmetric entrance 48 m wide. Semidiurnal tidal ranges of 2, 4 and 6 m were considered and the maximum water depth in the basin was set to 8 m. The corresponding tidal conditions in the laboratory model had a period of 708 s, a maximum water depth at high tide of 200 mm and tidal

Table 2

Summary of pollution exchange coefficients.

Prototype tidal range (m)	Non-dimensionalized freshwater flow	Pollution exchange coefficient, E	
		Observed	Predicted
2	0	0.221	0.220
4	0	0.454	0.451
6	0	0.670	0.699
4	$0.5P/T$	0.570	0.551
4	P/T	0.662	0.632
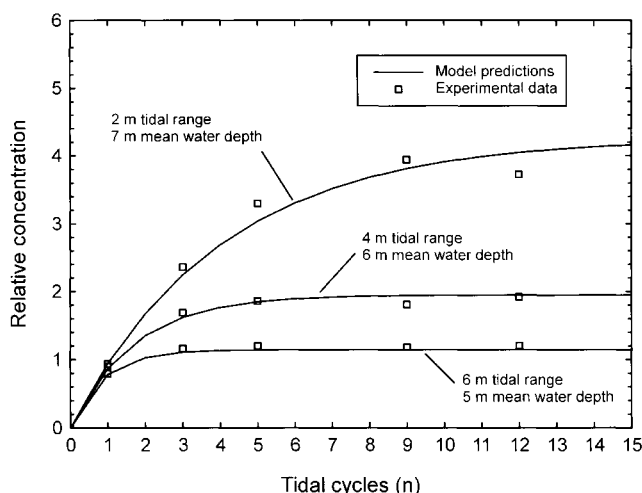
Figure 3. Experimental validation of proposed pollution discharge model (square harbor geometry).

ranges of 50, 100 and 150 mm respectively. Mean water depths in the harbor varied from 175 mm to 125 mm depending upon the tidal range.

Fig. 3 compares the observed and predicted fluorescein concentration data for the three tidal regimes. The experimental water quality sampling was conducted at high tide after 1, 3, 5, 9 and 12 complete tidal cycles in order to obtain a representative set of pollution data spanning the approach to limit-cycle conditions. To provide a logical method of interpreting the results, the water quality data have been non-dimensionalized and presented as graphs of relative concentration, $C/\overline{C}$, against the number of tidal cycles, n, where $\overline{C}$ is defined as the theoretical increase in pollutant concentration per cycle in the absence of tidal flushing, i.e.

$$\overline{C} = \frac{kT}{V_m + V_t} \tag{48}$$

High values of non-dimensionalized relative concentration, $C/\overline{C}$, indicate inefficient tidal flushing and suggest the embayment may be at risk from poor water quality.

The water quality predictions were computed using the same return-flow parameter as the pollution flushing studies ($b = 0.135$). The value of b was substituted into equation (47) to reduce the amplitude of the oscillatory tidal prism. Fig. 3 presents the results of the pollution discharge tests and shows good correlation between the analytical predictions and the observed pollution data. The stray experimental points for the smallest tidal range clearly demonstrate the difficulties in measuring the fluorescein dye concentrations even under carefully controlled laboratory conditions. Fig. 3 also demonstrates that the tidal range has a significant effect on the length of time required to achieve limit-cycle conditions. For example, the test involving the 2 m tide required in excess of 15 tidal cycles to reach steady state, while the test involving the 6 m tide reached steady state after only 4 tidal cycles.

To test whether the proposed analytical approach could be used for other geometries of tidal basins, a series of experiments were conducted using various rectangular-shaped embayments with different aspect ratios of length and breadth (Wearing, 2000). For example, Fig. 4 presents the results of a validation test conducted on a rectangular tidal embayment having an aspect ratio of 2:1. The experiment considered a prototype tidal basin having a rectangular area of 864 m x 432 m (37.3
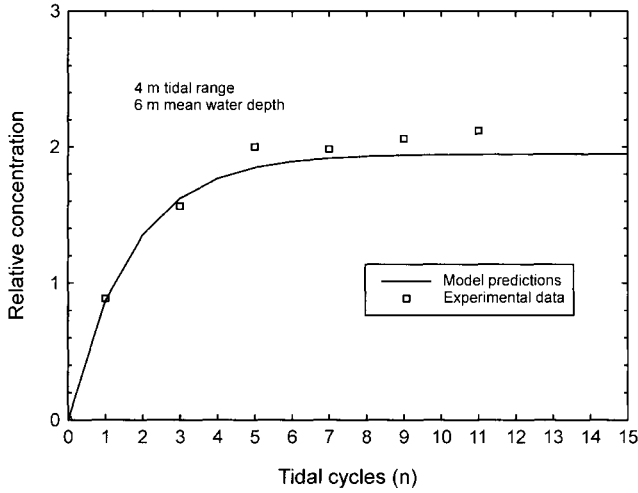
Figure 4. Experimental validation of proposed pollution discharge model (rectangular harbor geometry).

hectares) and an entrance 48 m wide half way along the longest side wall. A semidiurnal tidal range of 4 m was chosen and the maximum basin water depth was again set to 8 m. The corresponding conditions in the laboratory model had a tidal range of 100 mm and a maximum water depth of 200 mm. Once again, the close correlation between the experimental data and the analytical predictions demonstrates that the mathematical formulation offers a simple yet surprisingly accurate method of predicting the water quality response of well-mixed tidal embayments. Additional tests using different geometries confirm that the analytical technique is equally valid for other shapes of tidal basins.

5. NUMERICAL VALIDATION OF POLLUTION DISCHARGE MODEL

The analytical tidal prism model assumes the embayment is subjected to repetitive harmonic tides of constant amplitude. To generalize the mathematical formulation, a finite-difference scheme has also been developed to solve the water quality equations for distorted and non-repetitive tides. The finite-difference approach employs the same differential equations for volume and pollutant concentration presented earlier. Thus on the ebb tide, equation (24) can be discretized as

$$C^{(n+1)} = C^{(n)} + \frac{k\,\Delta t}{V^{(n)}} \tag{49}$$

while on the flood tide, equation (28) is discretized as

$$C^{(n+1)} = C^{(n)} \left(1 - \frac{\Delta t}{V^{(n)}} \cdot \left. \frac{dV}{dt}\right|^{(n)} \right) + \frac{k\,\Delta t}{V^{(n)}} \tag{50}$$

where $C^{(n)}$, $V^{(n)}$ and $(dV/dt)^{(n)}$ are the pollutant concentration, volume and rate of change of volume at time $t = n\Delta t$, $C^{(n+1)}$ is the concentration at time $t = (n+1)\Delta t$ and Δt is the time step. To obtain an accurate solution of the water quality response equations, the selected time step has to be very much less than the tidal period. Preliminary calibration of the finite-difference model showed
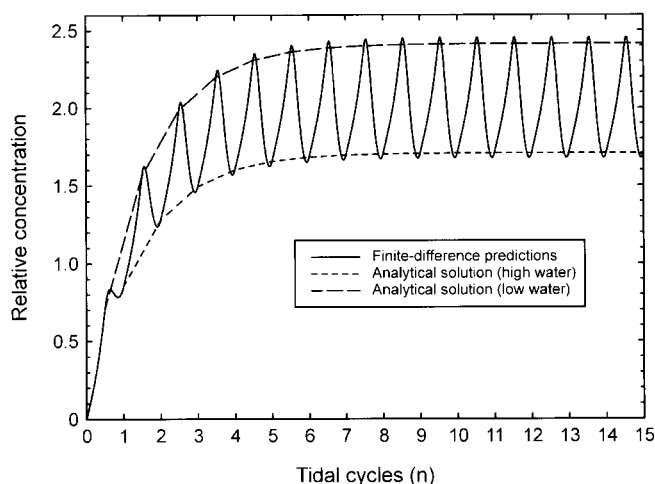
Figure 5. Comparison of analytical and finite-difference water quality predictions.

that predictions were independent of the selected time step when Δt was approximately 10^4 times smaller than the tidal period, T.

The analytical formulation was validated against the finite-difference model to ensure the two schemes were consistent. The numerical tests were conducted on the same idealized flat-bottomed harbor considered previously; namely a square planform area of 432 m x 432 m. Validation tests were performed using a tidal range of 4 m and a maximum water depth of 8 m. The pollution loading rate, k, was set to $1/T$ kg/s corresponding to a loading rate of 1 kg of pollutant per tidal cycle and the return-flow factor was assumed to be zero. Fig. 5 illustrates the predicted water quality response of the embayment over the first 15 tidal cycles, and clearly indicates the periodic variation of concentration on the flood and ebb tides. As before, the pollution data have been non-dimensionalized and presented as graphs of relative concentration, $C/\overline{C}$, against the number of tidal cycles, n.

Fig. 6 presents an enlarged view of the limit-cycle water quality response and demonstrates that the analytical and finite-difference models are consistent with each other at high and low water. However, it is also apparent that the minimum and maximum spatially-averaged pollutant concentrations in the tidal embayment do not occur at the exact times of high and low water. Instead, the maximum concentration occurs just after low water while the minimum concentration occurs just before high water. This can be explained by the fact that during the initial stages of a flood tide (when the inflow discharge is relatively small) the dilution effects of the incoming unpolluted water will be insufficient to counteract the pollution loading rate, k, and therefore the pollutant concentration in the basin will continue to increase beyond the time of low water. As the strength of the flood tide increases, the dilution effect of the incoming unpolluted water will eventually have an effect on the pollutant concentration that then starts to fall during the remainder of the flood tide. However, a similar phenomenon occurs during the final stages of the flood tide, when the dilution effects of the incoming water are again insufficient to counteract the pollution loading rate, k, leading to a minimum pollutant concentration before the time of high water. It can therefore be concluded that although the analytical model provides an accurate solution for the pollutant concentrations at both high and low water, the analytical formulation only provides an approximation to the actual limit-cycle pollution envelope. Fig. 6 also shows that the temporal variation of pollutant concentration in the embayment is asymmetric. This can be attributed to the fact that the pollution flux balance equations are markedly
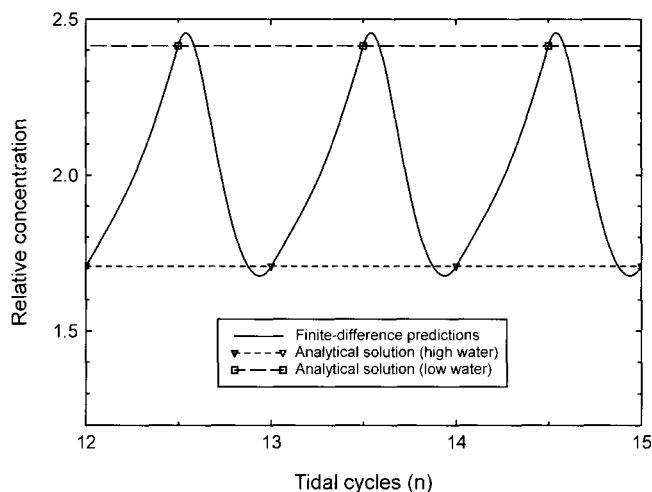
Figure 6. Detail of limit-cycle water quality response.
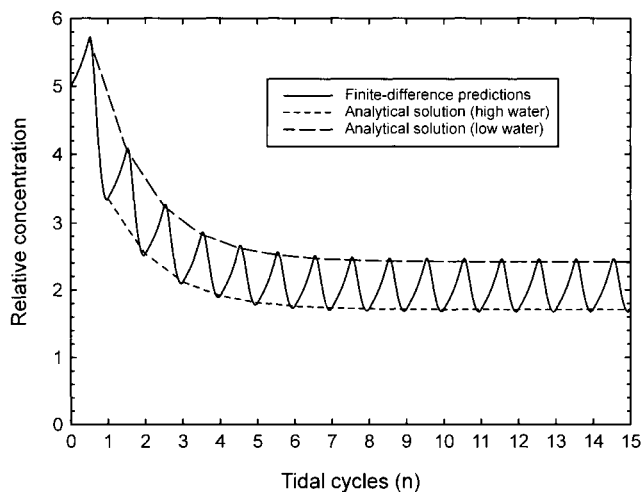
Figure 7. Comparison of analytical and finite-difference water quality predictions for $C_0/\overline{C} = 5$.

different on the flood and ebb cycles: unpolluted water is imported during the flood interval while the water exported during the ebb cycle has a varying basin concentration.

Fig. 7 presents the results of a second numerical validation test using the same tidal regime as before but starting from an initial non-dimensionalized pollutant concentration of $C_0/\overline{C} = 5$, well above the limit-cycle pollution envelope. The influence of the initial concentration becomes less significant as the number of tidal cycles increases and the water quality response soon adopts the same limit-cycle conditions shown in Fig. 5. The numerical validation exercise thus provides an increased understanding of the pollution flushing characteristics of well-mixed tidal basins and enables the analytical model to be used with greater confidence.

6. MODEL APPLICATION TO CENTREPORT HARBOR

To demonstrate a practical application of the proposed mathematical model, the technique has been used to estimate the water quality response of Centreport Harbor in the Huntington Bay Complex—a series of interconnected tidal embayments along the northern shore of Long Island, New York, USA. Centreport Harbor is a natural tidal basin that serves as both a recreational and commercial port as well as a productive shellfish habitat. The inevitable conflicts between the economic and environmental aspirations of the local community create problems when managing the aquatic ecosystem.

Centreport Harbor is connected to Huntington Bay by a narrow inlet extending some 500 m into the interior of the basin. The overall dimensions of the harbor are approximately 1270 m long, 250 m wide with a mean low water depth of 0.6 m. The mean tidal range is 2.2 m while the spring tidal range is approximately 2.6 m. There are no significant freshwater streams entering the harbor, but a limited amount of freshwater enters the embayment in the form of direct surface runoff and groundwater seepage. Using the mathematical notation developed earlier in this chapter, the spring tide conditions in the harbor can be characterized by the following parameters: average surface area of basin, $A = 317\,500$ m^2; mean volume of water, $V_m = 539\,750$ m^3 and volume of oscillatory component of tidal volume, $V_t = 412\,750$ m^3.

DiLorenzo et al. (1995) reported the results of a field experiment carried out in Centreport Harbor to address some of the environmental concerns. Tidal elevations were continuously sampled in the embayment, while an instantaneous dye-release experiment was performed by injecting 1.8 kg (4 lbs) of rhodamine WT dye into the upstream tributary at high water on a spring tide. The resultant spatial distributions of the rhodamine dye were sampled until the concentration approached the limit of detection (approximately two tidal cycles after the initial release). The field survey revealed that the semidiurnal tides in Centreport Harbor are almost identical (in both magnitude and phase) to the tides in the adjacent coastal bay, demonstrating that the embayment may be classified as a 'hydraulically efficient' system by virtue of its unattenuated tidal response. This was quite an important finding since DiLorenzo et al. (1994) had previously shown that hydraulically efficient tidal basins were generally less susceptible to water quality problems in comparison to 'hydraulically constricted systems' which have an attenuated tidal response.

DiLorenzo et al. (1995) used the results of the rhodamine dye experiment to estimate the pollution-return parameter for Centreport Harbor. The return-flow factor, b, was found to be approximately 0.1 indicating relatively efficient mixing between the effluent plume and surrounding coastal waters just outside the embayment. Knowledge of the return-flow parameter then enables the pollution susceptibility of the harbor to be determined. The steady state Pollution Susceptibility (or PS), first suggested by Weyl (1976), can be defined as the spatially and temporally averaged concentration of a dissolved conservative pollutant which results from a unit rate of discharge. For example, a PS of 10 ppb cyc/kg indicates that a steady discharge of 1 kg of conservative pollutant per tidal cycle would result in an average basin contamination of 10 ppb (10^{-2} ppm). The concept can therefore be used to identify tidal embayments at risk from potential water quality problems.

By applying the Simplified Tidal Embayment Assessment Model (STEAM) to a hydraulically efficient embayment, DiLorenzo et al. (1994) were able to derive an expression for the pollution susceptibility of a tidal basin in terms of the volume of the tidal prism, the pollution return-flow factor and the freshwater inflow rate. They demonstrated that the pollution susceptibility could be written as

$$PS = \frac{10^6}{2(1-b)V_t + Q_f} \text{ ppb cyc/kg} \tag{51}$$

where Q_f is expressed in units of cubic meters per tidal cycle. Applying equation (51) to Centre-port Harbor and assuming that the freshwater inflow is negligible yields a pollution susceptibility of 1.35 ppb cyc/kg. In other words, a toxic discharge of 1 kg/cycle of a conservative substance (for example, lead) would increase the pollutant concentration in Centreport Harbor by about 1.4 parts-per-billion (ppb).

To apply the present tidal prism formulation to the estimation of pollution susceptibility, the con-taminant loading rate is assumed to be equal to $k = 1/T$ kg/s corresponding to a loading rate of 1 kg of pollutant per tidal cycle. The limit-cycle pollutant concentrations presented in Section 2.2.3 are measured in kg/m^3 and so a conversion factor of 10^6 ppb m^3/kg (based upon an assumed water density of 1000 kg/m^3) must be applied to maintain the desired units for pollution susceptibility (ppb cyc/kg). Equations (45) and (46) can thus be recast as limit-cycle pollution susceptibilities as follows

$$PS_{(high\ water)} = \left(\frac{10^6}{2\sqrt{V_m^2 - V_t^2}} + \frac{10^6}{2(V_m - V_t)} \right) \left(\frac{V_m - V_t}{2V_t} \right) \tag{52}$$

and

$$PS_{(low\ water)} = \left(\frac{10^6}{2\sqrt{V_m^2 - V_t^2}} + \frac{10^6}{2(V_m - V_t)} \right) \left(\frac{V_m - V_t}{2V_t} \right) + \frac{10^6}{2\sqrt{V_m^2 - V_t^2}} \tag{53}$$

The present mathematical formulation has the advantage over more traditional tidal prism models of being able to estimate the average basin concentration at the end of both the flood and ebb tides. However, it should be noted that equations (52) and (53) omit the dilution effects of any freshwa-ter inflow and therefore the resulting pollution susceptibilities would tend to be conservative esti-mates.

Applying equations (52) and (53) to Centreport Harbor and assuming a 10% reduction in the oscil-latory tidal volume to account for the return-flow effect yields pollution susceptibilities of 0.96 ppb cyc/kg at the end of the flood tide (high water) and 2.24 ppb cyc/kg at the end of the ebb tide (low wa-ter). While the pollution susceptibilities could be averaged to obtain a temporal mean value of 1.6 ppb cyc/kg, it is generally more appropriate to express the water quality response of an embayment in terms of both these values. The mean pollution susceptibility agrees reasonably well with DiLorenzo et al.'s (1995) estimate for Centreport Harbor. However, the present analytical model suggests that the water quality in the harbor deteriorates considerably during the ebb tide, with the pollution sus-ceptibility increasing well in excess of the value predicted by equation (51). The ebb tide pollution susceptibility equation (53) would provide a more stringent estimate of the likely long-term maxi-mum pollution levels in the harbor and would therefore highlight any potential water quality issues at an earlier threshold than existing tidal prism models.

7. CONCLUSIONS

This chapter has detailed a tidal prism model for predicting the water quality response of well-mixed tidal embayments. Two separate analytical approaches have been presented—the first con-siders the water quality response when the embayment is subjected to an instantaneous release of contaminant, such as a sudden chemical spillage, while the second considers the situation where the embayment is subjected to a continuous release of pollution.

Predictions from the mathematical technique are compared with experimental pollution data from a 1:400 scale laboratory model of a generic square tidal basin. The results from the validation tests

are very encouraging and show that the model is able to replicate the observed flushing characteristics irrespective of the tidal range and freshwater inflow. In addition, the results have demonstrated that the analytical tidal prism model offers an accurate method of estimating the pollution exchange coefficient over a wide range of tidal regimes. The validation of the second tidal prism procedure is equally encouraging and demonstrates that the analytical model is able to predict the limit-cycle pollutant concentrations for a continuous release of pollution. Tests using different geometries of tidal basins have confirmed that the analytical technique is equally valid for other shapes of embayment. In addition, the model has been applied to Centreport Harbor on the east coast of the USA to determine the pollution susceptibility of the embayment. The proposed analytical formulation provides an increased understanding of the pollution flushing characteristics of well-mixed tidal basins and could be used as a design tool for conducting preliminary environmental impact assessments.

Further investigations are required to test whether the proposed mathematical techniques are appropriate for complex harbor geometries having less internal mixing. Such harbors are likely to experience large internal gradients in pollutant concentration, with areas remote from the entrance flushing at a slower rate than that predicted by the present analytical model. An extension of the tidal prism approach could be feasible using two or more separate 'prisms' to represent the behavior of a system of interconnecting tidal basins. However, the problem of estimating the individual return-flow factors in such a model may be unacceptably empirical. Further development of the model may be required to simulate particular geometric details but the author considers the present analytical approach is appropriate for a wide range of problems involving the estimation of tidal flushing in semi-enclosed embayments. The model has been shown to provide accurate estimates of pollution flushing over a wide range of tidal regimes and can produce water quality predictions quickly with the minimum of computational effort.

LIST OF SYMBOLS

A	—	average surface area of tidal embayment
b	—	pollution return-flow factor
C	—	pollutant concentration
$C^{(n)}$	—	pollutant concentration at time, $t = n\Delta t$ in finite-difference scheme
C_0	—	initial pollutant concentration
C/C_0	—	non-dimensionalized pollutant concentration for pollution flushing studies
$C/\overline{C}$	—	non-dimensionalized pollutant concentration for pollution discharge studies
$C_{e(n)}$	—	pollutant concentration after n ebb tides
$C_{f(n)}$	—	pollutant concentration after n flood tides
$\overline{C}$	—	theoretical increase in pollutant concentration in the absence of tidal flushing
Δt	—	time step in finite-difference scheme
E	—	pollution exchange coefficient
H	—	tidal range
k	—	pollution loading rate
n	—	number of tidal cycles or time step index
P	—	volume of inter-tidal prism
PS	—	pollution susceptibility of tidal basin
Q	—	flow rate through entrance
Q_f	—	freshwater inflow rate
t	—	time
T	—	tidal period
V	—	volume of tidal embayment at time, t

V_m —   mean volume of tidal embayment

V_t —   amplitude of oscillatory component of tidal volume

ω —   tidal angular frequency $= 2\pi/T$

REFERENCES

Barber, R.W., and Wearing, M.J., 2000. Laboratory validation of a pollution flushing model for small tidal harbours. In: Bentley, L.R., Gray, W.G., Pinder, G.F., and Sykes, J.F. (Editors), Computational Methods in Water Resources, Vol. 2, pp. 1001–1008. Rotterdam: Balkema.

Blumberg, A.F., and Mellor, G.L., 1987. A description of a three-dimensional coastal ocean circulation model. In: Heaps, N. (Editor), Topics in Three Dimensional Coastal Ocean Models, Vol. 5, pp. 1–16. Washington, DC: American Geophysical Union.

Callaway, R.J., 1981. Flushing study of South Beach Marina, Oregon. Journal of Waterway, Port, Coastal and Ocean Engineering, 107 (2): 47–58.

Casulli, V., and Cheng, R.T., 1992. Semi-implicit finite-difference methods for three dimensional shallow water flow. International Journal for Numerical Methods in Fluids, 15: 629–648.

Chiang, W.L., and Lee, J.J., 1982. Simulation of large-scale circulation in harbours. Journal of Waterway, Port, Coastal and Ocean Engineering Division, 108 (1): 17–31.

Dias, J.M., Lopes, J.F., and Dekeyser, I., 1996. Numerical modelling of tidal fluxes and passive pollutant concentrations in Ria de Aveiro, Portugal. In: Ferrante, A.J., and Brebbia, C.A. (Editors), Environmental Problems in Coastal Regions, pp. 285–294. Southampton, UK: Computational Mechanics Publications.

DiLorenzo, J.L., Huang, P., and Najarian, T.O., 1989. Water quality models for small tidal inlet systems. Journal of Environmental Engineering, 115 (1): 192–209.

DiLorenzo, J.L., Ram, R.V., Huang, P., and Najarian, T.O., 1994. Pollution susceptibility of well-mixed tidal basins. Journal of Waterway, Port, Coastal and Ocean Engineering, 120 (4): 404–422.

DiLorenzo, J.L., Hasbrouck, E., and Najarian, T.O., 1995. Water quality screening methodology for a coastal boat basin. In: Blain, W.R. (Editor), Proceedings of the 3rd International Conference on the Planning, Design and Operation of Marinas, pp. 151–160. Southampton, UK: Computational Mechanics Publications.

Dyer, K.R., 1973. Estuaries: A Physical Introduction. New York: John Wiley and Sons.

European Community, 1976. Council directive of 8th December 1975 concerning the quality of bathing waters. Official Journal of the European Communities, 31/1-1-31/7.

Falconer, R.A., 1993. Application of numerical models for water quality studies. Proceedings of the Institution of Civil Engineers, Vol. 93, pp. 163–170.

Falconer, R.A., and Yu, G.P., 1991. Effects of depth, bed slope and scaling on tidal currents and exchange in a laboratory model harbour. Proceedings of the Institution of Civil Engineers, Vol. 91, pp. 561–576.

Fuentes, M.O.A., Carrillo, S.J.J., and de Luna, C.F., 1999. Calculations of concentrations of a pollutant and volume of seawater that enters a marina. In: Brebbia, C.A., and Anagnostopoulos, P. (Editors), Proceedings of the 4th International Conference on Coastal Engineering and Marina Developments, pp. 535–544. Southampton, UK: W.I.T. Press.

Harleman, D.R.F., 1966. Pollution in estuaries. In: Ippen, A.T. (Editor), Estuary and Coastline Hydrodynamics, pp. 630–647. New York: McGraw-Hill.

Hinwood, J.B., and McLean, E.J., 1996. A parametric hydrodynamic model of a complex estuary. In: Zanetti, P., and Brebbia, C.A. (Editors), Computer Techniques in Environmental Studies VI, pp. 277–286. Southampton, UK: Computational Mechanics Publications.

Isaji, T., and Spaulding, M.L., 1981. A simplified model for assessing the impact of breachway modifications on coastal pond circulation and flushing dynamics. Proceedings of Oceans '81, Boston, USA, pp. 824–828.

Koutitas, C.G., 1988. Mathematical Models in Coastal Engineering. London: Pentech Press.

van de Kreeke, J., 1983. Residence time: Application to small boat basins. Journal of Waterway, Port, Coastal and Ocean Engineering Division, 109 (4): 416–428.

Lacey, P., 1992. Marinas: An overview. In: Blain, W.R. (Editor), Proceedings of the 2nd International Conference on Marina Technology, pp. 3–11. Southampton, UK: Computational Mechanics Publications, co-published with London: Thomas Telford.

Li, C.W., and Falconer, R.A., 1995. Depth-integrated modelling of tide-induced circulation in a square harbour. Journal of Hydraulic Research, 33 (3): 321–332.

Lin, B., and Falconer, R.A., 1996. Numerical modelling of three-dimensional suspended sediment for estuarine and coastal waters. Journal of Hydraulic Research, 34 (4): 435–455.

Nece, R.E., and Falconer, R.A., 1989. Modelling of tide-induced depth averaged velocity distributions in a square harbour. In: Falconer, R.A., Goodwin, P., and Matthew, R.G.S. (Editors), Proceedings of the International Conference on Hydraulic and Environmental Modelling of Coastal, Estuarine and River Waters, pp. 56–66. Aldershot, UK: Gower Publishing.

Ozhan, E., 1989. Flushing of marinas with weak tidal motion. In: Blain, W.R., and Webber, N.B. (Editors), Marinas: Planning and Feasibility, pp. 485–498. Southampton, UK: Computational Mechanics Publications.

Rajar, R., 1997. The role of mathematical models, physical models and field measurements in water pollution problems. In: Rajar, R., and Brebbia, C.A. (Editors), Proceedings of the 4th International Conference on Water Pollution, pp. 545–555. Southampton, UK: Computational Mechanics Publications.

Rajar, R., and Sajovic, A., 1995. Modelling of circulation and water exchange in marinas. In: Wrobel, L.C., and Latinopoulos, P. (Editors), Proceedings of the 3rd International Conference on Water Pollution, pp. 237–244. Southampton, UK: Computational Mechanics Publications.

Rajar, R., and Sirca, A., 1996. Hydrodynamic and pollutant transport models applied to coastal seas. In: Ferrante, A.J., and Brebbia, C.A. (Editors), Environmental Problems in Coastal Regions, pp. 251–262. Southampton, UK: Computational Mechanics Publications.

Sanford, L.P., Boicourt, W.C., and Rives, S.R., 1992. Model for estimating tidal flushing of small embayments. Journal of Waterway, Port, Coastal and Ocean Engineering, 118 (6): 635–654.

U.S. EPA., 1985. Coastal Marinas Assessment Handbook. Atlanta, GA: United States Environmental Protection Agency, Region IV.

Wearing, M.J., 2000. Modelling of pollution transport in small tidal harbours. Ph.D. Thesis. Salford, UK: University of Salford.

Wearing, M.J., and Barber, R.W., 1999. Analytical modelling of steady-state pollution levels within a small tidal harbour. In: Brebbia, C.A., and Anagnostopoulos, P. (Editors), Proceedings of the 4th International Conference on Coastal Engineering and Marina Developments, pp. 523–534. Southampton, UK: W.I.T. Press.

Weyl, P.K., 1976. Pollution susceptibility: An environmental parameter for coastal zone management. Coastal Zone Management Journal, 2 (4): 327–343.

Wu, J., and Tsanis, I.K., 1994. Pollutant transport and residence time in a distorted scale model and a numerical model. Journal of Hydraulic Research, 32 (4): 583–598.

This Page Intentionally Left Blank

Chapter 18

Advances in Water Quality Modeling in the Coastal Environment

Mark S. Dortch

Department of the Army, Corps of Engineers, Engineer Research and Development Center, Waterways Experiment Station, 3909 Halls Ferry Road, Vicksburg, MS 39180–6199, USA

1. INTRODUCTION

Over half of the U.S. population now resides in coastal communities (National Research Council, 2000). This population shift toward the coastal zone, with concomitant municipal and industrial development and land use changes in coastal watersheds, has created serious anthropogenic stress on the coastal environment. This stress has resulted in a host of coastal problems, including eutrophication, beach closures due to pathogens, contamination of fin- and shellfish, loss of habitat, invasions by non-indigenous species, and harmful algal blooms. Coastal eutrophication is the primary problem and has received widespread attention in many U.S. coastal waters, including Chesapeake Bay, Long Island Sound, the dead zone of the Gulf of Mexico, and other sites. Nitrogen is the limiting nutrient in coastal eutrophication. It is estimated that human fixation of nitrogen through production of fertilizer, combustion of fossil fuels, and production of nitrogen-fixing agricultural crops, has increased globally 2- to 3-fold from 1960 to 1990 (National Research Council, 2000).

These concerns have dramatically increased the use of mathematical models to gain an improved understanding of coastal processes, predict the impacts of further development, and evaluate the effectiveness of various management strategies to reduce adverse impacts. As a result, there has been substantial advancement in modeling of the coastal environment. Since pollution, or eutrophication, is the central factor that has contributed to coastal environmental problems, the major emphasis in coastal environmental modeling has centered on water quality models. Thus, this chapter focuses on advances made in the past 20 years in water quality modeling in the coastal environment in the United States.

The discussions herein are limited to mechanistic, deterministic mathematical water quality models, rather than statistical, empirical and stochastic models. Mechanistic models usually have greater predictive power than statistical models since they are based on generalized process descriptions of first principles that should be applicable for conditions that may be different from the calibration conditions. Statistical models usually have less predictive power since they do not include process descriptions. For example, mechanistic water quality models depend on transport as affected by circulation, or changes in circulation as may occur with channel modifications or bathymetric alterations. Statistical models usually cannot capture such influences. However, it is easier to consider stochastic variations and uncertainty when using statistical models.

Mechanistic, mathematical water quality modeling has progressed significantly over the past 20 years due primarily to advances in computer power, and the pursuit of specialists to make the models more comprehensive through the addition of new process descriptions. It is becoming common practice, especially for the coastal modeler, to apply water quality models as part of a broader, linked, modeling suite that includes hydrodynamics, waves, and sediment transport. Application of three-dimensional (3-D) models is now common in the coastal zone. Advances in water quality modeling in the coastal zone are discussed from the aspects of computing power, linkages among models, model frameworks, and process descriptions. The fundamentals of water quality modeling are not

discussed herein; rather the reader is referred to well-known textbooks, such as those by Thomann and Mueller (1987) and Chapra (1997) as two excellent examples.

2. COMPUTING POWER

The advances in computer power have had the greatest influence in advancing coastal zone modeling. Twenty years ago, modelers were using mainframes and minicomputers that did not have the power and speed of personal computers (PCs) of today. For example, the Digital Equipment Corporation's VAX 750 had a processor speed of approximately 0.2 megaflops (10^6 floating-point operations per second), whereas the 2000 MHz PCs of today have speeds of roughly 500 megaflops or more. The availability of vector-based supercomputers during the late 1980's, such as the Cray Y-MP, provided the first major opportunity to advance the models. The vector-based supercomputers had processor speeds of approximately 80 megaflops. With these processing speeds, it became practical to apply 3-D models of large systems with considerable spatial and process definition as indicated in Box 1.

The vector-based supercomputers eventually yielded to serial, multi-processor machines. With programs running in parallel on multi-processor machines (referred to as high performance computing or HPC), approximately two orders of magnitude improvement in speed has been obtained over the vector-based, single processor supercomputers. The advent of HPC machines and methods made it practical to increase spatial resolution even further while adding more process descriptions with longer simulation times. Box 2 provides an example of computational gains provided by HPC. The disadvantage of HPC was that the programs had to be modified to run massively parallel which required significant code development and testing. Conversion to parallel computing was achieved by combining a single program with multiple data (SPMD) execution, also referred to as data domain decomposition. The Message Passing Interface (MPI) library was used to exchange inter-processor

---

Box 1: Chesapeake Bay numerical hydrodynamic and water quality models executed on a Cray supercomputer

The Chesapeake Bay numerical models included an indirectly linked 3-D hydrodynamic model (Johnson et al., 1993) and a water quality model (Cerco and Cole, 1993). Both models used the same computational grid, which had 4,073 computational cells (729 cells in plan view with a maximum of 15 layers). The hydrodynamic model solved coupled conservation equations for momentum, continuity, energy (temperature), and salt balance and yielded solution of the time-varying water surface elevation, 3-D velocities, temperature, and salinity. The water quality model solved conservation of mass equations for 22 state variables including various forms of nutrients, three phytoplankton groups, and dissolved oxygen. Additionally, the water quality model included a diagenetic benthic sediment model to compute nutrient fluxes and sediment oxygen demand (DiToro and Fitzpatrick, 1993). Tidally averaged hydrodynamics were corrected for Stokes drift to maintain proper intertidal transport and used to drive the water quality model (Dortch et al., 1992). The time step of the hydrodynamic model was 5 minutes, whereas that of the water quality model was variable but averaged about 30 minutes. The hydrodynamic model required approximately 12 hours to simulate one year on a Cray Y-MP. The water quality model required about 4 hours per year of simulation on the same machine. For this study, three years were simulated with the hydrodynamic model and used to construct a 10-year period used by the water quality model for simulating each management scenario (Cerco, 1995).

Box 2: Chesapeake Bay numerical hydrodynamic and water quality models executed on HPC multi-processor machines

The Chesapeake Bay numerical 3-D hydrodynamic model of Johnson et al. (1993) was upgraded to provide more spatial resolution, especially in the tributaries (Cerco et al., 2002; Wang and Johnson, 2002), resulting in 12,920 computational cells (2961 cells in plan view). The hydrodynamic model was used to simulate a 10-year record from 1985-1995. The water quality model of Cerco and Cole (1993) was revised to include submerged aquatic vegetation, epiphytes, two zooplankton groups, and two benthos compartments (benthic filter feeders and deposit feeders). The revised water quality model (Cerco, 2000; Cerco et al., 2002) had 36 state variables and operated on the same grid as the revised hydrodynamic model. Twenty-year simulations were run with the water quality model for each management scenario. The first 10 years were used to spin-up initial conditions for the benthic sediments as a result of altered nutrient loading conditions. With the finer grid, the time step of the water quality model was smaller than in the first model study (Box 1), and averaged about 15 minutes. Thus, with the finer grid, increased number of state variables, smaller time step, and longer scenario simulation periods, the total computational demand had increased about 20-fold over the previous model discussed in Box 1. With improvements in processor speed, the revised water quality model required about 15 hours per simulation year. Each 20-year scenario simulation would have required about 12 days on a single processor, which would have been impractical. However, using 32 processors on the HPC machines, these run times were reduced to about 10 hours, a practical execution time.

---

information. The METIS multi-level graph-partitioning package from the University of Minnesota was used for grid domain decomposition (Karypis and Kumar, 1995a; 1995b). Dortch and Gerald (2002) describe the HPC methods used and give benchmarks for three machines.

It appears that parallel computing is here to stay. Methods for code conversion have improved, and many codes have now been converted for massively parallel computing. Processor and memory caching speeds continue to improve, as more processor and greater memory are added. Advancements in computing power continue to outpace our ability to advance the process descriptions. It is doubtful that the use of increased spatial resolution will improve the processes in water quality models if the resolution is already fine enough to accurately capture the transport.

One of the biggest effects of advancement in computer power was to make 3-D modeling rather common. There is no question that the inclusion of all three dimensions improved model performance in terms of increased realism for simulating spatial variations, as well as transient behavior such as internal seiches. Additionally, inclusion of more dimensions tends to reduce requirements for model parameterization.

3. MODEL LINKAGES

Linkage to hydrodynamic models is of paramount importance for water quality modeling since flow regimes are required for transport. However, direct linkage, where hydrodynamic and water quality computations are conducted concurrently within the same code, can be computationally demanding for 3-D models and may not be necessary. Water density arising from total dissolved solids (TDS) or salinity, total suspended solids (TSS) and temperature can affect hydrodynamics. In estuarine and coastal systems, where salinity has the predominant influence on water density and hydro-

dynamics, water quality can be uncoupled from the hydrodynamic solution. Most density-dependent hydrodynamic models include salinity and temperature in their solution for density. In freshwater systems, (for example, lakes and reservoirs) density differences are much less and can be significantly affected by water quality variables that affect TDS and TSS, as well as temperature. Additionally, short wave light attenuation and penetration can be influenced by dissolved and suspended matter, which affects the vertical distribution of heat, water density, and consequentially the hydrodynamics. Thus, for deep freshwater systems, it is preferable to keep hydrodynamics and water quality dynamically coupled, as is the case with most reservoir water quality models, such as the CE-QUAL-W2 model (Cole and Buchak, 1995). However, for 3-D models of estuarine and coastal waters, the common practice is to execute the models in a sequential, uncoupled fashion, where the hydrodynamic model is run first, output is saved, and the output is supplied later to the water quality model. This procedure is referred to as indirect coupling or linkage. Indirect linkage reduces the computational time considerably for each model, especially for 3-D models. The benefits of indirect linkage are quite evident when considering the large number of calibration runs typically required with water quality models. Some two-dimensional (2-D) models, such as CE-QUAL-W2, execute relatively quickly compared with 3-D models so that there may not be a need to consider indirect linkage.

The easiest and most accurate practice for indirect linkage is for the water quality model to use the same spatial grid as the hydrodynamic model, i.e., a one-to-one spatial linkage. In this case, hydrodynamic velocities or flows and diffusivities have a direct correspondence for the water quality model computational cells. If a different grid is used for the water quality model, precautions must be taken to ensure that the transport is properly preserved, and that local mass conservation is preserved. Water quality models often are required to perform long-term simulations that may not be practical using the finer hydrodynamic model grid. In such cases, a coarser water quality model grid may be used, and the hydrodynamic model may be applied for shorter periods of seasonal, average, or extreme conditions, and the hydrodynamic conditions applied to the water quality model in a recurring fashion. If it becomes necessary to use a water quality model grid or mesh that is coarser than that of the hydrodynamic model, then the preferred approach is to use a congruent overlay of the hydrodynamic model grid or mesh. Examples of coarser water quality model computational cells that congruently overlay a finer hydrodynamic model finite difference grid and finite element mesh are shown in Figs. 1 and 2, respectively. The hydrodynamic and water quality model meshes are shown separately for Florida Bay (Figs. 2a and 2b) to better discern the meshes. However, it should be realized that the water quality mesh does exactly overlay the hydrodynamic computational mesh but with coarser resolution. It is possible to link this particular water quality model (CE-QUAL-ICM) to finite difference and finite element models since the water quality model is based on the finite volume method. If the water quality model grid/mesh is made very coarse relative to that of the hydrodynamic model, it is theoretically necessary to compute and add in dispersion resulting from spatial-averaging of velocities to maintain proper transport. However, in reality, spatial aggregation often results in excessive numerical diffusion. Output from tracer transport simulations conducted by the hydrodynamic and water quality models should be compared to verify preservation of proper transport properties. Of course, it is also highly advisable to validate results against observed natural tracers such as salinity.

Water quality models solve the mass conservation equation over each computational cell for each water quality state variable. Preservation of water continuity as a result of flows through cell boundaries and water level change is critically important for mass conservation. Since finite difference hydrodynamic models usually satisfy water and mass continuity locally (i.e., over a computational cell), linkage to such models will usually satisfy local mass continuity within the water quality model. Conventional finite element models ensure mass conservation globally, but may not guarantee local conservation around each computational element. Thus, linkage to these models may be problematic. A method has been developed to adjust the flow fields slightly to ensure local mass conservation
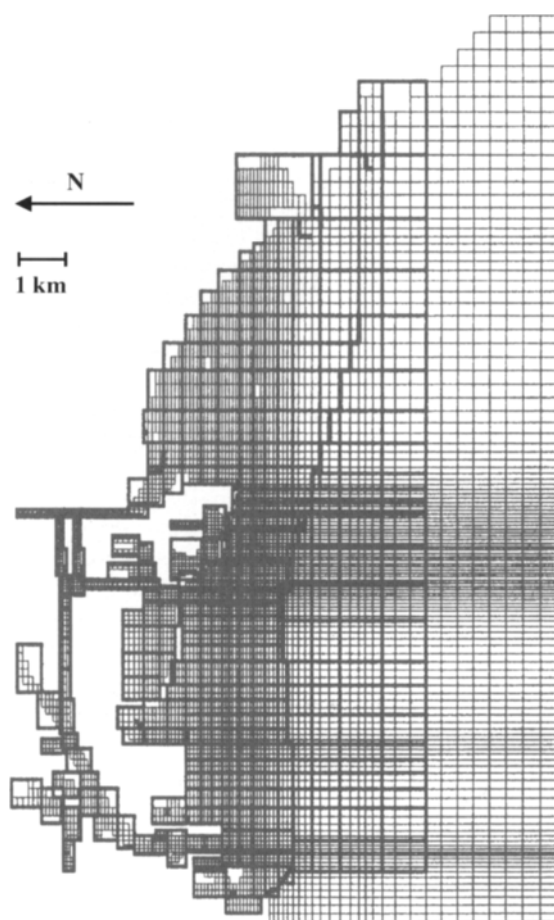
Figure 1. San Pedro Bay, CA (Los Angeles—Long Beach Harbors), hydrodynamic model grid overlain by water quality model grid (ocean boundary is on the right).

when projecting flows from a hydrodynamic model finite element mesh to a transport model grid or mesh, while allowing the meshes/grids to be different (Carey et al., 2001). This projection method was used for a hydrodynamic and water quality model of Florida Bay (Cerco et al., 2000). Berger and Howington (2002) point out that if the discrete approximation of flux given by the finite element statement remains consistent with the finite element formulation, then the resulting flux estimates will preserve mass balance locally.

Water quality models usually operate at different time scales than hydrodynamic models. For example, water quality models generally use larger time steps and are run for longer periods. Additionally, boundary condition updates may be less frequent for water quality models. Although hydrodynamic models typically have time steps on the order of minutes, hourly hydrodynamic updates are sufficiently accurate for water quality model transport (Dortch et al., 1992). More frequent updates are wasteful of disk space; even hourly updates can require substantial disk space (for example, on the order of tens of gigabytes for a single hydrodynamic period). When hydrodynamic update peri-

(a)

(b)
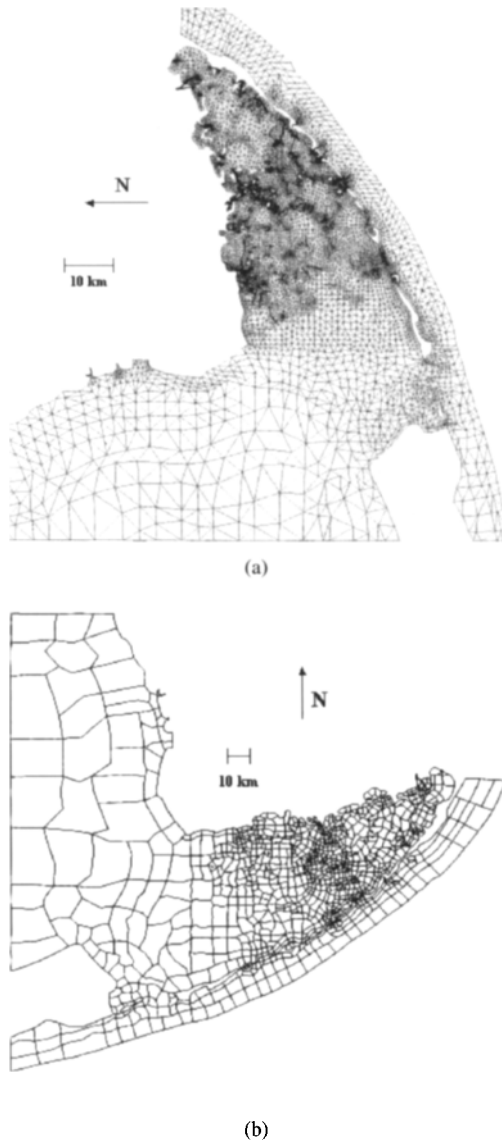
Figure 2. (a) Florida Bay numerical hydrodynamic model computational mesh. (b) Florida Bay numerical water quality model mesh, coarser overlay of hydrodynamic model mesh.

ods are greater than the hydrodynamic model time step, it is necessary to compute the average water velocities or flows for each update interval so that water continuity is maintained for each update interval (Dortch, 1990). It is possible to compute Lagrangian residual (inter-tidal) flows that preserve the proper transport thus allowing update intervals on the order of a tidal period (Dortch et al., 1992). Tidally averaged flow fields reduced disk space requirements for indirect linkage by an order of magnitude, which was an important aspect 10 years ago when disk space was less abundant. However,

given the much more abundant and cheap data storage media of today, such considerations are no longer an issue.

There are other model linkages that may be of interest as input for water quality models, such as linkage of comprehensive sediment transport models with contaminant (potentially toxic substances such as organic chemicals and trace metals) transport and fate models that are highly dependent on sediment transport and fate. Additionally, watershed model linkages are of interest to provide input for nonpoint source loading. There are examples today of linkage of watershed and water quality models of receiving waters, such as for Chesapeake Bay (Cerco, 1995; Donigian et al., 1991). Output from water quality models are being linked to other types of models, such as living resource population models (Luo et al., 2001) and food chain models for conducting human and ecological health risk assessment (Chapra, 1997).

4. MODEL FRAMEWORKS

Great progress has been made in the past 10 years as related to the development of modeling system frameworks and user interfaces. Many of the more popular coastal zone models now have graphical user interfaces (GUI), although usually a license fee must be paid to obtain these systems to help cover costs for development and maintenance. Examples of GUI modeling systems for multi-dimensional hydrodynamic and water quality models applicable to the coastal zone include:

1. the Surface Water Modeling System (SMS) developed by the Environmental Modeling Research Laboratory of Brigham Young University through support primarily from the U.S. Army Engineer Research and Development Center (http://chl.wes.army.mil/software/sms/download.htp),
2. a suite of modeling systems developed by Applied Science Associates, Inc. of Narragansett, RI which includes models for hydrodynamics (HYDROMAP), water quality (WQMAP), chemical and oil spill fate/transport (CHEMMAP and OILMAP), several models for sediment dredging and disposal operations (DREDGEMAP), and other modeling systems (http://www.appsci.com/),
3. GEMSS (Generalized Environmental Modeling System for Surface Waters) by J.E. Edinger & Associates, Inc. (JEEAI) of Wayne, PA (http://www.jeeai.com/), and
4. MIKE21 and MIKE3 of the DHI Water & Environment of Hørsholm, Denmark (http://www.dhisoftware.com/).

The SMS is referred to as a modeling environment that goes beyond a model GUI. The SMS provides a host of generic modeling tools that interface to more than one model. There are several models for hydrodynamics, as well as models for sediment transport, wave processes, and water quality. The SMS includes tools for GIS-based mapping, data import and manipulation, grid/mesh generation and editing, visualization of observed and computed data, and interfacing to each model for input, output, and execution.

Model frameworks have taken on new meaning in recent years. Model frameworks are more than model GUI and modeling environments, rather recent developments suggest that they are systems that allow linkage and application of disparate models. Model frameworks may also allow access to disparate databases to facilitate model application. The Framework for Risk Assessment Modeling of Environmental System (FRAMES) is an example of a modeling framework that allows linkage of models for multimedia fate/transport, exposure, uptake, and effects framework to assess human and ecological health impacts/risk (Whelan et al., 1999) (http://mepas.pnl.gov:2080/framesv1). FRAMES serves as the framework upon which the components of the Army Risk Assessment Modeling System (ARAMS), as well as risk assessment methods of other U.S. federal agencies, are based (Dortch, 2001) (http://www.wes.army.mil/el/arams/). Other model frameworks exist or are under development by various federal agencies in the U.S., such as:

1. the Modular Modeling System (MMS) (http://wwwbrr.cr.usgs.gov/mms),

2. the Object Modeling System (OMS) (http://oms.ars.usda.gov/), and
3. the Common Delivery Framework (CDF) being developed by the U.S. Army Engineer Research and Development Center (https://cdf.usace.army.mil/index.jsp).

Frameworks that allow linkage of disparate models and databases will greatly facilitate the ability to link models and data of different types thus improving the capability to simulate and analyze diverse phenomena to address environmental issues of increasing complexity.

5. PROCESS DESCRIPTIONS

Water quality models can be generally classified as two types: conventional pollutants including nutrients, eutrophication, and pathogens; and toxic substances, such as organic chemicals and trace metals. Recent developments in each of these classes are discussed briefly.

Models of conventional pollutants and eutrophication have evolved significantly in the past 20 years. The greatest change is the increased number of state variables and processes. For example, the number of state variables has more than doubled, increasing from roughly a dozen to two dozen or more. Nutrients are described in greater detail, including more inorganic and organic forms, as well as particulate and dissolved forms. Additionally, multiple algal groups are often included in addition to other plant forms, such as periphyton (Cerco and Seitzinger, 1997) and submerged aquatic plants (SAV) (Cerco and Dortch, 1998; Cerco and Moore, 2001), including attached epiphytes that cause shading of light available to SAV. Other life forms also have been included in the Chesapeake Bay model (Cerco, 2000), such as multiple zooplankton (micro- and meso-zooplankton) and benthos groups (filter and deposit feeders).

Process descriptions have also become more detailed. For example, the CE-QUAL-ICM model was modified to simulate the effects of water color in a black water system (the Lower St. Johns River Estuary as described in Box 3). A model of Florida Bay included the effect of bottom sediment resuspension on light and sea grass growth (Cerco et al., 2000).

Probably the greatest advancement in process descriptions in recent years has been the development of models for benthic sediment diagenesis. DiToro (2001) describes the processes for such models, which are driven by organic matter deposition and mineralization (i.e., diagenesis). Diagenesis generates nutrients, which can flux across the sediment-water interface, and oxygen demand, which can have three fates: exertion of sediment oxygen demand (SOD) on overlying water column; export of chemical oxygen demand (for example, sulfide) in the absence of dissolved oxygen in the overlying water column; and burial. DiToro and Fitzpatrick (1993) developed a benthic diagenesis sub-model that was dynamically coupled (as a suite of subroutines) to the Chesapeake Bay water quality model to provide continuous interaction between the bed and overlying water column.

Prior to the development of benthic diagenesis models, SOD and nutrient fluxes had to be specified, rather than computed. These specifications were adjusted during model calibration until water column dissolved oxygen (DO) and nutrient concentrations were brought into agreement with observations. Specifying these bottom boundary conditions resulted in models of limited predictive capability for future pollutant loading scenarios, especially for stratified water bodies with slow flushing characteristics (i.e., long residence times). The development of benthic diagenesis models brought much greater realism for future loading scenarios since SOD and nutrient fluxes are predicted based on organic matter deposition as a result of altered loading and internal production.

Increased numbers of state variables and more detailed process descriptions do not necessarily translate into greater model accuracy, rather more complete information. The goal is to increase model accuracy while reducing the amount of parameterization by including more complete closure of ecological processes. Experience has shown that with more process descriptions, models tend to take on a life of their own, meaning that they are less sensitive to calibration parameters. This was

---

Box 3: Modifications to the CE-QUAL-ICM model for the Lower St. Johns River Estuary (Martin et al., 2002).

One of the characteristics of black water systems, such as the Lower St. Johns River estuary, is the presence of high concentrations of colored dissolved organic matter derived primarily from terrestrial organic matter loadings. Colored dissolved organic matter (CDOM) resulting from humic substances is considered to be relatively refractory when compared to other forms of organic matter. In order to incorporate the impacts of CDOM in the application of the CE-QUAL-ICM model to the Lower St. Johns River, the state variables in the original model (Cerco and Cole, 1993) for dissolved organic carbon, nitrogen, and phosphorus were fractionated into labile and refractory forms, where the refractory forms are considered analogous to CDOM. This allowed specification of different degradation rates for each of these forms, as well as their separate impact on other modeled state variables.

One effect of high concentrations of CDOM is an increase in light attenuation, which can affect primary production. Light attenuation is extremely high in colored surface waters, where PAR (photosynthetically active radiation) vertical diffuse light attenuation coefficients over 4 m^{-1} are not uncommon. To include this effect, the model light formulation was modified to include an attenuation coefficient to relate predicted concentrations of refractory dissolved organic carbon to light attenuation.

While refractory CDOM is resistant to microbial degradation, it has been found to exhibit substantial susceptibility to photochemical decomposition or "bleaching", and the rates may exceed that of microbial decomposition alone in dystrophic systems, thus, enhancing microbial decomposition through creation of labile, low molecular weight organic compounds. Algorithms were added to the model to simulate the impact of photochemical decomposition by including a light-mediated photochemical decomposition rate for refractory dissolved organic carbon (RDOC).

Literature reports of flocculation of CDOM were supported by observed non-conservative behavior of color across the longitudinal salinity gradient in the lower St. Johns River, suggesting an increase in the percent of RDOC removed as salinity increases. A maximum removal rate of 7 percent of the freshwater RDOC was estimated at a salinity of about 15 ppt (Hendrickson, 2001). The impact of this process was included in the revised model through inclusion of salinity-moderated transfer rates of RDOC to the particulate form (RPOC).

The numerical model grid for the Lower St. Johns River model is shown in Fig. 3. This grid was developed for use by the EFDC hydrodynamic model applied by Sucsy and Morris (2002). The water quality model used a one-to-one overlay of this grid.

---

certainly the case when the benthic diagenesis sub-model was added to the Chesapeake Bay water quality model.

Toxic substances (i.e., contaminants) tend to sorb to sediment particles and concentrate in benthic sediments. As a result, robust contaminant models of today simulate both suspended and benthic sediment and the interactions between the water column and bed (sediment deposition, resuspension, and burial). Likewise, contaminant mass should be tracked in both the water column and the bed. Sediment bed processes, such as bioturbation and sediment mixing, deep burial, pore water diffusion within the bed and across the bed-water interface, and compaction with pore water extrusion, are
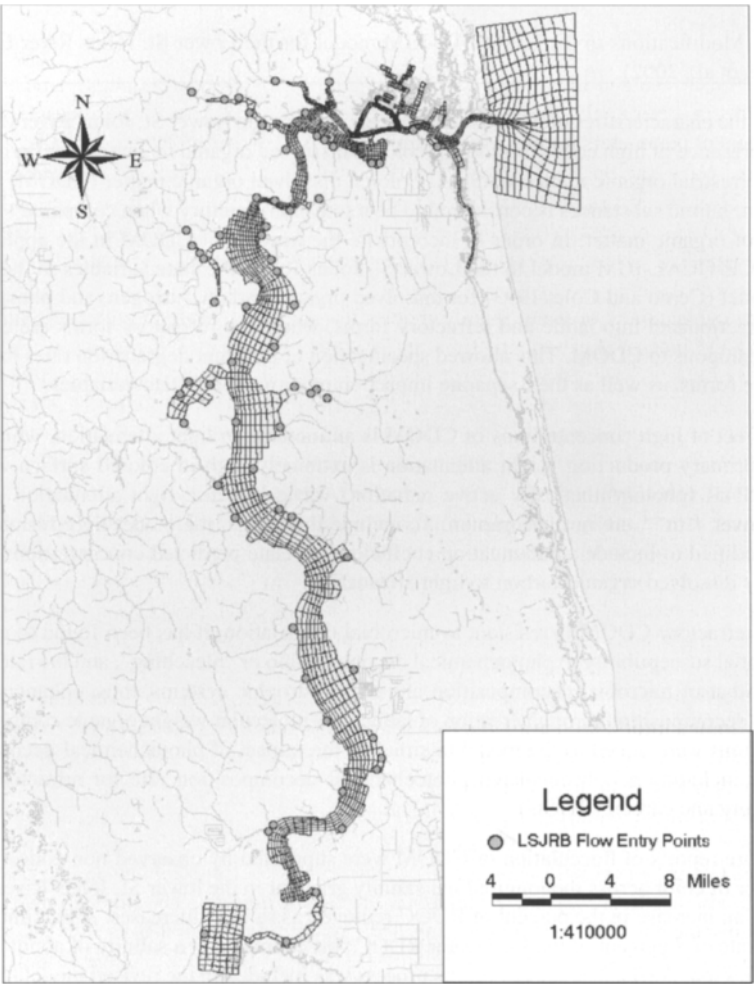
Figure 3. Lower St. Johns River numerical model grid.

important relevant to contaminant transport and fate (Thomann and Mueller, 1987; Chapra, 1997). Contaminants can sorb to and transport with solids and dissolved organic carbon. Other losses and degradation pathways, such as volatilization across the water-air interface, hydrolysis, photolysis, oxidation, and biodegradation, should be taken into account. Recent model developments, such as RECOVERY (Boyer et al., 1994) and CE-QUAL-ICM/TOXI (Dortch et al., 1998; 2002), discretize the bed with multiple layers to more accurately capture benthic sediment and contaminant processes.

Sediment transport processes within most existing contaminant models are relatively rudimentary for cohesive sediments. For example, processes such as flocculation, hindered settling, bed sorting and armoring, and bed-depth-variable critical shear stress are neglected. However, much progress has been made in recent years to include such process detail in engineering sediment transport models. As a result, there is much interest today in linking comprehensive sediment transport models with contaminant fate/transport models.

6. CONCLUSION

Further development in the area of process descriptions is one of the greatest needs for future improvements in water quality modeling. The complexity of biogeochemical processes still requires large numbers of parameters for process equations as a result of incomplete knowledge of the process relationships. For example, substrate limitation of growth in biological kinetics can be described well by the Monod model (Chapra, 1997). However, the maximum growth rate and half-saturation constant used in this model must still be specified with optimal values usually decided through model calibration. Hopefully, some day rate coefficients can be automatically adjusted based upon ambient site-specific conditions.

Although the accuracy of water quality models has improved through advancements in process descriptions and increased experience from applications, the accuracy is not as good as that of hydrodynamic models. For example, the relative error for chlorophyll was on the order of 0.45 for Chesapeake Bay (Cerco and Cole, 1993), where a perfect match has a relative error of 0.0. In comparison, the relative error for salinity computations was on the order of 0.1 or less (Johnson et al., 1993). Part of the reason for this level of error in chlorophyll is probably insufficient process descriptions that fail to capture all of the complex biochemical mechanisms that affect phytoplankton concentrations. Additionally, phytoplankton chlorophyll, which models usually compute, is only a surrogate indicator of phytoplankton biomass or carbon, and it varies with species and other factors, such as nutrient availability, thereby making it difficult to predict. Multiple phytoplankton species are lumped into a few classes in models, which also contributes to the difficulty of making more accurate predictions. Predictions for nutrients are generally better than for chlorophyll, but not as good as predictions for salinity, temperature, and dissolved oxygen.

Although computer technology has made long-term (i.e., multi-decade) simulations feasible, there is still very limited information available to validate water quality models for such extended periods. More research is needed to get a better understanding of long-term water quality processes and the ability of models to capture long-term trends.

Ultimately, resource managers are more interested in sustaining aquatic living resources and protecting human and ecological health rather than meeting water quality standards, although water quality standards are of interest as indicators of aquatic health. For this reason, there is increasing interest in predicting future aquatic populations and health impacts. The time is opportune for advancing environmental models by developing linkages from water quality models to various types of living resource models, such as bioenergetics and population models. These linkages should be dynamic with feedback between water quality and living resources. Not only does ambient water quality affect aquatic living resources, but also aquatic living resources can affect ambient water quality through predation on phytoplankton, dissolved oxygen utilization, and carbon and nutrient cycling. In some cases, "top-down" control of eutrophication may be viable, and models that include such interactions will be required to better evaluate these strategies. Such advancements in water quality models may potentially improve model robustness by inclusion of more processes that can affect water quality.

REFERENCES

Berger, R.C., and Howington, S.E., 2002. Discrete fluxes and mass balance in finite elements. Journal of Hydraulic Engineering, 128 (1): 1–6.

Boyer, J.M., Chapra, S.C., Ruiz, C.E., and Dortch, M.S., 1994. RECOVERY, a mathematical model to predict the temporal response of surface water to contaminated sediments. Technical Report W-94-4. Vicksburg, MS: U.S. Army Engineer Waterways Experiment Station.

502

Carey, G.F., Bicken, G., Carey, V., Berger, R., and Sanchez, J., 2001. Locally constrained projections on grids. International Journal of Numerical Methods in Engineering, 50: 549–577.

Cerco, C.F. 1995. Response of Chesapeake Bay to nutrient load reductions. Journal of Environmental Engineering, 121 (8): 549–557.

Cerco, C.F. 2000. Tributary refinements to Chesapeake Bay model. Journal of Environmental Engineering, 126 (2): 164–174.

Cerco, C.F., Bunch, B.W., Teeter, A.M., and Dortch, M.S., 2000. Water quality model of Florida Bay. Report number ERDC/EL TR-00-10. Vicksburg, MS: U.S. Army Engineer Research and Development Center.

Cerco, C.F. and Cole, T., 1993. Three-dimensional eutrophication model of Chesapeake Bay. Journal of Environmental Engineering, 119 (6): 1006–1025.

Cerco, C.F., and Dortch, M.S. 1998. A model of suspended solids, light, and SAV. In: Abt, S.R., Young-Pezeshk, J., and Watson, C.C. (Editors), Water Resources Engineering 98, Proceedings of the International Water Resources Engineering Conference, pp. 838–843. Reston, VA: American Society of Civil Engineers.

Cerco, C.F., Johnson, B.J., and Wang, H., 2002. Tributary refinements to the Chesapeake Bay Model. Technical Report ERDC TR-02-4. Vicksburg, MS: US Army Engineer Research and Development Center.

Cerco, C.F., and Moore, K., 2001. System-wide submerged aquatic vegetation model for Chesapeake Bay. Estuaries, 24 (4): 522–534.

Cerco, C.F., and Seitzinger, S.P., 1997. Measured and modeled effects of benthic algae on eutrophication in Indian River-Rehoboth Bay, Delaware. Estuaries, 20 (1): 231–248.

Chapra, S.C. 1997. Surface Water Quality Modeling. New York, NY: McGraw-Hill.

Cole, T.M., and Buchak, E.M., 1995. CE-QUAL-W2: A two-dimensional, laterally averaged, hydrodynamic and water quality model. Version 2.0. Instruction Report EL-95-1. Vicksburg, MS: U.S. Army Engineer Waterways Experiment Station.

DiToro, D.M. 2001. Sediment Flux Modeling. New York, NY: Wiley-Interscience.

DiToro, D.M., and Fitzpatrick, J.J., 1993. Chesapeake Bay sediment flux model. Contract Report EL-93-2. Vicksburg, MS: U.S. Army Engineer Waterways Experiment Station.

Donigian, A., Jr., Bicknell, B.R., Patwardhan, A.S., Linker, L.C., Alegre, D.Y., Chang, C.H., and Reynolds, R., 1991. Chesapeake Bay Program Watershed Model Application to Calculate Bay Nutrient Loadings. Prepared by AQUA TERRA Consultants for US EPA Chesapeake Bay Program, Annapolis, MD.

Dortch, M.S., 1990. Three-dimensional, Lagrangian residual transport computed from an intratidal hydrodynamic model. Technical Report EL-90-11. Vicksburg, MS: U.S. Army Engineer Waterways Experiment Station.

Dortch, M.S., 2001. Army Risk Assessment Modeling System (ARAMS). In: Linkov, I., and Palma-Oliveira, J. (Editors), Assessment and Management of Environmental Risks, Cost Efficient Methods and Applications. Amsterdam, The Netherlands: Kluwer Academic Publishers in cooperation with NATO Scientific Affairs Division.

Dortch, M.S., Chapman, R.S., and Abt, S.R., 1992. Application of three-dimensional Lagrangian residual transport. Journal of Hydraulic Engineering, 118 (6): 831–848.

Dortch, M.S., and Gerald, T., 2002. Comparison of HPC methods for long-term contaminant modeling. In: Spaulding, M.L. (Editor), Proceedings of the 7th International Conference on Estuarine and Coastal Modeling. Reston, VA: American Society of Civil Engineers.

Dortch, M.S., Ruiz, C.E., Gerald, T., and Hall, R., 1998. Three-dimensional contaminant transport/fate model. In: Spaulding, M.L., and Blumberg, A.R. (Editors), Proceedings of 5th International Conference on Estuarine and Coastal Modeling. Reston, VA: American Society of Civil Engineers.

Dortch, M.S., Wang, P.F., Martin, J.L., and Wool, T., 2002 (in press). Three-dimensional contaminant model for surface water, CE-QUAL-ICM/TOXI: Model theory and user Guide. Draft Technical Report. Vicksburg, MS: US Army Research and Development Center.

Hendrickson, J., 2001. Rate of transfer of refractory organic carbon from the dissolved to the particulate pool along the salinity gradient of the Lower St. Johns River: Supplement to USACE WES Water Quality Modeling Project. Palatka, FL: St. Johns River Water Management District.

Johnson, B.H., Kim, K.W., Heath, R.E., Hsieh, B.B., and Butler, H.L., 1993. Validation of three-dimensional hydrodynamic model of Chesapeake Bay. Journal of Hydraulic Engineering, 119 (1): 2–20.

Karypis, G., and Kumar, V., 1995a. METIS: Unstructured graph partitioning and sparse matrix ordering system. Technical Report. Minneapolis, MN: University of Minnesota, Department of Computer Science.

Karypis, G., and Kumar, V., 1995b. A fast and high quality multilevel scheme for partitioning irregular graphs. Technical Report TR 95-035. Minneapolis, MN: University of Minnesota, Department of Computer Science.

Luo, J., Hartman, K., Brandt, S., Cerco, C., and Rippetoe, T., 2001. A spatially-explicit approach for estimating carrying capacity: An approach for the Atlantic menhaden (*Brevoortia tyrannus*) in Chesapeake Bay. Estuaries, 24 (4): 545–556

Martin, J., Tillman, D., Cerco, C., Hendrickson, J., and Dortch. M., 2002. A three-dimensional water quality model for estimating TMDLs in a black water river estuary, the Lower St. Johns River, FL. In: Spaulding, M.L. (Editor), Proceedings of the 7th International Conference on Estuarine and Coastal Modeling. Reston, VA: American Society of Civil Engineers.

National Research Council, 2000. Clean Coastal Waters: Understanding and Reducing the Effects of Nutrient Pollution. Washington, DC: National Academy Press.

Sucsy, P.V., and Morris, F.W., 2002 (in press). Calibration of a three-dimensional circulation and mixing model of the Lower St. Johns River. St. Johns River Water Management District Technical Memorandum. Palatka, FL.

Thomann, R.V., and Mueller, J.A., 1987. Principles of Surface Water Quality Modeling and Control. New York, NY: Harper and Row Publishers.

Wang, H.V., and Johnson, B.H., 2002. Validation and application of the second generation three-dimensional hydrodynamic model of Chesapeake Bay. Journal of Water Quality and Ecosystem Modeling, 1 (1–4): 51-90.

Whelan, G., Buck, J., Gelston, G., and Castleton, K., 1999. Framework for risk analysis in multimedia environmental systems. Training Manual. Richland, WA: Pacific Northwest National Laboratory.

This Page Intentionally Left Blank

505

Chapter 19

Neural Network Applications in Coastal Ecological Modeling

Michele Scardi

Department of Biology, University of Rome "Tor Vergata", Via della Ricerca Scientifica, 00133 Rome, Italy

1. INTRODUCTION

In this chapter some applications of neural networks (NN) to modeling processes in coastal ecology will be presented to demonstrate the potential of this approach and to identify some of its limitations. Some of these applications have been presented in detail elsewhere (Barciela et al., 1999; Scardi and Harding, 1999; Scardi, 2000; Scardi, 2001), whereas others are new or unpublished. In all the cases, however, while the original features of the neural network applications will be emphasized, the methodological issues will only be briefly summarized. This approach will help the reader to determine which kind of problems are suitable for neural network applications without overloading the presentation with details that can be retrieved from the literature.

At first, this chapter introduces neural networks as computational tools, providing a general and accessible description of their main features, while more technical details are available in Appendix 1. Existing ecological applications of neural networks and, in particular, applications to coastal ecosystems are then reviewed briefly. Although dynamic modeling in coastal ecosystems is being advocated (see, for instance, the seminal and comprehensive study on Narragansett Bay by Kremer and Nixon, 1978) emphasis will, nevertheless, be placed on steady state models because they are by far the most common NN ecological applications in coastal ecosystems. In the next sections some neural network models of phytoplankton primary production are presented and compared to conventional models, as well as other examples of neural network models applied to coastal ecosystems. Then a comparison between conventional, dynamic models and neural networks is outlined using some phytoplankton biomass models for a coastal embayment as examples. Finally, the state-of-the-art in neural network modeling is discussed, as well as some perspectives in their future development. Useful links to neural network resources are presented in Appendix 2.

1.1. What Are Neural Networks?

Neural networks (NNs) or, according to a more precise definition, *artificial* neural networks (ANNs) have been defined in many different ways, although none of the definitions has been accepted universally. According to Haykin (1994)

> "A neural network is a massively parallel distributed processor that has a natural propensity for storing experiential knowledge and making it available for use. It resembles the brain in two respects: (1) knowledge is acquired by the network through a learning process and (2) interneuron connection strengths known as synaptic weights are used to store the knowledge."

In general, a NN can be regarded as a network of simple units that operate on data either stored locally or received via the connections to other units. This kind of structure is somewhat related to the nervous systems of living organisms, and the development of NNs has been influenced by the idea that artificial systems could mimic the activity of their biological counterpart. It is worth noting that today, even though most NNs are commonly regarded as mere computational tools, many

terms in the NN jargon express this conceptual relationship. For instance, a NN *learns* from examples presented during a *training* procedure when the *synaptic* weights in the connections between *neurons* are optimized. Such a training procedure is usually based on rules that define the way the weights of the connections are adjusted when the examples (i.e., the data) are passed to the network.

Several practical applications of NNs involve some form of supervised learning. In other words, the training data include values both for the predictive variables and for the variables to be predicted. When the training phase is completed successfully and some input values are passed to the NN, the latter returns output values that approximate the desired outputs. These NNs are effective in solving nonlinear regression problems, but they are also useful for classification and pattern recognition. The most common supervised NN is the multilayer perceptron, whereas the error back-propagation is by far the most common training algorithm for those NNs. Therefore, the majority of the real world NN applications are based on the combination of the two, and we refer to this combination as an error back-propagation NN (or EBP NN).

Multilayer perceptrons can be modified in several different ways when dynamic systems are to be modeled. Since the previous state of a system is a very important source of information in deterministic modeling, it can be taken into account using *recurrent* NNs (Pineda, 1987). These NNs use some form of feedback control based on output values or hidden layer synaptic weights from a previous state of the system to enhance their ability to model dynamic systems.

Other NNs are able to learn without supervision, i.e., they are able to adjust their weights according to the data sets used for training. The most common unsupervised NN is the Self Organizing Map (SOM), which is usually applied to classification or ordination problems.

From a computational point of view, NN applications are usually intensive. As in the case of other empirical modeling tools, the quality of the results depends on the amount and quality of available data. However, NNs require two independent data sets for learning and validation when they are used as generalized regression tools[1]. Obviously, a third, independent data set is still needed for testing the results of the NN model and for comparing them to those provided by other models. As for the need for an independent test data set, it should be stressed that this is not a special requirement for NNs, even though many modelers tend to overlook it when using conventional regression tools.

Finally, parallel implementations of NNs are effective because the computations that are done within each NN unit are partly independent of each other.

More details on the NNs that have been used for the applications that are presented in this chapter and links to useful web sites and resources are provided in Appendix 2.

1.2. What Role Do Neural Networks Play in Ecological Modeling?

Neural network applications to ecological modeling or, more generally, to ecology are relatively recent approaches. The first references to the potential use of neural networks cannot be found in ecological literature before the early 1990s (for example, Colasanti, 1991). However, only a few years later, while Edwards and Morse (1995) had identified that NNs could play an important role in computer-aided biodiversity research, the first ecological applications appeared. They were developed in different fields and involved different tasks, such as classifying benthic community data (Chon et al., 1996), predicting various parameters in brown trout management (Baran et al., 1996; Lek et al., 1996b), modeling spatial dynamics of fish (Giske et al., 1998), predicting phytoplankton production (Scardi, 1996; Recknagel et al., 1997), predicting fish diversity (Guégan et al., 1998), predicting production:biomass (P:B) ratio of animal populations (Brey et al., 1996), etc.

The majority of the first NN ecological applications were aimed at showing that NNs performed better than conventional modeling methods. Therefore their focus was mainly on the comparison between NNs and other methods. Recently, however, the use of NNs in ecological applications has become more common, even though most ecologists are still not familiar with these tools. In particu-

lar, it is interesting that NN applications are more abundant in terrestrial and freshwater ecology than in marine ecology.

From a general point of view, however, the context of ecological modeling is quite different from that of other NN applications, as data sets and knowledge are often very limited with respect to the complexity of the real processes. This implies that relationships between variables are only partly known and understood and that they are usually studied by analyzing correlations rather than by defining causal pathways in a deterministic framework. As Lek et al. (1996a) pointed out, NNs are effective in modeling such relationships by "learning" the underlying processes—which are often highly nonlinear—independently of the modeler's knowledge. Of course, good results can only be obtained when enough good data are available and a correct procedure has been used for "training" the model. A quick, but comprehensive introduction to the use of NNs in ecological modeling applications can be found in Lek and Guégan (1999).

While most of the existing NN applications deal with steady state modeling, other types of NN applications are emerging, as those based on Self Organizing Maps (SOMs) and recurrent NNs. SOMs have been recently used both to ordinate and to classify ecological data (Giraudel and Lek, 2001), whereas recurrent NNs, which proved to be effective in modeling time series and dynamic systems (Recknagel, 2001), have been applied successfully to model phytoplankton dynamics in freshwater ecosystems (for example, Jeong et al., 2001; Walter et al., 2001).

1.3. Neural Network Applications to Coastal Modeling

As for coastal ecosystem modeling, only a few NN applications are available, even though coastal ecosystems have always been a favorite target for modelers as they normally function as interfaces between catchments and marine systems. Some applications have focused on coastal data sets, but they do address problems that are not strictly coastal (for example, Brey et al., 1996; Scardi, 1996; Brey and Gerdes, 1998). A few applications, however, deal with typical coastal problems, for instance, the propagation of the green alga *Caulerpa taxifolia* in the northwestern Mediterranean Sea (Aussem and Hill, 1999; 2000); the suitability of the coastline for breeding by New Zealand fur seals (Bradshaw et al., 2002); phytoplankton primary production in Chesapeake Bay (U.S.A.) (Scardi and Harding, 1999), in the Gulf of Napoli (Italy) (Scardi, 2000) or in a coastal embayment affected by upwelling (Barciela et al., 1999); the estimation of chlorophyll concentration and turbidity in coastal waters using Thematic Mapper imagery (Keiner and Yan, 1998); the estimation of coastal water quality on the basis of nutrient concentrations (Aguilera et al., 2001) or estimating relevant hydrological variables by means of remotely sensed data (Zhang et al., 2002).

Several NN applications to coastal geology, physical oceanography and marine engineering have also been presented. These deal mainly with tools that allow a better exploitation of the existing data sets with respect to conventional models. Examples of these applications are on the enhancement of the available bathymetric information using remotely sensed imagery (Sandidge and Holyer, 1998; Kingston et al., 2000), the assessment of salinity variations in tidal rivers (Huang and Foo, 2002), the prediction of sea level (Ultsch and Röske, 2002), the prediction of tides (Lee and Jeng, 2002) or waves (Deo and Sridhar Naidu, 1999; Deo et al., 2001) and breakwater design (Mase et al., 1995; Mase and Kitano, 1999).

2. MODELING PHYTOPLANKTON PRIMARY PRODUCTION IN COASTAL WATERS

2.1. Overview

In marine ecosystems phytoplankton primary production (PP) plays a fundamental role in supporting the whole food web. Coastal marine ecosystems are not exceptions to this rule, especially

where the environmental conditions do not allow seagrasses or macroalgae to sustain a robust benthic primary production.

Therefore, models of phytoplankton PP have long played an important role in oceanographic research, both because of their theoretical value and the fact that direct measurements of this process can be difficult, expensive and time consuming. In particular, empirical models that estimate PP on the basis of other variables are often needed. Typical applications are in post-processing phytoplankton biomass data (for example, by remote sensing) or in supporting direct measurements of photosynthetic efficiency (for example, by pump-and-probe fluorometry).

Many empirical models of phytoplankton PP have been developed using conventional approaches. Early models relied on simple formulations based largely on phytoplankton biomass (for example, Smith and Baker, 1978), or on more complex linear relationships that included terms for phytoplankton biomass and light availability as surface irradiance and water transparency (for example, Cole and Cloern, 1984; 1987).

Multiple linear regression (Eppley et al., 1985) and more complex formulations have also been tested using other predictive variables (such as day length or physiological parameters) to improve the accuracy of the estimates. A recent example of this category of models is the Vertically Generalized Production Model (VGPM), developed by Behrenfeld and Falkowski (1997)

$$\sum PP = 0.66125 \cdot P_{opt}^{B} \cdot \frac{I_0}{I_0 + 4.1} \cdot Chl \cdot Z_{eu} \cdot Dl \tag{1}$$

The VGPM provides estimates of phytoplankton PP integrated down to the photic zone depth (Z_{eu}, i.e., the depth at which irradiance is 1% of the surface value) based on surface values for chlorophyll concentration (Chl), irradiance (I_0), temperature and day length (Dl). Sea surface temperature is not directly used, but it allows estimating P_{opt}^{B} (i.e., the maximum, observed primary productivity rate in the water column normalized to biomass), whereas Z_{eu} may be estimated from surface chlorophyll concentrations, assuming that the water column transparency is principally affected by the phytoplankton biomass (this is generally not the case in coastal ecosystems where other sources of dissolved and particulate organic and inorganic materials contribute to light attenuation).

Depth-integrated models such as the VGPM assume the distribution of the phytoplankton biomass throughout the water column is homogeneous. This assumption is not always true in open waters, but it is more often reasonably close to reality in shallow coastal ecosystems. On the other hand, the role that some physical (water circulation, wind stress, waves, turbidity, etc.), and chemical (for example, nutrient inputs regulated by terrestrial runoff, biogeochemical cycles, etc.) processes play in driving primary production is more important in coastal ecosystems than in open waters. Therefore, modeling phytoplankton primary production in coastal waters can be a challenging task for conventional models.

NN models, however, are much more flexible than conventional models, because the modeler must not define a formulation a priori (i.e., the level of complexity, the "shape", etc.). Therefore, NN models are able to reproduce complex responses accurately and to handle easily predictive co-variables that account for forcing functions that are not taken into account directly (Scardi, 2001). The latter feature, for instance, allows using the distance from the coastline as a proxy for nutrient concentrations (via the relationships with terrestrial runoff), mixing in the water column (via the relationships with depth and waves), etc. Of course, this strategy could be applied to conventional models as well, but in that case it is often more difficult (if not impossible) to define a suitable formulation for taking relationships involving co-variables into account.

The application of NN models to phytoplankton PP modeling in coastal ecosystems has produced good results (Scardi, 1996; Barciela et al., 1999; Scardi and Harding, 1999; Scardi, 2000), but it is worth mentioning that similar applications have been developed for dynamic modeling of freshwater ecosystems (for example, Yabunaka et al., 1997; Recknagel et al., 1998; Walter et al., 2001). In this

chapter some of the methods and results that are presented in greater detail in Scardi (2000) and Scardi and Harding (1999) are outlined briefly.

2.2. Methods

All the NN models presented in this chapter were trained using the most popular algorithm i.e., error back-propagation (EBP) (Rumelhart et al., 1986). This is not really a relevant detail, however, because the selection of the NN training algorithm seldom plays a relevant role in ecological applications, in which the amount and quality of the data sets are usually the limiting factors for optimal learning. For the same reason, fine-tuning the parameters that control the way the model learns (i.e., the way the optimal set of NN weights is found) rarely has a significant impact on the final result. Therefore, a unit learning rate and no momentum were used in the majority of the models that will be described in this chapter.

The ecological data that were used for training and validating the models (as well as those that were used for testing them) are usually affected by significant errors due to sampling strategies, analytical procedures, instrument accuracy, etc. Using highly variable data for training a NN model may induce "overfitting" (i.e., *overtraining* in NN jargon), especially with small data sets. In fact, NNs are sufficiently flexible in their responses that they are likely to reproduce local data patterns (including noise) rather than to generalize (i.e., to learn the overall trend). Therefore, several techniques have been applied simultaneously to preserve or to enhance the generalization capabilities of all the NN models presented in this chapter:

(1) only a subset of the whole training set was selected randomly for each training cycle (*epoch*) and submitted to the NN in random order,

(2) the training procedures were done according to an *early stopping* strategy with respect to a validation data set that was independent of the training data set (i.e., the training was stopped as soon as the error with respect to the validation set stopped decreasing), and

(3) a small amount of Gaussian noise ($\mu = 0$) and ($\sigma = 0.01$) was added to the normalized input patterns before passing them to the NN during the training (Györgyi, 1990).

The latter procedure (*jittering* in NN jargon) contributed to the NN regularization by producing an unlimited number of "artificial" training patterns that were similar, but not identical, to the real ones.

All the input and output variables were normalized with respect to their observed ranges to train the NNs using only values in the [0,1] interval.

All the NN models had a single hidden layer, and the number of units in this layer was defined after empirical tests. The optimal structure was determined as that which provided the smallest mean square error (MSE) for the phytoplankton PP estimates.

All NN units in the hidden and output layer had sigmoid activation functions, namely

$$f(a) = \frac{1}{1 + e^{-a}} \tag{2}$$

In all the cases, the available data were divided into three subsets for training, validation and testing (consisting of 50%, 25% and 25% of the data, respectively).

The sampling date, when included among the predictive variables, was expressed in two new variables, which allow us to map the day of the year onto a unit diameter circle (i.e., a sort of yearly "clock"), as follows

$$date_1 = \frac{1}{2}\left[\cos\left(\frac{2\pi \cdot day}{365}\right) + 1\right] \tag{3}$$

$$date_2 = \frac{1}{2}\left[\sin\left(\frac{2\pi \cdot day}{365}\right) + 1\right] \tag{4}$$

2.3. Phytoplankton Primary Production Modeling in the Gulf of Napoli (Italy)

Oceanographic data were collected routinely in the Gulf of Napoli (Italy) at a fixed station, from January 1984 to November 1988. The sampling station was located in the inner part of the Gulf of Napoli and it was not directly influenced by terrestrial runoff. The final data set consisted of 825 records for phytoplankton biomass (both as chlorophyll-*a* and phaeopigment concentrations) and PP. Pigments concentrations as well as PP and downwelling irradiance data were measured at different depths, from the surface to 60 m. Temperature profiles were obtained using a CTD probe. The data set included 116 surface records and a similar number of records, subject to slight changes due to missing data, for other depths (2, 5, 10, 20, 40 and 60 m).

2.3.1. Basic Primary Production Modeling: Neural Networks vs. Linear Models

At first a linear model based on surface phytoplankton biomass (B_0, mg Chl m^{-3}), irradiance (I_0, E m^{-2} day^{-1}) and water temperature (T_0, °C) was developed, assuming that surface PP (PP$_0$) was directly proportional to all of these variables

$$PP_0 = 6.79 + 0.0287 \cdot B_0 \cdot I_0 \cdot T_0 \tag{5}$$

This linear model was obtained using 85 records that were randomly selected from the 116 available (i.e., 75% of the available data). The remaining records (n=29, i.e., 25% of the available data) were used as an independent test set for comparisons of models.

The same predictive variables were used as inputs for an EBP NN. The NN model, which had 4 units in the hidden layer, was trained on the same data that were used in the linear model. However, only 58 records out of 85 (i.e., 50% of the available data) were used to train the NN model, whereas the remaining 29 records were included in the validation set for an *early stopping* procedure. The same records (n=29, i.e., 25% of the available data) were used to test both the linear model and the NN model.

The accuracy of the linear model was apparently good ($R^2 = 0.792$), but the result was quite different ($R^2 = 0.379$) when it was evaluated on the basis of the test set data. The linear model was not adequately generalized and provided biased estimates, especially in the case of large PP values. On the other hand, the difference in R^2 values between training and test data was much smaller in the case of the NN model ($R^2 = 0.918$ and $R^2 = 0.768$, respectively). Estimated PP values, both for the linear and the NN model, were plotted against the test set observed values in Fig. 1 (the diagonal line, that has a unit slope, shows the perfect match between estimated and observed values).

These results showed that not only was the NN model able to fit the available data better than the linear model, but that it was correctly generalized, i.e., able to provide accurate PP estimates when independent test data were used. This example also shows that too often the real performance of conventional models is not correctly evaluated. In fact, their MSE and/or R^2 are often computed on the basis of the same data used by the fitting procedure. In other words, these models are not validated after calibration, whereas the correct procedure, involving independent data sets for validation and calibration, has traditionally been applied to NN training.

Although a linear model did not perform well in this case, there are cases in which simple models have provided accurate estimates of PP, especially when the environmental conditions were homogeneous and changes in biomass and light were the main influences on PP. The flexibility of the NN approach, on the other hand, allows us to embed complex relationships into the models implicitly, as shown in the following example.

Excluding equatorial regions, sea surface temperature and surface irradiance show strong seasonality. Seasonal climatic conditions, in turn, affect the vertical structure of the water column and the way nutrients, phytoplankton biomass and PP are distributed. Moreover, diffuse terrestrial runoff and river discharge also undergo seasonal changes and they can significantly affect PP in coastal ecosystems.
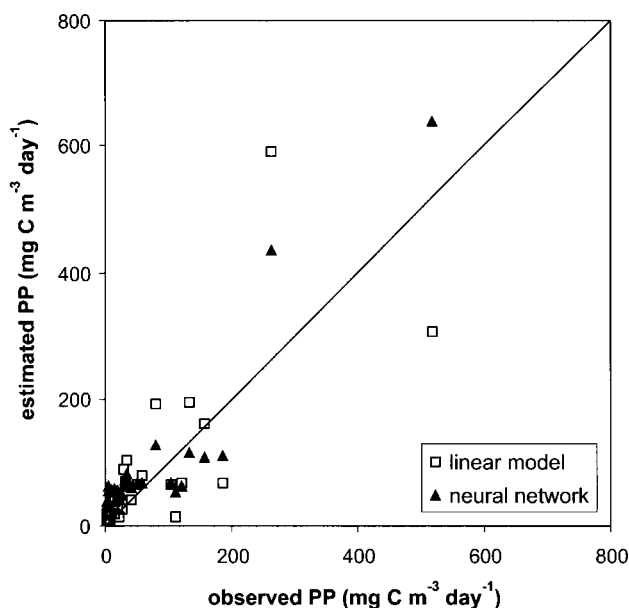
Figure 1. Predicted vs. observed values for surface phytoplankton primary production in the Gulf of Napoli (Italy). Results for the test data set (n=29) are shown for both the linear model (white squares, $R^2 = 0.379$) and the neural network model (black triangles, $R^2 = 0.768$).

Therefore, the same level of phytoplankton surface PP can be observed in different seasonal conditions, associated with different vertical distributions of PP and depth-integrated values. The example in Fig. 2 was extracted from the Gulf of Napoli data set and clearly shows that a subsurface peak can significantly contribute to depth-integrated PP (295 and 912 mg C m^{-2} day^{-1} on March 20, 1985 and on July 9, 1985, respectively).

Using only the surface predictive variables mentioned in the previous example, a NN model was developed to estimate depth-integrated PP. A linear model was also developed and compared to the NN model using the test procedure described above (Fig. 3).

The resulting NN did not perform as well as that for surface PP, but it still delivered an acceptable level of accuracy, especially compared to the large sampling and measurement errors that are usually found in PP data. R^2 for the NN model was 0.449, whereas the linear model had R^2 of 0.206. It is clear that the linear model was not able to cope with the complexity of the problem in this case, as it visibly overestimated low PP values and underestimated high PP values. On the other hand, NN estimates are affected by errors that are not systematic and that are of the same magnitude of the errors in direct PP measurements.

2.3.2. A Depth-Resolved Primary Production Model

Although estimating depth-integrated PP using surface data only can be useful (for example, when remote sensing data are used as inputs), it is obvious that the highest accuracy in PP modeling cannot be attained on that basis. The most relevant predictive data in PP modeling are measures of phytoplankton biomass that can be easily obtained from *in vivo* fluorometric vertical profiles. Therefore, a depth-resolved NN model was developed using this kind of information (chlorophyll-*a* and phaeopigment concentrations) as well as sea surface temperature, irradiance and depth. Day of year
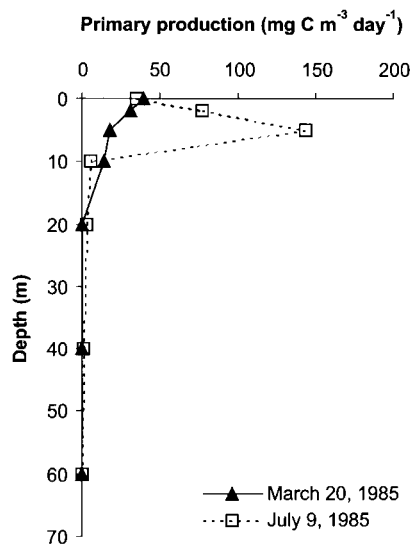
Figure 2. Two vertical profiles of phytoplankton primary production in the Gulf of Napoli (Italy) with similar surface values and different vertical distributions. A subsurface maximum is often present in summer (dotted line with white squares), whereas in other seasons the values tend to decrease monotonically according to depth (solid line with black triangles).
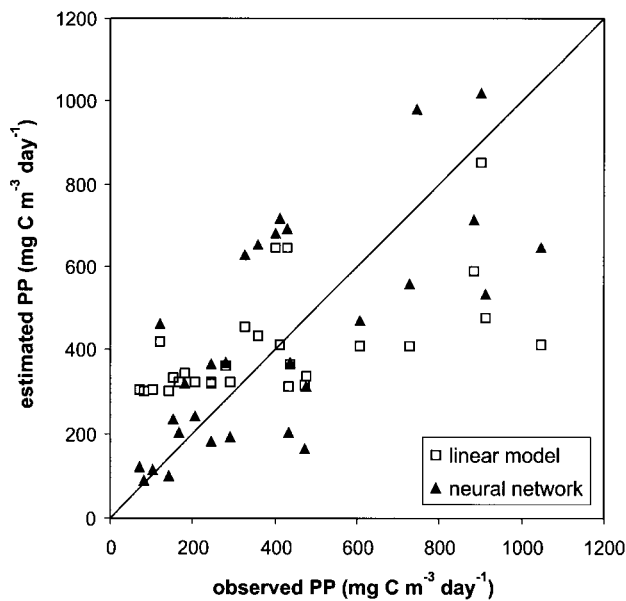
Figure 3. Predicted vs. observed values for depth-integrated phytoplankton primary production in the Gulf of Napoli (Italy). Results for the test data set (n=29) are shown for both the linear model (white squares, $R^2 = 0.206$) and the neural network model (black triangles, $R^2 = 0.449$).

was also included as a predictive variable, using the sine and cosine transformations described above. Finally, a heuristic index for daily variability of the irradiance and average chlorophyll-*a* concentration above the considered depth completed the set of predictive variables. Further details about the above-mentioned heuristic index and a more complete presentation of the methods for this depth-resolved NN model can be found in Scardi (2000).

All the data on photosynthetic pigments and PP were log-transformed before training the NN model. The rationale for this approach is not related to the expected "shape" of the relationships to be modeled (as in the case of conventional models), but only to the way the differences between NN output and target values have to be evaluated and the MSE has to be computed. In fact, EBP NNs are able to approximate any function, so they do not require log-transformations to linearize the relationships to be modeled. However, using raw instead of log-transformed PP data would have overemphasized the role of the highest PP values—which have proportionally large measurement errors—in driving the learning procedure. Moreover, a spatial bias would also have been introduced as large PP values are only found in the upper part of the water column. As the observed PP values span at least three orders of magnitude, using log-transformed data allows us to take into account the complete range of PP. Pigment concentrations were also log-transformed, but this choice was only related to the need to simplify the NN training (in fact, they are the NN input variables most closely related to PP), as they are not involved in the error computations.

The resulting model, which had 7 units in the hidden layer, was able to predict PP accurately on the basis of nine predictive variables (Fig. 4). In fact, even though the model was able to explain a large fraction of the PP variance ($R^2 = 0.907$), its actual quality was probably still underestimated as
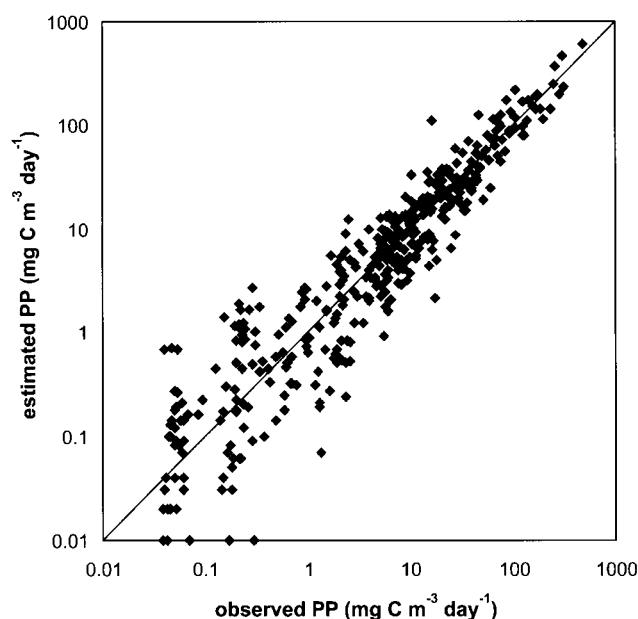
Figure 4. Neural network predicted vs. observed values for depth-resolved phytoplankton primary production in the Gulf of Napoli (Italy). Results for the test data set (n=413) are shown ($R^2 = 0.907$). Both axes have log scales because primary production values as well as pigment concentrations were log transformed before training the neural network model to reduce the influence of high primary production values in driving the training procedure.

primary production (mg C m^{-3} day^{-1})

March   **August**   **November**
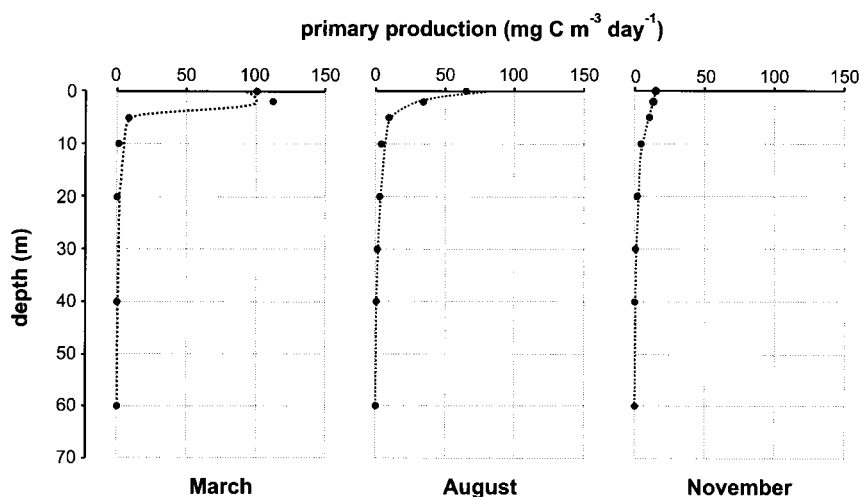
Figure 5. Three vertical profiles of phytoplankton primary production in the Gulf of Napoli (Italy). Neural network modeled profiles (dotted line) fitted very well the observed data (black circles).

the largest errors selectively affected PP values that were too small to be measured accurately (i.e., PP < 1 mg C m^{-3} day^{-1}).

In practical applications the resulting model proved to be accurate and more than 80% of the deviations of the estimated PP values from the observed ones were negligible (< 10 mg C m^{-3} day^{-1}). Some vertical profiles of PP computed by this model are presented in Fig. 5 (dotted lines), where observed values are also shown (black circles). It is clear that different vertical PP patterns, which correspond to different seasonal conditions, were reproduced accurately by the NN model on the basis of surface data for all the predictive variables except for pigment concentrations.

2.4. A More Complex Coastal Model: Phytoplankton Primary Production Modeling in Chesapeake Bay (U.S.A.)

The PP models for the Gulf of Napoli were based on the same variables that were used by the majority of the conventional empirical PP models. However, the most important advantage of a NN approach over a conventional one is its flexibility that allows the use of heterogeneous sources of information to enhance predictive capabilities. Moreover, NNs are not as sensitive as conventional models to non-independent (i.e., correlated) predictive variables. This is not only true because NNs do not require matrix inversions, but also from a more general point of view, because they are robust with respect to redundant predictive variables. In fact, if properly trained, NNs are able to define appropriate weights of the connections between other units and the correlated inputs, so that the latter can act correctly as a single source of information. All these properties, obviously, can be fully exploited only when enough data are available for training a NN model.

A more complex model that shows how the above-mentioned properties reveal themselves in practical applications deals with the phytoplankton primary production in Chesapeake Bay (U.S.A.). This model followed a first "toy" model that was aimed at demonstrating that NN could provide an alternative to conventional approaches for PP modeling (Scardi, 1996).

The NN PP model for Chesapeake Bay was based on 12 predictive variables that are listed in Table 1 and more details about it can be found in Scardi and Harding (1999).

Table 1

Input and output variables and units for the Chesapeake Bay (U.S.A.) neural network model of phytoplankton primary production. Variable names followed by ($\log_{10}$) indicate that raw values have been log-transformed before normalizing them to a [0,1] interval.

	Variable	Units
INPUT	$1/2\,[\cos(2\pi \cdot \text{day}/365) + 1]$	*none*
	$1/2\,[\sin(2\pi \cdot \text{day}/365) + 1]$	*none*
	latitude	*degrees*
	longitude	*degrees*
	station depth	*m*
	water temperature	$^{\circ}C$
	salinity	*PSU*
	surface chlorophyll concentration ($\log_{10}$)	$mg\,m^{-3}$
	total chlorophyll in the photic zone ($\log_{10}$)	$mg\,m^{-2}$
	surface downwelling irradiance	$E\,m^{-2}\text{day}^{-1}$
	light extinction coefficient	m^{-1}
	photic zone depth	*m*
OUTPUT	phytoplankton primary production ($\log_{10}$)	$mg\,C m^{-2}\text{day}^{-1}$

Among the predictive variables there are some that are not common in empirical PP models. The geographical coordinates, for instance, account implicitly for variations in complex environmental characteristics that are observed in different parts of the Bay and that are not easy to describe using field data. Photic zone depth and light extinction coefficient, on the other hand, are strictly related to each other; the only exception are those sampling sites where the photic zone depth was larger than the actual depth: in those cases the latter was assumed as the real photic zone depth (from an operative point of view, photic zone depth is a function of the inverse of the light extinction coefficient, but its upper limit is the sampling-site depth).

The subsequent model was trained and validated using data collected from 1982 to 1996. It had a 12–5–1 structure, i.e., 12 inputs, one output (see Table 1) and 5 units in the hidden layer. The NN model was reasonably accurate, with MSE=0.0771 and $R^2 = 0.6717$ (Fig. 6a). As in other similar cases, the final model was defined after a series of tests with different numbers of units in the hidden layer and the final set of synaptic weights was selected after a large number of iterations of the training procedure.

The generalization ability of the model was tested with new data collected during 1997 that were not available while developing the model. The model fit the new data even better than expected, as shown in Fig. 6b (MSE=0.0370 and $R^2 = 0.8423$), and also performed well with data collected in 1998, 1999 and 2000 (Figs. 6c-e), as indicated by MSE and R^2 values for these new data sets that were better than the original ones.

On the basis of these independent tests, the NN Chesapeake Bay phytoplankton PP model can be considered as a very reliable tool[2], ready for practical applications (for example, it has been used for estimating PP on the basis of remotely sensed data on phytoplankton biomass).

The model was able to reproduce a wide spectrum of relationships among biomass, other variables and PP in different regions of Chesapeake Bay and in different seasons. A comparison between the PP estimates in summer and fall conditions is shown in Fig. 7 and it clearly shows that the response of the model is very flexible (these plots can be regarded as a family of curves in which the steeper ones correspond to higher photosynthetic efficiencies). Because a single mean daily irradiance value was used for each plot, this variable did not play a role in determining the intra-plot variability, that

516
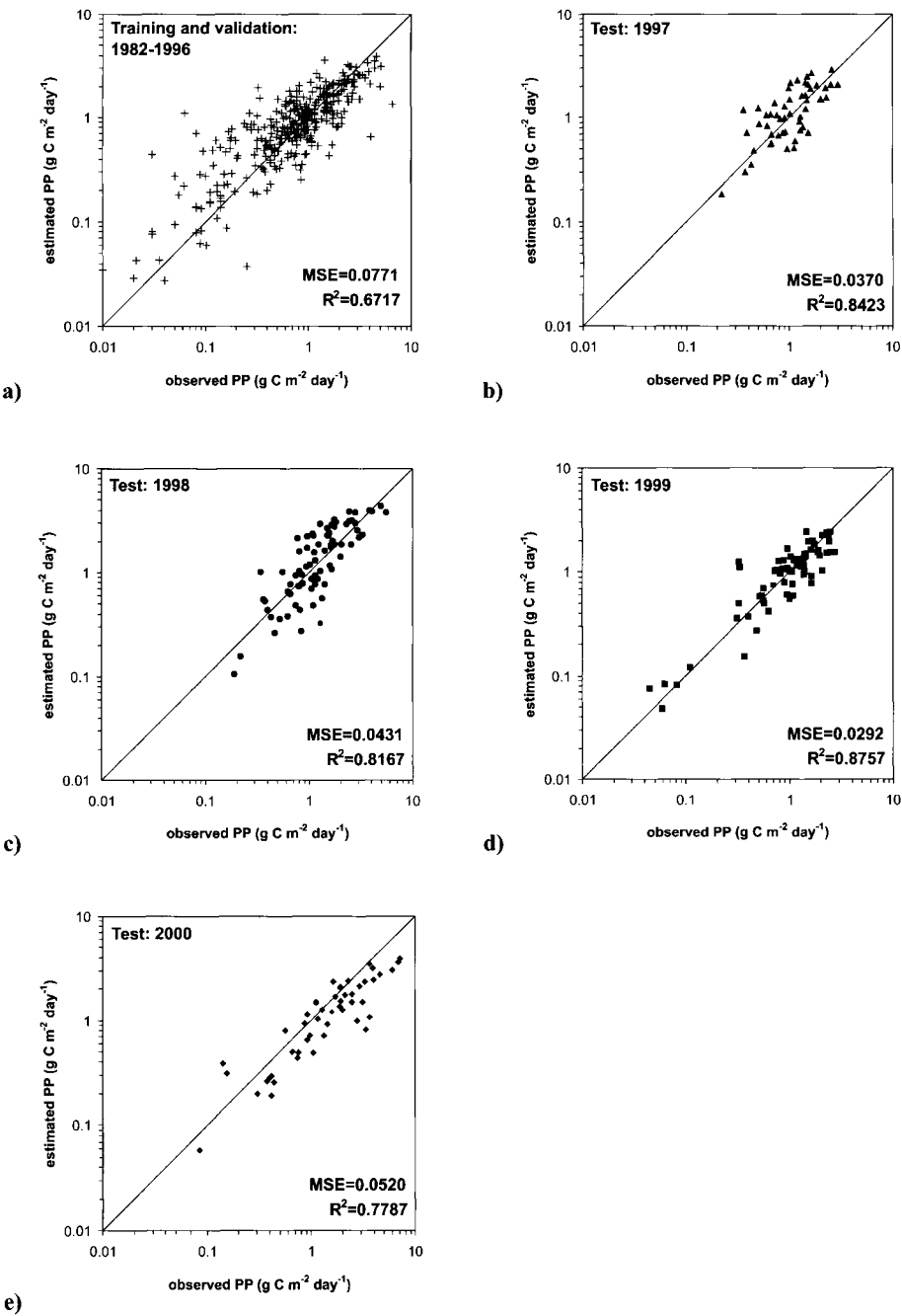
Figure 6. Neural network predicted vs. observed values for depth-integrated phytoplankton primary production in Chesapeake Bay (U.S.A.). The original neural network model (a) provided good results ($R^2 = 0.672$), but the results were even more accurate ($R^2 = 0.779 \div 0.876$) when the model was tested on data sets collected well after the end of its development (b-e).
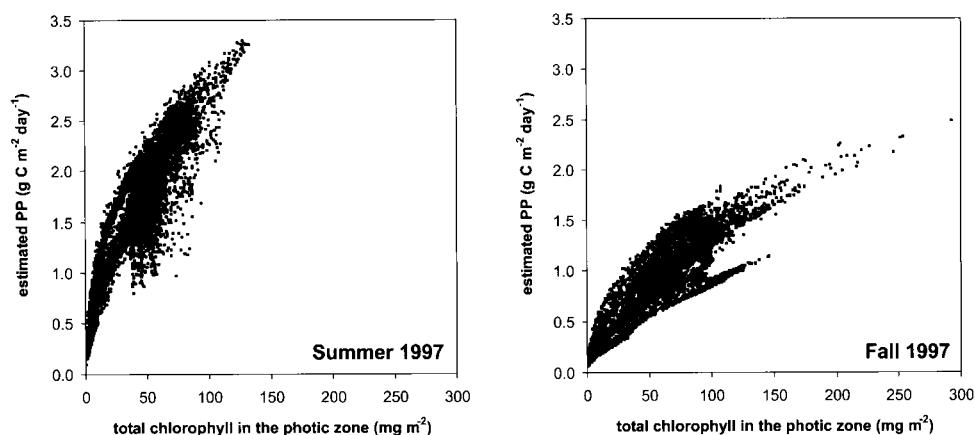
Figure 7. Neural network predicted phytoplankton primary production vs. observed total chlorophyll in the photic zone in Chesapeake Bay (U.S.A.). Two different seasonal scenarios were considered in this figure: summer 1997 (a) and fall 1997 (b). In each plot more than 7000 points were shown, corresponding to different locations in Chesapeake Bay. The position of each point depended on the photosynthetic efficiency of the whole water column and a steeper overall slope implied a higher photosynthetic efficiency, as in the summer plot (a). It was interesting to note that each plot actually consisted of a set of curves that represented different site-specific nonlinear relationships.

was actually due to other variables that are directly (for example, photic zone depth) or indirectly (for example, latitude, that is a proxy for freshwater inputs and nutrient load) related to PP.

To elucidate the role of the predictive variables in NN models, several procedures have been proposed (Garson, 1991; Dimopoulos et al., 1995; Hammitt and Bartlett, 1995; Balls et al., 1996; Lek et al., 1996a; 1996b; Dimopoulos et al., 1999; Scardi and Harding, 1999), but in the case of the Chesapeake Bay model the one proposed by Scardi and Harding (1999) was applied.

According to this procedure, the available data for predictive variables were perturbed before passing them to a trained NN and computing a new MSE value. In particular, only one of the variables was perturbed at each run, while the others were not perturbed. Changes in the input values range from small adjustments (for example, 1% of the normalized range, i.e., ±0.01) to larger ones (usually 50% of the normalized range, i.e., ±0.5). Moreover, they can be fixed (only two modified values for each level of perturbation) or random (white noise in the desired range is added to the input value). When a small change in one of the input values produces a large change in the NN output, it can be inferred that the modified input variables play a relevant role in determining the response of the model. This kind of evidence obviously does not imply causal relationships and only accounts for first-order interactions between NN inputs and outputs. However, the results of such a sensitivity analysis can provide useful insights into the mechanics of the modeled system, and can also help to evaluate the robustness of the model with respect to errors in predictive variables.

The line plot in Fig. 8 shows the results of a sensitivity analysis that was done on the Chesapeake Bay phytoplankton PP model. In this case fixed perturbations of the NN inputs were applied, ranging from ±1% to 50% of the normalized interval (i.e., from ±0.01 to ±0.5). It is clear that the majority of the curves overlap with the exception of the curve for the total chlorophyll in the photic zone (open circles). This result is not surprising as it implies that the amount of phytoplankton biomass that is able to carry out photosynthetic activity is the most influential variable in determining phytoplankton PP in Chesapeake Bay. Salinity and longitude, in contrast, are the least influential among the predictive variables.
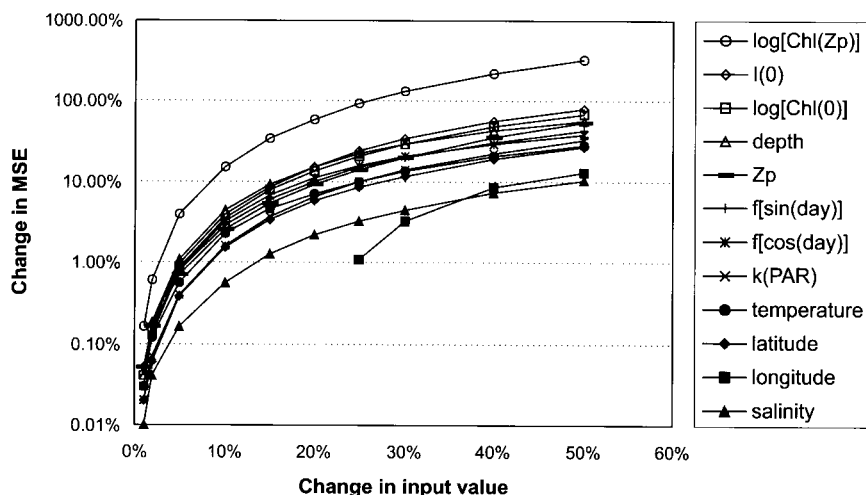
Figure 8. Sensitivity analysis of the neural network model of phytoplankton primary production for Chesapeake Bay (U.S.A.). Each curve represented the relative increase in mean square error (MSE) that was caused by different changes in the input values for a given predictive variable. Changes in input values smaller than 5% caused minor variations in MSE (i.e., in the model response). The labels in the plot legend were sorted according to the sensitivity of the predictive variables they represent. For instance, the most sensitive predictive variable was the total chlorophyll concentration in the photic zone, that was represented by the first label in the legend, i.e., log[Chl(Zp)] (marked with white circles).

Defining the relative importance of each predictive variable in determining phytoplankton PP is certainly an interesting achievement, but other useful information can be derived from a NN sensitivity analysis. For instance, it is clear that small changes in the input values for a particular predictive variable have minor effects on PP estimates, even in the case of the most sensitive variable (i.e., log-transformed total chlorophyll in the photic zone). This implies that the NN model is very robust with respect to sampling and measurement errors, that seldom exceed this magnitude and that have a negligible effect on model estimates.

It has to be stressed, as far as the reasons for this robustness are concerned, that the NN ability to accept predictive variables that are closely related to each other generates some redundancy in the input information that, in turn, helps in making the model more robust.

3. OTHER APPLICATIONS OF NEURAL NETWORK MODELS IN COASTAL ECOSYSTEMS

3.1. Sediment Organic Matter

Available information about relevant ecological variables usually refers to specific areas where studies have been done. Therefore, if reference values are needed for other areas, the only possible solution is to accept values that have been reported elsewhere, assuming that they approximate the local ones correctly. In some cases it can be useful to interpolate known values either heuristically or by means of sophisticated techniques like kriging or co-kriging, while in others the desired variable can be approximated by means of suitable models. NNs solve the problem by applying both approaches simultaneously. In fact, a NN model can easily take profit of the information about both

spatial structures and correlations between variables. A simple example will demonstrate such a procedure.

Several hundreds of records of sediment organic matter (SOM) are available in the literature for Italian coastal ecosystems, but obviously very little or no information can be retrieved for the majority of coastal sites. Therefore, it is not possible to define correctly—even on the basis of analogies—a range for the expected values.

An empirical model based on an EBP NN was trained to solve this problem, using a set of predictive variables that were selected among the most widely available ones: latitude and longitude (in degrees), depth, sand percentage in sediment, distance from the coastline, distance of the 200 m isobath from the coastline and three variables that account for the morphology of the coastline. The latter variables were weighted to make them less influential in sites that are too close to the coastline (because of the high small-scale variability) or too far from it (because of the reduced influence of the coastline morphology). It is important to notice that except for sand percentage in the sediment, all the predictive variables can be easily derived from maps or geographical information systems (GIS). However, the predictive variables can be regarded as two separate, but not fully independent, subsets that play different roles. The first one, which included the geographical coordinates and the depth, was needed to make the NN model behave like an interpolator, thus reproducing large-scale patterns, whereas the second one, which included the site-specific information, was needed to fine tune the estimates on the basis of predictive variables that account for the local characteristics of the seafloor and for the dynamics of the processes that determine the SOM concentration (for example, sand percentage, grain size, seafloor slope, etc.).

The training procedure was done using 352 records, with 177 records used for validation during the training, to stop the procedure as soon as the validation error began to increase, and 178 were preserved for testing only. Several NN architectures were tested, but the best results were obtained using a 9–7–1 NN and using log-transformed SOM concentrations[3]. A multiple linear regression was also applied to the same data, to compare its results with those provided by the NN. Plots for the estimated vs. observed values in the independent test set, both for the regression and for the NN model, are shown in Fig. 9.
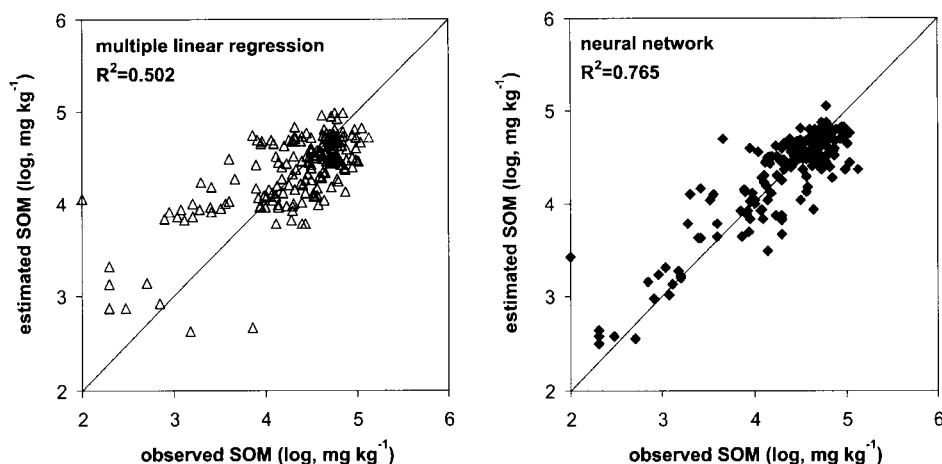
Figure 9. Predicted vs. observed concentrations of sediment organic matter (SOM) in surface sediments of the Italian seas. Results for the test data set (n=178) are shown for both the multiple linear regression model (on the left, white triangles, $R^2 = 0.502$) and the neural network model (on the right, black diamonds, $R^2 = 0.765$).
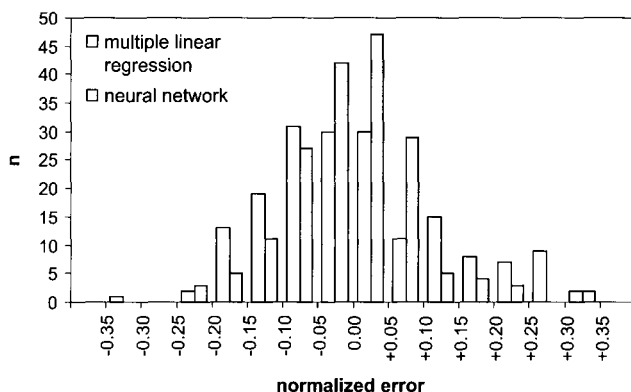
Figure 10. Error distributions for the multiple linear regression (white bars) and the neural network model (grey bars) of sediment organic matter (SOM) in Italian seas. The error distribution was referred to the test set only (n=178) and it was expressed in normalized units (i.e., in the [0,1] interval). The majority (81%) of the deviations from the observed values for the NN model were in the [-0.1,+0.1] interval (i.e., they did not exceed 10% of the SOM concentration range). The multiple linear regression model did not perform as well and only 57% of the deviations were in the [-0.1,+0.1] interval.

It is clear that the neural network model not only provided better predictions than the multiple linear regression in terms of overall accuracy ($R^2 = 0.765$ and $R^2 = 0.502$, respectively), but it was also more consistent when low SOM values were taken into account. In fact, the error distribution for the NN model was more leptokurtic, symmetrical and unbiased than the one for the multiple linear regression model, as shown in Fig. 10.

3.2. Benthic Macro-Invertebrates

Modeling species composition in aquatic communities is becoming a common task in freshwater ecology. In streams and rivers the physical description of a site (for example, slope, distance from the source, vegetation cover, etc.) accounts for a large share of its ecological properties, which in turn allow for predicting fauna and flora composition (see, for instance, Sen and Smeins, 1996; Manel et al., 1999; Hoang et al., 2001; Pearson et al., 2002; etc.). In marine ecosystems this task is more difficult to carry out, mainly because the environmental information cannot be acquired by means of quick visual assessments, but it is still feasible if some suitable predictive data are available.

A sample application aimed at predicting the presence of a benthic macroinvertebrate species in a Mediterranean coastal ecosystem demonstrates the potential of this approach. *Lumbrineris latreilli* (Audouin and Milne Edwards, 1834) is a Polychaete worm that is common in muddy sediments, both in marine and brackish ecosystems. Its distribution, as for most benthic macro-invertebrates, is closely related to edaphic factors. Therefore, information about the sediment can be used to predict the presence of this species.

Six predictive variables were selected: depth, abundance of vegetal and shell detritus (both as percentage of sediment weight) and sediment grain size (three size classes were used, namely gravel, very coarse to fine sand and very fine sand to clay, i.e., $\phi < 0$, $0 \leqslant \phi < 3$ and $\phi \geqslant 3$). Data from 107 records were divided into three sets for training, validating and testing a NN model (54, 27 and 26 records, respectively).

An EBP NN with seven units in the hidden layer provided the best results because it allowed for the correct prediction of the presence of *Lumbrineris latreilli* in 83% of the cases in the training and validation sets and in 77% of the cases in the test set.

It is worth noticing that the output of an EBP NN is actually continuous (i.e., it is a value in the [0,1] interval), which can be regarded as an estimate of the probability of species presence. This way to express species presence is actually closer to the reality than a binary datum, as it takes into account the effects of species density, sample size, spatial heterogeneity, sampling avoidance, etc. A continuous output can be turned easily into a binary form by applying a step function with a 0.5 threshold.

Even though the above-mentioned results were apparently satisfying, it was necessary to check whether they differed significantly from a random choice or not. This problem seems trivial, but it must be carefully taken into account especially when rare or common species are modeled. In fact, if the ratio between presence and absence records is too small or too large, the learning will be biased by the most common instance. In other words, the model—any model, not only a NN one—will always predict absence for very rare species and presence for very common species, independently of environmental predictive data. A "lazy" learning (or calibration, in case of conventional models) makes perfect sense from a purely computational point of view. For instance, if a species is present in only 1% of the records, a model that always predict absence will be right in 99% of the cases. Therefore, producing an almost constant presence prediction is the easiest way to minimize the error if MSE or the percentage of correctly classified instances is used as a criterion.

The only way to avoid training biased models is to train (i.e., to calibrate) them providing a balanced mix of species presence and absence records even when the real proportion is far from unity. In other words, the modeler must provide enough information about the environmental conditions that are related to the rarest response of the species whose presence or absence is to be predicted.

The *Lumbrineris latreilli* model was trained, validated and tested on data in which the balance between presence and absence records was close to optimal (46 presence and 61 absence records). Therefore, the model was not biased and it was able to predict correctly most of both presence and absence cases (Table 2).

However, to evaluate the predictive capabilities of the model a specific test was needed, so the Kappa statistics (Cohen, 1960) was applied. The Kappa statistics is probably the most common criterion for evaluating the performance of models that predict species presence or absence and it allows defining the probability of chance agreement. In the case of the *Lumbrineris latreilli* model, the Kappa statistics computed using the test data in Table 2 was highly significant (K = 0.549, p < 0.001). Hence, the probability that the response of the model is random was very small, so the model can be considered a very good predictor.

4. A COMPARISON BETWEEN NEURAL NETWORKS AND CONVENTIONAL DYNAMIC MODELS

Most NN models are inspired by an empirical modeling approach. In other words, they are used to solve nonlinear regression problems in which one or more variables are estimated on the basis of a set of predictive variables. The steady state models that were presented in the previous sections of this chapter are examples for this kind of approach. However, NNs also have a potential as dynamic modeling tools, especially if their architecture is adapted to this kind of application. For instance, it is possible to add information about the previous states of a system to the values for the forcing functions to improve the predictions for the next state of the system, according to a sort of semi-Markovian scheme. Recurrent NNs are adapted to this way of functioning, as some of their connections link the output units (or the hidden units) to the input ones, according to a typical feedback scheme.

Barciela et al. (1999) presented an interesting comparison between the results of dynamic and NN PP modeling for a coastal embayment. The dynamic model they used was a rather complex one-dimensional, carbon based, size-dependent and compartmental model that was physically forced by

Table 2

Confusion matrices for the neural network model predicting the presence or absence of the benthic Polychaete worm *Lumbrineris latreilli* in a Mediterranean coastal ecosystem on the basis of environmental variables. The results for the training and validation sets are shown in the top table, whereas those for the test set are shown in the bottom table. The model was able to correctly predict species presence or absence in 67 out of 81 cases (82.7%) in the training and validation sets and in 20 out of 26 cases (77.0%) in the test set.

Training and validation sets		Prediction	
		Present	*Absent*
Observation	*Present*	32 (39.5%)	3 (3.7%)
	Absent	11 (13.6%)	35 (43.2%)

Test set		Prediction	
		Present	*Absent*
Observation	*Present*	10 (38.5%)	1 (3.8%)
	Absent	5 (19.2%)	10 (38.5%)

solar radiation, temperature, vertical advection and mixed layer depth. The model had eight state variables: six represented different biotic entities (i.e., mussels and five categories of planktonic organisms), whereas the remaining variables accounted for dissolved inorganic nitrogen and dissolved organic carbon.

The NN approach was based on three different models. Each model was trained on phytoplankton biomass data integrated over a different time interval (i.e., daily, weekly and yearly means were used).

The NN models had six input variables: temperature, irradiance, mixed layer depth, an "upwelling index" and a feedback variable for phytoplankton biomass. The latter was the previous output of the NN model, i.e., the one obtained using values from the previous state of the system (for example, from the day before, in the case of the daily model) for all the other predictive variables. The number of hidden layers (one or two) and the number of units in each hidden layer were determined empirically.

The comparison between dynamical and NN models was done by computing the correlation coefficients between observed and modeled values for both model types. The results showed that the NN models, especially when daily estimates were taken into account, outperformed the conventional dynamic models ($r = 0.36$ for the dynamic model and $r = 0.99$, $r = 0.71$ and $r = 0.32$ for the daily-, weekly- and yearly-integrated NN models, respectively).

These findings support the conclusion that although dynamic simulation models contributed to a better understanding of ecological processes, their predictive potential was low due to uncertainty in the estimation of model parameters, some of which were actually impossible to measure (for example, phytoplankton natural mortality rate). On the other hand, NN models provided very good results, especially for short time scales (i.e., when complex patterns in the time series have to be reproduced), but they cannot contribute as much insight into ecosystem functioning as the dynamic models.

5. DISCUSSION AND CONCLUSIONS

5.1. State-of-the-Art

It would be both tempting and overly simplistic to conclude that NN models are always better than other models. NNs can certainly play a major role in a modeler's "toolbox", but there are certainly many cases in which other approaches are simpler, more accurate or faster.

NNs are particularly effective when a generalized, nonlinear regression problem has to be solved, hence they can be used effectively in empirical modeling (i.e., when values for one or more variables have to be predicted on the basis of values for other variables to which they are linked by known causal relationships or correlations).

The examples given for phytoplankton PP and SOM demonstrated this type of application. However, there are cases in which NN models do not provide results that are significantly different from those that can be obtained by means of more conventional models, while retaining a greater computational burden. For instance, Harding et al. (2002) developed phytoplankton PP models based on multiple linear regression on log-transformed data for Chesapeake Bay. Even though the NN model described in Section 2.4 provided better results than these conventional models, it was able to deliver more accurate predictions because it was using more predictive variables. On the other hand, when a NN model was trained using the same predictive variables as in Harding et al. (2002), the improvement in accuracy over the conventional regressive model was actually marginal. Obviously, in such a case there are viable and simpler alternatives to NN models that may yield comparable results.

Another case in which the NN approach may not be the most suitable is the one that involves the formulation of explicit relationships among variables, thus embedding knowledge about relevant ecological processes in the model. Even though it is possible to use theoretical knowledge for improving NN models (see, for instance, Scardi et al., in press), it is not possible to constrain them completely while retaining all their useful properties.

When species distribution is to be modeled, the available theoretical background is usually very limited. Therefore, an empirical approach based on NN models can be effective in building single species models (Olden and Jackson, 2002), that can provide useful ecological information, especially when modeling key species, such as in the case of *Lumbrineris latreilli*. If sufficient data are available (unfortunately this is rare), it is possible to predict simultaneously more than one species and, in theory, a single NN model with many outputs could model the whole community. In practice, this approach is actually feasible when only a subset of species is selected (for example, a syntaxon, the most abundant species, the most sensitive species, etc.). However, there is evidence of improved accuracy of these more complex models compared to a set of single-species models because unknown interactions among species can be represented implicitly by the complex structure of the connections between the units of a NN. In theory, training a complex NN model involves the estimation of a large number of weights, which can be successfully done only if based on large data sets. In practice, species tend to occur in a rather small number of combinations that are obviously determined by inter-specific interactions. Hence, the real complexity of the problem to be solved is often much lower than expected and training the NN model is feasible even when a more limited (but still large enough) number of records is available.

However, even single-species models can play a very useful role. For instance, modeling a species that is sensitive to pollution using only information from pristine sites provides a tool for defining the expected distribution of that species assuming that no pollution exists. Therefore, deviations from the expected distribution can be easily recognized and related to potential pollution sources.

Other machine-learning techniques are now competing with NNs as new tools for ecological modeling. They are not only aimed at solving generalized regression problems, and significantly broaden the spectrum of potential modeling applications. Applications of decision trees, genetic algorithms, case-based reasoning and artificial life, for instance, provide interesting ecological results and they

certainly can play a role in coastal modeling too (Fielding, 1999). However, more research is needed because none of these methods has been so widely applied to ecological research as NNs.

Finally, when compared to conventional dynamic models for ecological applications, NNs easily outperformed, especially when the response of modeled variables to predictive variables is complex and nonlinear.

5.2. Perspectives

The majority of the existing applications are based on common types of NN, namely EBP NNs and SOMs. The latter have been used for ordination and/or classification tasks, whereas EBP NNs have been used mainly for generalized regression and pattern recognition tasks. Recurrent NNs, that are closely related to basic EBP NNs can also be useful in modeling dynamic systems. Of course, other types of NNs have also been used (for example, Radial Basis Function NNs), as well as other training algorithms (for example, Quickprop), but their ecological applications are rarely exploited. This probably depends on the fact that ecological data are often so variable that minor differences between NN modeling techniques are really difficult to detect.

Nevertheless, sometimes the usual modeling tools (EBP NNs in the case of the applications that have been presented in this chapter) can still be improved in the light of the specific problems that have to be solved. According to Scardi (2001), at least three different enhancements of a NN model should be considered.

Co-predictors (i.e., variables that are easily available and tend to co-vary with the variables to be modeled), although not explicitly relevant from a causal or even logical point of view, should be carefully considered as supplementary input variables.

Available knowledge about the relationships that are to be modeled can be used to constrain the usual NN training procedures. For instance, the compliance of the NN outputs with an expected response (for example, monotonic) can be checked instead of (or in addition to) MSE or similar criteria to validate the training procedure. Another effect of a *constrained training* procedure is that using knowledge instead of data for validation makes more data available for training, so that the accuracy of a NN model may be increased.

NNs are perfect tools for developing *metamodeling* applications. In fact, in many cases not only data, but also one or more models are available for describing a given ecological process. A NN model can easily "learn" from both data and other models, working as a sort of "envelope" for all the available information with no need to specify an explicit formulation. This approach can benefit from real data when they are available and use estimates provided by models when data are scarce or absent. A NN *metamodeling* approach can also be useful when a consensus model is to be developed on the basis of other models.

Finally, specific adaptations of NN training and validation procedures should be developed to take the peculiarities of coastal ecological data into account. For instance, in both NN and conventional models the error computation is usually focused only on dependent variables (i.e., on the output variables in NNs). This implies that the independent variables (i.e., the input variables in NNs) are not affected by measurement errors. In reality, of course, this is not the case. In coastal marine ecosystems most variables are affected not only by measurement errors, but also by a very high variability in time and space. Therefore, measuring the errors with respect to both dependent and independent variables could be more efficient and ecologically sound (such an approach is used when the major axis or the reduced major axis is used instead of a linear regression). In the same way, suitable distance or similarity measures should be used instead of MSE when comparing records that involve presence or abundance of species, because this kind of data cannot be processed as mere quantitative information.

In conclusion, NN models are powerful and flexible tools for coastal ecological modeling because they are able to cope with complex, ill-defined, nonlinear problems. Like all the other types of empirical models, NN models are just as good as the data on which they are based, but they have

additional potential that can be easily exploited by modelers for incorporating ecological knowledge, integrating different sources of information and handling very complex relationships.

ACKNOWLEDGMENTS

ENDNOTES

1. Strategies for using all the data for both training and validation exist, but they are only to be considered when not enough data are available.
2. A Java applet is available for running the model from your browser (http://www.mare-net.com/mscardi/work/nn/cbjavann.htm).
3. As already mentioned in Section 2.3.2, the rationale for log-transforming the variable to be predicted is related to the way the errors are to be computed. Log-transformed data allow one to assign a (relatively) smaller weight to deviations in large values (that are affected by the largest sampling and measurement errors).

LIST OF SYMBOLS AND ACRONYMS

ϕ	—	measure of grain size in sediment analysis
μ	—	exact value of the mean
σ	—	exact value of the standard deviation
B_0	—	surface phytoplankton biomass
Dl	—	day length
I_0	—	surface downwelling irradiance
K	—	Kappa statistics (Cohen, 1960)
Chl	—	chlorophyll-a concentration
P_{opt}^B	—	maximum observed primary productivity rate in the water column normalized to biomass
PP_0	—	surface phytoplankton primary production
r	—	Bravais-Pearson correlation coefficient
R^2	—	determination coefficient, i.e., the square of the correlation coefficient or the fraction of variance explained by a model
T_0	—	surface water temperature
Z_{eu}	—	the depth at which irradiance is 1% of the surface value
i	—	input values
h	—	hidden units outputs
o	—	output values
W	—	input to hidden layer synaptic weights
Z	—	hidden to output layer synaptic weights
y	—	expected output values
n_i	—	number of units in the input layer
n_h	—	number of units in the hidden layer

n_o	—	number of units in the output layer
δ_l^o	—	output to hidden layer synaptic weight adjustment
δ_k^h	—	hidden to input layer synaptic weight adjustment
η	—	learning rate
ANN	—	Artificial Neural Network
CTD	—	Conductivity, Temperature, Depth (used for oceanographic probes)
EBP	—	Error Back-Propagation
GIS	—	Geographical Information System
MSE	—	Mean Square Error
NN	—	Neural Network
PP	—	Primary Production
SOM	—	(1) Self-Organizing Map; (2) Sediment Organic Matter
VGPM	—	Vertically Generalized Production Model

APPENDIX 1

An Introduction to Error Back-Propagation Neural Networks

The multilayer perceptrons are certainly the most widespread neural networks (NNs) and the error back-propagation (EBP) is by far the most common algorithm in all kind of applications. These NNs consist of three or more (but usually no more than four) layers of units. In particular, all the EBP NNs have one input layer (**i**) and one output layer (**o**), whereas they can have one or more hidden layers (**h**). Very often, however, there is only one hidden layer, as shown in the example in Fig. 11. Units in the hidden and output layer receive the outputs of the units in the previous layer (input and hidden, respectively), whereas units in the input layer obviously receive inputs from the user.

The connections between units are associated to coefficients (**W** and **Z** in Fig. 11), often called *synaptic weights* because of the obvious analogies with real neurons, that are iteratively adjusted during the training process, i.e., as long as their changes allow to obtain output values that are closer to the expected ones.
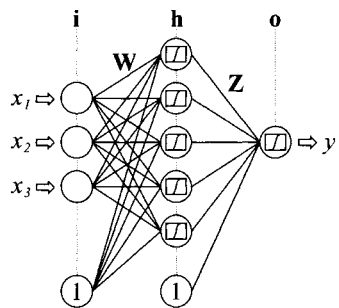
Figure 11. The multilayer perceptron is the most common type of neural network. It is very often trained using the error back-propagation algorithm (see text). The multilayer perceptron shown in this figure has a 3–5–1 structure (i.e., it has three input units (**i**), a single hidden layer with five units (**h**) and a single output unit (**o**)). The connections between units (solid lines) are associated to synaptic weights (**W, Z**) that are iteratively adjusted during the training procedure. Two bias units are also shown (labeled with 1, i.e., their output value). The role of bias units is similar to the one of the constant term in regression models. The small plots shown within the units in the hidden and output layers represent the activation functions.

The NN in Fig. 11 has three units in the input layer, five units in the hidden layer and a single output unit. Therefore, its structure can be summarized as 3–5–1. Additional units with a constant output (usually 1), called *bias units*, are also shown in the input and hidden layers. Their role in these NNs is very similar to that of the constant term in multiple regression (i.e., they allow to shift the origin of the space defined by the input variables).

Each unit in hidden and output layers passes the sum of its inputs to an *activation function* (i.e., a differentiable function that returns the output from that unit). Several functions can be used as activation functions, but the most common choice is a sigmoid function (see equation (2), this chapter).

Provided that enough data are available for training, that the activation functions of the hidden layer units are nonlinear and that the number of the units in the hidden layer(s) is large enough, an EBP NN is able to approximate any nonlinear function (Hornik et al., 1989).

A NN works at its best if all its synaptic weights have been properly tuned. The error back-propagation algorithm is a way to compute these weights and involves four steps:
(1) the network is initialized by assigning random values to its synaptic weights;
(2) a training pattern is passed to the NN input layer and propagated through the network to compute an output value for each output unit;
(3) computed outputs are compared with the expected outputs;
(4) a backward pass through the network is performed, changing the synaptic weights on the basis of the observed output errors.
Steps 2 through 4 are iterated for each pattern in the training set, then the network performance is checked (usually on the basis of a mean squared error criterion) and a new set of training patterns is submitted to the network (i.e., a new *epoch* is started), if further optimization is needed.

Focusing on the most common case (i.e., on EBP NNs with a single hidden layer), the first step in the forward propagation calculations involves the computation of the weighted sums of input values that are passed to the hidden layer

$$h_k = \sum_{j=1}^{n_j+1} i_j \, w_{jk} \qquad (k = 1, \ldots, n_h) \tag{6}$$

where i_j are the NN inputs (included the bias unit, that is always equal to 1) and w_{jk} are the weights of the connections between input and hidden layers. To compute the outputs from the hidden layer, these weighted sums are passed to the activation function, except the one for the bias unit that is forced to have an output equal to 1

$$h_k = f(h_k) \tag{7}$$

$$h_{n_h+1} = 1 \tag{8}$$

Then, the network outputs are computed in the same way

$$o_l = \sum_{k=1}^{n_h+1} h_k \, z_{kl} \qquad (l = 1, \ldots, n_o) \tag{9}$$

$$o_l = f(o_l) \tag{10}$$

After the forward propagation, the estimated outputs o_l are compared with the expected outputs y_l and a mean square error *MSE* for the current pattern is computed as

$$MSE = \frac{1}{n_o} \sum_{l=1}^{n_o} (y_l - o_l)^2 \tag{11}$$

528

Then, in the back-propagation step, all the synaptic weights are adjusted to follow a gradient descent on the error surface. Therefore, for the connections between hidden and output layers, the weights z_{kl} are changed into

$$z_{kl} = z_{kl} + \eta \, \delta_l^o \, h_k \qquad (k = 1, \dots, n_h + 1; \quad l = 1, \dots, n_o) \tag{12}$$

where η is a constant (learning rate) and

$$\delta_l^o = (y_l - o_l) \cdot f'(o_l) \tag{13}$$

The weights w_{jk} of the connections between hidden and input layer are also adjusted

$$w_{jk} = w_{jk} + \eta \, \delta_k^h \, i_j \qquad (k = 1, \dots, n_h + 1; \quad j = 1, \dots, n_i + 1) \tag{14}$$

where δ_k^h are computed as

$$\delta_k^h = f'(h_k) \cdot \sum_{l=1}^{n_o} \delta_l^o z_{kl} \tag{15}$$

At the beginning of the training procedure the NN weights are randomly initialized and the available data are divided into three sets for training, validation, and testing, respectively. The training data are then passed to the NN to compute the output values. The deviations of those output values from the expected ones (i.e., from the observed data) in the training set are used in order to tune the error back-propagation (i.e., the learning procedure), whereas the deviations from the validation set are used as a criterion for stopping the learning procedure. In other words, as long as an EBP NN keeps improving with respect to the validation set, the learning phase can be continued and the training data can be submitted to the NN again. The network training is iterated until a given condition is met. Minimization of the mean square error is usually involved, but other criteria can also be used.

It has to be stressed, however, that the weight adjustment process does not always return the same result as many non-deterministic factors (for example, different starting values of the synaptic weights) affect the network training. This means that the trajectory of the gradient descent on the error surface is often attracted by local minima. Therefore, repeating the learning procedure as many times as possible is usually a good practice.

APPENDIX 2

A Few Useful Links to Web Resources
- Information and links about ecological applications of NNs can be found on a dedicated page on the web site of the Author of this chapter. (http://www.mare-net.com/mscardi/work/nn/nn.htm)
- Other useful resources about NNs and other machine learning techniques to ecology are listed in the Links page at the web site of the 3rd Conference of the International Society for Ecological Informatics (http://www.isei3.org/links.htm).
- A huge amount of basic and advanced information about NN theory as well as news about books, software, etc. can be found in the NN FAQ maintained by Warren Sarle at SAS Institute (ftp://ftp.sas.com/pub/neural/FAQ.html).
- Finally, the Fortran source code for a simple EBP NN implementation, which can be used as a basis for further development, can be requested from the Author (mscardi@mclink.it)

REFERENCES

Aguilera, P.A., Garrido Frenich, A., Torres, J.A., Castro, H., Martinez Vidal, J.L., and Canton, M., 2001. Application of the Kohonen neural network in coastal water management: Methodological development for the assessment and prediction of water quality. Water Research, 35 (17): 4053–4062.

Aussem, A., and Hill, D., 1999. Wedding connectionist and algorithmic modelling towards forecasting *Caulerpa taxifolia* development in the north-western Mediterranean sea. Ecological Modelling, 120: 225–236.

Aussem, A., and Hill, D., 2000. Neural-network metamodelling for the prediction of *Caulerpa taxifolia* development in the Mediterranean sea. Neurocomputing, 30: 71–78.

Balls, G.R., Palmer Brown, D., and Sanders, G.E., 1996. Investigating microclimatic influences on ozone injury in clover (*Trifolium subterraneum*) using artificial neural networks. New Phytology, 132: 271–280.

Baran, P., Lek, S., Delacoste, M., and Belaud, A., 1996. Stochastic models that predict trouts population densities or biomass on macrohabitat scale. Hydrobiologia, 337: 1–9.

Barciela, R.M., García, E., and Fernández, E., 1999. Modelling primary production in a coastal embayment affected by upwelling using dynamic ecosystem models and artificial neural networks. Ecological Modelling, 120: 199–211.

Behrenfeld, M.J., and Falkowski, P.G., 1997. Photosynthetic rates derived from satellite-based chlorophyll concentration. Limnology and Oceanography, 42 (1): 1–20.

Bradshaw, C.J.A., Davis, L.S., Purvis, M., Zhou, Q., and Benwell, G.L., 2002. Using artificial neural networks to model the suitability of coastline for breeding by New Zealand fur seals (*Arctocephalus forsteri*). Ecological Modelling, 148: 111–131.

Brey, T., and Gerdes, D., 1998. High Antarctic macrobenthic community production. Journal of Experimental Marine Biology and Ecology, 231: 191–200.

Brey, T., Jarre-Teichmann, A., and Borlich, O., 1996. Artificial neural network versus multiple linear regression: Predicting P:B ratios from empirical data. Marine Ecology Progress Series, 140: 251–256.

Chon, T.-S., Park, Y.S., Moon, K.H., and Cha, E.Y., 1996. Patternizing communities by using an artificial neural network. Ecological Modelling, 90: 69–78.

Cohen, J., 1960. A coefficient of agreement of nominal scales. Educational and Psychological Measurement, 20: 37–46.

Colasanti, R.L., 1991. Discussions of the possible use of neural network algorithms in ecological modelling. Binary, 3: 13–15.

Cole, B.E., and Cloern J.E., 1984. Significance of biomass and light availability to phytoplankton productivity in San Francisco Bay. Marine Ecology Progress Series, 17: 15–24.

Cole, B.E., and Cloern J.E., 1987. An empirical model for estimating phytoplankton productivity in estuaries. Marine Ecology Progress Series, 36: 299–305.

Deo, M.C., and Sridhar Naidu, C., 1999. Real time wave forecasting using neural networks. Ocean Engineering, 26: 191–203.

Deo, M.C., Jha, A., Chaphekar, A.S., and Ravikant, K., 2001. Neural networks for wave forecasting. Ocean Engineering, 28: 889–898.

Dimopoulos, I., Bourret, P., and Lek, S., 1995. Use of some sensitivity criteria for choosing networks with good generalization ability. Neural Processing Letters, 2: 1–4.

Dimopoulos, I., Chronopoulos, J., Chronopoulou Sereli, A., and Lek, S., 1999. Neural network models to study relationships between lead concentration in grasses and permanent urban descriptors in Athens city (Greece). Ecological Modelling, 120 (2–3): 157–165.

Edwards, M., and Morse, D.R., 1995. The potential for computer-aided identification in biodiversity research. Trends in Ecological Evolution, 10 (4): 153–158.

Eppley, R.W., Stewart, E., Abbott, M.R., and Heyman, U., 1985. Estimating ocean primary production from satellite chlorophyll. Introduction to regional differences and statistics for the Southern California Bight. Journal of Plankton Research, 7: 57–70.

Fielding, A.H., 1999. An introduction to machine learning methods. In: Fielding, A.H. (Editor), Machine Learning Methods for Ecological Applications, pp. 1–35. Boston, Dordrecth, London: Kluwer Publishers.

Garson, G.D., 1991. Interpreting neural network connection weights. Artificial Intelligence Expert, 6: 47–51.

Giraudel, J.L., and Lek, S., 2001. A comparison of self-organizing map algorithm and some conventional statistical methods for ecological community ordination. Ecological Modelling, 146: 329–339.

Giske, J., Huse, G., and Fiksen, O., 1998. Modelling spatial dynamics of fish. Reviews in Fish Biology and Fisheries, 8: 57–91.

Guégan, J.F., Lek, S., and Oberdorff, T., 1998. Energy availability and habitat heterogeneity predict global riverine fish diversity. Nature, 391: 382–384.

Györgyi, G., 1990. Inference of a rule by a neural network with thermal noise. Physical Review Letters, 64: 2957–2960.

Hammitt, A.M., and Bartlett, E.B., 1995. Determining functional relationships from trained neural networks. Mathematical and Computer Modelling, 22: 83–103.

Harding, L.W., Jr., Mallonee, M.E., and Perry, E.S., 2002. Toward a predictive understanding of primary productivity in a temperate, partially stratified estuary. Estuarine, Coastal and Shelf Science, 55: 437–463.

Haykin, S., 1994. Neural Networks: A Comprehensive Foundation. New York, NY: Macmillan/IEEE Press, 696p.

Hoang, H., Recknagel, F., Marshall, J., and Choy, S., 2001. Predictive modelling of macroinvertebrate assemblages for stream habitat assessments in Queensland (Australia). Ecological Modelling, 195: 195–206.

Hornik, K., Stinchcombe, M., and White, H., 1989. Multilayer feedforward networks are universal approximators. Neural Networks, 2: 359–366.

Huang, W., and Foo, S., 2002. Neural network modeling of salinity variation in Apalachicola River. Water Research, 36: 356–362.

Jeong, K.-S., Joo, G.-J., Kim, H.-W., Ha, K., and Recknagel F., 2001. Prediction and elucidation of phytoplankton dynamics in the Nakdong River (Korea) by means of a recurrent artificial neural network. Ecological Modelling, 146: 115–129.

Keiner, L.E., and Yan, X.-H., 1998. Neural network model for estimating sea surface chlorophyll and sediments from Thematic Mapper imagery. Remote Sensing in the Environment, 66: 53–165.

Kingston, K.S., Ruessink, B.G., van Enckevort, I.M.J., and Davidson, M.A., 2000. Artificial neural network correction of remotely sensed sandbar location. Marine Geology, 169: 137–160.

Kremer, J.N., and Nixon, S.W., 1978. A Coastal Marine Ecosystem: Simulation and Analysis. New York: Springer-Verlag, 217p.

Lee, T.L., and Jeng, D.S., 2002. Application of artificial neural networks in tide-forecasting. Ocean Engineering, 29: 1003–1022.

Lek, S., Delacoste, M., Baran, P., Dimopoulos, I., Lauga, J., and Aulagnier, S., 1996a. Application of neural networks to modelling nonlinear relationships in ecology. Ecological Modelling, 90 (1): 39–52.

Lek, S., Belaud, A., Baran, P., Dimopoulos, I., and Delacoste, M., 1996b. Role of some environmental variables in trout abundance models using neural networks. Aquatic Living Research, 9: 23–29.

Lek, S., and Guégan, J.F., 1999. Artificial neural networks as a tool in ecological modelling. An introduction. Ecological Modelling, 120: 65–73.

Manel, S., Dias, J.-M., and Ormerod, S.J., 1999. Comparing discriminant analysis, neural networks and logistic regression for predicting species distributions: A case study with a Himalayan river bird. Ecological Modelling, 120: 337–347.

Mase, H., and Kitano, T., 1999. Prediction model for occurrence of impact wave force. Ocean Engineering, 26: 949–961.

Mase, H., Sakamoto, M., and Sakai, T., 1995. Neural network for stability analysis of rubble-mound breakwaters. Journal of Waterway, Port, Coastal and Ocean Engineering, 121: 294–299.

Olden, J.D., and Jackson, D.A., 2002. A comparison of statistical approaches for modelling fish species distributions. Freshwater Biology, 47: 1976–1995.

Pearson, R.G., Dawson, T.P., Berry, P.M., and Harrison, P.A., 2002. SPECIES: A spatial evaluation of climate impact on the envelope of species. Ecological Modelling, 154: 289–300.

Pineda, F., 1987. Generalization of backpropagation to recurrent neural networks. Physical Review Letters, 19 (59): 2229–2232.

Recknagel, F., 2001. Applications of machine learning to ecological modeling. Ecological Modelling, 146: 303–310.

Recknagel, F., French, M., Harkonen, P., and Yabunaka, K.I., 1997. Artificial neural network approach for modelling and prediction of algal blooms. Ecological Modelling, 96: 11–28.

Recknagel, F., Fukushima, T., Hanazato, T., Takamura, N., and Wilson, H., 1998. Modelling and prediction of phyto- and zooplankton dynamics in Lake Kasumigaura by artificial neural networks. Lakes & Reservoirs, 3: 123–133.

Rumelhart, D.E, Hinton, G.E., and Williams, G.E., 1986. Learning representations by back-propagating errors. Nature, 323: 533–536.

Sandidge, J.C., and Holyer, R.J., 1998. Coastal bathymetry from hyperspectral observations of water radiance. Remote Sensing of the Environment, 65: 341–352.

Scardi, M., 1996. Artificial neural networks as empirical models of phytoplankton production. Marine Ecology Progress Series, 139: 289–299.

Scardi, M., 2000. Neuronal network models of phytoplankton primary production. In: Lek, S., and Guégan, J.-F. (Editors), Artificial Neuronal Networks: Application To Ecology And Evolution, pp. 115–129. Berlin/Heidelberg: Springer-Verlag.

Scardi, M., 2001. Advances in neural network modeling of phytoplankton primary production. Ecological Modelling, 146: 33–45.

Scardi, M., and Harding, L.W., Jr., 1999. Developing an empirical model of phytoplankton primary production: A neural network case study. Ecological Modelling, 120: 213–223.

Scardi, M., Lek, S., Park., Y.S., Verdonschot, P., and Jørgensen, S.E., in press. Improving neural network models by means of theoretical ecological knowledge. Ecological Modelling, in press.

Sen, S.T., and Smeins, F.E., 1996. Predicting grassland community changes with an artificial neural network model. Ecological Modelling, 84: 91–97.

Smith, R.C., and Baker, K.S., 1978. The bio-optical state of ocean waters and remote sensing. Limnology and Oceanography, 23 (2): 247–259.

Ultsch, A., and Röske, F., 2002. Self-organizing feature maps predicting sea levels. Information Sciences, 144: 91–125.

Walter, M., Recknagel, F., Carpenter, C., and Bormans, M., 2001. Predicting eutrophication effects in the Burrinjuck Reservoir (Australia) by means of the deterministic model SALMO and the recurrent neural network model ANNA. Ecological Modelling, 146: 97–113.

Yabunaka, K., Masaaki, H., and Murakami, A., 1997. Novel application of a back-propagation artificial neural network model formulated to predict algal blooms. Water Science Technology, 36 (5): 89–97.

Zhang, Y., Pulliainen, J., Koponen, S., and Hallikainen, M., 2002. Application of an empirical neural network to surface water quality estimation in the Gulf of Finland using combined optical data and microwave data. Remote Sensing of the Environment, 81: 327–336.

Chapter 20

Space-Time Transfer Function Models of Beach and Shoreline Data for Medium-Term Shoreline Monitoring Programs

Placido D. Lavalle

Department of Earth Sciences, School of Physical Sciences, University of Windsor, Windsor, Ontario, Canada N9B 3P4

1. INTRODUCTION

Although it is necessary to gain insights on the long-term temporal and spatial dynamics of the nearshore system by fitting models to collected data there is, nevertheless, a paucity of research work on space-time series modeling of beach and shoreline data (Finkl, 2002). This could be attributed to the fact that most researchers have concentrated only on analyzing short-term (less than 10 years) beach and shoreline data with various statistical techniques. For example, several researchers have used the empirical eigenfunction technique to analyze large data sets that describe variations in beach profile configurations (Winant et al., 1975; Aubrey, 1979; Bowman, 1981; Fisher et al., 1984; Wood and Weishar, 1984; Aubrey and Ross, 1985; Lins, 1985; Ostrowski et al., 1990; Pruszak, 1993; Hsu et al., 1994; Reeve et al., 2001). While eigenfunction analysis can provide valuable insights on the dissimilarities of profile lines and their responses, the technique relies on interpretations regarding the processes influencing morphological changes.

Another statistical method, the theory of regional variables or geostatistics, has been used by Dolan et al. (1992). Geostatistics, based on the spatial continuity of natural phenomena, has been found to be effective to estimate the alongshore rates of change and spatial variations along profile transects. Shoreline rates of change which exhibit a nearest neighbor effect or spatial autocorrelation can be highlighted with the theory of regionalized variables which uses the random function concept to model the influence of nearby points. "The autocorrelation phenomenon reflects the spatial continuity of the driving processes which produce a measurable response such as shoreline change" (Dolan et al., 1992, p. 264). Swales (2002) used geostatistical methods to deal with short-term changes in beach morphology, but the method is not suited to the discrimination between spatial effects and the various time series movements over a relatively long time period.

Spectral analysis techniques are also applicable for analyzing a time series of data from topographic profiles, and other natural time series (for example, river discharge, daily temperature, lake turbidity, river planform) with a uniform sampling interval (Hegge and Masselink, 1996). The results of the spectral analysis represent the amount of variance of the time series as a function of frequency. The time series analysis techniques of parametric spectra, autocorrelation, and cross-correlation were utilized by Walton (1999) to investigate shoreline planform advance and recession rates for a coastal segment of Florida. The analysis of the spatial data allowed for the identification of low frequency rhythmic patterns in the shoreline. The low frequency shoreline oscillations were found to be non-stationary in time. Spectral analysis assumes that deterministic processes are operating in the system and that the data set is continuous. Evidently, our beach data are discrete and stochastic, so spectral methods may not be appropriate.

Transfer function models have been employed to study serial relationships between system inputs and outputs for stream flow data and space-time studies in agricultural and medical geography.

Gurnell and Fenn (1984) analyzed serial relationships between stream suspended sediment concentrations and pro-glacial streams discharge in Norway, while Lemke (1990; 1991) utilized transfer function models to examine relationships between sediment loads and stream discharge in Iowa. Martin and Oeppen (1976) utilized transfer function methods to study space-time patterns of fowl pest disease infestations in Britain as well as patterns of beef fat-stock supply in Britain. In another study, Bennett (1979) provides a detailed treatment describing how many time-space systems might be analyzed using transfer function models, while Lai (1979) presents a simpler discussion of the mechanics of transfer function modeling, which is based on the seminal work by Box and Jenkins (1970; 1976).

While different statistical techniques can be used to analyze beach and shoreline data far more research remains to be done in explaining what types of statistical models best fit long-term beach and shoreline data. This chapter will, therefore, concentrate on utilizing Box-Jenkins (1976) transfer function modeling procedures to identify models which best describe a moderately long time series (1978–2001) of beach sediment flux and shoreline change data. The data to be modeled are from the Northeast Beach, Point Pelee, Lake Erie, Canada. Before presenting the procedures and results of the Box-Jenkins modeling approach the chapter provides a brief description of the study area and the data collection methodology.

2. THE NORTHEAST BEACH STUDY AREA

Point Pelee is located south of the forty-second parallel, and extends 10 km into the western basin of Lake Erie (Fig. 1). Point Pelee contains a large marsh, and is flanked by beach systems, including the Northeast Beach. The Northeast Beach is characterized by periodic episodes of erosion. Consequently, a shoreline monitoring program was initiated in 1978 when an artificial berm-beach complex was constructed over a major breach in the barrier beach system (LaValle and Lakhan, 1997a). To assess changes in the shoreline and morphology of the beach Kuznik et al. (1986) examined the collected data and indicated that the sediment changes along the profiles of the Northeast Beach exhibited distinctive patterns of erosion and degradation. Since the report by Kuznik et al. (1986), research by LaValle and Lakhan (1997b) has shown that sediment renourishment programs, construction and replacement of infrastructure erosional control devices, and high lake levels have combined to affect the spatial and temporal variability at the Northeast Beach.

3. DATA COLLECTION METHODOLOGY

Since May, 1978, a cooperative shoreline monitoring program involving the University of Windsor and Parks Canada has been carrying out semiannual topographic and bathymetric surveys at the Northeast Beach, Point Pelee. Semiannual topographic and bathymetric data are collected over a predetermined grid established by Setterington (1978). This shoreline monitoring program is designed to assess the relative effectiveness of the various erosion control programs encountered along Point Pelee. The monitoring program entails the following procedures:

- the establishment of a standardized set of survey baselines and sampling grids along key beach sites;
- the establishment of standardized data collection and data analysis procedures which are inexpensive and require only simple equipment; and
- the utilization of standardized analytical procedures for spatial-temporal data analysis to isolate any significant trends and patterns of change along the beach systems.
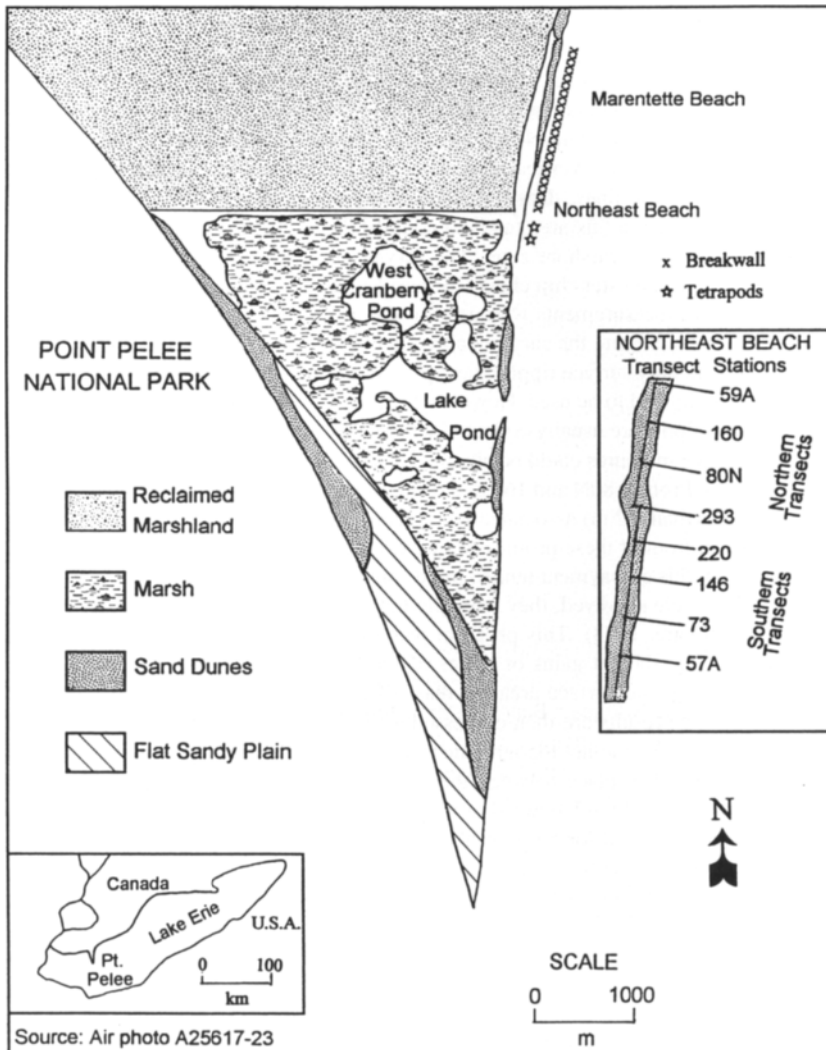
Figure 1. The Northeast Beach at Point Pelee, Lake Erie, Canada.

Data collection was limited mainly to semiannual simple topographic and bathymetric surveys on the pre-established grid, because funding constraints imposed by Parks Canada allowed only two beach surveys to be executed per annum.

The data for this chapter were obtained semiannually from seven profile transects (hereinafter referred to as profiles) on the Northeast Beach for all years between May 1978 and November 2001. Early May and November were selected, because these periods fall roughly midway between the lake level maxima in mid-July and the lake level minima in mid-January The seven profiles (57A, 73, 146, 220, 293, 80N, and 160) shown in Fig. 1 are oriented perpendicular to the shoreline, and are between Park Survey Monument 59A (north) and Park Survey Monument 57A (south). Data from the seven

beach profiles, which are 74–80 m apart, were collected in May and November of each year. Standard leveling methods, using an automatic level, were employed to collect land measurements along each profile. Measurements were taken at 5 m intervals or at each major change of slope. Since the longest distance between the instrument and any rod point rarely exceeded 30 m, horizontal distances could be estimated to within 1–3 cm, and elevations could be read to the nearest centimeter. The profile transect graphs were drafted at a vertical scale of 1:100, and a horizontal scale of 1:500.

By extending the profile lines, data were also collected for at least 100 m or until a depth of 4.3 m was reached, which in this area tends to identify the seaward limit of significant cross-shore sediment movement in the nearshore zone. The survey into the nearshore zone was done with the aid of a motorized boat, Foresters hip chain (for horizontal control) and a long stadia rod (for depth measurements). Depth measurements were read to the nearest 5 cm and rounded off to the nearest 0.1 m mark. In order to execute the survey, calm conditions were chosen with offshore winds being less than 15 km/h, and only surface ripples were present. In both May and November meteorological windows of opportunity had to be used. However, the two variables (beach flux and shoreline change used in this investigation were usually collected within 10–15 m of the shoreline so reasonable accurate depth and distance measures could be obtained. The exception to this situation occurred between 1985 and 1987 along Profiles 80N and 160 as a result of the development of a large very shallow embayment (depths less than 1.2 m) associated with record high water levels and the failure of a line of concrete tetrapods in front of these profiles. Under calm conditions, depth measurements shoreward from the tetrapods in this embayment tended to be consistent in several trials.

Once the profiles were surveyed, they were plotted using a microcomputer program titled GRA-PHER (Golden Software, 1988). This program was used to plot two successive surveys for each profile, and to calculate the net gains or losses of sedimentary material along the profile line. By using elevation changes and surface area the mass of material gained or lost between observation times is calculated. The results are then expressed as beach net sediment flux (B) for each profile. For this study B represents the net topographic volumetric change per square meter of a one meter wide transect that has taken place between the most lakeward shoreline position observed during the survey time interval, and the landward terminus of the beach. In addition to B data, changes in shoreline position are obtained for each profile by determining the net difference in the distance of the shoreline from the baseline for successive surveys. Net shoreline positional change (S) can thus be taken as being the net displacement of the shoreline observed over the survey interval.

4. DATA ANALYSIS

The data set for analysis represents one of the longest continuous records of shoreline change and beach sediment supply fluctuations collected using a standardized methodology. While the data set is not as long as that preferred by Leatherman et al. (1997) for long-term trend analysis using regression methods, it is longer than most of the detailed short-term quantitative shoreline studies cited by Finkl (2002). An examination of the trend analysis described by Leatherman et al. (1997) leads to the consideration of whether the regression coefficient estimating the rate of change is not biased by serial autocorrelation effects. If this is so then Box-Jenkins (1976) time series analysis methods may be more appropriate. On the other hand, Smith and Benson (2000) argue that monthly surveys are necessary to adequately sample short-term variations in beach systems. Monthly surveys would have yielded better data, but as mentioned above, the timing of the surveys and the sampling grid were decided on by Parks Canada.

In analyzing the collected data (LaValle, 1978-2001) transfer function models are used because they allow the investigator to simultaneously assess seasonal or longer term cyclical or pseudo-cyclical movements through time or space in systems characterized by very strong random processes

which are described by discrete data sets, if sufficient data are available. Also, they can be used to estimate the relative limits of predictability in a system characterized by strong random processes.

Both serial and spatial autocorrelation effects will be assessed, thereby enhancing the explanatory power of medium long-term shoreline monitoring programs, while identifying the random component of the shoreline dynamics. In fact, transfer function methodology could also be employed in short-term monthly studies (5–10 years) with more than 48 surveys or long-term annual studies with at least 50 years of record. In the case of monthly surveys, this methodology will enable the investigator to differentiate between seasonal and long-term serial processes.

5. REMARKS ON THE BOX-JENKINS MODELING APPROACH

In summarizing the use of standard Box-Jenkins (1970; 1976) univariate time series modeling procedures, LaValle et al. (2001) stated that the autocorrelation coefficients are plotted against the lag intervals on a graph called a correlogram, and the resulting function is called the autocorrelation function (ACF). In addition, the partial autocorrelation coefficients are calculated for the same number of lag intervals where a partial autocorrelation for lag i represents the autocorrelation at lag i with the effects of the autocorrelations at lag intervals 1 through $i-1$ filtered out. (This is similar in nature to a partial correlation coefficient). The partial autocorrelation coefficients are plotted against the lag intervals on a partial correlogram depicting the partial autocorrelation function (PACF). Based on an examination of the ACF and the PACF a model is fit to the data. If the ACF decays exponentially to near zero and the PACF shows a distinct spike at lag 1, then a long memory Markov process may characterize the data, and a first-order autoregressive model AR(1) might adequately describe the data. Such a model would have the form: $Z_t = \phi Z_{t-1} \pm \epsilon$, where ϕ is the autoregressive parameter and ϵ is the residual or error term. If such a model is to be accepted then the ϵ terms should not be autocorrelated.

In some cases "transients" or random shocks associated with short memory moving averages processes (MA) may produce an ACF with a single significant spike at lag 1 and no significant autocorrelations elsewhere. In this case one may fit a first-order moving averages model which has the form: $Z_t = \epsilon_t \pm \theta \epsilon_{t-1} \pm e$ where θ is the estimated moving average parameter and ϵ_{t-1} is the residual at lag $t-1$ while ϵ_t is the residual term and e is an error term. As mentioned previously, after the model is fitted, the error terms should not be autocorrelated if the model is to be accepted. Complex correlograms and partial correlograms may suggest that a combination of autoregressive (AR) and moving averages (MA) processes may be present which would call for the application of an autoregressive moving averages model (ARMA). To simultaneously examine k time series variables, the multivariate form of ARMA or Box-Jenkins analysis would be used. Pfeifer and Deutsch (1980), Kendall and Ord (1991) and Cressie (1993) suggest adding spatial dimensions to the model. To do this the time series of the study variable, measured at different locations, can be treated as a set of variables in a multivariate time series analysis.

Cressie (1993) provides details on how ARMA (Box-Jenkins, 1976) models can be generalized to include spatial location. There are space-time autoregressive (STAR) models and space-time autoregressive moving averages (STARMA) models. The STARMA model uses an observation $Z(s_i, t)$ taken at spatial location s_i and time t, and defines $Z(t) = [Z(s_i, t) \ldots Z(s_n, t)]$. The STARMA model takes the form

$$Z(t) = \sum_{k=0}^{\rho} \sum_{j=1}^{\lambda} \xi_{kj} W_{kj} Z(t-k) - \sum_{l=0}^{q} \sum_{j=1}^{\mu} \phi_{lj} V_{lj} \epsilon(t-1) + \epsilon(t) \tag{1}$$

where W_{kj} and V_{lj} are given weight matrices, λ_k is the extent of spatial lagging on the autoregressive component, μ_l is the extent of spatial lagging on the moving average component, the residuals,

$\epsilon(t) = [\epsilon(s_i, t) \ldots \epsilon(s_n, t)]$ and ξ_{kj} is the autoregressive parameter while ϕ_{lj} is the moving average parameter. Martin and Oeppen (1976) described how such a model can be generalized to introduce the effects of a lagged independent regressor variable X_{t-k}. Such a model would be characterized a STARMAR model or a space-time autoregressive-moving average and regression model and would take the form

$$Z(s, t) = \sum \sum \xi_{kj} \, W_{kj} \, Z_{t-k} - \sum \sum \phi_{ij} \, V \epsilon_{t-k} + \epsilon(t) + \theta_{ij} \, X_{t-k} \tag{2}$$

where X_{t-k} is the lagged regressor variable.

Bennett (1979, p. 42) presents an alternative approach to the analysis of space-time systems through the employment of transfer function models which can be expressed as

$$Z_t = \sum_{k=1}^{k=p} \phi_k \, Z_{t-k} + \sum_{k=0}^{k=q} \psi_k \, X_{t-k} \pm \epsilon \tag{3}$$

where ϕ_k is the kth order autoregressive term for Z_{t-k}, the system output and ψ_{t-k} is the kth order autoregressive term for X_{t-k}, the system input which is the spatial lag = 1 updrift value of Z_t while ϵ is the error term or residual which should not be autocorrelated.

In this chapter, the transfer function approach is utilized because the spatial aspect is unidimensional. It is assumed that the system operates in a time-space continuum. Since only 7 survey transects are used in this study, only a simple first-order spatial autoregressive (SAR1) or spatial autoregressive process (SAR1) is expected in the system [in order to use a higher-order SAR2 parameter at least 9 profiles should be in the data set if the convention that the number of autocorrelations that are considered must be less than or equal to the number of significant observation points divided by four (i.e., N/4 rule)], but in this case, the input variable X_t may be serially autocorrelated in the same manner as the output variable Z_t such that both variables may exhibit possible seasonal and longer term cyclical movements. Thus one might expect more complex pseudo-cyclic patterns to characterize the temporal behavior of the system such as would be described by a temporal Yule-Walker temporal second-order autoregressive model with a possible cyclical component (TAR2 or TAR2CA1). This should be the case, because X_t, the input variable is generated from the time series of the adjacent updrift transect of Z_t, the output variable. The combination of these processes into a single model would yield a STAR2CAR model. Thus the approach of Martin and Oeppen (1976) may not be the most efficient in this situation. However, the transfer modeling approach would circumvent this problem.

Lai (1979) presents a simple step by step procedure to execute a transfer function analysis, which is as follows:

(a) Examine the autocorrelation functions (ACF) for both Z_t and X_t as well as the partial autocorrelation functions (PACF);

(b) Fit an AR(k) (k is the order of the AR fit) model to the input series X_t;

(c) This will yield an error series $\epsilon_{xt} = X_t - \sum \psi_k \, X_{t-k}$;

(d) Using the same AR(k) filter that was used for X_t fit the same AR(k) model to Z_t yielding the error series ϵ_{zt};

(e) Cross-correlate ϵ_{xt} with ϵ_{zt};

(f) Multiply the significant cross-correlations by the ratio of the standard deviations of ϵ_{zt} to the standard deviation of ϵ_{xt} yielding the impulse function which is regressed against Z_t;

(g) In this study the significant spatial impulses were mainly found at serial lag 0 (a pure spatial autocorrelation effect), so the X at $t = 0$ impulse parameter provides a measure of the strength of the spatial autocorrelation in the system where the effects of the serial autocorrelations are filtered out;

(h) If the only significant impulse parameters are at lag 0, then one can regress Z_t against X_t and fit an SARTARCAR model to the residuals;

(i) Once this is done, check the final set of error terms or residuals for significant autocorrelation;

(j) If the model is satisfactory, this will yield an estimate of the total variance accounted for by the serial aspect of the system which is then added to the amount of variance accounted for by the spatial process.

6. MODELING PROCEDURES AND RESULTS

After the specific model parameter values are determined, the Box-Jenkins method provides statistical tests for verifying the appropriateness of the chosen model (see Box and Jenkins, 1976; Hoff, 1983; Pankratz, 1983). The procedures used in this study can be adapted to either SPSS (SPSS, 1999) or STATISTICA (StatSoft, Inc., 1995) statistical software packages.

To determine the best fitting model for the beach data and for the shoreline data it is reasonable to consider the spatial series to be unidimensional, and that the dominant movement of sediment is unidirectional from north to south. In essence, the cumulative effects of the processes that produce change at profile 160 (distance = zero) should significantly influence the observed response at the other profiles. This influence decreases away from 160 starting at profile 80N which is 80 m south of 160. Field investigations showed that at any given time (T_i) interval, the profile (P) changes at distances one through seven exhibited seasonal variations as well as biennial variations. If monthly surveys could have been carried out, seasonal movement patterns could have been assessed. Hence, the data collected at the seven profile transects shown in Fig. 1 for forty-seven different time intervals (semiannually from 1978–2001) are represented in the modified Box-Jenkins model as

$$T_1: \quad P1, P2, P3, P4, P5, P6, P7,$$
$$T_2: \quad P1, P2, P3, P4, P5, P6, P7,$$
$$\vdots$$
$$T_{47}: P1, P2, P3, P4, P5, P6, P7,$$

This approach could be adapted to monthly data to differentiate between seasonal patterns and long-term patterns while identifying the spatial character of these patterns, if such a data set were available. Since the data set was collected at discrete spatial and temporal intervals, this method may be appropriate. With the use of the STATISTICA software (StatSoft Inc., 1995) best fit models are obtained through a process that involves examination of the autocorrelation functions (ACFs), partial autocorrelation functions (PACFs), and cross-correlation functions (CCFs) to select a number of tentative model identifications and parameter estimations. After several experimental runs the results show that a spatial autoregressive (SARTAR2CAR1) model best describes the beach net sediment flux (B data). Based on the ACFs (see Figs. 2 and 3a) for both beach flux (B) and updrift adjacent profile beach flux (b), they were fitted to similar TAR2CAR1 models, because both B and b exhibited significant autocorrelation peaks at lags 1, 2 and 4. It should be noted that b represents the standardized updrift adjacent beach flux values. When the effects of the spatial autocorrelation were introduced (see Fig. 3b), significant serial autocorrelations persisted at lags serial 2 and 4 in the pattern of residuals.

Since the predominant direction of longshore drift along this beach runs north to south, standardized beach flux data for the updrift adjacent profile were correlated with the nearest northern profile in the survey grid. Fig. 4 presents the cross-correlation function (CCF) between the residuals of B and b based on the coefficients associated with the TAR2CAR1 model fitted to b. Then a SARTAR2CAR

Autocorrelation Function

Standardized Beach Net Sediment Flux (B)

(Standard errors are white-noise estimates)

Lag	Corr.	S.E.		Q	p
1	+.132	.0549		5.80	.0160
2	-.149	.0548		13.20	.0014
3	+.018	.0547		13.31	.0040
4	+.180	.0546		24.17	.0001
5	+.028	.0545		24.43	.0002
6	-.034	.0545		24.82	.0004
7	-.034	.0544		25.22	.0007
8	-.010	.0543		25.25	.0014
9	-.080	.0542		27.41	.0012
10	-.098	.0541		30.65	.0007
11	-.098	.0540		33.94	.0004
12	-.138	.0540		40.47	.0001
13	-.012	.0539		40.52	.0001
14	+.013	.0538		40.57	.0002
15	-.121	.0537		45.67	.0001

-1.0   -0.5   0.0   0.5   1.0

Figure 2. Autocorrelation function: Standardized beach sediment flux (B).

transfer function model was fitted to the beach flux B data and the residuals were examined for autocorrelation (see Fig. 5). This model took the form $B_t = -0.161B_{t-2} + 0.184B_{t-4} + 0.396b_t \pm \epsilon$ which accounted for 19% ($R^2 = 0.193$) of observed spatial-temporal variation of (B) values (see Table 1). Here b is the updrift profile beach flux and ϵ is the residual or error term. Fig. 5 indicates that no significant autocorrelation exists in the pattern of residuals from the model. The model results highlight the fact that localized stochastic processes have some control on beach net sediment fluxes. If the profile spacing on the grid were larger, then the spatial term would not have been significant. With closer spacing in the profiles and shorter intervals between surveys, a much higher degree of explained variation may have been observed, but the costs associated with such surveys would be prohibitive. These processes operate through space, and it is evident that there are interrelated spatial patterns of erosion and accretion through time.

One of the implications derived from the aforementioned model is that beach flux levels in adjacent sites are interdependent, and partially represent the cumulative spatial effects of a number of different sediment flow events. These processes operating at the Northeast Beach are variations in longshore drift as well as persistent localized sediment circulation cells, which may vary in the long run in a random or possibly a nonlinear fashion. However, the statistically significant but weak long-term relationship suggests that strong random processes operate in the system, and that short-term (monthly surveys over less than 5 years) detailed assessments of beach changes may not be adequate for long-term prediction. However, if transfer function methodology had been applied to data collected on a monthly basis over a finer grid pattern, it would have possible to detect detailed spatial effects on the shoreline dynamics, and the degree of explained variation in the spatial-temporal pattern should be higher unless the randomness in the system is not due to a lack of data. In any case, transfer function models can be adapted to any data set, and the investigator will have an opportunity to assess the level of randomness in the system as well as spatial, seasonal and other temporal effects.

Autocorrelation Function
Spatial Lag=1 Standardized Beach Net Sediment Flux (b)
(Standard errors are white-noise estimates)

Lag	Corr.	S.E.		Q	p
1	+.126	.0549		5.29	.0214
2	-.121	.0548		10.21	.0061
3	+.041	.0547		10.77	.0131
4	+.137	.0546		17.05	.0019
5	+.018	.0545		17.15	.0042
6	-.015	.0545		17.23	.0085
7	-.037	.0544		17.70	.0134
8	+.003	.0543		17.71	.0236
9	-.063	.0542		19.07	.0246
10	-.139	.0541		25.62	.0043
11	-.075	.0540		27.57	.0038
12	-.096	.0540		30.73	.0022
13	-.069	.0539		32.37	.0021
14	-.019	.0538		32.49	.0034
15	-.099	.0537		35.92	.0018

-1.0   -0.5   0.0   0.5   1.0

(a)

Autocorrelation Function
Standardized Beach Net Sediment Flux (B) Residuals from
Spatial Autoregressive (SAR) Model: $B_t = 0.396b_t$
B_t = Sediment Flux; b_t = Sediment flux at Updrift Spatial Lag =1
(Standard errors are white-noise estimates)

Lag	Corr.	S.E.		Q	p
1	+.067	.0549		1.47	.2248
2	-.165	.0548		10.59	.0050
3	-.010	.0547		10.62	.0140
4	+.189	.0546		22.58	.0002
5	+.012	.0545		22.63	.0004
6	+.018	.0545		22.74	.0009
7	-.066	.0544		24.21	.0010
8	+.032	.0543		24.57	.0018
9	-.051	.0542		25.45	.0025
10	-.032	.0541		25.81	.0040
11	-.097	.0540		29.02	.0023
12	-.097	.0540		32.27	.0013
13	+.020	.0539		32.41	.0021
14	+.077	.0538		34.48	.0018
15	-.112	.0537		38.81	.0007

-1.0   -0.5   0.0   0.5   1.0

(b)

Figure 3. (a) Autocorrelation function: Beach sediment flux spatial lag 1, standardized beach net sediment flux (*b*). (b) Standardized beach net sediment flux (*B*) residuals from spatial autoregressive (SAR) model: $B_t = 0.396b_t$.

Cross-Correlation Function

First : Residuals from: $B_t = 0.140B_{t-1} - 0.127B_{t-2} + 0.121B_{t-4}$

Lagged: Residuals from: $b_t = 0.140b_{t-1} - 0.127b_{t-2} + 0.121b_{t-4}$

Lag	Corr.	S.E.
-15	-.093	.0564
-14	-.071	.0563
-13	-.021	.0563
-12	-.054	.0562
-11	-.033	.0561
-10	-.165	.0560
-9	-.020	.0559
-8	-.074	.0558
-7	.0016	.0557
-6	-.024	.0556
-5	.0022	.0556
-4	-.008	.0555
-3	.0973	.0554
-2	-.042	.0553
-1	.0596	.0552
0	.3823	.0551
1	.1132	.0552
2	.0450	.0553
3	-.001	.0554
4	.0025	.0555
5	.0615	.0556
6	-.098	.0556
7	.0627	.0557
8	-.046	.0558
9	-.058	.0559
10	-.067	.0560
11	.0064	.0561
12	-.154	.0562
13	-.055	.0563
14	-.022	.0563
15	-.008	.0564

-1.0   -0.5   0.0   0.5   1.0

Figure 4. Cross-correlation function residuals of beach sediment flux model fits.

Autocorrelation Function

Residuals from: $B_t = -0.161B_{t-2} + 0.182B_{t-4} + 0.396b_t$

B= Standardized Beach Sediment Flux

b= Space Lag 1 Standardized Beach Sediment flux

Lag	Corr.	S.E.	Q	p
1	+.002	.0549	.00	.9699
2	-.003	.0548	.00	.9981
3	+.015	.0547	.08	.9941
4	-.002	.0546	.08	.9992
5	-.005	.0545	.09	.9999
6	+.063	.0545	1.45	.9630
7	-.074	.0544	3.30	.8564
8	+.030	.0543	3.60	.8916
9	-.080	.0542	5.79	.7609
10	-.057	.0541	6.92	.7333
11	-.064	.0540	8.34	.6828
12	-.111	.0540	12.55	.4027
13	+.024	.0539	12.74	.4681
14	+.094	.0538	15.79	.3266
15	-.131	.0537	21.70	.1161

-1.0   -0.5   0.0   0.5   1.0

Figure 5. Autocorrelation function: Beach sediment flux model residuals.

Table 1
Spatial-temporal analysis of beach net sediment flux (B) patterns.

Beach Sediment Flux Model	B_t	=	$0.155B_{t-1} - 0.153B_{t-2} + 0.165B_{t-4} \pm \epsilon$ ($R^2 = 0.072$) (0.056) (0.057) (0.057)	
Spatial Lag 1 Beach Sediment Flux Model	b_t	=	$0.139b_{t-1} - 0.153B_{t-2} + 0.165B_{t-4} \pm \epsilon$ ($R^2 = 0.050$) (0.056) (0.056) (0.056)	
Beach Sediment Flux SARTAR2CAR Model	B_t	=	$-0.161B_{t-2} + 0.184B_{t-4} + 0.396b_t \pm \epsilon$ ($R^2 = 0.193$) (0.056) (0.056) (0.056)	

Note: $t - 4$ represents the cyclical effect. Numbers in brackets represent the standard error terms associated with the above coefficients. B is the standardized beach net sediment flux; b is the updrift adjacent profile standardized net sediment flux; SARTAR2CAR represents a first-order spatial autoregressive, second-order temporal autoregressive model with an autoregressive cyclical component (the cycle here represents two years).

Although the level of explained variation seems to be relatively small, it does identify the fact that a substantial degree of randomness exists in the spatial-temporal behavior of this beach system, and the statistically significant levels of spatial and temporal autocorrelation suggests that the estimates of the parameters associated with deterministic predictive models could be biased and limit their predictive effectiveness. Increases in survey frequency as well as decreases in profile spacing may produce somewhat higher levels of explained variation, but the cost involved with such changes may be excessive.

The spatial and temporal variations explained by the model for the B data can be visualized on a space-time metamap (Fig. 6). The space-time metamap is a variant of the Minkowski space-time diagram (see Mills, 1994, p. 52–56) which is used to summarize the salient patterns of variables which change through time and space. A similar graphic presentation was used by Reeve et al. (2001). The profile locations, survey time and B data were input as variables into the STATISTICA software package (StatSoft, Inc., 1995) to produce a two-dimensional contour plot. A cubic spline subroutine was used to smooth the contour lines presented in the metamap (Fig. 6). The overall spatial-temporal trends presented in the metamap are indicative of the net erosion and accretion patterns which have occurred through time and space. Low rates of erosion in the first 100 m south of 160 give way to modest accretion, especially for areas beyond the 260 m mark for the months before May 1985. Another aggradational pattern can be seen in the first 260 m of the beach for the months after May 1987. The broad pattern of erosion, observed in the central part of the metamap, developed between May 1985 and November 1986. This erosion is attributed to record high water levels which caused artificial structures to fail and a large embayment to develop. This promoted a reduction in the normal north to south movement of sediment.

To determine which model best fits the net shoreline positional change (S) data the same set of procedures utilized for the beach flux (B) data are followed. An examination of the ACF for the net shoreline positional change (S) (Fig. 7) and the ACF for the spatially lagged net shoreline change (s) (Fig. 8a) indicates that both variables exhibit similar temporal patterns. However, when the residuals from the spatial autoregressive (SAR) initial model were fitted to the shoreline change data (Fig. 8b), the pattern of residuals indicated a significant autocorrelation at lag $t = 2$, so both variables (S and s) were fitted to an TAR2 model (see Table 2). Next a cross-correlation analysis was run on the residuals of both S and s fitted to the TAR2 model associated with the serial analysis of s (spatially lag 1 shoreline change data) (see Fig. 9). Based on the CCF, and the models fitted to S and s, a SARTAR2 model was fitted to the shoreline change (S) data which has the form:

Beach Sediment Flux Metamap (m^3/m^2)

Spline
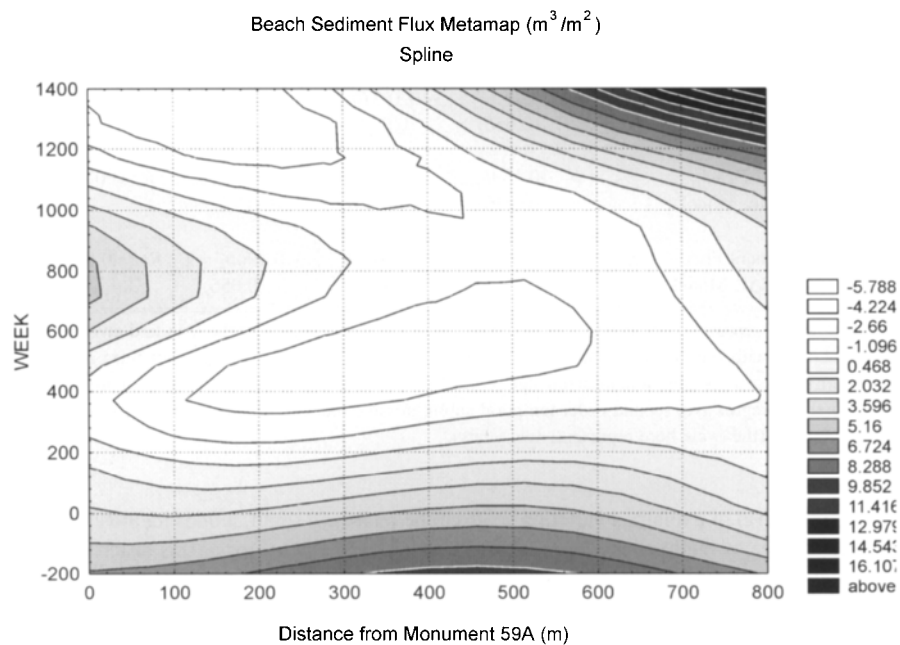
Figure 6. Space-time metamap of beach net sediment flux, Northeast Beach.

Autocorrelation Function

Standardized Net Shoreline Change S

(Standard errors are white-noise estimates)

Lag	Corr.	S.E.		Q	p
1	+.195	.0549		12.57	.0004
2	-.082	.0548		14.82	.0006
3	+.008	.0547		14.84	.0020
4	+.079	.0546		16.94	.0020
5	-.028	.0545		17.21	.0041
6	-.061	.0545		18.46	.0052
7	-.093	.0544		21.38	.0033
8	-.088	.0543		24.01	.0023
9	-.052	.0542		24.93	.0031
10	+.015	.0541		25.00	.0054
11	-.087	.0540		27.58	.0038
12	-.168	.0540		37.33	.0002
13	-.045	.0539		38.04	.0003
14	+.031	.0538		38.37	.0005
15	-.088	.0537		41.09	.0003

-1.0   -0.5   0.0   0.5   1.0

Figure 7. Autocorrelation function: Standardized net shoreline change (S).

Autocorrelation Function
Standardized Space Lag 1 Net Shoreline Position Change (s)
(Standard errors are white-noise estimates)

Lag	Corr.	S.E.		Q	p
1	+.261	.0549		22.66	.0000
2	-.033	.0548		23.02	.0000
3	-.007	.0547		23.03	.0000
4	+.027	.0546		23.28	.0001
5	-.067	.0545		24.81	.0002
6	-.067	.0545		26.31	.0002
7	-.060	.0544		27.53	.0003
8	-.075	.0543		29.44	.0003
9	-.062	.0542		30.73	.0003
10	-.024	.0541		30.93	.0006
11	-.086	.0540		33.44	.0004
12	-.142	.0540		40.35	.0001
13	-.097	.0539		43.57	.0000
14	+.022	.0538		43.73	.0001
15	-.050	.0537		44.61	.0001

-1.0   -0.5   0.0   0.5   1.0

(a)

Autocorrelation Function
Net Shoreline Change (S) Residuals from A Spatial
Autoregressive Model (SAR): $S_t = 0.497s_t$
S_t = Shoreline Change; s_t = Shoreline change at Updrift Spatial Lag =1
(Standard errors are white-noise estimates)

Lag	Corr.	S.E.		Q	p
1	+.052	.0549		.88	.3470
2	-.148	.0548		8.16	.0169
3	-.037	.0547		8.62	.0347
4	+.088	.0546		11.24	.0240
5	+.013	.0545		11.30	.0457
6	-.013	.0545		11.36	.0779
7	-.147	.0544		18.69	.0092
8	-.001	.0543		18.69	.0167
9	-.001	.0542		18.69	.0280
10	+.019	.0541		18.81	.0428
11	-.052	.0540		19.74	.0491
12	-.131	.0540		25.60	.0122
13	-.037	.0539		26.08	.0166
14	+.095	.0538		29.21	.0098
15	-.066	.0537		30.74	.0096

-1.0   -0.5   0.0   0.5   1.0

(b)

Figure 8. (a) Autocorrelation function: Standardized shoreline change spatial lag 1, net shoreline position change (s). (b) Net shoreline change (S) residuals from a spatial autoregressive model (SAR): $S_t = 0.497s_t$.

Table 2

Spatial-temporal analysis of net shoreline positional change(s) patterns.

TAR2				
Model of Net Shoreline Change	S_t	$=$	$0.235S_{t-1} - 0.132S_{t-2} \pm \epsilon$ (0.057) $\quad$ (0.057)	$(R^2 = 0.058)$
TAR2				
Spatial Lag 1 Shoreline Change	s_t	$=$	$0.302s_{t-1} - 0.115s_{t-2} \pm \epsilon$ (0.057) $\quad$ (0.057)	$(R^2 = 0.083)$
SARTAR2				
Model of Net Shoreline Change	S_t	$=$	$-0.156S_{t-2} + 0.497s_t + 0.123s_{t-1} \pm \epsilon$ (0.056) $\quad$ (0.056) $\quad$ (0.056)	$(R^2 = 0.339)$

Numbers in brackets represent the standard error terms associated with the above coefficients. S represents standardized net shoreline change; s represents the updrift adjacent profile standardized net shoreline change; TAR2 represents a second-order temporal autoregressive process; SARTAR2 represents a spatial autoregressive second-order serial autoregressive process.

Cross-Correlation Function

First : Residuals = S_t - 0.302*S_{t-1} +0.115*S_{t-2}

Lagged: Residuals= s_t - 0.302*s_{t-1} +0.115*s_{t-2}

Lag	Corr.	S.E.
-15	-.088	.0564
-14	-.046	.0563
-13	-.037	.0563
-12	-.064	.0562
-11	-.096	.0561
-10	-.005	.0560
-9	-.049	.0559
-8	-.096	.0558
-7	.0305	.0557
-6	-.039	.0556
-5	-.072	.0556
-4	.0252	.0555
-3	.0826	.0554
-2	.0163	.0553
-1	.0904	.0552
0	.4974	.0551
1	.1241	.0552
2	-.035	.0553
3	.0012	.0554
4	.0395	.0555
5	-.017	.0556
6	-.098	.0556
7	.0445	.0557
8	-.127	.0558
9	-.045	.0559
10	.0349	.0560
11	-.015	.0561
12	-.124	.0562
13	-.002	.0563
14	.0236	.0563
15	-.038	.0564

-1.0 $\qquad$ -0.5 $\qquad$ 0.0 $\qquad$ 0.5 $\qquad$ 1.0

Figure 9. Cross-correlation function residuals of shoreline change models fits.

$S_t = -0.156S_{t-2} + 0.497s_t + 0.123s_{t-1} \pm \epsilon$ where ϵ is a residual term. All other non-significant terms were deleted. The residuals from this model are depicted in Fig. 10. Although there is one small statistically significant residual autocorrelation at lag = 7, the Box-Lung statistics and the

Autocorrelation Function

$$S_t = -0.171S_{t-2} + 0.497s_t + 0.123s_{t-1}$$

(Standard errors are white-noise estimates)

Lag	Corr.	S.E.		Q	p
1	-.006	.0549		.01	.9110
2	+.011	.0548		.05	.9742
3	-.037	.0547		.51	.9169
4	+.050	.0546		1.34	.8549
5	-.011	.0545		1.38	.9265
6	+.007	.0545		1.40	.9660
7	-.135	.0544		7.60	.3694
8	+.005	.0543		7.61	.4727
9	-.029	.0542		7.89	.5452
10	+.005	.0541		7.90	.6385
11	-.039	.0540		8.41	.6761
12	-.111	.0540		12.65	.3953
13	-.055	.0539		13.67	.3974
14	+.084	.0538		16.12	.3059
15	-.076	.0537		18.12	.2565

-1.0   -0.5   0.0   0.5   1.0

Figure 10. Autocorrelation function: Shoreline change model residuals.

probabilities associated with them suggest that the model is adequate. Overall, this model accounted for 34.9% of the spatial-temporal variation in the shoreline change data ($R^2 = 0.339$).

The observed spatial and temporal patterns can be associated with dynamic temporal processes which cumulatively impact particular spatial locations. Shoreline positional change and total sediment flux tend to be more sensitive to short-term fluctuations in sediment dynamics between spatial locations. The existence of a temporal term in the SARTAR2 model can be explained by the fact that a large-scale shoreline positional change can develop quite rapidly, but the change can persist for an extended period of time. The adjustments of the shoreline toward its original state will occur at a relatively slow rate. At the Northeast Beach the tetrapods which were emplaced to protect the shoreline now constitute an artificial reef, and these artificial structures have mitigated against the process of beach and shoreline restoration.

The shoreline change S results from the SARTAR2 model can also be highlighted on a space-time metamap (Fig. 11). These results show that there is a pattern of initial shoreline advance giving way to retreat, followed by a pattern of reduced shoreline advance through time. Along the spatial dimension, the intensity of shoreline retreat extends for about 260 m, starting at profile 59A. Shoreline advance is restricted to the first 18 months of the monitoring period (May 1978 to November 2001). This advance can be attributed to relatively low lake levels.

Between May 1982 and May 1991 shoreline retreat dominated the Northeast Beach with pronounced retreat occurring between zero and 260 m. The distinctive "thumb print" configuration which represents rapid shoreline retreat is located wholly within that part of the beach which is served by the tetrapods. This reach of massive shoreline retreat may be associated with the combined effects of the armour stone breakwater, tetrapod failure and unusually high lake levels. Since 1977, Lake Erie water levels have been rising at a rate of 0.06 m per annum. Thornburn (1986) reported that Lake Erie water levels exceeded record levels by 0.06 to 0.37 m from June through October 1986. As

Net Shoreline Change Metamap (m)
Spline
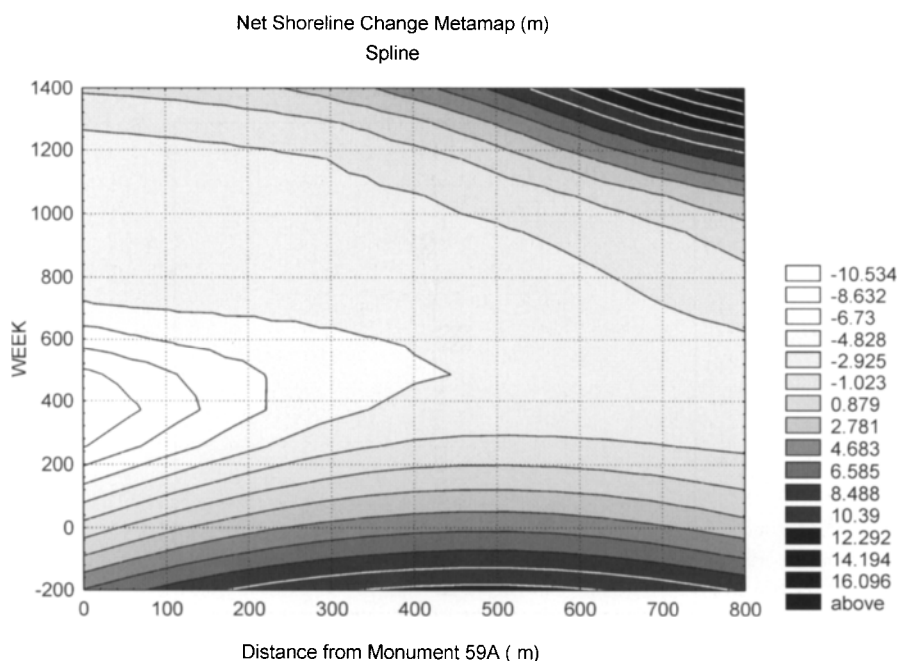
Figure 11. Space-time metamap of net shoreline positional change, Northeast Beach.

the water levels peaked in 1986 the tetrapods became submerged and waves started to break over the sunken tetrapods. A large embayment developed behind the line formerly occupied by the concrete tetrapod system. With only relatively moderate rates of shoreline retreat beyond the 160 m mark it can be claimed that the beach areas not protected by the tetrapod system experienced less erosion than the areas with artificial structures.

7. CONCLUSIONS

Temporal and spatial variations in the beach and shoreline environment are produced by a combination of highly complex interactions between the influences of anthropogenic activities, and the initial morphodynamic state of the beach governed by natural processes, among them changes in water levels, tides, waves, currents, winds and sediment supply (LaValle et al., 2001). Understanding the stochastic character of these changes is important because "in addition to being fundamental to understanding the morphodynamics of beaches, the spatial and temporal behavior of the beach profile has direct application in coastal engineering projects involving beach nourishment and in the siting of coastal structures" (Larson and Kraus, 1994, p. 76).

Actually, if a beach system fluctuated through time and space in a purely random manner around a constant mean with a constant variance, the system would be in a state of quasi-dynamic equilibrium. One advantage of the Box-Jenkins approach is that it is designed to cope with discrete spatial-temporal data, while assessing the random and non-random spatial-temporal movements. Also, one can utilize standard statistical packages to execute such an analysis. If sufficient data are available, this approach can be adapted to detailed short-term studies (less than 5–10 years) where the spatial-temporal effects of storms are measured, or in long-term (50–100 years) studies of shoreline changes

using annual data. In this medium-term study (20–50 years), semiannual data were examined to assess medium-term spatial-temporal movements as well as to identify the random processes in the system which could limit the predictive power of any deterministic model. Sometimes it is more important to know the limits of predictability in a natural open system than to generate a deterministic model with possibly biased parameters whose predictive power may disappear at the whim of nature.

The findings of this study emphasize the fact that an assessment of beach and shoreline stability requires examining a medium long time series of data (more than 20 years). The study also suggests that such a long-term analysis should be based on data characterized by uniform survey methods on the same sampling grid. The transfer function approach provides a reasonably simple method of dealing with long-term complex spatial-temporal patterns using available statistical software packages, when data on other predictor variables are in short supply due to time and monetary constraints placed on their collection. Since wave action, longshore currents, and freshwater lake levels are directly or indirectly related to meteorological phenomena which are characterized by strong random components, one would expect to encounter substantial random elements in beach dynamics, so knowing the extent of these random processes may be quite important to the coastal manager, because such knowledge will enable the coastal manager to know the limits to which the system can be predicted.

The procedures employed in this chapter are appropriate for application elsewhere because they provide results which will enable a shoreline manager to ascertain whether localized stochastic spatial processes operate in the beach and nearshore system or a combination of stochastic spatial and temporal processes interact to produce a complex pattern of beach change. The Box-Jenkins transfer function modeling approach results highlight the influence of temporal stochastic processes on the long range of beach and shoreline variations. For instance, temporal processes, such as high water levels can have the effect of shifting a beach away from a state of dynamic equilibrium, while spatial variations in the antecedent beach state may add a spatial element to the temporal relations. Since many natural beaches can attain dynamic equilibrium conditions (see for example, Lakhan and Trenhaile, 1989; Larson, 1991; Pilkey et al., 1993) it is vital to utilize space-time modeling procedures in order to detect shifts in phase states which occur through time and space. In this case, the transfer modeling approach can easily handle this situation. Admittedly, one problem with traditional philosophies associated with coastal management technologies is that many of the models used to predict beach behavior are predicated on maximizing predictive power by assuming that a beach is a closed system at the expense of respecting the random element in shoreline behavior. In the long run, it might be better to know the limits of predictability in a system, which could be revealed by some transfer function models, than to use a biased but highly predictive model that fails catastrophically when natural conditions deviate from expected norms. A beach in a state of dynamic equilibrium would exhibit zero trends and non-significant serial autocorrelations outside of seasonal movements, which would be detected by a transfer function model. The weak level of explained variation in the beach flux (B) model may not be as ominous as it would be if a very strong and catastrophic event occurs and cause the system to self-destruct. However, the presence of the weak relationship could alert the coastal manager as to the probabilities associated with non-random events.

LIST OF SYMBOLS AND ACRONYMS

ϵ — is a residual or error term
ϕ — is a serial autoregressive parameter
ψ — is a spatial autoregressive parameter
θ — is a serial moving average parameter
λ — is a spatial lagging factor
AR — is an autoregressive process

ACF	—	is the autocorrelation function
B	—	is the beach net sediment flux (m^3/m width of transect)
b	—	is the adjacent updrift beach net sediment flux (m^3/m width of transect)
CAR	—	is a cyclical autoregressive process (here the cycle is two years)
CCF	—	is the cross-correlaton function
MA	—	is a moving average process
S	—	is the net shoreline change (m)
s	—	is the updrift adjacent profile shoreline change (m)
SAR	—	is a spatial autoregressive process
SARTAR2	—	is a spatial autoregressive - second-order temporal autoregressive process
SARTAR2CAR	—	is a spatial autoregressive - second-order temporal autoregressive process with a cyclical component (in this case two years)
TAR	—	is a temporal autoregressive process
TAR2	—	is a second-order temporal process
TAR2CAR	—	is a second-order temporal process with a cyclical component

REFERENCES

Aubrey, D.G., 1979. Seasonal patterns of onshore/offshore sediment movement. Journal of Geophysical Research, 84: 6347–6354.

Aubrey, D.G., and Ross, R.M., 1985. The quantitative description of beach cycles. Marine Geology, 69: 155–170.

Bennett, R.J., 1979. Spatial Time Series: Analysis—Forecasting—Control. London: Pion.

Bowman, D., 1981. Efficiency of eigenfunctions for discriminant analysis of subaerial non-tidal beach profiles. Marine Geology, 39: 243–258.

Box, G.E.P., and Jenkins, G.M., 1970. Time Series Analysis: Forecasting and Control. San Francisco, CA: Holden-Day.

Box, G.E.P., and Jenkins, G.M., 1976. Time Series Analysis: Forecasting and Control. Revised edition. San Francisco, CA: Holden-Day.

Cressie, N.A.C., 1993. Statistics for Spatial Data. New York: John Wiley Interscience.

Dolan, R., Fenster, M.S., and Holme, S.J., 1992. Spatial analysis of shoreline recession and accretion. Journal of Coastal Research, 8: 263–285.

Finkl, C.W., 2002. Long term analysis of trends in shore protection based on papers appearing in the Journal of Coastal Research, 1984–2000. Journal of Coastal Research, 18 (2): 211–224.

Fisher, N., Dolan, R., and Hayden, B.P., 1984. Variations in large-scale beach amplitude along the coast. Journal of Sedimentary Petrology, 54: 73–85.

Golden Software, Inc., 1988. Grapher. Version 1.75. Golden Software, Inc., USA.

Gurnell, A.M., and Fenn, C.R., 1984. Box-Jenkins transfer function models applied to suspended sediment concentration—Discharge relationships in a proglacial stream. Arctic and Alpine Research, 16: 93–106.

Hegge, B.J., and Masselink, G., 1996. Spectral analysis of geomorphic time series: Auto-spectrum. Earth Surface Processes and Landforms, 21: 1021–1040.

Hoff, J.C., 1983. A Practical Guide to Box-Jenkins Forecasting. Belmont, CA: Lifetime Learning Publications, 316p.

Hsu, T.-W., Ou, S.-H., and Wang, S.-K., 1994. On the prediction of beach changes by a new 2-D empirical eigenfunction model. Coastal Engineering, 23: 255–270.

Kendall, M., and Ord, J.K., 1991. Time Series. Oxford, UK: Oxford University Press.

Kuznik, F., Lakhan, V.C., and LaValle, P.D., 1986. Spatial and temporal variability of the Northeast Beach, Point Pelee. In: Ricketts, P.J. (Editor), Studies in Marine and Coastal Geography, pp. 14–36. Halifax, NS: St. Mary's University.

Lai, P.-W., 1979. Transfer Function Modelling: Relationship Between Time Series Variables. Concepts And Techniques In Modern Geography, Vol. 22. London: Institute of British Geographers, 49p.

Lakhan, V.C., and Trenhaile, A.S., 1989. Models and the coastal system. In: Lakhan, V.C. and Trenhaile, A.S. (Editors), Applications in Coastal Modeling, pp. 159–213. Amsterdam, The Netherlands: Elsevier Science Publishers.

Larson, M., 1991. Equilibrium profile of a beach with varying grain size. Proceedings. Coastal Sediments '91, ASCE, New York, pp. 905–919.

Larson, M., and Kraus, N.C., 1994 Temporal and spatial scales of beach profile change, Duck, North Carolina. Marine Geology, 117: 75–94.

LaValle, P.D., 1978-2001. Monitoring Shoreline Erosion at the Northeast Beach, Point Pelee. Unpublished Reports to Parks Canada, Ottawa, Ontario, Canada.

LaValle, P.D., and Lakhan, V.C., 1997a. Utilizing microcomputer-based models to simulate changes in the nearshore environment. Environmental Modelling and Software, 12 (1): 19–26.

LaValle, P.D., and Lakhan, V.C., 1997b. A spatial-temporal analysis of the development of a log-spiral shaped embayment. Earth Surface Processes and Landforms, 22: 657–667.

LaValle, P.D., Lakhan, V.C., and Trenhaile, A.S., 2001. Space-time series modeling of beach and shoreline data. Environmental Modelling and Software, 16: 299–307.

Leatherman, S.P., Douglas, B.C., and Crowell, M., 1997. Beach erosion trends and shoreline forecasting. Journal of Coastal Research, 13 (4): iii–iv.

Lemke, K.A., 1990. An evaluation of transfer function—Noise models of suspended sediment concentration. Professional Geographer, 43 (2): 324–336.

Lemke, K.A., 1991. Transfer function models of suspended sediment concentration. Water Resources Research, 27 (3): 293–305.

Lins, H.F., 1985. Storm-generated variations in nearshore beach topography. Marine Geology, 62: 13–29.

Martin, R.L., and Oeppen, J.E., 1976. The identification of regional forecasting models using space time correlation functions. Transactions of the Institute of British Geographers, 66: 95–118.

Mills, R., 1994. Space Time and Quanta: An Introduction to Contemporary Physics. New York: W.H. Freeman and Company, 482p.

Ostrowski, R., Pruszak, Z., and Zeidler, R.B., 1990. Multi-scale nearshore and beach changes. Proceedings of the 22nd International Conference on Coastal Engineering, ASCE, pp. 2101–2116.

Pankratz, A., 1983. Forecasting with Univariate Box-Jenkins Models. New York: John Wiley & Sons.

Pfeifer, P.E., and Deutsch, S.J., 1980. A three stage iterative procedure for space-time modeling. Technometrics, 22 (1): 35–47.

Pilkey, O.H., Young, R.S, Riggs, S.R., Smith, A.W.S, Wu, H., and Pilkey, W.D., 1993. The concept of shoreface profile of equilibrium: A critical review. Journal of Coastal Research, 9 (1): 245–278.

Pruszak, Z., 1993. The analysis of beach profile changes using Dean's method and empirical orthogonal functions. Coastal Engineering, 19: 245–261.

Reeve, D., Li, B., and Thurston, N., 2001. Eigenfunction analysis of decadal fluctuations in sandbank morphology at Great Yarmouth. Journal of Coastal Research 17(2): 371–382

Setterington, W.J., 1978. Erosion Survey at the Point Pelee National Park. Unpublished Report to Parks Canada, Ottawa, Canada.

Smith, R.K., and Benson, 2000. Beach profile monitoring: How frequent is sufficient. International Coastal Symposium (ICS 2000), Challenges for the 21st Century in Coastal Science. Journal of Coastal Research Special Issue 34, pp. 573–579.

SPSS, 1999. SPSS Version 9 for Windows. Chicago, IL: SPSS Inc.

StatSoft, Inc., 1995. STATISTICA for Windows. Tulsa, OK: StatSoft, Inc.

Swales A., 2002. Geostatistical estimation of short term changes in beach morphology and sand budget. Journal of Coastal Research 18 (2): 338–351

Thornburn, G., 1986. Governments ask for a new IJC study of the Great Lakes water levels. Focus on International Joint Commission Activities, 131: 1–3.

Walton, T.L. Jr., 1999. Shoreline rhythmic pattern analysis. Journal of Coastal Research, 15 (2): 379–387.

Winant, C.D., Inman, D.L., and Nordstrom, C.E., 1975. Description of seasonal beach changes using empirical eigenfunctions. Journal of Geophysical Research, 8 (15): 1979–1986.

Wood, W.L., and Weishar, L.L., 1984. Beach response to long period lake-level variation. Proceedings of the 19th International Conference on Coastal Engineering, ASCE, pp. 1571–1583.

553

Chapter 21

Progress in Geographical Information Systems and Coastal Modeling: An Overview

David R. Green and Stephen D. King

Centre for Marine and Coastal Zone Management, Department of Geography and Environment, University of Aberdeen, Elphinstone Road, AB24 3UF, Aberdeen, Scotland, UK

1. INTRODUCTION

Geographical Information Systems (GIS) are rapidly becoming an all-pervasive technology. A review of recent literature shows that there is a growing number of applications for nearly all disciplines, for example, landscape ecology, environmental impact assessment (EIA), nature conservation (European Union NATURE-GIS project) and coastal zone management (CZM). GIS brings the geographical dimension or spatial element to data exploration, analysis and problem solving, together with a suite of spatial mapping, analysis and visualization tools. It is this geographical dimension that is considered to have potential for developing a new perspective on a problem, whether it be simply through undertaking exploratory data analysis, examining data in a spatial context (for example, patterns or distributions revealed in graphs or maps, or resulting from geostatistical analysis). As noted by Pullar and Springer (2000, pp. 451–452) "...all too often predictive models do not examine the problems in a geographical context. A GIS coupled with an environmental model provides a tool to run a simulation and to interpret the results in a spatial context".

Although maps are most often associated with the output from GIS applications, GIS software is increasingly being used to manage, process, analyze and visualize a wide range of environmental data in two or more dimensions. Growing end-user demand and emphasis is also being placed upon developing the environmental modeling applications (see for example, Clarke et al., 2002; Skidmore, 2002) and visualization capabilities of GIS for scientific and decision-making processes (Huang and Jiang, 2002). In the past, GIS software has generally been considered to be a relatively weak environment for modeling work. Despite GIS software being used for the spatial analysis of data, and some simple modeling applications, development of simulation and process models is not straightforward in a software environment (GIS) that is not optimized for computationally intensive and integrative programming (Livingstone and Kidd, 1999). In part this is due to the fact that most mathematical models of environmental processes were developed prior to or independent of, mainstream GIS (Livingstone and Kidd, 1999). However, rapidly developing computer technology has provided considerable scope to either extend GIS to incorporate more sophisticated modeling tools with the aid of programming, or opportunities to couple existing, externally developed, models with GIS software via, for example, context-specific interfaces, as well as to reproduce existing process models within GIS software. Advances in computer interoperability, for example, now also provide the means to develop the flexible and interactive spatial data handling framework required for modeling development (Livingstone and Kidd, 1999).

Not only has evolution of computer technology aided in the development of more complex models and enabled links to be forged with GIS software, but it has also provided the means by which it has been possible to evolve simulation and prediction exercises into fully operational desktop

tools for use by both scientists and others, for example engineers and coastal practitioners. The migration of these software tools from the so-called 'scientific backrooms' into the everyday work environment (Manuels, 2002) has facilitated the use of both GIS and models by practitioners and the non-specialist community alike, helping to broaden the operational applications of the software to a wider community. But, this also has some significant implications for future use, since it places sophisticated modeling tools in the hands of the non-specialist who, although practically able to use the software with the aid of intuitive and user-friendly interfaces, together with online help files and tutorials, may ultimately be unable to put the software to its appropriate use, and may experience considerable difficulty when interpreting the output results.

The development and application of coastal feature and process models has made a great deal of progress in the last few years. Major achievements have been made toward modeling the evolution of coastal features such as beaches and spits, as well as currents, waves, and sediment transport both at the coast and within estuarine environments. An improved knowledge and understanding of coastal processes has also played an important part in the study and management of our coastal environments (for example, ecology and habitat), as well as in environmental impact studies involving, for example, oil spill monitoring and mapping. The advances made in knowledge and understanding have all been possible as a direct result of our capability to gather environmental data, and to process it with the aid of information technology (IT).

The scope to make even greater practical and operational use of both GIS and coastal modeling tools (either together or on their own) is now being rapidly facilitated by developments in Internet technology, allowing greater access to environmental data sets and information resources via online catalogues, databases, mapping and Decision Support Systems (DSS), vast quantities of environmental data acquired by a new generation of remote sensing instruments with higher spatial, spectral and temporal resolution, and most recently important opportunities to develop collaborative, distributed modeling (Barthel and Lehfeldt, 2000). This has also opened up the potential to build upon multiple sources of expertise and environmental data to help both develop and test models, as well as to improve feedback and allow for further refinement and utilization of such models in the workplace.

This chapter presents a brief overview of some of the advances in the application of GIS software and modeling to the study of the coastal environment. It begins by providing some basic definitions of the terms GIS and modeling in the context of coastal studies and management. The role of geographical data and information is considered for the study of the coastal environment, and the significant benefits obtained from integrating GIS and coastal modeling tools. Perceived limitations of current GIS for modeling applications are also discussed. The rapid developments in computer technology (microprocessors, data capture, storage, display, etc.) and software (mathematical, statistical, modeling, mapping, and visualization) are used as the basis for understanding the factors driving the development of, and requirement for, more powerful GIS-based coastal modeling tools. With the rapid growth in desktop processing power, developments in user-interfaces, and latterly the Internet, there will be even greater demand for operational applications of GIS and modeling for monitoring, management, planning and decision-making. Accompanying such developments will be the need to ensure that user-interfaces facilitate ease-of-use and interaction at all possible levels. Moreover, it will also be necessary to ensure that the end-user community carefully considers the limitations of the tools (GIS and models), are able to interpret the output generated, and clearly understand the importance of data quality and error in the context of modeling work. The Internet provides one way in which it will be possible to address the growing application of modeling techniques through access to documentation, data, tools and expertise (Fig. 1).
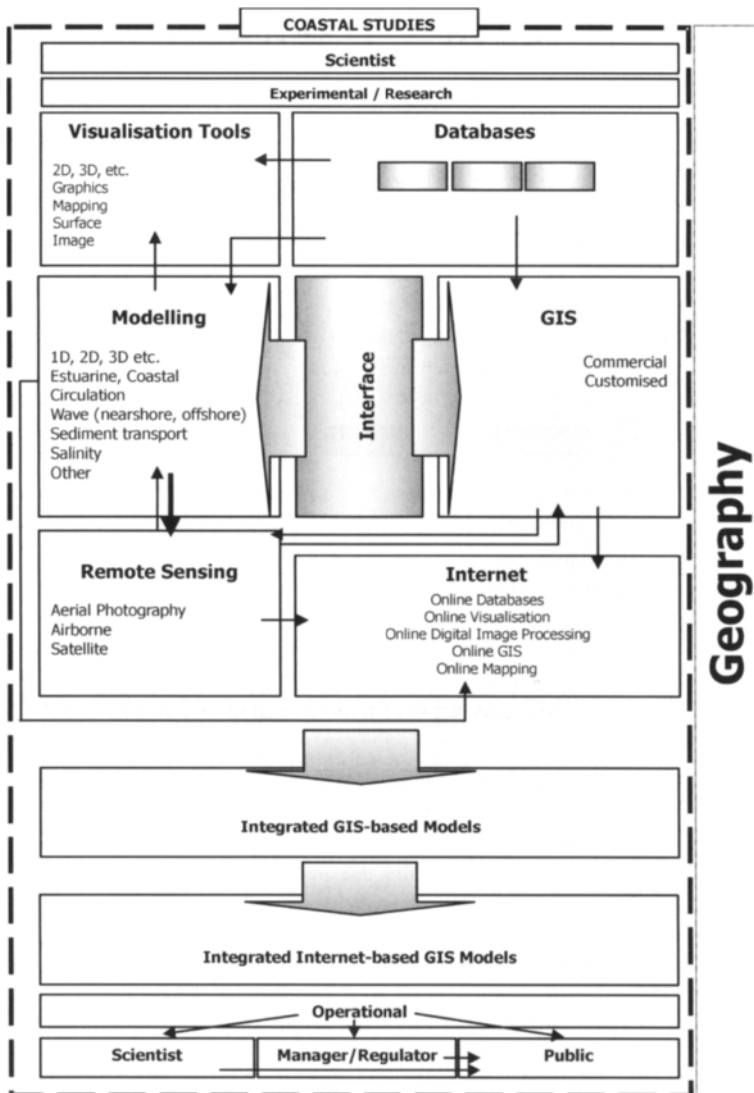
Figure 1. Linking GIS and coastal modeling.

2. THE COASTAL SYSTEM

Defining the coastal environment and the coastal system provides an essential starting point for further discussion, and a contextual setting to help define the domain of the coastal modeler and their perceived requirement to develop links between coastal process modeling and GIS tools.

The coastal environment is a unique one and is a special geographical area, described by Chua (1993) as comprising five main zones: inland areas, coastal lands, coastal waters, offshore waters, and the high seas. These five zones include lagoons, bays, estuaries, wetlands, beaches, spits, bars,

The Coastal System
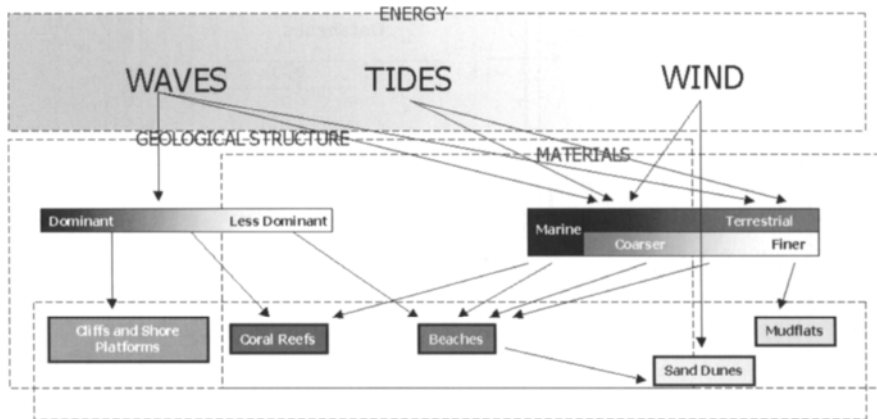
Figure 2. The coastal system (courtesy of Cambridge University Press and Jim Hansom, University of Glasgow, after Figure 1.6 in French (1997)).

dunes, and reefs, a diverse and dynamic environment. To help understand the processes active in the formation and evolution of a coastal environment, French (1997) suggests that coasts may be studied in several different ways, one of which is through a process-based classification. Hansom (1988) describes these coastal processes as part of the coastal system (Fig. 2).

Besides providing a physical description of the coastal environment and the processes operating within, the coastal system is also considered as comprising complex subsystems (Lakhan, 1989) interacting as a dynamic web of interrelationships between human activities, societal demands, natural resources, and external and human inputs that are involved in our use of the coastal landscape. Furthermore, the significance of coastal areas to our livelihood and survival over time means that coastlines around the world are increasingly coming under more pressure. Our growing attraction to the coast for tourism, recreation and leisure activities, and the resultant pressures being placed upon this unique environment are further complicated by global warming and sea level rise.

Understanding the coastal system is difficult, as the interface between the marine, terrestrial, atmospheric and human environments is both complex and dynamic over space and time. The coexistence of natural systems and human activities in marine, coastal, and estuarine environments inevitably brings conflicts of interest requiring ways to alleviate problems that arise (wldelft.nl/cons/area/cos/inex.html). In order to understand the complexity of the coastal environment and the processes operating there, multidisciplinary research studies of the coast, especially GIS, need to be carried out and links made to the management community charged with stewardship of the coastal environment.

3. WHAT DOES GEOGRAPHY BRING TO THE STUDY OF THE COASTAL SYSTEM?

In order to provide a contextual setting for the potential role of GIS in coastal studies in general and modeling, it is also important to consider at the outset why geography is important to the study of the coastal system and coastal zone management. Geography is about processes over space and

through time and is both an integratory discipline and a spatial science. The coastal zone comprises an environment of objects, features and processes that interact and occur across space and through time. It is a spatial environment, and geography is a spatial discipline. Coastal management by definition is spatial management (Fedra and Feoli, 1998). Geography, therefore, adds a new and very important dimension to studies of the coastal zone. Golledge (2002, pp. 6–10) observes the following:

(1) In short, geographic thinking and reasoning has provided a basis for understanding-or reasoning out-why there are spatial effects, not just finding what they are! Further, it enables us to reveal patterns in spatial distributions and spatial behaviors that may not be obvious to a casual observer in the real world.

(2) Geographic knowledge is useful for two fundamental reasons: (i) to establish where things are, (ii) to remember where things are and to help us in the process of making decisions and solving problems.

(3) Other aspects consist of making us aware of the spatial relations among things, the regional or categorical classes to which things belong, the extent to which things interact, and the extent to which things are co-related in terms of their spatial occurrence and distribution.

To date, geographers have been involved in a very wide range of different studies of the coastal and marine environment. Psuty et al. (2002) note that much work has been carried out on coastal geomorphology including: the mechanics of sediment interaction, coastal sand dunes, barrier beach systems, nearshore and offshore, coastal change, bays and estuaries, coastal erosion, coastal dynamics, shoreline change, as well as human and environmental aspects of industrial location and settlement, plant and wildlife habitat. What differentiates a geographer's work from other disciplines concerned with the coastal and marine environment is the emphasis upon spatial location.

Effective modeling of the coastal system has been found to require both a mathematical component and increasingly a geographical component. The geographical component places processes in a wider environmental context. At present many mathematical process models often cannot incorporate locational constraints operating at the different spatial and temporal scales (Livingstone and Kidd, 1999).

4. WHAT DO THE GEOSPATIAL TECHNOLOGIES BRING TO COASTAL STUDIES?

Geographers have always been involved in the collection of data, the processing of the data into information, and modeling and simulation work. However, rapid developments in IT have had a major impact upon the range and power of the tools available to the geographer, as well as the ease and efficiency with which it is now possible to handle, analyze and display a wide range of spatial data.

Increasingly, geographical research has focused on the gathering of environmental data at many different resolutions, spatial and temporal scales, and the use of new data collection, processing, analysis, simulation and display tools such as remote sensing, GIS, modeling software, Global Positioning Systems (GPS), digital mapping, and visualization. The availability of IT has provided the geographer with a powerful suite of data processing and integration tools to facilitate geospatial analysis and new opportunities to derive insight into environmental processes at a variety of different scales and resolutions. Significant advantages of geospatial technologies are: high resolution, spatial and temporal data collection, spatial data input, storage, management, processing and visualization tools, integration, and networking and communication.

4.1. Environmental Data Sources: Remote Sensing

Data and information underpins nearly everything we do. Over time our ability to collect environmental data has grown exponentially. There are many data sources available now, and increasingly these are becoming available over the Internet. A comprehensive overview of geographical

data sources for environmental modeling and assessment is provided by Reed et al. (2002). One of these sources is remotely sensed data. Remote sensing is a unique source of environmental data and includes aerial photography, airborne and satellite imagery. We have the capability to both acquire and process very large volumes of environmental data from many different remote sensors with different spectral, spatial, and temporal resolutions for monitoring and mapping purposes (for example, Landsat, Coastal Zone Color Scanner (CZCS), Advanced Very High Resolution Radiometer (AVHRR), SeaWiFs). There are now opportunities for real-time satellite data acquisition as well. A detailed examination of the many different sources of environmental data from remote sensing for environmental modeling is given in van der Meer et al. (2002).

To date the data and imagery acquired have been used very successfully for numerous different applications to the coastal and marine environment including water quality studies, bathymetric mapping, modeling shoreline protection and retreat, coastal flooding, sea bed mapping, sediment movement, ocean feature (currents and waves) detection, ecosystem monitoring, inter-tidal morphology and sedimentation studies, and coastal change among many others (see Abdullah et al., 2000; Narongrit and Tokunaga, 2001). Remotely sensed data is also useful for resource identification, developing exploitation strategies, environmental management, coastal services and surveillance, as well the monitoring of short-term and long-term changes in the coast (UNESCO, 2002). Notable among the current generation of sensors that provide information about the coastal zone are RADARSAT (Radarsat International, 1999), CASI (Compact Airborne Spectrographic Imager), and LiDAR (Light Detection and Ranging). Earth Observation Sensors (EOS), in particular, potentially facilitate regular operational monitoring and mapping of coastal environments, and are becoming a crucial component of coastal management as a result of frequent data acquisition, rapid processing, and availability of a wide range of imaging options. LiDAR, for example, is providing new opportunities for vertically accurate (15 cm and better) shoreline surveys (for example, the rapid production of detailed Digital Elevation Models (DEMs)), and mapping to help in the identification of the impact of severe storms, the success of erosion control using groins and jetties, and the effectiveness of beach nourishment projects, coastal erosion and accretion, and human land use intervention (Geodan, 1999; Eiser et al., 2000). Coastal topography, derived from LiDAR data, is available from the NOAA/USGS coastal mapping program (www.csc.noaa.gov/crs/tcm/about_ldart.html) for use in GIS with the aid of simple tools (for example, for ArcView there is an extension: LiDAR Data Handler).

In many cases remote sensing provides a cost-effective tool to obtain data that cannot be acquired in any other way. Today, EOS have become a crucial component for coastal mapping and management. They are also an important potential data source for coastal models and GIS. However, until relatively recently the lack of long-term data, poor resolution of the data acquired (both spatial and temporal), together with problems associated with extracting information from the data and acquiring data that is suitable for models has not helped to fully realize the potential of remotely sensed data in this context. Higher resolution data will, however, help to overcome such drawbacks and there is now the potential for large spatial coverage with high resolution. Also, as noted by Southgate et al. (2000), for example, there are now opportunities to measure nearshore bathymetry using LiDAR and using new photogrammetric systems.

However, the use of remote sensing is still largely the domain of the expert users based in research establishments using complex and expensive hardware and software. New approaches to information extraction will link process-models to the extraction process (for example, coastal erosion models to shoreline detection), thereby helping to improve the speed with which it is possible to extract accurate shorelines from remotely sensed data (Marghany, 2000). Similar uses for coastal models are described by De Valk and Wensink (2002) relating to the use of SAR imagery for sea bed mapping.

4.2. Geographical Information Systems (GIS)

Reference to Bartlett (1994) reveals that the application of GIS to coastal studies is not new. Over the years many different geospatial technologies have been successfully used to aid in coastal research and coastal zone management. With the rapid development of information technology, the number of applications and their scope has grown very rapidly. As Fabbri (1998, p. 54) observes:

> "Given the complexities of coastal systems and the multidisciplinarity required for sustainable coastal development, computerized systems are necessary for the integration and distribution of vast amounts of data and expert knowledge. They are also vital for performing analyses to aid decision makers in their difficult task of providing optimal and comprehensive coastal management solutions."

Coastal studies involving the use of GIS typically cite their value for: storing and managing data input and results; preprocessing of input data including editing, transformation, interpolation, and the derivation of parameters; spatial analyses; visualization; and a computational environment with tools for animation and simulation. An additional benefit of GIS lies with the tools that are available for analyzing and modeling the interrelationships between individual layers of data; for example, map algebra, overlays, animations, regression analyses, and models. GIS are also considered to be tools for the integration of both data and information from multiple disparate sources. Multimedia GIS, for example, enable text, graphics, images, maps, and video to be overlain or geolinked. Increasingly, there is an opportunity to examine multi-dimensional and multi-temporal data sets and it is now possible to incorporate remote sensing, video imagery, tabular data (for example, the results of oceanographic surveys), satellite imagery and seafloor mapping in a single data handling and processing environment. GIS also provide a means by which it is possible to utilize and display topographic and statistical surfaces, (i.e., DEMs). Furthermore, morphodynamic models can be seen as part of, or interfacing with, software such as GIS, site-specific databases or decision support tools (Southgate et al., 2000).

Another very significant use of GIS software is for visualization purposes. This may be very simple (i.e., for data exploration, or for plotting a graph or map), or complex (i.e., for using three or more dimensions, or draping information over a surface). While there are already many software packages for visualizing geospatial data and information available, often with a very specific application (i.e., mapping or surface generation), GIS provides the end-user with a more 'bundled approach' that is directly linked with the data handling functionality of the tools, minimizing the need for import and export routines. It is the powerful all-round data-handling capabilities of GIS that distinguish it from other geospatial software packages.

One benefit in the context of modeling applications, is the possibility to take advantage of the high quality graphics and animation capabilities included with GIS. Advanced visual analysis of data is facilitated through the provision of interactive manipulation of the visual environment parameters such as the viewing position, z-scale, cutting planes, light position, brightness, color and animation tools. Different representations of data can be examined in multiple viewports, and data can be 'visually mined'. Another advantage lies with helping people to understand the output from spatial analyses and models, which may include complex spatial relationships, patterns, and distributions, as well as to facilitate communication with a wider audience (Jung, 1996). Most commercial GIS software now comprises very sophisticated and easy to use visualization tools. However, care must be taken when using these tools in practice. For example, only certain visualization techniques are appropriate for some data. Knowledge, understanding and careful choice of the correct visualization option is usually important. There is currently a need to provide the end-user with some guidance for the use of visualization tools, in the form of tutorials and even expert systems, to ensure that the end-user chooses and uses the most appropriate technique to represent the data for analysis and interpretation. At present there is all too little guidance to assist the end-user community, many of

whom have very little or no experience in the visual representation of data, either in the form of a map or a graphic. Guidance that does exist is often deemed inadequate (Jung, 1996), providing little in the way of helpful explanations, or offering display alternatives. To this end more advanced, albeit experimental rather than operational, solutions have been devised (for example, VIZARD by Jung, 1996).

A GIS is also much more than simply a vector or raster data-handling and processing toolbox, or mapping software package. Today, GIS, together with modeling and visualization software, and the Internet provide the basis for the development of a range of online mapping tools, web-based portals to data and image catalogues, and DSS designed to provide access to spatial data and information for wider use. For example, proven GIS capabilities such as inventory, storage, digital display, correction and overlays can be used to contribute more effectively to coastal decision-making if supplemented with information about coastal data structures, analytical routines, and decision-making interfaces into DSS (Terfai and Schrimpf, 1997). Coastal management, for example, is about answering 'what if' questions and making 'informed decisions' based on the data and information available. In this context, GIS provides a unique interactive work environment that offers the end-user an interactive or intelligent map or graphic that can be interrogated and mined. Increasingly also, the GIS software can be tailored to provide the basis for developing an information service to the public. This can be used to convey information, or to help link the scientific research community to the layman to explain the meaning of research. GIS has also been shown to provide a unique stimulus for the work environment, encouraging greater interaction with spatial data, by presenting the end-user with a simple interface to data and information, and new ways to investigate and study environmental data sets. While this may be considered to be simply an extension of the paper map into an electronic environment, GIS provides an integrative framework and toolbox that allows the end-user to examine data in a simple or complex way, offering a wide range of tools from the user menus, as well as providing the means to customize the examination process in ways specific to the task in hand. This provides a toolbox with a scientific basis but also with the means to communicate results to a wider audience (i.e., the layman) where the tool reflects the science while also being comprehensible as it may affect the day-to-day decisions of the end-users. There is a growing desire now to be able to inform the wider end-user community, including businessmen, policy-makers and non-scientists of the results of scientific research (i.e, scenarios generated by models). The Internet is providing some of the opportunities needed to network the end-user community, to facilitate communication, and provide access to data and information.

But there are also a number of key weaknesses in many of the GIS. Firstly, there is a lack of many analytical tools already widely available in specialized geostatistical software packages (Variowin, GSLIB, Geopack, ISATIS), and mathematical software (MatLab, Maple 8) that are not yet part of GIS. This is gradually changing, however, with the announcement of products such as ArcGIS Geostatistical Analyst by Environmental Research Systems Institute (ESRI), and add-on modules or extensions to ArcView. Also, at present most GIS do not handle time or temporal data very well beyond simply allowing the end-user to compare data sets from different dates, and to undertake simple change detection via differencing methods. Various different solutions have been advanced to try and accommodate the temporal dimension into GIS via the development of new methods (Mitasova et al., 1995; Mitasova, 2000) or specialized software such as the Spatio-Temporal Mapper software (STEMgis), recently developed by Kevin Morris of Discovery Software (www.discoverysoftware.co.uk, personal communication, 2003). The integration of dynamic models within a static GIS also provides a temporal capability.

Nevertheless, despite the current limitations of GIS, they do provide a means to pursue the data into an information pathway and a suite of valuable tools that can be used in coastal modeling studies.

5. INTEGRATION, GIS AND COASTAL MODELING

The capability to integrate multiple disparate data sources, providing an ideal basis for studying complex environmental problems is the reason most often cited in support of utilizing the functionality of a GIS in the context of coastal modeling applications. The term 'integration' can also be extended to include the possibilities that exist for integrating process models within a GIS environment to take advantage of the spatial data handling, mapping, and visualization capabilities. Taking advantage of the spatial analytical tools has increasingly been recognized by many researchers who have advocated integration of models with GIS. For example, Pullar and Springer (2000) observe that the integration of models into a desktop GIS provides a better interface and visualization capability in a user-friendly environment. It also assists in validating model data input and model calibration.

There are now a number of examples in the literature that demonstrate the combination of GIS and coastal modeling tools. However, despite this, it is notable that in a recent publication on environmental modeling and GIS by Skidmore (2002) there are no chapters dealing with coastal applications. An earlier, more specialized coastal GIS applications text by Wright and Bartlett (2000) does, however, include some examples where successful links between GIS and models have been developed. Despite this, Wright and Bartlett (2000) note that, in contrast to many of the techniques used, work involved in coupling coastal models to GIS is still poorly investigated or understood, and as a result the benefits arising from integration have rarely been seen. Furthermore, Yoon (1996), notes that most early attempts to develop such links were not successful. Today, modeling is supported by most commercially available software, especially those with raster subsystems (for example, Idrisi, Clark Labs, 2002). However, full integration of complex models in a GIS generally requires extensions to the standard GIS functionality such as support for temporal, three-dimensional and four-dimensional data, and meshes for finite element methods.

A number of different approaches toward the integration of GIS with models have been pursued. These include: providing an interface between the GIS software and the model; programming the model within the GIS; and developing custom GIS-based modules that interface directly with models, thereby helping the end-user to transfer model results and output quickly and easily from the manipulation to the visualization stage without the need for import and export options.

There are three main model/GIS integration architectures described in the literature. These are defined as low, medium or high level integration. In low level integration, the two components (model and GIS) are linked together through data transfer between the two independent systems. Medium level integration involves an embedded two component architecture that allows a master component to utilize the capabilities of an agent component. The GIS can be either the master or the agent component, depending on the required output and capabilities of the model being used; for example, when a GIS calls the model or the model calls the GIS. In high level integration, the two elements are tightly combined, sharing components such as a database management system and output system (Grover, 2002).

The terms low, medium and high level integration, are more usually described as loose-coupled, tight-coupled, and embedded-coupling (Pullar and Springer, 2000; Huang and Jiang, 2002). Coupling methodologies for environmental models are discussed at some length by Brandmeyer and Karimi (2000), and five types are considered: **one-way data transfer**; **loose coupling**; **shared coupling; joined coupling** and **tool coupling**. The type signifies the extent to which the model and GIS software are integrated. The loose-coupled models are where the GIS is used to retrieve and preprocess data into the form required by the model structure, data being written to files, and subsequently used as inputs to the model program (which may even reside on another computer system). The model computes the results and returns the files of data for display or visualization to the GIS software. For the end-user of this combination, the advantages are that there is little knowledge of programming required, operation is quick, and the models are highly portable. However, while this

option may initially seem fairly simple, a great deal of work is usually involved in altering the data formats and structure, a process that is very time consuming if the model requires to be run on different occasions. Furthermore, as noted by Huang and Jiang (2002), the exchange of data files (often ASCII text) is usually not user-friendly and is cumbersome. A tightly-coupled model involves full integration of the GIS and model. Usually the model is developed outside the GIS, with its own data structures and exchange mechanisms for data. As noted by Huang and Jiang (2002) the models are usually developed in Dynamic Link Libraries (DLLs) using FORTRAN or C/C++ and linked to a GIS macro-language. Interaction between the model and the GIS is hidden from the end-user. Data is usually exported from the GIS to the model, with the results being returned to the former for display or visualization. One benefit is that access to the spatial database is direct (Huang and Jiang, 2002). Despite the apparently closer integration, however, disadvantages include the significant investment required in programming and data management, and the portability limitations, as well as difficulties in linking the GIS macro-languages and the DLLs, and the need for a transparent interface to the GIS data structures (Huang and Jiang, 2002). Full integration, known as embedded-coupling, means that the model is written using the analytical engine of the GIS or, alternatively a simple GIS may be developed and added to the modeling system. The main reason for this use of the GIS is as the means to display results and provide interactive control for the user. The advantages are that you do not have to transform the data to other formats, data structures do not have to be matched, and end-users can make 'on-the-fly' changes. The primary disadvantage of internalizing a model program within the GIS environment is that it usually requires the programming of the existing model which may be cost prohibitive.

All three of these approaches to modeling have been successfully used. In reality, despite the attraction of developing the model within the GIS environment, the costs in terms of time and effort involved may be disproportionate since significant effort would have to be extended to duplicate the existing coastal model, (perhaps developed over many years at some considerable cost) within the GIS. Furthermore, an extensive knowledge of the GIS environment would be required to achieve this goal. In practice, however, as noted by Goodchild (quoted in Macmillan, 1997, p. 23), more often than not the environmental modeler who wishes to take advantage of GIS functionality will likely write their model code in a programming language such as FORTRAN or C++, providing a link to the GIS software to be used for processing and analyzing the data and displaying the model results. This type of link between GIS and models probably characterizes the majority of efforts in environmental simulation modeling. A good example of this is the work carried out by Gilman (2002) which involved linking a coastal wave model to the GIS software ArcView via the development of a user-friendly interface. Such an approach is usually considered to be the most logical one, taking advantage of an already well-developed individual model and GIS software components without the need to re-write and test software, as well as wasting time reinventing the wheel. A rule is that if good models already exist, then either loose or tight coupling is the best approach (Huang and Jiang, 2002). Direct linkages between GIS and models generally facilitate better data storage, manipulation and analysis than conventional methods. Opening of data formats and incorporation of customization and application development tools stimulate coupling of commercial GIS and modeling. Use of object-oriented (OO) technology facilitates more efficient GIS implementation and merges the different levels of coupling.

Another approach, developed by Yates and Bishop (1997) sets out to develop a means for integrating existing GIS and modeling systems that have typically been developed in isolation, with their own specifications, interfaces, data models and data types. Using the implementation of the application and database layers of the OGIS (Open GIS Consortium: www.opengis.org) guide they explore the key issues such as importance of data access, interoperability[1], integration, process management, user-interface design, and security to develop 'wrappers' that allow the software to control the systems being integrated as well as to communicate with external processes.

While interfacing existing software products seems to be the approach most often favored when considering linking long-standing and well-established coastal process models with GIS, simpler models, those that often form the basis of commercial modeling software products, seem to rely on a different approach, one that develops new GIS software components or modules for the process models. For example, products developed by Applied Science Associates (ASA) in the United States make use of a specialized GIS module designed specifically to interface with the coastal process models, with the intention of facilitating mapping and visualization of model outputs. The primary reasons cited to support this approach are to take advantage of GIS functionality and also to minimize the need for the end-user to seek software to visualize the model outputs. Similar examples have been developed by the Danish Hydraulic Institute (DHI) to provide successful linkages between coastal models and GIS functionality for example, MIKE 21 (www.dhisoftware.com/mike21/) and MIKE INFO COAST (www.dhisoftware.com/mikeinfo/index.htm).

6. THE IMPACT OF INFORMATION TECHNOLOGY ON GEOGRAPHICAL INFORMATION SYSTEMS AND MODELS

Information technology has evolved very rapidly over the last five years. The microprocessor, for example, at the heart of the modern desktop computer environment, and latterly the mobile workstation and now the personal digital assistant (PDA), has largely been responsible for providing the opportunities to both develop, as well as link, coastal modeling tools and GIS. Faster, lower cost microprocessors have led to powerful desktop computer systems, with number processing capabilities far in excess of the computer systems of only a few years earlier, as well as parallel computer systems (Pirozzi and Zicarelli, 2000). Cheaper and larger data storage capacity as well as data compression software now provide the means to handle far greater volumes of data than were possible only a few years ago. Lower cost and higher resolution computer display systems with graphics cards and on-board RAM, together with more powerful and functional visualization software have provided for significant advances in display alternatives. The use of OpenGL for developing interactive 2-D and 3-D graphics applications, as well as rendering capabilities, has also greatly enhanced the visualization possibilities. Developments in communications and networking technology have also facilitated greater access to and sharing of data and information, and in the context of the Internet, technologies such as Java, CORBA and IDL[2] have all been useful in modeling applications. Together the tools now available more closely match the characteristics of coastal and marine data, namely large volumes of multi-dimensional, multi-variable data at a variety of scales in both space and time. The significant increase in the magnitude, speed, and economics of high performance computing has also unlocked the potential for computationally intensive analyses of a geographical nature. Among the applications set to benefit from the increased capability are artificial intelligence (AI) techniques replacing conventional modeling tools in GIS (Moore et al., 1997). They describe, for example, the development of the expert system COAMES (Coastal Management Expert System) for the extraction of beach landforms from DEMs.

Growing functionality of software development tools is now also allowing the developer to do much more in terms of processing, number crunching and increasing the speed at which all this can be undertaken, as well as extending the functionality and visualization possibilities; for example, sampling, interpolation, regeneration from grids, and scope for animation sequences. Enhancements to visualization tools also provide unparalleled opportunities for studying model output, techniques that offer new insight into the data. More sophisticated visualization and 3-D graphics tools are now required to help depict the important scientific content of data. Advances in this area are very important because of the vast amounts of analyzed or model data that otherwise make it very difficult to extract and present relevant scientific information. According to Wang et al. (1999), this presents

a substantial challenge for scientific visualization applications, especially since the development of visualization tools has provided the means to communicate scientific results to a wider audience including managers and non-scientists. Such a visualization capability is an invaluable asset for the future management of the coastal and marine environment.

Another important impact of IT is that the developments in visualization technology are also changing the way science is undertaken in many areas of research. The power and flexibility of the new visualization tools is revealing a gradual shift in emphasis away from simply the communication of results to the development of a more active role in the research process for example, through visual data exploration.

Until recently, information technology available on the desktop in the everyday work environment has also limited the ease with which both models and GIS can be utilized by a wider audience. With the developments in both hardware and software, resulting in greater access to the necessary tools, it is now possible to link the scientist's world to that of the real world. Not only do researchers have more choice available to them for the display of data and choice of representation, but also greater interest from the non-scientist is being stimulated through the opportunities to interact with and utilize previously unavailable software and to access data and information.

7. MODELING

In the context of a GIS, a model may be a linear combination of themes or layers that, when combined (using map algebra), lead to the generation of a composite layer or output. The integrated GIS and digital image processing (DIP) software Erdas Imagine (www.erdas.com) includes an interactive graphic model-maker module that allows end-users to 'model' image analysis processes (for example, Intensity Hue Saturation (IHS) transform or image fusion). Alternatively, one or more mathematical equations may represent a model. In the context of the remaining discussion, the term 'model' is considered to be that defined as a simplified description of an observed relation or process.

Models may be conceptual, physical, analytical, numerical, or mathematical (CoOp, 1998). They may be described as empirical, or deterministic and stochastic process-based, rule-based, or simulation. There are different types of models: regression techniques, box-type models and process-based models (Guan et al., 2001). The modeling process generally involves calibration, validation, sensitivity analysis, error propagation and uncertainty. Models may be simple (highly aggregated) or complex describing specific processes. A single model may also comprise several different sub-models.

Models have many different roles and purposes. For example, models can be used to digest large volumes of data into more usable forms. They also help us to conceptualize, integrate, and generalize knowledge. Models allow hypotheses to be refined and sampling plans to be tested. They can play a critical role in isolating data inputs and help us to understand weaknesses in our reasoning, provide direct observations in real-time, and can also be used for interpolation to provide a more complete picture of a process. Computer simulations are considered by Mitasova and Mitas (2001) to be the 'third way' of performing research leading to analysis and understanding, testing of hypotheses and theories. Simulation models have been successfully used by the scientific community for many years, but although once the domain of the specialist modeler and programmer, are now becoming more attractive to others (i.e., coastal managers). Models are also widely used outside of the scientific domain in operational decision-making and as a management tool.

A number of technical issues associated with models still exist (Nielsen, 2000). Some examples are the quality of data, the physics and mathematical basis of models, and the experience of the model end-user. There are also problems associated with the management and presentation of the data and the model results. In the past, the development of complex process models has often been limited by the large amount of data that is often required to run a simulation, and also the lack of

computer processing power. Other difficulties have related to writing, debugging and calibrating large simulation programs. Models also generate large quantities of output. Such quantities of information can become difficult to manage, interpret, analyze, and display. Combining models, to accommodate complexity and efficiency, is also very challenging in terms of the development of easy to use and intuitive interfaces, and the use of computer languages. With commercial uses of models growing, there are also problems associated with the ability of the general public or non-technical layman to interpret the output from such models. While some of the simpler models are easy to understand and use, more complex models require much greater knowledge and understanding of the underlying fundamentals of the model. Involving the layman can also undermine confidence in the modeling process. However, many of the problems encountered in modeling are now being overcome with the increasing availability of data at a wide variety of different scales, often from remote sensing platforms, and the rapid development of computer-based hardware and software.

7.1. Coastal Models

Over the past decades, our knowledge and understanding of coastal morphodynamic behavior, over both space and time has increased considerably and has been elaborated into a wide variety of physical-numerical models. Many different coastal modeling exercises have been carried out over the years and there are many examples cited in this book and the general literature. These include studies of the hydrodynamics of the coast (Keen and Glenn, 2002), coastal vulnerability to sea level rise (Bryan et al., 2001), wave modeling (Gilman, 2002), sediment transport, landform formation, simulation of the nearshore environment (LaValle and Lakhan, 1997), beaches and shorelines (LaValle et al., 2001), tidal currents (Wu et al., 2001), seawater intrusion in coastal aquifers (Ghazali, 2001), wave-driven currents and sea bed evolution (Aelbrecht and Denot, 2000), groundwater effects on swash sediment transport and beach profile changes (Li et al., 2002), surf and swash zone mechanics (see SASME, 2001), and the transport of beach materials, among many others. Such models offer an opportunity to achieve a better understanding of coastal processes and better predictions of coastal behavior. Models have been developed at a variety of different scales from the global (marine) to the local (coastal/estuarine) scale. This modeling is built around knowledge and understanding of the physical processes active on time scales of seconds to days and on distances of meters to kilometers. Our knowledge and understanding of 'coastal geomorphology', for example, has been largely based upon both 'process-based laboratory and modeling studies', and 'conceptual models based upon empirical relationships between wave and/or sedimentary parameters and coastal morphology' (Moller, 2002). As with all models their acceptability is limited by our understanding of the processes that are active in the coastal environment, the scales at which these processes operate, and the degree to which the processes have been modeled; for example the degree of generalization and accuracy. Indeed, many of the coastal processes of interest are now considered to be well understood (Southgate et al., 2000).

While many of the early studies were purely research-based activities, aimed at developing a more comprehensive and detailed understanding of the physical processes active in the onshore, nearshore and offshore environment, there is growing interest in developing both the practical and operational application of such models in the context of coastal zone management (CZM). CZM is a response to the many pressures and adverse effects now being faced with the potential to help sustain coastal environments for future generations. Integrated Coastal Zone Management (ICZM) is an effort to achieve sustainable development of the coastal zone. Together, knowledge and understanding are essential to our use of the coastal environment serving to aid in the better implementation of coastal management policies. Such understanding comes from data collected about the coast that are subsequently turned into information, thereby contributing to our body of knowledge. As noted by Gibbs (2002) many modeling studies now focus on gaining an understanding of the environmental patterns

and processes to facilitate operational and strategic management of the coastal zone and impact assessment. According to Manuels (2002) present day coastal zone management is now intensively supported by process-based modeling and for larger scales as well.

Complex numerical models are available that can simulate a wide range of hydraulic processes, including the movement of tide and wind-driven currents in coastal regions, the propagation of waves approaching a coastline, and the movement of pollutants, objects or sediments in the water (Nielsen, 2000). There are many different examples of models for the same process. Each one is differentiated by its origin and development over time, the physics and mathematical equations used, scale (local or regional), assumptions, simplicity/complexity, data sources and input required, output generated, constraints and computational efficiency, support, and availability (code, cost). They may also differ on the basis of the governing equations, the model structure, numerical methods and physical parameterizations used.

Apart from models developed by academic researchers, there are many examples of the use of coastal models by research institutions and consulting agencies. Some are briefly mentioned below to illustrate the breadth of coastal modeling work. It is not the purpose of this overview to describe the details of each model, so the reader is, therefore, directed to the websites of each organization or company for further details.

Delft Hydraulics

The Delft3D model suite by Delft Hydraulics is designed to simulate water flow, waves, sediment transport, water quality, morphology and ecology in coastal and estuarine areas. Two different wave models are available within this suite of software. These are the second generation HISWA (HIndcast Shallow WAter Waves) wave model and the third generation SWAN model. Delft3D also has support tools for: Visualization (Delft-GPP); a Grid generator (Delft-RGFGRID); and a Bathymetry generator (Delft-QUICKIN).

- The SED module is designed to model the transport of cohesive and non-cohesive sediments.
- The MOR module integrates the effects of waves, currents, and sediment transport on the morphological development of estuaries and coasts over time.
- PHAROS is a wave model designed for investigating the penetration of shortwave or longwave energy into large complex harbor layouts and harbor basins.
- DELFT-STREAM is designed for the prediction and visualization of tidal stream patterns and can be used for tidal port, harbor, estuary, coastal sea and sea strait environments.
- The FLOW module of Delft3D is a multi-dimensional (2-D or 3-D) hydrodynamic (and transport) simulation program. A user-interface for the SWAN wave model (see below) is also integrated into the Delft3D-WAVE module.

DELFT-WAVE is a suite of wave models for the simulation of wave climate, generation and propagation in coastal regions, wave penetration in harbors, and wave interaction with coastal structures. It consists of the modules:

- TRITON, a Boussinesq-type wave model for harbors and coastal regions;
- HYPAN (Hydrodynamic Panel-Method Wave Model) in which water motion due to waves is described by a potential flow; and
- SKYLLA a wave model that simulates wave motion on coastal structures such as dikes and breakwaters.

In addition, there are two tidal analysis models. GETIJSYS is a general purpose tidal analysis and prediction package, and TRIAMA is an online tidal analysis program.

The UNIBEST package consists of the following three modules:

- UNIBEST-LT ("Uniform Beach Sediment Transport—Longshore Transport"),
- UNIBEST-CL ("Uniform Beach Sediment Transport—Coastal Dynamics"), and

- UNIBEST-TC ("Uniform Beach Sediment Transport—Transport Cross-Shore"), a powerful sediment balance modeling tool to model longshore sediment transport and the morphodynamics of coastlines.

SWAN (see Chapter 5 for details) is a third generation wave model used for the simulation of wave generation, propagation and dissipation in coastal areas especially in the nearshore area and for use as a wave hindcast model in intermediate and shallow depth water. The SWAN model can be readily nested within other models (i.e., WAM). It generates a wide variety of numerical output, including geographical plots. SEDMOC (SEDiment Transport MOdelling in Coastal Environments) is a joint-European approach to basic research and development applicable in a variety of coastal environments, including wave- or current-dominated, offshore or nearshore areas.

Delft University of Technology

The WAVEWATCH series of models originated with version I at the Delft University of Technology and was subsequently developed into WAVEWATCH II at the NASA Goddard Space Flight Center and later WAVEWATCH III by NOAA (see below).

National Ocean and Atmospheric Administration (NOAA)

WAVEWATCH III is a third generation wave model aimed at oceanic applications but using different formulations and numerical techniques to WAM. WAM is also a third generation ocean wave forecasting model for deep and shallow water developed at the Max-Planck-Institut für Meteorologie in Hamburg, Germany (see WAMDI Group, 1988).

Coastal and Hydraulics Laboratory, US Army Engineer Research and Development Center

The following models are part of a commercial coastal engineering software product entitled the Coastal Engineering Design and Analysis System (CEDAS) (chl.wes. army.mil/). ACES (Automated Coastal Engineering System) is an environment for coastal engineering design and analysis technologies in the areas of: Wave Prediction, Wave Theory, Wave Transformation, Structural Design, Wave Runup, Transmission, and Overtopping, Littoral Processes, Inlet Processes and Harbor Design. The Inlet Processes Module comprises:
- SBAS (Sediment Budget Analysis System);
- NMLong-CW (Numerical Model for Simulating Longshore Current Wave Interaction), and
- DYNLET (DYNamic Behavior of Tidal Flow at InLETs) a powerful 1-D hydrodynamic model for riverine, estuarine, or coastal problems.
  The Beach Processes Module comprises:
- SBEACH (Storm-induced BEAch CHange Model);
- BMAP (Beach Morphology Analysis Package);
- NEMOS (Nearshore Evolution Modeling System) and includes GENESIS (GENEralized Model for SImulating Shoreline Change) a beach evolution model,
- RCPWAVE (Regional Coastal Processes Monochromatic WAVE Model), and
- STWAVE (STeady State Irregular WAVE Model).

Danish Hydraulic Institute (DHI)

The Coastal and Inland Waters section of DHI has developed a number of coastal models including MIKE 21 that consists of modules covering: coastal hydrodynamics, environmental hydraulics, sediment processes and wave processes. It can be used to study a wide range of phenomena related to coastal hydraulics including: tidal exchange and currents, storm surge, heat and salt recirculation, water quality, wave disturbance, seiche, breakwater alignment, sediment erosion, transport and deposition. A number of wave models are included: the Offshore Spectral Wave Module (OSW), and the Boussinesq Wave Module (BW).

The Elliptic Mild-Slope Module (EMS) may be used to calculate wave fields in smaller coastal areas where diffraction and wave breaking are important. The Parabolic Mild-Slope Module (PMS) is a simplified version of the EMS model. MIKE 3 is a 3-D Modeling System for Estuaries, Coasts and Oceans. LITPACK is a Sediment Transport and Littoral Processes model. It comprises:

- STP the deterministic sediment transport model,
- LITDRIFT the littoral sediment module,
- LITLINE the coastline evolution model,
- LITTREN the non-equilibrium trench sedimentation model, and
- LITPROF the profile evolution model.

LITPACK is also fully compatible with MIKE 21.

HR Wallingford

HR Wallingford developed a number of products (either alone or in collaboration with other institutes) for wave and beach processes, and sediment transport. These include:

- TELEMAC (developed in close partnership with Electricite de France - Laboratoire National d'Hydraulique), which allows for the simulation of currents, sediment transport, wave and water quality patterns and comprises modules on:
  - Hydrodynamics;
  - Water quality;
  - Sediment transport;
  - Dispersion of pollutants;
  - Wave dynamics, and
  - Pre and post-processing.

  It includes the Seaworks (1–6) modules that deal with wind and wave prediction, wave transformation, wave disturbance, wave energy dissipation, long-term shoreline changes, and sediment transport in the surf zone.
- TOMAWAC is a prediction model for Offshore and Nearshore Storm Waves but uses different numerical techniques to the other wave models.
- SandCalc is designed to calculate sediment transport dynamics and includes solutions for currents, waves and waves-with-currents acting on mud, sand and shingle and may be applied to the coastal zone and offshore.
- FloodWorks is for real-time flood forecasting and warning. It combines data assembly, validation and management, advanced hydrological and hydrodynamic simulation engines, geographical analysis and a relational database within a single environment.

HR Wallingford has also been involved in a project known as CAMELOT (Coastal Area Modeling for Engineering in the Long Term) (Southgate et al., 2000) for the development and testing of numerical models for long-term morphodynamic predictions. The project is also linked to other projects such as SASME (Surf and Swash Zone Mechanics, see SASME, 2001), COAST3D and PACE, as well as BEACHPLAN (planshape) designed for both research and commercial use.

Alkyon Hydraulic Consultancy & Research

In conjunction with Delft Hydraulics and others, the Alkyon consultancy developed a number of wave models. These include HYDROBASE with tools for statistical analysis, data presentation and simple models for various wave generation and propagation effects, DIFFRAC2DH a two-dimensional model for the wave penetration of harbors including diffraction and partial reflection, and PONTOS an integrated model for shoreline management.
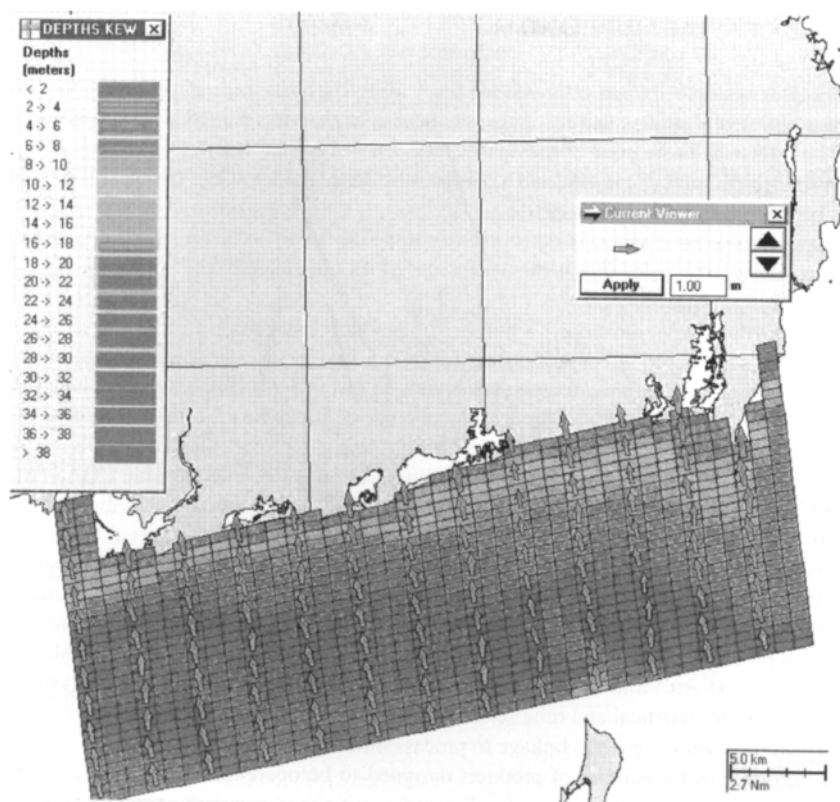
Figure 3. A screenshot from WAVEMAP (courtesy of ASA Limited).

Applied Science Associates (ASA)

By contrast to some of the more research-based models mentioned above, ASA have developed a range of commercially oriented models. These include: Hydromap—a globally re-locatable hydrodynamic model; and WQMAP (Water Quality Mapping and Analysis Package)—a set of hydrodynamic and water quality models integrated with a geographical information and environmental data system through a graphical user interface. WQMAP includes:

- BFGRID: Boundary Fitted Coordinate Grid Generation,
- BFHYDRO: Boundary Fitted Hydrodynamic Model,
- BFMASS: Boundary Fitted Pollutant Transport Model, and
- BFWASP: Boundary Fitted Eutrophication Model.

WAVEMAP (Fig. 3) is a wave-modeling software package integrated with a Geographical Information System (GIS).

EIA Limited

EIA Ltd. has produced a model system comprising a 3-D hydrodynamic and water quality model including a coupled ecological and wave erosion model with a spatially varying grid size and nested model for local accuracy. The EIA model base for coastal modeling consists of closely integrated 3-D flow and 3-D water quality models, data visualization and analysis.

8. GIS AND COASTAL MODELING

A number of examples of coastal modeling work using GIS have been described in the literature. Most are experimental studies that recognize the benefit of the links and set out to demonstrate how they can be established using one of the approaches detailed earlier. For example, Hart and Zilkoski (1994) described the linking of a GIS and a coastal subsidence model, while Gilman (2002) discusses the links between GIS and wave models.

Other applications have increasingly been based upon the use of commercially available modeling software tools that are developed specifically to utilize GIS functionality (i.e., for convenience) built-into the software package.

ASA for example, have developed a number of products in addition to those described earlier. COASTMAP is a PC-based integrated system for marine and freshwater environmental monitoring, modeling and management providing the user with an easy-to-use capability to manage environmental data and process models in a geographical context. It can be customized to reflect the data processing and modeling needs of the user, the purpose being to provide the user with software tools to perform environmental modeling and technical analyses on environmental data. COASTMAP has a mapping system and GIS built-in to it. Applications can include estuarine systems with scales of kilometers, to bays, seas and continental shelves, with scales of tens to hundreds of kilometers. The GIS that is embedded allows the user to input, store, manipulate, analyze and display geographically referenced information, as with any other GIS, and is designed to be user-friendly, interactive and fast. A suite of tools is provided within the system to import, export and manipulate environmental data and it is possible to share data with other commercial GIS applications such as MapInfo and ESRI's ArcInfo, and ArcView. COASTMAP contains a suite of functionality for analysis and display tasks, including statistical and time series analysis as well as correlation. The software has also been designed to provide a general linkage to process models.

ASR Ltd. developed a number of products designed to be operational in the workplace. These include 2DBeach, a beach circulation and sediment transport model with the capacity to predict features such as rip currents, sand bar movement, beach transformations, storm erosion and the post storm build-up of beaches. 3DD is a three-dimensional, hydrodynamic numerical model forming a major part of the hydrodynamic modeling suite providing simulations of a range of processes over time scales of minutes to weeks. It is possible to model headland eddies, microscale circulation over wave-induced ripples, and thermally stratified continental shelf circulation and freshwater plumes on open coasts. Graphic capabilities allow animated model outputs for ease of interpretation and communication for non-scientific people. 3DD can also be coupled with dispersal, sediment transport, oil spill and wave refraction and wave generation models for transfer of model-generated information between all the suite of models. An interesting inclusion is the MatLab graphical interface for the presentation of results. The wave generation model WGEN3DD (Wave GENeration coupled to 3DD) was developed for use in shorter fetches in estuaries and bays. It can be coupled to the hydrodynamic and sediment dynamic models 3DD and POL3DD (Pollution dispersal coupled to 3DD), the dispersal and sediment transport model and WGEN3DD or the wave refraction model (WBEND).

DHI's MIKE INFO Coast, a GIS based on ArcView, is designed for shoreline management applications and is a tool for the management of the morphological evolution of the coastal zone, including the impact from nourishment schemes, harbors and coastal protection works. It contains modules for all the data types used in coastal engineering, including: coastline position, coastal profiles, coastal structures, land use data, waves, currents, water levels and winds, sediment properties, photographs, aerial photographs, and maps. MIKE INFO Coast also contains input modules to interface with traditional methods of coastline surveys and digitizing modules. To extend this system with powerful modeling capabilities it can be linked directly to the LITPACK and MIKE 21 models.

In the context of extending the capabilities of commercial GIS to coastal modeling, there are an increasing number of external modules being developed for ESRI's ArcView GIS. One such example, is the Dune Hazard Assessment Tool (DHAT) developed by NOAA's Coastal Services Center and The Oregon Department of Land Conservation and Development. It uses the ESRI Spatial Analyst module and is a decision-making tool based on a foredune erosion model and traditional ground survey beach elevation data. Subsequently it has been modified to include remotely sensed LIDAR data. Model parameters included are significant wave height, wave period, mean sea level, beach slope, dune toe elevation, dune crest elevation, angle of repose, recession rate, and planning period. It can be used for making dune profiles based upon LIDAR-based DEMs, and can be used to assist coastal managers and planners to identify the relative risk from coastal erosion to oceanfront properties and developments. It is a GIS tool designed to aid in policy development and policy decisions (www.csc.noaa.gov/beachmap/html/dhav4.html).

Mack and Marcy (2002) have developed a beach morphology analysis package, BMAP together with the ArcView image analyst module, BeachTools, for shoreline and profile change analysis.

GIS and modeling can also be considered in the context of public participation systems designed to aid in planning studies. Examples make use of the powerful toolbox provided in a GIS to visualize the results as the basis for communicating information to the public. Visual images are usually considered to be a more direct medium for communicating the complex results of spatial analyses to end-users. Increasingly, images are becoming useful for landscape simulations using remotely sensed imagery draped over digital elevation models, fly-throughs or flybys where the user can fly over or through a landscape, often being able to interact and control the flight path. In other examples, the end-user is able to interact directly with a model using the graphical or visualization tools as the means to view the results of a model simulation or scenario.

Although still in its infancy the synergies between GIS and participatory three-dimensional (3-D) modeling offer the potential to increase public participation to help improve spatial data and information gathering and decision making, as well as to raise awareness about the linkage between modeling and reality (Rambaldi and Tarr, 2000). The linkage between the 3-D modeling process and its output into, for example, GIS provide the foundation to release the full potential of the modeling/GIS combination, permitting local stakeholders to interact more widely with local, national and international institutions.

9. INTERNET

Technical developments in IT have led to increased amounts of digital data and information, as well as enhanced networking and communication and data transfer between distributed locations (Purvis et al., 2001). The Internet has provided the modeling community with a number of potentially useful new resources. For example, in recent years the Internet has provided a means by which it is possible to locate and access data from numerous different sources. Data is an important input to models in order to run simulations and to undertake validation. The availability of data, and at the right scale, has been limited in the past. The reason for this is that the data is often costly to collect. Furthermore, despite there being a considerable amount of data in existence, more often than not the whereabouts and the availability of the data are not always known. The Internet has, therefore, provided an online portal to many digital data sets. For the modeling community, the most useful resource that the Internet can provide is the availability of 'signposts', usually in the form of a data catalogue. A data catalogue that lists the available data sets at the local, regional, national, and even global scale is a very useful resource that can act as a 'locator' for data sets to be used as input to models. Moreover a data catalogue that includes metadata (information about information) is potentially even more useful because it describes the data sets in their entirety: for example the date

of collection and update, sampling, scale, analysis, etc., information that is very important if the data is to be used as input to a model.

The Internet has also provided a range of tools that allow online access to data, mapping, GIS software, imagery, and digital image processing software. Use of embedded technologies like CGI, ActiveX, ASP, Java, and JavaScript provide for more efficient distributed project handling (Sellerhoff et al., 1998). More recently, this has been extended to include access to modeling software. Purvis et al. (2001), for example, describe the development of an integrated distributed spatial information modeling and analysis system using an open software environment. While most of these tools are still at a relatively early stage in their development, they are beginning to provide access to data and information as well as important tools for a much wider end-user community than ever before. For example, access to the data catalogues provides the end-user with the means to search for and locate data sets of interest and use. Metadata provides the end-user with valuable information allowing them to decide whether or not such data are suitable for an application. Increasingly more and more digital data sets are becoming available online. Downloadable data sets provide the end-user with direct access to data that may then be placed on a local computer for input to a model. Data in the form of remotely sensed imagery, for example, are increasingly available via searchable catalogues and can be downloaded from a remote machine for local processing. Specialized tools have also been developed that allow the end-user to select imagery from a catalogue and then to process it online to yield information. Online mapping tools have become an increasingly popular way for end-users on the Internet to gain access to spatial data and information in the form of maps at varying different scales. An extension to this has been the development of online GIS and DSS that permit the end-user to interact with and integrate the data with other data sets. Online GIS also provide the means for searching, locating, and displaying geospatial data in the form of maps and imagery that can be displayed as layers or themes, analyzed and interpreted.

It is now possible to undertake online modeling and simulation studies. Simple examples allow the end-user to input data and to run a model by typing in values and selecting options, displaying the results in the form of a static or animated graphic. More sophisticated examples allow the end-user to specify values for input to a model, the results of which are then displayed in a variety of different formats as a table, graphic or map. Models often require many different data sets from different sources. These can be acquired through the Internet using metadata catalogues and online databases and services (e.g. COASTWATCH—www.coastwatch.info). Lehfeldt and Piasecki (2001) describe the use of web portals for coastal studies. An integral part of IT infrastructures for coastal zone management require online operation of simulation models as prediction tools for the generation of scenarios. Embedding the handling of field data model input and results together with reports and other documents in a single unified working environment, such as a Web portal, can make working and assessment procedures more efficient. Distributed Interactive Visualization Environments (DIVE) (Chiou et al., 1999) offer the potential to integrate the interactive visualization of three-dimensional terrain models for communication permitting collaborative visualization that allows interaction between end-users and applications. In effect, the Internet becomes the computer and the World Wide Web (WWW) becomes the operating system. Furthermore, through the Internet, distributed expert knowledge from all areas of numerical modeling software utilities becomes readily available and can be used as part of an integrated approach to modeling techniques for evaluation, communication and the development of new projects. Modern communication technologies, therefore, help to bridge the gap between the model makers and the model users, something that is not easy to achieve in any other way.

There are a number of examples where the Internet brings together the geographical context with coastal modeling. The webpage Stormsurf, for example, provides online access to the Pacific Ocean NOAA Wave Models based on the WAVEWATCH III model. Online menus provide the interface for the end-user to generate surf forecasts and reports for the Atlantic, Indian, and Pacific Ocean in the form of map or graphic output for ease of interpretation and
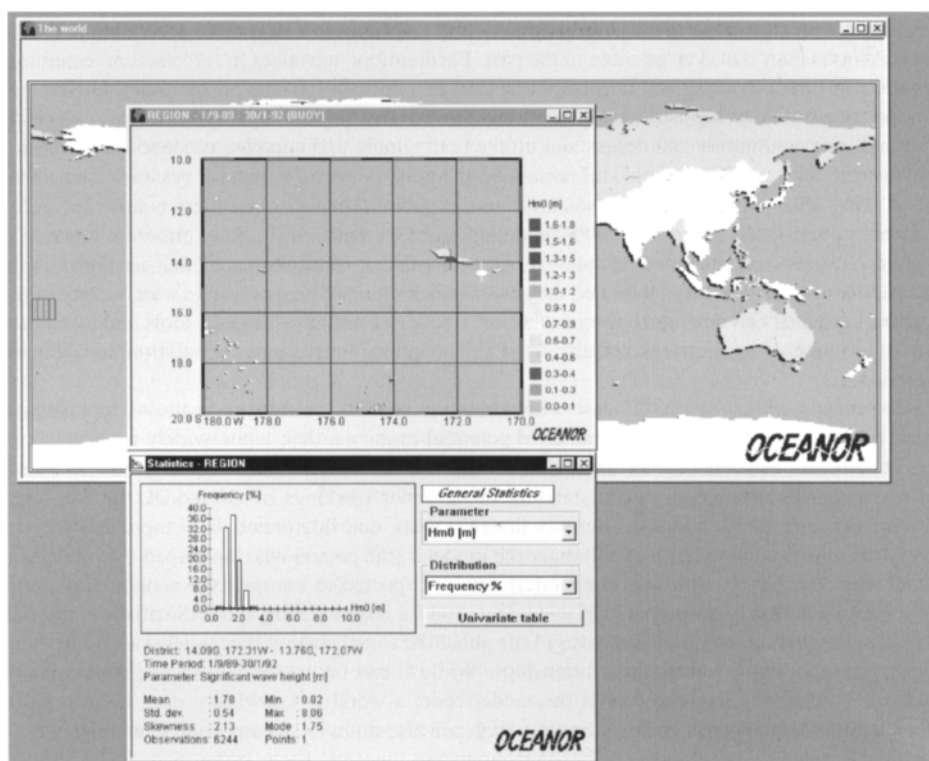
Figure 4. A screenshot from OCEANOR World Wave Atlas (WWA).

communication (www.stormsurf.com/page2/page2.html). The Oceanor World Wave Atlas (WWA) (Fig. 4) uses a global database of wind and wave climate statistics suitable for the coastal engineer (www.oceanor.no/products/software/wwa) and can be used in the context of coastal defense works, harbor design, coastal operations, coastal erosion, wave climate trends, and the calibration of wave models. WorldWaves, a new software package, designed to be a global extension of EuroWaves, will be launched soon for shallow water (coastal) wave analyses (for further details see World Wave Atlas: www.oceanor.no/wwa; EUROWAVES: www.oceanor.no/eurowaves, and World-Waves: www.oceanor.no/projects/eurowaves/index.htm). Similarly, NOAA's Center for Operational Oceanographic Products and Services Tides Online (www.co-ops.nos.noaa.gov) includes tidal prediction accuracy. Other examples are the United Kingdom Hydrographic Office's (UKHO) Easy Tide (www.ukho.gov.uk/tideprediction.cfm) and Wave Climate (www.waveclimate.com/clams/frames/location.html). Argoss (www.argoss.nl), involved in coastal mapping and marine information generation, uses global databases of observations of wind, waves, sea level and currents, with input from altimeter data acquired from Geosat, Jason-1/GFO, ERS1, ERS and Topex Poseidon satellites.

10. PROBLEMS

As scientific tools, coastal models and GIS are very well-established research and applications tools. Information technology, in the form of both hardware and software, has provided the means

by which it is now possible to develop both modeling and GIS tools into more accessible and more practical forms than was ever possible in the past. Furthermore, advances in information technology have brought both modeling and GIS from the specialist domain into the public arena. Lower costs and more powerful desktop and networked computer systems provide the platform upon which the wider end-user community can access and utilize both simple and complex models. Only the most sophisticated and complex models still remain on the most powerful computer systems. The advantage of being able to move from the scientific to the public domain is that there is now far greater awareness of the value and role of both modeling and GIS than ever before, either as separate or integrated entities, and in a practical applications environment. User-interfaces, that are both simpler and easier to use, have largely facilitated the ease with which more people from a wide variety of different backgrounds can now make use of what are frequently complex models, tools and techniques for a wide range of applications ranging from visualization, to mapping, simulation and scenario generation.

Unfortunately, access to and the ease with which the layman can now make use of sophisticated models and software also brings a number of potential problems that, while widely recognized, do necessitate solutions sooner rather than later. Ideally, the use of any model requires the end-user to have a detailed knowledge and understanding of the inner workings of the model, the data input requirements, as well as the use of the visualization tools, and interpretation of the output results. More often than not, however, it is no longer the modeler (the person who developed the model) but the end-user (the person who uses the model) who is expected to interpret the results (Kamphuis, 2000). Despite access to accompanying documentation for the modeling and GIS software, tutorials and books, the average user may know very little about the actual code of the model or the underlying science, physics, mathematics and relationships. While it can be argued that the end-user may no longer need to know very much about the model code, a working knowledge does help to aid in understanding. All too often, however, most models are also not well documented. Choice of options other than defaults will obviously affect the output but the end-user may be unaware of this. To overcome such problems, the model interfaces, error messaging, help files, and tutorials should help to minimize the opportunities to make mistakes. In other cases the model may have been developed by specialists who know little about the applications to which the model may eventually be put. Quite often models developed for one application may eventually find many other applications. Another example is when models are utilized by end-users who are not specialists in that particular field. The ease with which it is possible to utilize a model may also give the end-user a false idea about their expertise which is based solely upon their ability to operate the model.

Further problems may arise when both the end-user, and perhaps a client, are overcome by the aesthetics of the output graphics. Attractive and very clever representations of reality using color graphics, animations and imagery, may lull the end-user into a false sense of security, as well as making the results very difficult to question or dispute, leading to unquestioning acceptance of the results as being correct. For example, attractive and convincing graphics can be generated by questionable models, run by users who are not experts in their field, and based upon data with large uncertainties; what do the output graphics really mean in such a case? It is also important for end-users to understand whether the model is simple or complex. For example, there are examples of wave models that provide simple results which are markedly different from the results generated by more complex models that incorporate a more detailed understanding of the processes at work. Without an understanding of the workings of a model it may also be difficult to compare and contrast output generated by several different models. In fact, many commercial products utilize relatively simple models of reality. While there is nothing wrong in this, it is important for the end-user community to be aware of the nature of the model they are using such that they do not draw inappropriate conclusions from the results generated. Any end-user who wishes to utilize both models and GIS should also be aware of the need for a detailed knowledge and understanding of the technology, the models,

the software and the visualization tools in order to be able to utilize them correctly. Increasingly, it is very easy for any person with a limited knowledge of modeling tools, and a limited experience with interpreting the results to make use of a model and to convince others of the output. While there are many advantages to be gained from making modeling and GIS far more accessible and much easier to use, there are also significant disadvantages that require greater attention to ensure that there are additional ways to raise awareness, educate and guide the end-user community toward the correct use of such powerful tools.

The purpose of modeling software is to gain a better understanding of how a particular environment (for example, the coastal environment) will be affected by certain changes, by imitating those conditions in advance on a computer screen. Simple models are often considered to be better to work with, at least initially, because they usually involve simpler software, and work well for small and simple problems. However, the real world is rarely simple and applying a simple model to a more complex set of conditions usually leads to a decrease in the accuracy and reliability of the model results. Furthermore, simple models often depend upon steady state and linear assumptions. In extreme conditions, dynamic modeling also becomes essential and to accommodate this requires more advanced software. In reality such software is also becoming increasingly easy to use despite the advanced functionality it contains to address the most complex of modeling scenarios (Southgate et al., 2000).

11. FUTURE DEVELOPMENTS AND CONSIDERATIONS

The potential of GIS-based modeling is growing very rapidly. The driving force for this rapid evolution and availability is largely based upon computer hardware and software. More and more tools are allowing for the development of other software packages that will greatly enhance the power of the standard GIS and modeling toolbox. In the coming years there will be better examples of the integration of data, modeling, simulation and GIS software providing the basis for real-time simulations, distributed online modeling, complex systems that provide for integrated models of interacting processors, dynamic systems in three-dimensional space, and object-oriented reusable model development environments. Rapid developments in computer technology have undoubtedly provided the basis upon which all the geospatial technologies have been able to evolve in the last five years. More powerful desktop computers, faster processors, finer resolution data gathering, better and high resolution display devices, new software, and the Internet have all been responsible for enabling the researcher to build more sophisticated models. While complex models were once difficult to utilize and remained the domain only of the specialist with access to a powerful mainframe or minicomputer, this is no longer the case, and models, while still developed by specialists can be accessed by other people: the non-specialist and the practitioner. The development of user-friendly interfaces to both models and geographical information systems as well as to the Internet has provided the capability to make use of models that once required a special computer, the knowledge of programming, and a working knowledge of the underlying fundamentals. A major development has been that of visualization. Output from models in the past was often difficult to interpret, especially in the form that was comprehensible to a wider audience. Now it is possible to represent output from models in a wide variety of different ways that can, if necessary, be tailored to the end-user or audience. With developments in visualization software, as well as greater awareness of the use of graphic and visual communication techniques, together with the growing use of maps and multi-dimensional visualizations, it is now possible to communicate the results of modeling exercises, scenarios and simulations in a variety of different ways that permit the results to be more easily and more meaningfully represented. The ease with which the non-specialist can now access and run the model, change the input data, and visualize the results, all presented in a visually familiar way has also greatly enhanced the

awareness that models can play in managing the coastal environment. In so doing, a wider end-user community can now begin to appreciate the advantages and disadvantages of models in the context of planning and decision making. Furthermore, they are able to appreciate the need for high-quality data input to models.

However, there are still problem areas. As noted by Southgate et al. (2000) increasing complexity of models means that many are still scientific research tools rather than for use in routine practical studies. Furthermore, the intelligent use of models in practice requires specialized knowledge. They also note that "...We are a long way from having 'expert systems' in which (*for example*) coastal geomorphological models can be incorporated into wider management modeling suites and used by the non-specialists". In a chapter by Bregt et al. (2002), discussing the issues surrounding environmental modeling, they identify a number of problems and proposed solutions. These include problems surrounding data (for example, lack of data, implementation of remote sensing observations), modeling (i.e., scaling, validation, incorporation of dynamic models in GIS), technology, and expertise. Solutions proposed include more data observations, new models, and increased use of GIS in environmental and resource modeling, as well as improvements in remote sensing data quality, better education and more interdisciplinary work.

Bregt et al. (2002) also reflect upon the perceived problems associated with GIS-based modeling in the last decade and find that, despite considerable progress in, for example, computer hardware, many of the past issues such as GIS tools falling short of what users require are still the same issues faced today. Among these are problems associated with lack of data and data quality, gaps in spatial and temporal data, no focus on systematic data collection, and incompatibility from different data sources. In the context of modeling, many models are still considered not to be good enough to study the real world and to undertake dynamic modeling (Kamphuis, 2002). Furthermore, analysis techniques to analyze spatial time series are still limited. Such observations are also confirmed by Mitasova (personal communication, 2002) who suggests that in its present form, GIS is not yet very useful for coastal modeling except for some pre-processing of data. As seen earlier, this is one of the main uses of GIS functionality at present. The reason given for this observation is that support for floating point grids, essential for modeling, is considered unreliable and support for time series and meshes is still generally poor. Furthermore, Mitasova considers that there is still too much focus on working with maps and data represented by categories (traditional geography) rather than the multivariate fields required for modeling. As a direct result of such shortcomings, those who are developing coastal models also develop GIS functionality to directly support their models or link them with a commercial product such as ESRI's ArcView to make the data processing more efficient.

To conclude, while it is clear that considerable progress has undoubtedly been made toward integrating GIS and coastal modeling tools at one level, namely by utilizing the pre-processing, data handling, mapping and visualization functionality available, there are still a number of more fundamental areas that will now require further attention in order to help fully realize the potential of utilizing a GIS environment for coastal modeling.

ENDNOTES

1. Interoperability is defined by Brandmeyer and Karimi (2000, p. 480) who quoted Howie et al. (1996). It is defined as being the capability with which two or more programs can share and process information irrespective of their implementation language and platform.
2. Java is an object-oriented, platform independent programming language; CORBA is an industry-standard distributed object model providing the standard for clients to interact with servers and to implement remote objects to perform tasks such as accessing and updating complex databases; IDL is the Interactive Data Language used to generate graphic plots, and supports the development of custom Graphic User Interfaces (GUIs) (www.nodc.noaa.gov/col/scitech/).

REFERENCES

Abdullah, K., Din, Z.B., Mahamod, Y., Rainis, R., and MatJafri, M.Z., 2000. Remote Sensing of Total Suspended Solids in Penang Coastal Waters, Malaysia. GIS Development. 6p.

Aelbrecht, D., and Denot, T., 2000. 3D Wave-Driven Currents and Seabed Evolution Modeling Around a Groyne System. SASMW Book of Abstracts. Topic 2.2—Project 4, EDF-LNHE. 4p.

Barthel, V., and Lehfeldt, R., 2000. MorWin—An Integrated Approach to Coastal Morphodynamics. Proceedings of the 27th International Conference on Coastal Engineering, 3p.

Bartlett, D., 1994. GIS and the Coastal Zone: Past, Present and Future. London: AGI Publication, 30p.

Brandmeyer, J.E., and Karimi, H.A., 2000. Coupling methodologies for environmental models. Environmental Modelling and Software, 15: 479–488.

Bregt, A.K., Skidmore, A.K., and Nieuwenhuis, G., 2002. Environmental Modelling: Issues and Discussion. Chapter 12. In: Skidmore, A. (Editor), Environmental Modelling with GIS and Remote Sensing, pp. 252–259. London: Taylor and Francis.

Bryan, B., Harvey, N., Belperio, T., and Bourman, B., 2001. Distributed process modelling for regional assessment of coastal vulnerability to sea-level rise. Environmental Modelling and Assessment, 6: 57–65.

Chiou, P-H., Tsai, J-J., Huang, C-A., Liang, S-J., and Molkenthin, F., 1999. Development and Application of Distributed Interactive Visualization Environment: Using Tamshui River and Baltic Sea Ruegen Terrain Models as an Example. (www.bauinf.tu-cottbus.de/taiger/Publications/Taipeh12_99/TaiGerCS.html) 15p.

Chua, Thia-Eng, 1993. Essential elements of integrated coastal zone management. Ocean & Coastal Management, 21: 81–108.

Clark Labs, 2002. Idrisi 32 Software. Worcester, MA: Clark University.

Clarke, K.C., Parks, B.O., and Crane, M.P., 2002. Geographic Information Systems and Environmental Modelling. New York: Prentice Hall. 306p.

CoOP, 1998. Coastal Ocean Processes (CoOP): Wind-Driven Transport Science Plan. CoOP Report Number 6, July 1998. Technical Report, UMCES TS-170-98. University of Maryland. 23p.

De Valk, C.F., and Wensink, H.G., 2002. Measuring the bathymetry of shallow seas using radar imagery from satellite and aircraft. Offshore Technology Conference (OTC) 2002—Deep into the Future, May 6–9, 2002. Geohazards and Seafloor Imaging Session. Technical Paper 14276. Houston, TX.

Eiser, W.C., Eslinger, D. L., and Goss, H., 2000. Beach Management Decision Support Using LIDAR. EOM Archives. (www.eomonline.com/Common/Archives/August00/goss.htm)

Fabbri, K.P., 1998. A methodology for supporting decision making in integrated coastal zone management. Ocean & Coastal Management, 39: 51–62

Fedra, K., and Feoli, E., 1998, GIS technology and spatial analysis in coastal zone management. EEZ Technology. Vol. 3, pp. 65–80. UK: ICG Publishing Ltd.

French, P.W., 1997. Coastal and Estuarine Management. London: Routledge, 208p.

Geodan, 1999. Airborne Laser Scanning—Applications in Coastal Zone Management. Geo Information Solutions. Acrobat Reader PDF file, 32p.

Ghazali, A.M., 2001. Modelling of Contaminant Transport and Seawater Intrusion in Coastal Aquifers. (ewre-www.cv.ic.ac.uk/news/2001.htm)

Gibbs, M., 2002. (www.cawthron.org.nz/profiles_coastal_markg.htm)

Gilman, J., 2002. GIS-based Wave Modelling for Coastal Management. D.Phil. Thesis. London: University College, 322p.

Golledge, R.G., 2002. The nature of geographic knowledge. Annals of the Association of American Geographers, 92 (1): 1–14.

Grover, S., 2002. Perspectives of GIS modelling in hydrology. (www.gisdevelopment.net /application/nrm/water/surface/watsw0004.htm) 2p.

Guan, W.B., Wong L.A., and Xu D.F., 2001. Modeling Nitrogen and Phosphorus Cycles and Dissolved Oxygen in the Pearl River Estuary, Part I: Model Development. Part II: Model Results (ccar.ust.hk/cis/doc/31_ i.pdf) 8p. and Part II (ccar.ust.hk/cis/doc/31_ii.pdf) 11p.

Hansom, J., 1988. Coasts. Cambridge: Cambridge University Press, 96p.

Hart, D., and Zilkoski, D., 1994. Mapping a Moving Target: The Use of GIS to Support Development of a Subsidence Model in the New Orleans Region. URISA 1994 Annual Conference Proceedings. Washington, D.C.: Urban and Regional Information Systems Association, 1994, 1:555–569, or wwwsgi.ursus.maine.edu/gisweb/spatdb/urisa/ur94049.html. 12p.

Howie, C.T., Kunz, J.C., Law, K.H., 1996. Software Interoperability. Stanford, CA: Stanford University. Prepared for Rome Laboratory (www.dacs.dtic.mil/techs/interop/title.shtml).

Huang, B., and Jiang, B., 2002. AVTOP: A full integration of TOPMODEL into GIS. Environmental Modelling and Software, 17: 261–268.

Jung, V., 1996. Guiding Users in the Visualization of Geographic Data. Extended Abstracts from the 1st International Conference on GeoComputation. Leeds, UK: University of Leeds. (http://www.ashville.demon.co.uk/gc1996/abs051.htm)

Kamphuis, J.W., 2000. Coastal Modelling into the Next Millennium. Unpublished paper. 13p.

Keen, T.R., and Glenn, S.M., 2002. A Quantitative Skill Assessment of Numerical Hydrodynamic Models of Coastal Currents. www7320.nrlssc.navy.mil/html/vhr4d/Papers/ecm4/ecm4.html

Lakhan, V.C., 1989. Modeling and simulation of the coastal system. In: Lakhan, V.C., and Trenhaile, A.S. (Editors), Applications in Coastal Modeling, pp. 17–41. Amsterdam, The Netherlands: Elsevier Science Publishers.

LaValle, P.D., Lakhan, V.C, and Trenhaile, A.S., 2001. Space-time series modelling of beach and shoreline data. Environmental Modelling and Software, 16: 299–307.

LaValle, P.D., and Lakhan, V.C., 1997. Utilizing microcomputer-based models to simulate changes in the nearshore environment. Environmental Modelling and Software, 12, (1): 19–26.

Lehfeldt, R., and Piasecki, M., 2001. Web Portals for Coastal Studies. Paper presented at the 7th International Conference on Estuarine and Coastal Modeling, ASCE, November 5–7, 2001, St. Petersburg, Florida, USA.

Li, L., Barry, D.A., Pattiaratchi, C.B., and Masselink, G., 2002. BeachWin: Modelling groundwater effects on swash sediment transport and beach profile changes. Environmental Modelling and Software, 17: 313–320.

Livingstone, D., and Kidd, D., 1999. 'Top Down' Meets 'Bottom Up': A Strategic Project to Handle the Geocomputational Requirements of Environmental Modellers. GISRUK'99. 4p.

Mack, C., and Marcy, D., 2002. Application of Beach Morphology Analysis Package (BMAP) and ArcView Image Analysis (w/BeachTools) for Shoreline and Profile Change Analyses. Proceedings of Shoreline Change Conference. Session IV: Coastal Processes. NOAA Coastal Services Center. 7p. (www.csc.noaa.gov/shoreconf/session4.html).

Macmillan, W.D., 1997. Computing and the Science of Geography: The Postmodern Turn and the Geocomputational Twist. Proceedings of GeoComputation'97 and SIRC'97, pp. 15-25. New Zealand: University of Otago.

Marghany, M., 2000. Operationlisation Model of Coastal Erosion Studies by SAR Polarised Data. GIS Development, 7p. (www.gisdevelopment.net/magazine/gisdev/2000/aug/omces.shtml)

Manuels, P., 2002. Long-Term Coastal Modelling Central Dutch Coast. DHV Infrastructure and Environment. Thesis. Amersfoort, The Netherlands, 55p.

Mitasova, H.L., Mitas, L., Brown, B.M., Gerdes, D.P., and Kosinovsky, I., 1995. Modeling spatially and temporally distributed phenomena: New methods and tools for GRASS GIS. International

Journal of Geographical Information Systems: A special issue on integration of environmental modeling and GIS, 9 (4): 443–446.

Mitasova, H., 2000. Multi-Scale Characterization and Simulation of Near-Shore Environment Using Advanced GIS Technology. Detailed Proposal, 3p. (skagit.meas.ncsu.edu/~helena/publwork/coast02/finnrc.html).

Mitasova, H., and Mitas, L., 2001. Modeling physical systems. In: Parks, B., Crane, M., and Clarke, K. (Editors), Geographic Information Systems and Environmental Modeling, pp. 189–210. New York: Prentice Hall.

Moller, I., 2002. Research Home Page. (www.geog.cam.ac.uk/people/moeller/research.html).

Moore, T., Morris, K., Blackwell, G., and Gibson, S., 1997. Extraction of Beach Landforms from DEMs using a Coastal Management Expert System. Proceedings of GeoComputation'97 and SIRC'97, the Second Annual Conference of GeoComputation, pp. 15–24. New Zealand: University of Otago.

Narongrit, C., and Tokunaga, M., 2001. Fusion of Nighttime AVHRR Data and Daytime TM Data for Studying Coastal Environments. Paper presented at the 22nd Asian Conference on Remote Sensing. November 5-9, 2001. Singapore, 6p.

Nielsen, C., 2000. The Application of GIS techniques in the Analysis and Presentation of Complex Hydraulic Models. Paper Presented at AURISA 2000—the 28th Annual Conference of AURISA Hyatt Coolum Resort. Coolum, Queensland, November 20–24, 2000, 7p.

Pirozzi, M.A., and Zicarelli, M., 2000. Environmental modelling on massively parallel computers. Environmental Modelling and Software, 15: 489–496.

Psuty, N., Steinberg, P, and Wright, D., 2002. Coastal and marine geography: More than just flotsam and jetsam. In: Gaile, G.L., and Willmott, C.J. (Editors), Geography in America at the Dawn of the 21st Century. New York: Oxford University Press, 16p.

Pullar, D., and Springer, D., 2000. Towards integrating GIS and catchment models. Environmental Modelling and Software, 15: 451–459.

Purvis, M.K., Zhou, Q., Cranefield, S.J.S, Ward, R., Raykov, R., and Jessberger, D., 2001. Spatial information modelling and analysis in a distributed environment. Environmental Modelling and Software, 16: 439–445.

Radarsat International, 1999. Coastal Zone Monitoring. Application Profile, Brochure, Canada. 6p. (www.rsi.ca/resources/marine/czm_case.pdf).

Rambaldi, G., and Tarr, J., 2000. Exploring the Synergies of GIS and Participatory 3-D Modeling to Increase Local Communication Capacity. Paper presented at the 5th Seminar on GIS and Developing Countries, GISDECO 2000, IRRI, Los Baños, Philippines, 9p.

Reed, B.C., Brown, J.F., and Loveland, T.R., 2002. Geographic Data for Environmental Modelling and Assessment. Chapter 4. In: Skidmore, A. (Editor), Environmental Modelling with GIS and Remote Sensing, pp. 52–69. London: Taylor and Francis.

SASME, 2001. (www.hrwallingford.co.uk/projects/SASME/).

Sellerhoff, F., Milbradt, P., Lehfeldt, R., 1998. Model validation in web environment—Progress in distributed modeling. In: Holz, P.-P. et al. (Editors), Advances in Hydro-Science and–Engineering, Vol III, ICHE98, Cottbus/Berlin. University of Mississippi, Center for Computational Hydroscience and Engineering.

Skidmore, A. (Editor), 2002. Environmental Modelling with GIS and Remote Sensing. London: Taylor and Francis, 268p.

Southgate, H., Millard, K.T., and Soulsby, R.L., 2000. CAMELOT (Coastal Area Modelling for Engineering in the Long Term). MAFF Final Project Report (CSG 15 Form) on Commission FD1001. March 2000. 22p.

Terfai, L., and Schrimpf, W., 1997. The Use of Geographic Information Systems and Remote Sensing Imagery Data for Development of Decision Support Systems for Environmental Management.

Case Study: Coastal Zone Management. Joint Research Centre of the European Commission, Italy. (http://www.unesco.org/webworld/public_domain/tunis97/com_43/com_43.html)

UNESCO, 2002. Environment and Development in Coastal Regions and in Small Islands: Guidelines for Busy Decision Makers. (www.unesco.org/csi/wise/wise3.htm)

Van der Meer, F., Schmidt, K.S., Bakker, W., and Bijker, W., 2002. New Environmental Remote Sensing Systems. Chapter 3. In: Skidmore, A. (Editor), Environmental Modelling with GIS and Remote Sensing, pp. 27–51. London: Taylor and Francis.

WAMDI Group, 1988. The WAM model—A third generation ocean wave prediction model. Journal of Physical Oceanography, 18: 1775–1810.

Wang, H., Lau, K., and Chan, W., 1999. A PC Based Visualization System for Coastal Ocean and Atmospheric Modeling. Center for Coastal and Atmospheric Research, Hong Kong University of Science & Technology, Clear Water Bay, Kowloon, Hong Kong. Paper presented at 6th International Conference of Estuarine and Coastal Modeling, November 3–5, 1999, New Orleans, USA. Also presented at the Symposium on Coastal Ocean Resources and Environment SCORE 1999, 17–18 November 1999, Guangzhou, China. 10p.

Wright, L.D., and Bartlett, D., 2000. Marine and Coastal Geographical Information Systems. London: Taylor and Francis, 384p.

Wu, Y., Falconer, R.A., and Struve, J., 2001. Mathematical modelling of tidal currents in mangrove forests. Environmental Modelling and Software, 16: 19–29.

Yates, P., and Bishop, I., 1997. A Method for the Integration of Existing GIS and Modelling Systems. Proceedings Second Annual Conference of GeoComputation '97 and SIRC'97, pp. 191–197. New Zealand: University of Otago.

Yoon, J., 1996. Watershed-Scale Nonpoint Source Pollution Modelling and Decision Support System Based on a Model-GIS-RDBMS Linkage. AWRA Symposium on GIS and Water Resources. Ft. Lauderdale, FL, 10p.

Subject Index

This Page Intentionally Left Blank